

Special Issue Reprint

Advanced Thermoplastic Polymers and Composites

Edited by
Somen K. Bhudolia and Sunil Chandrakant Joshi

www.mdpi.com/journal/polymers

Advanced Thermoplastic Polymers and Composites

Advanced Thermoplastic Polymers and Composites

Editors

Somen K. Bhudolia

Sunil Chandrakant Joshi

MDPI • Basel • Beijing • Wuhan • Barcelona • Belgrade • Manchester • Tokyo • Cluj • Tianjin



Editors

Somen K. Bhudolia
Materials Science Lab
Halliburton
Singapore
Singapore

Sunil Chandrakant Joshi
Mechanical and Aerospace
Engineering
Nanyang Technological
University
Singapore
Singapore

Editorial Office

MDPI
St. Alban-Anlage 66
4052 Basel, Switzerland

This is a reprint of articles from the Special Issue published online in the open access journal *Polymers* (ISSN 2073-4360) (available at: www.mdpi.com/journal/polymers/special_issues/Thermoplast_Polym_Compos).

For citation purposes, cite each article independently as indicated on the article page online and as indicated below:

LastName, A.A.; LastName, B.B.; LastName, C.C. Article Title. <i>Journal Name</i> Year , Volume Number, Page Range.
--

ISBN 978-3-0365-8059-3 (Hbk)

ISBN 978-3-0365-8058-6 (PDF)

© 2023 by the authors. Articles in this book are Open Access and distributed under the Creative Commons Attribution (CC BY) license, which allows users to download, copy and build upon published articles, as long as the author and publisher are properly credited, which ensures maximum dissemination and a wider impact of our publications.

The book as a whole is distributed by MDPI under the terms and conditions of the Creative Commons license CC BY-NC-ND.

Contents

About the Editors	ix
Preface to "Advanced Thermoplastic Polymers and Composites"	xi
Rudy A. Gómez-López, Camilo E. Montilla-Buitrago, Héctor S. Villada-Castillo, Aidé Sáenz-Galindo, Felipe Avalos-Belmontes and Liliana Serna-Cock Co-Plasticization of Starch with Glycerol and Isosorbide: Effect on Retrogradation in Thermo-Plastic Cassava Starch Films Reprinted from: <i>Polymers</i> 2023 , <i>15</i> , 2104, doi:10.3390/polym15092104	1
Chih-Jen Chang, Jayashree Chandrasekar, Chia-Jung Cho, Manikandan Venkatesan, Pin-Shu Huang and Ching-Wei Yang et al. Reinforcing a Thermoplastic Starch/Poly(butylene adipate-co-terephthalate) Composite Foam with Polyethylene Glycol under Supercritical Carbon Dioxide Reprinted from: <i>Polymers</i> 2022 , <i>15</i> , 129, doi:10.3390/polym15010129	21
Haitao Lang, Xianlei Chen, Jiarong Tian, Jing Chen, Mengna Zhou and Fangfang Lu et al. Effect of Microcrystalline Cellulose on the Properties of PBAT/Thermoplastic Starch Biodegradable Film with Chain Extender Reprinted from: <i>Polymers</i> 2022 , <i>14</i> , 4517, doi:10.3390/polym14214517	35
Madara Žiganova, Remo Merijs-Meri, Jānis Zicāns, Tatjana Ivanova, Ivan Bochkov and Mārtiņš Kalniņš et al. Characterisation of Nanoclay and Spelt Husk Microfiller-Modified Polypropylene Composites Reprinted from: <i>Polymers</i> 2022 , <i>14</i> , 4332, doi:10.3390/polym14204332	49
Somen K. Bhudolia, Goram Gohel, Durga Vasudevan, Kah Fai Leong and Pierre Gerard On the Mode I and Mode II Delamination Characteristics and Surface Morphological Aspects of Composites with Carbon-Thermoplastic Hybrid Fabrics and Innovative Liquid Thermoplastic Resin Reprinted from: <i>Polymers</i> 2022 , <i>14</i> , 4155, doi:10.3390/polym14194155	69
Syed Zulfiqar Hussain Shah, Puteri S. M. Megat-Yusoff, Saravanan Karuppanan, Rizwan Saeed Choudhry and Zubair Sajid Off-Axis and On-Axis Performance of Novel Acrylic Thermoplastic (Elium®) 3D Fibre-Reinforced Composites under Flexure Load Reprinted from: <i>Polymers</i> 2022 , <i>14</i> , 2225, doi:10.3390/polym14112225	91
Mohd Nazri Ahmad, Mohamad Ridzwan Ishak, Mastura Mohammad Taha, Faizal Mustapha, Zulkiflle Leman and Debby Dyne Anak Lukista et al. Application of Taguchi Method to Optimize the Parameter of Fused Deposition Modeling (FDM) Using Oil Palm Fiber Reinforced Thermoplastic Composites Reprinted from: <i>Polymers</i> 2022 , <i>14</i> , 2140, doi:10.3390/polym14112140	109
Philip Bean, Roberto A. Lopez-Anido and Senthil Vel Integration of Material Characterization, Thermoforming Simulation, and As-Formed Structural Analysis for Thermoplastic Composites Reprinted from: <i>Polymers</i> 2022 , <i>14</i> , 1877, doi:10.3390/polym14091877	125

Anesh Manjaly Poulouse, Hamid Shaikh, Arfat Anis, Abdullah Alhamidi, Nadavala Siva Kumar and Ahmed Yagoub Elnour et al. Effect of Compatibilizer on the Persistent Luminescence of Polypropylene/Strontium Aluminate Composites Reprinted from: <i>Polymers</i> 2022 , <i>14</i> , 1711, doi:10.3390/polym14091711	151
Ozan Erartsın, Jamal Sayyed Monfared Zanjani and Ismet Baran Thermoset/Thermoplastic Interphases: The Role of Initiator Concentration in Polymer Interdiffusion Reprinted from: <i>Polymers</i> 2022 , <i>14</i> , 1493, doi:10.3390/polym14071493	161
Qinghua Song, Weiping Liu, Jiping Chen, Dacheng Zhao, Cheng Yi and Ruili Liu et al. Research on Void Dynamics during In Situ Consolidation of CF/High-Performance Thermoplastic Composite Reprinted from: <i>Polymers</i> 2022 , <i>14</i> , 1401, doi:10.3390/polym14071401	171
Somen K. Bhudolia, Goram Gohel, Durga Vasudevan, Kah Fai Leong and Pierre Gerard Behaviour of Rectangular Hollow Thin Ply Carbon Thermoset and Thermoplastic Composite Tubes Subjected to Bending Reprinted from: <i>Polymers</i> 2022 , <i>14</i> , 1386, doi:10.3390/polym14071386	187
Guan-Yan Liou, Chi-Wei Su, Po-Wei Huang, Sheng-Jye Hwang, Chao-Tsai Huang and Hsin-Shu Peng Fabrication and Property Characterization of Long-Glass-Fiber-Reinforced Polypropylene Composites Processed Using a Three-Barrel Injection Molding Machine Reprinted from: <i>Polymers</i> 2022 , <i>14</i> , 1251, doi:10.3390/polym14061251	201
Jian-Jun He, Hai-Xia Yang, Feng Zheng and Shi-Yong Yang Dielectric Properties of Fluorinated Aromatic Polyimide Films with Rigid Polymer Backbones Reprinted from: <i>Polymers</i> 2022 , <i>14</i> , 649, doi:10.3390/polym14030649	219
Zhenxue Zhang, Eleni Gkartzou, Simon Jestin, Dionisis Semitekolos, Panagiotis-Nektarios Pappas and Xiaoying Li et al. 3D Printing Processability of a Thermally Conductive Compound Based on Carbon Nanofiller-Modified Thermoplastic Polyamide 12 Reprinted from: <i>Polymers</i> 2022 , <i>14</i> , 470, doi:10.3390/polym14030470	233
Yawei Shi, Aijun Hu, Zhiyuan Wang, Kedi Li and Shiyong Yang Closed-Cell Rigid Polyimide Foams for High-Temperature Applications: The Effect of Structure on Combined Properties Reprinted from: <i>Polymers</i> 2021 , <i>13</i> , 4434, doi:10.3390/polym13244434	249
Takumitsu Kida, Takeyoshi Kimura, Ayaka Eno, Khunanya Janchai, Masayuki Yamaguchi and Yasuhiko Otsuki et al. Effect of Ultra-High-Molecular-Weight Molecular Chains on the Morphology, Crystallization, and Mechanical Properties of Polypropylene Reprinted from: <i>Polymers</i> 2021 , <i>13</i> , 4222, doi:10.3390/polym13234222	265
Somen K. Bhudolia, Pavel Perrotey, Goram Gohel, Sunil C. Joshi, Pierre Gerard and Kah Fai Leong Optimizing Bladder Resin Transfer Molding Process to Manufacture Complex, Thin-Ply Thermoplastic Tubular Composite Structures: An Experimental Case Study Reprinted from: <i>Polymers</i> 2021 , <i>13</i> , 4093, doi:10.3390/polym13234093	283

Kamil Dydek, Paulina Latko-Durałek, Agata Sulowska, Michał Kubiś, Szymon Demski and Paulina Kozera et al. Effect of Processing Temperature and the Content of Carbon Nanotubes on the Properties of Nanocomposites Based on Polyphenylene Sulfide Reprinted from: <i>Polymers</i> 2021 , <i>13</i> , 3816, doi:10.3390/polym13213816	301
Dalia Niazy, Ahmed Elsabbagh and Mostafa R. Ismail Mono–Material 4D Printing of Digital –Memory Components Reprinted from: <i>Polymers</i> 2021 , <i>13</i> , 3767, doi:10.3390/polym13213767	315
Mohd Nazri Ahmad, Mohamad Ridzwan Ishak, Mastura Mohammad Taha, Faizal Mustapha and Zulkiflle Leman Rheological and Morphological Properties of Oil Palm Fiber-Reinforced Thermoplastic Composites for Fused Deposition Modeling (FDM) Reprinted from: <i>Polymers</i> 2021 , <i>13</i> , 3739, doi:10.3390/polym13213739	329
Zhanna Kurdanova, Azamat Zhansitov, Kamila Shakhmurzova, Azamat Slonov, Artur Baykaziev and Svetlana Khashirova Synthesis and Properties of Copolyphenylene Sulphones with Cardo Fragments Reprinted from: <i>Polymers</i> 2021 , <i>13</i> , 3689, doi:10.3390/polym13213689	343
Marco Valente, Jordi Puiggalí, Luis J. del Valle, Gioconda Titolo and Matteo Sambucci Recycled Porcine Bone Powder as Filler in Thermoplastic Composite Materials Enriched with Chitosan for a Bone Scaffold Application Reprinted from: <i>Polymers</i> 2021 , <i>13</i> , 2751, doi:10.3390/polym13162751	351
Minghui Xu, Xianming Lu, Ning Liu, Qian Zhang, Hongchang Mo and Zhongxue Ge Fluoropolymer/Glycidyl Azide Polymer (GAP) Block Copolyurethane as New Energetic Binders: Synthesis, Mechanical Properties, and Thermal Performance Reprinted from: <i>Polymers</i> 2021 , <i>13</i> , 2706, doi:10.3390/polym13162706	367
Noemi Jardón-Maximino, Gregorio Cadenas-Pliego, Carlos A. Ávila-Orta, Víctor Eduardo Comparán-Padilla, Luis E. Lugo-Urbe and Marissa Pérez-Alvarez et al. Antimicrobial Property of Polypropylene Composites and Functionalized Copper Nanoparticles Reprinted from: <i>Polymers</i> 2021 , <i>13</i> , 1694, doi:10.3390/polym13111694	381
Weimin Gao, Lijing Wang, Jolanta K. Coffey, Hongren Wu and Fugen Daver Finite Element Modelling and Experimental Validation of Scratches on Textured Polymer Surfaces Reprinted from: <i>Polymers</i> 2021 , <i>13</i> , 1022, doi:10.3390/polym13071022	395
Tamer A. Sebaey, Mohamed Bouhrara and Noel O’Dowd Fibre Alignment and Void Assessment in Thermoplastic Carbon Fibre Reinforced Polymers Manufactured by Automated Tape Placement Reprinted from: <i>Polymers</i> 2021 , <i>13</i> , 473, doi:10.3390/polym13030473	413
Marco Valente, Ilaria Rossitti and Matteo Sambucci Different Production Processes for Thermoplastic Composite Materials: Sustainability versus Mechanical Properties and Processes Parameter Reprinted from: <i>Polymers</i> 2023 , <i>15</i> , 242, doi:10.3390/polym15010242	425
Katherine E. Rivadeneira-Velasco, Christian A. Utreras-Silva, Antonio Díaz-Barrios, Alicia E. Sommer-Márquez, Juan P. Tafur and Rose M. Michell Green Nanocomposites Based on Thermoplastic Starch: A Review Reprinted from: <i>Polymers</i> 2021 , <i>13</i> , 3227, doi:10.3390/polym13193227	449

Tyser Allami, Ahmed Alamiery, Mohamed H. Nassir and Amir H. Kadhum Investigating Physio-Thermo-Mechanical Properties of Polyurethane and Thermoplastics Nanocomposite in Various Applications Reprinted from: <i>Polymers</i> 2021 , <i>13</i> , 2467, doi:10.3390/polym13152467	485
Edgar Adrian Franco-Urquiza Clay-Based Polymer Nanocomposites: Essential Work of Fracture Reprinted from: <i>Polymers</i> 2021 , <i>13</i> , 2399, doi:10.3390/polym13152399	509
Yi Di Boon, Sunil Chandrakant Joshi and Somen Kumar Bhudolia Review: Filament Winding and Automated Fiber Placement with In Situ Consolidation for Fiber Reinforced Thermoplastic Polymer Composites Reprinted from: <i>Polymers</i> 2021 , <i>13</i> , 1951, doi:10.3390/polym13121951	549
Edgar Adrián Franco-Urquiza, Perla Itzel Alcántara Llanas, Victoria Rentería-Rodríguez, Raúl Samir Saleme, Rodrigo Ramírez Aguilar and Cecilia Zarate Pérez et al. Innovation in Aircraft Cabin Interior Panels. Part II: Technical Assessment on Replacing Glass Fiber with Thermoplastic Polymers and Panels Fabricated Using Vacuum Forming Process Reprinted from: <i>Polymers</i> 2021 , <i>13</i> , 3258, doi:10.3390/polym13193258	579
Edgar Adrián Franco-Urquiza, Annika Dollinger, Mauricio Torres-Arellano, Saúl Piedra, Perla Itzel Alcántara Llanas and Victoria Rentería-Rodríguez et al. Innovation in Aircraft Cabin Interior Panels Part I: Technical Assessment on Replacing the Honeycomb with Structural Foams and Evaluation of Optimal Curing of Prepreg Fiberglass Reprinted from: <i>Polymers</i> 2021 , <i>13</i> , 3207, doi:10.3390/polym13193207	595

About the Editors

Somen K. Bhudolia

Dr. Somen Kumar Bhudolia received his PhD in Composite Materials from Nanyang Technological University (NTU), Singapore, in 2017. He received his MSc in Aerospace Engineering from Nanyang Technological University (NTU), Singapore, and the Technical University of Munich, Germany (Joint Degree Programme). He is currently working as Sr. Material Scientist Non-Metallics at Halliburton Singapore. Prior to that, he worked as a Research Fellow at Nanyang Technological University for five years and, as a lead member of the composites research team, completed many R&D projects in collaboration with leading industries. He has worked on projects related to advanced composites manufacturing, material innovation, automation, and digitalization towards Industry 4.0. He is a professional member of the Institute of Materials, Minerals, and Mining, UK, and has also achieved his Chartered Scientist (C.Sci.) and Chartered Engineer (C.Eng.) registrations. He has published more than 50 journals and conference papers in high-quality journals and conferences.

His research interests are the design, fabrication, and testing of advanced composite materials, out-of-autoclave processes, thermoplastics, thin-ply NCFs, microwave curing of composites, elastomers, and non-metallic materials for energy transition.

Sunil Chandrakant Joshi

Dr. Sunil C. Joshi received his doctorate in 1999 from Monash University (Clayton), Australia, for his work on advanced composite manufacturing processes. Prior to that, he obtained an M. Tech. in aeronautical engineering from the Indian Institute of Technology (Bombay), Mumbai, and worked as a scientist at the National Aerospace Laboratories, Bangalore, India, from 1988 to 1994. After his Ph.D., Dr. Sunil joined Nanyang Technological University, Singapore, in 2000 as a faculty member in the School of Mechanical and Aerospace Engineering. His teaching encompasses aerospace materials, structures, and manufacturing. Prof. Sunil has worked on several R&D projects funded by external agencies and industries. He was the team leader responsible for designing and developing thermal controls for XSAT, Singapore's first fully designed and built microsatellite. XSAT was successfully launched in 2011 and has since completed its intended mission. Dr. Sunil has more than 200 research publications (journals, conferences, books, and patents) to his credit, and he is often invited to be a reviewer by international journals and conferences. Besides teaching and research, Dr. Sunil has held concurrent school management positions. He was the Assistant Chair (Graduate Studies) from 2014 to 2017 and the Associate Chair (Academic) from 2017 to 2020. He has chaired the School Accreditation Committee twice, in 2011 and 2016, where he worked towards preparing for the full accreditation of the B.Eng. (Aerospace Eng.) programme under the Washington Accord.

Preface to “Advanced Thermoplastic Polymers and Composites”

In the last decade, design and material innovations for manufacturing composites have reached new heights. Thermoplastic polymers and their composites have become the most in-demand materials in recent times as they provide numerous advantages over thermoset composites. Thermoplastic polymers have a high damage tolerance, high impact resistance, recyclability, formability, weldability, repairability, and cost-effectiveness compared with thermoset composites. Thermoplastic polymers and composites are widely used in automotive, aerospace, electrical and electronics, industrial, and medical applications. Thermoplastic composites are estimated to grow from USD 28.0 billion in 2019 to USD 36.0 billion by 2024. High-performance thermoplastic materials are used in conjunction with a multitude of manufacturing processes like injection moulding, thermoforming, prepreg, liquid injection processes (especially reactive thermoplastics), automated tape placement, filament winding, pultrusion, additive manufacturing, and other processes. The material limits, design, and assembly requirements, as well as the processing constraints, are significantly important for the realisation of novel product development using a manufacturing process by simultaneously optimising reliability, safety, and other performance-related issues. The current thermoplastic material systems and manufacturing techniques still have plenty of room for optimisation and advancement. This reprint presents the latest scientific and technical advances in thermoplastic materials and their composites, processing, characterisation, product development, and manufacturing process parameter optimisations.

Somen K. Bhudolia and Sunil Chandrakant Joshi

Editors

Article

Co-Plasticization of Starch with Glycerol and Isosorbide: Effect on Retrogradation in Thermo-Plastic Cassava Starch Films

Rudy A. Gómez-López ^{1,*}, Camilo E. Montilla-Buitrago ¹, Héctor S. Villada-Castillo ¹, Aidé Sáenz-Galindo ², Felipe Avalos-Belmontes ² and Liliana Serna-Cock ³

¹ Grupo de Investigación Ciencia y Tecnología de Biomoléculas de Interés Agroindustrial, (CYTBIA), Departamento de Ingeniería Agroindustrial, Facultad de Ciencias Agrarias, Universidad del Cauca, Cauca 190017, Colombia

² Facultad de Ciencias Químicas, Universidad Autónoma de Coahuila, Boulevard Venustiano Carranza y José Cárdenas Valdés, Colonia República, Saltillo 25280, México

³ Facultad de Ingeniería y Administración, Universidad Nacional de Colombia Sede Palmira, Palmira 763533, Colombia

* Correspondence: rgomezl@unal.edu.co; Tel.: +57-3104393909

Abstract: Thermoplastic starch (TPS) has emerged as an essential alternative to produce environmentally friendly packaging; however, retrogradation is a disadvantage that affects its shelf life. This study analyzed the co-plasticizing effect of isosorbide on the mechanical, thermal, physicochemical, and microstructural properties and the retrogradation of films obtained by blown film extrusion from thermoplasticized starch with mixtures of glycerol and isosorbide in different ratios (3:0, 2:1, 1:2, and 0:3, respectively). The results showed that the higher concentration of isosorbide significantly increased the tensile strength; however, it reduced the elongation. Retrogradation modeled using the Avrami equation showed that the presence of isosorbide reduced the retrogradation rate (k) and modified the recrystallization mechanism (n). The relative crystallinity in the plasticized TPS films was reduced to 89%, and the adsorption significantly decreased. Isosorbide was very important in reducing the retrogradation of TPS. The best performance was obtained with the 2:1 ratio of glycerol/isosorbide due to the synergistic effect between the plasticizers. The results would allow tuning the properties of TPS films by combining glycerol/isosorbide in different ratios, which enables the design of materials tailored to potential application requirements.

Keywords: thermoplastic starch; retrogradation; extrusion; co-plasticization; isosorbide

Citation: Gómez-López, R.A.; Montilla-Buitrago, C.E.; Villada-Castillo, H.S.; Sáenz-Galindo, A.; Avalos-Belmontes, F.; Serna-Cock, L. Co-Plasticization of Starch with Glycerol and Isosorbide: Effect on Retrogradation in Thermo-Plastic Cassava Starch Films. *Polymers* **2023**, *15*, 2104. <https://doi.org/10.3390/polym15092104>

Academic Editors: Somen K. Bhudolia and Sunil Chandrakant Joshi

Received: 20 December 2022

Revised: 24 February 2023

Accepted: 26 February 2023

Published: 28 April 2023



Copyright: © 2023 by the authors. Licensee MDPI, Basel, Switzerland. This article is an open access article distributed under the terms and conditions of the Creative Commons Attribution (CC BY) license (<https://creativecommons.org/licenses/by/4.0/>).

1. Introduction

There are considerable concerns about synthetic plastics, which have prompted research into new and more environmentally friendly polymers [1]. In recent years, the development of polymers from renewable sources such as starch has attracted the attention of researchers due to their origin, biodegradability, low cost, and ease of handling [2]. Starch in its native form is partially crystalline [3] and cannot be considered a thermoplastic polymer due to intermolecular and intramolecular hydrogen-bond interactions in the amylose and amylopectin chains [4,5]. Therefore, it cannot be processed using conventional technologies to produce plastic materials [6,7]. The incorporation of plasticizers helps to overcome this problem [8]. The primary function of plasticizers is to reduce the interaction between polymer chains, decreasing their intra- and intermolecular forces, which promotes the mobility, flexibility, elongation, and ductility of plasticized materials [9]. This is possible because plasticizers have polar groups in their structure (OH, COOH, and NH₂ groups) with the ability to form hydrogen-bond-like interactions with the –OH of the glycosidic units of the polysaccharide chains [10]. The use of polyols [11], amines [9], amides [12], carboxylic acids or salts [9], ionic liquids [13], eutectic solvents [14], amino acids [15], sugars [16], and sugar-based mixtures (fructose, glucose, sucrose, and glycerol) have been

reported [17]. Co-plasticization is a strategy in which the properties of two or more plasticizers are combined to produce a synergistic effect, minimizing their disadvantages and enhancing their benefits [18,19].

Glycerol is the most widely used plasticizer for obtaining thermoplastic starch due to its high boiling point, high solubility in starch chains, low cost, and availability [11]. However, its use has a disadvantage due to the high rate of retrogradation [8].

Several studies have investigated the mixing of plasticizers to transform thermoplastic starch [8,11,20,21]. The sorbitol–glycerol co-plasticization approach has helped to find a balance between the microstructural and thermo-mechanical properties of plasticized starch because the problems caused by the weak interaction of glycerol with the starch chains are reduced; thus, the addition of sorbitol provides a higher modulus of elasticity (E), thermal stability, and resistance to retrogradation [11]. A study has also been reported using the addition of sugars (sucrose, fructose, and glucose) as co-plasticizers with glycerol, showing that the E increased. At the same time, the glass transition temperature (T_g) decreased, and the microstructure of the films was more homogeneous. By co-plasticizing sugar–glycerol, it is possible to reduce the cohesive forces of the polymer, demonstrating efficient plasticization [21]. In another study by Mikus et al., glycerol was mixed with sorbitol, in which there was a balance between the mobility of the chains promoted by the presence of glycerol and an increase in molecular cohesion provided by sorbitol [20]. Schmitt et al. used starch with glycerol–sorbitol mixtures by extrusion and injection that produced mechanical properties intermediate between materials plasticized with a single plasticizer [8]. In addition, it was reported that urea/ethanolamine blends led to balanced mechanical properties with less variation during storage time [8].

Isosorbide is a fused bicyclic diol and one of the three isomeric forms of 1,4–3,6 dihydroxitol characterized by two OH groups and two oxygen atoms intercalated on the carbon rings [22,23]. It is a promising compound as a co-plasticizer due to its biological origin, water solubility, and low melting point (approximately 65 °C). This compound is thermally stable and can withstand the process conditions required to prepare TPS [24,25]. Some studies report the use of isosorbide as a plasticizer for starch due to the interaction of starch chains and isosorbide through hydrogen bridges, suggesting an effective plasticization and a positive effect on reducing the retrogradation of the material [22,23,26,27]. The high cost of raw materials used in the production of isosorbide (corn, wheat, potato, and sorbitol) continues to be an obstacle to the growth of the co-plasticizer market [26]. Therefore, replacing a proportion of glycerol with isosorbide may be a promising alternative to improve the properties of starch-based biodegradable materials and reduce the effects of time on thermoplastic starch retrogradation. In this sense, this work aimed to evaluate the effect of co-plasticization of starch with glycerol and isosorbide on the properties of thermoplastic cassava starch films and demonstrate their ability to reduce the retrogradation process.

2. Materials and Methods

2.1. Materials

The materials used were cassava starch with 12% water on a wet basis (provided by CODIPSA, Asunción, Paraguay), commercial grade glycerol with 99.5% purity (provided by DISAN, Cali, Colombia), and isosorbide with 98.5% purity (supplied by Haihang Industry Co. Ltd., Jinan City, China).

2.2. Sample Preparation

The starch was dried at 80 °C for 16 h until it reached a humidity of less than 2%. The dried starch was mixed with plasticizers: glycerol and isosorbide in a ratio of 70:30 (starch/plasticizer). For co-plasticization (glycerol–isosorbide), different mixtures were made in the proportions presented in Table 1. The starch with the different proportions of plasticizers was mixed for 10 min in a KITCHEN AID (Benton Harbor, MI, USA) mixer and stored in hermetically sealed PET containers for 48 h [27–29]. The obtained starch was processed in a single screw extruder (compression ratio 5:1 and L/D of 25) (HAAKE™

PolyLab™ QC, Thermo Fisher Scientific, Herzogenaurach, Germany) and adapted to a bead die and a nozzle with a 3 mm diameter orifice. The process conditions are described in Table 1. The material obtained was granulated and stored in airtight containers until further processing.

Table 1. Glycerol–isosorbide ratio as starch co-plasticizers and processing conditions.

Sample	Starch (wt. %)	Plasticizer		Temperature Profile (°C)	Speed (rpm)
		Glycerol (wt. %)	Isosorbide (wt. %)		
TPS-G	70	30	0	110–155–145–109	45
TPS-i10	70	20	10		
TPS-i20	70	10	20		
TPS-i30	70	0	30	110–160–155–109	

The pellets were extruded to obtain films by extrusion blowing with a single screw extruder coupled to a blow die. The temperature profile was 130, 157, 153, and 149 °C from the feeding zone to the die. The speed was 35 rpm. The films obtained were stored in a chamber at an average ambient temperature of 20 °C and relative humidity (RH) of 60%.

2.3. Mechanical Properties of Tension

The tests were performed according to norm ASTM D-882-10 on a universal machine (Shimadzu EZ-L, Kyoto, Japan) at a deformation speed of 25 mm/min. The jaw spacing was 50 mm. The product obtained was cut in the machine direction (DM) and transverse to the machine (DT), with dimensions 20 mm wide and 70 mm long. The tests were carried out at room temperature.

2.4. Moisture Absorption

This method dried TPS samples cut to 20 mm × 50 mm in a forced convection oven at 80 °C for 24 h. The initial weight of each sample was taken, and the samples were immediately placed in a chamber with a relative humidity of 60% and 90%. Moisture contents of 60 and 90% were fixed using saturated solutions of magnesium nitrate (Mg(NO₃)₂) and potassium chloride (KCl), respectively. All solutions were prepared with distilled water. Samples were weighed periodically every 24 h for the first 8 days and then at 15 and 30 days of storage. The percentage of moisture absorption (*H*) expressed in percent was calculated according to Equation (1) below, where *W_t* is the weight at time *t*, and *W_i* is the weight in weight of dry material:

$$H (\%) = \left(\frac{W_t - W_i}{W_i} \right) \times 100 \quad (1)$$

2.5. Fourier Transform Infrared Spectroscopy (FTIR)

The films and raw materials were analyzed by Fourier transform infrared spectroscopy with a spectrometer (IRAffinity-1S, Shimadzu, Japan) coupled to an ATR device. The spectra of all samples were recorded with 4 cm^{−1} resolution in the spectral range of 500–4000 cm^{−1}.

2.6. X-ray Diffraction (XRD)

The crystallinity of the starch and TPS films was analyzed by X-ray diffraction. An XRD diffractometer (Panalytical, Empyrean) was used at a current of 30 mA and a voltage of 40 kV. Scans were performed at 2θ between 7 and 40°. Relative crystallinity (*RC*) was estimated using Equation (2) below, where *C_A* corresponds to the crystalline area, and *A_A* is an amorphous area:

$$RC (\%) = \left(\frac{C_A}{C_A + A_A} \right) \times 100 \quad (2)$$

2.7. Differential Scanning Calorimetry (DSC)

Phase transitions were performed according to norm D3418-08 using a TA Instruments Q20 calorimeter (New Castle, DE, USA). A scan was performed from $-60\text{ }^{\circ}\text{C}$ to $250\text{ }^{\circ}\text{C}$ at a heating rate of $20\text{ }^{\circ}\text{C}/\text{min}$. The parameters of retrogradation kinetics were calculated from the enthalpy results (ΔH). The degree of retrogradation (DR) was calculated by Equation (3) [30]:

$$DR = \frac{\Delta H_t - \Delta H_0}{\Delta H_{\infty} - \Delta H_0} \quad (3)$$

where ΔH_t is the melting enthalpy (J/g) of the sample after retrograding for different times, ΔH_0 is the melting enthalpy (J/g) of the sample without retrogradation, and ΔH_{∞} is the melting enthalpy (J/g) of the sample after retrograding for 30 days. The analysis of the retrogradation kinetics was carried out by applying the theory of Avrami, expressed in Equations (4) and (5) [30]:

$$DR = 1 - \exp(-kt^n) \quad (4)$$

$$\ln[-\ln(1 - DR)] = \ln k + n \ln t \quad (5)$$

where DR is the degree of retrogradation, and k and n indicate the crystallization rate constant and Avrami exponent, respectively. The $\ln k$ corresponds to the intersection, and the n value is the slope of plotting $\ln[-\ln(1 - DR)]$ versus $\ln(t)$.

2.8. Thermogravimetric Analysis (TGA)

The TGA was performed by norm ASTM E1131 (2008) using a thermogravimetric analyzer TA Instruments TGA Q50 (New Castle, DE, USA). Samples of 4 to 6 mg were deposited in a platinum capsule inside the sample holder of the equipment. Heating was performed from room temperature to $600\text{ }^{\circ}\text{C}$ at a heating rate of $20\text{ }^{\circ}\text{C}/\text{min}$ in a nitrogen atmosphere.

2.9. Scanning Electron Microscopy Morphology (SEM)

The morphology of the films obtained was analyzed on the surface using a Field-emission scanning electron microscope (FE-SEM) Hitachi UHR 8010 (Hitachi, Tokyo, Japan). The samples were vacuum dried at a pressure of 25 psi and gold–palladium coated using a Quorum machine Q150-ES (Quorum International, Fort Worth, TX, USA).

2.10. Statistical Analysis

The experimental results of the mechanical tension properties were analyzed by ANOVA. Tukey's test (p -value < 0.05) was used to evaluate the difference between the mean values of the mechanical properties of the films.

3. Results and Discussion

3.1. Mechanical Properties of Tension

While obtaining the sample, films were obtained with all the treatments except for TPSi-30, where isosorbide was the only plasticizer, so it was impossible to analyze the samples; this was because the 70/30 starch plasticizer mixture generated an excessive increase in torque, which exceeded the maximum allowed by the equipment. This phenomenon has been reported by other authors, who attribute it to an increase in the viscosity of the molten material caused by a low concentration of plasticizer to form hydrogen bonds with the starch, which decreases the mobility of the chains [22].

The obtained results are compiled in Figure 1 and Table 2. Figure 1 shows the extruded films' longitudinal and transverse tensile strength vs. elongation at break. The curves in Figure 1 were built with the average of the data collected for each treatment to show the tendency of the mechanical behavior of the material. Previously, the films were aged at different periods according to the experimental section. Here, it is observed that as the amount of isosorbide in the film formulation increases, the stress increases and the strain decreases. The use of isosorbide caused an increase in the elastic modulus (E). The E value

was twice higher in the case of TPS-i10 and up to four times higher for TPS-i20 films. The same behavior was observed for the tensile strength (σ) values.

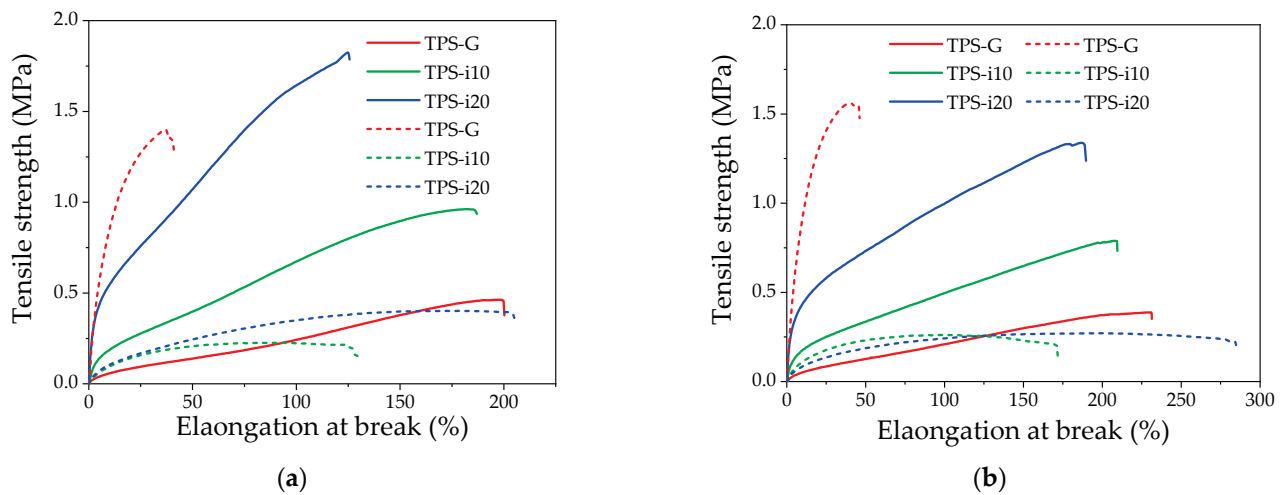


Figure 1. Mechanical properties of TPS films co-plasticized with glycerol/isosorbide: (a) orientation in the machine direction; (b) orientation in the transverse direction. The solid line and dashed line correspond to day 2 and day 30 of the conditioning of the samples, respectively.

Table 2. Mechanical properties of TPS films.

Sample	Day	E (Mpa)	σ (Mpa)	\mathcal{E} (%)	Thickness (mm)
TPS-G	2	7.51 ± 1.13	0.47 ± 0.02	200 ± 7	0.31 ± 0.03
	30	123.89 ± 4.49	1.57 ± 0.05	42 ± 3	0.42 ± 0.02
TPS-i10	2	14.22 ± 1.01	0.96 ± 0.05	188 ± 3	0.24 ± 0.02
	30	14.07 ± 1.10	0.23 ± 0.02	128 ± 2	0.26 ± 0.02
TPS-i20	2	32.54 ± 3.19	1.76 ± 0.17	125 ± 21	0.21 ± 0.01
	30	9.62 ± 0.64	0.40 ± 0.01	203 ± 29	0.30 ± 0.05
Orientation in Transverse Direction					
TPS-G	2	5.70 ± 1.08	0.37 ± 0.04	231 ± 47	0.31 ± 0.04
	30	140.37 ± 5.90	1.40 ± 0.07	40 ± 1	0.30 ± 0.01
TPS-i10	2	12.49 ± 0.71	0.79 ± 0.07	212 ± 15	0.25 ± 0.02
	30	12.17 ± 1.86	0.26 ± 0.01	164 ± 8	0.27 ± 0.01
TPS-i20	2	24.32 ± 0.84	1.35 ± 0.04	192 ± 14	0.22 ± 0.01
	30	7.99 ± 0.22	0.27 ± 0.01	285 ± 6	0.34 ± 0.01

In contrast, the strain value (\mathcal{E}) decreased by 6% for TPS-i10 and 37% for TPS-i20; this indicates that the behavior of films with isosorbide tends to be stiffer, which is in agreement with the results reported by other authors [23,27,31]. González et al. reported values for E , σ , and \mathcal{E} of 55 MPa, 2.7 MPa, and 72.4%, respectively, for isosorbide-plasticized films obtained by extrusion and compression molding. The above values were higher than those observed for films plasticized with glycerol [23]. In another study by González et al., values for E , σ , and \mathcal{E} of 8.7 MPa, 2.7 MPa, and 142.4%, respectively, were reported. However, in the latter case, the TPS preparation technique was by casting. In both cases, the authors attributed this behavior to the compatibility of the bonds formed between plasticizer and starch [23,27]. The differences between the values reported in the scientific

literature and those found in this research could be related to factors such as the TPS preparation technique, amount of plasticizer, and plasticizing system, among other factors.

The results show that the stiffness, E , and strength (σ) (Table 2) of films plasticized only with glycerol increased significantly (p -value < 0.05) after 30 days of storage, while the strain (\mathcal{E}) was reduced by approximately 80%; this suggests that the TPS-G materials underwent a higher degree of retrogradation, due to the reorganization of the structures that had been destroyed during starch extrusion and plasticization [32]. In addition to the molecular structure of starch, the ability of the plasticizer and polymer to form hydrogen bridges plays an important role in retrogradation [8,33]. The stronger the hydrogen bridge energy, the less recrystallization will occur during storage [34]. As previously cited, TPS-G films showed a higher retrogradation rate than samples containing some proportion of isosorbide. In this case, retrogradation is favored by the more significant amount of water, which acts as a plasticizer promoting retrogradation [11,35].

In the TPS-i10 films, after 30 days of storage, the E value did not undergo considerable changes. In TPS-i20, the E value for day 30 was reduced by 70%. Tensile strength was the parameter most affected by time, with a decrease of 76 and 77% (for TPS-i10 and TPS-i20, respectively). With the 1:2 glycerol/isosorbide ratio, the elongation of the films increased with time and reached the highest value (203.3%). In general, the TPS-i10 films (glycerol/isosorbide ratio of 2:1) were the least susceptible to time-induced changes, which could indicate a lower degree of retrogradation. Among the polyols, sorbitol has been shown to slow the rate of recrystallization best in the TPS [8] because it decreases water absorption and postpones the formation of V_H crystals, which contain more water molecules [11]. Isosorbide has been found to prevent crystal structure change after nine months of storage [23,31]. This agrees with XRD results, where TPS-G films had the highest increase in crystallinity. In addition, co-plasticization has been reported to be an effective strategy to prevent retrogradation, preventing the material from becoming stiff and less ductile [8].

3.2. Moisture Absorption

Figure 2 shows the behavior of TPS-G, TPS-i10, and TPS-i20 in moisture absorption versus time plots. The water-absorption capacity of TPS films co-plasticized with different glycerol/isosorbide ratios stored in environments with two relative humidities (60 and 90% RH) was evaluated. The amount of moisture absorbed varied according to the RH of the environment and the co-plasticization system. The TPS samples showed rapid absorption in the first 24 h of storage. Subsequently, the water absorption rate decreased notably, remaining relatively stable until the last day of measurement. This behavior is in agreement with other results reported by other authors [36,37]. At 60% RH, moisture absorption ranged from 9 to 12% and was much lower than at 90% RH. Although the difference in the amount of water absorbed at 60% RH was minimal, it is observed to decrease with an increasing amount of isosorbide. In the 90% RH environment, the amount of water absorbed by the films increased on average by almost three times. This behavior is attributed to the larger molecular size of the isosorbide and the lower amount of OH groups available to water, which allows for lower affinity to water [38,39].

Few studies have reported the water-absorption capacity of starch-based materials plasticized with isosorbide. It has been reported that films plasticized with isosorbide showed lower water absorption than when glycerol was used [31]. The lowest water absorption was 4.5% at 25% RH, while the highest was 22.8% at 75% RH. At 50% RH, the isosorbide-containing films absorbed 8.8% water [31]. In films obtained by casting [23], it has been found that after four weeks of storage at 43% RH, the films plasticized with 35% isosorbide went from having a wetting of 4.71 to 3.87%, while the films plasticized with glycerol went from 7.68 to 5.96% of absorbed water. This behavior was attributed to more significant interaction and homogeneity of the isosorbide-plasticized films [23].

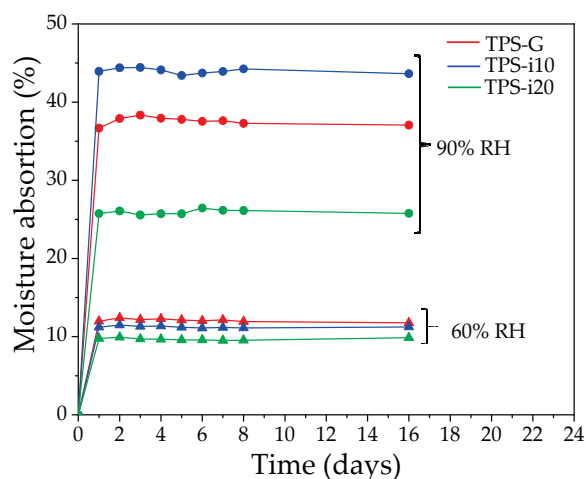


Figure 2. Moisture-absorption curves for TPS films at different %RH.

3.3. Fourier Transform Infrared Spectroscopy (FTIR)

One of the functions of plasticizers is to break the hydrogen-bonding forces existing in native starch to convert it into a thermoplastic material [8,40]. Infrared spectroscopy was used to estimate the influence of the type and amount of plasticizer. Figure 3 shows the FTIR-ATR spectra corresponding to native starch and the thermoplastic starch films evaluated.

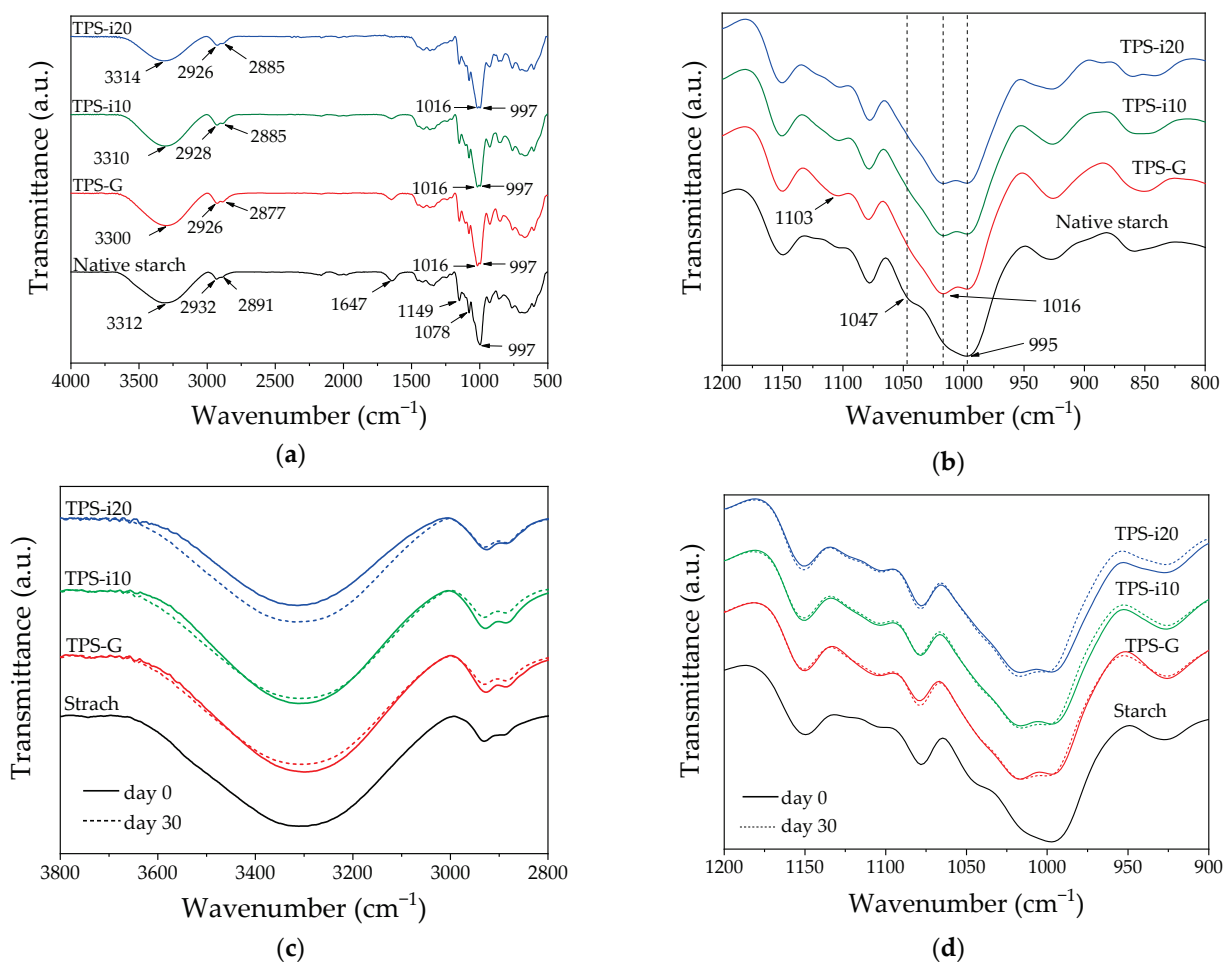


Figure 3. FTIR–ATR spectra of native starch and co-plasticized TPS films for day 0: (a) 4000–500 cm^{-1} ; (b) 1200–800 cm^{-1} ; and for days 0 and 30: (c) 3800–2800 cm^{-1} ; (d) 1200–900 cm^{-1} .

Three absorption bands were observed at 3312, 1149, and 997 cm^{-1} , characteristic of starch [41]. The absorption band between 3600 and 3100 cm^{-1} corresponds to the stretching of the free OH groups of the starch structure [15]. It is associated with forming intra- and intermolecular hydrogen bonds between the starch chains [30]. This band shifted slightly in the TPS to a lower wavenumber (3300 cm^{-1}) when the starch was plasticized with glycerol. Other authors have observed this behavior in potato starch materials plasticized with glycerol [42]. The addition of isosorbide increased the wavenumber assigned to stretching the O–H bond. This behavior does not agree with the results of other investigations, in which it has been reported that a higher concentration of plasticizer decreases the wave number and increases the intensity of the peak related to the hydroxyl group; this indicates a better interaction between the plasticizer and the starch chains since the number of hydrogen bridges is increased [43]; however, other authors have reported that the plasticizer composition does not significantly alter the band related to the hydroxyl group [8,17]. The absorption band at 1647 cm^{-1} in starch decreased in intensity in the TPS as the isosorbide content increased; this is related to less water absorbed by the amorphous regions of the plasticized starch [44] since this band is associated with the vibration of water bonds [30], as verified by absorption tests.

In the region from 1200 to 800 cm^{-1} (Figure 3b), changes were observed in the characteristic absorption bands of native starch (1149, 1078, and 997 cm^{-1} and two undefined shoulders at 1047 and 1016 cm^{-1}), which could indicate the molecular interaction between plasticizer and starch. The bands at 1149 cm^{-1} and 1078 cm^{-1} correspond to the C–O stretching of the C–O–H group. The absorption band between 920 and 936 cm^{-1} was assigned to the C–O bond stretching vibration of the C–O–C $\alpha(1,6)$ bond between the anhydroglucose rings of native starch [45]. In the TPS samples, the band at 1016 cm^{-1} corresponding to the C–O stretching of the C–O–C group of the starch anhydroglucose ring was intensified [11,35]; this is caused by newly formed hydrogen bonds between plasticizers and the C–O group of native starch [11,46], indicating stable hydrogen bonds between the plasticizer and both O corresponding to C–O–H and the O on the O–C of the anhydroglucose ring in starch molecules [46]. The absorption band between 1016 and 1021 cm^{-1} is associated with plasticization [21], and its appearance indicates low crystallinity [15]. A new band located at 1103 cm^{-1} was observed in the TPS, corresponding to glycerol functional groups [47]. The shoulder located around 1047 cm^{-1} decreased almost entirely when starch was plasticized, regardless of the type of plasticizer. The 1047 cm^{-1} absorption band is sensitive to the number of starch crystals [47], since the native starch crystallinity may have been destroyed and replaced by amorphous zones due to the action of the plasticizers (glycerol and isosorbide).

The FTIR spectra of the TPS were evaluated on day 30, and their typical absorption bands did not change drastically. Although the interaction associated with the wavelength range between 3800 and 2800 cm^{-1} is not directly related to plasticization [21], in samples containing only glycerol (TPS-G), the absorption band shifted from 3300 to 3307 cm^{-1} , indicating an increase in recrystallization and an increase in the intermolecular strength of hydrogen bonds between starch chains [30]. The above behavior did not occur in the samples containing isosorbide (TPS-i10 and TPS-i20). The band located at 1149 cm^{-1} shifted towards a slightly higher wavenumber for all samples, whereas the absorption bands at 1078 and 1016 cm^{-1} did not change substantially with time. Although it has been reported that, during TPS aging, the height of these three bands increases [40,48,49], no significant changes in the transmittance of the corresponding absorption bands were observed, regardless of the plasticization system.

3.4. X-ray Diffraction (XRD)

Figure 4 shows the XRD patterns of isosorbide and native starch and the different TPS films. The XRD spectrum of isosorbide was characterized by diffraction peaks mainly at 10.6, 19.1, and 20.8°, indicating the high crystallinity of this plasticizer [31]. In the spectrum of native starch, two peaks were observed at 15.3 and 23.2°. In addition, an undefined

double peak at 17.3 and 18.1° corresponds to the presence of type C crystalline structures (a combination of type A and B crystals). These polymorphic structures are typical of starches from roots [50].

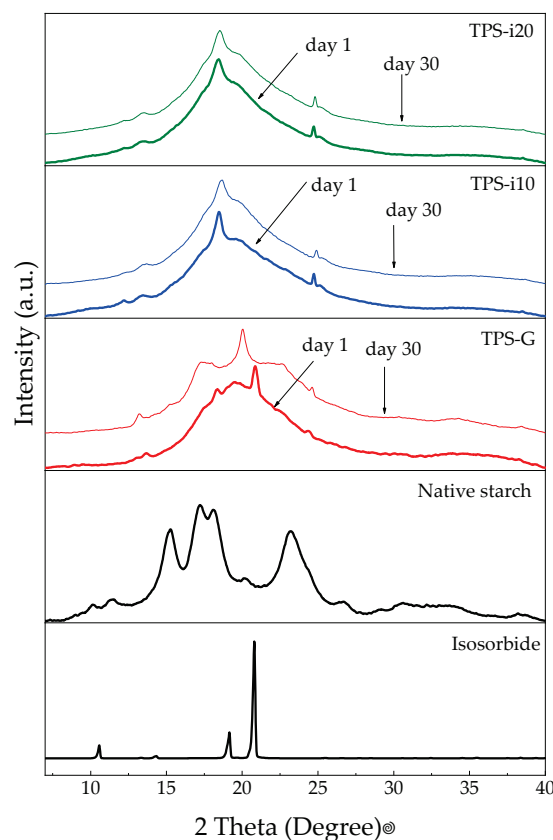


Figure 4. XRD diffraction spectra for TPS films and their components.

Compared to native starch, all samples' amorphous area (A_A) was higher. In contrast, the crystalline area (C_A) decreased (Table 3), demonstrating the transformation of the semi-crystalline structure of starch into predominantly amorphous areas. Three processing-induced crystalline structures were identified: V_H , V_A , and E_H [51,52]. Differences were found between the diffraction patterns of TPS films, confirming the effect of plasticizer type and amount on TPS crystallinity. The TPS-G films present a large amorphous halo with a small peak at 18.3° due to residual crystallinity caused by incomplete plasticization of some native starch granules. The shoulder, located at 19.5°, with a smaller peak at 13.4°, corresponds to crystalline structures induced by V_H -thermomechanical-type processing and generated by the crystallization of amylose into a simple helical structure [27,53]. In addition, a new peak was observed at 20.2° that could be attributed to V_A -type crystalline structures, which appear immediately after processing at high temperatures and in the presence of glycerol due to the formation of hydrogen bridges between the plasticizer and the starch [30].

In the XRD diffractograms of the films co-plasticized with glycerol/isosorbide (TPS-i), a small peak at 24° was observed, attributed to residual crystallinity due to incomplete destructuring of native starch granules, which is also evident in the analysis of SEM pictures. Contrary to TPS-G films, TPS-i materials presented a single intense peak located around 18°, which is associated with E_H -type crystallinity [31], a product of processing under higher shear stresses than those necessary to form V_H -type structures [27]. According to González et al., the molecular weight of isosorbide and the bulky geometry produces an increase in the viscosity of the melt, which, in turn, causes higher shear stresses during extrusion; this favors the appearance of E_H -type structures rather than V_H -type structures [27]. The

size of the molecule could prevent more plasticizer molecules from being available for the amylose chains [22].

Table 3. Amorphous area (A_A), crystalline area (C_A), and relative crystallinity (RC) of TPS films before and after storage time.

Sample	Time (Days)	A_A	C_A	RC (%)
Starch	-	5.82	2.38	29.05
TPS-G	1	7.57	0.23	2.93
	30	7.81	0.58	6.89
TPS-i10	1	7.48	0.24	3.10
	30	7.34	0.26	3.38
TPS-i20	1	7.25	0.28	3.71
	30	7.32	0.29	3.82

Table 2 shows that the relative crystallinity calculated for native starch was 29.05%. Lin et al., reported an RC value of 25.6% [54]; other authors have reported values higher than 32% [50]. However, RC values between 15 and 49% have been reported [55]. The differences between the values have been attributed to the analysis and calculation methods [55]. Films plasticized only with glycerol presented a more effective plasticization since the RC value was lower than those found with samples containing isosorbide. As the proportion of isosorbide in the TPS increased, the crystallinity increased by 19%; this indicates that, under the processing conditions employed in this investigation, the effectiveness of plasticization was reduced with increasing isosorbide. However, co-plasticization with glycerol and isosorbide could promote a synergistic effect between the plasticizers, in which the advantages of each are exploited. This synergistic effect has been reported by other authors using other plasticizers [8,11,19,21,56].

In TPS-i10 and TPS-i20 films, the type of crystalline structures (E_H) did not change with storage time. Crystallinity (Table 3) increased by 9 and 2% in TPS-i10 and TPS-i20 films, respectively. Although the crystallinity was higher in samples with higher isosorbide content (TPS-i20), the variation with time was the lowest; this suggests that retrogradation has less of an effect when the isosorbide ratio is higher. In TPS-G, the most significant changes as a function of time were observed. The characteristic DRX peaks were modified, suggesting the appearance of other crystal structures. The diffraction patterns indicate the transformation of V_A -type crystals into V_H -type structures due to the retrogradation process; this is promoted by a higher amount of water absorbed in the glycerol-plasticized TPS [8]. Although the materials containing TPS-G presented a lower initial RC (Table 3), the RC increased by almost 135% after storage time; this is due to the weakening of hydrogen bonding interactions between the plasticizer and the starch and the consequent release of the starch chains by the recrystallization of amylopectin [41].

3.5. Differential Scanning Calorimetry (DSC)

A calorimetric analysis was performed to know the thermal transitions of the TPS after processing and at different storage times. Figure 5 shows the DSC thermograms and retrogradation kinetics of the films. Endothermic melting peaks were identified, around 160 °C and above 180 °C. The first peak could be associated with the firmly bound water evaporation enthalpy, which occurs between 80 and 180 °C [57]. The second peak could be attributed to the melting the remaining crystalline domains [58] and structures resulting from the co-crystallization of amylose and amylopectin during film formation [59]. These peaks are explained by the rearrangement of the starch molecules that form crystalline structures in the presence of water and by the passage of time [30].

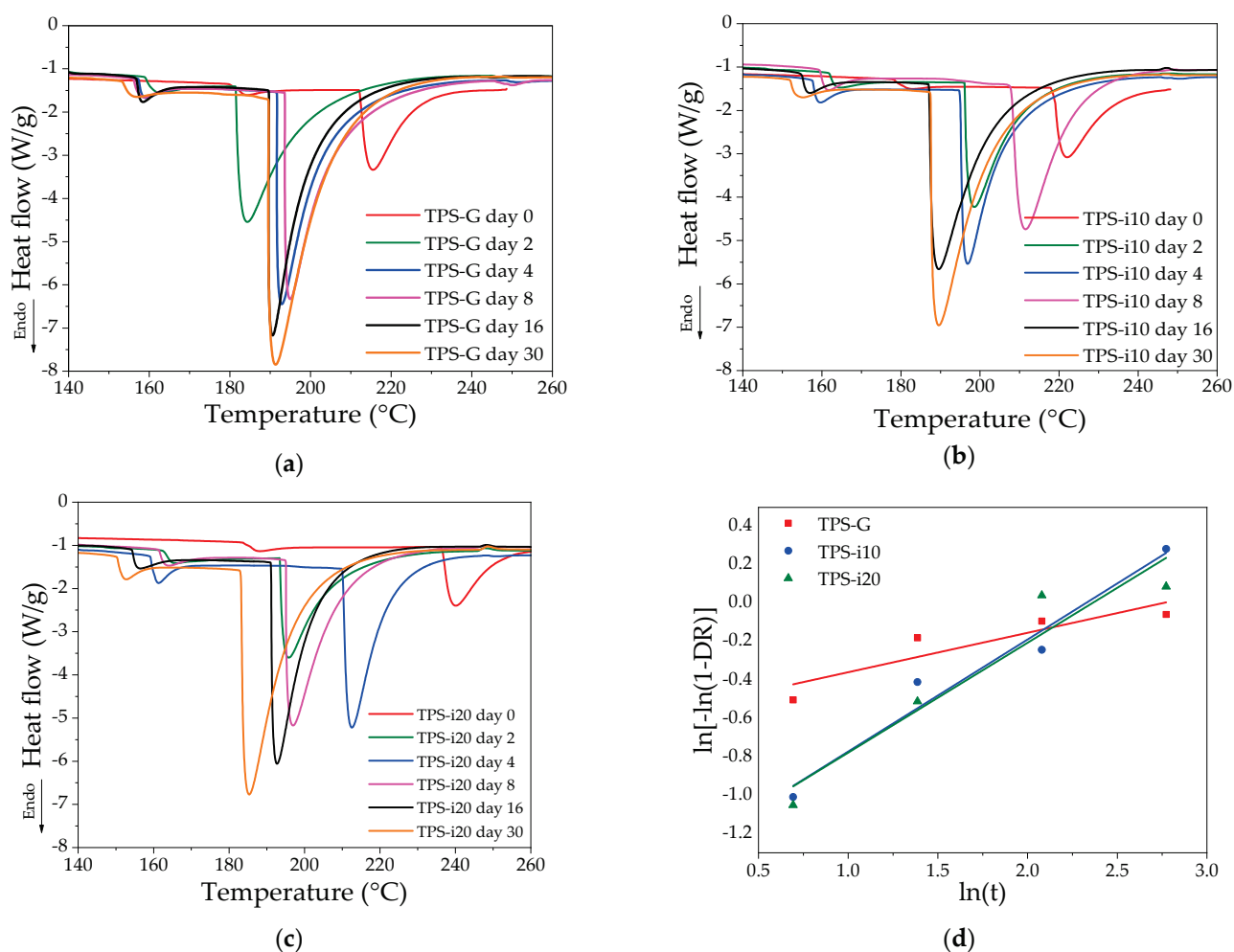


Figure 5. DSC thermograms and retrogradation kinetics of glycerol- and isosorbide-plasticized films: (a) glycerol-plasticized starch; (b) glycerol/isosorbide TPS-i10; (c) glycerol/isosorbide TPS-i20; (d) plots for $\ln[-\ln(1 - DR)]$ versus $\ln(t)$.

The partial substitution of glycerol by isosorbide drastically modified the melting temperature (T_m) and the heat or melting enthalpy (ΔH_m), due to the interactions created by the addition of isosorbide, through hydrogen bridges between the starch and plasticizer chain [60]. Although no clear trend is observed concerning the values found for all samples, it is possible to show that the T_m of the TPS-G treatment films tends to be lower than the isosorbide-plasticized films. In addition, it is observed that the T_m of all samples decreases strongly during the first two days of storage; subsequently, it has minor variations over time until reaching a very close value for all samples on day 30. This behavior coincides with the water absorption results in Figure 2, where a substantial variation is observed in the first days and tends to stabilize with time; the effect could explain this effect that the absorbed water can have on the recrystallization of the starch chains since the reorganization of the starch chains is lower when the water content is reduced [32,61].

Moreover, the reduction of ΔH_m could indicate an enhanced effect of co-plasticization produced by isosorbide incorporation, which occurs when starch–starch interactions are replaced by a new starch-plasticizer [62,63]. The molar mass and bulky geometry of isosorbide cause higher shear stress during extrusion, which promotes more significant destruction of starch granules [27]. The destruction of starch granules could allow the glycerol to penetrate the starch chains [11], increasing the plasticizing capacity of the glycerol/isosorbide system; this suggests a synergistic effect during starch plasticization, where the properties of plasticizers complement each other [11,19,21,41].

The TPS samples' retrogradation behavior (Figure 5d) was evaluated using the Avrami model, which has been employed to analyze variations in the molecular rearrangement process [8,30,64]. The kinetic parameters of the Avrami model (Table 4) were calculated from the ΔH_m values at different storage times. The coefficient of determination values (R^2 , 0.8173, 0.9619, and 0.9136 for TPS-G, TPS-i10, and TPS-i20, respectively) were close to 1, indicating a high fit of the experimental data in the model. However, the fit for the TPS-G treatment was lower, possibly due to the high moisture absorption capacity mainly produced in the first days of storage, which causes a rapid retrogradation [8]. The Avrami exponent (n) provides qualitative information about nucleation and crystallite growth [65]. The values of n were less than 1 in all samples, being lower for TPS-G. In TPS-i10 and TPS-i20 films, the exponent n was almost three times higher than TPS-G, which shows that the incorporation of isosorbide influenced the nucleation mechanism and crystallization processes during TPS retrogradation.

Table 4. Thermal properties and retrogradation kinetic parameters for starch-, glycerol-, and isosorbide-based films.

Sample	Parameter	Time (Day)						n	k
		0	2	4	8	16	30		
TPS-G	T_m (°C)	215	184	193	195	191	191	0.21	0.52
	ΔH_m (J/g)	55	131	150	155	157	222		
	DR	-	0.45	0.57	0.60	0.61	-		
TPS-i10	T_m (°C)	222	198	197	211	180	190	0.62	0.24
	ΔH_m (J/g)	52	96	123	131	159	198		
	DR	-	0.31	0.48	0.54	0.73	-		
TPS-i20	T_m (°C)	240	196	213	196	193	185	0.55	0.24
	ΔH_m (J/g)	41	79	100	125	127	171		
	DR	-	0.29	0.45	0.65	0.66	-		

These observations are consistent with the XRD results, suggesting the formation of different crystalline structures according to the plasticizer. Values of n less than one could indicate that the formation of nucleation points followed an instantaneous mechanism during starch recrystallization, and the latter occurred mainly in the initial stage of storage [66]. The crystallization rate (k) decreased drastically with the addition of isosorbide, with similar values for TPS-i10 and TPS-i20 films, indicating a reduction in the retrogradation rate [64]; this is possibly due to plasticizer–starch interactions and the large size of the isosorbide molecule restricting the movement of the starch chains [31], as evidenced by FTIR spectra. In addition, this behavior could have been favored by the low amount of water adsorbed in the isosorbide-containing films. The low amount of water in the films reduces the short- and long-term rearrangement capacity of amylose and amylopectin, respectively [41,67]. Similar n and k values in order of magnitude have been reported for glycerol-plasticized and SiO₂-added TPS films obtained by compression molding [30]. In films extruded with different plasticizers (glycerol, urea, and sorbitol), the k values calculated based on the storage modulus were much lower. However, the k for the TPS containing glycerol was higher than the other plasticizers [8], which coincides with the behavior of the results found in this study.

3.6. Thermogravimetric Analysis (TGA)

Thermogravimetric analysis was performed to study the influence of the plasticizer on the thermal degradation of TPS films co-plasticized with glycerol/isosorbide. The results were plotted using TGA curves (Figure 6). The thermal degradation behavior at day 0 (Figure 6a) was very similar for all samples analyzed. Mainly three stages were distinguished, with some variations according to the co-plasticization system. The first stage, produced around 100 °C, corresponds to water loss, although it is poorly visible

due to the low humidity of the sample. The second stage corresponds to the thermal degradation of the phase with high glycerol and isosorbide content, which occurs between 190 and 320 °C, and the third stage is observed at temperatures above 320 °C, where thermal decomposition of the starch occurs [22,23,31].

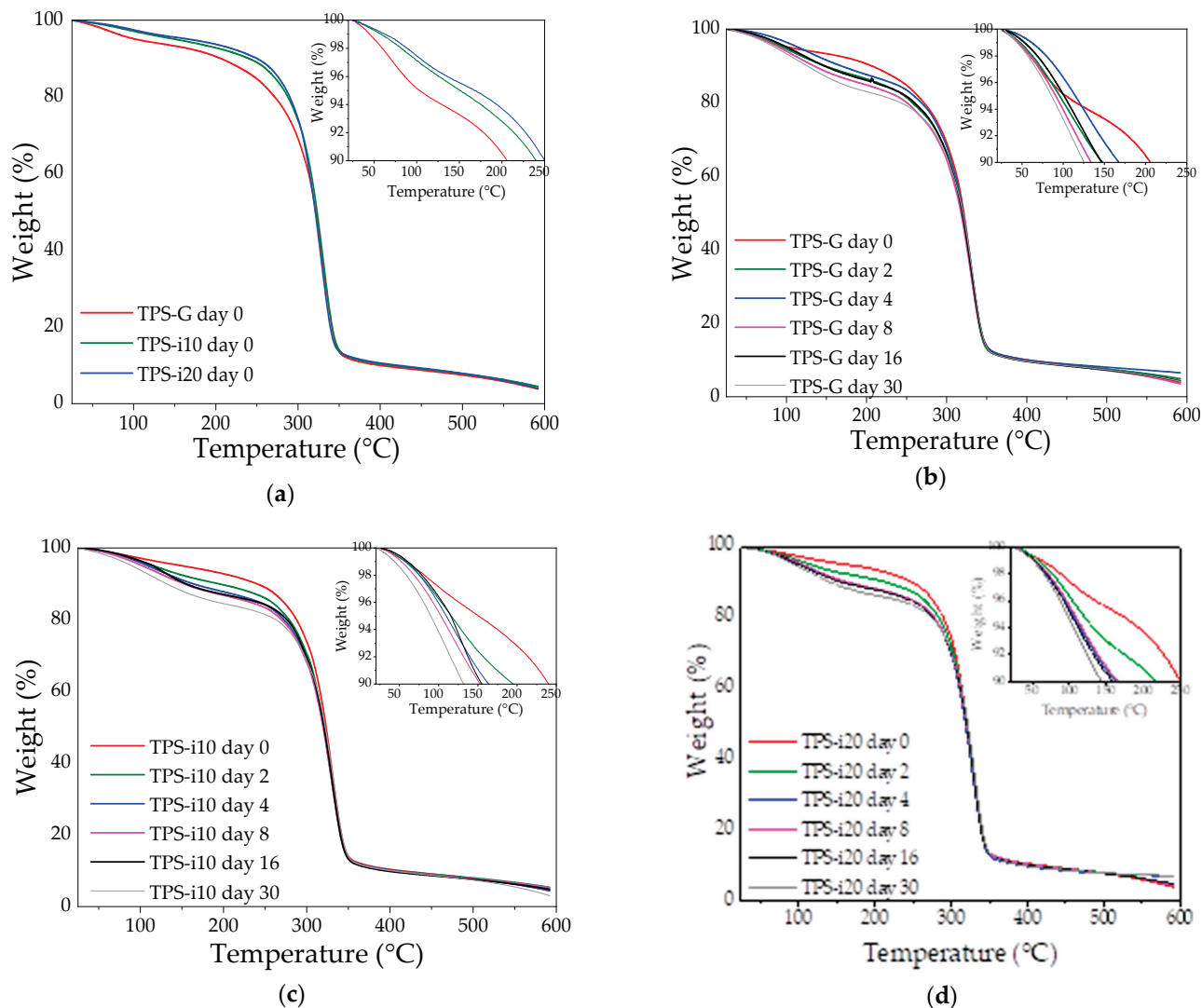


Figure 6. Thermogravimetric curves at day 0: (a) TPS films; and day 0–30: (b) TPS-G, (c) TPS-i10, (d) TPS-i20.

The data extracted from the TGA curves are summarized in Table 5. Comparison parameters were established: $T_{10\%}$, $T_{50\%}$, and $T_{90\%}$, indicating the temperature at which 10%, 50%, and 90% mass were lost, respectively. T_{max} is the maximum degradation temperature. The residue (%) is the fraction remaining after heating to 591.5 °C (maximum test temperature). The most significant changes were observed in the first stage of thermal degradation ($T_{10\%}$, integrated plot in Figure 6a), which increased by approximately 10 to 20 °C upon the incorporation of isosorbide. An increase in $T_{10\%}$ for films containing isosorbide could be related to the lower volatility of this plasticizer but also suggests higher thermal stability of TPS-i10 and TPS-i20 films [27].

Table 5. TGA data for starch-, glycerol- and isosorbide-based TPS films.

Variable	Sample	Time (Days)					
		0	2	4	8	16	30
T _{10%} (°C)	TPS-G	230	148	168	134	147	125
	TPS-i10	240	194	164	153	155	132
	TPS-i20	250	217	162	166	159	143
T _{50%} (°C)	TPS-G	322	319	321	318	319	320
	TPS-i10	323	321	320	319	321	322
	TPS-i20	321	321	319	320	320	322
T _{90%} (°C)	TPS-G	411	390	402	392	388	388
	TPS-i10	412	407	404	402	394	401
	TPS-i20	421	418	395	416	406	399
T _{max} (°C)	TPS-G	331	331	331	330	331	332
	TPS-i10	331	330	330	330	330	333
	TPS-i20	328	329	328	330	329	331
Residue	TPS-G	3.6	4.9	6.5	3.5	4.3	4.2
	TPS-i10	4.5	5.4	4.4	5.2	4.8	3.0
	TPS-i20	4.0	4.6	7.1	4.5	4.8	7.1

Previous studies indicate that isosorbide effectively integrates starch and plasticizer into a single phase, where the plasticizer molecules are trapped inside the starch [22]; this is because the interaction between isosorbide and starch chains is much larger, thus making plasticization more efficient [31]. In addition, the bulky geometry of the isosorbide molecule plays an essential role in this behavior. It reduces its mobility compared to glycerol, making its release after the plasticization process more complex [23].

The thermal stability of the films as a function of time (Figure 6b–d) shows significant changes mainly at the stage of volatilization of water and the phase with high plasticizer content (integrated graphs). Although T_{10%} decreased with time, indicative of a loss of thermal stability of the materials, the T_{10%} of the films containing isosorbide remained above the T_{10%} of the films containing only glycerol as the plasticizer; this suggests that the initial starch–isosorbide interactions were more stable than the starch–glycerol interactions. Lower water absorption of TPS-i films favors this behavior, since a low amount of water reduces the ability of starch chains to reorganize [32,61].

3.7. Scanning Electron Microscopy Morphology (SEM)

The surface morphology of the glycerol/isosorbide co-plasticized TPS films was studied by scanning electron microscopy (Figure 7). A compact surface was observed, with a predominantly smooth layer and variable relief product of the tension action generated during blowing and subsequent shrinkage due to retrogradation [32]. In addition, the shear stress typical of extrusion-blown processing is noted [50].

The plasticizer's processing and presence destructured most of the starch granules. However, residual starch granule structures were observed outside the matrix (Figure 7b,d,f) and inside the matrix (Figure 7a,c,e). The residual granules result from insufficient mixing and shearing typical of single-screw extrusion [68]. This process still has room for improvement. The presence of starch granules could also indicate incomplete plasticization [69]. Starch granules that were not plasticized and remained outside the polymeric matrix were observed (Figure 7b,d,f). In them, small changes on their surface could suggest the damage caused by shearing in the extrusion and changes concerning the plasticization system employed. As the amount of isosorbide increased, the starch granules suffered

more significant damage to their structure (Figure 7b,d,f); the increase in viscosity causes this and the high shear stresses when isosorbide is used [22,27,31].

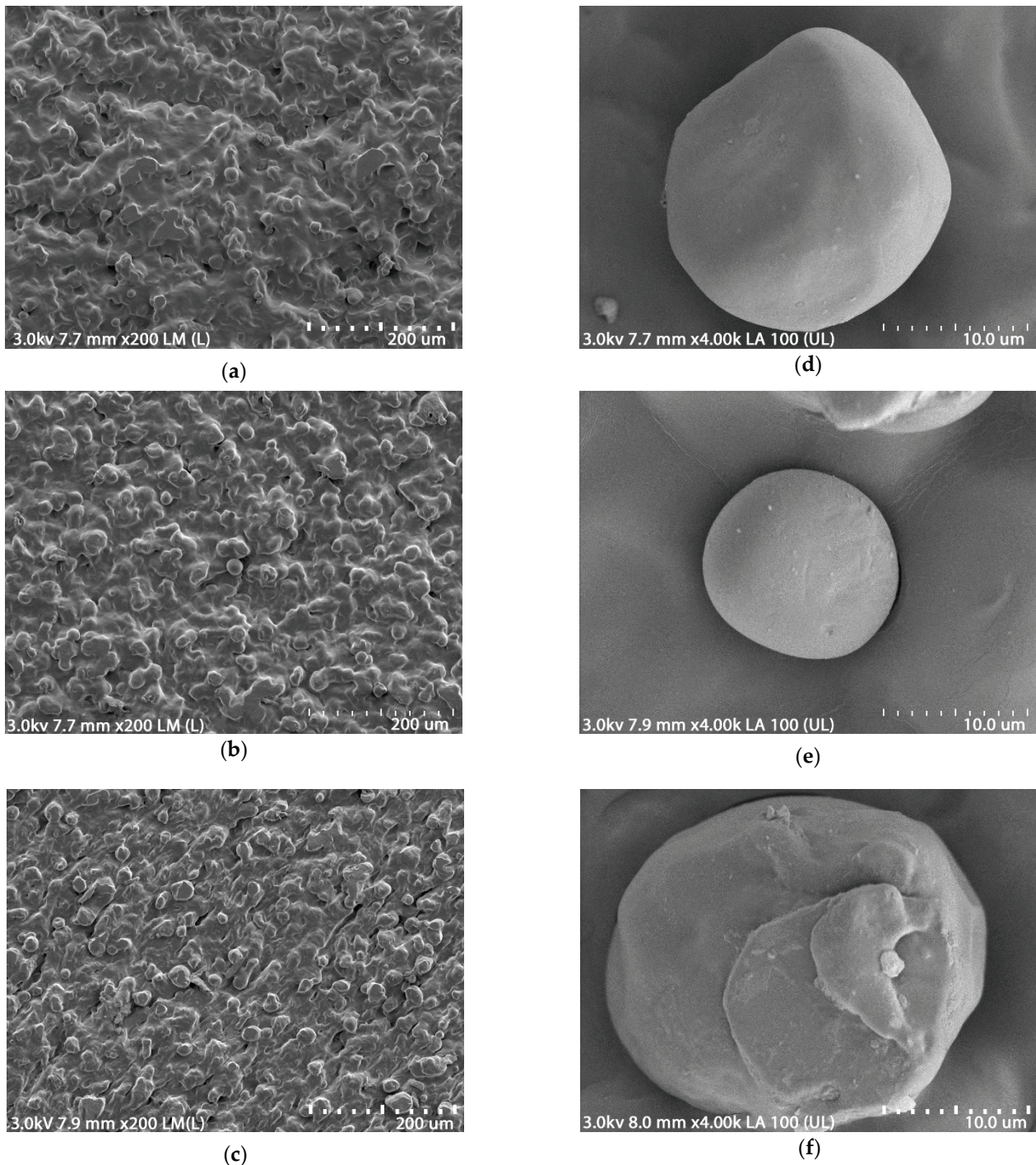


Figure 7. SEM micrographs of films at magnification 200 \times : (a) TPS-G; (c) TPS-i10; (e) TPS-i20; and 4000 \times : (b) TPS-G, (d) TPS-i10, (f) TPS-i20.

4. Conclusions

This study obtained environmentally friendly bio-composites using raw materials of renewable origin, such as cassava starch. In addition, implementing a co-plasticization system with glycerol and isosorbide allowed complementing of the plasticizing properties of glycerol and the anti-retrogradation effect of isosorbide to obtain thermoplastic starch-

based materials. Isosorbide promoted changes in the mechanical tension properties of TPS as a function of the glycerol/isosorbide ratio. Although the elongation decreased with an increasing amount of isosorbide, the presence of glycerol in the co-plasticization system allowed for obtaining a sufficiently flexible material with higher re-strength.

A partial modification of the recrystallization mechanism was identified with isosorbide, promoting the formation of predominantly E_H-type crystalline structures, which are more stable over time and reduce the effects of retrogradation. A glycerol/isosorbide ratio of 2:1 is effective in achieving adequate starch plasticization, comparable to other plasticizing systems. This evidence suggests a synergistic effect between glycerol and isosorbide.

The results obtained are promising and helpful in the search for biodegradable materials for different applications; however, other parameters should be evaluated according to the specific application, such as oxygen or water vapor permeability, color, and transparency in the case of food packaging.

Author Contributions: Conceptualization, R.A.G.-L., C.E.M.-B. and H.S.V.-C.; methodology, R.A.G.-L. and C.E.M.-B.; software, R.A.G.-L. and C.E.M.-B.; validation, R.A.G.-L., C.E.M.-B. and H.S.V.-C.; formal analysis, R.A.G.-L. and C.E.M.-B.; investigation, R.A.G.-L., C.E.M.-B., F.A.-B., L.S.-C. and A.S.-G.; resources, H.S.V.-C., F.A.-B. and A.S.-G.; data curation, R.A.G.-L. and C.E.M.-B.; writing—original draft preparation, R.A.G.-L.; writing—review and editing, R.A.G.-L.; visualization, R.A.G.-L.; supervision, C.E.M.-B., H.S.V.-C. and L.S.-C.; project administration, H.S.V.-C. and R.A.G.-L.; funding acquisition, H.S.V.-C. All authors have read and agreed to the published version of the manuscript.

Funding: This research was funded by Project “Consolidación de procesos de transferencia de conocimiento y tecnologías para la producción de materiales biodegradables desarrollados en el Departamento del Cauca” [Grand No. 2018000100042], executed by Universidad del Cauca, Gobernación del Cauca and Sistema General de Regalías (SGR).

Institutional Review Board Statement: Not applicable.

Informed Consent Statement: Not applicable.

Data Availability Statement: The data presented in this study are available on request from the corresponding author.

Acknowledgments: The authors would like to acknowledge the Sistema General de Regalías (SGR) and the Gobernación del Cauca for their financial support, the Universidad del Cauca for allowing the use of its facilities and equipment, and the Universidad Nacional de Colombia, Palmira Campus, for contributing to the training and academic guidance received.

Conflicts of Interest: The authors declare no conflict of interest.

References

1. Ferri, J.M.; Garcia-Garcia, D.; Sánchez-Nacher, L.; Fenollar, O.; Balart, R. The Effect of Maleinized Linseed Oil (MLO) on Mechanical Performance of Poly(Lactic Acid)-Thermoplastic Starch (PLA-TPS) Blends. *Carbohydr. Polym.* **2016**, *147*, 60–68. [CrossRef] [PubMed]
2. Isotton, F.S.; Bernardo, G.L.; Baldasso, C.; Rosa, L.M.; Zeni, M. The Plasticizer Effect on Preparation and Properties of Etherified Corn Starches Films. *Ind. Crops Prod.* **2015**, *76*, 717–724. [CrossRef]
3. Kahvand, F.; Fasihi, M. Plasticizing and Anti-Plasticizing Effects of Polyvinyl Alcohol in Blend with Thermoplastic Starch. *Int. J. Biol. Macromol.* **2019**, *140*, 775–781. [CrossRef]
4. Zhang, B.; Xie, F.; Zhang, T.; Chen, L.; Li, X.; Truss, R.W.; Halley, P.J.; Shamshina, J.L.; McNally, T.; Rogers, R.D. Different Characteristic Effects of Ageing on Starch-Based Films Plasticised by 1-Ethyl-3-Methylimidazolium Acetate and by Glycerol. *Carbohydr. Polym.* **2016**, *146*, 67–79. [CrossRef]
5. Zhang, L.; Wang, X.-F.; Liu, H.; Yu, L.; Wang, Y.; Simon, G.P.; Qian, J. Effect of Plasticizers on Microstructure, Compatibility and Mechanical Property of Hydroxypropyl Methylcellulose/Hydroxypropyl Starch Blends. *Int. J. Biol. Macromol.* **2018**, *119*, 141–148. [CrossRef]
6. Genovese, L.; Dominici, F.; Gigli, M.; Armentano, I.; Lotti, N.; Fortunati, E.; Siracusa, V.; Torre, L.; Munari, A. Processing, Thermo-Mechanical Characterization and Gas Permeability of Thermoplastic Starch/Poly(Butylene Trans-1,4-Cyclohexanedicarboxylate) Blends. *Polym. Degrad. Stab.* **2018**, *157*, 100–107. [CrossRef]
7. González-Seligra, P.; Guz, L.; Ochoa-Yepes, O.; Goyanes, S.; Famá, L. Influence of Extrusion Process Conditions on Starch Film Morphology. *LWT* **2017**, *84*, 520–528. [CrossRef]

8. Schmitt, H.; Guidez, A.; Prashantha, K.; Lacrampe, M.F.; Krawczak, P. Studies on the Effect of Storage Time and Plasticizers on the Structural Variations in Thermoplastic Starch. *Carbohydr. Polym.* **2015**, *115*, 364–372. [CrossRef]
9. Edhirej, A.; Sapuan, S.M.; Jawaid, M.; Zahari, N.I. Effect of Various Plasticizers and Concentration on the Physical, Thermal, Mechanical, and Structural Properties of Cassava-Starch-Based Films. *Starch-Stärke* **2017**, *69*, 1–11. [CrossRef]
10. Zdanowicz, M.; Johansson, C. Mechanical and Barrier Properties of Starch-Based Films Plasticized with Two- or Three Component Deep Eutectic Solvents. *Carbohydr. Polym.* **2016**, *151*, 103–112. [CrossRef]
11. Esmaeili, M.; Gholamreza, P.; Bagheri, R. Optimizing the Mechanical and Physical Properties of Thermoplastic Starch via Tuning the Molecular Microstructure through Co-plasticization by Sorbitol and Glycerol. *Polym. Int.* **2017**, *66*, 809–819. [CrossRef]
12. Adamus, J.; Spychaj, T.; Zdanowicz, M.; Jędrzejewski, R. Thermoplastic Starch with Deep Eutectic Solvents and Montmorillonite as a Base for Composite Materials. *Ind. Crops Prod.* **2018**, *123*, 278–284. [CrossRef]
13. Ismail, S.; Mansor, N.; Man, Z. A Study on Thermal Behaviour of Thermoplastic Starch Plasticized by [Emim] Ac and by [Emim] Cl. *Procedia Eng.* **2017**, *184*, 567–572.
14. Zdanowicz, M. Starch Treatment with Deep Eutectic Solvents, Ionic Liquids and Glycerol. A Comparative Study. *Carbohydr. Polym.* **2020**, *229*, 115574. [CrossRef]
15. Niazi, M.; Broekhuis, A. Oxidized Potato Starch Based Thermoplastic Films: Effect of Combination of Hydrophilic and Amphiphilic Plasticizers. *Starch/Stärke* **2016**, *68*, 785–795. [CrossRef]
16. Maniglia, B.C.; Tessaro, L.; Ramos, A.P.; Tapia-Blácido, D.R. Which Plasticizer Is Suitable for Films Based on Babassu Starch Isolated by Different Methods? *Food Hydrocoll.* **2019**, *89*, 143–152. [CrossRef]
17. Zdanowicz, M.; Staciwa, P.; Spychaj, T. Low Transition Temperature Mixtures (LTTM) Containing Sugars as Potato Starch Plasticizers. *Starch/Stärke* **2019**, *71*, 1900004. [CrossRef]
18. Ivanič, F.; Jočec-Mošková, D.; Janigová, I.; Chodák, I. Physical Properties of Starch Plasticized by a Mixture of Plasticizers. *Eur. Polym. J.* **2017**, *93*, 843–849. [CrossRef]
19. Giroto, A.S.; Garcia, R.H.S.; Colnago, L.A.; Klamczynski, A.; Glenn, G.M.; Ribeiro, C. Role of Urea and Melamine as Synergic Co-Plasticizers for Starch Composites for Fertilizer Application. *Int. J. Biol. Macromol.* **2020**, *144*, 143–150. [CrossRef]
20. Mikus, P.-Y.; Coqueret, X.; Alix, S.; Krawczak, P.; Soulestin, J.; Lacrampe, M.F.; Dole, P. Deformation Mechanisms of Plasticized Starch Materials. *Carbohydr. Polym.* **2014**, *114*, 450–457. [CrossRef]
21. Gao, W.; Liu, P.; Li, X.; Qiu, L.; Hou, H.; Cui, B. The Co-Plasticization Effects of Glycerol and Small Molecular Sugars on Starch-Based Nanocomposite Films Prepared by Extrusion Blowing. *Int. J. Biol. Macromol.* **2019**, *133*, 1175–1181. [CrossRef]
22. Area, M.R.; Rico, M.; Montero, B.; Barral, L.; Bouza, R.; López, J.; Ramírez, C. Corn Starch Plasticized with Isosorbide and Filled with Microcrystalline Cellulose: Processing and Characterization. *Carbohydr. Polym.* **2019**, *206*, 726–733. [CrossRef]
23. González, K.; Martín, L.; González, A.; Retegi, A.; Eceiza, A.; Gabilondo, N. D-Isosorbide and 1,3-Propanediol as Plasticizers for Starch-Based Films: Characterization and Aging Study. *J. Appl. Polym. Sci.* **2017**, *134*, 1–10. [CrossRef]
24. Vazifehasl, Z.; Hemmati, S.; Zamanloo, M.; Dizaj, S.M. New Series of Dimethacrylate-Based Monomers on Isosorbide as a Dental Material: Synthesis and Characterization. *Int. J. Compos. Mater.* **2013**, *3*, 100–107. [CrossRef]
25. Wnuk, A.J.; Rane, S.Y.; Terry, J. Isosorbide-Plasticized Starch and Uses Thereof. Patent Application US20120178858A1, 12 July 2012.
26. Delbecq, F.; Khodadadi, M.R.; Rodriguez Padron, D.; Varma, R.; Len, C. Isosorbide: Recent Advances in Catalytic Production. *Mol. Catal.* **2020**, *482*, 110648. [CrossRef]
27. González, K.; Iturriaga, L.; González, A.; Eceiza, A.; Gabilondo, N. Improving Mechanical and Barrier Properties of Thermoplastic Starch and Polysaccharide Nanocrystals Nanocomposites. *Eur. Polym. J.* **2020**, *123*, 109415. [CrossRef]
28. Arboleda, G.A.; Montilla, C.E.; Villada, H.S.; Varona, G.A. Obtaining a Flexible Film Elaborated from Cassava Thermoplastic Starch and Polylactic Acid. *Int. J. Polym. Sci.* **2015**, *2015*, 627268. [CrossRef]
29. Estevez-Areco, S.; Guz, L.; Famá, L.; Candal, R.; Goyanes, S. Bioactive Starch Nanocomposite Films with Antioxidant Activity and Enhanced Mechanical Properties Obtained by Extrusion Followed by Thermo-Compression. *Food Hydrocoll.* **2019**, *96*, 518–528. [CrossRef]
30. Liu, Y.; Fan, L.; Mo, X.; Yang, F.; Pang, J. Effects of Nanosilica on Retrogradation Properties and Structures of Thermoplastic Cassava Starch. *J. Appl. Polym. Sci.* **2017**, *135*, 45687. [CrossRef]
31. Battagazzore, D.; Bocchini, S.; Nicola, G.; Martini, E.; Frache, A. Isosorbide, a Green Plasticizer for Thermoplastic Starch That Does Not Retrograde. *Carbohydr. Polym.* **2015**, *119*, 78–84. [CrossRef] [PubMed]
32. Liu, Y.; Fan, L.; Pang, J.; Tan, D. Effect of Tensile Action on Retrogradation of Thermoplastic Cassava Starch/Nanosilica Composite. *Iran. Polym. J.* **2020**, *29*, 171–183. [CrossRef]
33. Domene-López, D.; García-Quesada, J.C.; Martín-Gullon, I.; Montalbán, M.G. Influence of Starch Composition and Molecular Weight on Physicochemical Properties of Biodegradable Films. *Polymers* **2019**, *11*, 1084. [CrossRef]
34. Ma, X.; Yu, J. The Effects of Plasticizers Containing Amide Groups on the Properties of Thermoplastic Starch. *Starch/Stärke* **2004**, *56*, 545–551. [CrossRef]
35. Zdanowicz, M.; Staciwa, P.; Jędrzejewski, R.; Spychaj, T. Sugar Alcohol-Based Deep Eutectic Solvents as Potato Starch Plasticizers. *Polymers* **2019**, *11*, 1385. [CrossRef]
36. Abera, G.; Woldeyes, B.; Demash, H.D.; Miyake, G. The Effect of Plasticizers on Thermoplastic Starch Films Developed from the Indigenous Ethiopian Tuber Crop Anchote (*Coccinia Abyssinica*) Starch. *Int. J. Biol. Macromol.* **2020**, *155*, 581–587. [CrossRef] [PubMed]


37. Ridhwan, J.; Sapuan, S.M.; Jawaid, M.; Ishak, M.R.; Sahari, J. Thermal, Mechanical, and Physical Properties of Seaweed/Sugar Palm Fibre Reinforced Thermoplastic Sugar Palm Starch/Agar Hybrid Composites. *Int. J. Biol. Macromol.* **2017**, *97*, 606–615. [CrossRef]
38. Rico, M.; Rodríguez-Llamazares, S.; Barral, L.; Bouza, R.; Montero, B. Processing and Characterization of Polyols Plasticized-Starch Reinforced with Microcrystalline Cellulose. *Carbohydr. Polym.* **2016**, *149*, 83–93. [CrossRef] [PubMed]
39. Baran, A.; Vrabel, P.; Koval'aková, M.; Hutníková, M.; Fričová, O.; Olčák, D. Effects of Sorbitol and Formamide Plasticizers on Molecular Motion in Corn Starch Studied Using NMR and DMTA. *J. Appl. Polym. Sci.* **2020**, *137*, 48964. [CrossRef]
40. Warren, F.J.; Gidley, M.J.; Flanagan, B.M. Infrared Spectroscopy as a Tool to Characterise Starch Ordered Structure-A Joint FTIR-ATR, NMR, XRD and DSC Study. *Carbohydr. Polym.* **2016**, *139*, 35–42. [CrossRef] [PubMed]
41. Zhang, K.; Zhang, K.; Cheng, F.; Lin, Y.; Zhou, M.; Zhu, P. Aging Properties and Hydrophilicity of Maize Starch Plasticized by Hyperbranched Poly(Citrate Glyceride). *J. Appl. Polym. Sci.* **2019**, *136*, 1–8. [CrossRef]
42. Altayan, M.M.; Al Darouich, T.; Karabet, F. On the Plasticization Process of Potato Starch: Preparation and Characterization. *Food Biophys.* **2017**, *12*, 397–403. [CrossRef]
43. Montilla-buitrago, C.E.; Gómez-lópez, R.A.; Solanilla-duque, J.F. Effect of Plasticizers on Properties, Retrogradation, and Processing of Extrusion-Obtained Thermoplastic Starch: A Review. *Starch-Stärke* **2021**, *2100060*, 1–15. [CrossRef]
44. Chuang, L.; Panyoyai, N.; Katopo, L.; Shanks, R.; Kasapis, S. Calcium Chloride Effects on the Glass Transition of Condensed Systems of Potato Starch. *Food Chem.* **2016**, *199*, 791–798. [CrossRef] [PubMed]
45. Ren, J.; Zhang, W.; Lou, F.; Wang, Y.; Guo, W. Characteristics of Starch-Based Films Produced Using Glycerol and 1-Butyl-3-Methylimidazolium Chloride as Combined Plasticizers. *Starch/Stärke* **2017**, *69*, 1–8. [CrossRef]
46. Ma, X.; Yu, J.; He, K.; Wang, N. The Effects of Different Plasticizers on the Properties of Thermoplastic Starch as Solid Polymer Electrolytes. *Macromol. Mater. Eng.* **2007**, *292*, 503–510. [CrossRef]
47. Castillo, L.A.; López, O.V.; García, M.A.; Barbosa, S.E.; Villar, M.A. Crystalline Morphology of Thermoplastic Starch/Talc Nanocomposites Induced by Thermal Processing. *Heliyon* **2019**, *5*, e01877. [CrossRef]
48. Qin, Y.; Zhang, H.; Dai, Y.; Hou, H.; Dong, H. Effect of Silane Treatment on Mechanical Properties. *Materials* **2019**, *12*, 1–13.
49. Xie, F.; Flanagan, B.M.; Li, M.; Sangwan, P.; Truss, R.W.; Halley, P.J.; Strounina, E.V.; Whittaker, A.K.; Gidley, M.J.; Dean, K.M.; et al. Characteristics of Starch-Based Films Plasticised by Glycerol and by the Ionic Liquid 1-Ethyl-3-Methylimidazolium Acetate: A Comparative Study. *Carbohydr. Polym.* **2014**, *111*, 841–848. [CrossRef]
50. Mina, J.H.; Valadez, A.; Herrera-Franco, P.J.; Toledano, T. Influence of Aging Time on the Structural Changes of Cassava Thermoplastic Starch. *Mater. Res. Soc. Symp. Proc.* **2012**, *1372*, 21–27.
51. Ghanbari, A.; Tabarsa, T.; Ashori, A.; Shakeri, A.; Mashkour, M. Preparation and Characterization of Thermoplastic Starch and Cellulose Nanofibers as Green Nanocomposites: Extrusion Processing. *Int. J. Biol. Macromol.* **2018**, *112*, 442–447. [CrossRef]
52. Hulleman, S.H.D.; Kalisvaart, M.G.; Janssen, F.H.P.; Feil, H.; Vliegthart, J.F.G. Origins of B-Type Crystallinity in Glycerol-Plasticized, Compression-Moulded Potato Starches. *Carbohydr. Polym.* **1999**, *39*, 351–360. [CrossRef]
53. Van Soest, J.J.G.; Hulleman, S.H.D.; De Wit, D.; Vliegthart, J.F.G. Changes in the Mechanical Properties of Thermoplastic Potato Starch in Relation with Changes in B-Type Crystallinity. *Carbohydr. Polym.* **1996**, *29*, 225–232. [CrossRef]
54. Lin, R.H.; Fan, Y.Y.; Liu, T.; Yang, H.; Ma, L.J.; Huang, X.J.; Liu, Y. Structural Characterization of Controlled Decrystallization of Cassava Starch. *Starch/Stärke* **2020**, *72*, 1–7. [CrossRef]
55. Zhu, F. Composition, Structure, Physicochemical Properties and Modifications of Cassava Starch. *Carbohydr. Polym.* **2015**, *122*, 456–480. [CrossRef] [PubMed]
56. Shamsuri, A.A.; Daik, R. Plasticizing Effect of Choline Chloride/Urea Eutectic-Based Ionic Liquid on Physicochemical Properties of Agarose Films. *BioResources* **2012**, *7*, 4760–4775. [CrossRef]
57. Turco, R.; Ortega-Toro, R.; Tesser, R.; Mallardo, S.; Collazo-Bigliardi, S.; Boix, A.C.; Malinconico, M.; Rippa, M.; Di Serio, M.; Santagata, G. Poly (Lactic Acid)/Thermoplastic Starch Films: Effect of Cardoon Seed Epoxidized Oil on Their Chemico-physical, Mechanical, and Barrier Properties. *Coatings* **2019**, *9*, 574. [CrossRef]
58. Li, M.; Liu, P.; Zou, W.; Yu, L.; Xie, F.; Pu, H.; Liu, H.; Chen, L. Extrusion Processing and Characterization of Edible Starch Films with Different Amylose Contents. *J. Food Eng.* **2011**, *106*, 95–101. [CrossRef]
59. Seligra, P.G.; Medina Jaramillo, C.; Famá, L.; Goyanes, S. Biodegradable and Non-Retrogradable Eco-Films Based on Starch-Glycerol with Citric Acid as Crosslinking Agent. *Carbohydr. Polym.* **2016**, *138*, 66–74. [CrossRef]
60. Jumaidin, R.; Sapuan, S.M.; Jawaid, M.; Ishak, M.R.; Sahari, J. Characteristics of Thermoplastic Sugar Palm Starch/Agar Blend: Thermal, Tensile, and Physical Properties. *Int. J. Biol. Macromol.* **2016**, *89*, 575–581. [CrossRef]
61. Hornung, P.S.; do Prado Cordoba, L.; da Silveira Lazzarotto, S.R.; Schnitzler, E.; Lazzarotto, M.; Ribani, R.H. Brazilian Dioscoreaceas Starches: Thermal, Structural and Rheological Properties Compared to Commercial Starches. *J. Therm. Anal. Calorim.* **2017**, *127*, 1869–1877. [CrossRef]
62. Gamarano, D. de S.; Pereira, I.M.; da Silva, M.C.; Mottin, A.C.; Ayres, E. Crystal Structure Transformations in Extruded Starch Plasticized with Glycerol and Urea. *Polym. Bull.* **2019**, *77*, 4971–4992. [CrossRef]
63. Ismail, S.; Mansor, N.; Majeed, Z.; Man, Z. Effect of Water and [Emim][OAc] as Plasticizer on Gelatinization of Starch. In Proceedings of the Procedia Engineering; Elsevier B.V.: Amsterdam, The Netherlands, 2016; Volume 148, pp. 524–529.
64. Berski, W.; Witczak, M.; Gambu, H. International Journal of Biological Macromolecules The Retrogradation Kinetics of Starches of Different Botanical Origin in the Presence of Glucose Syrup. *Int. J. Biol. Macromol.* **2018**, *114*, 1288–1294. [CrossRef]

65. Zhang, H.; Sun, B.; Zhang, S.; Zhu, Y.; Tian, Y. Inhibition of Wheat Starch Retrogradation by Tea Derivatives. *Carbohydr. Polym.* **2015**, *134*, 413–417. [CrossRef] [PubMed]
66. Zhang, Y.; Zhang, Y.; Li, B.; Xu, F.; Zhu, K.; Tan, L.; Wu, G.; Dong, W.; Li, S. Retrogradation Behavior of Amylopectin Extracted Different Jackfruit Cultivars Seeds in Presence on the Same Amylose. *LWT* **2019**, *114*, 108366. [CrossRef]
67. Halley, P.J.; Avérous, L.R. *Starch Polymers: From the Field to Industrial Products*; Taylor & Francis: Abingdon, UK, 2014; ISBN 9780444537300.
68. Giles, H.F.; Wagner, J.R.; Mount, E.M. *Extrusion: The Definitive Processing Guide and Handbook*, 2nd ed.; Willian Andrew: New York, NY, USA, 2013; ISBN 9781437734812.
69. Ceballos, R.L.; Ochoa-Yepes, O.; Goyanes, S.; Bernal, C.; Famá, L. Effect of Yerba Mate Extract on the Performance of Starch Films Obtained by Extrusion and Compression Molding as Active and Smart Packaging. *Carbohydr. Polym.* **2020**, *244*, 116495. [CrossRef] [PubMed]

Disclaimer/Publisher’s Note: The statements, opinions and data contained in all publications are solely those of the individual author(s) and contributor(s) and not of MDPI and/or the editor(s). MDPI and/or the editor(s) disclaim responsibility for any injury to people or property resulting from any ideas, methods, instructions or products referred to in the content.

Article

Reinforcing a Thermoplastic Starch/Poly(butylene adipate-co-terephthalate) Composite Foam with Polyethylene Glycol under Supercritical Carbon Dioxide

Chih-Jen Chang ^{1,†} , Jayashree Chandrasekar ^{1,†}, Chia-Jung Cho ^{2,*,†} , Manikandan Venkatesan ¹ , Pin-Shu Huang ², Ching-Wei Yang ¹, Hsin-Ta Wang ¹ , Chang-Ming Wong ³ and Chi-Ching Kuo ^{1,*} 

¹ Institute of Organic and Polymeric Materials, Research and Development Center of Smart Textile Technology, National Taipei University of Technology, Taipei 10608, Taiwan

² Institute of Biotechnology and Chemical Engineering, I-Shou University, Kaohsiung 84001, Taiwan

³ CoreTech System Co., Ltd., Hsinchu 30265, Taiwan

* Correspondence: ppaul288@isu.edu.tw (C.-J.C.); kuocc@mail.ntut.edu.tw (C.-C.K.)

† These authors contributed equally to this work.

Abstract: Biodegradable foams are a potential substitute for most fossil-fuel-derived polymer foams currently used in the cushion furniture-making industry. Thermoplastic starch (TPS) and poly(butylene adipate-co-terephthalate) (PBAT) are biodegradable polymers, although their poor compatibility does not support the foam-forming process. In this study, we investigated the effect of polyethylene glycol (PEG) with or without silane A (SA) on the foam density, cell structure and tensile properties of TPS/PBAT blends. The challenges in foam forming were explored through various temperature and pressure values under supercritical carbon dioxide (CO₂) conditions. The obtained experimental results indicate that PEG and SA act as a plasticizer and compatibilizer, respectively. The 50% (TPS with SA + PEG)/50% PBAT blends generally produce foams that have a lower foam density and better cell structure than those of 50% (TPS with PEG)/50% PBAT blends. The tensile property of each 50% (TPS with SA + PEG)/50% PBAT foam is generally better than that of each 50% (TPS with PEG)/50% PBAT foam.

Keywords: starch; polyethylene glycol; poly(butylene adipate-co-terephthalate); supercritical CO₂; foam

Citation: Chang, C.-J.; Chandrasekar, J.; Cho, C.-J.; Venkatesan, M.; Huang, P.-S.; Yang, C.-W.; Wang, H.-T.; Wong, C.-M.; Kuo, C.-C. Reinforcing a Thermoplastic Starch/Poly(butylene adipate-co-terephthalate) Composite Foam with Polyethylene Glycol under Supercritical Carbon Dioxide.

Polymers **2023**, *15*, 129. <https://doi.org/10.3390/polym15010129>

Academic Editors: Somen K. Bhudolia and Sunil Chandrakant Joshi

Received: 2 November 2022

Revised: 19 December 2022

Accepted: 26 December 2022

Published: 28 December 2022



Copyright: © 2022 by the authors. Licensee MDPI, Basel, Switzerland. This article is an open access article distributed under the terms and conditions of the Creative Commons Attribution (CC BY) license (<https://creativecommons.org/licenses/by/4.0/>).

1. Introduction

Recently, conventional plastics prepared by the petrochemical industry have been utilized for many everyday products, such as multifunctional sensors [1,2], optoelectronic devices [3], wearable electronic devices [4], etc. However, petrochemical plastics are difficult to degrade and inconvenient to collect and store for recycling. Developing biopolymeric materials as an alternative to these materials can reduce the use of non-biodegradable polymers [5], which has become one of the world's major goals. In particular, the key advantages of biodegradable polymer-based foams are their compatibility [6], biodegradability, and renewability [7].

Starch, which can be obtained with ease, is a cost-effective biodegradable polymer. It consists of a large number of glucose components and two different structures, i.e., amylose and amylopectin. Amylose is a much smaller molecule than amylopectin, but amylose molecules in starch are more numerous than amylopectin molecules. The granular structures of starch are observed in nature and are very difficult to process directly by extrusion or injection due to the very large molecular weight. TPS consists of starch granules mixed with plasticizers, such as water or glycerin, to reduce the interaction among starch granules, and it can further be processed to obtain products. Biodegradable plastics for daily products can be an good alternative to address the difficult degradation of regular plastics, causing environmental problems. The foam products obtained from

biodegradable plastics for packing and other applications have received much attention in the industrial world.

Many works associated with starch-based foams [7–19] include TPS foams produced by starch with high amylose content [7,10,12,13,15–17,19] or by grafting poly(methyl acrylate) on starch or grafting polystyrene on starch [18]. The performance of starch loose-fill foams was also investigated [11]. PBAT is a soft, biodegradable, and hydrophobic resin, but it is expensive. However, when mixed with other cheap materials, such as TPS, the PBAT/TPS blends may offer promise for many applications. TPS is a hydrophilic material. When TPS is mixed with PBAT to form blends, modification of either TPS or PBAT is required to enhance the compatibility between the two materials. Malleated TPS with PBAT [20–22] and TPS with malleated PBAT [15,19] are used to produce a film or foam.

Polyethylene glycol (PEG) is a water-soluble polyether compound having a nontoxic, biocompatible, and biodegradable nature. The molecular weight of PEG can lead to a liquid or a solid form, which can contribute to the melting temperature of PEG. There are plenty of applications for PEG, such as lubricants for industrial uses, excipients in pharmaceutical products, dispersants in toothpastes, antifoaming agents in food or industrial processes, binders, etc. Poly(lactic acid) (PLA) is a biodegradable thermoplastic material with excellent optical properties and high tensile strength [23–25]. Although the rigidity and low ductility of PLA limit its applications, when mixed with PEG, it acts as a plasticizer and has received much attention towards current research [26–34].

It is found that PEG can lower the glass transition temperature and the temperature of crystallization of PLA [26–34]. In addition, it can accelerate the crystallization process and increase the crystallinity of PLA [30,34], but it does not cause any significant change in the melt temperature of PLA [26,29–34]. The tensile modulus, tensile strength at break [26–28,30–34], flexural strength [27], and Izod impact strength of PLA/PEG are lower in comparison with PLA. However, the elongation at break among the tensile properties [26–28,30–34] either increases or decreases for PLA/PEG blends depending on the molecular weight of PEG and the amount of PEG in the PLA/PEG blend. Supercritical CO₂ foaming of PLA/PEG blends with a higher amount of PEG achieved more open cells in the foam [34]. The foams of polystyrene/PEG blends show a bimodal cellular structure, with large and small cells coexisting, and a large cell embracing a PEG particle [35]. However, very little attention has been paid to (TPS with PEG)/PBAT blends and their foams in the literature.

In this study, we used an inexpensive industrial starch that was thermally plasticized into thermoplastic starch (TPS), acting as the main foaming material. Further, the problem of the insufficient structural melt strength of TPS was solved by the addition of biodegradable PEG or PEG with a compatibilizer. The elasticity and buffering properties of the PEG/TPS/biodegradable polyester composite were improved by expanding the molecular chains and generating intermolecular entanglements with each other. Energy saving, reduced carbon emissions, and recycling are key advantages of the presented work due to the bioplastic foaming material used. Thus, this work provides an eco-friendly material and technique for a variety of applications.

2. Experimental Preparation

2.1. Materials and Procedure

Polyethylene glycol (PEG) was purchased from Echo Chemical Co., LTD., Kaohsiung, Taiwan; tapioca starch/TPS (thermoplastic starch) from the Roi Et Group, Yan-nawa, Thailand; poly(butylene adipate-co-terephthalate (PBAT; Ecoflex) from BASF, Lemförde, Germany; and Silane A 6040 (SA) (236.34 g/mol) from Ya-Hu-Chi Industrial Co., Zhubei, Taiwan.

SA contains trimethoxysilyl inorganic functional groups and one reactive glycidoxo organic functional group at the other end. The crystallinity and compatibility of TPS can be altered based on the molecular weight of PEG; therefore, the effect of the molecular weight (Mw: 1000, 2000, 3000, named PEG-10, PEG-20, and PEG-30, respectively) was studied.

The PEG with different molecular weights was blended with TPS with a known amount of 10 PHR (per hundred resin) with respect to the TPS concentration. However, SA with a small amount (5 PHR) is inevitable to improve the compatibility of PEG-modified TPS with PBAT.

The composite blending ratios are displayed in Table 1. Sheets of TPS/PBAT, PEG-TPS/PBAT, and (SA/PEG-TPS)/PBAT blends were produced by a hot press at a temperature of 140–160 °C, as shown in Figure S1. The sheet area and thickness were fixed at 75 mm × 75 mm and 3 mm, respectively. These sheets were directly used for foaming under CO₂ supercritical conditions. This foam preparation experiment was repeated five times with fixed parameters to achieve a high degree of accuracy in the results, and it exhibited excellent reproducibility.

Table 1. The composite material composition ratio and corresponding symbols list.

Symbols	Blends (by Weight) Ref.
[N-1]	50% TPS/50% PBAT [36]
[P-1]	50% (TPS with 10PHR PEG-10)/50% PBAT
[P-2]	50% (TPS with 10PHR PEG-20)/50% PBAT
[P-3]	50% (TPS with 10PHR PEG-30)/50% PBAT
[SP-1]	50% (TPS with 5PHR SA + 5PHR PEG-10)/50% PBAT
[SP-2]	50% (TPS with 5PHR SA + 5PHR PEG-20)/50% PBAT
[SP-3]	50% (TPS with 5PHR SA + 5PHR PEG-30)/50% PBAT

2.2. Surface and Functional Group Modification of TPS

First, the starch was uniformly plasticized into TPS commercially with the addition of available starch raw material to a binary solvent of water/glycerin in a plastic spectrometer (Barbender MIX, Kulturstraße, Germany). Then, the chemical structures of TPS blends were remodified based on our previous studies [36]. A functional group modifier–coupling agent of SA and different PEG (Mw: 1000, 2000, 3000) was added to the foam to enhance the number of porous cells, which afforded high flexibility (Table 1). The reaction temperature was optimized in the range of 55–70 °C, and the reaction time was 30–60 min. The pelletizer was modified and pelletized to produce surface-modified PEG/TPS and SA-PEG/TPS blends. The complete reaction mechanisms are given in Figure S2.

2.3. The (SA-PEG/TPS)/PBAT Biodegradable Polyester Composite Mixing

Chemical structure modifying agents were prepared by blending pre-prepared TPS and pre-mixed SA with PEG-10, PEG-20, and PEG-30 in a 1:1 ratio. Then, they were further mixed with PBAT biodegradable polyester at a 50% weight ratio. The composite mixture was transferred into a plastic spectrometer blending machine. The SA-PEG/TPS and the biodegradable polyester were uniformly mixed and dispersed into the composite. The mixing machine plastic spectrometer temperature was set at 90 °C to 145 °C, and the granulation screw speed was 50–100 rpm. Similarly, a control sample of unmodified TPS was blended with PBAT (50% TPS/50% PBAT).

2.4. The (SA-PEG/TPS)/PBAT Composite Foam Test Piece and Supercritical Foaming Experiment

The evenly mixed (SA-PEG/TPS)/PBAT composite was placed into a hot pressing machine to foam a film. The hot pressing process took place at a temperature of 140 °C to 165 °C; the retrieved sample appeared square in shape, with an area and thickness of 75 mm × 75 mm and 3 mm, respectively.

Then, the test samples were treated with supercritical CO₂ using foaming equipment (200-ton capacity, Tainan City, Jing Day Machinery Industrial Co., Ltd., Taiwan) to achieve highly flexible, porous foam materials. The foaming process was controlled by adopting adequate parameters, namely a foaming temperature from 80 °C to 105 °C at two different pressure conditions of 17 MPa and 23.8 MPa. The impregnation chamber was maintained

at a constant foaming temperature and pressure for 60 min. This time was sufficient to ensure that the CO₂ in the material reached a saturated state.

2.5. The (SA-PEG/TPS)/PBAT Composite Foam Appearance and Internal Structure SEM Analysis

A scanning electron microscope (SEM, using a Hitachi TM4000 Plus, Hitachi High-Tech Fielding Corporation, Nagano, Japan; the WD parameter was 15.6 mm, and the HV voltage was 5.0 kV) was used to examine the foam cells' structure, the size of the bubbles, and the dispersion of TPS in the composite foam samples after supercritical foaming.

3. Results and Discussion

3.1. FTIR Study of (P/TPS) and (SP/TPS)

The functional groups of PEG/TPS (P/TPS) prior to surface modification and after modification with SA are shown in Figure 1a by the FT-IR spectrum. In P/TPS, the peaks of IR at 3362, 2916, 1654, and 1381 cm⁻¹ represent the stretching of O–H, asymmetric stretching of C–H, –CH₂, C=O stretching, and –CH₂-deformation, while the position of the peak at 1031 cm⁻¹ may be due to the stretching of C–O–H in starch. There is a slight shift in the IR peaks of modified SA-PEG/TPS (SP/TPS to 3355 cm⁻¹ (O–H stretching), 2896 cm⁻¹ (C–H and –CH₂ asymmetric stretching), 1643 cm⁻¹ (C=O stretching), 1372 cm⁻¹ (–CH₂-deformation), and 1033 cm⁻¹ (C–O–H stretching), respectively), indicating the interaction of SA with the TPS functional groups. The interaction is further confirmed by the shift in the peak position from 1030 to 1115 cm⁻¹. The corresponding peak position of the SA modifier was observed at a low frequency. This frequency of the SA modifier is close to the peaks in P/TPS, where C–H reflects the –CH₂– asymmetric expansion and C–O–C expansion and contraction.

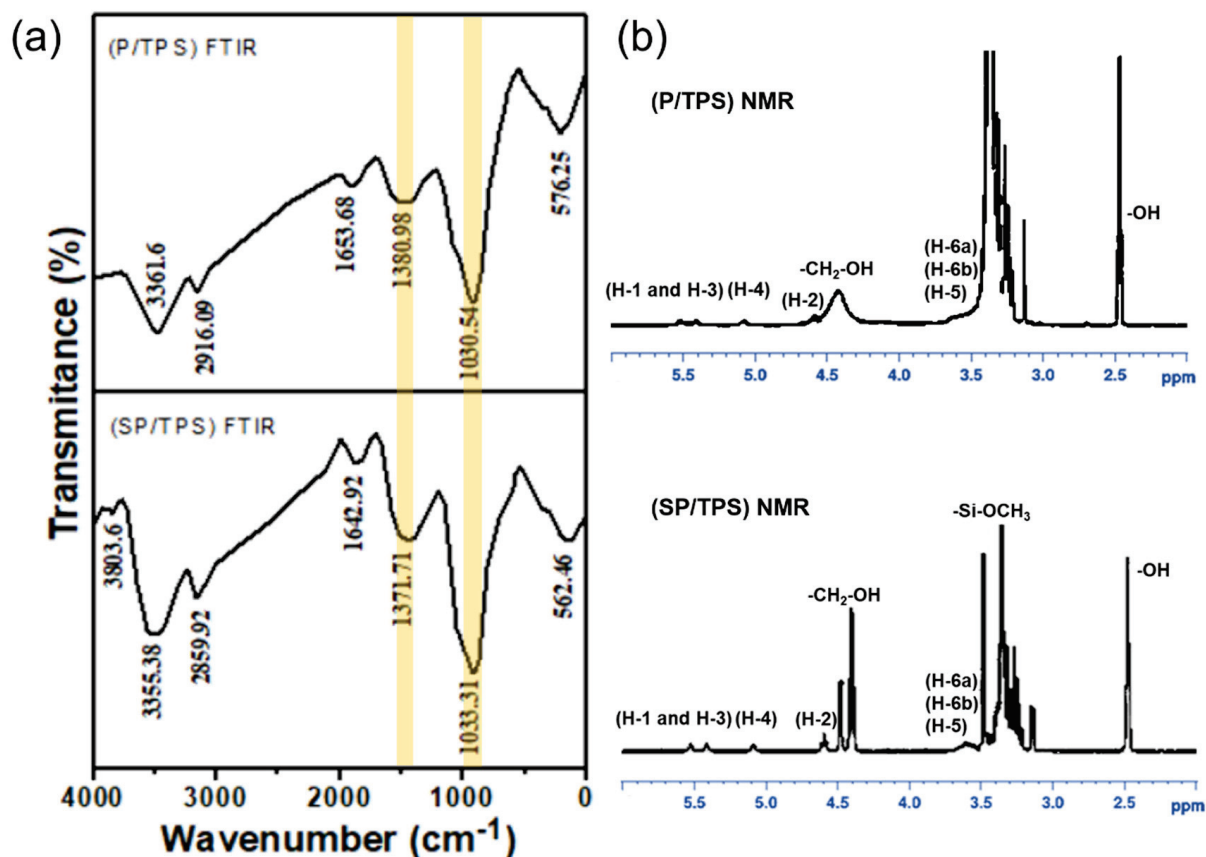


Figure 1. Schematic of chemical modification for analysis of TPS functional groups. (a) FTIR of (P/TPS) and (SP/TPS). (b) NMR of (P/TPS) and (SP/TPS).

H NMR Investigation of (P/TPS) and (SP/TPS).

Figure 1b shows the NMR spectrum of PEG/TPS (P/TPS). DMSO- d_6 was used as a solvent. Compared to the literature data [37], small signals appear at 3.62 (H-6a, H-6b, and H-5), 4.6 (H-2), 5.08 (H-4), and 5.41–5.52 (H-1 and H-3) ppm, indicating the starch. The small signals at 2.49 and 3.33 ppm correspond to the –OH (hydrogen bond and water) in DMSO and starch, respectively, and the signal from the terminal proton of the –CH₂–OH group appears at 4.44 ppm.

The NMR of SP/TPS is revealed in Figure 1b, where SA-PEG/TPS is dissolved in the DMSO- d_6 solvent. The starch resonance is represented by a small signal at 3.6 (H-6a, H-6b, and H-5), 4.6 (H-2), 5.08 (H-4), and 5.41–5.52 (H-1 and H-3) ppm [37]. The NMR peak at 2.49 corresponds to the –OH group of DMSO and the 3.38 ppm peak is related to that of –OH (hydrogen bond and water) in starch. The terminal functional group bearing a proton resonates at 4.40 and 4.47 ppm, and the SA modifier proton of the –Si–OCH₃ functional group shows a signal at 3.49 ppm.

3.2. The Foam Density of (P/TPS)/PBAT

3.2.1. The Density of Foamed PBAT

In a previous study, we evaluated the density changes in PBAT foams with impregnated CO₂ at different temperatures with two different foaming pressures [36]. The foam density of PBAT was affected proportionally by the increase in temperature under the above pressure conditions. Furthermore, the foam density obtained declined from 350 to 160 Kg/m³.

3.2.2. The Composite Foam Density of (PEG/TPS)/PBAT

The effect of foaming temperatures ranging from 80 °C to 105 °C at a foam pressure of 17MPa and 23.8 MPa on the foam density of the four blends, i.e., 50% TPS/50% PBAT [N-1], 50% (TPS with 10PHR PEG-10)/50% PBAT [P-1], 50% (TPS with 10PHR PEG-20)/50% PBAT [P-2], 50% (TPS with 10PHR PEG-30)/50% PBAT [P-3], is illustrated in Figure 2. The highest foam density in the study for the four blends occurs at a temperature of 80 °C, in comparison with other foaming temperatures, under the two foaming pressures of 17 MPa (shown in Figure 2a) and 23.8 MPa (shown in Figure 2b). As the foaming temperature increases, the foam density for the four blends reduces. In essence, the foams produced at the foaming pressure of 23.8 MPa for the four blends have a lower foam density than those produced at the foaming pressure of 17 MPa under the same foam temperature. The lowest foam density under the foaming pressure of 17 MPa for the four blends is obtained around the foaming temperature of 100 °C; however, for a foaming pressure of 23.8 MPa, it is observed around the foaming temperature of 95 °C. Generally, the lowest foam density values of the three 50% (TPS with 10PHR PEG)/50% PBAT blends are very close to one another under the foaming conditions. The foam density of the four blends rises again when the foaming temperature increases. The enhancement in the foam density indicates that the foam structure becomes weak and the shrinkage of the foam occurs at high temperatures.

3.2.3. The Foam Density of (SA-PEG/TPS)/PBAT Composite

Figure 2c,d depict the foam density of the [N-1] blend and three 50% (TPS with 5PHR SA and 5PHR PEG-10, PEG-20, or PEG-30)/50%PBAT blends, i.e., [SP-1], [SP-2], and [SP-3], at six foaming temperatures and the foaming pressure of 17 MPa and 23.8 MPa, respectively. It is observed that the foam density of the [N-1] blend is higher than that of the three 50% (TPS with 5PHR SA and 5PHR PEG)/50% PBAT blends. The [SP-1] foam has the lowest foam density among the three 50% (TPS with 5PHR SA and 5PHR PEG)/50% PBAT foams. However, the [SP-2] and [SP-3] foams have a similar foam density. The lowest foam density in the study for the four foams occurs at 100 °C when the foaming pressure is at 17 MPa; when the foaming pressure is increased to 23.8 MPa, the foaming temperature shifts to 95 °C. From this, it can be seen that the four blends generate a lower foam density at the foaming

pressure of 23.8 MPa than that at the foaming pressure of 17 MPa. This phenomenon is corroborated by the SEM images.

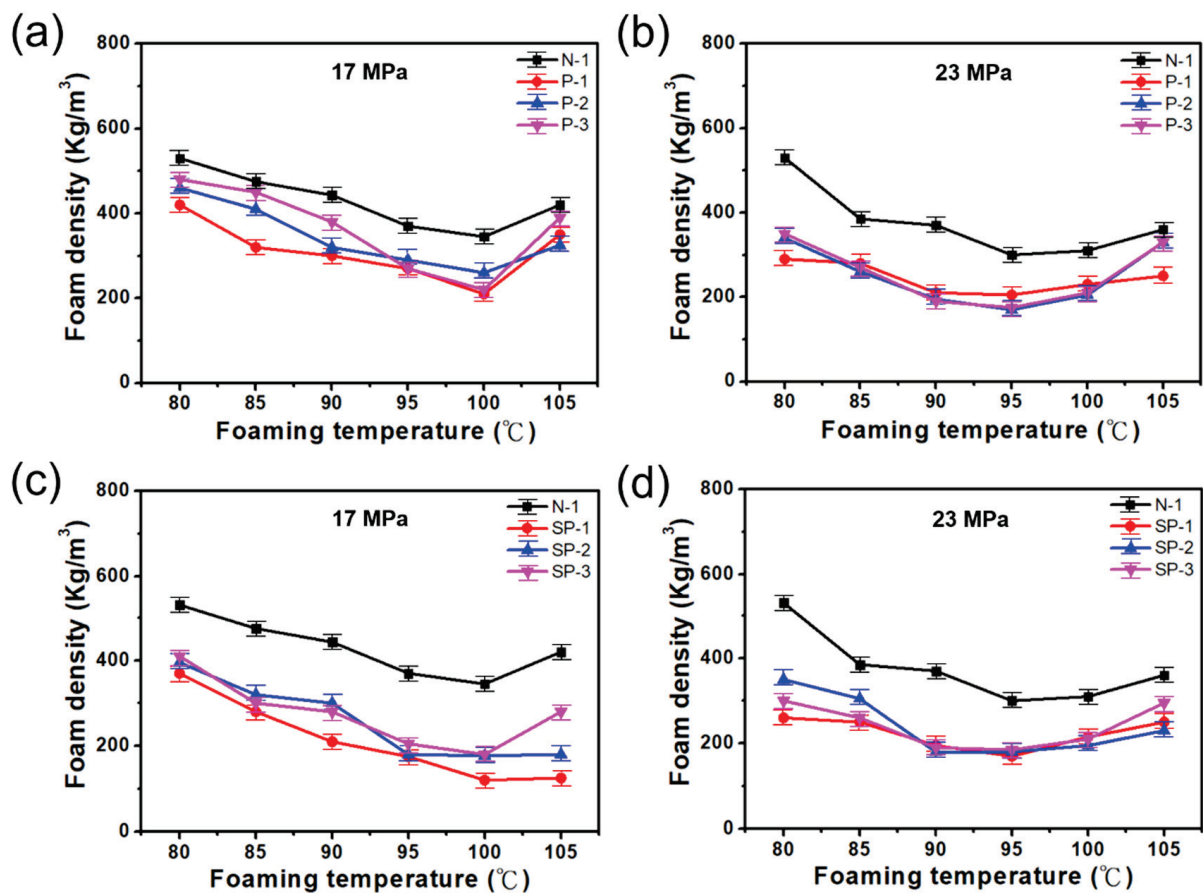


Figure 2. Dependence of (PEG-TPS)/PBAT and (PEG-TPS with SA)/PBAT composite foam density under six foaming temperatures and different foaming pressures. (a,c) Variation in composite foam density at 17 MPa. (b,d) Variation in composite foam density at 23 MPa.

3.2.4. The Density of Composite Foams at Different Foaming Temperatures and PBAT Ratios (PEG/TPS)

Figure S3a–d show the foams (N-1), (P-1), (P-2), and (P-3), respectively. These foams are produced at various foaming temperatures ranging from 80 °C to 105 °C, at a foam pressure of 17 MPa. A good appearance and shape of the foams appeared under the foaming temperatures of 90 °C and 95 °C.

Figure S4a–d show the foams (N-1), (P-1), (P-2), and (P-3), respectively, and the foams were produced at various foaming temperatures at a fixed foam pressure of 23.8 MPa. The sizes of the foams, without warpage or breakage, obtained at a foam pressure of 23.8 MPa were larger than those prepared at a foam pressure of 17 MPa under the same foaming temperatures. The foams with the (P-3) composition had a better appearance and shape than those with other compositions. A poor appearance and shape for the foams can be observed above 95 °C.

3.2.5. The Effect of Foaming Temperature on the Density of SA-Modified Composite Foams with Different PBAT Ratios (SA-PEG/TPS)

Figure S5a–c present the foams with (SP-1), (SP-2), and (SP-3), respectively, and the foams were produced at various foaming temperatures ranging from 80 °C to 105 °C and a foam pressure of 17 MPa. Similarly, the (SP-1), (SP-2), and (SP-3) foams under the same temperature variation at a foam pressure of 23.8 MPa are shown in Figure S6a–c. The foams with (SP-1), (SP-2), and (SP-3) generally exhibit a good appearance and shape at the

foaming conditions in the study, except at the foaming temperature of 105 °C and foam pressure of 23.8 MPa. The foams with the (SP-1), (SP-2), and (SP-3) compositions are much better in appearance and shape than those with (N-1), (P-1), (P-2), and (P-3) under the same foaming conditions, even at the high foaming temperatures applied in the study.

Moreover, with the TGA result, we can see that the reason is that SA is an epoxy-based modifier and its structural thermal stability is better. It can also increase the compatibility of TPS and PBAT and generate more entanglement characteristics between molecules (shown in Figures S7–S9).

In general, a poor appearance and shape for the foams is observed at high foaming temperatures, such as 100 °C and 105 °C. When two foams are produced at the same foaming temperature, but at a different foam pressure of 17 MPa and 23.8 MPa, the foam produced at the higher foam pressure shows the worst appearance and structure.

3.3. External and Internal Structure of (PEG/TPS)/PBAT Composite Foam

(TPS/PBAT) and (PEG/TPS) Foam

The cell structure for the [N-1] foam obtained at 95 °C and the foaming pressure of 17 MPa is displayed in Figure 3a. In Figure 3a, many large openings and small TPS particles scattered in the foam can be seen. The magnified view of Figure 3a shows that the large cells and small cells exist simultaneously; TPS particles can be seen distinctly in the foam, with a clear boundary between TPS particles and cells. Figure S10a exhibits the cell structure for the [N-1] foam produced at 95 °C and the foaming pressure of 23.8 MPa. Cells in the foam obtained at the foaming pressure of 23.8 MPa are more uniform and smaller than those obtained at the foaming pressure of 17 MPa. However, TPS particles are still separated from cells that arise from PBAT foaming and can generate large pores in the foam.

Figure 3b shows the cell structure for the [P-1] foam produced at the temperature of 95 °C and pressure of 17 MPa. Numerous large (TPS/PEG-10) particles are randomly scattered in the foam observed in Figure 3b, and the size of the (TPS/PEG-10) particles in the foam is generally larger than that of the TPS particles in the [N-1] foam. A gap at the boundary between (TPS/PEG-10) particles and cells for the [P-1] foam clearly exists and is similar to that of the TPS particles and cells in the [N-1] foam. However, the cell structure for the [P-1] foam exhibits a bimodal nature in terms of the cell size. One is that (TPS/PEG-10) particles generate many large pores, for which the pore sizes can be larger than 200 µm; the other is that many small cells can be seen and the cell sizes are less than 15 µm.

Figure S10b presents the cell structure for the [P-1] foam produced at the foaming temperature of 95 °C and the foaming pressure of 23.8 MPa. Many large pores and small cells are scattered in the foam produced under the above-mentioned foaming conditions; however, the mean size of cells obtained at a pressure of 23.8 MPa is smaller than that of cells obtained at 17 MPa. The cell structure is shown in Figure S10b, which is similar to that shown in Figure 3b. Therefore, TPS modified by PEG with a low molecular weight, 0.3 Kg/mole, does not improve the dispersion and compatibility of TPS in PBAT.

Figure 3c is the cell structure for the [P-2] foam obtained at 95 °C and a pressure of 17 MPa. When the cell structure of the [P-2] foam is compared with that of the [P-1] foam, the [P-2] foam generally has smaller (TPS/PEG-20) particles and fewer large pores than the [P-1] foam. The result indicates that TPS with P20 can obtain a better dispersive property in PBAT than that of TPS with P10. The increase in the number of (TPS/PEG-20) particles can lead to the destruction of the bimodal structure of cells observed in Figure 3b.

Figure S10c represents the cell structure for the [P-2] foam obtained at the temperature of 95 °C and pressure of 23.8 MPa. Essentially, the foam produced at the foaming pressure of 23.8 MPa has a better cell structure than that of the foam produced at the foaming pressure of 17 MPa under the same foaming temperature. A bimodal structure of the cell is observed again, probably because the [P-2] foam has smaller cells from PBAT foaming produced at the high foaming pressure of 23.8 MPa than those of the foam produced at the low foaming pressure of 17 MPa.

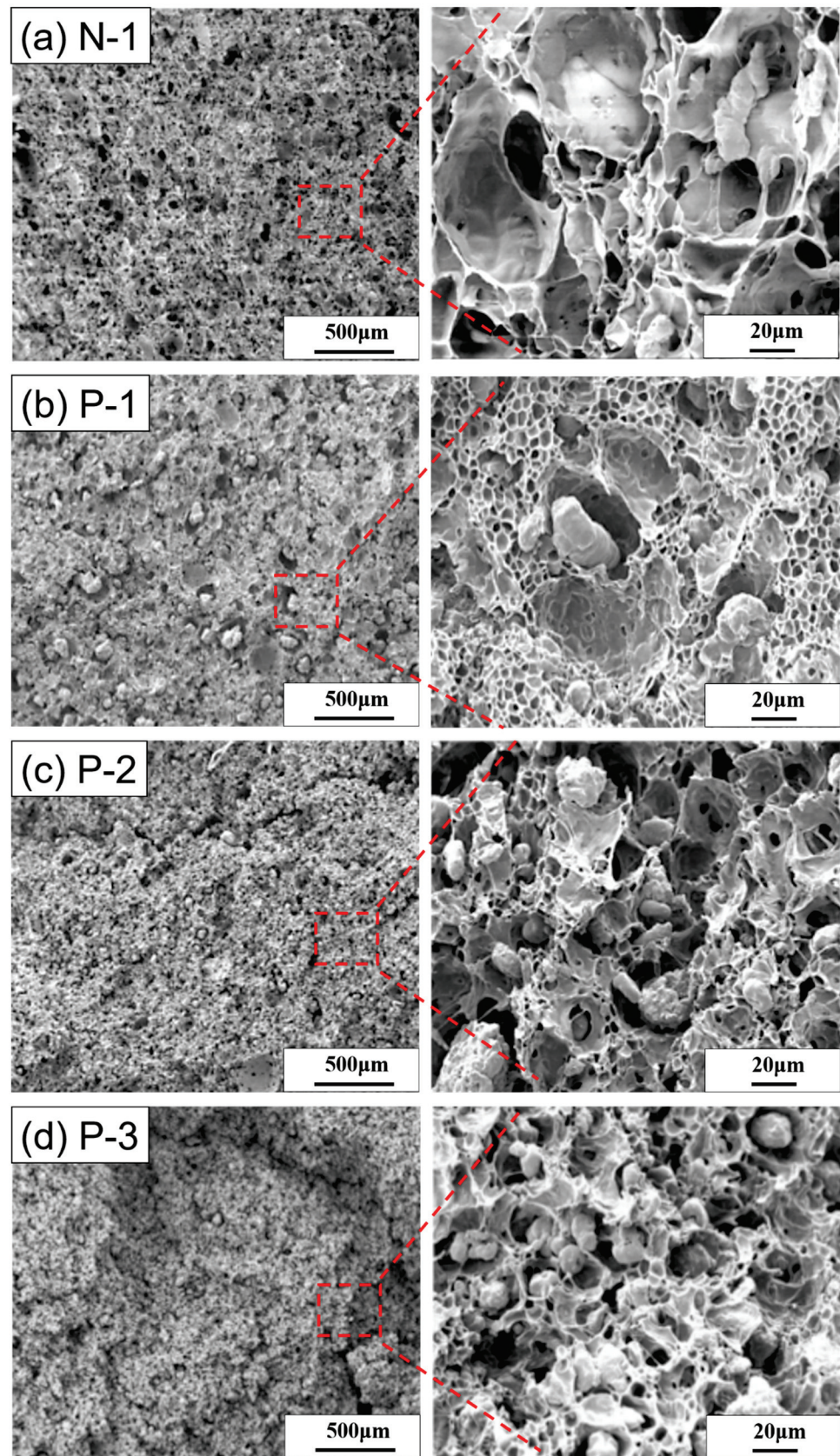


Figure 3. SEM images of cell structure of (a) [N-1], (b) [P-1], (c) [P-2], and (d) [P-3] at the foaming temperature of 95 °C and the foaming pressure of 17 MPa.

Cell structures for the [P-3] foam obtained at the foaming temperature of 95 °C and the two foaming pressures of 17 MPa and 23.8 MPa are shown in Figures 3d and S10d, respectively. In comparison with the effect of the three PEG components with different MWs on the TPS/PBAT blend, it is found that the particle size of TPS modified by PEG with a high MW is more uniform and smaller than that of TPS modified by PEG with a low MW in the 50% (TPS with 10PHR PEG)/50% PBAT foam. However, the aggregation of small (TPS/PEG-30) particles occurs and they resemble a large particle. The [P-3] foam has a better cell structure than the [P-1] and [P-2] foams. Generally, 50% (TPS with or without PEG)/50% PBAT foams produced at a high foaming pressure have a better cell structure than foams produced at a low foaming pressure.

SEM images for the 50% (TPS with 10PHR PEG)/50% PBAT foams reveal (TPS/PEG) particles at the boundary, without interaction with cells. PEG acts as a plasticizer in the blend. The increase in MW for PEG can lead to an enhancement in the viscosity of PEG. Therefore, TPS mixed with different types of PEG can yield different viscosity levels for (TPS/PEG), which may result in differences in dispersion for (TPS/PEG) in 50% (TPS/PEG)/50% PBAT blends.

3.4. External and Internal Structure of (SA-PEG/TPS)/PBAT Composite Foam

(SA-PEG/TPS)/PBAT Foams with Different (SA-PEG/TPS) Ratios

The cell structure for [SP-1] foamed at a temperature of 95 °C and the foaming pressure of 17 MPa is shown in Figure 4a. It is found that (TPS/SA + PEG-10) particles become small, and large (TPS/SA + PEG-10) particles almost disappear in the foam; the boundary between (TPS/SA + PEG-10) particles and cells becomes indistinct, and (TPS/SA + PEG-10) particles seem to be embedded in the foam. In general, the cell structure of the [SP-1] foam is more uniform than that of the [P-1] foam shown in Figure 3b. Figure S11a represents the cell structure for [SP-1] foamed at 95 °C and a pressure of 23.8 MPa. It is observed that the two foams shown in Figures 4 and S11 have a similar structure, but the foam obtained at a high foaming pressure exhibits smaller cells than the foam obtained at a low foaming pressure. Therefore, SA, as a compatibilizer, can enhance the miscibility between (TPS/SA + PEG-10) particles and PBAT and further contribute to the good dispersion of (TPS/SA + PEG-10) particles in PBAT.

Figures 4b and S11b display the cell structure for [SP-2] foamed at a temperature of 95 °C and pressures of 17 MPa and 23.8 MPa, respectively. It is found that the gap at the boundary between (TPS/SA + PEG-20) particles and cells becomes clear and large. The size of (TPS/SA + PEG-20) particles and the number of large cells increase, when the cell structure of the [SP-2] foam is compared with that of the [SP-1] foam. Therefore, due to the increase in the MW of PEG, (TPS/SA + PEG-20) particles show poor dispersion in the (TPS/SA + PEG-20)/PBAT blend. However, the cell structure of [SP-2] is better than that of the [P-2] foam. Figures 4c and S11c, respectively, exhibit the cell structures for [SP-3] foams obtained at the foaming temperature of 95 °C and the foaming pressures of 17 MPa and 23.8 MPa. The (TPS/SA + PEG-30) particles in the foam are observed more distinctly than (TPS/SA + PEG-10) particles in the [SP-1] foam. The aggregation of (TPS/SA + PEG-30) particles resulted in an increase in the number of large pores in the foam. In particular, the [SP-3] foam obtained at the foaming pressure of 23.8 MPa shows a bimodal cell structure, where small cells and large cells coexist. Moreover, the cell structure of the [SP-3] foam is close to that of the [P-2] foam in the study. The results indicate that TPS mixed with both SA and PEG with a high MW can result in poor dispersion and miscibility for (TPS/SA + PEG) particles in the (TPS/SA + PEG)/PBAT blend.

3.5. Tensile Properties and Elongation at Break of TPS/PBAT and SA-Modified (SA-PEG/TPS)/PBAT Composite Foam

Table 2 shows the tensile strength and elongation at break of five foams, i.e., the [N-1], [P-1], [P-2], and [P-3] foams achieved at the foaming pressure of 17 MPa(A) and the [P-1] foam obtained at the foaming pressure of 23.8 MPa(*), under the foaming temperature

of 95 °C. Essentially, the three 50% (TPS with PEG)/50% PBAT foams have better tensile strength and more than twice the elongation at break compared to the 50% TPS/50% PBAT foam. Among the three 50% (TPS with PEG)/50% PBAT foams achieved at the foaming pressure of 17 MPa, the [P-3] foam shows better ultimate tensile strength and elongation at break than the [P-1] and [P-2] foams. The tensile strength of [P-1] is poor and, even at the foaming pressure of 23.8MPa, it does not show an improvement in the tensile property. These results of the tensile properties are consistent with the cell structures displayed in Figures 3b–d and S6b.

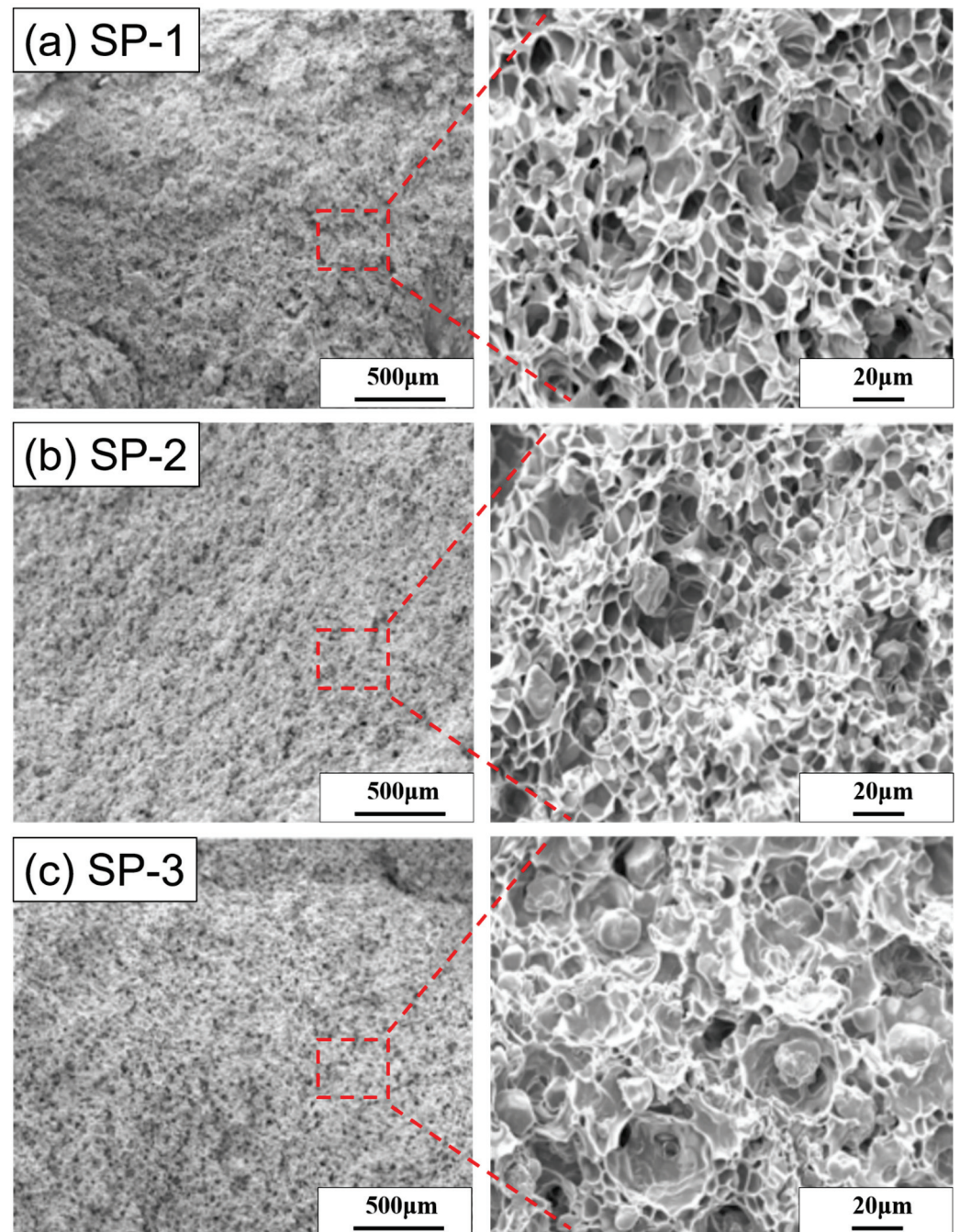


Figure 4. SEM images of cell structure at the foaming temperature of 95 °C and the foaming pressure of 17 MPa. (a) [SP-1], (b) [SP-2], and (c) [SP-3].

Table 2. The mechanical properties of the (TPS/SA/PEG)/PBAT composite foams.

	Tensile Strength (kPa)	Elongation (%) Ref.
[N-1] (F)	226 ± 35	20 ± 3 [36]
[P-1] * (F)	308 ± 43	42 ± 2
[P-1] (F)	294 ± 45	45 ± 1
[P-2] (F)	363 ± 41	43 ± 2
[P-3] (F)	431 ± 42	45 ± 3
[SP-1] * (F)	760 ± 40	48 ± 1
[SP-1] (F)	745 ± 45	45 ± 2
[SP-2] (F)	637 ± 52	44 ± 1
[SP-3] (F)	608 ± 44	46 ± 1

(*): The foaming temperature of 95 °C and the foaming pressure of 23.8 MPa.

The ultimate tensile strength and elongation at break for the [N-1], [SP-1], [SP-2], and [SP-3] foams were achieved at the foaming pressure of 17 MPa(A), and the [SP-1] foam was also obtained at the foaming pressure of 23.8 MPa(B) under the foaming temperature of 95 °C. The tensile strength and elongation at break of the three 50% (TPS with 5PHR SA and 5PHR PEG)/50% PBAT foams are much better than those of the 50% TPS/50% PBAT foam. In addition, the tensile strength is also better than that of the 50% (TPS with 10PHR PEG)/50% PBAT foams. Distinctly, the [SP-1] foam has the best tensile strength among the three 50% (TPS with 5PHR SA and 5PHR PEG)/50% PBAT foams. However, it shows a similar elongation at break to the [SP-2] and [SP-3] foams obtained under the foaming pressure of 17 MPa. It is also observed that the [SP-1] foam produced at a foaming pressure of 23.8 MPa is slightly better in terms of tensile strength and elongation at break the [SP-1] foam produced at a foaming pressure of 17 MPa. These results for the tensile properties reflect the cell structure of the [SP-1] foam, which has small cells and also good dispersion and miscibility for (TPS/SA + PEG-10) particles with PBAT in blends, as indicated in Figures 4a and S11a.

4. Conclusions

Three different molecular weights of PEG, namely PEG-10, PEG-20, and PEG-30, as a plasticizer, and SA as a compatibilizer, are used to modify TPS. PEG-10 and PEG-30 have the lowest and the highest molecular weight, respectively, and PEG-20 has an intermediate molecular weight. Moreover, 50% TPS, 50% (TPS with 10 PHR different PEGs), or 50% (TPS with 5PHR SA and 5PHR different PEGs) are mixed with 50% PBAT by weight to form blends. These blends are foamed by supercritical CO₂ at foaming temperatures ranging from 80 °C to 105 °C and foaming pressures of 17 MPa and 23.8 MPa. The 50% (TPS with PEG-10)/50% PBAT foam has the lowest foam density among the three 50% (TPS with PEG)/50% PBAT foams under the foaming conditions, and the 50% (TPS with SA and PEG-10)/50% PBAT foam also shows the lowest foam density among the three 50% (TPS with SA and PEG)/50% PBAT foams. The foam density of the 50% (TPS with SA and PEG)/50% PBAT foam is generally lower than that of the 50% (TPS with PEG)/50% PBAT foam. The lowest foam density for those blends obtained at a foaming pressure of 17MPa is obtained at around the foaming temperature of 100 °C. However, at a high foaming pressure of 23.8 MPa, the lowest foam density for the blends occurs at a foaming temperature of 95 °C.

The tensile property and elongation at break for the three 50% (TPS with PEG)/50% PBAT foams are ultimately better than those of the 50% TPS/50% PBAT foam. The tensile strength of the three 50% (TPS with SA + PEG)/50% PBAT foams is much better than that of the three 50% (TPS with PEG)/50% PBAT foams; however, both foams have a similar elongation at break. The cell structure and tensile property of the 50% (TPS with SA + PEG-10) and 50% PBAT foam are better in comparison with those of other foams.

Supplementary Materials: The following supporting information can be downloaded at: <https://www.mdpi.com/article/10.3390/polym15010129/s1>, Figure S1: Schematic representation of foaming system, the processing system is used for CO₂ batch foaming; Figure S2: Chemical structure of foam forming process; Figure S3: Dependence of TPS/PBAT and (PEG-TPS)/PBAT foam appearance on six foaming temperatures and the foaming pressure of 17 MPa; Figure S4: Dependence of TPS/PBAT and (PEG-TPS)/PBAT foam appearance on six foaming temperatures and the foaming pressure of 23.8 MPa; Figure S5: Dependence of (PEG-TPS with SA)/PBAT foam appearance on six foaming temperatures and the foaming pressure of 17 MPa; Figure S6: Dependence of (PEG-TPS with SA)/PBAT foam appearance on six foaming temperatures and the foaming pressure of 23.8 MPa; Figure S7: TGA of [N-1]; Figure S8: TGA of [P-1]; Figure S9: TGA of [SP-1]; Figure S10: The SEM images of cell structure at the foaming temperature of 95 °C and the foaming pressure of 23.8 MPa; Figure S11: The SEM images of cell structure at the foaming temperature of 95 °C and the foaming pressure of 23.8 MPa.

Author Contributions: Conceptualization, C.-C.K. and C.-J.C. (Chia-Jung Cho) conceived and supervised the project. C.-J.C. (Chih-Jen Chang), M.V., C.-J.C. (Chia-Jung Cho) and H.-T.W. conceived and designed the experiments. C.-J.C. (Chih-Jen Chang), J.C., C.-W.Y. and C.-M.W. performed and analyzed the experiments. P.-S.H., J.C. and C.-M.W. assisted with sample preparation, analyzing the SEM morphology and the other measurements. C.-J.C. (Chih-Jen Chang) wrote the paper. C.-J.C. (Chih-Jen Chang), C.-C.K. and C.-J.C. (Chia-Jung Cho) discussed the results and revised or commented on the manuscript. All authors have read and agreed to the published version of the manuscript.

Funding: This work was supported by (1) the Ministry of Science and Technology, Taiwan (Contracts: MOST 109-2221-E-027-114-MY3, MOST 110-2222-E-214-001-MY2, MOST 110-2622-E-027-019) and (2) I-Shou University (Contract: ISU 111-S-01). The authors also thank the National Science Council of Taiwan (NSC-108-2221-E-182A-002) for financially supporting this research.

Institutional Review Board Statement: Not applicable.

Data Availability Statement: Not applicable.

Conflicts of Interest: The authors declare no conflict of interest.

References

1. Cho, C.-J.; Lu, S.-T.; Kuo, C.-C.; Liang, F.-C.; Chen, B.-Y.; Chu, C.-C. Pyrene or rhodamine derivative–modified surfaces of electrospun nanofibrous chemosensors for colorimetric and fluorescent determination of Cu²⁺, Hg²⁺, and pH. *React. Funct. Polym.* **2016**, *108*, 137–147. [CrossRef]
2. Venkatesan, M.; Veeramuthu, L.; Liang, F.-C.; Chen, W.-C.; Cho, C.-J.; Chen, C.-W.; Chen, J.-Y.; Yan, Y.; Chang, S.-H.; Kuo, C.-C. Evolution of electrospun nanofibers fluorescent and colorimetric sensors for environmental toxicants, pH, temperature, and cancer cells—A review with insights on applications. *Chem. Eng. J.* **2020**, *397*, 125431. [CrossRef]
3. Cho, C.-J.; Chen, S.-Y.; Kuo, C.-C.; Veeramuthu, L.; Au-Duong, A.-N.; Chiu, Y.-C.; Chang, S.-H. Morphology and optoelectronic characteristics of organic field-effect transistors based on blends of polylactic acid and poly(3-hexylthiophene). *Polym. J.* **2018**, *50*, 975–987. [CrossRef]
4. Venkatesan, M.; Chen, W.-C.; Cho, C.-J.; Veeramuthu, L.; Chen, L.-G.; Li, K.-Y.; Tsai, M.-L.; Lai, Y.-C.; Lee, W.-Y.; Chen, W.-C.; et al. Enhanced piezoelectric and photocatalytic performance of flexible energy harvester based on CsZn_{0.75}Pb_{0.25}I₃/CNC–PVDF composite nanofibers. *Chem. Eng. J.* **2022**, *433*, 133620. [CrossRef]
5. Lu, W.C.; Chuang, F.S.; Venkatesan, M.; Cho, C.J.; Chen, P.Y.; Tzeng, Y.R.; Yu, Y.Y.; Rwei, S.P.; Kuo, C.C. Synthesis of Water Resistance and Moisture-Permeable Nanofiber Using Sodium Alginate-Functionalized Waterborne Polyurethane. *Polymers* **2020**, *12*, 2882. [CrossRef]
6. Chan, H.W.; Cho, C.J.; Hsu, K.H.; He, C.L.; Kuo, C.C.; Chu, C.C.; Chen, Y.H.; Chen, C.W.; Rwei, S.P. Smart Wearable Textiles with Breathable Properties and Repeatable Shaping in In Vitro Orthopedic Support from a Novel Biomass Thermoplastic Copolyester. *Macromol. Mater. Eng.* **2019**, *304*, 1900103. [CrossRef]
7. Motloung, M.P.; Ojijo, V.; Bandyopadhyay, J.; Ray, S.S. Cellulose Nanostructure-Based Biodegradable Nanocomposite Foams: A Brief Overview on the Recent Advancements and Perspectives. *Polymers* **2019**, *11*, 1270. [CrossRef]
8. Boonprasertpoh, A.; Pentrakoon, D.; Junkasem, J. Effect of PBAT on physical, morphological, and mechanical properties of PBS/PBAT foam. *Cell. Polym.* **2019**, *39*, 31–41. [CrossRef]
9. Combrzynski, M.; Matwijczuk, A.; Wojtowicz, A.; Oniszczuk, T.; Karcz, D.; Szponar, J.; Niemczynowicz, A.; Bober, D.; Mitrus, M.; Kupryaniuk, K.; et al. Potato Starch Utilization in Ecological Loose-Fill Packaging Materials—Sustainability and Characterization. *Materials* **2020**, *13*, 1390. [CrossRef]


10. Diyana, Z.N.; Jumaidin, R.; Selamat, M.Z.; Ghazali, I.; Julmohammad, N.; Huda, N.; Ilyas, R.A. Physical Properties of Thermoplastic Starch Derived from Natural Resources and Its Blends: A Review. *Polymers* **2021**, *13*, 1396. [CrossRef]
11. Gunawardene, O.H.P.; Gunathilake, C.; Amaraweera, S.M.; Fernando, N.M.L.; Wanninayaka, D.B.; Manamperi, A.; Kulatunga, A.K.; Rajapaksha, S.M.; Dassanayake, R.S.; Fernando, C.A.N.; et al. Compatibilization of Starch/Synthetic Biodegradable Polymer Blends for Packaging Applications: A Review. *J. Compos. Sci.* **2021**, *5*, 300. [CrossRef]
12. Li, Y.; Zhang, Z.; Wang, W.; Gong, P.; Yang, Q.; Park, C.B.; Li, G. Ultra-fast degradable PBAT/PBS foams of high performance in compression and thermal insulation made from environment-friendly supercritical foaming. *J. Supercrit. Fluids* **2022**, *181*, 105512. [CrossRef]
13. Lourdin, D.; Della Valle, G.; Colonna, P. Influence of amylose content on starch films and foams. *Carbohydr. Polym.* **1995**, *27*, 261–270. [CrossRef]
14. Meimoun, J.; Wiatz, V.; Saint-Loup, R.; Parcq, J.; Favrelle, A.; Bonnet, F.; Zinck, P. Modification of starch by graft copolymerization. *Starch-Stärke* **2018**, *70*, 1600351. [CrossRef]
15. Nabar, Y.; Raquez, J.M.; Dubois, P.; Narayan, R. Production of Starch Foams by Twin-Screw Extrusion: Effect of Maleated Poly(butylene adipate-co-terephthalate) as a Compatibilizer. *Biomacromolecules* **2005**, *6*, 807–817. [CrossRef]
16. Prasong, W.; Ishigami, A.; Thumsorn, S.; Kurose, T.; Ito, H. Improvement of Interlayer Adhesion and Heat Resistance of Biodegradable Ternary Blend Composite 3D Printing. *Polymers* **2021**, *13*, 740. [CrossRef]
17. Sagnelli, D.; Hebelstrup, K.H.; Leroy, E.; Rolland-Sabate, A.; Guilois, S.; Kirkensgaard, J.J.K.; Mortensen, K.; Lourdin, D.; Blennow, A. Plant-crafted starches for bioplastics production. *Carbohydr. Polym.* **2016**, *152*, 398–408. [CrossRef] [PubMed]
18. Thanpitcha, T.; Kritchayanon, N.; Pentrakoon, D.; Pimpan, V. An Initial Study of Starch-g-polystyrene Foam Prepared by a Steaming Process. *J. Met. Mater. Miner.* **2003**, *12*, 1–6.
19. Wu, F.; Misra, M.; Mohanty, A.K. Tailoring the toughness of sustainable polymer blends from biodegradable plastics via morphology transition observed by atomic force microscopy. *Polym. Degrad. Stab.* **2020**, *173*, 109066. [CrossRef]
20. Hu, D.; Xue, K.; Liu, Z.; Xu, Z.; Zhao, L. The essential role of PBS on PBAT foaming under supercritical CO₂ toward green engineering. *J. CO₂ Util.* **2022**, *60*, 101965. [CrossRef]
21. Raquez, J.-M.; Nabar, Y.; Narayan, R.; Dubois, P. In situ compatibilization of maleated thermoplastic starch/polyester melt-blends by reactive extrusion. *Polym. Eng. Sci.* **2008**, *48*, 1747–1754. [CrossRef]
22. Stagner, J.A.; Alves, V.D.; Narayan, R. Application and performance of maleated thermoplastic starch-poly(butylene adipate-co-terephthalate) blends for films. *J. Appl. Polym. Sci.* **2012**, *126*, E135–E142. [CrossRef]
23. Kim, S.J.; Kwak, H.W.; Kwon, S.; Jang, H.; Park, S.I. Characterization of PLA/PBSeT Blends Prepared with Various Hexamethylene Diisocyanate Contents. *Materials* **2021**, *14*, 197. [CrossRef] [PubMed]
24. Nofar, M.; Salehiyan, R.; Ciftci, U.; Jalali, A.; Durmuş, A. Ductility improvements of PLA-based binary and ternary blends with controlled morphology using PBAT, PBSA, and nanoclay. *Compos. Part B Eng.* **2020**, *182*, 107661. [CrossRef]
25. Zhang, J.; Hirschberg, V.; Rodrigue, D. Mechanical fatigue of biodegradable polymers: A study on polylactic acid (PLA), polybutylene succinate (PBS) and polybutylene adipate terephthalate (PBAT). *Int. J. Fatigue* **2022**, *159*, 106798. [CrossRef]
26. Banpean, A.; Takagi, H.; Shimizu, N.; Igarashi, N.; Sakurai, S. Small- and wide-angle X-ray scattering studies on confined crystallization of Poly(ethylene glycol) in Poly(L-lactic acid) spherulite in a PLLA/PEG blend. *Polymer* **2021**, *229*, 123971. [CrossRef]
27. Bijarimi, M.; Ahmad, S.; Rasid, R.; Khushairi, M.A.; Zakir, M. Poly(lactic acid)/Poly(ethylene glycol) blends: Mechanical, thermal and morphological properties. *AIP Conf. Proc.* **2016**, *1096*, 020002. [CrossRef]
28. Hassouna, F.; Raquez, J.-M.; Addiego, F.; Dubois, P.; Toniazzo, V.; Ruch, D. New approach on the development of plasticized polylactide (PLA): Grafting of poly(ethylene glycol) (PEG) via reactive extrusion. *Eur. Polym. J.* **2011**, *47*, 2134–2144. [CrossRef]
29. Hu, Y.; Hu, Y.S.; Topolkarav, V.; Hiltner, A.; Baer, E. Crystallization and phase separation in blends of high stereoregular poly(lactide) with poly(ethylene glycol). *Polymer* **2003**, *44*, 5681–5689. [CrossRef]
30. Martin, O.; Avérous, L. Poly(lactic acid): Plasticization and properties of biodegradable multiphase systems. *Polymer* **2001**, *42*, 6209–6219. [CrossRef]
31. Park, B.-S.; Song, J.C.; Park, D.H.; Yoon, K.-B. PLA/chain-extended PEG blends with improved ductility. *J. Appl. Polym. Sci.* **2012**, *123*, 2360–2367. [CrossRef]
32. Pillin, I.; Montrelay, N.; Grohens, Y. Thermo-mechanical characterization of plasticized PLA: Is the miscibility the only significant factor? *Polymer* **2006**, *47*, 4676–4682. [CrossRef]
33. Taki, K.; Nitta, K.; Kihara, S.-I.; Ohshima, M. CO₂ foaming of poly(ethylene glycol)/polystyrene blends: Relationship of the blend morphology, CO₂ mass transfer, and cellular structure. *J. Appl. Polym. Sci.* **2005**, *97*, 1899–1906. [CrossRef]
34. Zhang, W.; Chen, B.; Zhao, H.; Yu, P.; Fu, D.; Wen, J.; Peng, X. Processing and characterization of supercritical CO₂ batch foamed poly(lactic acid)/poly(ethylene glycol) scaffold for tissue engineering application. *J. Appl. Polym. Sci.* **2013**, *130*, 3066–3073. [CrossRef]
35. Xu, L.; Qian, S.; Zheng, W.; Bai, Y.; Zhao, Y. Formation Mechanism and Tuning for Bimodal Open-Celled Structure of Cellulose Acetate Foams Prepared by Supercritical CO₂ Foaming and Poly(ethylene glycol) Leaching. *Ind. Eng. Chem. Res.* **2018**, *57*, 15690–15696. [CrossRef]

36. Chang, C.J.; Venkatesan, M.; Cho, C.J.; Chung, P.Y.; Chandrasekar, J.; Lee, C.H.; Wang, H.T.; Wong, C.M.; Kuo, C.C. Thermoplastic Starch with Poly(butylene adipate-co-terephthalate) Blends Foamed by Supercritical Carbon Dioxide. *Polymers* **2022**, *14*, 1952. [CrossRef]
37. Dehouche, N.; Idres, C.; Kaci, M.; Zembouai, I.; Bruzard, S. Effects of various surface treatments on Aloe Vera fibers used as reinforcement in poly(3-hydroxybutyrate-co-3-hydroxyhexanoate) (PHBHHx) biocomposites. *Polym. Degrad. Stab.* **2020**, *175*, 109131. [CrossRef]

Disclaimer/Publisher's Note: The statements, opinions and data contained in all publications are solely those of the individual author(s) and contributor(s) and not of MDPI and/or the editor(s). MDPI and/or the editor(s) disclaim responsibility for any injury to people or property resulting from any ideas, methods, instructions or products referred to in the content.

Article

Effect of Microcrystalline Cellulose on the Properties of PBAT/Thermoplastic Starch Biodegradable Film with Chain Extender

Haitao Lang ^{1,†}, Xianlei Chen ^{2,†}, Jiarong Tian ¹, Jing Chen ¹, Mengna Zhou ², Fangfang Lu ² and Shaoping Qian ^{1,*} 

¹ School of Materials Science and Chemical Engineering, Ningbo University, Ningbo 315211, China

² Zhoushan Institute of Calibration and Testing for Quality and Technology Supervision, Zhoushan 316000, China

* Correspondence: qianshaoping@nbu.edu.cn

† These authors contributed equally to this work and should be considered first co-authors.

Abstract: Poly (butylene adipate-co-terephthalate) (PBAT) is a fully biodegradable polymer with toughness and ductility. It is usually compounded with thermoplastic starch (TPS) to balance the cost for manufacturing biodegradable films such as disposable plastic bags. However, blending with TPS reduces valuable tensile strength, which limits the bearing capacity of PBAT film. In this study, microcrystalline cellulose (MCC) was employed as a reinforcement to strengthen the PBAT/TPS biodegradable film. The effect of MCC content on the mechanical, thermal, and morphological properties of the composite film were investigated. The optimal tensile strength and elongation at break reached 5.08 MPa and 230% when 4% MCC was added. The thermal stability and thermal resistance were improved with the addition of MCC; for example, T_{\max} increased by 1 °C and T_{onset} increased by 2–8 °C. Moreover, good compatibility among PBAT, TPS, and MCC can be achieved when the MCC content was below 6%. Consequently, the optimal MCC content was found to be 4%. These results could provide experimental data and method support for preparing high-performance PBAT hybrid films.

Keywords: PBAT; starch; microcrystalline cellulose; composite; biodegradable

Citation: Lang, H.; Chen, X.; Tian, J.; Chen, J.; Zhou, M.; Lu, F.; Qian, S. Effect of Microcrystalline Cellulose on the Properties of PBAT/Thermoplastic Starch Biodegradable Film with Chain Extender. *Polymers* **2022**, *14*, 4517. <https://doi.org/10.3390/polym14214517>

Academic Editor: Paola Scarfato

Received: 11 October 2022

Accepted: 23 October 2022

Published: 25 October 2022

Publisher's Note: MDPI stays neutral with regard to jurisdictional claims in published maps and institutional affiliations.



Copyright: © 2022 by the authors. Licensee MDPI, Basel, Switzerland. This article is an open access article distributed under the terms and conditions of the Creative Commons Attribution (CC BY) license (<https://creativecommons.org/licenses/by/4.0/>).

1. Introduction

Poly (butylene adipate-co-terephthalate) (PBAT) is a copolyester of polybutylene adipate and polybutylene terephthalate, and its mechanical properties are similar to low-density polyethylene. PBAT is the most popular polymer that can be used for biodegradable plastic film bags due to its high elongation, excellent toughness, and good heat resistance [1]. However, high cost and poor tensile strength become obstacles, limiting its wide application. As a consequence, many kinds of fillers have been employed to improve the properties of the PBAT composites, including silane [2], lignin [3], nanoclay [4], calcium carbonate [5], fermented soybeans [6], etc. The tensile strength of the hybrid film can be increased by 30–60%, making it technically comparable to polyethylene (PE) film. Nonetheless, due to the limitation of filler content (usually less than 30% to avoid the excessive degradation of certain performances [7]), the issue of high cost still exists [8]. Strategies for synchronously reducing cost and maintaining the biodegradability of PBAT remain to be further investigated.

Starch is considered as an attractive biodegradable filler for PBAT to cut down the cost. Due to the hydrogen bonding inter- and intra-molecules, natural starch molecules crystallize into microparticles, making it agglomerate and difficult to homodisperse in a PBAT matrix. Consequently, plasticizers (such as water and glycerin [9]) are often employed to prepare thermoplastic starch (TPS), which is much easier to compound with PBAT. Even

so, the weak interfacial compatibility between PBAT and TPS significantly decreases the properties of the composites, especially tensile strength. Thus, the additional amount of starch is usually less than 40% in industrial manufacturing [10]. The extension of a molecule chain and the introduction of high-efficiency reinforcements can improve the mechanical properties of PBAT/TPS composite films, and further increase the TPS additive amount to reduce costs.

Microcrystalline cellulose (MCC) is considered as a desirable reinforcement for improving the mechanical properties of polymer composites because of excellent biodegradability, high strength and low cost [11–14]. Vincenzo Titone et al. [15] found that MCC could congruently embed in the PBAT matrix with a good adhesion so that the particles tripled the elastic modulus of the composites with 20% MCC. Chen et al. [16] investigated the best increase in the tensile strength of TPS film reinforced with 6% MCC. They found that a strong solid hydrogen bonding network between cellulose and TPS was formed. Reis et al. [17] prepared a PBAT/TPS/MCC composite through a two-step method, and found that MCC with a mass fraction below 5% had no significant enhancement effect. In addition, chain extenders such as maleic anhydride [18], polyvinyl alcohol [19], reactive epoxy compatibilizer (L-335A) [1], and tartaric acid [20] were used to improve the interface property of PBAT composites. The commercially available ADR-4386 is widely used to extend the molecular chain of polyesters to increase the properties of biodegradable composites; for example, it has been proven to improve the elongation at a break from 23.5% to 410.3% of PBAT/poly(lactic acid) composites [21]. However, the effect of ADR-4386 in the PBAT/TPS/MCC system still remains to be investigated. In addition, the reinforcement effect of MCC with high TPS contents (>50%) seems unclear as well.

In this study, the effects of MCC and chain-extender in the PBAT/TPS composites were investigated. Different contents of MCC were adopted to fabricate PBAT/TPS/MCC composites by melt-blending and the extrusion method, and the commercially available ADR 4368 was used as chain-extending agent. The surface chemical and morphological characteristics were studied by Fourier transform infrared spectroscopy (FT-IR) and scanning electron microscopy (SEM). The mechanical properties, thermal properties, thermal degradation properties, and crystallization properties of the composites were characterized as well. Based on these results, the optimal usage amount of MCC was gained accordingly. The results of this study could provide theoretical guidance for the preparation and practical application of PBAT composite films.

2. Materials and Methods

2.1. Materials

PBAT (TH801T) was produced by Lanshan Tunhe, Co., Ltd. (Xinjiang, China). The density was 1200–1280 kg/m³ (ISO 1183), and the melt flow rate was 2–5 g/10 min (2.16 kg, 190 °C). MCC (Alfa-A17730) was provided by Sinopharm Chemical Reagent, Co., Ltd. (Shanghai, China), and the particle size was Ca. 50 µm. Wheat starch, produced by Ganzhiyuan Sugar, Co., Ltd. (Nanjing, China), was a food-grade ingredient available in local supermarkets. Glycerin and urea, ACS grade, were used as bought (Aladdin, Shanghai, China). The commercial chain-extending agent (Joncryl-ADR-4368) was provided by BASF SE (Ludwigshafen, Germany), and the molecular weight was 6800. All other reagents and solvents were used as received from the commercial source.

2.2. Preparation of TPS

According to previous work [22], starch, glycerin, and urea were mixed at a weight ratio of 70:25:5. A mixture of 4 g was fed into a WLG10A co-rotating twin screw extruder (Xinshuo Co., Ltd., Shanghai, China) under 120 °C and 100 rpm. The diameter of the screw was 20 mm and the length–diameter ratio was 27:1. Then, the mixture was blended, extruded, and granulated into TPS particles by hand with a size of Ca. 3 mm.

2.3. Preparation of PBAT/TPS/MCC Composites

PBAT, TPS, MCC, and ADR-4368 were weighed in proportions according to Table 1. Then, the mixture was fed into a co-rotating twin screw extruder system (HAAKE PolyLab OS, Karlsruhe, Germany) with a diameter of 20 mm and a length–diameter ratio of 35:1. The temperature zone was set to 120 °C/125 °C/130 °C/140 °C/145 °C/150 °C/150 °C/145 °C/140 °C/125 °C. The rotation speed was set at 100 rpm. After melt-blending, the compounds were extruded to film with a thickness of 0.3–0.5 mm through a cast film die.

Table 1. Experimental formula of PBAT/TPS/MCC composites.

Sample Name	PBAT wt%	TPS wt%	MCC wt%	ADR wt%
0% MCC	40	60	0	0.5
2% MCC	40	58	2	0.5
2% MCC-N	40	58	2	0
4% MCC	40	56	4	0.5
6% MCC	40	54	6	0.5
8% MCC	40	52	8	0.5

Note: The amounts of added components are based on dried weight.

In the investigation of the impact of a chain extender (ADR-4386), the experimental group with 2% MCC was selected as a comparison. During the experiment, the performance representatives of this group can fully reflect the role of chain extenders.

2.4. Tensile Tests

Tensile tests of PBAT/TPS/MCC composite films were performed by a universal testing machine at room temperature (CMT4503, MTS Inc., Shenzheng, China). The films were cut along the extruding direction into dumb-bell-shaped specimen with a length of 50 mm, cross-sectional width of 4.0 mm, and initial gauge length of 30 mm [23]. Five specimens were tested, and the average value was taken for analysis with a settled tensile crosshead rate of 50 mm/min.

2.5. X-ray Diffraction (XRD)

X-ray diffraction patterns of PBAT/TPS/MCC composites were obtained using the Xpert PRO (D8 Advance, Bruker, Karlsruhe, Germany) machine with Cu (k_{α}) radiation ($\lambda = 0.15406$ nm) operating at room temperature, 50 mA and 40 kV. The scanned 2θ region ranged from 5.0° to 60.0° with the rate of 0.01°/s. The relative crystallinity index (CI) was calculated by using Equation (1) [24],

$$CI(\%) = \frac{A_c}{A_t} \times 100 = \frac{A_c}{A_c + A_a} \times 100 \quad (1)$$

where A_c means the crystalline area, A_a means the amorphous area, and A_t means the total area.

2.6. Scanning Electron Microscopy (SEM)

A field emission scanning electron microscope (S-8010, Hitachi, Tokyo, Japan) was used to observe both the surface and the fractured surface of PBAT/TPS/MCC composites. The fractured surface observation sample was collected after tensile test. Before observation, samples were coated with a golden layer. The emission voltage of the electron microscopy was 4.0 kV.

2.7. Fourier Transform Infrared Spectroscopy (FT-IR)

The Thermo Scientific FT-IR (Nicolet6700/870, Nicolet, Rhinelander, WI, USA) was used to examine the surface functional groups of the PBAT/TPS/MCC composites. The scanning wavenumber of 4000–400 cm^{-1} with a 4 cm^{-1} spectral resolution was tested.

Before scanning, samples were ground into powder, and compressed with KBr powder into thin slices. Each sample was scanned 64 times.

2.8. Thermo-Gravimetric Analysis (TGA)

The thermal stability of the PBAT/TPS/MCC composites was determined by a thermo-gravimetric analyzer (STA 2500 Regulus, Netzsch, Selb, Germany). Approximately 10.00 mg of the sample was weighed in a standard alumina crucible and heated from 30 °C to 600 °C at a heating rate of 10 °C/min under a nitrogen atmosphere. An empty crucible was used as a reference.

2.9. Differential Scanning Calorimetry (DSC)

The thermal properties of the composites were tested by DSC (200F3, Netzsch, Selb, Germany). Approximately 10.00 mg samples were heated from room temperature to 180 °C at a rate of 10 °C/min, kept for 3 min, and then cooled down to −60 °C at a rate of 10 °C/min. Subsequently, it was heated again to 180 °C at a rate of 10 °C/min. Nitrogen was used as a protecting and purging gas. The second DSC thermograms were recorded for further evaluation. An empty crucible was used as a reference. The PBAT crystallinity (X_c) was estimated according to the following Equation (2):

$$X_c(\%) = \frac{\Delta H_c}{\Delta H_0 \times X_{PBAT}} \times 100 \quad (2)$$

where ΔH_c refers to the crystallization enthalpy of composites; ΔH_0 refers to the enthalpy value during 100% crystallization of PBAT, which is 114 J/g [25]; X_{PBAT} refers to the weight ratio of PBAT in composites.

3. Results and Discussion

3.1. Mechanical Properties Analysis

The tensile properties including tensile strength, Young's modulus, and elongation at break are tabulated in Table 2, and the typical curves of the stress–strain of different samples are shown in Figure 1. It indicates that the tensile strain tends to be lowered, whereas stress exhibits an enhancement with the increase in MCC content. The tensile strength is enhanced by Ca. 30% (from 4.03 MPa to 5.78 MPa) along with the MCC content increase from 0% to 6%, which obviously suggests that MCC acts as a reinforcement in the composites. Moreover, a steady increase in Young's modulus is noticed as well. It is remarkably improved by Ca. 200% when compared the film with 6% MCC to that without MCC. This is quite different from the effect of MCC in the polylactic acid matrix, which showed decreases in both tensile strength and modulus [15]. This might be contributed to the interaction of MCC with TPS. As we know, TPS is a ductile material with low modulus, whereas MCC exhibits high stiffness, crystallinity, and modulus [26]. More importantly, they have a similar surface functional group. Thus, MCC and TPS are likely to form hydrogen bonds and mechanical interactions when compounding. These analyses corroborate the results of FTIR and the micromorphology analysis.

Table 2. Mechanical properties of PBAT/TPS/MCC composites.

Samples	Tensile Strength (MPa)	Young's Modulus (MPa)	Elongation at Break (%)
0% MCC	4.03 ± 0.13 ^a	10.38 ± 0.3 ^a	556 ± 20 ^a
2% MCC	4.52 ± 0.22 ^b	10.18 ± 0.3 ^a	543 ± 23 ^b
2% MCC-N	4.58 ± 0.21 ^b	15.04 ± 0.4 ^b	303 ± 10 ^c
4% MCC	5.08 ± 0.36 ^c	20.58 ± 0.7 ^c	230 ± 46 ^d
6% MCC	5.78 ± 0.12 ^d	30.78 ± 0.6 ^d	87 ± 45 ^e
8% MCC	5.64 ± 0.24 ^d	34.99 ± 1.5 ^d	78 ± 2 ^e

Note: Data are the mean of replicate determinations ± standard deviation. ^{a,b,c,d,e} The same letter in the same column indicates no significant difference at the $p < 0.05$ level.

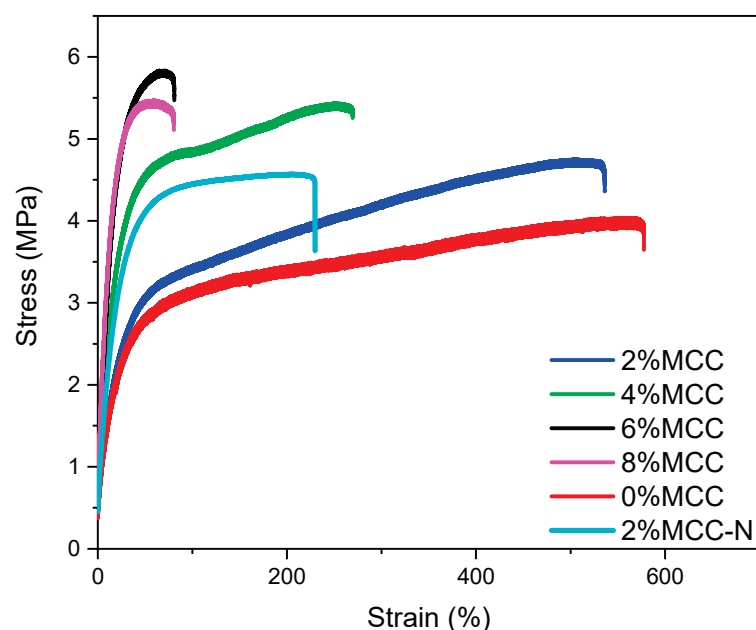


Figure 1. The stress to strain curves of typical film samples with different MCC content.

Notably, the elongation at break of the samples decreases, especially when the MCC content exceeds 4%. Additionally, when the MCC content is 8%, the elongation at break reaches a minimum. Perhaps the aggregation of MCC decreases the continuity of the different phases of the composites, leading to stress concentrations [27]. Furthermore, in the absence of the chain extender case, the tensile elongation of the composites decreases by Ca. 80%, and the tensile strength remains almost unchanged, indicating that a chain extender mainly plays the role of increasing the ductility. This could be attributed to the fact that the chain extender ADR-4368 improves the compatibility of PBAT and TPS. Wei et al. [10] also found that the chain extender had a cross-linking effect on the PBAT and TPS molecular chains, which also helped tensile elongation. However, it is also worth to consider questioning an efficient approach to premix MCC with the granular PBAT and TPS matrices before melt-blending. The optimal content is found to be 4% after a comprehensive comparison of the tensile strength, modulus, and elongation at break.

3.2. XRD Analysis

By the X-ray diffraction technique, the results of the crystalline structures of the composites are shown in Figure 2. Four diffraction angles corresponding to the 2θ at 13.4° , 17.6° , 21.4° , and 23.2° are observed in the PBAT/TPS/MCC composites. The peaks identified at 17.6° and 23.2° are the characteristic diffraction angles of the PBAT crystalline structure. The diffraction angle of cellulose is supposed to be shown at 2θ of 22.5° , which is overlapped by the PBAT crystalline peak [17]. The relative crystallinity index of composites without MCC addition is Ca. 9.7%, which can be increased to Ca. 11% after introducing MCC.

The crystal diffraction peaks of the PBAT/TPS without MCC are very weak and basically present an amorphous dispersion feature. This may be due to the weak crystallization capacity of TPS and PBAT—crystal nuclei can hardly form in the system. Garalde et al. [28] also reported a weak crystal diffraction peak, as the addition of TPS was 40% in the PBAT matrix. With the addition of MCC, PBAT crystallization is facilitated by the heterogeneous nucleation, and the crystalline diffraction peaks at 17.6° and 23.2° are strengthened. This is quite different from the observation of Reis et al. [17]. With the crystallization of PBAT, the tensile strength of the composites gradually increases and the tensile elongations decreases. Interestingly, without the chain extender, the crystal diffraction peaks become small, indicating the weakening of crystallization. Souza et al. [29] also reported an increase in crystallinity once the chain extender was added. It is worth noting that starch itself is

a crystalline particle; generally, there are crystalline diffraction peaks at 13.1° and 19.8° . However, in this study, because of the thermoplastic processing, the typical crystalline diffraction peak ($2\theta = 13.4^\circ$) for starch is too weak to be seen in the composites. Therefore, it can be deduced that starch has been plasticized during thermoplastic processing. This is beneficial to the processing properties of PBAT/TPS composites.

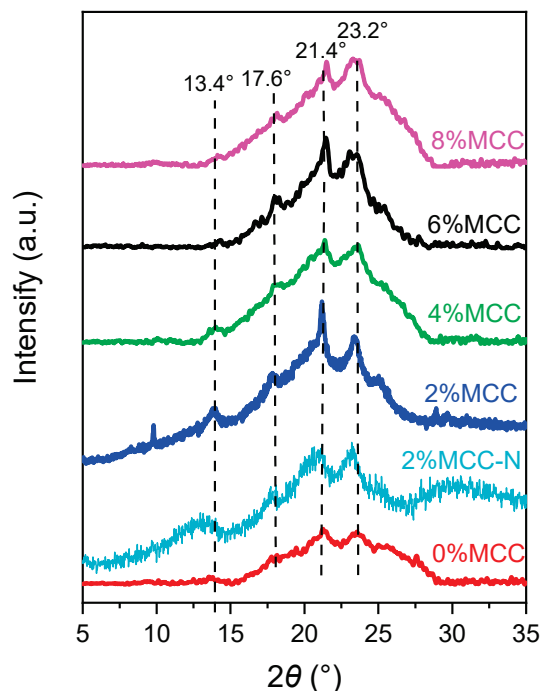


Figure 2. XRD patterns of the samples.

3.3. Micromorphological Analysis

The surface morphology of TPS, PBAT, and MCC are exhibited in Figure 3a–c, and the fractural surface morphology of the composites with 2% and 8% MCC additions are shown in Figure 3d,e. The surfaces of TPS (Figure 3a) and PBAT (Figure 3b) are nearly smooth. Small particle-like features can be noticed on the TPS surface; possibly, this could be partially crystallized starch due to the crystallization of the aging process. This is a common phenomenon in thermoplastic starch materials and it will limit the mechanical properties such as elongation at break and tensile strength. MCC (Figure 3c) exhibits a rod-like structure with rough surface; the length is estimated to be 50–300 μm . The fractural surface of the sample with 2% MCC (Figure 3d) shows typical ductile characteristics with obvious wire drawings, filaments, and a few holes resulting from the slippage of PBAT molecules. No obvious phase separation and agglomeration of MCC particles are found, indicating the good interfacial adhesion between TPS and PBAT as well as the uniform dispersion of MCC. The improvement in tensile ductility could be attributed to the hydrogen-bond interactions between plenty of hydroxyl groups of MCC and the carbonyl groups of PBAT under a suitable proportion [30]. Furthermore, the roughness of the MCC contributes to good mechanical adhesion as well, when the addition is not in excess [31]. On the contrary, the fractural surface of the sample with 8% MCC (Figure 3e) is comparatively flat. Filamentous features can merely be seen. Instead, a great number of cellular orifices that are filled with rod-like MCC and voids between MCC and the polymer matrix can be found. Excessive MCC agglomerates and causes cavitation—this could be considered to be a defect in the composite [15], and could be adopted to explain the decline in mechanical properties, especially the elongation-at-break decrease from 543% to 78%. Giri et al. [32] also reported a similar condition—that the possible interspace formation led to the drastic reduction in the ductility. Crack initiation and propagation were prone to happen with MCC content over 20% in the PBAT matrix.

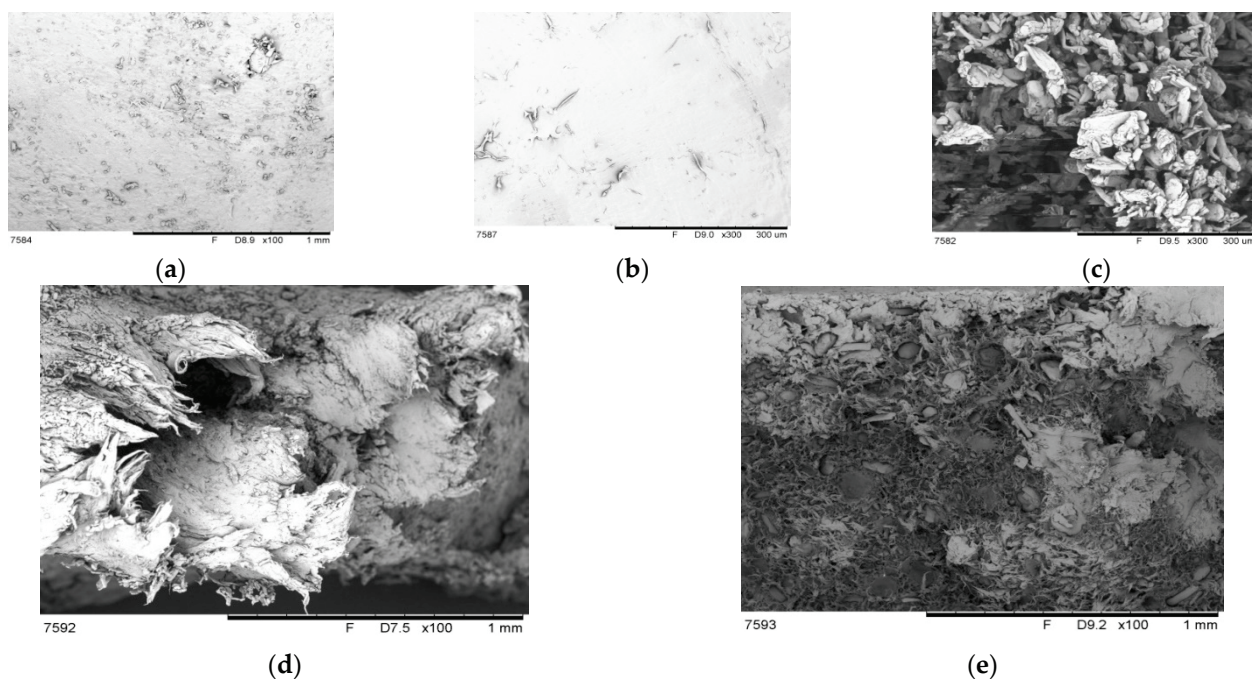


Figure 3. SEM micrographs of the surface of (a) TPS, (b) PBAT, (c) MCC, and the fracture surfaces of the samples with (d) 2% MCC and (e) 8% MCC.

3.4. FT-IR Analysis

Figure 4 shows the surface functional group characteristic of the PBAT/TPS/MCC composites. Characteristic bands associated with the -OH stretching vibration, C-O bending vibration, and -OH bending vibration on the pyranose ring of cellulose and starch are found near 3500 cm^{-1} , 1080 cm^{-1} , and 1101 cm^{-1} , respectively. Additionally, the characteristic bands associated with ether C-O-stretching vibration bands are observed in 1160 cm^{-1} and 930 cm^{-1} . These absorption bands are the evidence of TPS, MCC, and PBAT in the composites. With the increase in MCC content, the absorption bands near 3500 cm^{-1} are enhanced. This could be explained by the increase in the number of -OH and hydrogen bonds. The change in absorption bands reveals the interaction among starch, PBAT, and MCC. However, the difference in the IR spectrum is generally small, which is similar to the findings of Reis et al. [17]. They concluded that there was no chemical bond breakage and formation, and only a physical entanglement between the three phases existed, except for hydrogen bonds. In addition, there are two absorption bands near 2945 cm^{-1} and 2850 cm^{-1} with respect to the asymmetric- and symmetric-stretching vibrations of aliphatic C-H bonds. The C=O-stretching vibration bands of unsaturated polyester are observed at 1714 cm^{-1} , corresponding to the PBAT, which is associated with the in-plane bending vibration of CH_2 bonds near the 1453 cm^{-1} and 1410 cm^{-1} region. According to the analysis from Ning et al. [33], the bands at 728 cm^{-1} can be contributed to the out-of-plane deformation of the benzene ring on the PBAT.

3.5. Thermal Stability Analysis

The thermal stability of the composites is analyzed by thermogravimetry (TGA) and its derivative curves (DTG), as shown in Figure 5a,b. The thermal degradation parameters are listed in Table 3. Dehydration and low-molecule weight compound evaporation occur at $50\text{ }^{\circ}\text{C}$ to $250\text{ }^{\circ}\text{C}$. This is quite commonly seen in the cellulose and starch composites. Subsequently, the low temperature peak from $270\text{ }^{\circ}\text{C}$ to $320\text{ }^{\circ}\text{C}$ can be attributed to the thermal degradation of TPS. The composites with 2% MCC have the lowest T_{onset} value, which is probably due to the good compatibility between TPS/PBAT/MCC. This promotes heat conduction and thermal degradation. Coincidentally, this is consistent with the mechanical result that the composite with 2% MCC has the highest elongation at break. By increasing

the MCC content, a closer interaction between MCC, TPS, and PBAT requires a higher level of energy to break down, thus, presenting a stable thermal degradation performance. The degradation step of PBAT exists between the temperatures from 370 °C to 410 °C; the degradation rate between the composites is found to be similar. It may be that MCC is more compatible with hydrophilic TPS compared with hydrophobic PBAT, and it is inclined to form tough structures with TPS under the action of a chain extender. As a result, the curves at the degradation step of PBAT are close and cannot be separated because they are too near. No separate degradation stage of the cellulose can be found in TGA curves, which indicates that cellulose has been completely covered [34]. Generally, the addition of MCC strengthens the thermal stability of the composites, which is represented by the increase in starting temperature (T_{onset}), the temperature range of thermal degradation, and the temperature of the maximum thermal degradation rate (T_{max}). This could be attributed to MCC promoting the heat transfer in the composites. Importantly, the thermal stability of samples with 4% and 6% MCC are satisfied. Excessive MCC (8%) may inhibit the chain slip because of agglomeration, leading to weaker thermal stabilities. However, its thermal stability is still better than the composites without MCC. Furthermore, the thermal stability decreases without chain extender, according to a lower T_{onset} , T_{max} and a higher rate of thermal decomposition. At last, the residues at 550 °C are the fixation of carbon in TPS and PBAT polymers.

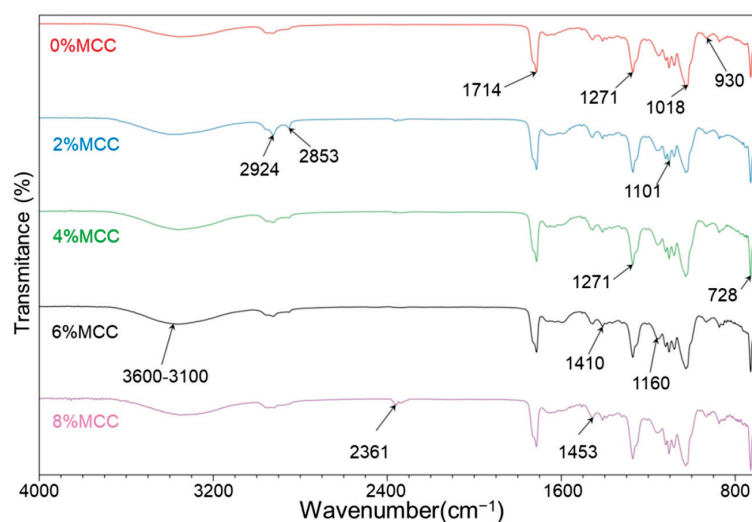


Figure 4. FT-IR spectra of PBAT/TPS/MCC composites.

Table 3. The parameters of the thermogravimetric analysis of PBAT/TPS/MCC composites.

Samples	Peak	T_{onset} (°C)	Temperature Range (°C)	T_{max} (°C)	Mass Loss at 550 °C (%)
0% MCC	1	283.9	283.9–304.7	295.3	94.8
	2	372.3	372.3–407.8	391.9	
2% MCC	1	282.6	282.6–307.0	297.0	97.5
	2	373.3	373.3–405.5	393.9	
2% MCC-N	1	280.5	280.5–318.9	302.4	99.9
	2	374.2	374.2–408.5	393.6	
4% MCC	1	284.3	284.3–308.0	303.0	91.2
	2	374.4	374.4–410.0	393.9	
6% MCC	1	283.8	283.8–308.8	298.1	94.8
	2	372.9	372.9–406.8	394.0	
8% MCC	1	285.4	285.4–306.7	294.9	93.8
	2	376.4	376.4–408.2	394.4	

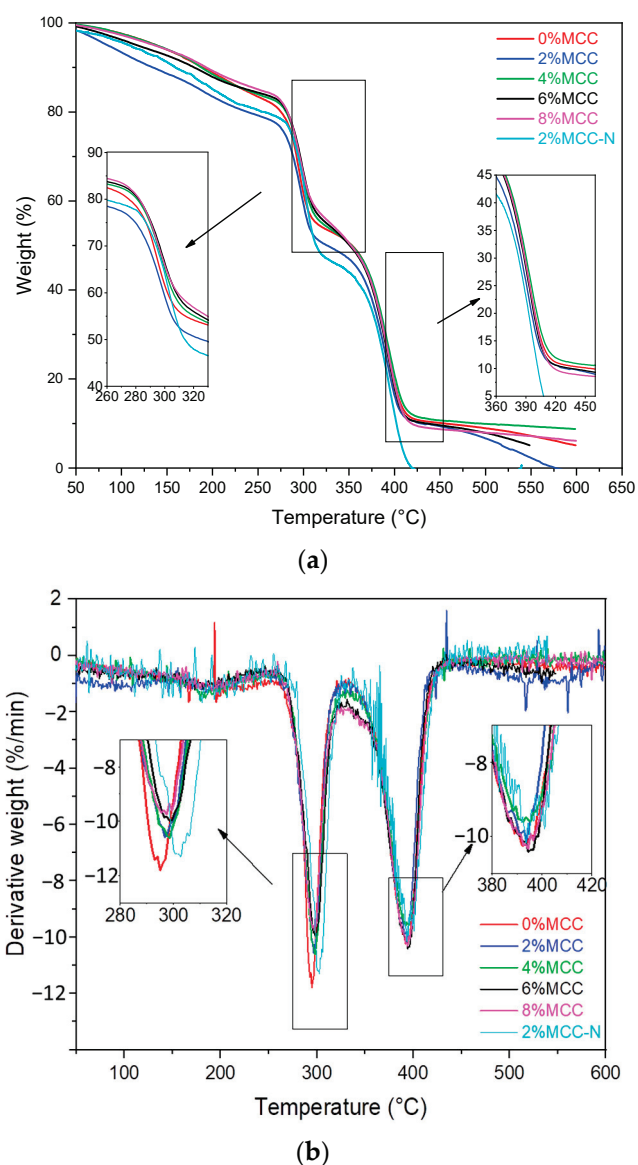


Figure 5. The curves of thermogravimetric analysis (TGA) (a) and DTG (b).

3.6. DSC Analysis

The DSC curves of the composites are shown in Figure 6a,b, corresponding to the crystallization transition and melting transition, respectively. Thermal parameters are listed in Table 4. The crystallization transition of the neat PBAT and the pure TPS commonly occur at Ca. 45 °C and Ca. 99 °C [35], whereas the crystallization transition temperature of the composites is obtained at Ca. 87 °C. Most likely, the reason could be the fact that MCC and ADR-4368 enhance the binding capacity of PBAT and TPS, making the two phases more homogeneous in the composites [36]. However, Garalde et al. reported an increase in T_c from 83 °C to 90.3 °C without the chain extender [28]. Obviously, the T_c and T_m of the composites are decreased, and X_c is increased by the addition of the MCC. With 6% MCC, they decreased from 90.3 °C to 88.6 °C and 147.2 °C to 125.7 °C, respectively. Meanwhile, X_c increases from 9.77% to 11.41%, which is similar to that of the PBAT/TPS composites without the chain extender [1]. This can be interpreted as the nucleating effect of the MCC of the PBAT [37]. Contextually, the same effect has been reflected in Figure 6b. With the 6% MCC addition, the endothermic peaks shift to the high temperature, which can also be attributed to the formation of hydrogen bonds between the matrix and MCC. Furthermore, X_c is almost equal to the CI. This demonstrates that the processing of the

composite has little effect on the crystalline properties of the composite itself, suggesting that the composite has good processability. The addition of MCC shows less influence on the melting transition of the composites.

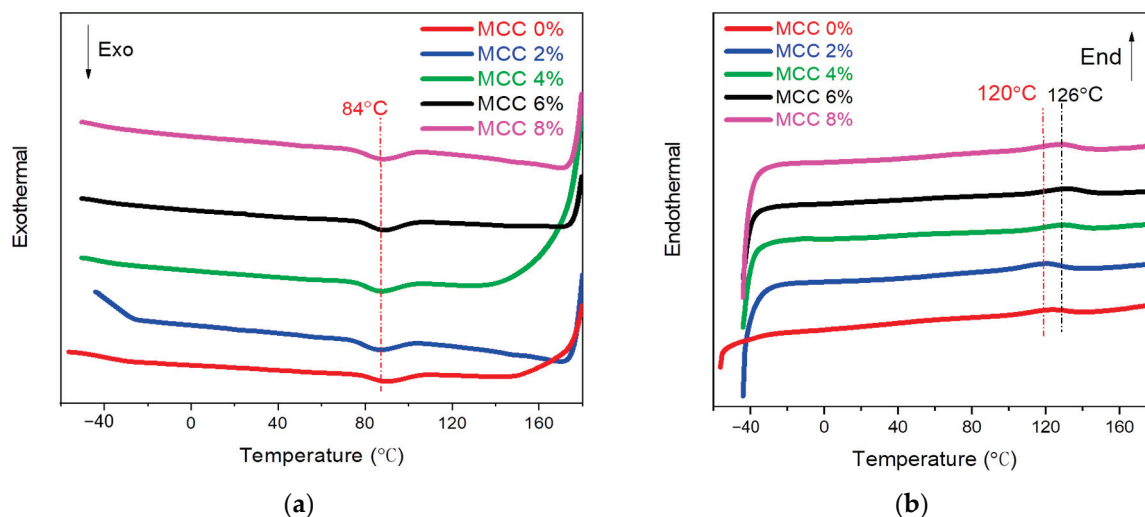


Figure 6. The DSC curves of samples, (a) the cooling round and the second heating round (b).

Table 4. Thermal behaviors of the PBAT/TPS/MCC composites.

Samples	T_c (°C)	ΔH_c (J/g)	X_c (%)	CI (%)	T_m (°C)	ΔH_m (J/g)
0% MCC	90.3	4.456	9.77	9.68	123.0	2.571
2% MCC	86.5	5.133	11.26	11.28	120.2	3.193
4% MCC	87.2	5.373	11.78	11.82	123.2	2.738
6% MCC	88.6	5.183	11.37	11.41	125.7	3.336
8% MCC	88.5	5.354	11.74	11.80	120.6	3.089

3.7. Comparison of PABT/TPS Composites with/without the Chain Extender

The performance comparison of the composites with and without the chain extender is shown in Figure 7. These comparisons are based on the same addition of 2% MCC. Both ductility and thermal properties of the composites with the chain extender achieve a remarkable improvement. Notably, the ductility of the composites is nearly two times higher than that without the chain extender. This seems to be slightly lower than the findings of Li et al. [34]. They found that the elongation of the PLA/PBAT composite was improved by ten-fold after the chain extender was added. As we know, there is a contradiction between the tensile strength and ductility. However, tensile strength remains nearly unchanged as ductility improves, which may contribute to the enhancement effect of the chain extender. Furthermore, a lower decomposition rate indicates an improvement in thermal stability by the addition of the chain extender. It also increases the crystallinity of the composites, which might contribute to the enhancement of mechanical properties. As a result, after taking mechanical and thermal properties into consideration, the addition of a chain extender is a potential strategy to strengthen PBAT/TPS composites.

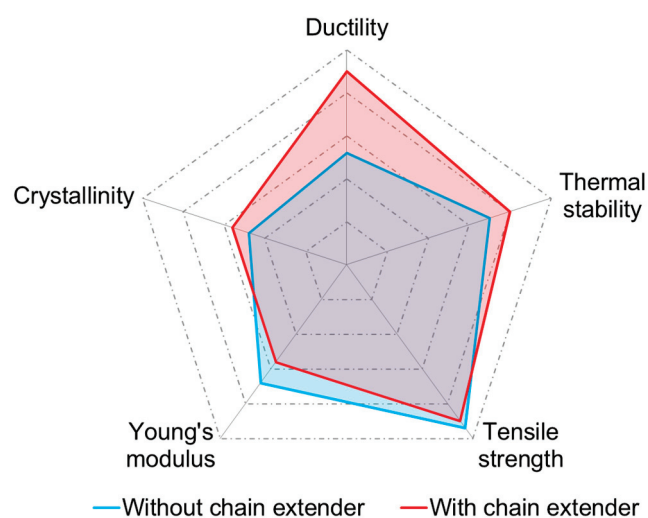


Figure 7. The performance comparison between the no-chain extender and 0.5% chain extender additions.

4. Conclusions

PBAT/TPS/MCC composite films with chain extender ADR-4368 were fabricated by one-step melt-blending and extrusion. The effect of MCC addition and chain extender was comprehensively evaluated. The results of the mechanical properties showed that the addition of MCC and chain extender enhanced the mechanical properties of the composites to a certain extent, and reached saturation when the addition of MCC reached 6%. Meanwhile, the thermal stability in terms of the melting temperature and thermal degradation temperature were improved with the increase in MCC content (<6%). Although excessive MCC had a certain backlash, most properties were better than those without MCC. Moreover, the results of the XRD analysis, FT-IR analysis, and SEM analysis indicated that PBAT, TPS, and MCC, with the action of a chain extender, formed a new tough interaction, which had good compatibility. The chain extender ADR-4368 improved the ductility, thermal stability, tensile strength, and crystallinity of the composites. Finally, the optimal MCC content was found to be 4%. This study provided a simple strategy to obtain low-cost and high-performance biodegradable films, and it would be helpful to expand the application of PBAT composites in the packaging, mulch field, etc.

Author Contributions: H.L. and X.C.: Investigation, Data Curation, Writing—Original Draft, Visualization, Funding. J.T. and J.C.: Investigation, Data Curation, Writing—Original Draft. M.Z. and F.L.: Writing—Review and Editing, Supervision. S.Q.: Writing—Review and Editing, Supervision, Funding. All authors have read and agreed to the published version of the manuscript.

Funding: This work was financially supported by the Fund for Scientific Research in the Public Interest of Ningbo (No. 2021S067, 2022S150), the Foundation of the Department of Education of Zhejiang Province (Y202148281), and the Science and Technology Project of Zhoushan (2022C31068).

Institutional Review Board Statement: Not applicable.

Informed Consent Statement: Not applicable.

Data Availability Statement: Not applicable.

Conflicts of Interest: The authors declare no conflict of interest.

References

- Bai, J.; Pei, H.; Zhou, X.; Xie, X. Reactive compatibilization and properties of low-cost and high-performance PBAT/thermoplastic starch blends. *Eur. Polym. J.* **2021**, *143*, 110198. [CrossRef]
- Qian, S.; Sheng, K. PLA toughened by bamboo cellulose nanowhiskers: Role of silane compatibilization on the PLA bionanocomposite properties. *Compos. Sci. Technol.* **2017**, *148*, 59–69. [CrossRef]

3. Xiong, S.J.; Bo, P.; Zhou, S.J.; Li, M.K.; Yang, S.; Wang, Y.Y.; Shi, Q.T.; Wang, S.F.; Yuan, T.Q.; Sun, R.C. Economically Competitive Biodegradable PBAT/Lignin Composites: Effect of Lignin Methylation and Compatibilizer. *ACS Sustain. Chem. Eng.* **2020**, *8*, 5338–5346. [CrossRef]
4. Fukushima, K.; Wu, M.H.; Bocchini, S.; Rasyida, A.; Yang, M.C. PBAT based nanocomposites for medical and industrial applications. *Mater. Sci. Eng. C Mater. Biol. Appl.* **2012**, *32*, 1331–1351. [CrossRef]
5. Titone, V.; La Mantia, F.P.; Mistretta, M.C. The Effect of Calcium Carbonate on the Photo-Oxidative Behavior of Poly(butylene adipate-co-terephthalate). *Macromol. Mater. Eng.* **2020**, *305*, 2000358. [CrossRef]
6. Mekonnen, T.; Misra, M.; Mohanty, A.K. Fermented Soymeals and Their Reactive Blends with Poly(butylene adipate-co-terephthalate) in Engineering Biodegradable Cast Films for Sustainable Packaging. *ACS Sustain. Chem. Eng.* **2016**, *4*, 782–793. [CrossRef]
7. Mittal, V.; Chaudhry, A.U.; Matsko, N.B. “True” Biocomposites with Biopolyesters and Date Seed Powder: Mechanical, Thermal, and Degradation Properties. *J. Appl. Polym. Sci.* **2014**, *131*, 40816. [CrossRef]
8. Sheng, K.; Zhang, S.; Qian, S.; Fontanillo Lopez, C.A. High-toughness PLA/Bamboo cellulose nanowhiskers bionanocomposite strengthened with silylated ultrafine bamboo-char. *Compos. Part B Eng.* **2019**, *165*, 174–182. [CrossRef]
9. Moscicki, L.; Mitrus, M.; Wojtowicz, A.; Oniszczuk, T.; Rejak, A.; Janssen, L. Application of extrusion-cooking for processing of thermoplastic starch (TPS). *Food Res. Int.* **2012**, *47*, 291–299. [CrossRef]
10. Wei, D.; Wang, H.; Xiao, H.; Zheng, A.; Yang, Y. Morphology and mechanical properties of poly(butylene adipate-co-terephthalate)/potato starch blends in the presence of synthesized reactive compatibilizer or modified poly(butylene adipate-co-terephthalate). *Carbohydr. Polym.* **2015**, *123*, 275–282. [CrossRef]
11. Zhao, T.; Chen, Z.Z.; Lin, X.R.; Ren, Z.Y.; Li, B.; Zhang, Y.Y. Preparation and characterization of microcrystalline cellulose (MCC) from tea waste. *Carbohydr. Polym.* **2018**, *184*, 164–170. [CrossRef] [PubMed]
12. Tian, J.; Cao, Z.; Qian, S.; Xia, Y.; Zhang, J.; Kong, Y.; Sheng, K.; Zhang, Y.; Wan, Y.; Takahashi, J. Improving tensile strength and impact toughness of plasticized poly(lactic acid) biocomposites by incorporating nanofibrillated cellulose. *Nanotechnol. Rev.* **2022**, *11*, 2469–2482. [CrossRef]
13. Xu, L.; Zhao, J.; Qian, S.; Zhu, X.; Takahashi, J. Green-plasticized poly(lactic acid)/nanofibrillated cellulose biocomposites with high strength, good toughness and excellent heat resistance. *Compos. Sci. Technol.* **2021**, *203*, 108613. [CrossRef]
14. Qian, S.; Zhang, H.; Yao, W.; Sheng, K. Effects of bamboo cellulose nanowhisker content on the morphology, crystallization, mechanical, and thermal properties of PLA matrix biocomposites. *Compos. Part B Eng.* **2018**, *133*, 203–209. [CrossRef]
15. Botta, L.; Titone, V.; Mistretta, M.C.; La Mantia, F.P.; Modica, A.; Bruno, M.; Sottile, F.; Lopresti, F. PBAT Based Composites Reinforced with Microcrystalline Cellulose Obtained from Softwood Almond Shells. *Polymers* **2021**, *13*, 2643. [CrossRef]
16. Chen, J.; Wang, X.; Long, Z.; Wang, S.F.; Zhang, J.X.; Wang, L. Preparation and performance of thermoplastic starch and microcrystalline cellulose for packaging composites: Extrusion and hot pressing. *Int. J. Biol. Macromol.* **2020**, *165*, 2295–2302. [CrossRef]
17. Reis, M.O.; Zanela, J.; Olivato, J.; Garcia, P.S.; Yamashita, F.; Grossmann, M.V.E. Microcrystalline Cellulose as Reinforcement in Thermoplastic Starch/Poly(butylene adipate-co-terephthalate) Films. *J. Polym. Environ.* **2014**, *22*, 545–552. [CrossRef]
18. Fourati, Y.; Tarres, Q.; Mutje, P.; Boufi, S. PBAT/thermoplastic starch blends: Effect of compatibilizers on the rheological, mechanical and morphological properties. *Carbohydr. Polym.* **2018**, *199*, 51–57. [CrossRef]
19. Nordqvist, D.; Sanchez-Garcia, M.D.; Hedenqvist, M.S.; Lagaron, J.M. Incorporating Amylopectin in Poly(lactic Acid) by Melt Blending Using Poly(ethylene-co-vinyl Alcohol) as a Thermoplastic Carrier. (I) Morphological Characterization. *J. Appl. Polym. Sci.* **2010**, *115*, 1315–1324. [CrossRef]
20. Zhang, S.; He, Y.; Lin, Z.; Li, J.; Jiang, G. Effects of tartaric acid contents on phase homogeneity, morphology and properties of poly (butylene adipate-co-terephthalate)/thermoplastic starch bio-composites. *Polym. Test.* **2019**, *76*, 385–395. [CrossRef]
21. Li, X.; Yan, X.Y.; Yang, J.; Pan, H.W.; Gao, G.H.; Zhang, H.L.; Dong, L.S. Improvement of compatibility and mechanical properties of the poly(lactic acid)/poly(butylene adipate-co-terephthalate) blends and films by reactive extrusion with chain extender. *Polym. Eng. Sci.* **2018**, *58*, 1868–1878. [CrossRef]
22. Niazi, M.B.K.; Zijlstra, M.; Broekhuis, A.A. Understanding the role of plasticisers in spray-dried starch. *Carbohydr. Polym.* **2013**, *97*, 571–580. [CrossRef] [PubMed]
23. Huang, Y.; Pan, P.; Shan, G.; Bao, Y. Polylactide-b-poly(ethylene-co-butylene)-b-poly(lactide) thermoplastic elastomers: Role of polylactide crystallization and stereocomplexation on microphase separation, mechanical and shape memory properties. *RSC Adv.* **2014**, *4*, 47965–47976. [CrossRef]
24. Müller, C.M.O.; Laurindo, J.B.; Yamashita, F. Effect of nanoclay incorporation method on mechanical and water vapor barrier properties of starch-based films. *Ind. Crop. Prod.* **2011**, *33*, 605–610. [CrossRef]
25. Chivrac, F.; Kadlecova, Z.; Pollet, E.; Averous, L. Aromatic copolyester-based nano-biocomposites: Elaboration, structural characterization and properties. *J. Polym. Environ.* **2006**, *14*, 393–401. [CrossRef]
26. Cheng, Q.; Wang, S.; Rials, T.G. Poly(vinyl alcohol) nanocomposites reinforced with cellulose fibrils isolated by high intensity ultrasonication. *Compos. Part A Appl. Sci. Manuf.* **2009**, *40*, 218–224. [CrossRef]
27. Haafiz, M.K.M.; Hassan, A.; Zakaria, Z.; Inuwa, I.M.; Islam, M.S.; Jawaid, M. Properties of polylactic acid composites reinforced with oil palm biomass microcrystalline cellulose. *Carbohydr. Polym.* **2013**, *98*, 139–145. [CrossRef]

28. Garalde, R.A.; Thipmanee, R.; Jariyasakoolroj, P.; Sane, A. The effects of blend ratio and storage time on thermoplastic starch/poly(butylene adipate-co-terephthalate) films. *Heliyon* **2019**, *5*, e01251. [CrossRef]
29. de Souza, A.G.; Nunes, E.D.D.; Rosa, D.D. Understanding the effect of chain extender on poly(butylene adipate-co-terephthalate) structure. *Iran. Polym. J.* **2019**, *28*, 1035–1044. [CrossRef]
30. Nunes, F.C.; Ribeiro, K.C.; Martini, F.A.; Barrioni, B.R.; Ferreira Santos, J.P.; Carvalho, B.M. PBAT/PLA/cellulose nanocrystals biocomposites compatibilized with polyethylene grafted maleic anhydride (PE-g-MA). *J. Appl. Polym. Sci.* **2021**, *138*, 51342. [CrossRef]
31. Mathew, A.P.; Oksman, K.; Sain, M. Mechanical properties of biodegradable composites from poly lactic acid (PLA) and microcrystalline cellulose (MCC). *J. Appl. Polym. Sci.* **2005**, *97*, 2014–2025. [CrossRef]
32. Giri, J.; Lach, R.; Le, H.H.; Grellmann, W.; Saiter, J.M.; Henning, S.; Radusch, H.J.; Adhikari, R. Structural, thermal and mechanical properties of composites of poly(butylene adipate-co-terephthalate) with wheat straw microcrystalline cellulose. *Polym. Bull.* **2021**, *78*, 4779–4795. [CrossRef]
33. Ning, W.; Jiugao, Y.; Xiaofei, M.; Ying, W. The influence of citric acid on the properties of thermoplastic starch/linear low-density polyethylene blends. *Carbohydr. Polym.* **2007**, *67*, 446–453. [CrossRef]
34. Cao, X.D.; Habibi, Y.; Lucia, L.A. One-pot polymerization, surface grafting, and processing of waterborne polyurethane-cellulose nanocrystal nanocomposites. *J. Mater. Chem.* **2009**, *19*, 7137–7145. [CrossRef]
35. Liu, W.; Liu, S.; Wang, Z.; Dai, B.; Liu, J.; Chen, Y.; Zeng, G.; He, Y.; Liu, Y.; Liu, R. Preparation and characterization of reinforced starch-based composites with compatibilizer by simple extrusion. *Carbohydr. Polym.* **2019**, *223*, 115122. [CrossRef]
36. Akrami, M.; Ghasemi, I.; Azizi, H.; Karrabi, M.; Seyedabadi, M. A new approach in compatibilization of the poly(lactic acid)/thermoplastic starch (PLA/TPS) blends. *Carbohydr. Polym.* **2016**, *144*, 254–262. [CrossRef]
37. Koschek, K. Design of natural fiber composites utilizing interfacial crystallinity and affinity. *Compos. Part A Appl. Sci. Manuf.* **2015**, *69*, 21–29. [CrossRef]

Article

Characterisation of Nanoclay and Spelt Husk Microfiller-Modified Polypropylene Composites

Madara Žiganova ^{1,*} , Remo Merijs-Meri ¹ , Jānis Zicāns ¹, Tatjana Ivanova ¹, Ivan Bochkov ¹, Mārtiņš Kalniņš ¹, Andrzej K. Błędzki ² and Paulius P. Danilovas ³

¹ Institute of Polymer Materials, Faculty of Materials Science and Applied Chemistry, Riga Technical University, 3 Paula Valdena Street, LV-1048 Riga, Latvia

² Institute of Materials Science, West Pomeranian University of Technology, Department of Materials Engineering, 19 Piastów Avenue, 70310 Szczecin, Poland

³ Polymer Competence Center, Gradauciznos k. 7, LT-60430 Raseiniu R., Lithuania

* Correspondence: madara.ziganova@rtu.lv; Tel.: +37-167-089-2525

Abstract: Current research is devoted to the investigation of spelt husk (SH) and nanoclay-modified compatibilised polypropylene (PP) binary and ternary composites for injection-moulding applications. PP composites were obtained using twin-screw extrusion. The content of mechanically milled SH microfiller with aspect ratio within 2 and 6 was fixed at 40 wt.%, whereas the amount of nanoclay functional filler in the polypropylene matrix was changed in the range from 0.5 to 5 wt.%. Nanoclay filler was introduced in the polypropylene matrix either in the form of nanoclay powder (C) or as a masterbatch (M). Regular distribution of the clay nanofiller within the polymer matrix has been observed, disregarding its form and concentration. The effects of the individual or combined addition of SH microreinforcement and nanoclay fillers on the rheological, mechanical, calorimetric, and thermal properties of the developed PP composites were investigated. It is revealed that the addition of the nanoclay fillers insignificantly influences the viscosity of both PP nanocomposites and hybrid composites with SH. Additionally, for PP nanocomposites, remarkable increases in tensile and flexural modules and strength are observed by maintaining considerable ultimate deformations, mainly in the case of M-containing systems. Concomitantly, because of the addition of the nanoclay filler, the improvement in thermal stability of PP nanocomposites and PP hybrid composites with SH is observed. As a result of SH addition, considerable increases in tensile and flexural modules are also observed. Results of the research demonstrate the potential of the use of natural materials (agricultural residues and clay minerals) for the development of PP composites with increased stiffness and thermal properties.

Keywords: reinforcements; mechanical properties; thermal properties; biobased polymer composites; polymer modification

Citation: Žiganova, M.; Merijs-Meri, R.; Zicāns, J.; Ivanova, T.; Bochkov, I.; Kalniņš, M.; Błędzki, A.K.; Danilovas, P.P. Characterisation of Nanoclay and Spelt Husk Microfiller-Modified Polypropylene Composites. *Polymers* **2022**, *14*, 4332. <https://doi.org/10.3390/polym14204332>

Academic Editors: Somen K. Bhudolia and Sunil Chandrakant Joshi

Received: 8 September 2022

Accepted: 4 October 2022

Published: 14 October 2022

Publisher's Note: MDPI stays neutral with regard to jurisdictional claims in published maps and institutional affiliations.



Copyright: © 2022 by the authors. Licensee MDPI, Basel, Switzerland. This article is an open access article distributed under the terms and conditions of the Creative Commons Attribution (CC BY) license (<https://creativecommons.org/licenses/by/4.0/>).

1. Introduction

The current demand for environmentally friendly materials makes researchers and commercialists focus on alternate options to synthetic materials, particularly polymers, which are commonly derived from fossil sources. Over past decades, polymers have replaced many conventional materials such as metals, glass, and wood in various applications starting from low-cost consumer articles and ending with high-tech customized products for transport, construction, and energy sectors. In transport and construction sector applications, polymers are often used as matrices of composite materials that meet the demand for high-performance materials with increased mechanical, thermal, and other valuable properties. Increased use of polymers and polymer-based materials in almost every branch of the national economy has led to a generation of a great amount of post-consumer polymer waste, particularly originating from sources of short-term applications

such as packaging and disposables. Nevertheless, the use of polymer-based products in durable construction and transport applications represents a delayed threat of generating polymer waste, as these durable materials tend to appear in the waste stream several years after the start of their application. Consequently, in the design of new products, several aspects should be taken into account, meeting the demands of environmental friendliness, cost efficiency, technological prevalence over the existing materials, and market viability. Considering the case of durable products, increased environmental friendliness may be ensured by developing polymer-based composites, which are reinforced with natural fibres, while only limited biodegradability in a specified environment is accepted in order not to compromise the longevity of the product. Cost efficiency is usually ensured by developing polymer composites based on low-cost recycled or waste products, such as postconsumer polymers, biomass waste, etc. Technological prevalence is achieved by ensuring sufficient interaction between the components of the developed polymer composite as well as by modifying the polymer matrix with synergistically interacting and mutually completing ingredients. Market viability, in turn, is largely dependent on environmental awareness and the customers' willingness to pay, even if the proposed product is more expensive than its environmentally less friendly counterpart. These aspects were based on the current research on the compatibilized polypropylene (PP)-based hybrid composites reinforced with grain husk-derived lignocellulosic microfiller and nanoclay. According to the recent review by Yashas Gowda et al. [1], PP is one of the most widely used matrices for the development of natural-fibre-reinforced polymer composites because of its recyclability, moderate processing temperatures, as well as relatively high mechanical properties. Considerable increase in mechanical properties, particularly modulus, tensile, and flexural strength, has been reported, especially in the case of compatibilized systems [2]. Various approaches have been used to increase compatibility between nonpolar PP matrix and highly polar natural microfibres, including fibre pretreatment by physical [3,4] or chemical [5,6] means, as well as the addition of a separate compatibiliser [7]. Although various chemical compatibilisers have been used to increase interfacial adhesion between PP matrix and natural fibres, with respect to cost/performance ratio, the maleic anhydride groups containing compounds have shown the greatest efficiency [8]. Consequently, maleic-anhydride-grafted PP copolymer has been chosen as the compatibiliser also in the current research.

With respect to natural fibre reinforcement, a great variety of lignocellulosic materials have been used to enhance the properties of PP and other polymer composites [9]. Wood flour is an abundant, low-cost lignocellulosic material that has been used for years as a reinforcement of polypropylene, primarily in an injection-moulded product market. The amount of natural fibre was chosen by considering the limitations of injection moulding. According to the literature, the amount of natural fibres in the thermoplastic polymer composites is usually limited to ca. 40–45 wt.% [10,11], while at higher reinforcements content, the quality of the injection-moulded products may be reduced, and the configuration complexity is limited. The residue of crop farming is another waste source of lignocellulosic materials. An important advantage of agricultural waste-derived fillers is their availability and annual renewability. According to estimates [12], wheat, rice and barley straw, corn stover, sorghum stalks, coconut husks, sugarcane bagasse, and pineapple and banana leaves are among the major lignocellulosic agricultural residues. Rice husks are probably the most widely used agricultural residue for the development of bio-based polymer composites because of their abundance as well as some specific properties, such as intrinsic SiO₂ content, which lead to reduced moisture sensitivity [12,13]. Bledzki et al. [14,15] considered rice, rye, and wheat husks as potential alternative fillers for softwood fibre in bio-based PP composites, demonstrating better deformability and increased impact strength. Similarly, in our previous research, it was demonstrated that the addition of either mechanically milled or steam-explosion-treated oat or spelt husk flat microfibres allows more than a twofold increase in the modulus of elasticity, as well as an improvement in tensile and flexural strength of PP composites in comparison with the neat polymer matrix. In contrast,

the ultimate elongation of the grain husk microfiller-containing systems was larger than that of the wood flour filler-modified counterpart [16].

Natural-fibre-reinforced polymer composites unfortunately also have certain drawbacks, for example, moisture and thermal sensitivity. Consequently, to reduce the negative effects of moisture uptake and thermal degradation during processing, adding an extra additive should be considered. Layered silicates, such as montmorillonite nanoclay, offer a high surface-to-volume area, a high aspect ratio of monolayers (as high as 448 in the case of montmorillonite [17]), high stiffness (178 GPa [18]), and impermeability to gases and solvent vapours [19]. This makes montmorillonite nanoclay suitable for increasing mechanical and thermal barriers and other properties of polymers. In order to increase compatibility between polar montmorillonite nanoclay particles and nonpolar polypropylene matrix, a variety of approaches have been used, based on both organofunctionalization of the mineral filler and introduction of customized compatibiliser in the composite. Functionalisation of montmorillonite particles is based on ion exchange reaction to replace originally occurring inorganic cations in the interlaminar space of the silicate mineral with low- or high-molecular organic surfactants, leading to an increase in the distance between the clay monolayers. This aids penetration of polymer chains into the clay interlaminar space, facilitating further separation of nanoplatelets and yielding intercalated or even exfoliated structures under applied shear stresses during the manufacturing of polymer nanocomposites. In addition to the organomodification of nanoclay, customized compatibiliser is another common approach for improving dispersibility and increasing interaction between montmorillonite nanoclay and polypropylene matrix. Although various interfacial agents have been used, including silane (mostly trialkoxysilanes) [20], titanate, and zirconate coupling agents [21,22], maleic-anhydride-grafted polypropylene still demonstrates remarkable technological efficiency at reasonable costs.

As previously mentioned, increased attention has been paid recently to the development of environmentally friendly hybrid composites containing polypropylene matrix, lignocellulosic reinforcement, and clay nanofiller. In recent comprehensive reviews on natural-fibre and nanoclay-reinforced polymer hybrid composites [19,23], modifications of polypropylene simultaneously with almond shell flour and organically modified montmorillonite [24], wood fibre and nanoclay [25], poplar sawdust and nanoclay [26], wood flour and nanoclay [27,28], pine cone fibres and nanoclay [29], reed fibres and nanoclay [30], bagasse and nanoclay [31], coir fibre, wood fibre, and montmorillonite [32], and carbon fibres, glass fibres, montmorillonite and wood fibre [33] have been demonstrated. In these research works, an increase in mechanical (particularly stiffness) and a decrease in water sensitivity, along with the addition of nanoclay, are generally demonstrated. At the same time, the increase in the mentioned properties in some cases is rather moderate; additionally, a significant increase in thermal properties is observed to a considerably lesser extent. Analysis of rheological properties of natural fibre and nanoclay-modified polypropylene hybrid composites is also not sufficiently performed. Consequently, only a limited number of investigations exists related to grain husk microfillers and nanoclay-modified polypropylene hybrid composites. Therefore, the current research analyzes how the addition of locally obtained spelt husk microreinforcements, as well as montmorillonite nanoclay, affects the rheological, thermal, and mechanical properties of polypropylene. It is expected that the use of a simple melt mixing method for the development of PP composites with SH and its hybrid composites with nanoclay will promote the utilization of agricultural residues (grain husk) for the development of value-added composites with improved stiffness and thermal stability. Furthermore, it is expected that this approach could be further extended to recycled polyolefin matrices.

2. Materials and Methods

2.1. Materials

Injection-moulding-grade polypropylene homopolymer (PP, *Moplen* HP400R, Bassel Orlen Co., Płock, Warsaw, Poland) was used as a matrix. This homopolymer exhibits good

stiffness and high fluidity (MFR = 25 (230 °C/2.16 kg), necessary for injection-moulding applications. Polypropylene-graft-maleic anhydride (PPgMA, Clariant Co., Licocene PP MA 6452, Muttentz, Switzerland) in the amount of 3.3 wt.% in relation to the matrix was used as a coupling agent between the nonpolar matrix and polar lignocellulosic fibres. Spelt husks (SH, Amilina AB Co., Panevėžys, Lithuania) microfiller used as lignocellulosic reinforcement was obtained by mechanical milling. Two types of organoclays containing fillers, neat nanoclay (C, Nanomer I.44P, Nanocor Co., Hoffman Estates, IL, USA), and organoclay masterbatch (M, Masterbatch I.44P, Nanocor Co., Hoffman Estates, IL, USA), were used as co-modifiers. A visual summary of all the raw materials is shown in Figure 1, along with their main physical characteristics.

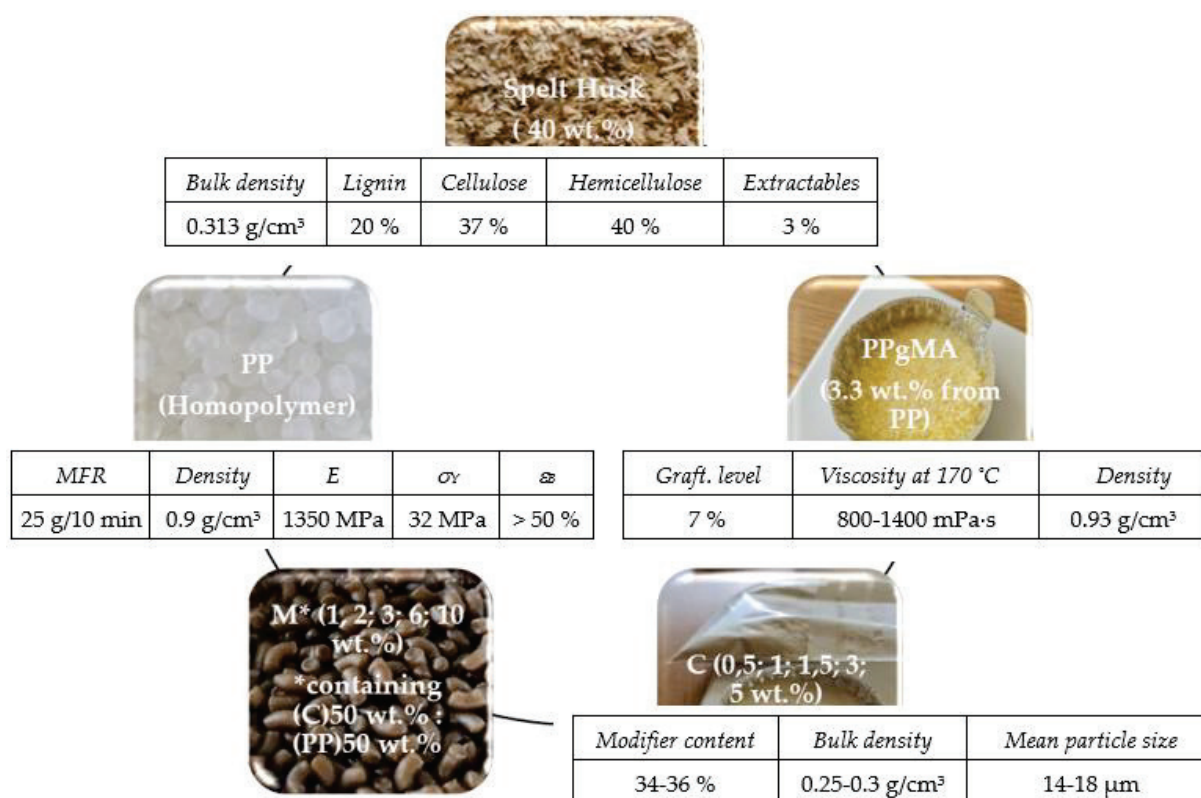


Figure 1. Schematic presentation of raw materials used for research.

2.2. Preparation of the Composites

Before obtaining the bio-based composites, raw SH was mechanically sieved through 3 mm and 2 mm sieves to remove coarse impurities on the one hand and dust and grain residues on the other hand. Thus, isolated SH were ground at 700 rpm using Retsch (Retsch GmbH, Haan, Germany) cutting mill SM300 with a 0.25 mm sieve. Sieve analysis of the milled SH was performed using pneumatic sieve shaker LPzB-2e (Multiserv-Morek Jan Morek, Brzeźnica, Poland) equipped with a number of sieves within the following size range: 0.05 mm–1.0 mm. Considering that in the case of injection moulding of the investigated composites considerable rise in viscosity is expected, the amount of SH in PP composites was fixed to 40 wt.%, not exceeding the 45 wt.% limit accepted by the industry [10,11]. In the case of M and C, the maximum concentration in the PP matrix was limited to 5 wt.% in accordance with the manufacturer’s specifications. It is known that at higher nanofiller content, increased agglomeration may be observed.

Before further melt processing, the milled SH microfillers were dried overnight in an oven at 60 °C. The organoclay containing fillers were dried at 60 °C in a vacuum oven for 3–4 h.

SH microfiller and nanostructured organoclays at certain ratios, as shown in Table 1, were compounded with PP matrix in the presence of PPgMA compatibiliser using Thermo Electron Corporation (now Thermo Fischer Scientific Inc., Waltham, MA, USA) twin-screw co-rotating extruder PRISM TSE 16 at the screw rotation speed of 40 rpm and the following temperature profile over the 5 heating zones: 170–175–180–185–190 (die) °C. The extrudates obtained at the above-mentioned compounding conditions were cooled in a water bath and pelletized. Thus, obtained pellets were dried in a vacuum oven for 4 h under 80 °C before further processing by injection moulding using an injection-moulding machine Minijector 55 (Miniature Plastic Molding, Farmington Hills, MI, USA) at the following temperatures of the barrel heating zones: 165–190–200 (die) °C. Dimensions of injection-moulded flexural test bars were 80 mm × 10 mm × 4 mm, in accordance with EN ISO 178, whereas the dimensions of tensile dog-bone test specimens were in accordance with EN ISO 527-2 (Type 5A).

Table 1. Codes and composition of the composites.

Code	PP (wt.%)	PPgMA (wt.%)	C (wt.%)	M (wt.%)	SH (wt.%)
PP	100	-	-	-	-
PPSH	56.7	3.3	-	-	40
PP0.5C	96.2	3.3	0.5	-	40
PP0.5M	95.7	3.3	-	1	40
PP1C	95.7	3.3	1	-	40
PP1M	94.7	3.3	-	2	40
PP1.5C	95.2	3.3	1.5	-	40
PP1.5M	93.7	3.3	-	3	40
PP 3C	93.7	3.3	3	-	40
PP 3M	90.7	3.3	-	6	40
PP5C	91.7	3.3	5	-	40
PP 1C SH	55.7	3.3	1	-	40
PP1M SH	54.7	3.3	-	2	40
PP3C SH	53.7	3.3	3	-	40
PP3M SH	50.7	3.3	-	6	40

2.3. Characterization of the Composites

2.3.1. Light Microscopy

Inspection of the isolated fractions of sieve analysis of SH was performed by LEICA optical microscope Leica DM RM (Leica Microsystems GmbH, Wetzlar, Germany) at 5× magnification by performing at least 20 length-to-width measurements per individual microfiller particle. For shape analysis of SH microparticles open-source image analysis tool Fiji (Fiji is just ImageJ, ImageJ, Eliceiri/LOCI group at the University of Wisconsin-Madison, Jug group at Human Technopole in Milan, and Tomancak lab at the MPI-CBG in Dresden) was used.

2.3.2. Scanning Electron Microscopic Analysis (SEM)

Morphology was studied using Mira\LMU field emission scanning electron microscope (TESCAN a.s., Brno, Czechia), operated at 15 kV and magnification of 5000. The investigated polymer nanocomposite test specimens for SEM measurements were obtained by breaking rectangular test bars cooled in liquid nitrogen in order to obtain a brittle fracture surface. The samples were sputter-coated with gold using an Emitech K550X sputter coating unit (Quorum Technologies Ltd., Lewes, United Kingdom).

2.3.3. Fourier Transform Infrared Spectroscopy (FTIR)

The spectra were obtained by Nicolet 6700 spectrometer (Thermo Fisher Scientific Inc., Waltham, MA, USA) with the Attenuated Total Reflectance (ATR) technique. All the spectra were recorded in the range 650–4000 cm⁻¹ with a resolution of 4 cm⁻¹.

2.3.4. Rheological Tests—Capillary Rheometer

Visco-elastic properties in melt state at 190 °C were determined using Malvern capillary rheometer RH7 (Malvern Panalytical Ltd, Malvern, Worcestershire, UK). Rheological behaviour was tested at 7 different shear rates, changed stepwise from 120 s⁻¹ to 12,000 s⁻¹. During the experiment, shear viscosity μ , shear stress τ , and flow index n within the mentioned shear rate γ range were determined. The procedure was repeated at least three times for each material tested.

2.3.5. Differential Scanning Calorimetry

The melting and crystallization behaviour of the investigated composites was evaluated using differential scanning calorimeter DSC 1/200W (Mettler Toledo, Greifensee, Switzerland). The specimen of approximately 10 mg was sealed in an aluminium pan and subjected to the following temperature cycles: (1) heating from 25 °C to 200 °C at a rate of 10 °C/min and holding at the corresponding target temperature for 5 min, (2) cooling to 25 °C at a rate of 10 °C/min and holding at the corresponding target temperature for 5 min, followed by (3) second heating from 25 °C to 200 °C at a rate of 10 °C/min. The DSC measurements were performed underneath a nitrogen atmosphere.

Crystallinity (X_c) of the PP composites and hybrid composites was calculated using the following equation:

$$X_c = \frac{\Delta H_c}{\Delta H_m^0(1 - W)} \times 100\% \quad (1)$$

where ΔH_c is the melting/crystallization enthalpy of the measured composite sample, ΔH_m^0 is the theoretical melting enthalpy of PP crystal, assumed as 190 J/g, and W is the weight fraction of the additives (nanoclay and spelt husks).

2.3.6. Thermogravimetric Analysis

The thermal stability of the investigated composites was analyzed using thermogravimetric analyzer TGA1/SF (Mettler Toledo, Greifensee, Switzerland). Specimens of approximately 10 mg were heated from ambient temperature to 800 °C at a heating rate of 10 °C/min under an inert atmosphere (nitrogen gas flow). The material weight loss was calculated using the original software following the ASTM D3850.

2.3.7. Flexural Test

Stress–strain characteristics of the studied compositions in bending were determined using universal material testing machine BDO—FB020 TN (Zwick Roell Group, Ulm, Germany) in accordance with EN ISO 178 at a deformation speed of 1 mm/min. Flexural modulus E_L , maximum flexural stress σ_{ML} , and corresponding relative deformation ε_{ML} were analysed. Demonstrated values represent the averaged results of the measurements performed on 10 test specimens for each type of composite material.

2.3.8. Tensile Test

Tensile stress–strain characteristics of the compositions were determined at a temperature of 20 °C using material testing equipment BDO—FB020TN (Zwick Roell Group, Ulm, Germany) equipped with pneumatic grips in accordance with EN ISO 527. Type 5A test specimens were stretched at a constant deformation speed of 50 mm/min. Tensile modulus E , stress at break σ_B , relative elongation at break ε_B , yield stress σ_y , and the relative elongation at yield ε_y whenever appropriate were analysed. Demonstrated values represent the averaged results of the measurements performed on 10 test specimens for each type of composite material.

3. Results and Discussion

3.1. Light microscopy

Light microscopy images of the used lignocellulosic microfiller particles are demonstrated in Figure 2, representing main size fractions of SH obtained after milling.

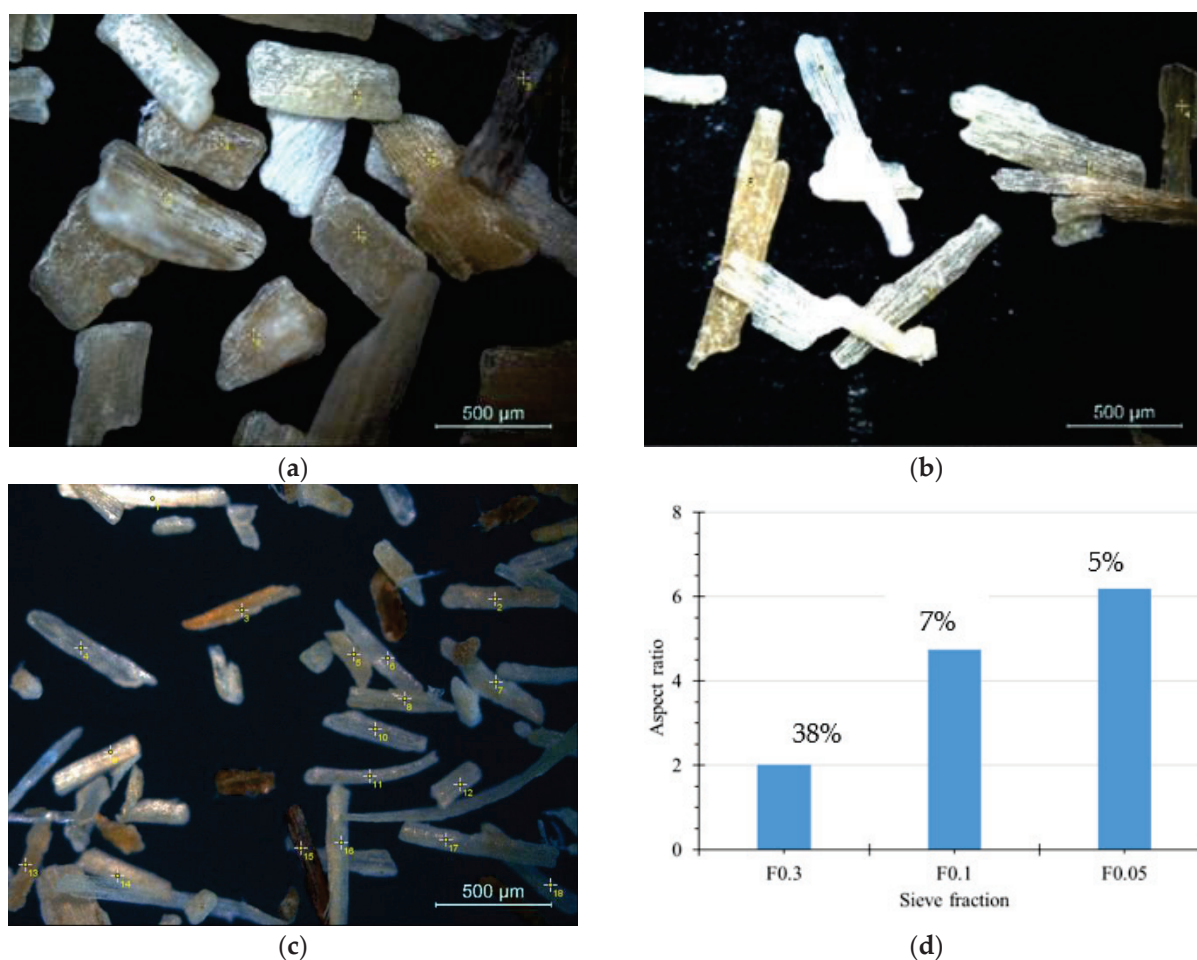


Figure 2. Light microscopy images of SH after sieving through 0.5 mm (a), 0.3 mm (b), and 0.1 mm (c); size sieves and calculated average aspect ratios of the respective sieve fractions and their per cent amounts (d).

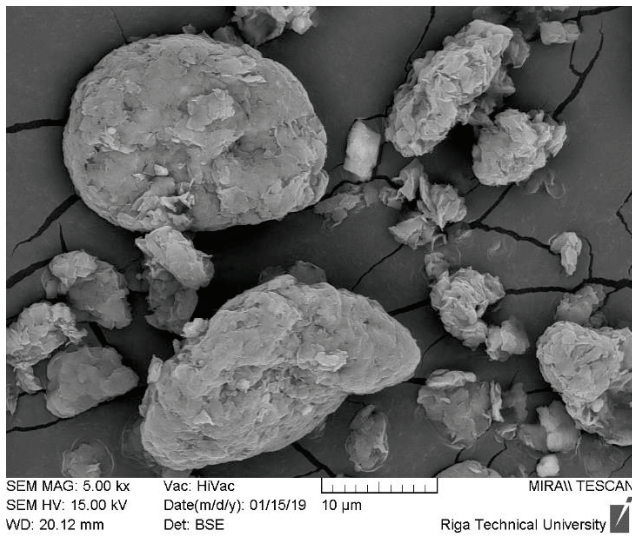
As one can see, milling of SH flat microfibres at 700 rpm yields micron-sized reinforcements with a rather broad spectrum of particle sizes and aspect ratios. Thus, after milling average dimensions of SH flat microfibres have been considerably reduced from the initial ca. 10 mm in length and ca. 3 mm in width. Although lateral and axial dimensions of the used SH microparticles are reduced because of milling, it is revealed that the microfibrillar morphology of SH microfibre reinforcement is maintained at each of the isolated fractions. Along with changes in its dimensions, considerable changes in the aspect ratio of the used SH flat microfibres are observed. Considering the obtained amounts of the separate sieve fractions, it was concluded that the further development of PP composites uses SH microfibres in size range of 0.05–0.3, building up more than 50% of the total amount of the sieved material.

3.2. SEM

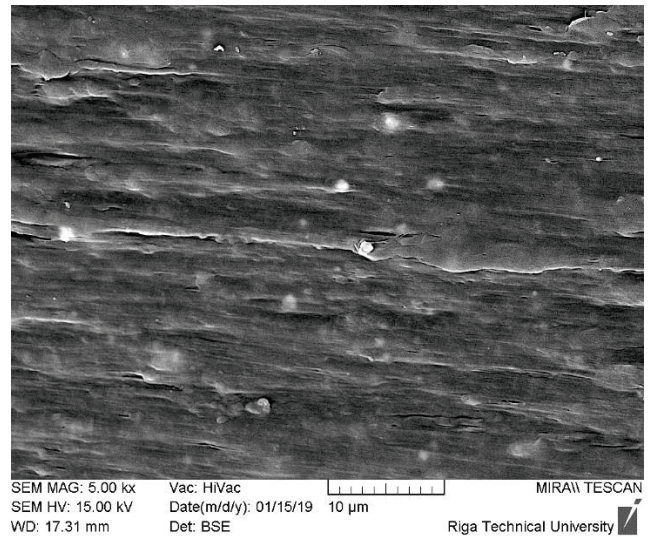
The surface morphology of C and M used for the development of PP nanocomposites is depicted in Figure 3. Before melt compounding with polymer matrix, C is in the form of large agglomerates with great variety in particle sizes. In Figure 3a, one can see that the agglomerates consist of a great number of plate-like C particles, which need to be separated during melt compounding. In the case of commercially marketed M (Figure 3b), one can observe that these clay particles are evenly distributed within the PP matrix, disregarding its high content (50 wt.%). Bright spots in the SEM images may be attributed to electron

backscattering from the lateral surfaces of clay nanoparticles. In Figure 3c, the smooth surface morphology of a neat PP matrix is demonstrated.

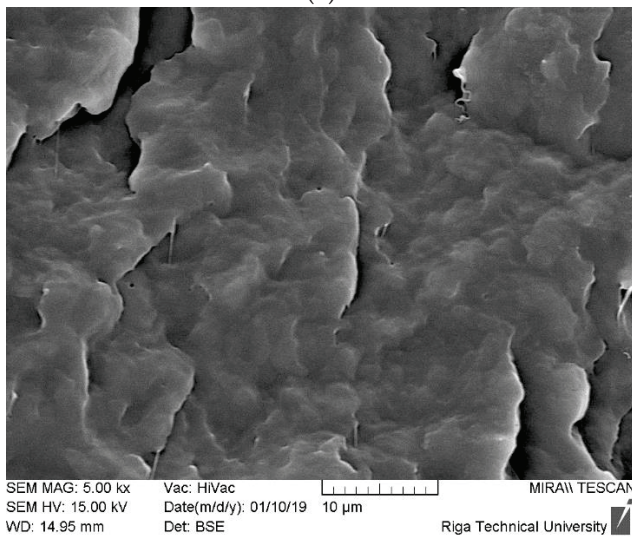
The effect of nanoclay addition on the investigated melt compounded PP composites is demonstrated in Figure 3d–f. As one can see, regular distribution of the nanofiller within the PP matrix is observed, disregarding the type of the used particulate modifier (C or M) or its concentration in the polymer (0.5 wt.% or 5 wt.%). This testifies that the chosen processing conditions were sufficient to ensure regular distribution of both C and M within the used PP homopolymer matrix.



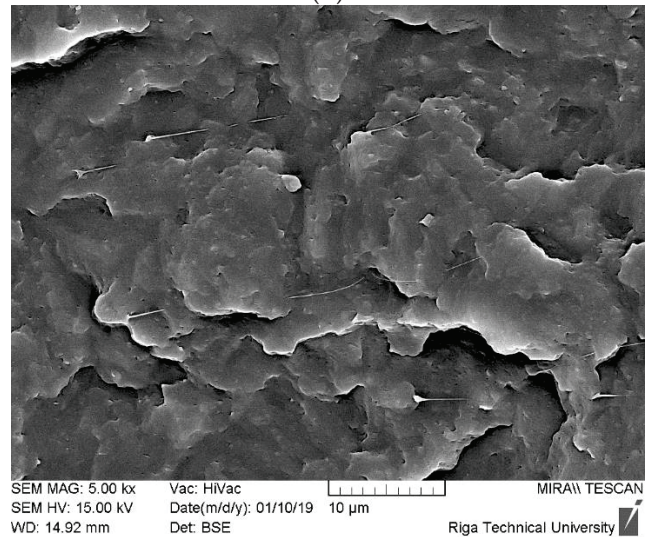
(a)



(b)



(c)



(d)

Figure 3. Cont.

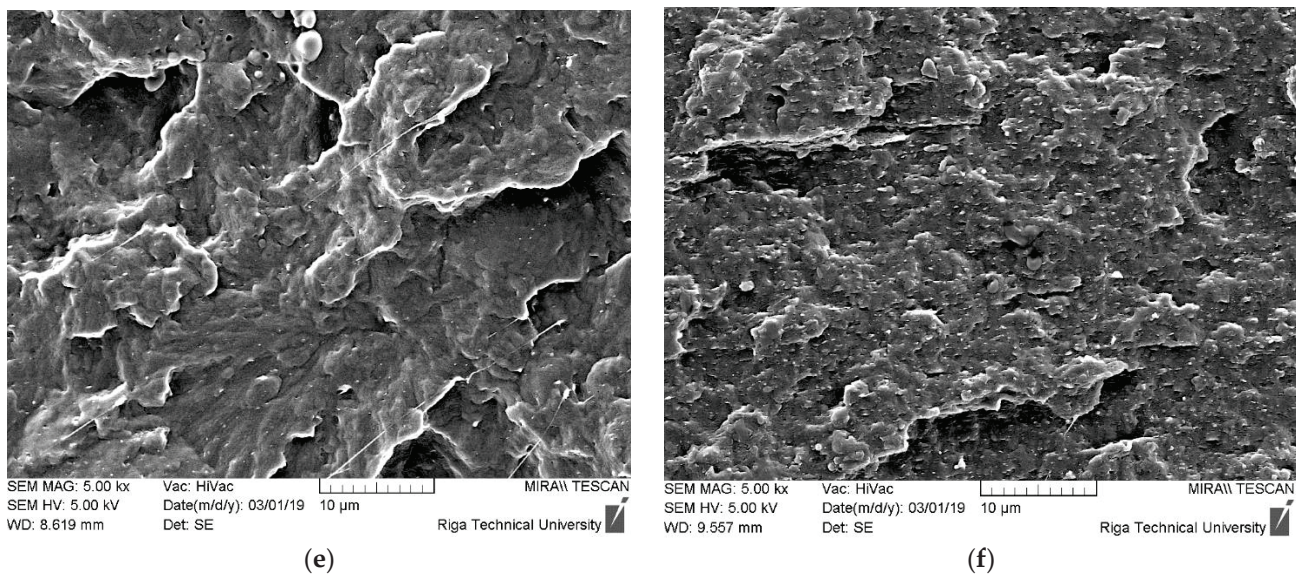


Figure 3. Surface morphology of C (a), M (b), and PP (c); its composites with 0.5%C and MAH (d), 0.5%M and MAH (e), and 5%M and MAH (f).

3.3. FTIR

FTIR spectra in the region of absorption of carbonyl groups of SH, PPSH, and PPgMA are summarized in Figure 4. It has been well accepted that interaction between hydroxyl groups of lignocellulosic filler and maleic anhydride functional groups in PPgMA occurs via an esterification reaction leading to the formation of ester carbonyl groups. In Figure 4, it is demonstrated that absorption of the maleic anhydride groups grafted to PP occurs in the range between 1760 cm^{-1} and 1800 cm^{-1} , with broad maxima from 1772 cm^{-1} to 1780 cm^{-1} . After compounding with SH, absorption in this region is considerably decreased, whereas new signals have been observed in the range between 1744 cm^{-1} and 1746 cm^{-1} . These signals may be attributed to the esterification reaction between free hydroxyl groups of SH and maleic anhydride functional groups of PPgMA.

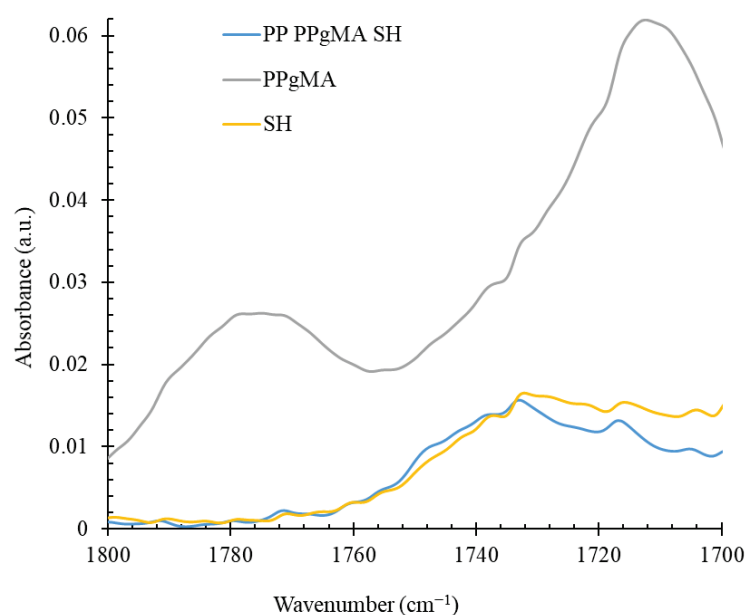


Figure 4. FTIR spectra of SH, PPgMA, and PPSH composite.

3.4. Rheological Characterization

Figure 5 shows the shear rate dependence of viscosity, shear stress, as well as flow behaviour index for neat PP and PP composites, determined at 190 °C. The range of shear rates examined is characteristic for both polymer extrusion and injection moulding.

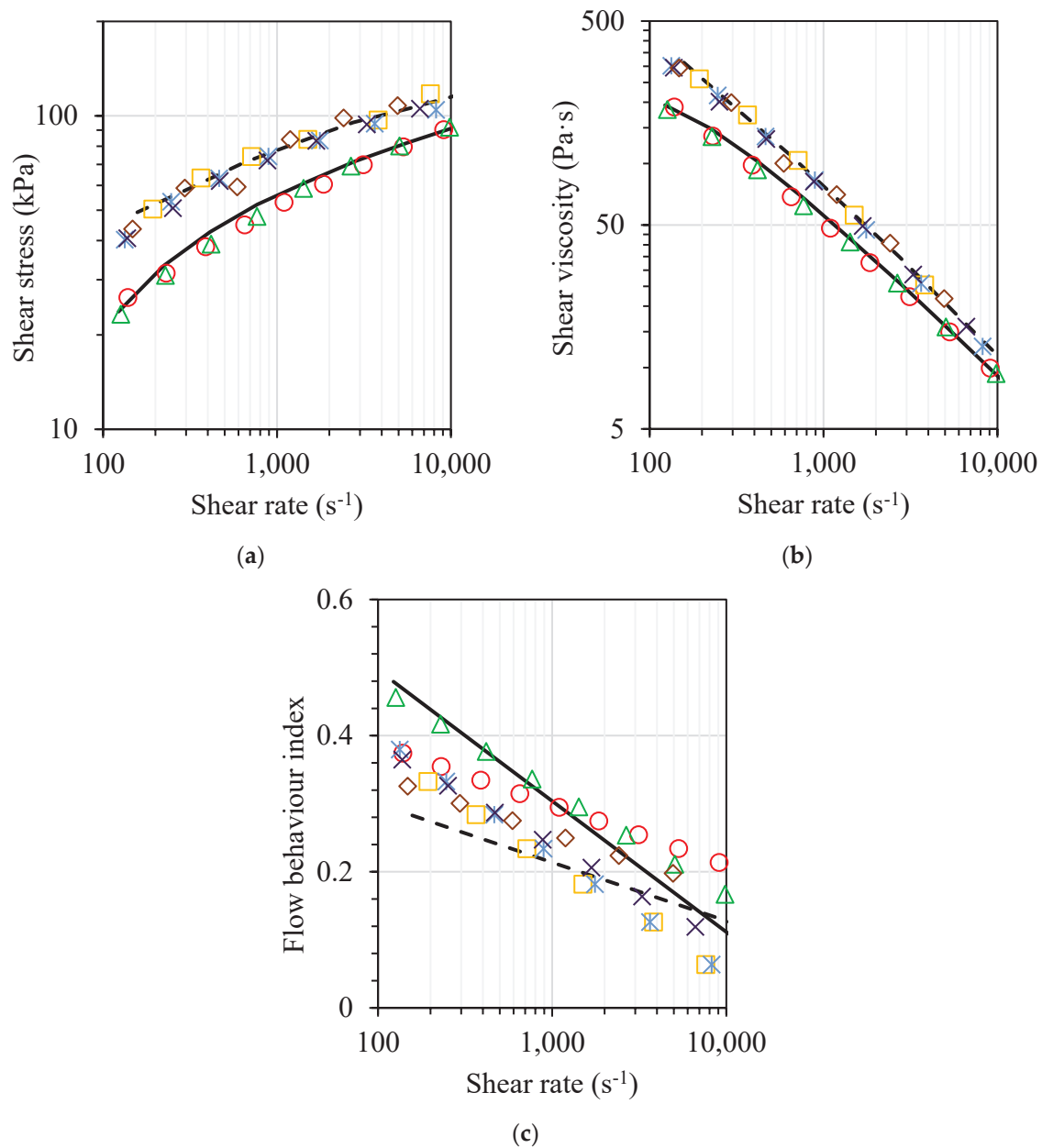


Figure 5. Shear stress (a), shear viscosity (b), and flow behaviour index (c) of PP (solid line), PP composite with SH (dashed line), PP nanocomposites with 5 wt.% of C (○) or M (Δ), PP hybrid composites with SH and 1 wt.% of C (□) or M (◊), and PP hybrid composites with SH and 3 wt.% of C (◇) or M (×) as functions of shear rate.

As depicted in Figure 5, in the investigated shear rate range, all the examined materials show a shear-thinning non-Newtonian behaviour caused by the disentanglement process and an increase in the average end-to-end distance of polymer chains as a result of shearing. Considerable shear stress and viscosity increase is observed along with the introduction of 40 wt.% of SH in the polymer matrix, whereas the effect of the addition of high surface area nanostructured nanoclay filler (C or M) is much lower.

However, it should be mentioned that at larger shear rate values approaching $10,000 \text{ s}^{-1}$, viscosities of SH, C- and M-containing systems become rather similar. Evidently, at larger shear stress values, due to the orientation of the microphase lignocellulosic filler, its effect on the flow behaviour of the polymer composite melt becomes smaller. By analysing the viscosity and shear stresses of M- and C-containing systems, one can observe somewhat smaller data scatter. Hence, a more stable flow is observed in the case of clay masterbatch (M)-modified systems, especially in the case of hybrid composites with SH (see Figure 5a). By considering that in the certain shear rate region $\tau(\dot{\gamma})$ and $\eta(\dot{\gamma})$ relationships are linear, the power law model is applied, allowing the determination of pseudoplasticity of the investigated systems. As demonstrated in Figure 5c, considerable differences in the pseudoplastic behaviour of the investigated systems are observed after the introduction of both SH and nanoclay containing reinforcing fillers. Upon the addition of micron-sized SH in the PP matrix melt, considerable changes in pseudoplastic behaviour are observed at lower shear rates range, whereas at high shear rates approaching $10,000 \text{ s}^{-1}$, the value of flow behaviour index of the lignocellulosic filler-containing composite almost coincides with that of neat PP matrix. It is also worth mentioning that because of better dispersibility, the addition of the clay nanofiller in the form of masterbatch influences the pseudoplasticity of PP nanocomposites and PP hybrid composites considerably less in comparison with the systems containing neat nanoclay filler.

3.5. Thermal Properties

3.5.1. Differential Scanning Calorimetry

DSC thermograms of PP, PPgMA, and their composites with SH, C, and M are reported in Supplementary Materials Figures S1–S3. A summary of DSC results for PP and PP composites modified with SH, C, and M is also reported in Table 2. It is found that PP modified with SH, C, and M demonstrate no considerable differences in melting behaviour. On first heating melting peak temperature T_m of the PP matrix phase changes within the range of 167–169 °C, whereas after eliminating thermal prehistory on the second heating T_m range is lower – 163–165 °C. Somewhat larger changes, fluctuating in the range from 36% to 53%, are observed for crystallinities X_C of the melting PP phase. In general, on the introduction of either lignocellulosic flat microfibrils or nanoclay particles, the crystallinity degree of the PP matrix is decreased, most probably because of the additive hindering formation of PP spherulites. However, during the cooling run crystallisation of the PP matrix is somewhat promoted as the cooling peak temperature of the polymer matrix phase is increased from 113 °C (PP) to 117 °C–119 °C (PP nanocomposites) and 116 °C–117 °C (the SH flat microfibre-reinforced and the hybrid composites). A somewhat greater increase in PP crystallisation peak temperature in the nanocomposites case evidently is associated with the prevalence of high-surface-area nanosized clay as nucleants. An increase in the X_C of PP with the incorporation of rigid fillers has also been reported by other authors [3,34].

Table 2. Calorimetric properties of the investigated PP and PP composites.

Sample	Heating Run 1		Heating Run 2		Cooling Run	
	T_m (°C)	X_C (%)	T_m (°C)	X_C (%)	T_m (°C)	X_C (%)
PP	167	45	162	51	113	52
PPgMA	135	61	132	63	99	65
PPSH	167	42	164	43	117	53
PP1.5C	170	36	164	42	118	51
PP1.5M	168	42	164	46	118	50
PP1C	169	46	163	51	118	49
PP1M	169	40	164	46	118	47
PP1.5C	168	44	165	49	118	52
PP1.5M	168	43	163	47	117	51

Table 2. Cont.

Sample	Heating Run 1		Heating Run 2		Cooling Run	
	T_m (°C)	X_C (%)	T_m (°C)	X_C (%)	T_m (°C)	X_C (%)
PP3C	168	45	165	49	117	50
PP3M	169	42	165	42	119	53
PP5C	169	41	165	42	118	51
PP5M	169	42	166	45	117	51
PP1CSH	168	36	165	40	116	45
PP1MSH	166	40	164	41	117	50
PP3CSH	167	40	165	49	117	51
PP3MSH	168	40	166	45	116	52

3.5.2. Thermogravimetric Analysis

TGA and TGA derivative thermograms of PP, PPgMA, and their composites with SH, C, and M are reported in Supplementary Materials Figures S4 and S5. Summary TGA results of PP and PP composites modified with SH, C, and M are also reported in Table 3. Initially, it should be mentioned that all the investigated compositions are sufficiently stable at the compounding temperatures used; according to the performed TGA experiments, less than 1% of the weight is lost at 220 °C. As expected, the SH-containing PP composite demonstrated the lowest thermal stability that was due to thermal degradation of thermally sensitive fractions of lignocellulose, particularly hemicelluloses, as described more in detail in numerous previous investigations, for example, [12,14]. Consequently, 5% of weight loss in PPSH composite is fixed at 271 °C, which is 1.5 times lower than for neat PP matrix (405 °C). Although the maximum degradation temperature T_d of the composite after the introduction of SH does not change much (454 °C for PPgMA and 451 °C for PPSH), it should be mentioned that the remaining mass at 800 °C in the case of PPSH is considerably larger (11%) in comparison with PP (almost 0%). The thermal stability of the composite is increased with the addition of nanoclay in the system due to the ability of nanoclay to form combustible gases impermeable layer of char. As a result, the thermal stability of the investigated PP nanocomposites is considerably improved with the addition of nanoclay, especially M. It is important to mention that even a small amount of nanoclay (i.e., 0.5 wt.%) is sufficient to ensure a rise in thermal stability. Further increase in nanoclay filler content does not lead to a significant rise in thermal stability. At higher content of the nanoclay filler, thermal stability may even decrease due to the increased possibility of agglomeration of the nanofiller because of its high surface activity [34]. However, considering that according to SEM investigations, no notable agglomeration is observed for PP nanocomposites, a more plausible reason for somewhat reduced thermal stability is the presence of trace metal ions within clays. It has also been observed that the addition of nanoclay in the form of masterbatch ensured somewhat higher thermal stability in comparison with the systems containing pristine nanoclay. The addition of nanoclay in either form (C or M) is also effective in the case of the investigated hybrid composites. It is important to mention that in comparison with PPSH, a considerable increase of $T_{50\%}$ and $T_{75\%}$ is observed with the addition of clay nanofiller. Evidently, clay nanofiller, together with SH, promotes the development of a solid char layer. Consequently, hybrid composites demonstrate the highest T_d values in comparison with all other investigated materials.

Table 3. Thermogravimetric properties of the investigated PP and PP composites.

Test Specimen Identification	Weight Loss Temperatures				Maximum Degradation Temperature
	$T_{5\%}$ (°C)	$T_{10\%}$ (°C)	$T_{50\%}$ (°C)	$T_{75\%}$ (°C)	T_d (°C)
PP	405	422	453	461	453
PPgMA	323	385	444	457	454
SH	271	294	434	458	451
PPSH	271	294	434	472	451
C	303	328	-	-	404
M	363	405	437	433	436
PP0.5C	426	433	446	449	449
PP0.5M	429	434	445	449	447
PP1C	424	430	439	446	440
PP1M	424	430	440	447	441
PP1.5C	423	428	437	453	440
PP1.5M	426	431	443	445	446
PP3C	422	428	438	442	440
PP3M	426	432	443	451	446
PP5C	421	428	436	435	442
PP5M	419	427	435	433	440
PP1CSH	273	295	457	474	465
PP1MSH	267	291	458	475	467
PP3CSH	266	291	462	480	474
PP3MSH	272	293	464	482	474

3.6. Mechanical Properties

3.6.1. Flexural Test

Analysis of the results of the flexural test is depicted in Figures 6 and 7. The addition of either lignocellulosic flat microfibrils or nanoclay fillers to PP results in increased stiffness and strength of the composites compared with neat PP. By considering nanoclay-modified polymer composites, a smooth increase in the modulus of elasticity and maximum flexural strength are observed by increasing the nanoclay content. Consequently, at the nanofiller content of 0.5 wt.% increase in flexural modulus is around 20%, while at maximum nanofiller content (5 wt.%) ca. 1.5-fold growth is observed. As expected, the modulus increase is larger in the case of clay masterbatch containing PP nanocomposites. It is worth noting that in the case of nanoclay-containing systems average reinforcing efficiency of the filler is 11% per 1 wt.% of the filler added, which is considerably more than in the case of lignocellulosic flat microfibre-containing systems for which ca. 3.0% increase per 1 wt.% of the added SH is observed. The introduction of the nanoclay filler in the PP matrix leads to a notable increase in maximal flexural stress, whereas strain at maximal flexural stress is slightly decreased, as depicted in Figure 7. However, it should be mentioned that all investigated PP nanocomposites, either with C or with M, were not broken during the test. Despite the high modulus values of hybrid composites (up to 3090 MPa for compatibilized PP composite with 40 wt.% SH and 3 wt.% M), unfortunately, an increase in brittleness accompanied by a reduction in maximal flexural stress and strain values is observed by rising the nanoclay content.

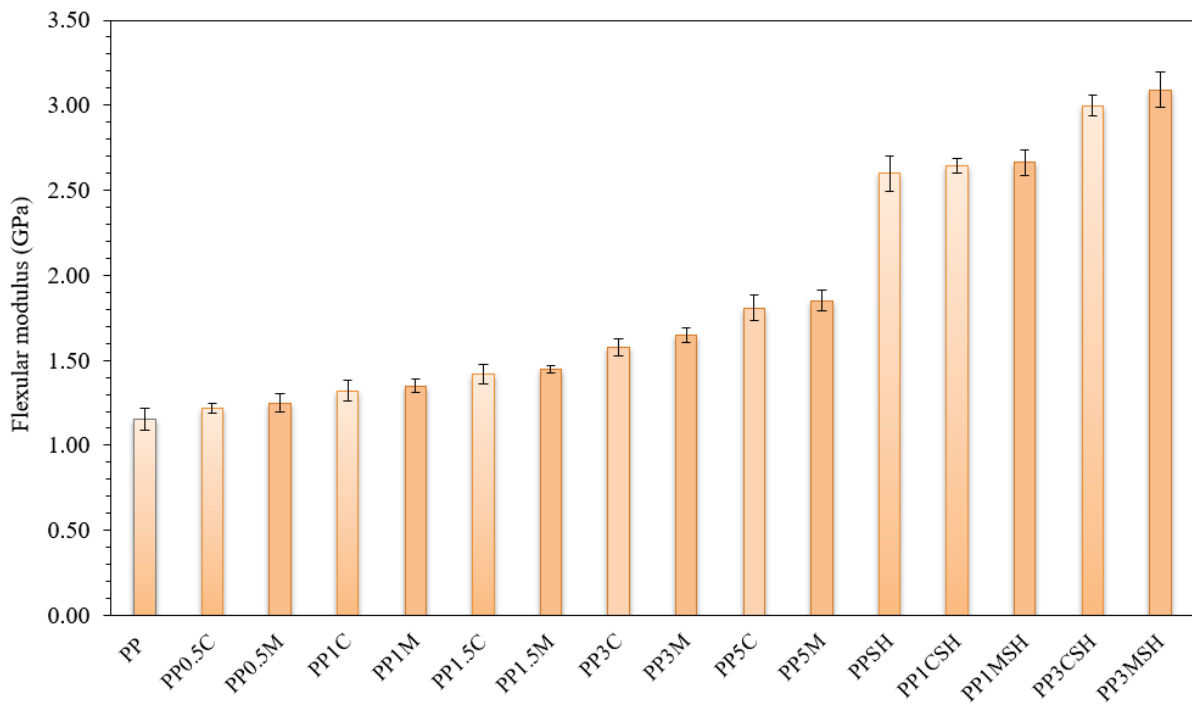


Figure 6. Flexural modulus of PP composites compared to neat PP; darker bars are related to the masterbatch-containing systems.

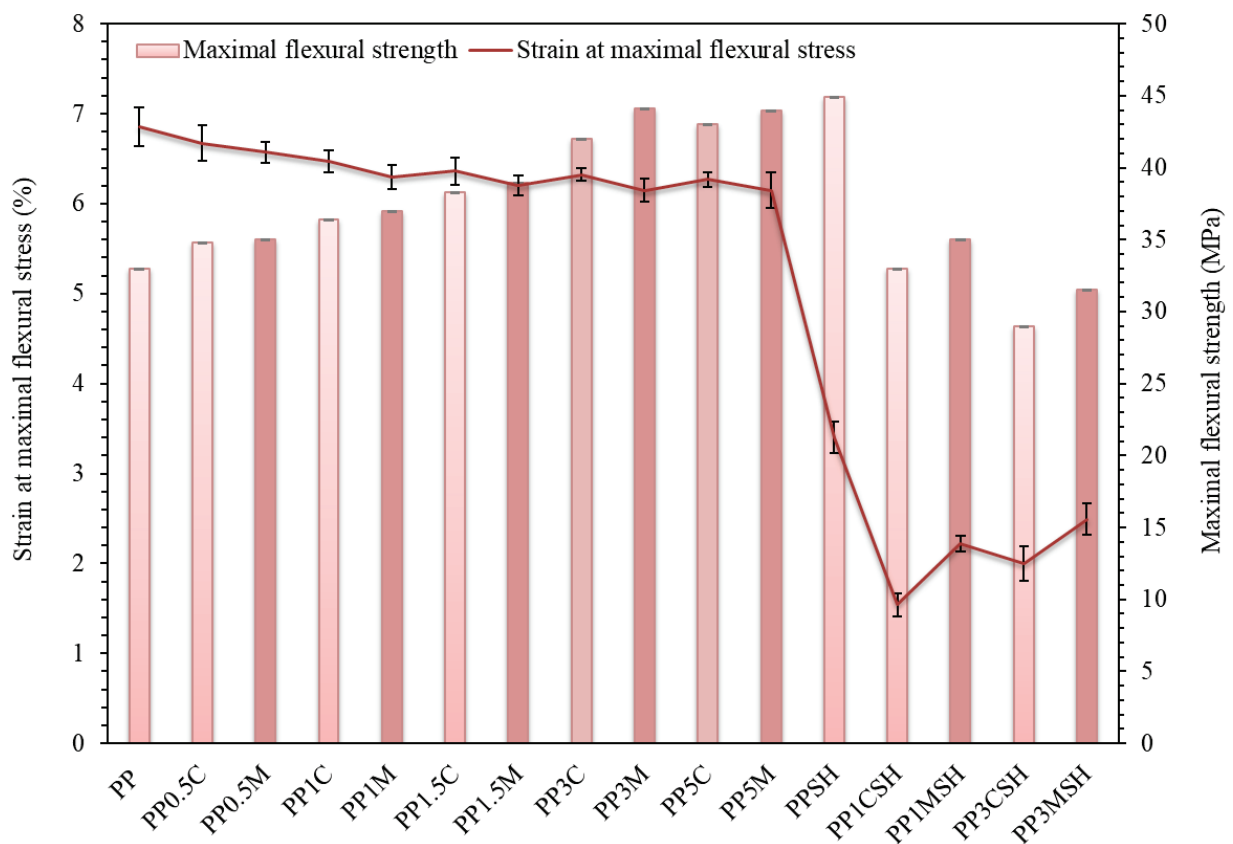


Figure 7. Strain at maximal flexural stress and maximal flexural strength of PP composites and neat PP; darker bars are related to the masterbatch-containing systems.

3.6.2. Tensile Test

Exemplary tensile stress–strain diagrams are depicted in Figure 8. As one can see, the addition of C and M caused an increase in yield strength but a certain decrease in the ultimate elongation of the investigated composites. A larger influence on the improvement of mechanical properties is observed in the case of masterbatch-containing systems, most probably due to better distribution of nanoclay within the polymer matrix. An increase in the nanoclay content in the polymer matrix above 1 wt.% considerably limits the reinforcing capability of the composite after yielding is achieved. However, this influence is small in comparison with that of SH addition. The addition of SH considerably increases the stiffness of the composite, as clearly shown in Figure 8c from the considerably raised slope of the σ - ϵ curves. Unfortunately, stiffness increase occurs, greatly compromising the deformability of the composites.

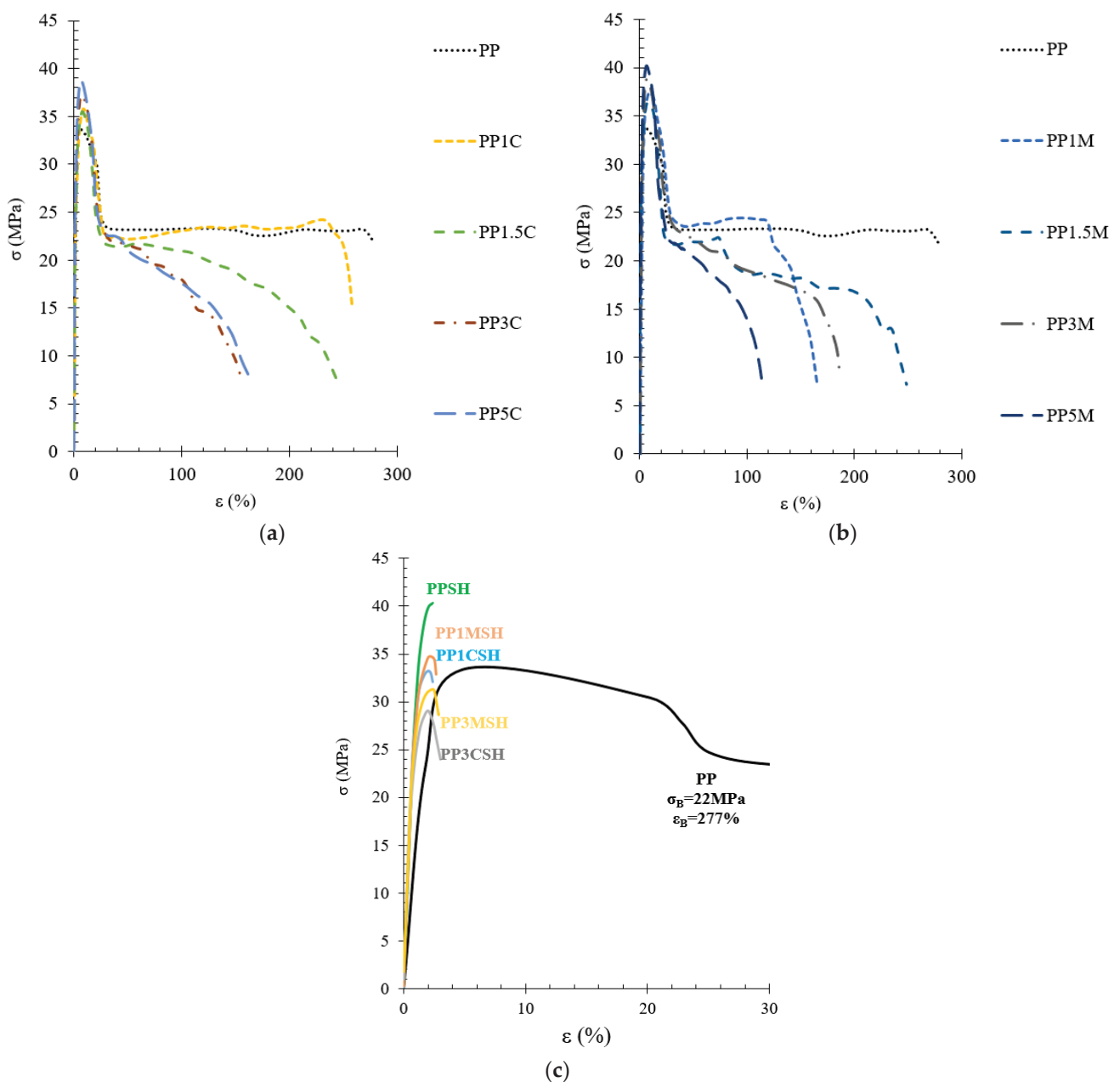


Figure 8. Tensile stress–strain diagrams of PP nanocomposites with C (a), M (b), and PP hybrid composites with SH and nanoclay (c).

A more detailed analysis of the results of the tensile test is depicted in Figures 9 and 10. Tensile modulus, as well as the maximal tensile stress and strain values, are analysed. It is worth mentioning that in the case of the nanoclay-reinforced binary composites, the corresponding stress–strain values are attributed to the upper yield point, whereas in the case of hybrid composites, the corresponding stress–strain values are attributed to the fracture point. In general, the tensile behaviour of the investigated PP composites has similar trends to flexural behaviour. Consequently, the addition of only nanoclay results in increased modulus and strength of the nanocomposite by maintaining remarkable ultimate deformation values (even up to 150% at the highest nanofiller content), whereas the addition of nanoclay nanofiller to SH-containing PP composites further increases its brittleness (Figures 9 and 10).

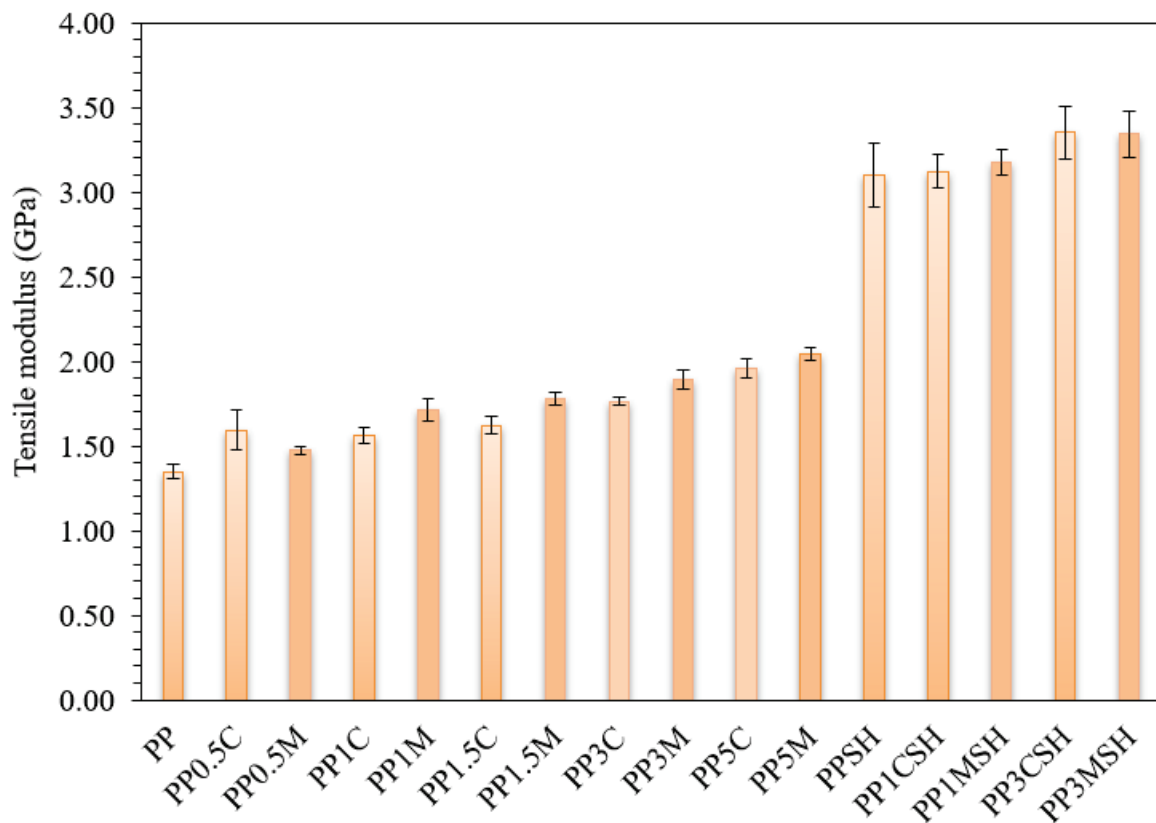


Figure 9. Tensile modulus of PP composites compared to neat PP; darker bars are related to the masterbatch-containing systems.

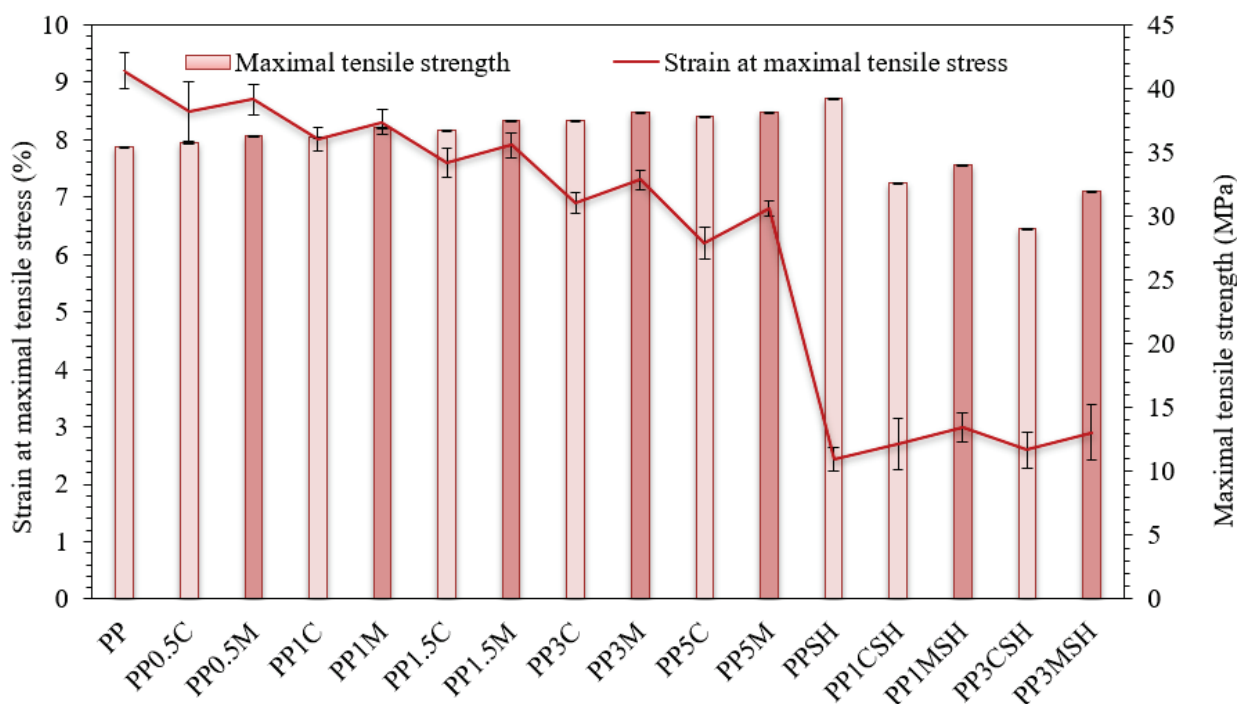


Figure 10. Strain at maximal tensile stress and maximal tensile strength of PP-modified composites and neat PP; darker bars are related to the masterbatch-containing systems.

4. Conclusions

In this research, the efficiency of modification of PP by SH (40 wt.%), C, and M (1 and 3 wt.%) in the presence of PPgMA (3 wt.%) compatibiliser is demonstrated. The following results have been obtained:

- (1) The addition of the nanoclay fillers does not considerably reduce melt viscosities of PP nanocomposites as well as PP hybrid composites with SH because of the regular dispersion of C or M particles within the polymer matrix, as demonstrated by SEM analysis;
- (2) Increased modulus of elasticity of the nanoclay-modified composites is a result of the reinforcement effect of high-aspect-ratio plate-like clay nanoparticles, oriented in the direction of the flow, as well as the perfection of the crystalline structure of the polymer matrix, as demonstrated by the increase in melting peak temperature of PP crystalline phase;
- (3) Increased modulus of elasticity of hybrid composites is due to the reinforcement effect of high-aspect-ratio nanoclay particles and isodiametric SH particles (aspect ratio within the range 2–6) oriented in the direction of the flow;
- (4) Reduced strength of the investigated nano- and hybrid composites is a result of the constraint in deformability (ultimate elongation values) of PP matrix introduced in the presence of rigid fillers;
- (5) Improved thermal stability of PP nano- and hybrid composites is attributed to the thermal barrier effect of plate-like nanoclay, increasing the 5% weight loss temperature ($T_{5\%}$) of PP nanocomposites on the one hand and promoting more intense development of impermeable char layer related to increased maximal degradation temperature (T_d) of PP hybrid composites on the other hand.

Consequently, the developed hybrid composites can be regarded as environmentally friendly alternative materials for the development of injection-moulded products requiring increased thermal stability and stiffness.

Supplementary Materials: The following supporting information can be downloaded at: <https://www.mdpi.com/article/10.3390/polym14204332/s1>, Figure S1: DSC heating run 1 of PP, PPgMA, and its composites with SH, C, and M, Figure S2: DSC cooling run of PP, PPgMA and its composites with SH, C, and M, Figure S3: DSC heating run 2 of PP, PPgMA and its composites with SH, C, and M, Figure S4: TGA thermograms of PP, PPgMA and its composites with SH, C, and M, Figure S5: TGA derivative thermograms of PP, PPgMA and its composites with SH, C, and M.

Author Contributions: Conceptualization, J.Z., M.K., P.P.D. and A.K.B.; methodology, I.B., M.Ž. and T.I.; investigation, M.Ž. and I.B.; resources, J.Z., P.P.D. and A.K.B.; data curation, M.Ž. and I.B.; writing—original draft preparation, M.Ž.; writing—review and editing, R.M.-M.; visualization, T.I. and R.M.-M.; supervision, J.Z.; project administration, J.Z., P.P.D. and A.K.B.; funding acquisition, A.K.B., J.Z. and P.P.D. All authors have read and agreed to the published version of the manuscript.

Funding: This research was funded by the M-ERA.NET project HyBiCo; This research was funded by the project for students for research capacity building of scientific staff of RTU, Nr. ZM-2020/9.

Data Availability Statement: The data presented in this study are available on request from the corresponding author.

Conflicts of Interest: The authors declare no conflict of interest.

References

- Gowda, T.G.Y.; Sanjay, M.R.; Bhat, K.S.; Madhu, P.; Senthamaraiannan, P.; Yogesha, B. Polymer matrix-natural fiber composites: An overview. *Cogent. Eng.* **2018**, *5*, 1446667. [CrossRef]
- Zaghloul, M.Y.M.; Zaghloul, M.M.Y.; Zaghloul, M.M.Y. Developments in polyester composite materials—An in-depth review on natural fibres and nano fillers. *Compos. Struct.* **2021**, *278*, 114698. [CrossRef]
- Molina, S. Modification of Natural Fibers Using Physical Technologies and Their Applications for Composites. In *Lignocellulosic Fibers and Wood Handbook: Renewable Materials for Today's Environment*, 1st ed.; Belgacem, N., Pizzi, A., Eds.; Wiley: Hoboken, NJ, USA, 2016; Volume 12, pp. 323–344.
- Mukhopadhyay, S.; Fanguero, R. Physical modification of natural fibers and thermoplastic films for composites—A review. *J. Thermoplast. Compos. Mater.* **2009**, *22*, 135–162. [CrossRef]
- Bledzki, A.K.; Jaszkiwicz, A.; Murr, M.; Sperber, V.E.; Lützendorf, R.; Reußmann, T. Processing techniques for natural- and wood-fibre composites. In *Properties and Performance of Natural-Fibre Composites*, 1st ed.; Pickering, K.L., Ed.; Woodhead Publishing: Cambridge, UK, 2008; Volume 4, pp. 163–192. [CrossRef]
- Kalia, I.K.S.; Kaith, B.S. Pretreatments of Natural Fibers and their Application as Reinforcing Material in Polymer Composites—A Review. *Polym. Eng. Sci.* **2009**, *49*, 1253–1272. [CrossRef]
- Zaghloul, M.M.Y.M. Mechanical properties of linear low-density polyethylene fire-retarded with melamine polyphosphate. *J. Appl. Polym. Sci.* **2018**, *135*, 46770. [CrossRef]
- El-Sabbagh, A. Effect of coupling agent on natural fibre in natural fibre/polypropylene composites on mechanical and thermal behaviour. *Compos. Part B Eng.* **2014**, *57*, 126–135. [CrossRef]
- Malalli, C.S.; Ramji, B.R. Mechanical characterization of natural fiber reinforced polymer composites and their application in Prosthesis: A review. *Mater. Today: Proc.* **2022**, *62*, 3435–3443. [CrossRef]
- Andrzejewski, J.; Barczewski, M.; Szostak, M. Injection Molding of Highly Filled Husk and Wood Flour Filler: A Comparison of Agricultural and Wood Industry Waste Utilization. *Polymers* **2019**, *11*, 1881. [CrossRef]
- Santulli, C.; Sarasini, F.; Puglia, D.; Kenny, J.M. 8 Injection moulding of plant fibre composites. In *Advanced Composite Materials: Properties and Applications*; De Gruyter Open Poland: Warsaw, Poland, 2017; pp. 420–439. [CrossRef]
- Panthapulakkal, S.; Sain, M. The use of wheat straw fibres as reinforcements in composites, 2015. In *Biofiber Reinforcements in Composite Materials*, 1st ed.; Faruk, O., Sain, M., Eds.; Woodhead Publishing: Cambridge, UK, 2015; Volume 14, pp. 423–453. [CrossRef]
- Arjmandi, R.; Hassan, A.; Majeed, K.; Zakaria, Z. Rice Husk Filled Polymer Composites. *Int. J. Polym. Sci.* **2015**, *2015*, 501471. [CrossRef]
- Bledzki, A.K.; Mamun, A.A.; Bonnia, N.N.; Ahmad, S. Basic properties of grain by-products and their viability in polypropylene composites. *Ind. Crops Prod.* **2012**, *37*, 427–434. [CrossRef]
- Bledzki, A.K.; Mamun, A.A.; Volk, J. Physical, chemical and surface properties of wheat husk, rye husk and soft wood and their polypropylene composites. *Compos. Part A Appl. Sci. Manuf.* **2010**, *41*, 480–488. [CrossRef]
- Merijs-Meri, R.; Zicans, J.; Ivanova, T.; Bochkov, I.; Varkale, M.; Franciszczak, P.; Bledzki, A.K.; Danilovas, P.P.; Gravitis, J.; Rubenis, K.; et al. Development and Characterization of Grain Husks Derived Lignocellulose Filler Containing Polypropylene Composites. *Polym. Eng. Sci.* **2019**, *59*, 2467–2473. [CrossRef]
- Veghte, D.P.; Freedman, M.A. Facile method for determining the aspect ratios of mineral dust aerosol by electron microscopy. *Aerosol Sci. Technol.* **2014**, *48*, 715–724. [CrossRef]

18. Zare, Y. Effects of imperfect interfacial adhesion between polymer and nanoparticles on the tensile modulus of clay/polymer nanocomposites. *Appl. Clay Sci.* **2016**, *129*, 65–70. [CrossRef]
19. Saba, N.; Jawaid, M.; Asim, M. Recent Advances in Nanoclay/Natural Fibers Hybrid Composites. In *Nanoclay Reinforced Polymer Composites: Natural Fibre/Nanoclay Hybrid Composites*, 1st ed.; Jawaid, M., Qaiss, A.K., Bouhfid, R., Eds.; Springer: Singapore, 2016; Chapter 1; pp. 1–28. [CrossRef]
20. Xie, Y.; Hill, C.A.S.; Xiao, Z.; Militz, H.; Mai, C. Silane coupling agents used for natural fiber/polymer composites: A review. *Compos. Part A Appl. Sci. Manuf.* **2010**, *41*, 806–819. [CrossRef]
21. Fuad, M.Y.A.; Zawawi, M.T.; Rahmad, S.; Norazlan, R.; Ismail, Z. Effect of silane, titanate and zirconate coupling agents in polypropylene composites. *J. Ind. Technol.* **1997**, *6*, 1–13.
22. DeArmitt, C.; Rothon, R. Surface Modifiers for Use with Particulate Fillers. In *Fillers for Polymer Applications*, 1st ed.; Rothon, R., Ed.; Springer: Cham, Switzerland, 2017; Chapter 2; pp. 29–50.
23. Rajeshkumar, G.; Seshadri, S.A.; Ramakrishnan, S.; Sanjay, M.R.; Siengchin, S.; Nagaraja, K.C. A comprehensive review on natural fiber/ nano-clay reinforced hybrid polymeric composites: Materials and technologies. *Polym. Compos.* **2021**, *42*, 3687–3701. [CrossRef]
24. Jawaid, M.; Paridah, M.T.; Saba, N. Introduction to biomass and its composites. In *Lignocellulosic Fibre and Biomass-Based Composite Materials*, 1st ed.; Jawaid, M., Tahir, P.M., Saba, N., Eds.; Woodhead Publishing: Sawston, UK, 2017; Chapter 1; pp. 1–11. [CrossRef]
25. Nafchi, H.R.; Abdouss, M.; Najafi, S.K.; Gargari, R.M.; Mazhar, M. Effects of nano-clay particles and oxidized polypropylene polymers on improvement of the practical properties of wood-polypropylene composite. *Adv. Compos. Mater.* **2015**, *24*, 239–248. [CrossRef]
26. Bari, E.; Taghiyari, H.R.; Schmidt, O.; Ghorbani, A.; Aghababaei, H. Effects of nano-clay on biological resistance of woodplastic composite against five wood-deteriorating fungi. *Maderas Cienc. Tecnol.* **2015**, *17*, 205–212. [CrossRef]
27. Tabari, H.Z.; Nourbakhsh, A.; Ashori, A. Effects of Nanoclay and Coupling Agent on the Physico-Mechanical, Morphological, and Thermal Properties of Wood Flour/Polypropylene Composites. *Polym. Eng. Sci.* **2010**, *51*, 272–277. [CrossRef]
28. Fallis, A. Mechanical and Physical Properties of Wood-Plastic Composites Made of Polypropylene, Wood Flour and Nanoclay. *J. Chem. Inf. Model.* **2013**, *53*, 1689–1699.
29. Arrakhiz, F.Z.; Benmoussa, K.; Bouhfid, R.; Qaiss, A. Pine cone fiber/clay hybrid composite: Mechanical and thermal properties. *Mater. Des.* **2013**, *50*, 376–381. [CrossRef]
30. Najafi, A.; Kord, B.; Abdi, A.; Ranaee, S. The impact of the nature of nanoclay on physical and mechanical properties of polypropylene/reed flour nanocomposites. *J. Thermoplast. Compos. Mater.* **2012**, *25*, 717–727. [CrossRef]
31. Yang, Z.; Peng, H.; Wang, W.; Liu, T. Crystallization behavior of poly(ϵ -caprolactone)/layered double hydroxide nanocomposites. *J. Appl. Polym. Sci.* **2010**, *116*, 2658–2667. [CrossRef]
32. Islam, M.S.; Ahmad, M.B.; Hasan, M.; Aziz, S.A.; Jawaid, M.; Haafiz, M.K.M.; Zakaria, S.A.H. Natural fiber-reinforced hybrid polymer nanocomposites: Effect of fiber mixing and nanoclay on physical, mechanical, and biodegradable properties. *BioResources* **2015**, *10*, 1394–1407. [CrossRef]
33. Turku, I.; Kärki, T. The effect of carbon fibers, glass fibers and nanoclay on wood flour-polypropylene composite properties. *Eur. J. Wood Wood Prod.* **2014**, *72*, 73–79. [CrossRef]
34. Chrissafisa, K.; Bikiaris, D. Can nanoparticles really enhance thermal stability of polymers? Part I: An overview on thermal decomposition of addition polymers. *Thermochim. Acta* **2011**, *523*, 1–24. [CrossRef]

Article

On the Mode I and Mode II Delamination Characteristics and Surface Morphological Aspects of Composites with Carbon-Thermoplastic Hybrid Fabrics and Innovative Liquid Thermoplastic Resin

Somen K. Bhudolia ^{1,*}, Goram Gohel ¹, Durga Vasudevan ², Kah Fai Leong ¹ and Pierre Gerard ³

¹ School of Mechanical and Aerospace Engineering, Nanyang Technological University, 50, Nanyang Avenue, Singapore 639798, Singapore

² School of Mechanical and Aerospace Engineering, Technical University of Munich Asia, 25 International Business Park Rd, Singapore 609916, Singapore

³ Groupement de Recherche de Lacq, Arkema, Route Départementale 817, BP 34, 64170 Lacq, France

* Correspondence: somenkum001@e.ntu.edu.sg

Abstract: In the current research, the delamination behavior under Mode I and Mode II loading for the hybrid carbon-thermoplastic fabrics in conjunction with novel liquid thermoplastic acrylic Elium[®] resin processable at ambient conditions was studied. The experimentation by incorporating doublers methodology, studying the performance under Mode I and Mode II loading, and understanding failure mechanisms using surface morphological fractography is deliberated. Hybrid Carbon-Ultra-high molecular weight polyethylene (UHMWPP)/Elium[®] composite has shown a 22.81% higher G_{IC} and a 22.2% higher G_{IIC} than Carbon-UHMWPP/Epoxy composite. On the contrary, the Carbon_Ultra-high molecular weight polypropylene (UHMWPE)/Elium[®] has shown an 11.11% higher Mode I critical energy release rate (G_{IC}) and a 7.58% higher Mode II critical energy release rate (G_{IIC}) than Carbon_UHMWPE/Epoxy composite. Hybrid fiber reinforced thermoplastic composites have shown severe plastic deformation of the matrix, rough fracture surface, and micro-cracks on the de-bonding surface, extensive fiber bridging, and crack branching which contributed to the improvement in the delamination behavior. Hybrid fiber architecture is also found to be detrimental by inducing crack arresting mechanisms including the tortuous crack path and the resin-rich pockets path due to the mismatch of the size of the fiber yarns.

Keywords: hybrid fibers; hybrid composites; thermoplastic resin; vacuum assisted resin infusion (VARI); fracture toughness; fractography

Citation: Bhudolia, S.K.; Gohel, G.; Vasudevan, D.; Leong, K.F.; Gerard, P. On the Mode I and Mode II Delamination Characteristics and Surface Morphological Aspects of Composites with Carbon-Thermoplastic Hybrid Fabrics and Innovative Liquid Thermoplastic Resin. *Polymers* **2022**, *14*, 4155. <https://doi.org/10.3390/polym14194155>

Academic Editor: Victor Tcheryntsev

Received: 23 August 2022

Accepted: 25 September 2022

Published: 4 October 2022

Publisher's Note: MDPI stays neutral with regard to jurisdictional claims in published maps and institutional affiliations.



Copyright: © 2022 by the authors. Licensee MDPI, Basel, Switzerland. This article is an open access article distributed under the terms and conditions of the Creative Commons Attribution (CC BY) license (<https://creativecommons.org/licenses/by/4.0/>).

1. Introduction

Composite materials with carbon as a reinforcement material are significantly used in many industries in wide applications ranging from automotive, aerospace, marine and offshore, and many others as they have lightweight characteristics along with high specific mechanical properties, such as strength and stiffness. Although considered by many as a wonder material along with the obsession of industries to use them, there occurs a challenge in terms of cost along with their brittle nature which leads to catastrophic failure with low strain to failure under different loading scenarios. While the polymeric fibers including ultra-high molecular weight polyethylene (UHMWPP), ultra-high molecular weight polypropylene (UHMWPE), Polyester (Diolen) are ultra-lightweight in nature, have excellent impact and toughness characteristics, and have a high elongation to break, and consequently are appealing for sporting goods, body armors, and ballistic applications [1,2]. However, they also have certain limitations with extremely low shear and compressive strength and hence are not ideal for structural load carrying applications. More recently, the hybridization route has been explored by many textile industries, such as DSM, Innegra

Tech and others, to manufacture hybrid thermoplastic fabrics in conjunction with carbon fiber which could mitigate the effect of brittleness and bring in ductility to the reinforcement system while simultaneously improving the in-plane compressive and shear properties as well [3,4]. If effectively used, the hybridization technique could result in optimized properties as there is a greater degree of design space using this route.

Woven ultra-high molecular weight polypropylene (UHMWPP), commercially known as Innegra™, is a thermoplastic fiber made from polyolefin polypropylene. Innegra™ is a very lightweight fiber, with a density of 0.84 g/cm³ and a high elongation to break of 9.5%, when compared to other commonly used fibers in fiber reinforced polymer (FRP) laminate composites. It is also non-electrical and hydrophobic, due to its limited moisture absorption property. However, because of its low tensile strength of 667 MPa and modulus of 15 GPa when compared to other composite fibers, Innegra™ is frequently employed in hybrid composites, which are made up of two or more distinct fibers that are reinforced in a resin matrix. Various other characteristics of Innegra™ include high toughness, high crystallinity, and excellent impact properties. Innegra™ is frequently utilized in a hybrid fiber system, such as a carbon fiber/UHMWPP hybrid weave because of their low modulus. For specific applications, this combines the desirable qualities of both fibers, namely, carbon fiber's high flexural modulus and Innegra's high impact resistance. Innegra™ fiber reinforced composites are generally used in kayaks, ice-hockey sticks, helmets, and many more. DSM's Dyneema® fiber is an extremely strong ultra-high molecular weight polyethylene (UHMWPE) fiber that provides maximum strength with less weight [5]. As a result, the number of viable applications is practically limitless. Dyneema® fiber is made using a gel spinning process that involves drawing, heating, elongating, and cooling the fibers. Low density, high crystallization, and molecular alignment are the results of stretching and spinning. Extremely long molecular chains found in Dyneema® transfer load more efficiently to the polymer backbone. As a result, Dyneema® outperforms competing materials in terms of strength while also being lighter. In the fiber direction, Dyneema® has high strength and modulus (resistance to deformation). Because of its low density, it has an incredibly high strength per unit of weight, making it one of the strongest man-made fibers. The elongation at break is modest, but the energy to break is high due to the high strength. The mechanical properties of this synthetic fiber are unaffected by the presence of water, unlike those of conventional synthetic fibers. The modulus and strength in the transverse direction are lower than in the fiber direction due to the anisotropic nature of the fibers. Dyneema® finds its application in various products, such as helmets, soft and hard armors, and anchor ropes. Generally, Dyneema® fibers are also hybridized with carbon fibers to achieve the desired properties of both the fibers.

Using the thermoplastic polymer fabrics with thermoplastic resin can potentially lead to wholly thermoplastic structures and even the usage of hybrid thermoplastics can keep the overall proportion of thermoplastic presence higher compared to that with pure carbon or with a thermosetting matrix variant. High-performance thermoplastic resins, such as PEEK, CBT, and PU are extensively used to manufacture composite laminates [6–8]. Yet, the liquid injection processes can be employed directly with these matrices as they are accessible in pellet or film form and in turn must be processed at high-temperature ranges [9]. An acrylic thermoplastic Elium® was recently developed by ARKEMA [10–18] to address the challenges associated with manufacturing with the potential to cure at room temperature. Elium® composites have been shown to have superior fracture toughness, impact resistance, and vibration damping qualities [11,16,19] compared to the composites with thermosetting epoxy as matrix material. Fracture toughness [9,11,20], vibration [19,21], flexural properties [13,21,22], tensile properties [18,23], weldability [21] and other mechanical properties for acrylic-based composites were all comprehensively researched.

For any material system to be readily adopted by industries, it is of paramount importance to understand the bonding characteristics of the fabrics and the matrix system. If there is good compatibility, the structure will carry a significant load otherwise there significant delamination will occur. The delamination phenomenon initiates due to poor

interfacial adhesion during Mode I (peel mode), Mode II (shear mode), and Mode III (torsion mode) type of loading scenarios [24,25]. There is limited work on understanding the bonding characteristics of a thermoplastic matrix with only the bonding capability of thermoplastic Elium[®] resin with UHMWPE fabrics studied by Shanmugam et al. [20]. They have determined that UHMWPE fabrics have relatively weak bonding with Elium[®] matrix and the reason is the lack of the polar functional group on the fabrics [26]. Whereas in another study the surface treated UHMWPE fabric improved the bonding characteristics. In Mode I fracture toughness tests, Somen K. Bhudolia et al. [9] observed that thin ply Elium[®] composite had a 30% greater ILFT than thick ply Elium[®] composite. In addition, thin Elium[®] composites have a 72% improvement in ILFT when compared to thin Epoxy composites. Logesh Shanmugam et al. [20] researched enhancing the fracture toughness in Mode I of Elium[®] composite by enhancing the fiber/matrix bonding with the help of surface treatments. This resulted in an improvement in G_{IC} by 19.6% and 42.5% for the PDA surface-treated sample and PDA with 0.03 wt% of MWCNT ingrained, respectively, compared to non-treated composite laminate. A detailed study was carried out by L.C.M. Barbosa et al. [11] regarding the fracture toughness in Mode II of Elium[®]-based composites. In this study, for composite laminate a reinforcement carbon fiber along with thermoplastic Elium resin and thermoset Epoxy resin were used. Mode II fracture toughness of Carbon/Elium[®] composites was obtained to be 214.22 J/m², which is 40% higher compared to the Carbon/Epoxy composites.

Concerning the hybrid composites with hybrid fabrics (carbon + thermoplastic fabrics), the majority of the work which has been reported in the literature is concentrated on studying the tensile, fatigue, impact, and damping characteristics of these hybrid composite structures [2,18,27–32]. However, there is very limited research on understanding the fracture toughness attributes of composites with hybrid thermoplastic fabrics. Recently, Zhao et al. studied the Mode I and Mode II attributes of the carbon-Dyneema hybrid composites with thermosetting epoxy resin as the matrix material and concluded the usage of Dyneema could potentially act as a toughening mechanism to improve delamination resistance characteristics. They have shown that using the hybridization of carbon fabrics with Dyneema fabrics can potentially increase the Mode I and Mode II performance by 65% and 40%, respectively, compared to that with pure carbon [3]. In another study by Zou et al., the performance of hybrid carbon-Dyneema composites was studied with an emphasis on understanding the details of failure mechanisms governing the increase in the Mode II properties due to hybridization [4]. In addition, they have shown that the J-integral technique and digital image co-relation techniques lead to more consistent fracture toughness results.

After a detailed literature review and addressing the research gaps, there is no research reported on understanding the fracture toughness attributes in Mode I and Mode II of hybrid thermoplastic composites with acrylic Elium[®] resin. In the current investigation, authors have researched the characteristics, in Mode I and II, of the composites manufactured with the hybrid fabrics (carbon + UHMWPP and carbon + UHMWPE) and using novel acrylic resin, Elium[®] as the matrix material to understand their adhesion characteristics. Current work also utilizes a testing methodology using doublers to avoid the large displacement and compression failure constraints. Failure mechanisms are also studied in detail under electron microscopy and SEM and the comparisons are performed with a thermosetting epoxy variant. The usage of these hybrid thermoplastic fabrics with thermoplastic Elium[®] resin could potentially further improve the impact and damping characteristics and could be a tremendous material system for automotive, sporting goods, helmets, bicycle frames, and lightweight armor applications. Hence, the current investigation is an important step to understanding the delamination behavior of these fabrics with acrylic Elium[®] resin and accessing their suitability to be used for the above-mentioned applications.

2. Materials and Manufacturing

2.1. Materials

In this current research, two hybrid configurations of thermoplastic fibers, UHMWPP and UHMWPE with carbons were manufactured and investigated (refer Figure 1). It is to be noted that the ratio of the thermoplastic fiber to the carbon fabrics in hybrid configurations is 1:1. The densities of the hybrid UHMWPP and Hybrid UHMWPE reinforcements are 1.31 g/cm^3 and 1.38 g/cm^3 .

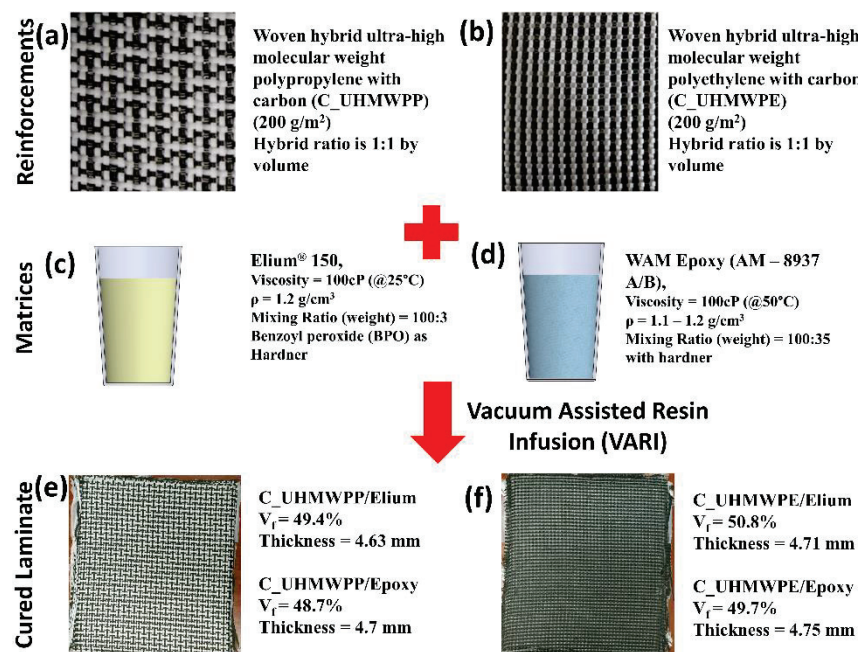


Figure 1. Properties of different fibers, resin system and laminates (a,b) C_UHMWPP and C_UHMWPE reinforcement system (c,d) Elium 150 and Epoxy matrix system (e,f) C_UHMWPP/Elium and C_UHMWPE/Elium cured laminates.

Thermoplastic and thermoset matrices were used in the current project along with hybrid reinforcement for manufacturing the composite panels. A liquid thermoplastic resin at room temperature (RT) Elium® 150, from Arkema, France with a viscosity of 100 cP at RT was used as a thermoplastic variant [9,16,33,34]. On the other hand, Epoxy (AM-8937 A/B) resin, procured from Wells Advanced Materials Co., Ltd., Shanghai, China, is employed as a thermoset variant for composite manufacturing. For creating an artificial crack into the manufactured laminate Polytetrafluoroethylene (PTFE) film of $25.4 \mu\text{m}$ thickness was used for Mode I and $12.5 \mu\text{m}$ thickness was used for Mode II. The adhesive utilized for the gluing of the composite laminates to aluminum doublers is Bostik's SAF 30 ultimate M10 grade and aluminum 6065 sheets with a thickness of 1.2 mm were used as doublers for the fracture toughness tests—Mode I and Mode II.

2.2. Manufacturing

For the fracture toughness tests, the hybrid thermoplastic and thermoset composites were fabricated using the conventional vacuum-assisted resin infusion (VARI) manufacturing process, as illustrated in Figure 2. PTFE film was inserted in the central layer of the dry hybrid fabric preform as shown in Figure 2a.

Before manufacturing, the mould was prepared by applying multiple layers of the mould releasing agent. Then, the fibers were laid on a mould; inlet, and outlet tubes were connected; and the VARI setup was prepared as depicted in Figure 2b,c. Lastly, the entire set-up was sealed using sealant and a vacuum bag and a leak test was performed. Once the leak test was cleared the setup was ready for infusion. It is to be noted that 12 layers of hybrid reinforcements were used based on the required thickness of the laminates.

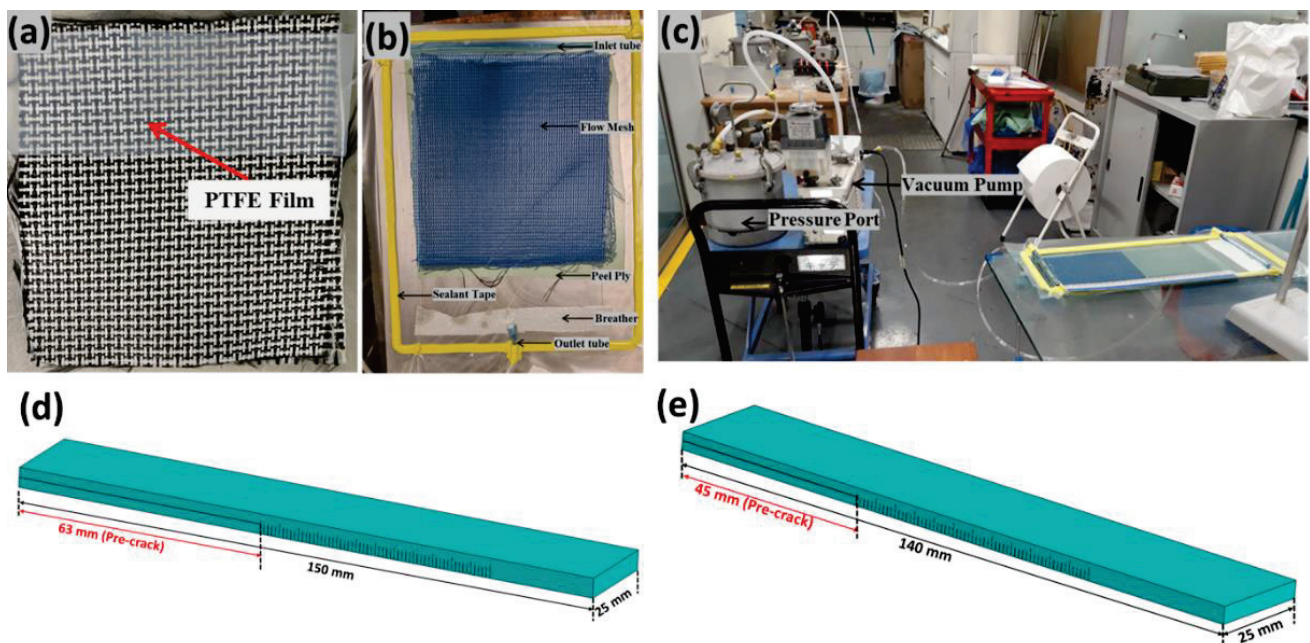


Figure 2. (a) Placement of PTFE film inserted in the central layer of the preform (b,c) Resin Infusion setup (d) Manufactured laminate cut to the dimension for Mode I (e) Manufactured laminate cut to the dimension for Mode II.

Thermoplastic hybrid composite laminate configurations using Elium[®] 150 resin were manufactured at RT. After mixing the resin with hardener at a weight ratio 100:3, it was injected into the preform at full vacuum. After injection, the laminate was let to cure at RT for approximately one hour and the cured laminate was demoulded and then post-cured at 60 °C for an hour. Similarly, a heated cycle was employed for thermoset hybrid composite laminate, containing epoxy as the matrix. The mould temperature before injection was raised to 50 °C and the prepared resin by mixing it with hardener at a weight ratio of 100:35 was also kept at 50 °C. Further, the laminate was injected at this temperature and once the injection was completed, the mould temperature was increased to 110 °C and was held at this temperature for nearly 10 min. Furthermore, the mould was brought to RT and was then demoulded.

The manufactured hybrid composite configurations were cut to the required dimensions of Mode I and Mode II based on ASTM D 5528-13 [35] and JIS K7086 [36] standards, as shown in Figures 2d and 2e, respectively. The manufactured laminates configurations with their fiber volume fraction (V_f) and thickness are illustrated in Table 1. For testing of the manufactured laminate for Mode I and Mode II testing, an aluminum doubler of thickness 1.2 mm was required to be glued to increase the stiffness, which will be explained in more detail in Section 3.

Table 1. Manufactured laminates configurations with their thickness, fiber volume fraction, and nomenclature used in current research.

Reinforcement System	Resin System	Layers	Fiber Volume Fraction (%)	Thickness (mm)	Terminology
Carbon-UHMWPP	WAM Epoxy	12	48.7	7.3	Carbon_UHMWPP/Epoxy
	Elium [®]		49.4	7.2	Carbon_UHMWPP/Elium [®]
Carbon-UHMWPE	WAM Epoxy	14	49.7	7.3	Carbon_UHMWPE/Epoxy
	Elium [®]		50.8	7.2	Carbon_UHMWPE/Elium [®]

Note: Thickness indicated in the table is the total laminate thickness inclusive of Al doubler.

3. Experimental Details

In the current research work, a Mode I (Double Cantilever Beam) fracture toughness test and a Mode II (End-Notched Flexure) fracture toughness test were performed. Because of the low stiffness of the thermoplastic fibers, there are chances of the composite laminate manufactured using thermoplastic reinforcement to be failed prematurely under compression failure without any crack propagation under Mode I/flexure testing [37,38]. To find the solution to this problem different methods were tried, one method is the manufacturing of a thicker sample, which will increase the stiffness of the laminate; but, for the Mode I sample, such a sample thickness with hybrid layers is difficult to manufacture, and the chances of manufacturing defects will increase, which is not ideal for fracture toughness test. Similarly, for Mode II specimens, it may cause difficulty during testing due to the requirement of a higher support span to width ratio [38]. Additionally, the bending of the thicker sample would not be as desired and which will result in incorrect fracture toughness results. Hence, to improve the bending stiffness aluminum doublers were added to the laminate [37]. Aluminum sheets were bonded to the laminates using a control adhesive. The extra factors influenced by the doubler plates are also taken into consideration and the equations were modified [37]. With the addition of the doubler plate, the specimen will no longer be homogenous, and the critical change will be the increase in EI, and the bending stiffness. Furthermore, the addition of doubler plates alters the compliance of the composite specimen and thus the data reduction formulae will be revised. The modified equations considering the addition of the doubler for the bending stiffness were used [37].

3.1. Double Cantilever Beam/Mode I Fracture Toughness Test

The fracture toughness test, Mode I, was carried out utilizing an Instron 5569 machine with a load cell of 50 kN, using a 3-point bending fixture following the ASTM D 5528-13 [35] standard. According to the standard, the length of the artificial delamination or crack has to be 63 mm for the Mode I test. With a cyanoacrylate adhesive, two metal blocks with through-holes were bonded to the split ends of each specimen. Figure 3b depicts the schematic of the sample dimensions. To correctly track the crack propagation of the laminate during testing, the sides of the laminates were painted with white correction fluid and the scale with each millimeter were marked as can be seen from Figure 3a.

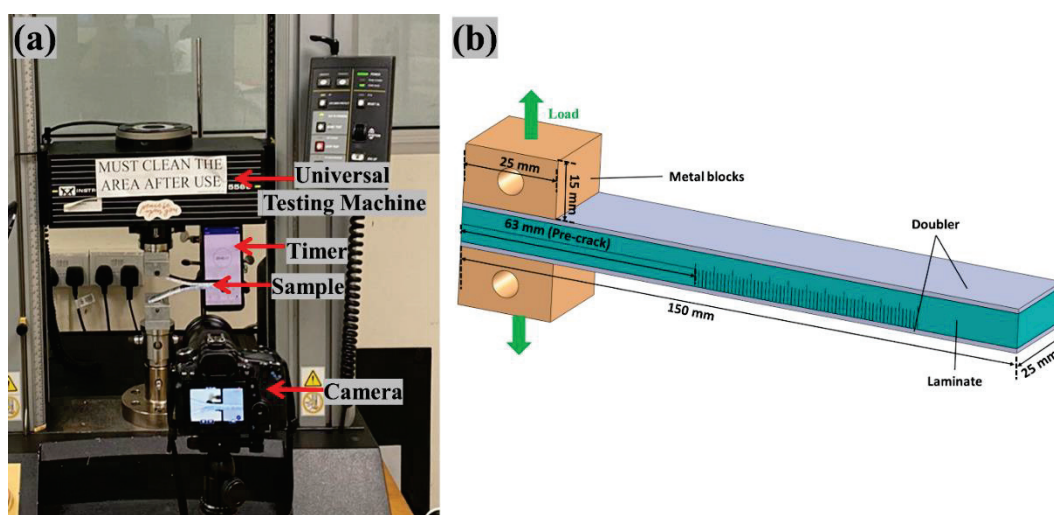


Figure 3. (a) Mode I test setup (b) Schematic of Mode I sample with doublers and metal block attached.

The DCB specimen in Mode I was peeled by pulling the two metal blocks at a constant feed rate of 2 mm/min. The load and crosshead displacement was observed and noted using the data-acquisition system. To aid in the observation of crack propagation over time, a digital camera was positioned in front of the specimen (Figure 3a) [38].

The ASTM D 5528-13 standard was utilized to determine the inter-laminar fracture energy in Mode I [35]. Figure 4a,b depicts the premature failure of the hybrid composite laminate when tested under Mode I without doublers due to low in-plane stiffness as explained above. Figure 4c,d shows the Mode I sample glued with the doubler and when tested it undergoes the desired testing, respectively. A modified beam theory expression with correction factors for significant displacement correction and end block correction was applied. The modified equation using the doublers was shown by the equation below:

$$G_{IC} = \left(\frac{L^2 * (a + (\chi * h))^2}{w * EI_{del(doubler)}} \right) \quad (1)$$

where L : load for crack growth (N), a : corresponding crack length (mm), w : width of the specimen (mm), h : Half-thickness of the specimen (mm), χ is the correction factor.

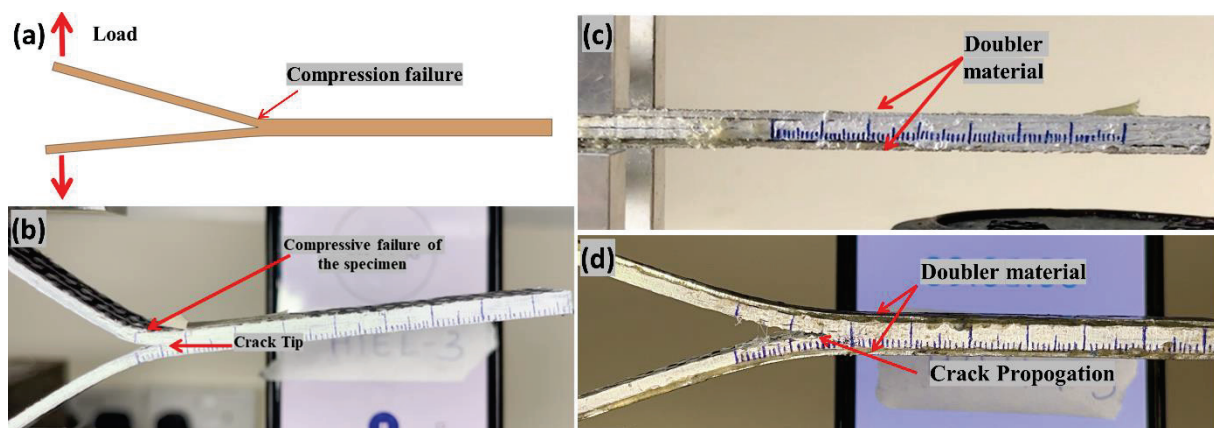


Figure 4. (a,b) Schematic and testing showing the compression failure of the specimen under Mode I testing without doubler respectively (c) Hybrid composite specimen with aluminum doubler (d) Mode I testing of the hybrid composite laminate with doublers.

It should be noted that the χ is the correction factor, which is affected by the inclusion of the doubler, but since this factor is very small, it is neglected in the current research work.

3.2. End Notched Flexure/Mode II Fracture Toughness Test

The Mode II fracture toughness test was carried out following JIS K7086 [36] standard. Instron 5569 machine, a 3-point bending fixture, was used to perform Mode II test. Artificial delamination of 45 mm using PTFE film was created during the manufacturing for Mode II specimens. To correctly track the crack propagation of the laminate for Mode II specimens during testing, the sides of the laminates were painted with white correction fluid and the scale with each millimeter were marked as can be seen from Figure 5b. To reduce the friction between crack surfaces during Mode II test, the PTFE film of 20 μm thickness was removed, and a thick PTFE film was placed between the crack surfaces [38]. Figure 5a–c depicts the Mode II schematic, test setup, and a specimen undergoing the Mode II test, respectively. To facilitate in the observing of crack propagation with respect to time, a digital camera is positioned in front of the specimen for both the fracture toughness tests, Mode I and II [38].

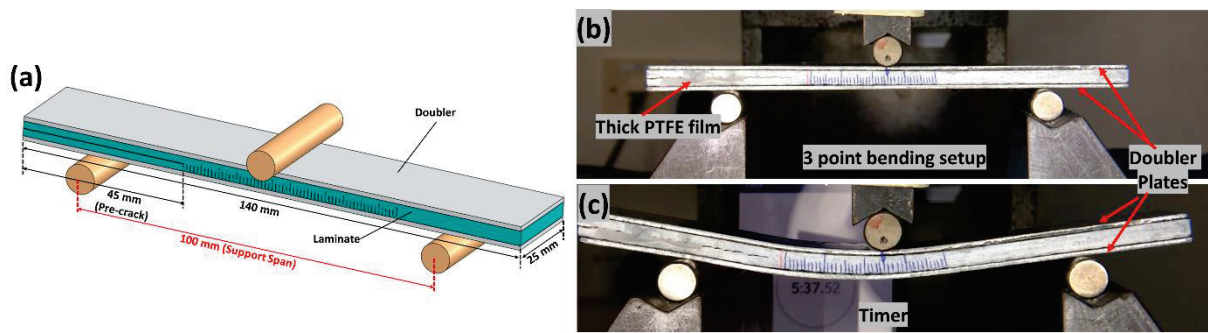


Figure 5. (a) Schematic of the Mode II tests sample with dimensions (b) Mode II test setup and (c) Specimen undergoing Mode II test.

The Mode-II is analyzed based on the beam theory as shown in Equation (2), with the crack length correction in accordance to JIS standard [39].

$$G_{IIC} = \frac{9 * L^2 * C * a^2}{2 * w * ((2 * S^3) + (3 * a^3))} \quad (2)$$

Compliance is given by Equation (3) [39].

$$C = \frac{(2 * L^3) + (3 * a^3)}{8 * E_L * w * h^3} \quad (3)$$

where L is load (N), a is the total crack length (mm), S is the half support span (mm), C is the compliance (mm/N), E_L is the longitudinal elastic modulus (MPa), and h : is half of the thickness of the laminate (mm).

Based on the beam theory, the original equation for Mode-II ILFT is assessed as shown in Equation (2), JIS standard [39]. Homogeneous stiffness of the laminate is assumed in Equation (2) and therefore this equation is required to be modified to include the doubler parameter to avoid the premature compression failure (refer Figure 6a,b), which is explained in detail in our recently published work [38].

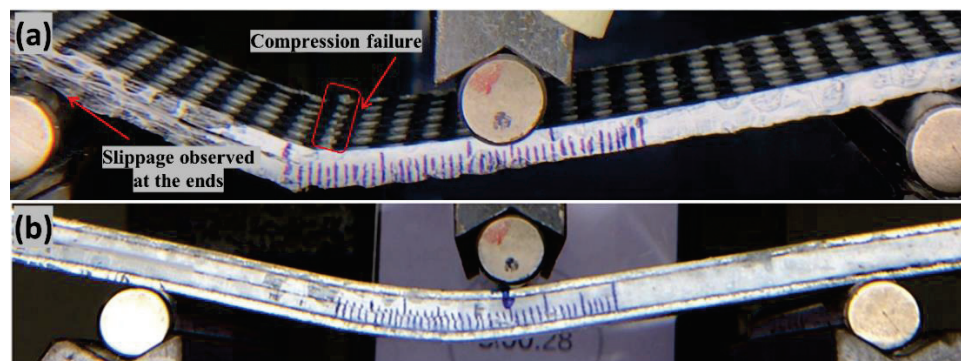


Figure 6. (a) Hybrid composite premature compression failure under mode II testing without doubler (b) Hybrid composite specimen under Mode II with doubler.

For each wholly thermoplastic composite configuration, a minimum of three specimens were tested under Mode II testing to obtain better repeatability of the result. During testing, a support span of 100 mm was used and the tensile modulus (E_L) of the composites were calculated following the ASTM D3039 [40] standard. The calculated average tensile modulus of Carbon_UHMWPP/Elium[®] and Carbon_UHMWPE/Elium[®] composites are 17.96 GPa and 27 GPa, respectively. Additionally, for Carbon_UHMWPP/Epoxy and Carbon_UHMWPE/Epoxy composites are 18.95 GPa and 27.94 GPa, respectively. A scanning electron microscope (SEM) was further used on the failed samples tested under Mode I and II loading to perform a detailed surface morphological study.

4. Results and Discussions

The test results of various mechanical characterization tests are discussed in this section. A comparative study on the performance of thermoplastic composites against thermosetting composites is also performed. In addition, the various failure mechanisms of the tested composites were carried out through a comprehensive microscopic study.

4.1. Double Cantilever Beam/MODE I Test

4.1.1. Load vs. Displacement Characteristics

The load vs. displacement graphs for Carbon_UHMWPP and Carbon_UHMWPE reinforced Elium[®] and Epoxy composites are shown in Figure 7a,b, respectively. A minor non-linearity is noticed prior to the fracture propagation, following which the specimen exhibited acceptable linear behavior. The load-displacement curve of the hybrid fiber reinforced composite also shows the stick-slip behavior connected with unstable crack jumps in the weaving structure [3]. As shown in Figure 7a, peak load to failure is higher for Carbon_UHMWPP/Elium[®] composites when compared to Carbon_UHMWPP/Epoxy composites. This could be attributable to the better fiber/matrix bonding in thermoplastic composites. Whereas Carbon_UHMWPE/Elium[®] and Carbon_UHMWPE/Epoxy composites have a lesser difference for the peak load to failure (refer Figure 7b). Some of the load reductions and Mode I fracture resistance development with increasing crack length could generally be due to secondary energy-dissipation processes such as tow rupture and/or de-bonding occurrences [23,41,42].

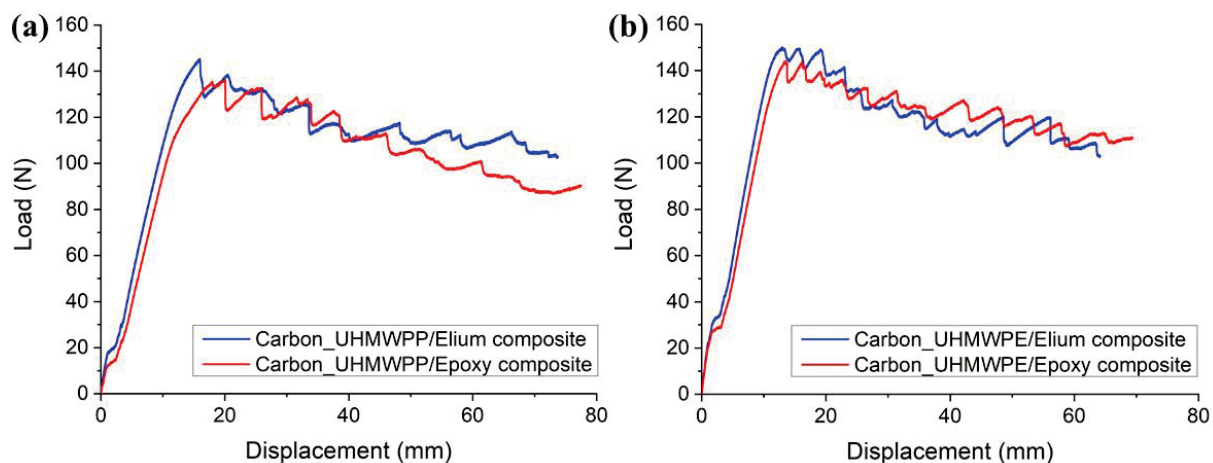


Figure 7. Load vs. displacement graphs for (a) Hybrid Carbon_UHMWPP (b) Hybrid Carbon_UHMWPE composite configurations.

The resistance curves (R-curves) of Carbon_UHMWPP and Carbon_UHMWPE reinforced Elium[®] and Epoxy composites are depicted in Figure 8a,b, respectively. The hybridization of UHMWPP and UHMWPE fibers with carbon fiber results in a significant rise in G_{IC} values. Due to the disparity in carbon and thermoplastic yarn diameter and geometries, a resin-rich zone is created at hybrid interfaces, which in turn promotes a cohesive failure at the hybrid interfaces [3]. Figure 9a,b shows the average mode I fracture toughness values of various hybrid composites. For Carbon_UHMWPP/Elium[®] composite has a G_{IC} value of 2.616 kJ/m², which is 22.81% higher than Carbon_UHMWPP/Epoxy composite. However, Carbon_UHMWPE/Elium[®] and Carbon_UHMWPE/Epoxy have G_{IC} values of 2.957 kJ/m² and 2.661 kJ/m², respectively (11.11% for Elium[®] based hybrid composite).

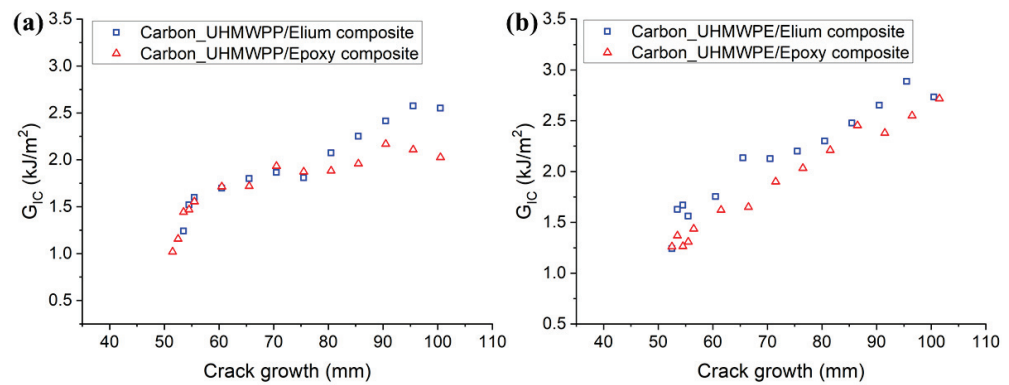


Figure 8. Resistance graphs for (a) Hybrid Carbon_UHMWPP (b) Hybrid Carbon_UHMWPE composite configurations.

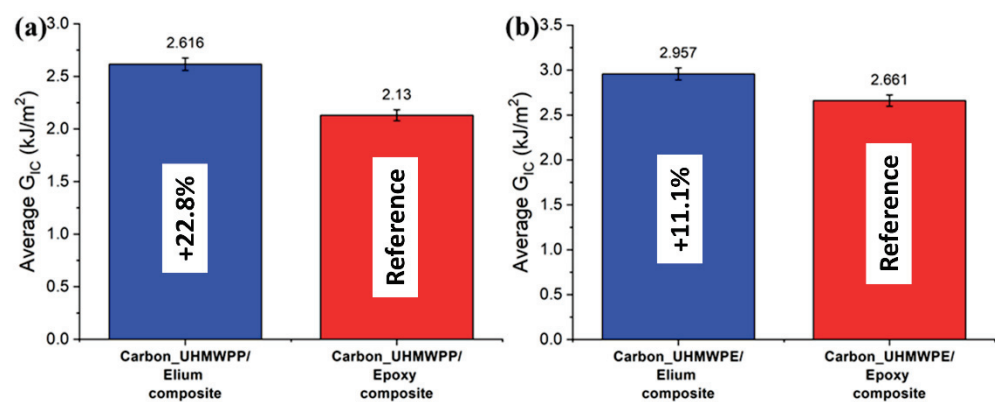


Figure 9. Average critical energy release rates for (a) Carbon_UHMWPP (b) Carbon_UHMWPE composite configurations.

4.1.2. Failure Mechanisms

All the hybrid laminated composite configurations have shown stick-slip characteristics (refer Figure 7a,b) which is a very well-known phenomenon occurring particularly for the composites with woven fabric due to its weave architecture [3,4]. There is more resistance to crack propagation as the crack front is typically discontinuous and jumps in between the fiber tows in longitudinal and transverse directions. The interfaces of the hybrid composite configuration with both the matrix systems have the same amount of UHMWPP or UHMWPE fibers and carbon fibers. Figure 10a–d shows the microscopic images of the different laminate configurations. For Carbon_UHMWPP and Carbon_UHMWPE reinforced Elium® composites (refer Figure 10a,b), extensive fiber bridging, and fiber breakage and the pull-out phenomenon were observed, which results in significantly resisting the crack propagation. It is evident for all the laminate configurations that the layers with the interweaving of UHMWPE and UHMWPP with carbon fibers have formed a tortuous interface as there is a presence, are matrix/resin-rich sites, as well as the varied ranges of yarn sizes as well as differences in the adhesion characteristic of these reinforcements with acrylic thermoplastic and thermosetting epoxy resins (refer Figure 10a,b,d). This is also one of the reasons for the laminated configurations showing very strong stick-slip characteristics. The fiber failure sites at the resin-rich areas are observed along with the pull out of the UHMWPE yarns with the epoxy matrices highlighting the poor adhesion resins (refer Figure 10d).

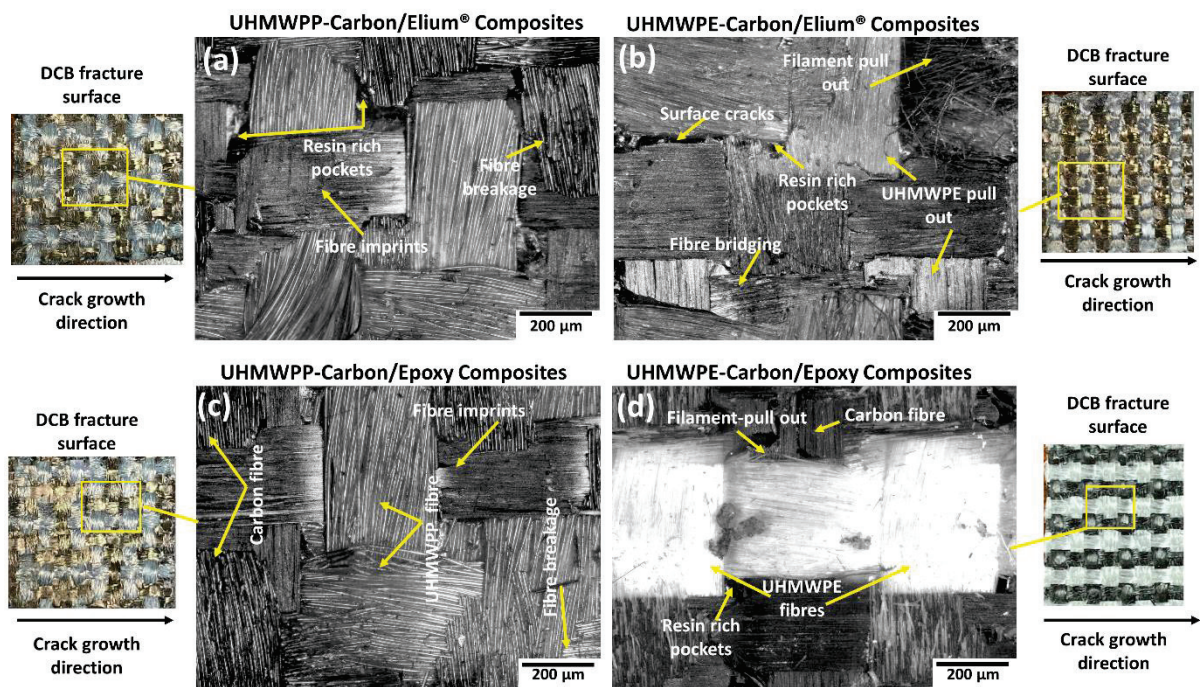


Figure 10. Micrographic images of the failed surfaces of (a) Carbon_UHMWPP/Elium[®] (b) Carbon_UHMWPE/Elium[®] (c) Carbon_UHMWPP/Epoxy and (d) Carbon_UHMWPE/Epoxy reinforced composite configurations under Mode I loading.

To better understand the failure mechanisms, several macro and micro photographs of the side surface of the specimen were taken. Figure 11a–c shows the macro-photographs of hybrid fiber reinforced thermoplastic composites, which highlight the features, such as fiber bridging and pull out, formation of multiple cracks sites, crack branching, and others that are important crack arresting mechanisms. The resistance to fracture growth is also aided by localized filament pull-out and splitting of thermoplastic yarns [3].

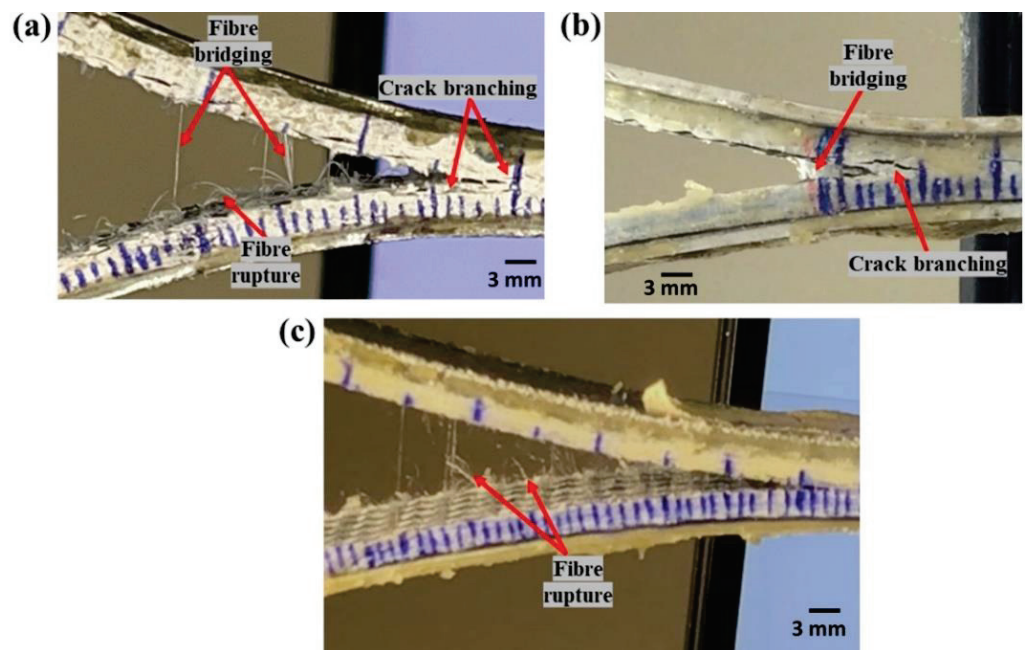


Figure 11. Macro-photographs of side surfaces of (a,b) Carbon_UHMWPP and (c) Carbon_UHMWPE reinforced thermoplastic composites.

Microphotographs of Carbon_UHMWPP and Carbon_UHMWPE reinforced thermoplastic composites with multiple cracks, fiber pull-outs are described in Figure 12a–c, respectively. The typical features shown by Carbon_UHMWPP reinforced composites included multiple cracks and crack deflection along with fiber pull-outs and bridging. While Carbon_UHMWPE reinforced composites exhibit only moderate fiber pull-out and rupture due to the poor adhesion characteristics of the UHMWPE fabrics with both the thermoplastic and thermoset variants.

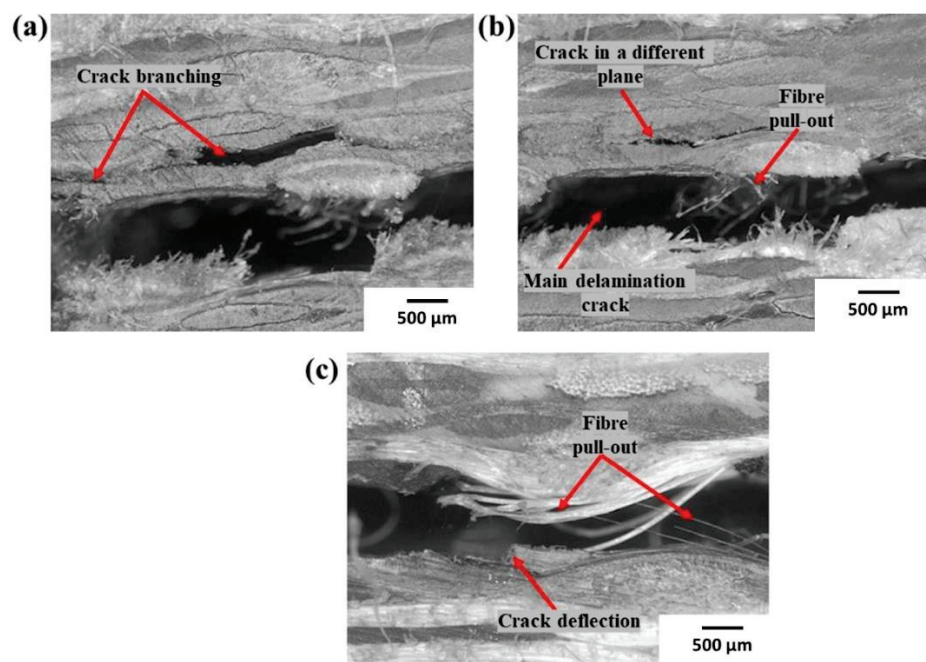


Figure 12. Micro-photographs of side surfaces of (a,b) Carbon_UHMWPP and (c) Carbon_UHMWPE reinforced thermoplastic composites.

The initial crack deflection sites and the subsequent crack branching significantly contribute to improving the delamination resistance of the hybrid fabric with acrylic Elium[®] resin [9,20]. The crack advancement in the interlayers is highly resisted due to the higher fracture toughness of Elium[®] resin (0.5 kJ/m^2) compared to thermoset epoxy resin (0.2 kJ/m^2) [9,20,23].

To further understand the failure processes, a scanning electron microscopic analysis was used to examine the tested specimens in detail. The different failure modes of hybrid fiber reinforced composites are depicted in Figures 13a–f and 14a–d. Hybrid fiber reinforced thermoplastic composites shows severe plastic deformation of the matrix, rough fracture residue and micro-cracks on the de-bonding surface (refer Figures 13a,b,d,e and 14a), which in turn confirms better fiber/matrix bonding. Figure 13a shows a resin-rich region at the hybrid interface of the Elium[®] composite, indicating the possibility of a cohesive failure. Localized surface fractures are also observed immediately after crack initiation sites, which are prevented by fiber pull-outs, bridging, and a strong fiber-matrix bonding (refer Figures 13a,d and 14a,c).

Sharp step features, such as scarp (refer Figure 14a) and the textured microflow sites, are also observed for the acrylic-based composites (refer Figure 14c). While hybrid fiber reinforced epoxy composites exhibit hackle markings and clean fiber fracture with smooth surface and pull-outs, which is a typical characteristic of a brittle thermoset matrix system [9,23] as shown in Figures 13f and 14b. Fiber imprints were noticed for all the laminated composite configurations (refer Figures 13c,d and 14c,d) with matching surfaces being exposed with one leaving with a significant amount of fibers while the other has it imprints [43].

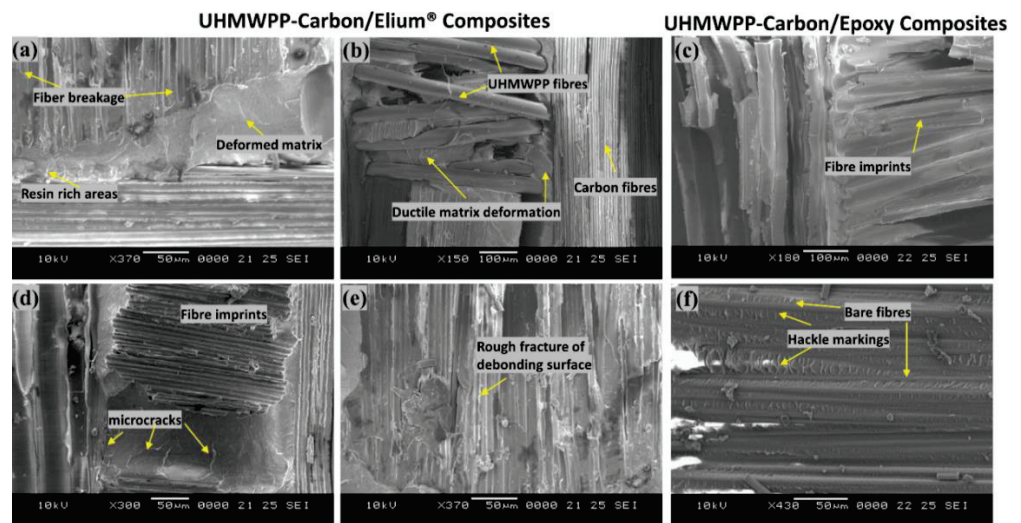


Figure 13. Surface morphological images of fractured surfaces of composites using Scanning Electron Microscopic approach of (a,b,d,e) Carbon_UHMWPP/ Elium® (c,f) Carbon_UHMWPP/Epoxy composites under Mode I loading.

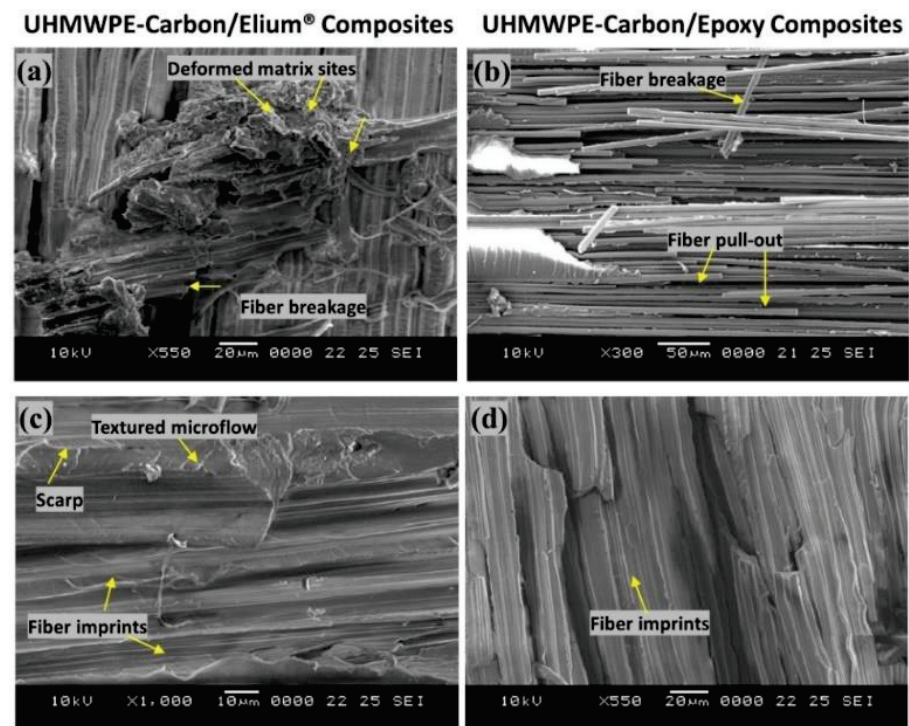


Figure 14. Surface morphological images of fractured surfaces of composites using Scanning Electron Microscopic approach of (a,c) Carbon_UHMWPE/Elium® (b,d) Carbon_UHMWPE/Epoxy composite under Mode I loading.

4.2. End Notched Flexure/MODE II Test

4.2.1. Load vs. Displacement Characteristics

The load vs. displacement graphs for Carbon_UHMWPP and Carbon_UHMWPE reinforced Elium® and Epoxy composites under Mode II loading are shown in Figure 15a,b, respectively.

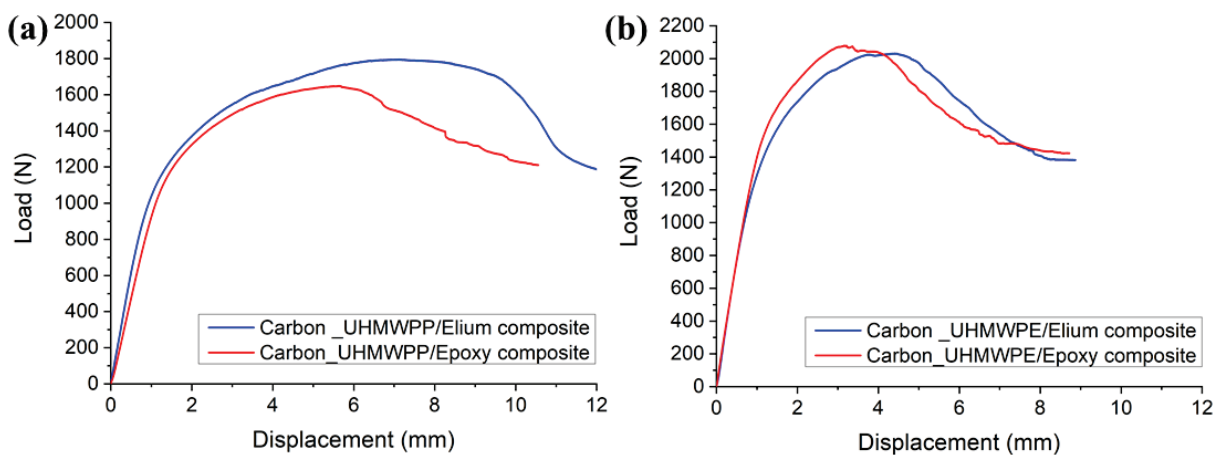


Figure 15. Load vs. Displacement graphs for (a) Carbon_UHMWPP (b) Carbon_UHMWPE fiber reinforced composite configurations.

The load vs. displacement graphs of hybrid fiber reinforced composites exhibit a linear growth followed by a non-linear portion, which is more noticeable in the case of thermoplastic composites, before the onset of crack propagation. However, the non-linearity observed in Elium[®] composites is indicative of the thermoplastic resin plastic deformation which delays the unstable crack propagation to a greater displacement value [11], as shown in Figure 15a,b. The highest peak load is found for Carbon_UHMWPP reinforced composites using Elium[®] as the matrix, suggesting an 8.88% increase in load-bearing capability above the baseline of Carbon_UHMWPP reinforced epoxy composite. However, Carbon_UHMWPE/Epoxy composite has a higher peak load of 2.079 kN, which is 2.36% greater than that of Carbon_UHMWPE/Elium[®].

Figure 16a,b depict the resistance curves for Carbon_UHMWPP and Carbon_UHMWPE reinforced Elium[®] and Epoxy composites, respectively. The crack growth is found to be relatively more unstable for Elium[®] composites. A considerable increase in the fracture toughness values is observed for based hybrid fiber composites. This could be due to the resin pockets created by the difference in the carbon and thermoplastic fiber diameters and the tortuous crack propagation [4].

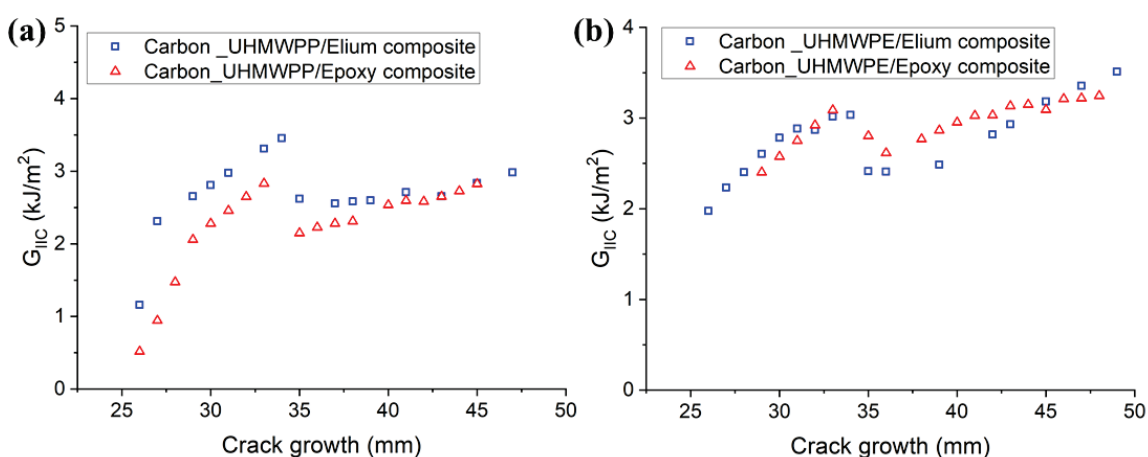


Figure 16. R-curves for (a) Carbon_UHMWPP (b) Carbon_UHMWPE composites configurations.

The results of all the laminated configurations compared to the Mode I test results are more dispersed due to the complexity of the toughening mechanisms for hybrid thermoplastic composites. The non-linearity as observed from the R-curves of the hybrid composites could be attributed to the moderate to poor bonding of the thermoplastic yarns with acrylic Elium[®] and Epoxy resin, respectively, as well as the significantly lower

transverse and shear properties of UHMWPE and UHMWPP fibers, and the same has been reported in a research performed by Zhou et al., while investigating the Mode II performance of hybrid carbon-UHMWPE/epoxy composite [4]. The average mode II fracture toughness values of hybrid fiber reinforced composites are illustrated in Figure 17a,b, respectively. The G_{IIC} value of the Carbon_UHMWPP/Elium[®] composite is 3.433 kJ/m² which is 22.21% higher than the G_{IIC} value of the Carbon_UHMWPP/Epoxy composite. However, Carbon_UHMWPE/Elium[®] and Carbon_UHMWPE/Epoxy have G_{IIC} values of 3.496 kJ/m² and 3.231 kJ/m², respectively. The increase in the Mode II fracture toughness for the acrylic-based hybrid composites is attributed to the difference in their chemical structures with Elium[®] absorbing more energy as there is comparatively a much larger free volume between the polymeric chains and hence leads to additional plastic deformation absorption linked to the crack propagation, while the thermoset epoxy-based composites have cross-linked structure inducing brittle characteristics leading to lower fracture toughness [9,11,44]. The fracture toughness for hybrid composites is relatively higher than the pure carbon variants due to the extra resistance arising from the frictional sliding of the expanding contact area of the woven fabric of the failure surfaces [3,4,9]. Thermoplastic fabrics are known to improve the friction between the surfaces of the fracture zones in contrast with the smooth surface in the case of conventional carbon fabrics [3,4].

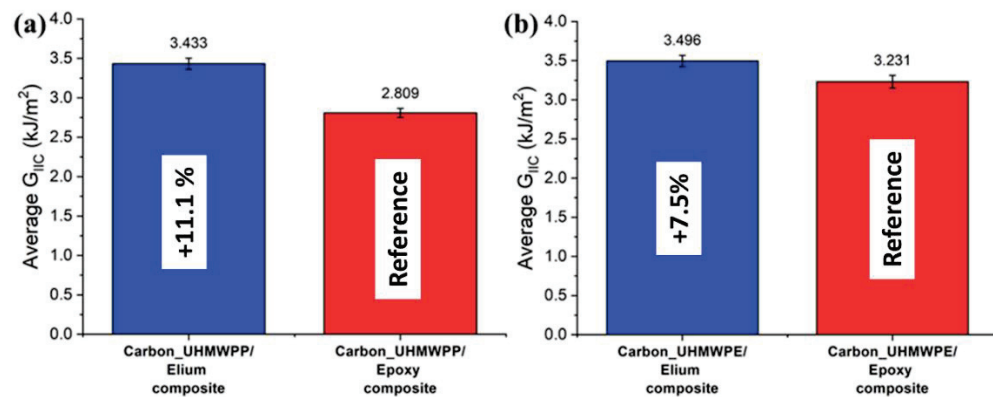


Figure 17. Average critical energy release rates for (a) Carbon_UHMWPP (b) Carbon_UHMWPE composites configurations.

4.2.2. Failure Mechanisms

Macro-photographs of crack growth of Carbon_UHMWPE reinforced composites taken during the Mode II test are shown in Figure 18a–c. Figure 18a,b represent Carbon_UHMWPE/Elium[®] sample at the beginning of the test and at a test duration of $t = 480$ s, respectively, whereas Figure 18c represents the Carbon_UHMWPE/Epoxy sample at a test duration of $t = 480$ s. A crack propagation of 18 mm and 23 mm can be observed in the same time duration for Carbon_UHMWPE/Elium[®] and Carbon_UHMWPE/Epoxy, respectively; thus, demonstrating the higher resistance to crack propagation offered by Elium[®] composites even when they are reinforced with the same hybrid fibers.

The microphotographs as seen from Figure 19a,b shows significant fiber bridging for the acrylic-based hybrid composite configurations. The fabric yarns and filaments are seen to be pulled out being adjoined to the crack surfaces along with the transverse yarn damage and signals that at the delamination front there must have been a formation of bridging zones which is an important crack resistance mechanism (refer Figure 19a,b). Due to mismatches in the yarn sizes of the UHMWPE or UHMWPP with carbon, large resin pockets or resin-rich areas (refer Figure 19a,b,d) are introduced which is an important driver to improving the fracture toughness by aiding in an increased fracture process zone. For the epoxy-based hybrid composites, the fiber dominating crack enhancing mechanisms along with imprints remains intact but the presence of bare fibers deprived of the resin signals a poor adhesion of the thermoplastic fabrics with epoxy resin similar to the earlier reported mechanisms for Mode I results (refer Figure 19c,d).

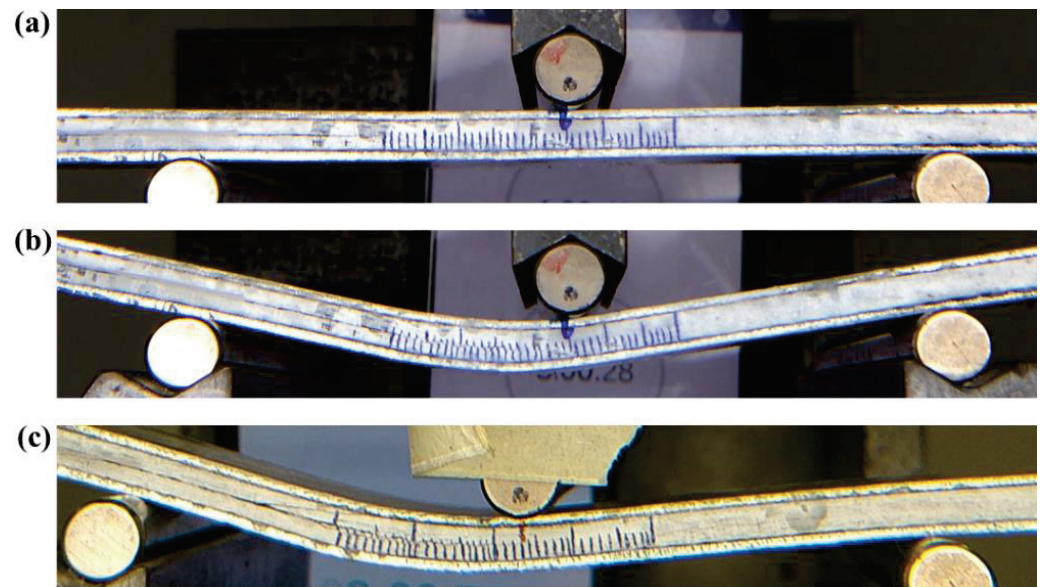


Figure 18. Macro-photographs of (a) Carbon_UHMWPE/Elium® composite at the start of the test (t = 0 s) (b) Carbon_UHMWPE/Elium® composite between testing (t = 480 s) (c) Carbon_UHMWPE/Epoxy composite between testing (t = 480 s).

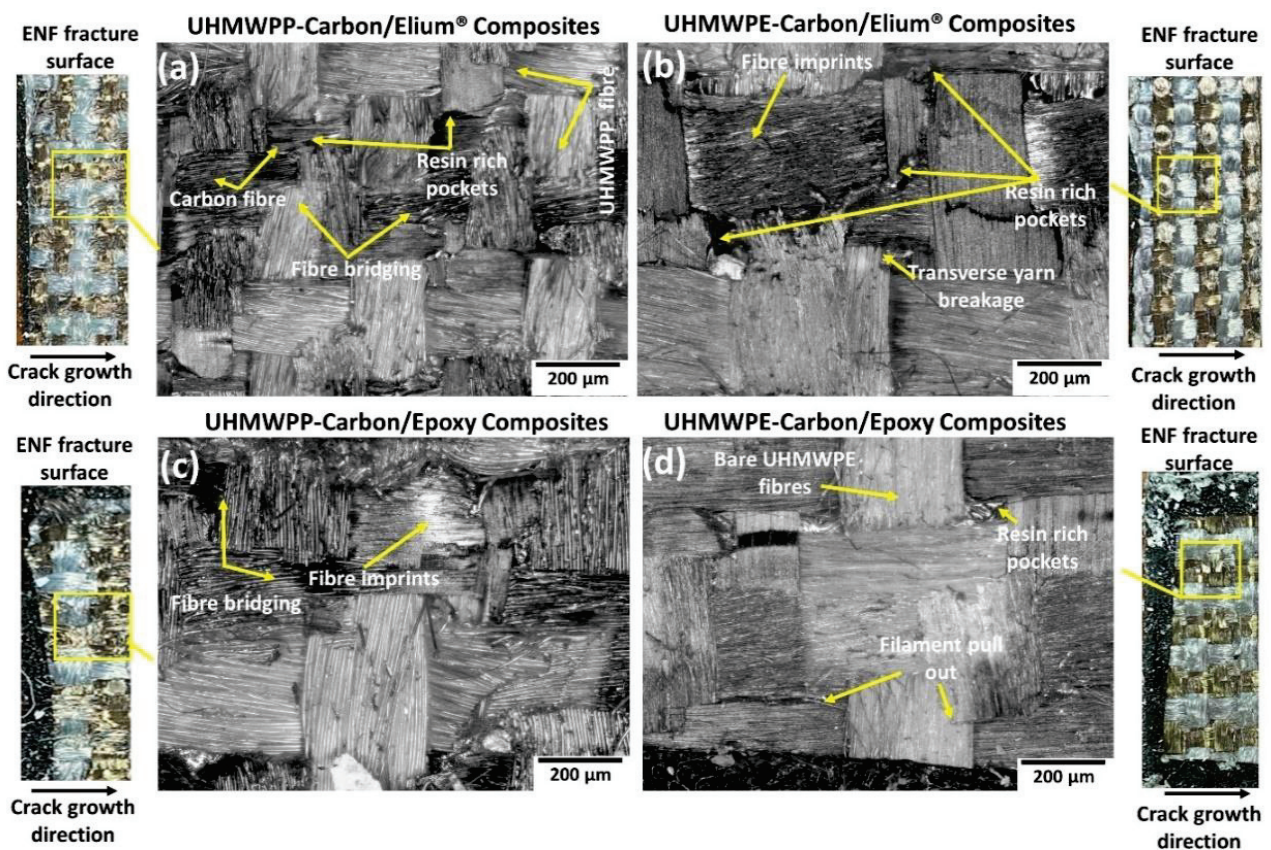


Figure 19. Micrographic images of the failed surfaces of (a) Carbon_UHMWPP/Elium® (b) Carbon_UHMWPE/Elium® (c) Carbon_UHMWPP/Epoxy and (d) Carbon_UHMWPE/Epoxy reinforced composite configurations under Mode II loading.

For a better comprehension of the failure mechanisms of the various hybrid composite configurations, an elaborate Scanning Electron Microscopy study was conducted, as illustrated in Figures 20a–f and 21a–d. Figures 20a–f and 21a–d depict the presence of shear

cusps, river line marking converging to form scarps, fiber imprints, and fiber pull-out, which are all common Mode II failure features. Strong fiber/matrix adhesion of Elium[®] composites is observed in Figures 20e and 21c. Figure 21c depicts the severe ductile plastic deformation underwent by the Elium[®] matrix. Figures 20c,f and 21b,d shows the various failure modes observed in Epoxy composites including the shear cusps and fiber imprints. The smooth de-bonding surface illustrated the bare fiber (refer Figure 20f) which substantiates the poor fiber/matrix adhesion of the thermosetting composite. One can observe the presence of the bare fibers resulting from the shear failure of the matrix under consideration but on the contrary, the surfaces were found to be significantly rougher in acrylic Elium[®] based hybrid composites owing to significant yarn splitting of the thermoplastic fibers. Thermoplastic fibers, such as UHMWPE and UHMWPP are chemically inert and tend to form weaker bonds with the thermosetting epoxy as well as acrylic Elium[®] resin in the current investigation [3,4]. The fracture surfaces are also found to be partially covered with a very thin epoxy or acrylic resin layer along with the fiber imprints of the fibers, which were debonded from the mating layer and confirm the delamination growth or propagation on the bottom fiber/matrix interface (refer Figures 20b,c,e,f and 21a–d). At a higher magnification, thermoplastic fibers are observed to be pulled out and are nicely correlated to the macro photographic fiber bridging aspects, which are discussed earlier (refer Figures 20b,c and 21c).

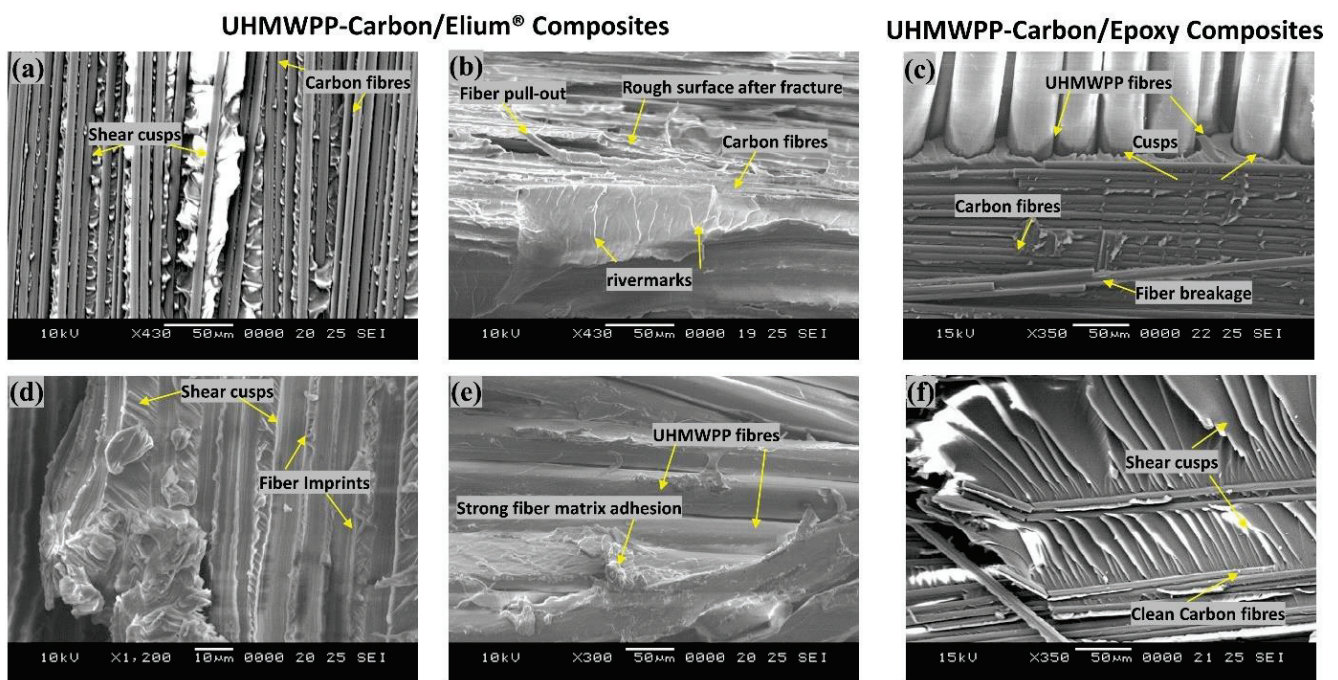


Figure 20. Surface morphological images of fractured surfaces of composites using Scanning Electron Microscopic approach of (a,b,d,e) Carbon_UHMWPP/Elium[®] composite (c,f) Carbon_UHMWPP/Epoxy composite under Mode II loading.

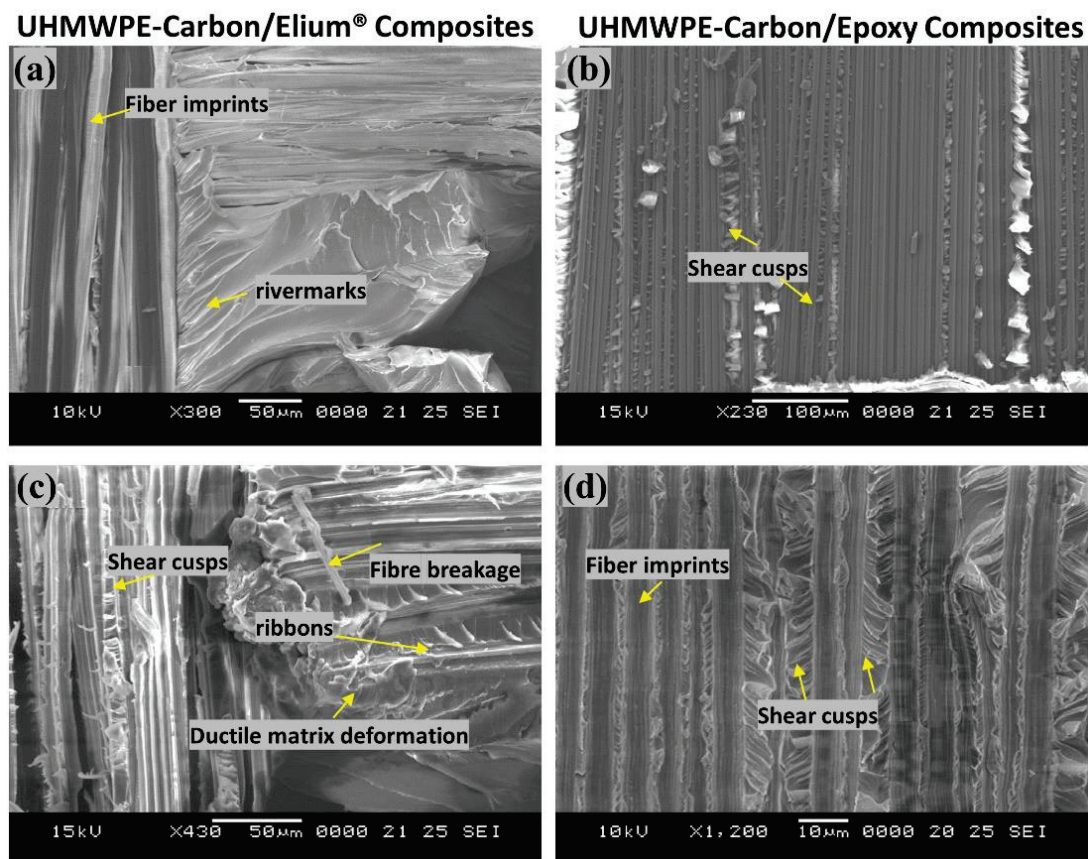


Figure 21. Surface morphological images of fractured surfaces of composites using Scanning Electron Microscopic approach of (a,c) Carbon_UHMWPE/Elium[®] composite (b,d) Carbon_UHMWPE/Epoxy composite under Mode II loading.

5. Conclusions

In the current research, hybrid fiber reinforced Elium[®] composites are manufactured using a vacuum-assisted resin infusion (VARI) process, and their fracture toughness attributes are studied under Mode I and II loading. The details of the experimental study using the doubler methodology are also presented to test the hybrid laminated composite configurations. The failure mechanisms of the composites under each of the above-mentioned loading scenarios are understood by the detailed microscopic investigation to comprehend the bonding efficacy of thermoplastic Elium[®] resin with the hybrid thermoplastic fibers along with the baseline comparison carried out with the composites manufactured using thermosetting epoxy matrix. Important findings are summarized below:

The stiffness of the composite laminates is modified by including aluminum doublers and the Mode I and II tests were successfully carried out for all the hybrid laminated composite configurations by eradicating the concerns of large displacement and compression failure during the tests.

Hybrid Carbon_UHMWPP/Elium[®] composite has shown 22.81% higher G_{IC} and 22.2% higher G_{IIC} than Carbon_UHMWPP/Epoxy composite. While the Carbon_UHMWPE/Elium[®] has shown an 11.11% higher G_{IC} and a 7.58% higher G_{IIC} than Carbon_UHMWPE/Epoxy composite.

The initial crack deflection sites and the subsequent crack branching contribute significantly to improving the delamination resistance of the hybrid fabric with acrylic Elium[®] resin under the Mode I loading scenario. Hybrid fiber reinforced thermoplastic composites shows severe plastic deformation of the matrix, rough fracture residue, and micro-cracks on the de-bonding surface, which resulted in the improved fracture toughness for the hybrid

thermoplastic-based composites while the hybrid fiber reinforced epoxy composites exhibit hackle markings and clean fiber fracture with smooth surface and pull-out.

In general, hybrid fiber architecture is also found to be contributing significantly to increasing the overall fracture toughness as it induced the tortuous crack path due to the mismatch of the fiber yarns and the generation of resin-rich sites which has a major positive say on the fracture toughness attributes.

The development of hybrid fiber reinforced thermoplastic composites and their acceptable bonding with the thermoplastic acrylic resin could be an excellent alternative to the conventionally used thermosetting material systems owing to their ease of manufacturing at room temperature along with the typical thermoplastic advantages they will offer in terms of impact, damping, recyclability, and many others which could have tremendous application in automotive, sporting equipment, and protective gear and ballistic applications.

Author Contributions: S.K.B.: Conceptualization, Methodology, Investigation, Original draft preparation, Writing—Review and Editing; G.G.: Conceptualization, Methodology, Investigation, Writing—Review and Editing; D.V.: Original draft preparation; Methodology, Investigation, K.F.L.: Supervision, Funding acquisition; P.G.: Resources. All authors have read and agreed to the published version of the manuscript.

Funding: The authors would like to acknowledge financial support from Nanyang Technological University, Singapore and Arkema, France under the industry collaboration project with Arkema (NTU REF: REQ0232981). This research is also supported by A*STAR under the Research Innovation Enterprise (RIE) 2020 Plan, Advanced Manufacturing and Engineering (AME) Domain—Industry Alignment Fund—Pre-positioning (IAF-PP) Polymer Matrix Composites Program, Grant number A19C9a0044, Work Package 1–2.

Institutional Review Board Statement: Not applicable.

Informed Consent Statement: Not applicable.

Data Availability Statement: The raw data required to reproduce these findings cannot be shared at this time as the data also forms part of an ongoing study.

Acknowledgments: The authors would like to acknowledge support from Nanyang Technological University, Singapore; Arkema, France; and A*STAR, under the Research Innovation Enterprise (RIE) 2020 Plan, Advanced Manufacturing and Engineering (AME) Domain—Industry Alignment Fund—Pre-positioning (IAF-PP) Polymer Matrix Composites Program.

Conflicts of Interest: The authors declare no conflict of interest.

References



- Lässig, T.; Nguyen, L.; May, M.; Riedel, W.; Heisserer, U.; van der Werff, H.; Hiermaier, S. A non-linear orthotropic hydrocode model for ultra-high molecular weight polyethylene in impact simulations. *Int. J. Impact Eng.* **2015**, *75*, 110–122. [CrossRef]
- Larsson, F.; Svensson, L. Carbon, polyethylene and PBO hybrid fibre composites for structural lightweight armour. *Compos. Part A: Appl. Sci. Manuf.* **2002**, *33*, 221–231. [CrossRef]
- Zhao, Y.; Cao, M.; Lum, W.P.; Tan, V.B.C.; Tay, T.E. Interlaminar fracture toughness of hybrid woven carbon-Dyneema composites. *Compos. Part A Appl. Sci. Manuf.* **2018**, *114*, 377–387. [CrossRef]
- Zhou, H.X.; Li, S.P.; Xie, K.; Lu, X.; Zhao, Y.; Tay, T.E. Mode II interlaminar fracture of hybrid woven carbon-Dyneema composites. *Compos. Part A Appl. Sci. Manuf.* **2020**, *131*, 105785. [CrossRef]
- Campbell, F.C. *Chapter 10—Thermoplastic Composites: An Unfulfilled Promise, in Manufacturing Processes for Advanced Composites*; Campbell, F.C., Ed.; Elsevier Science: Amsterdam, the Netherlands, 2004; pp. 357–397.
- Friedrich, K.; Gogeva, T.; Fakirov, S. Thermoplastic impregnated fiber bundles: Manufacturing of laminates and fracture mechanics characterization. *Compos. Sci. Technol.* **1988**, *33*, 97–120. [CrossRef]
- Ma, Y.; Yang, Y.; Sugahara, T.; Hamada, H. A study on the failure behavior and mechanical properties of unidirectional fiber reinforced thermosetting and thermoplastic composites. *Compos. Part B: Eng.* **2016**, *99*, 162–172. [CrossRef]
- Yao, S.-S.; Jin, F.-L.; Rhee, K.Y.; Hui, D.; Park, S.-J. Recent advances in carbon-fiber-reinforced thermoplastic composites: A review. *Compos. Part B Eng.* **2018**, *142*, 241–250. [CrossRef]
- Bhudolia, S.K.; Perrotey, P.; Joshi, S.C. Mode I fracture toughness and fractographic investigation of carbon fibre composites with liquid Methylmethacrylate thermoplastic matrix. *Compos. Part B Eng.* **2018**, *134*, 246–253. [CrossRef]
- Kinvi-Dossou, G.; Boumbimba, R.M.; Bonfoh, N.; Koutsawa, Y.; Eccli, D.; Gerard, P. A numerical homogenization of E-glass/acrylic woven composite laminates: Application to low velocity impact. *Compos. Struct.* **2018**, *200*, 540–554. [CrossRef]

11. Barbosa, L.C.M.; Bortoluzzi, D.B.; Ancelotti, A.C. Analysis of fracture toughness in mode II and fractographic study of composites based on Elium[®] 150 thermoplastic matrix. *Compos. Part B Eng.* **2019**, *175*, 107082. [CrossRef]
12. Shah, S.Z.H.; Megat-Yusoff, P.S.M.; Karuppanan, S.; Choudhry, R.S.; Din, I.U.; Othman, A.R.; Sharp, K.; Gerard, P. Compression and buckling after impact response of resin-infused thermoplastic and thermoset 3D woven composites. *Compos. Part B Eng.* **2021**, *207*, 108592. [CrossRef]
13. Bhudolia, S.K.; Gohel, G.; Leong, K.F.; Joshi, S.C. Damping, impact and flexural performance of novel carbon/Elium[®] thermoplastic tubular composites. *Compos. Part B Eng.* **2020**, *203*, 108480. [CrossRef]
14. Khalili, P.; Blinzler, B.; Kádár, R.; Bisschop, R.; Försth, M.; Blomqvist, P. Flammability, smoke, mechanical behaviours and morphology of flame retarded natural Fibre/Elium[®] composite. *Materials* **2019**, *12*, 2648. [CrossRef]
15. Matadi Boumbimba, R.; Coulibaly, M.; Khabouchi, A.; Kinvi-Dossou, G.; Bonfoh, N.; Gerard, P. Glass fibres reinforced acrylic thermoplastic resin-based tri-block copolymers composites: Low velocity impact response at various temperatures. *Compos. Struct.* **2017**, *160*, 939–951. [CrossRef]
16. Bhudolia, S.K.; Joshi, S.C. Low-velocity impact response of carbon fibre composites with novel liquid Methylmethacrylate thermoplastic matrix. *Compos. Struct.* **2018**, *203*, 696–708. [CrossRef]
17. Bhudolia, S.K.; Gohel, G.; Kantipudi, J.; Leong, K.F.; Gerard, P. Mechanical performance and damage mechanisms of thin rectangular carbon/Elium[®] tubular thermoplastic composites under flexure and low-velocity impact. *Thin-Walled Struct.* **2021**, *165*, 107971. [CrossRef]
18. Kazemi, M.E.; Shanmugam, L.; Lu, D.; Wang, X.; Wang, B.; Yang, J. Mechanical properties and failure modes of hybrid fiber reinforced polymer composites with a novel liquid thermoplastic resin, Elium[®]. *Compos. Part A Appl. Sci. Manuf.* **2019**, *125*, 105523. [CrossRef]
19. Bhudolia, S.K.; Perrotey, P.; Joshi, S.C. Enhanced vibration damping and dynamic mechanical characteristics of composites with novel pseudo-thermoset matrix system. *Compos. Struct.* **2017**, *179*, 502–513. [CrossRef]
20. Shanmugam, L.; Kazemi, M.E.; Rao, Z.; Lu, D.; Wang, X.; Wang, B.; Yang, L.; Yang, J. Enhanced mode I fracture toughness of UHMWPE fabric/thermoplastic laminates with combined surface treatments of polydopamine and functionalized carbon nanotubes. *Compos. Part B Eng.* **2019**, *178*, 107450. [CrossRef]
21. Bhudolia, S.K.; Gohel, G.; Leong, K.F.; Barsotti, R.J., Jr. Investigation on ultrasonic welding attributes of novel Carbon/Elium[®] composites. *Materials* **2020**, *13*, 1117. [CrossRef]
22. Bhudolia, S.K.; Joshi, S.C.; Bert, A.; Boon, Y.D.; Makam, R.; Gohel, G. Flexural characteristics of novel carbon methylmethacrylate composites. *Compos. Commun.* **2019**, *13*, 129–133. [CrossRef]
23. Obande, W.; Mamalis, D.; Ray, D.; Yang, L.; Ó Brádaigh, C.M. Mechanical and thermomechanical characterisation of vacuum-infused thermoplastic- and thermoset-based composites. *Mater. Des.* **2019**, *175*, 107828. [CrossRef]
24. Joshi, S.C.; Dikshit, V. Enhancing interlaminar fracture characteristics of woven CFRP prepreg composites through CNT dispersion. *J. Compos. Mater.* **2012**, *46*, 665–675. [CrossRef]
25. Dikshit, V.; Bhudolia, S.; Joshi, S. Multiscale polymer composites: A review of the interlaminar fracture toughness improvement. *Fibers* **2017**, *5*, 38. [CrossRef]
26. Shanmugam, L.; Feng, X.; Yang, J. Enhanced interphase between thermoplastic matrix and UHMWPE fiber sized with CNT-modified polydopamine coating. *Compos. Sci. Technol.* **2019**, *174*, 212–220. [CrossRef]
27. Swolfs, Y.; Gorbatikh, L.; Verpoest, I. Fibre hybridisation in polymer composites: A review. *Compos. Part A Appl. Sci. Manuf.* **2014**, *67*, 181–200. [CrossRef]
28. Swolfs, Y.; Verpoest, I.; Gorbatikh, L. Recent advances in fibre-hybrid composites: Materials selection, opportunities and applications. *Int. Mater. Rev.* **2019**, *64*, 181–215. [CrossRef]
29. Ellis, R.L. *Ballistic Impact Resistance of Graphite Epoxy Composites with Shape Memory Alloy and Extended Chain Polyethylene Spectra Hybrid Components*; Virginia Tech: Blacksburg, VA, USA, 1996.
30. Peijs, A.A.J.M.; de Kok, J.M.M. Hybrid composites based on polyethylene and carbon fibres. Part 6: Tensile and fatigue behaviour. *Composites* **1993**, *24*, 19–32. [CrossRef]
31. Jang, J.; Moon, S.-I. Impact behavior of carbon fiber/ultra-high modulus polyethylene fiber hybrid composites. *Polym. Compos.* **1995**, *16*, 325–329. [CrossRef]
32. Lu, S.-H.; Liang, G.-Z.; Zhou, Z.-W.; Li, F. Structure and properties of UHMWPE fiber/carbon fiber hybrid composites. *J. Appl. Polym. Sci.* **2006**, *101*, 1880–1884. [CrossRef]
33. Bhudolia, S.K.; Perrotey, P.; Joshi, S.C. Optimizing polymer infusion process for thin ply textile composites with novel matrix system. *Materials* **2017**, *10*, 293. [CrossRef]
34. Van Rijswijk, K.; Bersee, H.E.N. Reactive processing of textile fiber-reinforced thermoplastic composites—An overview. *Compos. Part A Appl. Sci. Manuf.* **2007**, *38*, 666–681. [CrossRef]
35. *ASTM D5528-13*; Standard Test Method for Mode I Interlaminar Fracture Toughness of Unidirectional Fiber-Reinforced Polymer Matrix Composites. ASTM International: West Conshohocken, PA, USA, 2022.
36. *JSA-JIS K 7086*; Testing Methods for Interlaminar Fracture Toughness of Carbon Fibre Reinforced Plastics. Japanese Industrial Standard Group, Japanese Standards Association: Tokyo, Japan, 1993.
37. Reeder, J.R.; Demarco, K.; Whitley, K.S. The use of doubler reinforcement in delamination toughness testing. *Compos. Part A Appl. Sci. Manuf.* **2004**, *35*, 1337–1344. [CrossRef]

38. Bhudolia, S.K.; Gohel, G.; Vasudevan, D.; Leong, K.F.; Gerard, P. On the mode II fracture toughness, failure, and toughening mechanisms of wholly thermoplastic composites with ultra-lightweight thermoplastic fabrics and innovative Elium[®] resin. *Compos. Part A Appl. Sci. Manuf.* **2022**, *161*, 107115. [CrossRef]
39. JSA-JIS K 7086; ERTA. Testing Methods for Interlaminar Fracture Toughness of Carbon Fibre Reinforced Plastics. Japanese Industrial Standard Group, Japanese Standards Association: Tokyo, Japan, 2008.
40. Fiedler, B.; Hojo, M.; Ochiai, S.; Schulte, K.; Ando, M. Failure behavior of an epoxy matrix under different kinds of static loading. *Compos. Sci. Technol.* **2001**, *61*, 1615–1624. [CrossRef]
41. Andrew, J.J.; Alhashmi, H.; Schiffer, A.; Kumar, S.; Deshpande, V.S. Energy absorption and self-sensing performance of 3D printed CF/PEEK cellular composites. *Mater. Des.* **2021**, *208*, 109863. [CrossRef]
42. Andrew, J.J.; Verma, P.; Kumar, S. Impact behavior of nanoengineered, 3D printed plate-lattices. *Mater. Des.* **2021**, *202*, 109516. [CrossRef]
43. Greenhalgh, E.S. 4—Delamination-dominated failures in polymer composites A2. In *Failure Analysis and Fractography of Polymer Composites*; Greenhalgh, E.S., Ed.; Woodhead Publishing: Cambridge, UK, 2009; pp. 164–237.
44. Meyers, M.A.; Chawla, K.K. *Mechanical Behavior of Materials*, 2nd ed.; Cambridge University Press: Cambridge, UK, 2008.

Article

Off-Axis and On-Axis Performance of Novel Acrylic Thermoplastic (Elium[®]) 3D Fibre-Reinforced Composites under Flexure Load

Syed Zulfiqar Hussain Shah ¹, Puteri S. M. Megat-Yusoff ^{1,*}, Saravanan Karuppanan ¹, Rizwan Saeed Choudhry ² 
and Zubair Sajid ¹ 

¹ Mechanical Engineering Department, Universiti Teknologi PETRONAS, Seri Iskandar 32610, Perak, Malaysia; syedzulfiqar.shah@utp.edu.my (S.Z.H.S.); saravanan.karuppanan@utp.edu.my (S.K.); zubair_17005303@utp.edu.my (Z.S.)

² School of Computing and Engineering, Mechanical Engineering Discipline, College of Science and Engineering, University of Derby, Derby DE22 1GB, UK; r.choudhry@derby.ac.uk

* Correspondence: puteris@utp.edu.my

Abstract: The flexure response of novel thermoplastic (Elium[®]) 3D fibre-reinforced composites (FRC) was evaluated and compared with a conventional thermoset (Epolam[®])-based 3D-FRC. Ten different types of sample 3D-FRC were prepared by varying fibre orientations, i.e., 0°, 30°, 45°, 60° and 90°, and resin system, i.e., thermoplastic and thermoset. The bending characteristics and failure mechanisms were determined by conducting a three-point bend test. Results elucidate that the on-axis specimens show linear response and brittle failure; in contrast, the off-axis specimens depicted highly nonlinear response and ductile failure. The thermoplastic on-axis specimen exhibited almost similar flexure strength; in comparison, the off-axis specimens show ~17% lower flexure strength compared to thermoset 3D-FRC. Thermoplastic 3D-FRC shows ~40% higher energy absorption, ~23% lower flexure modulus and ~27% higher flexure strains as compared to its thermoset counterpart.

Keywords: 3D composites; thermoplastic; thermoset; off-axis flexure behaviour; on-axis flexure behaviour

Citation: Shah, S.Z.H.; Megat-Yusoff, P.S.M.; Karuppanan, S.; Choudhry, R.S.; Sajid, Z. Off-Axis and On-Axis Performance of Novel Acrylic Thermoplastic (Elium[®]) 3D Fibre-Reinforced Composites under Flexure Load. *Polymers* **2022**, *14*, 2225. <https://doi.org/10.3390/polym14112225>

Academic Editors: Somen K. Bhudolia and Sunil Chandrakant Joshi

Received: 25 April 2022

Accepted: 10 May 2022

Published: 30 May 2022

Publisher's Note: MDPI stays neutral with regard to jurisdictional claims in published maps and institutional affiliations.



Copyright: © 2022 by the authors. Licensee MDPI, Basel, Switzerland. This article is an open access article distributed under the terms and conditions of the Creative Commons Attribution (CC BY) license (<https://creativecommons.org/licenses/by/4.0/>).

1. Introduction

The use of 3D-FRC has increased in recent years thanks to their superior transverse properties (impact resistance) and damage tolerance in comparison with 2D-FRC [1–5]. However, their in-plane properties were reduced, which was attributed to the waviness caused by the z-binder [6–9]. Following this direction, researchers focused their attention on improving their in-plane properties [10–12]. Meanwhile, their failure mechanisms and bending behaviour are still unclear [13]. The 3D-FRCs are orthotropic, and their load-carrying capacity varies with the fibre orientation. In addition to fibre orientation, resin toughness significantly affects bending characteristics. Therefore, it is desirable to understand the effect of fibre orientation and resin toughness on the flexure properties of 3D-FRC for their design and different applications.

The thermoset polymers took the lead as a matrix for FRC due to their ease in manufacturing processes in comparison with thermoplastic polymers. The thermoplastic FRC offers attractive advantages, i.e., higher impact resistance, damage tolerance and the ability to be recycled at the end of life [14–16]. However, the major roadblock is the manufacture of thermoplastic FRC, as the viscosity of the thermoplastic matrix in its molten state is high. In particular, the manufacture of 3D-FRC with thermoplastic is challenging due to poor impregnation [17]. Currently, post-impregnation is generally used to manufacture 3D-FRC, as long as the thermoplastic polymers are in the form of powder/fibre or film [18]. This limits the manufacture of 3D-FRC with thermoset matrix using conventional manufacturing processes, i.e., resin infusion and resin transfer moulding [19,20].

In past years, the flexure properties of thermoset-based 3D-FRC were widely studied [21]. Several researchers studied their on-axis (warp and fill) flexure properties [22–26] and concluded that delamination resistance and bending properties were improved by introducing a z-binder in the fabric architecture [27,28]. Apart from the on-axis flexure properties, the off-axis bending behaviour of 3D-FRC was rarely discussed. Recently, Zhang et al. [13] studied the on-axis (0° and 90°) off-axis (30° and 45°) flexure behaviour of 3D-FRC and found that the on-axis specimen shows a brittle response compared to off-axis specimens. All the studies discussed above were limited to thermoset-based 3D-FRC. Very few researchers discussed the flexure properties of thermoplastic-based 3D-FRC [17,18,28,29]. The flexure modulus of thermoplastic FRC is generally lower than thermoset FRC, which was attributed to the higher toughness of the thermoplastic matrix. Kuo et al. [18] studied the flexure properties of polyamide-based 3D-FRC and reported a reduction in fibre kinking. Qian et al. [28] studied polypropylene-based 3D-FRC and found that the flexure properties improved. Both studies highlight an improper impregnation of 3D fabric due to the higher viscosity of polypropylene and Polyamide resin. Archer et al. [29] compared the flexure properties of thermoset (epoxy) and thermoplastic (polybutylene terephthalate) based on 3D-FRC. They observed that the flexure strength of thermoplastic-based 3D-FRC was 46% less than that of thermoset 3D-FRC due to the highly crystalline microstructure and voids produced during the fabrication process. Luo et al. [17] investigated PEEK based on 3D-FRC and reported an improper impregnation of yarns. Moreover, they used 3D fabric with a small thickness (2 mm) and low fibre volume fraction (36%). Hence, manufacturing 3D-FRC with higher thickness and fibre volume fraction using post-impregnation process (such as hot compression molding) is again a challenging task.

To address these limitations, Arkema recently developed acrylic thermoplastic resin (Elium), which is in liquid form at room temperature and can be employed to manufacture thermoplastic 3D-FRC by using conventional manufacturing processes, i.e., vacuum infusion. Elium[®] has tremendous potential for a wide range of applications in composite industries such as aerospace, automotive, wind power, sports and marine industries, etc. In particular, it is beneficial for the wind power industry where it can be used to manufacture wind turbine blades using a conventional resin-assisted vacuum infusion process. These wind turbine blades will not only provide better fatigue life and resistance against the extreme environment but also resolve the recycling problem at the end of their life span. Furthermore, it offers a unique advantage to assembling composite parts by using resistance or ultrasonic welding, which are particularly significant for aerospace, wind power and automotive industries [30].

Recent studies highlighted that the novel resin-infused thermoplastic-based 3D-FRC is a suitable material to manufacture composite structures for superior impact resistance [2,31], damage tolerance [32] and energy absorption [33] applications. Murray et al. [34] studied the flexure properties of a novel acrylic thermoplastic-based 2D-FRC and reported that the flexure strength and flexure modulus were almost similar. To the best of the author's knowledge, no study has been dedicated to evaluating the flexure performance of novel acrylic thermoplastic-based 3D-FRC and their comparison with thermoset-based 3D-FRC. Therefore, it is important to evaluate the bending characteristics and delamination resistance of this novel acrylic resin (Elium[®])-based 3D-FRC before they are considered for practical applications.

Following these directions, the objective of this paper is to determine the combined effect of fibre orientation (on-axis/off-axis) and matrix toughness (Elium[®] and Epolam[®]) on the flexure properties of 3D-FRC. Ten different types of 3D-FRC samples with different fibre orientations (0° , 30° , 45° , 60° and 90°) and matrix (Elium[®] and Epolam[®]) were tested using a three-point bend test. For both thermoplastic and thermoset 3D-FRC, only one fibre volume fraction has been investigated. The results were compared in terms of flexure strength, flexure modulus, flexure strain and stress-deflection curves. Moreover, a detailed macroscopic and microscopic damage characterization was performed using digital and

Scanning Microscopy (SEM) images to identify the effect of both factors on the damage mechanisms of 3D-FRC under flexure load.

1.1. Flexure Response of FRC

The flexure response of 3D-FRC depends on the fabric architecture, fibre orientation (on-axis and off-axis), resin toughness (thermoplastic and thermoset) and tensile/compressive properties. Under flexure load, the top surface of the specimen experiences compressive load, whereas the bottom surface undergoes tensile load [35]. Figure 1. shows the schematic diagram of the stress–strain curve under flexural load, which provides a complete failure response of 3D-FRC (damage initiation and propagation). Figure 1a depict the on-axis flexural stress-strain curve of 3D-FRC. The flexure load increases linearly until it reaches the maximum value, which is called flexure yield stress " σ_Y^f ". As the load increases further, the nonlinear region begins and the flexure modulus decreases due to fibre kinking (at/near the top surface) or matrix cracking (at the bottom surface). During this process, the stress reached its ultimate value called ultimate flexure stress " σ^f ". After this point, the transverse crack on the bottom surface propagates upward and transfers all loads to yarns/fibres, which results in their failure. This fibre/yarn breakage produces a sudden load drop ($\sim 20\%$) in the stress–strain curve as a result of kink band formation, which is the strongest limiting factor. The strain at this point is called flexural strains " ε^f ". Figure 1b depicts the off-axis flexural response of 3D-FRC. After reaching the ultimate flexure stress, the damage propagates in the form of crack extension, debonding and fibre kinking. During this stage, no catastrophic failure occurs, and the load-bearing capacity of a material decreases. The stress–strain curve shows a large plateau during this stage due to geometric deformation and re-orientation of yarns, which is also called the "scissoring effect" [13]. This large plateau indicates that the off-axis specimen absorbs more energy and exhibited significant high impact resistance and damage tolerance.

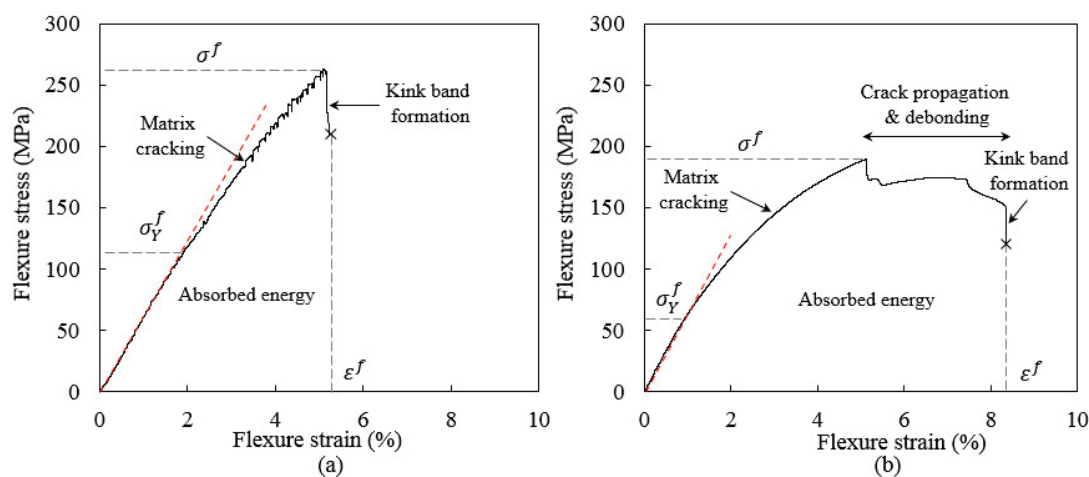


Figure 1. Schematic diagram of typical flexural stress/strain curve of 3D-FRC: (a) on-axis S-D curves of 3D-FRC and (b) off-axis stress/displacement curves of 3D-FRC.

2. Materials and Methods

2.1. Material Used

The 3D fabric used in this study is orthogonal E-glass woven fabric (3D-9871) obtained from TexTech[®] Industries, Winthrop, ME, USA. The actual fabric and schematic diagrams of 3D orthogonal woven fabric are depicted in Figure 2. The areal weight of the fabric is 5200 g/m², and the overall thickness of a single layer is ~ 4 mm. In this study, the 3D-FRC panels were fabricated using both thermoplastic and thermoset resin systems, i.e., a recently developed acrylic thermoplastic liquid resin Elium[®] 188x0 from Arkema, Colombes, France, and thermoset epoxy resin system Epolam[®] 5015/5015 from Axson, Shanghai, China. Elium[®] 188x0 is an acrylic monomer that was mixed with a peroxide

initiator to initiate the polymerization process at room temperature. The mechanical properties of both resin systems are summarised in Table 1.

Table 1. Summary of mechanical properties of the thermoplastic matrix (Elium[®] 188x0) and thermoset matrix (Epolam[®] 5015).

Property	Elium [®] 188x0	Epolam [®] 5015/5015
Tensile strength (MPa) ^a	76	80
Tensile modulus (GPa) ^a	3.3	3.1
Elongation at failure (%) ^c	6	3.1
Flexural strength (MPa) ^a	130	100
Flexural modulus (GPa) ^a	3.25	2.6
Fracture toughness (kJ/m ²) ^b	0.5	0.12
Rockwell Hardness ^d	99	119
Density (g/cc) ^d	1.17	1.15

^a Material technical datasheet. ^b Reported in the literature [36]. ^c Reported in the literature (Elium[®] 188x0 [37] and Epolam[®] 5015/5015 [38]). ^d In-house testing.

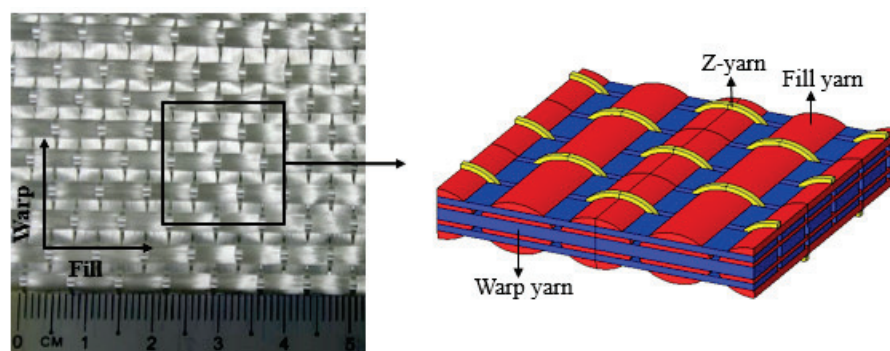


Figure 2. 3D orthogonal woven fabric (3D-9871).

2.2. Fabrication Process

Elium[®] and Epolam[®] based 3D-FRCs were manufactured by using a vacuum-assisted resin transfer moulding (VARTM) process. The mixed viscosity of Elium[®] 188x0 and Epolam[®] 5015 are 200 mPa.s and 210 mPa.s, respectively, which is ideal for the VARTM process. A rectangular panel of 400 mm × 500 mm was fabricated. The resin systems were mixed carefully for two-three minutes to obtain a homogenous mixture. In the case of the Elium[®] based 3D-FRC, resin was degassed for 15 min due to its short pot life (60–70 min). The resin infusion was carried out at 100 mbar to avoid resin boiling and the process was completed in 25 min. The panels were left at room temperature to complete the polymerization process, followed by post-curing in an oven at 80 °C for four hours to achieve maximum mechanical properties. In contrast, for the manufacture of Epolam[®]-based 3D-FRC, Epolam[®] resin was degassed for 25 min to remove air bubbles, which may degrade the final mechanical properties. The resin infusion was performed at 450 mbar and completed in 7 min. Epolam[®]-based 3D-FRC panels were left for twelve hours to fully cure at room temperature and then post-cured in an oven at 80 °C for eight hours. Figure 3 also shows a comparison of infusion time in the Elium[®] and Epolam[®]-based FRCs. The Elium[®] based 3D-FRC took approximately fourfold to completely infuse the panel because low vacuum pressure was used to avoid void/bubble formation during the polymerization process. More details on the fabrication process can be found in our earlier publications [6,31,32,39].

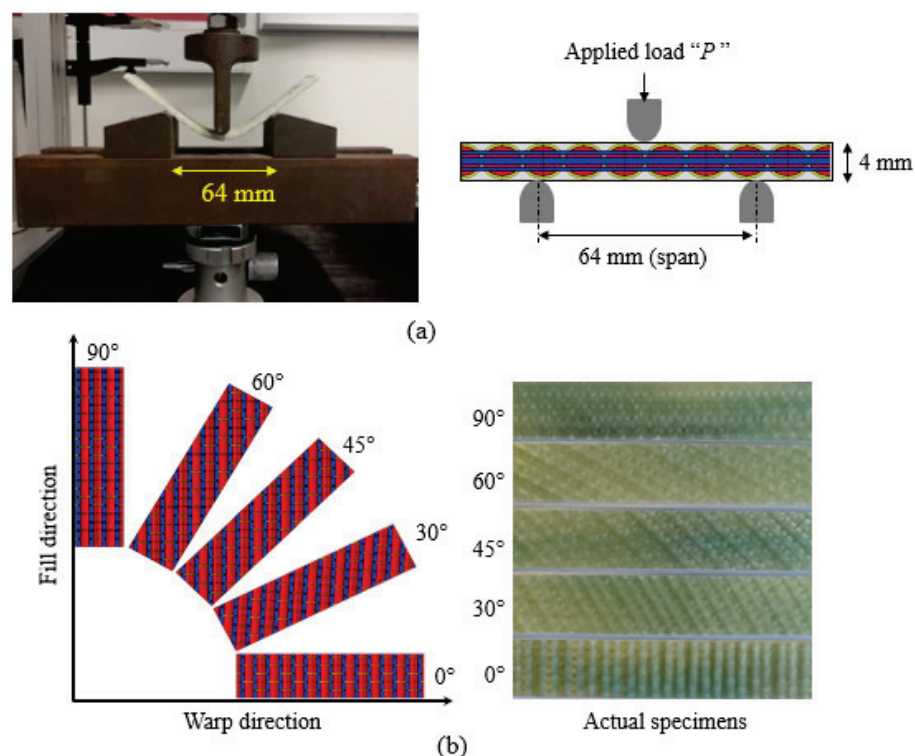


Figure 3. Samples prepared for the flexure testing of 3D-FRC: (a) 3D fabric architecture with different fibre orientations and actual specimens cut into different orientations and (b) flexure testing setup and schematic diagram of three-point bend test.

2.3. Physical Parameters of the Cured Panels and Samples

After the panels were fully cured, they were checked for defected regions, and physical parameters such as density, fibre volume fraction and thickness of the panel were measured. The fibre volume fraction of fabricated panels was measured using the burn-off method according to ASTM D3171, and density was measured using the water displacement method according to ASTM D792-08. Ten samples were cut from different panels, and the average void content, density and fibre volume fractions were measured. In Elium[®]-based 3D-FRC, the void content was less than 3.7%; in comparison, in Epolam[®]-based 3D-FRC, the void content was less than 1%. The fibre volume fraction of Elium[®] and Epolam[®]-based 3D-FRC are $52 \pm 1.5\%$ and $52 \pm 0.4\%$, respectively. The thickness of the cured panels was measured at different locations, and the average values are 4 ± 0.05 mm. The densities of the cured Elium[®] and Epolam[®]-based 3D-FRC were 1.86 g/cc and 1.92 g/cc, respectively, and they were measured using the water displacement method.

2.4. Flexural Testing

The flexure test was performed according to ASTM standard D7264 (procedure A, i.e., three-point bend test), which requires a rectangular specimen [40]. The specimen rests on two vertical supports, while the load was applied halfway between vertical supports, as shown in Figure 3a. The span to thickness ratio used was 1:16 as recommended by the standard. The total length of the specimen should be 10% longer than the span length from each side of the vertical support. The final dimensions of a rectangular specimen were 100 mm × 25 mm × 4 mm. The load rate used was 2 mm/min. Three samples were tested for both 3D-FRC materials at each orientation. The properties measured from the flexure test were flexure strength, modulus and deflection. The flexure strength and modulus can be calculated using Equations (1) and (2), respectively:

$$\sigma_f = \frac{3FL}{2bd^2} \quad (1)$$

$$E_f = \frac{L^3}{4bd^3} \frac{\Delta P}{\Delta \delta} \quad (2)$$

where “ L ”, “ b ”, “ d ” and “ F ”, represent support span, specimen width, specimen thickness and applied load, respectively. “ ΔP ” and “ $\Delta \delta$ ” represent load increments and deflection increments, respectively. In this study, thirty samples were prepared (three samples for each fibre orientation, i.e., 0° , 30° , 45° , 60° and 90°) for both materials (Elium[®] and Epolam[®] based 3D-FRC). Figure 3b shows the 3D fabric architecture, fibre orientation in each sample and actual sample prepared for testing. The specimens were cut from panels using a diamond tip disc cutter, which provides an excellent surface finish.

2.5. Damage Evaluation Method

To further understand the failure mechanisms in both 3D composites, a comprehensive fractography was performed. The failure mechanisms were classified into intralaminar and interlaminar failure mechanisms. A collection of digital photographs obtained following mechanical tests was used to examine the macro-damage morphologies of failed specimens. Meanwhile, SEM was used to examine the micro-failure processes. Because both types of 3D composites were made with insulating glass fibres, the specimens’ surfaces were covered with a 40 nm gold layer to make them conductive. The voltage and maximum magnification used during SEM analysis are 10 keV and 200 \times , respectively.

3. Results and Discussion

3.1. Comparison of the Stress-Displacement Curve

Figure 4 depict the flexure stress-deflection curves of Elium[®] and Epolam[®] based 3D-FRC. The stress-displacement curve provides comprehensive details about the damage process of 3D-FRC under flexure load, as discussed in Section 1.1. Each stress-displacement curve in Figure 4 represents different fibre orientations and matrix systems, which highlight that flexure properties were sensitive to both matrix toughness and fibre orientation. All stress-displacement curves show linear behaviour initially, followed by non-linear behaviour after 1% to 1.5% of flexure deflection.

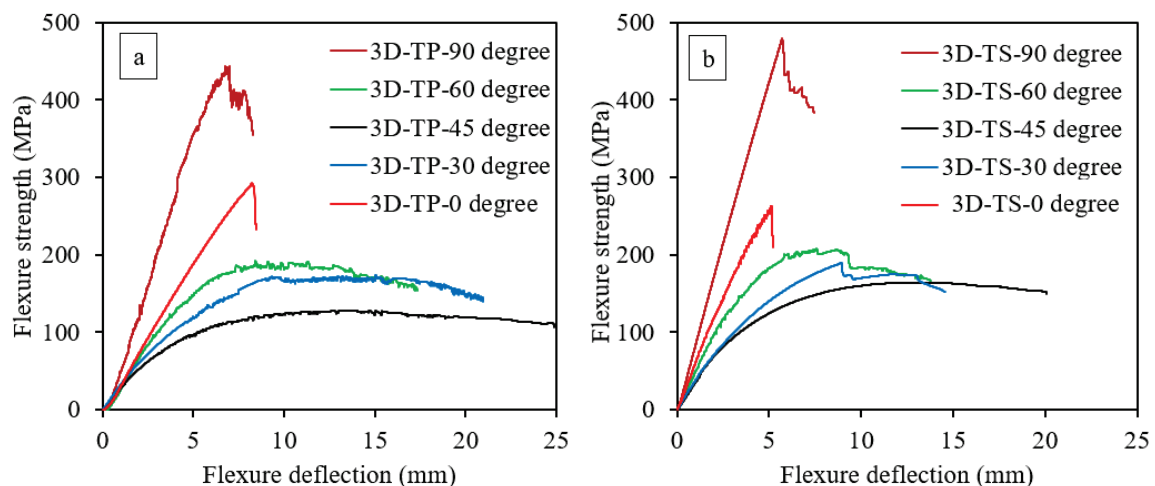


Figure 4. Effect of fibre orientation on the flexure properties of 3D-FRC, (a) S-D curves of 3D thermoplastic FRC and (b) S-D curves of 3D thermoset FRC.

The on-axis specimens (0° and 90°) show higher bending stiffness and load-bearing capacity than the off-axis specimen (30° , 45° and 60°). It was observed that on-axis specimens failed in a brittle manner (that is with a sudden fast fracture and little signs of progressive damage or plastic deformation as compared to off-axis specimens). The stress-displacement curve of on-axis specimens shows linear behaviour up to a maximum value (ultimate strength), followed by the sudden load drop caused by the tensile fibre failure at the bottom surface of the specimen. Such brittle behaviour of on-axis specimens is due to fibre-

dominant characteristics, and a similar observation was made by Zhang et al. [13]. This sudden failure of the on-axis specimen may represent structure damage and is completely lost in the load-bearing capacity of the material. In comparison, the off-axis specimen shows a plateau in the stress–strain curve analogous to the plastic plateau observed in ductile metals. In this case, the plateau is formed due to the progressive failure of the matrix and fibres, which results in a larger strain to final failure, bending deflection, lower bending stiffness and lower peak loads compared to the on-axis specimens. This large deflection represents the matrix dominant characteristics of off-axis specimens, which is consistent with references [13,41]. The ranking for the maximum flexure strength at different fibre orientation is as follows: $90^\circ > 0^\circ > 60^\circ > 30^\circ > 45^\circ$. This is consistent for both types of 3D-FRC.

Regarding the effect of matrix toughness on flexural properties, the thermoplastic 3D-FRC on-axis specimen shows almost similar ultimate flexural strength; in contrast, the off-axis specimens depict lower ultimate stress as compared to the thermoset counterpart (see Figure 4). The bending stiffness of thermoplastic 3D-FRC was lower, whereas the flexure deflection is higher due to the plastic deformation of a ductile matrix (see Figure 4a). The thermoset 3D-FRC specimens (30° and 60°) undergo a sudden load drop, as shown in Figure 4b. This is postulated to be due to kinking and yarn/matrix interface debonding. In contrast, the thermoplastic 3D-FRC specimens (30° and 60°) continue to deform without catastrophic damage, as shown in Figure 4a. This behaviour of thermoplastic 3D-FRC is due to their higher interlaminar fracture toughness, which delays crack propagation [29]. Moreover, the thermoplastic 3D-FRC specimen (45°) shows the highest bending deflection and lowest peak load. The ranking for the maximum flexure modulus at different fibre orientations is the same as flexure strength, i.e., $90^\circ > 0^\circ > 60^\circ > 30^\circ > 45^\circ$.

3.2. Comparison of Flexure Strength, Modulus and Failure Strain

The results obtained from flexure tests in terms of modulus, ultimate stress, yield stress and strains were summarised in Table 2. The values in the parenthesis represent the coefficient of variance (COV) among three tested specimens for each configuration. The on-axis specimens show higher COV due to fibre dominant characteristics and sensitivity to the geometric variabilities. In contrast, the off-axis specimens depict less variation, which was attributed to the progressive nonlinear damage due to the reorientation of yarns.

Table 2. Summary of flexure test results. Value in the parenthesis represents the co-efficient of variance in data.

Material	Fibre Orientation (Degree)	Flexure Modulus (GPa)	Flexure Yield Strength (MPa)	Flexure Strength (MPa)	Flexure Strain (%)
3D-TP-FRC	0°	7.3 (6.1%)	117 (14.5%)	249 (15%)	4.3 (12%)
	30°	5.6 (4.7%)	55 (9.0%)	176 (1.9%)	11 (12%)
	45°	5.4 (6.6%)	45 (4.5%)	136 (6.0%)	13.4 (9.2%)
	60°	7.2 (11%)	86 (2.5%)	184 (6.5%)	9.6 (3.7%)
	90°	11.6 (5.7%)	272 (20%)	418 (8.0%)	5.0 (3.0%)
3D-TS-FRC	0°	9.4 (14%)	94 (6.5%)	225 (14%)	3.4 (17%)
	30°	6.7 (3.0%)	65 (8.0%)	176 (6.4%)	9.9 (14%)
	45°	6.5 (5.0%)	61 (5.0%)	162 (1.3%)	11.7 (3.5%)
	60°	9.2 (1.0%)	101 (2.5%)	208 (2.8%)	8.3 (7.3%)
	90°	14.2 (8.2%)	378 (8.0%)	455 (4.9%)	4.3 (2.3%)

The results depict that the on-axis specimens show the highest flexure strength in both 3D-FRCs. The flexural strengths of Elium[®] and Epolam[®]-based 3D-FRC were 249 MPa and 225 MPa when loaded along the warp direction and 418 MPa and 455 MPa when loaded along fill direction, respectively. The off-axis specimens experience the lowest bending strength due to the in-plane shear induced in these composites, which manifests itself in the re-orientation of angled yarns (warp and fill) towards the principal directions. This has been referred to in the literature as the scissoring effect [13,42]. During this re-orientation process,

the specimen experiences additional flexural strains due to geometrical deformation, which is followed by yarn/matrix debonding. Both these phenomena are responsible for the large deflection of the specimen under flexure loads. Among the off-axis specimens, the 45° fibre orientation specimen depicts the lowest flexure strength (130–170 MPa), modulus (5.4–6.5 GPa) and strain (11–14%).

In order to evaluate the effect of resin toughness on the flexure properties of 3D-FRC, the flexural strength, modulus and strain were compared, as shown in Figure 5. The thermoplastic 3D-FRC possesses lower ultimate flexural stress compared to thermoset 3D-FRC except at 0° and 30°, whereas the thermoplastic composite shows higher ultimate stress, as shown in Figure 5a. The warp-loaded thermoplastic and thermoset composite specimens exhibited 40% and 50% lower ultimate flexural stress, as compared to fill-loaded specimens, respectively. One possible reason for this lower stress is the difference in the fabric architecture in both directions. In warp-loaded specimens, the resin-rich pockets at the top/bottom surface were parallel to the applied load. Under flexural load, the cracks developed in the brittle Epolam® matrix propagate more rapidly, leading to the earlier failure at lower ultimate stress. In contrast, the ductile thermoplastic matrix undergoes plastic deformation and delays the propagation of cracks, which results in relatively higher ultimate stress along the warp direction.

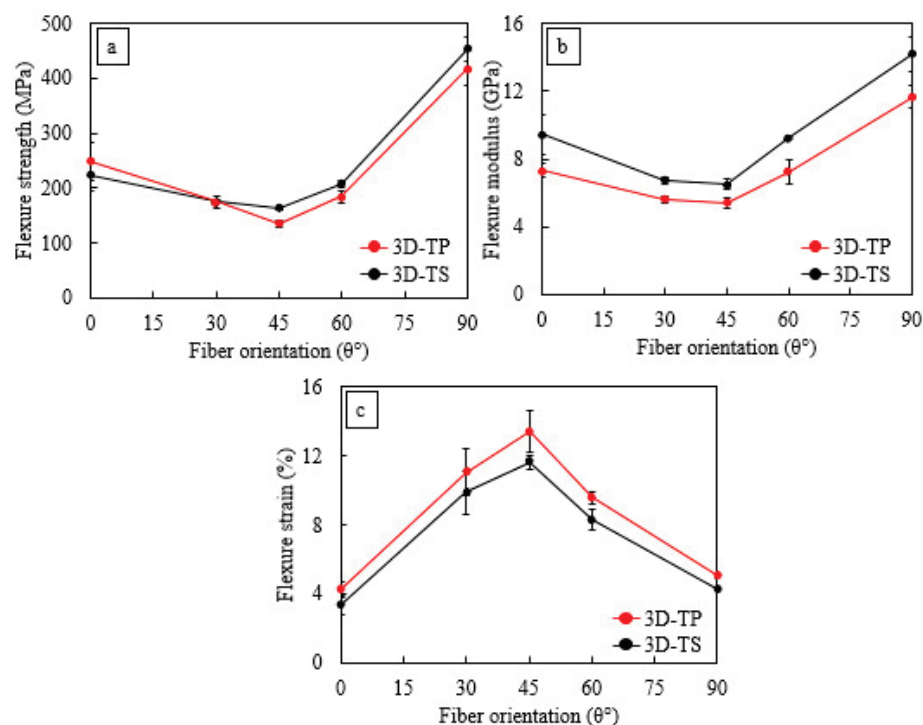


Figure 5. Variation of flexure strength, modulus and failure strain as a function of fibre orientation in 3D-FRC. (a) Flexural strength, (b) Flexural modulus and (c) Flexural strain.

Figure 5b shows the comparison of flexural modulus. The flexure modulus of Elium®-based 3D-FRC was 16–29% lower than the thermoset counterpart. The 3D fabric used in the study exhibited the same areal density along the warp and fill direction; theoretically, the flexure modulus should be the same. However, it is worth noting that the flexure moduli of warp-loaded thermoplastic and thermoset composites were 38% and 34% lower than fill-loaded specimens, respectively. A probable explanation of the lower flexure modulus is that the middle yarn warps as it runs through the neutral axis of the specimen. The cross-sectional area of the middle warp yarn is twice as large as compared to the top/bottom warp yarn. Thus, 50% of the main load-carrying yarn was not fully utilised/loaded under flexure load. Figure 5c depicts the comparison of flexure strains. Thermoplastic 3D-FRC possesses 15–30% higher flexure strains due to the ductile matrix and higher fracture toughness.

In comparison, the brittle Epolam[®] matrix failed earlier due to the rapid propagation of micro-cracks, which led to an early failure of 3D-FRC. The ranking for the maximum flexure strain at different fibre orientations is almost opposite to the flexure strength and modulus, i.e., $45^\circ > 30^\circ > 60^\circ > 90^\circ > 0^\circ$. This ranking is the same for both types of 3D-FRC.

Normalizing the flexure properties of the thermoset 3D-FRC with thermoplastic 3D-FRC is one possible comparison to evaluate the performance of both materials when undergoing different loadings. Moreover, it clearly highlights the performance of both 3D-FRC in terms of flexure strength, modulus and strain at maximum stress, as shown in Figure 6. The visual comparison clearly indicates that the ultimate flexural stress of on-axis novel Elium[®]-based 3D-FRC was only 9% lower (see Figure 6a), as compared to 46% lower ultimate stress as reported by Archer et al. [29]. The flexure modulus of Elium[®] based 3D-FRC was ~23% lower, as shown in Figure 6b. In comparison, the flexure strain of Elium[®]-based 3D-FRC was ~27% higher, as shown in Figure 6c.

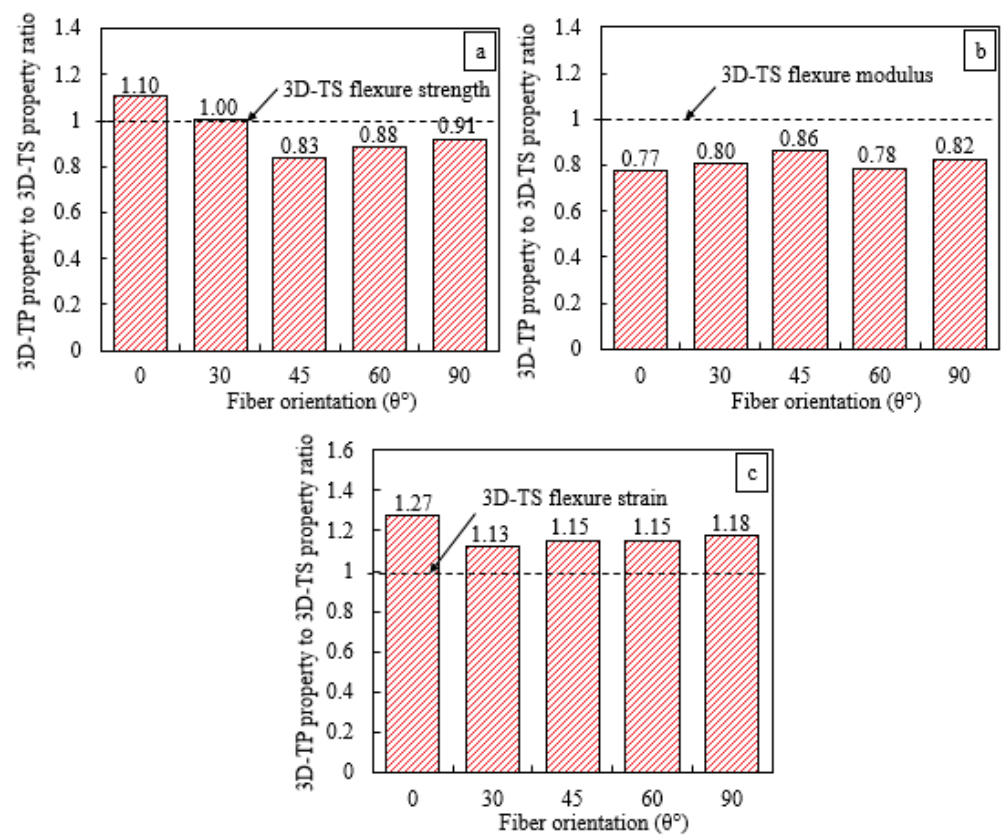


Figure 6. Comparison of normalised flexure strength, modulus and failure strain of 3D-FRC. (a) Flexural strength, (b) Flexural modulus and (c) Flexural strain.

3.3. Flexural vs. Yield Strength of 3D-FRC

Figure 7 depicts the comparison between ultimate flexure stress and flexural yield stress as a function of fibre orientation. The error bars represent the variation in the data. The flexure yield stress in the stress–displacement curve represents a point where the curve lost its linearity, as discussed in Section 1.1. Overall, the thermoplastic 3D-FRC possesses lower flexural yield stress compared to the thermoset counterpart, as shown in Figure 7a,b. The flexural yield stresses of fill loaded thermoset and thermoplastic-based 3D-FRC were 82% and 65% of the ultimate flexure stress. In comparison, the flexural yield stresses of warp loaded Epolam[®] and Elium[®]-based 3D-FRCs were 42% and 45% of ultimate yield stress. This lower yield stress along the warp direction is due to the resin-rich pockets on the top/bottom surface of the specimens. Matrix cracks developed in these resin pockets grew rapidly, which leads to lower flexure yield stress. In the case of off-axis specimens, the flexure yield stress varies between 30 and 50% of the ultimate flexure stress.

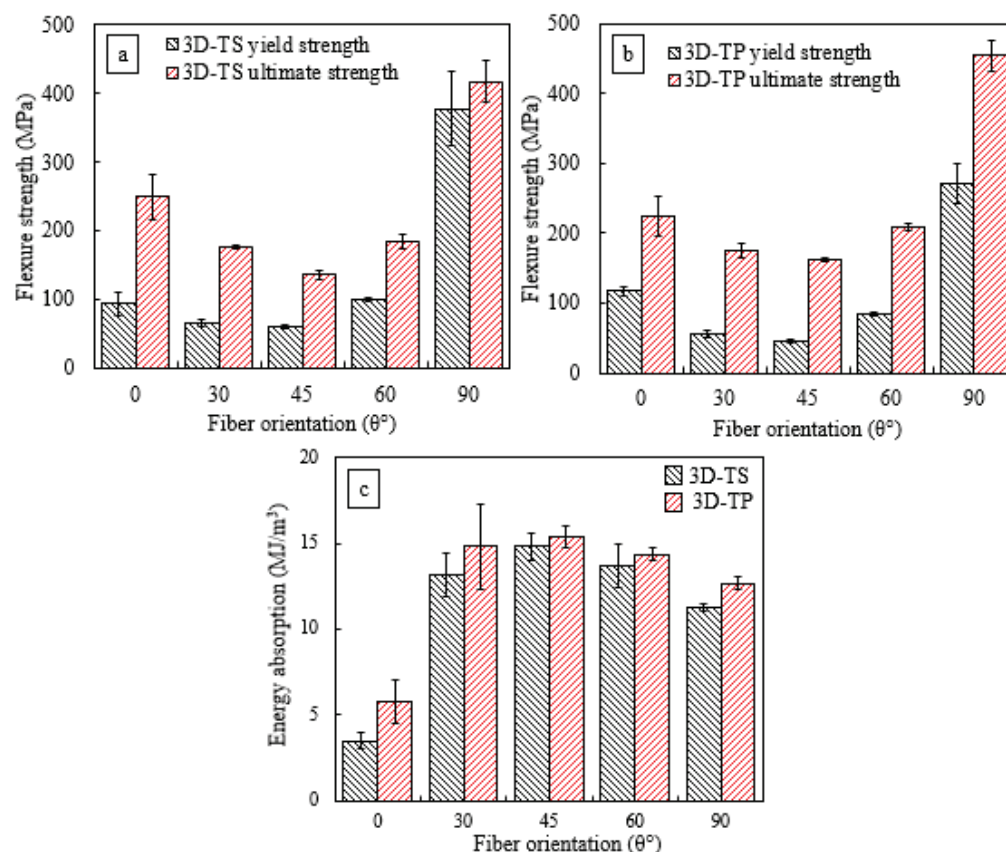


Figure 7. Comparison of flexure strength and flexure yield strength as a function of fibre orientation, (a) 3D thermoplastic FRC, (b) 3D thermoset FRC and (c) comparison of energy absorbed by 3D-FRC under flexure load.

3.4. Effect of Resin Toughness on Energy Absorption

Figure 7c shows the comparison of energy absorbed by 3D-FRC per unit volume (MJ/m^3), which was calculated through the area under the stress/strain curve, up to complete failure. Overall, Elium[®]-based 3D-FRC absorbed up to 40% higher energy compared to Epolam[®]-based 3D-FRC. The on-axis specimens absorbed less energy compared to off-axis specimens due to fibre-dominant characteristics. This higher energy absorption of off-axis specimens was due to the scissoring effect, as discussed earlier. The off-axis thermoplastic 3D-FRC absorbs almost two-times higher energy compared to on-axis specimens. In comparison, the off-axis thermoset 3D-FRC absorbs around three-times higher energy than on-axis specimens, which was attributed to the sudden brittle failure of on-axis specimens at much lower flexure deflections. The above findings indicate the following: (i) the thermoplastic 3D-FRC exhibited much better energy absorption capability; (ii) the off-axis specimens are the better choice for composite structures, where higher energy absorption is the prime requirement.

3.5. Failure Mechanisms in TP and TS 3D Composites under Flexure Load

The failure mechanisms in 3D-FRC under flexural loads have been shown in Figure 8. The figure shows the combination of macro- and micro-failure mechanisms. The main damage mechanisms in the thermoset 3D-FRC were yarn kinking, yarn tensile failure, matrix cracking, debonding/delamination and re-orientation of yarns. In comparison, the failure mechanisms in thermoplastic-3D-FRC were yarn kinking, yarn tensile failure, matrix plastic deformation and re-orientation of yarns. The bottom surface of the specimen experiences the highest damage due to tensile stress developed under flexural loads. The presence of various failure mechanisms made it challenging to evaluate damage mechanisms by changing fibre orientation under flexural loads. Therefore, the failure

mechanisms were divided into two main recognised categories, i.e., intralaminar failure mechanisms (micro and macro damages of fibre and matrix in impregnated yarn and matrix regions) and interlaminar failure mechanisms (delamination as well as debonding due to reorientation of yarns). These failure mechanisms for all cases have been summarised in Table 3 and are discussed in the following section.

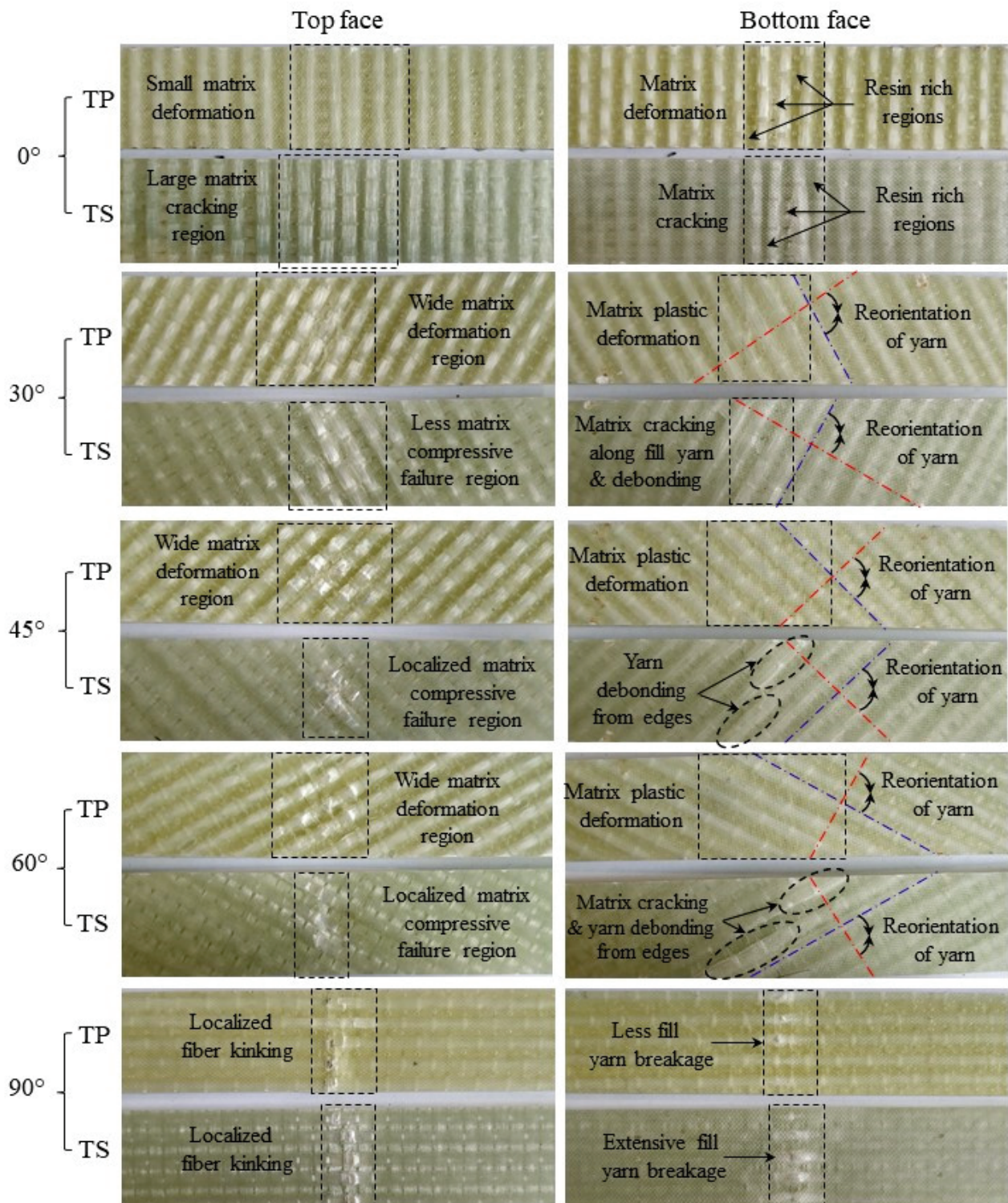


Figure 8. Comparison of macroscopic damage patterns in 3D-FRC. Blue-line represents fill yarn, and the red line represents warp yarn.

Table 3. The relative severity of damage mechanisms for changing fibre orientation.

Mat.	Damage Type	Damage Mechanisms	Case-1 (0°)	Case-2 (30°)	Case-3 (45°)	Case-4 (60°)	Case-5 (90°)
3D-TP-FRC	Intralaminar	Fibre breakage	Moderate	None	None	None	Moderate
		Plasticization	Some	Moderate	Significant	Moderate	Some
		Matrix cracking	None	None	Some	None	None
	Interlaminar	Kinking	Some	None	None	None	Some
		Yarn debonding	Some	None	None	Moderate	Moderate
		Yarn re-orientation	None	Moderate	Significant	Moderate	None
3D-TS-FRC	Intralaminar	Matrix deformation	Some	Moderate	Significant	Moderate	Some
		Fibre breakage	Moderate	None	None	None	Significant
		Plasticization	None	None	None	None	None
	Interlaminar	Matrix cracking	Moderate	Significant	Significant	Significant	Moderate
		Kinking	Some	None	None	None	Some
		Yarn debonding	Moderate	Moderate	Moderate	Significant	Some
	Yarn reorientation	None	Moderate	Significant	Moderate	None	
	Matrix comp. failure	Some	Moderate	Significant	Moderate	Some	

3.5.1. Intralaminar Failure Mechanisms

The behaviour of 3D-FRC, when loaded along the on-axis direction, can be described in a general sense as linear, elastic and brittle due to straight yarns, which carry the majority of the load and allow for little deformation before catastrophic failure (see Figure 4). The on-axis specimens (0° and 90°) show localised damage zone on the top and bottom surface, due to fibre breakage in warp or fill yarns (see Figure 9). In the case of warp-loaded specimens (0°), the resin-rich pockets between the fill yarn undergo micro-cracking or elastoplastic deformation, which transfers all the load to warp yarn. In thermoset 3D-FRC, this micro-crack propagates rapidly, which results in catastrophic failure in the form of fibre breakage (see Figure 9d,e) at a lower deflection. On the other hand, the resin-rich pockets in thermoplastic 3D-FRC deform instead of cracking and delay crack propagation in the form of yarn debonding and kinking (see Figure 9a–c). Hence, these composites failed at a relatively higher flexural strain. In the case of fill-loaded specimens (90°), the fill yarns fail in compression due to kink band formation on the top surface and tensile failure at the bottom surface (see Figure 9f,g). However, in thermoset 3D-FRC, extensive fill yarn failure and yarn debonding were observed on the top and bottom surface due to the brittle matrix (see Figure 9h,i).

The off-axis specimens (30°, 45° and 60°) undergo large deflection under bending loads, which results in higher damage. Among the off-axis specimens, the 45° specimens show the highest damage at the top and bottom face (see Figure 8). In comparison, the 30° specimen depicts the highest matrix compressive failure zone at the top surface, whereas the 60° specimens show the highest damage at the bottom surface. The thermoplastic off-axis specimens show a wider matrix compressive failure region on the top surface due to the ductile matrix (see Figure 8) and yarn debonding (see Figure 10d–f), whereas the bottom surface undergoes large plasticization (see Figure 10a,b). In comparison, thermoset 3D-FRC depicts a relatively small matrix compressive failure region (see Figure 8) and matrix cracking (see Figure 10h) on the top surface due to the brittle (Epolam[®]) matrix. In contrast, the bottom surface of the specimen undergoes extensive matrix cracking, yarn debonding and z-binder breakage, as shown in Figure 10e,h.

3.5.2. Interlaminar Failure Mechanisms

The off-axis behaviour of the 3D orthogonal woven composite is highly nonlinear due to the plasticization of resin-rich pockets and progressive damage of the matrix, which was attributed to the re-orientation of yarns. During the re-orientation process, the debonding/delamination of yarns and matrix occurs (see Figures 9 and 10). The re-orientation between warp and fill yarns is shown in Figure 8. (Represented with blue and red lines). Moreover, Elium[®]-based 3D-FRC shows significantly reduced delamination (see Figure 9f,g) due to their higher interlaminar fracture toughness and strong fibre/matrix

interface [43]. In contrast, extensive fill yarn debonding was identified in the Epolam[®]-based 3D-FRC due to the re-orientation of warp and fill yarns (Figure 9h,i). The off-axis specimens (45° and 60°) show significant debonding of fill yarns at the edges of the specimens in both 3D textile composites, as shown in Figure 11. Thermoplastic off-axis specimens show large out-of-plane permanent deformation after unloading due to the locking of yarns caused by plasticization during the loading process.

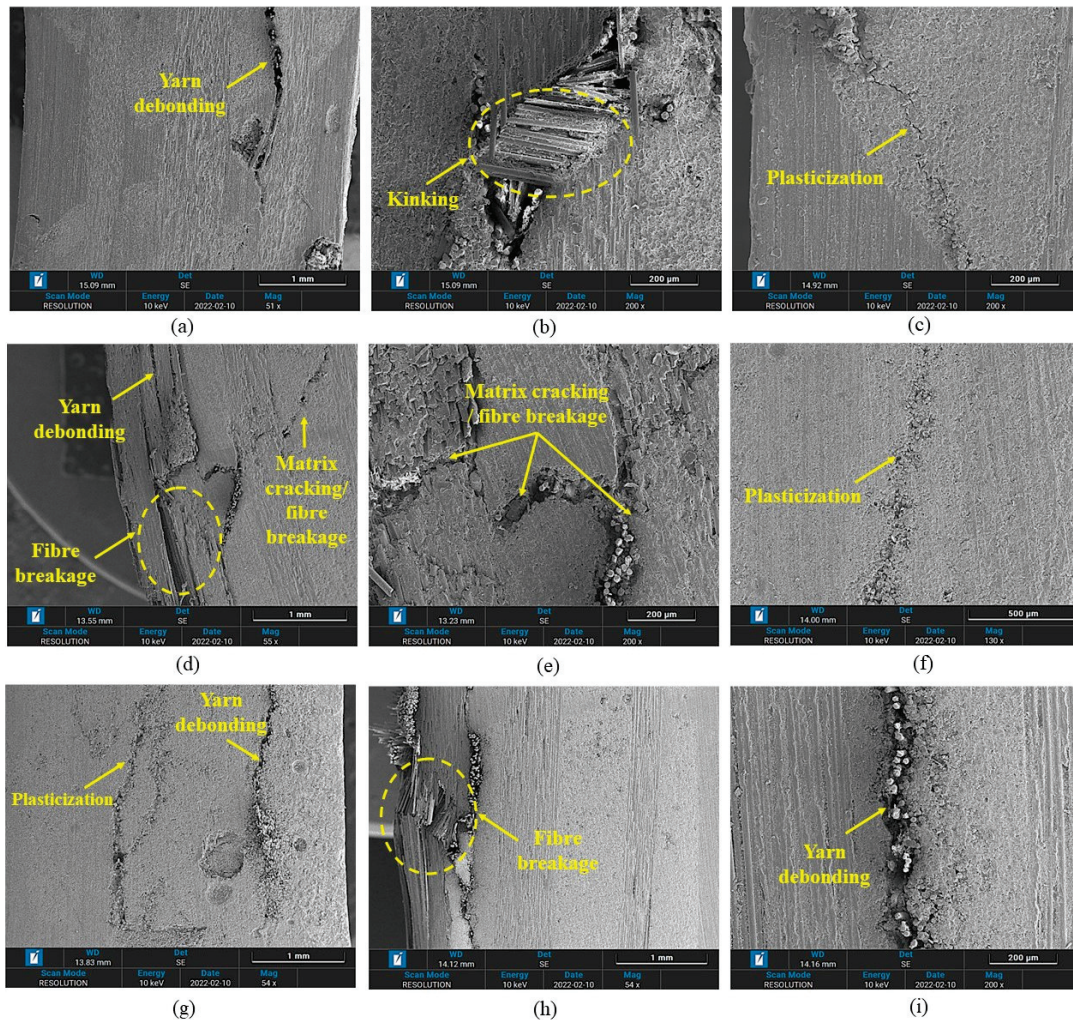


Figure 9. Comparison of intralaminar/interlaminar failure mechanisms in on-axis (0° and 90°) specimens. (a–c) 0° TP-3D-FRC, (d,e) 0° TS-3D-FRC, (f,g) 90° TP-3D-FRC and (h,i) 90° TS-3D-FRC.

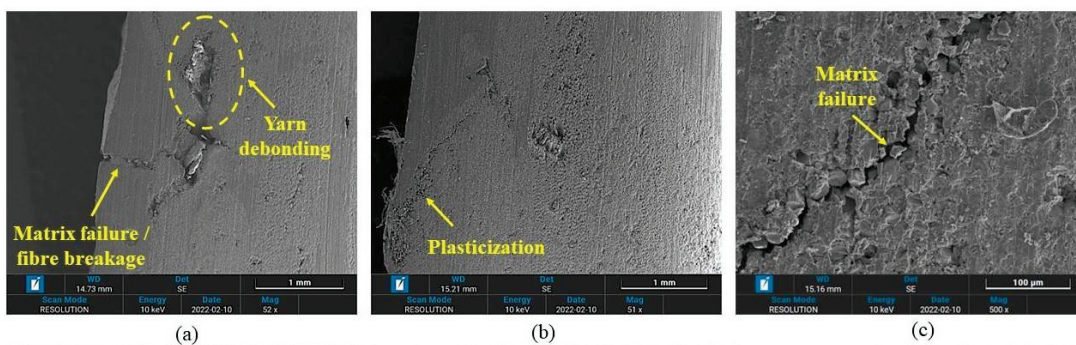


Figure 10. Cont.

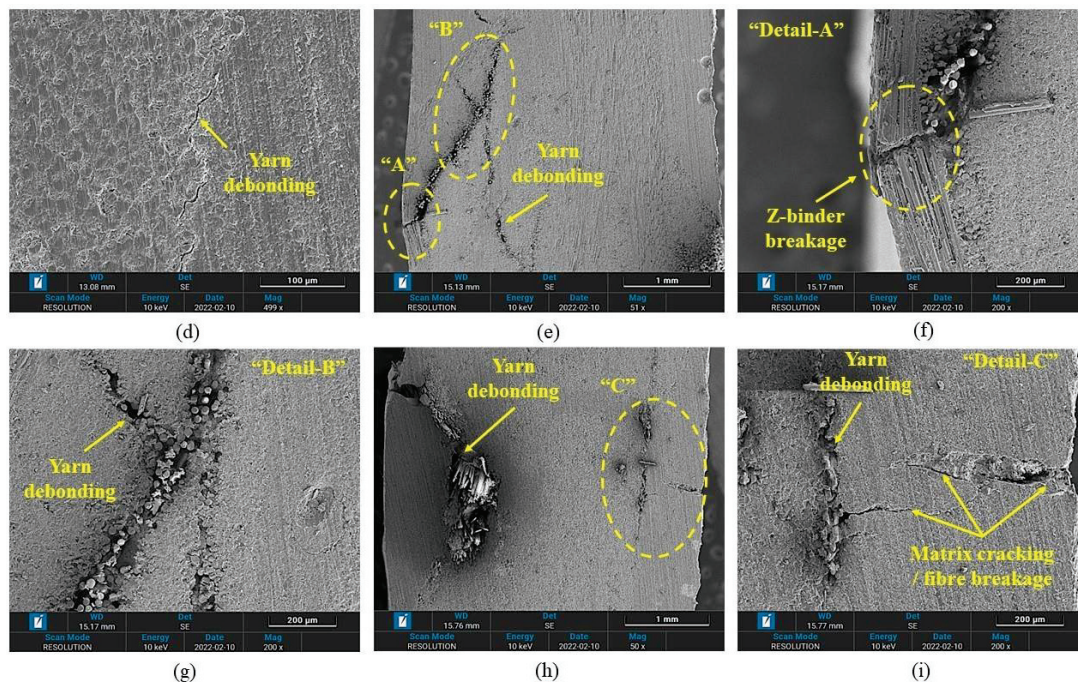


Figure 10. Comparison of intralaminar/interlaminar failure mechanisms in off-axis (30°, 45° and 90°) specimens. (a–d) TP-3D-FRC and (e–i) TS-3D-FRC.

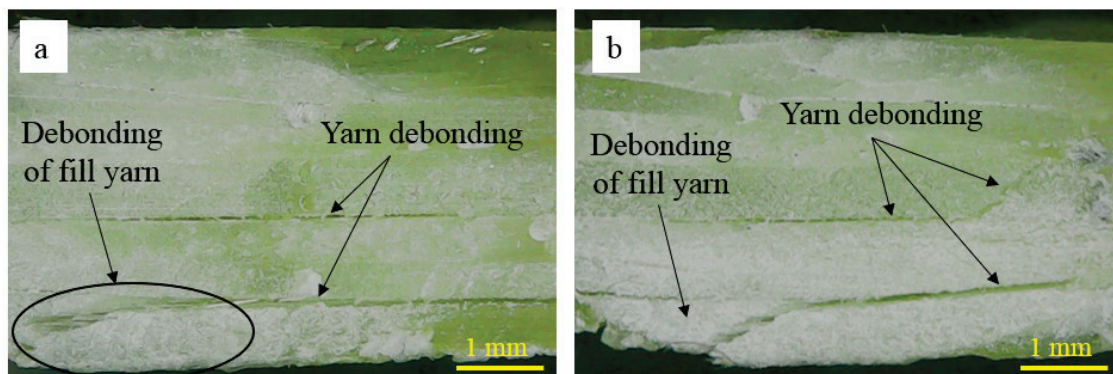


Figure 11. Interlaminar failure in off-axis specimens under flexure load. (a) Thermoplastic 3D-FRC and (b) thermoset 3D-FRC.

This study elucidates that the novel thermoplastic 3D-FRC exhibited significantly improved bending properties as compared to conventional Elium[®] based 3D-FRC. Although the bending properties of novel thermoplastic 3D-FRC were almost similar to the thermoset counterparts, it provides an additional advantage of superior impact resistance, damage tolerance and recyclability at the end of service life.

4. Conclusions

This work presents the experimental investigation on the effect of resin toughness and fibre orientation on the flexure properties of 3D-FRC. The on-axis specimens show the highest flexure strength and modulus due to brittle response, whereas the off-axis specimens undergo higher flexural strains, which were attributed to ductile characteristics. The thermoplastic on-axis 3D-FRC exhibited almost similar flexure strength, ~23% lower flexural modulus and ~27% higher flexural strains compared to thermoset 3D-FRC. In comparison, thermoplastic off-axis 3D-FRC demonstrated ~17% lower flexural strength, ~22% lower flexural modulus and ~15% lower flexural strains. On the other hand, in terms of energy absorption, thermoplastic 3D-FRC absorbs up to ~40% higher energy

compared to the thermoset counterpart. The main damage mechanism in the thermoset 3D-FRC was matrix cracking, fill yarn failure and a significant delamination of fill yarn. In comparison, thermoplastic 3D-FRC shows plasticization, fill yarn failure and slight delamination. This improved performance of novel thermoplastic composites was attributed to strong fibre/matrix interface properties and higher interlaminar fracture toughness. This study highlights that the novel Elium[®] matrix improves the bending properties of 3D-FRC compared to the conventional thermoplastic matrix. Hence, this novel thermoplastic 3D-FRC can be used in different applications, where higher flexure properties and energy absorptions are required.

Author Contributions: Conceptualisation, S.Z.H.S.; methodology, S.Z.H.S. and R.S.C.; investigation, P.S.M.M.-Y. and S.K.; resources, Z.S.; writing—original draft preparation, S.Z.H.S. and R.S.C.; writing—review and editing, R.S.C. and S.K.; visualisation, S.Z.H.S.; supervision, P.S.M.M.-Y., S.K. and R.S.C.; project administration, S.Z.H.S. and P.S.M.M.-Y.; funding acquisition, P.S.M.M.-Y. All authors have read and agreed to the published version of the manuscript.

Funding: The authors would like to express their gratitude to Universiti Teknologi PETRONAS, Malaysia, for the financial support under Yayasan Universiti Teknologi PETRONAS (YUTP) grant number 015LC0-351.

Data Availability Statement: The presented in this study are available upon request from the corresponding author.

Acknowledgments: The authors are grateful to Barsotti J Robert and Pierre Gerard from Arkema for providing Elium[®] resin for this research work and the Centre for Advanced and Functional Materials, Institute of Sustainable Buildings, Universiti Teknologi PETRONAS.

Conflicts of Interest: The authors declare no conflict of interest.

References

1. Shah, S.Z.H.; Choudhry, R.S.; Khan, L.A. Challenges in compression testing of 3D angle-interlocked woven-glass fabric-reinforced polymeric composites. *ASTM J. Test. Eval.* **2017**, *5*, 1502–1523. [CrossRef]
2. Shah, S.Z.H.; Karuppanan, S.; Megat-Yusoff, P.; Sajid, Z. Impact resistance and damage tolerance of fiber reinforced composites: A review. *Composite* **2019**, *217*, 100–121. [CrossRef]
3. Sajid, Z.; Karuppanan, S.; Sallih, N.; Kee, K.E.; Shah, S.Z.H. Role of washer size in mitigating adverse effects of bolt-hole clearance in a single-lap, single-bolt basalt composite joint. *Compos. Struct.* **2021**, *266*, 113802. [CrossRef]
4. Ud Din, I.; Tu, S.; Hao, P.; Panier, S.; Khan, K.A.; Umer, R.; Shah, S.Z.H.; Franz, G.; Aamir, M. Sequential damage study induced in fiber reinforced composites by shear and tensile stress using a newly developed Arcan fixture. *J. Mater. Res. Technol.* **2020**, *9*, 13352–13364. [CrossRef]
5. Sajid, Z.; Karuppanan, S.; Shah, S.Z.H. Open-Hole and Filled-Hole Failure Envelopes of BFRP and GFRP: A Comparative Study. In *Advances in Manufacturing Engineering. Lecture Notes in Mechanical Engineering*; Emamian, S., Awang, M., Yusof, F., Eds.; Springer: Singapore, 2020. [CrossRef]
6. Shah, S.Z.H.; Megat-Yusoff, P.S.M.; Karuppanan, S.; Choudhry, R.S.; Ahmad, F.; Sajid, Z. Mechanical Properties and Failure Mechanisms of Novel Resin-infused Thermoplastic and Conventional Thermoset 3D Fabric Composites. *Appl. Compos. Mater.* **2021**, *29*, 515–545. [CrossRef]
7. Cox, B.N.; Dadkhah, M.S.; Morris, W. On the tensile failure of 3D woven composites. *Compos. Part A Appl. Sci. Manuf.* **1996**, *27*, 447–458. [CrossRef]
8. Kuo, W.S.; Tse-Hao, K. Compressive damage in 3-axis orthogonal fabric composites. *Compos. Part A Appl. Sci. Manuf.* **2000**, *31*, 1091–1105. [CrossRef]
9. Shah, S.; Lee, J. Stochastic lightning damage prediction of carbon/epoxy composites with material uncertainties. *Compos. Struct.* **2022**, *282*, 115014. [CrossRef]
10. Stig, F.; Hallström, S. Assessment of the mechanical properties of a new 3D woven fibre composite material. *Compos. Sci. Technol.* **2009**, *69*, 1686–1692. [CrossRef]
11. Ladani, R.B.; Pingkarawat, K.; Nguyen, A.T.; Wang, C.H.; Mouritz, A.P. Delamination toughening and healing performance of woven composites with hybrid z-fibre reinforcement. *Compos. Part A Appl. Sci. Manuf.* **2018**, *110*, 258–267. [CrossRef]
12. Shah, S.Z.H.; Megat Yusoff, P.S.M.; Karuppanan, S.; Sajid, Z. Elastic Constants Prediction of 3D Fiber-Reinforced Composites Using Multiscale Homogenization. *Processes* **2020**, *8*, 722. [CrossRef]
13. Zhang, D.; Sun, M.; Liu, X.; Xiao, X.; Qian, K. Off-axis bending behaviors and failure characterization of 3D woven composites. *Compos. Struct.* **2019**, *208*, 45–55. [CrossRef]

14. Zaghloul, M.M.Y.; Zaghloul, M.M.Y. Influence of flame retardant magnesium hydroxide on the mechanical properties of high density polyethylene composites. *J. Reinf. Plast. Compos.* **2017**, *36*, 1802–1816. [CrossRef]
15. Shah, S.Z.H.; Choudhry, R.S.; Mahadzir, S. A new approach for strength and stiffness prediction of discontinuous fibre reinforced composites (DFC). *Compos. Part B Eng.* **2020**, *183*, 107676. [CrossRef]
16. Obande, W.; Mamalis, D.; Ray, D.; Yang, L.; Bradaigh, C.M.O. Mechanical and thermomechanical characterisation of vacuum-infused thermoplastic and thermoset-based composites. *Mater. Des.* **2019**, *175*, 107828. [CrossRef]
17. Luo, H.; Xiong, G.; Yang, Z.; Raman, S.R.; Li, Q.; Ma, C.; Li, D.; Wang, Z.; Wan, Y. Preparation of three-dimensional braided carbon fiber-reinforced PEEK composites for potential load-bearing bone fixations. Part I. Mechanical properties and cytocompatibility. *J. Mech. Behav. Biomed. Mater.* **2014**, *29*, 103–113. [CrossRef]
18. Kuo, W.S.; Jiunn, F. Processing and characterization of 3D woven and braided thermoplastic composites. *Compos. Sci. Technol.* **2000**, *60*, 643–656. [CrossRef]
19. Sajid, Z.; Karuppanan, S.; Kee, K.E.; Sallih, N.; Shah, S.Z.H. Carbon/basalt hybrid composite bolted joint for improved bearing performance and cost efficiency. *Compos. Struct.* **2021**, *275*, 114427. [CrossRef]
20. Sajid, Z.; Karuppanan, S.; Shah, S.Z.H. Effect of Washer Size and Tightening Torque on Bearing Performance of Basalt Fiber Composite Bolted Joints. *J. Nat. Fibers* **2021**, 1–18. [CrossRef]
21. Zaghloul, M.Y.M.; Zaghloul, M.M.Y.; Zaghloul, M.M.Y. Developments in polyester composite materials—An in-depth review on natural fibres and nano fillers. *Compos. Struct.* **2021**, *278*, 114698. [CrossRef]
22. Kuo, W.-S.; Ko, T.-H.; Cheng, K.-B.; Hsieh, K.-Y. Flexural behavior of three-axis woven carbon/carbon composites. *J. Mater. Sci.* **2001**, *36*, 2743–2752. [CrossRef]
23. Umer, R.; Alhusein, H.; Zhou, J.; Cantwell, W.J. The mechanical properties of 3D woven composites. *J. Compos. Mater.* **2016**, *51*, 1703–1716. [CrossRef]
24. Dai, S.; Cunningham, P.; Marshall, S.; Silva, C. Influence of fibre architecture on the tensile, compressive and flexural behaviour of 3D woven composites. *Compos. Part A Appl. Sci. Manuf.* **2015**, *69*, 195–207. [CrossRef]
25. Jin, L.; Hu, H.; Sun, B.; Gu, B. Three point bending fatigue behavior of 3D angle interlock woven composite. *J. Compos. Mater.* **2012**, *46*, 883–894. [CrossRef]
26. Wang, Y.; Zhao, D. Effect of Fabric Structures on the Mechanical Properties of 3-D Textile Composites. *J. Ind. Text.* **2006**, *35*, 239–256. [CrossRef]
27. Adanur, S.; Tam, C.A. On-machine interlocking of 3D laminate structures for composites. *Compos. Part B Eng.* **1997**, *28*, 497–506. [CrossRef]
28. Zhang, Q.; Fang, X.; Sun, X.; Sun, B.; Qiu, Y. Comparison of the Mechanical Properties between 2D and 3D Orthogonal Woven Ramie Fiber Reinforced Polypropylene Composites. *Polym. Polym. Compos.* **2014**, *22*, 187–192. [CrossRef]
29. Archer, E.; Mulligan, R.; Dixon, D.; Buchanan, S.; Stewart, G.; McIlhagger, A.T. An investigation into thermoplastic matrix 3D woven carbon fibre composites. *J. Reinf. Plast. Compos.* **2012**, *31*, 863–873. [CrossRef]
30. Bhudolia, S.K.; Gohel, G.; Kah Fai, L.; Barsotti, R.J. Fatigue response of ultrasonically welded carbon/Elium[®] thermoplastic composites. *Mater. Lett.* **2020**, *264*, 127362. [CrossRef]
31. Shah, S.Z.H.; Megat-Yusoff, P.; Karuppanan, S.; Choudhry, R.; Ahmad, F.; Sajid, Z.; Gerard, P.; Sharp, K. Performance comparison of resin-infused thermoplastic and thermoset 3D fabric composites under impact loading. *Int. J. Mech. Sci.* **2020**, *189*, 105984. [CrossRef]
32. Shah, S.Z.H.; Megat-Yusoff, P.; Karuppanan, S.; Choudhry, R.; Ud Din, I.; Othman, A.; Gerard, P.; Sharp, K. Compression and buckling after impact response of resin-infused thermoplastic and thermoset 3D woven composites. *Compos. Part B Eng.* **2021**, *207*, 108592. [CrossRef]
33. Shah, S.Z.H.; Megat-Yusoff, P.S.M.; Choudhry, R.S.; Sajid, Z.; Din, I.U. Experimental investigation on the quasi-static crush performance of resin-infused thermoplastic 3D fibre-reinforced composites. *Compos. Commun.* **2021**, *28*, 100916. [CrossRef]
34. Murray, R.E.; Penumadu, D.; Cousins, D.; Beach, R.; Snowberg, D.; Berry, D.; Suzuki, Y.; Stebner, A. Manufacturing and Flexural Characterization of Infusion-Reacted Thermoplastic Wind Turbine Blade Subcomponents. *Appl. Compos. Mater.* **2019**, *26*, 945–961. [CrossRef]
35. Zhang, D.; Waas, A.M.; Yen, C.-F. Progressive damage and failure response of hybrid 3D textile composites subjected to flexural loading, part I: Experimental studies. *Int. J. Solids Struct.* **2015**, *75–76*, 309–320. [CrossRef]
36. Bhudolia, S.K.; Perrotey, P.; Joshi, S.C. Optimizing polymer infusion process for thin ply textile composites with novel matrix system. *Materials* **2017**, *10*, 293. [CrossRef] [PubMed]
37. Kazemi, M.E.; Shanmugam, L.; Lu, D.; Wang, X.; Wang, B.; Yang, J. Mechanical properties and failure modes of hybrid fiber reinforced polymer composites with a novel liquid thermoplastic resin, Elium[®]. *Compos. Part A Appl. Sci. Manuf.* **2019**, *125*, 105523. [CrossRef]
38. Zhang, H.; Yang, J. Development of self-healing polymers via amine–epoxy chemistry: II. Systematic evaluation of self-healing performance. *Smart Mater. Struct.* **2014**, *23*, 065004. [CrossRef]
39. Shah, S.Z.H.; Megat-Yusoff, P.; Karuppanan, S.; Choudhry, R.; Sajid, Z. Multiscale damage modelling of 3D woven composites under static and impact loads. *Compos. Part A Appl. Sci. Manuf.* **2021**, *151*, 106659. [CrossRef]
40. ASTM D7264/D7264M-07; Standard Test Method for Flexural Properties of Polymer Matrix Composite Materials. ASTM International: West Conshohocken, PA, USA, 2007. Available online: www.astm.org (accessed on 20 April 2022).

41. Turner, P.; Liu, T.; Zeng, X. Collapse of 3D orthogonal woven carbon fibre composites under in-plane tension/compression and out-of-plane bending. *Compos. Struct.* **2016**, *142*, 286–297. [CrossRef]
42. Hufner, D.R.; Accorsi, M.L. A progressive failure theory for woven polymer-based composites subjected to dynamic loading. *Compos. Struct.* **2009**, *89*, 177–185. [CrossRef]
43. Bhudolia, S.K.; Perrotey, P.; Joshi, S.C. Mode I fracture toughness and fractographic investigation of carbon fibre composites with liquid Methylmethacrylate thermoplastic matrix. *Compos. Part B Eng.* **2018**, *134*, 246–253. [CrossRef]

Article

Application of Taguchi Method to Optimize the Parameter of Fused Deposition Modeling (FDM) Using Oil Palm Fiber Reinforced Thermoplastic Composites

Mohd Nazri Ahmad ^{1,2,3,*} , Mohamad Ridzwan Ishak ^{1,4,5,*}, Mastura Mohammad Taha ², Faizal Mustapha ¹, Zulkifile Leman ^{6,7} , Debby Dyne Anak Lukista ², Irianto ^{8,*} and Ihwan Ghazali ² 

- ¹ Department of Aerospace Engineering, Faculty of Engineering, Universiti Putra Malaysia, Serdang 43400, Selangor, Malaysia; faizalms@upm.edu.my
 - ² Faculty of Mechanical and Manufacturing Engineering Technology, Universiti Teknikal Malaysia Melaka, Hang Tuah Jaya, Durian Tunggal 76100, Melaka, Malaysia; mastura.taha@utem.edu.my (M.M.T.); debbydyne2024@gmail.com (D.D.A.L.); ihwan@utem.edu.my (I.G.)
 - ³ Centre of Smart System and Innovative Design, Universiti Teknikal Malaysia Melaka, Hang Tuah Jaya, Durian Tunggal 76100, Melaka, Malaysia
 - ⁴ Aerospace Malaysia Research Centre (AMRC), Universiti Putra Malaysia, Serdang 43400, Selangor, Malaysia
 - ⁵ Laboratory of Biocomposite Technology, Institute of Tropical Forestry and Forest Products (INTROP), Universiti Putra Malaysia, Serdang 43400, Selangor, Malaysia
 - ⁶ Department of Mechanical and Manufacturing Engineering, Faculty of Engineering, Universiti Putra Malaysia, Serdang 43400, Selangor, Malaysia; zleman@upm.edu.my
 - ⁷ Advanced Engineering Materials and Composites Research Centre, Faculty of Engineering, Universiti Putra Malaysia, Serdang 43400, Selangor, Malaysia
 - ⁸ Department-General Education, Faculty of Resilience, Rabdan Academy, Abu Dhabi 22401, United Arab Emirates
- * Correspondence: mohdnazri.ahmad@utem.edu.my (M.N.A.); mohdridzwan@upm.edu.my (M.R.I.); iharny@ra.ac.ae (I.)

Citation: Ahmad, M.N.; Ishak, M.R.; Mohammad Taha, M.; Mustapha, F.; Leman, Z.; Anak Lukista, D.D.; Irianto; Ghazali, I. Application of Taguchi Method to Optimize the Parameter of Fused Deposition Modeling (FDM) Using Oil Palm Fiber Reinforced Thermoplastic Composites. *Polymers* **2022**, *14*, 2140. <https://doi.org/10.3390/polym14112140>

Academic Editors: Somen K. Bhudolia and Sunil Chandrakant Joshi

Received: 13 April 2022

Accepted: 20 May 2022

Published: 24 May 2022

Publisher's Note: MDPI stays neutral with regard to jurisdictional claims in published maps and institutional affiliations.



Copyright: © 2022 by the authors. Licensee MDPI, Basel, Switzerland. This article is an open access article distributed under the terms and conditions of the Creative Commons Attribution (CC BY) license (<https://creativecommons.org/licenses/by/4.0/>).

Abstract: Fused Deposition Modeling (FDM) is capable of producing complicated geometries and a variety of thermoplastic or composite products. Thus, it is critical to carry out the relationship between the process parameters, the finished part's quality, and the part's mechanical performance. In this study, the optimum printing parameters of FDM using oil palm fiber reinforced thermoplastic composites were investigated. The layer thickness, orientation, infill density, and printing speed were selected as optimization parameters. The mechanical properties of printed specimens were examined using tensile and flexural tests. The experiments were designed using a Taguchi experimental design using a L_9 orthogonal array with four factors, and three levels. Analysis of variance (ANOVA) was used to determine the significant parameter or factor that influences the responses, including tensile strength, Young's modulus, and flexural strength. The fractured surface of printed parts was investigated using scanning electron microscopy (SEM). The results show the tensile strength of the printed specimens ranged from 0.95 to 35.38 MPa, the Young's modulus from 0.11 to 1.88 GPa, and the flexural strength from 2.50 to 31.98 MPa. In addition, build orientation had the largest influence on tensile strength, Young's modulus, and flexural strength. The optimum printing parameter for FDM using oil palm fiber composite was 0.4 mm layer thickness, flat (0 degree) of orientation, 50% infill density, and 10 mm/s printing speed. The results of SEM images demonstrate that the number of voids seems to be much bigger when the layer thickness is increased, and the flat orientation has a considerable influence on the bead structure becoming tougher. In a nutshell, these findings will be a valuable 3D printing dataset for other researchers who utilize this material.

Keywords: FDM; Taguchi; DOE; oil palm fiber composites; ABS

1. Introduction

Additive Manufacturing (AM) is layer by layer-oriented or layered manufacturing, which was first established as rapid prototyping technology towards the end of the 1980s. It delivers minimal cost, adaptable goods; as a result, the application of this technology to build enhanced parts has been a popular trend in recent years [1]. Figure 1 depicts a schematic representation of FDM. It is particularly useful in the formation of thermoplastics such as ABS, polylactic acid (PLA), and polypropylene (PP) [2,3]. Anisotropic characteristics were found on an ABS specimen created using FDM [4]. The quantitative and qualitative properties of thermoplastic specimens are determined by the experimental optimization of the FDM input parameters. The proper setup of the process parameters helped to provide a consistent and accurate finished ABS product, enhance process sustainability, and decrease post-processing activity [5–7]. Layer thickness, raster width, orientation, and infill density percentage all had an impact on the mechanical characteristics of thermoplastic when processed with FDM [8]. The use of thermoplastic cellulose-based composite filaments in FDM is exciting, since it reduces raw material cost [9,10] and has good impact on the environment [11–14], reduces warping after processing [15], and preserves the material's mechanical attributes [16].

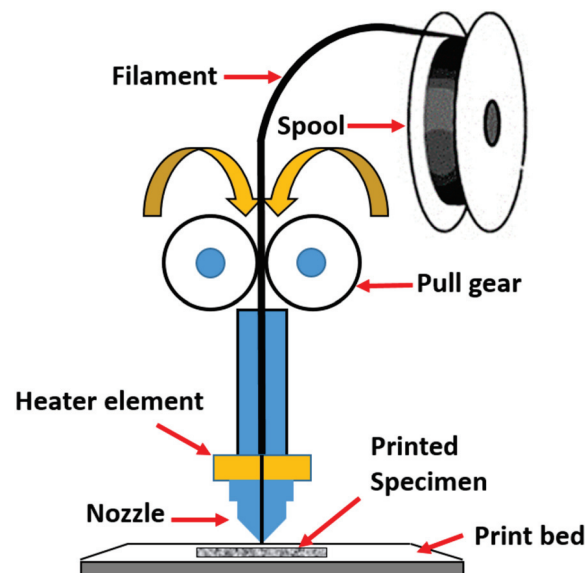


Figure 1. Schematic of a FDM 3D printing.

Recently, many researchers employed natural fiber reinforced composite (NFRC) materials such as PLA/pineapple [17], iron/nylon [18], ABS/fiberglass [19], ABS/carbon fibers [1], and PLA/wood [20] to create specimens for mechanical testing using FDM. All of these factors should be optimized and controlled efficiently in FDM to produce high dimensional accuracy, quality of printed parts, less distortion, reduced porosity, and superior mechanical properties [21]. Many researchers had concentrated on the optimization of the machine's process parameters and were concerned with understanding the link between different processing factors and their impacts on the final product. Accordingly, the study mostly focused on characteristics such as ambient temperature [22], layer thickness [23], extrusion temperature [24], printing speed [25], reinforced particle size [26], orientation of raster [27], road width [28], and raster air gap [29]. Huynh et al. [30] investigated the impact of printing speed, pattern, and layer thickness on the dimensional accuracy of the printed parts. Meanwhile, Raut et al. [31] investigated the mechanical properties and the processing time of printed specimens. El-Kassas and Elsheikh [32] investigated the rice straw fiber composite utilizing a novel approach that offers several benefits over traditional procedures, including the absence of chemicals or heat treatments, a minimum manufacturing area, and lower production costs.

The solution to optimize the FDM input parameters involved applying several design of experiments (DOE), including ANOVA, fuzzy logic, full factorial design, response surface methodology (RSM), and the Taguchi method [33]. Because of its robustness, tolerance, and dimensional control, Taguchi's design of experiments approach was commonly used to optimize the FDM parameters setting [34]. Ahmad et al. [35] used the Taguchi approach to improve surface roughness of the printed parts by optimizing the printing parameters of FDM. On the other hand, the Taguchi approach is a descriptive survey that identifies a product or process in order to enhance its usability. The Taguchi technique is employed since it is simple and a problem-solving technique to help improve process performance, to increase efficiency and productivity. The approach is known as the factorial outline of the test. The orthogonal technique is used to select the level combination of information plan variables for each experiment [36]. Taguchi's major goal is to optimize a process's parameters to attain maximum efficiency [37]. The Taguchi technique was used to optimize the FDM input parameters such as a printing pattern, printing speed, layer thickness and orientation of raster. The results demonstrated that layer thickness had a substantial impact on Young's modulus at a 20° displacement angle [38,39]. The lowest layer thickness improves tensile strength while also conserving raw material [40]. Kumar et al. [41] investigated the effect of five factors on the surface integrity of ABS parts manufactured using FDM. To understand the influence of the treated parameter, he employed Taguchi analysis and did analysis of variance (ANOVA). ANOVA also was used to identify the significant factor contributing to the experimental conditions [42].

The use of NFRC in FDM is impressive since it reduces cost of feedstock material and has a low environmental effect [9,10]. It also reduces warping after processing though perhaps keeping the material's mechanical strengths [16]. However, production process becomes problematic owing to issues shared with typical cellulose-based composites, such as feedstock drying non-uniformity in filler distribution, void formation, and temperature control [43,44]. Recently, several researchers have been focusing on the creation of novel materials to increase mechanical performance. There has not been enough study done to discover the process parameter interdependence on various materials in order to enhance the mechanical characteristics of printed parts by FDM. Additionally, no previous research has investigated the optimal parameter settings for FDM to print products manufactured from oil palm fiber reinforced thermoplastic composites. Thus, it is vital to investigate the optimum printing parameters for new materials like oil palm fiber composite in order to get the best results and to provide primary data to other researchers that use this material.

2. Materials and Methods

2.1. Materials

The oil palm fibers or known as *Elaeis guineensis* used in this research were obtained from a local estate. Meanwhile, the ABS types PA-747H were supplied by a local supplier that is imported from the Chi Mei Corporation. The material preparation process of oil palm fiber composite in granules form include the method of fiber treatment, mixing, hot pressing, crushing, as was explained in our previous study [45]. The oil palm fiber composite filament was fabricated using a twin screw extruder. The extruder was built locally in Malaysia, using a Siemens PLC controller that was imported from China. Figure 2 shows the process flow of this study for fabrication and optimization of oil palm fiber reinforced thermoplastic composites. The method of research starts with the material pre-processing of the fiber and the compounding process. Then, it continues with the fabrication of the filament by an extrusion process, printing specimens, application of DOE, performing mechanical test, and lastly evaluating the fractured surface of specimens by SEM. For this study, 3wt% of oil palm fiber was used to study the printing optimization using an FDM 3D printer.

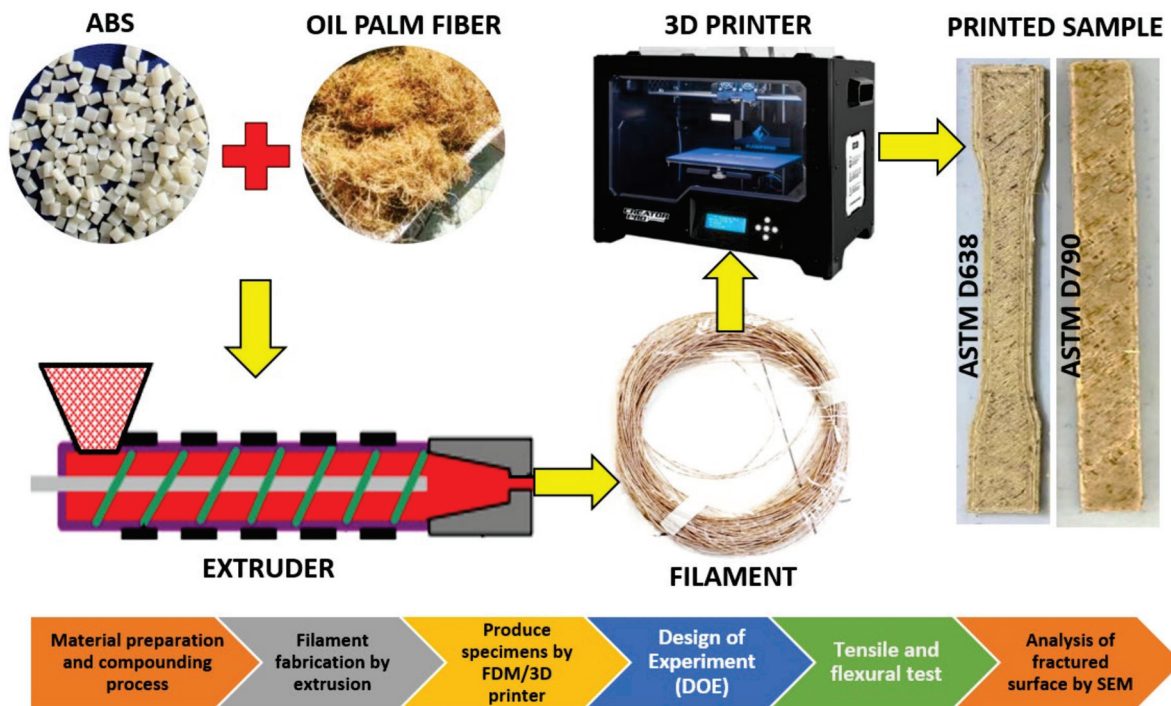


Figure 2. Process flow for fabrication and optimization of oil palm fiber reinforced thermoplastic composites.

2.2. Design of Experiment (DOE)

The relation between the experimental factors and their response was evaluated using the Taguchi method. The design of experiments was carried out using Minitab-16 software to examine the effect on mechanical strength of the oil palm fiber composite specimens. Orthogonal array design L_9 was generated by Minitab software by referring to the four factors and three levels. It is selected in this study because it contains a minimum number of experiments so that it becomes more affective, reducing experiment time and cost. Figure 3 shows the graph of tensile strength, Young's modulus, and the flexural strength based on the nine design runs. According to the literature, the strength of composites is determined by numerous characteristics such as nozzle temperature, raster orientation, raster angle, contour width, infill density, orientation, printing speed, layer height, and thermal conductivity. There were four key characteristics that determine the strength of the printed specimens that were addressed in this investigation, including layer thickness, orientation, infill density, and printing speed, as shown in Table 1. The tests were carried out according to the design matrix, and the results are also reported. Table 2 shows the number of experiments for orthogonal array L_9 (3^4) as well as the response values for nine design runs. The Taguchi approach includes using a rigorous experimental design to optimize process parameters. Tensile strength, Young's modulus, and flexural strength were chosen as responses to calculate the percentage contribution of each factor. The selection of levels of each factor is based on the minimum, medium and maximum range of printing parameters using an FDM 3D printer. The signal-to-noise (S/N) ratio is a quality metric for assessing the impact of input variables towards responses. All of the output responses in this investigation are quality characteristics of the 'larger the better' type. Equation (1) was used to estimate the S/N ratios for this characteristic,

$$S/N = -10 \log_{10} \left(\sum_{i=1}^n Y_i^2 \right) \quad (1)$$

where S/N is signal-to-noise; i is 1, 2, 3, ... n ; Y is output response value.

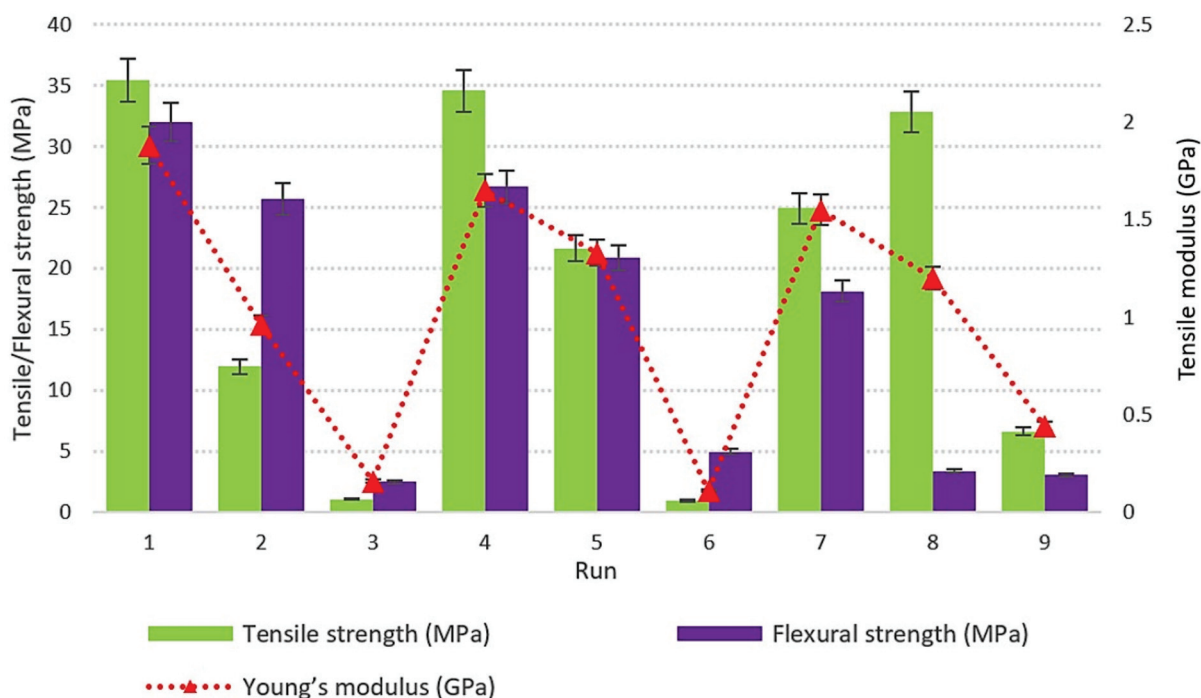


Figure 3. Graph of tensile strength, Young’s modulus and flexural strength of oil palm fiber reinforced thermoplastic composites.

Table 1. Factors and their levels.

Factors		Levels		
		1	2	3
A	Thickness of Layer (mm)	0.2	0.3	0.4
B	Orientation on Z-axis (°)	0	45	90
C	Infill Density (%)	100	50	0
D	Printing Speed (mm/s)	10	50	100

Table 2. Orthogonal array design L₉ (3⁴).

Run	Layer Thickness (mm)	Orientation (°)	Infill Density (%)	Printing Speed (mm/s)	Responses		
					Tensile Strength (MPa)	Young’s Modulus (GPa)	Flexural Strength (MPa)
1	0.2	0	100	10	35.38	1.88	31.98
2	0.2	45	50	50	11.94	0.96	25.67
3	0.2	90	0	100	1.06	0.16	2.50
4	0.3	0	50	100	34.55	1.65	26.67
5	0.3	45	0	10	21.64	1.33	20.88
6	0.3	90	100	50	0.95	0.11	4.97
7	0.4	0	0	50	24.92	1.55	18.12
8	0.4	45	100	100	32.83	1.20	3.40
9	0.4	90	50	10	6.64	0.44	3.04

2.3. 3D Printing

A 3D printer, model FlashForge, Creator Pro (Zhejiang Flashforge 3D Technology Co., Ltd., Jinhua City, China) was used to print all specimens. The selected printing parameters of FDM to be optimized are orientation, infill density, layer thickness, and printing speed, as shown in Figure 4a–d. The printing orientations were 0, 45, and 90°, with layer thicknesses (0.2, 0.3, and 0.4 mm), infill density (0, 50 and 100%) and printing speed (10, 50, 100 mm/s),

respectively. A FlashPrint, version 5.3.1 software (Zhejiang Flashforge 3D Technology Co., Ltd., Jinhua City, China) was used to integrate with 3D printer. It provides a simple and easy to use user interface for preparing of 3D designs for printing on the FlashForge 3D printers. The tensile and flexural samples were printed according to ASTM 638 and ASTM 790 standards.

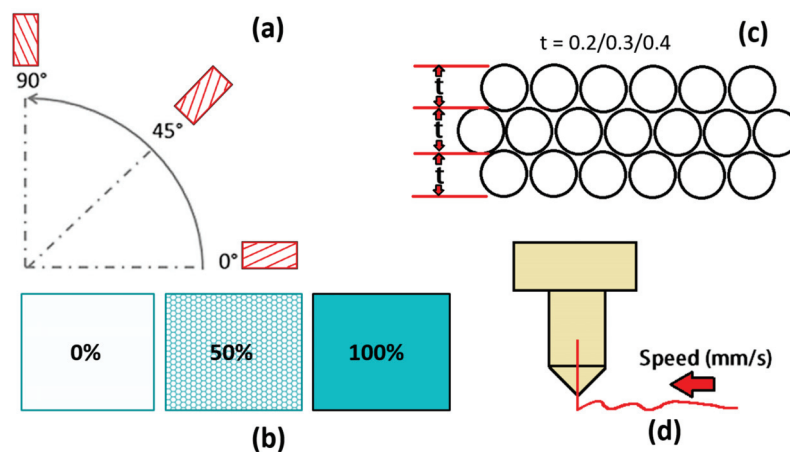


Figure 4. Printing parameter (a) orientation (b) infill density percentage (c) layer thickness and (d) printing speed.

2.4. Tensile Testing

The tensile properties of the samples were analyzed following a standard procedure of ASTM D-638 and the dimension of printed specimens can be referred to Table 3. The determinations of tensile strength and modulus as well as elongation were performed in a universal testing machine (Shimadzu Autograph AGSX, Shimadzu Corporation, Kyoto, Japan) with a 50 kN load cell and constant crosshead speed of 5 mm/min. Tensile strength is a measurement of a material’s ability to withstand stretching or the extent to which it can be stretched before failing. The composites’ tensile characteristics, such as stiffness, ductile modulus, and prolongation at breaking point, were measured. The formulae for calculating tensile strength and modulus of elasticity are Equations (2) and (3).

$$\sigma = F/A \tag{2}$$

where σ is the tensile strength at yield; F is the force applied (kN); A is the cross-section area in rectangular.

$$E = \sigma/\epsilon \tag{3}$$

where E is the young’s modulus (MPa); σ is the stress applied on printed specimen; ϵ is the strain of the specimen (mm/mm).

Table 3. Dimension of ASTM D638 and ASTM D790 standard specimen.

Dimension (mm)	ASTM D638	ASTM D790
Overall length	165	130
Overall width	19	13
Distance between grips	115	-
Gage length	50	-
Length of narrow section	57	-
Thickness	3.2	3
Radius of fillet	76	-
Gage width	13	-

2.5. Flexural Testing

A flexural test, also known as a three-point bending test, was used to measure the bending strength and modulus of printed specimens made from ABS-oil palm fiber composite using

FDM. The flexural properties of the samples were analyzed according to a standard procedure of ASTM D-790 and the dimension of printed specimens as in Table 3. A universal testing machine (Shimadzu Autograph AGSX, Shimadzu Corporation, Kyoto, Japan) equipped with a 50 kN load cell was used to conduct flexural tests at 23 ± 1 °C temperature and of $50 \pm 5\%$ relative humidity. Yield and fracture parameters were evaluated at a crosshead speed of 5 mm/min. The ability of a material to tolerate twisting in the opposite direction of its axial center is known as flexural ability. Furthermore, when a bar-shaped test piece with a straight shaft is exposed to a twisting force opposed to the bar, the maximum pressure is formed [46]. Two support beams were used to hold the printed specimens. The specimens were then loaded using a loading nose in the middle. The span-to-depth ratio (R) of the structure was 16:1. Equation (4) was used to compute the rate of crosshead motion for each specimen. Equation (5) was used to compute the flexural stress from the observed load, whereas Equation (6) was used to determine the flexural modulus.

$$R = \frac{ZL^2}{6d} \quad (4)$$

$$\sigma_{max} = \frac{3PL}{2bd^2} \quad (5)$$

$$E_H = \frac{L^2P}{4bd^3} \quad (6)$$

where E_H is the flexural modulus (MPa); L is the support span (mm); P is the load at yield; σ_{max} is the flexural strength (MPa); d is the thickness (mm); b is the width (mm) ($a^2 + b^2 = c^2$); R is the rate of crosshead motion, mm/min; Z is the rate of straining of the outer fiber, mm/min; and Z is 0.01.

2.6. Scanning Electron Microscope (SEM)

The morphology of the fractured surface of ABS-oil palm fiber composite was observed using a scanning electron microscope, model ZEISS LEO 1455 VPSEM (Jena, Germany) at 10 kV acceleration voltage. All samples were cut to a standard size and platinum-coated on the surface prior to the experiment. All test samples were stored in zip plastic bags after inspection.

3. Results and Discussion

3.1. Interaction Plots, Probability Plots and ANOVA

The interaction plots for tensile strength, Young's modulus, and flexural strength as a function of four parameters considered in this study are shown in Figure 5. In this interaction plot, the lines were not parallel, which indicates the good relationship among the factors to the value of tensile strength, Young's modulus, and flexural strength. However, there was no interaction between the orientation-infill and the orientation-printing speed towards mean of tensile strength and Young's modulus. Parameter setting for 0.2 mm layer thickness, 0° of build orientation, 100% infill density indicate the 10 mm/s speed gave the higher tensile strength, Young's modulus and flexural strength. Irfan et al. [47] found that there was no interaction between fiber mass and feeding zone to the tensile strength of kenaf-polypropylene composites.

Probability plots quantify the dispersion of experimental results of tensile strength, Young's modulus, and flexural test of oil palm fiber composite specimens. Normal probability plots are utilized to determine if data comes from a normal distribution. The statistical technique is based on the assumption of a normal underlying distribution [48]. As a result, normal probability plots can either give comfort that the assumption is justified or provide a warning that the assumption has flaws. Normal probability plots and hypothesis tests for normalcy are usually combined in a normality study. An assumption of normality is plausible in a normal probability plot if all of the data points lie around the line. Otherwise, the points will curve away from the line, eliminating the need for a normalcy assumption. The Anderson Darling (AD) test is used to validate the normalcy assumption [49]. It is a sophisticated statistical technique used to discover outliers from normality. Figure 6 indicates that the experimental data for all answers is close to the fitted line, the AD statics

values are low, and the p -value of the test is larger than 0.05, implying that the data follows a normal distribution. As a result, the data may be subjected to additional analysis and optimization. The normal probability plots show that all points are close to a straight line and are evenly distributed, with no outliers. On the other hand, it means that the errors are distributed normally. This pattern also shows that residuals are evenly distributed throughout all runs. Montgomery [50] used ANOVA to demonstrate how the two factors influence Young’s modulus and tensile strength.

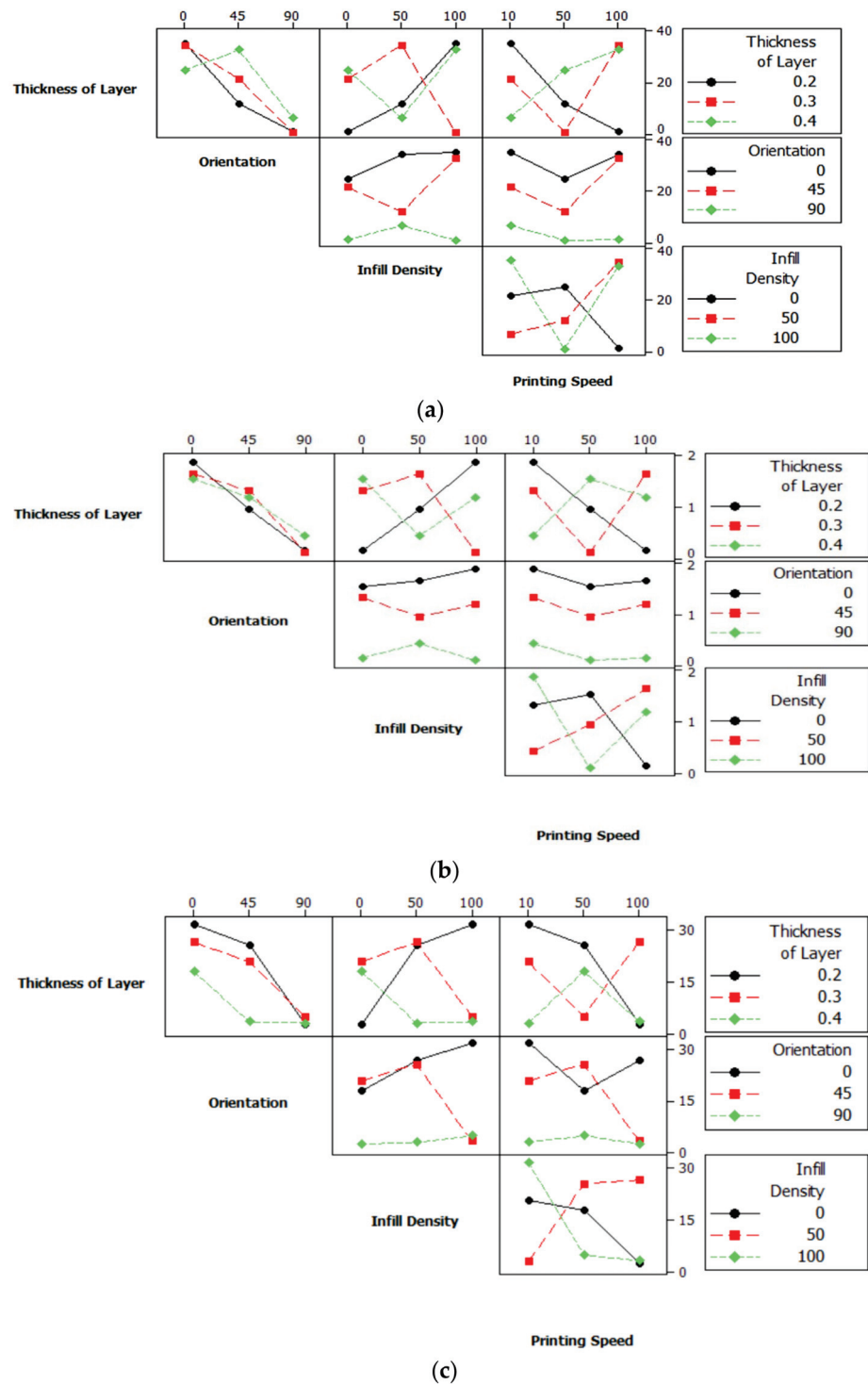


Figure 5. Interaction plots of (a) tensile strength (b) Young’s modulus and (c) flexural strength.

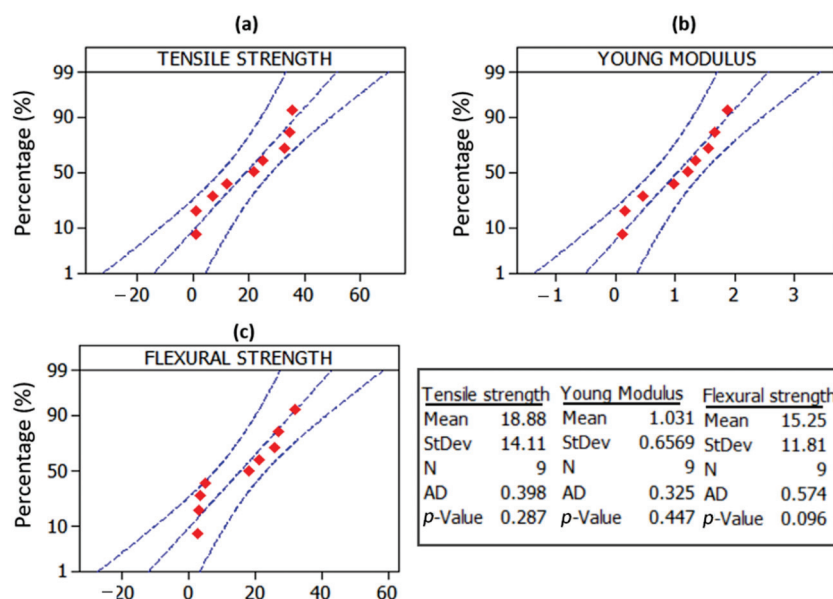


Figure 6. Normal probability plots of (a) tensile strength (b) Young’s modulus and (c) flexural strength.

To investigate the primary influence of input parameters on individual response, an ANOVA with a 95% confidence interval was used. The ANOVA values for tensile strength, Young’s modulus, and flexural strength are shown in Table 4. If the *p*-value is less than 0.05, the parameter is significant in terms of responses. The most significant factor influencing the value of tensile strength in this investigation was orientation, which contributed 67.7%. The remaining factors, such as layer thickness, printing speed, and infill density, were not significant according to *p*-values larger than 0.05. The greater influence parameter for Young’s modulus response was also orientation, with a 45.5% contribution and a *p*-value less than 0.05. Furthermore, other parameters were minor, contributing a lesser percentage of contribution. This also applied to flexural strength value, where part orientation was the most influential parameter, accounting for 49.6% of the response. This finding was in agreement with Chacón et al. [51], who had observed the effect of layer thickness, built orientation, and feed rate on the strength of the printed parts by FDM. He found that the 0° of build orientation was the influencing parameter as relates to the value of tensile strength.

Table 4. ANOVA for each response.

Response	Source	DoF	Adj SS	Adj MS	F-Value	p-Value	% Contribution	Remarks
Tensile strength	Layer thickness	2	43.0	21.0	0.08	0.921	2.26	Insignificant
	Orientation	2	1286.2	643.1	12.55	0.007 *	67.67	Significant
	Infill density	2	83.0	42.0	0.17	0.851	4.37	Insignificant
	Printing speed	2	181.0	91.0	0.38	0.696	9.52	Insignificant
	Error	6	307.4	51.2			16.17	
	Total	8	1900.6				100	
Young’s modulus	Layer thickness	2	0.006	0.003	0.01	0.995	0.09	Insignificant
	Orientation	2	3.262	1.631	51.23	0.000 *	48.51	Significant
	Infill density	2	0.005	0.002	0.00	0.996	0.07	Insignificant
	Printing speed	2	0.180	0.090	0.17	0.851	2.68	Insignificant
	Error	6	3.272	1.726			48.65	
	Total	8	6.725				100	
Flexural strength	Layer thickness	2	234.0	117.0	0.80	0.494	15.68	Insignificant
	Orientation	2	740.6	370.3	5.91	0.038 *	49.62	Significant
	Infill density	2	47.0	23.0	0.13	0.880	3.15	Insignificant
	Printing speed	2	95.0	48.0	0.28	0.765	6.36	Insignificant
	Error	6	376.0				25.19	
	Total	8					100	

* Source of variance with *p*-value less than 0.05 is significant; DoF is degree of freedom; Adj SS is the adjusted sum of square; Adj MS is the adjusted mean square.

3.2. Main Effect Plots for Means

A main effects plot is a graph that displays the mean response values for each level of a design parameter of FDM. It is useful for comparing the relative strength of several factors' impacts. Figure 7a–c show the main effect plot of means for tensile strength, Young's modulus, and flexural strength, respectively. The result shows that the tensile strength increases when layer thickness, infill density and printing speed increase from low to high level. However, when the orientation parameter increases from low to high, the value of tensile strength decreases. The graph for Young's modulus demonstrates that the value of the modulus rose from level 2 to 3 for layer thickness, speed, and infill density, but not for orientation. Furthermore, the main effect plot of means for flexural strength reveals that when the level is increased from 2 to 3, the mean values for all parameters decrease. Overall, printing orientation (0°) contributes a greater value of tensile strength, Young's modulus, and flexural strength. This result was consistent with the findings by Chacón et al. [51], who discovered that the 0° of printing orientation was the most contributing parameter to the tensile strength value.

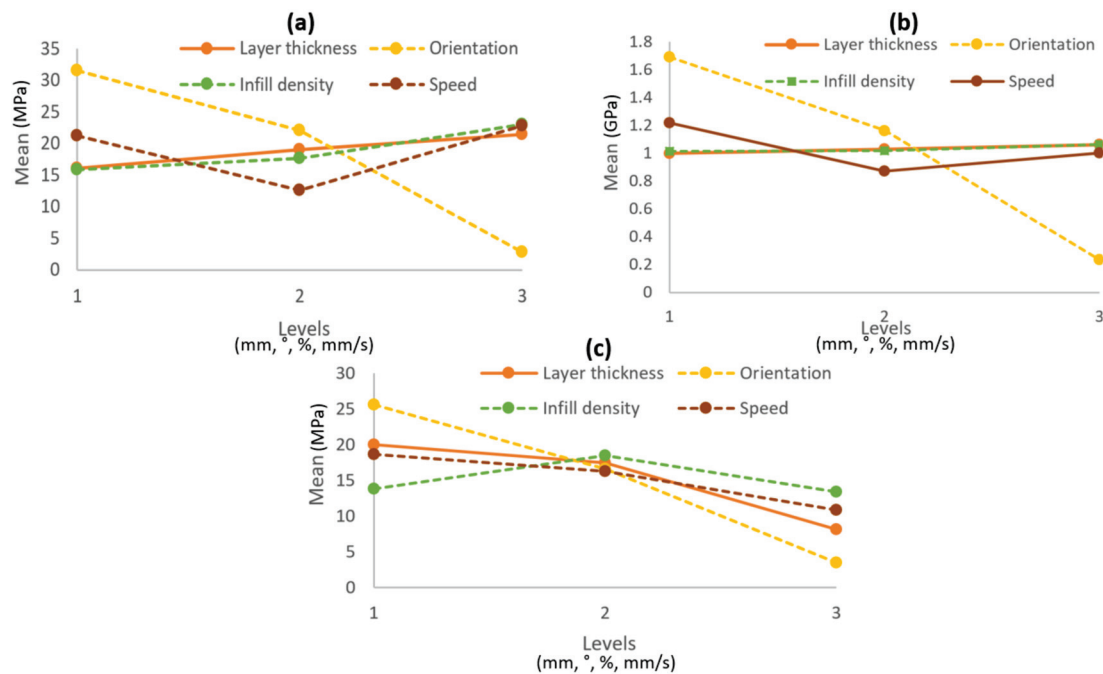


Figure 7. Main effect plot of means for (a) tensile strength (b) Young's modulus and (c) flexural strength.

3.3. Taguchi Optimization by S/N Ratio

Figure 8 shows the main effects plots for the S/N ratios of tensile strength, Young's modulus, and flexural strength with printing parameter such as layer thickness, orientation, infill density, and printing speed. Since the aim of the study is to maximize the value of responses such as tensile strength, Young's modulus, and flexural strength, the S/N ratio was selected to be 'larger the better'. The optimal levels are obtained by computing the average values of the S/N ratios for each response at each level, and the higher values of the S/N ratios show good quality characteristics. Irfan et al. [47] studied the compounding parameters of kenaf fiber composite. They applied the S/N ratio to analyze the results as a function of the factors and levels for tensile strength and modulus. Figure 8a,b show the S/N ratio for tensile strength and Young's modulus. Meanwhile, Figure 8c shows the S/N ratio for flexural strength and trend posters the decreasing the value of the S/N ratio from level 1 to level 3. Overall, the optimum printing parameter for FDM using oil palm fiber composite filament was 0.4 mm layer thickness, flat (0°) of orientation, 50% infill density and 10 mm/s printing speed. Among all the factors, build orientation became

the most significance parameter towards responses including tensile strength, Young's modulus, and tensile strength. This result was similar to the research finding on FDM optimization by Chacón et al. [51], Domingo et al. [52], Tymrak et al. [53] and Lanzotti et al. [54]. They found that the build orientation plays the main role in the performance of mechanical properties of the printed parts by FDM. The flat (0°) orientation parameter contributes the higher tensile strength rather than increasing the degree ($^\circ$) of orientation.

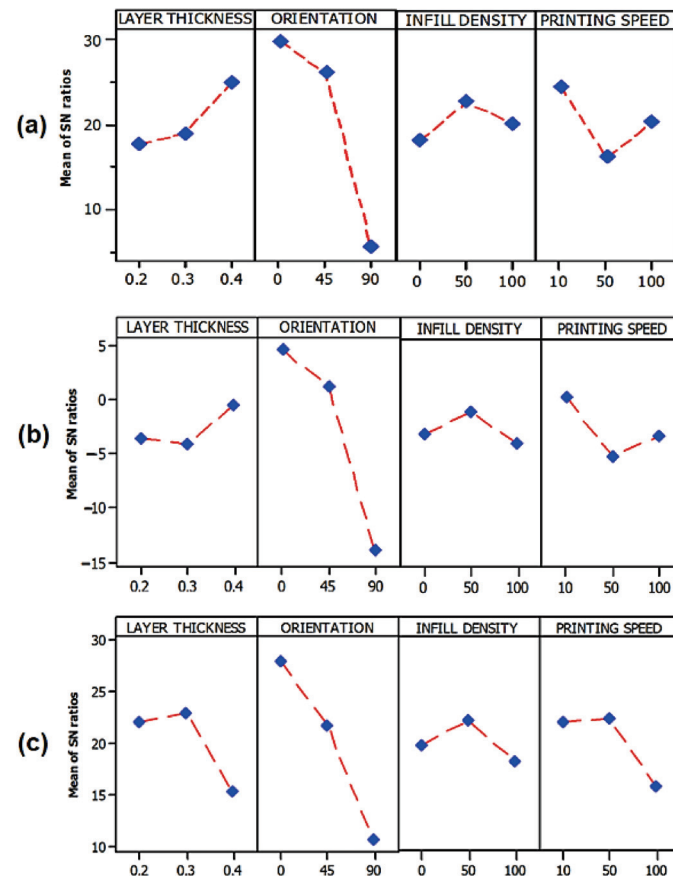


Figure 8. Main effects plot for the S/N ratios (larger the better) of (a) tensile strength (b) Young's modulus and (c) flexural strength.

3.4. SEM Analysis of Fractured Surfaces

Figure 9 shows SEM images of the specimen's fractured surfaces. Figure 9a–d indicate the fractured surfaces of S1, S4, S7, and S8 specimens from design experiment runs 1, 4, 7, and 8, respectively. The fractured fiber can clearly be observed on Figure 9b,c. It was caused by the extrusion, compounding, and fiber treatment processes [55,56]. The microstructural changes in all specimens with different parameter settings were seen in the cross section images of the samples. Figure 9d shows a cross section pattern with a 45° printing orientation, 0.4 mm layer thickness, 100 mm/s and 100% infill density. It demonstrates that the interlayer printing beads were misaligned as a result of the increased printing speed. However, Figure 9a with parameter 0° orientation shows the tougher bead structure and looks more ductile when compared to the 45° orientation. Microscopic images reveal the presence of voids between beads, resulting in a reduction in the element's net section and real density, as well as the existence of a cavity at the interaction of beads [57]. The adhesion force between filaments can be reduced by a type of defect, which is most likely connected to the extrusion temperature. When comparing layer thicknesses of 0.2 mm and 0.4 mm, the number of voids appeared to be significantly higher. This finding is in accordance with that of Tekinalp et al. [58], who discovered that the FDM printed fiber reinforced composites had lower inter-layer porosity but higher inner-layer porosity. As

shown in the SEM images, the parameter of thickness 0.4 mm, orientation 0°, infill 0.5, and printing speed 10 mm/s was the optimal configuration, with reduced void and good layer arrangement after applying stress. Figure 9b–d show the fiber pull out on the images of the printed specimens. It is due to the poor bonding between fiber and matrix, and when these fibers pull out, the structure’s strength will decrease. If the interfacial adhesion is good, a significant amount of energy is required.

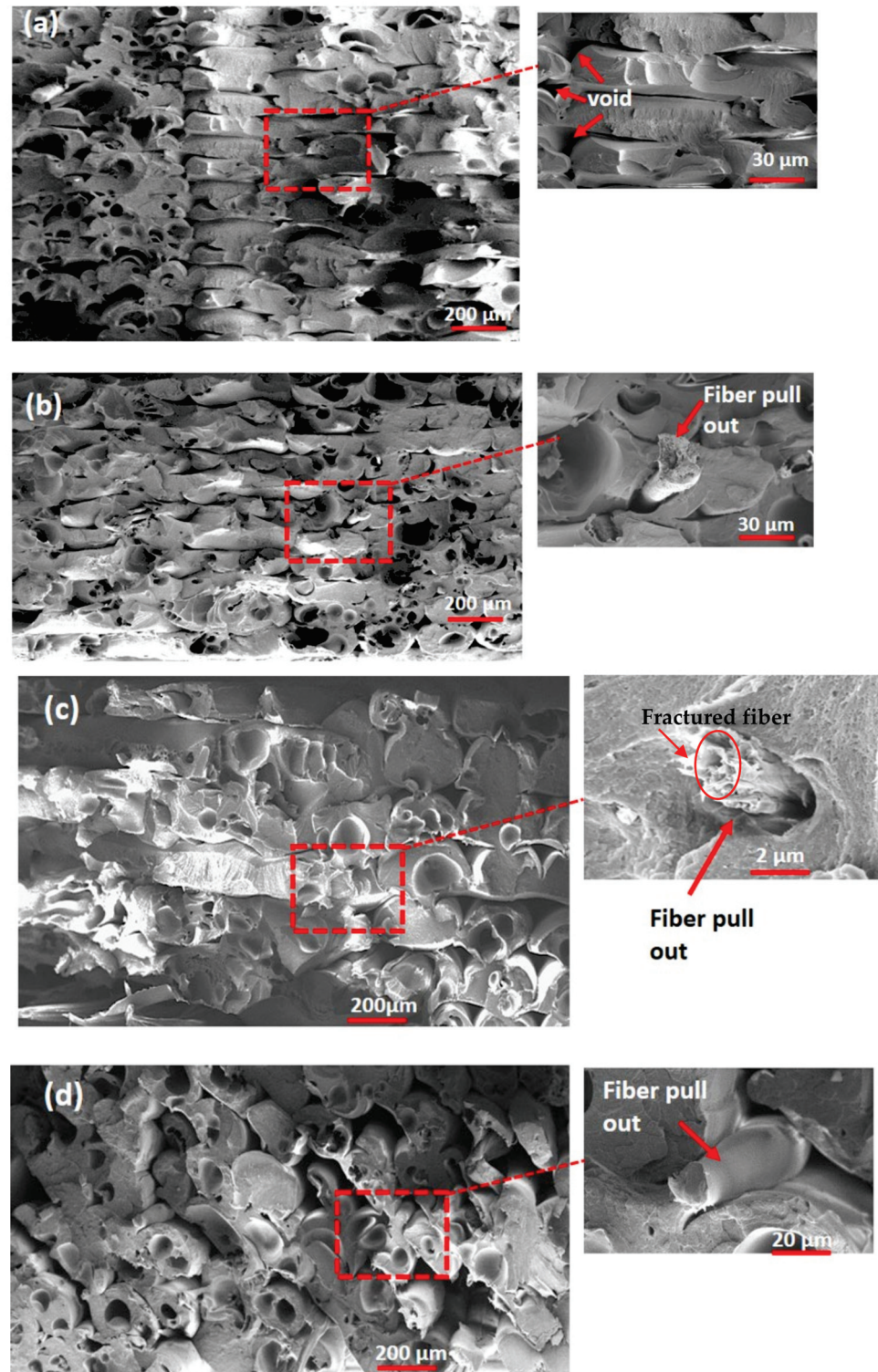


Figure 9. SEM images of (a) S1 (b) S4 (c) S7 and (d) S8 specimens with fractured surfaces.

4. Conclusions

The Taguchi approach was used to improve the process parameters of FDM, which use oil palm fiber reinforced thermoplastic composites as feedstock. Through the use of an orthogonal array L_9 (3^4) to explore the impact of process factors on variable behavior, four parameters with three levels were investigated: layer thickness, orientation, infill density, and printing speed. According to ANOVA analysis, the most significant input variable is build orientation, with p -values less than 0.05 for all responses including tensile, Young's modulus, and flexural strength. According to the normal probability plots, all points are near to a straight line and distributed evenly, with no outliers. The tensile strength of the composites ranged from 0.95 to 35.38 MPa, while Young's modulus was 0.11 to 1.88 GPa and the flexural strength was 2.50 to 31.98 MPa. The best printing parameters for FDM using oil palm fiber composite filament based on the S/N ratio were 0.4 mm layer thickness, flat (0°) orientation, 50% infill density, and 10 mm/s printing speed. The microscopic views show the existence of voids between beads, causing a reduction in the element's net section and actual density, as well as the presence of a cavity at the bead interface. Finally, SEM images revealed that the 0° build orientation has a stronger bead structure and seems more ductile when compared to 45° orientations. As a result, the study would provide experts and researchers with accurate data when dealing with this novel material as a feedstock for FDM.

Author Contributions: Conceptualization, M.N.A.; methodology, M.N.A.; validation, M.N.A., M.R.I., M.M.T., F.M. and Z.L.; formal analysis, M.N.A.; investigation, M.N.A.; resources, M.N.A. and D.D.A.L.; data curation, M.N.A.; writing—original draft preparation, M.N.A.; writing—review and editing, M.N.A., M.R.I. and M.M.T.; visualization, M.N.A., D.D.A.L., I. and I.G.; supervision, M.R.I., M.M.T., F.M. and Z.L.; project administration, M.N.A.; funding acquisition, M.R.I., M.M.T., F.M. and Z.L. All authors have read and agreed to the published version of the manuscript.

Funding: This research was funded by the Fundamental Research Grant Scheme (FRGS), grant no. FRGS/1/2019/TK05/UPM/02/11 (5540205).

Institutional Review Board Statement: Not applicable.

Informed Consent Statement: Not applicable.

Data Availability Statement: The data presented in this study are available on request from the corresponding author.

Acknowledgments: The authors are grateful for the help from all staff and technicians at Universiti Putra Malaysia as well as to Universiti Teknikal Malaysia Melaka and the Ministry of Higher Education (Malaysia) for providing the scholarship awarded to the principal author of this project. Additionally, we would like to thank our families and friends for their moral support during this research.

Conflicts of Interest: The authors declare no conflict of interest.

References

1. Ning, F.; Cong, W.; Qiu, J.; Wei, J.; Wang, S. Additive manufacturing of carbon fiber reinforced thermoplastic composites using fused deposition modeling. *Compos. Part B Eng.* **2015**, *80*, 369–378. [CrossRef]
2. Nath, S.D.; Nilufar, S. An overview of additive manufacturing of polymers and associated composites. *Polymers* **2020**, *12*, 2719. [CrossRef] [PubMed]
3. Leite, M.; Varanda, A.; Ribeiro, A.R.; Silva, A.; Vaz, M.F. Mechanical properties and water absorption of surface modified ABS 3D printed by fused deposition modelling. *Rapid Prototyp. J.* **2018**, *24*, 195–203. [CrossRef]
4. Ziemian, C.; Sharma, M.; Ziemi, S. Anisotropic mechanical properties of ABS parts fabricated by Fused Deposition Modelling. *Mech. Eng.* **2012**, *23*, 159–180.
5. Abeykoon, C.; Sri-Amphorn, P.; Fernando, A. Optimization of fused deposition modeling parameters for improved PLA and ABS 3D printed structures. *Int. J. Lightweight Mater. Manuf.* **2020**, *3*, 284–297. [CrossRef]
6. Camposeco-Negrete, C. Optimization of printing parameters in fused deposition modeling for improving part quality and process sustainability. *Int. J. Adv. Manuf. Technol.* **2020**, *108*, 2131–2147. [CrossRef]
7. Dey, A.; Yodo, N. A systematic survey of FDM process parameter optimization and their influence on part characteristics. *J. Manuf. Mater. Process.* **2019**, *3*, 64. [CrossRef]

8. Khan, I.; Kumar, N. Fused deposition modelling process parameters influence on the mechanical properties of ABS: A review. *Mater. Today Proc.* **2020**, *21*, 1659–1672. [CrossRef]
9. Gkartzou, E.; Koumoulos, E.P.; Charitidis, C.A. Production and 3D printing processing of bio-based thermoplastic filament. *Manuf. Rev.* **2017**, *4*, 2016020. [CrossRef]
10. Guo, R.; Ren, Z.; Bi, H.; Song, Y.; Xu, M. Effect of toughening agents on the properties of poplar wood flour/poly (lactic acid) composites fabricated with fused deposition modeling. *Eur. Polym. J.* **2018**, *107*, 34–45. [CrossRef]
11. Gardan, J.; Roucoules, L. 3D printing device for numerical control machine and wood deposition. *Julien Gardan Int. J. Eng. Res. App.* **2014**, *4*, 123–131.
12. Wimmer, R.; Steyrer, B.; Woess, J.; Koddenberg, T.; Mundigler, N. 3D Printing and wood. *Pro Ligno* **2015**, *11*, 144–149.
13. Gardan, J.; Nguyen, D.C.; Roucoules, L.; Montay, G. Characterization of wood filament in additive deposition to study the mechanical behavior of reconstituted wood products. *J. Eng. Fibers Fabr.* **2016**, *11*, 56–63. [CrossRef]
14. Rosenthal, M.; Henneberger, C.; Gutkes, A.; Bues, C.T. Liquid deposition modeling: A promising approach for 3D printing of wood. *Eur. J. Wood Wood Prod.* **2018**, *76*, 797–799. [CrossRef]
15. Stoof, D.; Pickering, K. Sustainable composite fused deposition modelling filament using recycled pre-consumer polypropylene. *Compos. Part B* **2018**, *135*, 110–118. [CrossRef]
16. Daver, F.; Lee, K.P.M.; Brandt, M.; Shanks, R. Cork-PLA composite filaments for fused deposition modelling. *Compos. Sci. Technol.* **2018**, *168*, 230–237. [CrossRef]
17. Suteja, J.; Firmanto, H.; Soesanti, A.; Christian, C. Properties investigation of 3D printed continuous pineapple leaf fiber-reinforced PLA composite. *J. Thermoplast. Compos. Mater.* **2020**. [CrossRef]
18. Masood, S.H.; Song, W.Q. Development of new metal/polymer materials for rapid tooling using fused deposition modelling. *Mater. Des.* **2004**, *25*, 587–594. [CrossRef]
19. Zhong, W.; Li, F.; Zhang, Z.; Song, L.; Li, Z. Short fiber reinforced composites for fused deposition modeling. *Mater. Sci. Eng. A* **2001**, *301*, 125–130. [CrossRef]
20. Tao, Y.; Wang, H.; Li, Z.; Li, P.; Shi, S.Q. Development and application of wood flour-filled polylactic acid composite filament for 3D printing. *Materials* **2017**, *10*, 339. [CrossRef]
21. Subramanian, M.; Karuppan, S.; Eswaran, P.; Appusamy, A.; Shankar, A.N. State of art on fusion deposition modeling machines process parameter optimization on composite materials. *Mater. Today Proc.* **2021**, *45*, 820–827. [CrossRef]
22. Sun, Q.; Rizvi, G.M.; Bellehumeur, C.T.; Gu, P. Effect of processing conditions on the bonding quality of FDM polymer filaments. *Rapid Prototyp. J.* **2008**, *14*, 72–80. [CrossRef]
23. Tian, X.; Liu, T.; Yang, C.; Wang, Q.; Li, D. Interface and performance of 3D printed continuous carbon fiber reinforced PLA composites. *Compos. A Appl. Sci. Manuf.* **2016**, *88*, 198–205. [CrossRef]
24. Garg, H.; Singh, R. Investigations for melt flow index of Nylon6-Fe composite based hybrid FDM filament. *Rapid Prototyp. J.* **2016**, *22*, 338–343. [CrossRef]
25. Ning, F.; Cong, W.; Hu, Y.; Wang, H. Additive manufacturing of carbon fiber reinforced plastic composites using fused deposition modeling: Effects of process parameters on tensile properties. *J. Compos. Mater.* **2017**, *51*, 451–462. [CrossRef]
26. Hill, N.; Haggi, M. Deposition direction-dependent failure criteria for fused deposition modeling polycarbonate. *Rapid Prototyp. J.* **2014**, *20*, 221–227. [CrossRef]
27. Chockalingam, K.; Jawahar, N.; Praveen, J. Enhancement of anisotropic strength of fused deposited ABS parts by genetic algorithm. *Mater. Manuf. Processes* **2016**, *31*, 2001–2010. [CrossRef]
28. Anitha, R.; Arunachalam, S.; Radhakrishnan, P. Critical parameters influencing the quality of prototypes in fused deposition modelling. *J. Mater. Process. Technol.* **2001**, *118*, 385–388. [CrossRef]
29. Mohamed, O.A.; Masood, S.H.; Bhowmik, J.L. September. Experimental investigation of the influence of fabrication conditions on dynamic viscoelastic properties of PC-ABS processed parts by FDM process. *IOP Conf. Ser. Mater. Sci. Eng.* **2016**, *149*, 012122. [CrossRef]
30. Huynh, H.N.; Nguyen, A.T.; Ha, N.L.; Ha Thai, T.T. Application of fuzzy Taguchi method to improve the dimensional accuracy of fused deposition modeling processed product. In Proceedings of the 2017 International Conference on System Science and Engineering, ICSSE 2017, Ho Chi Minh City, Vietnam, 21–23 July 2017.
31. Raut, S.; Jatti, V.S.; Khedkar, N.K.; Singh, T.P. Investigation of the effect of built orientation on mechanical properties and total cost of FDM parts. *Procedia Mater. Sci.* **2014**, *6*, 1625–1630. [CrossRef]
32. El-Kassas, A.M.; Elsheikh, A.H. A new eco-friendly mechanical technique for production of rice straw fibers for medium density fiberboards manufacturing. *Int. J. Environ. Sci. Technol.* **2021**, *18*, 979–988. [CrossRef]
33. Alafaghani, A.; Qattawi, A. Investigating the effect of fused deposition modeling processing parameters using Taguchi design of experiment method. *J. Manuf. Process.* **2018**, *36*, 164–174. [CrossRef]
34. Hamza, I.; Abdellah, E.G.; Mohamed, O. Experimental optimization of fused deposition modeling process parameters: A Taguchi process approach for dimension and tolerance control. In Proceedings of the International Conference on Industrial Engineering and Operations Management, Paris, France, 26–27 July 2018; pp. 2992–2993.

35. Ahmad, M.N.; Ab Rahman, M.H.; Maidin, N.A.; Osman, M.H.; Wahid, M.K.; Mohamed Saiful Firdaus, H.; Abd Aziz, N.A. Optimization on Surface Roughness of Fused Deposition Modelling (FDM) 3D printed parts using taguchi approach. In Proceedings of the Symposium on Intelligent Manufacturing and Mechatronics, Melaka, Malaysia, 8 July 2019; Springer: Singapore, 2019; pp. 230–243.
36. Uttarwar, P.B.; Raini, S.K.; Malwad, D.S. Optimization of process parameter on Surface Roughness (Ra) and Wall Thickness on SPIF Using Taguchi method. *Int. Res. J. Eng. Technol.* **2015**, *2*, 781–784.
37. Naiju, C.D.; Anil, P.M. Influence of operating parameters on the reciprocating sliding wear of direct metal deposition (DMD) components using Taguchi method. *Procedia Eng.* **2017**, *174*, 1016–1027. [CrossRef]
38. Lee, B.H.; Abdullah, J.; Khan, Z.A. Optimization of rapid prototyping parameters for production of flexible ABS object. *J. Mater. Process. Technol.* **2005**, *169*, 54–61. [CrossRef]
39. Uddin, M.S.; Sidek, M.F.R.; Faizal, M.A.; Ghomashchi, R.; Pramanik, A. Evaluating mechanical properties and failure mechanisms of fused deposition modeling acrylonitrile butadiene styrene parts. *J. Manuf. Sci. Eng.* **2017**, *139*, 081018. [CrossRef]
40. Onwubolu, G.C.; Rayegani, F. Characterization and optimization of mechanical properties of ABS parts manufactured by the fused deposition modelling process. *Int. J. Manuf. Eng.* **2014**, *2014*, 1–13. [CrossRef]
41. Kumar, S.; Kannan, V.N.; Sankaranarayanan, G. Parameter optimization of ABS-M30i parts produced by fused deposition modeling for minimum surface roughness. *Int. J. Curr. Eng. Technol.* **2014**, *3*, 93–97.
42. Osman, M.H.; Ab Rahman, M.H.; Ahmad, M.N.; Wahid, M.K.; Maidin, N.A. Optimization of drilling parameters on diameter accuracy in dry drilling process of AISI D2 tool steel. *Int. J. Appl. Eng. Res.* **2017**, *12*, 9644–9652.
43. Depuydt, D.; Balthazar, M.; Hendrickx, K.; Six, W.; Ferraris, E.; Desplentere, F.; Ivens, J.; van Vuure, A.W. Production and characterization of bamboo and flax fiber reinforced polylactic acid filaments for fused deposition modeling (FDM). *Polym. Compos.* **2019**, *40*, 1951–1963. [CrossRef]
44. Filgueira, D.; Holmen, S.; Melbø, J.K.; Moldes, D.; Echtermeyer, A.T.; Chinga-Carrasco, G. Enzymatic-assisted modification of thermomechanical pulp fibers to improve the interfacial adhesion with poly-(lactic acid) for 3D printing. *ACS Sustain. Chem. Eng.* **2017**, *5*, 9338–9346. [CrossRef]
45. Ahmad, M.N.; Ishak, M.R.; Taha, M.M.; Mustapha, F.; Leman, Z. Rheological and Morphological Properties of Oil Palm Fiber-Reinforced Thermoplastic Composites for Fused Deposition Modeling (FDM). *Polymers* **2021**, *13*, 3739. [CrossRef] [PubMed]
46. Ahmad, M.N.; Wahid, M.K.; Maidin, N.A.; Ab Rahman, M.H.; Osman, M.H. Mechanical characteristics of oil palm fiber reinforced thermoplastics as filament for fused deposition modeling (FDM). *Adv. Manuf.* **2020**, *8*, 72–81. [CrossRef]
47. Irfan, M.S.; Umer, R.; Rao, S. Optimization of Compounding Parameters for Extrusion to Enhance Mechanical Performance of Kenaf-Polypropylene Composites. *Fibers Polym.* **2021**, *22*, 1378–1387. [CrossRef]
48. Montgomery, D.C. *Design and Analysis of Experiments*; John Wiley & Sons: Hoboken, NJ, USA, 2017.
49. Stephens, M.A. EDF statistics for goodness of fit and some comparisons. *J. Am. Stat. Assoc.* **1974**, *69*, 730–737. [CrossRef]
50. Montgomery, D.C. *Introduction to Statistical Quality Control*; John Wiley & Sons: Hoboken, NJ, USA, 2007.
51. Chacón, J.M.; Caminero, M.A.; García-Plaza, E.; Núñez, P.J. Additive manufacturing of PLA structures using fused deposition modelling: Effect of process parameters on mechanical properties and their optimal selection. *Mater. Des.* **2017**, *124*, 143–157. [CrossRef]
52. Domingo-Espin, M.; Puigoriol-Forcada, J.M.; Garcia-Granada, A.A.; Llumà, J.; Borros, S.; Reyes, G. Mechanical property characterization and simulation of fused deposition modeling Polycarbonate parts. *Mater. Des.* **2015**, *83*, 670–677. [CrossRef]
53. Tymrak, B.M.; Kreiger, M.; Pearce, J.M. Mechanical properties of components fabricated with open-source 3-D printers under realistic environmental conditions. *Mater. Des.* **2014**, *58*, 242–246. [CrossRef]
54. Lanzotti, A.; Grasso, M.; Staiano, G.; Martorelli, M. The impact of process parameters on mechanical properties of parts fabricated in PLA with an open-source 3-D printer. *Rapid Prototyp. J.* **2015**, *21*, 604–617. [CrossRef]
55. Sgriccia, N.; Hawley, M.; Misra, M. Characterization of natural fibre surfaces and natural fibre composites. *Compos. Part A Appl. Sci. Manuf.* **2008**, *39*, 514–522. [CrossRef]
56. Taj, S.; Munawar, M.A.; Khan, S. Review: Natural fibre reinforced polymercomposites. *Proc. Pak. Acad. Sci.* **2007**, *44*, 129–144.
57. Casavola, C.; Cazzato, A.; Moramarco, V.; Renna, G. Mechanical behaviour of ABS-Fused Filament Fabrication compounds under impact tensile loadings. *Materials* **2019**, *12*, 1295. [CrossRef] [PubMed]
58. Tekinalp, H.L.; Kunc, V.; Velez-Garcia, G.M.; Duty, C.E.; Love, L.J.; Naskar, A.K.; Ozcan, S. Highly oriented carbon fiber–polymer composites via additive manufacturing. *Compos. Sci. Technol.* **2014**, *105*, 144–150. [CrossRef]

Article

Integration of Material Characterization, Thermoforming Simulation, and As-Formed Structural Analysis for Thermoplastic Composites

Philip Bean , Roberto A. Lopez-Anido  and Senthil Vel Advanced Structures and Composite Center, University of Maine, Orono, ME 04469, USA
rla@maine.edu (R.A.L.-A.); senthil.vel@maine.edu (S.V.)

* Correspondence: philip.m.bean@maine.edu

Abstract: An improved simulation-based thermoforming design process based on the integration of material characterization and as-formed structural analysis is proposed. The tendency of thermoplastic composites to wrinkle during forming has made simulation critical to optimized manufacturing, but the material models required are complex and time consuming to create. A suite of experimental methods has been developed for measurement of several required properties of the molten thermoplastic composite. These methods have the potential to enhance thermoplastic composites manufacturing by simplifying and expediting the process. These material properties have been verified by application to thermomechanical forming predictions using commercial simulation software. The forming predictions showed improved agreement with experimental results compared to those using representative material properties. A tool for using thermoforming simulations to inform more accurate structural models has been tested on a simple case study, and produced results that clearly differ from those of models using idealized fiber orientations and thicknesses. This provides evidence that this type of as-formed analysis may be necessary in some cases, and may be further investigated as an open source alternative to commercial analysis software.

Keywords: composite; thermoplastic; thermoforming; simulation

Citation: Bean, P.; Lopez-Anido, R.A.; Vel, S. Integration of Material Characterization, Thermoforming Simulation, and As-Formed Structural Analysis for Thermoplastic Composites. *Polymers* **2022**, *14*, 1877. <https://doi.org/10.3390/polym14091877>

Academic Editors: Somen K. Bhudolia and Sunil Chandrakant Joshi

Received: 17 March 2022

Accepted: 29 April 2022

Published: 4 May 2022

Publisher's Note: MDPI stays neutral with regard to jurisdictional claims in published maps and institutional affiliations.



Copyright: © 2022 by the authors. Licensee MDPI, Basel, Switzerland. This article is an open access article distributed under the terms and conditions of the Creative Commons Attribution (CC BY) license (<https://creativecommons.org/licenses/by/4.0/>).

1. Introduction

Continuous fiber reinforced thermoplastic composite materials (CFRTPs) contain fiber reinforcement in a meltable thermoplastic matrix, which differs from the more common thermoset composites in which the reinforcing fibers are embedded in a matrix of a chemically-cured resin. This difference gives CFRTPs some unique advantages including higher fracture toughness than their thermoset counterparts [1]; better recyclability [2]; a variety of rapid-manufacturing technologies; and the ability to assemble or repair by welding [3] (in addition to conventional methods like adhesive-bonding or bolting). Thermoplastics also have the ability to be manufactured by a process called thermoforming, wherein a flat thermoplastic composite 'blank' is heated and pressed to shape between press-molds. This versatile process allows for rapid production with cycle times as low as five minutes [4,5], which is much faster than typical thermoset processes. One of the largest drawbacks to thermoforming is the difficulty in forming complex shapes without defects, due to the composites being nearly inextensible along the fiber directions [6–9]. This forces the material to conform to a shape almost exclusively by shear deformation, which has a tendency to cause wrinkles that can compromise the structural integrity of the part. These kinds of defects can often be mitigated by altering the forming process with different temperatures, speeds, or simpler geometry [10–12]. These alterations have traditionally been implemented in a "trial and error"-type manner as shown in Figure 1. This can be costly and time consuming due to the need for iterative physical manufacturing [13–15].

In addition, it requires a high level of experience-based intuition. In order to increase process efficiency, then, the trial and error method has been replaced by computer simulations. In fact, the Consortium for Manufacturing Innovation in Structural Thermoplastics (CMIST) concluded during roadmapping workshops that simulation software and experimental characterization of the requisite material processing properties are a significant need [16]. To be useful, these simulations must accurately predict a variety of behaviors including wrinkling and fiber reorientation. These predictions can allow the costly manufacturing processes to be removed from the design loop (as shown in Figure 2), thus improving efficiency, and allowing for better process optimization. This simulation-based design process has recently been gaining traction in industry as the simulation tools have matured [14].

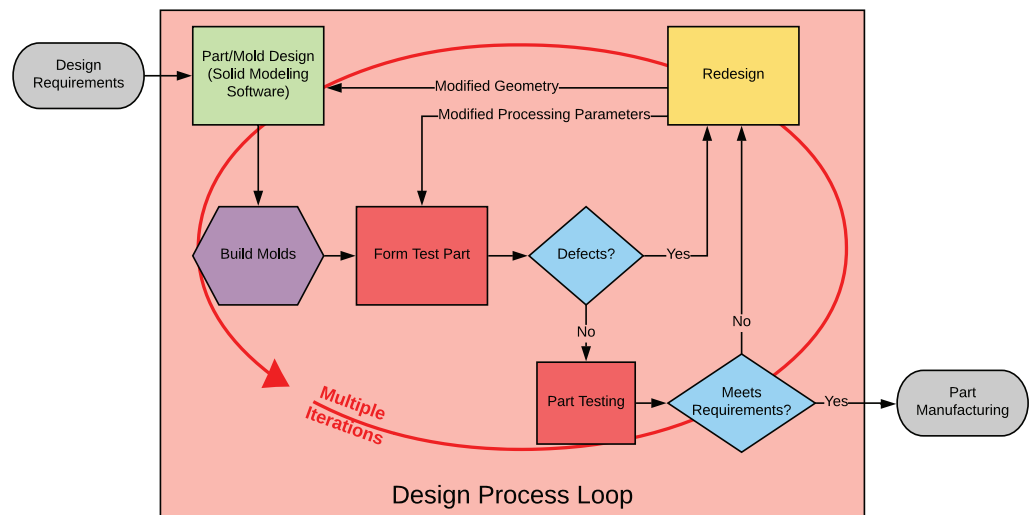


Figure 1. Flowchart of the traditional thermoforming design process.

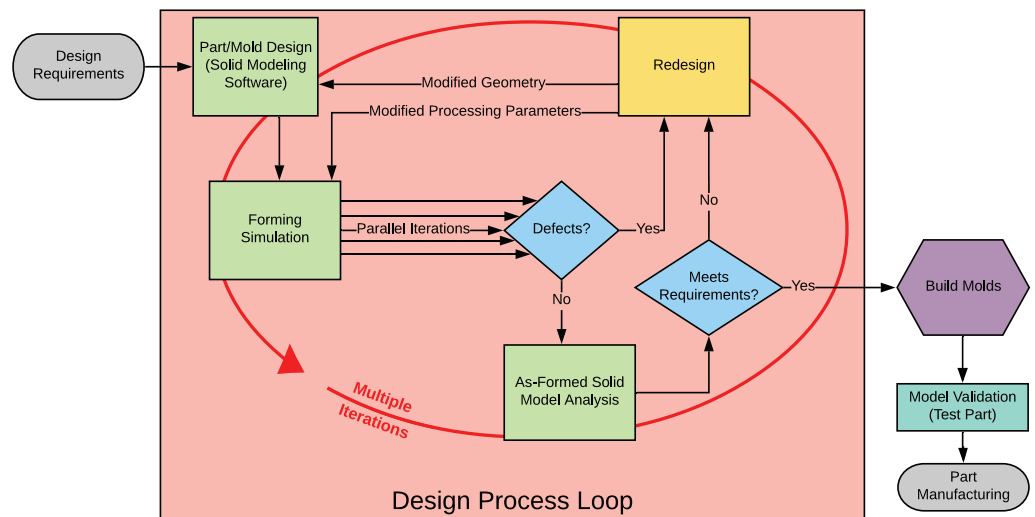


Figure 2. Flowchart of the simulation-based thermoforming design process.

The goal of this research is to aid in the development of simulation methods, which can help this promising technology become more widespread. This work then approaches that goal in a threefold manner. First, to collect a novel set of methods for characterizing material properties for forming analysis. Second, to verify the usefulness of these material properties in thermomechanical forming predictions using commercial simulation software. Third, to extend the use of simulation results for use in structural analysis of the as-formed part.

In order to properly simulate the forming process, material properties must be measured accurately at the processing temperature. These properties can be measured using a standard tensile test frame in a variety of ways including tests like the picture-frame shear test [6,7,17–22] or bias extension test [20,23–26]. Unfortunately, this can present some difficulty, as it requires the use of a high temperature environment chamber so the experiments can be performed at the material forming temperature. Therefore, a set of experimental methods has been proposed to simplify the measurement of these properties. These experiments utilize dynamic mechanical analysis (DMA) techniques.

These material characterizations needed verification to be used in simulations. To this end, two case-study parts were simulated using industrial simulation software, and the results were compared against actual formed parts. A commercial simulation software package was chosen in order to focus on the integration of the entire process, rather than on developing new software. An additional benefit of this is that the methods discussed here could be easily implemented into an existing workflow.

Forming simulation results, while traditionally only used for tuning the manufacturing process, also contain detailed data regarding the final as-formed part. Rather than ignore this data, it is also useful to inform a structural analysis of the as-formed part, since fiber alignment changes during forming [27–30]. To this end, we developed a tool that uses the local fiber alignment and thickness predictions from the forming simulation to build a structural model. This is expected to better predict the final part's performance than a structural model that uses the initial ply thicknesses and fiber orientations, since fiber angle and volume fraction are significant factors in composite material behavior. Thus, the usefulness of a forming simulation is extended.

2. Experimental Characterization Methods

In order to accurately simulate forming, several material properties must be known. These are primarily in-plane properties of the laminae (layers). Here, the focus is on the in-plane shear modulus (G_{12}), the tensile moduli in longitudinal (fiber) and transverse directions (E_1^t and E_2^t), and the bending moduli in the longitudinal and transverse directions (E_1^b and E_2^b). While there have been many different methods proposed for measuring these properties, we chose to use a set of dynamic mechanical analysis (DMA) experiments. DMA, despite being well established as a method, and having several advantages over alternative methods, has not been utilized extensively in the thermoforming field. The primary benefits of DMA are as follows: First, DMA machines typically have high temperature thermal control thus eliminating the need to fit a tensile test frame with an environment chamber. Second, the oscillatory nature of the DMA process allows for a single specimen to be tested continually through a wide range of temperatures and strain-rates, thus decreasing the number of experiments needed. Third, DMA samples are much smaller than typical specimens, thus further decreasing the amount of material needed for characterization. The data from these dynamic experiments comes in the form of the 'storage modulus' and 'loss modulus'. The storage modulus is of interest to this work as it can serve as a proxy for the corresponding elastic modulus (tensile, shear, or bending). While not investigated here, the loss modulus is useful in characterizing the viscous behavior of the material. The polymer material selected was polypropylene, which is a commodity semi-crystalline thermoplastic. These experiments were performed using unidirectional E-glass fiber reinforced polypropylene (Avient prepreg unidirectional tape IE 6034) for use with an automated tape layup machine (hereafter referred to as "PP/glass"). These tapes have a nominal fiber content of 65% by weight. The various experiments are summarized in Table 1 and detailed below.

Table 1. Summary of various material characterization experiments.

Experiment	Target Properties	Specimen Dimensions	Swept Temperatures	Repeats
Dynamic Torsion (Prismatic)	Shear Modulus	10 × 4 × 35 mm	80–200 °C	9
Dynamic Torsion (Dogbone)	Shear Modulus	4 × 4 × 35 mm	80–200 °C	3
Dynamic Tension (Fiber)	Longitudinal Modulus	8 × 0.3 × 30 mm	40–200 °C	8
Dynamic Tension (Transverse)	Transverse Modulus	8 × 0.3 × 30 mm	40–200 °C	3
Dynamic Bending (Fiber)	Longitudinal Bending Modulus	15 × 0.3 × 50 mm	40–200 °C	8

2.1. Shear Modulus

Due to the high longitudinal modulus, continuous-fiber reinforced composites must rely on their ability to deform in an in-plane shear mode (shear strain γ_{12}) in order to conform to complex geometries [6,21,24]. This phenomenon can be avoided by using chopped-strand, knitted, or stretch-broken (aligned discontinuous) fibers. Each of these is more formable than (equivalent) continuous fiber materials because of their ability to stretch in-plane. These are generally not used in high performance applications due to their decreased mechanical properties; however, some stretch-broken-fiber materials have been shown to have strength values comparable to equivalent continuous-fiber systems [31–33]. The importance of shear modulus has prompted investigation of a variety of measurement methods, including picture-frame, bias-extension, and torsion experiments. It has been shown to be difficult to adapt the former two methods to unidirectional materials [34–36]; however, Haanappel et al. [35] have found promising results using torsion experiments. For this reason, torsional rheometry was used in this research.

Torsion experiments were performed on a Bohlin Gemini II rheometer (Figure 3) using the extended-temperature cell (ETC) in order to achieve the desired conditions. This machine was used to run an oscillatory strain-controlled deformation while sweeping through different temperatures or frequencies. These tests were first performed using the temperature sweep, and then later using frequency sweeps at the various temperatures in order to fully capture the behavior and inform a data lookup table for the simulation. The samples measured were unidirectional PP/glass composite manufactured by stamp-thermoforming to consolidate 18 layers into a 4 mm thick panel. This thermoforming process involved pressing a 180–190 °C blank between ambient-temperature platens at a target of 0.69 MPa (100 psi) surface pressure for 1–5 min until cool. The resulting panels were then cut into samples using a CNC waterjet cutter. After cutting, the samples were then conditioned in a standard laboratory environment (23 °C and 50% humidity) for a minimum of 40 h in accordance with ASTM D618-13 Procedure A [37]. Two sample geometries were used: a 10 mm by 4 mm rectangular prismatic section, and a dogbone with a 4 mm square prismatic gage section. Both samples had a 35 mm gage length.

When analyzing the heating-curve data gathered using samples from different panels, it is clear that there are significant differences between each panel. In Figure 4, we can see that each dataset from any given panel varies only slightly from the others, whereas the differences between panels is quite large. It is speculated that this variation may be driven by crystallinity differences due to cooling-rate changes when the panels were consolidated. Since these panels were manufactured as separate batches, variations in thermal history are likely. For the purposes of this research, we decided to simply average the data from each individual panel, and use them as separate datasets.

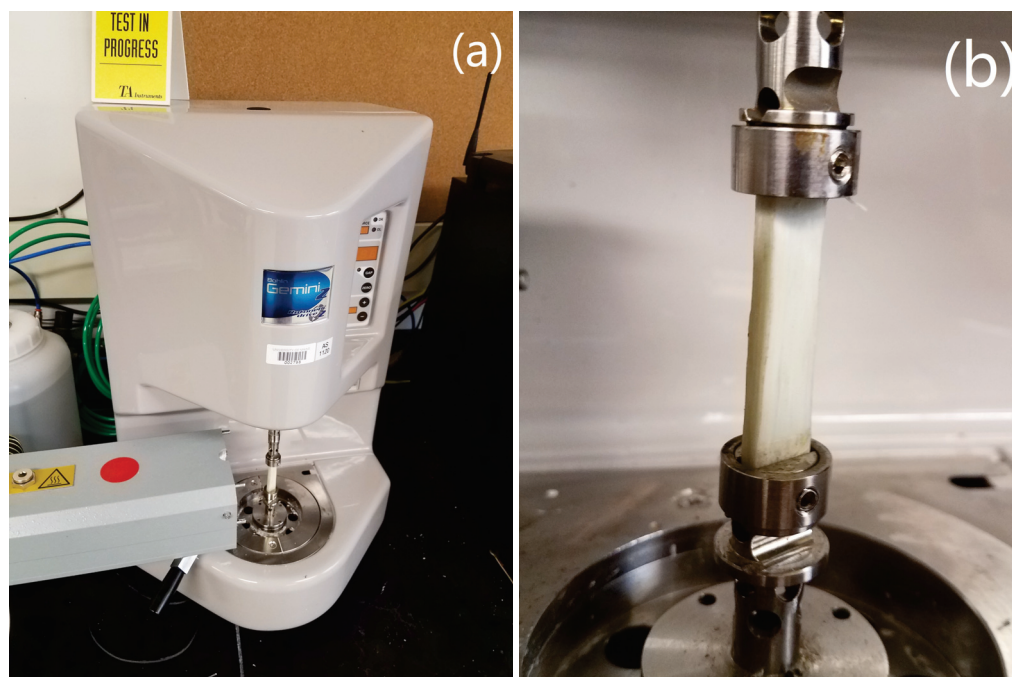


Figure 3. Photos of the torsional rheometer experimental setup. (a) Bohlin rheometer with ETC; (b) 10 mm × 4 mm × 35 mm specimen installed in fixture clamps.

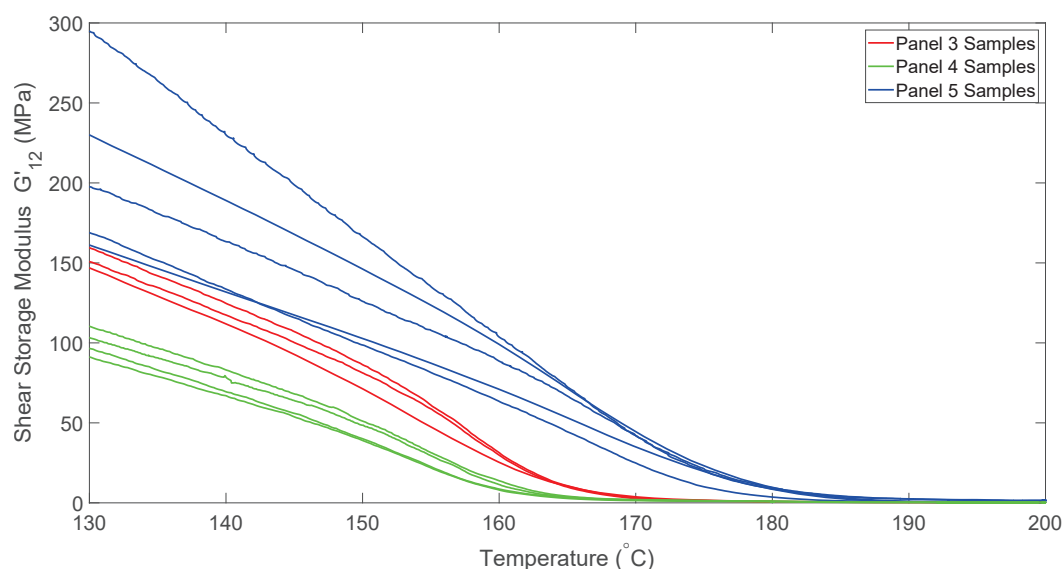


Figure 4. Shear modulus for samples from different panels as a function of temperature.

2.2. Tensile Modulus

The longitudinal tensile modulus in unidirectional thermoplastic composites tends to be orders of magnitude higher than the shear modulus at processing temperatures, thus mandating that the material will deform primarily in shear. This means that the accuracy of the longitudinal modulus is much less critical to the model predictions than the shear modulus. The transverse modulus, however, will still be relatively low, therefore accurate measurements are required.

In order to measure these properties, a DMA (Q-800 DMA by TA Instruments) machine was used. This machine, like the rheometer, utilizes an oscillating deformation, and gathers a continuous stream of data on the material response as temperature and other parameters are varied. The only difference being that the DMA machine fixture adopted applies a tensile load rather than a torsional one. For the tension DMA, thin samples

were manufactured by hot-pressing single tapes of the same PP/glass in order to remove the spool-curl from the material and to smooth the surface for more reliable thickness measurements. This is similar to the process used for the torsion specimens, with the notable difference that only a single layer was utilized rather than multiple. The resulting panels were approximately 0.3 mm thick. Samples were made to the largest allowable size (8 mm × 30 mm) for measurements in both the longitudinal and transverse directions.

Figure 5 shows the temperature dependence of the longitudinal tensile modulus obtained from the DMA experiments. Note that these values are several orders of magnitude higher than the shear moduli, thus demonstrating the relative inextensibility of the fibers, which forces shear deformation.

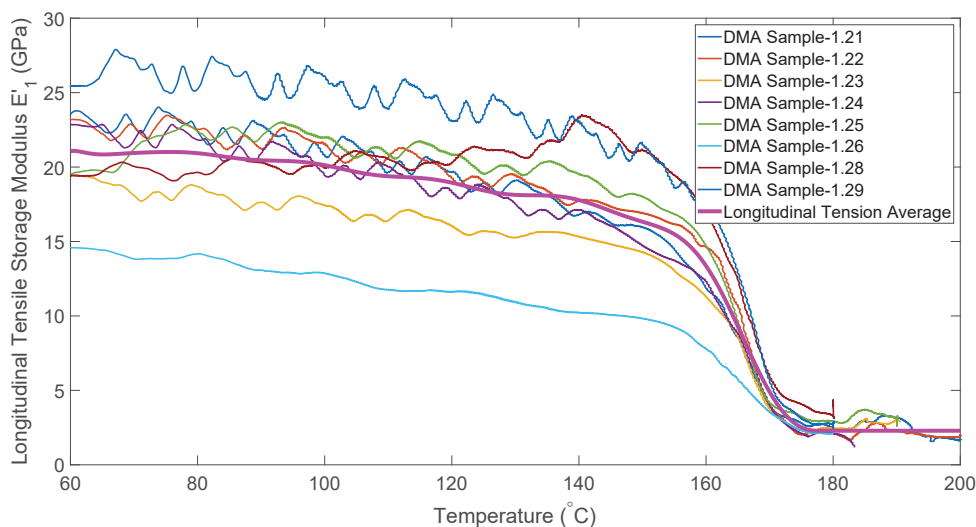


Figure 5. Temperature dependence of longitudinal tensile modulus.

Figure 6 shows the temperature dependence of the transverse tensile modulus obtained from the DMA experiments. One important difference from the longitudinal data is that the transverse tensile modulus actually goes to zero near the processing temperature (180–190 °C), unlike the longitudinal modulus where the fibers provide residual stiffness even after the matrix is molten. It is also worth noting that there is significant scatter in the data. This may be driven by defects in the matrix that also cause some specimens to be quite fragile in this direction.

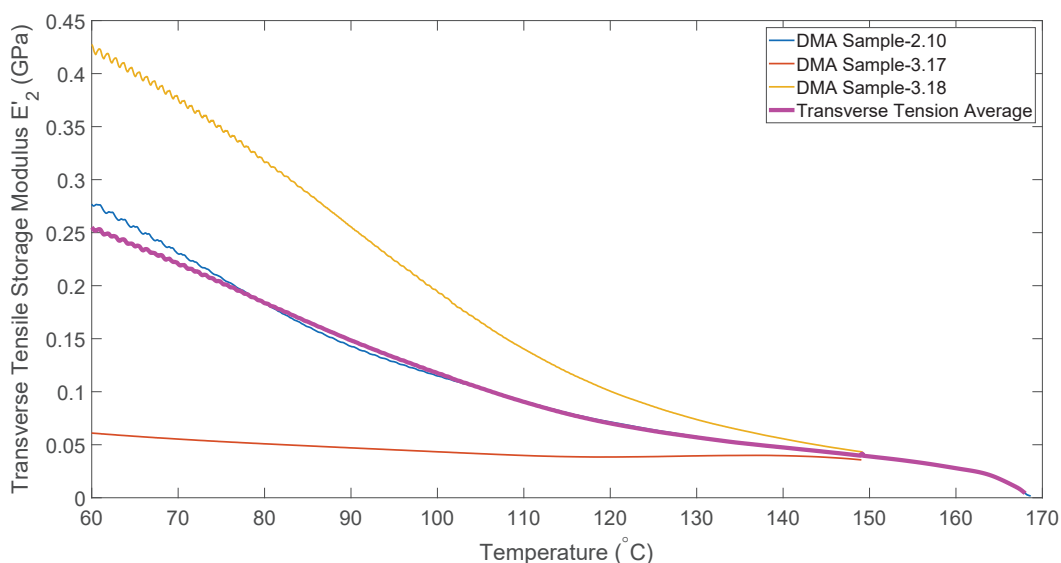


Figure 6. Temperature dependence of transverse tensile modulus.

2.3. Bending Modulus

The modulus of the individual layers in bending is also an important property, since, while the shear deformation determines the critical areas for wrinkling, the bending is what drives the size and distribution of wrinkles in the high shear areas [11,38,39]. Unlike homogeneous materials, however, the bending rigidity of molten composite laminae cannot be directly inferred from the tensile modulus. Due to interactions between the fibers and matrix as well as fiber migration, the modulus in bending can often be significantly smaller than the corresponding tensile moduli. This necessitates a separate series of experiments for the bending modulus of the tapes. For this, the Q-800 DMA machine was utilized using a 3-point bending fixture (see Figure 7) with $15\text{ mm} \times 0.3\text{ mm} \times 50\text{ mm}$ samples, which were manufactured identically to the tension samples. Note also that this unidirectional material had insufficient strength in the transverse direction for any bending experiments. Since the composite in question is unidirectional, there is no reinforcement in the transverse direction, making this tensile-modulus matrix-controlled [40]. Therefore, transverse-bending modulus would also be matrix driven. Since the difference between bending and tensile moduli is a reinforcement-controlled phenomenon, the transverse moduli (tensile and bending) should not exhibit this difference. For this reason, we make the assumption that transverse-tensile modulus can be substituted for transverse-bending modulus.

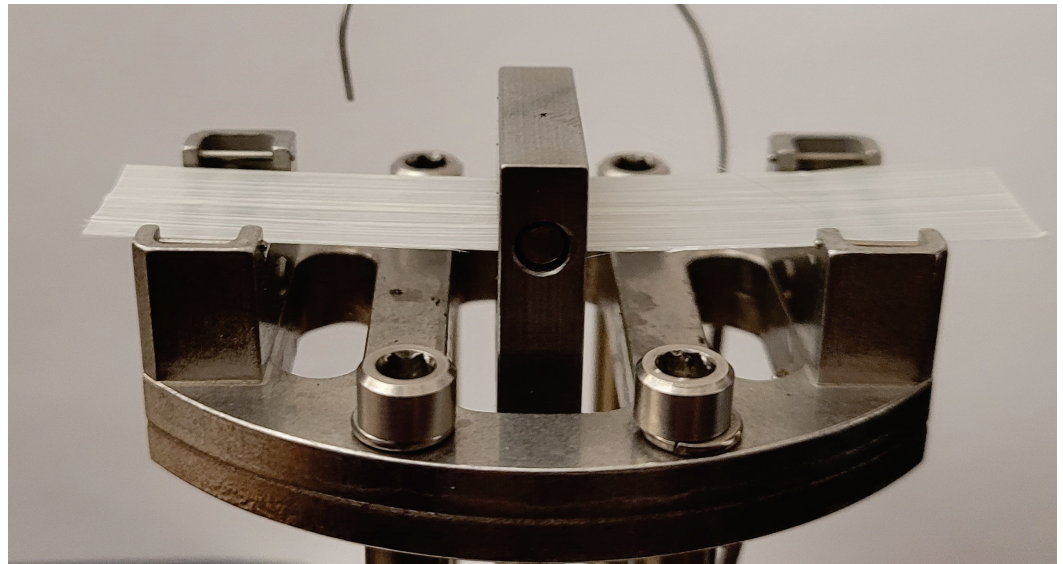


Figure 7. $15\text{ mm} \times 0.3\text{ mm} \times 50\text{ mm}$ specimen installed in 3-point bending DMA fixture.

The bending data in Figure 8 follows a similar trend to all previous data, with the exception of its erratic behavior above melt temperature (approximately $170\text{ }^{\circ}\text{C}$). This is due to the sample with molten matrix being too compliant to be stable in the fixture. In order to generate data for use in simulations at processing temperature ($180\text{--}190\text{ }^{\circ}\text{C}$), the relationship between this curve and the tension curve was used. Figure 9 shows that for much of the heating curve, the bending modulus is lower than the tensile modulus, but near the melt temperature the two curves converge. This behavior was utilized in order to predict the bending modulus at higher temperatures by fitting a curve to follow the bending modulus for lower temperatures, and then smoothly transition to following the tensile modulus.

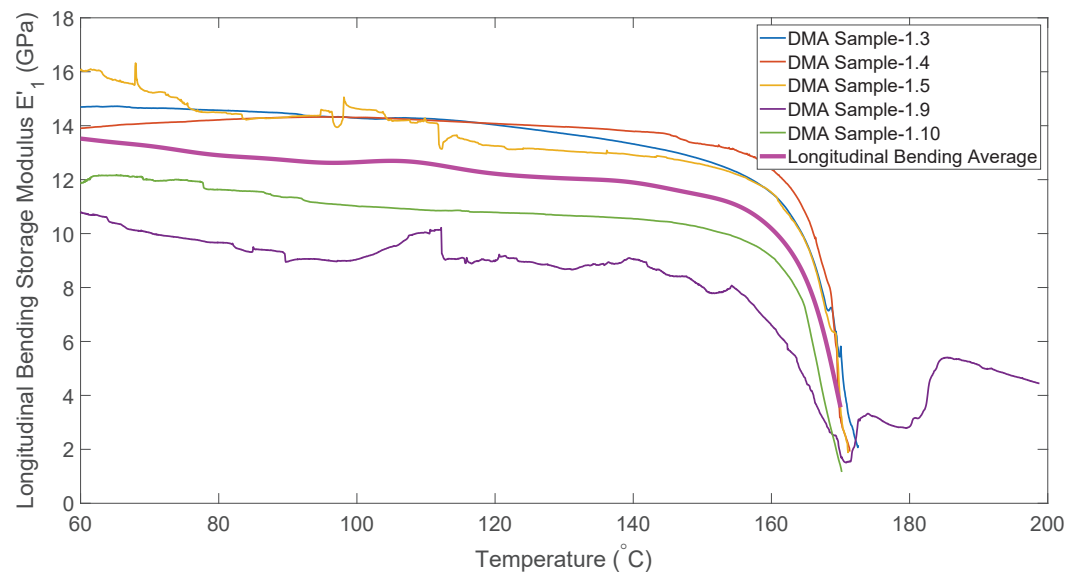


Figure 8. Temperature dependence of the longitudinal bending modulus.

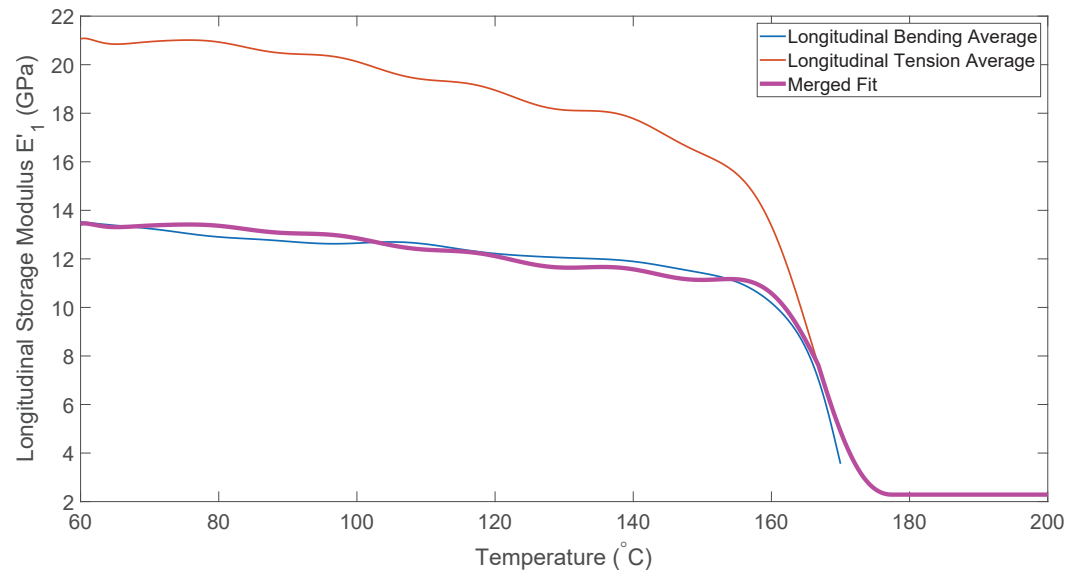


Figure 9. Curve fit for longitudinal bending modulus.

Some other properties to define include contact interactions and thermal properties. The contact interactions determine how the plies will slide relative to the mold, and relative to each other. Contact in forming is a very complex topic due to the interaction between sliding friction, external pressure, and viscous flow, which all vary with temperature [41–43]. Due to the complexity and lack of existing data, we decided to use an estimated constant friction parameter to approximate the contact forming interactions. This was implemented as a constant gluing stress of 1 MPa (which simulates adhesion by forcing plies together once they contact one another), and friction coefficient $\mu = 0.8$, which were chosen by qualitative comparison of simulations using various options. Thermal properties are necessary to simulate processes in which thermal gradients and cooling effects are significant (such as rapid processes with fast cooling times). In these instances, the thermal behavior must be accounted and additional properties are needed. These include thermal conductivities of the blank and mold, conductivities of the blank-mold and ply-ply interfaces, and specific heats of the blank and mold. For a large number of forming applications, however, these effects are relatively small and the simulation remains accurate despite idealizing the process as isothermal [44]. In this research, the modeling has been idealized as isothermal for simplicity.

3. Thermoforming Simulations

The forming behavior of thermoplastic composites is governed by the complex interaction of the fiber-structure and the matrix viscosity. To completely model this complex system using finite element analysis (FEA), everything would need to be modeled at the meso-scale (scale of fiber-structure). This model would be prohibitively complex for any but the simplest designs, requiring far too much computing time. Commercial forming simulation software bypass this issue by approximating the behavior with the effective properties of the overall composite (i.e., “homogenized” or “average” properties), thus allowing for the use of much larger elements, and producing viable models. Some alternative methods (including kinematic, hybrid, and membrane models) have also been developed in order to simplify the simulation process [34,39,45–47].

In a typical orthotropic material model, Poisson’s effects cause coupling between the longitudinal and transverse stress and strain components in the plane of the lamina. In this work, however, we model the composite as an orthotropic material without any coupling effects. This approximation retains simplicity for setup and computation, while also providing accurate results as seen in [48,49]. The stress–strain relationship in each direction, then, is governed by only the modulus in that direction, and is completely independent of the stress in the other directions. The moduli may also be functions of other variables like strain, strain-rate, and temperature. These variations are implemented in a lookup table, wherein the values of the moduli for each element are chosen based on its current state.

One implementation of this simplified model exists in the industrial software PAM-Form [50], which is an explicit finite element analysis software with additional tools to facilitate forming simulations (such as advanced contact modeling and a dedicated composites material model MAT140). By utilizing this software, we focus on integrating the simulation with the material characterization and later structural analysis, rather than on developing a new simulation tool.

The decoupled modeling is very simple for elastic materials, but additional complexity is introduced by the inclusion of viscoelasticity. While other options exist in PAM-Form, we chose to utilize the “lookup-table” functionality, wherein the modulus is determined by interpolation between stress/strain curves measured at different strain-rates and temperatures; thus capturing a portion of the viscous behavior. This empirical method was chosen due to the directness of the approach, as experimental data can be input directly as a table of values [50].

Advanced contact modeling tools make it possible to simulate forming of multi-layered laminates with inter-ply slip. This capability is one reason that explicit solvers are sometimes preferred over implicit solvers [13,48,51].

3.1. Simulation Framework

All models were simulated using 4-noded quadrilateral shell elements. Each individual layer was modeled separately so as to allow inter-ply slip and fiber realignment, though this was moderated by the contact definition, which imposed a friction and gluing stress between the layers and with the tooling. The details of the friction parameters were discussed in Section 2. These models were run isothermally at 180 °C using parameters measured in Section 2 and the density, which is derived from published constituent densities and fiber content. The data is summarized in Table 2.

One difficulty in using a software like PAM-Form is that the models can occasionally become unstable. While this can occur in an unpredictable way, it is often caused when significant wrinkles or excessive stresses arise. These can cause the model to crash, as it cannot account for the extremely large stresses and rotations involved, and so stops calculation. These failed models, then, are quite informative. Since the solver is capable of predicting real wrinkles, it follows that wrinkles large enough to crash the solver correspond to significant defects in a real part.

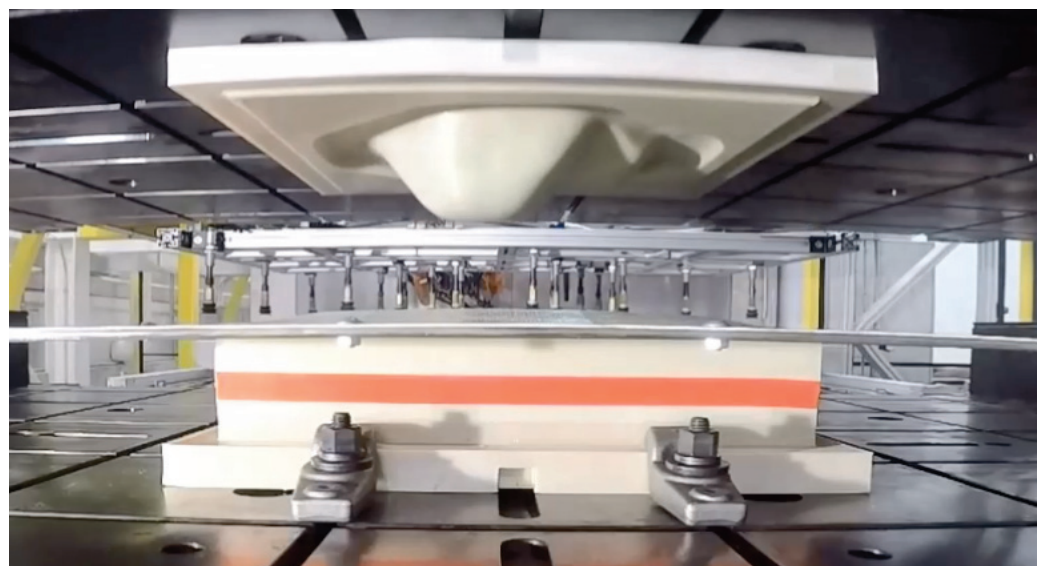
Table 2. Isothermal forming properties for various material models at 180 °C.

		Measured Material (Panel-3)	Measured Material (Panel-4)	Measured Material (Panel-5)
G_{12}	In-plane shear modulus	21.14 MPa	0.922 MPa	45.19 MPa
E_1^t	Fiber-direction tensile modulus		2.288 GPa	
E_1^b	Fiber-bending modulus		2.288 GPa	
E_2^t	Transverse tensile modulus		4.13 MPa	
E_2^b	Transverse-bending modulus		4.13 MPa	
ρ	Density		1.41 g/cm ³	
V_{fo}	Initial Fiber Volume Fraction		0.36	

3.2. Simulation Case Studies

Two different forming simulations have been performed in this research, both to demonstrate the capabilities of the simulations, and as validation tools to check the correctness of the material characterizations.

The first case-study is an automotive part. Specifically it is the cover for the rear differential of a pickup truck. The geometry used was derived from measurements of an existing metal part, and direct composite replacements were thermoformed using 3D printed tooling (Figure 10). The original steel part and thermoformed composite part are seen in Figure 11.

**Figure 10.** Differential cover mold mounted in press.

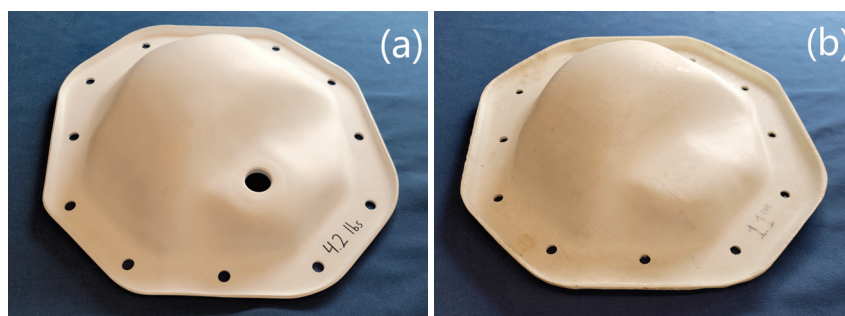


Figure 11. Comparison of 300 mm wide (12") differential covers. (a) Original steel part; and (b) thermoformed composite part.

The forming of this part was simulated with 17 layers using a 10 mm target element size. Initial simulations were run using a set of generic-composite properties modified from an example file from PAM-Form. These were later replaced with those measured experimentally as discussed in Section 3.1. Before analyzing the numerical results, qualitative inspection of results reveals some useful information. First, several of the defects exhibited by the real differential cover were also exhibited by the model. For example, the separation between tapes within a layer that was visible in early iterations of the process was also visible in the model (see Figure 12). The figure shows a PAM-Form model result in which the different plies are rendered in different colors. The top layer (blue) is a partial ply that was added to help mitigate the ply separation. Next, we see the first full layer (pink), which has developed gaps that reveal the underlying layer (gray).

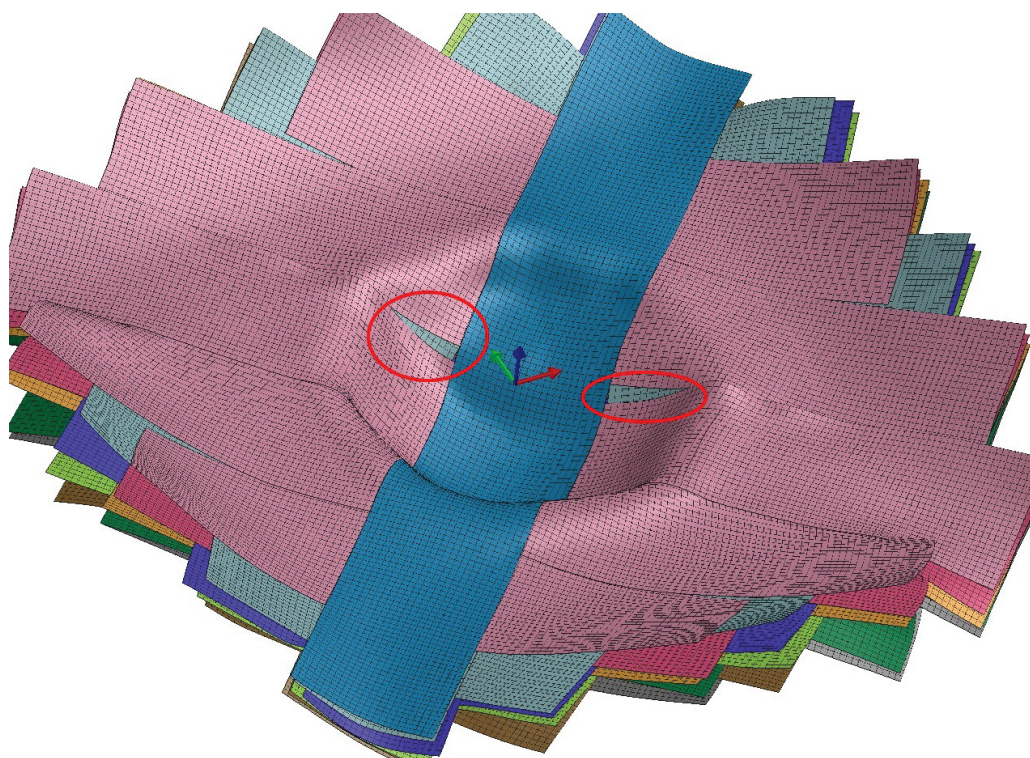


Figure 12. Tape separation exhibited by the differential cover model.

Second, stress concentrations appear in an area found to be one critical for ply splitting/tearing (Figure 13). It is unclear what mechanism causes the longitudinal stress banding to translate to transverse splitting, however, the simulation clearly shows that these regions are important in terms of stress concentration. Further investigation of thermoforming failure modes may be of value in furthering the predictive value of the simulation.

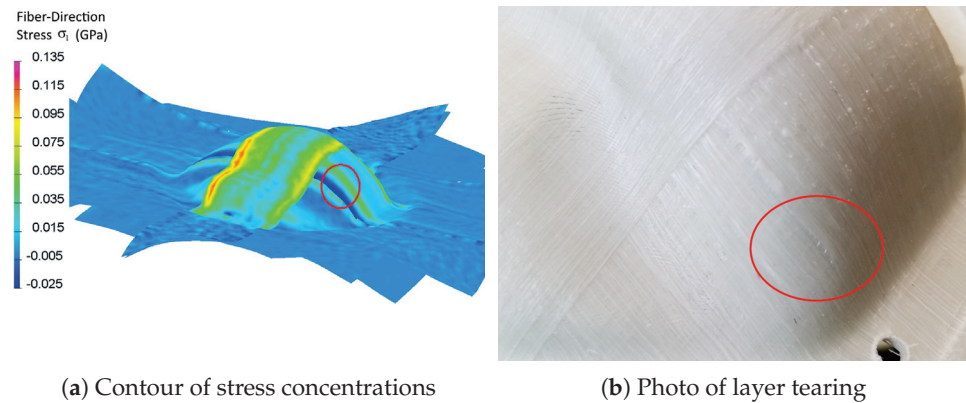


Figure 13. Comparison between simulated stress and forming defects in a differential cover.

Lastly, the general trend of thickness variation at critical pinching locations is exhibited in both model and formed-part.

These qualitative observations appear even in models run using the generic material properties, thus indicating that some useful approximations, and critical-locations can be predicted without full material characterization, and also that certain behaviors are heavily geometry dependent, rather than material dependent. For smaller defects, such as wrinkles, it is assumed that accurate material data is necessary.

In order to validate the models, a numerical comparison was needed for relating the simulated results with experimental ones. The comparison chosen was to use full-field non-contact digital image correlation (DIC) to measure the displacement field in an experimental part (full-size) from before and after forming. This is then converted to a strain field from which shear angle is taken for comparison to simulations [52]. Note that shear angle is simply the shear strain (typically presented in radians) converted to degrees for better readability.

The locations chosen for inspection were known critical locations for wrinkling, also being the regions in which the highest shear-angles are observed. In addition to this, the shear angle in the patch (along the crest) was also inspected. See Figure 14 for the locations of these inspection-points.

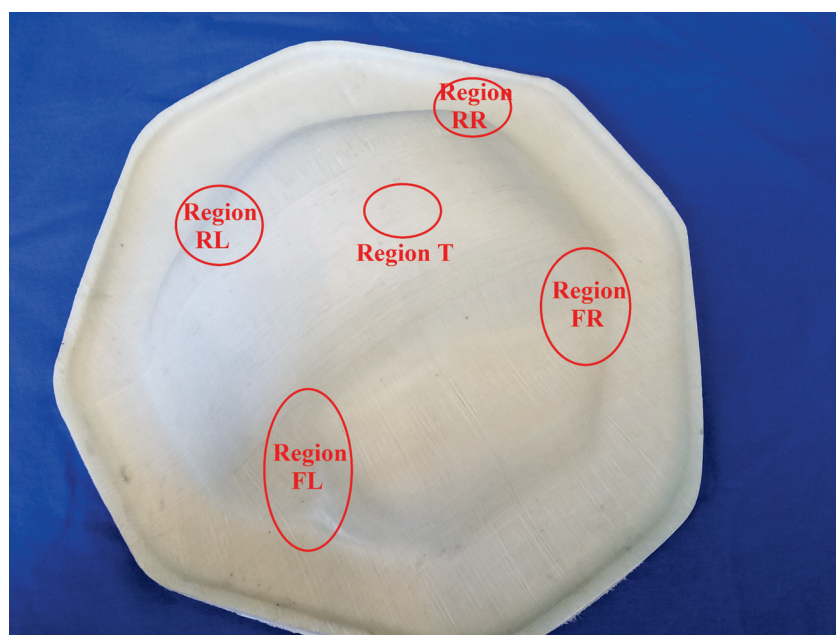


Figure 14. Critical regions in differential cover forming.

Using a DIC system, the peak shear-angle magnitude from each of the critical regions was taken. Measurements were averaged from two formed parts. The number of specimens was limited by the amount of available material for forming. These measured values were then compared with those taken from the surface layers of PAM-Form models, thus determining which material model best simulates the actual material. As discussed in Section 2, the data necessitated there be 3 different material models in which the shear modulus (G_{12}) is defined using the experimental results of samples from the three different panels (labeled 3, 4, and 5). Table 3 shows the results of this comparison. Note that panel-4 material is omitted due to numerical instability in the corresponding model, which prevented its completion.

Table 3. Shear angle at critical locations in a differential cover.

a Top Surface				
Region	Measured Angle (Experiments)	Predicted Angle (Generic Material)	Predicted Angle (Measured Material) (Panel 3)	Predicted Angle (Measured Material) (Panel 5)
T	7.64°	12.0°	15.6°	8.83°
FR	21.2°	29.0°	13.2°	8.02°
FL	21.5°	25.9°	10.9°	8.42°
RR	18.0°	36.1°	12.2°	10.5°
RL	10.8°	32.9°	17.3°	11.0°
b Bottom Surface				
Region	Measured Angle (Experiments)	Predicted Angle (Generic Material)	Predicted Angle (Measured Material) (Panel 3)	Predicted Angle (Measured Material) (Panel 5)
Region				
T	6.89°	13.5°	9.72°	7.77°
FR	24.0°	34.1°	11.6°	8.72°
FL	26.0°	23.2°	13.6°	9.00°
RR	19.7°	34.0°	13.5°	11.7°
RL	28.0°	37.8°	11.8°	11.8°

From the table, the differences between the different measured properties' model and the generic properties' model can be seen.

The first thing to note is that all the models overestimate the shear in the top point of the part. This can be explained in that the peak of the part contacts the mold first, thus facilitating a more rapid cooldown and limiting the shear deformation at this point. Since the simulations treated the process as isothermal, this phenomenon was not captured. For this reason, this point will not be included in the average error measure.

Additionally, with the exception of the top point, the measured material models tend to underestimate the shear, where the generic-material overestimates it. This would suggest that the actual shear modulus in the part is below that found in the measured models, but above that in the generic-material model.

Finally, an average was taken over the magnitudes of the errors from each material model, in order to have a single quantity on which to judge each model's merit. The results are as follows:

- Generic Material had an average error of 60%;
- Panel-5 Material had an average error of 51%;
- Panel-3 Material had an average error of 43%.

From this, it is clear that the panel-3 material is the best of the models here tested. In addition, since there is an assortment of under- and overpredictions of angle, the error average (rather than average magnitude) shows that holistically, the predictions are slightly better (58%, 48%, and 30%, respectively).

The next case study is a hemisphere, which is a relatively simple shape that also exhibits double-curvature (where the part curves in multiple directions) as most real-world parts do. Simplicity combined with double-curvature has made the hemisphere a common forming case-study [41]. Our hemisphere was 76.2 mm (3") diameter, a size which balanced material usage and deformation visibility. By trial and error, the layup and processing parameters were optimized to achieve good consolidation and shape. For this study, a simplified manual process was utilized whereby a preconsolidated blank with a layup of $[\pm 45^\circ]_5$ was placed in a convection oven set at 200 °C for 5 min. The softened blank was then carefully transferred to a 10-ton pneumatic press, and stamped between a set of hemispherical aluminum molds. The forming of this part was simulated with 10 layers using a 5 mm target element size.

Due to the mold shape, the material is not restrained at the region of transition between the hemispherical and flat portions of the mold. As a result, the material in the transition region is quite wrinkled (Figure 15). This issue means that the comparisons from model to forming will be restricted to the hemisphere itself, and the adjacent regions will be ignored.

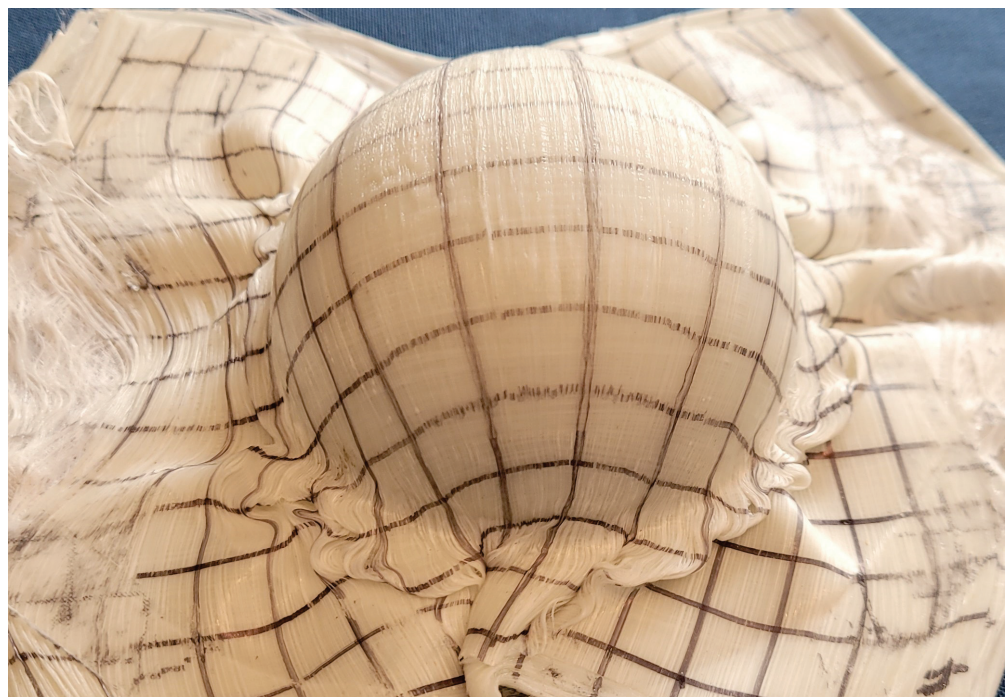


Figure 15. Formed hemisphere.

As with the differential cover, hemispherical parts were formed from PP/glass, and shear measurements taken using DIC (Figure 16). These measurements were then compared to simulated results using the several material models (with the exception of M5, which failed by unstable wrinkling behavior). Unlike the differential cover, however, the symmetric nature of this part means that there are no distinct locations to compare. Instead, the peak magnitude of shears in the bias directions (the $\pm 45^\circ$ directions as shown in Figure 17) were averaged to generate a comparison criterion. The results of the comparison can be found in Table 4.

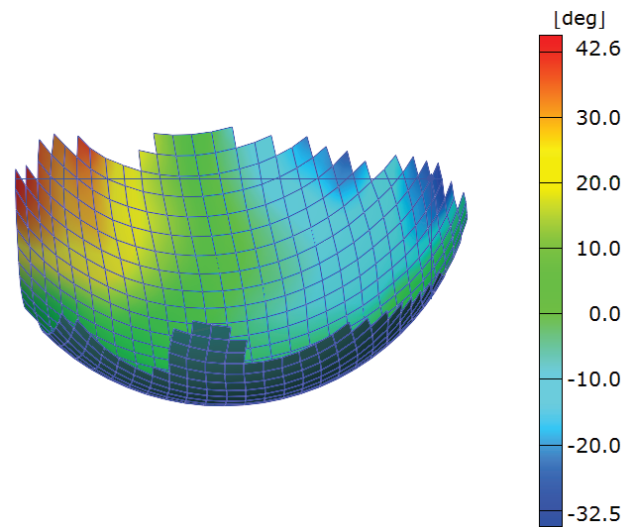


Figure 16. Shear angle field in a hemispherical part.

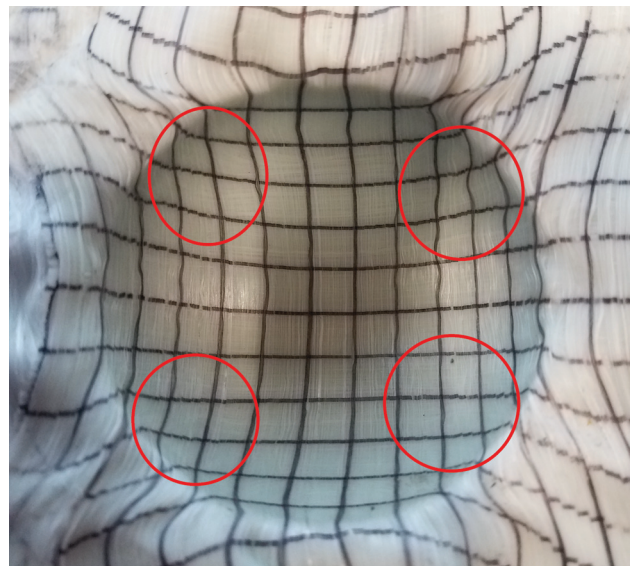


Figure 17. Critical regions in hemisphere forming.

Table 4. Shear angle at critical locations in a hemisphere.

	Measured Angle (Experiments)	Predicted Angle (Generic Material)	Predicted Angle (Measured Material) (Panel 3)	Predicted Angle (Measured Material) (Panel 4)
Angle	32.8°	44.6°	19.0°	44.7°

Here, notice that panel-3 properties no longer produce the best results, but performs slightly worse than both other materials. Additionally, the relative predictions of the different models can give a bit more insight into the other models. Since panel-3 properties cause underprediction of shear, and panel-4 properties cause overprediction of shear, these two models were combined to infer a shear modulus that falls between them. Using weighted average of these two produces an average error of only 29% in the differential cover and 12% in the hemisphere, thus proving that the true shear modulus does, in fact, lie between those measured. As discussed in Section 2, the material variations have been hypothesized to be due to differences in crystallinity due to the rate of cooling during the forming process.

It should be noted here that the errors measured here are larger than those expected for a predictive tool. These predictions, however, would typically not be used as quantitative predictions, but rather as a qualitative indicator of potential problem areas in a given manufacturing process. For this reason it is possible to gain valuable insights even from the generic materials, but any improvement on this can greatly benefit the model's usefulness. There are a number of possible ways in which this disagreement could arise, which are potentially valuable topics of further research. The first possible source of error is the sliding friction between individual layers, as well as between the blank and tool. Since this was beyond the scope of this research, an approximate friction value was used (as discussed in Section 2). It may be that a better contact model could produce a more accurate simulation. The second possible source of error is in the isothermal nature of the simulations [53]. It is possible, as discussed regarding the differential-cover's measurements on 'point-T', that the cooling as the part interacts with the mold has a significant effect on the shearing behavior. Third, the discrepancies in the shear modulus between different sample panels is likely another source of error. Each of these sources could be investigated, along with possible simple methods of characterization, to further improve the models. Finally, it is possible that some error arose from the limited sample size (two samples for each case-study) of the DIC experiments.

4. Structural Analysis of the As-Formed Part Model

In order to conduct structural simulations of the "as-formed" part, we integrated the results of the forming simulation software (PAM-Form) with a structural finite element analysis software (Abaqus) [54]. This is important, since variations in fiber-orientation, fiber-density, and part-thickness influence the strength of any structural member. Properly including this information, which is readily available from forming simulation results, in the structural analysis is expected to make the model more accurate in comparison to the "idealized" part. In order to translate these details between the forming and structural simulation softwares' formats, a script was developed.

The first step in transferring results of the forming simulation into a structural analysis model involves translating the mesh information from the format used by PAM-Form to that used by the Abaqus software. This begins by gathering the data from the PAM-Form database. One of the main challenges in transferring the results of the forming simulation to a finite element analysis is that PAM-Form simulates a multi-layered blank as many shell-meshes (in order to include sliding contact between layers). While it is possible to model a laminate this way in Abaqus, it requires tie constraints to establish perfect bonding between the layers. This process is made overly complex when the finite element meshes of the individual layers are misaligned, which is inevitable after a forming simulation. Another option would involve tied contact constraints, but this method fails to capture the layer thickness and volume fraction variations caused by matrix migration during the forming process. One solution which can account for this is to first consolidate the layered mesh into a single shell mesh to represent the entire laminate, including fiber orientation and layer-thickness information. This mesh is then used to model the part in Abaqus.

4.1. Mesh Conversion Process

The conversion process was performed using a custom computer program whose function is summarized in Figure 18. To simplify the process, a 2D projection is used wherein the z-coordinate of the nodes are neglected when translating the mesh. Ignoring z works nicely for many shapes, but has difficulty in resolving near-vertical faces. Typical stamp formed parts, though, are designed to avoid these kinds of steep inclines, which are difficult to form, making the 2D assumption valid for typical parts. For this reason, we consider these assumptions to be sufficient for this proof of concept, but for completeness, commercial implementations would need to account for steep inclines as well. The remainder of the translation process is summarized by a few critical points. The nodes in the generated single-layer mesh are defined to fall at the midpoint between the multi-layer

meshes, thus this single-layer mesh forms the midsurface of the part. Each element in this midsurface mesh is then defined to have composite properties including multiple layers, each of which has its own orientation and thickness. These are 4-noded tetrahedral elements, with their “section” property defined as a laminate whose properties are based on the layers of the mesh from forming simulation. Local thicknesses are determined by taking the spacing between the individual layer-meshes. It is assumed that as long as proper consolidation is maintained, this spacing will be driven primarily by matrix flow and can be captured in the layer thickness parameter. The layer thickness is evaluated separately for each element of the structural mesh. This accounts for thickness and layup variation at every point across the part, including things like dropped plies. Since the meshes typically do not all align, the local orientations are determined using a weighted average of corresponding elements. The weighting factors are determined as the portion of the area of the new element that each contributing element occupies (see Figure 19). The fiber volume fraction is determined using the volumetric strains and thickness change, modified by an “overlap fraction”, which takes into account any layer self-overlapping caused by wrinkles. Finally, each layer of the composite is given material properties based on micromechanical approximations using typical properties for polypropylene [55,56] and E-glass [57]. Local elastic properties are approximated using the Mori-Tanaka method [58], while local strengths are defined using a method adapted in [59] from [40,57]. This micromechanics approach was necessary, as forming-induced matrix flow causes the local layer thicknesses and fiber volume fractions to vary across the part, and therefore, any given location possesses different structural properties than the unformed material.

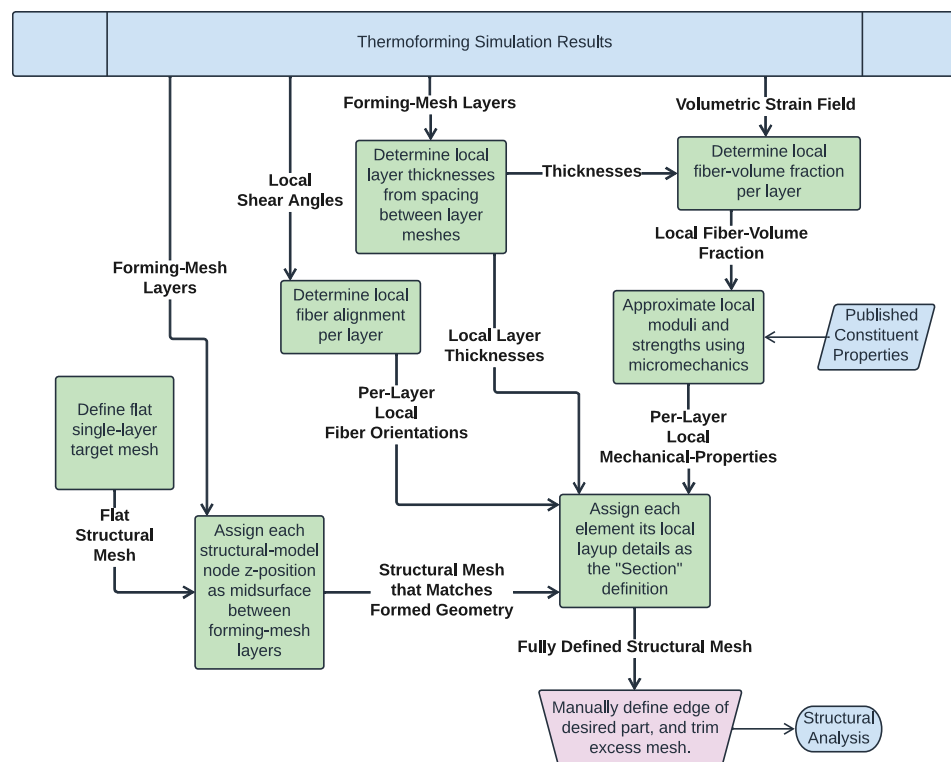


Figure 18. Flowchart of the mesh conversion process.

4.2. Case Study for Implementing As-Formed Analysis

Since the purpose of this study is to demonstrate the value in using as-formed models versus the idealized models (where the fiber alignment and thicknesses are exactly as designed), a case study was required. To this end, a simple geometry was chosen which could be relatively easily formed and tested. This geometry, seen in Figure 20, consists of a flat plate 254 mm × 76.2 mm (10" × 3") with an incomplete hemisphere (spherical cap) pressed in the center. This specimen simulates a variety of real-world parts wherein bumps

or ridges are added to plates for stiffening. The purpose for this particular form-factor, though, was to produce a part which is not only formable, but also testable, since the plate size is within the limits of a standard tension test frame's grips.

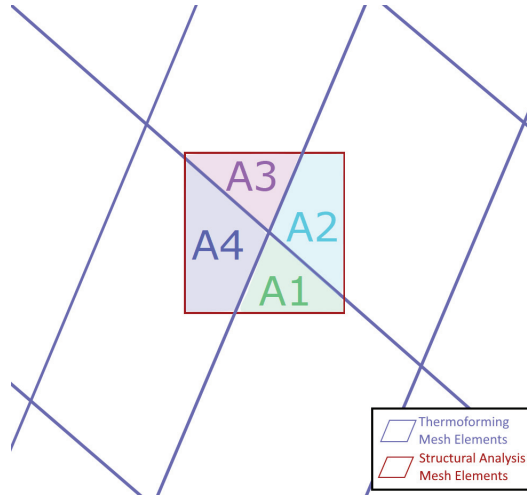


Figure 19. Element area contributions for mesh conversion.

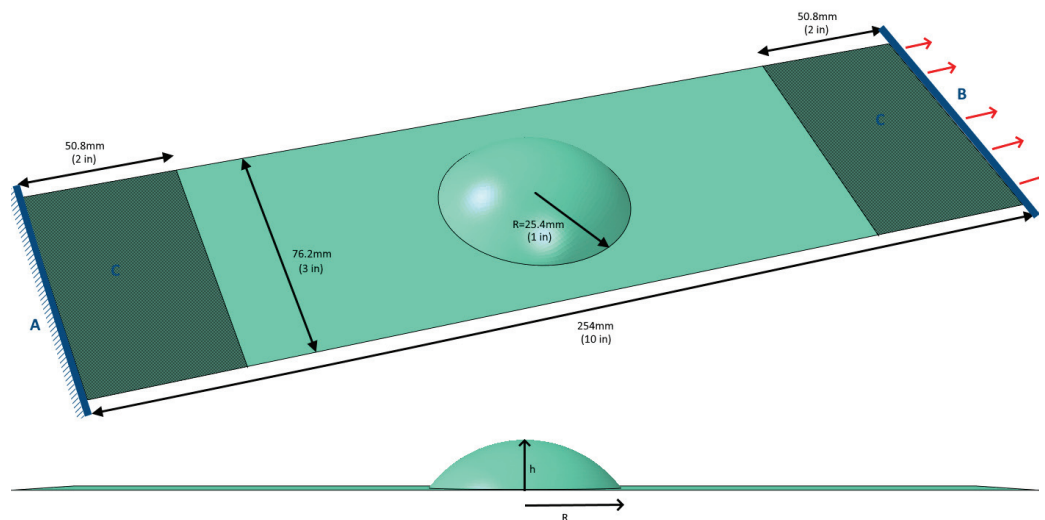


Figure 20. A CAD rendering of the proposed case-study geometry including boundary conditions.

The hemisphere, which will hereafter be referred to as the “bump”, intersects the plate with a radius of 25.4 mm (1”). The height of the bump was varied as a fraction of this intersection radius between different models, and has been tested for values of $h/R = 0.25, 0.5, \text{ and } 0.75$. A model with a full hemispherical bump ($h/R = 1$) was also attempted, but wrinkled excessively, so as to be unusable. A $[\pm 45^\circ]_2$ layup was used for all models.

4.2.1. Model Specifications

In order to demonstrate the differences between as-formed and idealized modeling, two methods needed to be utilized. First, PAM-Form was used to simulate stamp-forming of the part (using the weighted-average material properties determined above), the forming results were translated into an Abaqus model, and a structural test was performed. The boundary conditions used were chosen to represent gripping in a tension test machine:

- A Displacements and rotations of nodes along one end of the model were fixed.
- B Displacements and rotations of nodes along the opposite end, were fixed except for displacement in the direction of the plate’s longitudinal axis. The longitudinal displacement was set to 0.5 mm. This corresponds with a tensile strain of 0.2% in

the equivalent flat plate. Note also that this is an elastic quasi-static analysis, so all dynamic effects are considered negligible, and no velocity is defined.

- C A region 50.8 mm (2") from either end was fixed to all out-of-plane motion to approximate the restriction caused by a tension tester's grips.

Next, an equivalent model was generated directly in Abaqus CAE. The fiber directions were assigned to be at $\pm 45^\circ$ in the global coordinate system, thus presenting an "idealized" part. The part was meshed using 4 node quadrilateral elements (since these are the type generated from the PAM-Form conversion), and the same boundary conditions were used. After a mesh convergence study, a nominal element size of 1 mm was selected for all models. This corresponds to 19,300 elements in Figure 21.

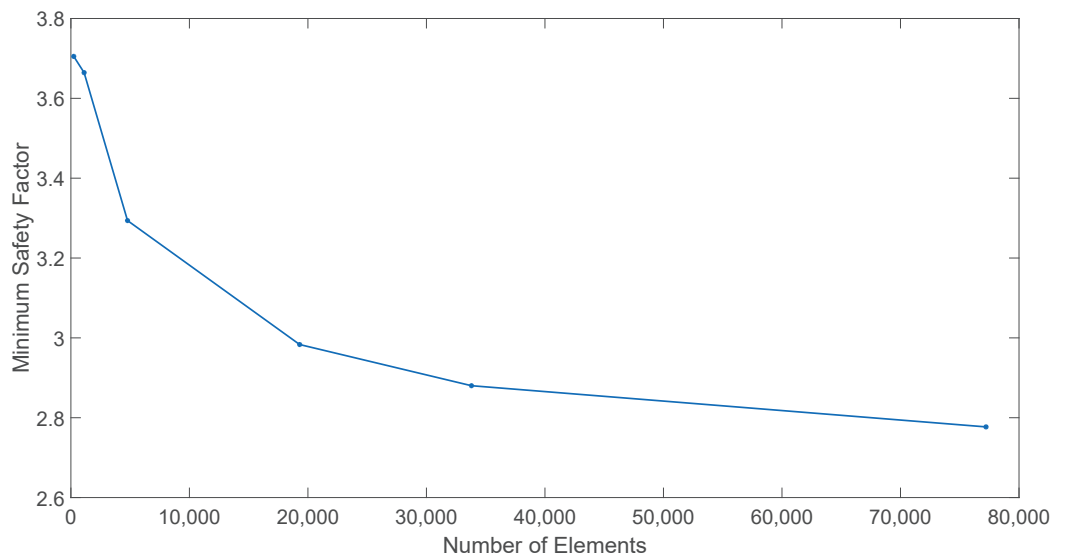
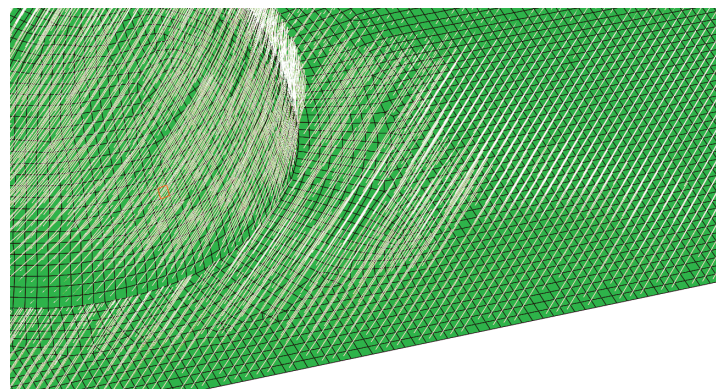


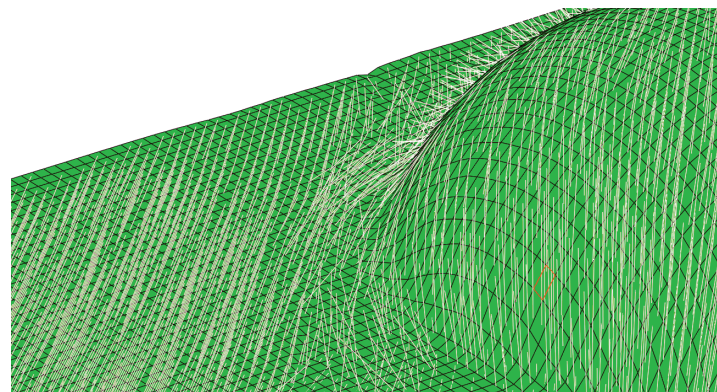
Figure 21. Convergence plot of minimum safety factor ($h/R = 0.5$).

The first thing to look at when inspecting these models is the fiber directions. In the idealized model, the fiber direction is established at the given angle, and is largely unaffected by the bump, whereas for the formed model, the fiber directions near the bump are much different from those further away. This effect becomes more pronounced as the bump height increases, and is particularly vivid for the bump with $h/R = 0.75$ as seen in Figure 22, where the fiber directions are rendered as white lines. As can be expected, those models containing a shallow bump demonstrate this effect to a smaller degree, since they require less fiber displacement to form.



(a) Ideal fiber directions

Figure 22. Cont.



(b) As-formed fiber directions

Figure 22. Comparisons of fiber orientation between model types ($h/R = 0.75$, $[\pm 45^\circ]_2$ layup).

4.2.2. Comparison of Stress Concentrations

The first parameter used to compare the two models was the level of stress concentration near the bump as compared with the stress in an equivalent flat plate (whose stress is given as σ_0). The concentration factor is calculated as $K = \sigma/\sigma_0$. Note that the stress field and fiber architecture near the discontinuity in the part are more complicated than can be fully represented by shell elements, so some parts may require a complete 3D analysis for useful predictions. Within the scope of this research, however, it is assumed that the shell assumptions provide a reasonable approximation. Figure 23 shows a representative plot of the in-plane shear stress within the model. While the stresses vary slightly between the layers, and other stress components produce different patterns, they all share the concentration region near the edge of the bump.

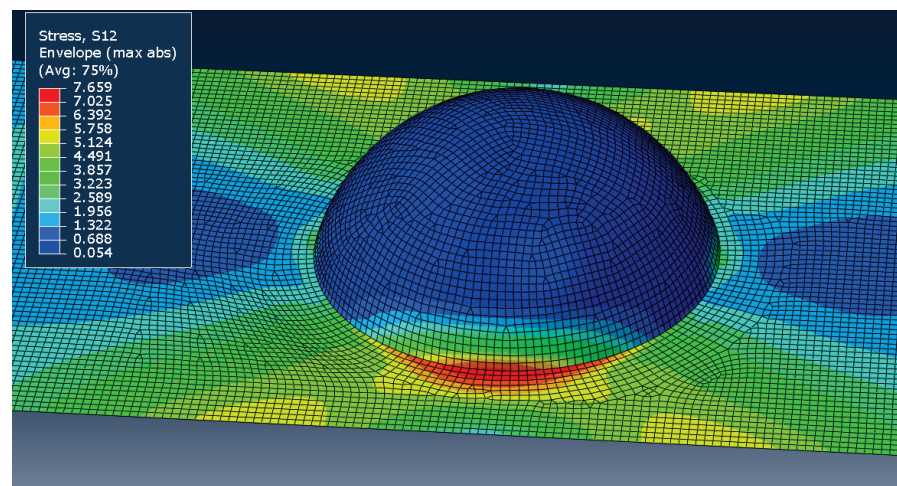


Figure 23. Shear stress (MPa) envelope showing concentration region in an idealized model ($h/R = 0.75$, $[\pm 45^\circ]_2$ layup).

The results of each model were analyzed, and a stress concentration factor generated for each in-plane stress component (longitudinal stress σ_1 , transverse stress σ_2 , and shear stress τ_{12}). These factors were taken by averaging the stress over several most-stressed elements in each model. Note that the stresses taken were the largest magnitudes seen through the thickness, rather than from an individual layer. The end results are shown in Figure 24.

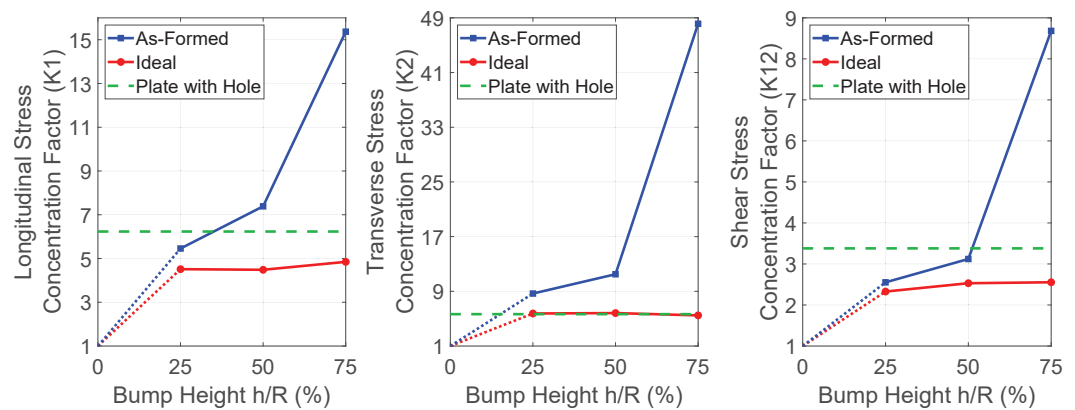


Figure 24. Stress concentration comparisons ($[\pm 45^\circ]_2$ layup).

Looking at these plots, a clear pattern emerges. For the bump with $h/R = 0.25$, the ideal and formed part share a similar concentration factor, but as the bump-height increases, the stress concentration factor increases for the formed part at a much larger rate than does the ideal part. This seems to align with intuition, since the smaller bump requires less fiber migration, and therefore the formed and ideal parts are quite similar. Taller bumps require more fiber migration, differentiating the two further.

For comparison, the equivalent model where a hole replaces the bump was also simulated in the same manner, and results are plotted as a horizontal green line in Figure 24. The ideal part generally hovers near or below this value, while the formed-part generally becomes much higher for the larger bumps. This is likely due to fiber migration decreasing the efficiency with which the part can carry load.

In order to determine the effect of layup on the model behavior, the process was repeated using a $[0^\circ/90^\circ]_2$ layup. These models were generated identically to those discussed above, except the layup.

In the $[0^\circ/90^\circ]_2$ case, there is less difference between models. As seen in Figure 25, the stress concentration factors remain similar for most cases. Note that for a flat plate with $[0^\circ/90^\circ]_2$ layup, the shear stresses will be negligible. This, then, would create meaningless values of shear stress concentration, so these have been omitted. This indicates that the fiber deviation is a significant factor in determining these values, since the values diverge significantly in those models having significant fiber migration, whereas they remain similar for these models, which have less fiber migration. The only exception to the similarity of concentrations is in the transverse stress in the model with the largest bump, which we attribute to the wrinkles that appeared in the forming model.

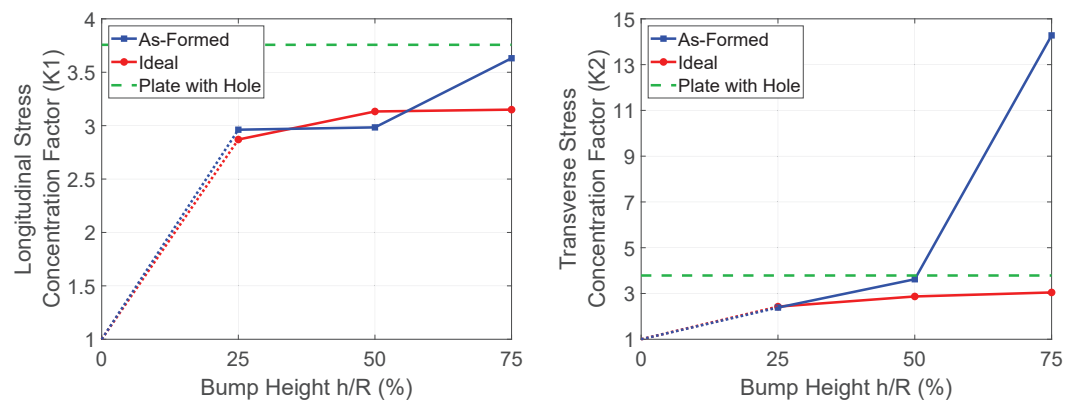


Figure 25. Stress concentration comparisons ($[0^\circ/90^\circ]_2$ layup).

4.2.3. Tsai-Wu First Ply Failure

Next, first-ply failure in the part was assessed. To do this, the Abaqus intrinsic Tsai-Wu failure model was implemented. Tsai-Wu uses a quadratic formulation to calculate a

failure index within the part [40]. Based on this model, the safety factor for proportional increase of stresses (S_f) is given as the reciprocal of the failure index. Note that the strength values used here were those determined by micromechanics during the model conversion, and these vary across the part.

Since the failure index (and thus safety factor) is determined by the relationship between all of the stresses within any given element, it is expected for these metrics to follow similar patterns as the underlying stresses. This pattern can be seen in Figure 26. Based on this, the minimum safety factor has been used to compare the strength to first failure. The data is seen in Table 5, which shows that the as-formed part weakens with larger bumps, whereas the idealized part retains significant strength in all configurations.

Table 5. Factors of safety for various models with a $[\pm 45^\circ]_2$ layup.

h/R	Idealized Model		As-Formed Model	
	S_f^{min}	Ply	S_f^{min}	Ply
0.25	4.01	1	3.61	1
0.50	3.62	1	2.98	1
0.75	3.51	1	1.02	2

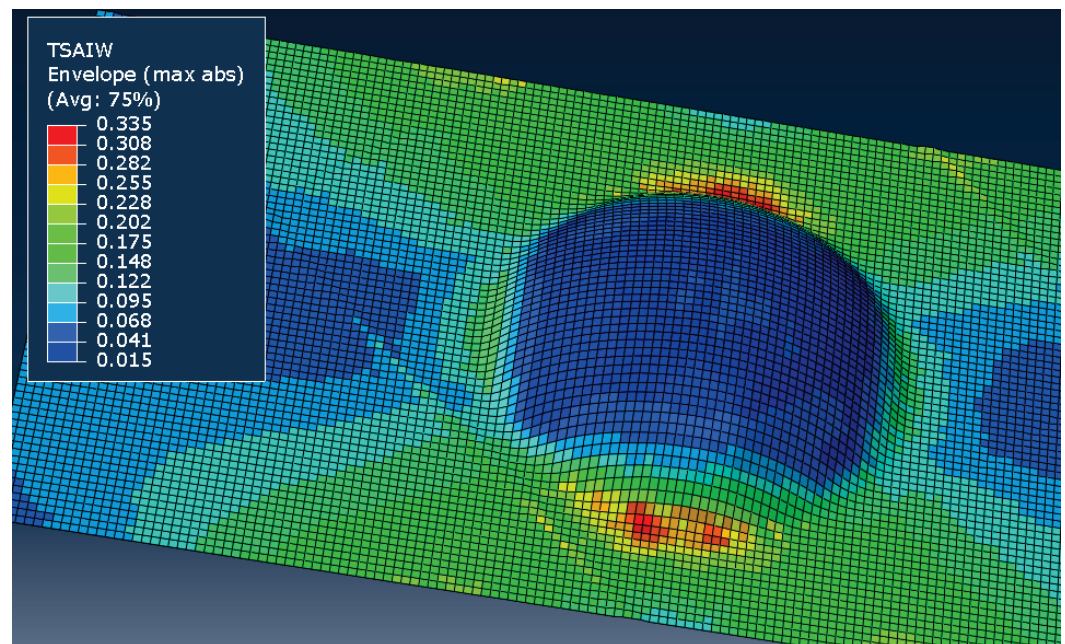


Figure 26. Failure index envelope for the as-formed model ($h/R = 0.5$, $[\pm 45^\circ]_2$ layup).

Lastly, Table 6 shows the safety factors for the models using a $[0^\circ/90^\circ]_2$ layup. It is important to note that, since these were modeled in displacement control, so there are different levels of stress depending on the layup. This means that comparing the safety factors between these two layups does not correlate to comparing strengths. It does, however, illustrate the power of this method in allowing the strength of a given part to be predicted.

It is worth noting that the wrinkled model is the weakest by far, having already failed at the applied displacement. This failure is seen to occur within the wrinkled region, as well as happening within a 0° layer (L3) unlike all of the other models which fail in a 90° layer (L2 or L4). Again, this highlights the weakening effect of the wrinkles within the part.

Table 6. Factors of safety for various models with a $[0^\circ/90^\circ]_2$ layup.

h/R	Idealized Model		As-Formed Model	
	S_f^{min}	Ply	S_f^{min}	Ply
0.25	2.55	2	2.62	2
0.50	2.12	2	1.82	4
0.75	1.96	2	0.65	3

4.3. Discussion

These results demonstrate that there is value in using the as-formed geometry in structural analyses. This type of analysis is expected to be very situation dependent, making it crucial for accurate prediction in some processes, and unnecessary for others, with the determining factor being the amount of fiber reorientation. The value of using as-formed fiber geometry for structural analysis is clear [27–29], and has recently even been implemented commercially [60,61]. Due to the usefulness of this technique, it will likely become universally utilized in designing complex parts for thermoforming.

5. Conclusions and Recommendations

An improved simulation-based thermoforming design process based on the integration of material characterization and as-formed structural analysis has been proposed.

A novel suite of material characterization methods, which relies on DMA techniques, for thermoforming simulations has been implemented and shown capable for measuring several of the required properties. The material model generated by this method has been tested, and after interpolating the shear data, it performed quite well in comparison to the formed parts. This suite, then, can provide an alternative means of material characterization with limited equipment.

The simulation of thermoformed parts using these measured properties in commercial simulation software has been shown to predict critical regions for wrinkling, tearing, and ply separation, and also to predict the shear deformation with reasonable accuracy. This is encouraging in terms of the usability of these methods for industrial design.

A tool for using thermoforming simulation results to inform more accurate structural models has been tested on a simple case study, and produced results that clearly differ from those of ideal models. This provides evidence that this type of analysis may be necessary in some cases. This tool, then, has demonstrated value, and should be investigated for further development and validation as an open source alternative to commercially available solutions.

The tendency of thermoplastic composites to wrinkle has made simulation a must for optimized manufacturing, but the material models required are complex, and time consuming to create. The methods described here have the potential to enhance thermoplastic composites manufacturing by simplifying and expediting the process. In addition, the usefulness of these models is being extended into the realm of bettering predictions of the part's actual performance, thus improving the design process as well.

This work has demonstrated the value of integrating simple characterization methods with thermoforming simulation toward as-formed structural analysis, but there remain several avenues of research that are beyond the scope of this work, but which would be critical in improving the method toward industrial use. The following recommendations are proposed: Firstly, the discrepancy on shear stiffness between different processing batches warrants further investigation with consideration of the thermal history. Additionally, a friction model which incorporates thermally-varying viscous flow behavior would enhance the accuracy of the simulations. This model would ideally use material properties derived from simple rheometric viscosity experiments. Finally, while isothermal analyses like ours are commonly used, and produce reasonable results [44,53], it is clear that further accuracy could be achieved by implementing a thermal analysis in order to capture the

effects of contact-induced local cooling. While analysis software packages often have these thermo-mechanical capabilities, material properties (like thermal conductivity, and heat capacity) are not readily available. A collection of simple methods for measuring these properties would be invaluable for including thermal behavior into the analyses.

Author Contributions: The following is a list of the contributions by the various authors: Conceptualization, R.A.L.-A., S.V. and P.B.; methodology, P.B.; software, P.B.; formal analysis, P.B.; investigation, P.B.; resources, R.A.L.-A. and S.V.; data curation, P.B.; writing—original draft preparation, P.B.; writing—review and editing, R.A.L.-A., S.V. and P.B.; visualization, P.B.; supervision, R.A.L.-A. and S.V.; project administration, R.A.L.-A. and S.V.; funding acquisition, R.A.L.-A. All authors have read and agreed to the published version of the manuscript.

Funding: This research was funded through the Harold W. Alford Graduate Research Assistantship and the Malcolm G. Long '32 Professorship in Civil Engineering.

Data Availability Statement: Not applicable.

Acknowledgments: This research was done in partnership with the University of Maine Advanced Structures and Composites Center. Special thanks to David Erb, Nick Fitzpatrick, and the Thermoplastic Composites Manufacturing Team.

Conflicts of Interest: The authors declare no conflict of interest.

References

- Chang, I.Y.; Lees, J.K. Recent Development in Thermoplastic Composites: A Review of Matrix Systems and Processing Methods. *J. Thermoplast. Compos. Mater.* **1988**, *1*, 277–296. [CrossRef]
- Chabin, M.; Gerard, P.; Clerc, P. Simulation boosts the use of thermoplastic composites in mass production. *JEC Compos. Mag.* **2017**, *54*, 32–33.
- Warren, K.C. Resistance Welding of Thermoplastic Composites for Industrial Scale Wind Turbine Blades. Master's Thesis, University of Maine, Orono, ME, USA, November 2012.
- Diaz, J.; Rubio, L. Developments to manufacture structural aeronautical parts in carbon fibre reinforced thermoplastic materials. *J. Mater. Process. Technol.* **2003**, *143–144*, 342–346. [CrossRef]
- Kropka, M.; Muehlbacher, M.; Neumeier, T.; Altstaedt, V. From UD-tape to Final Part—A Comprehensive Approach Towards Thermoplastic Composites. *Procedia CIRP* **2017**, *66*, 96–100. [CrossRef]
- McGuinness, G.; ÓBrádaigh, C. Characterisation of thermoplastic composite melts in rhombus-shear: the picture-frame experiment. *Compos. Part A Appl. Sci. Manuf.* **1998**, *29*, 115–132. [CrossRef]
- McGuinness, G.B.; ÓBrádaigh, C.M. Development of rheological models for forming flows and picture-frame shear testing of fabric reinforced thermoplastic sheets. *J. Non-Newton. Fluid Mech.* **1997**, *73*, 1–28. [CrossRef]
- Roberts, R.W.; Jones, R.S. Rheological characterization of continuous fibre composites in oscillatory shear flow. *Compos. Manuf.* **1995**, *6*, 161–167. [CrossRef]
- Sunderland, P.; Yu, W.; Mnson, J.A. A thermoviscoelastic analysis of process-induced internal stresses in thermoplastic matrix composites. *Polym. Compos.* **2001**, *22*, 579–592. [CrossRef]
- Sjölander, J.; Hallander, P.; Åkermo, M. Forming induced wrinkling of composite laminates: A numerical study on wrinkling mechanisms. *Compos. Part A Appl. Sci. Manuf.* **2016**, *81*, 41–54. [CrossRef]
- Haanappel, S.P.; Ten Thije, R.; Sachs, U.; Rietman, B.; Akkerman, R. Formability analyses of uni-directional and textile reinforced thermoplastics. *Compos. Part A Appl. Sci. Manuf.* **2014**, *56*, 80–92. [CrossRef]
- Yin, H.; Peng, X.; Du, T.; Chen, J. Forming of thermoplastic plain woven carbon composites: An experimental investigation. *J. Thermoplast. Compos. Mater.* **2015**, *28*, 730–742. [CrossRef]
- Pickett, A.K.; Queckbörner, T.; De Luca, P.; Haug, E. An explicit finite element solution for the forming prediction of continuous fibre-reinforced thermoplastic sheets. *Compos. Manuf.* **1995**, *6*, 237–243. [CrossRef]
- Okine, R.K. Analysis of Forming Parts from Advanced Thermoplastic Composite Sheet Materials. *J. Thermoplast. Compos. Mater.* **1989**, *2*, 50–76. [CrossRef]
- Liu, L.; Chen, J.; Li, X.; Sherwood, J. Two-dimensional macro-mechanics shear models of woven fabrics. *Compos. Part A Appl. Sci. Manuf.* **2005**, *36*, 105–114. [CrossRef]
- Wehrle, M. CMIST Structural Thermoplastics Roadmapping Report. 2017. Available online: <https://composites.umaine.edu/wp-content/uploads/sites/20/2017/11/v5CMIST-Roadmapping-November-Report-Full.pdf> (accessed on 16 March 2022).
- Milani, A.S.; Nemes, J.A.; Abeyaratne, R.C.; Holzapfel, G.A. A method for the approximation of non-uniform fiber misalignment in textile composites using picture frame test. *Compos. Part A Appl. Sci. Manuf.* **2007**, *38*, 1493–1501. [CrossRef]
- Dangora, L.M.; Hansen, C.J.; Mitchell, C.J.; Sherwood, J.A.; Parker, J.C. Challenges associated with shear characterization of a cross-ply thermoplastic lamina using picture frame tests. *Compos. Part A Appl. Sci. Manuf.* **2015**, *78*, 181–190. [CrossRef]

19. Peng, X.Q.; Cao, J.; Chen, J.; Xue, P.; Lussier, D.S.; Liu, L. Experimental and numerical analysis on normalization of picture frame tests for composite materials. *Compos. Sci. Technol.* **2004**, *64*, 11–21. [CrossRef]
20. Glaser, R.; Caccese, V. Experimental determination of shear properties, buckling resistance and diagonal tension field of polyurethane coated nylon fabric. *J. Text. Inst.* **2014**, *105*, 980–997. [CrossRef]
21. Stanley, W.F.; Mallon, P.J. Intraply shear characterisation of a fibre reinforced thermoplastic composite. *Compos. Part A Appl. Sci. Manuf.* **2006**, *37*, 939–948. [CrossRef]
22. Willems, A.; Lomov, S.V.; Verpoest, I.; Vandepitte, D. Picture frame shear tests on woven textile composite reinforcements with controlled pretension. In *AIP Conference Proceedings*; American Institute of Physics: College Park, MD, USA, 2007; Volume 907. [CrossRef]
23. Cao, J.; Akkerman, R.; Boisse, P.; Chen, J.; Cheng, H.S.; de Graaf, E.F.; Gorczyca, J.L.; Harrison, P.; Hivet, G.; Launay, J.; et al. Characterization of mechanical behavior of woven fabrics: Experimental methods and benchmark results. *Compos. Part A Appl. Sci. Manuf.* **2008**, *39*, 1037–1053. [CrossRef]
24. Lebrun, G.; Bureau, M.N.; Denault, J. Evaluation of bias-extension and picture-frame test methods for the measurement of intraply shear properties of PP/glass commingled fabrics. *Compos. Struct.* **2003**, *61*, 341–352. [CrossRef]
25. Lomov, S.V.; Boisse, P.; Deluycker, E.; Morestin, F.; Vanclooster, K.; Vandepitte, D.; Verpoest, I.; Willems, A. Full-field strain measurements in textile deformability studies. *Compos. Part A Appl. Sci. Manuf.* **2008**, *39*, 1232–1244. [CrossRef]
26. Larberg, Y.; Åkermo, M. In-plane deformation of multi-layered unidirectional thermoset prepreg—Modelling and experimental verification. *Compos. Part A Appl. Sci. Manuf.* **2014**, *56*, 203–212. [CrossRef]
27. Aridhi, A.; Arfaoui, M.; Mabrouki, T.; Naouar, N.; Denis, Y.; Zarroug, M.; Boisse, P. Textile composite structural analysis taking into account the forming process. *Compos. Part B Eng.* **2019**, *166*, 773–784. [CrossRef]
28. Cartwright, B.K.; Lex Mulcahy, N.; Chhor, A.O.; Thomas, S.G.F.; Suryanarayana, M.; Sandlin, J.D.; Crouch, I.G.; Naebe, M. Thermoforming and Structural Analysis of Combat Helmets. *J. Manuf. Sci. Eng.* **2015**, *137*, 277–279. [CrossRef]
29. Sisca, L.; Locatelli Quacchia, P.T.; Messana, A.; Airale, A.G.; Ferraris, A.; Carello, M.; Monti, M.; Palenzona, M.; Romeo, A.; Liebold, C.; et al. Validation of a Simulation Methodology for Thermoplastic and Thermosetting Composite Materials Considering the Effect of Forming Process on the Structural Performance. *Polymers* **2020**, *12*, 2801. [CrossRef]
30. Hineno, S.; Yoneyama, T.; Tatsuno, D.; Kimura, M.; Shiozaki, K.; Moriyasu, T.; Okamoto, M.; Nagashima, S. Fiber deformation behavior during press forming of rectangle cup by using plane weave carbon fiber reinforced thermoplastic sheet. *Procedia Eng.* **2014**, *81*, 1614–1619. [CrossRef]
31. Duhovic, M. Deformation Characteristics of Knitted Fabric Composites. Ph.D. Thesis, University of Auckland New Zealand, Auckland, New Zealand, 2004.
32. Wang, P.; Hamila, N.; Boisse, P.; Chaudet, P.; Lesueur, D. Thermo-mechanical behavior of stretch-broken carbon fiber and thermoplastic resin composites during manufacturing. *Polym. Compos.* **2015**, *36*, 694–703. [CrossRef]
33. Black, S. Aligned discontinuous fibers come of age. *High-Perform. Compos.* **2008**, *16*, 42–47.
34. Willems, A. Forming Simulation of Textile Reinforced Composite Shell Structures. Ph.D. Thesis, University of Leuven, Leuven, Belgium, 2008.
35. Haanappel, S.P. Forming of UD Fibre Reinforced Thermoplastics. Ph.D. Thesis, University of Twente, Enschede, The Netherlands, 2013.
36. Haanappel, S.P.; Akkerman, R. Shear characterisation of uni-directional fibre reinforced thermoplastic melts by means of torsion. *Compos. Part A Appl. Sci. Manuf.* **2014**, *56*, 8–26. [CrossRef]
37. *ASTM D618-13*; Standard Practice for Conditioning Plastics for Testing. American Society for Testing and Materials: West Conshohocken, PA, USA, 2013.
38. Liang, B.; Hamila, N.; Peillon, M.; Boisse, P. Analysis of thermoplastic prepreg bending stiffness during manufacturing and of its influence on wrinkling simulations. *Compos. Part A Appl. Sci. Manuf.* **2014**, *67*, 111–122. [CrossRef]
39. Boisse, P.; Hamila, N.; Vidal-Salle, E.; Dumont, F. Simulation of wrinkling during textile composite reinforcement forming. Influence of tensile, in-plane shear and bending stiffnesses. *Compos. Sci. Technol.* **2011**, *71*, 683–692. [CrossRef]
40. Barbero, E.J. *Introduction to Composite Materials Design*, 2nd ed.; CRC Press: Boca Raton, FL, USA, 2011.
41. Chen, Q.; Boisse, P.; Park, C.H.; Saouab, A.; Breard, J. Intra/inter-ply shear behaviors of continuous fiber reinforced thermoplastic composites in thermoforming processes. *Compos. Struct.* **2011**, *93*, 1692–1703. [CrossRef]
42. Lightfoot, J.S.; Wisnom, M.R.; Potter, K. A new mechanism for the formation of ply wrinkles due to shear between plies. *Compos. Part A Appl. Sci. Manuf.* **2013**, *49*, 139–147. [CrossRef]
43. Larberg, Y.R.; Åkermo, M. On the interply friction of different generations of carbon/epoxy prepreg systems. *Compos. Part A Appl. Sci. Manuf.* **2011**, *42*, 1067–1074. [CrossRef]
44. Isogawa, S.; Aoki, H.; Tejima, M. Isothermal forming of CFRTP sheet by penetration of hemispherical punch. *Procedia Eng.* **2014**, *81*, 1620–1626. [CrossRef]
45. Potluri, P.; Sharma, S.; Ramgulam, R. Comprehensive drape modelling for moulding 3D textile preforms. *Compos. Part A Appl. Sci. Manuf.* **2001**, *32*, 1415–1424. [CrossRef]
46. Wang, J.; Paton, R.; Page, J. The draping of woven fabric preforms and prepreps for production of polymer composite components. *Compos. Part A Appl. Sci. Manuf.* **1999**, *30*, 757–765. [CrossRef]

47. Cherouat, A.; Billoët, J.L. Mechanical and numerical modelling of composite manufacturing processes deep-drawing and laying-up of thin pre-impregnated woven fabrics. *J. Mater. Process. Technol.* **2001**, *118*, 460–471. [CrossRef]
48. Margossian, A.; Bel, S.; Hinterhoelzl, R. On the characterisation of transverse tensile properties of molten unidirectional thermoplastic composite tapes for thermoforming simulations. *Compos. Part A Appl. Sci. Manuf.* **2016**, *88*, 48–58. [CrossRef]
49. Thagard, J.; Liu, Q.; Liang, Z.; Okoli, O.; Wang, H. Simulation of the Resin Infusion Between Double Flexible Tooling Process and Experimental Validation. In Proceedings of the AmeriPAM Conference, Troy, MI, USA, 3–4 November 2003.
50. ESI-Group. *PAM-Form User Guide*; ESI-Group: Rungis, France, 2015.
51. Yu, W.R.; Pourboghra, F.; Chung, K.; Zampaloni, M.; Kang, T.J. Non-orthogonal constitutive equation for woven fabric reinforced thermoplastic composites. *Compos. Part A Appl. Sci. Manuf.* **2002**, *33*, 1095–1105. [CrossRef]
52. GOM GmbH. *GOM Testing—Technical Documentation as of V8 SR1, Digital Image Correlation and Strain Computation Basics*; GOM mbH: Braunschweig, Germany, 2016.
53. Nishi, M.; Kaburagi, T.; Kurose, M.; Hirashima, T.; Kurasiki, T. Forming simulation of thermoplastic pre-impregnated textile composite. *Int. J. Mater. Text Eng.* **2014**, *8*, 779–787.
54. Dassault System. *ABAQUS User Guide*, Version 6.14; Dassault System: Velizy-Villacoublay, France, 2014.
55. Ineos Olefins & Polymers USA. *Typical Engineering Properties of Polypropylene*; Ineos Olefins & Polymers USA: Fort Worth, TX, USA, 2014.
56. Boedeker Plastics Inc. Specifications for Polypropylene-Natural. Available online: <https://www.boedeker.com/Product/Polypropylene-Natural> (accessed on 16 March 2022).
57. Daniel, I.M.; Ishai, O. *Engineering Mechanics of Composite Materials*, 2nd ed.; Oxford University Press Inc.: New York, NY, USA, 2006.
58. Chen, T.; Dvorak, G.J.; Benveniste, Y. Mori-Tanaka Estimates of the Overall Elastic Moduli of Certain Composite Materials. *J. Appl. Mech.* **1992**, *59*, 539. [CrossRef]
59. Seigars, C. Feasibility of Hybrid Thermoplastic Composite-Concrete Load Bearing System. Master’s Thesis, University of Maine, Orono, ME, USA, 2018.
60. ESI Group PAM Composites Software Catalog. Available online: <https://www.esi-group.com/products/composites> (accessed on 16 March 2022).
61. Ansys Inc. Connecting Composite Forming Simulations in AniForm with Ansys Structural Simulation. Available online: <https://www.ansys.com/de-de/resource-center/webinar/connecting-composite-forming-simulations-in-aniform-with-ansys-structural-simulation> (accessed on 16 March 2022).

Article

Effect of Compatibilizer on the Persistent Luminescence of Polypropylene/Strontium Aluminate Composites

Anesh Manjaly Poulouse ^{1,*} , Hamid Shaikh ¹ , Arfat Anis ¹ , Abdullah Alhamidi ¹, Nadavala Siva Kumar ² , Ahmed Yagoub Elnour ²  and Saeed M. Al-Zahrani ¹

¹ SABIC Polymer Research Center, Department of Chemical Engineering, King Saud University, Riyadh 11421, Saudi Arabia; hamshaikh@ksu.edu.sa (H.S.); aarfat@ksu.edu.sa (A.A.); akfhk90@hotmail.com (A.A.); szahrani@ksu.edu.sa (S.M.A.-Z.)

² Department of Chemical Engineering, King Saud University, Riyadh 11421, Saudi Arabia; snadavala@ksu.edu.sa (N.S.K.); aelnour@ksu.edu.sa (A.Y.E.)

* Correspondence: apoulouse@ksu.edu.sa

Abstract: There is a demand for long afterglow composites due to their potential applications in nighttime signal boards, sensors, and biomedical areas. In this study, Polypropylene (PP)/strontium aluminate-based composites [SrAl₂O₄:Eu²⁺/Dy³⁺ (SAO₁) and Sr₄Al₁₄O₂₅:Eu²⁺, Dy³⁺ (SAO₂)] with maleic anhydride grafted PP compatibilizer (PRIEX) were prepared, and their auto-glowing properties were examined. After UV excitation at 320 nm, the PP/5PRIEX/SAO₁ composites showed green emission at 520 nm, and blue emission was observed for PP/5PRIEX/SAO₂ around 495 nm. The intensity of phosphorescence emission and phosphorescence decay was found to be proportional to the filler content (SAO₁ and SAO₂). The FTIR analysis excluded the copolymerization reaction between the SAO₁ and SAO₂ fillers and the PP matrix during the high-temperature melt mixing process. The SAO₁ and SAO₂ fillers decreased the overall crystallinity of the composites without affecting the T_m and T_c (melting and crystallization temperature) values. The thermal stability of the composites was slightly improved with the SAO₁ and SAO₂ fillers, as seen from the TGA curve. Due to the plasticizing effect of the compatibilizer and the agglomeration of the SAO₁ and SAO₂ fillers, the tensile modulus, tensile strength, and storage modulus of the composites was found to be decreased with an increase in the SAO₁ and SAO₂ content. The decreasing effect was more pronounced, especially with the bulk-sized SAO₂ filler.

Keywords: phosphorescent composites; compatibilizer; thermal and mechanical

Citation: Poulouse, A.M.; Shaikh, H.; Anis, A.; Alhamidi, A.; Kumar, N.S.; Elnour, A.Y.; Al-Zahrani, S.M. Effect of Compatibilizer on the Persistent Luminescence of Polypropylene/Strontium Aluminate Composites.

Polymers **2022**, *14*, 1711.

<https://doi.org/10.3390/polym14091711>

polym14091711

Academic Editors:

Somen K. Bhudolia and

Sunil Chandrakant Joshi

Received: 29 March 2022

Accepted: 19 April 2022

Published: 22 April 2022

Publisher's Note: MDPI stays neutral with regard to jurisdictional claims in published maps and institutional affiliations.



Copyright: © 2022 by the authors. Licensee MDPI, Basel, Switzerland. This article is an open access article distributed under the terms and conditions of the Creative Commons Attribution (CC BY) license (<https://creativecommons.org/licenses/by/4.0/>).

1. Introduction

Strontium aluminates doped with rare earth metals can store energy once excited by UV, thermal, or mechanical stimulation [1–5]. These materials show persistent luminescence once the excitation energy is released as light in the visible wavelength range, especially during nighttime. Unlike ZnS, these materials have good chemical stability, are non-radioactive, and have long-lasting afterglow properties (≥ 16 h) even after the excitation source is stopped [6]. They find potential applications in emergency signs, medical diagnostics, luminous paints, optical detectors, textiles, etc. [7–12]. After the discovery of green phosphor, SrAl₂O₄:Eu²⁺/Dy³⁺, in the 1990s, the need for multi-colored persistent phosphor encouraged rapid growth in this area [13]. In recent years, different rare-earth such as Pr³⁺, Ce³⁺, Sm²⁺, Nd³⁺ doped luminescent materials were developed, and their emission colors were dependent upon the raw materials chosen, stoichiometry, the synthesis methods, and their crystalline structure [14–16]. Due to the shorter afterglow time and lower luminescent intensity, these were not suited for practical application purposes. So far, mainly SrAl₂O₄:Eu, Dy, and Sr₄Al₁₄O₂₅:Eu, Dy phosphors were successfully commercialized due to their superior afterglow characteristics. Lepphoto et al. compared the effect of doping different trivalent rare-earth (Re³⁺, Dy³⁺, Nd³⁺, Gd³⁺, Sm³⁺, Ce³⁺,

Er³⁺, Pr³⁺, and Tb³⁺) on BaAl₂O₄:Eu²⁺ phosphors and found that the highest intensity was obtained for the Er³⁺ and Dy³⁺ doped ones. When comparing both the luminescence intensity and decay effect, the Dy³⁺ doped ones showed better luminescence intensity as well as slow decaying [17].

For the long-term application side, these luminescent particles need to be combined with the polymer matrix to prevent hydrolysis in the presence of humidity, and the polymeric encapsulation method yields good mechanical strength, support, and flexibility to these composites [18]. When the polymer organic moieties and inorganic phosphor materials are physically mixed, they often deteriorate the mechanical properties due to the weaker interaction between the polymer and filler (immiscibility). Thus, designing a phosphors/polymer composite with good physical properties is still challenging. Furthermore, the melt-blending of phosphor fine powder with polymers often results in an agglomeration effect inversely affecting the physical properties of the composites. In the literature, different polymers were incorporated with luminescent materials to facilitate better adhesion and support [19]. Polyurethane (PU) with amino-functionalized SrAl₂O₄:Eu²⁺, Dy³⁺ exhibits good compatibility between the phosphor and PU and imparts better mechanical properties than non-functionalized phosphor/PU composites [20]. Bem et al. employed LDPE and PMMA as polymer support for the SrAl₂O₄:Eu, Dy phosphor, and the results show that the LDPE/phosphor has higher luminous intensity as it forms a three-dimensional phosphor network in the LDPE matrix [21]. In a recent study, SiO₂ modified SrAl₂O₄:Eu²⁺, Dy³⁺ showed better dispersion in PLA and PMMA and improved the mechanical properties of the composites with better antibacterial properties and hydrophobicity [19,22]. In another study, SrAl₂O₄:Eu²⁺, Dy³⁺ phosphor with TiO₂ in the PMMA matrix considerably improved the luminescence emission intensity. The TiO₂ nanoparticles act as a light-harvesting agent enriching the light absorption capacity of the phosphor [23]. Recently, PP/SrAl₂O₄:Eu²⁺, Dy³⁺ long afterglow composites were prepared and studied. It was found that the resultant composites showed long afterglow properties, but their tensile strength and modulus decreased significantly [24]. PEG plasticizer was also added, aiming to improve the dispersion of the phosphor, but it inversely affected the intensity of emission [24]. In this paper, maleic anhydride grafted PP was added to virgin PP and melt-blended with SrAl₂O₄:Eu²⁺, Dy³⁺, and Sr₄Al₁₄O₂₅:Eu²⁺, Dy³⁺, aiming to improve the compatibility of the phosphor with the PP matrix and thereby on the mechanical features of the resulting long-lasting luminescent composites.

2. Materials and Methods

2.1. Materials

Poly (propylene) (PP) matrix, supplied by TASNEE Company, Saudi Arabia (Grade: PP H4120), was chosen for the present study. PP with a density of 0.9 g/cm³ and a melt flow rate (MFR) of 12 g/10 min was employed as the polymer matrix. Two strontium aluminate phosphor materials; SrAl₂O₄:Eu²⁺, Dy³⁺ (Mw = 209.11 g/mol) (SAO₁), and Sr₄Al₁₄O₂₅:Eu²⁺, Dy³⁺ (1139.55 g/mol) (SAO₂) from Sigma Aldrich company were used as luminescent fillers. Maleic Anhydride Grafted PP homopolymer (PRIEX 20097; Addcomp polymer additive solutions, Nijverdal, Netherlands) was used as a compatibilizer with an MFR of 20–30 g/10 min.

2.2. Methods

2.2.1. Preparation of the Composites

PP pellets and phosphor powders (SAO₁ and SAO₂; 1, 3, 5, and 10 wt. %) were mixed physically before feeding into the melt-mixing chamber. The PRIEX compatibilizer weight percentage was fixed as 5 for the entire study. The DSM Xplore micro-compounder (15cc) (Sittard, The Netherlands) with a co-rotating twin-screw was utilized for the melt-mixing process. The melt-mixing process was carried out for 3 min at a temperature of 200 °C (screw speed of 50 rpm). The collected melt was then introduced to an injection-molding machine (DSM Xplore microinjection molder, 12cc, Sittard, The Netherlands) for

the preparation of the ASTM, Type1 tensile testing specimen. Thin films of a thickness (0.6 cm) for the phosphorescence measurements were prepared using COLLIN Press (Maitenbeth, Germany) by applying 100 bar pressure at 200 °C.

2.2.2. Characterization of Composites

Phosphorescence and Decay Measurements

A Fluorescence Spectrophotometer (Agilent Technologies, Santa Clara, CA, USA) was used to measure the phosphorescence in the prepared composites. The emission spectra (visible range) were collected after exciting the samples using a UV source at a wavelength of 320 nm. The phosphorescence decay studies were conducted in this machine with the gate time and delay time set as 10,000 ms and 0.1 ms. The emission intensity decay was examined in 1800 s, selecting the excitation and emission wavelength as 320 nm and 490 nm, respectively.

Scanning Electron Microscope (SEM)

The phosphor dispersion and the morphology of the PP-5PRIEX/SAO₁ and PP-5PRIEX/SAO₂ composites were monitored with the help of the SEM (VEGA II LSU, TESCAN, Libusina, Czech Republic) at an accelerating voltage of 10 kV. The thin-sliced specimens were placed on sample holder stubs using double-sided adhesive carbon tape and were then coated with a fine layer of gold for 40 s to eliminate the charging effect.

Fourier Transform Infrared Spectroscopy (FTIR)

Fourier transform infrared spectroscopy (ATR-FTIR) analysis was carried out for the composites using a Nicolet iN10 FTIR microscope (Thermo-Scientific, Winsford, UK) with a Germanium micro tip accessory, and the scanning range was between 400 and 4000 cm⁻¹ wavelengths.

Differential Scanning Calorimetry (DSC)

The DSC-60A model (Shimadzu, Tokyo, Japan) was operated for the thermal characterization of the studied composites. The composites were heated from 30 to 250 °C with a heating rate of 10 °C/min. At 250 °C, the samples were kept for 4 min to erase the memory effect and were then cooled to 30 °C at the same rate. The degree of crystallinity (X_c) was calculated using the following equation:

$$X_c = \frac{(\Delta H_m)}{(1 - \varnothing)\Delta H_m^o} \times 100 \quad (1)$$

where ΔH_m is the melting enthalpy, and ΔH_m^o is the enthalpy of melting for a 100% crystalline PP which is 207 J/g [25]. \varnothing is the phosphor content (wt. %) present in the composites.

Thermo-Gravimetric Analysis (TGA)

The thermal stability of the PP-5PRIEX/SAO₁ and PP-5PRIEX/SAO₂ composites was investigated as a function of phosphors contents using a thermo-gravimetric analyzer, Mettler Toledo AG, Analytical CH-8603, Schwerzenbach, Switzerland. The composites (9–11 mg) were scanned in an aluminium pan from 30 to 700 °C, at a heating rate of 10° C/min under an inert Argon gas flow rate of 50 mL/min. The weight loss against the temperature was monitored.

Tensile Testing

Tensile tests were carried out in a universal testing machine (UTM) (Tinius-Olsen, Horsham, Pennsylvania, USA, Model: H100KS). The test was conducted according to the ASTM D638-14 testing method for the tensile properties of plastics. The reported values are an average of five measurements.

3. Results

3.1. FTIR, DSC, and TGA Studies in PP/PRIEX/SAO₁ and PP/PRIEX/SAO₂ Composites

The ATR-FTIR data of PP/PRIEX/SAO₁ and PP/PRIEX/SAO₂ composites are shown in Figure 1. For all the composites studied, the FTIR peaks were identical, and one can say that the chemical reaction between the phosphor particles SAO₁ and SAO₂ and the PP/PRIEX matrix did not take place during the high-temperature mixing process. As there is no new peak formation visible in the FTIR spectrum of the composites, only physical mixing was taking place during the high-temperature processing of all the composites.

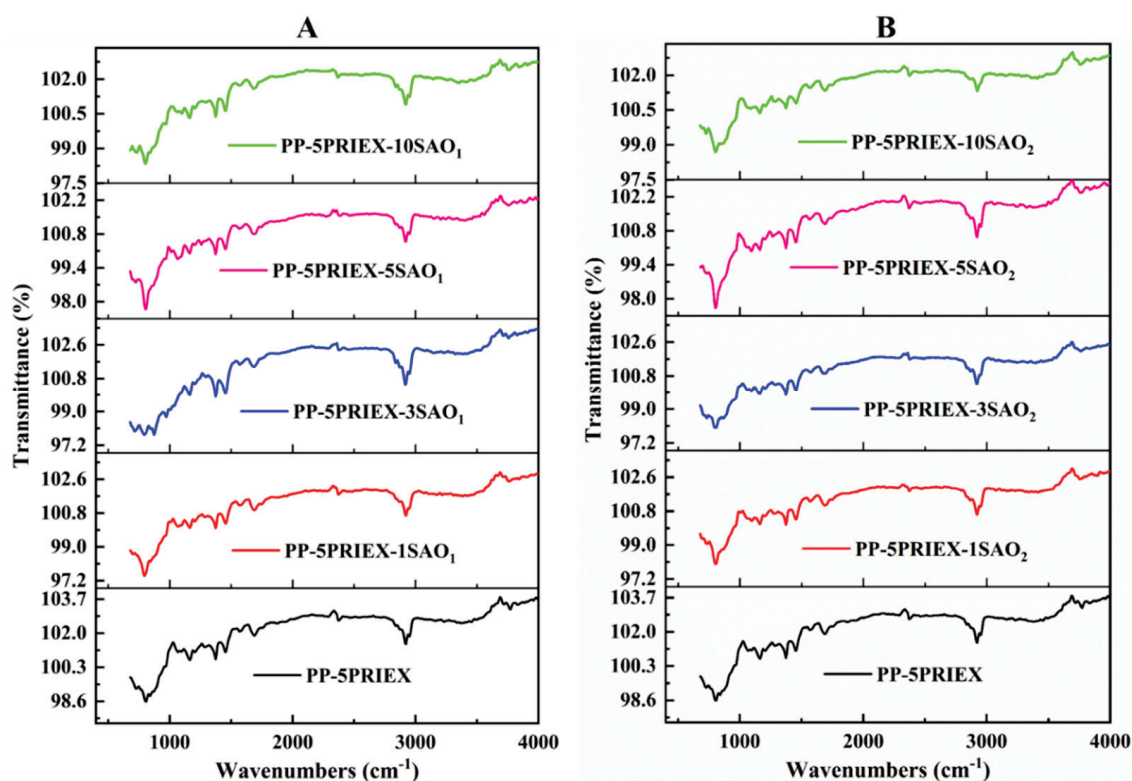


Figure 1. ATR-FTIR data of PP/PRIEX/SAO₁ (A) and PP/PRIEX/SAO₂ (B) composites.

The DSC data for the SAO₁ and SAO₂ composites are presented in Tables 1 and 2, respectively. The SAO₁ and SAO₂ fillers did not affect the melting and crystalline temperature (T_m and T_c) of the composites, which is also evidence of the physical mixing process. The chemical reaction altered the T_m and T_c values due to the structural modification taking place during the reaction, and in turn, it affected the composite's crystallization process [26]. As seen in Tables 1 and 2, the SAO₁ and SAO₂ fillers decreased the overall crystallinity of the resultant composites. The reason was due to the SAO₁ and SAO₂ fillers interception, which restricted the PP chain mobility, hindered the chain packing and spherulites formation, and decreased the overall crystallinity of the composites [27].

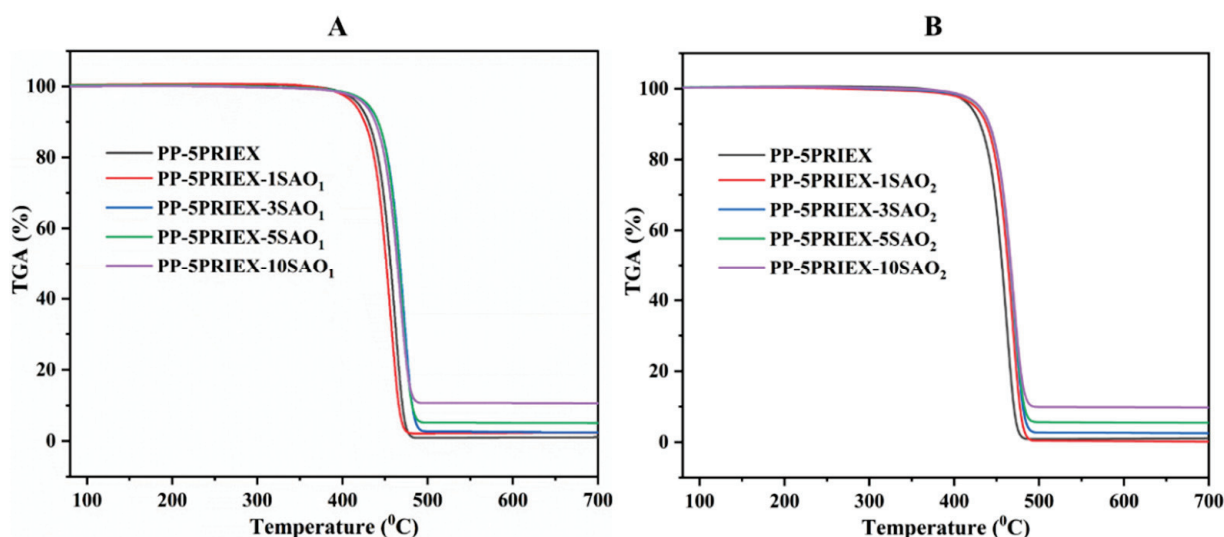
Table 1. DSC data on PP/5PRIEX/SAO₁ composites.

Material	T_c (°C)	T_m (°C)	ΔH_m (J/g)	X_c (%)
PP-5PRIEX	116.1	158.8	99.4	48.0
PP-5PRIEX/1SAO ₁	115.1	160.2	87.9	42.5
PP-5PRIEX/3SAO ₁	114.0	160.8	70.5	34.1
PP-5PRIEX/5SAO ₁	114.8	159.2	67.6	32.7
PP-5PRIEX/10SAO ₁	114.4	160.1	62.1	30.0

Table 2. DSC data on PP/5PRIEX/SAO₂ composites.

Material	T _c (°C)	T _m (°C)	ΔH _m (J/g)	X _c (%)
PP-5PRIEX	116.1	158.8	99.4	48.0
PP-5PRIEX/1SAO ₂	114.5	160.2	81.2	39.2
PP-5PRIEX/3SAO ₂	115.4	159.8	79.9	38.6
PP-5PRIEX/5SAO ₂	115.3	159.6	75.6	36.5
PP-5PRIEX/10SAO ₂	115.8	159.1	72.1	34.8

The TGA data for the PP/PRIEX/SAO₁ and PP/PRIEX/SAO₂ composites are in Figure 2A,B. For all the composites studied, the degradation process was taking place in a single step. The inorganic fillers (SAO₁ and SAO₂) which act as thermal barriers, slightly improved the thermal stability of the studied composites [22]. The onset of degradation was slightly shifted towards a higher temperature as seen in Figure 2. The SAO₁ and SAO₂ fillers are thermally stable inorganic materials and the residues left over after heating was directly proportional to the amount of SAO₁ and SAO₂ fillers used.

**Figure 2.** TGA results of PP/PRIEX/SAO₁ (A) and PP/PRIEX/SAO₂ (B) composites.

3.2. Tensile Strength, Tensile Modulus and Storage Modulus of PP/PRIEX/SAO₁ and PP/PRIEX/SAO₂ Composites

The tensile strength (TS) and tensile modulus (TM) of the PP/PRIEX/SAO₁ and PP/PRIEX/SAO₂ composites are shown in Figure 3A,B. Both TS and TM decrease with an increase in the weight percentage of SAO₁ and SAO₂ in the studied composites. The TS decreases from 34 MPa to 32.1 for SAO₁ composites and 34 to 31.6 for SAO₂ composites with the highest filler loading (10 wt. %). For the highest filler loading, the TM decreases from 1.1 to 0.93 GPa for SAO₁ and 1.1 to 0.88 GPa for SAO₂ composites. Due to the presence of the PRIEX compatibilizer, the decrease in the tensile properties (TS and TM) is not very pronounced, and the agglomeration of SAO₁ and SAO₂ exists, as seen in Figure 4, which could be the reason for the existing decreasing effect. The incompatibility among the inorganic fillers (SAO₁ and SAO₂) with the organic polymeric moieties can also impart mechanical property deterioration [24].

The storage modulus of the PP/PRIEX/SAO₁ and PP/PRIEX/SAO₂ composites from the rheological studies are shown in Figure 5. The rheological properties also follow the tensile properties trend, i.e., a slight decrease in storage modulus exists, which could be due to the agglomeration of SAO₁ and SAO₂ fillers in PP (Figure 4).

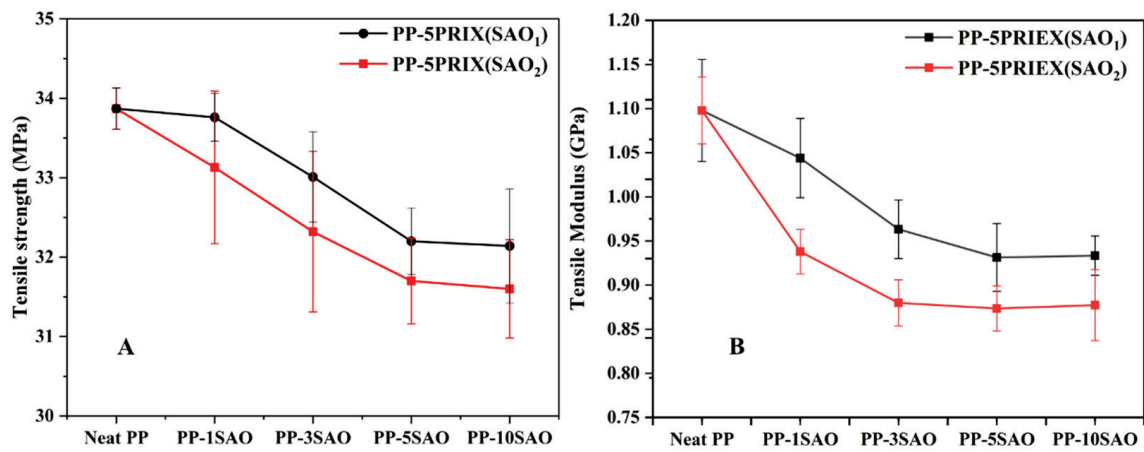


Figure 3. The tensile strength (A) and tensile modulus (B) of PP/PRIEX/SAO₁ and PP/PRIEX/SAO₂.

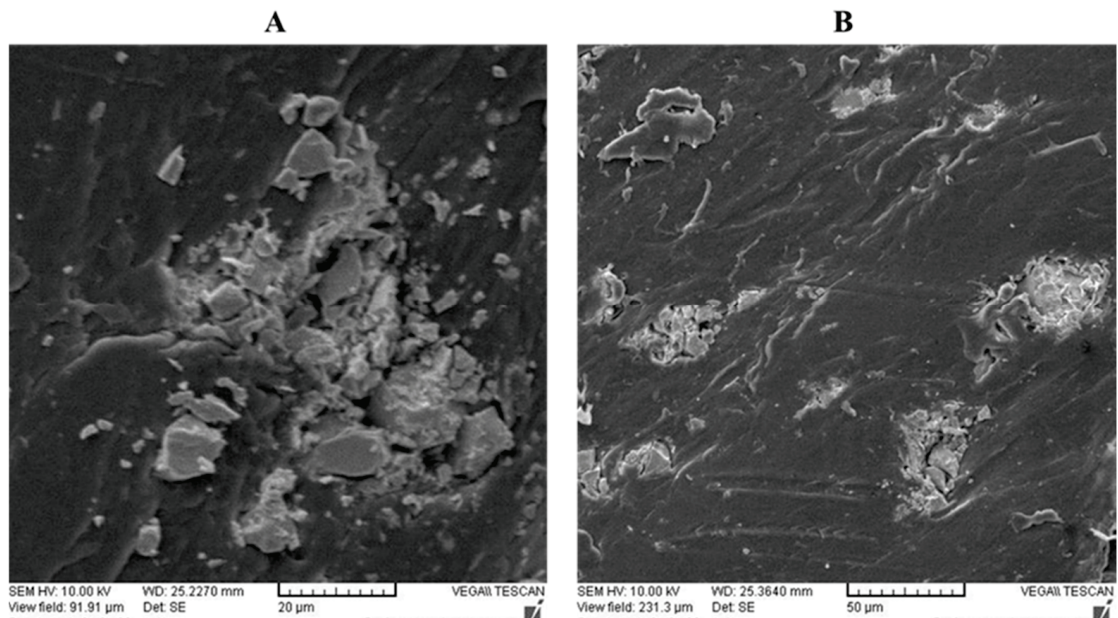


Figure 4. The SEM pictures were taken on PP/PRIEX/10 SAO₁ (A) and PP/PRIEX/10SAO₂ (B).

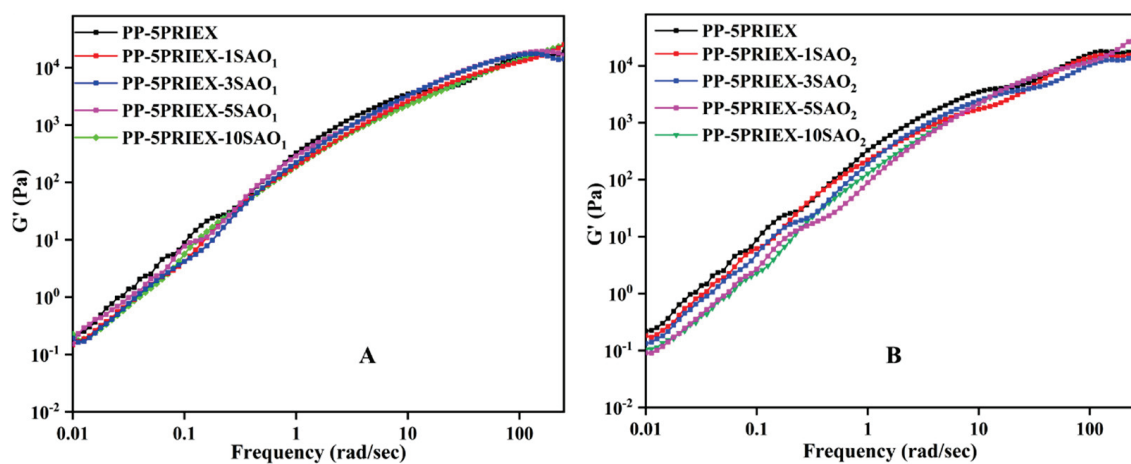


Figure 5. The storage modulus of PP/PRIEX/SAO₁ (A) and PP/PRIEX/SAO₂ (B) composites.

3.3. Phosphorescence Emission and Their Decay Studies in PP/PRIEX/SAO₁ and PP/PRIEX/SAO₂ Composites

The phosphorescence emission spectra of PP/5PRIEX/SAO₁ and PP/5PRIEX/SAO₂ were collected after exciting the composites at an excitation wavelength of 320 nm (UV). The emission spectra of both the composites are shown in Figure 6A,B. The emission spectra of the PP/5PRIEX/SAO₁ composites showed a green emission at 520 nm, and for PP/5PRIEX/SAO₂, a blue emission was observed around 495 nm and the intensity of the emission increased with the SAO₁ and SAO₂ phosphor content. The reported mechanisms for the phosphorescence emission are controversial [13,28,29], but it is widely accepted that Eu²⁺ luminescence center transition (5d–4f) is responsible for the broadband at the visible wavelength range. Later, Yuan et al. suggested the important role of Dy³⁺ in the long-lasting afterglow process. They suggested that these Dy³⁺ ions act as luminescence centers and introduce new electron traps and significantly increase the concentration of electron or hole traps. The electrons can be excited from the valence band (VB) to the conduction band (CB), creating excited electrons and holes. These can be non-radiatively captured by the electron or hole traps by the quantum tunneling process known as the trapping process. Once the trapped electrons and holes are released from their traps, they combine radiatively with the result of afterglow, and the depths of these electron and hole traps are critically important for this process [30,31]. For the PP/5PRIEX/10SAO₁ and PP/5PRIEX/10SAO₂ samples, once they were excited in outside sunlight for 10 min and kept under darkness, the phosphorescence emission was found to last for above 2 h, as shown in Figure 7.

The phosphorescence intensity decay with time for the studied composites is displayed in Figure 8. The decay rate was found to be directly proportional to the filler (SAO₁ and SAO₂) content in the studied PP/PRIEX matrix. With the gradual increase of the SAO concentration, the initial afterglow intensity gradually decreased, as shown in Figure 8. This is probably because one part of the excitation energy was absorbed and reflected by the host PP and PRIEX interaction with the rare-earth-doped particles. The part of the energy emitted by the SAO phosphors was also absorbed and reflected by the host matrix [32]. As shown in Figure 8, the phosphorescence decay curve shows two distinct behaviors, initially a faster decay followed by slow decay. Once the excitation of the low trap energy level was completed, the thermal disturbance initiated the release of the electrons. The low trap level had a shallow depth, low energy, and small binding effects on the electrons. Therefore, the reason for the faster decay of the original brightness could be related to the faster escape of the electrons from the low trap energy level [33]. The final intensity did not reach zero within the period used for the decay studies, as the afterglow properties lasted for hours in these composites [34].

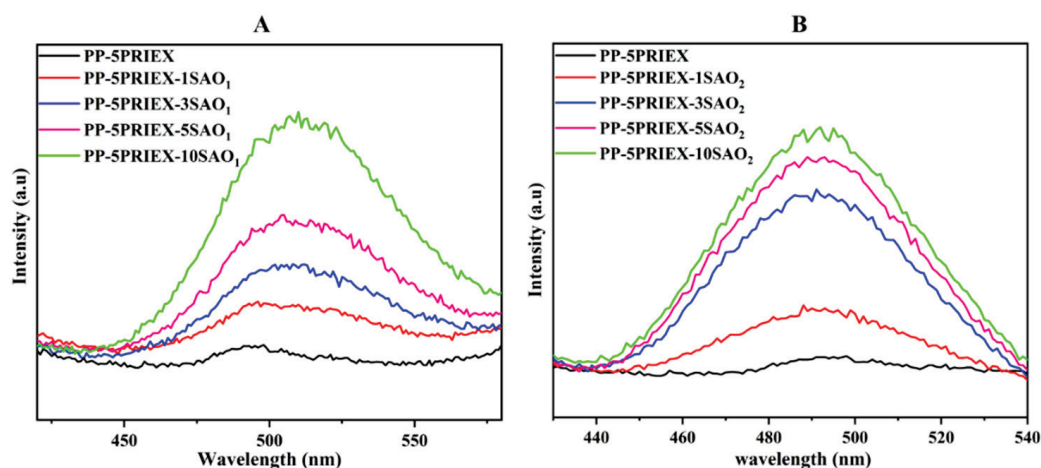


Figure 6. The phosphorescence emission spectra of PP/5PRIEX/SAO₁ (A) and PP/5PRIEX/SAO₂ (B) composites.

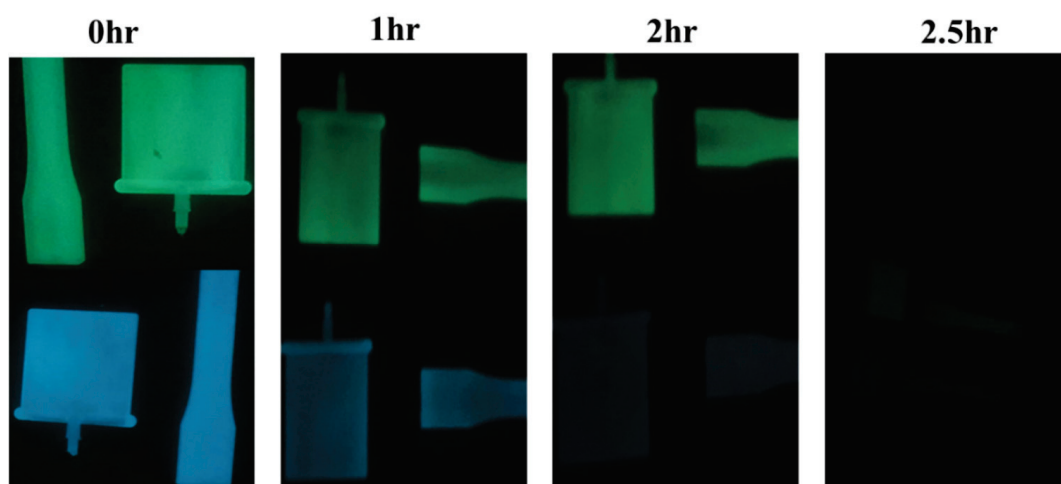


Figure 7. The green and blue emission decay at different times for PP/5PRIEX/10SAO₁ and blue PP/5PRIEX/10 SAO₂ composites (after excited in outside sunlight for 10 min and kept in a dark room).

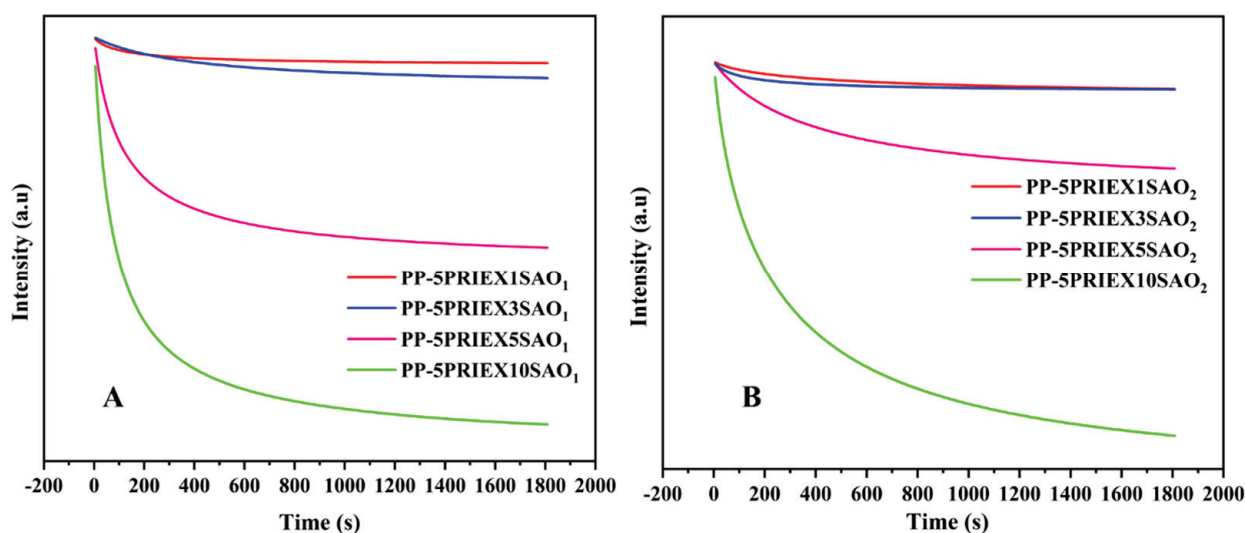


Figure 8. The phosphorescence intensity decay with time for PP/PRIEX/SAO₁ (A) and PP/PRIEX/SAO₂ (B) composites.

4. Conclusions

PP/Maleated PP encapsulated strontium aluminate fillers (SAO₁ and SAO₂) with long-lasting afterglow properties were prepared via the melt-blending process. The intention of using maleated PP was to improve the dispersion of SAO₁ and SAO₂ fillers in the PP matrix and thereby have a positive effect on the mechanical properties of the resultant composites. As visible from the SEM figures, the agglomeration of these fine SAO₁ and SAO₂ fillers and the incompatibility among fillers and matrix inversely affected the mechanical properties (tensile strength, tensile modulus, and storage modulus) of the resultant composites, especially with the bulk-sized SAO₂ filler. Though chemically modified maleated PP was used in this study, no chemical reaction took place between the SAO₁ and SAO₂ fillers and the PP matrix. This was confirmed from the FTIR and DSC studies, and from TGA studies, it was found that the onset of degradation was slightly shifted to a higher temperature with the filler percentage. The fillers inversely affected the total crystallinity of the composites without changing the T_m and T_c values. As expected, the intensity of phosphorescence emission and their decay rate were enhanced with the phosphor filler content. Though economically viable long-lasting composites based on PP

and maleated PP were fabricated, the efforts must be continued to improve the dispersion of phosphor fillers and, thereby, the mechanical properties of the composites.

Author Contributions: Conceptualization, A.M.P.; investigation, A.A. (Abdullah Alhamidi) and A.Y.E.; writing—original draft preparation, A.M.P.; writing—review and editing, A.M.P., H.S., N.S.K. and A.A. (Arfat Anis); supervision, A.M.P. and S.M.A.-Z.; project administration, A.M.P. All authors have read and agreed to the published version of the manuscript.

Funding: This project was funded by the National Plan for Science, Technology, and Innovation (MAARIFAH), King Abdulaziz City for Science and Technology, Kingdom of Saudi Arabia (13-ADV1044-02).

Institutional Review Board Statement: Not applicable.

Informed Consent Statement: Not applicable.

Data Availability Statement: The data presented in this study are available on request from the corresponding author.

Acknowledgments: This project was funded by the National Plan for Science, Technology, and Innovation (MAARIFAH), King Abdulaziz City for Science and Technology, Kingdom of Saudi Arabia, Award Number (13-ADV1044-02).

Conflicts of Interest: The authors declare no conflict of interest.

References

- Lu, B.; Shi, M.; Pang, Z.; Zhu, Y.; Li, Y. Study on the optical performance of red-emitting phosphor: $\text{SrAl}_2\text{O}_4:\text{Eu}^{2+}, \text{Dy}^{3+}/\text{Sr}_2\text{MgSi}_2\text{O}_7:\text{Eu}^{2+}, \text{Dy}^{3+}$ /light conversion agent for long-lasting luminous fibers. *J. Mater. Sci. Mater. Electron.* **2021**, *32*, 17382–17394. [CrossRef]
- Chang, C.-C.; Yang, C.-Y.; Lu, C.-H. Preparation and photoluminescence properties of $\text{Sr}_4\text{Al}_{14}\text{O}_{25}:\text{Eu}^{2+}$ phosphors synthesized via the microemulsion route. *J. Mater. Sci.* **2013**, *24*, 1458–1462. [CrossRef]
- Yeşilay Kaya, S.; Karacaoglu, E.; Karasu, B. Effect of Al/Sr ratio on the luminescence properties of $\text{SrAl}_2\text{O}_4:\text{Eu}^{2+}, \text{Dy}^{3+}$ phosphors. *Ceram. Int.* **2012**, *38*, 3701–3706. [CrossRef]
- Xue, Z.; Deng, S.; Liu, Y. Synthesis and luminescence properties of $\text{SrAl}_2\text{O}_4:\text{Eu}^{2+}, \text{Dy}^{3+}$ nanosheets. *Phys. B Condens. Matter* **2012**, *407*, 3808–3812. [CrossRef]
- Dutczak, D.; Milbrat, A.; Katelnikovas, A.; Meijerink, A.; Ronda, C.; Jüstel, T. Yellow persistent luminescence of $\text{Sr}_2\text{SiO}_4:\text{Eu}^{2+}, \text{Dy}^{3+}$. *J. Lumin.* **2012**, *132*, 2398–2403. [CrossRef]
- Katsumata, T.; Nabae, T.; Sasajima, K.; Komuro, S.; Morikawa, T. Effects of Composition on the Long Phosphorescent $\text{SrAl}_2\text{O}_4:\text{Eu}^{2+}, \text{Dy}^{3+}$ Phosphor Crystals. *J. Electrochem. Soc.* **1997**, *144*, L243–L245. [CrossRef]
- Nance, J.; Sparks, T.D. Comparison of coatings for $\text{SrAl}_2\text{O}_4:\text{Eu}^{2+}, \text{Dy}^{3+}$ powder in waterborne road striping paint under wet conditions. *Prog. Org. Coat.* **2020**, *144*, 105637. [CrossRef]
- Nance, J.; Sparks, T.D. From streetlights to phosphors: A review on the visibility of roadway markings. *Prog. Org. Coat.* **2020**, *148*, 105749. [CrossRef]
- Tan, H.; Wang, T.; Shao, Y.; Yu, C.; Hu, L. Crucial Breakthrough of Functional Persistent Luminescence Materials for Biomedical and Information Technological Applications. *Front. Chem* **2019**, *7*, 387. [CrossRef]
- Soni, A.K.; Singh, B.P. Luminescent Materials in Lighting, Display, Solar Cell, Sensing, and Biomedical Applications. In *Luminescence-OLED Technology and Applications*; Pyshkin, S., Ed.; IntechOpen: London, UK, 2019.
- Mokhtar, O.M.; Attia, Y.A.; Wassel, A.R.; Khattab, T.A. Production of photochromic nanocomposite film via spray-coating of rare-earth strontium aluminate for anti-counterfeit applications. *Luminescence* **2021**, *36*, 1933–1944. [CrossRef]
- Liu, J.; Lécuyer, T.; Seguin, J.; Mignet, N.; Scherman, D.; Viana, B.; Richard, C. Imaging and therapeutic applications of persistent luminescence nanomaterials. *Adv. Drug Deliv. Rev.* **2019**, *138*, 193–210. [CrossRef] [PubMed]
- Matsuzawa, T.; Aoki, Y.; Takeuchi, N.; Murayama, Y. A New Long Phosphorescent Phosphor with High Brightness, $\text{SrAl}_2\text{O}_4:\text{Eu}^{2+}, \text{Dy}^{3+}$. *J. Electrochem. Soc.* **1996**, *143*, 2670–2673. [CrossRef]
- Chen, W.; Wang, Y.; Zeng, W.; Han, S.; Li, G.; Guo, H.; Li, Y.; Qiang, Q. Long persistent composite phosphor $\text{CaAl}_2\text{O}_4:\text{Eu}^{2+}, \text{Nd}^{3+}/\text{Y}_3\text{Al}_5\text{O}_{12}:\text{Ce}^{3+}$: A novel strategy to tune the colors of persistent luminescence. *New J. Chem.* **2016**, *40*, 485–491. [CrossRef]
- Zhao, Z.; Wang, Y. The synthesis and afterglow luminescence properties of a novel red afterglow phosphor: $\text{ZrO}_2:\text{Sm}^{3+}, \text{Sn}^{4+}$. *J. Lumin.* **2012**, *132*, 2842–2846. [CrossRef]
- Zheng, R.; Xu, L.; Qin, W.; Chen, J.; Dong, B.; Zhang, L.; Song, H. Electrospinning preparation and photoluminescence properties of $\text{SrAl}_2\text{O}_4:\text{Ce}^{3+}$ nanowires. *J. Mater. Sci.* **2011**, *46*, 7517–7524. [CrossRef]
- Lephoto, M.A.; Ntwaaborwa, O.M.; Pitale, S.S.; Swart, H.C.; Botha, J.R.; Mothudi, B.M. Synthesis and characterization of $\text{BaAl}_2\text{O}_4:\text{Eu}^{2+}$ co-doped with different rare earth ions. *Phys. B Condens. Matter* **2012**, *407*, 1603–1606. [CrossRef]

18. Poulouse, A.M.; Shaikh, H.; Anis, A.; Alhamidi, A.; Kumar, N.S.; Elnour, A.Y.; Al-Zahrani, S.M. Long Persistent Luminescent HDPE Composites with Strontium Aluminate and Their Phosphorescence, Thermal, Mechanical, and Rheological Characteristics. *Materials* **2022**, *15*, 1142. [CrossRef]
19. Cheng, L.-X.; Liu, T.; Li, L.; Yang, L.; He, H.-W.; Zhang, J.-C. Self-repairing inorganic phosphors/polymer composite film for restructuring luminescent patterns. *Mater. Res. Express* **2021**, *8*, 065302. [CrossRef]
20. Tian, S.; Wen, J.; Fan, H.; Chen, Y.; Yan, J.; Zhang, P. Sunlight-activated long persistent luminescent polyurethane incorporated with amino-functionalized SrAl₂O₄:Eu²⁺, Dy³⁺ phosphor. *Polym. Int.* **2016**, *65*, 1238–1244. [CrossRef]
21. Bem, D.B.; Swart, H.C.; Luyt, A.S.; Coetzee, E.; Dejene, F.B. Properties of green SrAl₂O₄ phosphor in LDPE and PMMA polymers. *J. Appl. Polym. Sci.* **2010**, *117*, 2635–2640. [CrossRef]
22. Wan, M.; Jiang, X.; Nie, J.; Cao, Q.; Zheng, W.; Dong, X.; Fan, Z.H.; Zhou, W. Phosphor powders-incorporated polylactic acid polymeric composite used as 3D printing filaments with green luminescence properties. *J. Appl. Polym. Sci.* **2019**, *137*, 48644. [CrossRef]
23. Oguzlar, S.; Ongun, M.Z.; Keskin, O.Y.; Delice, T.K.; Azem, F.A.; Birlik, I.; Ertekin, K. Investigation of Spectral Interactions between a SrAl₂O₄:Eu(2+), Dy(3+) Phosphor and Nano-Scale TiO₂. *J. Fluoresc.* **2020**, *30*, 839–847. [CrossRef] [PubMed]
24. Poulouse, A.M.; Anis, A.; Shaikh, H.; Alhamidi, A.; Siva Kumar, N.; Elnour, A.Y.; Al-Zahrani, S.M. Strontium Aluminate-Based Long Afterglow PP Composites: Phosphorescence, Thermal, and Mechanical Characteristics. *Polymers* **2021**, *13*, 1373. [CrossRef] [PubMed]
25. Paukkeri, R.; Lehtinen, A. Thermal behaviour of polypropylene fractions: 1. Influence of tacticity and molecular weight on crystallization and melting behaviour. *Polymers* **1993**, *34*, 4075–4082. [CrossRef]
26. Lee, S.S.; Kim, J.; Park, M.; Lim, S.; Choe, C.R. Transesterification Reaction of the BaSO₄-Filled PBT/Poly(ethylene terephthalate) Blend. *J. Polym. Sci. Part B Polym. Phys.* **2001**, *39*, 2589–2597.
27. Zhu, J.; Abeykoon, C.; Karim, N. Investigation into the effects of fillers in polymer processing. *Int. J. Lightweight Mater. Manuf.* **2021**, *4*, 370–382. [CrossRef]
28. Clabau, F.; Rocquefelte, X.; Jobic, S.; Deniard, P.; Whangbo, M.H.; Garcia, A.; Le Mercier, T. Mechanism of Phosphorescence Appropriate for the Long-Lasting Phosphors Eu²⁺-Doped SrAl₂O₄ with Codopants Dy³⁺ and B³⁺. *Chem. Mater.* **2005**, *17*, 3904–3912. [CrossRef]
29. Tuomas Aitasalo, J.H. Hogne Jungner, Mika Lastusaari, Janne Niittykoski, Mechanisms of persistent luminescence in Eu²⁺, RE³⁺ doped alkaline earth aluminates. *J. Lumin.* **2001**, *94–95*, 59–63. [CrossRef]
30. Huang, Y.M.; Ma, Q.-l. Long afterglow of trivalent dysprosium doped strontium aluminate. *J. Lumin.* **2015**, *160*, 271–275. [CrossRef]
31. Xu, J.; Tanabe, S. Persistent luminescence instead of phosphorescence: History, mechanism, and perspective. *J. Lumin.* **2019**, *205*, 581–620. [CrossRef]
32. Ni, Z.; Fan, T.; Bai, S.; Zhou, S.; Lv, Y.; Ni, Y.; Xu, B. Effect of the Concentration of SrAl₂O₄: Eu²⁺ and Dy³⁺ (SAO) on Characteristics and Properties of Environment-Friendly Long-Persistent Luminescence Composites from Polylactic Acid and SAO. *Scanning* **2021**, *2021*, 6337768. [CrossRef] [PubMed]
33. Francisco, L.H.C.; Moreira, R.P.; Felinto, M.C.F.C.; Teixeira, V.C.; Brito, H.F.; Malta, O.L. SrAl₂O₄: Eu²⁺, Dy³⁺ persistent luminescent materials functionalized with the Eu³⁺(TTA)-complex by microwave-assisted method. *J. Alloy. Compd.* **2021**, *882*, 160608. [CrossRef]
34. Eftimov, T.; Kostova, I.; Arapova, A.; Patronov, G. Rise and decay time responses of Sr aluminate phosphorescent materials. *J. Lumin.* **2021**, *235*, 117985. [CrossRef]

Thermoset/Thermoplastic Interphases: The Role of Initiator Concentration in Polymer Interdiffusion

Ozan Erartsın *, Jamal Sayyed Monfared Zanjani  and Ismet Baran * Faculty of Engineering Technology, University of Twente, 7500 AE Enschede, The Netherlands;
j.seyyedmonfaredzanjani@utwente.nl

* Correspondence: o.erartsin@utwente.nl (O.E.); i.baran@utwente.nl (I.B.)

Abstract: In the co-bonding of thermoset and thermoplastic polymers, the interdiffusion of the polymers results in the formation of an interphase between them. Understanding the factors influencing the interdiffusion and the resulting interphase is crucial in order to optimize the mechanical performance of the bond. Herein, for the first time, the effect of the initiator concentration of the thermoset resin-initiator mixture on the interphase thickness of co-bonded thermoset-thermoplastic polymers is investigated. The dependence of the gelation time on the initiator concentration is determined by rheometer measurements. Differential scanning calorimetry measurements are carried out to determine the speed of cure. To co-bond the polymers, pieces of already-manufactured thermoplastic plates are embedded in a resin-initiator mixture. The interphase thickness of the co-bonded polymers is measured with an optical microscope. The results of this study show that the gelation time decreases as the initiator concentration increases. This decrease leads to a significant reduction in both interphase thickness and diffusivity. For instance, increasing the initiator/resin weight ratio from 1% to 3% reduces the gelation time by 74% and the interphase thickness by 63%.

Citation: Erartsin, O.; Zanjani, J.S.M.; Baran, I. Thermoset/Thermoplastic Interphases: The Role of Initiator Concentration in Polymer Interdiffusion. *Polymers* **2022**, *14*, 1493. <https://doi.org/10.3390/polym14071493>

Academic Editors: Somen K. Bhudolia and Sunil Chandrakant Joshi

Received: 23 February 2022

Accepted: 4 April 2022

Published: 6 April 2022

Publisher's Note: MDPI stays neutral with regard to jurisdictional claims in published maps and institutional affiliations.



Copyright: © 2022 by the authors. Licensee MDPI, Basel, Switzerland. This article is an open access article distributed under the terms and conditions of the Creative Commons Attribution (CC BY) license (<https://creativecommons.org/licenses/by/4.0/>).

Keywords: thermosetting resins; thermoplastics; co-bonding; interphase; diffusion; adhesion

1. Introduction

Fiber-reinforced polymer composites (FRPC) provide not only a high strength-to-weight ratio but also exceptional properties such as high durability, stiffness, and corrosion resistance. While knowledge of the manufacturing of individual FRPC parts has reached a level of maturity, the integration and assembly of different FRPC parts is far less developed, particularly considering the co-bonding process. Co-bonding is a bonding technique in which a prefabricated part (in this case, a thermoplastic (TP) polymer) is bonded with a (neat or fiber-reinforced) thermoset polymer through a curing reaction of the thermoset resin [1–4]. The areas of application of this technique involve the bond between the pultruded profiles at the blade root, spar cap, and leading edge protection (LEP) layer and the over-infused main body of the wind turbine blade [5,6]. Although co-bonding may refer to the bonding of two parts with or without an adhesive between them [1–4,7], in this work we will focus on co-bonding without adhesives, where bonding takes place by the interdiffusion of polymers that are in contact as the curing takes place. The interdiffusion of the bonded polymers, and, subsequently, the curing of the resin result in the formation of an interphase [2,4,8–12]. The size and morphology of the interphase have been shown to depend on the gelation time and viscosity of the resin, the thermodynamic affinity between the polymers, and the physical state of the thermoplastic [2,4,8–10]. For instance, high levels of thermodynamic affinity may promote homogeneous mixing, whereas phase separation may take place at lower levels of affinity [9]. The gelation time and viscosity of the resin have competing effects on the interphase thickness [2]. Higher gelation times allow more time for the interdiffusion to take place, which eventually promotes an increase in the interphase thickness. Conversely, an increase in the resin viscosity hampers the diffusion of resin into the thermoplastic, leading to a lower interphase thickness.

It is of the utmost importance to investigate the influence of the aforementioned parameters on the TP-TS interphases. This is necessary in order to optimize the design of co-bonded hybrid composites, closing the knowledge gap in this field and promoting their more widespread use. To illustrate, for the accurate prediction of the residual stresses and the resulting process-induced deformations in the co-bonded composites, the size and the mechanical properties of the interphase are essential inputs [1,13]. Another reason why understanding the interphase is important is that the interphase morphology, which is influenced by processing conditions, plays a major role in the resulting bond strength [14]. As it is highly desirable to have stronger bonds in the joining of composites, determining the factors leading to optimum bond performance is crucial.

One way to control the cure speed of a resin-initiator mixture is to change the concentration of initiator in the mixture [15,16]. For instance, in vacuum-assisted resin transfer molding, the initiator concentration can be tuned to delay the gelation of the resin to allow sufficient time for the resin to fill the mold [15]. In the literature, studies on the effect of initiator concentration on the gelation time of neat resins are available [15–18]. Nevertheless, the effect of initiator concentration on the interphase morphology, which is crucial for the co-bonded parts, since the interphase morphology is also affected by the gelation time, has not been studied so far.

One benefit of changing the initiator concentration to tune the gelation time is that it allows one to control the gelation time without affecting other parameters controlling the interdiffusion. For instance, decreasing the temperature to increase the gelation time also reduces the viscosity of the resin, which has an adverse effect on the interphase thickness [2,19]. Tuning the initiator concentration eliminates this problem and, hence, enables one to investigate the effect of gelation time on the interdiffusion exclusively.

This study aims to investigate the effect of initiator concentration of a resin-initiator mixture on the interphase thickness of co-bonded unsaturated polyester resin (UPR) and polycarbonate (PC). UPR is a resin that is commonly used in wind turbine blades and PC is a TP polymer that could potentially be used for LEP applications. Initially, the gelation time of the resin at different initiator concentrations is measured and DSC tests are conducted to determine the cure behavior (cure speed and degree of cure). Resin-initiator mixtures with different initiator concentrations are co-bonded to PC and the interphase thickness is measured using optical microscopy. To investigate the diffusion kinetics, the diffusivity of the mixtures is calculated based on Fick's second law of diffusion using the measured interphase thicknesses and gelation times. Finally, the measured interphase thickness and gelation time are correlated.

2. Experiments, Methodology and Background

2.1. Materials

The curing process of unsaturated polyester resin (UPR) is free radical chain-growth crosslinking polymerization. In this reaction, styrene is used as a crosslinking agent to link the polyester molecules [20]. The curing starts with the opening of highly reactive initiator (peroxide) molecules, which leads to free radical formation. These radicals interact with the styrene molecules to form new radicals. Eventually, the new radicals make contact with the polyester chains and open their unsaturated C=C bonds. This leads polyester chains to be linked via styrene bridges; hence, crosslinking takes place [20].

The UPR used in this study was 40–45% styrene by weight; it is used in the industry for manufacturing large parts through vacuum-assisted resin transfer molding. Methyl ethyl ketone peroxide (MEKP) was used as an initiator. UPR and MEKP were mixed in certain ratios for 3 min to obtain the UPR-MEKP mixture to be cured. In this study, the initiator concentration was varied by using different initiator/resin weight ratios ranging from 0.5% (0.5 g initiator/100 g of UPR) up to 3%.

As the TP material used for the co-bonded samples, a LEXAN™ PC plate with a thickness of 2 mm was used. This material was chosen since it was shown to have a strong thermodynamic affinity to UPR [2].

2.2. Cure Kinetics (DSC) Measurements

Isothermal differential scanning calorimetry (DSC) measurements were conducted at 25 °C using a Mettler Toledo DSC to characterize the cure kinetics of the mixtures with different initiator concentrations. Mixtures had weights of about 20 mg and the DSC scans lasted for 24 h. A total of 3 specimens were tested at the initiator/resin weight ratio of 1.5%, whereas either 1 or 2 specimens were tested at the other ratios (0.5%, 1%, 2%, 2.5%, 3%). From the DSC scans, the time the DSC peak started and reached its maximum was obtained to investigate the speed of curing. In addition, to gain more insight into the cure behavior, the heat and degree of cure were calculated.

2.3. Gelation Time Measurements

Gelation time measurements of UPR–MEKP mixtures with different initiator/resin weight ratios were carried out utilizing an Anton Paar-Physica MCR 501 rheometer in “plate-plate” oscillatory mode. Plates had a diameter of 25 mm with a spacing of 0.5 mm between them. A strain of 1% and a frequency of 1 Hz were used. Tests were carried out isothermally at 23 °C. Storage and loss moduli were recorded, from which the gelation time was obtained as the time when the storage modulus equaled (and subsequently exceeded) the loss modulus. A total of 3 specimens were tested at initiator/resin weight ratios of 1.5%, 2%, 2.2%, and 3%; 2 specimens were tested at ratios of 1% and 2.5%.

2.4. Co-Bonding

The co-bonding of TP and TS polymers was carried out by embedding pieces of TP plates in the TS resin in cylindrical cups 25 mm in diameter. Initially, pieces of PC plates with dimensions of 18 mm × 18 mm were cut making use of a paper cutter. Later, each of the TP plate pieces was placed in the middle of the cylindrical cups with the help of metallic holders, as shown in Figure 1. Finally, the resin-initiator (UPR-MEKP) mixtures with various initiator/resin weight ratios were poured on the TP pieces up to a height of about 20 mm. The TP pieces embedded in resin were left for curing at room temperature for 24 h. At least three specimens were prepared per initiator/resin weight ratio (at 1%, 1.5%, 2%, 2.5%, 3%), except at 0.5%, where two specimens were prepared.

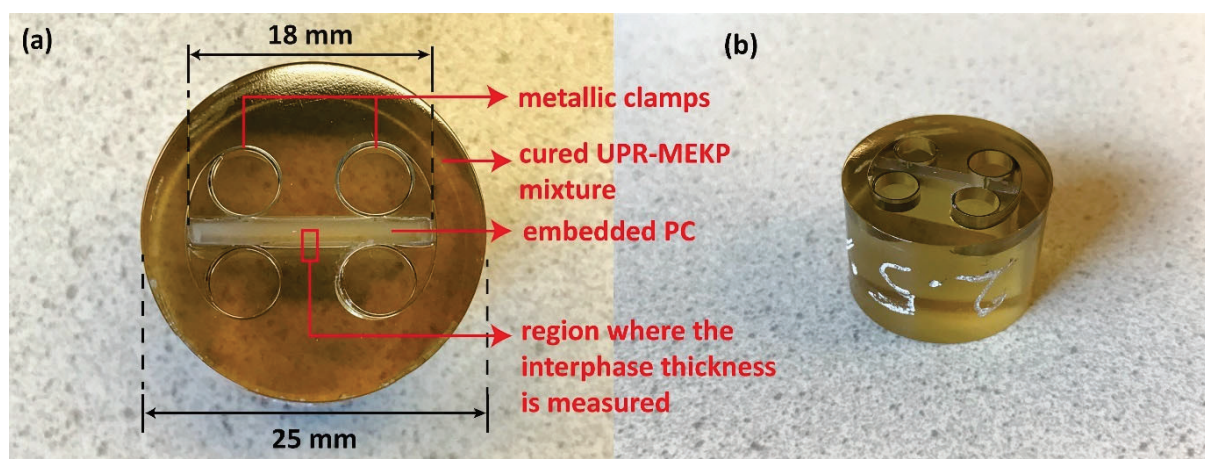


Figure 1. (a) Top and (b) isometric views of the co-bonded PC and UPR-MEKP.

2.5. Interphase Thickness Measurements

The interphase thickness was measured using a Keyence VHX-7000 digital optical microscope equipped with a VH-100UR lens. Before microscopy, the co-bonded samples were polished using a Struers Tegramin 30 polisher. The polishing procedure involved grinding with SiC paper (500, 1000, 2000, and 4000 grits, respectively) and polishing later using several different polishing clothes with diamond solutions. Final polishing was obtained using an MD-Chem cloth with a colloidal silica suspension. During the

measurements, the interphase thickness was obtained from the middle point of the cross-section, as marked in Figure 1, where the interphase thickness reached a maximum (as it was away from the metallic clamps that prevented interdiffusion).

2.6. Diffusivity of UPR into Thermoplastic Polymers

The diffusivity of the UPR-MEKP mixture into PC was estimated to evaluate the diffusion kinetics at different initiator/initiator/resin weight ratios. It was shown by Zanjani, J.S.M., Baran, I. and Akkerman, R. [2] that the diffusion of UPR into PC is Fickian. Fick's second law of diffusion, which was used to model the diffusion kinetics, is as follows:

$$\frac{\partial C}{\partial t} = -D \frac{\partial^2 C}{\partial x^2}, \quad (1)$$

where C is the concentration of the diffusing species and D is the diffusivity (diffusion coefficient) [21]. The diffusivity D is a proportionality factor between the mass flux and the concentration gradient [21]. In other words, the larger the D is, the larger the mass flux is, given a certain concentration gradient. Assuming that D is constant, C at a certain time and location can be solved when D is known and the boundary conditions are input [4,21]. In our case, the interphase thickness (diffusion length) and the gelation time are known, while D is unknown. Hence, assuming that the interphase development stops at the gelation time [22] and using the gelation time and interphase thickness measurements, the diffusivity D can be calculated, as presented in detail in [4].

3. Results and Discussion

3.1. Cure Kinetics and Gelation Time

DSC curves of UPR-MEKP mixtures with different initiator/resin weight ratios are shown in Figure 2. All curves exhibit exothermic peaks, which correspond to the heat flow resulting from the curing reaction. According to the figure, the peaks start and reach their highest point earlier as the initiator/resin weight ratio is increased, which means that curing takes place faster. The heat of the cure is calculated as the area below the DSC peaks. For this, initially, a baseline is drawn for each DSC curve. After constructing the baselines and calculating the area between the DSC curves and the baseline, the heat of the cure is calculated, the values of which are presented in Table 1. The DSC tests carried out at the initiator/resin weight ratio of 1.5%, involving multiple specimens, had a very low scatter, showing the good repeatability of the test. Note that for the mixture with 0.5% initiator, curing was not completed (see the incomplete peak corresponding to 0.5% in Figure 2); hence, the heat of the cure was not calculated for this case. Considering the other cases, the heat of cure was seen to increase with an increase in the initiator/resin weight ratio, which is agreement with the findings of Vilas et al. [17]. This means that a higher degree of cure is reached at higher initiator/resin weight ratios, where the normalized degree of cure for different initiator/resin ratios is calculated as the ratio of the heat of cure at a certain concentration to that at the concentration of 3% (Table 1). While the initiator/resin weight ratio of 1% led to a significantly low degree of cure (0.58), for higher ratios high degrees of cure above 0.90 were obtained for all cases.

The acceleration of curing was also confirmed by the gelation times measured in rheometer tests at a wide range of initiator/resin weight ratios. Figure 3a presents the evolution of storage and loss modulus with time from these measurements. It can be observed that the crossover time of the storage and loss modulus, which is a commonly used indicator of gelation time, is lower at a higher initiator/resin weight ratio. The gelation times taken from these measurements are plotted against the initiator/resin weight ratio in Figure 3b. It can be seen that the gelation time decreases with an increasing initiator/resin weight ratio, with the decrease being more dramatic at lower ratios. This is in agreement with the previous observations made by Kuppusamy and Neogi [15]. To illustrate, according to Figure 3b, the gelation time decreases by 47% (from 4.30 h to 2.27 h)

in the initiator/resin weight ratio range of 1–1.5%, while the decrease is only 6% (from 1.21 h to 1.14 h) in the initiator/resin ratio range of 2.5–3%.

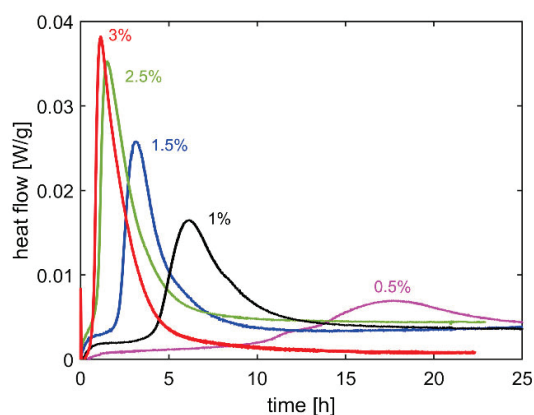


Figure 2. DSC curves of UPR-MEKP mixture for different MEKP/UPR weight ratios.

Table 1. Heat of cure calculated from the DSC curves and the degree of cure normalized with respect to the heat of cure of mixture with 3% initiator (table shows mean values. Only for 1.5%, ± one standard deviation is also given, as 3 specimens were tested at that ratio).

Initiator/Resin Weight Ratio	Heat of Cure [J/g]	Normalized Degree of Cure [-]
1%	149.7	0.58
1.5%	233.4 ± 2.9	0.90 ± 0.01
2.5%	249.1	0.96
3%	259.9	1

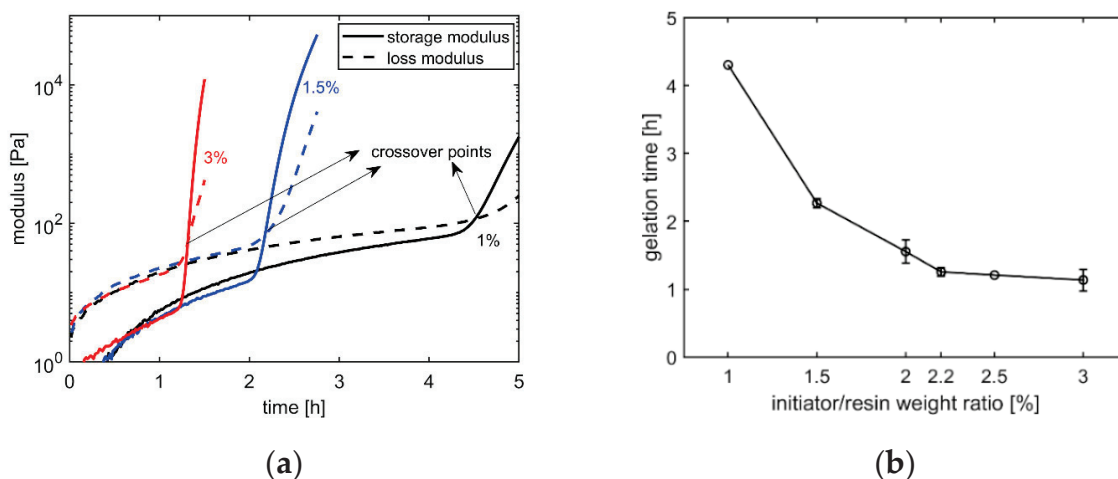


Figure 3. (a) The evolution of storage and loss modulus with time in rheometer tests and (b) gelation times of UPR-MEKP mixture for different MEKP/UPR weight ratios. Markers represent mean values and error bars represent ± one standard deviation (no error bar at 1% and 2.5%, since only 2 specimens were tested at these ratios).

3.2. Interphase Morphology

The interphase between the co-bonded PC and UPR-MEKP mixtures with initiator/resin weight ratios of 0.5%, 1.5%, 2.5%, and 3% can be seen in the optical micrographs shown in Figure 4. In all micrographs, it can be seen that the interphase comprises two regions, one with a dark color and the other one with a lighter color and a pit-like morphology. When the dark region is focused during microscopy analysis, a single phase is observed, signifying that the mixing is homogeneous. On the other hand, the other

region exhibits a nodular, phase-separated morphology resulting from the limited solubility of PC in the UPR–MEKP mixture [2]. The interphase thicknesses measured from the optical micrographs are plotted against the initiator/resin weight ratio in Figure 5a. Figures 4 and 5a both demonstrate that the interphase thickness decreases nonlinearly with the initiator/resin weight ratio.

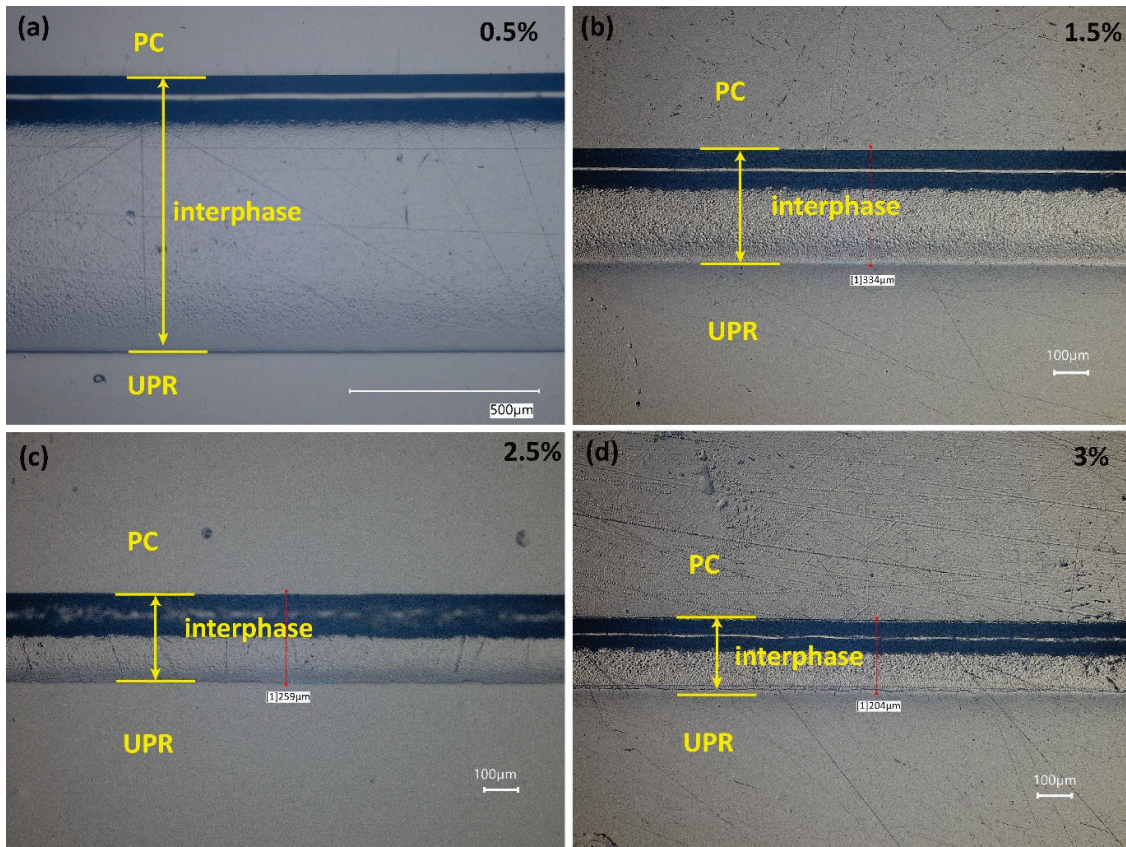


Figure 4. Optical micrographs of UPR–MEKP mixture for MEKP/UPR weight ratios of (a) 0.5%, (b) 1.5%, (c) 2.5%, and (d) 3%.

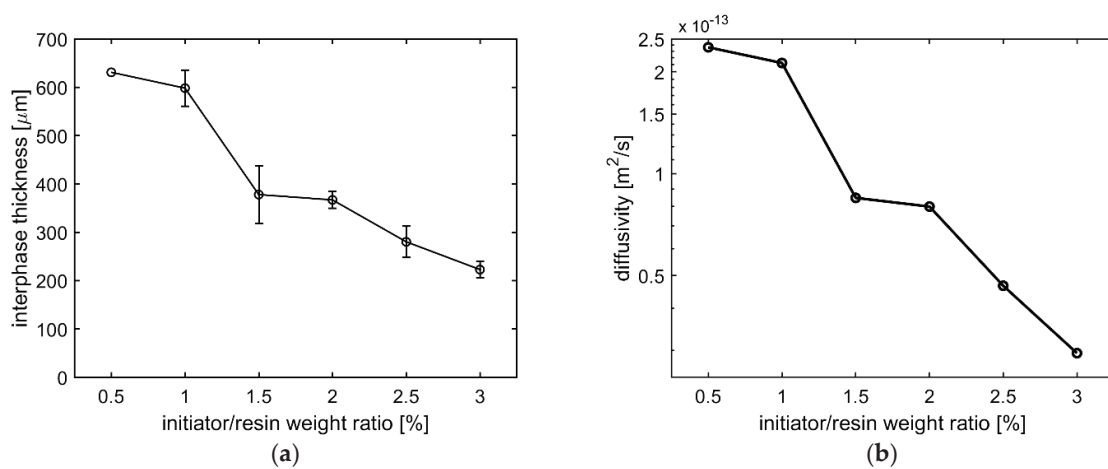


Figure 5. (a) Interphase thickness vs. MEKP/UPR weight ratio. Markers represent mean values and error bars represent \pm one standard deviation (no error bar at 0.5%, since only 2 specimens were tested at that ratio). (b) Diffusivity vs. initiator/resin weight ratio calculated based on Equation (1) using the gelation times in Figure 3b and interphase thicknesses in Figure 5a.

Interphase thickness is known to be influenced by the physical state of the TP (for instance, its temperature with respect to the glass transition temperature), the temperature-dependent viscosity, and the gelation time of the resin [2,4,10,19]. In this study, since the temperature and the TP material used were the same for experiments with different initiator/resin weight ratios, the first two factors were not effective in the observed interphase thickness vs. initiator ratio trend. Nevertheless, as also shown in Figure 3b, gelation time was highly reduced with an increasing initiator/resin weight ratios, which is considered to be the main reason for the decrease in interphase thickness. A decrease in gelation time allows less time for interdiffusion to take place, eventually leading to a lower interphase thickness [2]. In Figure 5a, the steepest decrease in the interphase thickness (by 37%, from 598 μm to 378 μm) can be observed in the initiator/resin weight ratio range of 1–1.5%, which corresponds to the range where the steepest decrease in gelation time took place in Figure 3b. The peak times of the DSC curves shown in Figure 2, which show a similar trend to the gelation times shown in Figure 3b, also agree with the trend of interphase thickness change with the initiator/resin ratio shown in Figure 5a. Although the degree of cure is low (0.58) for the mixture with initiator/resin weight ratio of 1% (Table 1), this is not thought to have contributed to the high interphase thickness via a lower viscosity of the mixture. This is because the interphase thickness evolution ceases at gelation [22,23], which takes place at a far lower degree of cure (0.15 [1] for the material system studied; it is assumed to be constant for different cure conditions based on [24,25]). Furthermore, at gelation, the complex viscosities of the resin–initiator mixtures with different initiator/resin weight ratios measured by the rheometer were in the range of 10–100 Pa·s for all initiator ratios, which is a small range considering the fast increase of viscosity at gelation. In future work, in situ interphase development should be studied for resin–initiator mixtures with different initiator/resin weight ratios to verify the cessation of interdiffusion for the material studied in this work.

Using the gelation times shown in Figure 3b and the interphase thicknesses shown in Figure 5a, the diffusivity of the resin into PC was calculated based on Equation (1), which is shown in Figure 5b. It can be seen that the diffusivity also decreases with an increase in the initiator/resin weight ratio, similar to the interphase thickness. In fact, the trends of diffusivity vs. initiator/resin weight ratio (Figure 5b) and interphase thickness vs. initiator/resin weight ratio (Figure 5a) can be seen to be quite similar. A decreasing diffusivity with an increasing initiator/resin weight ratio shows that higher ratios are less favorable for the diffusion of resin.

4. Conclusions

In this study, the effect of the initiator (MEKP) concentration of the resin–initiator mixture (initiator/resin weight ratio) on the interphase thickness of the co-bonded TP-TS (UPR-PC) was investigated for the first time. Gelation time was found to decrease with an increasing initiator concentration. Co-bonded polymers with higher initiator concentrations showed lower interphase thicknesses, which correlated well with the decrease seen in the gelation time. Investigating the effect of initiator concentration on the diffusion kinetics, the diffusivity of the resin was also seen to decrease with an increasing initiator concentration, showing a similar trend to that of the interphase thickness. Varying the initiator concentration helped us to exclusively investigate the effect of gelation time on the interphase thickness.

In future work, we recommend studying other TPs to check if the trend of decreasing interphase thickness with an increase in initiator concentration can be observed as well. Considering that the physical state of the thermoplastics and their affinity toward the thermoset resin both play a significant role in the interphase formation [2,8,9], investigating thermoplastics with different affinities and physical states is recommended. Furthermore, the method used for controlling the interphase thickness by varying the initiator concentration paves the way for investigating the effect of interphase thickness on the processing-induced deformations of the co-bonded TP-TS composites [3].

Author Contributions: Conceptualization, O.E., J.S.M.Z. and I.B.; methodology, O.E., J.S.M.Z. and I.B.; investigation, O.E. and J.S.M.Z.; resources, I.B.; writing—original draft preparation, O.E.; writing—review and editing, O.E., J.S.M.Z. and I.B.; supervision, I.B.; project administration, I.B.; funding acquisition, I.B. All authors have read and agreed to the published version of the manuscript.

Funding: This research was funded by the Netherlands Organization for Scientific Research (NWO) Veni Talent Programme with Grant Number 15897. The APC was covered by an author voucher.

Institutional Review Board Statement: Not applicable.

Informed Consent Statement: Not applicable.

Data Availability Statement: The data presented in this study are available on request from the corresponding author.

Acknowledgments: The authors would like to thank Elsemiek Verheijen for conducting gelation time measurements as part of her MSc thesis.

Conflicts of Interest: The authors declare no conflict of interest.



References

- Baran, I. Warpage prediction in over-infusion process of glass/polyester composite laminates. In Proceedings of the 21st ICCM International Conference on Composite Materials, Xi'an, China, 20–25 August 2017.
- Zanjani, J.S.M.; Baran, I.; Akkerman, R. Characterization of interdiffusion mechanisms during co-bonding of unsaturated polyester resin to thermoplastics with different thermodynamic affinities. *Polymer* **2020**, *209*, 122991. [CrossRef]
- Erartsin, O.; Zanjani, J.S.M.; Baran, I. Warpage of fiber-reinforced thermoset polymers co-bonded to thermoplastics. In Proceedings of the SAMPE EUROPE Conference and Exhibition 2021, Baden, Switzerland, 29–30 September 2021.
- Zanjani, J.S.M.; Baran, I. Co-bonded hybrid thermoplastic-thermoset composite interphase: Process-microstructure-property correlation. *Materials* **2021**, *14*, 291. [CrossRef] [PubMed]
- Nielsen, M.W. Prediction of Process Induced Shape Distortions and Residual Stresses in Large—With Application to Wind Turbine Blades. Ph.D. Thesis, Technical University of Denmark, Lyngby, Denmark, 2013.
- Haag, M.D. A Wind Turbine Blade Having an Erosion Shield. U.S. Patent 20180209400A1, 26 July 2018.
- Li, J.; Yao, X.; Liu, Y.; Cen, Z.; Kou, Z.; Dai, D. A study of the integrated composite material structures under different fabrication processing. *Compos. Part A Appl. Sci. Manuf.* **2009**, *40*, 455–462. [CrossRef]
- Deng, S.; Djukic, L.; Paton, R.; Ye, L. Thermoplastic—Epoxy interactions and their potential applications in joining composite structures—A review. *Compos. Part A Appl. Sci. Manuf.* **2015**, *68*, 121–132. [CrossRef]
- Vandi, L.J.; Hou, M.; Veidt, M.; Truss, R.; Heitzmann, M.; Paton, R. Interface diffusion and morphology of aerospace grade epoxy co-cured with thermoplastic polymers. In Proceedings of the 28th Congress of the International Council of the Aeronautical Sciences 2012 (ICAS 2012), Brisbane, Australia, 23–28 September 2012; pp. 1–9.
- Zweifel, L.; Brauner, C. Investigation of the interphase mechanisms and welding behaviour of fast-curing epoxy based composites with co-cured thermoplastic boundary layers. *Compos. Part A Appl. Sci. Manuf.* **2020**, *139*, 106120. [CrossRef]
- Farooq, U.; Heuer, S.; Teuwen, J.; Dransfeld, C. Effect of a Dwell Stage in the Cure Cycle on the Interphase Formation in a Poly(ether imide)/High Tg Epoxy System. *ACS Appl. Polym. Mater.* **2021**, *3*, 6111–6119. [CrossRef]
- Zweifel, L.; Brauner, C.; Teuwen, J.; Dransfeld, C. In Situ Characterization of the Reaction-Diffusion Behavior during the Gradient Interphase Formation of Polyetherimide with a High-Temperature Epoxy System. *Polymers* **2022**, *14*, 435. [CrossRef] [PubMed]
- Twigg, G.; Poursartip, A.; Fernlund, G. Tool-part interaction in composites processing. Part II: Numerical modelling. *Compos. Part A Appl. Sci. Manuf.* **2004**, *35*, 135–141. [CrossRef]
- Voleppe, Q.; Ballout, W.; Van Velthem, P.; Bailly, C.; Pardoën, T. Enhanced fracture resistance of thermoset/thermoplastic interfaces through crack trapping in a morphology gradient. *Polymer* **2021**, *218*, 123497. [CrossRef]
- Kuppusamy, R.R.P.; Neogi, S. Influence of curing agents on gelation and exotherm behaviour of an unsaturated polyester resin. *Bull. Mater. Sci.* **2013**, *36*, 1217–1224. [CrossRef]
- Ramis, X.; Salla, J.M. Effect of the initiator content and temperature on the curing of an unsaturated polyester resin. *J. Polym. Sci. Part B Polym. Phys.* **1999**, *37*, 751–768. [CrossRef]
- Vilas, J.L.; Laza, J.M.; Garay, M.T.; Rodríguez, M.; León, L.M. Unsaturated polyester resins cure: Kinetic, rheologic, and mechanical-dynamical analysis. 1. Cure kinetics by DSC and TSR. *J. Appl. Polym. Sci.* **2001**, *79*, 447–457. [CrossRef]
- Cook, W.D.; Lau, M.; Mehrabi, M.; Dean, K.; Zipper, M. Control of gel time and exotherm behaviour during cure of unsaturated polyester resins. *Polym. Int.* **2001**, *50*, 129–134. [CrossRef]
- Ballout, W.; Coulon, B.; Janssens, Y.-A.; Van Velthem, P.; Sclavons, M.; Magnin, D.; Pardoën, T.; Bailly, C. Quantitative characterization of interdiffusion at the resin–resin and resin–prepreg interphases of epoxy systems processed by model SQ-RTM. *Polym. Eng. Sci.* **2016**, *56*, 1061–1069. [CrossRef]
- Campbell, F.C. Thermoset resins: The glue that holds the strings together. *Manuf. Processes Adv. Compos.* **2004**, 63–101. [CrossRef]
- Crank, J. *The Mathematics of Diffusion*, 2nd ed.; Oxford University Press: Oxford, UK, 1979; ISBN 0-19-853344-6.

22. Rajagopalan, G.; Narayanan, C.; Gillespie, J.W.; McKnight, S.H. Diffusion and reaction of epoxy and amine in polysulfone-transport modeling and experimental validation. *Polymer* **2000**, *41*, 8543–8556. [CrossRef]
23. Lestriez, B.; Chapel, J.P.; Gérard, J.F. Gradient interphase between reactive epoxy and glassy thermoplastic from dissolution process, reaction kinetics, and phase separation thermodynamics. *Macromolecules* **2001**, *34*, 1204–1213. [CrossRef]
24. Baran, I.; Akkerman, R.; Hattel, J.H. Material characterization of a polyester resin system for the pultrusion process. *Compos. Part B Eng.* **2014**, *64*, 194–201. [CrossRef]
25. Ramis, X.; Salla, J.M. Time-temperature transformation (TTT) cure diagram of an unsaturated polyester resin. *J. Polym. Sci. Part B Polym. Phys.* **1997**, *35*, 371–388. [CrossRef]

Article

Research on Void Dynamics during In Situ Consolidation of CF/High-Performance Thermoplastic Composite

Qinghua Song ¹, Weiping Liu ^{1,*}, Jiping Chen ¹, Dacheng Zhao ², Cheng Yi ¹, Ruili Liu ¹, Yi Geng ¹, Yang Yang ¹, Yizhu Zheng ¹ and Yuhui Yuan ¹

¹ Composites Center, COMAC Shanghai Aircraft Manufacturing Co., Ltd., Shanghai 201324, China; songqinghua@comac.cc (Q.S.); chenjiping@comac.cc (J.C.); yicheng@comac.cc (C.Y.); liuruili@comac.cc (R.L.); gengyi@comac.cc (Y.G.); yangyang@comac.cc (Y.Y.); zhengyizhu@comac.cc (Y.Z.); yuanyuhui@comac.cc (Y.Y.)

² College of Material Science and Engineering, Donghua University, Shanghai 201620, China; 18817831097@163.com

* Correspondence: liuweiping@comac.cc

Abstract: Automated fiber placement (AFP) in situ consolidation of continuous CF/high-performance thermoplastic composite is the key technology for efficient and low-cost manufacturing of large thermoplastic composites. However, the void in the in situ composite is difficult to eliminate because of the high pressure and the short consolidation time; the void content percentage consequently is the important defect that determines the performance of the thermoplastic composite parts. In this paper, based on the two-dimensional Newtonian fluid extrusion flow model, the void dynamics model and boundary conditions were established. The changes of the void content percentage were predicted by the cyclic iteration method. It was found that the void content percentage increased gradually along the direction of the layers' thickness. With the increasing of the laying speed, the void content percentage increased gradually. With the increasing of the pressure of the roller, the void content percentage gradually decreased. When the AFP speed was 11 m/min and the pressure of the compaction roller reached 2000 N, the void content percentage of the layers fell below 2%. It was verified by the AFP test that the measured results of the layers' thickness were in good agreement with the predicted results of the model, and the test results of the void content percentage were basically equivalent to the predicted results at different AFP speeds, which indicates that the kinetic model established in this paper is representative to predict the void content percentage. According to the metallographic observation, it was also found that the repeated pressure of the roller was helpful to reduce the void content percentage.

Keywords: thermoplastic composites; automated fiber placement; in situ consolidation; void content; processing parameters

Citation: Song, Q.; Liu, W.; Chen, J.; Zhao, D.; Yi, C.; Liu, R.; Geng, Y.; Yang, Y.; Zheng, Y.; Yuan, Y. Research on Void Dynamics during In Situ Consolidation of CF/High-Performance Thermoplastic Composite. *Polymers* **2022**, *14*, 1401. <https://doi.org/10.3390/polym14071401>

Academic Editors: Somen K. Bhudolia and Sunil Chandrakant Joshi

Received: 21 February 2022

Accepted: 22 March 2022

Published: 30 March 2022

Publisher's Note: MDPI stays neutral with regard to jurisdictional claims in published maps and institutional affiliations.



Copyright: © 2022 by the authors. Licensee MDPI, Basel, Switzerland. This article is an open access article distributed under the terms and conditions of the Creative Commons Attribution (CC BY) license (<https://creativecommons.org/licenses/by/4.0/>).

1. Introduction

Automated fiber placement (AFP) in situ consolidation of continuous CF/high-performance thermoplastic composite (Figure 1) [1–5], which is based on continuous fiber-reinforced thermoplastic prepreg, positioning, laying-up, and consolidation by automatic placement equipment according to the requirements of the mathematical model, components are manufactured in the thickness direction by layer accumulation, and the manufacturing is accomplished when the thickness reaches the designed value; thus, the traditional manufacturing process of first laying-up and then curing in the autoclave is no longer needed [6–12]. This technology will bring about an unprecedented change in composite components' manufacturing, especially in the aerospace applications of composite materials.

The thermoplastic composite has outstanding characteristics, which are different from the traditional thermosetting composite, such as high toughness, high strength, fast forming, and recyclability [13–18]. It is a new type of composite material with high performance, low cost, and environmental protection and becomes an ideal material for civil aircraft

structure components manufacturing, which can reduce weight effectively and improve processing efficiency [19,20]. Airbus, Boeing, etc., have developed special AFP equipment, which was applied to manufacture the aircraft secondary bearing structure.

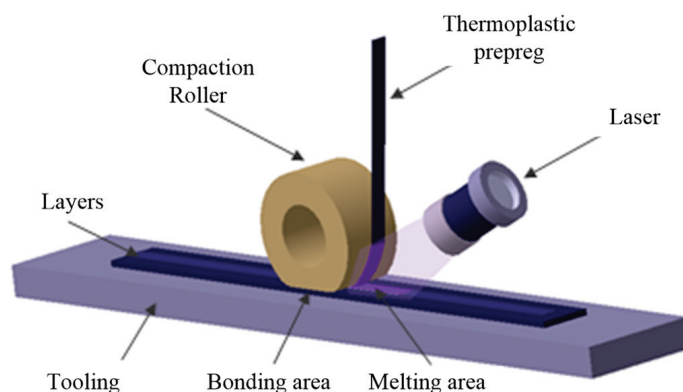


Figure 1. Schematic diagram of AFP in situ consolidation.

Although the application of thermoplastic composite materials in civil aircraft has gradually aroused an upsurge in research upsurge abroad and in the future, the large-scale application of thermoplastic composite materials in civil aircraft is the inevitable result of the development of advanced materials and the progress of manufacturing technology. Nevertheless, the continuous fiber-reinforced thermoplastic composite in situ consolidation technology has not been applied in the manufacturing of civil aircraft structural components effectively at present [21,22]. The reason is the significant difference between the AFP in situ consolidation process of thermoplastic composite and the AFP of thermosetting composite. The AFP of thermosetting composite is a process of shaping, only completing the pre-forming of structural components, and the forming is completed mainly in the autoclave. Despite the fact that the process of AFP in situ consolidation of thermoplastic composite is very complex, the high melting point and melting viscosity of the high-performance thermoplastic resin matrix requires high temperature and pressure; thus, the requirements for manufacturing equipment are more demanding.

In addition, the residual air bubbles or dissolved air, as well as water or other volatiles will lead to an increase of the void content of the structural components manufactured by in situ consolidation. Void content is one of the most important defects that determines the structural component properties of thermoplastic composites. Consequently, it is necessary to reduce the void content of the layers as much as possible, to improve the mechanical properties [23–26].

The void content of thermoplastic composites has been studied by many scholars. Qinghao He [27] quantified the adverse effects of voids on 3D-printed continuous fiber-reinforced polymer composites. Vipin Kumar [28] produced a large-scale multimaterial by additive manufacturing (AM) undergoing compression molding (CM) to produce high-performance thermoplastic composites reinforced with short carbon fibers. Zhu Liu [29] established a microscale unit cell with a random distribution of fibers, interfaces, and voids based on the random sequential adsorption algorithm to investigate the quantitative effects of void content on the strength and modulus under the loading of transverse tension.

In the process of in situ consolidation, the prepreg and the substrate are melted in the bonding area under the heating of the heat source, and pressure is applied through the compaction roller, then the layers are bonded together in the bonding area and finally cooled and consolidated simultaneously, to realize the in situ consolidation. As a result, the void content due to the reasons mentioned above can be reduced by increasing the pressure under the compaction roller. In the forming process of thermosetting composite, due to the low viscosity of the resin matrix, Darcy's law can be used to describe the process of resin impregnation. In contrast, the melting viscosity of the thermoplastic resin matrix is high, and the resin and the fiber are not relatively independent during the forming

process; they generally move with the external pressure [30]. Hence, Balasubramanyam [31] and Barnes [32] thought that the fiber, resin, and voids in fiber-reinforced thermoplastic composite can be approximated as a uniform continuum, and this is a more valuable way to describe the flow of the resin as the flow of the continuum in the process of forming. Tierney [33] also pointed out that, compared with Darcy's law model, they believed that the squeeze flow model was more suitable for analyzing the change of void content in the processing of thermoplastic composites. Muhammad [34] established a two-dimensional Newtonian fluid squeeze flow model for the processing of thermoplastic composites.

In this paper, the objective of this work was establishing a two-dimensional Newtonian fluid squeeze model to describe the void dynamics during the in situ consolidation process. The variety of the void content with the processing parameters during the in situ consolidation process was predicted through the cyclic iterative method.

2. Void Dynamics Model

2.1. Void Formation Mechanisms

In the in situ consolidation process, voids are usually inter-laminar and intra-laminar. The intra-laminar voids mainly contribute to the following aspects: (1) softening of the resin matrix, (2) primary voids in the prepreg, and (3) dissolved air. The inter-laminar voids are mainly caused by the fact that the intimate contact between layers has not reached to one (Figure 2) [35]; hence, there exists residual air between the layers.

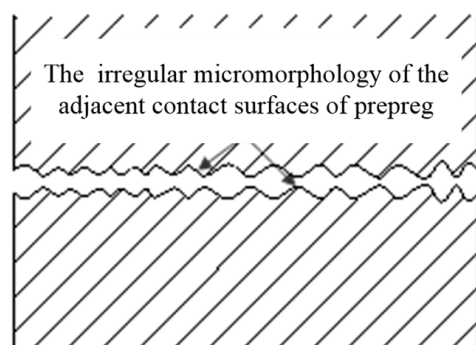


Figure 2. Schematic diagram of the contact between two layers.

During the in situ consolidation process, the prepreg and the substrate are melted by the heat source first and bonded together by the compaction roller, and then, the bonded layers are cooled and crystallized. Before the pressure is applied, the resin matrix of the prepreg experiences softening, thermal expansion, and melting in a short heating time; at the same time, the dissolved volatiles and the air remaining in the prepreg are released, and the voids in the layer begin to appear simultaneously. Subsequently, the pressure of the compaction roller plays a significant role in both preventing the voids' growth and eliminating the inter-laminar and intra-laminar voids (Figure 3).

In Figure 3, the initial thickness of the layers is h_i , the width is w_i , x is the width direction, y is the direction of movement, z is the thickness direction, and the placement speed is v . As the compaction roller passes through the bonding area, the thickness of the layer is reduced to h_f and the width changes to w_f . The consolidation pressure compresses the voids and changes the thickness and width of the layers. Since the layer dimension in the y direction is much larger than the x and z directions, the y direction flow may be neglected. Due to the high matrix resin viscosity, the flow may be treated as creeping motion. In other words, the inertial effects can be neglected. Since the y direction flow can be neglected, the in situ consolidation process can be treated as a sequence of two-dimensional squeeze flow problems in the $x - z$ plane. The squeeze speed in the z direction is governed by the placement speed v .

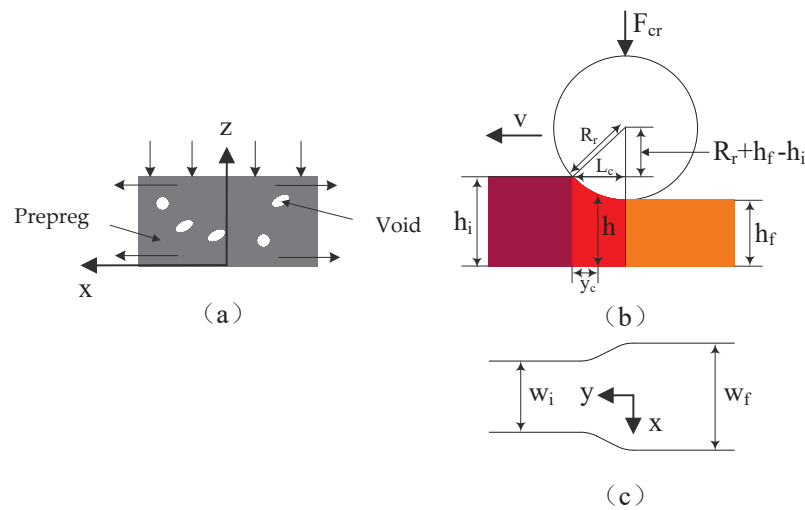


Figure 3. Geometric sketch of the in situ consolidation process: (a) The thermoplastic prepreg layer; (b) The pressure is applied by compaction roller; (c) The prepreg is widened under the pressure.

From Figure 3, the contact length L_c between the compaction roller and prepreg can be described as:

$$L_c = [R_r^2 - (R_r - h_i + h_f)^2]^{1/2} \tag{1}$$

Similarly, the height h of the layer may be expressed as:

$$h = R_r + h_f - [R_r^2 - (L_c - y_c)^2]^{1/2} \tag{2}$$

where y_c represents the distance between the contact point of the prepreg and the front of the compaction roller (the position where the thickness of the layer is h).

Differentiating both sides with respect to time t and equating dy_c/dt to the placement velocity v , we can obtain:

$$\dot{h} = \frac{dh}{dt} = -v \frac{[R_r^2 - (R_r - h + h_f)^2]^{1/2}}{(R_r - h + h_f)} \tag{3}$$

Equation (3) is an expression of the closing speed \dot{h} at the layer interface.

Besides, the width w of the prepreg during in situ consolidation can be obtained by the average speed of the free boundary condition of the prepreg, which can be expressed as:

$$\frac{dw}{dt} = \frac{1}{h} \left[\int_0^h v_x dz \right]_{x=w} \tag{4}$$

where v_x is the speed of the squeeze flow of the resin matrix under the pressure of the compaction roller.

By integrating the contact length between the compaction roller and the prepreg and the real-time width of the prepreg, the pressure on the layers during the in situ consolidation process can be determined as:

$$F_c = 2 \int_0^{L_c} \int_0^w P(x, y) dx dy \tag{5}$$

where $P(x, y)$ is the pressure distribution under the compaction roller.

Therefore, in this work, the in situ consolidation process was simplified as a two-dimensional Newtonian fluid squeeze flow process under the pressure provided by the

compaction roller. In this process, the changes of the layer thickness and width were considered, and the change of the layer length was neglected. Simultaneously, the changes of the height and width were related to the squeeze flow velocity of the resin and the pressure distribution under the compaction roller. Thus, the macro void dynamics model, containing the squeeze flow model of the resin and the pressure distribution model, is proposed. To solve the model, the velocity boundary condition and the pressure boundary condition were also considered. Finally, the void dynamics model was solved by the cyclic iteration method to predict the variety of layer void content during the in situ consolidation process. The flowchart of the proposed models is shown in Figure 4.

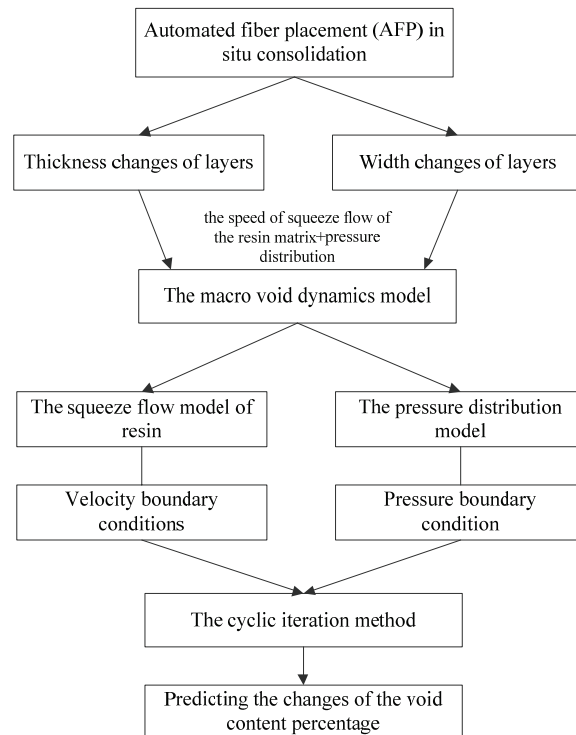


Figure 4. The flowchart of the proposed models.

2.2. Void Dynamics Model

The momentum equations that govern the flow of the continuum under the compaction roller, neglecting the inertia and body terms, can be written as:

$$\frac{\partial \rho}{\partial t} + \frac{\partial}{\partial x}(\rho v_x) + \frac{\partial}{\partial z}(\rho v_z) = 0 \tag{6}$$

$$\frac{\partial P}{\partial x} = \frac{\partial}{\partial z} \left(\mu \frac{\partial v_x}{\partial z} \right) \tag{7}$$

where the density of the continuum is given by ρ , the viscosity of the resin matrix by μ , the compaction roller pressure by P , and the placement velocity by v .

By integrating Equation (7) with respect to z :

$$\mu \left[\frac{\partial v_x}{\partial z} \right] = z \frac{dP}{dx} + C_1(x) \tag{8}$$

Integrating Equation (8) once more with respect to z , the flow velocity model of resin squeeze during in situ consolidation can be obtained:

$$v_x(z) = v_x(0) + \frac{dP}{dx} \int_0^z \frac{\xi}{\mu} d\xi + C_1(x) \int_0^z \frac{1}{\mu} d\xi \tag{9}$$

Integrating Equation (6) in the thickness direction from 0 to h , the governing equation describing the instantaneous thickness of the layer can be obtained:

$$h \frac{\partial \rho}{\partial t} + \int_0^h \left[\frac{\partial}{\partial x} (\rho v_x) \right] dz + \rho(v_z) \Big|_{z=0}^{z=h} = 0 \tag{10}$$

The velocity v_z at $z = 0$ is 0 and at $z = h$ is close to the closing speed between the two bounding surfaces, so assuming $v_z = \dot{h}$. Thus, substituting variables and changing the order of integration and differentiation in Equation (10), the following expression can be obtained:

$$h \frac{\partial \rho}{\partial t} + \frac{\partial}{\partial x} \left(\rho \int_0^h v_x dz \right) + \rho \dot{h} = 0 \tag{11}$$

Substituting the velocity variable in Equation (9) into Equation (11) to eliminate the velocity variable:

$$h \frac{\partial \rho}{\partial t} + \frac{\partial}{\partial x} \left(\rho \int_0^h \left[v_x(0) + \frac{dP}{dx} \int_0^z \frac{\xi}{\mu} d\xi + C_1(x) \int_0^z \frac{1}{\mu} d\xi \right] dz \right) + \rho \dot{h} = 0 \tag{12}$$

where h is the instantaneous thickness of the layer; $C_1(x)$ and $v_x(0)$ can be obtained from two velocity boundary conditions. Because Equation (12) is a second-order integral equation, so two pressure boundary conditions are also needed.

Defining a non-dimensional density ρ^* of layer:

$$\rho^* = \frac{\rho}{\rho_f} \tag{13}$$

where ρ^* is the initial density of prepreg. Therefore, Equation (12) can be modified as:

$$h \frac{\partial \rho^*}{\partial t} + \frac{\partial}{\partial x} \left(\rho^* \int_0^h \left[v_x(0) + \frac{dP}{dx} \int_0^z \frac{\xi}{\mu} d\xi + C_1(x) \int_0^z \frac{1}{\mu} d\xi \right] dz \right) + \rho^* \dot{h} = 0 \tag{14}$$

Equation (14) is considered as the governing equation of the pressure distribution model under the compaction roller during in situ consolidation.

2.3. Boundary Conditions

Two velocity boundary conditions and two pressure boundary conditions are needed for the solution of the void dynamics model.

2.3.1. Velocity Boundary Conditions

Barone J.R. [36] established a velocity boundary condition between the fluid and solid in the compression molding process, since the contact between the prepreg and the compaction roller during the in situ consolidation process is similar to compression molding; therefore, based on Barone’s theory, the velocity boundary condition in this work was described by a friction factor boundary condition and expressed as:

$$\frac{\partial v_x}{\partial z} = \frac{K}{\mu} (v_x)_{z=h} \tag{15}$$

The ratio $\frac{K}{\mu}$ determines the type of boundary condition. If the friction at the layer interface is very high, i.e., $\frac{K}{\mu} \rightarrow \infty$, this is equivalent to a no-slip boundary condition, then $(v_x)_{z=h}$ is expressed as:

$$(v_x)_{z=h} = 0 \tag{16}$$

On the other hand, if the friction is expected to be very low, i.e., $\frac{\kappa}{\mu} \rightarrow 0$, this is equivalent to a perfect boundary condition:

$$\frac{\partial v_x}{\partial z} = 0 \quad (17)$$

2.3.2. Pressure Boundary Condition

If the layers are assumed to be unrestricted along the width direction, then the appropriate boundary condition would be to impose atmospheric pressure at the free surfaces, which could be expressed as:

$$P_{\text{edges}} = P_{\text{atm}} \quad (18)$$

Since the width of the compaction roller is not less than the layer, so it was assumed that the pressure of compaction roller along the layers' width direction is uniformly applied.

3. Materials and Methods

3.1. Material

The material selected in this paper was CF/PPS prepreg with a width of 6.35 mm. Relevant parameters required for the model simulation are given in Table 1. Figure 5 is the metallographic micrograph (Metalloscope, OLYMPUS, Tokyo, Japan) of the void content of the initial prepreg. It could be calculated that the initial void content of the prepreg was about 0.8% by the metallographic observation.

Table 1. Relevant parameters required for the model prediction.

Parameters	Symbol	Value
Number of layers	N	6
Compaction pressure, N	F_{cr}	500–1000
Density of prepreg, $\text{g}\cdot\text{cm}^{-3}$	ρ	1.62

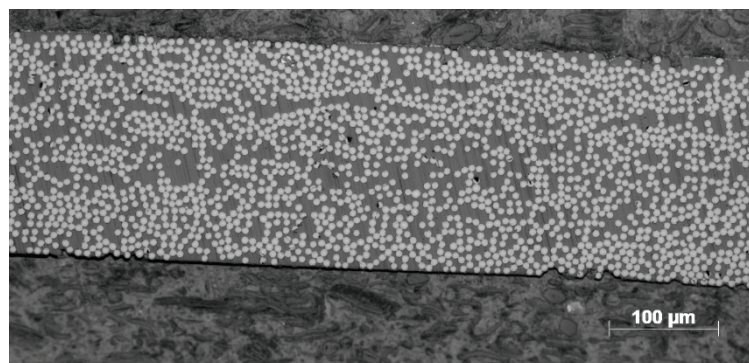


Figure 5. Metallographic micrograph of initial prepreg.

3.2. Model Prediction Methods

Figure 6 is the computational flowchart of void dynamics model prediction. Before prediction, the ratio h_f/h_i of the layer compressed by the roller can be assigned an initial value, and a roller pressure F_{cr} was applied. Then, the geometric parameters of the layer under the pressure of the compaction roller can be obtained according to Equations (1) and (2); the change in thickness of the layers can be derived from Equation (3); the squeeze flow speed of the resin matrix along the width direction can be predicted using Equation (9); accordingly, combined with Equation (4), the variety of prepreg width in the process of in situ consolidation was obtained; the variety of the layer in the y direction was neglected, that is assuming the prepreg dimension is constant along the length direction. Therefore, the changes of the layer volume in the process of in situ consolidation can be predicted by combining the change of the layer width and thickness. In addition, the resin matrix was

assumed to be incompressible, so according to the law of the conservation of mass, the density of the layer can be obtained. Since the density and void content of the original prepreg are known, the change in the void content of the layer during the in situ consolidation process can be solved.

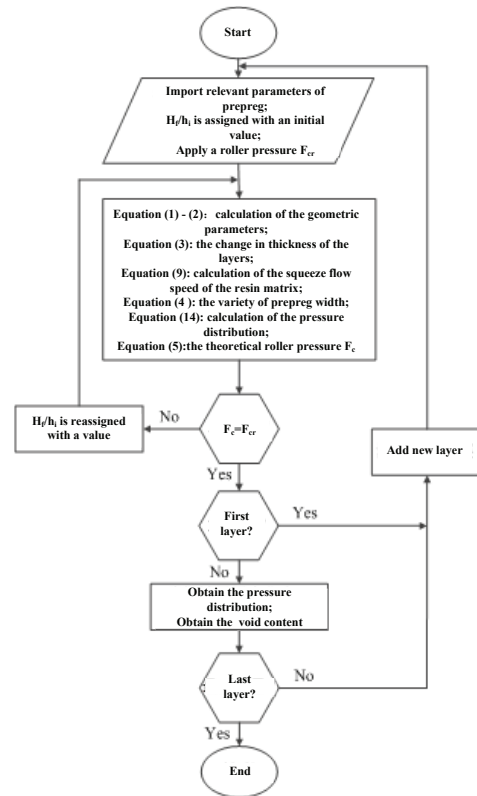


Figure 6. Calculation flowchart of the void dynamics model.

The pressure distribution under the compaction roller can be obtained by Equation (14), and then, combined with Equation (5), the theoretical roller pressure F_c can be calculated. Comparing the theoretical roller pressure F_c with the actual roller pressure F_{cr} , if they are not equal, h_f/h_i will be reassigned and recalculated until $F_c = F_{cr}$. When the roller leaves the bonding area, the layers are exposed to the air, and the real-time variety of layers' void content and density can still be solved by the void dynamics model. The method mentioned above was used to predict the void content of each layer.

3.3. Experimental Section

3.3.1. Thickness Measurement

Three specimens with a size of $400 \times 400 \text{ mm}^2$ were manufactured at different placement parameters to verify the void dynamics model, as shown in Table 2. The prepreg was unidirectional carbon-fiber-reinforced polyphenylene sulfide composite (CF/PPS). Six layers of prepreg were laid on the flat tooling under the 4 tows of the AFP equipment shown in Figure 7 (M·Torres, Navarra, Spain). The main purpose of this test was to verify the effect of different placement speeds on the void content of the layer.

Table 2. Manufacturing parameters of the specimens.

No.	Placement Speed ($\text{m} \cdot \text{min}^{-1}$)	Laser Power (kW)	Pressure (N)
1	11	6	1000
2	13	6	1000
3	15	6	1000



Figure 7. The equipment 4 tows of the AFP.

During the manufacturing process of the specimens, the thickness vernier caliper (Mitutoyo, Kawasaki City, Japan) was used to measure the thickness of each layer of prepreg after placement, as shown in Figure 8.

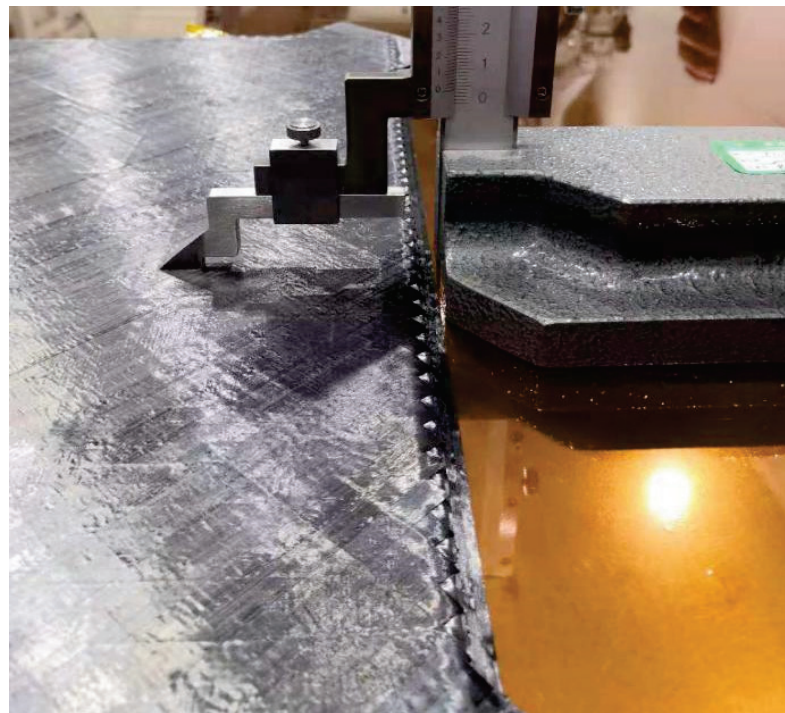


Figure 8. The thickness vernier caliper.

3.3.2. Metallographic Observation

Metallographic observation samples were prepared by cutting, inlaying, grinding, polishing, and other processes according to the GB 3365-2008 standard (Figure 9).

Figure 8. The thickness vernier caliper.

3.3.2. Metallographic Observation

Metallographic observation samples were prepared by cutting, inlaying, grinding, polishing, and other processes according to the GB 3365-2008 standard (Figure 9).

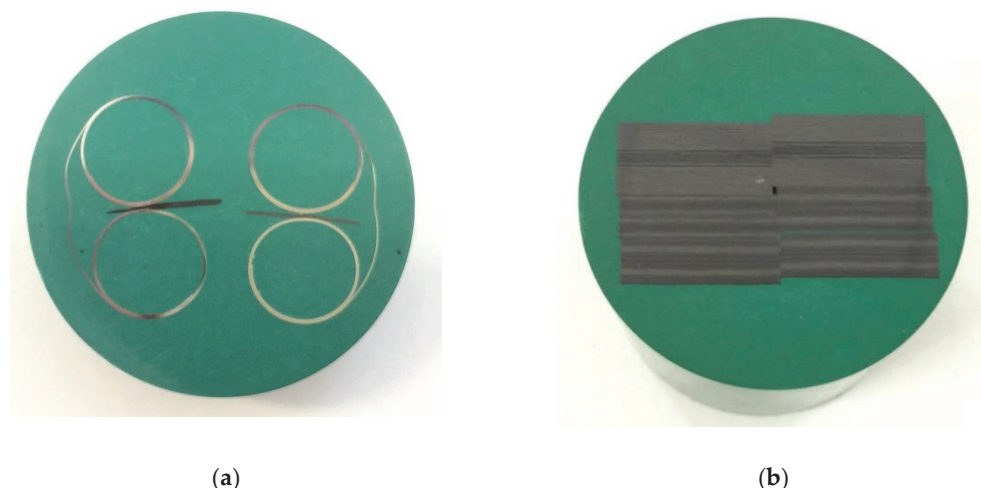


Figure 9. The metallographic observation samples: (a) one layer; (b) six layers.

4. Results and Discussion

4. Results and Discussion

4.1. Model Prediction

4.1.1. Model Prediction. The through-thickness void content distribution with the change of prediction. The compaction roller pressure was set to a value of 6 kW, and the placement speed to 11 m/min,

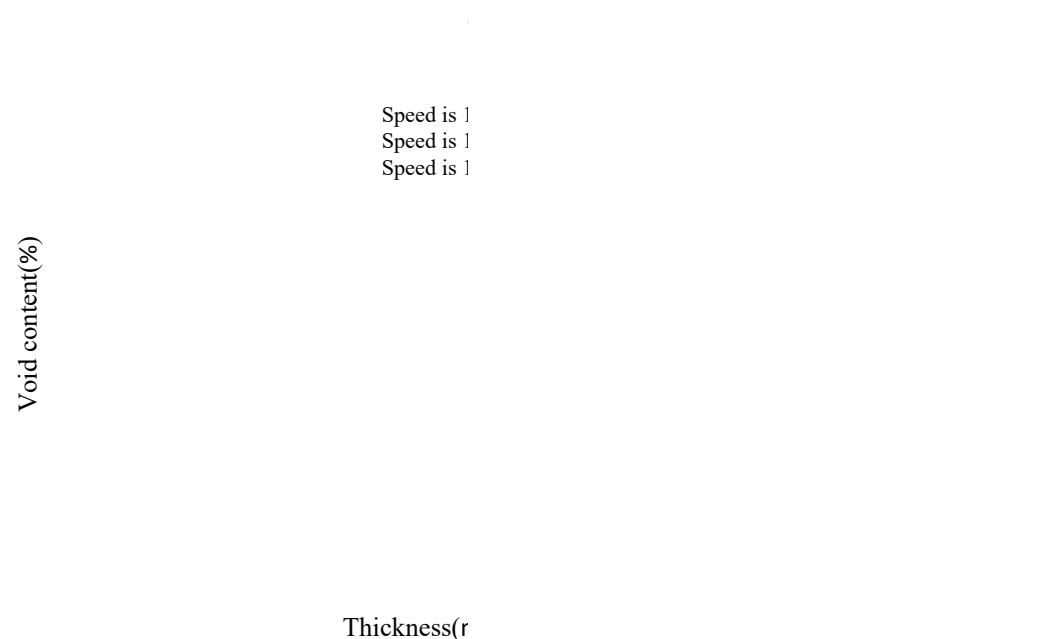


Figure 10. Through-thickness void content distribution.

Figure 10. Through-thickness void content

It can be seen from Figure 10 that placement speed had a significant effect on the void content. The results of the temperature field [37] and inter-laminar bonding strength analysis [35] indicated that the consolidation of the layers resulted in a combination of temperature and pressure. On the one hand, at higher velocities, the heat input was significantly reduced, and the insufficient heat led to a high resin viscosity, which restricted the elimination of the voids; on the other hand, a higher placement speed reduced the pressure application time, leading to a higher void content.

Figure 10 also indicates that the void content of the bottom layer and the upper layers along the thickness direction was slightly higher. On account of the direct contact between the first layer and the mold, resulting in the lower heating temperature that caused the high resin viscosity, the void content was consequently high. When laying the second layer, the

temperature increased and the resin viscosity decreased due to the heat insulation of the first layer, so the void content decreased. However, due to the heat accumulation effect of the layer, the temperature of the layers gradually increased with the increase of the layers' thickness, which was responsible for the extremely high temperature of the layers even if the roller left the bonding area. Furthermore, if the temperature of the layers was still above the melting point, the molten resin would dissolve the air, and thus, the void content would increase.

Figure 11 shows that the void content varied with the laser power and compaction roller pressure. The placement speed was set to 11 m/min.

Figure 11. Void content varies with laser power and compaction roller pressure.

It can be seen from Figure 11 that the void content was relatively high when the pressure under the compaction roller was small. The reason lied in that during the process of in situ consolidation, due to the resin being in a molten state in the bonding area when the pressure roller had not passed through, the voids inside the layer were not constrained by external pressure and began to expand, resulting in a higher void content; when the roller passed through the bonding area, the pressure under the compaction roller was not enough to discharge most of the voids; on the other hand, due to the high pressure inside the voids, the binding force of the voids decreased when the roller left the bonding area, so the voids began to expand, leading to a higher void content. The result in the figure also indicates that a lower the layer void content could be obtained by increasing the pressure under the compaction roller; however, the layer void content could be reduced to less than 2% only when the pressure under the compaction roller reached 2000 N or higher. In addition, increasing the heating power reduced the effect of pressure on the void content. This was due to the viscosity of the resin increasing due to sufficient heat input at a high laser power, which was beneficial to eliminate the voids; additionally, it is manifest from the figure that the void content of the layers at a maximum laser power of 6 kW and a small roller pressure was still greater than that at a heating power of 4 kW with larger roller pressure, which indicates that the void content can be attributed to the coupling effect of

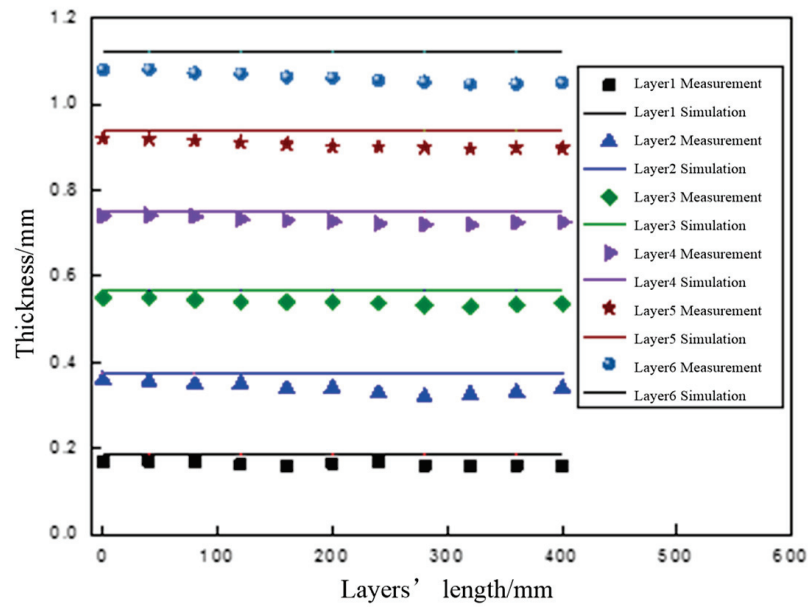
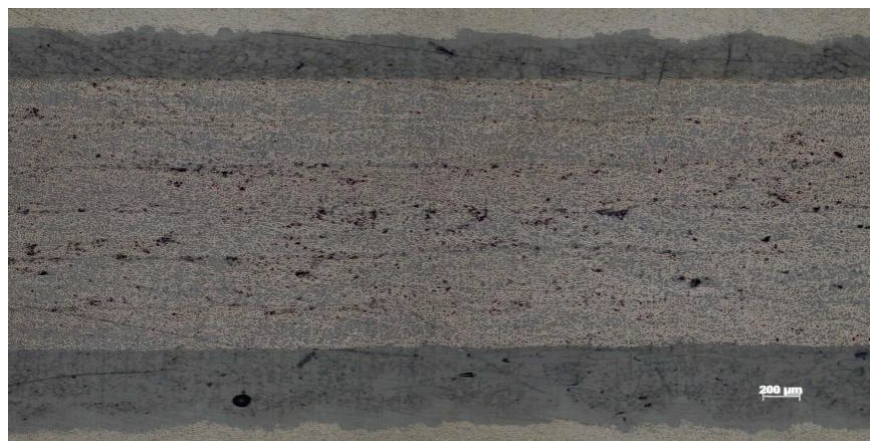


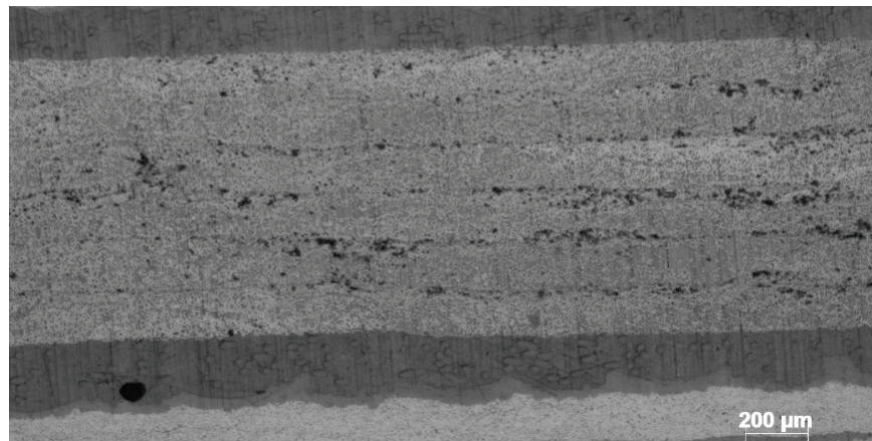
Figure 12. The comparison of the measured values and predicted values (speed is 11 m/min).

Figure 13 shows images of the void content of the specimens manufactured by the process parameters shown in Table 2. It is obvious that void content of the layers gradually increased with the increasing placement speed. Nonetheless, none of the three figures show the trend of higher void content in the bottom layer, as shown in Figure 10. The reason for the preliminary analysis was that the first layer in Figure 10 was only rolled once by the compaction roller, so the void content of the first layer was high. On the contrary, with the increasing of the number of layers, the number of times that the bottom layer prepreg was rolled increased. After the repeated pressure of the roller, the void content of the bottom layer accordingly decreased, whereas the number of rolls on the upper layer reduced less gradually; therefore, the void content increased gradually with the increase of the number of layers. The results of the metallographic test thereby were similar to the simulation results shown in Figure 6, except for the bottom prepreg.

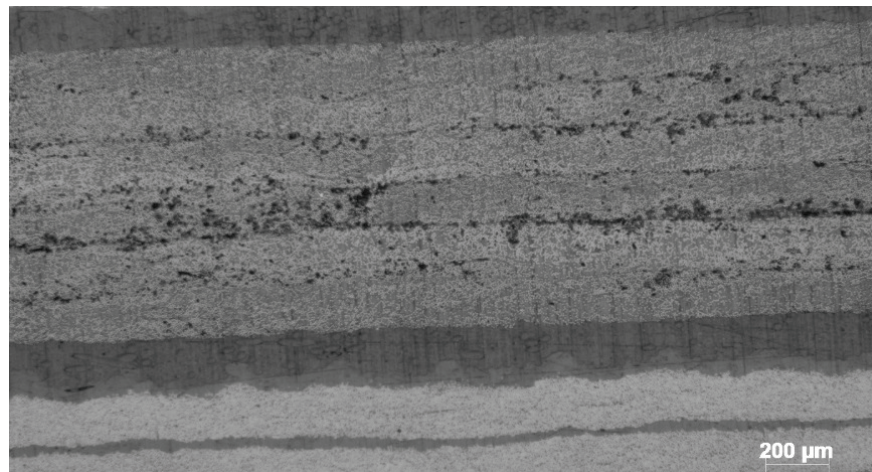


(a)

Figure 13. Cont.



(b)



(c)

Figure 13. The images of the void content of the specimens manufactured at different speeds (laser power is 6 kW, pressure is 1000 N): (a) speed is 11 m/min; void content is 3.1%; (b) speed is 13 m/min; void content is 4.2%; (c) speed is 15 m/min; void content is 5.5%.

Figure 14 shows the comparison between the void content test results of the specimens manufactured by different placement speeds and the simulation results of the model. It is obvious that the void content showed an increasing trend when the placement speed increased. It can also be seen that the test results were equivalent to the simulation results, which proves that the dynamics model established in this work had a certain representativeness for predicting the void content of the layer, but the prediction results were always slightly lower than the measurement results, which was related to the simplification of the model, such as the change of the layer along the length direction being neglected; however, the fact is that during the in situ consolidation process, the layer would become longer along the length direction, which would result in a higher predicted density; thereby, the void content obtained by the model was slightly lower.

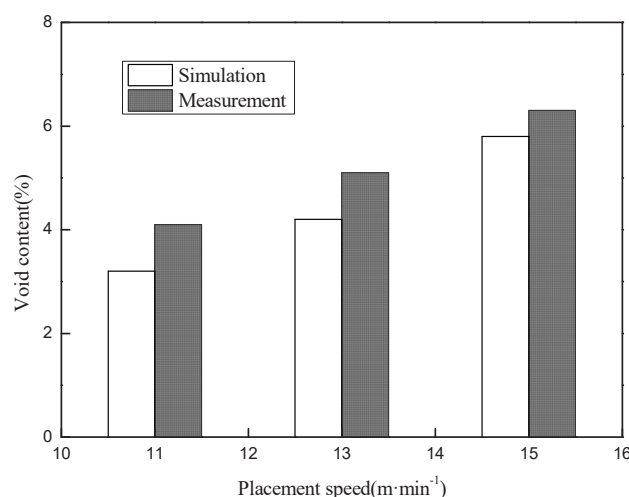


Figure 14. The void content varies with placement speed (laser power is 6 kW, pressure is 1000 N).

5. Conclusions

A void dynamics model and boundary conditions during the process of in situ consolidation were established based on the two-dimensional Newtonian fluid squeeze flow model. The cyclic iteration method was used to predict the variety of the void content during the process of in situ consolidation. The experimental measurement results of the layers' thickness were in good agreement with the prediction results, and the void content test results of the specimens manufactured at different placement speeds were equivalent to the prediction results, which means the void dynamics model established in this work has certain representativeness for predicting the void content; the metallographic observation results also indicated that the repeated pressure of the compaction roller was beneficial to reduce the void content.

Author Contributions: Conceptualization, Q.S. and W.L.; methodology, Q.S. and D.Z.; software, J.C.; validation, Q.S. and C.Y.; formal analysis, Q.S. and Y.G.; data curation, Q.S.; writing—original draft preparation, Q.S.; writing—review and editing, Y.Y. (Yang Yang); visualization, R.L.; supervision, Y.Y. (Yuhui Yuan); project administration, Y.Z.; funding acquisition, J.C. All authors have read and agreed to the published version of the manuscript.

Funding: This research was funded by the Shanghai Collaborative Innovation Center of High Performance Fibers and Composites (Province-Ministry Joint) (Project#: X12812101/022), the Shanghai Sailing Program (Project#: 19YF1417100), the Commercial Aircraft Corporation of China, Ltd. (COMAC) innovation funds (Project#: Y20GS14), and the Project of China's Ministry of Science and Technology (Project#: 2020YFB0311500).

Institutional Review Board Statement: Not applicable.

Informed Consent Statement: No applicable.

Data Availability Statement: The data presented in this study are available upon request from the corresponding author.

Conflicts of Interest: The authors declare no conflict of interest.

References

- Han, Z.; Sun, S.; Li, W.; Zhao, Y.; Shao, Z. Experimental Study of the Effect of Internal Defects on Stress Waves during Automated Fiber Placement. *Polymers* **2018**, *10*, 413. [CrossRef] [PubMed]
- Sun, S.; Han, Z.; Fu, H.; Jin, H.; Dhupia, J.S.; Wang, Y. Defect Characteristics and Online Detection Techniques During Manufacturing of FRPs Using Automated Fiber Placement: A Review. *Polymers* **2020**, *12*, 1337. [CrossRef] [PubMed]
- Sebaey, T.A.; Bouhrara, M.; O'Dowd, N. Fibre Alignment and Void Assessment in Thermoplastic Carbon Fibre Reinforced Polymers Manufactured by Automated Tape Placement. *Polymers* **2021**, *13*, 473. [CrossRef] [PubMed]
- Boon, Y.D.; Joshi, S.C.; Bhudolia, S.K. Review: Filament Winding and Automated Fiber Placement with In Situ Consolidation for Fiber Reinforced Thermoplastic. *Polymer Composites. Polymers* **2021**, *13*, 1951. [CrossRef] [PubMed]

5. Xiao, R.; Shi, J.; Xiao, J. Study of Allowable Interlaminar Normal Stress Based on the Time–Temperature Equivalence Principle in Automated Fiber Placement Process. *Polymers* **2021**, *13*, 4180. [CrossRef]
6. Comer, A.J.; Ray, D.; Obande, W.O.; Jones, D.; Lyons, J.; Rosca, I.; Higgins, R.M.O.; McCarthy, M.A. Mechanical characterisation of carbon fibre-PEEK manufactured by laser-assisted automated-tape-placement and autoclave. *Compos. Part A Appl. Sci. Manuf.* **2015**, *69*, 10–20. [CrossRef]
7. Grouve, W.J.B.; Warnet, L.; Rietman, B.; Visser, R.; Akkerman, R. Optimization of the tape placement process parameters for carbon-PPS composites. *Compos. Part A Appl. Sci. Manuf.* **2013**, *50*, 44–53. [CrossRef]
8. Negin, A.; Cedric, C.; John, G.; David, R.M.; Natalie, L.J. Transmission laser welding of amorphous and semi-crystalline poly-ether-ether-ketone for applications in the medical device industry. *Mater. Des.* **2010**, *31*, 4823–4830.
9. Qureshi, Z.; Swait, T.; Scaife, R.; El-Dessouky, H. In situ consolidation of thermoplastic prepreg tape using automated tape placement technology: Potential and possibilities. *Compos. Part B Eng.* **2014**, *66*, 255–267. [CrossRef]
10. Bhandari, S. Feasibility of Using 3D Printed Molds for Thermoforming Thermoplastic Composites. Master’s Thesis, The University of Maine, Orono, ME, USA, 2017.
11. Ebrahim, O.; Ulf, G.B.G.P. Porosity analysis of carbon fibre-reinforced polymer laminates manufactured using automated fibre placement. *J. Mater. Res. Technol.* **2020**, *54*, 1217–1231.
12. Eichenhofer, M.; Wong, J.C.H.; Ermanni, P. Exploiting cyclic softening in continuous lattice fabrication for the additive manufacturing of high performance fibre-reinforced thermoplastic composite materials. *Compos. Sci. Technol.* **2018**, *164*, 248–259. [CrossRef]
13. Showaib, E.A.; Elsheikh, A.H. Effect of surface preparation on the strength of vibration welded butt joint made from PBT composite. *Polymer Test.* **2020**, *83*, 106319. [CrossRef]
14. Elsheikh, A.H.; Elaziz, M.A.; Ramesh, B.; Egiza, M.; Al-Qaness, M.A. Modeling of drilling process of GFRP composite using a hybrid random vector functional link network/parasitism-predation algorithm. *J. Mater. Res. Technol.* **2021**, *14*, 298–311. [CrossRef]
15. Kamal, A.; Ashmawy, M.S.S.; Algazzar, A.M.; Elsheikh, A.H. Fabrication techniques of polymeric nanocomposites: A comprehensive review. *Proc. Inst. Mech. Eng. Part C J. Inst. Mech. Eng. Sci.* **2021**, *1*, 1–19. [CrossRef]
16. Stelea, L.; Filip, I.; Lisa, G.; Ichim, M.; Drobotă, D.; Sava, C.; Augustin, M. Characterisation of Hemp Fibres Reinforced Composites Using Thermoplastic Polymers as Matrices. *Polymers* **2022**, *14*, 481. [CrossRef]
17. Zhi, Q.; Li, Y.; Shu, P.; Tan, X.; Tan, C.; Liu, Z. Double-Pulse Ultrasonic Welding of Carbon-Fiber-Reinforced Polyamide 66 Composite. *Polymers* **2022**, *14*, 714. [CrossRef]
18. Guessasma, S.; Abouzaid, K.; Belhabib, S.; Bassir, D.; Nouri, H. Interfacial Behaviour in Polymer Composites Processed Using Droplet-Based Additive Manufacturing. *Polymers* **2022**, *14*, 1013. [CrossRef]
19. Dilimulati, A.; Duan, Y.-G.; Li, D.-C.; Lu, Z.L. Overview of In-situ Curing Manufacturing Technology for Resin Matrix Composites. *J. Mater. Eng.* **2011**, *2011*, 84–90.
20. Lee, K.-S.; Shin, M.-S.; Lee, J.-Y.; Ryu, J.-J.; Shin, S.-W. Shear bond strength of composite resin to high performance polymer PEKK according to surface treatments and bonding materials. *J. Adv. Prosthodont.* **2017**, *9*, 350–357. [CrossRef]
21. Rizzolo, R.H.; Walczyk, D.F. Ultrasonic consolidation of thermoplastic composite prepreg for automated fiber placement. *J. Thermoplast. Compos. Mater.* **2016**, *29*, 1480–1497. [CrossRef]
22. Shadmehri, F.; Hoa, S.V.; Fortin-Simpson, J.; Ghayoor, H. Effect of in situ treatment on the quality of flat thermoplastic composite plates made by automated fiber placement (AFP). *Adv. Manuf. Polym. Compos. Sci.* **2018**, *4*, 41–47. [CrossRef]
23. Dell’Anna, R.; Lionetto, F.; Montagna, F.; Maffezzoli, A. Lay-Up and Consolidation of a Composite Pipe by In Situ Ultrasonic Welding of a Thermoplastic Matrix Composite Tape. *Materials* **2018**, *11*, 786. [CrossRef] [PubMed]
24. Patoua, J.; Bonnaire, R.; Luyckerb, E.D. Influence of consolidation process on voids and mechanical properties of powdered and commingled carbon/PPS laminates. *Compos. Part A* **2019**, *117*, 260–275. [CrossRef]
25. Miao, Q.; Dai, Z.; Ma, G.; Niu, F.; Wu, D. Effect of consolidation force on interlaminar shear strength of CF/PEEK laminates manufactured by laser-assisted forming. *Compos. Struct.* **2021**, *266*, 113779. [CrossRef]
26. Oromiehie, E.; Gain, A.K.; Donough, M.J. Fracture toughness assessment of CF-PEEK composites consolidated using hot gas torch assisted automated fibre placement. *Compos. Struct.* **2022**, *279*, 114762. [CrossRef]
27. He, Q.H.; Wang, H.J.; Fu, K.K. 3D printed continuous CF/PA6 composites: Effect of microscopic voids on mechanical performance. *Compos. Sci. Technol.* **2020**, *191*, 108077. [CrossRef]
28. Kumar, V.; Alweka, S.P.; Kunc, V. High-performance molded composites using additively manufactured preforms with controlled fiber and pore morphology. *Addit. Manuf.* **2021**, *37*, 101733. [CrossRef]
29. Liu, Z.; Lei, Y.; Zhang, X. Effect Mechanism and Simulation of Voids on Hygrothermal Performances of Composites. *Polymers* **2022**, *14*, 901. [CrossRef]
30. Clancy, J.G.; Peeters, D.; Oliveri, V.; Jones, D.; O’Higgins, R.M.; Weaver, P.M. A study of the influence of processing parameters on steering of carbon Fibre/PEEK tapes using laser-assisted tape placement. *Compos. Part B Eng.* **2019**, *163*, 243–251. [CrossRef]
31. Balasubramanyam, R.; Jones, R.S.; Wheeler, A.B. Modelling transverse flows of reinforced thermoplastic composite materials. *Composites* **1989**, *20*, 33–37. [CrossRef]
32. Barnes, J.A.; Cogswell, F.N. Transverse flow processes in continuous fibre reinforced thermoplastic composites. *Composites* **1989**, *20*, 38–42. [CrossRef]

33. Tierney, J.; Gillespie, J.W. Modelling of in situ strength development for thermoplastic composites tow placement process. *J. Compos. Mater.* **2006**, *40*, 1487–1506. [CrossRef]
34. Khan, M.A.; Mitschang, P.; Schledjewski, R. Tracing the void content development and identification of its effecting parameters during in situ consolidation of thermoplastic tape material. *Polym. Polym. Compos.* **2010**, *18*, 1–15.
35. Song, Q.; Liu, W.; Liu, X.; Liu, K.; Yang, Y.; Chen, J. Interlaminar bonding strength for thermoplastic composite in an in-situ consolidation process. *Acta Aeronaut. Astronaut. Sin.* **2019**, *40*, 259–267.
36. Barone, J.R.; Schmidt, W.F.; Liebner, C.F.E. Compounding and molding of polyethylene composites reinforced with keratin feather fiber. *Compos. Sci. Technol.* **2005**, *65*, 683–692. [CrossRef]
37. Song, Q.; Liu, W.; Chen, J.; Liu, K.; Yang, Y. Temperature field for laser heating of carbon fiber reinforced polyphenyl sulphide matrix composite in an automated fiber placement process. *Acta Mater. Compos. Sin.* **2019**, *36*, 283–292.

Article

Behaviour of Rectangular Hollow Thin Ply Carbon Thermoset and Thermoplastic Composite Tubes Subjected to Bending

Somen K. Bhudolia ^{1,*}, Goram Gohel ¹, Durga Vasudevan ², Kah Fai Leong ¹ and Pierre Gerard ³

¹ School of Mechanical and Aerospace Engineering, Nanyang Technological University, 50, Nanyang Avenue, Singapore 639798, Singapore; goram001@e.ntu.edu.sg (G.G.); mkfleong@ntu.edu.sg (K.F.L.)

² Technical University of Munich Asia, 25 International Business Park Rd, Singapore 609916, Singapore; dv.527699@tum-asia.edu.sg

³ Groupement de Recherche de Lacq, Arkema, Route Départementale 817, BP 34, 64170 Lacq, France; pierre.gerard@arkema.com

* Correspondence: somenkum001@e.ntu.edu.sg

Abstract: Tubular composites are widely used in many industrial applications, and there is need to use new material and reliable manufacturing processes to improve the performance and process aspects. The current research presents a detailed study to understand the flexure response of rectangular tubular composites based on thin ply carbon fibres and Elium[®] resin. Another aim was to understand the failure mechanisms of novel tubular thermoplastic composite systems and carry out a baseline comparison with Epoxy-based tubular systems. In the current research, a bladder-assisted resin transfer moulding process was used to manufacture hollow thermoplastic composite tubes, and the bending behaviour of thin ply carbon (TPC) composite parts with novel Elium[®] (EL) and Epoxy (EP) resin as the matrix material was studied using a detailed experimental study. A testing method with optimized support span and a saddle was used to carry out three-point bending tests on the tubular composite structures. The TPC/EL composite tubes have shown 10% higher bending strength, with a noticeable increase in deformation due the presence of extended plasticity attributes for acrylic Elium resin. Failure mechanisms studied with the detailed microscopic investigation have shown severe catastrophic failure for epoxy-based composite tubes; however, acrylic Elium[®]-based composite tubes have shown different damage modes such as fibre splitting, resin infragmentation, and fibre resin-interfacial cracking.

Keywords: hollow composite tubes; thermoplastic resin; bending; failure mechanisms

Citation: Bhudolia, S.K.; Gohel, G.; Vasudevan, D.; Leong, K.F.; Gerard, P. Behaviour of Rectangular Hollow Thin Ply Carbon Thermoset and Thermoplastic Composite Tubes Subjected to Bending. *Polymers* **2022**, *14*, 1386. <https://doi.org/10.3390/polym14071386>

Academic Editor: Miguel Ángel López Manchado

Received: 15 March 2022

Accepted: 26 March 2022

Published: 29 March 2022

Publisher's Note: MDPI stays neutral with regard to jurisdictional claims in published maps and institutional affiliations.



Copyright: © 2022 by the authors. Licensee MDPI, Basel, Switzerland. This article is an open access article distributed under the terms and conditions of the Creative Commons Attribution (CC BY) license (<https://creativecommons.org/licenses/by/4.0/>).

1. Introduction

Hollow composite structures are extensively used in many engineering applications such as marine, automobile, aerospace industries and especially in sporting equipment [1,2]. From an engineering point of view, fibre provides outstanding properties in an in-plane direction (x , y -axis). Additionally, the resin system plays a crucial role in the thickness direction (in the z -axis direction) and provides support to hold the fibres to reduce delamination between the layers. The type of resin also determines the manufacturing processes, pressure, and temperature limits. The appropriate usage of both is very significant to achieve a composite system with optimized mechanical properties. Hollow composite structures can be manufactured by different processes. The most widely used processes are filament winding process, pultrusion process, and bladder resin transfer moulding process [3]. Inflatable bladder-assisted resin transfer moulding (B-RTM) was chosen for better surface finishing quality and uniform thickness [4].

Thin carbon fibre plies are available in thicknesses from 0.12 mm to 0.5 mm, and as per the European patent, thin plies are the ones with a thickness of one-sixth of the thicker plies. For the thin plies spreading, the first ply is oriented in one specific direction, and the next layer is placed with respect to the first ply direction. Composites that are manufactured

from thin plies possess excellent capabilities in both static and dynamic load cases to overcome microcracking and delamination challenges [5–8]. In carbon-based composites, the structures fail at 2% strain, but micro-cracks initiate at an early strain level of 0.5% [5]. Thermoplastic resins are challenging to use due to the higher associated temperature curing cycles [9,10]. However, they offer improved damping [11,12], higher crack critical energy rates to arrest crack propagations [13,14], reshapability [15], impact and damage tolerance [16–21], the ability to be welded [22–25], and are recyclable [26,27]. Elium[®] liquid resin is a recent invention from ARKEMA to manufacture thermoplastic composite parts. It is available in a liquid state with low viscosity and possesses significantly higher impact, fracture toughness, and vibration damping attributes [12,18,22–25,28–35].

Dejun Yin et al. studied the flexural response of carbon fibre-reinforced tubes filled with Al foam and showed that the bending stiffness and the energy-absorbing capability of the tubes with the addition of foam fillers increased, and the increase was more substantial with the increase in the foam density of the metal [36]. In another study, the performance of flax-reinforced epoxy composite tubes is studied by adopting the four-point bending test [37]. Libo Yan et al. demonstrated from their study that the results at the tubular and the flat scale are very similar to brittle catastrophic failure. It was also concluded from their study that the increase in thickness leads to a simultaneous increase in the load and deflection to failure characteristics. Ali Amiri et al. carried out research investigating the benefits of hybridization of the carbon fibres with the flax fibres [38]. They showed that there was an increase in the load-carrying ability with hybridization, but it cannot be fully determined whether the added benefits are due to the addition of flax fibres or the higher thickness in the case of the hybridized tube. M. Stefanovska et al. investigated the flexural performance of glass/epoxy tubular composites manufactured using the filament winding process [39]. The effect of winding angle was studied, and the bending stiffness was found to be increased with the decrease in the winding angle. The failure mechanisms involved matrix cracking, fibre splitting, and inter- and intra-ply delamination. Zhenyu Wu et al. have investigated the gradient effect on the bending response of over-braided composite tube with two layers of $\pm 40^\circ$ layers [40]. The layer that was in direct contact with the loading pin had a detrimental effect on the flexural properties and the damage mechanisms. Bhudolia et al. investigated the bending response of carbon acrylic Elium[®] composite tubes and compared its performance with epoxy-based composite parts [12,41,42]. The flexural properties were very similar, barring the ability of the acrylic-based composite to take larger displacement before the failure, but the details of the failure mechanisms were not studied. The current research presents a detailed study to understand the flexure response of rectangular tubular composites based on thin ply carbon fibres and Elium[®] resin. It was also intriguing to develop a detailed interpretation of the failure mechanisms of novel tubular thermoplastic composite systems and carry out a baseline comparison with Epoxy-based tubular systems; hence, a detailed microscopic investigation is also carried out.

2. Materials and Manufacturing

Composite tubes are manufactured using a combination of uni-directional thin ply (144 gsm) and C-Ply[™] BX30 bi-angle ply (150 gsm) (Refer Figure 1a,b) [41]. Thermoplastic Elium[®] 150 acquired from Arkema, France was used as a matrix system. Elium[®] resin has a viscosity of 100 cP and is in a liquid state at room temperature (RT) [18,43–45]. On the other hand, similar to thermoplastic composites, the same fibre architecture but with epoxy sizing was used to manufacture the thermoset composite tubes. Epoxy (AM-8937 A/B) resin used as a thermoset matrix was obtained from Wells Advanced Materials Co. Ltd, Shanghai, China. Figure 1c,d show the individual layer thicknesses and the angles under the microscope.

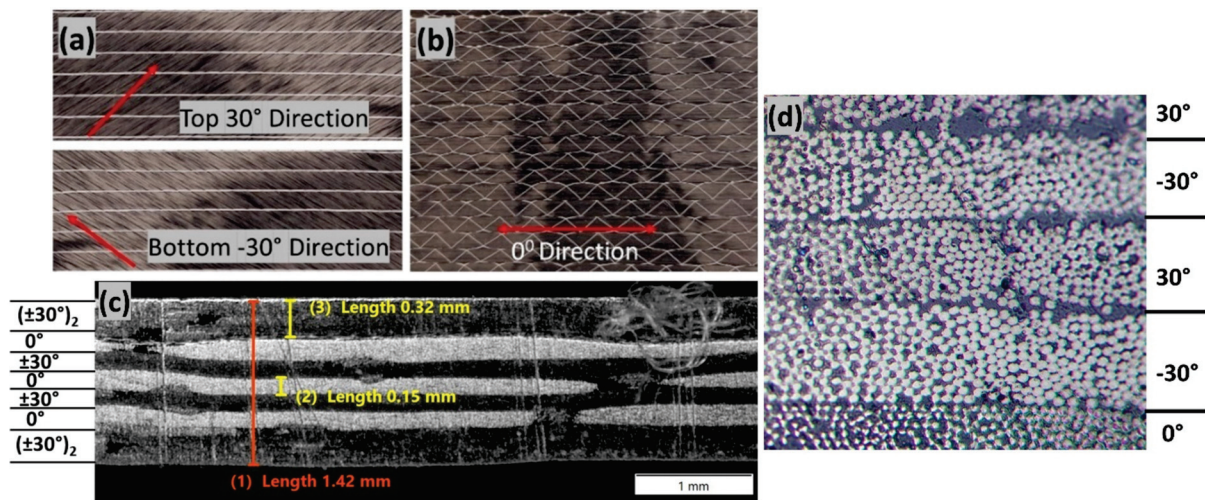


Figure 1. (a) BX 30 C-plyTM fabric (b) UD (0°) fabric (c,d) microscopic images showing the individual layers and the cross-sectional details.

Thermoset and thermoplastic composite tubes were manufactured using the bladder resin transfer moulding (BRTM) manufacturing process. Several samples were manufactured to optimize the injection and bladder pressure with thin ply fabric tubes impregnated with either thermoplastic or thermoset resin. The overall process steps of B-RTM are shown in Figure 2.

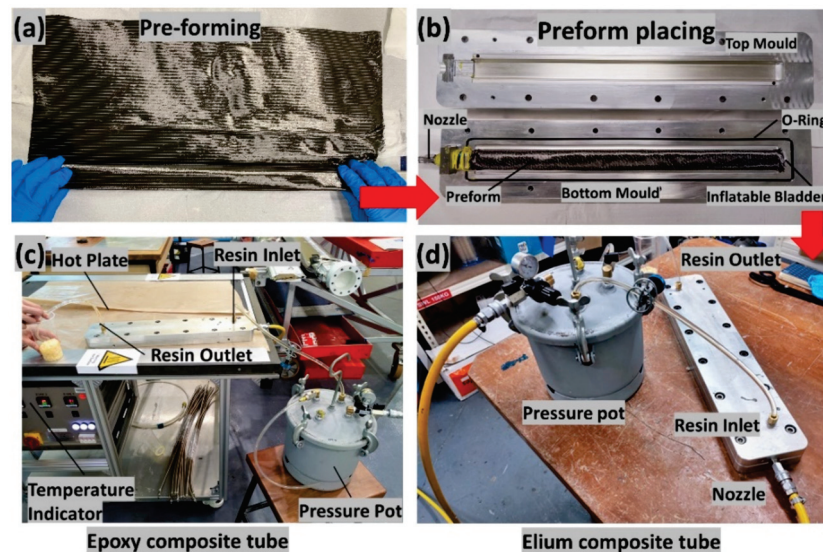


Figure 2. B-RTM manufacturing steps and set-up.

A two-part aluminium mould was used for the manufacturing of tubular composites. For manufacturing of the tubular composite, the first step was mould preparation; the mould release was applied onto the mould surface for ease of the demoulding of the manufactured part, followed by dry fibre preforming. Preforming of dry fibres was carried out over the mandrel to obtain the fibre layup of $[(\pm 30^\circ)_2 / 0^\circ / \pm 30^\circ / 0^\circ / \pm 30^\circ / 0^\circ / (\pm 30^\circ)_2]$ (refer Figure 2a). Once the preform was made, it was taken out of the mandrel and was placed into the mould, as shown in Figure 2b. The mould was then closed, and the bladder was initially inflated (3 bar) to properly compact the fibres over the mould. Then, the resin was injected (2.8 bar) into the mould at the required injection pressure. Once the part was filled, the injection was stopped, and the bladder pressure was further increased for consolidation (5 bar) to allow the excess resin to squeeze out and to obtain the uniform thickness and V_f (54%) of the part. To manufacture the thermoplastic composite part,

injection was carried out at room temperature (RT), followed by post-curing at 65 °C for 1 hr (refer Figure 2c). For epoxy composite, the injection was carried out with mould at 50 °C (refer Figure 2d). Once the part was filled, the mould temperature was raised to 100 °C for curing for 10 min, followed by cooling to RT and demoulding. The final thickness (t) and the fibre volume fraction (V_f) of the manufactured composites tubes were 1.4 ± 0.2 mm and $54 \pm 0.93\%$, respectively. Additionally, ASTM D792 [46] and ASTM D2734-09 [47] tests were carried out, and the porosity for the manufactured tubes was found to be less than 1% and was used for mechanical testing. The two different configurations investigated are Thin ply_Carbon/Elium[®] (TPC/EL) composite and Thin ply_Carbon/Epoxy (TPC/EP) composite.

3. Experimental Setup

The flexural properties of the composite rectangular tube were investigated following the ASTM D 790 [8] standard. The three-point bending flexural testing of the composite tube using the saddle support was performed using an Instron 5569 machine (refer Figure 3a). As shown in Figure 3a, the saddles were positioned onto the rollers of the fixture, and tubes were placed into the saddles and are aligned. The dimensions of the saddle and the loading pin are shown in Figure 3b. The load (kN) and displacement (mm) data are acquired from the Bluehill 4 software from the machine. The bending response of the tubular composite sample is highly dependent on the support span of the specimen during the test. Currently, the widely used ASTM D790 standard is suitable for flat laminate testing and may not be directly applicable to tubular geometries. However, many researchers have used a similar standard to determine the fundamental flexural response of the tubular structures [39,40,48]. Support span is essentially required to be optimized for the geometry under consideration to avoid shear and localized bending and crushing effects. These effects dominate when a shorter support span is used during the testing and must be eradicated. Damage analysis was carried out on the failed samples under flexure using an optical microscope (OLYMPUS SZX7) to understand the failure mechanism.

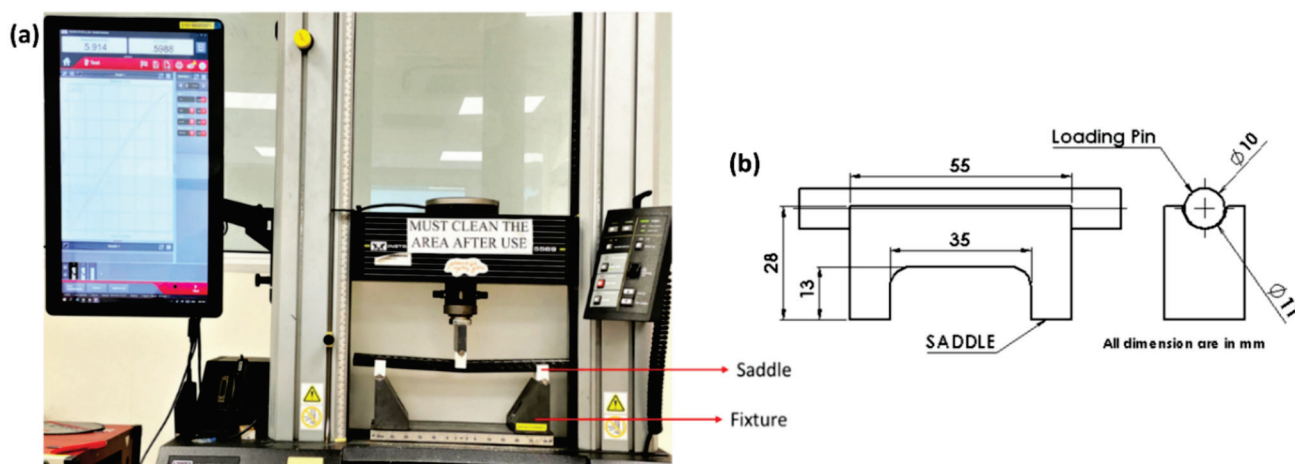


Figure 3. (a) Flexure experimental test set-up with saddle supports for testing tubular composites (b) dimensions of the saddle and the loading pin.

4. Results and Discussion

For flexural testing, two different configurations were investigated: TPC/EL and TPC/EP composite tube. During flexure testing of the tubular structures, the cracks were propagated in both transverse and longitudinal directions. Flexure tests were carried out to calculate the bending stresses and the modulus of the manufactured tubular configurations. It was also important to understand the differences in the flexural behaviour along with the failure mechanisms of the composite tubes manufactured with Elium[®] and Epoxy resin systems. One of the key factors that has a major effect on the flexural behaviour

of the composite structures is the support span used during the testing. Following the standard [49], the maximum recommended span to thickness ratio of 60:1 was chosen in the current investigation. A larger support span was used because it eliminates the possible shear effect, considering the peculiar nature of the geometry under consideration as well the concentrated and undesired localized bending.

The maximum thickness of the manufactured tube under consideration was 1.4 mm, and hence the first tests were carried out with a support span of 90 mm with an overhanging length of 30 mm on each side of the support rollers. This overhanging length was always ensured to be at least 10% of the support span following the ASTM D790 [49]. The initial study was carried out using one TPC/EL configuration, and once the optimised support span was defined, the comparison study was carried out for different tubular configurations using the optimised support span. Two strategies were considered to optimise the real bending scenario of the composite tube: (1) by increasing the support span (refer Figure 4a,c) and (2) using saddles. Saddles, as shown in Figure 4d, were used to reduce the concentrated effect of the roller pins on the composite tube created during the bending rather than creating a global bending behaviour. Support spans of 90 mm, 150 mm, 200 mm, and 300 mm were used in the current investigation, with a minimum overhanging length of at least 10% of the corresponding configuration. The load–displacement curves for the different configurations of TPC/EL composite tubes are shown in Figure 5a. The tubes tested with a support span of 90 mm and 150 mm without using a saddle have shown a peak load of 2.62 kN and 2.85 kN, respectively, with a significant flexural displacement of up to 30 mm. The tube with a 200 mm support span without using a saddle has shown 3.1 kN with a flexural displacement of up to 8.5 mm. The tube tested without saddle and 300 mm support span has shown more linear behaviour until the first major failure with a peak load of 2.9 kN. Increasing the support span from 90 mm to 150 mm, it was evident from the failure modes, as shown in Figure 5a, that the samples with lower support span have undergone localized crushing rather than pure global bending of the tube. With the increase in support span, the localized crushing of the tube was seen to diminish. However, to fully eradicate the concentrated bending behaviour, the saddles were symmetrically used on both the support rollers as well as the loading pin.

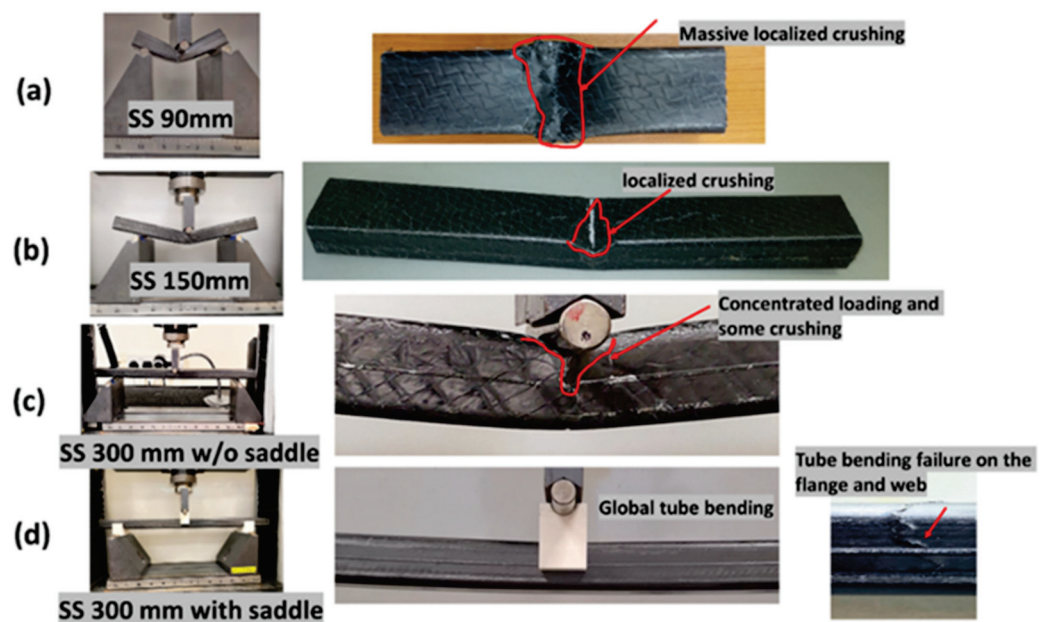


Figure 4. (a–d) Tube bending failure behaviour with different support span and the use of saddle.

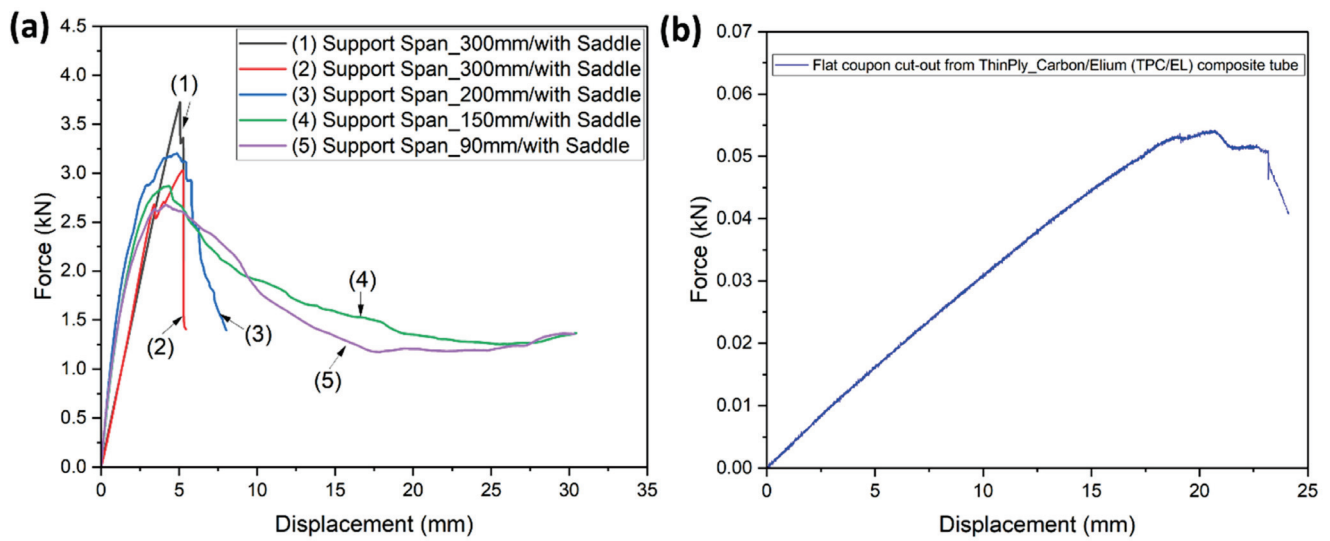


Figure 5. Load vs. displacement curve for (a) TPC/EL composite tube with different support spans and with the saddle arrangement (b) flat coupon cut-out from TPC/EL composite tube.

The load–displacement curve for the sample with a 300 mm support span with the saddles has shown a peak load of 3.67 kN with failure mode, showing pure global bending behaviour until the complete failure of the tubular structure. Furthermore, a flat sample was cut from the tubular configuration, and flexural tests were carried out to check the flexural modulus, which is independent of the geometry of the structure (refer Figure 5b). The flexural modulus for TPC_EL_SS300_SAD configuration and the flat coupon cut from the same tube was calculated to be 36.3 GPa and 36.1 Gpa, respectively, showing good agreement between the results and the adequacy of the defined support span and the saddle arrangement for carrying out further tests on other tubular composite configurations.

It can be concluded from the initial test study that the recommended span for flat specimens cannot be directly applied to tubular configurations, and there could easily be an under-estimation of the peak load and an over-estimation of the flexural modulus during the testing of the composite tubes with shorter support spans. Once the support span and the testing methodology were defined from the initial tests, a detailed investigation was carried out for TPC/EL and TPC/EP tubular composite configurations. Figure 6 shows the load–displacement curve for both the composite tubular configurations.

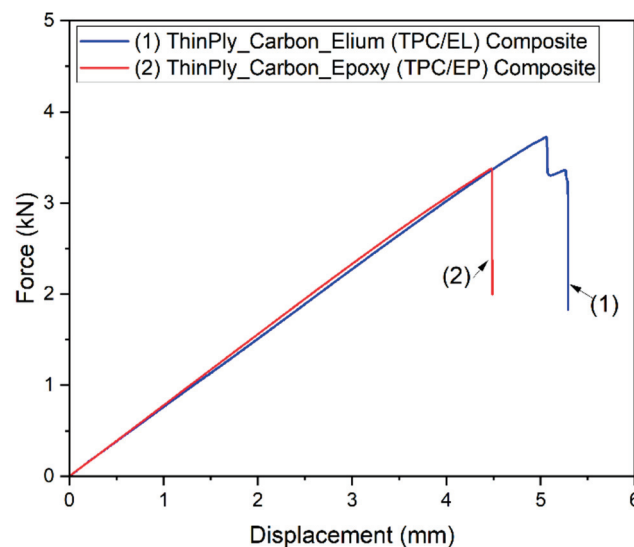


Figure 6. Load vs. displacement curves for TPC/EL and TPC/EP tubular composite configurations.

It should be noted that, for each tubular configuration, three tubes were tested, and Figure 6 represents the best representative curve of the three tubes, which is closer to the average values. The slope of the two configurations is very similar and hence so is the flexural modulus (refer to Table 1), whereas the TPC/EL configuration shows a 10.4% higher maximum bending strength compared to TPC/EP. It is evident from the load–displacement curve with no striations or kinks in the elastic region that there were no induced slipping mechanisms or the associated breakage of the network of molecules of the matrix. It also shows that there is synergetic deformation of the interfacial region (reinforcement/matrix), and the load is progressively transferred. The global bending behaviour of the tube can be noticed at different instances (refer Figure 7) where TPC/EL composite tube is seen to undergo pure bending and it noticeably undergoes more deformation (5.3 mm), as opposed to 4.5 mm in case of the TPC/EP configuration. The final state of failure modes for flange and web are found to be very similar for TPC/EL and TPC/EP composites, although more severe crack and localized failure in the flange was noticed for the TPC/EP composite, which must be due to the more brittle nature of thermoset epoxy matrix in the case of the latter (refer to Figure 7). The global bending at different instances of displacements and the final damage modes are shown in Figure 7.

Table 1. Flexural test results of different tubular composite configurations under 3-point bending.

Tubular Configuration	Thickness (mm)/V _f (%)	Slope (from L vs. d Curve)	Maximum Bending Stress (σ_{max}) (Mpa)	Flexural Modulus (E) (Gpa)	Bending Stiffness/Flexural Rigidity (EI) (Nmm ²)
TPC/EL	1.4/54	756.61	522.42 ± 3.7	36.16 ± 1.78	425,595.2 ± 234.7
TPC/EP	1.4/54	778.90	473.31 ± 2.8	37.23 ± 1.23	438,135.8 ± 398.3

TPC/EL: Thin Ply Carbon/Elium[®]; TPC/EP: Thin Ply Carbon/Epoxy.

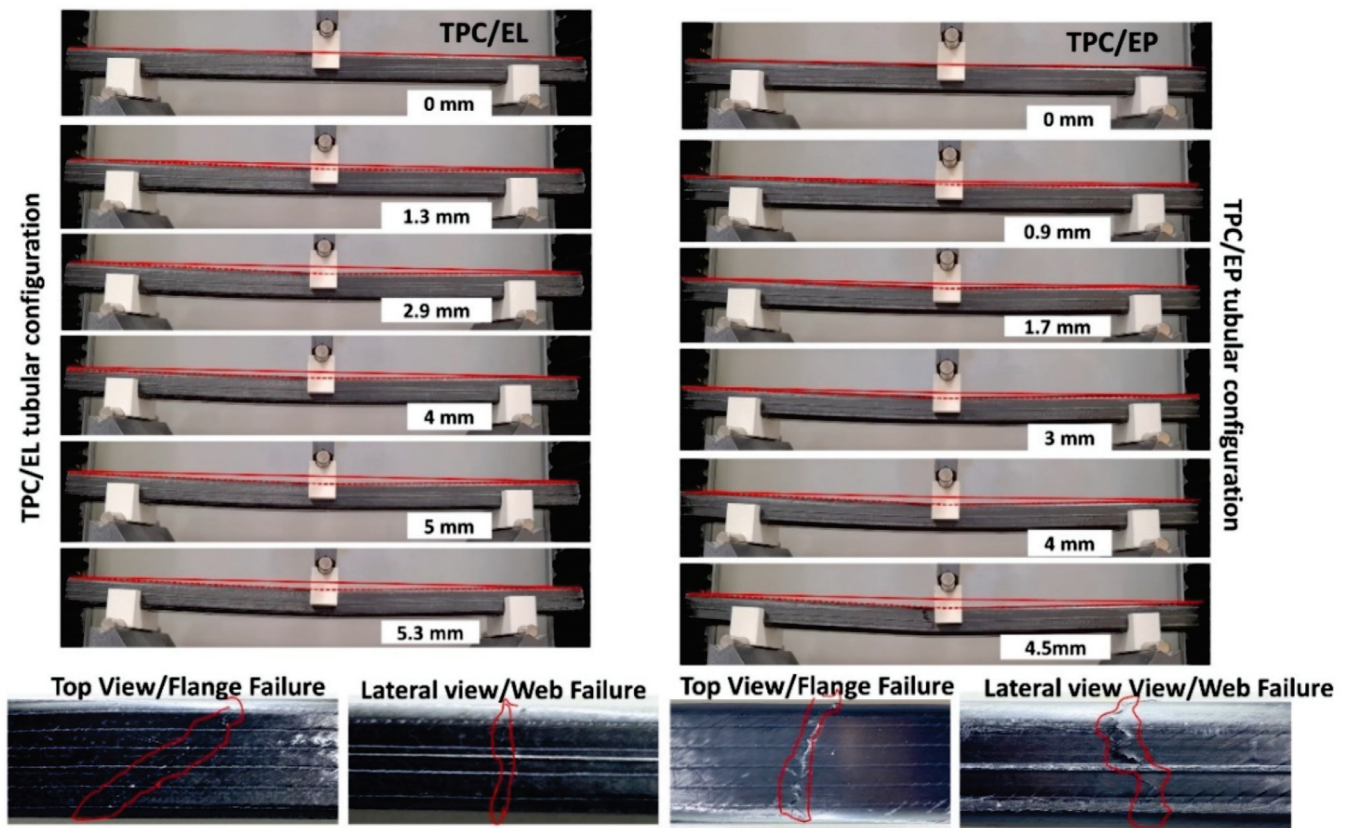


Figure 7. Global bending behaviour with the web and flange failure modes for the Thin Ply Carbon/Elium[®] (TPC/EL) and Thin Ply Carbon/Epoxy (TPC/EP) composite tubes.

There is a clear improvement offered by thermoplastic Elium[®] composite tube in terms of flexural deformation until failure when used with thin plies, as in the current investigation, which can also be related to previous studies carried out with woven reinforcement [42]. It was intriguing to further our investigation to understand the details of the failure mechanism. This was carried out by investigating the cross-section damaged morphologies of the different tubular configurations at the loading position (section view) and along the longitudinal direction (20 mm away from the loading position). Figure 8a,b show the web and the flange failures for the TPC/EL and TPC/EP configurations, respectively.

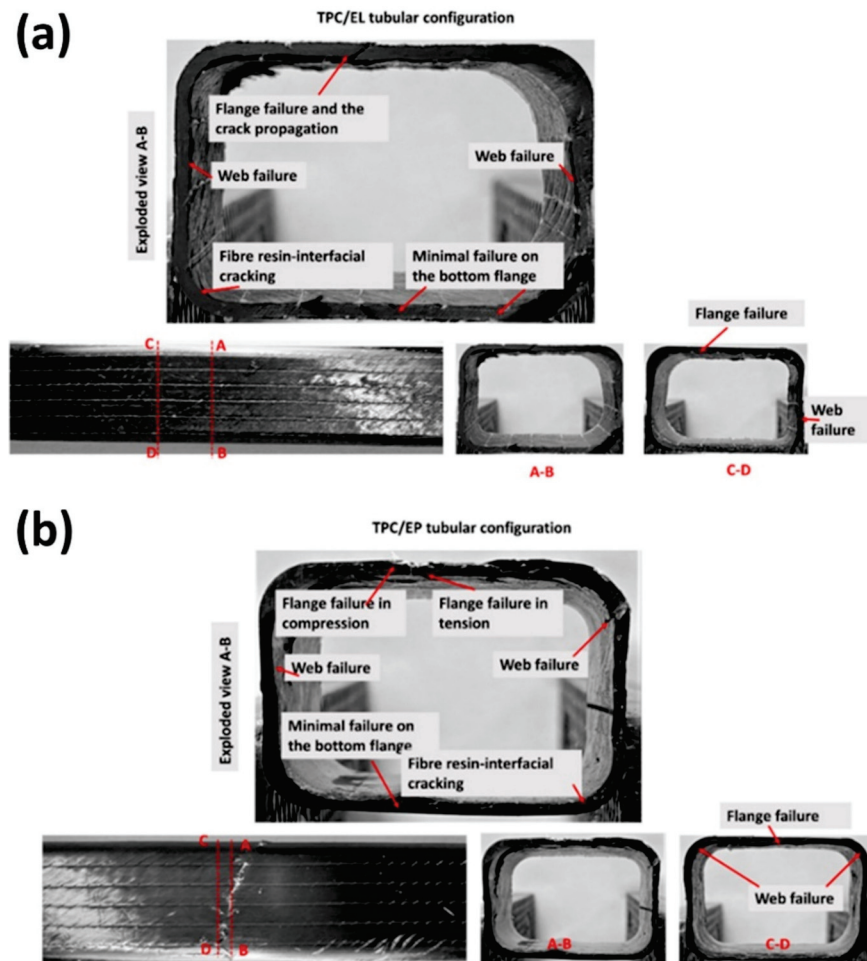


Figure 8. Morphology of the damaged cross-section of (a) TPC/EL and (b) TPC/EP tubular configuration at the loading position (section view) and the different cross-section along the longitudinal direction.

The section view of section A–B shows that the failure of the flange in the direction of the outer layer (BX30 or $\pm 30^\circ$). There was a minimum failure on the bottom flange, whereas the load transfer from the outer flange to the web resulted in evident fibre/matrix interfacial cracks. The same feature was also seen in the cross-section C–D, with evident flange and web failure, showing that these cracks can be transferred away from the central flexural region in the longitudinal direction. Shifting the focus to TPC/EP configuration, the failure modes for the top flange are very different, with more catastrophic failure in both compression and tension. Similar features were seen for the web failure, as noticed in the case of TPC/EL configuration. For both the configurations, the downward loading of the roller caused the top surface of the flange’s failure, which is evident with the majority of $\pm 30^\circ$ and 0° layers in the TPC configuration. Herein, crack propagation is mostly in the longitudinal direction, followed by the load transfer to the web.

Further, a microscopic investigation was carried out to understand the failure mechanisms in more detail. As seen from Figure 9, clear crack propagation in the direction of the fibre of the outer layer was noticed in the case of the flange of the TPC/EL composite tube, and clear tensile failure of the top flange of the tube was also noticed. The matrix cracking sites were observed on the web of the TPC/EL configuration due to the excessively higher strains developed at the corner of the tubes, which are generally more resin-rich due to the corner thickening effect in the case of the bladder moulding process (refer Figure 9) [3]. Figure 10 shows micrographs of the bottom flange and a web for the TPC/EL configuration, showing no to very minimal failure. Moving to the TPC/EP configuration, severe cracks and delamination can be seen on the top flange and the web, and the bottom flange and web also did not undergo any noticeable damage (refer Figure 10).

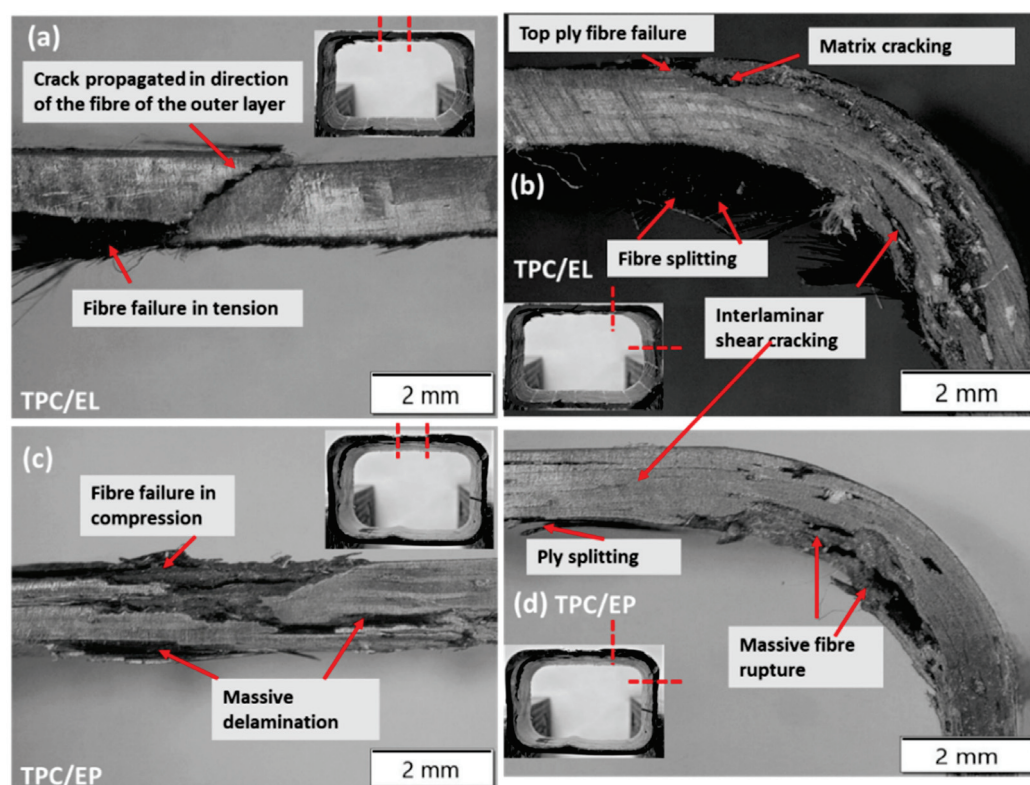


Figure 9. Microscopy pictures of damaged tubular C/S of TPC/EL and TPC/EP tubular configuration at the (a,c) top flange and the (b,d) top web positions.

The detailed flexural study showed two important aspects that are distinguishable. Firstly, the effect of fibre architecture plays a major role in deciding the failure propagation modes. For TPC architecture, top surface failure was noticed, but there was minimal damage propagated to the bottom flange. Another important aspect is the usage of Elium[®] resin to arrest the catastrophic failure mode [14,17,28,32,33,42,50–52] to a more spread failure with more flexural deformation, notably with TPC fibre reinforcement, owing to their chemical structure and presence of inherent micro ductility. SEM investigation was used to confirm the distinctive thermoplastic features for Elium[®]-based composites. Whereas the flexure test is dominated by the reinforcement effect, with samples undergoing tensile and compressive failure (Figure 11a), fibre matrix interfacial bonding is enhanced in the case of thermoplastic composite due to the presence of microductility, induced due to significant plastic deformation of the acrylic Elium[®] resin (Figure 11a–c).

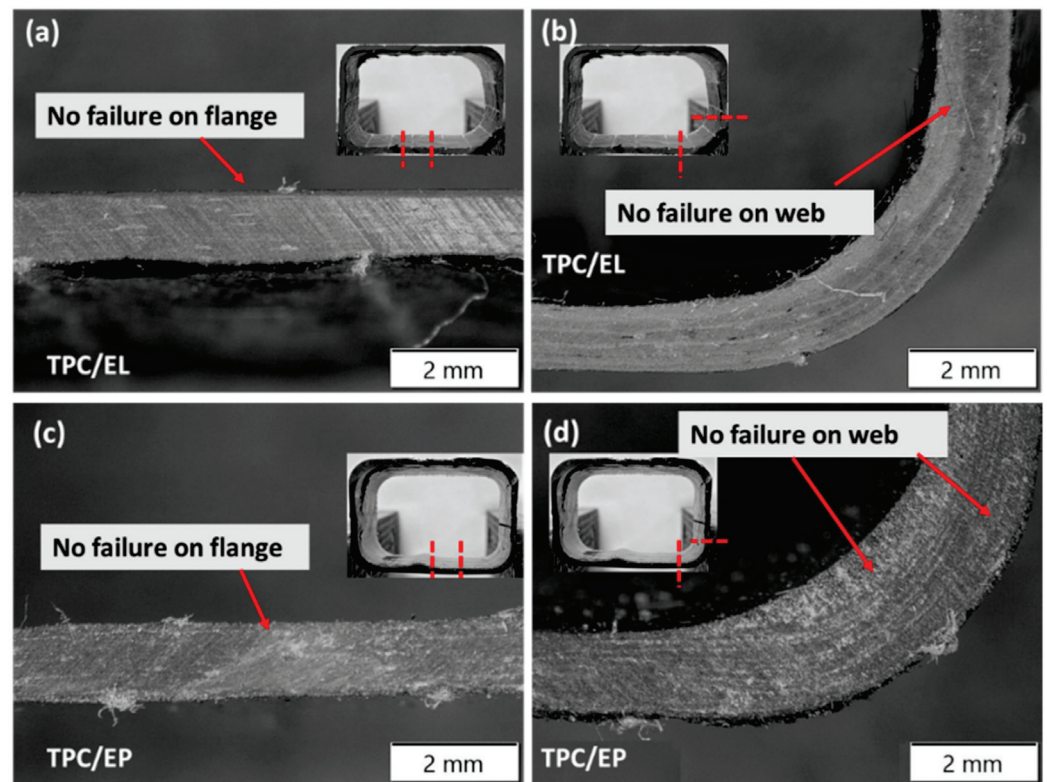


Figure 10. Microscopy pictures of damaged tubular C/S of TPC/EL and TPC/EP tubular configuration at the (a,c) bottom flange and the (b,d) bottom web positions.

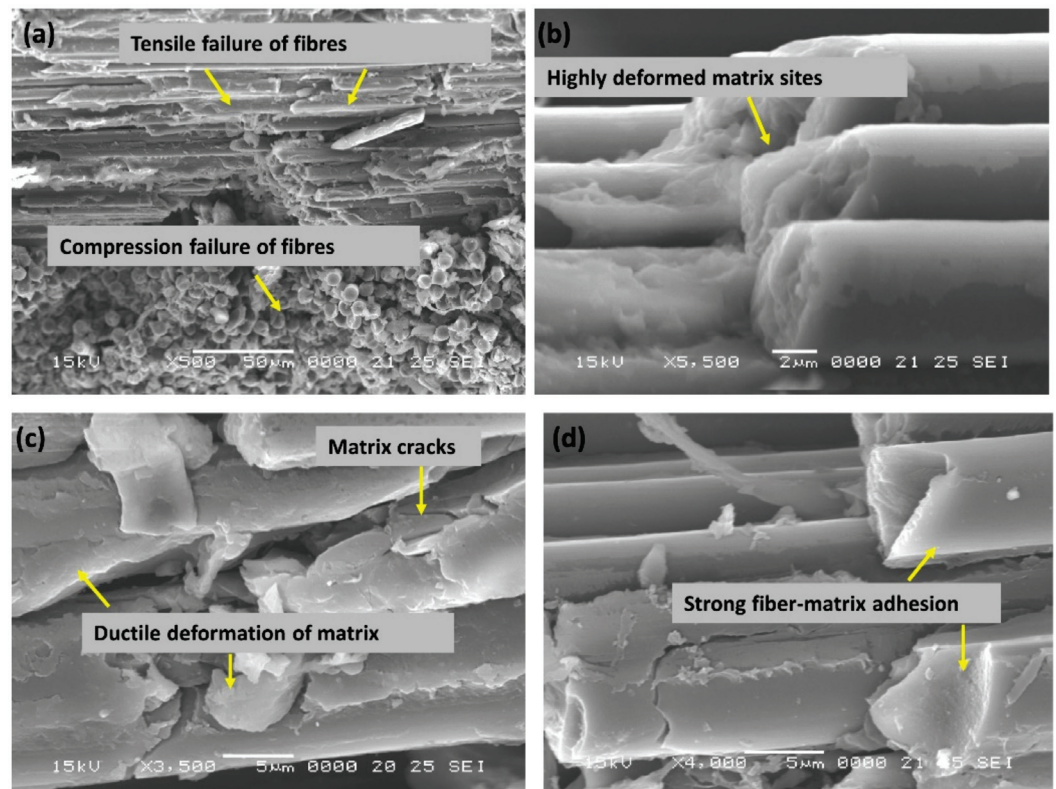


Figure 11. (a–d) SEM pictures of damaged TPC/EL tubular composite tube under flexural loading.

5. Conclusions

Thin ply hollow composite tubes with Elium[®] and epoxy resin were successfully manufactured using the B-RTM process, and their bending response was studied. It was concluded from the initial test results that the span used for flat specimens cannot be directly applied to the tubular configurations, and there could easily be an under-estimation of the peak load and over-estimation of the flexural modulus during the testing of the composite tubes with shorter support spans. Hence, an experimental setup methodology was developed by optimising the support span and the usage of saddle mechanism to induce the overall bending behaviour in the tubular composite structure. The effect of fibre architecture plays a major role in deciding the failure propagation modes. TPC/EL configuration has 10.4% higher maximum bending strength, very similar bending modulus, but has noticeably undergone more deformation owing to the extended plasticity in the case of acrylic Elium[®] resin. The global bending behaviour of the tube was noticed at different instances where TPC/EL composite tube is seen to undergo pure bending and underwent more deformation as opposed to TPC/EP configuration. Top surface failure was noticed with minimal damage to the bottom flange, and the usage of Elium[®] resin helps in arresting the catastrophic failure with more flexural deformation-dominated failure, notably owing to their chemical structure and presence of inherent micro ductility, which is confirmed from the SEM investigation.

Author Contributions: Conceptualization, S.K.B.; methodology, S.K.B. and G.G.; investigation, S.K.B., G.G. and D.V.; experiments, S.K.B., G.G. and D.V.; writing—original draft preparation, S.K.B.; writing—review and editing P.G. and K.F.L.; supervision, P.G. and K.F.L.; funding acquisition, K.F.L. All authors have read and agreed to the published version of the manuscript.

Funding: The authors would like to acknowledge the financial support from Nanyang Technological University, Singapore, and Arkema, France for financial support under the RCA18/46. This research is also supported by A*STAR under the Research Innovation Enterprise (RIE) 2020 Plan, Advanced Manufacturing and Engineering (AME) Domain—Industry Alignment Fund-Pre-positioning (IAF-PP) Polymer Matrix Composites Programme, Grant number A19C9a0044, Work Package 1–2.

Institutional Review Board Statement: Not applicable.

Informed Consent Statement: Not applicable.

Data Availability Statement: The data presented in this study are available on request from the corresponding author.

Acknowledgments: The authors would like to acknowledge the support from Nanyang Technological University, Singapore, Arkema, France and A*STAR, Singapore.

Conflicts of Interest: The authors declare no conflict of interest.

References


1. Kim, G.; Barocio, E.; Pipes, R.B.; Sterkenburg, R. 3D printed thermoplastic polyurethane bladder for manufacturing of fiber reinforced composites. *Addit. Manuf.* **2019**, *29*, 100809. [CrossRef]
2. Bhudolia, S.K.; Perrotey, P.; Gohel, G.; Joshi, S.C.; Gerard, P.; Leong, K.F. Optimizing bladder resin transfer molding process to manufacture complex, thin-ply thermoplastic tubular composite structures: An experimental case study. *Polymers* **2021**, *13*, 4093. [CrossRef]
3. Lehmann, U.; Michaeli, W. Cores lead to an automated production of hollow composite parts in resin transfer moulding. *Compos. Part A Appl. Sci. Manuf.* **1998**, *29*, 803–810. [CrossRef]
4. Schillfahrt, C.; Fauster, E.; Schledjewski, R. Influence of process pressures on filling behavior of tubular fabrics in bladder-assisted resin transfer molding. *Adv. Manuf. Polym. Compos. Sci.* **2017**, *3*, 148–158. [CrossRef]
5. Tsai, S.W. Thin ply composites. In Proceedings of the 46th AIAA/ASME/ASCE/AHS/ASC Structures, Structural Dynamics & Materials Conference, Austin, TX, USA, 18–21 April 2005.
6. Sih, S.; Kim, R.Y.; Kawabe, K.; Tsai, S.W. Experimental studies of thin-ply laminated composites. *Compos. Sci. Technol.* **2007**, *67*, 996–1008. [CrossRef]
7. Yokozeki, T.; Aoki, Y.; Ogasawara, T. Experimental characterization of strength and damage resistance properties of thin-ply carbon fiber/toughened epoxy laminates. *Compos. Struct.* **2008**, *82*, 382–389. [CrossRef]

8. Yokozeki, T.; Kuroda, A.; Yoshimura, A.; Ogasawara, T.; Aoki, T. Damage characterization in thin-ply composite laminates under out-of-plane transverse loadings. *Compos. Struct.* **2010**, *93*, 49–57. [CrossRef]
9. Lystrup, A.; Andersen, T.L. Autoclave consolidation of fibre composites with a high temperature thermoplastic matrix. *J. Mater. Proc. Technol.* **1998**, *77*, 80–85. [CrossRef]
10. Díaz, J.; Rubio, L. Developments to manufacture structural aeronautical parts in carbon fibre reinforced thermoplastic materials. *J. Mater. Proc. Technol.* **2003**, *143–144*, 342–346. [CrossRef]
11. Chou, P.J.C.; Ding, D.; Chen, W.S. Damping of moisture-absorbed composite rackets. *J. Reinf. Plast. Compos.* **2000**, *19*, 848–862. [CrossRef]
12. Bhudolia, S.K.; Gohel, G.; Leong, K.F.; Joshi, S.C. Damping, impact and flexural performance of novel carbon/elium[®] thermoplastic tubular composites. *Compos. Part B Eng.* **2020**, *203*, 108480. [CrossRef]
13. Friedrich, K.; Gogeva, T.; Fakirov, S. Thermoplastic impregnated fiber bundles: Manufacturing of laminates and fracture mechanics characterization. *Compos. Sci. Technol.* **1988**, *33*, 97–120. [CrossRef]
14. Barbosa, L.C.M.; Bortoluzzi, D.B.; Ancelotti, A.C. Analysis of fracture toughness in mode II and fractographic study of composites based on elium[®] 150 thermoplastic matrix. *Compos. Part B Eng.* **2019**, *175*, 107082. [CrossRef]
15. Sadighi, M.; Rabizadeh, E.; Kermansaravi, F. Effects of laminate sequencing on thermoforming of thermoplastic matrix composites. *J. Mater. Proc. Technol.* **2008**, *201*, 725–730. [CrossRef]
16. Taillemite, S. Arkema Gains Ground in Composites and Launches a Revolutionary Range of Elixir Liquid Resins. Available online: <http://www.arkema.com/en/media/news/news-details/Arkema-gains-ground-in-composites-and-launches-a-revolutionary-range-of-Eluxim-liquid-resins/> (accessed on 12 February 2017).
17. Matadi Boumbimba, R.; Coulibaly, M.; Khabouchi, A.; Kinvi-Dossou, G.; Bonfoh, N.; Gerard, P. Glass fibres reinforced acrylic thermoplastic resin-based tri-block copolymers composites: Low velocity impact response at various temperatures. *Compos. Struct.* **2017**, *160*, 939–951. [CrossRef]
18. Bhudolia, S.K.; Joshi, S.C. Low-velocity impact response of carbon fibre composites with novel liquid methylmethacrylate thermoplastic matrix. *Compos. Struct.* **2018**, *203*, 696–708. [CrossRef]
19. Obande, W.; Ray, D.; O’Brádaigh, C.M. Viscoelastic and drop-weight impact properties of an acrylic-matrix composite and a conventional thermoset composite—A comparative study. *Mater. Lett.* **2019**, *238*, 38–41. [CrossRef]
20. Kinvi-Dossou, G.; Matadi Boumbimba, R.; Bonfoh, N.; Garzon-Hernandez, S.; Garcia-Gonzalez, D.; Gerard, P.; Arias, A. Innovative acrylic thermoplastic composites versus conventional composites: Improving the impact performances. *Compos. Struct.* **2019**, *217*, 1–13. [CrossRef]
21. Kinvi-Dossou, G.; Matadi Boumbimba, R.; Bonfoh, N.; Koutsawa, Y.; Eccli, D.; Gerard, P. A numerical homogenization of e-glass/acrylic woven composite laminates: Application to low velocity impact. *Compos. Struct.* **2018**, *200*, 540–554. [CrossRef]
22. Gohel, G.; Bhudolia, S.K.; Kantipudi, J.; Leong, K.F.; Barsotti, R.J. Ultrasonic welding of novel carbon/elium[®] with carbon/epoxy composites. *Compos. Commun.* **2020**, *22*, 100463. [CrossRef]
23. Bhudolia, S.K.; Gohel, G.; Kah Fai, L.; Barsotti, R.J. Fatigue response of ultrasonically welded carbon/elium[®] thermoplastic composites. *Mater. Lett.* **2020**, *264*, 127362. [CrossRef]
24. Bhudolia, S.K.; Gohel, G.; Kantipudi, J.; Leong, K.F.; Barsotti, R.J. Ultrasonic welding of novel carbon/elium[®] thermoplastic composites with flat and integrated energy directors: Lap shear characterisation and fractographic investigation. *Materials* **2020**, *13*, 1634. [CrossRef] [PubMed]
25. Bhudolia, S.K.; Gohel, G.; Leong, K.F.; Barsotti, R.J. Investigation on ultrasonic welding attributes of novel carbon/elium[®] composites. *Materials* **2020**, *13*, 1117. [CrossRef]
26. Campbell, F.C. Chapter 10—Thermoplastic composites: An unfulfilled promise. In *Manufacturing Processes for Advanced Composites*; Campbell, F.C., Ed.; Elsevier Science: Amsterdam, The Netherlands, 2003; pp. 357–397.
27. Offringa, A.R. Thermoplastic composites—Rapid processing applications. *Compos. Part A Appl. Sci. Manuf.* **1996**, *27*, 329–336. [CrossRef]
28. Bhudolia, S.K.; Joshi, S.C.; Bert, A.; Yi Di, B.; Makam, R.; Gohel, G. Flexural characteristics of novel carbon methylmethacrylate composites. *Compos. Commun.* **2019**, *13*, 129–133. [CrossRef]
29. Cousins, D.S.; Suzuki, Y.; Murray, R.E.; Samaniuk, J.R.; Stebner, A.P. Recycling glass fiber thermoplastic composites from wind turbine blades. *J. Clean. Prod.* **2019**, *209*, 1252–1263. [CrossRef]
30. Khalili, P.; Blinzler, B.; Kádár, R.; Bisschop, R.; Försth, M.; Blomqvist, P. Flammability, smoke, mechanical behaviours and morphology of flame retarded natural fibre/elium[®] composite. *Materials* **2019**, *12*, 2648. [CrossRef] [PubMed]
31. Khalili, P.; Blinzler, B.; Kádár, R.; Blomqvist, P.; Sandinge, A.; Bisschop, R.; Liu, X. Ramie fabric elium[®] composites with flame retardant coating: Flammability, smoke, viscoelastic and mechanical properties. *Compos. Part A Appl. Sci. Manuf.* **2020**, *137*, 105986. [CrossRef]
32. Bhudolia, S.K.; Gohel, G.; Joshi, S.C.; Leong, K.F. Quasi-static indentation response of core-shell particle reinforced novel nccf/elium[®] composites at different feed rates. *Compos. Commun.* **2020**, *21*, 100383. [CrossRef]
33. Shah, S.Z.H.; Megat-Yusoff, P.S.M.; Karuppanan, S.; Choudhry, R.S.; Ud Din, I.; Othman, A.R.; Sharp, K.; Gerard, P. Compression and buckling after impact response of resin-infused thermoplastic and thermoset 3d woven composites. *Compos. Part B Eng.* **2021**, *207*, 108592. [CrossRef]

34. Bhudolia, S.K.; Joshi, S.C.; Bert, A.; Gohel, G.R.; Raama, M. Energy characteristics and failure mechanisms for textile spread tow thin ply thermoplastic composites under low-velocity impact. *Fibers Polym.* **2019**, *20*, 1716–1725. [CrossRef]
35. Bhudolia, S.K.; Gohel, G.; Joshi, S.C.; Leong, K.F. Manufacturing optimization and experimental investigation of ex-situ core-shell particles toughened carbon/elium[®] thermoplastic composites. *Fibers Polym.* **2021**, *13*, 4093. [CrossRef]
36. Yin, D.; Zheng, J.; Xiong, C.; Yin, J.; Li, B.; Deng, H.; Zhu, X. Analytical, numerical, and experimental investigations on transverse bending responses of cfrp square tube filled with aluminum foam. *Math. Probl. Eng.* **2020**, *2020*, 8764349. [CrossRef]
37. Yan, L.; Chouw, N.; Jayaraman, K. On energy absorption capacity, flexural and dynamic properties of flax/epoxy composite tubes. *Fibers Polym.* **2014**, *15*, 1270–1277. [CrossRef]
38. Amiri, A.; Krosbakken, T.; Schoen, W.; Theisen, D.; Ulven, C.A. Design and manufacturing of a hybrid flax/carbon fiber composite bicycle frame. *Proc. Inst. Mech. Eng. Part P J. Sports Eng. Technol.* **2017**, *232*, 28–38. [CrossRef]
39. Stefanovska, M.; Risteska, S.; Samakoski, B.; Maneski, G.; Kostadinovska, B. Theoretical and Experimental Bending Properties of Composite Pipes. *Int. J. Environ. Ecol. Eng.* **2015**, *9*, 706–710.
40. Wu, Z.; Shen, Y.; Pan, Z.; Hu, X. Three-point bending behavior and energy absorption capacity of composite tube reinforced by gradient braided structure in radial direction. *Fibers Polym.* **2019**, *20*, 1455–1466. [CrossRef]
41. Bhudolia, S.K.; Gohel, G.; Kantipudi, J.; Leong, K.F.; Gerard, P. Manufacturing and investigating the load, energy and failure attributes of thin ply carbon/elium[®] thermoplastic hollow composites under low-velocity impact. *Mater. Des.* **2021**, *206*, 109814. [CrossRef]
42. Bhudolia, S.K.; Gohel, G.; Kantipudi, J.; Leong, K.F.; Gerard, P. Mechanical performance and damage mechanisms of thin rectangular carbon/elium[®] tubular thermoplastic composites under flexure and low-velocity impact. *Thin-Walled Struct.* **2021**, *165*, 107971. [CrossRef]
43. Van Rijswijk, K.; Bersee, H.E.N. Reactive processing of textile fiber-reinforced thermoplastic composites—An overview. *Compos. Part A Appl. Sci. Manuf.* **2007**, *38*, 666–681. [CrossRef]
44. Bhudolia, S.K.; Perrotey, P.; Joshi, S.C. Mode I fracture toughness and fractographic investigation of carbon fibre composites with liquid methylmethacrylate thermoplastic matrix. *Compos. Part B Eng.* **2018**, *134*, 246–253. [CrossRef]
45. Bhudolia, S.K.; Perrotey, P.; Joshi, S.C. Optimizing polymer infusion process for thin ply textile composites with novel matrix system. *Materials* **2017**, *10*, 293. [CrossRef] [PubMed]
46. *Astm-D792-2020*; Standard Test Methods for Density and Specific Gravity (Relative Density) of Plastics by Displacement. ASTM International: West Conshohocken, PA, USA, 2020.
47. *Astm D2734-09*; Standard Test Methods for Void Content of Reinforced Plastics. ASTM International: West Conshohocken, PA, USA, 2011.
48. Scărlătescu, D.D.; Modrea, A.; Stanciu, M.D. Three-point bend test to determine the mechanical behavior of the tubes used in water supply networks. *Procedia Manuf.* **2019**, *32*, 179–186. [CrossRef]
49. Bakavos, D.; Prangnell, P.B. Mechanisms of joint and microstructure formation in high power ultrasonic spot welding 6111 aluminium automotive sheet. *Mater. Sci. Eng. A* **2010**, *527*, 6320–6334. [CrossRef]
50. Gohel, G.; Bhudolia, S.K.; Elisetty, S.B.S.; Leong, K.F.; Gerard, P. Development and impact characterization of acrylic thermoplastic composite bicycle helmet shell with improved safety and performance. *Compos. Part B Eng.* **2021**, *221*, 109008. [CrossRef]
51. Bhudolia, S.K.; Gohel, G.; Subramanyam, E.S.B.; Leong, K.F.; Gerard, P. Enhanced impact energy absorption and failure characteristics of novel fully thermoplastic and hybrid composite bicycle helmet shells. *Mater. Des.* **2021**, *209*, 110003. [CrossRef]
52. Gohel, G.; Bhudolia, S.K.; Leong, K.F.; Gerard, P. On the structural damping response of hollow carbon composite shafts with room temperature curable novel acrylic liquid thermoplastic resin. *Compos. Commun.* **2021**, *29*, 100990. [CrossRef]

Article

Fabrication and Property Characterization of Long-Glass-Fiber-Reinforced Polypropylene Composites Processed Using a Three-Barrel Injection Molding Machine

Guan-Yan Liou ¹, Chi-Wei Su ¹, Po-Wei Huang ² , Sheng-Jye Hwang ^{1,*}, Chao-Tsai Huang ³ and Hsin-Shu Peng ²

¹ Department of Mechanical Engineering, National Cheng Kung University, Tainan 70101, Taiwan; n16094182@gs.ncku.edu.tw (G.-Y.L.); hyde00155@gmail.com (C.-W.S.)

² Department of Mechanical and Computer-Aided Engineering, Feng Chia University, Taichung 40724, Taiwan; bowei8915@gmail.com (P.-W.H.); hspeng@fcu.edu.tw (H.-S.P.)

³ Department of Chemical and Materials Engineering, Tamkang University, New Taipei 251301, Taiwan; cthuang@mail.tku.edu.tw

* Correspondence: jimppl@mail.ncku.edu.tw; Tel.: +886-6-2757575 (ext. 62184)

Abstract: Processing equipment and parameters will highly influence the properties of long-fiber-reinforced injection-molded thermoplastic composites, leading to different fiber lengths and orientations. Thus, maintaining fiber length during the injection molding process is always a big challenge for engineers. This study uses long-glass-fiber-reinforced polypropylene with 25 mm fiber length and a special-built novel injection molding machine with a three-barrel injection unit, including a plasticizing screw, an injection plunger, and a packing plunger, to fabricate injection molding parts while retaining long fiber length. This study also discusses the influence of process parameters, such as back pressure, screw speed, melt temperature, and different flow paths, on the properties of long-glass-fiber-reinforced composites. The experiment results show that a higher screw speed and back pressure will reduce the fiber length in the injection-molded parts. However, using appropriate parameter settings can maintain the fiber length to more than 10 mm. It was found that by increasing the back pressure, the cross direction of the fiber orientation can be increased by up to 15% and the air trap volume fraction can be decreased by up to 86%. Setting appropriate back pressure under a low screw speed will increase the tensile strength. Finally, it was found that the single-edge-gate path results in a higher tensile strength than that of the single-sprue-gate path due to the retainment of longer fiber length in the injection-molded part.

Keywords: long-fiber-reinforced thermoplastic; fiber length; fiber orientation; injection molding; mechanical properties

Citation: Liou, G.-Y.; Su, C.-W.; Huang, P.-W.; Hwang, S.-J.; Huang, C.-T.; Peng, H.-S. Fabrication and Property Characterization of Long-Glass-Fiber-Reinforced Polypropylene Composites Processed Using a Three-Barrel Injection Molding Machine. *Polymers* **2022**, *14*, 1251. <https://doi.org/10.3390/polym14061251>

Academic Editors: Somen K. Bhudolia and Sunil Chandrakant Joshi

Received: 24 February 2022

Accepted: 17 March 2022

Published: 20 March 2022

Publisher's Note: MDPI stays neutral with regard to jurisdictional claims in published maps and institutional affiliations.



Copyright: © 2022 by the authors. Licensee MDPI, Basel, Switzerland. This article is an open access article distributed under the terms and conditions of the Creative Commons Attribution (CC BY) license (<https://creativecommons.org/licenses/by/4.0/>).

1. Introduction

The automotive industry has used many lightweight composite materials to reduce weight and improve fuel efficiency in recent years. Among them, fiber-reinforced thermoplastic composites are popular in the automotive industry. Fiber-reinforced composites have the characteristic of lightweight and can effectively improve the mechanical properties of the product [1–3]. Automobile components widely use plastic injection molding products. However, injection molding processing methods will change the fiber characteristics (fiber length, fiber orientation, and fiber weight fraction) and affect its mechanical properties. Therefore, the literature collected below studies the influence of fiber characteristics, the injection molding machine, mold design, and injection parameters on the mechanical properties of the fiber.

Fiber characteristics significantly affect the mechanical properties of the product. Thomason [4] and Sun et al. [5] mentioned that the mechanical properties of long-fiber-reinforced thermoplastics depend on three main factors, which are fiber length, fiber

orientation, and fiber weight fraction. Baillif and Oksman [6] found that both fiber length and fiber orientation affect mechanical properties but that the effect of fiber length is more significant. In the injection molding process, the melt flow process affects the degree of fiber orientation. Advani and Sozer [7] mentioned that injection-molded fiber-reinforced thermoplastic parts typically have a skin/shell/core structure. Jan et al. [8] mentioned that the degree of fiber alignment in the flow direction is sensitive to fiber weight fraction. Toll and Anderson [9] found that the core regions of samples made with long-fiber compounds have a higher fiber content and a more consistent fiber orientation along the flow direction than those made with short-fiber compounds. Wang et al. [10] showed that the fiber orientation in the loading direction is beneficial for improving the tensile strength and modulus of long-fiber-reinforced thermoplastic composites. Kumar et al. [11] noted that as the fiber content increases, the tensile strength and impact resistance of the molded parts also increase. Therefore, maintaining fiber integrity and achieving dense and uniform fiber orientation in the final product are critical challenges for injection molding.

The gate, the runner, the cavity design, and the injection molding machine are also essential. The flow path design of the composite material melt can damage the fiber. Hung and Tseng [12] pointed out that the threads of long-fiber-reinforced thermoplastic materials break when they move through the plasticizing screw, so it is not easy to use injection molding processing to inject long-fiber-reinforced thermoplastics. Güllü et al. [13] found that increasing the cross section of the gate can help produce a more extended fiber distribution and increase the tensile strength. Lafrance and Krawczak [14] showed that the quality of the product depends on the gate type and the design of the plasticizing unit. In addition, the gate location and size affect the composite's skin/shell/core structure during the filling stage. Huang et al. [15] investigated the effects of the process parameters on the fiber length and tensile strength of long-fiber-reinforced thermoplastic parts produced using a customized injection molding machine with a novel three-barrel-type injection unit. The results showed that the fibers in the molded part of the unit maintain an average length of more than 13 mm, given appropriate settings of the process parameters. According to the result of the references taken into consideration, this study uses an injection molding machine with a three-barrel injection molding unit, including a plasticizing screw, an injection plunger, and a packing plunger. This design of the injection unit can effectively avoid damaging the fiber and maintain the fiber length during the injection molding process.

The injection parameter setting is also a crucial part. Improper processing parameter setting may cause defects, such as fibers and bubbles, further reducing the product's mechanical properties. Some studies have pointed out the influence of injection molding process parameters on long-fiber-reinforced thermoplastic products. According to Sanou et al. [16], the melt temperature and the fiber content significantly affect the fiber orientation. Lafrance and Krawczak [17] mentioned that the most critical factors affecting bending strength and modulus are plasticizing, filling, and post-filling stages (melt temperature, volume flow, back pressure, and screw speed). Salleh et al. [18] found out that high-temperature processing can increase the tensile modulus of composite materials but the performance will decrease during low-temperature processing, especially under a high fiber content. Yilmazer and Cansever [19] showed that the average fiber length decreases when the shear rate increases on changing the screw speed or the feed rate. The impact strength, the tensile modulus, and the tensile strength increase, while the elongation at break decreases as the average fiber length increases. Rohde et al. [20] showed that backpressure harms fiber length and affects the energy absorption of long-fiber-reinforced thermoplastic parts. Hagstrand et al. [21] and Peng [22] mentioned that the existence of air traps in fiber-reinforced composites significantly damages their mechanical performance. According to the above literature review, the melt temperature, the back pressure, and the screw speed are important manufacturing parameters that affect the characteristics and mechanical properties of the fiber.

However, how to catch those fiber microstructures in the final parts is still challenging. In general, two methods have been used. One is the optical microscopy method, and the

other is the micro-computerized tomography scan method. Bernasconi [23] mentioned that the optical and micro-computed methods can provide similar results in fiber orientation. Huang et al. [24] mentioned the fiber orientation distribution using micro-computerized tomography scan and image analysis by Avizo software. The correlation between the fiber microstructure feature (particularly in fiber orientation) and tensile modulus and tensile stress for fiber-reinforced thermoplastic in the injection molding process can be validated. Since the fiber length of the samples used in this study is extremely long, a big volume of a sample part needed to be examined in order to calculate the fiber length and orientation in the sample. A high-resolution computerized tomography scan is not practical since it requires too many slices of a big cross section and the generated data size exceeds the handling capability of a modern computer. Therefore, this study uses the optical microscopy method and image analysis by Avizo software to examine the fiber microstructures.

Based on the literature collected above, the present study uses the three-barrel injection molding machine to identify the effects of the injection molding process parameters (namely, the backpressure, the screw speed, and the melt temperature) and two different melt flow paths (single-edge gate and single-sprue gate) on four fiber characteristics of molded long-fiber-reinforced thermoplastic parts: the fiber length, the fiber orientation, the fiber weight fraction, and the air trap. Finally, the tensile test for the long-fiber-reinforced thermoplastic samples is conducted. To validate the optical microscopy scan method in this study, the results are compared to the fiber length and fiber orientation measurement results using high-temperature sintering and computed tomography. The images of the optical microscopy scan and computed tomography are imported to Avizo software for fiber orientation analysis results. The fiber orientation defined by Advani and Tucker [25] presents a model based on even-order tensors to describe the average orientation of the fibers. The results showed that in terms of describing the fiber orientation distribution through the part thickness direction, the tensor components a_{11} , a_{22} , and a_{33} were sufficient for physical interpretation purposes, where axis 1 was aligned with the flow direction, axis 2 was aligned with the cross flow direction, and axis 3 was aligned with the thickness direction.

2. Materials and Methods

2.1. Material Fabrication

Long-glass-fiber-reinforced polypropylene was chosen for the experiment. LGP503NA250, which has a fiber content of 50 wt.%, was used as the molding material for the experiment. The length of the sample was 25 mm, and the diameter was 17 μm (as shown in Figure 1). The material was supplied by GECO (Great Eastern Resins Industrial Co. Ltd., Taichung, Taiwan).



Figure 1. Long-glass-fiber pellets.

2.2. Injection Molding Machine

A 180-ton injection molding machine was used for the experiment (CLF, Chuan Lih Fa Co., Ltd., Tainan, Taiwan) at a maximum injection speed of 150 mm/sec and a maximum injection pressure of 177 MPa. In an attempt to maintain the initial fiber length during the injection molding process, a three-barrel injection unit was designed and developed by the researchers (Figure 2). The injection unit consisted of a plasticization screw ($\varphi = 55$ mm), an injection plunger ($\varphi = 45$ mm), and a packing plunger ($\varphi = 40$ mm). The plasticization screw used in the injection unit was designed to have a low shear strain rate by reducing the compression ratio of the screw to minimize the fiber breakage rate. The screw does not move back and forth, so it does not have a check ring. The injection and packing plungers store and deliver composite melt into the mold cavity. This design of the injection unit can effectively avoid damaging the fiber and maintain the fiber length during the injection molding process. A cooling channel is designed and built in the packing plunger of the novel injection molding machine so the process cycle time can be almost the same as that of the traditional injection molding process, even though the gate size of the mold is considerably big.

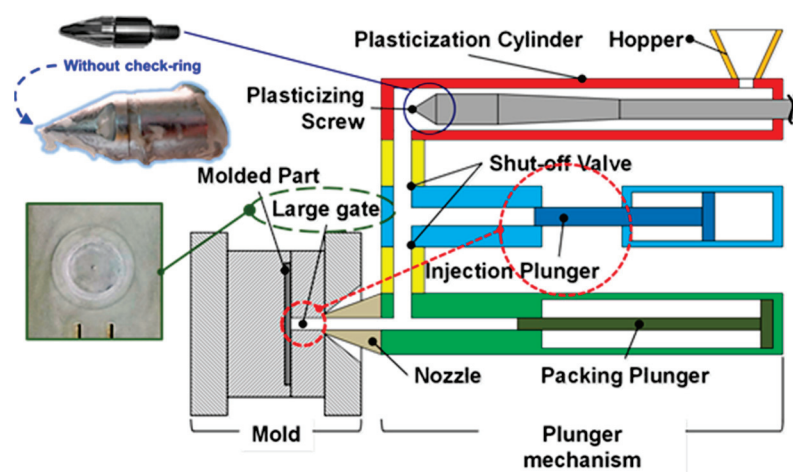


Figure 2. Design and application of the injection molding machine using a three-barrel injection mechanism (plasticization stage, filling stage, and packing stage).

2.3. Sample and Mold

To investigate the effects of the melt flow path on the mechanical properties of the long-fiber-reinforced thermoplastic components, a mold was designed with three different flow paths, (a) a single-edge gate, (b) a single-sprue gate, and (c) a double-edge gate, as shown in Figure 3 (Note that in designing the mold, the double-edge-gate path is intended to allow observation of the effects of the process parameters on the weld line. However, this issue is out of the scope of the present study, and the double-edge-gate path is, therefore, ignored in the remaining discussion).

2.4. Optical Microscopy Scan Method

The optical microscope scanner (shown in Figure 4) was developed with a PC-based control system with a $10\times$ magnification lens resolution of $2\ \mu\text{m}$. The typical single scanned picture was $0.9\ \text{mm} \times 0.9\ \text{mm}$ in size. The camera took some pictures in a large area by controlling the X and Y axes using a computer and then stitched them into a single image. The optical microscopy method was carried out by grinding and polishing the sample, after which, it was placed on the platform of the optical microscope to obtain a surface image. After the scanning process, we continued grinding and polishing ($0.2\ \text{mm}$ in depth). The entire process was repeated iteratively until sample images were acquired from the skin layer to the core layer. Finally, the images obtained using the optical microscopy method were imported to Avizo for analysis.

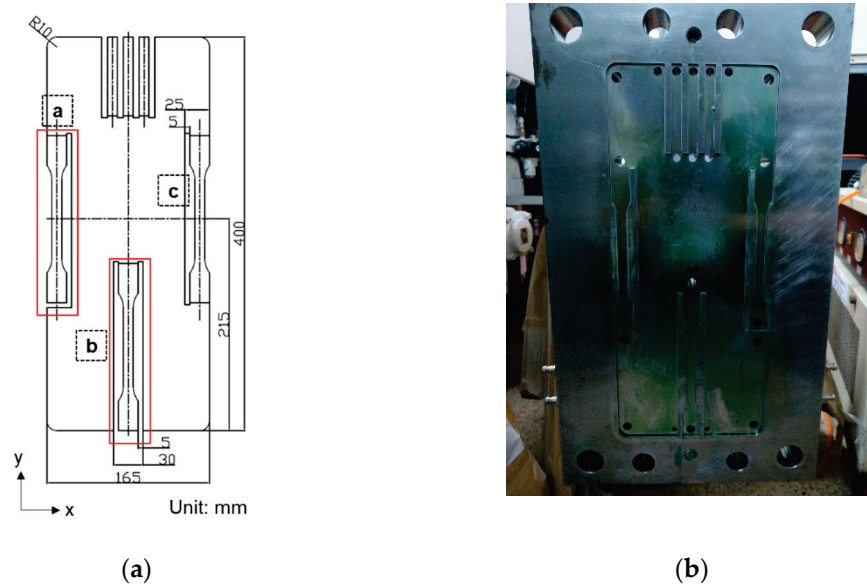


Figure 3. Schematic of tensile samples: (a) diagram of the sample designs (ISO 527-2 at a thickness of 3 mm) and (b) diagram of the mold cavity of the samples.

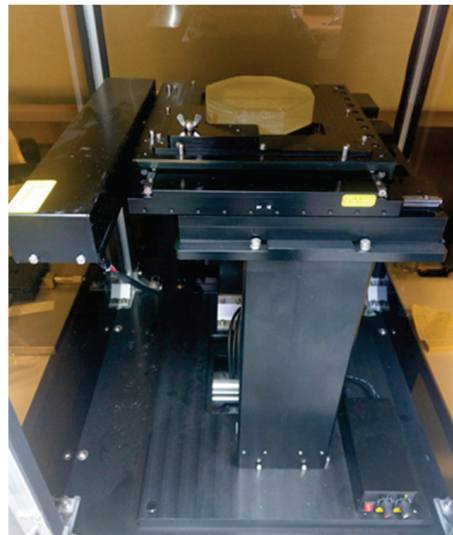


Figure 4. Optical microscopy scanner.

2.5. Image Analysis Software

Avizo (version 9.7.0, Thermo Fisher Scientific, Waltham, MA, USA) is a software program that enables users to perform interactive visualization and computation on 3D data sets. In the present study, the built-in fiber tracing module and the built-in thresholding module functions were used to analyze the fiber length, orientation, and weight fraction and the volume fraction of air the traps.

2.6. Experimental Parameters

The injection molding experiments considered the effects of three different process parameters on the fiber characteristics and mechanical properties of the long-glass-fiber-reinforced thermoplastic parts of interest, the back pressure (0–1.12 MPa), the plasticization screw speed (60–150 rpm), and the melt temperature (230–250 °C), as shown in Table 1. To validate the optical microscopy results for the fiber length and fiber orientation, high-temperature sintering and computed tomography, respectively, were used under the same

processing conditions. A back pressure of 0.7 MPa, a screw speed of 90 rpm, and a melt temperature of 230 °C were used.

Table 1. Configuration of the injection-molded long-glass-fiber-reinforced polypropylene composites.

A. Parameters						
Controllable Factors				Factors Maintained Constant		
Back pressure (MPa)	0	0.7	1.12	Injection pressure (%)	70	
Screw speed (rpm)	60	90	150	Injection speed (mm/s)	60	
Melt temperature (°C)	230	250		Injection time (s)	2	
				Packing pressure (%)	30	
				Packing time (s)	10	
				Mold temperature (°C)	80	
				Cooling time (s)	30	

B. The treatments used to mold the samples in random order			
Experiment	Back pressure (MPa)	Screw speed (rpm)	Melt temperature (°C)
1	0	90	230
2	0.7	90	230
3	1.12	90	230
4	0.7	60	230
5	0.7	150	230
6	0.7	90	250

2.7. Characterization of the Molded Parts

2.7.1. Fiber Length

To validate the feasibility of the optical microscopy method, the fiber length results after high-temperature sintering and optical microscopy scanning were compared. High-temperature sintering was carried out exposing the sample to a high temperature to make the polypropylene melt and leave only the glass fiber. The fiber length was obtained by measuring and averaging 200 fibers (shown in Figure 5). The fiber length was analyzed in this study by importing images from the optical microscopy scans into Avizo’s built-in fiber-tracking module.

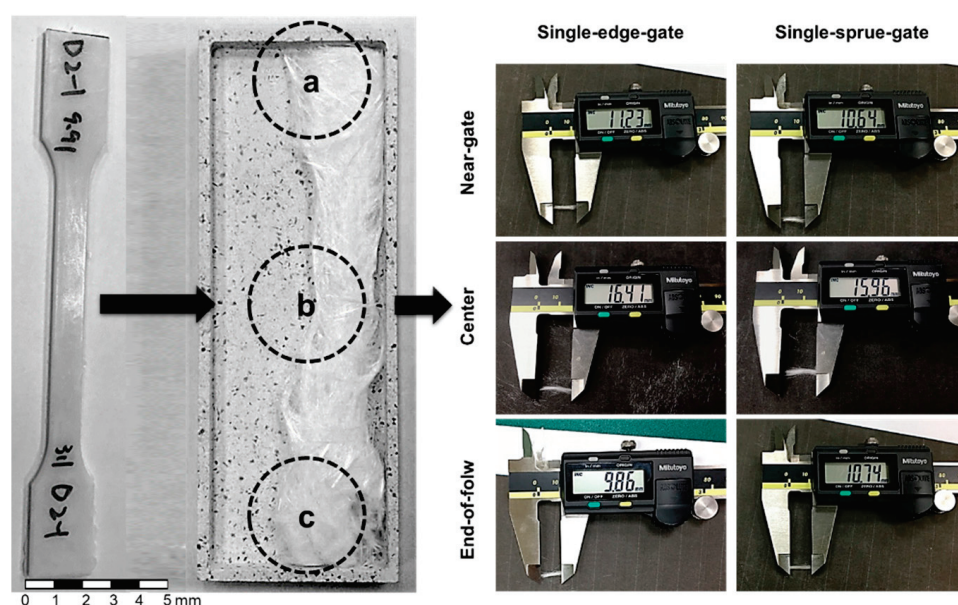


Figure 5. Measurement of the fiber length after high-temperature sintering for different melt flow paths: (a) the near-gate region, (b) the center region, and (c) the end-of-flow region.

2.7.2. Fiber Orientation

To validate the feasibility of the optical microscopy method, the fiber orientation results for the computerized tomography and the optical microscopy methods were compared. The computerized tomography scan was performed using the Zeiss Metrotom 800 scanner (Carl Zeiss AG, Jena, Germany). Table 2 shows the computerized tomography parameters. Since the fiber length of the samples used in this study can be extremely long, a big volume of a sample part needed to be examined in order to calculate the fiber length and orientation in the sample. A high-resolution computerized tomography scan is not practical since it requires too many slices of a big cross section and the generated data size exceeds the handling capability of a modern computer. The authors are perfectly aware of possible problems caused by not using a fine slicing computerized tomography scan to determine fiber length and orientation. Thus, this study not only used not-that-fine computerized tomography scan but also used an optical microscopy scan approach and high-temperature sintering to examine the fiber characteristics (fiber length and fiber orientation) in order to ensure the correctness of the analysis. The analysis of the fiber orientation was accomplished by importing images from computed tomography and optical microscopy into Avizo's built-in fiber-tracking module. Figure 6 shows the core layer images obtained using computed tomography and optical microscopy.

Table 2. Computerized tomography parameters.

Parameter	Value
Voltage	130
Current (mA)	120
Resolution (pixels)	1536 × 1920
Pixel size (mm)	0.127
Voxel size (μm)	42

The fiber orientation was examined using the model proposed by Advani and Tucker [10]. In theory, the second-order tensor represents a fiber orientation that is applied to rigid fibers only. Hence, strictly speaking, it cannot be used for the injection-molded long-fiber-reinforced thermoplastic composites considered in the present study since the fibers typically bend during the molding process and, therefore, do not always have a rigid rod shape. Nonetheless, the results still provide a useful qualitative description of the fiber orientation and were thus still retained in the present study.

2.7.3. Fiber Weight Fraction

The glass fibers appeared as white stripes in the optical microscopy images in the model and were detected automatically by setting appropriate threshold values for the grayscales of the scanned images in Avizo. The fiber fraction volume could then be determined by computing the data detected in white regions using Avizo's built-in thresholding modules. The fiber volume fraction within the various samples was determined by setting thresholding values for the grayscales and coloring the white-striped regions in the images in the Avizo model. Different from determining the air trap content, the white-striped regions in the images represented the glass fibers that could be detected and calculated using the built-in modules. The fiber weight fraction was then computed using polypropylene and glass fiber densities of 0.90 g/cm³ and 2.54 g/cm³, respectively.

2.7.4. Air Trap Volume Fraction

The air trapped within the sample appeared as black regions in the model and was detected automatically by setting appropriate threshold values for the grayscales of the scanned images in Avizo. The air trap volume fraction could then be determined by computing the data detected in the black regions using the built-in thresholding modules.

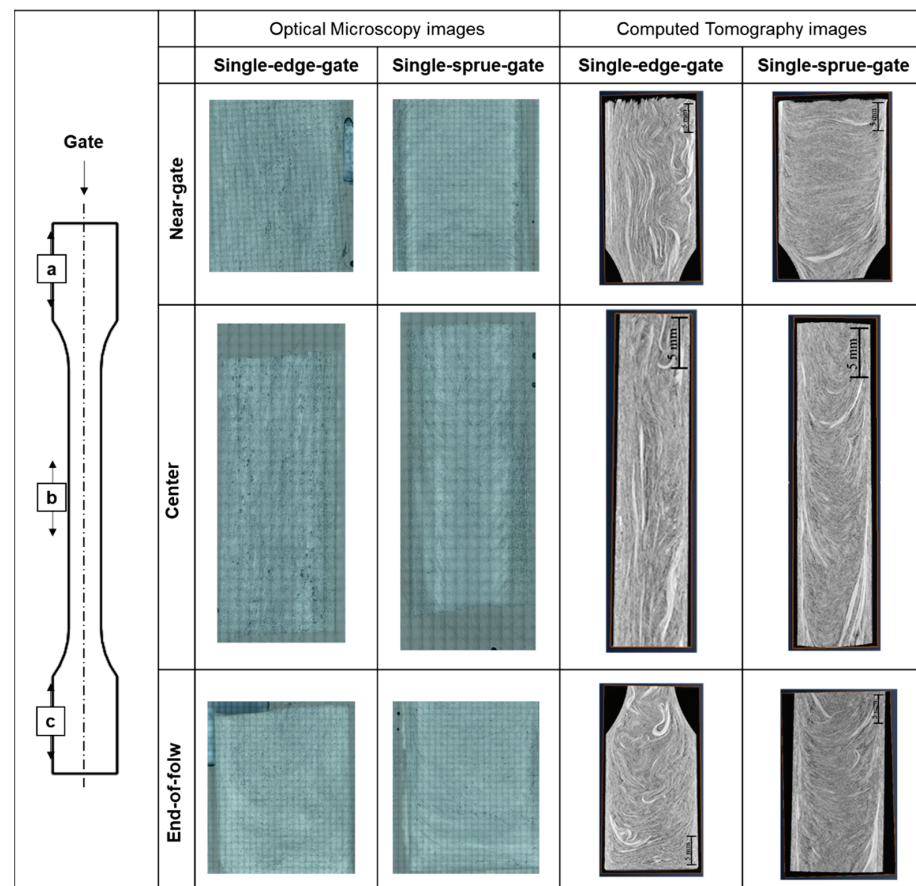


Figure 6. Observation of optical microscopy and computed tomography images (core layer) for different melt flow paths: (a) the near-gate region, (b) the center region, and (c) the end-of-flow region.

2.8. Tensile Test

In accordance with the ISO 527-2 standard, the test specimens were designed with a length of 170 mm, a width of 10 mm, and a thickness of 3 mm. The tensile tests were conducted on an AG-100 KN machine (Shimadzu Scientific Instruments Co. Ltd., Taipei, Taiwan) with a maximum load of 1000 kgf and a constant crosshead speed of 20 mm/min. For each set of experimental conditions and for both flow paths (i.e., the single-sprue gate and the single-edge gate), 20 tensile tests were performed, with the results averaged to obtain a final representative tensile strength value.

3. Results and Discussion

3.1. Comparison of High-Temperature Sintering and the Optical Microscopy Method

Figure 7 compares the fiber length results obtained from the high-temperature sintering and the optical microscopy images. It can be observed that the sample lengths after high-temperature sintering were longer than those measured using optical microscopy in each of the scanning locations. The difference between the two results is attributed to the greater interval (0.2 mm) between the sequential layers in the images obtained using optical microscopy. Consequently, fibers may be erroneously detected as discontinuous segments if they pass through multiple layers of the Avizo model. However, despite the difference in the absolute values of the fiber length, the two methods showed a similar trend in terms of the variations in the fiber length in different regions of the sample. The study shows that the central region of the sample has the longest fiber length. However, for the single-sprue-gate part, the optical microscopy result shows that the longest fiber length is at the end of the mold cavity. According to the results, the fiber lengths at the two locations are considerably

close. Thus, the trend that the central region of the sample has the longest fiber length can be justified.

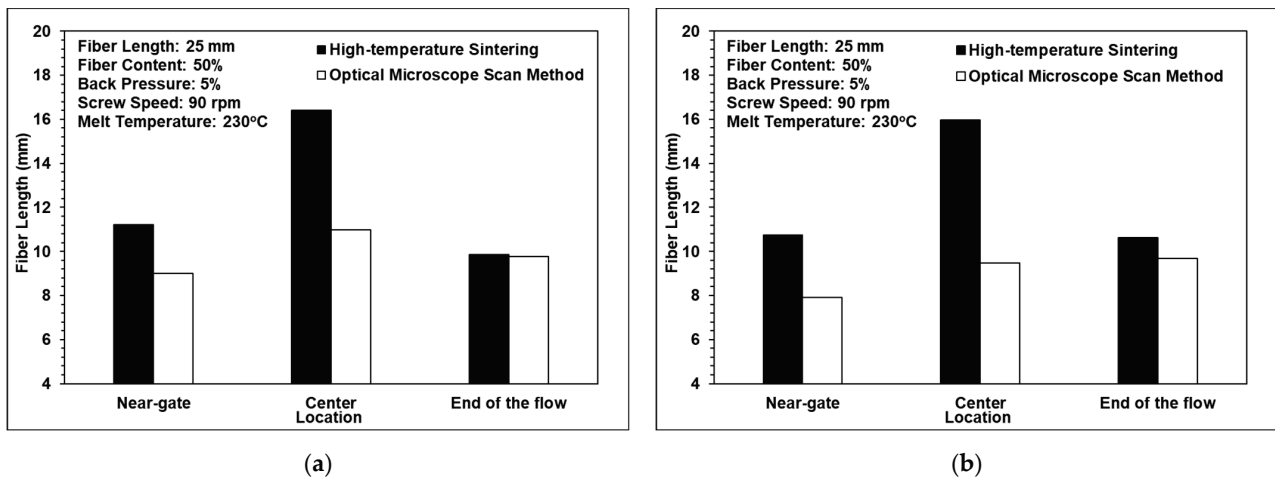


Figure 7. Comparison of fiber lengths using high-temperature sintering and optical microscopy for (a) the single-edge gate and (b) the single-sprue gate.

3.2. Comparison of the Computerized Tomography and Optical Microscopy Results

Figures 8 and 9 show the computed tomography and optical microscopy results for the fiber orientation within the single-edge-gate and simple-sprue-gate samples, respectively. Note that, as described in Section 1, notations a11, a22, and a33 refer to the flow direction, the cross flow direction, and the thickness direction, respectively. For both sample types, good qualitative agreement existed between the computed tomography image and each region of the sample. The number of fibers aligned in the flow direction was slightly higher in the computed tomography images than in the optical microscopy images since, in the latter case, the fibers may have been falsely identified as discontinuous segments due to the larger spacing distance between adjacent layers. For both models, and both sample types, the maximum number of fibers aligned in the flow direction in the central region due to the contraction of the specimen geometry, which constrains the flow in an axial direction [22]. In contrast, there were a11 tensor component reductions in the end-of-flow region due to the expansion of the specimen structure, which allowed freer flow in multiple directions as it filled the mold.

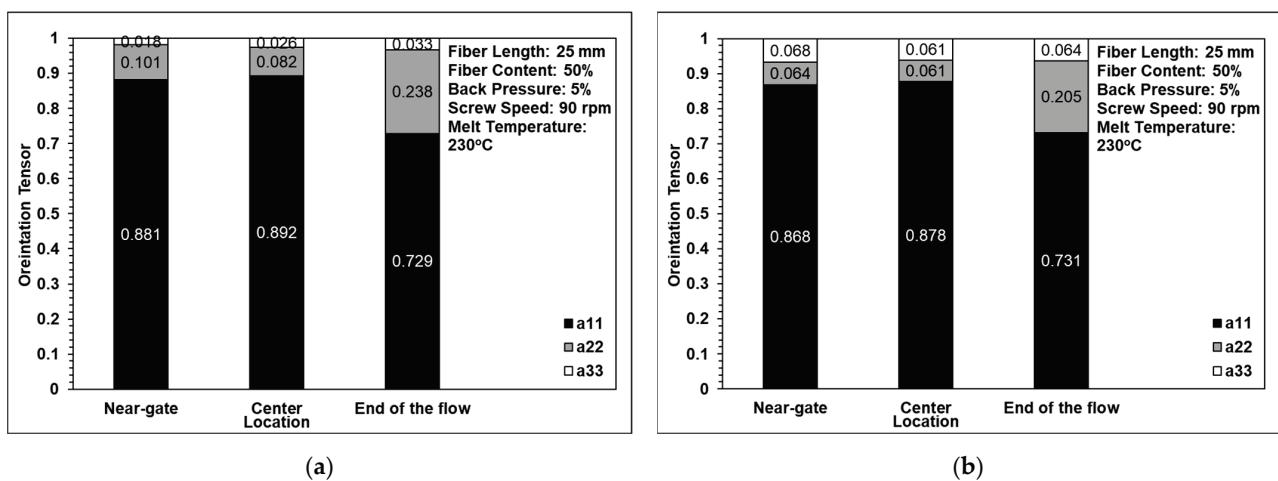


Figure 8. Comparison of orientation tensor in (a) computed tomography and (b) optical microscopy images of a single-edge gate.

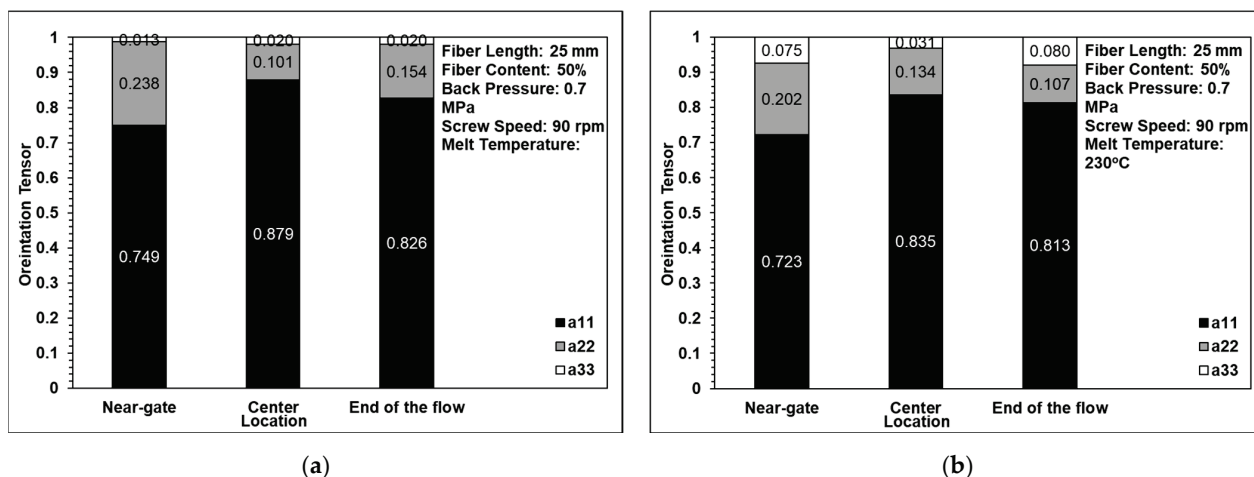


Figure 9. Comparison of the orientation tensor in (a) computed tomography and (b) optical microscopy images of a single-sprue gate.

3.3. Fiber Length Analysis

Figure 10 shows the effects of the back pressure, the screw speed, and the melt temperature on the fiber length. It can be observed that a fiber length of approximately 10 mm was maintained when the back pressure and the screw speed were assigned low values, of 0.7 MPa and 90 rpm, respectively. In other words, the three-barrel injection molding unit successfully protects the fibers from serious damage during the molding process provided that the processing conditions (back pressure and screw speed) are appropriately set. As the back pressure and the screw speed increase, the shear strain rate acting on the polymer melt also increases and, hence, the fibers tend to break. However, as shown in Figure 10c, the melt temperature had almost no effect on the fiber length. The result is similar to that of the previous research by Huang et al. [26].

For all three processing conditions, the fiber length in the central region of the single-edge-gate samples was longer than that in the single-sprue-gate samples. This finding is reasonable since the flow distance for the single-edge-gate cavity from the injection nozzle was longer than that for the single-sprue-gate cavity. As a result, the pressure gradient and the shear strain rate were both reduced and, hence, the fiber underwent less deformation and damage during the molding process.

3.4. Fiber Orientation Analysis

Figure 11 shows the effects of back pressure on the fiber orientation in the single-edge-gate and single-sprue-gate samples. Note that, as described in Section 1, notations a11, a22, and a33 refer to the flow direction, the cross flow direction, and the thickness direction, respectively. Figure 12 shows the equivalent results for the effects of screw speed, and Figure 13 shows the effects of the melt temperature. In general, the results indicate that, for all of the considered processing conditions, most of the fibers were aligned in the flow direction due to the shallow geometry of the tensile specimens and the long-fiber nature of the composite material. The number of fibers oriented perpendicularly to the flow direction increased slightly as the back pressure and the screw speed were increased since more severe fiber breakage leads to shorter fibers under such conditions. For example, when the back pressure values are set to 0, 0.7, and 1.12 MPa, the cross directions of the fiber orientation are 0.132, 0.016, and 0.208, respectively. This means that when the back pressure increased, the cross-direction fiber orientation of the single-edge gate and the single-sprue gate increased to 15% and 9%, respectively. When increasing the screw speed, the cross direction of the single-edge gate and the single-sprue gate increased to 4% and 8%, respectively. However, the melt temperature had little effect on the fiber orientation. The melt flow path also had only a minor effect on the orientation of the fibers in the

present study. When increasing the melt temperature, the cross-direction fiber orientation of the single-edge gate and the single-sprue gate changed to 1% and 7%, respectively. Sanou et al. [16] mentioned that the melt temperature affects the fiber orientation in the short-fiber-length case. However, in this study, the fiber length is considerably long, so the injection parameters will have only a small effect on the fiber orientation.

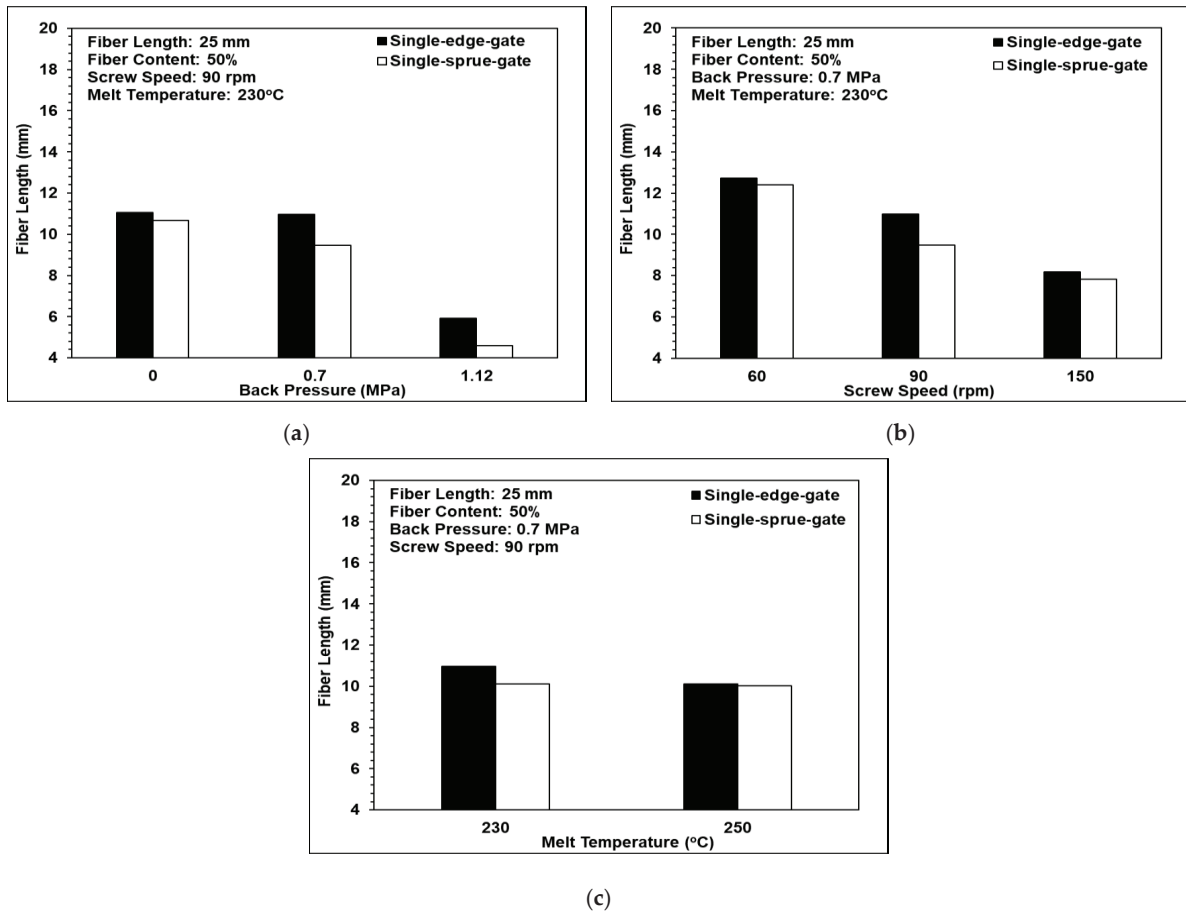


Figure 10. Effects of the different melt flow paths on fiber length: (a) back pressure variations, (b) screw speed variations, and (c) melt temperature variations.

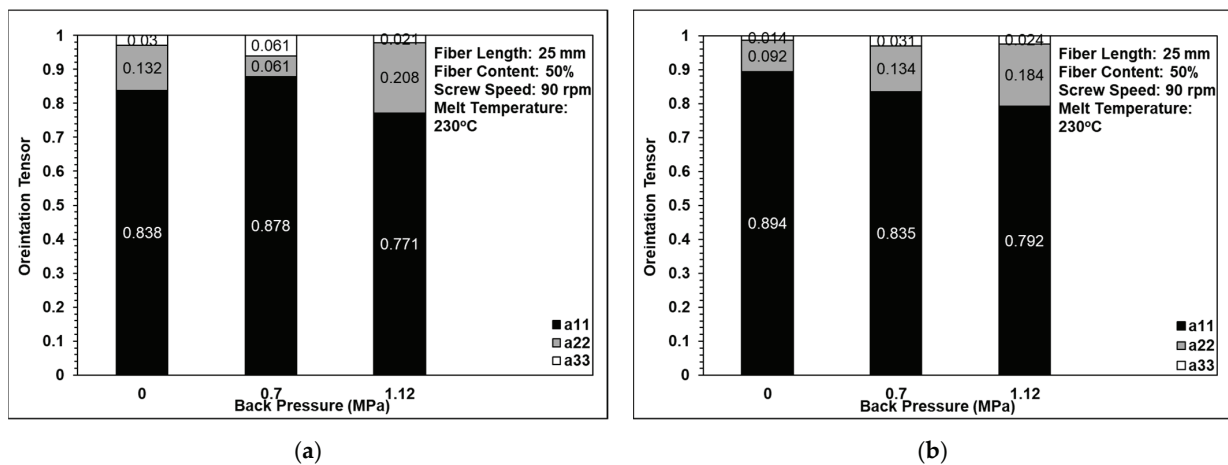


Figure 11. Effects of back pressure on fiber orientation in (a) the single-edge gate and (b) the single-sprue gate.

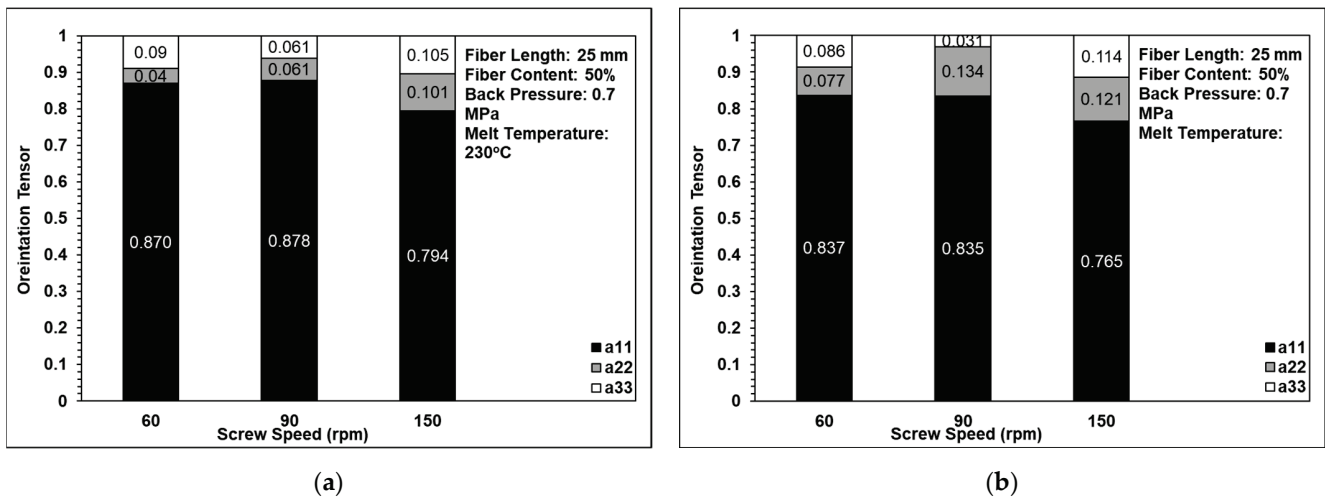


Figure 12. Effects of screw speed on fiber orientation in (a) the single-edge gate and (b) the single-sprue gate.

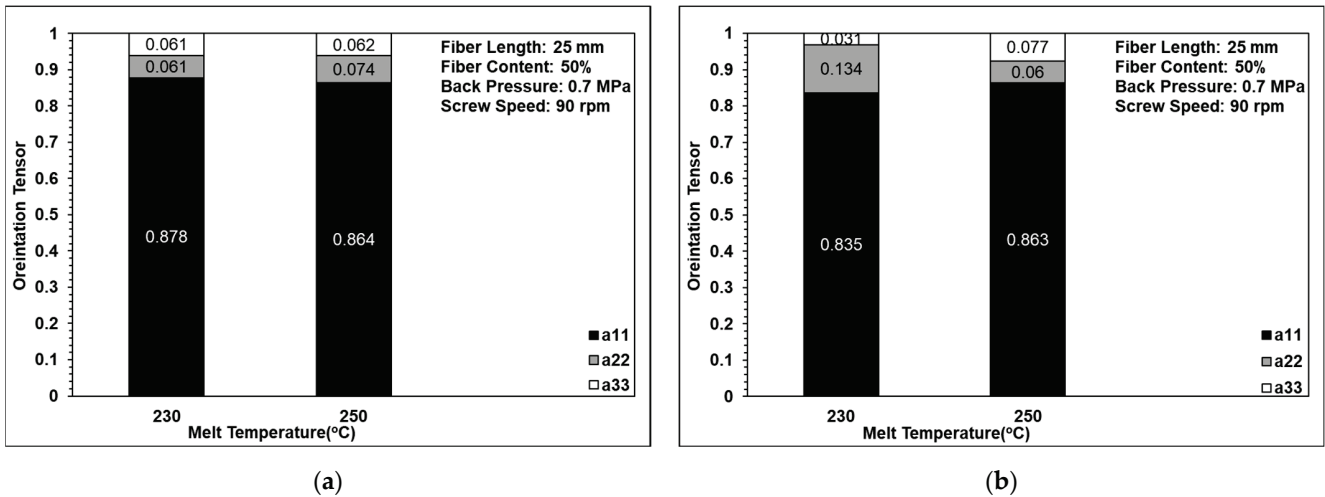


Figure 13. Effects of melt temperature on fiber orientation in (a) the single-edge gate and (b) the single-sprue gate.

3.5. Fiber Weight Fraction Analysis

Figure 14 shows the effects of back pressure, screw speed, and melt temperature, respectively, on the fiber weight fraction. In general, the results indicate that neither the process parameters nor the melt flow path significantly affect the weight fraction of the fibers. This study is more focused on the influence of fiber length and orientation on the properties of the injection-molded long-fiber-reinforced parts, and the fiber weight fraction analysis is just used to validate that the fiber content is close to 50 wt.%. According to the analysis results, the trends in the fiber weight fraction tend to be constant and do not change significantly under different process conditions. For example, the weight fraction of the single-sprue gate at 60, 90, and 150 rpm of screw speed resulted in 44, 46, and 45 wt.%, respectively.

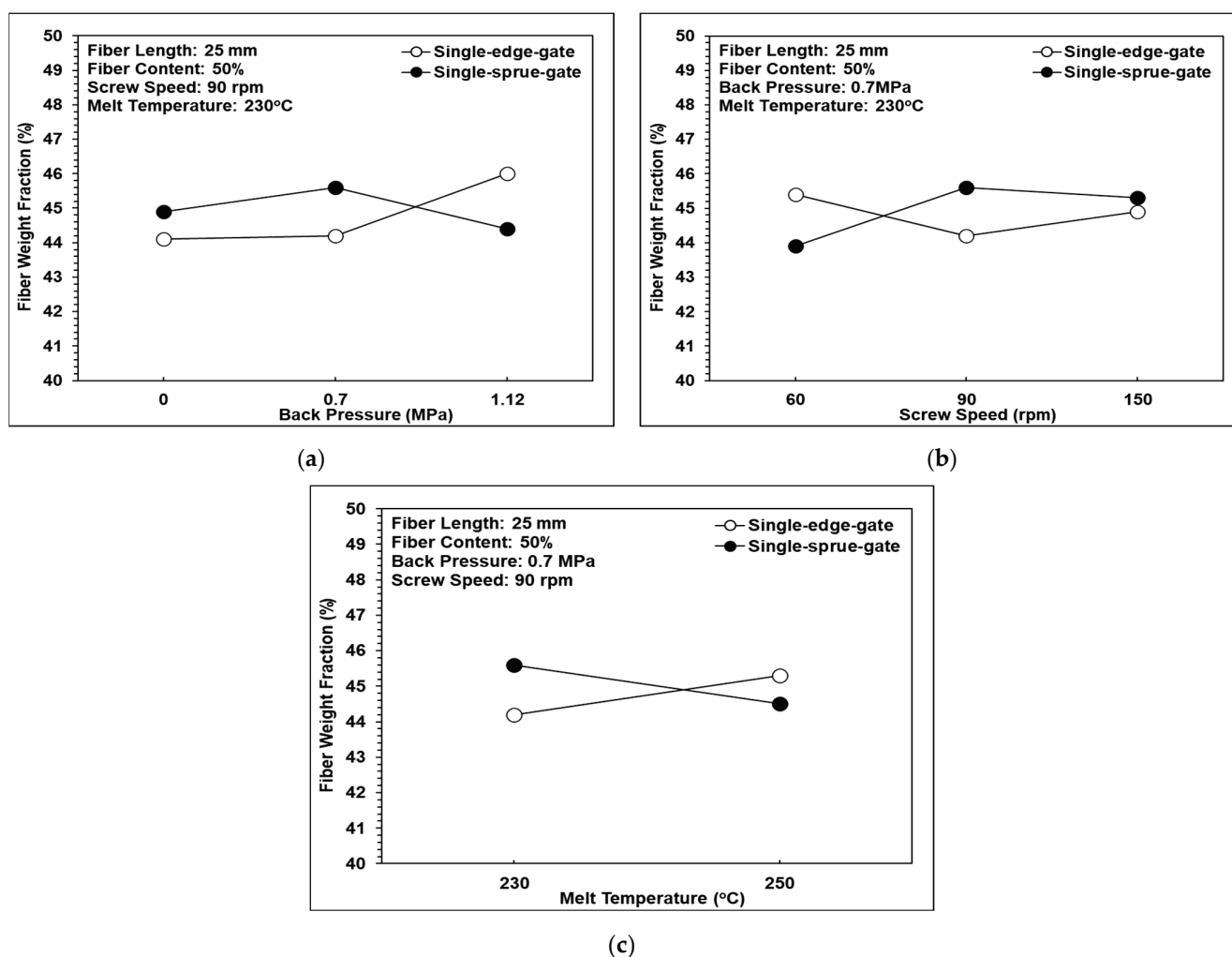


Figure 14. Effects of the different melt flow paths on the fiber weight fraction: (a) back pressure variations, (b) screw speed variations, and (c) melt temperature variations.

3.6. Air Trap Volume Fraction Analysis

The existence of air traps in fiber-reinforced composites significantly reduces their mechanical performance. Figure 15 shows the effects of back pressure, screw speed, and melt temperature, respectively, on the air trap volume fraction in the present samples. It can be observed that as the back pressure and the screw speed were increased, the volume fraction of the air traps reduced due to the corresponding increase in the pressure gradient, which expels the trapped air within the composite resin. However, the melt temperature had no obvious effect on the air trap volume fraction. The air trap volume fraction within the single-edge-gate samples was higher than that in the single-sprue-gate samples. This finding is reasonable since the flow path in the single-edge-gate cavity was longer than that in the single-sprue-gate cavity and, hence, the pressure gradient and the shear strain rate were smaller. Consequently, the trapped air was more difficult to expel.

3.7. Tensile Strength Analysis

Figure 16a shows that as the back pressure was increased from 0 to 0.7 MPa, the tensile strength also increased. However, as the back pressure was further increased, to 1.12 MPa, the tensile strength decreased. This tendency is reasonable since for back pressure values of 0–0.7 MPa, the fiber length remained approximately constant, at around 10 mm (see Figure 10a), while the volume fraction of the air traps reduced (see Figure 15a). However, at higher back pressure, the fiber length reduced dramatically, to around 5 mm, and hence, the tensile strength was reduced significantly despite the further reduction in the air trap

volume fraction. In addition, the tensile strength of the single-edge-gate specimens was higher than that of the single-sprue-gate specimens due to relatively longer fiber length in the single-edge-gate samples, as discussed in previous sections.

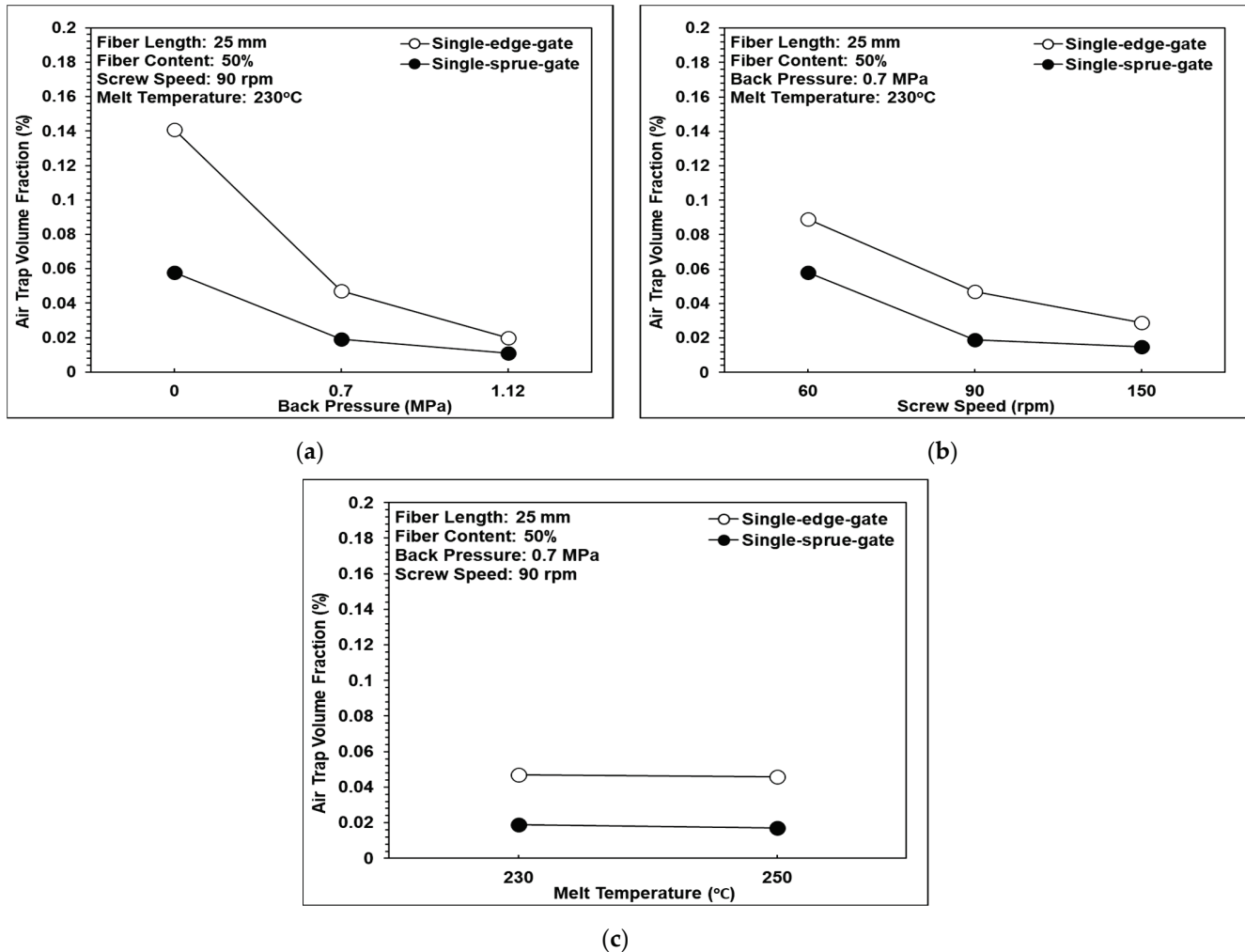


Figure 15. Effects of the different melt flow paths on the air trap volume fraction: (a) back pressure variations, (b) screw speed variations, and (c) melt temperature variations.

Figure 16b shows that as the screw speed was increased from 60 rpm to 150 rpm, the tensile strength was reduced. In Figures 10b and 15b, it can be observed that the rate of reduction in the volume fraction of the air traps with increases in the screw speed was greater than that of the fiber length. In the case of composite materials, a lower volume fraction of air traps increases the tensile strength, while a shorter fiber length reduces the tensile strength. Consequently, the results shown in Figure 16b suggest that in the long-fiber-reinforced thermoplastic parts investigated in this work, the tensile strength was dominated by the fiber length rather than the volume fraction of air traps.

Figure 16c shows that as the melt temperature was increased from 230 °C to 250 °C, the tensile strength also increased. The results presented above show that the melt temperature has no significant effect on the fiber length, fiber orientation, fiber weight fraction, or volume fraction of air traps. Hence, it can be inferred that the improved tensile strength of the long-fiber-reinforced thermoplastic parts at higher melt temperatures is the result of the greater fluidity and better bonding of the composite melt, which leads to a more uniform dispersion of the fibers within the matrix.

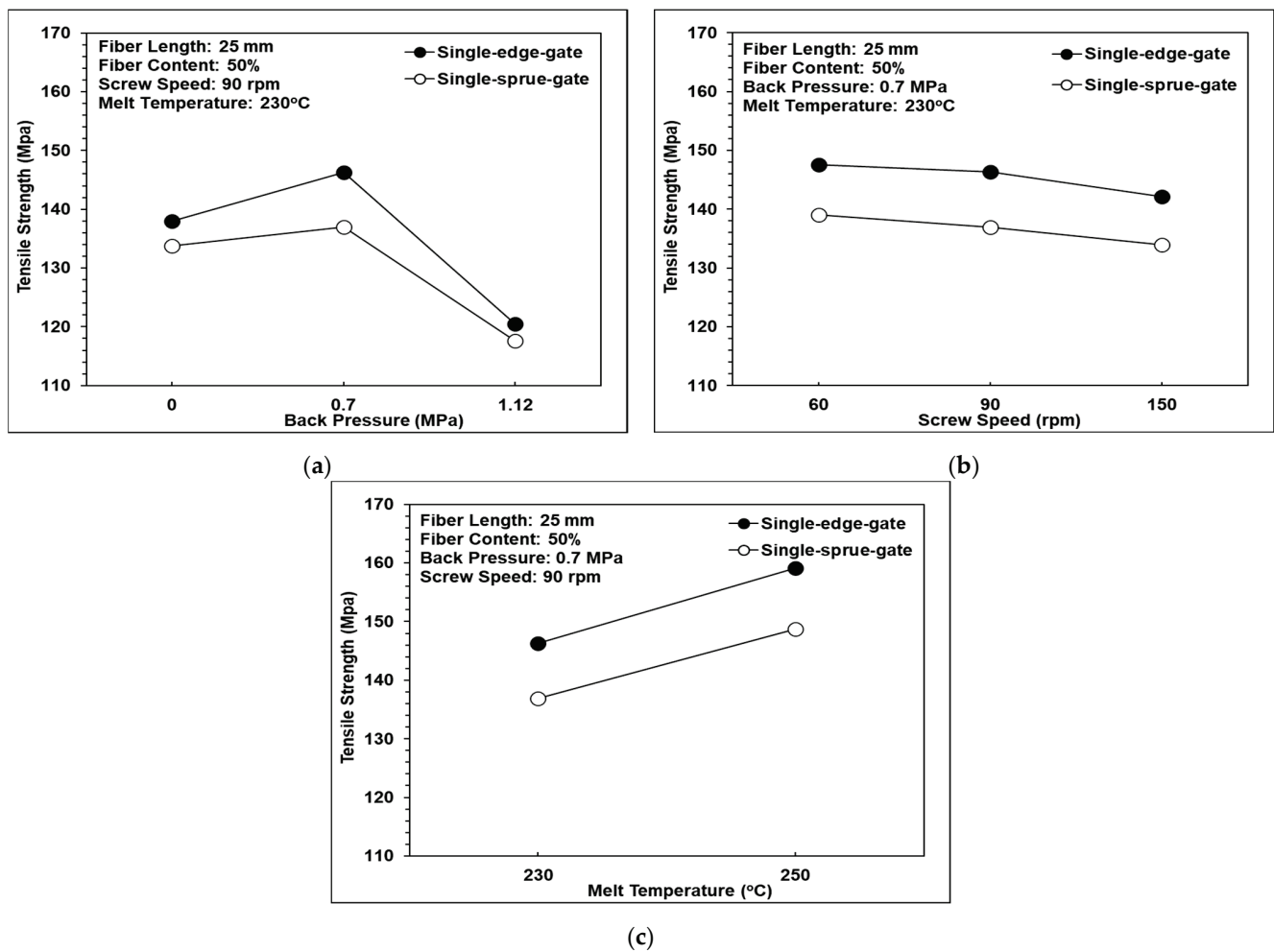


Figure 16. Effects of the different melt flow paths on tensile strength: (a) back pressure variations, (b) screw speed variations, and (c) melt temperature variations.

4. Conclusions

In this study, the effects of back pressure, screw speed, and melt temperature on the fiber characteristics and mechanical properties of long-fiber-reinforced thermoplastic parts were examined using a customized injection molding machine with a three-barrel injection system. The experiment results support the following significant findings and conclusions:

1. The experiments used 25 mm fiber length, and the results show that using the three-barrel injection molding machine, the fibers in the molded components retained a maximum average length of around 10 mm, which was much longer than that of the fibers in the parts produced using a traditional injection molding machine [8,20]. In other words, the effectiveness of the three-barrel-type injection unit in terms of minimizing the breakage of the reinforcing fibers is confirmed.
2. The fiber length results show that fiber breakage was dominated by the back pressure and the screw speed. By increasing the back pressure and the screw speed, the fiber length can be decreased to 57% and 37%, respectively. In contrast, the melt temperature had only a minor effect on the fiber length.
3. In fiber orientation results, it was found that most of the fibers within the long-fiber-reinforced thermoplastic parts were aligned in the flow direction due to the shallow geometry of the molded part (i.e., a tensile testing specimen) and the inherent long nature of the fibers. The back pressure, the screw speed, and the melt temperature do not significantly affect the fiber orientation because the fiber length is considerably long.

4. The air trap volume fraction results show that the volume fraction of the air traps in the single-edge-gate samples was higher than that in the single-sprue-gate samples due to the longer melt flow distance, which reduced both the pressure gradient and the strain rate during the molding process. In the case of both sample types, a higher back pressure and screw speed increased the pressure gradient and, therefore, reduced the volume fraction of the air traps. For example, increasing the back pressure from 0 to 1.12 MPa reduced the air trap volume fraction by 86% while increasing the screw speed from 60 to 150 rpm reduced the air trap volume fraction by 67%.
5. The tensile strength results show that as the back pressure was increased from 0 to 0.7 MPa, the fiber length was maintained and the volume fraction of the air traps was reduced. Consequently, the tensile strength of the molded components increased. However, as the back pressure was further increased, to 1.12 MPa, severe breakage of the fibers occurred. Hence, the tensile strength decreased. As the screw speed was increased from 60 to 150 rpm, the tensile strength also decreased since the dominant factor was the fiber length, even when the volume fraction of the air traps declined. The melt temperature had no significant effect on the fiber length, the fiber orientation, or the volume fraction of the air traps. However, as the melt temperature was increased, the fluidity of the melt increased and, hence, the fibers were dispersed more uniformly throughout the matrix. Consequently, the tensile strength increased.

Author Contributions: Methodology, G.-Y.L., C.-W.S., P.-W.H., S.-J.H., C.-T.H. and H.-S.P.; investigation, G.-Y.L.; formal analysis, G.-Y.L.; validation, S.-J.H.; writing—original draft preparation, G.-Y.L., C.-W.S. and S.-J.H.; writing—review and editing, G.-Y.L., C.-W.S., P.-W.H. and S.-J.H.; and supervision, S.-J.H. All authors have read and agreed to the published version of the manuscript.

Funding: This research was funded by the Ministry of Science and Technology of Taiwan, grant number MOST-107-2622-E-006-024-CC1.

Institutional Review Board Statement: The study did not require ethical approval.

Informed Consent Statement: Not applicable.

Data Availability Statement: The data presented in this study are available on request from the corresponding author.

Conflicts of Interest: The authors declare no conflict of interest.

References

1. Saba, N.; Tahir, P.M.; Jawaid, M. A Review on potentiality of nano filler/natural fiber filled polymer hybrid composites. *Polymers* **2014**, *6*, 2247–2273. [CrossRef]
2. Reale Batista, M.D.; Drzal, L.T.; Kiziltas, A.; Mielewski, D. Hybrid cellulose-inorganic reinforcement polypropylene composites: Lightweight materials for automotive applications. *Polym. Compos.* **2020**, *41*, 1074–1089. [CrossRef]
3. Wollan, E. Up Engineering Thermoplastics Using Glass and Carbon Fiber Reinforcement, July, 2015. Available online: <https://www.plasticomp.com/up-engineering-thermoplastics-using-glass-and-carbon-fiber-reinforcement/> (accessed on 23 February 2022).
4. Thomason, J. The influence of fibre length and concentration on the properties of glass fibre reinforced polypropylene: 7. Interface strength and fibre strain in injection moulded long fibre PP at high fibre content. *Compos. Part A Appl. Sci. Manuf.* **2007**, *38*, 210–216. [CrossRef]
5. Sun, Z.-Y.; Han, H.-S.; Dai, G.-C. Mechanical Properties of Injection-molded Natural Fiber-reinforced Polypropylene Composites: Formulation and Compounding Processes. *J. Reinf. Plast. Compos.* **2010**, *29*, 637–650. [CrossRef]
6. Le Baillif, M.; Oksman, K. The Effect of Processing on Fiber Dispersion, Fiber Length, and Thermal Degradation of Bleached Sulfite Cellulose Fiber Polypropylene Composites. *J. Thermoplast. Compos. Mater.* **2009**, *22*, 115–133. [CrossRef]
7. Advani, S.G.; Sozer, E.M. *Process Modeling in Composites Manufacturing*, 1st ed.; CRC Press: Boca Raton, FL, USA, 2002.
8. Teuwsen, J.; Goris, S.; Osswald, T. Impact of the process-induced microstructure on the mechanical performance of injection molded long glass fiber reinforced polypropylene. In Proceedings of the SPE-ANTEC, Material Science, Anaheim, CA, USA, 8–10 May 2017.
9. Toll, S.; Andersson, P.O. Microstructure of long- and short-fiber reinforced injection molded polyamide. *Polym. Compos.* **1993**, *14*, 116–125. [CrossRef]
10. Wang, J.; Geng, C.; Luo, F.; Liu, Y.; Wang, K.; Fu, Q.; He, B. Shear induced fiber orientation, fiber breakage and matrix molecular orientation in long glass fiber reinforced polypropylene composites. *Mater. Sci. Eng. A* **2011**, *528*, 3169–3176. [CrossRef]

11. Kumar, K.S.; Patel, V.; Tyagi, A.; Bhatnagar, N.; Ghosh, A.K. Injection Molding of Long Fiber Reinforced Thermoplastic Composites. *Int. Polym. Process.* **2009**, *24*, 17–22. [CrossRef]
12. Huang, C.-T.; Tseng, H.-C. Simulation prediction of the fiber breakage history in regular and barrier structure screws in injection molding. *Polym. Eng. Sci.* **2018**, *58*, 452–459. [CrossRef]
13. Güllü, A.; Özdemir, A.; Özdemir, E. Experimental investigation of the effect of glass fibres on the mechanical properties of polypropylene (PP) and polyamide 6 (PA6) plastics. *Mater. Des.* **2006**, *27*, 316–323. [CrossRef]
14. Lafranche, E.; Krawczak, P. Injection moulding of long glass fibre reinforced thermoplastics (LFT): Structure/processing conditions/mechanical properties relationship. In Proceedings of the ESAFORM Conference on Material Forming, Glasgow, UK, 26–28 April 2006.
15. Huang, P.W.; Peng, H.S.; Hwang, S.J.; Huang, C.T.; Chen, P.C.; Ke, Y.Y.; Pen, P.S.; Wu, C.C.; Tu, C.I. Study of the effect of process parameters on fiber length, fiber orientation and tensile strength of long glass fiber reinforced polypropylene molding. In Proceedings of the 77th Annual Technical Conference of the Society of Plastics Engineers, ANTEC 2019, Detroit, MI, USA, 18–21 March 2019.
16. Sanou, M.; Chung, B.; Cohen, C. Glass fiber-filled thermoplastics. II. Cavity filling and fiber orientation in injection molding. *Polym. Eng. Sci.* **1985**, *25*, 1008–1016. [CrossRef]
17. Lafranche, E.; Krawczak, P.; Ciolczyk, J.P.; Maugey, J. Injection moulding of long glass fiber reinforced polyamide 66: Processing conditions/microstructure/flexural properties relationship. *Adv. Polym. Technol. J. Polym. Process. Inst.* **2005**, *24*, 114–131. [CrossRef]
18. Salleh, F.M.; Hassan, A.; Yahya, R.; Azzahari, A.D. Effects of extrusion temperature on the rheological, dynamic mechanical and tensile properties of kenaf fiber/HDPE composites. *Compos. Part B Eng.* **2014**, *58*, 259–266. [CrossRef]
19. Yilmazer, U.; Cansever, M. Effects of processing conditions on the fiber length distribution and mechanical properties of glass fiber reinforced nylon-6. *Polym. Compos.* **2002**, *23*, 61–71. [CrossRef]
20. Rohde, M.; Ebel, A.; Wolff-Fabris, F.; Altstädt, V. Influence of Processing Parameters on the Fiber Length and Impact Properties of Injection Molded Long Glass Fiber Reinforced Polypropylene. *Int. Polym. Process.* **2011**, *26*, 292–303. [CrossRef]
21. Hagstrand, P.O.; Bonjour, F.; Månson, J.A. The influence of void content on the structural flexural performance of unidirectional glass fibre reinforced polypropylene composites. *Compos. Part A Appl. Sci. Manuf.* **2005**, *36*, 705–714. [CrossRef]
22. Peng, X.L. Study of the Orientation and Breakage History of Fibers through Runner and Cavity in Injection Molded Reinforced Thermoplastics. Master's Thesis, National Cheng Kung University, Tainan, Taiwan, 2017.
23. Bernasconi, A.; Cosmi, F.; Hine, P. Analysis of fibre orientation distribution in short fibre reinforced polymers: A comparison between optical and tomographic methods. *Compos. Sci. Technol.* **2012**, *72*, 2002–2008. [CrossRef]
24. Huang, C.-T.; Lai, C.-H. Investigation on the Coupling Effects between Flow and Fibers on Fiber-Reinforced Plastic (FRP) Injection Parts. *Polymers* **2020**, *12*, 2274. [CrossRef] [PubMed]
25. Advani, S.G.; Tucker, C.L., III. The use of tensors to describe and predict fiber orientation in short fiber composites. *J. Rheol.* **1987**, *31*, 751–784. [CrossRef]
26. Huang, P.-W.; Peng, H.-S.; Hwang, S.-J.; Huang, C.-T. The Low Breaking Fiber Mechanism and Its Effect on the Behavior of the Melt Flow of Injection Molded Ultra-Long Glass Fiber Reinforced Polypropylene Composites. *Polymers* **2021**, *13*, 2492. [CrossRef] [PubMed]

Article

Dielectric Properties of Fluorinated Aromatic Polyimide Films with Rigid Polymer Backbones

Jian-Jun He ^{1,2}, Hai-Xia Yang ^{1,*}, Feng Zheng ^{3,*} and Shi-Yong Yang ^{1,2}

¹ Key Laboratory of Science and Technology on High-Tech Polymer Materials, Institute of Chemistry, Chinese Academy of Sciences, Beijing 100190, China; hejianjun@iccas.ac.cn (J.-J.H.); shiyang@iccas.ac.cn (S.-Y.Y.)

² School of Chemical Engineering, University of Chinese Academy of Sciences, Beijing 100049, China

³ School of Chemical Science and Engineering, Tongji University, Shanghai 200092, China

* Correspondence: yanghx@iccas.ac.cn (H.-X.Y.); fzhen@tong.edu.cn (F.Z.)

Abstract: Fluorinated aromatic polyimide (FAPI) films with rigid polymer backbones have been prepared by chemical imidization approach. The polyimide films exhibited excellent mechanical properties including elastic modulus of up to 8.4 GPa and tensile strength of up to 326.7 MPa, and outstanding thermal stability including glass transition temperature (T_g) of 346.3–351.6 °C and thermal decomposition temperature in air (T_{d5}) of 544.1–612.3 °C, as well as high colorless transmittance of >81.2% at 500 nm. Moreover, the polyimide films showed stable dielectric constant and low dielectric loss at 10–60 GHz, attributed to the close packing of rigid polymer backbones that limited the deflection of the dipole in the electric field. Molecular dynamics simulation was also established to describe the relationship of molecular structure and dielectric loss.

Keywords: fluorinated aromatic polyimide; low dielectric loss; molecular chain orientation; molecular dynamics simulation

Citation: He, J.-J.; Yang, H.-X.; Zheng, F.; Yang, S.-Y. Dielectric Properties of Fluorinated Aromatic Polyimide Films with Rigid Polymer Backbones. *Polymers* **2022**, *14*, 649. <https://doi.org/10.3390/polym14030649>

Academic Editors: Somen K. Bhudolia and Sunil Chandrakant Joshi

Received: 16 December 2021

Accepted: 25 January 2022

Published: 8 February 2022

Publisher's Note: MDPI stays neutral with regard to jurisdictional claims in published maps and institutional affiliations.



Copyright: © 2022 by the authors. Licensee MDPI, Basel, Switzerland. This article is an open access article distributed under the terms and conditions of the Creative Commons Attribution (CC BY) license (<https://creativecommons.org/licenses/by/4.0/>).

1. Introduction

Aromatic polyimide films have been widely used in the microelectronic manufacturing and packaging industry due to its excellent thermal stability, combined mechanical properties, dimensional stability, chemical resistance and electrical insulating properties [1–4]. With the rapid advancement of communication technology, much attention has been focused on lowering the dielectric loss of polyimide films at high frequency.

It is an effective way to reduce the dielectric constant of the polymer by decreasing the molar polarizability or increasing the molar volume of the molecules. Hence, the dielectric constants of polyimides could be reduced by introducing fluorine [5–8], aliphatic/alicyclic structure [9–11], large side groups [12–16] or air [17–20] into polymer backbones. Zhi et al. [21] synthesized a series of semi-aromatic polyimide sheets, which were derived from the copolymerization of an alicyclic tetrahedral dianhydride (HBPDA) and an aromatic diamine mixture containing three flexible diamines. The copolyimide films showed dielectric constant of 2.56 and dielectric loss of 0.004 at 1 MHz. However, the glass transition temperatures of the films were lower than 290 °C and no mechanical properties were described. Ma et al. [22] prepared porous low-dielectric polyimide films by using microemulsion method, in which water droplets acted as template. Polyhedral oligomeric polysiloxane (POSS) with hierarchical porous structure was coated on both sides of planar polyimide (PI) films to prepare sandwich composite films. The films exhibited ultra-low dielectric constant (2.28) and dielectric loss (0.005) at 1 MHz, as well as low water absorption (0.56%). However, the composite films were brittle, having elongation at breakage of lower than 10%, and no dielectric properties at high frequencies were described.

Compared with dielectric constant, there are few reports on the reducing of dielectric loss of polyimide films at high frequencies (>10 GHz). Under the alternating electric field,

the dipole of the polymer chain is deflected back and forth. Dielectric loss mainly comes from the energy loss generated by the dipole in order to overcome the friction resistance and dissipated in the form of heat energy. Hence, it is reasonable to consider that the dipole deflection amplitude in alternating electric field can be limited by decreasing of the molecular chain spacing and increasing of the interchain interaction force, thus resulting in the low dielectric loss.

Fluorinated aromatic polyimides have been reported to exhibit low dielectric constant and low dissipation factor [23]. However, they have usually shown low modulus and high coefficient of thermal expansion, and are not suitable to be the base film of flexible printed circuit board. In this study, fluorinated aromatic polyimide films with high modulus and excellent dielectric properties at high frequency were prepared by introducing rigid rod-like structures in polymer backbone. Influence of the chemical structures on the combined properties of these films were systematically investigated. The relationship between the tight packing of polymer chains and the dielectric properties at high frequency was further illustrated by molecular dynamics simulation.

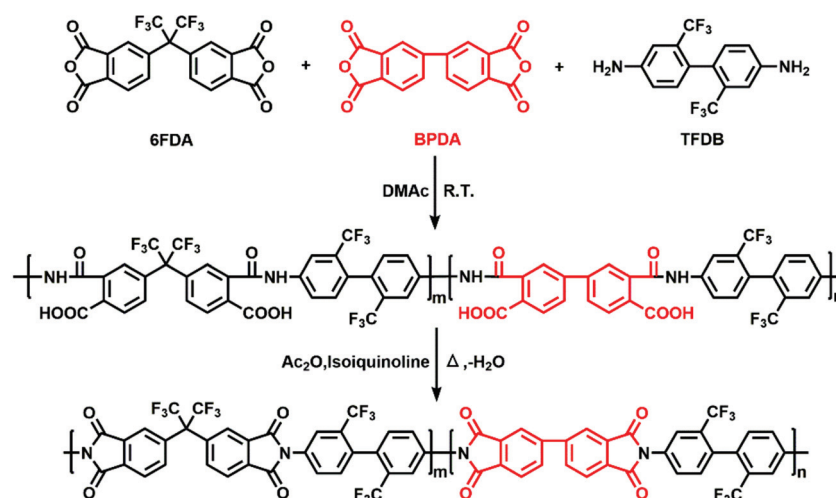
2. Materials and Methods

2.1. Materials

4,4'-(Hexafluoroisopropylidene) diphthalic anhydride (6FDA), 2,2'-Bis(trifluoromethyl)benzidine (TFDB) and 3,3',4,4'-Biphenyltetracarboxylic dianhydride (BPDA) was purchased from Chinatech (Tianjin, China) Chemical Co., Ltd. and dianhydrides including 6FDA and BPDA were used after vacuum drying at 160 °C for 3 h. Dimethylacetamide (DMAc) was purchased from Concord Technology (Tianjin, China) Co., Ltd. and used without distilled. Acetic anhydride was obtained from Sinopharm Chemical Reagent Co., Ltd. (Shanghai, China) while isoquinoline was obtained from Shanghai Aladdin Biochemical Technology Co., Ltd., (Shanghai, China) and both of them were directly used.

2.2. Methods

Fluorinated aromatic polyimide films were prepared by a two-step chemical imidization method displayed in Scheme 1. 32.02 g (100 mmol) of TFDB and 282 mL of DMAc were added into a three-neck round-bottom flask under a nitrogen atmosphere. After TFDB was completely dissolved, 13.33 g (30 mmol) of 6FDA and 20.60 g (70 mmol) of BPDA were added separately into the solution. The solution was mechanically stirred at room temperature for 24 h to give a homogeneous poly (amic acid) (PAA) solution with a solid content of 20% (FAPI-70).



Scheme 1. Synthesis of the fluorinated aromatic polyimide films.

The PAA solution, diluted by DMAc to 15% solid content, was mixed with a chemical imidization reagent (acetic anhydride: isoquinoline = 1:1, molar ratio), and then defoamed completely by a de-aerating mixer. The mixture was cast onto a dust-free glass plate with an adjustable doctor blade, and was then thermally baked in an oven with the following procedure: 65 °C/5 min, 75 °C/5 min, 85 °C/15 min. After most of the solvent was evaporated, a partially-cured film was peeled off from the glass plate, which was then fixed on the metal fixture and imidized completely in an oven with the following procedure to give the fluorinated aromatic polyimide (FAPI-70) film: 180 °C/5 min, 210 °C/3 min, 330 °C/3 min.

Similarly, a series of FAPI films with different molar ratios of BPDA/6FDA, including FAPI-0 (BPDA/6FDA = 0/100), FAPI-80 (BPDA/6FDA = 80/20), FAPI-90 (BPDA/6FDA = 90/10), FAPI-100 (BPDA/6FDA = 100/0), have been prepared, successively.

2.3. Characterization

Fourier transform infrared spectroscopy (FTIR) were carried out on TENSOR27 of Bruker Company with scanning wavenumber ranging from 3400 cm^{-1} to 600 cm^{-1} at Attenuated Total Reflection (ATR) mode to measure the imidization degree.

^{13}C NMR spectra were performed on a Bruker solid state NMR spectrometer AVANCE III 400 and collected at different spinning speeds to locating the chemical shift of spinning side bands.

Dielectric properties of FAPI films were measured on N5227B PNA Network Analyzer of Keysight Company equipped with cylindrical cavity resonance clamps at high frequencies of 10 GHz, 24 GHz, 40 GHz and 60 GHz, respectively.

Wide-angle X-ray diffraction (WAXRD) were executed in the range of 5°–50° at a scanning speed of 5 ($^{\circ}$) $\cdot\text{min}^{-1}$ on the Empyrean diffractometer of Malvern Panalytical Company with Cu $K\alpha$ radiation ($\lambda = 0.154 \text{ nm}$) at 40 kV.

Coefficients of thermal expansion (CTE) of FAPI films were undertaken on the Q400 thermomechanical analyzer with a heating rate of 5 $^{\circ}\text{C}\cdot\text{min}^{-1}$ and a load force of 0.05 N under a nitrogen flow. Before testing, the samples were treated at 150 °C for 5 min to remove the residual stress.

Birefringence index of FAPI films were measured by a prism coupler (Metric model PC-2000, Korea) at a wavelength of 633 nm.

Mechanical properties were measured on 5567 universal testing machines of Instron Company at a drawing rate of 2.0 $\text{mm}\cdot\text{min}^{-1}$.

Thermogravimetric analysis (TGA) was performed on a TA Q50 thermal analyzer in the range of 40 °C–800 °C with a heating rate of 20 $^{\circ}\text{C}\cdot\text{min}^{-1}$ in nitrogen and air, respectively. The sample was preheated to 150 °C for 5 min to remove moisture prior to testing.

Dynamic mechanical analysis (DMA) was performed on a TA Q800 thermal analyzer in the range of 40 °C–450 °C with a heating rate of 5 $^{\circ}\text{C}\cdot\text{min}^{-1}$ and a load frequency of 1 Hz under nitrogen atmosphere.

Ultraviolet-visible (UV-Vis) spectra of the FAPI films were recorded on a Hitachi U3900 spectrophotometer from 180 nm to 800 nm at room temperature with a sample's thickness of 25 μm . The yellowness and haze of the FAPI films were evaluated by X-rite Color i7 spectrophotometer, using an observational angle of 8° and a CIE (Commission International de l'Eclairage) standard D65 illuminant.

2.4. Computational Details

Molecular dynamics simulation was performed using Forcite module as implemented in Materials Studio 2019 software package. The molecular structures of FAPI films were constructed and their relevant parameters were calculated according to the following procedure:

Firstly, the repeating units of polyimides were built, and the single molecular chains containing 20 repeating units of two homopolymers (FAPI-0 and FAPI-100) were established

by the “homopolymer” tool [24,25] and followed by geometry optimization. Then, the amorphous polymeric models of FAPI-0 and FAPI-100 were constructed with 10 optimized chains using Amorphous Cell module. It's testified that reasonable molecular chain length and quantities are critical to simulate the real model, i.e., a short chain length can lead to end effects, whereas a long chain leads to increased simulation difficulties [26]. As for the random polymers, 10 molecular chains and 20 repeating units were adopted as well to the amorphous polymeric models with different probabilities on the basis of the copolymerization proportion of dianhydride monomers. All of the amorphous polymeric models were optimized ulteriorly to avoid convergence failure.

Molecular dynamics simulation was employed on the polyimide models to acquire the final equilibrium structures. As the initial polymeric models with the density of 0.5 g/cm^3 , a compressing procedure was carried out at 0.5 GPa under NPT ensemble. Afterwards, the frame with the closest density to the measured sample was exported for the NVT annealing dynamics with 10 cycles from 850 to 400 K to minimize the undesired inner stress between the chains. Then, the frame with the lowest potential energy was selected to run the final equilibration process under NVT ensemble at 0.0001 GPa and 298K for 500 ps. COMPASS II force field was utilized in the MD simulations. The Ewald method with an accuracy of 0.0001 kcal/mol was used to calculate both the non-bonded Van der Waals interactions and the non-bonded long-range electrostatic interactions. Furthermore, the Nosé thermostat and the Berendsen barostat were used to control the temperature and pressure at a time step of 1 fs, respectively.

Based on the final equilibrated PI models, Radius of gyration (R_g), Kuhn segment length (l_b), Cohesive Energy Density (CED) and Fractional Free Volume (FFV) were calculated.

3. Results and Discussion

3.1. Characterization

A series of fluorinated aromatic polyimides with different biphenyl group content in polymer backbone by changing the molar ratios of 6FDA/BPDA were successfully synthesized by chemical imidization method. Compared with the traditional thermal imidization method, chemical imidization method can initiate the imidization of PAA to polyimide at lower temperature. It is proved that the imidization procedure has been completed with the advent of 1778 cm^{-1} (C=O asymmetrical stretching of imide groups), 1720 cm^{-1} (C=O symmetrical stretching of imide groups), 1358 cm^{-1} (C–N stretching) and 737 cm^{-1} (C=O bending of imide rings) (Figure 1). No signal of –OH in –COOH ($3400\text{--}2500 \text{ cm}^{-1}$, a wide and uneven peak) was detected, implying that chemical imidization is a more effective pathway than thermal imidization.

Figure 2 depicts ^{13}C solid state NMR (SSNMR) spectra of the FAPI films. The peaks of ^{13}C in a variety of chemical environments have been detected, including the peaks at 166 ppm for C=O, 146 and 132 ppm for benzene rings, 124 ppm for $-\text{CF}_3$ and 65 ppm for the quaternary carbon atom of $-\text{C}(\text{CF}_3)_2$ group, respectively. The peak at 146 ppm is assigned to the carbon atoms which connected the benzene rings in the biphenyl unit. With increasing of biphenyl contents in the polymer backbones, the peak intensities became more and more obvious, meanwhile the intensity of $-\text{C}(\text{CF}_3)_2$ at 65 ppm decreased. The peak of the quaternary carbon atom of $-\text{C}(\text{CF}_3)_2$ group is not so visible due to the weak Nuclear Overhauser Effect (NOE) compared with other carbon atoms.

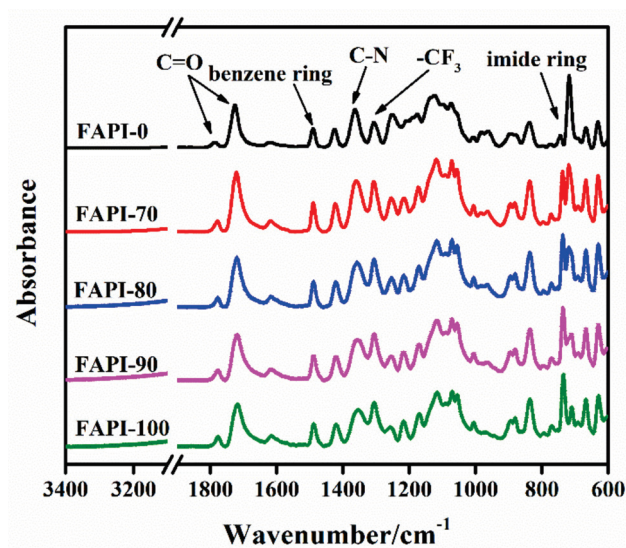


Figure 1. ATR-FTIR spectra of the FAPI films with different biphenyl group content in polymer backbone.

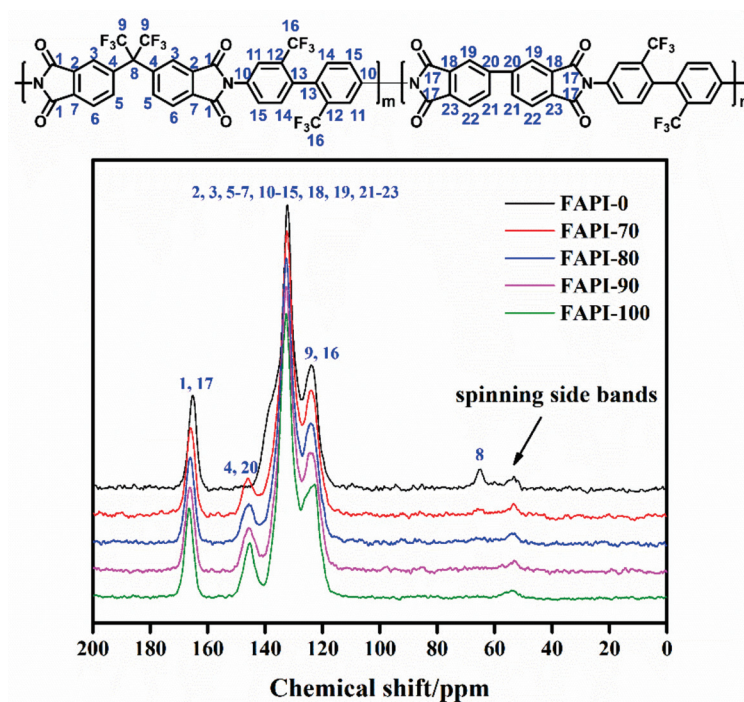


Figure 2. ^{13}C solid state NMR spectra of the FAPI films with different biphenyl group content in polymer backbone.

3.2. Mechanical and Optical Properties

Table 1 depicts the mechanical properties of the FAPI films including tensile modulus (T_M), tensile strength (T_s) and elongation at breakage (E_b). With the introduction of rigid rod-like biphenyl groups in the polyimide backbones, the FAPI films exhibited enhanced mechanical properties (Figure 3). It can be seen that both film modulus and strength have been improved gradually with increasing of the biphenyl contents in polymer backbones. For instance, FAPI-100 showed the highest T_M (8.4 GPa) and T_s (326.7MPa), compared with FAPI-80 ($T_M = 5.9$ GPa, $T_s = 203.3$ MPa) and FAPI-70 ($T_M = 4.9$ GPa, $T_s = 168.5$ MPa), respectively. The elongation at breakages was also enhanced by increasing the biphenyl group contents in polymer backbone from 16.5% (FAPI-70) to 43.2% (FAPI-100), probably

due to the higher polycondensation reactivity of the biphenyl-containing dianhydride monomer.

Table 1. Mechanical properties of the FAPI films.

FAPI Films	T_M /GPa	T_s /MPa	E_b /%	Thickness/ μm
FAPI-0	3.1	99.4	5.8	65.5
FAPI-70	4.9	168.5	16.5	55.0
FAPI-80	5.9	203.3	22.5	47.5
FAPI-90	7.1	256.4	36.2	48.0
FAPI-100	8.4	326.7	43.2	50.0

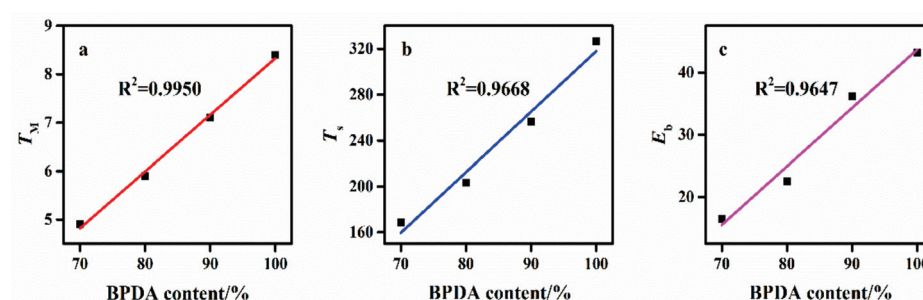


Figure 3. Relationship between mechanical properties and the biphenyl group content in polymer backbone.

Figure 4 shows the UV spectra of the FAPI films, which exhibits great visible transparency. With the increasing of the biphenyl contents in polyimide backbones, the light transmittance at 500 nm (T_{500}) was reduced gradually from 89.7% (FAPI-0) to 81.4% (FAPI-100) (Table 2), and the cutoff wavelength (λ_{cut}) was red-shifted from 334 nm (FAPI-0) to 381 nm (FAPI-100). Moreover, the yellowness (YI) increased from 1.3 (FAPI-0) to 6.9 (FAPI-100) and haze (HZ) from 1.7 (FAPI-0) to 4.1 (FAPI-100), respectively. Clearly, the optical transparency of FAPI films was deteriorated with the increasing of the biphenyl contents in polymer backbone, probably attributed to the higher bandgap energy of the biphenyl groups than the $-\text{CF}_3$ groups in polymer backbones.

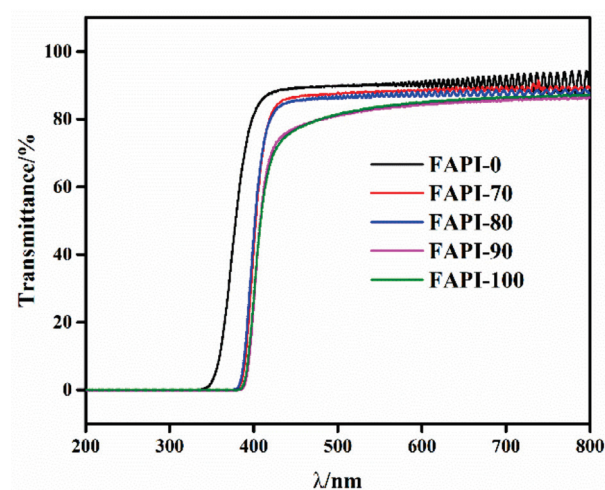


Figure 4. Ultraviolet-visible (UV-vis) spectra of the FAPI films with different biphenyl content in polymer backbone.

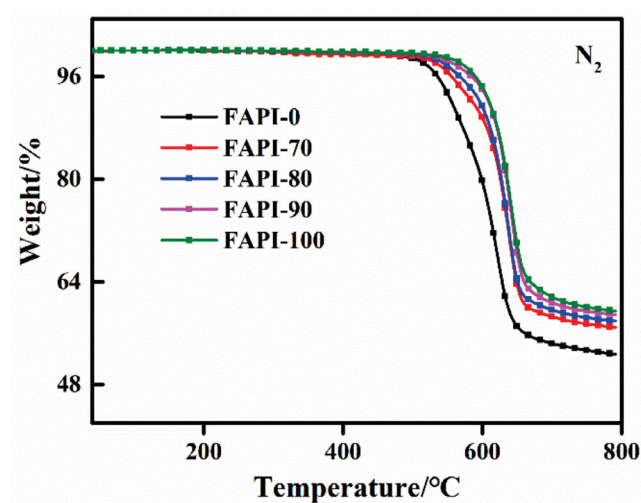
Table 2. Optical data of the FAPI films.

FAPI Films	T_{500} ^a /%	λ_{cut} ^b /nm	YI ^c	HZ ^d
FAPI-0	89.7	334	1.3	1.7
FAPI-70	87.7	379	2.6	1.3
FAPI-80	86.1	376	3.3	1.2
FAPI-90	81.2	381	6.4	4.7
FAPI-100	81.4	381	6.9	4.1

^a Transmittance at 500 nm; ^b Cutoff wavelength; ^c Yellowness; ^d Haze.

3.3. Thermal Properties

Figure 5 compares TGA curves of the FAPI films with different biphenyl contents in polymer backbones, and the corresponding thermal decomposition temperature (T_d) and glass transition temperature (T_g) are summarized in Table 3. The FAPI films showed great thermostability both in air and nitrogen. Moreover, no obvious weight loss was detected until the temperature was scanned up to 500 °C, implying that the imidization process was successfully completed and no residue of organic volatile existed in the films. As the $-CF_3$ groups are easily decomposed at high temperature, the T_d and R_{750} were found to increase gradually with the decreasing of $-CF_3$ groups in the polyimide backbones. The T_{d5} and T_{d10} were measured at 541.8 °C and 564.3 °C (FAPI-0), respectively, about 52–55 °C lower than that of FAPI-100 ($T_{d5} = 596.7$ °C, $T_{d10} = 616.7$ °C). At 750 °C, the FAPI films showed residual weights of 53.3 to 60.1%.

**Figure 5.** TGA curves of the FAPI films with different biphenyl content in polymer backbone.**Table 3.** Thermal properties of the FAPI films.

FAPI Films	T_g /°C	T_{d5} ^a /°C	T_{d10} ^b /°C	R_{750} ^c /%
FAPI-0	351.0	541.8	564.3	53.3
FAPI-70	354.2	563.8	598.0	57.5
FAPI-80	346.3	576.7	605.0	58.4
FAPI-90	348.4	593.4	616.0	59.4
FAPI-100	351.6	596.7	616.7	60.1

^a Decomposition temperature at 5% weight loss; ^b Decomposition temperature at 10% weight loss; ^c Residual weight at 750 °C.

The glass transition temperature of the FAPI films were measured at about 350 °C by DMA (Figure 6). The T_g values of the FAPI films were almost identical although the biphenyl contents varied. This could be attributed to the steric hindrance caused by the bulky $-CF_3$ groups linked at the biphenyl groups, which obstructed the twist moving of the polymer backbone and resulted in the high glass transition temperature. It is worth

noting that all of the FAPI films showed T_g values which are higher than the finally cured temperature (330 °C), indicating that the imidization process is a local process of cyclization and dehydration without much molecular chain moving ability [27].

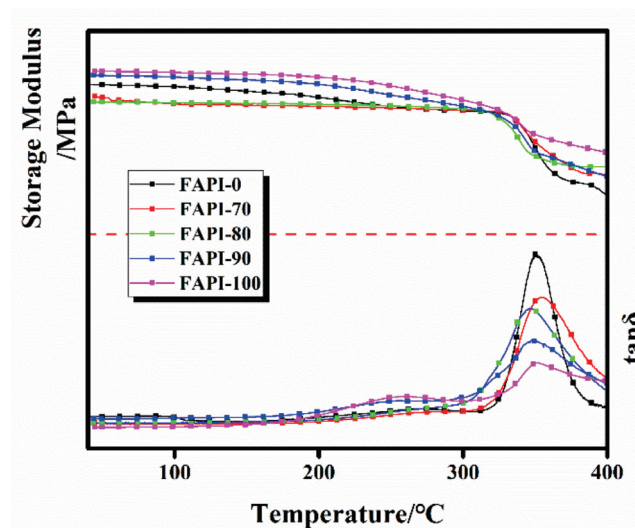


Figure 6. DMA curves of the FAPI films with different biphenyl content in polymer backbone.

3.4. Dielectric Properties

Dielectric properties of the FAPI films were measured on Network Analyzer of Keysight Company equipped with cylindrical cavity resonance clamps at high frequencies from 10 to 60 GHz, respectively (Table 4). Two interesting phenomena were attracted our attention. Compared with the dielectric properties of different films at one constant frequency, such as at 10 GHz, the dielectric constant (ϵ') increased gradually with the increasing of the biphenyl contents in polyimide backbones, while the dielectric dissipation factor ($\tan\delta$) decreased (Figure 7). Moreover, if comparing the same film at different frequency, the dielectric constant does not change obviously, but the $\tan\delta$ was increased about 42–56% from 10 to 60 GHz (Figure 7b). For instance, compared to both FAPI-80 and FAPI-90, FAPI-70 has a lower ϵ' (2.93) and higher $\tan\delta$ (5.9×10^{-3}) at 10 GHz. When the frequency increased from 10 GHz to 60 GHz, its ϵ' values kept almost constant, but the $\tan\delta$ increased from 5.9×10^{-3} to 8.4×10^{-3} .

Table 4. Dielectric properties of the FAPI films at high frequencies.

FAPI Films	10 GHz		24 GHz		40 GHz		60 GHz		F%	$W_a/\%$
	ϵ'	$\tan\delta$	ϵ'	$\tan\delta$	ϵ'	$\tan\delta$	ϵ'	$\tan\delta$		
FAPI-0	2.68	0.0059	2.73	0.0067	2.72	0.0076	2.70	0.0087	31.3	0.25
FAPI-70	2.93	0.0059	2.95	0.0069	2.96	0.0079	2.94	0.0084	23.2	0.30
FAPI-80	3.04	0.0047	3.11	0.0057	3.11	0.0065	3.03	0.0073	22.0	0.21
FAPI-90	3.14	0.0046	3.22	0.0054	3.22	0.0062	3.22	0.0072	20.8	0.40
FAPI-100	3.25	0.0045	3.24	0.0054	3.25	0.0060	3.23	0.0065	19.7	0.37

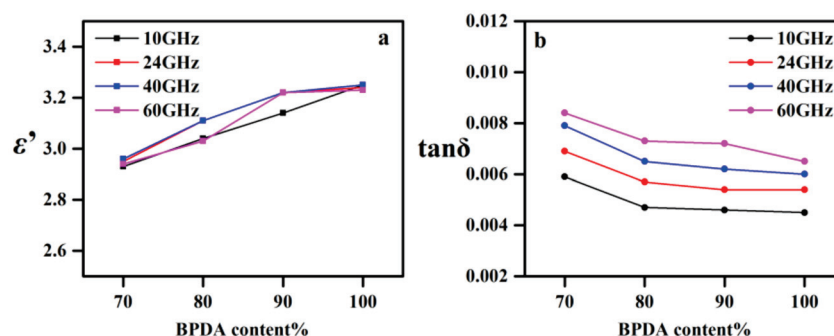


Figure 7. Dielectric constant (a) and dissipation factor (b) of the FAPI films at different high frequencies (10–60 GHz).

Introduction of $-\text{CF}_3$ groups in polymer backbones has been considered as an effective way to reduce the dielectric constant of polyimides. This is attributed to the strong electron absorption and large free volume of fluorinated groups. It can be seen that the dielectric constants of the FAPI films were changed from 2.68 (FAPI-0) to 3.25 (FAPI-100) at 10 GHz, which is closely related to the decline of the fluorine contents ($F\%$). The frequency also affects the dielectric constant. Under the applied electric field, dielectric properties of a polymer are mainly attributed by three kinds of polarization ways, namely orientation polarization, atomic polarization and electron polarization with the inherent frequencies of 10^9 Hz (1 GHz), 10^{12} Hz (10^3 GHz) and 10^{15} Hz (10^6 GHz), respectively [28]. The atomic polarization and electron polarization are also called deformation polarizations. In our research, the test frequencies (10–60 GHz) are dominantly located in the range of inherent frequencies of orientation polarization and atomic polarization. If the inherent frequency of orientation polarization of the FAPI films is lower than the frequency of the applied electric field, the dielectric constants of different testing samples would not change much. Furthermore, because the frequency of the applied electric field does not reach the inherent frequency of deformation polarization, the polarization of atoms and electrons has sufficient relaxation time, having no influence on dielectric constant (ϵ').

The dielectric loss of polymers originates from the energy loss generated to overcome intramolecular friction when dipoles, atoms and electrons are deflected in an alternating electric field. From this point of view, the internal factors affecting dielectric loss mainly lie in the number of dipoles and the deflection amplitude of dipoles. The more the dipoles and the greater the amplitude of deflection, the higher the dielectric loss. As shown in Table 4, the dielectric loss of FAPI films always decreases with the increase of the biphenyl content at each frequency, that means the introduction of rigid groups does help to weaken the deflection of dipoles. On the other hand, as the frequency was changed from 10 GHz to 60 GHz, the dielectric loss increased gradually. This could be interpreted that the frequency of atomic deflection increased with the increasing of test frequency, which intensified the internal friction between molecules.

Beside the structural factors which would affect the dielectric properties of a polymer, the water absorption is another key factor. The water absorption (W_a) of the FAPI films was measured in the range of 0.25–0.40% (Table 4). With the introduction of rigid biphenyl units, the W_a of the FAPI films are slightly improved on account of the reduction of $F\%$. At high frequencies, the influence of water molecules on dielectric loss cannot be ignored. Compared with polymer, water molecules with strong polarity are deflected more sharply under the alternating electric field, which is also positively correlated with frequency.

3.5. Effect of Polymer Chain Orientation on Dielectric Properties

Figure 8 compares the WXR spectra of the FAPI films. The crystal plane diffraction angle (2θ) of the FAPI films were gradually increased with the increasing of the biphenyl contents in polymer backbones (Table 5). As a consequence, the polymer chain spacing (d) decreased gradually from 6.7 Å to 4.8 Å according to the Bragg equation, indicating that

the introduction of biphenyl groups in polyimide backbones has effectively enhanced the polymer chain orientation and the inter-chain interactions, and thus increased the polymer chain packing density. The strong interchain interaction limited the deflection of the dipole, atoms and electrons in the electric field, resulting in a reduction of the energy consumed to overcome the friction in the polymer chains, thus lowering the dielectric loss.

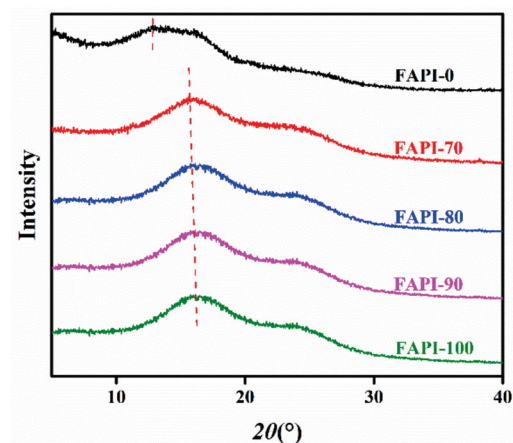


Figure 8. WXR D curves of the FAPI films with different biphenyl content in polymer backbone.

Table 5. WXR D, TMA and BR data of the FAPI films.

FAPI Films	$2\theta/^\circ$	$d/\text{\AA}$	n_{TE}	n_{TM}	Δn
FAPI-0	13.2	6.7	1.5613	1.5379	0.0234
FAPI-70	17.0	5.5	1.6543	1.5523	0.1020
FAPI-80	17.1	5.4	1.6669	1.5496	0.1173
FAPI-90	17.6	5.1	1.6813	1.5294	0.1518
FAPI-100	17.9	4.8	1.7303	1.5250	0.2053

Figure 9 compares the TMA curves (a) and CTE values (b) of the FAPI films. With the increasing of biphenyl content and the decreasing of $-\text{CF}_3$ groups in polyimide backbone, the CTE value of the FAPI films was decreased significantly from $58.6 \times 10^{-6}/^\circ\text{C}$ (FAPI-0) to $10.6 \times 10^{-6}/^\circ\text{C}$ (FAPI-70), and $6.4 \times 10^{-6}/^\circ\text{C}$ (FAPI-80), respectively, which is probably attributed to the reduction of the free volume of polymer structure [29]. The rigid polyimide backbones showed weaker in-plane expansion behavior and stronger in-plane orientation extent, resulted in low CTE. Surprisingly, the FAPI-90 and FAPI-100 showed a negative CTE values, implying that the polymer aggregate was shrank at high temperature.

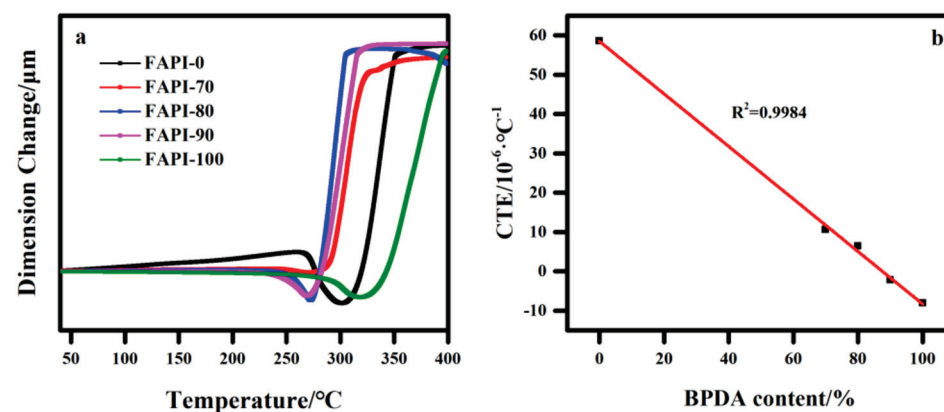


Figure 9. (a) TMA curve of the FAPI films; (b) The relationship between CTE and biphenyl content in polymer backbone.

Figure 10 compares the birefringence behaviors of the FAPI films measured by a prism coupler at a wavelength of 633 nm. With the increasing of biphenyl contents in polymer backbone, the in-plane refractive index (n_{TE}) of the FAPI films were increased gradually from 1.5613 (FAPI-0) to 1.7303 (FAPI-100), and the out-of-plane refractive index (n_{TM}) were reduced accordingly from 1.5379 (FAPI-0) to 1.5250 (FAPI-100). Thus, the Δn value was increased from 0.0234 (FAPI-0) to 0.2053 (FAPI-100), indicating that the polymer orientation extent was also increased gradually. The results further proved that the dielectric loss of the FAPI films at high frequencies could be reduced by enhancing the polymer chain orientation and stacking density, which limited the deflection of the dipole, atom, electron under alternating electric field.

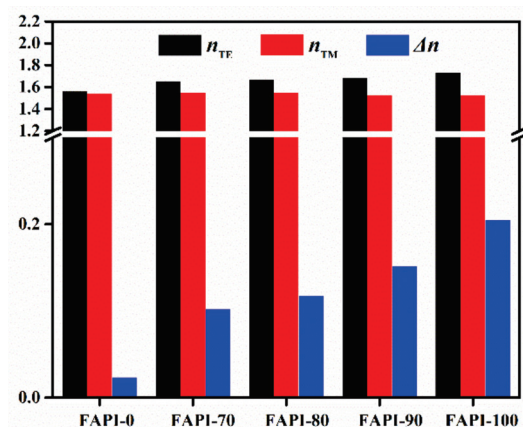


Figure 10. Birefringence index of the FAPI films with different biphenyl content in polymer backbone.

3.6. Molecular Simulation

Molecular Dynamics (MD) simulation was employed to demonstrate the above conclusion from a microscopic point of view. Firstly, a series of theoretical models of the FAPI films which are closed to the real state were established by validating appropriate parameters and conditions. Chain Rigidity, Intermolecular Force and Chain Stacking were then investigated by calculating the corresponding parameters.

3.6.1. Chain Rigidity

Radius of Gyration (R_g) and Kuhn segment length (l_b) were utilized to reflect the flexibility of molecular chains of studied PIs. R_g is defined as the distance from the point of concentration assumed by the differential mass of the object to the axis of rotation [30], and l_b is defined as the segment length of the polymer chain regarded as a free-connected chain with segments as statistical units. In general, the lower the R_g and l_b , the better the chain's flexibility. Table 6 compares the R_g and l_b values of the FAPI films with different biphenyl groups in the polyimide backbones. With the increasing of rigid rod-like biphenyl structures, R_g and l_b values were increased gradually from 41.26 (FAPI-0) to 56.42 (FAPI-90) except for FAPI-100, indicating that the rigid rod-like segments ensured the polymer chain conformation being more straightened and less twisted and tangled.

Table 6. Computational results of the FAPI films.

FAPI Films	$R_g/\text{Å}$	$l_b/\text{Å}$	$\frac{CED}{\times 10^8 \text{ J}\cdot\text{m}^{-3}}$	$V^a/\text{Å}^3$	$V_W^b/\text{Å}^3$	FFV^c
FAPI-0	41.26	23.85	3.13	171,000	100,477	23.61%
FAPI-70	49.06	35.05	3.56	141,940	89,624	17.91%
FAPI-80	53.31	42.44	4.25	137,822	88,157	16.85%
FAPI-90	56.42	50.47	3.92	134,362	86,610	16.20%
FAPI-100	51.40	46.76	4.34	127,904	84,962	13.65%

^a Total volume; ^b Van der Waals volume; ^c Fractional free volume, $FFV = (V - 1.3V_W)/V$.

3.6.2. Intermolecular Force

In order to better quantify the intermolecular forces, Cohesive Energy Density (*CED*) was calculated through the established models. *CED* is the energy required to overcome the intermolecular force of vaporization of 1 mol of aggregates per unit volume [31], which means that the aggregate structures with higher *CED* usually have stronger intermolecular forces. By replacing the $-CF_3$ group with biphenyl groups in the polyimide backbones, the *CED* of the FAPI films were increased from 3.13 (FAPI-0) to 4.34 (FAPI-100), testifying that the rigid-like biphenyl segments have effectively enhanced the intermolecular force and resulted in the reducing of the dipole deflection in the electric field.

3.6.3. Chain Stacking

In general, total volume (*V*) of a polymer can be divided into two parts, one part is occupied by atoms (V_W), the rest is the free volume. The fractional free volume (*FFV*) is the fraction of the free volume to the total volume, including the random distribution of unoccupied holes in polymer aggregate phase (static) and the space formed as the density of the material fluctuates and the molecules move (dynamic) [32], which represents the stacking degree of macromolecular chains. The *FFV* of the FAPI films reduced from 23.61% (FAPI-0) to 13.65% (FAPI-100) with the increase of the biphenyl groups in the polyimide backbones as depicted in Table 4. Figure 11 compares the 3D periodic boundary cell of the FAPI films. Clearly, the aggregate structures of the FAPI films became to denser stacking with less $-CF_3$ and more rigid-like biphenyl groups in the polymer backbones.

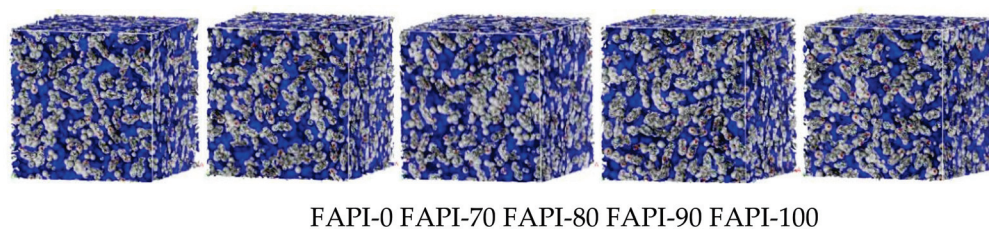


Figure 11. 3D periodic boundary cell of the FAPI films (gray part represents the molecule chain skeleton while blue part represents the free volume).

4. Conclusions

Fluorinated aromatic polyimide films with high modulus and excellent dielectric properties at high frequency have been prepared. The polyimide films exhibited great combined mechanical, thermal and colorless transparency properties, as well as dielectric properties, including tensile modulus of up to 8.4 GPa, strength of up to 326.7 MPa, glass transition temperature (T_g) of 346.3–351.6 °C, thermal decomposition temperature in air (T_{d5}) of 541.8–596.7 °C, as well as high colorless transmittance over 81.2% at 500 nm. Moreover, the polyimide films also showed dielectric constant of 2.68–3.25 which did not change obviously at frequency from 10 GHz to 60 GHz, and dielectric loss as low as 0.0045 at 10 GHz which is suitable for signal transportation applications at high frequencies. The relationship of molecular structure and dielectric loss was estimated by molecular dynamics simulations.

Author Contributions: Conceptualization, S.-Y.Y., H.-X.Y. and F.Z.; Project administration, S.-Y.Y., H.-X.Y. and J.-J.H.; Visualisation, J.-J.H.; Writing—original draft, J.-J.H.; Writing—review and editing, S.-Y.Y., F.Z. and H.-X.Y.; Funding acquisition, F.Z. and H.-X.Y. All authors have read and agreed to the published version of the manuscript.

Funding: This research was funded by the National Natural Science Foundation of China (51973225 and 52003196).

Institutional Review Board Statement: Not applicable.

Informed Consent Statement: Not applicable.

Data Availability Statement: The data presented in this study are available on request from the corresponding author.

Acknowledgments: The authors acknowledge the Southö African Centre for High Performance Computing (CHPC) for donating the computing facility, which was used to perform computational work presented in this article.

Conflicts of Interest: The authors declare no conflict of interest.

References

- Liaw, D.-J.; Wang, K.-L.; Huang, Y.-C.; Lee, K.-R.; Lai, J.-Y.; Ha, C.-S. Advanced polyimide materials: Syntheses, physical properties and applications. *Prog. Polym. Sci.* **2012**, *37*, 907–974. [CrossRef]
- Yang, S.-Y.; Yuan, L.-L. *Advanced Polyimide Materials*; Yang, S.-Y., Ed.; Elsevier: Beijing, China, 2018; pp. 1–66.
- Ni, H.-j.; Liu, J.-g.; Wang, Z.-h.; Yang, S.-y. A review on colorless and optically transparent polyimide films: Chemistry, process and engineering applications. *J. Ind. Eng. Chem.* **2015**, *28*, 16–27. [CrossRef]
- Hasegawa, T.; Horie, K. Photophysics, photochemistry, and optical properties of polyimides. *Prog. Polym. Sci.* **2001**, *26*, 259–335. [CrossRef]
- Zhang, S.-J.; Bu, Q.-Q.; Li, Y.-F.; Gong, C.-L.; Xu, X.-Y.; Li, H. High organosolubility and optical transparency of novel polyimides derived from 2',7'-bis(4-amino-2-trifluoromethylphenoxy)-spiro (fluorene-9,9'-xanthene). *Mater. Chem. Phys.* **2011**, *128*, 392–399. [CrossRef]
- Toltyo, M.; Sasaki, S.; Telegraph, S.; Corporation, T. Synthesis of Fluorinated Polyimides. Available online: http://www.op.titech.ac.jp/polymer/lab/sando/Book_Old/Sasaki_Polyimides.pdf (accessed on 10 December 2021).
- Bruma, M.; Fitch, J.W.; Cassidy, P.E. Hexafluoroisopropylidene-Containing Polymers for High-Performance Applications. *J. Macromol. Sci. Part C* **1996**, *36*, 119–159. [CrossRef]
- Maier, G. Low dielectric constant polymers for microelectronics. *Prog. Polym. Sci.* **2001**, *26*, 3–65. [CrossRef]
- Zhuang, Y.; Seong, J.G.; Lee, Y.M. Polyimides containing aliphatic/alicyclic segments in the main chains. *Prog. Polym. Sci.* **2019**, *92*, 35–88. [CrossRef]
- Matsumoto, T. Colorless Full-alicyclic Polyimides with Low Dielectric Constant. *J. Photopolym. Sci. Technol.* **2001**, *14*, 725–730. [CrossRef]
- Hasegawa, M.; Horiuchi, M.; Kumakura, K.; Koyama, J. Colorless polyimides with low coefficient of thermal expansion derived from alkyl-substituted cyclobutanetetracarboxylic dianhydrides. *Polym. Int.* **2014**, *63*, 486–500. [CrossRef]
- Liu, Y.; Qian, C.; Qu, L.; Wu, Y.; Zhang, Y.; Wu, X.; Zou, B.; Chen, W.; Chen, Z.; Chi, Z.; et al. A Bulk Dielectric Polymer Film with Intrinsic Ultralow Dielectric Constant and Outstanding Comprehensive Properties. *Chem. Mater.* **2015**, *27*, 6543–6549. [CrossRef]
- Bei, R.; Qian, C.; Zhang, Y.; Chi, Z.; Liu, S.; Chen, X.; Xu, J.; Aldred, M.P. Intrinsic low dielectric constant polyimides: Relationship between molecular structure and dielectric properties. *J. Mater. Chem. C* **2017**, *5*, 12807–12815. [CrossRef]
- Chen, W.; Zhou, Z.; Yang, T.; Bei, R.; Zhang, Y.; Liu, S.; Chi, Z.; Chen, X.; Xu, J. Synthesis and properties of highly organosoluble and low dielectric constant polyimides containing non-polar bulky triphenyl methane moiety. *React. Funct. Polym.* **2016**, *108*, 71–77. [CrossRef]
- Liu, Y.; Zhang, Y.; Lan, Q.; Liu, S.; Qin, Z.; Chen, L.; Zhao, C.; Chi, Z.; Xu, J.; Economy, J. High-Performance Functional Polyimides Containing Rigid Nonplanar Conjugated Triphenylethylene Moieties. *Chem. Mater.* **2012**, *24*, 1212–1222. [CrossRef]
- Goto, K.; Akiike, T.; Inoue, Y.; Matsubara, M. Polymer design for thermally stable polyimides with low dielectric constant. *Macromol. Symp.* **2003**, *199*, 321–332. [CrossRef]
- Shi, C.; Liu, S.; Li, Y.; Yuan, Y.; Zhao, J.; Fu, Y. Imparting low dielectric constant and high modulus to polyimides via synergy between coupled silsesquioxanes and crown ethers. *Compos. Sci. Technol.* **2017**, *142*, 117–123. [CrossRef]
- Chen, Z.; Zhu, D.; Tong, F.; Lu, X.; Lu, Q. Low Dielectric Constant Polyimide Hybrid Films Prepared by in Situ Blow-Balloon Method. *ACS Appl. Polym. Mater.* **2019**, *1*, 2189–2196. [CrossRef]
- Tsai, M.-H.; Whang, W.-T. Low dielectric polyimide/poly(silsesquioxane)-like nanocomposite material. *Polymer* **2001**, *42*, 4197–4207. [CrossRef]
- Leu, C.-M.; Chang, Y.-T.; Wei, K.-H. Polyimide-Side-Chain Tethered Polyhedral Oligomeric Silsesquioxane Nanocomposites for Low-Dielectric Film Applications. *Chem. Mater.* **2003**, *15*, 3721–3727. [CrossRef]
- Zhi, X.X.; Zhang, Y.; Zhang, X.M.; Wang, H.L.; Wu, L.; An, Y.C.; Wei, X.Y.; Liu, J.G. Preparation and properties of semi-alicyclic colorless polyimide films and light-colored sheets with low dielectric features for potential applications in optoelectronic integrated circuits. *Express Polym. Lett.* **2021**, *15*, 1051–1062. [CrossRef]
- Ma, Y.; He, Z.; Liao, Z.; Xie, J.; Yue, H.; Gao, X. Facile strategy for low dielectric constant polyimide/silsesquioxane composite films: Structural design inspired from nature. *J. Mater. Sci.* **2021**, *56*, 7397–7408. [CrossRef]
- Matsuura, T.; Hasuda, Y.; Nishi, S.; Yamada, N. Polyimide derived from 2,2'-bis(trifluoromethyl)-4,4'-diaminobiphenyl. 1. Synthesis and characterization of polyimides prepared with 2,2'-bis(3,4-dicarboxyphenyl)hexafluoropropane dianhydride or pyromellitic dianhydride. *Macromolecules* **1991**, *24*, 5001–5005. [CrossRef]
- Wang, X.-Y.; Veld, P.J.; Lu, Y.; Freeman, B.D.; Sanchez, I.C. A molecular simulation study of cavity size distributions and diffusion in para and meta isomers. *Polymer* **2005**, *46*, 9155–9161. [CrossRef]

25. Hofmann, D.; Ulbrich, J.; Fritsch, D.; Paul, D. Molecular modelling simulation of gas transport in amorphous polyimide and poly(amide imide) membrane materials. *Polymer* **1996**, *37*, 4773–4785. [CrossRef]
26. Ma, X.; Zheng, F.; van Sittert, C.; Lu, Q. Role of Intrinsic Factors of Polyimides in Glass Transition Temperature: An Atomistic Investigation. *J. Phys. Chem. B* **2019**, *123*, 8569–8579. [CrossRef]
27. Volksen, W.; Miller, R.D.; Dubois, G. Low Dielectric Constant Materials. *Chem. Rev.* **2010**, *110*, 56–110. [CrossRef]
28. Simpson, J.O.; St. Clair, A.K. Fundamental insight on developing low dielectric constant polyimides. *Thin Solid Film.* **1997**, *308-309*, 480–485. [CrossRef]
29. Hasegawa, M. Development of Solution-Processable, Optically Transparent Polyimides with Ultra-Low Linear Coefficients of Thermal Expansion. *Polymers* **2017**, *9*, 520. [CrossRef]
30. Mohammadi, M.; Davoodi, J.; Javanbakht, M.; Rezaei, H. Glass transition temperature of PMMA/modified alumina nanocomposite: Molecular dynamic study. *Mater. Res. Express* **2019**, *6*, 035309. [CrossRef]
31. Scatchard, G. Equilibria in Non-electrolyte Solutions in Relation to the Vapor Pressures and Densities of the Components. *Chem. Rev.* **1931**, *8*, 321–333. [CrossRef]
32. Thran, A.; Kroll, G.; Faupel, F. Correlation between fractional free volume and diffusivity of gas molecules in classy polymers. *J. Polym. Sci. Part B-Polym. Phys.* **1999**, *37*, 3344–3358. [CrossRef]

Article

3D Printing Processability of a Thermally Conductive Compound Based on Carbon Nanofiller-Modified Thermoplastic Polyamide 12

Zhenxue Zhang ^{1,*}, Eleni Gkartzou ², Simon Jestin ³, Dionisis Semitekolos ⁴, Panagiotis-Nektarios Pappas ⁵, Xiaoying Li ¹, Anna Karatza ², Panagiotis Zouboulis ², Aikaterini-Flora Trompeta ⁴, Nikolaos Koutroumanis ⁵, Costas Galiotis ⁵, Costas Charitidis ⁴ and Hanshan Dong ¹

¹ School of Metallurgy and Materials, University of Birmingham, Birmingham B15 2TT, UK; x.li.1@bham.ac.uk (X.L.); h.dong.20@bham.ac.uk (H.D.)

² BioG3D P.C., 1 Lavriou Str., Technological & Cultural Park of Lavrion, 19500 Lavrion, Greece; egkartzou@biog3d.gr (E.G.); akaratza@biog3d.gr (A.K.); pzouboulis@biog3d.gr (P.Z.)

³ CANOE, Le Centre Technologique Nouvelle Aquitaine Composites & Matériaux Avancés, Bât CHEMINNOV-ENSCBP, 33600 Pessac, France; jestin@plateforme-canoec.com

⁴ Research Lab of Advanced, Composites, Nanomaterials and Nanotechnology (R-NanoLab), School of Chemical Engineering, National Technical University of Athens, 9 Heroon Polytechniou Str., Zographos, 15780 Athens, Greece; diosemi@chemeng.ntua.gr (D.S.); ktrompeta@chemeng.ntua.gr (A.-F.T.); charitidis@chemeng.ntua.gr (C.C.)

⁵ FORTH/Institute of Chemical Engineering and High Temperature Chemical Processes, Stadiou Str., Rion, 26504 Patras, Greece; ppappas@iceht.forth.gr (P.-N.P.); nickkoutrou@iceht.forth.gr (N.K.); c.galiotis@iceht.forth.gr (C.G.)

* Correspondence: z.zhang.1@bham.ac.uk

Citation: Zhang, Z.; Gkartzou, E.; Jestin, S.; Semitekolos, D.; Pappas, P.-N.; Li, X.; Karatza, A.; Zouboulis, P.; Trompeta, A.-F.; Koutroumanis, N.; et al. 3D Printing Processability of a Thermally Conductive Compound Based on Carbon Nanofiller-Modified Thermoplastic Polyamide 12. *Polymers* **2022**, *14*, 470. <https://doi.org/10.3390/polym14030470>

Academic Editor: Somen K. Bhudolia

Received: 17 December 2021

Accepted: 17 January 2022

Published: 25 January 2022

Publisher's Note: MDPI stays neutral with regard to jurisdictional claims in published maps and institutional affiliations.

Abstract: A polyamide (PA) 12-based thermoplastic composite was modified with carbon nanotubes (CNTs), CNTs grafted onto chopped carbon fibers (CFs), and graphene nanoplatelets (GNPs) with CNTs to improve its thermal conductivity for application as a heat sink in electronic components. The carbon-based nanofillers were examined by SEM and Raman. The laser flash method was used to measure the thermal diffusivity in order to calculate the thermal conductivity. Electrical conductivity measurements were made using a Keithley 6517B electrometer in the 2-point mode. The composite structure was examined by SEM and micro-CT. PA12 with 15 wt% of GNPs and 1 wt% CNTs demonstrated the highest thermal conductivity, and its processability was investigated, utilizing sequential interdependence tests to evaluate the composite material behavior during fused filament fabrication (FFF) 3D printing processing. Through this assessment, selected printing parameters were investigated to determine the optimum parametric combination and processability window for the composite material, revealing that the selected composition meets the necessary criteria to be processable with FFF.

Keywords: polyamide 12; carbon nanofiller; carbon nanotube; graphene nanoplatelet; 3D printing; thermal conductivity; compound



Copyright: © 2022 by the authors. Licensee MDPI, Basel, Switzerland. This article is an open access article distributed under the terms and conditions of the Creative Commons Attribution (CC BY) license (<https://creativecommons.org/licenses/by/4.0/>).

1. Introduction

Conventional materials used for heat transfer applications, such as copper and aluminium, have the advantage of higher thermal conductivity but with higher cost and considerable weight. Low-cost thermoplastic composites with ease of manufacturability and recyclability are alternatives for such applications, although with lower thermal conductivity in comparison to the metallic materials [1,2]. The conduction of thermal energy in a polymer is achieved via a phonon transfer process rather than through vibration in the pure crystalline materials. However, the vibrational frequency mismatches at the interfaces between impurities and lattice defects cause significant phonon “scattering”

in polymer materials, which leads to the low thermal conductivities [2]. To enhance the thermal conductivity of polymers, incorporation of highly thermally conductive nanofillers in the host matrix by forming conduction paths is frequently selected as a cost-efficient bulk modification strategy to increase its thermal management applications, including in heat sinks and other components for electronics. The lightweight polymer nanocomposites offer highly specific properties that make them preferable for a wide range of applications. The 0.1 wt% CNTs reinforced polyamide 12 (PA12) nanocomposites prepared by laser sintering have an average 14.2% increase in thermal conductivity compared to that of neat PA12 at temperatures between 100 °C and 175 °C [3].

Recent advances in multi-material 3D printing present a potential extension of the product design beyond complex geometries, while functional, single-step manufacturing processes can be exploited by utilizing custom composite materials suitable for multifactorial applications. The fused filament fabrication (FFF) technique is of low cost with a large range of feedstock materials suitable for a wide range of 3D printing applications [4,5]. Thermoplastic materials, such as polylactic acid (PLA) and polyamide (PA) [6], can be melted and extruded as a strand through a nozzle in a line by line and layer by layer manner in FFF, and the extruded material (thermoplastic strands) rapidly solidifies and adheres with the surrounding material, which is especially useful for complex design and advanced functionality of smart products [4,7,8]. The utilization of micro/nanocomposites with multi-material FFF printing, combined with metamaterials and lattice structures, can lead to innovative functional parts for thermal management [9]. Different conductive filaments, carbon-based or metallic reinforcement, to reinforce composites have been utilized for shape morphing applications [10,11] and heat dissipation [12]. By utilizing composite filaments with 1D or 2D (nano) fillers through the FFF 3D printing process, the development of orthotropic components that improve the control of thermal conduction and heat management can be achieved. In this way, thermal pathways or barriers can be incorporated into the 3D printed part through material composition and material path deposition pattern from the FFF tool head [12]. Composite FFF materials with thermally conductive properties are also investigated for high-performance aerospace applications, in consideration of reduced manufacturing cost and weight and ease of fabrication. The influence of filler content on thermal conductivity is significant, indicating that a more thermally conductive filler leads to better thermal conductivity. However, the thermal conductivities of polymer/CNT nanocomposites are relatively low compared with expectations from the intrinsic thermal conductivity of CNTs. The challenge primarily comes from the large interfacial thermal resistance between the CNT and the surrounding polymer matrix, which hinders the transfer of phonon-dominating heat conduction in polymer and CNT [13]. Due to its excellent electrical and thermal conductivity, graphite platelets (GPs)/graphite nanoplatelets (GNPs) were also used to increase the electrical conductivity and mechanical properties of PA12 via selective laser sintering (SLS) [14]. However, the addition of graphite lowered the flowability and the mechanical properties of the PA12 composites compared to the CF-reinforced counterparts [15]. Guo [16] found that larger graphite flakes improved the electrical behavior of the composites to a greater extent than powdered graphite. Although the enhancement of composite performances is not always achieved, it is generally recognized that the synergistic effect can be achieved from the formation of percolative network structures within the polymer due to the presence of different conducting fillers with different aspect ratios and geometrical morphology [17]. Nano- and microfillers, such as carbon black, multiwalled CNTs, or GPs/GNPs, have been used together with CFs to improve the mechanical properties and thermal and electrical conductivities of thermal plastic composites [15].

To produce a printable filament for FFF technology with enhanced functionality, the filler content must also be adjusted according to rheological constraints imposed by the 3D printing technology [18]. In this context, an upper limit in terms of additive amount must be evaluated based on the application requirements, on the shape and size of fillers, and on matrix material properties [19]. A high dispersion and distribution

of the selected fillers, together with a low porosity of the final composite filament, are crucial for the improvement of mechanical and thermal properties of the produced material. Meanwhile, it is of high importance to assess FFF processability, since the inclusions alter melting and solidification dynamics through material viscosity alteration and thermal profile of the printed material [10]. Thermoplastic materials present differences in their viscosity and ease of flow during thermal processing, exhibiting a non-Newtonian shear thinning behavior when higher shear rates are applied and non-linear viscosity changes depending on processing temperature. There is plenty of research on the influence of the processing parameters (energy density/filling temperature, filling rate, filling pattern, layer thickness, infill percentage, nozzle size, and manufacturing orientation) on the geometrical accuracy (quality of the surface texture, roundness, and waviness), density, and mechanical properties in additive manufacturing plastic parts based on PLA or PA [20–23]. FFF process parameters are defined by the user in computer-aided manufacturing (CAM) software and involve a wide variety of toolpath and material processing parameters. However, in the majority of commercial FFF systems, open loop control of the process requires an experimental comparison of actual/nominal characteristics of the thermoplastic strands and compensation factors for each [24]. Taking into account melt viscosity dependence on temperature, shear rate, and pressure conditions, key FFF process parameters that directly affect material flow behavior are printing temperature, printing speed, and nozzle diameter, for a set combination of thermoplastic strand width and height [25]. These parameters define the shear rates and pressure drop imposed on the melt during extrusion and should be kept within a certain processing window for each material system in order to ensure consistent flow and intra-layer coalescence [26]. The printing temperature has also been identified as a main parameter which influences interlayer bonding, structural integrity, and fatigue lifetime of FFF specimens [21]. As heat transfer plays a particular role in determining the temperature history of the merging thermoplastic strands, the subsequent formation of bonds among individual strands arises from complex heat and mass transfer phenomena, coupled with thermal and mechanical stress accumulation and phase changes [27,28]. In this respect, material viscosity, melt strength, storage/loss modulus, melt temperature sensitivity, and phase transitions induced from temperature variation play a significant role in the final part structural integrity and dimensional accuracy. Furthermore, thermoplastic strand height (equal to layer height) and strand width are user-defined parameters that are subsequently employed by the CAM software for the automatic calculation of the filament feed rate; thus, an increase of these values is translated into a nominal increase in material volumetric flow rate to achieve the targeted strand volume [29]. However, material flow imposes physical limitations on the actual strand geometry that can be obtained, leading to over- or under-extrusion when the nominal volumetric flow rate is not in accordance with the actual volumetric flow rate [25]. Although GNPs and CNTs have been widely used to increase the electrical conductivity of PA12, there is hardly any report on improving their thermal conductivity nor the processability of GNP- and CNT-modified PA12 utilizing FFF.

Thermoplastic PA12 has a broad range of applications, such as cable covering and insulating material in the electronics field. In this paper, different nanofillers, in the forms of CNTs, CNT-modified CFs, and GNPs together with CNTs, were used to modify the thermoplastic PA12, and the fillers and the composite were characterized for improved structure and enhanced thermal conductivity. Finally, the processability for 3D printing (FFF) of a printable filament with the highest thermal conductivity, PA12_15%GNP+1%CNT, was assessed, and the processing parameters such as extrusion temperature, printing speed, strand height/width, extrusion multiplier, and retraction distance were optimized for a potential application in a heat sink.

2. Materials and Methods

2.1. The Materials

The CNT-based materials, either in powder form or grafted on CFs, were synthesized through the chemical vapor deposition (CVD) method. For the first case, the well-

established supported catalyst method was utilized, with Fe/zeolite catalyst and acetylene as carbon source [30]. On the contrary, in order to achieve a good grafting of CNTs onto the CFs, different approaches were investigated. Following the supported catalyst approach, the fibers (5–6 mm long) were impregnated in the catalyst solution (Fe particles embedded on zeolite, the same as the conventional procedure for CNT synthesis in powder form) and then left to dry. The coated fibers were spread on an inert substrate and inserted into the CVD reactor. Conventional experimental conditions were set ($T = 700\text{ }^{\circ}\text{C}$, flow rate of acetylene: 60 mL/min, flow rate of Ar: $\sim 200\text{ mL/min}$). According to the floating catalyst approach, both the ferrocene catalyst and the ethanol precursor were introduced simultaneously into the CVD system, similar to the configuration in [30]. For each batch, 20 g of chopped CFs was introduced into the center of the metallic tube of the CVD reactor. The furnace was heated up to $600\text{ }^{\circ}\text{C}$ in atmospheric air to remove the polymeric sizing on the CFs and to induce mild oxidation. Then, Ar was introduced into the system, which was sealed for 20 min to enable purging. The temperature was raised to $750\text{ }^{\circ}\text{C}$ [30], then the mixture of ethanol and ferrocene (1 g $\text{C}_{10}\text{H}_{10}\text{Fe}$ diluted in 100 mL $\text{C}_2\text{H}_5\text{OH}$) was boiled, and the vapor was transferred with the carrier gas (flow rate of Ar: $\sim 300\text{ mL/min}$) in the reactor. The reaction lasted for 2 h.

Graphene nanoplatelets (GNPs) were produced via wet shear exfoliation using graphite obtained from NGS Naturgraphit GmbH, Germany as raw material. The graphite particles exhibited an average lateral size of $500\text{ }\mu\text{m}$. The appropriate quantity of graphite was dissolved by manual stirring in an aqueous-based solution, and the mixture was transferred into the shear mixing device (Silverson) for the required high-shear stress field to be applied by a 4-blade rotor placed within a fixed screen (stator). At the initiation stage of the shear exfoliation process, the mixer head is driven towards the liquid solution into the vessel and operates at low rotational speed. The speed is gradually increased until the desired predetermined level is reached. The system runs at high speed throughout the remaining mixing time. The GNPs are obtained after drying under controlled temperature. The rotational speed parameters, as well as the duration of the steps of the process, were adjusted to result in GNPs with a maximum lateral size in the range of $10\text{ }\mu\text{m}$.

PA12, or Nylon 12, is a nylon polymer with the formula $[(\text{CH}_2)_{11}\text{C}(\text{O})\text{NH}]_n$. It has a melting point of $178\text{ }^{\circ}\text{C}$, thermal conductivity of 0.3 W/(mK) , and specific heat capacity of $1.7\text{ J/(g}\cdot^{\circ}\text{C)}$, while the linear CTE is $10^{-6}/\text{K}$ and service temperature up to $100\text{ }^{\circ}\text{C}$. The electrical resistivity is about $2.0\text{e}^{+15}\text{ ohm}\cdot\text{cm}$. In order to achieve accurate dosing of both polymers and fillers, PA12 polymer pellets (Rilsan AMNO TLD) were first ground into powders using a Retsch ZM200 lab-scale knife grinder equipped with a $500\text{ }\mu\text{m}$ sieve. A dry blend was then carried out at designed ratio by mixing the obtained powders and various reinforcement fillers: GNPs, CNTs, and CNT-modified chopped CFs. A masterbatch of highly concentrated polymer compound was manufactured by using a kneader-type extruder with the appropriate ratio of polymer and filler. The desired ratio of the filler was achieved by diluting the produced masterbatch with the base polymer on a twin-screw extruder, leading to higher shear forces and better filler dispersion. Two-millimeter thick plates were manufactured using thermal compression under press at $250\text{ }^{\circ}\text{C}$ for the evaluation of the thermal conductivity of this composite material.

2.2. Characterizations

A JEOL 7000 FE SEM and a Hitachi TM3030Plus SEM were used to characterize the enforcements of nano-inclusions/CFs and the composite. A Nikon XT H225 was used to scan the composite samples to carry out 3D characterization. The versatile XT H 225 systems offer a 225 kV microfocus X-ray source with $3\text{ }\mu\text{m}$ focal spot size. XT Software brings the fastest reconstruction of CT data with processing software, such as VolumeGraphics. It can be used for the inspection of internal faults of the plastic parts. The internal structural information of the samples was observed and collected by the compact desktop Bruker micro-CT, 3D X-ray scan system, SkyScan 1272 at NTUA. The system consists of a microfocus sealed X-ray source which operates at 20–100 kV and 10W, an X-ray

detector with a maximum resolution of 11 Mp (4032×2688 pixels), and a 14-bit cooled CCD fiber optically coupled to a scintillator.

Raman spectra were measured using a micro-Raman spectrometer (Invia Reflex, Renishaw, Wotton-under-Edge, UK). An Ar⁺ laser operating at 514.5 nm was employed as the light source. The laser beam was focused to an approximately 1 μm spot on the fiber surface using a microscope objective of $100\times$. The power of the incident light to the sample surface was retained below 1 mW to avoid local overheating.

2.3. Thermal Conductivity and Electrical Conductivity Test Methods

The laser flash method was used to measure thermal diffusivity. A laser flash delivers a short pulse of heat to the front of the sample, and an infrared scanner observes the temperature change at the rear face as a function of time. With a reference sample, specific heat can be determined (C_p), and with measured density (ρ) and thermal diffusivity (α), the thermal conductivity (K) at a certain temperature can be calculated with the following equation:

$$K = \alpha \cdot C_p \cdot \rho \quad (1)$$

where K is the thermal conductivity ($\text{W} \cdot \text{m}^{-1} \cdot \text{K}^{-1}$), α is the thermal diffusivity (m^2/s), C_p is the specific heat capacity ($\text{J} \cdot \text{kg}^{-1} \cdot \text{K}^{-1}$), and ρ is the density of the sample (kg/m^3). A NETZSCH thermal analyser DSC 404C was used to measure the specific heat capacity. A NETZSCH LFA 427 with a TASC 414/4 controller was used to measure the thermal diffusivity.

Electrical conductivity measurements were made using a Keithley 6517B electrometer in the 2-point measurement mode. Five-centimeter long compound extrudates (small rods) were covered on the edges using silver paste, and their diameter was measured. Resistance was measured under 1, 10, or 100 V depending on the compound conductivity. Volume conductivity σ is calculated as follows:

$$\sigma = L / (R \times S) \quad (2)$$

where L is the sample length in cm, R is the measured resistance in ohms, and S is the rod section in cm^2 . Conductivity values are given in S/cm^2 .

2.4. FFF Process Parameters

3D printing filament manufacturing was performed at 230 $^\circ\text{C}$ using a single-screw extruder with a water-cooling bath combined with a filament shaper to calibrate a diameter of 1.75 mm and 4 km long. The extrusion process and the produced spool of PA12_15%GNPs + 1%CNTs can be seen in Figure 1. The filament was evaluated by TGA and DSC, and the technical detail is listed in Table 1.

For FFF processability assessment, filament segments of 30 cm were cut and measured with a digital caliper to determine the average diameter of each segment. Filament drying was conducted by a hot-air drying oven at 80 $^\circ\text{C}$ for 12 h, and all segments were conditioned prior to testing in a low-humidity enclosure. The Raise 3D Pro 2 Plus FFF system was employed for the fabrication of testing specimens with different process parameters, and the generation of custom Gcode scripts was conducted through 3DOptimizer software (FabControl SIA). Firstly, a preliminary extrudability assessment was conducted for three nozzle diameters (0.4, 0.6, 0.8 mm) in order to assess flow consistency and extrusion temperature range. After the nozzle diameter (0.8 mm) was selected, seven different temperatures above the melting temperature (189 $^\circ\text{C}$ in Table 1) were tested, from 240 $^\circ\text{C}$ to 280 $^\circ\text{C}$, for printing quality examination. Subsequently, sequential interdependence tests were conducted by varying nozzle temperature, printing speed, extrusion multiplier (volumetric flow rate compensation factor), retraction, and thermoplastic strand width and height as seen in Figure 2. Precise leveling and calibration of the FFF system and first layer settings were conducted prior to each test. Stereomicroscope evaluation (S9 stereomicroscope, Leica Microsystems) was conducted to assess morphology and deposition consistency of

thermoplastic strands, aiming to identify parameter sets that eliminated structural defects related to over/under-extrusion and presented high strand uniformity.

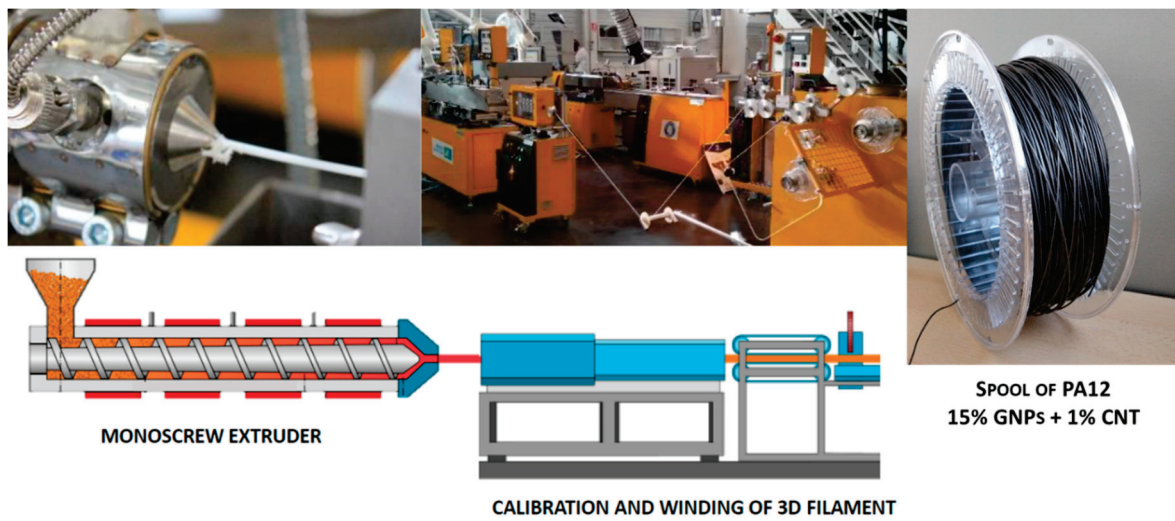


Figure 1. 3D printing fillers produced by a single-screw extruder combined with a filament shaper.

Table 1. Technical data of the PA12_15%GNPs + 1%CNTs filament.

Base Polymer Material	PA12 AMNO TLD
Fillers	15 wt% GNP + 1 wt% CNTs
Melting point (°C)-peak	189 °C
Glass transition temperature (°C)	51 °C
Max. printing temperature (°C)	280 °C
Diameter	1.75 mm
Color	Black
Translucency	No
Density (g/cm ³)	1.16
Humidity take-up (w%)	~0.35%

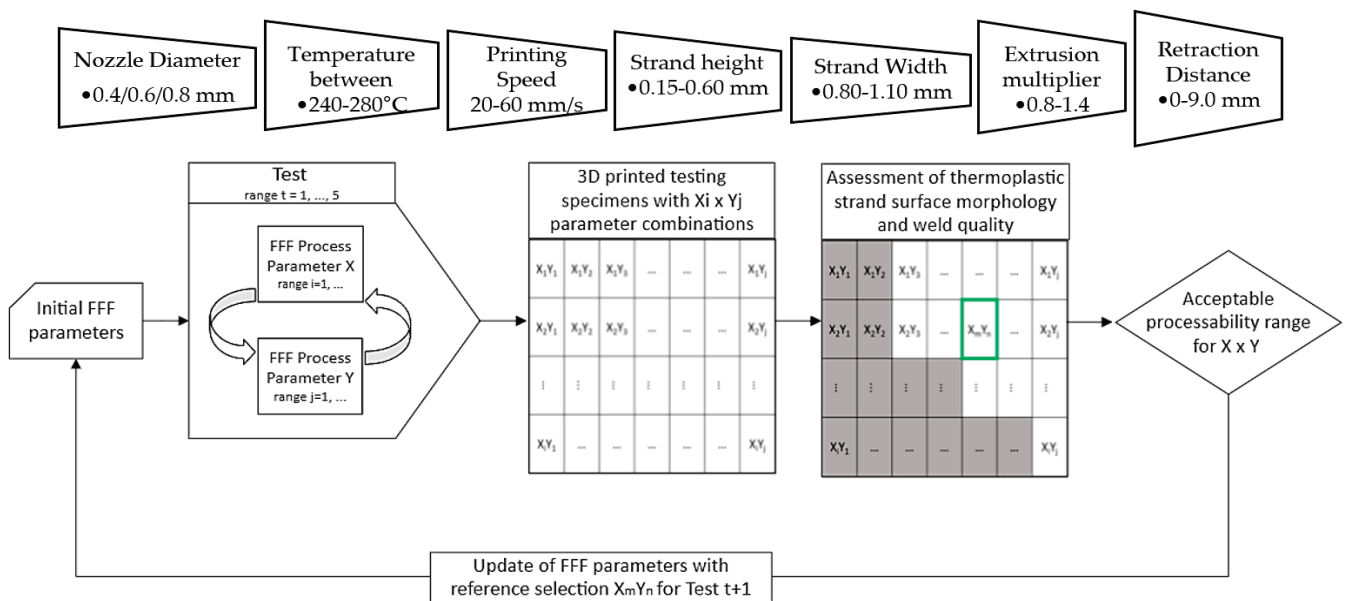


Figure 2. FFF Processability optimization path.

3. Results

3.1. Carbon-Based Nanofillers

Multiwalled carbon nanotubes (MWCNTs) were prepared with the supported catalyst approach and had an average diameter of 50–80 nm, as shown in Figure 3. They were in an entangled form, with embedded catalyst at their end caps, implying a tip growth mechanism.

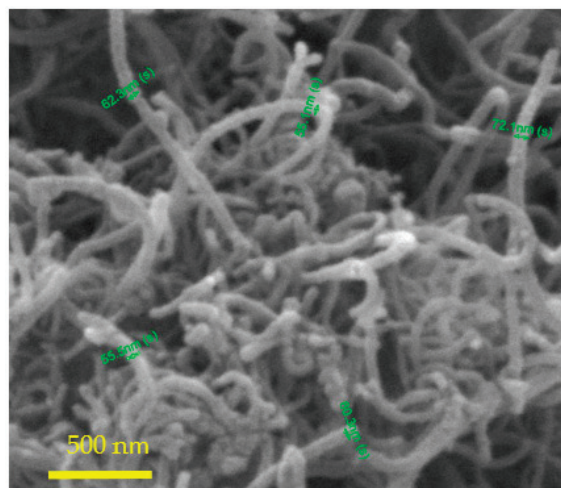


Figure 3. SEM images of MWCNTs prepared with the supported catalyst approach (Catalyst: Fe/zeolite; carbon source: acetylene).

The GNPs powders were dispersed on adhesive conductive tape for SEM characterization. The platelets had a lateral dimension within the range of 2–10 μm , with thickness of a few tens of nanometers. The material was partially exfoliated (or reaggregated), with platelets showing highly exfoliated regions together with thicker crystals (Figure 4a). The GNPs Raman spectra present very sharp and high-intensity G (1580 cm^{-1}) and 2D (2680 cm^{-1}) lines, which corresponds to high-crystallinity and low-defects surface structure (Figure 4b). The most prominent “disorder” Raman spectrum, D-line (1360 cm^{-1}), suggests an increase in the amount of crystallite boundaries with decreasing crystal size or to the presence of graphite edge planes perturbing the smoothly stratified crystallites.

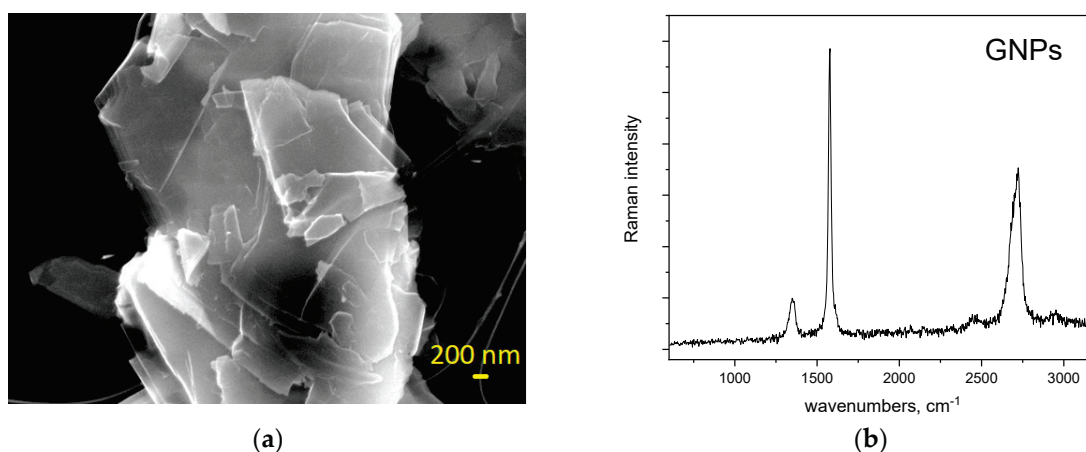


Figure 4. (a) SEM images of GNPs and (b) Raman spectra of the GNPs.

Different procedures were tested for the growth of CNTs on chopped CF surface. As displayed in Figure 5, the CFs grafted by the floating catalyst approach were homogeneously coated with thin CNTs, surrounding each monofilament.

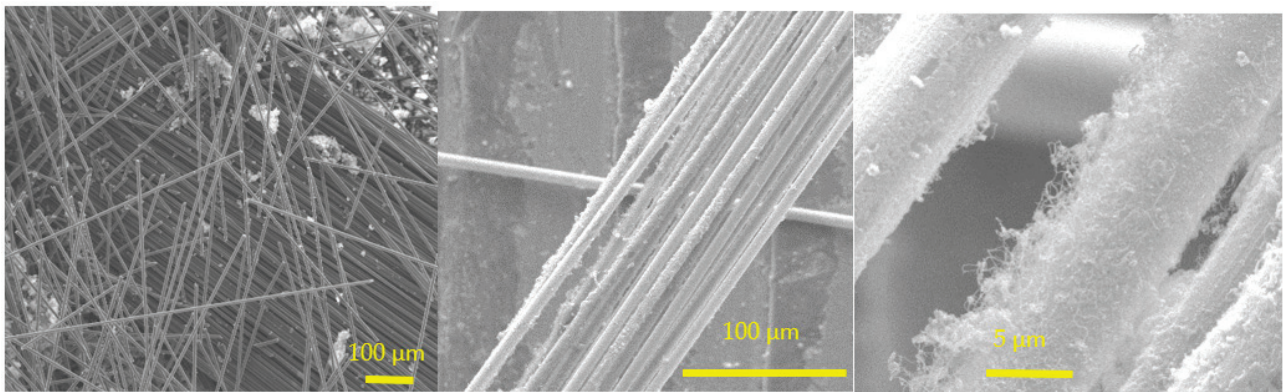


Figure 5. CNTs on chopped CFs (floating catalyst approach: catalyst: ferrocene; carbon source: ethanol).

3.2. Composite Structure Characterization by SEM/Micro-CT

PA12-based polymer composites with different functional additions (CNTs, CNTs@chopped CFs, and GNPs + CNTs) were made to enhance their thermal conductivity (Figure 6). The fractography of the PA12 neat composite and CNT-modified PA12 was observed by SEM, as shown in Figure 7a–c. The CNTs are evenly distributed in the PA12 composite, and no pore or agglomeration can be seen (Figure 7b,c). Although most of the chopped CFs are evenly distributed in the PA12 matrix, some space can be seen at the interface of the CFs and the resin as displayed in Figure 7d–f. Pores and agglomerations can also be seen in the matrix of 20wt%CNTs@CFs inclusion.



Figure 6. The fabricated coupons of PA12 and PA12 with 10% and 20% inclusions of CNTs@chopped CFs.

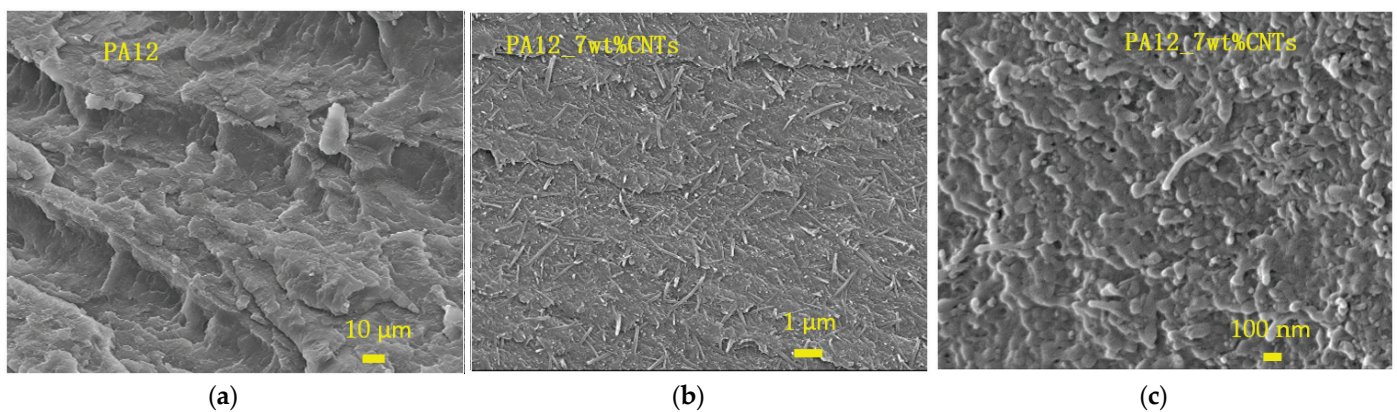


Figure 7. Cont.

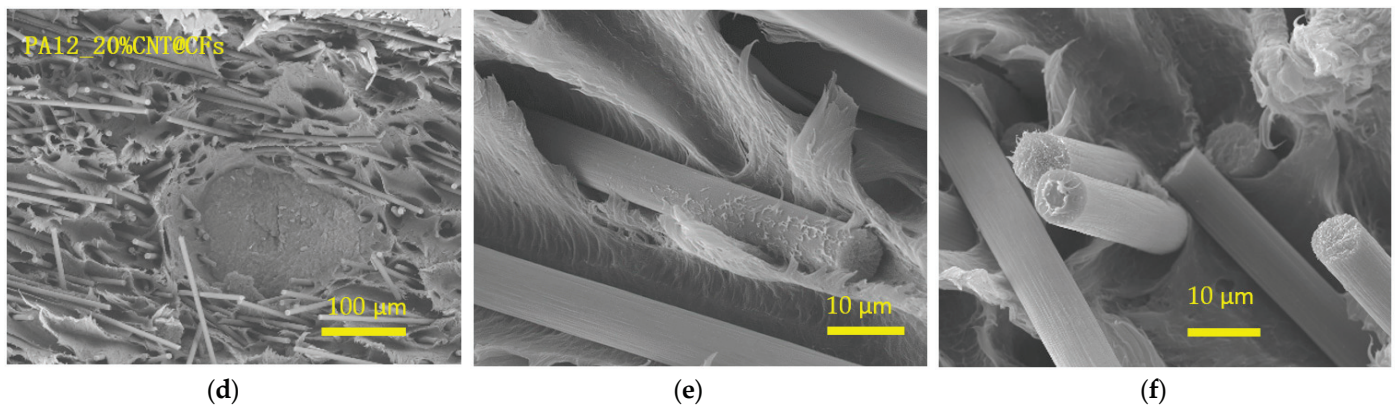


Figure 7. SEM fractography of (a) the neat PA12, (b,c) PA12 with 7 wt% CNTs, and (d–f) the PA12 with 20 wt% CNTs@CFs.

A layered structure can be seen on the fractography of the PA12_15%GNPs+1wt%CNT sample (Figure 8). The composite has a dense structure, and the CNTs are well embedded in the composite (Figure 8c).

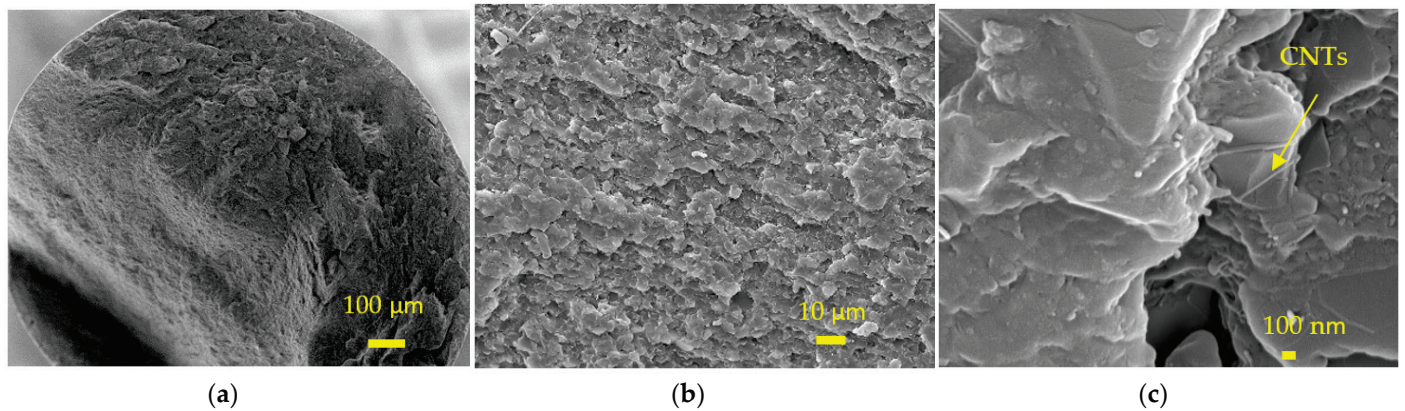


Figure 8. SEM fractography of the PA12-15wt%GNPs+1wt% CNT sample (a) the fracture, (b) an enlarged area, and (c) the CNTs in the composite.

The macro-scale observations regarding the surface quality of the filament are also confirmed through the micro-CT analysis (Figure 9 and Table 2). The shape of the filament appears to be circular and is within acceptable limits, as most areas are quite dense but some macrocracks can be seen in the pellet. Some defects and irregularities on the surface can be attributed to possible agglomerates that form during the manufacturing of the filament.

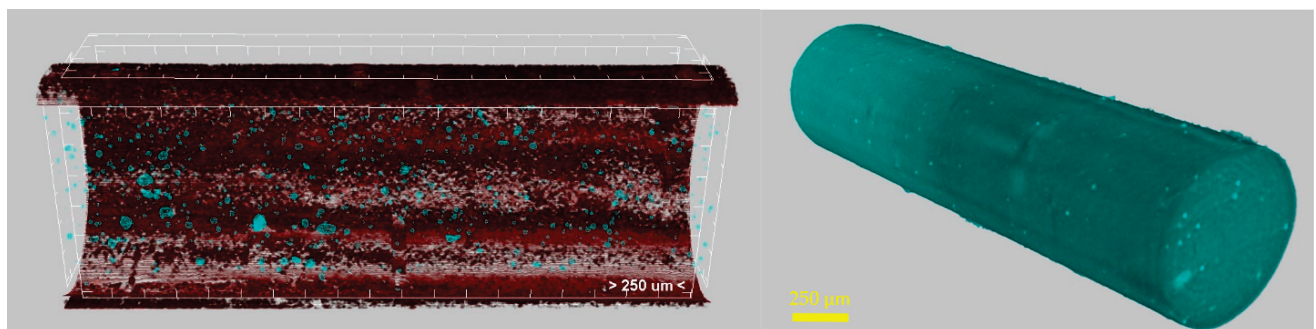
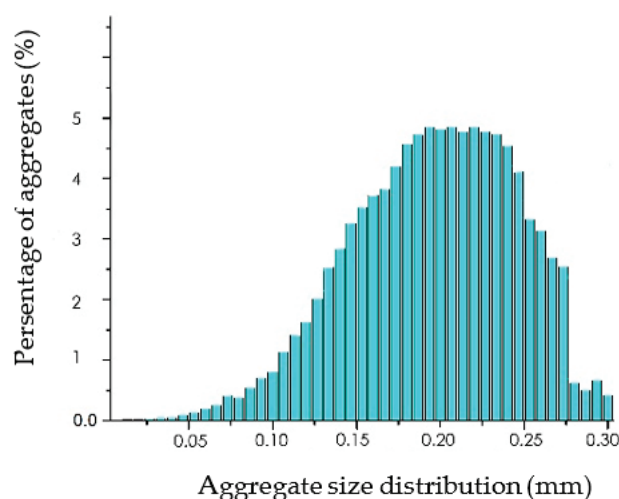


Figure 9. Micro-CT analysis images of PA12_15%GNPs + 1%CNTs.

Table 2. Micro-CT arithmetical results for the filament.

Parameters	Filament
Object Surface Density (mm^{-1})	3.82
Structure Thickness (mm)	0.58
Structure Separation (mm)	0.05
Structure Linear Density (mm^{-1})	1.72
Degree of Anisotropy	5.6
Fractal Dimension	2.09
Total Porosity (%)	0.18

Nanomaterial aggregation in the composite filament was also investigated, and its influence on the final products' properties was determined through CTAn software. The PA nanocomposite filament's aggregates constitute 1.2% in volume, with mid-range aggregation sizes placed at 0.18–0.25 mm (Figure 10). For this measurement, the similarity in structure between the organic polymer matrix and the carbon-based additives causes similar X-ray absorption between the two. From the 3D visualization and the indicative reconstructed slices (Figures 9 and 10), it is illustrated that the PA12 nanocomposite filament exhibits needle-like aggregations as well as clusters of aggregations near the filament surface, which may also cause surface morphological variations. Such defects increase the possibility of printing inconsistencies in the final product fabrication process, and, therefore, printing parameters (e.g., nozzle diameter) should be modified.

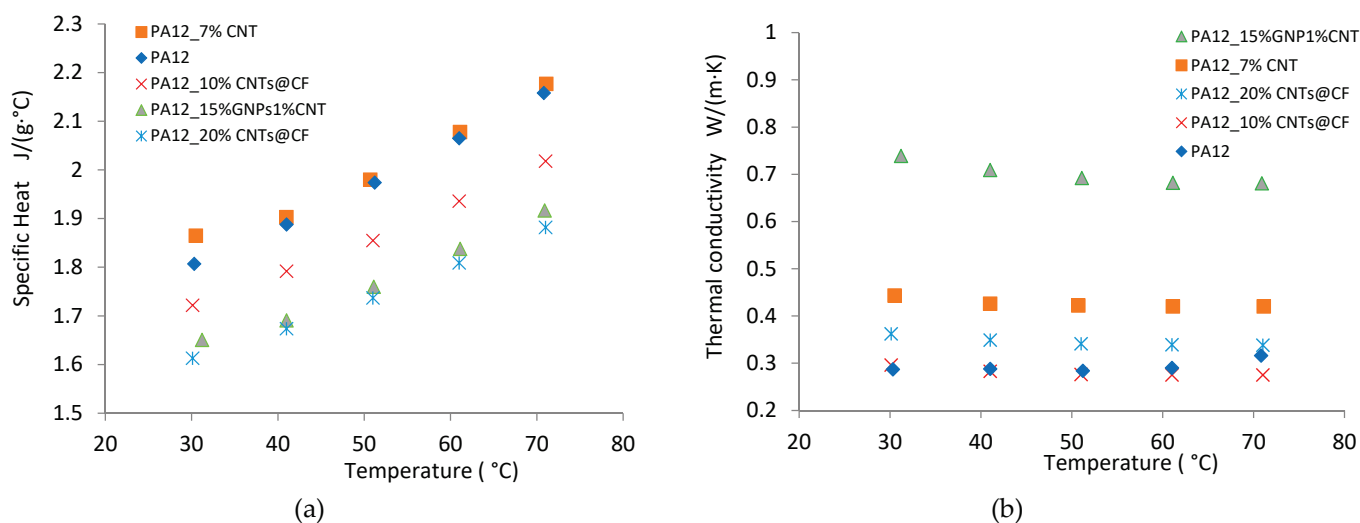
**Figure 10.** Aggregate size distribution for PA nanocomposite filament.

3.3. Thermal Conductivity and Electrical Conductivity Results

The density (Table 3), the specific heat, and the thermal diffusivity of the PA12-based composite were measured, and the thermal conductivities were calculated and plotted in Figure 11. In comparison with the neat PA12, 20 wt% CNTs@CFs inclusion increased the thermal conductivity of PA12 slightly, but 10 wt% CNTs @ CFs inclusion showed no improvement, especially at elevated temperature (Table 3 and Figure 11). Micro-CT scan and SEM examination indicated that there were many pores and agglomerations in the composite (Figure 7d–f), which resulted in less effective thermal conductivity enhancement. With 7 wt% CNTs inclusion, the thermal conductivity of PA12 increased significantly at the test temperature range of 30/40/50/60/70 °C. The CNTs were evenly distributed in the PA12 (Figure 7b), which led to a significant improvement in thermal conductivity. Furthermore, sample PA12_15GNPs + 1% CNTs performed best and nearly tripled the thermal conductivity value of the neat PA12 at the test range thanks to the inclusions of GNPs and CNTs (Figure 8).

Table 3. Summary of PA12 compounds modified by different filaments.

Sample	Detail	Density (g/cm ³)	Thermal Conductivity at 30 °C (W/mk)	Thermal Conductivity Improvement vs. Neat PA12
PA12	Neat	1.005	0.28	-
PA12_7% CNT	7 wt% CNTs	1.124	0.44	57%
PA12_15%GNP1%CNT	15 wt% GNPs + 1 wt% CNTs	1.065	0.73	161%
PA12_10%CNT@CFs	10 wt% CNTs @ CFs	0.988	0.3	7%
PA12_20%CNT@CFs	20 wt% CNTs @ CFs	1.117	0.37	32%

**Figure 11.** Thermal conductivity of PA12 incorporated with different reinforcements: (a) specific heat and (b) calculated thermal conductivity.

The measured electrical conductivity of neat PA12 compound was $1.00 \text{ E}^{-12} \text{ S/m}$, and it increased to $1.00 \text{ E}^{-10} \text{ S/m}$ for the 10 wt% CNTs @ CFs-modified PA12, while the value reached $6.00 \text{ E}^{-6} \text{ S/m}$ for the 15 wt% GNPs + 1 wt% CNTs-modified PA12 compound.

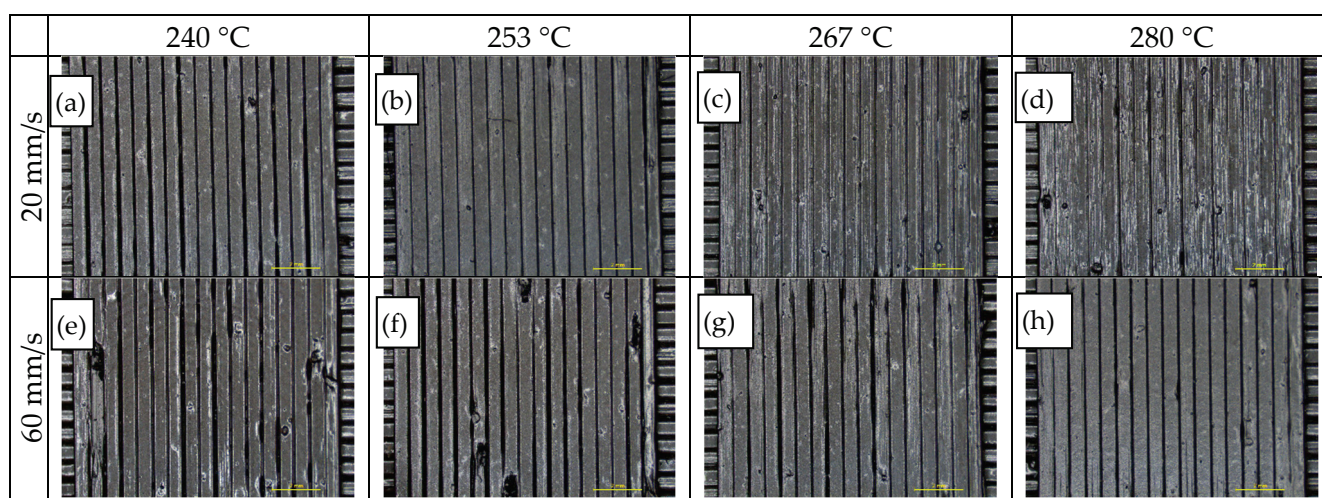
3.4. FFF Processability Assessment

Due to its improved thermal conductivity and low electrical conductivity, PA12 compound with 15 wt% of GNPs and 1 wt% CNTs was used for the FFF processability assessment. A range of process parameters were investigated for FFF processing, as shown in Figure 2 and Table 4. The upper and lower limits of each parameter value have been set from preliminary tests to ensure consistent flow through the nozzle and according to the FFF system operational range.

A total of 27 variants with seven extrusion temperatures and four different printing speeds were studied to find the effect of extrusion temperature and printing speed. As both parameters directly affect the maximum volumetric flow rate through the nozzle, the optimum range is obtained once printing speed is in balance with the maximum material throughput, while over- and under-extrusion is observed when this balance is disrupted. As shown in Figure 12a–h, for the upper (60 mm/s) and the lower (20 mm/s) printing speeds, the impact of the printing temperature increases, as demonstrated through a transition from gap formation to over-extrusion due to the associated variation in material melt viscosity. By inspection of thermoplastic strand surface morphology and weld quality among adjacent strands, the acceptable limits for printing temperature and speed were 253–280 °C and 20–47 mm/s respectively, while the combination of 280 °C and 33 mm/s was selected as reference for further assessment.

Table 4. List of 3D printing parameters in the FFF processability assessment for PA12 compound with 15 wt% of GNPs and 1 wt% CNTs.

Extrusion temperature (°C)	240	247	253	260	267	273	280
Printing speed (mm/s)	20	33	47	60	-	-	-
Strand height (mm)	0.15	0.22	0.30	0.37	0.45	0.52	0.60
Strand width (mm)	0.80	0.85	0.90	0.95	1.00	1.05	1.10
Extrusion multiplier	0.8	0.9	1.0	1.1	1.2	1.3	1.4
Retraction distance (mm)	0	1.5	3.0	4.5	6.0	7.5	9.0

**Figure 12.** Optical inspection via stereomicroscope (7 \times) of specimens obtained from varying extrusion temperatures (ET) and printing speeds (PS): (a–d) SP = 20 mm/s and ET = 240, 253, 267, 280 °C from left to right; (e–h) SP = 60 mm/s and ET = 240, 253, 267, 280 °C from left to right.

For the selected extrusion temperature, the effect of strand height was assessed for the same range of printing speeds by combining seven strand height values with four printing speed values investigated in the previous step, in a total of 27 variants. As the strand height value (equal to layer height) is employed for the automatic calculation of the filament feed rate, a variation of this value can lead to over- or under-extrusion when the nominal volumetric flow rate is not in accordance with the actual volumetric flow rate required to achieve the targeted strand volume. As shown in Figure 13a–h, for the two upper and lower limit values of printing speed, the effect of nominal strand height increase is demonstrated through a transition from increased overlapping of adjacent strands and rough surface morphology associated with over-extrusion to gap formation due to the associated deviation between nominal/actual volumetric flow rate. Acceptable limits for strand height and printing speed were defined as 0.30–0.45 mm and 20–47 mm/s, respectively. Furthermore, seven strand widths were studied at a printing speed of 33 mm/s and strand height of 0.3 mm, and it was found that the acceptable limits for strand width were between 1.00 and 1.10 mm.

For parameters selected in previous steps, the effect of strand width was assessed for seven strand width values, employed (along with the strand height) for the automatic calculation of the filament feed rate speed. As displayed in Figure 14a–d, for the selected printing speed of 33 mm/s and strand height of 0.3 mm, the effect of strand width increase is similarly demonstrated through a transition from increased overlapping of adjacent strands to uniform strand width deposition close to the nominal value. Acceptable limits for strand width were defined between 1.00 and 1.10 mm, while the value of 1.10 mm was selected as reference for further assessment.

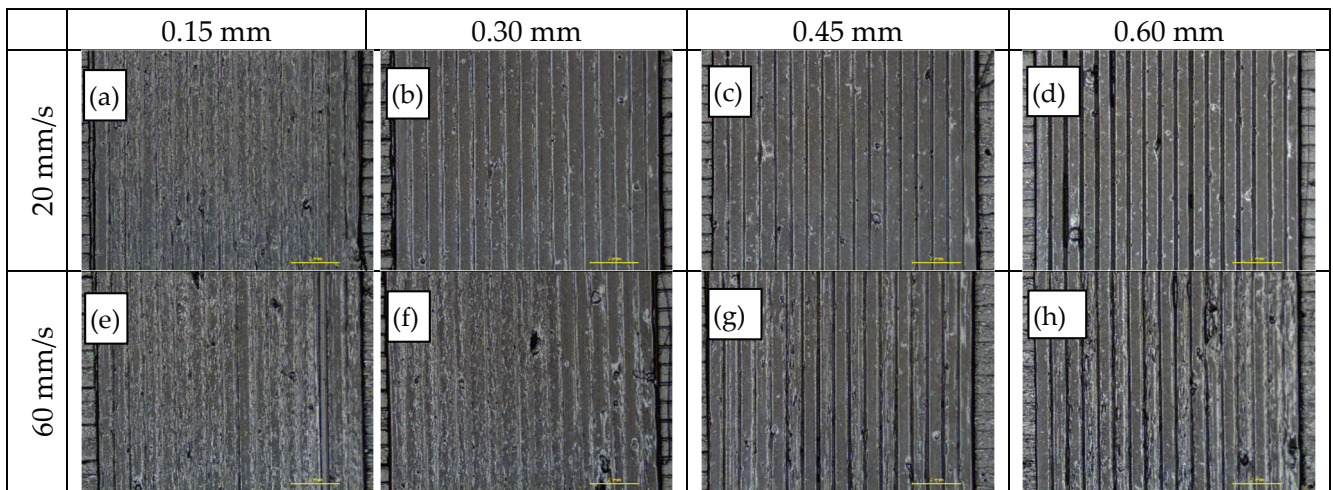


Figure 13. Optical inspection via stereomicroscope (7 \times) of specimens obtained from varying strand heights (SH) and printing speeds (PS): (a–d) SP = 20 mm/s and SH = 0.15, 0.30, 0.45, 0.60 mm from left to right; (e–h) SP = 60 mm/s and SH = 0.15, 0.30, 0.45, 0.60 mm from left to right.

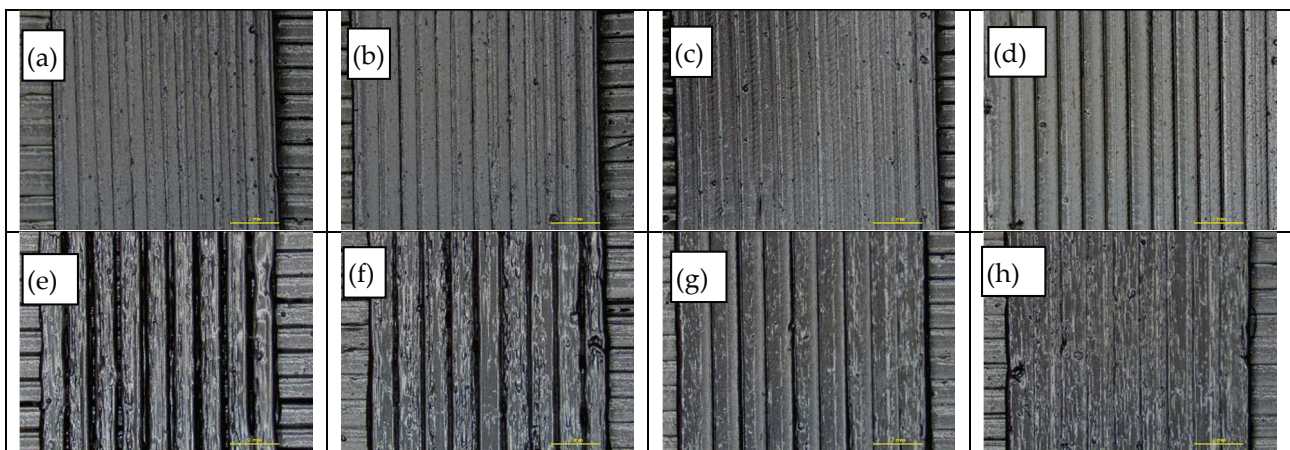


Figure 14. Optical inspection via stereomicroscope (7 \times) of specimens obtained from varying strand widths (SW) and the extrusion multiplier (EM): (a–d) SW = 0.80, 0.90, 1.00, 1.10 mm from left to right; (e–h) EM = 0.8, 1.0, 1.2, 1.4 from left to right.

In the next step, for parameters selected previously, the effect of a volumetric flow rate compensation factor (extrusion multiplier) was investigated for seven extrusion multiplier values. The extrusion multiplier allows for an automatic percentage adjustment of the nominal volumetric flow rate value by multiplying by a user-defined value. As depicted in Figure 14e–h, the effect of extrusion multiplier adjustment can be employed for further fine tuning of strand geometry and intra-strand coalescence. Acceptable limits for the extrusion multiplier were defined between 1.0 and 1.2, while the value of 1.2 was selected as reference for further assessment.

Finally, retraction distance was investigated for seven values, at the selected printing speed of 30 mm/s, as a parameter related to the length of filament (in mm) that is reverted and re-pushed through the FFF system feeding mechanism during the printing head non-extruding movements. Retraction distance is employed for the control of surface defects (e.g., blobs and strings) resulting from material remaining in the nozzle tip. As demonstrated in Figure 15a–d, by inspection of thermoplastic strand end points where defects are manifested, acceptable limits for retraction distance were defined between 4.5 and 7.5 mm, while further increases of the value did not present any further enhancement and some remaining defects were not eliminated.

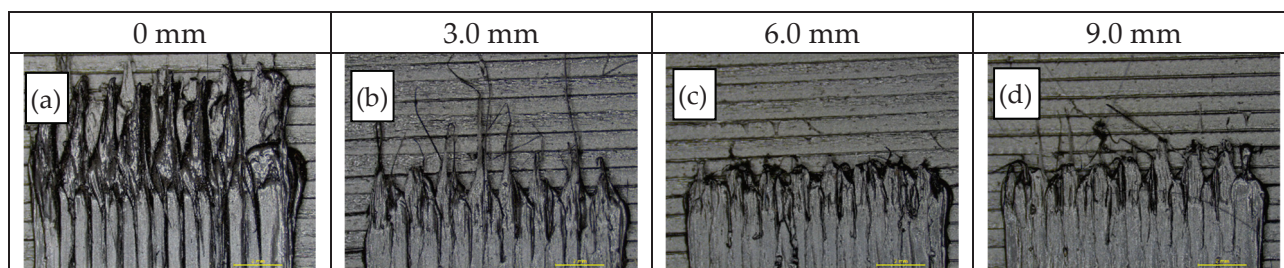


Figure 15. Optical inspection via stereomicroscope (7 \times) of specimens obtained from varying retraction distances (RD): (a–d) RD = 0.0, 3.0, 6.0, 9.0 mm from left to right.

In short, the extrusion temperature, printing speed, strand height and width, extrusion multiplier, and retraction distance all have an impact on the processability of FFF, and a combination of the optimized processing parameters is highlighted in Table 4.

4. Conclusions

Carbon-based nanofillers, CNTs, CNTS @ chopped CFs, and GNPs/CNTs were used to modify PA12 to improve its thermal conductivity. CNTs @ chopped CFs can improve the thermal conductivity of PA12 slightly, but a large amount is needed. Moreover, 7 wt% CNTs improved the thermal conductivity and electrical conductivity of the PA12, but they also led to agglomeration. PA12 with 15 wt% of GNPs and 1 wt% CNTs demonstrated the most improved thermal conductivity, and a processability assessment for FFF 3D printing technology was conducted to determine the processing window for the selected composition. Stereomicroscope optical inspection was conducted to assess morphology and deposition consistency of thermoplastic strands for a series of sequential interdependence tests varying nozzle temperature, printing speed, extrusion multiplier (volumetric flow rate compensation factor), retraction, and thermoplastic strand width and height. For the selected range of printing speeds, the impact of printing temperature increase was demonstrated through a transition from gap formation to over-extrusion, while the strand geometry obtained from different nominal strand height and width values provided insight into the actual volumetric flow rate and acceptable limits of nominal values to obtain strand uniformity. Finally, the effect of a volumetric flow rate compensation factor was investigated to further optimize inter-strand coalescence and filament retraction during printing head non-extruding movements; this indicated a moderate control of surface defects (e.g., blobs and strings) resulting from material remaining in the nozzle tip. Based on the results obtained, parameter sets were defined to achieve high strand uniformity and coalescence for the nanocomposite filament, eliminating most structural defects related to over-/under-extrusion and, thus, meeting the necessary criteria to be processable with FFF technology.

Author Contributions: Conceptualization, Z.Z. and H.D.; methodology, Z.Z.; validation, Z.Z., E.G., X.L. and A.-F.T.; formal analysis, Z.Z., E.G., S.J. and A.-F.T.; investigation, Z.Z., E.G., P.Z., S.J., D.S., P.-N.P., N.K. and A.K.; resources, Z.Z. and A.-F.T.; data curation, Z.Z., S.J. and P.Z.; writing—original draft preparation, Z.Z.; writing—review and editing, Z.Z., D.S., A.-F.T., E.G., S.J. and P.-N.P.; supervision, H.D.; project administration, C.C.; funding acquisition, C.G., H.D. and C.C. All authors have read and agreed to the published version of the manuscript.

Funding: This research was funded by the EU H2020 Project “Smart by Design and Intelligent by Architecture for turbine blade fan and structural components systems” (SMARTFAN) under Grant no. 760779.

Institutional Review Board Statement: Not applicable.

Informed Consent Statement: Not Applicable.

Data Availability Statement: Data are contained within this article.

Conflicts of Interest: The authors declare no conflict of interest. The funders had no role in the design of the study; in the collection, analyses, or interpretation of data; in the writing of the manuscript; or in the decision to publish the results.

References

- Vadivelu, M.A.; Kumar, C.R.; Joshi, G.M. Polymer Composites for Thermal Management: A Review. *Compos. Interfaces* **2016**, *23*, 847–872. [CrossRef]
- Kwon, Y.-J.; Park, J.-B.; Jeon, Y.-P.; Hong, J.-Y.; Park, H.-S.; Lee, J.-U. A Review of Polymer Composites Based on Carbon Fillers for Thermal Management Applications: Design, Preparation, and Properties. *Polymers* **2021**, *13*, 1312. [CrossRef] [PubMed]
- Bai, J.; Goodridge, R.D.; Yuan, S.; Zhou, K.; Chua, C.K.; Wei, J. Thermal Influence of CNT on the Polyamide 12 Nanocomposite for Selective Laser Sintering. *Molecules* **2015**, *20*, 19041–19050. [CrossRef] [PubMed]
- Tofail, S.A.M.; Koumoulos, E.P.; Bandyopadhyay, A.; Bose, S.; O'Donoghue, L.; Charitidis, C. Additive Manufacturing: Scientific and Technological Challenges, Market Uptake and Opportunities. *Mater. Today* **2018**, *21*, 22–37. [CrossRef]
- Feng, C.; Yu, S.-S. 3D Printing of Thermal Insulating Polyimide/Cellulose Nanocrystal Composite Aerogels with Low Dimensional Shrinkage. *Polymers* **2021**, *13*, 3614. [CrossRef] [PubMed]
- Vanaei, H.R.; Shirinbayan, M.; Deligant, M.; Khelladi, S.; Tcharkhtchi, A. In-Process Monitoring of Temperature Evolution during Fused Filament Fabrication: A Journey from Numerical to Experimental Approaches. *Thermo* **2021**, *10*, 21. [CrossRef]
- Bahadur, R.; Bar-Cohen, A. Orthotropic Thermal Conductivity Effect on Cylindrical Pin Fin Heat Transfer. *Int. J. Heat Mass Transf.* **2007**, *50*, 1155–1162. [CrossRef]
- Guo, R.; Ren, Z.; Jia, X.; Bi, H.; Yang, H.; Ji, T.; Xu, M.; Cai, L. Preparation and Characterization of 3D Printed PLA-Based Conductive Composites Using Carbonaceous Fillers by Masterbatch Melting Method. *Polymers* **2019**, *11*, 1589. [CrossRef]
- Rafiee, M.; Farahani, R.D.; Therriault, D. Multi-Material 3D and 4D Printing: A Survey. *Adv. Sci.* **2020**, *7*, 1902307. [CrossRef]
- Diogo José, H.; Pedro Paulo Andrade, J. 3D-Printed Conductive Filaments Based on Carbon Nanostructures Embedded in a Polymer Matrix: A Review. *IJANR* **2019**, *4*, 26–40. [CrossRef]
- Guo, H.; Lv, R.; Bai, S. Recent Advances on 3D Printing Graphene-Based Composites. *Nano Mater. Sci.* **2019**, *1*, 101–115. [CrossRef]
- Shemelya, C.; De La Rosa, A.; Torrado, A.R.; Yu, K.; Domanowski, J.; Bonacuse, P.J.; Martin, R.E.; Juhasz, M.; Hurwitz, F.; Wicker, R.B.; et al. Anisotropy of Thermal Conductivity in 3D Printed Polymer Matrix Composites for Space Based Cube Satellites. *Addit. Manuf.* **2017**, *16*, 186–196. [CrossRef]
- Han, Z.; Fina, A. Thermal Conductivity of Carbon Nanotubes and Their Polymer Nanocomposites: A Review. *Prog. Polym. Sci.* **2011**, *36*, 914–944. [CrossRef]
- Chen, B.; Davies, R.; Liu, Y.; Yi, N.; Qiang, D.; Zhu, Y.; Ghita, O. Laser Sintering of Graphene Nanoplatelets Encapsulated Polyamide Powders. *Addit. Manuf.* **2020**, *35*, 101363. [CrossRef]
- Lupone, F.; Padovano, E.; Ostrovskaya, O.; Russo, A.; Badini, C. Innovative Approach to the Development of Conductive Hybrid Composites for Selective Laser Sintering. *Compos. Part A: Appl. Sci. Manuf.* **2021**, *147*, 106429. [CrossRef]
- Guo, N.; Leu, M.C. Effect of Different Graphite Materials on the Electrical Conductivity and Flexural Strength of Bipolar Plates Fabricated Using Selective Laser Sintering. *Int. J. Hydrog. Energy* **2012**, *37*, 3558–3566. [CrossRef]
- Szeluga, U.; Kumanek, B.; Trzebicka, B. Synergy in Hybrid Polymer/Nanocarbon Composites. A review. *Compos. Part A Appl. Sci. Manuf.* **2015**, *73*, 204–231. [CrossRef]
- Dey, A.; Roan Eagle, I.N.; Yodo, N. A Review on Filament Materials for Fused Filament Fabrication. *J. Manuf. Mater. Process.* **2021**, *5*, 69. [CrossRef]
- Wang, J.; Mubarak, S.; Dhamodharan, D.; Divakaran, N.; Wu, L.; Zhang, X. Fabrication of Thermoplastic Functionally Gradient Composite Parts with Anisotropic Thermal Conductive Properties Based on Multicomponent Fused Deposition Modeling 3D Printing. *Compos. Commun.* **2020**, *19*, 142–146. [CrossRef]
- El Magri, A.; Vanaei, S.; Shirinbayan, M.; Vaudreuil, S.; Tcharkhtchi, A. An Investigation to Study the Effect of Process Parameters on the Strength and Fatigue Behavior of 3D-Printed PLA-Graphene. *Polymers* **2021**, *13*, 3218. [CrossRef]
- Vanaei, H.R.; Shirinbayan, M.; Vanaei, S.; Fitoussi, J.; Khelladi, S.; Tcharkhtchi, A. Multi-Scale Damage Analysis and Fatigue Behavior of PLA Manufactured by Fused Deposition Modeling (FDM). *Rapid Prototyp. J.* **2021**, *27*, 371–378. [CrossRef]
- Kozior, T. The Influence of Selected Selective Laser Sintering Technology Process Parameters on Stress Relaxation, Mass of Models, and Their Surface Texture Quality. *3D Print. Addit. Manuf.* **2020**, *7*, 126–138. [CrossRef]
- Adamczak, S.; Zmarzły, P.; Kozior, T.; Gogolewski, D. Assessment of Roundness and Waviness Deviations of Elements Produced by Selective Laser Sintering Technology. In Proceedings of the 23rd International Conference Engineering Mechanics, Svratka, Czech Republic, 15–18 May 2017; pp. 70–73.
- Turner, B.N.; Strong, R.; Gold, S.A. A Review of Melt Extrusion Additive Manufacturing Processes: I. Process Design and Modeling. *Rapid Prototyp. J.* **2014**, *20*, 192–204. [CrossRef]
- Bakrani Balani, S.; Chabert, F.; Nassiet, V.; Cantarel, A. Influence of the Printing Parameters on the Stability of the Deposited Beads in Fused Filament Fabrication of Poly(lactic) Acid. *Addit. Manuf.* **2019**, *25*, 112–121. [CrossRef]
- Ajinjeru, C.; Kishore, V.; Liu, P.; Lindahl, J.; Hassen, A.A.; Kunc, V.; Post, B.; Love, L.; Duty, C. Determination of Melt Processing Conditions for High Performance Amorphous Thermoplastics for Large Format Additive Manufacturing. *Addit. Manuf.* **2018**, *21*, 125–132. [CrossRef]

27. Gao, X.; Qi, S.; Kuang, X.; Su, Y.; Li, J.; Wang, D. Fused Filament Fabrication of Polymer Materials: A Review of Interlayer Bond. *Addit. Manuf.* **2021**, *37*, 101658. [CrossRef]
28. Rashid, A.A.; Koç, M. Fused Filament Fabrication Process: A Review of Numerical Simulation Techniques. *Polymers* **2021**, *13*, 3534. [CrossRef]
29. Comminal, R.; Serdeczny, M.P.; Pedersen, D.B.; Spangenberg, J. Numerical Modeling of the Strand Deposition Flow in Extrusion-Based Additive Manufacturing. *Addit. Manuf.* **2018**, *20*, 68–76. [CrossRef]
30. Trompeta, A.-F.; Koklioti, M.A.; Perivoliotis, D.K.; Lynch, I.; Charitidis, C.A. Towards a Holistic Environmental Impact Assessment of Carbon Nanotube Growth through Chemical Vapour Deposition. *J. Clean. Prod.* **2016**, *129*, 384–394. [CrossRef]

Article

Closed-Cell Rigid Polyimide Foams for High-Temperature Applications: The Effect of Structure on Combined Properties

Yawei Shi ^{1,2}, Aijun Hu ^{1,*}, Zhiyuan Wang ¹, Kedi Li ³ and Shiyong Yang ^{1,2,*}

¹ Key Laboratory of Science and Technology on High-Tech Polymer Materials, Institute of Chemistry, Chinese Academy of Sciences, Beijing 100190, China; shiywei@iccas.ac.cn (Y.S.); zhiyuan@iccas.ac.cn (Z.W.)

² School of Chemical Sciences, University of Chinese Academy of Sciences, Beijing 100190, China

³ Cashem Advanced Materials Hi-Tech Co., Ltd., Shaoxing 312369, China; ked.li@cashem.cn

* Correspondence: aijunhu@iccas.ac.cn (A.H.); shiyang@iccas.ac.cn (S.Y.)

Abstract: Closed-cell rigid polyimide foams with excellent thermal stability and combined properties were prepared by thermal foaming of a reactive end-capped polyimide precursor powder in a closed mold. The precursor powder was obtained by thermal treatment of a polyester-amine salt (PEAS) solution derived from the reaction of the diethyl ester of 2,3,3',4'-biphenyl tetracarboxylic dianhydride (α -BPDE) with an aromatic diamine mixture of p-phenylenediamine (PDA) and 2-(4-aminophenyl)-5-aminobenzimidazole (BIA) in the presence of an end-capping agent (mono-ethyl ester of nadic acid anhydride, NE) in an aliphatic alcohol. The effect of polymer mainchain structures on the foaming processability and combined properties of the closed-cell rigid polyimide foams were systematically investigated. The polyimide foams (100–300 kg/m³) with closed-cell rates of 91–95% show an outstanding thermal stability with an initial thermal decomposition temperature of ≥ 490 °C and a glass transition temperature of 395 °C. Polyimide foams with density of 250 kg/m³ exhibited compression creep deformation as low as 1.6% after thermal aging at 320 °C/0.4 MPa for 2 h.

Keywords: polyimide foam; rigid closed-cell foam; high temperature; benzimidazole

Citation: Shi, Y.; Hu, A.; Wang, Z.; Li, K.; Yang, S. Closed-Cell Rigid Polyimide Foams for High-Temperature Applications: The Effect of Structure on Combined Properties. *Polymers* **2021**, *13*, 4434. <https://doi.org/10.3390/polym13244434>

Academic Editors: Somen K. Bhudolia and Sunil Chandrakant Joshi

Received: 10 November 2021

Accepted: 12 December 2021

Published: 17 December 2021

Publisher's Note: MDPI stays neutral with regard to jurisdictional claims in published maps and institutional affiliations.



Copyright: © 2021 by the authors. Licensee MDPI, Basel, Switzerland. This article is an open access article distributed under the terms and conditions of the Creative Commons Attribution (CC BY) license (<https://creativecommons.org/licenses/by/4.0/>).

1. Introduction

Polyimide (PI) foams [1–4], due to the presence of the imide groups in the polymer mainchain, display excellent thermal stability, thermal insulating properties, non-flammability, radiation resistance, etc. and have found widespread application in aerospace, aviation, orbiting vehicles, and transportation [5–7]. There are two types of PI foams based on the cell morphology: an open-cell version and a closed-cell one [8,9]. Generally, most open-cell PI foams are soft. Closed-cell PI foams may have different closed-cell rates of less than 100%. The commercial SOLIMIDE[®] foams (BOYD Corporation) are a series of open-cell soft PI foams with density of 5 to 64 kg/m³, which can be maintained in long-term service at temperatures up to 300 °C [9,10]. Due to the open-cell structure and low strength, open-cell soft PI foams are usually used as heat insulation and sound absorbing materials. With the development of the aerospace industry, lightweight and high-strength foam materials have been required for applications such as cryogenic insulation and energy absorption. For example, the production of re-usable launch vehicles (RLVs) requires high performance structural insulation foam materials which may be subject to service temperatures ranging from –250 °C to 250 °C [11]. The construction of high speed aerospace vehicles requires a core-splice material with a density of 500 kg/m³ and a potting material with a density of 560 kg/m³, respectively [12]. Hence, rigid PI foams with excellent thermal stability and combined mechanical properties are required for application in the aerospace field.

DuPont started research on PI foams as early as the 1960s and later launched commercial rigid PI foams under the trade name Vespel[®] [13,14]. Vespel[®] PI foams possess an excellent compressive strength of 2.0 MPa with a density (ρ) of 300 kg/m³. The maximum service temperature is about 300 °C. The Langley Research Center at NASA has prepared

a series of closed-cell PI foams with closed-cell rates of <80% by foaming a salt-like precursor [9,15]. The salt-like precursor was synthesized by mixing the dimethyl ester of a dianhydride and a diamine in methanol. The compressive strength of the foam is in the range of 0.098–0.84 MPa, and the glass transition temperature (T_g) is ≤ 321 °C.

To improve the performance of PI foams, the incorporation of inorganic fillers such as silica, graphene, and carbon fibers [8,16–21] into the foam matrix has been utilized. PI/organoclay nanocomposite foams have been prepared through thermal foaming of a polyester amine salt (PEAS)/organoclay precursor [22]. Hydrogen bonding between the organoclay and the polymer matrix provided enhancements of both the T_g and decomposition temperature. However, property improvements were limited by the required dosage of the fillers, as the presence of fillers usually have negative effect on cell morphology [16].

The introduction of a cross-linked structure in the polyimide matrix can restrict the mobility of polymer chains, resulting in improvements in thermal stability and mechanical properties [23–29]. A series of crosslinked PI foams were prepared by copolymerization of a trifunctional diamine monomer 2,4,6-triaminopyrimidine (TAP) with BTDA-ODA to form a PI foam [23,24]. Both the T_g and tensile strength of the PI foam were increased. The PI foams (PIF-15) with 15% content of TAP displayed a T_g of 286.7 °C, compared with 272.6 °C for PIF-0 containing no TAP. A thermosetting/thermoplastic PI foam was prepared using in situ simultaneous orthogonal polymerization [25,30]. The precursor of linear PI and the monomer of cross-linked bismaleimide (BMI) were blended and foamed at high temperature. The T_g values for the PI foams increased with increasing BMI content, from 255.85 °C for neat PI foam to 285.12 °C for PIF-30 with a BMI content of 30 wt.%.

An approach for the production of closed-cell rigid PI foams by thermal foaming of nadimide end-capped polyimide oligomers (NPOs) has been reported. The NPOs were obtained by thermally treating an in situ polymerization of a monomeric reactant (PMR)-type polyester-amine salt (PEAS) solution [26,27]. The PEAS was synthesized from the reaction of the diethyl ester of aromatic dianhydride (α -BPDE) and aromatic diamines using mono-ethyl ester of cis-5-norbornene-endo-2,3-dicarboxylic anhydride (NE) as the reactive end-capping agent in ethyl alcohol. A crosslinking structure was formed through a reverse Diels–Alder reaction of the end-capped groups during the foaming process. The resulting rigid PI foams contained a uniform cellular structure with a closed-cell rate as high as 89%, along with a high thermal stability and good mechanical properties.

Heteroaromatic diamine monomers containing benzimidazole or the benzoxazole structure have also been employed as co-monomers to improve the closed-cell rigid PI combined properties. The incorporation of benzimidazole or the benzoxazole structure can increase the rigidity of polymer molecular segments and promote the formation of hydrogen bonds between polymer chains [28,31]. A series of PI foams containing the comonomer 2-(4-aminophenyl)-5-aminobenzoxazole (DAPBO) have been prepared [32]. The rigid PI foam with 60% DAPBO content displayed a T_g value of 368 °C, which was much higher than that of the pristine PI foam (273 °C). The compressive strength was also increased to 1.03 MPa from 0.3 MPa. Obviously, the introduction of a heterocyclic structure or crosslinked structure can improve the combined properties of the PI foams.

A heteroaromatic diamine, 2-(4-aminophenyl)-5-aminobenzimidazole (BIA), was employed as a comonomer to improve the combined properties of closed-cell PI foams possessing a crosslinked structure. The PI foams were produced by the thermal foaming of the nadimide end-capped polyimide oligomers (NPOs), which were prepared by the copolymerization of an aromatic dianhydride (α -BPDA) and an aromatic diamine mixture containing BIA and PDA using cis-5-norbornene-endo-2,3-dicarboxylic anhydride (NA) as the end-capping agent. The BIA content and the molecular weight (M_w) of the PI precursors had a significant effect on the cell morphology and overall performance of the PI foams.

2. Materials and Methods

2.1. Materials

2,3,3',4'-Biphenyl tetracarboxylic dianhydride (α -BPDA) was purchased from China-tech (Tianjin) Chemical Co., Ltd., (Tianjin, China) and dried at a reduced pressure at 160 °C for 8 h prior to use. *cis*-5-Norbornene-*endo*-2,3-dicarboxylic anhydride (NA) was purchased from Changzhou Sunlight Pharmaceutical Co., Ltd., (Changzhou, China) and dried at a reduced pressure at 80 °C for 8 h prior to use. *p*-Phenylenediamine (PDA) and 2-(4-aminophenyl)-5-aminobenzimidazole (BIA) were obtained from Changzhou Sunlight Pharmaceutical Co., Ltd., (Changzhou, China) and used as received. Ethyl alcohol was obtained from Beijing Chemical Reagents Co. (Beijing, China) and stored over 4 Å molecular sieves to remove the moisture.

2.2. Preparation of Nadimide End-Capped Polyimide Oligomers (NPOs)

α -BPDA (0.1 mol) (29.42 g) and NA (0.07 mol) (11.49 g) were combined in 63.58 g of ethanol (1.38 mol). The solution was stirred at solvent reflux for three hours to obtain a homogeneous solution. Then, 11.68 g of PDA (0.108 mol) and 6.06 g of BIA (0.027 mol) were added, and the solution was stirred at solvent reflux for another two hours to produce a homogeneous PEAS solution. After removing most of the solvent by rotating distillation, the viscous liquid was dried at a reduced pressure at 200 °C. The obtained solid resin was crushed into a fine powder and sieved, yielding a powder with a particle diameter of 50 to 200 μ m. In this experiment, the oligomer powder (NPO-2) had a BIA/(BIA + PDA) molar ratio of 20% and a calculated molecular weight (calcd M_w) of 1500 g/mol.

In addition, a series of NPO powders (NPO-0, NPO-1, and NPO-3) with a fixed calcd M_w of 1500 g/mol but different BIA/(BIA + PDA) molar ratios of 0%, 10%, and 30%, respectively, were prepared by adjusting the molar ratio of aromatic diamines. Moreover, a series of NPO powders with a fixed molar ratio of BIA/(BIA + PDA) (20%) but different calcd M_w were also prepared, including NPO-2-1000 (calcd M_w = 1000), NPO-2-1250 (calcd M_w = 1250), NPO-2-1500 (calcd M_w = 1500), NPO-2-1750 (calcd M_w = 1750), and NPO-2-2000 (calcd M_w = 2000), respectively.

2.3. Preparation of Closed-Cell Rigid PI Foams

The polyimide foams were prepared by thermal foaming of the NPO powder in a closed mold. The NPO powder was placed at the bottom of the mold, which was then heated in a hot press. The mold was heated stepwise to 350 °C and held for three hours with applied pressure. Then, the mold was cooled to room temperature and the rigid PI foam was removed and cut into the desired dimensions for testing.

The amount of NPO powder placed in the mold was determined according to the desired foam density and mold volume as well as the calculated amounts of organic volatiles evolved in the thermal foaming process. The foam density was determined by the amount of precursor and the size of the mold:

$$\rho = a \times m/V \quad (1)$$

where a is a constant factor determined by the mass loss during the foaming process and the volume shrinkage of the foam caused by the cooling process, m is the mass of the NPO precursor, and V represents the volume of the mold.

Hence, a series of rigid PI foams (PIF-0, PIF-1, PIF-2, and PIF-3) with a fixed calcd M_w of 1500 g/mol but different molar ratios of BIA/(BIA + PDA) of 0%, 10%, 20%, and 30% were prepared, respectively. Similarly, a series of rigid PI foams (PIF-2-1000, PIF-2-1250, PIF-2-1500, PIF-2-1700, and PIF-2-2000) with a fixed molar ratio of BIA/(BIA + PDA) of 20% but different calcd M_w were also prepared. Additionally, a series of rigid PI foams with a fixed BIA/(BIA + PDA) molar ratio of 20% and calcd M_w of 1500 g/mol but different densities (70, 150, 200, and 300 kg/m³) were prepared. Unless otherwise indicated, the density of the foam was 100 kg/m³.

2.4. Measurements

The chemical structures of the NPO precursors were characterized using a Bruker TENSOR27 Fourier transform infrared (FT-IR) spectrometer (Bruker, Karlsruhe, Germany). The measurements were performed in the range of 400–4000 cm^{-1} by averaging 32 scans. ^1H NMR spectra were obtained on a Bruker AVANCE 300 spectrometer (Bruker, Karlsruhe, Germany) using dimethyl sulfoxide (DMSO- d_6) (J&K Co, Beijing, China) as a solvent. The morphology of the PI foam cellular structure was observed using a Hitachi S-4800 scanning electron microscope (SEM) (Hitachi, Tokyo, Japan). The closed-cell rate of the PI foams was measured by a Micromeritics AccuPyc II 1340 pycnometer (Micromeritics, Norcross, GA, USA) according to GB/T 10799-2008 using specimens with the dimensions 25 mm \times 25 mm \times 25 mm and under 2.9 psi pressure.

The rheological behavior measurements of the NPO precursors at different temperatures were performed on a TA AR2000 rheometer (TA Instruments, New Castle, DE, USA) with a heating rate of 4 $^\circ\text{C}/\text{min}$. The specimen disks (25 mm in diameter and weighing 1 g) were prepared by compression molding of the NPO powder. The rheometer instrument was equipped with a 25 mm diameter parallel plate fixture. The upper plate was oscillated at a fixed strain of 0.1% and a constant angular frequency of 10 rad/s, while the lower plate was attached to a transducer that recorded the resultant torque and converted it to the complex viscosity.

Thermal gravimetric analysis (TGA) was performed on a TA Q50 thermal analysis system (TA Instruments, New Castle, DE, USA) with a heating rate of 20 $^\circ\text{C}/\text{min}$ under an air atmosphere with a gas flow rate of 40 mL/min. Dynamic mechanical analysis (DMA) was performed on a TA Q800 instrument (TA Instruments, New Castle, DE, USA) under an N_2 atmosphere with a heating rate of 5 $^\circ\text{C}/\text{min}$. A dual cantilever mode was employed using specimens with the dimensions 60.0 mm \times 15.0 mm \times 5.0 mm.

The mechanical properties of the PI foams were measured using an Instron 5567 universal testing machine (Instron, Norwood, MA, USA). The compression property measurement was performed according to GB T8813-2008 using specimens with a size of 25 mm \times 25 mm \times 25 mm at a compression rate of 2.5 mm/min. Dumbbell-shaped specimens were prepared to test the tensile properties of the PI foams with a tensile rate of 5 mm/min according to GB/T 9641-1988.

3. Results and Discussion

3.1. Characterization

The rigid PI foams were prepared by thermal foaming of the reactive end-capped NPO precursor powder at 350 $^\circ\text{C}$ for 3 h in a closed mold. As shown in Figure 1, the NPO powder was obtained by thermal treating of the polyester–amine salt (PEAS) solution derived from the reaction of the α -BPDA diethyl ester with PDA and BIA in the presence of an end-capping agent (monoethyl ester of nadic acid anhydride, NE) in aliphatic alcohol. The prepared foam showed a dense cell structure with a light-yellow color after the high-temperature foaming process.

The FT-IR spectra of the NPOs with different BIA contents are shown in Figure 2. The NPOs showed imide ring characteristic absorption peaks at 1778 cm^{-1} (C=O asymmetric stretching vibration), 1720 cm^{-1} (C=O symmetric stretching vibration), 1363 cm^{-1} (C–N stretching vibration), and 730 cm^{-1} (imide ring bending vibration), indicating the formation of an imide structure (Figure 2A). The peaks at 3100–3450 cm^{-1} were attributed to the asymmetric and symmetric stretching vibration of N–H as shown in Figure 2B [33,34]. The peak intensity increased with increasing BIA content in the NPOs, indicating the presence of benzimidazole moieties in the polymer backbones.

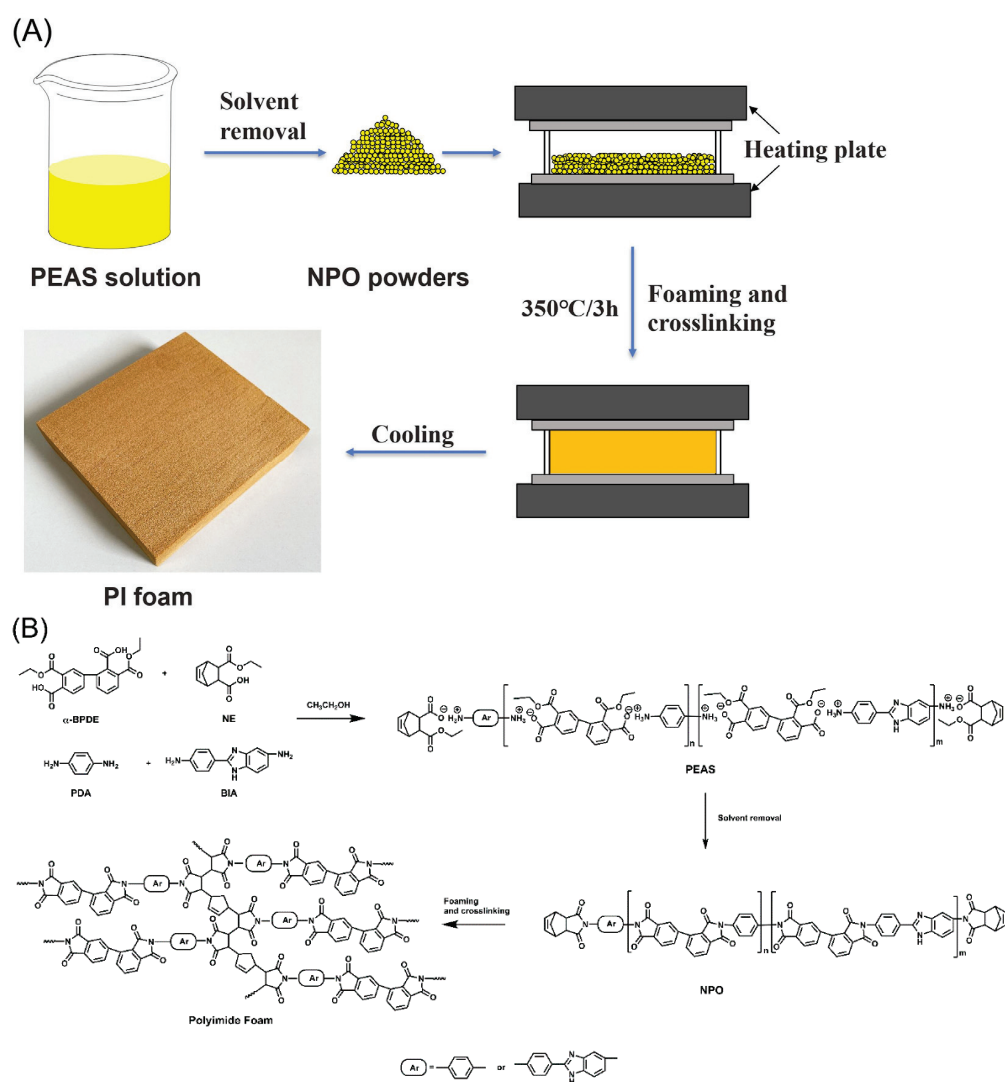


Figure 1. (A) Schematic diagram and (B) chemical reaction formula of procedure to fabricate the rigid PI foams. α -BPDE, diethyl ester of 2,3,3',4'-biphenyl tetracarboxylic dianhydride; NE, monoethyl ester of *cis*-5-norbornene-endo-2,3-dicarboxylic anhydride. α -BPDE and NE were obtained by reflux esterification of corresponding monomers in ethanol. The foam dimensions were 220 mm \times 220 mm \times 35 mm.

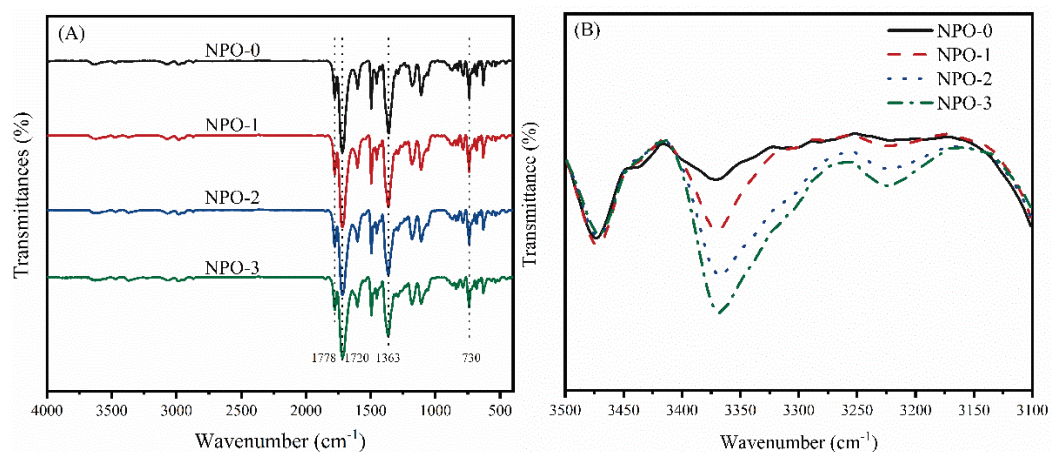


Figure 2. FT-IR spectra of NPOs with different BIA contents: (A) complete spectrum and (B) partial spectrum at 3100–3500 cm^{-1} .

The chemical structures of the NPOs were further confirmed by NMR spectra (Figure 3). The signals for H₁ to H₄ in the NA end-capping agent (Figure 3A) were detected in all NPO precursors. The signals at 13.26 ppm were attributed to H₅ in the BIA moiety, and the intensity was increased with the increase in BIA content. These results confirm the existence of the NA end-capping groups and BIA moiety in the polymer backbones.

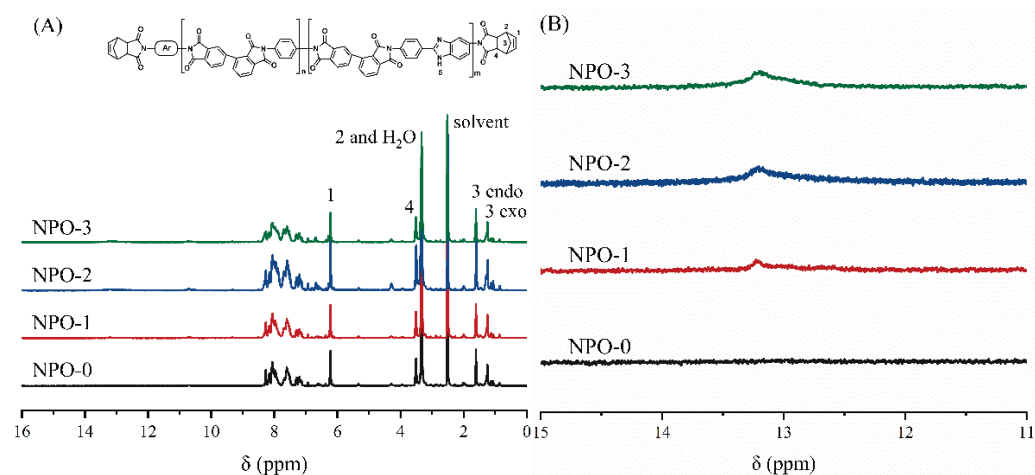


Figure 3. NMR spectra of NPOs with different BIA contents: (A) complete spectrum and (B) partial spectrum at 11–15 ppm.

The molecular weights of NPO-2 with a fixed BIA content of 20% and different calcd M_w of 1000–2000 g/mol were measured by GPC (Table 1). The measured M_n values showed the same trend as the calcd M_w , and the determined polydispersity ranged from 1.45 to 1.53.

Table 1. Measured molecular weight of NPO-2 with different calcd M_w .

Calcd M_w (g/mol)	M_n (g/mol)	M_w (g/mol)	Polydispersity
1000	1644	2385	1.45
1250	1662	2490	1.50
1500	1686	2508	1.49
1750	1688	2528	1.50
2000	1718	2626	1.53

3.2. Thermal Foaming Processability

The thermal foaming process of NPO-2 was monitored using a hot stage microscope with a heating rate of 10 °C/min. The temperature was increased to 320 °C, and the corresponding morphologies of the NPO powder at different temperatures are shown in Figure 4. The morphology of the NPO powder remained unchanged at temperatures below 280 °C, and some volume shrinkage was observed at 300 °C. At 320 °C, the NPO powder was completely melted and bubbles began forming. The foam bubbles gradually expanded from 0.5 to 10 min, implying that there was adequate strength maintaining the bubbles' intactness. The strength of the melt could be attributed to the crosslinking reaction of NPO during the foaming process [27]. In the foaming process, two types of foaming agents are produced: the byproducts of the imidization reaction, such as H₂O and CH₃CH₂OH, and the cyclopentadiene yielded by the thermal decomposition of the NA end-capping groups [35,36].

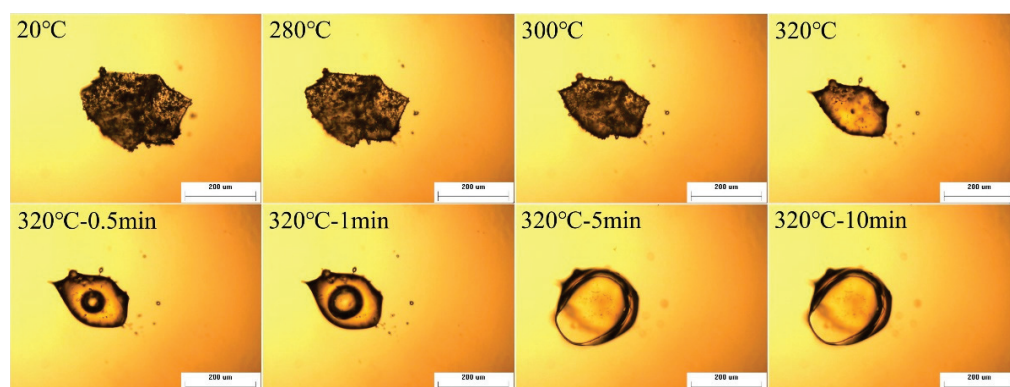


Figure 4. Foaming process of NPO-2 with increasing temperature.

Figure 5 compares the effect of BIA content on the NPO complex melt viscosities at 150–400 °C. The NPO powders began melting at temperatures higher than 250 °C; the melt viscosities decreased with the increase in temperature. After the minimum value, the melt viscosities were markedly increased due to the thermal crosslinking of the end-capping groups with a further increase in temperature, and the minimum melt viscosity was observed at 300–330 °C. Table 2 summarizes the minimum melt viscosity and the corresponding temperatures of the NPO powders with different BIA contents. Obviously, the minimum melt viscosity increased with the increase in BIA content in the polymer backbones. For instance, NPO-0 showed a minimum melt viscosity of 233 Pa·s at 317.3 °C, lower than that of NPO-1 (826 Pa·s at 324.1 °C), NPO-2 (5134 Pa·s at 328.9 °C), and NPO-3 (45,490 Pa·s at 304.6 °C).

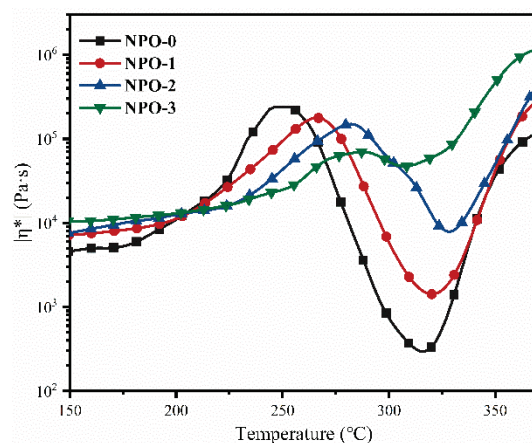


Figure 5. Rheological behaviors of melting for NPOs with different BIA contents.

Table 2. Minimum melt viscosity of powders NPO with different BIA contents and the corresponding temperature.

NPO	Minimum Melt Viscosity (Pa·s)	Temperature (°C)	$\eta_{(BIA)} : \eta_{(BIA+PDA)}$
NPO-0	233	317.3	0%
NPO-1	826	324.1	10%
NPO-2	5134	328.9	20%
NPO-3	45,490	304.6	30%

Closed-cell rigid PI foams—with different molar ratios of BIA/(BIA + PDA) (0% to 30%)—were successfully prepared by thermal foaming of the NPOs. However, when the molar ratio of BIA/(BIA + PDA) exceeded 40%, the NPOs could not be thermally foamed to yield PI foams—attributed to the lack of melt fluidity. Figure 6 compares the micro morphologies of the PI foams. The distribution of the cell sizes of the PI foams ranged from

50 to 600 μm , and most of the cell walls were intact without any broken holes or defects. The cell sizes and uniformity were significantly affected by the BIA content. The average cell diameter decreased with an increase in BIA content, along with the cell size uniformity. Obviously, PIF-3 showed an uneven cell structure.

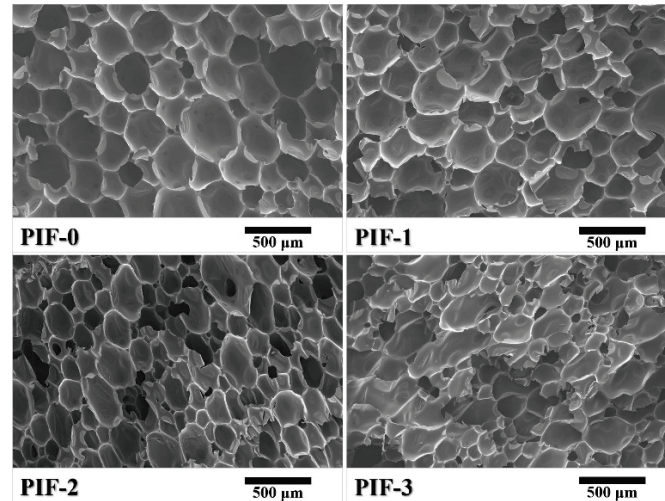


Figure 6. SEM images of the rigid PI foams with different BIA contents.

Figure 7 compares the complex melt viscosity of NPOs with different calcd M_w . The minimum melt viscosity increased with increasing calcd M_w . NPO-1000 showed the lowest minimum melt viscosity of 73 Pa·s at 301 $^{\circ}\text{C}$, compared with NPO-2-1250 (755 Pa·s at 311 $^{\circ}\text{C}$), NPO-2-1500 (5134 Pa·s at 328 $^{\circ}\text{C}$), and NPO-2-1750 (72,350 Pa·s at 318 $^{\circ}\text{C}$). The minimum melt viscosity of NPO-2-2000 was $>1.0 \times 10^5$ Pa·s at 325 $^{\circ}\text{C}$, resulting in a poor melt-flowing ability.

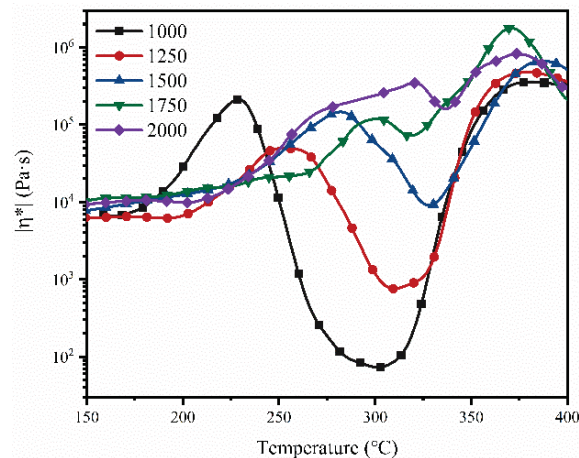


Figure 7. Melt viscosities of NPO-2 with different calcd M_w .

The NPO-2s with a calcd M_w of 1000–2000 g/mol could be thermally foamed to produce uniform rigid PI foams. Figure 8 compares the microscopic cell structures of the PI foams. The cell structures and cell diameter of the PI foams clearly changed with increasing calcd M_w . The cell size of PIF-2-1000 showed an obvious bimodal distribution comprising large-size cells (around 750 μm) and small-size cells (around 200 μm). The melt strength might not be strong enough to maintain cell integrity in the thermal foaming process, resulting in the occurrence of cell merging. PIF-2-1250 and PIF-2-1500 showed relatively uniform cell sizes, probably attributed to the moderate melt strength and blowing agent dosage.

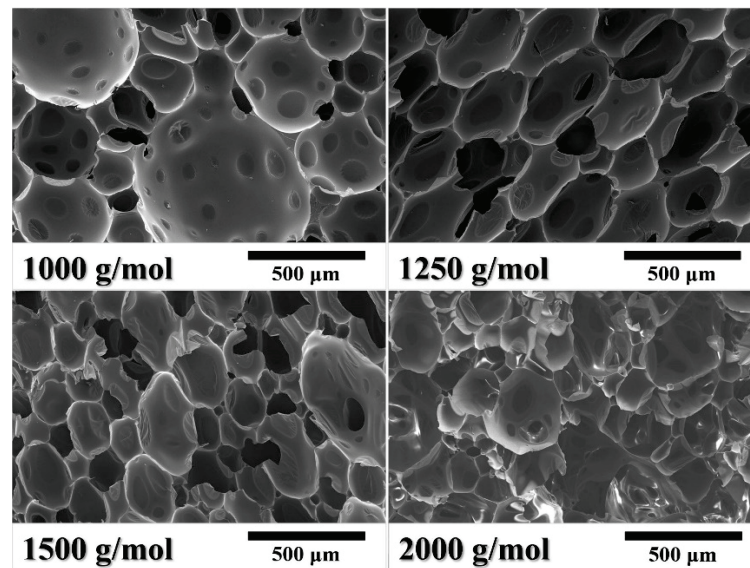


Figure 8. SEM images of rigid PI foams (NPO-2) with different calcd M_w .

Closed-cell rigid polymer foams are usually used as a core material of sandwich composites by co-curing of the foam core with carbon fiber prepreps. In this process, the high closed-cell rate is a crucial factor for reducing the weight of the finished product by preventing resin penetration into the foam core. Figure 9A compares the closed-cell rate of the PI foams with different BIA contents. The closed-cell rates of the PI foams were $\geq 80\%$, in which PIF-1 and PIF-2 showed closed-cell rates of 90% and 91%, respectively. The rapidly rising viscosity—due to the crosslinking of end-capping groups—might have accounted for the high closed-cell rate. NPO-0, which had the lowest melt viscosity, resulted in a PI foam with the lowest closed-cell rate. However, NPO-3 with the highest melt viscosity also resulted in PIF-3 with a lower closed-cell rate than PIF-1 and PIF-2, indicating that only an appreciable melt viscosity could produce PI foams with a high closed-cell rate. Figure 9B compares the closed-cell rate of the PI foams with different calcd M_w . The closed-cell rate increased from 85% for PIF-2-1000 to the highest value of 91% for PIF-2-1500. PIF-2-2000 showed a closed-cell rate of $<70\%$. This is consistent with the broken cell structure shown in Figure 8. Overall, the BIA content and the M_w had a significant influence on the rheological behavior of the precursor, which in turn affected the foam cell structure. Moderate melt viscosity could contribute to the formation of foam with a uniform cell structure and high closed-cell ratio.

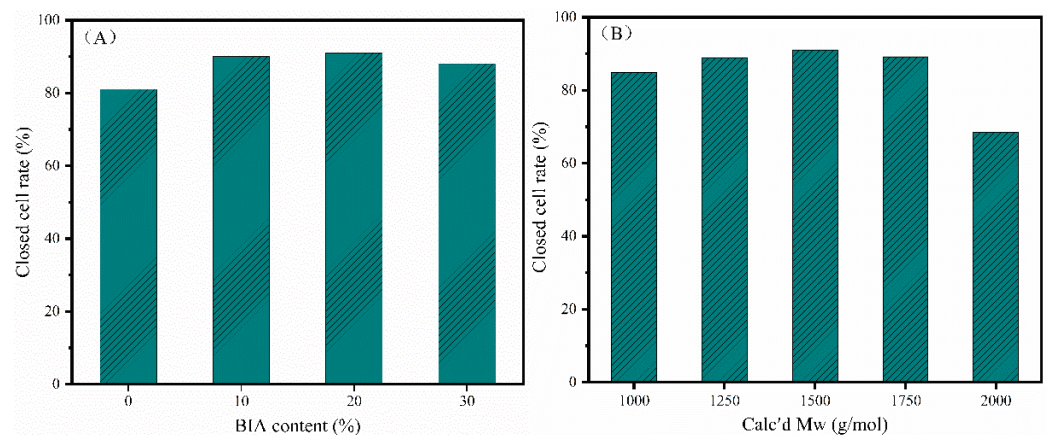


Figure 9. Closed-cell rates of the PI rigid foams according to (A) different BIA contents and (B) different calcd M_w .

3.3. Thermal Properties of the Rigid PI Foams

The thermal properties of the PI foams with different BIA contents are shown in Figure 10, and detailed data are listed in Table 3. No obvious weight loss was detected before 400 °C (Figure 10A), demonstrating the outstanding thermal oxidation stabilities of the foams. The T_g of the PI foams determined by tan δ in DMA was measured at ≥371.4 °C. The PI foams with higher BIA contents exhibited higher T_g values and thermal decomposition temperatures. For instance, PIF-3 showed a T_g of 402.9 °C, much higher than that of PIF-0 (371.4 °C) and PIF-1 (381.8 °C). The T_g of polymers is closely related to the rigidity of the polymer backbone. The BIA monomers used for polymerization enhanced the rigidity of the polyimide backbone. Additionally, the N–H groups in the BIA moiety can form hydrogen bonds with carbonyl groups in the imide ring, restricting the motion of polymer segments and increasing the T_g value [37].

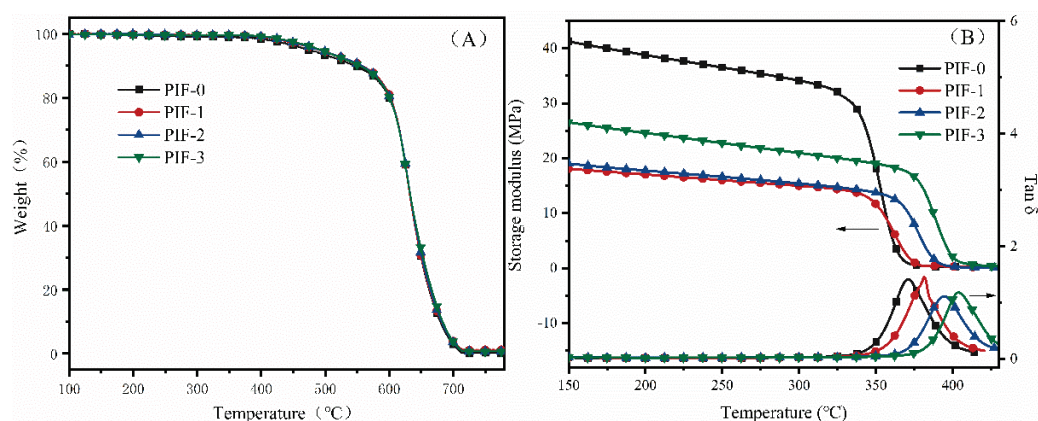


Figure 10. (A) TGA and (B) DMA curves of the rigid PI foams with different BIA contents.

Table 3. Thermal properties of polyimide foams with different BIA content and calcd M_w.

PIFs	TGA		DMA		n(BIA): n(BIA+PDA)	Calcd M _w (g/mol)
	T ₅ (°C)	T ₁₀ (°C)	E' (°C)	tan δ (°C)		
PIF-0	474.1	546.8	339.2	371.4	0%	1500
PIF-1	489.0	557.5	347.2	381.8	10%	1500
PIF-2	492.1	556.9	365.3	395.0	20%	1500
PIF-3	492.1	553.9	376.8	402.9	30%	1500
PIF-2-1000	479.1	521.8	378.2	409.3	20%	1000
PIF-2-1250	488.0	542.5	369.8	397.5	20%	1250
PIF-2-1500	492.1	556.9	365.3	395.0	20%	1500
PIF-2-1750	508.4	574.0	363.5	389.8	20%	1750
PIF-2-2000	512.9	578.5	362.8	387.0	20%	2000

Abbreviations: T₅, temperature at 5% loss of original weight; T₁₀, temperature at 10% loss of original weight; E', storage modulus; tan δ, tangent of loss angle.

The thermal properties of the PI foams with different calcd M_w can be seen in Table 3. T_g values were measured from 387.0 to 409.3 °C, which decreased with an increase in calcd M_w. For instance, PIF-2-2000 showed a T_g of 387.0 °C, much lower than PIF-2-1000 (409.3 °C) and PIF-2-1500 (395.0 °C), respectively. Thermal decomposition was restricted by increasing the M_w. The PI foams with lower M_w had a higher T_g but a lower thermal stability. Shortening the molecular chain could improve the degree of crosslinking and, thus, contribute to a high T_g. In addition, a lower M_w would increase the concentration of end-capping groups in the polymer backbone, resulting in a high ratio of aliphatic structure, which could be easily thermally decomposed at high temperatures [35]. Overall, increasing the BIA content and decreasing the M_w of the precursor are two effective methods to enhance the T_g of rigid PI foams.

3.4. Mechanical Properties of the Rigid PI Foams

Table 4 summarizes the mechanical properties of the PI foams. PIF-2 possessed the highest strengths, including a compression strength of 1.1 MPa and tensile strength of 0.9 MPa, and the highest elongation at breakage of 6.6%. The elongation at breakage increased from 3.0% for PIF-0 to 5.4% for PIF-1, and to 6.4% for PIF-3 and 6.6% (the highest) for PIF-2, implying that increasing the BIA content enhances the toughness of the foams. PIF-3 showed an obvious deterioration in mechanical properties when the BIA content was increased to 30%, accompanied by an irregular cell structure and lower closed-cell rate.

Table 4. Mechanical properties of PI foams with different BIA content and different calcd M_w .

PIFs	Compressive Properties		Tensile Properties		
	Strength (MPa)	Modulus (MPa)	Strength (MPa)	Modulus (MPa)	Elongation at Breakage (%)
PIF-0	1.0	31.0	0.6	21.5	3.0
PIF-1	1.0	35.7	0.6	15.3	5.4
PIF-2	1.1	24.7	0.9	17.0	6.6
PIF-3	0.6	9.8	0.6	11.2	6.4
PIF-2-1000	1.3	27.8	0.6	26.1	2.7
PIF-2-1250	1.1	28.2	1.0	28.6	4.0
PIF-2-1500	1.1	24.7	0.9	17.0	6.6
PIF-2-1750	1.4	35.9	0.6	15.7	4.8
PIF-2-2000	1.0	22.5	0.6	11.9	6.5

The PI foam mechanical properties were also influenced by M_w (Table 4). All PI foams showed a preferable compressive strength of ≥ 1.0 MPa. Increasing the M_w can lead to a decrease in tensile strength and enhanced toughness. This might be attributed to the non-uniformity of the cell structure and the decrease in crosslinking density, respectively. Overall, the mechanical properties of rigid PI foams were simultaneously affected by the chemical structure and cell structure of the foams. Generally, toughness can be improved by increasing the BIA content and the M_w of the precursors. An intact and uniform cell structure is essential to ensure the preferred mechanical properties of foam materials.

3.5. Mechanical Properties of the Closed-Cell Rigid PI Foams with Different Densities

Density is the most important factor determining the mechanical properties of foam materials [38,39]. A series of PI foams of different densities (70–300 kg/m³) were prepared. The precursor selected was NPO-2-1500 with a BIA content of 20% and calcd M_w of 1500 g/mol, for which the corresponding PI foam had the best combined properties. Figure 11A compares the SEM images of the PI foams with different densities. It is obvious that all the PI foams showed a uniform cell size distribution, in which the cell size was about 50–300 μm in diameter. In addition, the average cell size decreased with increasing density, and their sizes and their corresponding densities were 223 μm ($\rho = 70$ kg/m³), 216 μm ($\rho = 100$ kg/m³), 145 μm ($\rho = 150$ kg/m³), 136 μm ($\rho = 200$ kg/m³), and 132 μm ($\rho = 300$ kg/m³). The closed-cell rate of the PI foams with different densities can be seen in Figure 11B. All the rigid PI foams exhibited high closed-cell rates of $\geq 85\%$, which increased with increasing density. When the density exceeded 100 kg/m³, the closed-cell rates were $\geq 91\%$.

Figure 12 compares the compressive properties of the PI foams with different densities both at room temperature and 300 °C. The compressive strength and modulus increased with the increasing density, which is in accordance with the intensity being related to density as previously reported [38,39]. As the foam density increased from 70 to 300 kg/m³, the compressive strength and modulus increased by more than 10 times. The PI foam with 300 kg/m³ exhibited excellent mechanical properties with a compressive strength of 11 MPa and a compressive modulus of 215 MPa. Moreover, both the compressive strength and modulus retention at 300 °C were higher than 50%, demonstrating the outstanding thermodynamic properties of the rigid PI foams.

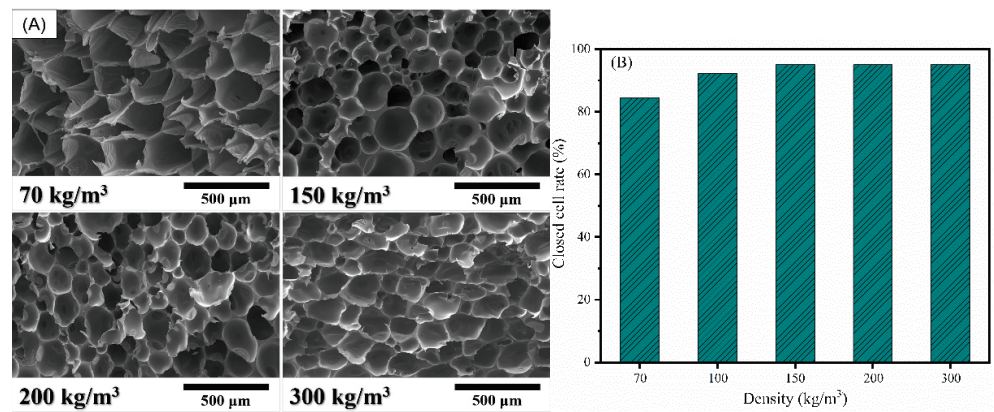


Figure 11. (A) SEM images and (B) closed-cell rate of the PI foams with different densities.

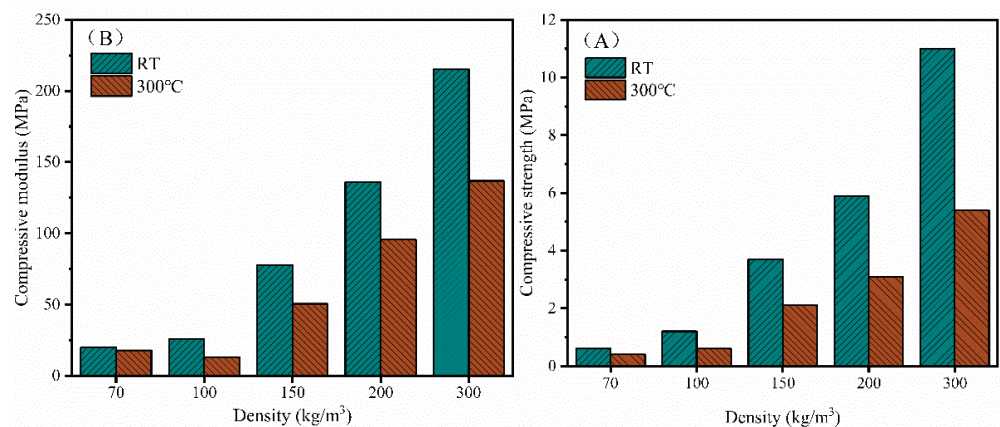


Figure 12. Compressive properties of the PI foams with different densities both at room temperature (RT) and 300 °C: (A) compressive strength and (B) compressive modulus.

The compression creep properties of the rigid PI foams with different densities are shown in Figure 13. The compression creep deformation decreased sharply with the increasing density. For instance, the creep deformation was 1.6% for a PI foam with 250 kg/m³ and 0.7% with a density of 300 kg/m³ after thermal aging at 320 °C/0.4 MPa for 2 h, compared with 11% with a density of 70 kg/m³. To ensure the stability of the sandwich composite material performance, the compression creep deformation of the foam core material should be lower than 2%. Hence, PI foams with a density of ≥ 250 kg/m³ are suitable as the foam core materials of carbon fiber reinforced polyimide sandwich composites processed at 320 °C.

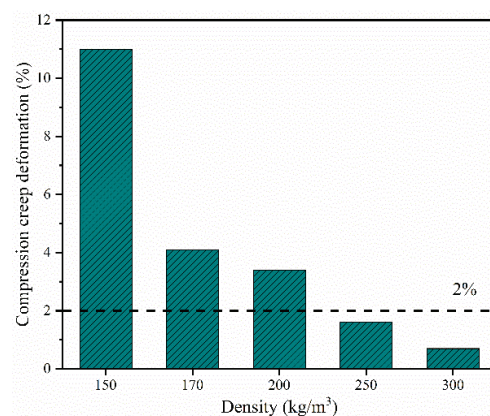


Figure 13. Compression creep deformation of the rigid PI foams with different densities after thermal aging at 320 °C/0.4 MPa for 2 h.

Table 5 compares the combined properties of PIF-2 in this work with those of other PI foams reported in the literature. PIF-2 shows the most optimally combined properties, including higher Tg values, higher closed-cell rates, and excellent mechanical properties. For instance, PIF-2 has a Tg of 395 °C, 21 °C higher than that of α -BPDA-PDA (374 °C) [31], 31 °C higher than that of α -BPDA-4,4'-ODA (364 °C) [27], 50 °C higher than that of BTDA-4,4'-ODA/BIA (345 °C) [28], and 89 °C higher than that of ODPDA-4,4'-ODA/BIA (306 °C) [32], respectively. PIF-2 also has a closed-cell rate of $\geq 91\%$, higher than those reported for other PI foams ($\leq 89\%$). In addition, when the density is similar, the compression performance of PIF-2 is better than for most other PI foams, such as BTDA-MDA/BDM [25], α -BPDA-3,4'-ODA [27], and α -BPDA-4,4'-ODA [27].

Table 5. Performance comparison of different PI foams.

PI Foams	Density (kg/m ³)	Closed-Cell Rate (%)	Tg (°C)	Compressive Strength (MPa)	Compressive Modulus (MPa)
PIF-2 (this work)	100	91	395	1.10	25.7
α -BPDA-PDA/BIA	150	95	395	3.70	77.6
α -BPDA-PDA [27]	100	89	374	1.34	37.1
α -BPDA-3,4'-ODA [27]	100	82	318	0.96	21.1
α -BPDA-4,4'-ODA [27]	100	86	364	0.70	16.3
BTDA-4,4'-ODA [15]	32	32	300	0.30	11.03
ODPA-3,4'-ODA [15]	80	-	237	0.84	6.13
	32	32	237	0.19	3.89
BTDA-MDA/BDM [25]	101	-	285	0.86	10.79
BTDA-4,4'-ODA/BIA [28]	243	-	345	7.45 ^a	23.8 ^a
ODPA-4,4'-ODA/BIA [31]	54	-	306	0.71	-
BTDA-4,4'-ODA/DAPBO [32]	77	-	368	1.03	-

Compressive properties were tested at 10% strain. ^a These compressive properties were measured at 15% strain. Abbreviations: ODPDA, 4,4'-oxydiphthalic anhydride; 3,4'-ODA, 3,4'-oxydianiline; 4,4'-ODA, 4,4'-oxydianiline; BTDA, 3,3',4,4'-benzophenonetetracarboxylic dianhydride; MDA, 4,4'-diaminodiphenyl methane; BDM, 4,4'-bismaleimidediphenylmethane; PDA, p-phenylenediamine; α -BPDA, 2,3,3',4'-biphenyl tetracarboxylic dianhydride; BIA, 2-(4-aminophenyl)-5-aminobenzimidazole; m-PDA, m-phenylenediamine; DAPBO, 2-(4-aminophenyl)-5-aminobenzoxazole.

4. Conclusions

In our study, rigid PI foams with different densities were prepared by thermal foaming of a nadimide end-capped polyimide precursor with an α -BPDA-PDA/BIA structure. The molar ratio of BIA/PDA and the M_w of the precursor were found to be two effective factors regulating the performance of PI foams. The prepared PI foams showed excellent combined properties, in which the initial thermal decomposition temperature was ≥ 490 °C and the Tg was 395.0 °C. PIF-2-1500 (300 kg/m³) showed outstanding mechanical properties with a compressive strength of 11 MPa and a compressive modulus of 215 MPa. Moreover, the foams with a density of ≥ 250 kg/m³ were suitable as foam core materials of carbon fiber reinforced polyimide sandwich composites co-cured at 320 °C/0.4 MPa.

Author Contributions: Conceptualization, S.Y.; data curation, Z.W.; funding acquisition, S.Y. and A.H.; resources, K.L. and Z.W.; project administration, K.L. and Z.W.; visualization, K.L. and Y.S.; formal analysis, Z.W. and Y.S.; investigation, Y.S.; methodology, S.Y., K.L. and A.H.; writing—original draft, Y.S.; writing—review and editing, S.Y. and A.H. All authors have read and agreed to the published version of the manuscript.

Funding: This research was funded by the National Natural Science Foundation of China, grant number 51803222.

Institutional Review Board Statement: Not applicable.

Informed Consent Statement: Not applicable.

Data Availability Statement: The data presented in this study are available on request from the corresponding author.

Conflicts of Interest: The authors declare no conflict of interest.



References

- Zhai, W.; Feng, W.; Ling, J.; Zheng, W. Fabrication of Lightweight Microcellular Polyimide Foams with Three-Dimensional Shape by CO₂ Foaming and Compression Molding. *Ind. Eng. Chem. Res. (ACS)* **2012**, *51*, 12827–12834. [CrossRef]
- Edward, A.L.; Paul, W.W. Cellular Polyimide Product. U.S. Patent 3310506, 21 March 1967.
- Caps, R.; Heinemann, U.; Fricke, J.; Keller, K. Thermal conductivity of polyimide foams. *Int. J. Heat Mass Transf.* **1997**, *40*, 269–280. [CrossRef]
- Cook, B.A.; Yudin, V.E.; Otaigbe, J.U. Thermal properties of polyimide foam composites. *J. Mater. Sci. Lett.* **2000**, *19*, 1971–1973. [CrossRef]
- Hower, R.T.; Hoang, S.V. Polyimide Foam-Containing Radomes. U.S. Patent 5662293, 2 September 1997.
- Gouzman, I.; Grossman, E.; Verker, R.; Atar, N.; Bolker, A.; Eliaz, N. Advances in Polyimide—Based Materials for Space Applications. *Adv. Mater.* **2019**, *31*, 1807738. [CrossRef] [PubMed]
- Indyke, D.M. Polyimide Foams and Their Production. U.S. Patent 4952611, 28 August 1990.
- Yang, J.Y.; Ye, Y.S.; Li, X.P.; Lu, X.Z.; Chen, R.J. Flexible, conductive, and highly pressure-sensitive graphene-polyimide foam for pressure sensor application. *Compos. Sci. Technol.* **2018**, *164*, 187–194. [CrossRef]
- Weiser, E.S.; Grimsley, B.W.; Pipes, R.B.; Williams, M.K. *Polyimide Foams from Friable Balloons*; Society for the Advancement of Material and Process Engineering Conference; SAMPE: Long Beach, CA, USA, 2002.
- Weiser, E.S.; Baillif, F.F.; Grimsley, B.W.; Marchello, J.M. High temperature structural foam. In Proceedings of the 43rd International SAMPE Symposium, Hampton, VA, USA, 31 May 1998; pp. 730–744.
- McConnell, V.P. NASA gets hands-on with X-33 design. *High Perf. Comp.* **1997**, *5*, 56–58.
- Fisher, K. Resin flow control is the key to RTM success. *High Perf. Comp.* **1997**, *5*, 34–38.
- Robert, H.W. Forming a Foamed Polyimide Article. U.S. Patent 3249561 A, 3 May 1966.
- Zhan, M.S.; Wang, K. *Polyimide Foam Materials*; National Defense Industry Press: Beijing, China, 2018; p. 5.
- Weiser, E.S.; Johnson, T.F.; St Clair, T.L.; Echigo, Y.; Kaneshiro, H.; Grimsley, B.W. Polyimide foams for aerospace vehicles. *High Perform. Polym.* **2000**, *12*, 1–12. [CrossRef]
- Li, J.W.; Zhang, G.C.; Li, J.T.; Zhou, L.S.; Jing, Z.X.; Ma, Z.L. Preparation and properties of polyimide/chopped carbon fiber composite foams. *Polym. Adv. Technol.* **2017**, *28*, 28–34. [CrossRef]
- Weng, L.; Wang, T.; Ju, P.H.; Liu, L.Z. Preparation and properties of polyimide/Fe₃O₄ composite foams. *Pigm Resin Technol.* **2018**, *47*, 173–179. [CrossRef]
- Ma, J.J.; Wang, K.; Zhan, M.S. A comparative study of structure and electromagnetic interference shielding performance for silver nanostructure hybrid polyimide foams. *RSC Adv.* **2015**, *5*, 65283–65296. [CrossRef]
- Pan, L.Y.; Zhan, M.S.; Wang, K. High-Temperature-Resistant Polyimide/Montmorillonite Nanocomposite Foams by Solid Blending. *Polym. Eng. Sci.* **2011**, *51*, 1397–1403. [CrossRef]
- Yan, L.; Fu, L.W.; Chen, Y.J.; Tian, H.F.; Xiang, A.M.; Rajulu, A.V. Improved thermal stability and flame resistance of flexible polyimide foams by vermiculite reinforcement. *J. Appl. Polym. Sci.* **2017**, *134*. [CrossRef]
- Xu, L.; Jiang, S.; Li, B.; Hou, W.; Li, G.; Memon, M.A.; Huang, Y.; Geng, J. Graphene Oxide: A Versatile Agent for Polyimide Foams with Improved Foaming Capability and Enhanced Flexibility. *ACS Chem. Mater.* **2015**, *27*, 4358–4367. [CrossRef]
- Qi, K.L.; Zhang, G.C. Effect of Organoclay on the Morphology, Mechanical, and Thermal Properties of Polyimide/Organoclay Nanocomposite Foams. *Polym. Compos.* **2014**, *35*, 2311–2317. [CrossRef]
- Chu, H.J.; Zhu, B.K.; Xu, Y.Y. Polyimide foams with ultralow dielectric constants. *J. Appl. Polym. Sci.* **2006**, *102*, 1734–1740. [CrossRef]
- Chu, H.J.; Zhu, B.K.; Xu, Y.Y. Preparation and dielectric properties of polyimide foams containing crosslinked structures. *Polym. Adv. Technol.* **2006**, *17*, 366–371. [CrossRef]
- Ou, A.; Huang, Z.; Qin, R.; Chen, X.; Li, Y.; Liu, Y.; Liu, X.; Wang, X. Preparation of Thermosetting/Thermoplastic Polyimide Foam with Pleated Cellular Structure via In Situ Simultaneous Orthogonal Polymerization. *ACS Appl. Polym. Mater.* **2019**, *1*, 2430–2440. [CrossRef]
- Wang, L.L.; Hu, A.J.; Fan, L.; Yang, S.Y. Structures and properties of closed-cell polyimide rigid foams. *J. Appl. Polym. Sci.* **2013**, *130*, 3282–3291. [CrossRef]
- Wang, L.L.; Hu, A.J.; Fan, L.; Yang, S.Y. Approach to produce rigid closed-cell polyimide foams. *High Perform. Polym.* **2013**, *25*, 956–965. [CrossRef]
- Li, J.; Yu, N.; Ding, Y.; Xu, T.; Zhang, G.; Jing, Z.; Shi, X. Fabrication of rigid polyimide foams with overall enhancement of thermal and mechanical properties. *J. Cell. Plast.* **2020**, *57*, 717–731. [CrossRef]
- Li, J.; Yu, N.; Jing, Z.; He, X.; Shi, X.; Zhang, G. Fabrication of rigid polyimide foams via thermal foaming of nadimide-end-capped polyester-amine precursor. *Polym. Bull.* **2020**, *77*, 5899–5912. [CrossRef]
- Wang, X.; Ou, P.A. Polyimide Foam and Preparation Method and Application Thereof. CN Patent 109880096 A, 21 April 2019.
- Li, J.W.; Zhang, G.C.; Yao, Y.; Jing, Z.X.; Zhou, L.S.; Ma, Z.L. Synthesis and properties of polyimide foams containing benzimidazole units. *RSC Adv.* **2016**, *6*, 60094–60100. [CrossRef]

32. Liu, J.N.; Wu, D.Y.; Liang, W.H.; Cao, J.H. Effect of DAPBO segment on the structure and performance enhancement of powder foamed BTDA—ODA polyimide. *J. Appl. Polym. Sci.* **2021**, *138*, 49911. [CrossRef]
33. Dong, J.; Yin, C.; Zhang, Z.; Wang, X.; Li, H.; Zhang, Q. Hydrogen—bonding interactions and molecular packing in polyimide fibers containing benzimidazole units. *Macromol. Mater. Eng.* **2014**, *299*, 1170–1179. [CrossRef]
34. Ahn, T.-K.; Kim, M.; Choe, S. Hydrogen-bonding strength in the blends of polybenzimidazole with BTDA-and DSDA-based polyimides. *Macromolecules* **1997**, *30*, 3369–3374. [CrossRef]
35. Dynes, P.; Panos, R.; Hamermesh, C. Investigation of the crosslinking efficiency of some additional curing polyimides. *J. Appl. Polym. Sci.* **1980**, *25*, 1059–1070. [CrossRef]
36. Wilson, D. PMR—15 processing, properties and problems—A review. *Br. Polym. J.* **1988**, *20*, 405–416. [CrossRef]
37. Luo, L.; Yao, J.; Wang, X.; Li, K.; Huang, J.; Li, B.; Wang, H.; Liu, X. The evolution of macromolecular packing and sudden crystallization in rigid-rod polyimide via effect of multiple H-bonding on charge transfer (CT) interactions. *Polymer* **2014**, *55*, 4258–4269. [CrossRef]
38. Williams, M.K.; Weiser, E.S.; Fesmire, J.E.; Grimsley, B.W.; Smith, T.M.; Brenner, J.R.; Nelson, G.L. Effects of cell structure and density on the properties of high performance polyimide foams. *Polym. Adv. Technol.* **2005**, *16*, 167–174. [CrossRef]
39. Swellam, M.; Yi, S.; Ahmad, M.F.; Huber, L.M. Mechanical properties of cellular materials. I. Linear analysis of hexagonal honeycombs. *J. Appl. Polym. Sci.* **1997**, *63*, 383–393. [CrossRef]

Article

Effect of Ultra-High-Molecular-Weight Molecular Chains on the Morphology, Crystallization, and Mechanical Properties of Polypropylene

Takumitsu Kida ^{1,*}, Takeyoshi Kimura ¹, Ayaka Eno ¹, Khunanya Janchai ^{1,2}, Masayuki Yamaguchi ¹, Yasuhiko Otsuki ³, Tokutaro Kimura ³, Tomoaki Mizukawa ³, Tomoya Murakami ³, Kazuki Hato ³ and Tomoya Okawa ³

¹ Japan Advanced Institute of Science and Technology, School of Materials Science, 1-1 Asahidai, Nomi 9231292, Japan; s2120012@jaist.ac.jp (T.K.); s2010016@jaist.ac.jp (A.E.); s1910444@jaist.ac.jp (K.J.); m_yama@jaist.ac.jp (M.Y.)

² Petrochemical and Polymer Science, Faculty of Science, Chulalongkorn University, Pathumwan, Bangkok 10330, Thailand

³ Packaging and Industrial Materials Laboratory, Prime Polymer Co., Ltd., 3 Chigusa-Kaigan, Ichihara 2990108, Japan; yasuhiko.otsuki@primepolymer.co.jp (Y.O.); tokutaro.kimura@primepolymer.co.jp (T.K.); tomoaki.mizukawa@primepolymer.co.jp (T.M.); tomoya.murakami@primepolymer.co.jp (T.M.); kazuki.hato@primepolymer.co.jp (K.H.); tomoya.okawa@primepolymer.co.jp (T.O.)

* Correspondence: tkida@jaist.ac.jp; Tel.: +81-761-51-1626; Fax: +81-761-51-1149

Citation: Kida, T.; Kimura, T.; Eno, A.; Janchai, K.; Yamaguchi, M.; Otsuki, Y.; Kimura, T.; Mizukawa, T.; Murakami, T.; Hato, K.; et al. Effect of Ultra-High-Molecular-Weight Molecular Chains on the Morphology, Crystallization, and Mechanical Properties of Polypropylene. *Polymers* **2021**, *13*, 4222. <https://doi.org/10.3390/polym13234222>

Academic Editors: Somen K. Bhudolia and Sunil Chandrakant Joshi

Received: 12 November 2021
Accepted: 27 November 2021
Published: 1 December 2021

Publisher's Note: MDPI stays neutral with regard to jurisdictional claims in published maps and institutional affiliations.



Copyright: © 2021 by the authors. Licensee MDPI, Basel, Switzerland. This article is an open access article distributed under the terms and conditions of the Creative Commons Attribution (CC BY) license (<https://creativecommons.org/licenses/by/4.0/>).

Abstract: The effects of the ultra-high-molecular-weight (UHMW) component of polypropylene (PP) on its rheological properties, crystallization behavior, and solid-state mechanical properties were investigated using various measurement techniques. The terminal relaxation time—determined by measuring the linear viscoelasticity—was increased by adding the UHMW component. The increase in the melt elasticity produced by adding the UHMW component was observed by measuring the steady-state shear flow, although the shear viscosity was not greatly affected. Owing to the long characteristic time of the Rouse relaxation of the UHMW component, PP with the UHMW component formed highly oriented structures through a shear-induced crystallization process. The addition of the UHMW component enhanced the orientation and regularity of crystalline structure for extruded films. Therefore, the Young's modulus, yield stress, and strength were higher in the PP film containing the UHMW component than in one without the UHMW component, irrespective of the direction of tensile deformation.

Keywords: ultra-high molecular weight component; rheological property; crystallization behavior; mechanical property; polypropylene

1. Introduction

Molecular weight and molecular weight distribution strongly affect various properties of polymeric materials [1] as well as branch structure [2,3] and the addition of nanofillers [4–7]. The physical and mechanical properties of polymeric materials such as viscosity, diffusion coefficient, drawability, and toughness are strongly influenced by the molecular weight and its distribution [8–11]. In particular, the processability and strength of a polymer are drastically improved by the addition of an ultra-high-molecular-weight (UHMW) component compared with samples with a monodispersed molecular weight distribution. Consequently, the influences of the UHMW component on the physical and mechanical properties of polymeric materials have been studied intensively [12–16].

The addition of UHMW chains significantly enhances strain hardening during the elongational flow process in various polymer melts [17–20]. The relaxation time of the Rouse mode (τ_R), which corresponds to the characteristic time for chain contraction,

strongly depends on the molecular weight described as $\tau_R \cong M^2$. Therefore, the stretching of the UHMW chains cannot be relaxed during elongational flow. This results in significant strain hardening. Moreover, it is well known that UHMW chains form the “shish” of a shish–kebab structure. The shish–kebab structure is composed of extended-chain crystals (shish) and folded-chain crystals (kebab) grown from the shish. This shish–kebab structure often appears by flow-induced crystallization, because the stretching of the UHMW chains remains during the crystallization process [21,22]. The formation of the shish structure by UHMW chains has been observed by small-angle neutron scattering in blends of low-molecular-weight hydrogenated polyethylene and UHMW deuterated polyethylene [23,24]. Because the formation of the shish–kebab structure results in significant improvements in the modulus and strength [25,26], the addition of UHMW chains is one of the most effective methods of modifying the mechanical properties of semi-crystalline polymers. However, the effects of UHMW chains on the morphology, crystallization behavior, and mechanical properties of such polymers have been investigated separately. In particular, the effects of the addition of a UHMW component on the structure–mechanical properties relationship of the products obtained by a conventional processing operation such as film formation have not yet been elucidated.

In the present study, the effects of a UHMW component on the rheological properties, crystallization behavior, and mechanical properties of PP samples were systematically investigated. The Rouse time of UHMW chains is considerably longer than the characteristic time of the flow process, resulting in the enhancement of the shish formation and the promotion of a highly oriented structure. Included herein is a discussion of the effects of a UHMW component on the structure and mechanical properties of a solid-state PP film based on its rheological properties and crystallization behavior.

2. Experimental

2.1. Materials

A commercially available low-molecular-weight PP (LPP) having an unimodal molecular weight distribution ($M_n = 0.43 \times 10^5$, $M_w = 3.1 \times 10^5$, and $M_z = 1.3 \times 10^6$) with a melt flow rate (MFR) at 230 °C under 2.16 kgf of 7 g/10 min, and high-molecular-weight PP (HPP) having a bimodal molecular weight distribution ($M_n = 0.33 \times 10^5$, $M_w = 7.2 \times 10^5$, and $M_z = 7.1 \times 10^6$) with an MFR of 3 g/10 min, were acquired from Prime Polymer Co., Ltd. It should be noted that the melting temperatures of LPP and HPP were 161 and 163 °C, respectively, suggesting that the isotacticity of the PP samples were almost the same. LPP and HPP were blended with a weight fraction of HPP of 15 wt% using a 50 mm single-screw extruder at 220 °C. All samples included phosphate and hindered phenol compounds as antioxidants. The MFR of the blend was 6.3 g/10 min.

LPP and LPP/HPP films (approximately 25 μm thick) were prepared using a 75 mm single-screw extruder with a T-shaped die at 250 °C. The screw torques were 37% and 36% of the maximum for LPP and LPP/HPP, respectively. The die width was 600 mm, and the die gap was 0.8 mm. The extruded film was stretched in the air gap (10 mm) at 150 m min^{-1} by winding rolls. The chill rolls were maintained at 30 °C. The shear rate on the die wall ($\dot{\gamma}_{\text{wa}}$), calculated using the following equation, was 590 s^{-1} :

$$\dot{\gamma}_{\text{wa}} = \frac{6Q}{H^2W}, \quad (1)$$

where Q is the volume flow rate, H is the die gap, and W is the width of the die.

The film density (ρ) values of LPP and LPP/HPP, which were measured using a density-gradient column at 23 °C, were 892 and 900 kg/m^3 , respectively.

Pellets of LPP and LPP/HPP were melt-pressed at 180 °C and 15 MPa for 5 min, then quenched at 25 °C to prepare sample sheets (approximately 0.8 mm thick) for melt-rheology measurements.

2.2. Measurements

The melt-state viscoelasticity values were measured using a stress-control rheometer (AR2000ex, TA Instruments, Inc., New Castle, DE, USA) equipped with a cone-and-plate system with a diameter of 25 mm and a cone angle of 4°. The frequency sweep was performed from 0.01 to 628.3 rad s⁻¹ at 180, 200, and 230 °C under a nitrogen atmosphere. The storage and loss moduli (G' and G'' , respectively) measured at various temperatures were horizontally shifted to construct the master curves using time–temperature superposition. The reference temperature (T_r) was set to 180 °C, which is above the melting temperature of PP samples. The shear stress and primary normal stress difference under a steady-state shear flow were also measured at different shear rates under the same conditions at 190 °C.

The transient elongational viscosity was measured using the stress-control rheometer with an extensional viscosity accessory (SER2-G, Xpansion Instruments, Tallmadge, OH, USA) under constant Hencky strain rates from 0.1 to 3.2 s⁻¹ at 190 °C. Rectangular specimens (10 mm wide, 15 mm length, and 0.8 mm thick) prepared by compression molding were used for the measurements.

Capillary extrusion was performed using a capillary rheometer (140 SAS-2002, Yasuda Seiki Seisakusho, Ltd., Nishinomiya, Japan) at 190 °C to determine the steady-state shear viscosity. Circular-shaped dies with length (L)-to-diameter (D) ratios of 40/1 and 10/1 were used. The flow curve during the capillary extrusion was calculated using Bagley–Rabinowitsch corrections. The drawdown force defined as the force required to stretch a molten strand extrudate from a capillary rheometer [27] was evaluated using a tension detector (DT-413 G-04-3, Nidec-Shimpo, Kyoto, Japan) and a set of rotating rolls at 190 °C with draw ratios of 10 and 30.

The crystallization behaviors of the samples with/without shear history were evaluated using a home-made machine comprising a polarized microscope (DM2700P, Leica Microsystems GmbH, Wetzlar, Germany), a shear stage with a temperature controller (CSS450, Linkam Scientific Instruments, Tadworth, Surrey, UK), and a photodetector (PM16-121, Thorlabs Inc., Newton, NJ, USA). A beam of light, which passed through the polarizer, the shear stage, and the analyzer, was directed into the photo detector, as shown in Figure 1. Parallel plates made of quartz were set in the stage, in which a circular window (2 mm in diameter) was provided to transmit the light. The center of this window was 10 mm from the center of the plate. A shear rate of 100 s⁻¹, which was calculated from the rotation speed of the bottom plate and the gap between the plates, was applied. The angle between the flow direction in the plates and the transmission axis of the polarizer was $\pi/4$. After passing through the analyzer at the crossed polar configuration, the light intensity was measured by the photo detector mounted in one of the eyepieces of the polarized microscope. A camera was set at another eyepiece to observe the morphology of the samples. The light transmittance (T) was calculated as follows:

$$T = \frac{I - I_{\perp}}{I_{\parallel} - I_{\perp}} \quad (2)$$

where I_{\perp} and I_{\parallel} are the light intensities without a sample under crossed polars and parallel polars, and I is the light intensity passing through the sample under crossed polars.

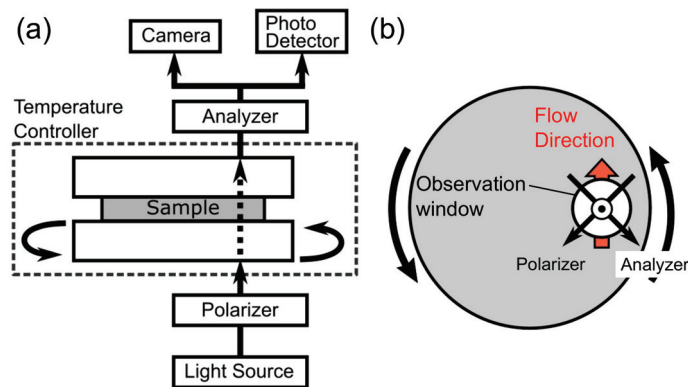


Figure 1. Schematics of the microscopic system combined with the shear stage viewed from (a) the side and (b) the top.

The melting and crystallization temperatures were evaluated using a differential scanning calorimetry (DSC) system (DSC8500, PerkinElmer Co., Ltd., Waltham, MA, USA) under a nitrogen atmosphere. A 5 mg piece of each sample film was heated from 25 to 230 °C at a rate of 10 °C min⁻¹ and was maintained at the isothermal temperature for 10 min. The sample was then cooled to 25 °C at a rate of 30 °C min⁻¹. The crystallinity was calculated using the following equation:

$$\chi_{\text{DSC}} = \frac{\Delta H_f}{\Delta H_f^0}, \quad (3)$$

where ΔH_f is the fusion enthalpy of the sample and ΔH_f^0 is the fusion enthalpy of a perfect sample of crystalline iPP (209 J g⁻¹) [28]. It should be noted that the DSC curves were measured in the first heating and cooling processes to evaluate the influences of the morphology of film samples on the melting and crystallization behaviors. The rigid amorphous fraction (χ_{RA}) was evaluated by temperature-modulated DSC measurements (step-scan mode) using the DSC8500 system. The step-scan procedure consisted of heating steps of 2 °C at 40 °C min⁻¹ and isothermal steps of 0.4 min. The heat capacity during the heating process was obtained using step-scan software. The specific heat capacity increment at T_g (Δc_p) was estimated from the reversible specific heat capacity curve obtained from the step-scan measurement. χ_{RA} was calculated using the following equation [29,30]:

$$\chi_{\text{RA}} = 1 - \chi_{\text{DSC}} - \frac{\Delta c_p}{\Delta c_{p,a}}, \quad (4)$$

where $\Delta c_{p,a}$ is the specific heat capacity increment at T_g of the fully amorphous iPP. The value of $\Delta c_{p,a}$ was taken from the ATHAS database and from previous studies [31,32]. It should be noted that the value of χ_{DSC} obtained from the step-scan measurement was almost the same as that from the conventional measurement using Equation (3).

Two-dimensional wide-angle X-ray diffraction (WAXD) and small-angle X-ray scattering (SAXS) patterns of the sample films were measured using an XRD machine (SmartLab, Rigaku Corp., Akishima, Japan). A graphite-monochromatized Cu K α radiation beam (45 kV and 200 mA) was directed into the sample film, and the diffraction patterns were collected with a detector (HyPix-400, Rigaku, Corp., Akishima, Japan). The exposure time for both the WAXD and SAXS measurements was 15 min. The crystallinity of each film was calculated using the following equation:

$$\chi_{\text{WAXD}} = \frac{\sum_i I_{ci}}{\sum_i I_{ci} + I_a}, \quad (5)$$

where I_{ci} and I_a are the integrated areas of the crystalline and amorphous peaks, respectively. The integrated area of each peak was obtained by fitting the sum of the Gaussian functions to the experimental integrated intensity profile. The Hermans' orientation function (f_{WAXD}) defined by the following equation was used to evaluate the orientation of the crystalline structure:

$$f_{WAXD} = \frac{3\langle \cos^2 \varphi \rangle - 1}{2}, \quad (6)$$

where φ is the angle between the crystalline axis and the machine, i.e., the flow direction (MD). Based on the Wilchinsky method [33], $\langle \cos^2 \varphi \rangle$ is described as:

$$\langle \cos^2 \varphi \rangle = 1 - 1.090 \langle \cos^2 \phi_{110} \rangle - 0.901 \langle \cos^2 \phi_{040} \rangle, \quad (7)$$

where $\langle \cos^2 \phi_{110} \rangle$ and $\langle \cos^2 \phi_{040} \rangle$ are calculated using the following equation: [34,35]

$$\langle \cos^2 \phi_{hkl} \rangle = \frac{\int_0^\pi I(\phi_{hkl}) \cos^2 \phi_{hkl} \sin \phi_{hkl} d\phi_{hkl}}{\int_0^\pi I(\phi_{hkl}) \sin \phi_{hkl} d\phi_{hkl}}. \quad (8)$$

Here, $I(\phi_{hkl})$ is the intensity distribution of the (hkl) plane at the azimuthal angle ϕ .

The polarized infrared (IR) spectrum of each film was measured using a Fourier-transform IR (FT-IR) spectrometer (Spectrum100, PerkinElmer Co., Ltd., Waltham, MA, USA) at 25 °C. The polarization direction of the incident laser was tuned to parallel and perpendicular to the MD using a polarizer. Each IR spectrum was accumulated 16 times with an exposure time of 2 s. The integrated intensity of each IR band was calculated by fitting the sum of the Voigt functions using Igor Pro software. The Hermans' orientation functions of the crystalline and amorphous chains were calculated using the following equation [36,37]:

$$f_{IR} = \frac{2}{3} \frac{D - 1}{\langle \cos^2 \alpha \rangle - 1} \frac{D - 1}{D + 2}, \quad (9)$$

where α is the angle between the molecular chain axis and the transition moment of each molecular vibration, and D is the IR dichroic ratio defined as $D = A_{||} / A_{\perp}$, where $A_{||}$ is the IR absorbance parallel to the stretching direction and A_{\perp} is the IR absorbance perpendicular to the stretching direction. In the present study, IR bands at 841 and 973 cm^{-1} assigned to the crystalline helical chains and the amorphous chains, respectively, were used to evaluate the orientation functions of the crystalline and amorphous chains ($f_{IR,c}$ and $f_{IR,a}$). It should be noted that the values of α of these IR bands are known to be 0° and 7.31° for 841 and 973 cm^{-1} , respectively [37,38]. The crystallinity was calculated using the following equation: [39]

$$\chi_{IR} = 0.614 \frac{A_{998}}{A_{973}}, \quad (10)$$

where A_{998} and A_{973} are the integrated intensities of the IR bands at 998 and 973 cm^{-1} , respectively.

Dynamic mechanical analysis (DMA) was performed using a DMA machine (Rheogel-E4000, UBM Co., Ltd., Muko, Japan) to evaluate the temperature dependences of the loss and storage moduli (E' and E'') in the tensile mode. The measurements were performed at 10 Hz in the temperature range from −80 to 160 °C at a constant heating rate of 2 °C min^{-1} . Rectangular specimens (width 4 mm and length 10 mm), which were cut from the films, were used for the measurements. Oscillatory strain was applied parallel and perpendicular to the MD and the transverse direction (TD) of the films to evaluate mechanical anisotropy.

Tensile tests were performed using a tensile machine (EZ-LX HS, Shimadzu Corp., Kyoto, Japan) at a constant crosshead speed of 10 mm min^{-1} at 25 °C to evaluate the stress–strain behavior of the films. Dumbbell-shaped specimens (gauge length 10 mm, width 4 mm, and thickness approximately 25 μm) were cut from the films along the MD and TD and used for the measurements. Drawn specimens were prepared by the following

procedure: each film specimen was drawn up to a strain of 1.5 and subjected to stress relaxation for 15 min; the drawn specimen was then removed from the tensile machine and kept for 1 day.

3. Results and Discussion

3.1. Rheological Properties

Figure 2 shows the angular frequency dependences of G' and G'' of LPP and LPP/HPP. Both G' and G'' decreased with decreasing the angular frequency and showed a cross point. The cross point for LPP/HPP was located at a lower frequency than that for LPP, suggesting that LPP/HPP has a longer relaxation time than LPP. Moreover, the modulus at the cross point for LPP/HPP was higher than for LPP. This is reasonable because LPP/HPP has a broad distribution of relaxation time. The slopes of G' and G'' in the terminal relaxation region were almost 1 and 2, respectively. This is typical viscoelastic behavior of a simple polymer melt. However, the slopes of G' and G'' in the low-frequency region of LPP/HPP were lower than those of LPP with an intense fashion of G' . This result was due to the long terminal relaxation time ascribed to the UHMW component of HPP. The broadening of the terminal relaxation region is a well-known effect of a UHMW component on rheological behavior [18]. Furthermore, the shift factors of both samples were almost the same, indicating both samples show a similar flow activation energy ($\cong 45$ kJ/mol).

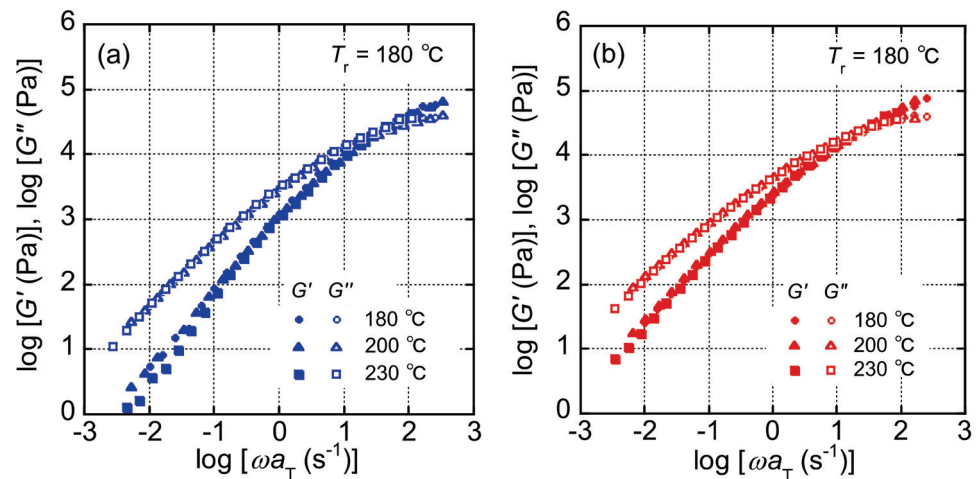


Figure 2. Angular–frequency dependences of the storage and loss moduli (G' and G'') of (a) LPP and (b) LPP/HPP (LPP is a unimodal PP and HPP is a bimodal PP). The reference temperature (T_r) was 180 °C.

The shear-rate ($\dot{\gamma}$) dependences of the shear stress (σ) and the primary normal stress difference (N) under steady-state shear flow are shown in Figure 3. Both σ and N increased with increasing $\dot{\gamma}$ for LPP and LPP/HPP. The values of σ were slightly higher for LPP/HPP than those for LPP in the low $\dot{\gamma}$ region, whereas the $\dot{\gamma}$ dependence of σ in the high $\dot{\gamma}$ region was almost the same for both PP samples. However, the values of N were higher for LPP/HPP than those for LPP over the whole $\dot{\gamma}$ region. This suggests that the increase in melt-state elasticity was caused by the addition of the UHMW component. These results corroborate those pertaining to linear viscoelasticity shown in Figure 2.

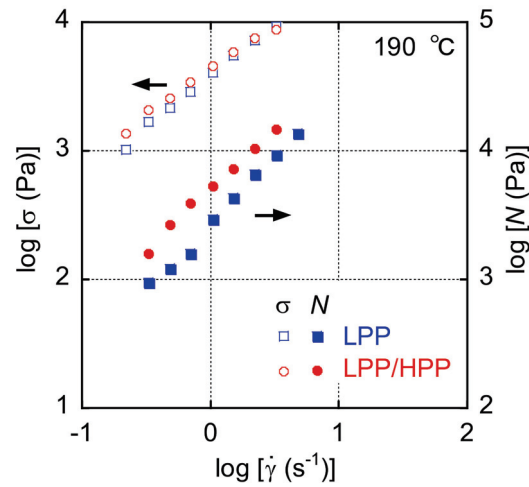


Figure 3. Shear-rate ($\dot{\gamma}$) dependences of the shear stress (σ) and the primary normal stress difference (N) of LPP and LPP/HPP at 190 °C (LPP is a unimodal PP and HPP is a bimodal PP).

Figure 4 shows the ratio of the diameter of the extruded strand (d) to the diameter of the die (D) plotted against the apparent shear rate on the wall ($\dot{\gamma}_{wa}$) when a die with a length of 40 mm was used. The d/D ratio increased monotonously as $\dot{\gamma}_{wa}$ increased in both samples, and the d/D ratio of LPP/HPP was obviously higher than that of LPP. This is attributed to the enhanced primary normal stress difference with a prolonged relaxation time.

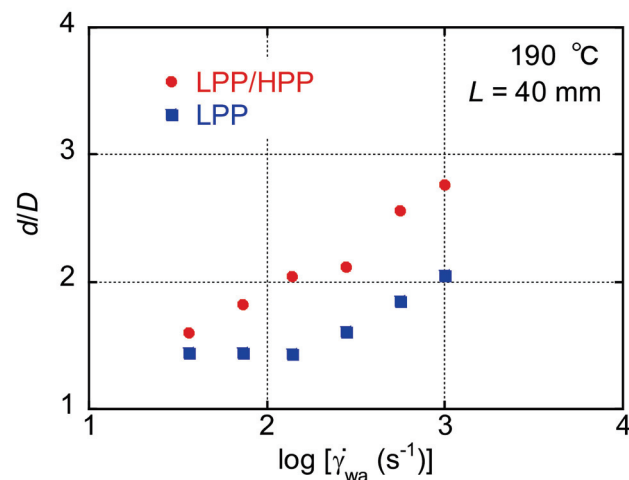


Figure 4. Ratio of the diameter of the extruded strand (d) and the die (D) plotted against the apparent wall shear rate ($\dot{\gamma}_{wa}$) during capillary extrusion.

The end-pressure drop (ΔP_e) at 190 °C evaluated using a Bagley plot is plotted against the apparent wall shear rate ($\dot{\gamma}_{wa}$) in Figure 5. ΔP_e increased with increasing $\dot{\gamma}_{wa}$, which is typical capillary extrusion behavior. Moreover, the ΔP_e value of LPP/HPP was higher than that of LPP in the $\dot{\gamma}_{wa}$ range, although σ was almost the same for both PPs, as shown in Figure 3. Considering that ΔP_e is determined by σ and N [40,41], this result is attributed to the enhancement of N by the addition of the UHMW component, as shown in Figure 3.

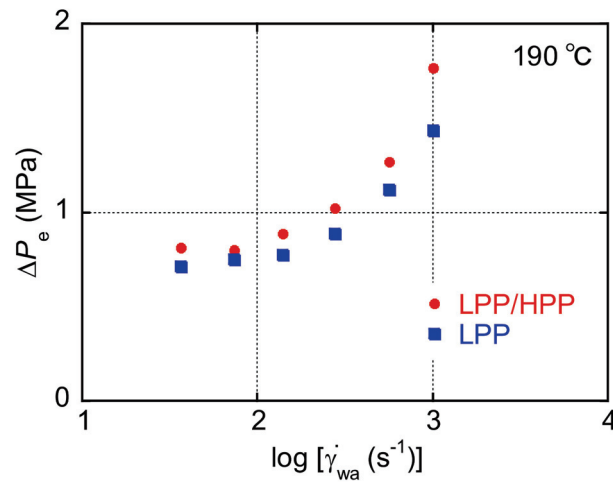


Figure 5. End-pressure drop (ΔP_e) for LPP and LPP/HPP plotted against the apparent wall shear rate ($\dot{\gamma}_{wa}$) at 190 °C (LPP is a unimodal PP and HPP is a bimodal PP).

The $\dot{\gamma}_w$ dependences of σ_w and η_w after Bagley–Rabinowitsch corrections are shown in Figure 6. Both σ_w and η_w showed almost the same $\dot{\gamma}$ dependence for LPP and LPP/HPP, and the values of σ_w for LPP/HPP were very close to those for LPP, corroborating the results for σ in the high shear-rate region during steady-state shear flow shown in Figure 3. This result corresponds to the extrusion torque during T-die extrusion; both PP samples showed the same torque values.

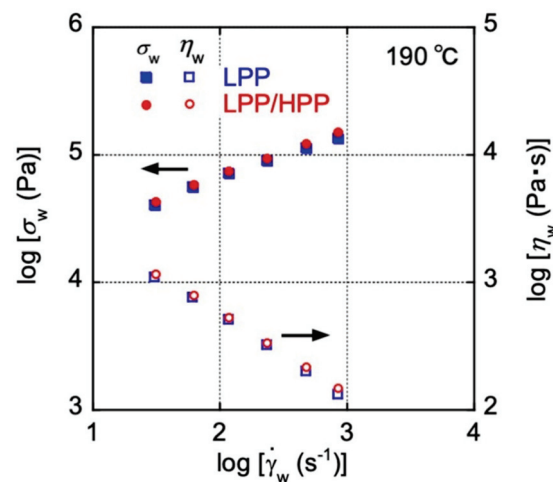


Figure 6. Steady-state shear stress (σ_w) and viscosity (η_w) plotted against the shear rate ($\dot{\gamma}_w$) during capillary extrusion at 190 °C for LPP and LPP/HPP (LPP is a unimodal PP and HPP is a bimodal PP).

The elongational viscosity growth curves at various strain rates under uniaxial elongational flow for both PP samples are shown in Figure 7. The solid line in Figure 7 represents $3\eta^+(t)$ calculated from G' and G'' shown in Figure 2 using the following equation [42,43]:

$$\eta^+(t) = t \left[G''(\omega) + 1.12G' \left(\frac{\omega}{2} \right) - 0.200G'(\omega) \right] \Big|_{\omega \rightarrow (1/t)} \quad (11)$$

The upward deviation of $\eta_E^+(t, \dot{\epsilon})$ from $3\eta^+(t)$ suggests the strain hardening. LPP showed almost no strain hardening during elongational flow because the flow curves were close to $3\eta^+(t)$ at all strain rates. On the other hand, LPP/HPP showed weak strain hardening at the strain rates from 0.4 to 3.2 s⁻¹, indicating that strain hardening was promoted by the stretching of the UHMW chains. The promotion of strain hardening by

the addition of UHMW chains has been reported for various polymeric materials [17–20,44]. It has been well known that the strain hardening is responsible for good processability at various processing operations. For example, the stability of tubular blown film is improved greatly, which makes it possible to produce a thin film [45,46].

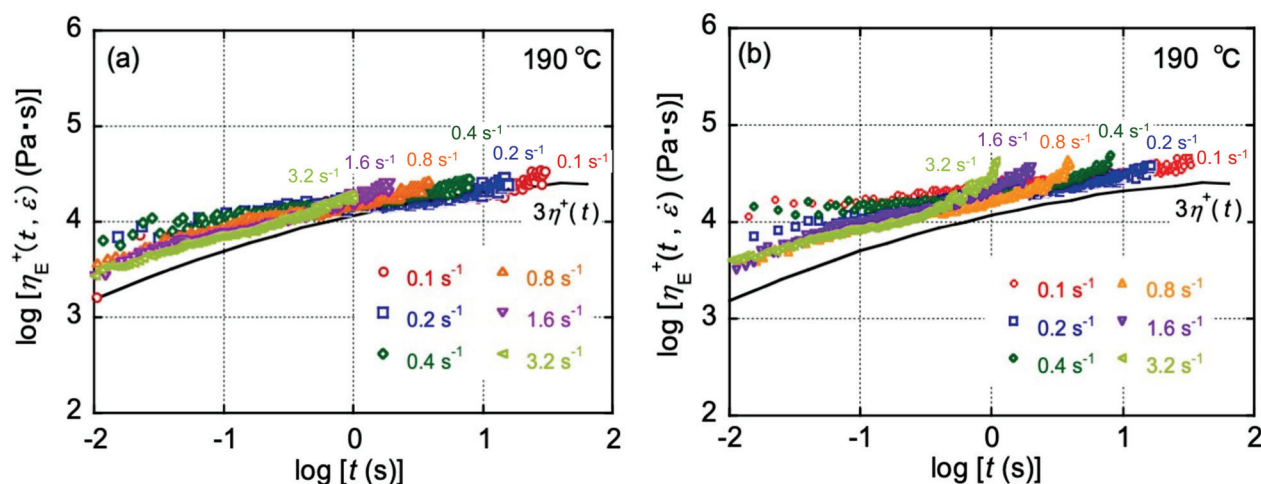


Figure 7. Transient uniaxial elongation viscosity ($\eta_E^+(t, \dot{\epsilon})$) at various Hencky strain rates ($\dot{\epsilon}$) at 190 °C for (a) LPP and (b) LPP/HPP (LPP is a unimodal PP and HPP is a bimodal PP). The solid line represents the calculated viscosity growth curve.

The values of the drawdown force during the capillary extrusion of both PP samples at draw ratios (DRs) of 10 and 30 are listed in Table 1. At both draw ratios, the values of the drawdown force were considerably higher for LPP/HPP than those for LPP. The markedly high drawdown force for LPP/HPP should be attributed to strain hardening during uniaxial elongation at the high strain rate, as shown in Figure 7, and/or the strain-induced crystallization of the UHMW chains [7,27].

Table 1. Drawdown force during the capillary extrusion of polypropylene (PP) samples at draw ratios (DRs) of 10 and 30.

Sample Code	Drawdown Force (mN)	
	DR = 10	DR = 30
LPP	56	70
LPP/HPP	86	96

3.2. Crystallization Behavior

The temperature dependence of light transmittance during non-isothermal crystallization without shear flow is shown in Figure 8. Each sample was initially heated to 230 °C for 10 min to erase its thermal history. The samples were then cooled at 30 °C min^{−1}, i.e., the same rate used for the DSC measurements. In each sample, the light intensity increased drastically at approximately 117 °C and reached an asymptotic value at below 107 °C, in good agreement with the DSC results discussed later, i.e., both PP samples had almost the same crystallization temperature at approximately 117 °C. Moreover, spherulites were observed in the polarized optical microscopy (POM) images of both PP samples at below 117 °C. These results are typical crystallization behavior for a semi-crystalline polymer in the absence of shear flow [47,48].

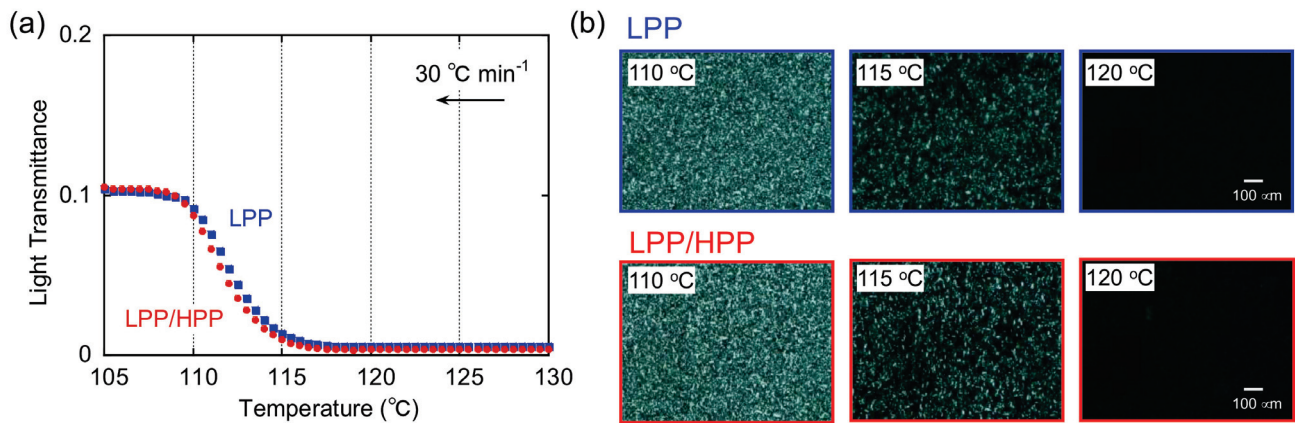


Figure 8. (a) Temperature dependence of light transmittance and (b) polarized optical microscopy (POM) images at 110, 115, and 120 °C during non-isothermal crystallization at 30 °C min⁻¹ in the absence of shear flow for both polypropylene (PP) samples.

Figure 9 shows the temperature dependence of light transmittance after exposure to shear flow during cooling from 230 to 160 °C. The shear rate was 100 s⁻¹. After the cessation of shear, the samples were cooled at the same rate. Therefore, the applied thermal history was the same as in Figure 8. Although it is not clear from the figure, light transmittance was unchanged at 160 °C, suggesting that flow-induced birefringence in the molten state was negligible. The onset crystallization temperature after the applied shear flow was obviously higher than that in the absence of shear for both PP samples, which is consistent with previous results of the flow-induced crystallization of PP [47]. Moreover, streak-like patterns caused by molecular orientation in the flow direction were observed in the POM images at 125 °C for both samples. These results indicate that the oriented molecular chains acted as nuclei for the formation of the shish-like structure, resulting in enhanced crystallization compared with crystallization in the absence of shear flow. When crystallization was almost completed (<115 °C), both highly oriented crystals and spherulites were observed in the POM image of LPP. However, highly oriented structure such as the shish-kebab structure was clearly observed in the LPP/HPP sample, owing to the strong orientation of the UHMW chains. The strong orientation of the molecular chains of LPP/HPP compared with those of LPP is consistent with the marked light transmittance below 115 °C for LPP/HPP. Reduced light scattering originating from the spherulite texture as well as a long correlation length resulted in high light transmittance.

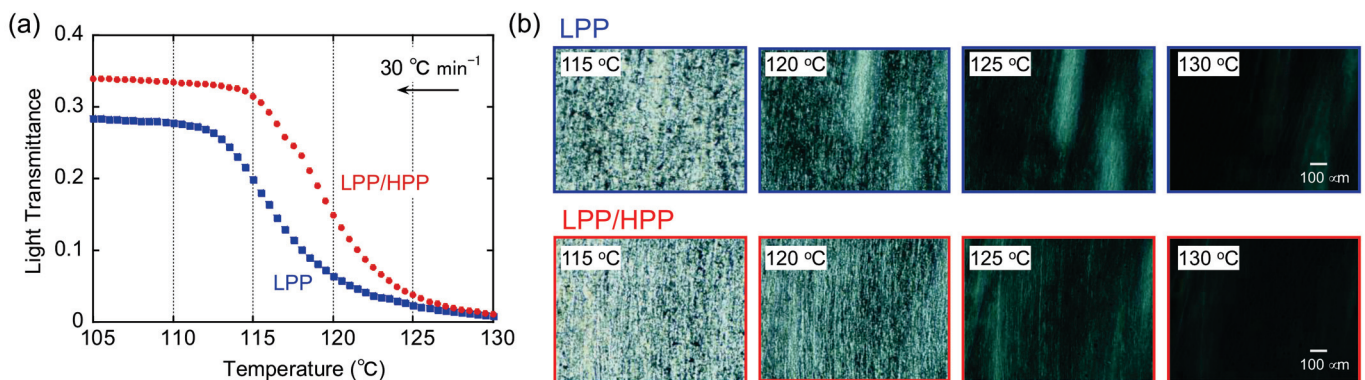


Figure 9. (a) Temperature dependence of light transmittance and (b) polarized optical microscopy (POM) images at 115, 120, 125, and 130 °C during non-isothermal crystallization at 30 °C min⁻¹ after the cessation of shear flow (100 s⁻¹) at 160 °C.

The Weissenberg number associated with the Rouse mode (Wi_R), defined as $Wi_R = \dot{\gamma}\tau_R$, is used as a critical factor for forming flow-induced crystalline structure [22]. It is known

that the flow-induced crystalline structure is formed at which Wi_R is larger than unity. The Wi_R values of both PP samples for the flow-induced crystallization process were calculated using the following equation [49]:

$$Wi_R = \dot{\gamma} \tau_e \left(\frac{M}{M_e} \right)^2, \quad (12)$$

where τ_e is the Rouse time of an entanglement strand and M_e is the entanglement molecular weight. For iPP, Wi_R was calculated using $\tau_e = 1.5 \times 10^{-7}$ s and $M_e = 5.25$ kg mol⁻¹ at 170 °C [50]. In the case of the present crystallization process, the critical molecular weight for flow-induced crystallization was approximately 1.3×10^6 , calculated using Equation (12). Considering that both PP samples included a small number of UHMW chains, the highly oriented crystalline structure observed in the POM image shown in Figure 9 was caused by stretching of the UHMW component. In particular, the LPP/HPP sample included a larger amount of the UHMW component than the LPP sample, which resulted in a significant degree of orientation in the flow direction and numerous highly oriented crystals in LPP/HPP compared with LPP.

3.3. Morphology and Mechanical Properties of Films

The DSC curves obtained during the heating and cooling processes of LPP and LPP/HPP films at heating and cooling rates of 10 and 30 °C min⁻¹, respectively, are shown in Figure 10. The melting and crystallization temperatures (T_m and T_c) were almost the same for both PP films, as denoted in Figure 10, which is in good agreement with the crystallization behavior demonstrated by the light transmittance shown in Figure 8. Moreover, as shown in Table 2, both PP samples had almost the same crystallinity, whereas the amount of rigid amorphous structure in LPP was higher than in LPP/HPP, suggesting that the LPP film included a large amount of imperfect crystalline structure compared with LPP/HPP.

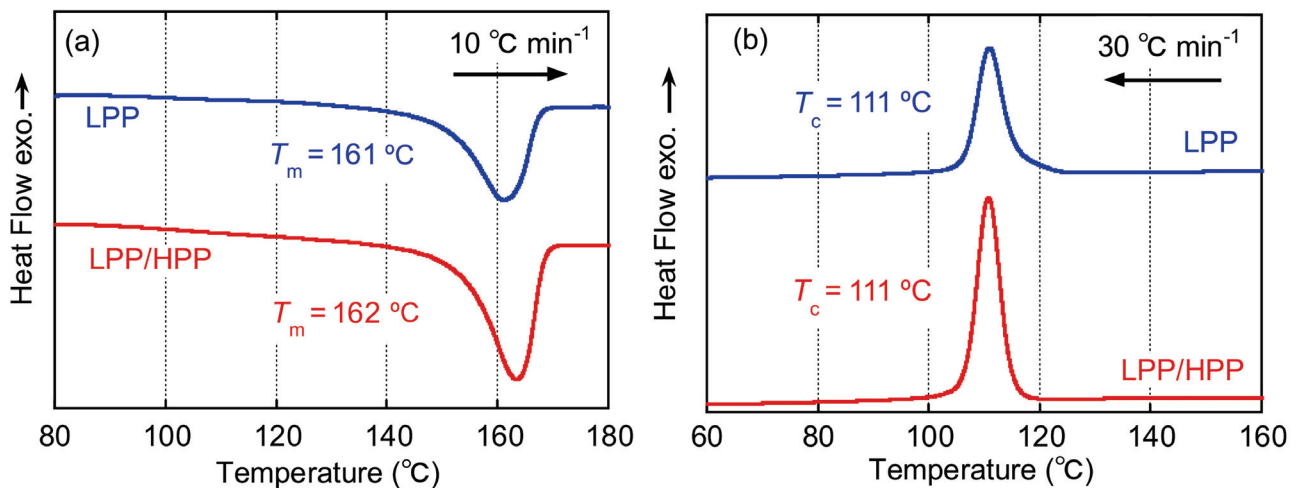


Figure 10. Differential scanning calorimetry (DSC) curves during (a) heating at 10 °C min⁻¹ and (b) cooling at 30 °C min⁻¹ for LPP and LPP/HPP (LPP is a unimodal PP and HPP is a bimodal PP).

Table 2. Characteristics of the LPP and LPP/HPP films (LPP is a unimodal PP and HPP is a bimodal PP).

Sample Code	χ_{DSC} (wt%)	χ_{RA} (wt%)	χ_{WAXD} (wt%)	χ_{IR} (wt%)	f_{WAXD}	$f_{IR,c}$	$f_{IR,a}$
LPP	34.3	59.5	49.3	51.8	0.12	0.22	0.15
LPP/HPP	34.5	54.1	52.1	53.6	0.18	0.28	0.16

The two-dimensional WAXD patterns of the LPP and LPP/HPP films are shown in Figure 11. Each PP film showed five diffraction peaks assigned to (110), (040), (130), (111), and (−131) of the PP α -crystals [51]. The integrated intensity profiles are plotted against 2θ in Figure 12. The figures in parentheses are the Miller indices. The crystalline diffraction peaks of LPP/HPP were sharper and stronger than those of LPP, although the crystallinity values calculated using Equation (3) were similar for each sample, as shown in Table 2. These results indicate that the crystalline regularity of LPP was imperfect compared with that of LPP/HPP. This corroborated the DSC results, which demonstrated that LPP included more rigid amorphous structure than HPP/LPP. It should be noted that the crystallinity determined by IR spectroscopy listed in Table 2 was similar for both PP samples, as corroborated by the DSC and WAXD results.

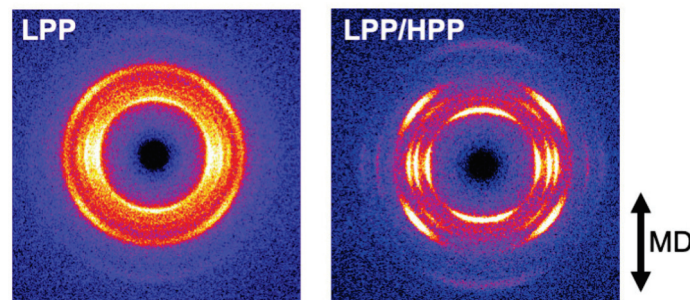


Figure 11. Two-dimensional wide-angle X-ray diffraction (WAXD) patterns of LPP (left) and LPP/HPP (right) (LPP is a unimodal PP and HPP is a bimodal PP).

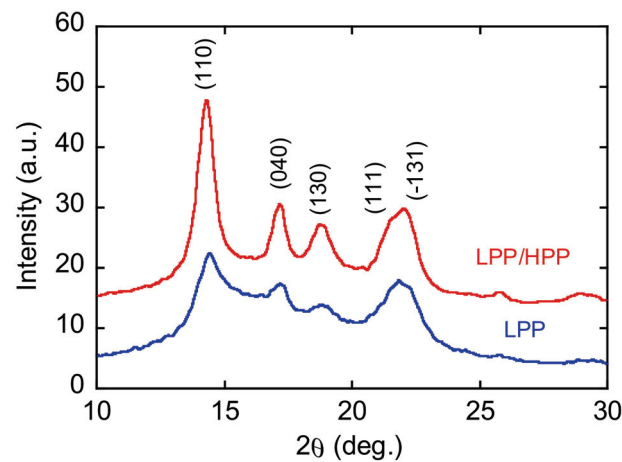


Figure 12. Integrated intensity profiles plotted against 2θ for LPP and LPP/HPP (LPP is a unimodal PP and HPP is a bimodal PP).

The azimuthal-angle dependence of the integrated intensity of the (040) diffraction peak is shown in Figure 13. There were sharp peaks in the intensity distribution at 90° and 270° , corresponding to the equator axis in Figure 11, for both PPs, suggesting that the c axis of the crystalline structure was oriented to the MD. The orientation of the crystalline structure was enhanced by the addition of the UHMW component because the peak width of the intensity profile of LPP/HPP was sharper than that of LPP. The orientation function values evaluated by WAXD and IR spectroscopy shown in Table 2 also suggest the enhancement of the crystalline structure orientation due to the addition of the UHMW component.

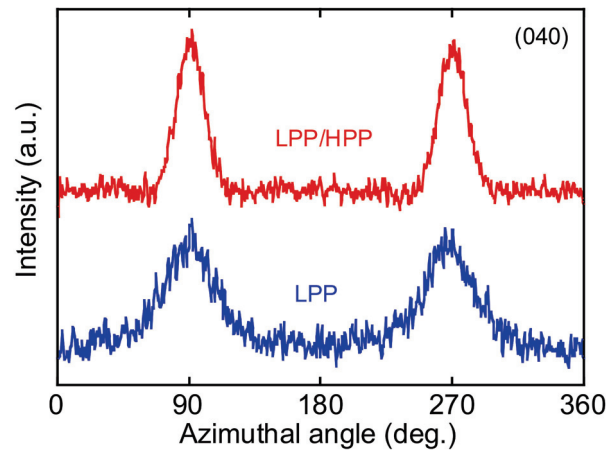


Figure 13. Azimuthal-angle distribution of the (040) diffraction plane of LPP and LPP/HPP α crystals (LPP is a unimodal PP and HPP is a bimodal PP).

The two-dimensional SAXS patterns of the oriented films are shown in Figure 14. LPP/HPP exhibited a strong two-peak pattern in the MD compared with LPP, indicating that the addition of the UHMW component enhanced the lamellar orientation to the perpendicular direction of the MD. Such lamellar orientation behavior is corroborated by the WAXD results.

According to the evaluation of the rheological and crystallization behaviors of LPP and LPP/HPP, the strong orientation of the UHMW chains to the MD should remain during film processing, which results in the improvement of the orientation of the lamellar crystalline structure by the addition of the UHMW component.

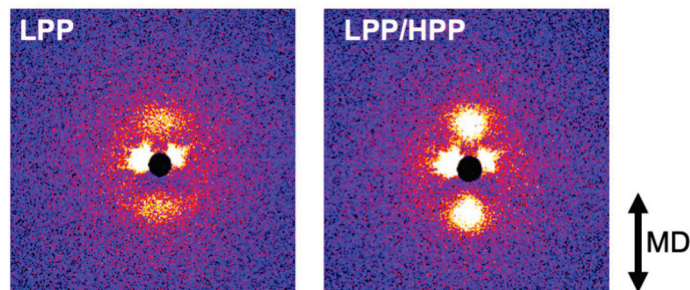


Figure 14. Two-dimensional small-angle X-ray scattering (SAXS) patterns of sample films of LPP (left) and LPP/HPP (right) (LPP is a unimodal PP and HPP is a bimodal PP).

The dynamic mechanical spectra of LPP and LPP/HPP films measured in the MD and TD are shown in Figure 15. Strain was applied along the MD and TD to investigate the effects of molecular orientation on solid-state viscoelasticity. For both PP samples, the E' and E'' values for MD stretching were higher than those for TD stretching owing to the orientation to the MD. Moreover, for both MD and TD stretching, the E' and E'' values for LPP/HPP were higher than those for LPP above the glass transition temperature at approximately 20 °C. These results were caused by the imperfect crystalline structure of LPP compared with that of LPP/HPP; disorder in the crystalline structure leads to low thermal stability.

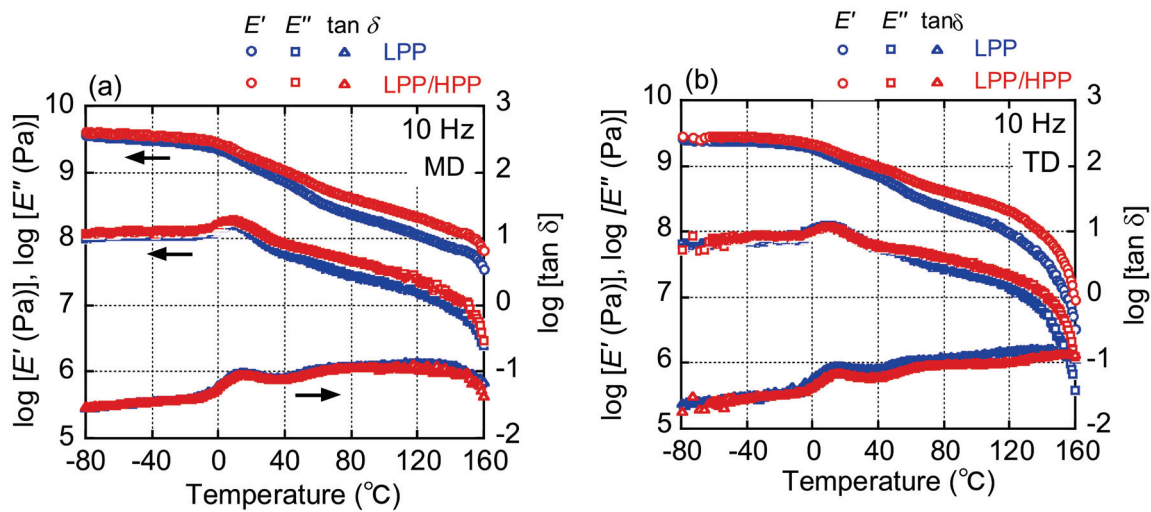


Figure 15. Temperature dependence of the storage modulus (E'), loss modulus (E''), and loss tangent ($\tan\delta$) at 10 Hz for LPP and LPP/HPP at the applied strain along (a) the machine direction (MD) and (b) the transverse direction (TD) (LPP is a unimodal PP and HPP is a bimodal PP).

Figures 16 and 17 show the stress–strain curves of LPP and LPP/HPP films stretched along the MD and TD, respectively. The Young's modulus, yield stress, and strength of LPP/HPP were higher than those of LPP with regard to MD stretching. As shown in Figure 18, the drawn specimens elongated up to $\varepsilon = 1.5$ along the MD exhibited homogeneous birefringence color without necking formation. Moreover, the two-dimensional WAXD patterns of the LPP and LPP/HPP films were almost the same as those of the undrawn films shown in Figure 11, suggesting that the initial crystalline structure of the undrawn films remained during the stretching process. These results indicate that the yielding deformation associated with MD stretching was caused by the pull-out of the molecular chains from the crystalline structure [52,53], because the pull-out deformation is homogeneously caused in all lamellar crystals. This is consistent with the homogeneous deformation without necking formation as observed in Figure 18a. Consequently, the improvements in the Young's modulus, yield stress, and strength following the addition of the UHMW component resulted from the higher molecular orientation and high regularity of the crystalline structure.

With regard to TD stretching, the Young's modulus, yield stress, and strength of LPP/HPP were increased by the addition of the UHMW component, as with MD stretching. However, in contrast to MD stretching, the stress–strain curve associated with TD stretching for each PP sample featured a neck-propagation region, and clear necking occurred in the drawn specimens of both samples elongated in the TD, as shown in Figure 18b. The two-dimensional WAXD patterns of the drawn specimens shown in Figure 19b suggest that the crystalline structure was highly oriented in the TD direction, and the orientation degree of LPP/HPP was higher than that of LPP. Moreover, the crystalline structure associated with TD stretching was significantly disordered in both samples because the diffraction peaks were obviously broadened. These results suggest that the initial crystalline structure that was highly oriented along the MD fragmented into smaller crystallites and reoriented in the TD direction, leading to the formation of necking [54–56]. The crystalline structure of the undrawn LPP film was disordered compared with that of the undrawn LPP/HPP, as shown in Figure 11. Therefore, the Young's modulus, yield stress, and strength of LPP/HPP were higher than those of LPP in the TD stretching. It should be noted that the orientation behavior of the drawn specimens of LPP and LPP/HPP evaluated by WAXD measurements were identical to those evaluated by birefringence measurements.

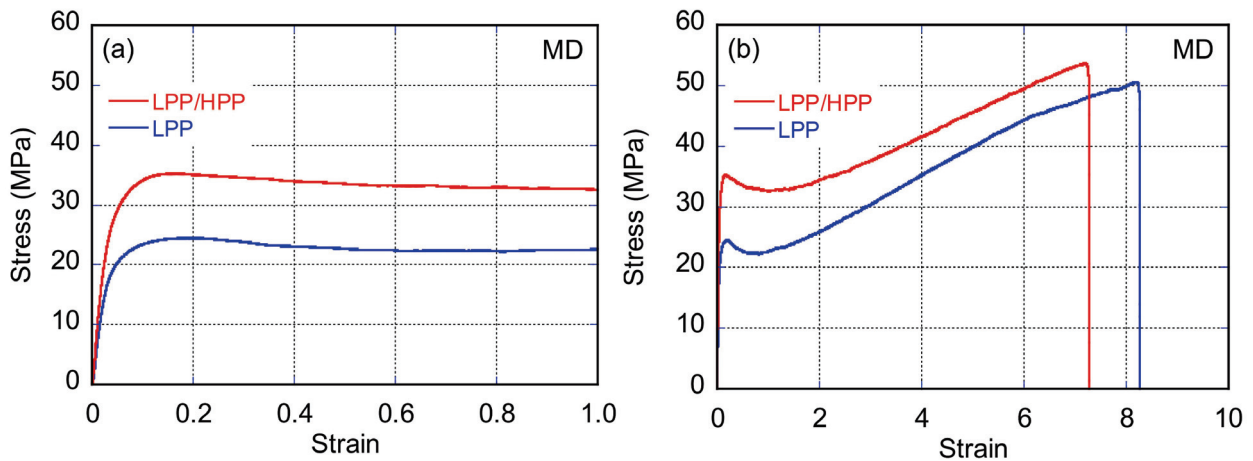


Figure 16. Stress–strain curves (a) in the yielding region and (b) up to the strain at break of LPP and LPP/HPP films stretched along the flow direction (MD) (LPP is a unimodal PP and HPP is a bimodal PP).

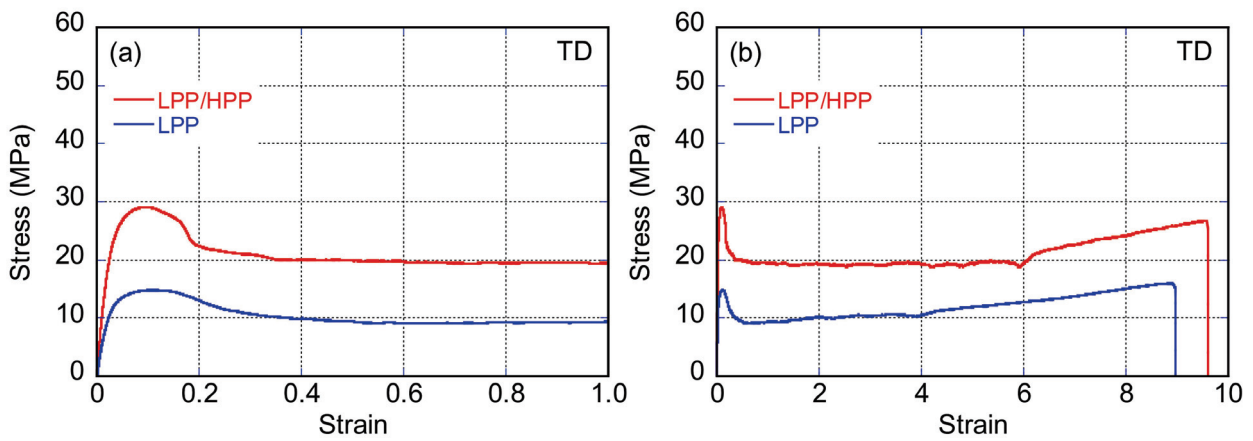


Figure 17. Stress–strain curves (a) in the yielding region and (b) up to the strain at break of LPP and LPP/HPP films stretched along the transverse direction (TD) (LPP is a unimodal PP and HPP is a bimodal PP).

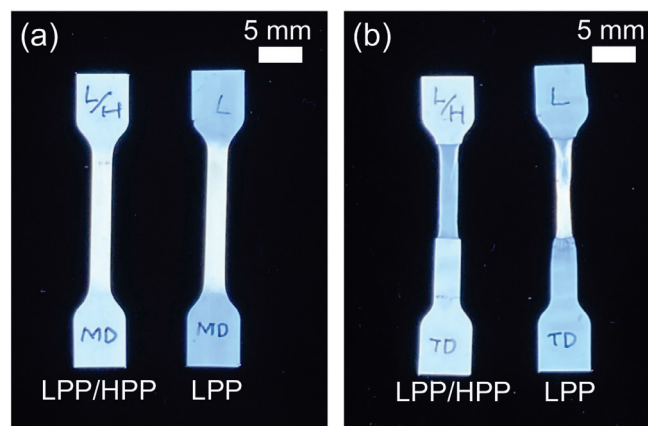


Figure 18. Polarized optical microscopy (POM) images of drawn specimens of LPP and LPP/HPP elongated up to a strain of 1.5 along (a) the flow direction (MD) and (b) the transverse direction (TD) (LPP is a unimodal PP and HPP is a bimodal PP).

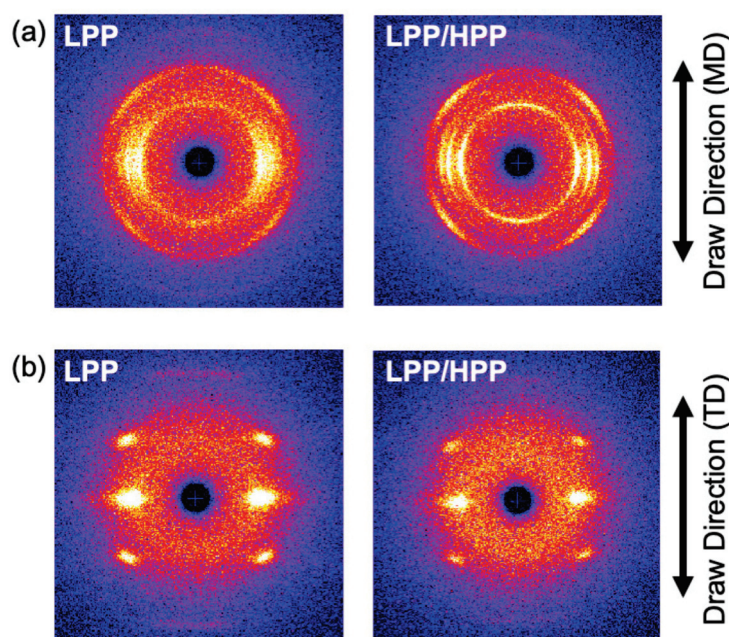


Figure 19. Two-dimensional wide-angle X-ray diffraction (WAXD) patterns of drawn LPP (left) and LPP/HPP (right) elongated along (a) the flow direction (MD) and (b) the transverse direction (TD) (LPP is a unimodal PP and HPP is a bimodal PP).

4. Conclusions

The present study comprised an investigation of the effects of a UHMW component on the rheological properties, crystallization behavior, and mechanical properties of PP. The elasticity of the melt state was improved by adding the UHMW component, as demonstrated by the higher values of the primary normal stress difference, the extrudate swell ratio, and the drop in end pressure of LPP/HPP than of LPP. It should be noted that the enhancements in rheological properties resulting from the addition of the UHMW component were achieved without an increase in the shear viscosity. Moreover, LPP/HPP exhibited strain hardening during uniaxial elongational flow in the high strain rate region. The strain hardening was due to that the orientation of the UHMW chains cannot be relaxed during uniaxial elongation owing to the characteristic long duration of the Rouse mode. With regard to the crystallization behavior, the addition of the UHMW component had no influence on the crystallization temperature, and spherulites were formed in both PP samples. However, the formation of a highly oriented structure was enhanced by the strong orientation of the UHMW chains during crystallization with shear flow. The enhancement of the molecular orientation by the addition of the UHMW component was also observed in the T-die films. Moreover, the numbers of crystalline defects and rigid amorphous structures decreased following the addition of the UHMW component, resulting in the strong orientation of crystalline structure in LPP/HPP compared with in LPP. Consequently, the Young's modulus and strength of the LPP/HPP films were higher than those of the LPP films for both MD and TD stretching. These results provide useful information for the improvement of the rheological and mechanical properties of semi-crystalline polymeric materials.

Author Contributions: Data curation, T.K. (Takeyoshi Kimura), A.E. and K.J.; Investigation, T.K. (Takumitsu Kida) and T.K. (Takeyoshi Kimura); Methodology, T.K. (Takumitsu Kida); Resources, T.K. (Tokutaro Kimura), T.M. (Tomoaki Mizukawa), T.M. (Tomoya Murakami), K.H. and T.O.; Software, Y.O.; Supervision, M.Y.; Writing—Original Draft, T.K. (Takumitsu Kida); Writing—Review and Editing, T.K. (Takumitsu Kida), M.Y. and Y.O. All authors have read and agreed to the published version of the manuscript.

Funding: This work was supported by the JSPS KAKENHI (grant number 20K15345).

Institutional Review Board Statement: Not applicable.

Informed Consent Statement: Not applicable.

Data Availability Statement: Not applicable.

Conflicts of Interest: The authors declare no conflict of interest.

References

- Gentekos, D.T.; Sifri, R.J.; Fors, B.P. Controlling polymer properties through the shape of the molecular-weight distribution. *Nat. Rev. Mater.* **2019**, *4*, 761–774. [CrossRef]
- Kennedy, M.A.; Peacock, A.J.; Failla, M.D.; Lucasji, J.C.; Mandelkern, L. Tensile Properties of Crystalline Polymers: Random Copolymers of Ethylene. *Macromolecules* **1995**, *28*, 1407–1421. [CrossRef]
- Hu, Y.; Shao, Y.; Liu, Z.; He, X.; Liu, B. Effect of short-chain branching on the tie chains and dynamics of bimodal polyethylene: Molecular dynamics simulation. *Eur. Polym. J.* **2018**, *103*, 312–321. [CrossRef]
- Zielińska, D.; Rydzkowski, T.; Thakur, V.K.; Borysiak, S. Enzymatic engineering of nanometric cellulose for sustainable polypropylene nanocomposites. *Ind. Crops Prod.* **2021**, *161*, 11388. [CrossRef]
- Nishikawa, R.; Aridome, N.; Ojima, N.; Yamaguchi, M. Structure and properties of fiber-reinforced polypropylene prepared by direct incorporation of aqueous solution of poly(vinyl alcohol). *Polymer* **2020**, *199*, 122566. [CrossRef]
- Iwasaki, S.; Inoue, M.; Takei, Y.; Nishikawa, R.; Yamaguchi, M. Modulus enhancement of polypropylene by sorbitol nucleating agent in flow field. *Polym. Cryst.* **2021**, *4*, e10170. [CrossRef]
- Phulkerd, P.; Nakabayashi, T.; Iwasaki, S.; Yamaguchi, M. Enhancement of drawdown force in polypropylene containing nucleating agent. *J. Appl. Polym. Sci.* **2019**, *136*, 1–7. [CrossRef]
- Colby, R.H.; Fetters, L.J.; Graessley, W.W. Melt Viscosity-Molecular Weight Relationship for Linear Polymers. *Macromolecules* **1987**, *20*, 2226–2237. [CrossRef]
- Pearson, D.S.; Ver Strate, G.; von Meerwall, E.; Schilling, F.C. Viscosity and Self-Diffusion Coefficient of Linear Polyethylene. *Macromolecules* **1987**, *20*, 1133–1141. [CrossRef]
- Anderews, J.M.; Ward, I.M. The cold-drawing of high density polyethylene. *J. Mater. Sci.* **1970**, *5*, 411–417. [CrossRef]
- Kennedy, M.A.; Peacock, A.J.; Mandelkern, L. Tensile Properties of Crystalline Polymers: Linear Polyethylene. *Macromolecules* **1994**, *27*, 5297–5310. [CrossRef]
- Diop, M.F.; Burghardt, W.R.; Torkelson, J.M. Well-mixed blends of HDPE and ultrahigh molecular weight polyethylene with major improvements in impact strength achieved via solid-state shear pulverization. *Polymer* **2014**, *55*, 4948–4958. [CrossRef]
- Tanaka, H.; Saijo, S.; Kakiage, M.; Yamanobe, T.; Uehara, H. In-situ analysis for melt-drawing behavior of ultra-high molecular weight polyethylene/normal molecular weight polyethylene blend films. *Polymer* **2021**, *213*, 123213. [CrossRef]
- Capaccio, G.; Ward, I.M. Preparation of ultra-high modulus linear polyethylenes; effect of molecular weight and molecular weight distribution on drawing behaviour and mechanical properties. *Polymer* **1974**, *15*, 233–238. [CrossRef]
- Sun, X.; Shen, H.; Xie, B.; Yang, W.; Yang, M. Fracture behavior of bimodal polyethylene: Effect of molecular weight distribution characteristics. *Polymer* **2011**, *52*, 564–570. [CrossRef]
- Kida, T.; Tanaka, R.; Hiejima, Y.; Nitta, K.-H.; Shiono, T. Improving the strength of polyethylene solids by simple controlling of the molecular weight distribution. *Polymer* **2021**, *218*, 123526. [CrossRef]
- Münstedt, H. Dependence of the Elongational Behavior of Polystyrene Melts on Molecular Weight and Molecular Weight Distribution. *J. Rheol.* **1980**, *24*, 847–867. [CrossRef]
- Minegishi, A.; Nishioka, A.; Takahashi, T.; Masubuchi, Y.; Takimoto, J.; Koyama, K. Uniaxial elongational viscosity of PS/a small amount of UHMW-PS blends. *Rheol. Acta* **2001**, *40*, 329–338. [CrossRef]
- Nielsen, J.K.; Rasmussen, H.K.; Hassager, O.; McKinley, G.H. Elongational viscosity of monodisperse and bidisperse polystyrene melts. *J. Rheol.* **2006**, *50*, 453–476. [CrossRef]
- Wingstrand, S.L.; Shen, B.; Kornfield, J.A.; Mortensen, K.; Parisi, D.; Vlassopoulos, D.; Hassager, O. Rheological Link between Polymer Melts with a High Molecular Weight Tail and Enhanced Formation of Shish-Kebabs. *ACS Macro Lett.* **2017**, *6*, 1268–1273. [CrossRef]
- Mykhaylyk, O.O.; Chambon, P.; Impradice, C.; Fairclough, J.P.A.; Terrill, N.J.; Ryan, A.J. Control of structural morphology in shear-induced crystallization of polymers. *Macromolecules* **2010**, *43*, 2389–2405. [CrossRef]
- Hamad, F.G.; Colby, R.H.; Milner, S.T. Onset of Flow-Induced Crystallization Kinetics of Highly Isotactic Polypropylene. *Macromolecules* **2015**, *48*, 3725–3738. [CrossRef]
- Matsuba, G.; Sakamoto, S.; Ogino, Y.; Nishida, K.; Kanaya, T. Crystallization of polyethylene blends under shear flow. Effects of crystallization temperature and ultrahigh molecular weight component. *Macromolecules* **2007**, *40*, 7270–7275. [CrossRef]
- Kanaya, T.; Matsuba, G.; Ogino, Y.; Nishida, K.; Shimizu, H.M.; Shinohara, T.; Oku, T.; Suzuki, J.; Otomo, T. Hierarchic structure of shish-kebab by neutron scattering in a wide Q range. *Macromolecules* **2007**, *40*, 3650–3654. [CrossRef]
- Bashir, Z.; Odell, J.A.; Keller, A. High modulus filaments of polyethylene with lamellar structure by melt processing; the role of the high molecular weight component. *J. Mater. Sci.* **1984**, *19*, 3713–3725. [CrossRef]

26. Bashir, Z.; Odell, J.A.; Keller, A. Stiff and strong polyethylene with shish kebab morphology by continuous melt extrusion. *J. Mater. Sci.* **1986**, *21*, 3993–4002. [CrossRef]
27. Seemork, J.; Siriprumpoonthum, M.; Lee, Y.; Nobukawa, S.; Yamaguchi, M. Effect of die geometry on drawdown force of polypropylene at capillary extrusion. *Adv. Polym. Technol.* **2015**, *34*, 1–7. [CrossRef]
28. Wunderlich, B. *Macromolecular Physics, Crystal Structure, Morphology, Defects*; Academic Press: New York, NY, USA, 1973.
29. Zia, Q.; Mileva, D.; Androsch, R. Rigid amorphous fraction in isotactic polypropylene. *Macromolecules* **2008**, *41*, 8095–8102. [CrossRef]
30. Di Lorenzo, M.L.; Righetti, M.C. Crystallization-induced formation of rigid amorphous fraction. *Polym. Cryst.* **2018**, *1*, 1–14. [CrossRef]
31. Wunderlich, B. The Athas database on heat capacities of polymers. *Pure Appl. Chem.* **1995**, *67*, 1019–1026. [CrossRef]
32. Wunderlich, B. *Thermal Analysis of Polymeric Materials*; Springer: New York, NY, USA, 1995.
33. Wilchinsky, Z.W. Measurement of Orientation in Polypropylene Film. *J. Appl. Phys.* **1960**, *31*, 1969–1972. [CrossRef]
34. Tanaka, M.; Young, R. Molecular orientation distributions in uniaxially oriented poly (L-lactic acid) films determined by polarized Raman spectroscopy. *Macromolecules* **2006**, *39*, 3312–3321. [CrossRef]
35. Arvidson, S.A.; Khan, S.A.; Gorga, R.E. Mesomorphic- α -monoclinic phase transition in isotactic polypropylene: A study of processing effects on structure and mechanical properties. *Macromolecules* **2010**, *43*, 2916–2924. [CrossRef]
36. Bower, D.I.; Maddams, W.F. *The Vibrational Spectroscopy of Polymers*; Cambridge University Press: New York, NY, USA, 1992.
37. Nitta, K.-H.; Sawada, T.; Yoshida, S.; Kawamura, T. Three dimensional molecular orientation of isotactic polypropylene films under biaxial deformation at higher temperatures. *Polymer* **2015**, *74*, 30–37. [CrossRef]
38. Parthasarthy, G.; Sevegney, M.; Kannan, R.M. Rheoptical Fourier transform infrared spectroscopy of the deformation behavior in quenched and slow-cooled isotactic polypropylene films. *J. Polym. Sci. Part B Polym. Phys.* **2002**, *40*, 2539–2551. [CrossRef]
39. Lanyi, F.J.; Wenzke, N.; Kaschta, J.; Schubert, D.W. A method to reveal bulk and surface crystallinity of Polypropylene by FTIR spectroscopy—Suitable for fibers and nonwovens. *Polym. Test.* **2018**, *71*, 49–55. [CrossRef]
40. Yamaguchi, M.; Takahashi, M. Rheological properties of low-density polyethylenes produced by tubular and vessel processes. *Polymer* **2001**, *42*, 8663–8670. [CrossRef]
41. Mieda, N.; Yamaguchi, M. Flow instability for binary blends of linear polyethylene and long-chain branched polyethylene. *J. Non-Newton. Fluid Mech.* **2011**, *166*, 231–240. [CrossRef]
42. Osaki, K.; Murai, A.; Bessho, N.; Kim, B.S. Linear Viscoelastic Relation Concerning Shear Stresses at the Start and Cessation of Steady Shear Flow. *Nihon Reoroji Gakkaishi (J. Soc. Rheol. Jpn.)* **1976**, *4*, 166–169. [CrossRef]
43. Yamaguchi, M. Flow instability in capillary extrusion of plasticized poly(vinyl chloride). *J. Appl. Polym. Sci.* **2001**, *82*, 1277–1283. [CrossRef]
44. Yamaguchi, M.; Suzuki, K.I. Enhanced strain hardening in elongational viscosity for HDPE/crosslinked HDPE blend. II. Processability of thermoforming. *J. Appl. Polym. Sci.* **2002**, *86*, 79–83. [CrossRef]
45. Yamaguchi, M. Material Strength in Molten State for Foam. In *Forum Extrusion: Principles and Practice*; Lee, S.-T., Park, C.B., Eds.; CRC Press: New York, NY, USA, 2014; p. 36, ISBN 9780429184703.
46. Kugimoto, D.; Kouda, S.; Yamaguchi, M. Modification of Poly(Lactic Acid) Rheological Properties Using Ethylene—Vinyl Acetate Copolymer. *J. Polym. Environ.* **2021**, *29*, 121–129. [CrossRef]
47. Seki, M.; Thurman, D.W.; Oberhauser, J.P.; Kornfield, J.A. Shear-Mediated Crystallization of Isotactic Polypropylene: The Role of Long Chain—Long Chain Overlap. *Macromolecules* **2002**, *35*, 2583–2594. [CrossRef]
48. Koscher, E.; Fulchiron, R. Influence of shear on polypropylene crystallization: Morphology development and kinetics. *Polymer* **2002**, *43*, 6931–6942. [CrossRef]
49. Doi, M.; Edwards, S.F. *The Theory of Polymer Dynamics*; Clarendon Press: Oxford, UK, 1986.
50. Fetters, L.J.; Lohse, D.J.; Graessley, W.W. Chain dimensions and entanglement spacings in dense macromolecular systems. *J. Polym. Sci. Part B Polym. Phys.* **1999**, *37*, 1023–1033. [CrossRef]
51. Pasquini, N. *Polypropylene Handbook*; Carl Hanser Verlag: Munich, Germany, 2005.
52. Takayanagi, M.; Nitta, K.-H. Application of a tie molecule model to the postyielding deformation of crystalline polymers. *Macromol. Theory Simul.* **1997**, *6*, 181–195. [CrossRef]
53. Nitta, K.-H.; Nomura, H. Stress–strain behavior of cold-drawn isotactic polypropylene subjected to various drawn histories. *Polymer* **2014**, *55*, 6614–6622. [CrossRef]
54. Strobl, G. *The Physics of Polymers: Concepts for Understanding Their Structures and Behavior*, 3rd ed.; Springer: Berlin, Germany, 2007.
55. Nitta, K.-H.; Takayanagi, M. Novel proposal of lamellar clustering process for elucidation of tensile yield behavior of linear polyethylenes. *J. Macromol. Sci. Phys.* **2003**, *42*, 107–126. [CrossRef]
56. Kuriyagawa, M.; Nitta, K.-H. Structural explanation on natural draw ratio of metallocene-catalyzed high density polyethylene. *Polymer* **2011**, *52*, 3469–3477. [CrossRef]

Article

Optimizing Bladder Resin Transfer Molding Process to Manufacture Complex, Thin-Ply Thermoplastic Tubular Composite Structures: An Experimental Case Study

Somen K. Bhudolia ^{1,*}, Pavel Perrotey ², Goram Gohel ¹, Sunil C. Joshi ¹, Pierre Gerard ³
and Kah Fai Leong ¹

¹ School of Mechanical and Aerospace Engineering, Nanyang Technological University, 50 Nanyang Avenue, Singapore 639798, Singapore; GORAM001@e.ntu.edu.sg (G.G.); mscjoshi@ntu.edu.sg (S.C.J.); MKFLEONG@ntu.edu.sg (K.F.L.)

² Carbon Axis, 34 Rue Jacques de Vaucanson, 17180 Perigny, France; pperrotey@carbon-axis.com

³ Groupement de Recherche de Lacq, Arkema Group, Route Départementale 817, 64170 Lacq, France; pierre.gerard@arkema.com

* Correspondence: somenkum001@e.ntu.edu.sg

Abstract: The bladder molding process is primarily used in sporting applications but mostly with prepregs. Bladder-Assisted Resin Transfer Molding (B-RTM) presents the tremendous potential to automate and mass produce the complex hollow-composite profiles. Thin-ply, non-crimp fabrics (NCFs) provide excellent mechanical, fracture toughness, and vibration damping properties on top of the weight saving it offers to a final product. However, these fiber architectures are difficult to inject due to the resistance they provide for the polymer flow using the liquid injection process. Therefore, it is mandatory to optimize the process parameters to reduce the time for injection and simultaneously achieve better consolidation. This work presents a first, detailed, experimental case study to successfully inject a low-permeability, thin-ply, complex, thermoplastic tubular structure, and the effect of process parameters, boundary conditions, the associated manufacturing challenges, and proposed solutions are deliberated in this paper.

Keywords: thermoplastic resin; resin transfer molding; non-crimp fabrics; consolidation

Citation: Bhudolia, S.K.; Perrotey, P.; Gohel, G.; Joshi, S.C.; Gerard, P.; Leong, K.F. Optimizing Bladder Resin Transfer Molding Process to Manufacture Complex, Thin-Ply Thermoplastic Tubular Composite Structures: An Experimental Case Study. *Polymers* **2021**, *13*, 4093. <https://doi.org/10.3390/polym13234093>

Academic Editor: Antonio Pizzi

Received: 29 October 2021

Accepted: 22 November 2021

Published: 24 November 2021

Publisher's Note: MDPI stays neutral with regard to jurisdictional claims in published maps and institutional affiliations.



Copyright: © 2021 by the authors. Licensee MDPI, Basel, Switzerland. This article is an open access article distributed under the terms and conditions of the Creative Commons Attribution (CC BY) license (<https://creativecommons.org/licenses/by/4.0/>).

1. Introduction

The utilization of a resin transfer molding (RTM) manufacturing technique is becoming more popular in composites' manufacturing industries [1–4]. In a RTM manufacturing technique, the polymer matrix is infused into the dry fiber preform at a certain pressure into the closed mold to impregnate the fabrics, in contrast to the traditional prepreg processing manufacturing technique [5].

Bladder-assisted resin transfer molding (B-RTM) is a manufacturing process variant specifically suited for the fabrication of hollow-composite, complex-shaped parts such as a hollow tube [4]. Hollow-composite structures are very fascinating and find tremendous applications in sailing ships (booms), wind turbine blades, pressure vessels, and in sports industries. The widely used manufacturing process for the hollow-composite profile is filament winding where the rovings are wound around the rotating mandrel to produce parts like drive shafts, tubes, and pressure vessels [6,7]. However, this process is associated with surface finishing issues, as there is no defined geometry, as well as the constraint on the fiber angle to be placed on the mandrel. Another effective process is a pultrusion process, which offers a substantially greater degree of automation for producing hollow-composite profiles [8]. However, the nature of the processing does not allow curvature within the composite structure. Although there exist some solutions such as bonding the structures together, it reduces the mechanical performance of the structure, due to existing joining lines, and there is no structural continuity. These processes are effective but do not fulfill

the growing needs of the industries, such as being reliable, with reproducible parts, and making the manufacturing process automated.

B-RTM is another interesting process that emerged to produce hollow-composite profiles using the Resin Transfer Molding Process with the aid of a bladder. This process is primarily used in industries with prepregs. The prepreg is wrapped around the inflatable bladder, which is consequently pressurized within a closed mold. Then, the mold is placed in the autoclave or hot press, whichever is appropriate depending on the mold geometry and the recommended cure cycle, to cure the hollow part. However, due to the sticky nature of the prepreg materials, there is a reduction in the drapability of the pre-impregnated fabrics. Although impregnated fabrics are always a solution, there is also poor reproducibility. However, B-RTM presents the tremendous potential to automate, and mass produce the complex hollow-composite profiles. The Schematic of the B-RTM process is shown in Figure 1. The major steps involve placing the preform inside the mold, pressurizing with the inflated bladder, injecting the resin, as with other liquid injection processes, and, finally, demolding the part.

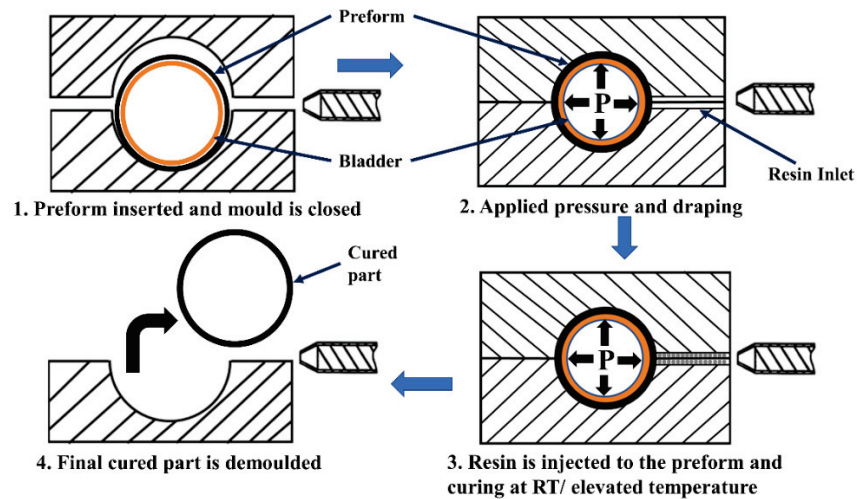


Figure 1. Schematic of the Bladder-assisted Resin Transfer Molding (B-RTM) process.

There is some research carried out on investigating the B-RTM process, but it is mostly focused on woven fabrics or bi-axial braided fabrics, which have high permeability [9–12]. The B-RTM process depends on a number of factors that affect the final manufactured part such as process parameters, such as injection pressure, bladder pressure, and consolidation pressure, and the intrinsic parameters including resin viscosity and the fiber permeability [9,10,13–15]. Christian Schillfahrt et al. investigated the impregnation behavior of a tubular preform with respect to variable injection and bladder pressures using biaxial braided sleeving and an elastomeric silicon bladder [10]. The moldability zone for the study with Toho Tenax HTS40 carbon/corn oil was described as the one where the consolidation pressure was greater than the minimum bladder compaction pressure, and the initial bladder compaction pressure should be greater than the minimum bladder pressure required for full compaction [10]. In another study, Schillfahrt et al. presented a methodology to determine the preform compaction behavior with an undersized elastomeric bladder during the B-RTM process [11].

However, there is minimal research carried on understanding the implications of injecting the fabrics, such as low permeability, thin-ply, non-crimp fabrics (NCFs). This research work presents a first attempt to carry out a detailed experimental case study to manufacture a composite tube mimicking a section of a racket shaft using thin-ply NCFs [8,16–18] as a reinforcement with novel thermoplastic Elium® [19–28] and thermoset epoxy resin. The details of the effective mold design and the development of injection strategy with controlled usage of process parameters are explained in detail. The effect of the process parameters governing the B-RTM process was deliberated and the final quality

of the manufactured parts was checked in terms of fiber volume fraction, void content, and surface finish. This case study will serve as a guide to effectively use bladder resin transfer molding to manufacture thin- as well as thick-ply composites with thermoset and thermoplastic resin with viscosity ≤ 250 cP.

2. Materials and Manufacturing

2.1. Materials

Thin-Ply, non-crimp fabric NCCFs (0/45 bi-angle ply C-Ply™, 200 gsm) and thick-ply NCCFs (0/45 bi-angle C-Ply™, 400 gsm) from CHOMARAT were the reinforcement material used in the current research. Woven, glass fibers were procured from Polymer Technologies, Singapore, and used in the initial phase of the manufacturing optimization. C-Ply™ fabrics with 0/45 orientation were sized especially to be compatible with the respective thermoset and thermoplastic resin systems. FOE sizing was used to manufacture thermoplastic composites and Epoxy-sized fibers were used to manufacture thermoset composites.

Elium® 150 resin from ARKEMA was used as a thermoplastic matrix system in the current investigation. This resin cured at room temperature (RT) by undergoing radical polymerization to form higher-molecular-weight acrylic co-polymers with the addition of a benzoyl peroxide initiator (refer to Figure 2) at a mixture ratio of resin to hardener by weight of 100:3 [29,30]. Epolam 5015/5015, a thermoset variant resin, was used in the current investigation. The resin was used with the hardener at a ratio of 100:30 by weight, with a curing time of 24 h at room temperature. Elium® 150 resin has a viscosity of 100 cP, while the mixed viscosity of epoxy resin was 210 cP.

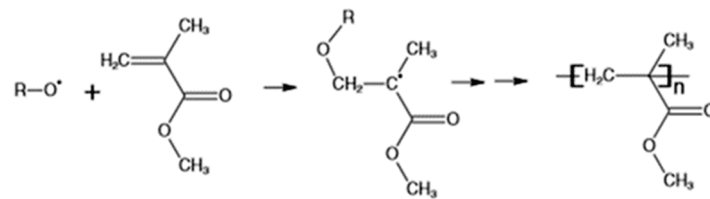


Figure 2. Radical polymerization of Elium matrix to form high-molecular-weight acrylic co-polymers with the addition of a benzoyl peroxide initiator [2,5,31].

A slightly over-sized nylon bladder with a perimeter of 60 mm was used for inflation during the manufacturing process to provide a better compaction, whereas the inner perimeter of the final part was 56.5 mm. Table 1 shows the permeability values for thick and thin NCCFs used in current research.

Table 1. Permeability values for thick and thin NCCFs.

Fabric Type	K_x (m ²)	K_y (m ²)	K_z (m ²)
Thin NCCFs (200 g/m ²)	1.27×10^{-11}	1.1×10^{-11}	2.1×10^{-13}
Thin NCCFs (400 g/m ²)	2.1×10^{-9}	8.7×10^{-10}	-

2.2. Theoretical Background

Parameters used during the injection process play a key role to perform the complete and fast injection of the composite part [9]. However, these parameters are needed to be optimized for the selected fiber and matrix systems. Darcy’s Law oversees the resin flow through the porous medium. In the RTM process, fabric preform is deemed as a porous media and the fabric permeability depends on fiber sizing, structure, and the required volume fraction required. As the permeabilities of the fabrics varied in different directions, the resin flow through the preform is considered an anisotropic. Darcy’s Law can be written as [3],

$$\bar{U} = -\frac{K}{\mu} \times \nabla P \tag{1}$$

where \bar{U} is averaged flow velocity, μ is the viscosity of the resin, ∇P is the pressure gradient, and K is the permeability tensor of the fabric preform. Therefore, based on Darcy's law equations, the resin flow velocity was highly dependent on the resin viscosity, preform permeability in two directions, and the pressure gradient.

2.2.1. Mold Design

B-RTM mold is required to be designed such that it is sealed and closed to resist pressure up to 20 bar, similarly to the RTM manufacturing process. However, using an internal bladder makes the design more complicated, as the bladder is passing through the mold, and makes the sealing more difficult. Figure 3 shows the mold used in the current research. The mold was manufactured of aluminum to reduce weight and to accelerate the heat transfer rate. The grooves were designed to insert a gasket (refer to Figure 3a) to seal the mold. The resin inlet and vacuum outlet are shown in Figure 3b, while the entire mold assembly is depicted in Figure 3c. The injection strategy was to inject the resin from one extremity of the beam and vent from the other extremity. A resin track was used to help spread the resin along the length, and the same track was added on the vacuum side to allow the excess resin to vent. It was also decided to first carry out the manufacturing trials on an acrylic prototype of the mold to visualize the resin injection and to verify if the injection strategy is working efficiently. Figure 4 shows the acrylic tubular section mold, where the cavity, as well as the resin inlet/vacuum outlet, is shown. Figure 4a shows the entire mold assembly, while Figure 4b shows the dry fiber preform placed in the mold cavity.

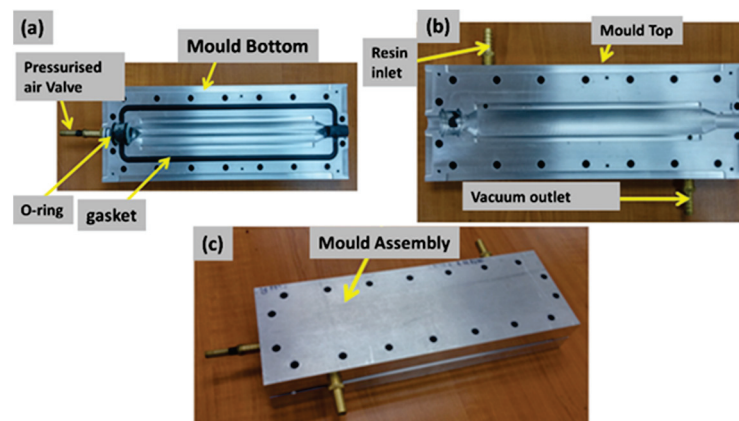


Figure 3. Mold design for manufacturing a tubular section (a) bottom mould (b) top mould (c) mould assembly.

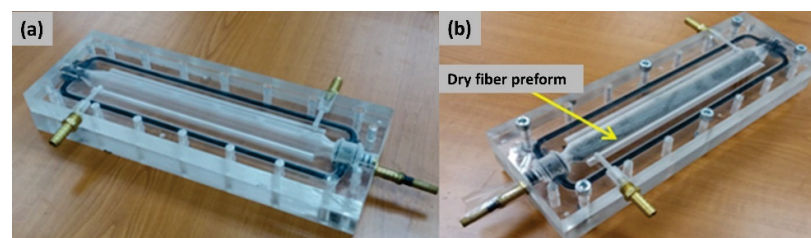


Figure 4. Acrylic mold prototype design for manufacturing a tubular section (a) mould without preform (b) mould with dry fabric preform.

2.2.2. Preforming, Fabrication, and Manufacturing

At first, the dry fabric NCCF layers were stacked depending on the required layup and thickness. Then, the preform was bound with an epoxy binder based on bisphenol A. After uniformly spreading the binder on the preform, it was activated at 85 °C using the heat gun. The binder was melted and subsequently bound to the preform to wind it

around the mandrel. The entire preform binding steps are shown in Figure 5. Figure 5a shows the preform without the binder sprinkled on it. Figure 5b shows the step where the binder was sprinkled on the preform. Figure 5c shows the binder was melted/activated on the preform with the heat application using the heat gun. Applying and activating the binder on the preform is significant to make a firm 3-D perform.

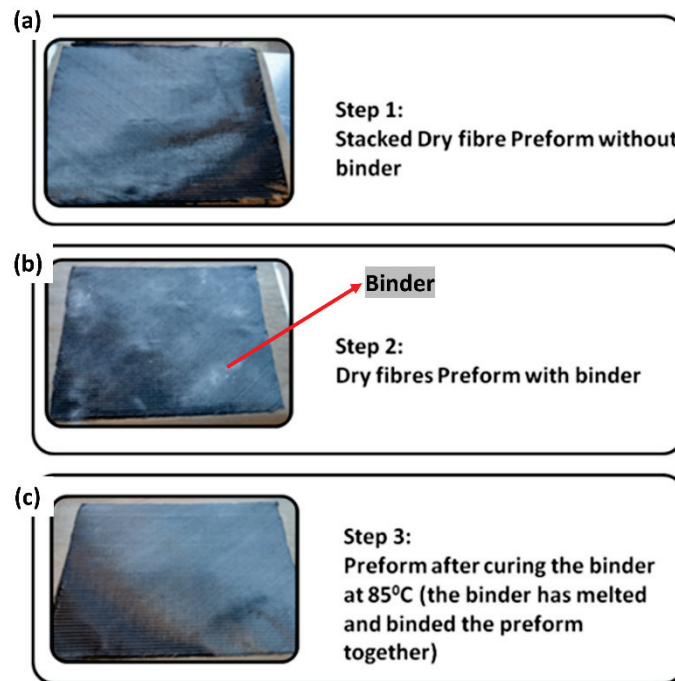


Figure 5. Preform binding steps for a tubular section.

The dimensions of the target tubular section mimicking a tennis racket section, the 3-D printed mandrel, and the preform are shown in Figure 6. The preform used was 250 mm long, having the same length as the mold cavity. The width of the preform was equal to the flank length of 226 mm, which corresponded to four layers when rolled, as the perimeter of the c/s is 56.52 mm. The fabrication steps to manufacture a tubular section are shown in Figure 7. First, the preform was wrapped as tightly as possible, and the binder was activated by heating with a heat gun at 85 °C. Once the preform was wrapped around the mandrel, it was vacuum bagged for compaction. The final adjustment for net-shape preforms was carried out manually. Then, the bagged preform was heated again to reactivate the binder. Finally, the bound preform was removed from the mandrel, as shown in the last step of Figure 7. Figure 8 shows the positioning of the final, bound preform in the mold cavity. The bladder was heat-sealed and folded at the end, as shown in Figure 8.

B-RTM setup for manufacturing a tubular section is shown in Figure 8. The RTM process, utilizing a pressure pot, was chosen to inject the resin in the mold. The pressure pot system used allowed a maximum injection pressure of 5 bar. The used pressure pot system is convenient while injecting small parts as it uses pre-mixed resin in relatively small quantities compared to a dedicated RTM machine with mixing in the head. Additionally, for the fast-curing resins, as the setup uses disposable pipes, there were no risks of damaging anything as the pipes containing cured resin will be thrown away after use.

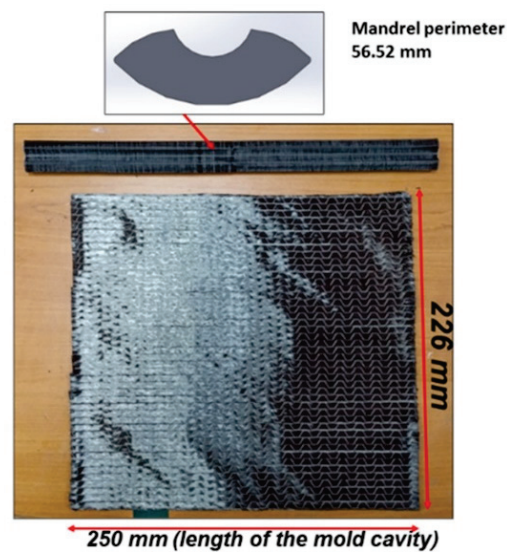


Figure 6. Section, mandrel, and preform dimensions.

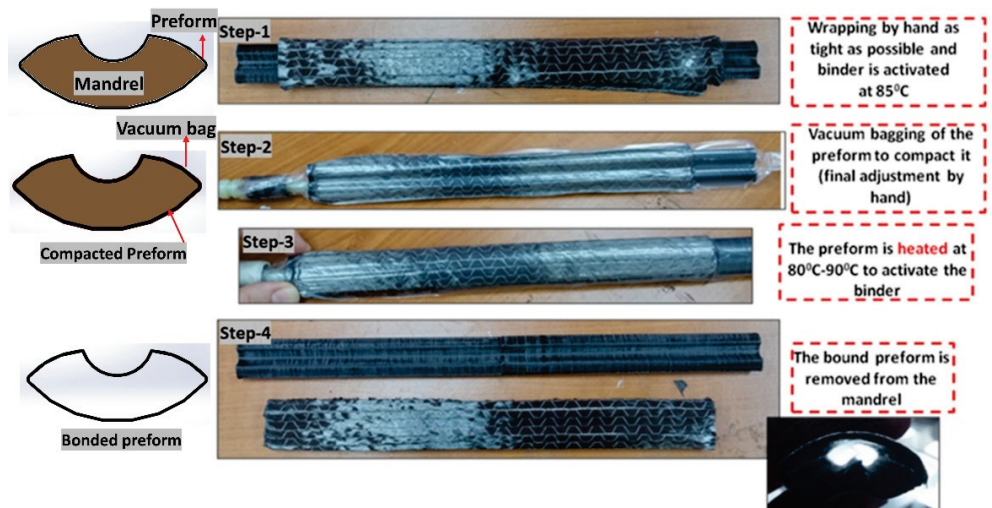


Figure 7. Fabrication steps to manufacture a tubular section.

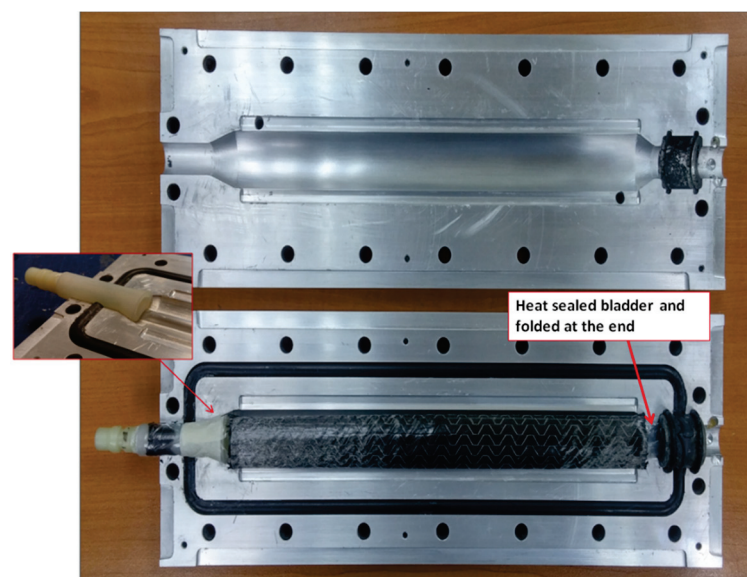


Figure 8. Preform positioning in the mold.

Figure 9 shows the complete test set-up for injecting a tubular section. As can be seen from Figure 9, the mold had a resin inlet, which was connected to the injection pressure pot, which, in turn, had compressed air from the air compressor. Additionally, there was a separate vacuum pot with an adjustable gauge to control the vacuum level in the outlet and a bladder valve attached to the air pressure line with a maximum capacity of 6 bar. At first, the preform was compacted with the pressurization of the inflated nylon bladder, followed by resin injection and further consolidation at higher bladder pressure to achieve a higher fiber volume fraction.

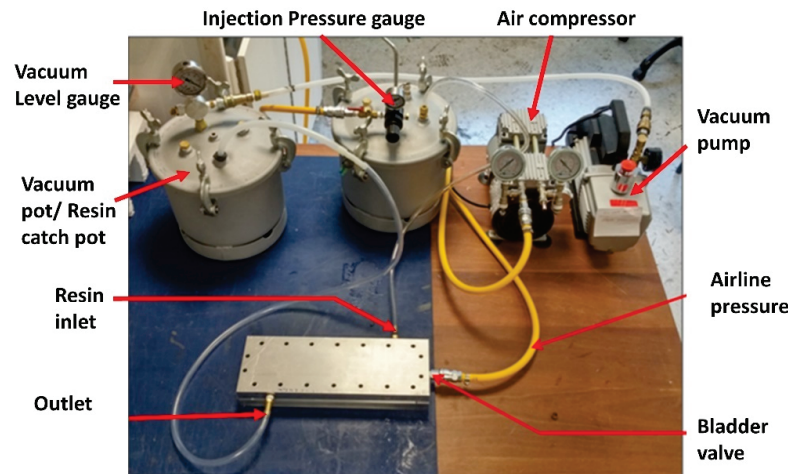


Figure 9. B-RTM setup for manufacturing a tubular section.

3. Experiments

The B-RTM process is influenced by many process parameters [9]. For the RTM process, the major process parameters that affect the impregnation, filling, quality, and fiber volume fraction of the laminates are typically (1) temperature of the mixed resin during the injection, (2) temperature of the mold, and (3) resin injection pressure or flow rate. For B-RTM, in addition to the abovementioned parameters, two more parameters arise due to the pressurization of the bladder, namely, the bladder pressure during the injection and the bladder pressure after the injection, i.e., during the curing stage [9]. There are a few studies carried out optimizing these parameters for high-permeability fabrics, such as mats, but a complete study is required to be carried out for low-permeability, Thin NCCF fabrics with novel Elium[®] and the epoxy resin.

3.1. Initial Trials

The initial trials of manufacturing Thick and Thin NCCF were carried out using the acrylic mold to check the draping and the impregnation behavior of the fabric preform and the injection strategy with TP and TS matrices. The advancement of the flow front was observed using a high-speed camera, which was set up perpendicularly to the transparent acrylic mold. An example of the above is shown in Figure 10, where the Thin NCCF preform was injected with epoxy matrix (Epolam 5015/5015).

Figure 10 shows the injection flow fronts at time $t = 0$ s, 10 s, 4 min, and 6 min. There were no anomalies observed, and the complete impregnation was achieved with the injection pressure of 3.8 bar and bladder pressure of 4 bar.

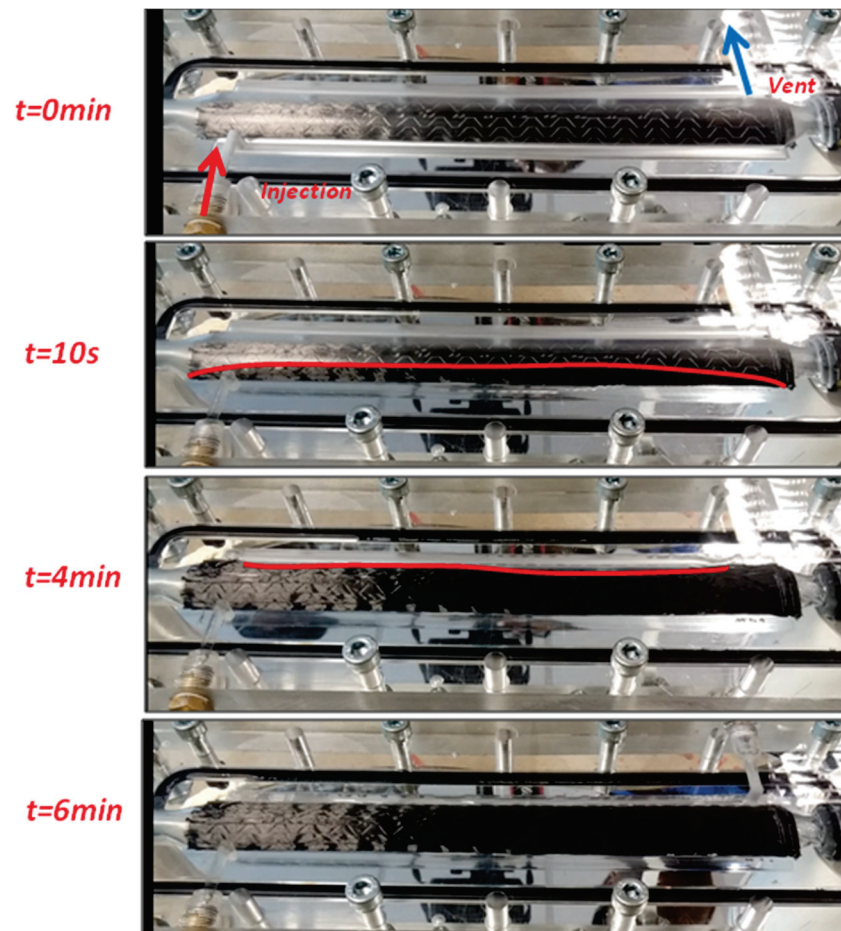


Figure 10. Flow front advancement for a tubular section using B-RTM process in an acrylic mold.

It should be noted that the whole study first started with a plain, glass weave followed by Thick and Thin NCCFs. As inferred from literature, it was essentially required that the bladder pressure should be higher than the resin injection pressure; otherwise, there are high chances that the bladder will collapse [9]. Hence, for all the trials, the bladder pressure was kept higher than the resin injection pressure. At this stage of the study, the major idea was to check the injection strategy, mold design used, and preform drapability. The consolidation of bladder pressure was also varied, depending on the injection and bladder pressure used. In total, 32 tubular beam sections were manufactured during the trial stage, and some of them are shown in Figure 11. Figure 11a shows the different manufactured hollow tubes, while Figure 11b shows the differences in the tube cross-sections with different consolidation pressures. Figure 11c–f shows the different views of tube and its cross-section depicting the uniform cross section and excellent surface finish. Additionally, the effect of bladder consolidation pressure can be seen with two different tubular sections consolidated at 2 bar and 5.5 bar, respectively (refer to Figure 11b). The target tubular section thickness was 1.5 mm and the ones achieved were 1.9 mm with 2 bar and 1.52 mm with 5.5 bar, respectively. The tubular section that was consolidated at 5.5 bar had 57% fiber volume fraction (V_f) compared to 51% of the one that was consolidated at 2 bar. It should be noted that the conventional B-RTM approach for manufacturing composite tubes with high-permeability fibers with a pressure difference of 2 bars was found not suitable for injecting low-permeability thin plies and the preform was not fully filled at the outlet even with the injection time of 22 min (Refer Figure 12).

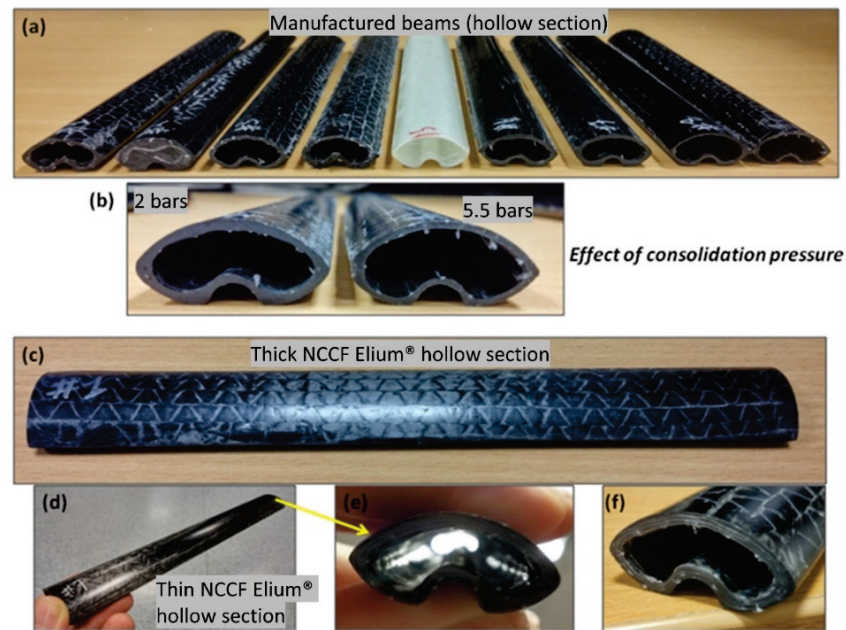


Figure 11. Manufactured Thin and Thick NCCF Elium[®] Composite tubular sections (beams) and effect of consolidation pressure (a) different beams (b) effect of consolidation pressure (c) thick NCCF Elium hollow section (d) Thin NCCF Elium hollow section (e,f) cross section of thin Elium tube.

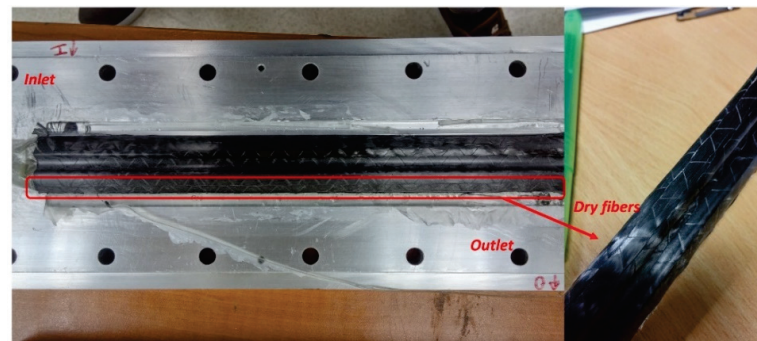


Figure 12. Cured part with process parameters (injection pressure 2 bar and bladder pressure 4 bar) showing unfilled preform at the outlet after the injection time of 22 min.

3.2. Process Parameters' Optimisation

Once the mold design and the injection strategy were checked to be working fine, the next major step was to identify the fixed and variable process parameters and optimize the variables. The identified fixed and variable process parameters are depicted in Table 2. The fixed parameters included the FOE-sized, Thin NCCF Fabrics (0/45) for the whole optimization study, and Elium[®] 150 as a TP resin with a fixed 2.5% benzoyl peroxide (BPO) as an initiator. Additionally, as the resin was cured at room temperature, the mold was kept at an ambient temperature. Furthermore, the post-fill bladder pressure was fixed at 5.5 bar for consolidation purpose, while the post-fill inlet boundary condition (BC) was clamped.

The important variable parameters, which were required to be optimized, were identified as filling resin pressure and filling bladder pressure, as recommended by various researchers [9,32,33]. Along with these major parameters, post-fill resin pressure, as well as filling and post-filling outlet boundary conditions, were required to be optimized. These parameters will not affect the impregnation time, but the quality of the tubular sections can be affected using different boundary conditions. The planned optimization cycle for producing high-quality and faster injection tubular sections is depicted in Table 3. The “tests” are referred as the specific condition at which the manufacturing was carried out.

Table 2. Fixed and Variable injection and post-injection parameters for manufacturing a tubular section.

Fixed Injection and Post-Injection Parameters		Variable Injection and Post-Injection Parameters
Post-fill bladder pressure	5.5 bar	Filling resin pressure
Post-fill inlet Boundary condition (BC)	Clamp	Filling bladder pressure
Fabric sizing	Thermoplastic FOE	Post-fill resin pressure
Mold temperature	Ambient	Filling outlet BC
BPO (%)	2.5%	Post-filling outlet BC

Table 3. Test Plan for optimizing B-RTM parameters for a tubular section.

Test	1	2	3	4	5	6	7
Bladder pressure during filling (bar)	4	4	3.8	3.8	3.8	4.2	4
Resin pressure during filling (bar)	4	4	3.8	4	4	4	3.8
Resin pressure post filling (bar)	500 mbar vacuum	Atm pressure	3	0	3	0	3

Several test plans, shown in Table 3, served to compare the various process parameter optimization schemes to finally decide the optimal strategy to inject a full tubular section. In this study, 49 tubular sections were manufactured using different injection, bladder, and consolidation pressures and with different clamping strategies. Below, sub-sections will give more insight into the various test cases. Out of 49 tubular sections manufactured, seven of them represented one of the particular test cases, as discussed in Table 3. The manufactured tubes were reproducible in terms of final thickness (1.5 ± 0.05 mm) and the fiber volume fractions (e.g., $54 \pm 0.8\%$) for a particular experiment repeated with the same boundary conditions.

3.2.1. Process Parameters during Injection

In the first attempt, process parameters during injection were optimized. Table 4 shows the details of all the variants of the optimization trials. It should be noted that for each test at least three beams were manufactured to check the accuracy of the particular test case. Test 6 and Test 2 showed the two comparison injection schemes. For Test 6, the bladder pressure > resin injection pressure, while, for Test 2, the injection and bladder pressure were kept the same. An important observation was that the tubular section injected with the same bladder and resin pressure was injecting faster primarily because of less resistance to the resin flow due to comparable bladder pressures, whereas the injection time was 1 min longer in the case of the tubular section manufactured with a higher bladder pressure. The quality of manufactured tubular sections was investigated by both microscopy and ASTM D792/D2734 and found to be very similar for both injection schemes, although a slightly higher volume fraction was attributed to better consolidation in the case of Test 2. The tubular section was cut using a water jet diamond cutter at both the inlet and the vent positions. At least three samples were tested for both the inlet and outlet side to quantify the void content. The standard void tests were conducted on the manufactured tube following ASTM D792 [34] and ASTM D2734-09 [35]. The microscopy images of the Test 6 tubular section can be seen in Figure 13. Void content was calculated using a digital microscopy technique using an Olympus SZX7 to cover the full cross section of the tubular section. The images were captured using a digital camera and the mosaic images were constructed by joining the images obtained using the microscope. This technique ensured a complete observation of the sample showing the distribution of voids [36].

Table 4. Results from the process parameter optimization for various test cases for manufacturing a tubular section.

	Test 1	Test 2	Test 3	Test 4	Test 5	Test 6	Test 6	Test 7	
Fibers			Thin NCCF 100/100 g/m ² (Elium [®] sized)					Thin NCCF 100/100 g/m ² (Epoxy sized)	Thin NCCF 100/100 g/m ² (Elium [®] sized)
Resin			Elium [®] 150					Epolam 5015/5015	Elium [®] 150
Bladder pressure (bar)	4	4	3.8	3.8	3.8	4.2	4.2	4	
Resin pressure (bar)	4	4	3.8	4	4	4	4	3.8	
Bladder pressure post-fill (bar)	5.5	5.5	5.5	5.5	5.5	5.5	5.5	5.5	
V _f (%)	57 ± 0.22	55 ± 0.35	57 ± 0.34	59 ± 0.72	49.2 ± 0.31	57 ± 0.21	62 ± 0.27	54 ± 0.21	
Injection time	5 min 35 s ± 21 s	3 min 40 s ± 11 s	4 min 20 s ± 14 s	2 min 30 s ± 8 s	50 s ± 3 s	4 min 4 s ± 12 s	6 min 30 s ± 12 s	6 min 30 s ± 10 s	
Clamping and consolidation strategy	Clamp inlet at 3 min and increase bladder pressure to 5.5 bar.	Clamp inlet at 6 min 30 s and increase bladder pressure to 5.5 bar	Clamp the outlet and let the pressure build in with resin pressure at 3 bar. Increase bladder pressure to 5.5 bar	Clamp inlet at 3 min and increase bladder pressure to 5.5 bar	Clamp the outlet and let the pressure build in with resin pressure at 3 bar. Increase bladder pressure to 5.5 bar	Clamp inlet at 8 min and increase bladder pressure to 5.5 bar	Clamp inlet at 10 min and increase bladder pressure to 5.5 bar	Clamped outlet and let the pressure build in with resin pressure at 3 bar. Increase bladder pressure to 5.5 bar	
Void Content (%) (Microscopy)	Inlet	<3	<2	<2	<2	<2	<3	<2	
	Outlet	<2	<2	<2	<2	<1	<2	<2	
Void Content (%) (ASTM D792/D2734)	Inlet	2.31 ± 0.53	1.14 ± 0.13	1.34 ± 0.19	1.19 ± 0.08	1.25 ± 0.13	2.31 ± 0.45	1.09 ± 0.11	
	Outlet	1.63 ± 0.27	1.31 ± 0.09	1.54 ± 0.30	1.07 ± 0.12	0.93 ± 0.11	1.04 ± 0.14	1.41 ± 0.16	

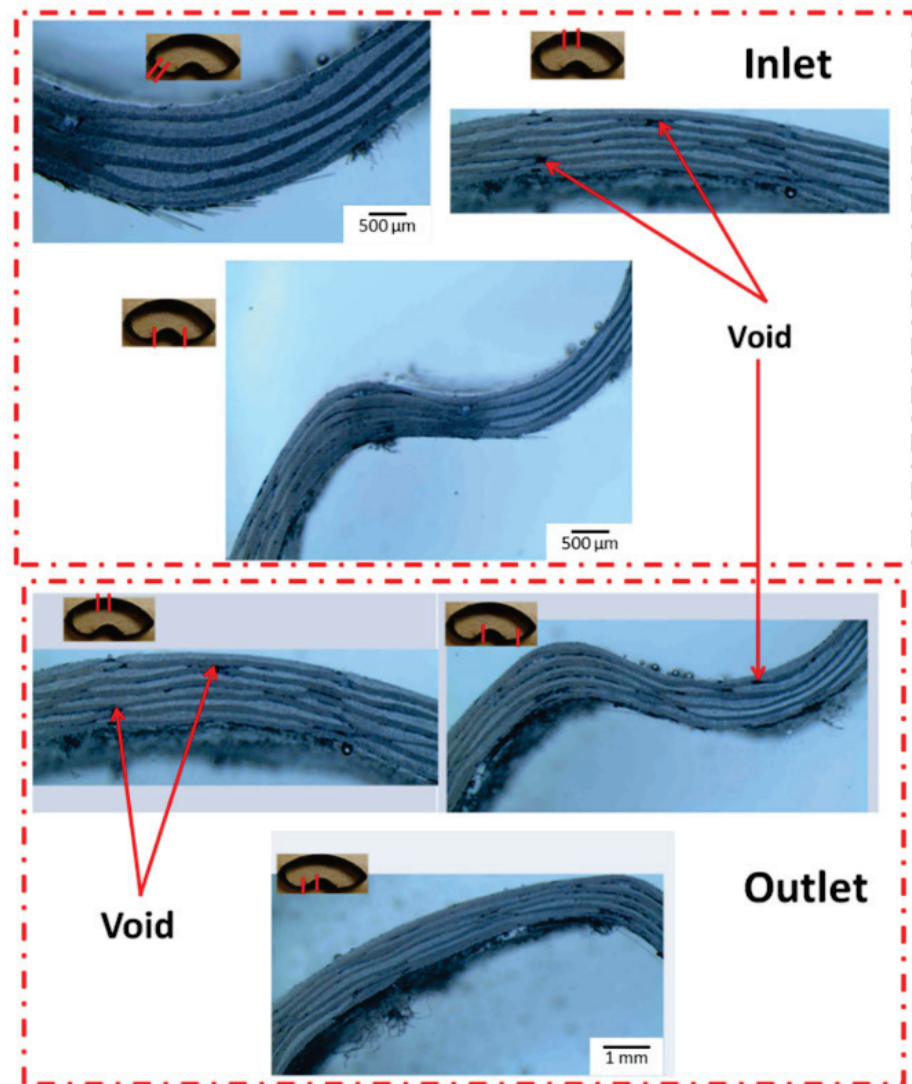


Figure 13. Microscopic images of the tubular section (Test 6) showing minimal void sites at multiple locations of the inlet and outlet sections.

3.2.2. Effect of Consolidation Pressure

Another important aspect of the B-RTM process is to check the effect of consolidation pressure during manufacturing [9,32,33]. To check the effect, the results of the tubular section manufactured using Test 4 and Test 5 parameters were compared. As can be seen from Table 4, during Test 5, after the injection was completed, the outlet was clamped, and the pressure was still building in at 3 bar. Therefore, the consolidation pressure was 2.5 bar (Bladder pressure–Resin pressure) as opposed to 4.5 bar in Test 4 where the inlet was clamped, and the bladder pressure was subsequently increased to 5.5 bar. Test 5 with 2.5 bar consolidation pressure yielded a very low fiber volume fraction of 49% compared to 4.5 bar of consolidation pressure where 59% V_f was achieved. Although a lower injection time was 2.5 times faster, injection was achieved, which is desirable for mass production of composite tubular sections. Still, there was a huge sacrifice in terms of fiber volume fraction, which may affect the mechanical performance. In our recent research, we showcased the effect of the fiber volume fraction, fiber architectures, and the resin systems on the mechanical and vibration damping properties of the tubular composite shafts [13–15,37]. Additionally, it was noticed that when the resin pressure was kept high, there were instances of the bladder collapsing, as shown in Figure 14.

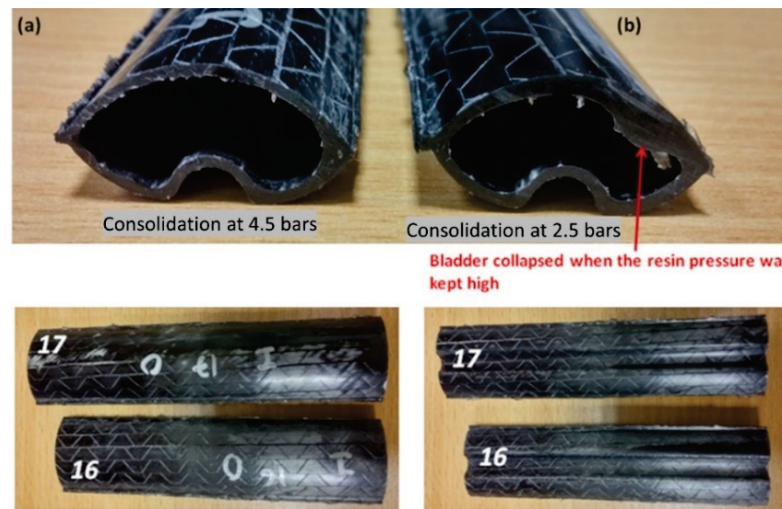


Figure 14. Effect of consolidation pressure on tubular sections manufactured using B-RTM process (a) consolidation at 4.5 bar (b) consolidation at 2.5 bar.

3.2.3. Effect of Outlet Boundary Conditions (BC)

In the majority of the RTM process, a vacuum was used as an aid in removing any entrapped air from the fabric preform during the preform compaction prior to the injection and during the complete curing cycle as well as the consolidation phase. Herein, Test 1 was carried out with the bladder and resin pressure at 4 bar during the injection phase. The inlet was clamped at 11 min, and the bladder pressure was increased to 5.5 bar. However, at the outlet, a 500-mbar vacuum was kept throughout the curing cycle. However, in the case of Test 2, the outlet was left at atmospheric pressure. The results, as shown in Table 4, conveyed that there was no significant effect of outlet boundary conditions during the B-RTM process. The void contents measured using both techniques were similar for both the testing conditions, although it was noticed that the tubular sections with the vacuum as the outlet BC had lesser surface porosities.

3.2.4. Effect of Matrix Systems

Although the main idea was to carry out the entire study with TP Elium[®] resin, a few tubular sections were also manufactured with TS epoxy Epolam 5015/5015 resin for baseline comparison. Test 6, which was carried out with Elium[®] resin, was repeated with the same process parameters but with TS epoxy resin. The NCCF epoxy tubular section took a slightly longer injection time than the NCCF Elium[®] tubular section due to the lower viscosity in the case of the Elium[®] 150 resin (100 cP) compared to 210 cP in the case of the Epolam 5015 resin. Additionally, the fiber volume fraction achieved with epoxy resin was higher due to the longer curing time of 24 h compared to 1.5 h in the case of Elium[®] resin. The excess resin was squeezed out of the laminate, as the epoxy resin had longer gel time resulted and, hence, the laminates had comparatively higher V_f .

3.3. Challenges and Solutions

Tubular sections were successfully manufactured using the above-discussed parameters with Thin NCCF (0/45) fibers as reinforcement and Elium[®] and epoxy as the matrices. However, it was noticed that there was still a huge room for improvement to fasten the injection process and to eliminate the resin pockets, which were observed in many trials during the optimization process. It was decided to use a larger preform (370 mm × 250 mm) compared to the older preforms of 330 mm × 250 mm dimensions used in the optimization study. With a larger preform, corners are seen to be better filled (refer to Figure 15) but still were slightly thicker than the top surface as the friction force with the bladder was higher in the corners (corner thickening effect), which is always the case with tubular geometries manufactured with concave tools [38]. The sections that were manufactured with some

collapsed bladder conditions tended to have more resin at the corners as well as at the collapsed region of the tube in the vicinity of the bladder collapse point. The thickness of the tube was found to be up to 2.1 mm as opposed to 1.5 mm due to a significant chunk of resin formation at the corners. To quicken the injection process, both the resin and bladder pressures during the injection were reduced with an aim to reduce the compactness of the fabric preform, which lowers the permeability of the fabric and, in turn, makes the injection longer. As seen from Table 5, Test 8 and Test 9 were repeated thrice with both the resin systems (TP and TS). During Test 8, higher resin injection and bladder pressures compared to Test 9 were used.

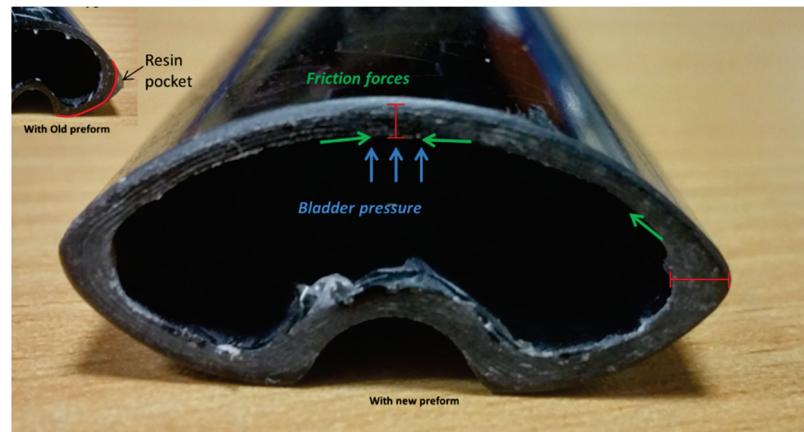


Figure 15. Tubular section showing better-filled corners with a larger preform.

Table 5. Injection results during B-RTM process with reduced bladder and injection pressures.

	Test 8	Test 8	Test 9	Test 9
Fibers	Thin NCCF Epoxy sized	Thin NCCF Elium [®] sized	Thin NCCF Epoxy sized	Thin NCCF Elium [®] sized
Resin	Epoxy	Elium [®] 150	Epoxy	Elium [®] 150
Bladder pressure (bar)	4.2	4.2	2.2	2.2
Resin pressure (bar)	4	4	2	2
Bladder pressure post-fill (bar)	5.5	5.5	5.5	5.5
V _f (%)	53	52	56	55
Injection time	4 min	2 min 29 s	1 min 5 s	51 s
Clamping strategy	Clamp inlet at 5 min and increase bladder pressure to 5.5 bar.	Clamp inlet at 4 min and increase bladder pressure to 5.5 bar.	Clamp inlet at 2 min and increase bladder pressure to 5.5 bar.	Clamp inlet at 2 min and increase bladder pressure to 5.5 bar.
	Clamp outlet at 7 min	Clamp outlet at 5 min 30 s	Clamp outlet at 5 min 30 s	Clamp outlet at 4 min 30 s
	Outlet kept at vacuum 500 mbar	Outlet kept at vacuum 500 mbar	Outlet kept at vacuum 500 mbar	Outlet kept at vacuum 500 mbar

Lower injection and bladder pressures quickened the injection process as the preform was less compacted. Bladder pressure significantly influenced the compaction of the fabric preform. With the higher bladder pressure, the layers of the preform were pressed, and the permeability of the compressed preform was reduced and affected the fiber impregnation time. During the draping, the preform touched the plane surface of the mold first. Surface pressure was created along with the frictional force, which existed due to the friction between the layers of the tubular section preform and the mold cavity surface. Preferably, this frictional force should be lower than the tensile forces, which help in the movement of

the preform into the edges of the mold cavity. If not, the drapability would be poorer with surface pressure preventing the draping into the edges [39]. There was lower permeability on the surface than the edges due to the strong fiber compaction at the planar surfaces. Hence, the choice of the bladder as well as reducing the bladder and resin pressure was significant for the desired flow front advancement.

Based on the detailed experimental investigation at different boundary conditions, a moldability zone diagram was constructed, as shown in Figure 16, showing an optimal zone for effectively processing Elium- and Epoxy-based composite tubes with a B-RTM process. Different zones with their boundary conditions, as shown in Figure 16, are explained below.

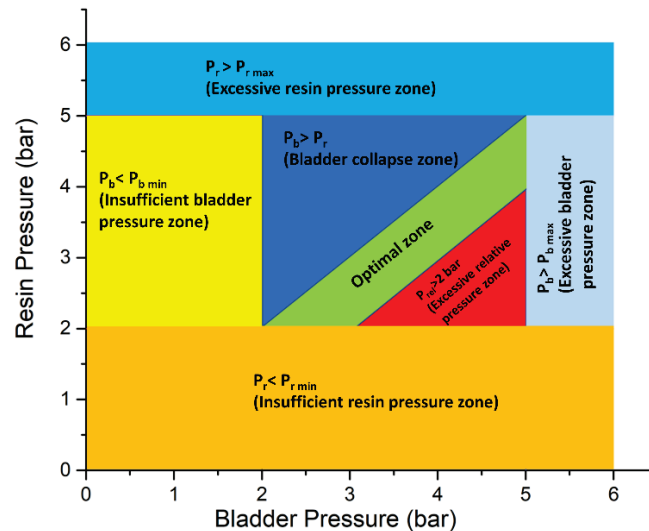


Figure 16. Manufacturing optimization zone diagram at different pressure boundary conditions during B-RTM process.

1. Insufficient resin pressure zone (Resin Pressure $P_r < \text{Minimum Resin Pressure } P_{r \min}$): Minimum of 2-bar resin pressure was required to impregnate the preform with low-permeability, thin-ply carbon fabrics. Usage of $P_r < 2$ bar resulted in unfilled parts and a significantly higher filling time.
2. Insufficient bladder pressure zone (Bladder Pressure $P_b < \text{Minimum bladder Pressure } P_{b \min}$): The minimum bladder pressure required to fully inflate the nylon bladder was 2 bar below which the preform was not fully compacted, there was race tracking of the resin, and the parts remained unfilled. It should be noted that the minimum bladder pressure is dependent on the part geometry, which held true for the current investigation.
3. Excessive bladder pressure zone (Bladder Pressure $P_b > \text{Maximum bladder Pressure } P_{b \max}$): This zone should be avoided as the bladder pressure above 5 bar led to excessive compaction of the preform and was undesirable, especially while using the low-permeability, thin-ply preforms.
4. Excessive resin pressure zone (Resin Pressure $P_r > \text{Maximum Resin Pressure } P_{r \min}$): Excessively higher resin pressure is to be avoided to minimize the chances of race tracking and wrinkling of the fabric preform.
5. Bladder collapse zone (Bladder Pressure $P_b > \text{Resin Pressure } P_r$): The bladder should not be kept higher than the resin pressure to avoid the collapsing of the preform during the injection.
6. Excessive relative pressure zone: The difference between bladder and resin pressures should be kept smaller. The parts injected at a higher pressure difference will significantly increase the injection time.

The optimization process for the tubular section deduced the following findings: Bladder pressure determines the preform compaction. It would be easy to impregnate

the fabrics at a lower bladder pressure, as that will cause less compaction of the fabric. However, at a lower bladder pressure it should be noted that, if resin pressure is higher than bladder pressure, there are chances of a bladder collapsing. Based on this optimization, the concluded scheme for injection of a tubular section is as shown below (Refer to Figure 17).

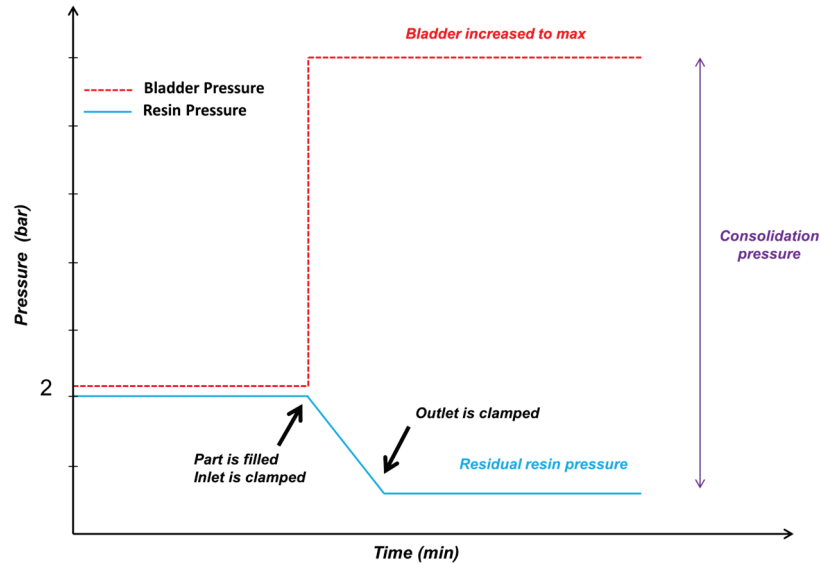


Figure 17. Deduced scheme for injecting a thin-ply tubular section with optimized parameters and boundary conditions.

1. Throughout the injection phase, bladder pressure (2.2 bar) was kept higher than the injection pressure (2 bar).
2. When the part was filled, then the inlet was clamped and, simultaneously, the bladder was increased to a maximum of 5.5 bar.
3. Clamp the outlet after step 2, such that maximum consolidation pressure is achieved.

4. Conclusions

The B-RTM process was used to successfully manufacture a complex tubular section with thin-ply NCFs as the reinforcement material and thermoplastic Elium resin as the matrix. A detailed case study was presented, showing the specifics regarding the effective mold design, recommended process parameters, associated challenges, and the proposed solutions. Following are the salient findings from the research case study.

1. An injection scheme was deduced to inject successfully the Thin NCCF Elium[®] and Epoxy composite sections. During the injection phase, bladder pressure (2.2 bar) should be kept higher than the resin injection pressure (2 bar). Once the part is filled, then the inlet should be clamped and, simultaneously, the bladder should be increased to a maximum of 5.5 to 6 bar or higher, depending on the final fiber volume fraction requirement. Further, the outlet should be clamped to achieve maximum consolidation pressure.
2. Using the optimized B-RTM process parameters, the tubular composite sections with minimal void content (<1%) and higher fiber volume fraction (>55%) can be manufactured using fibers with lower permeability and with thermoset and thermoplastic matrices of viscosity ≤ 250 cP.
3. Higher consolidation pressure is key to achieve an optimal fiber volume fraction, although there will be some sacrifice in terms of the injection speed. When the resin pressure was kept high at ≥ 3.8 bar, there were instances of the bladder collapsing.
4. There was no significant effect of outlet boundary conditions (500-mbar vacuum at an outlet or atmospheric pressure) during the B-RTM process. Both conditions had

similar fiber volume fractions and void content, barring lesser surface porosities in the case of the former.

Author Contributions: Conceptualization, S.K.B. and P.P.; methodology, S.K.B. and P.P.; investigation, S.K.B., P.P. and G.G.; experiments, S.K.B., P.P. and G.G.; investigation, S.K.B., P.P. and G.G.; writing—original draft preparation, S.K.B.; writing—review and editing, S.C.J., P.G. and K.F.L.; supervision, S.C.J., P.G. and K.F.L.; funding acquisition, S.C.J. and K.F.L. All authors have read and agreed to the published version of the manuscript.

Funding: The authors would like to acknowledge the financial support from Nanyang Technological University, Singapore, and Arkema, France, for financial support under the RCA18/46. This research was also supported by A*STAR under the Research Innovation Enterprise (RIE) 2020 Plan, Advanced Manufacturing and Engineering (AME) Domain—Industry Alignment Fund—Pre-positioning (IAF-PP) Polymer Matrix Composites Programme, Grant number A19C9a0044, Work Package 1-2.

Institutional Review Board Statement: Not applicable.

Informed Consent Statement: Not applicable.

Data Availability Statement: The data presented in this study are available on request from the corresponding author.

Acknowledgments: The authors would like to acknowledge Nanyang Technological University, Singapore; ARKEMA, France; and Agency for Science, Technology and Research (A*STAR) Singapore.

Conflicts of Interest: The authors declare no conflict of interest.

References

1. Kaynak, C.; Kas, Y.O. Effects of injection pressure in resin transfer moulding (rtm) of woven carbon fibre/epoxy composites. *Polym. Polym. Compos.* **2006**, *14*, 55–64. [CrossRef]
2. Van Rijswijk, K.; Bersee, H.E.N. Reactive processing of textile fiber-reinforced thermoplastic composites—An overview. *Compos. Part A Appl. Sci. Manuf.* **2007**, *38*, 666–681. [CrossRef]
3. Sozer, E.M.; Simacek, P.; Advani, S.G. 9—Resin transfer molding (rtm) in polymer matrix composites. In *Manufacturing Techniques for Polymer Matrix Composites (pmcs)*; Woodhead Publishing: Cambridge, UK, 2012; pp. 245–309.
4. Hammami, A.; Al-Zarouni, A. Investigation of the rtm/bladder molding process. In Proceedings of the 13th International Conference on Composite Materials, Beijing, China, 25–29 June 2001.
5. Bhudolia, S.K.; Perrotey, P.; Joshi, S.C. Optimizing polymer infusion process for thin ply textile composites with novel matrix system. *Materials* **2017**, *10*, 293. [CrossRef] [PubMed]
6. BBhudolia, S.K.; Fischer, S.; He, P.G.; Yue, C.Y.; Joshi, S.C.; Yang, J.L. Design, manufacturing and testing of filament wound composite risers for marine and offshore applications. *Mater. Sci. Forum* **2015**, *813*, 337–343. [CrossRef]
7. Son, D.S.; Chang, S.H. Evaluation of modeling techniques for a type iii hydrogen pressure vessel (70 mpa) made of an aluminum liner and a thick carbon/epoxy composite for fuel cell vehicles. *Int. J. Hydrogen Energy* **2012**, *37*, 2353–2369. [CrossRef]
8. Neacsu, V.; Fanucci, J.; Balonis, R.; Stronck, J. Pultrusion and resin film infusion (rfi) of bi-angle thin ply ncf. *JEC Compos. Mag.* **2011**, *68*, 59–61.
9. Lehmann, U.; Michaeli, W. Cores lead to an automated production of hollow composite parts in resin transfer moulding. *Compos. Part A Appl. Sci. Manuf.* **1998**, *29*, 803–810. [CrossRef]
10. Schillfahrt, C.; Fauster, E.; Schledjewski, R. Influence of process pressures on filling behavior of tubular fabrics in bladder-assisted resin transfer molding. *Adv. Manuf. Polym. Compos. Sci.* **2017**, *3*, 148–158. [CrossRef]
11. Schillfahrt, C.; Fauster, E.; Schledjewski, R. A methodology for determining preform compaction in bladder-assisted resin transfer molding with elastomeric bladders for tubular composite parts. *Int. J. Mater. Form.* **2019**, *12*, 1–15. [CrossRef]
12. Schillfahrt, C.; Fauster, E.; Schledjewski, R. Optical permeability measurement on tubular braided reinforcing textiles. In Proceedings of the 20th International Conference on Composite Materials, Copenhagen, Denmark, 19–24 July 2015.
13. Bhudolia, S.K.; Gohel, G.; Kantipudi, J.; Leong, K.F.; Gerard, P. Mechanical performance and damage mechanisms of thin rectangular carbon/ elium[®] tubular thermoplastic composites under flexure and low-velocity impact. *Thin-Walled Struct* **2021**, *165*, 107971. [CrossRef]
14. Bhudolia, S.K.; Gohel, G.; Kantipudi, J.; Leong, K.F.; Gerard, P. Manufacturing and investigating the load, energy and failure attributes of thin ply carbon/elium[®] thermoplastic hollow composites under low-velocity impact. *Mater. Des.* **2021**, *206*, 109814.
15. Bhudolia, S.K.; Gohel, G.; Leong, K.F.; Joshi, S.C. Damping, impact and flexural performance of novel carbon/elium[®] thermoplastic tubular composites. *Compos. Part B Eng.* **2020**, *203*, 108480. [CrossRef]
16. Camanho, P.; Arteiro, A.; Turon, A.; Costa, J.; Guillaumat, G. Structural integrity of thin ply laminates. *JEC Compos. Mag.* **2012**, *71*, 49–50.

17. Tsai, S.; Papila, M. Thin ply-ncf: Design for deformation through anisotropy. *JEC Compos. Mag.* **2011**, *68*, 66–67.
18. Sihh, S.; Kim, R.; Kawabe, K.; Tsai, S. Experimental studies of thin-ply laminated composites. *Compos. Sci. Technol.* **2007**, *67*, 996–1008. [CrossRef]
19. Bhudolia, S.K.; Perrotey, P.; Joshi, S.C. Experimental investigation on suitability of carbon fibre thin plies for racquets. *Proc. Inst. Mech. Eng. Part P. J. Sports Eng. Technol.* **2015**, *230*, 64–72. [CrossRef]
20. Bhudolia, S.K.; Perrotey, P.; Joshi, S.C. Enhanced Vibration damping and dynamic mechanical characteristics of composites with novel pseudo-thermoset matrix system. *Compos. Struct.* **2017**, *179*, 502–513. [CrossRef]
21. Matadi Boumbimba, R.; Coulibaly, M.; Khabouchi, A.; Kinvi-Dossou, G.; Bonfoh, N.; Gerard, P. Glass fibres reinforced acrylic thermoplastic resin-based tri-block copolymers composites: Low velocity impact response at various temperatures. *Compos. Struct.* **2017**, *160*, 939–951. [CrossRef]
22. Cousins, D.S.; Suzuki, Y.; Murray, R.E.; Samaniuk, J.R.; Stebner, A.P. Recycling glass fiber thermoplastic composites from wind turbine blades. *J. Clean. Prod.* **2019**, *209*, 1252–1263. [CrossRef]
23. Khalili, P.; Blinzler, B.; Kádár, R.; Bisschop, R.; Försth, M.; Blomqvist, P. Flammability, smoke, mechanical behaviours and morphology of flame retarded natural fibre/elium® composite. *Materials* **2019**, *12*, 2648. [CrossRef]
24. Bhudolia, S.K.; Gohel, G.; Joshi, S.C.; Leong, K.F. Quasi-static indentation response of core-shell particle reinforced novel nccf/elium® composites at different feed rates. *Compos. Commun.* **2020**, *21*, 100383. [CrossRef]
25. Gohel, G.; Bhudolia, S.K.; Elisetty, S.B.S.; Leong, K.F.; Gerard, P. Development and impact characterization of acrylic thermoplastic composite bicycle helmet shell with improved safety and performance. *Compos. Part B Eng.* **2021**, *221*, 109008. [CrossRef]
26. Kazemi, M.E.; Shanmugam, L.; Li, Z.; Ma, R.; Yang, L.; Yang, J. Low-velocity impact behaviors of a fully thermoplastic composite laminate fabricated with an innovative acrylic resin. *Compos. Struct.* **2020**, *250*, 112604. [CrossRef]
27. Shanmugam, L.; Kazemi, M.E.; Rao, Z.; Lu, D.; Wang, X.; Wang, B.; Yang, L.; Yang, J. Enhanced mode I fracture toughness of UHMWPE fabric/thermoplastic laminates with combined surface treatments of polydopamine and functionalized carbon nanotubes. *Compos. Part B Eng.* **2019**, *178*, 107450. [CrossRef]
28. Bhudolia, S.K.; Joshi, S.C.; Bert, A.; Gohel, G.R.; Raama, M. Energy characteristics and failure mechanisms for textile spread tow thin ply thermoplastic composites under low-velocity impact. *Fibers Polym.* **2019**, *20*, 1716–1725. [CrossRef]
29. Bhudolia, S.K.; Perrotey, P.; Joshi, S.C. Mode I fracture toughness and fractographic investigation of carbon fibre composites with liquid methylmethacrylate thermoplastic matrix. *Compos. B Eng.* **2018**, *134*, 246–253. [CrossRef]
30. Bhudolia, S.K.; Joshi, S.C. Low-velocity impact response of carbon fibre composites with novel liquid methylmethacrylate thermoplastic matrix. *Compos. Struct.* **2018**, *203*, 696–708. [CrossRef]
31. Bhudolia, S.K.; Gohel, G.; Fai, L.K.; Barsotti, R.J., Jr. Investigation on ultrasonic welding attributes of novel carbon/elium® composites. *Materials* **2020**, *13*, 1117. [CrossRef]
32. Ghiasi, H.; Lessard, L.; Pasini, D.; Thouin, M. Optimum structural and manufacturing design of a braided hollow composite part. *Appl. Compos. Mater.* **2010**, *17*, 159–173. [CrossRef]
33. Pham, X.-T.; Trochu, F. Analysis of the consolidation in flexible bladder process for thin composite parts by finite element method. *J. Reinf. Plast. Compos.* **2000**, *19*, 182–218. [CrossRef]
34. *Astm d792 Standard Test Methods for Density and Specific Gravity (Relative Density) of Plastics by Displacement*; ASTM International: West Conshohocken, PA, USA, 2008.
35. *Astm d2734-09 Standard Test Methods for Void Content of Reinforced Plastics*; ASTM International: West Conshohocken, PA, USA, 2009.
36. Paciornik, S.; Mauricio, M.H.P. Digital Imaging. In *Asm Handbook: Metallography and Microstructures*; ASM International: Materials Park, OH, USA, 2004.
37. Gohel, G.; Bhudolia, S.K.; Leong, K.F.; Gerard, P. On the structural damping response of hollow carbon composite shafts with room temperature curable novel acrylic liquid thermoplastic resin. *Compos. Commun.* **2021**, 100990. [CrossRef]
38. Baran, I.; Cinar, K.; Ersoy, N.; Akkerman, R.; Hattel, J.H. A review on the mechanical modeling of composite manufacturing processes. *Arch. Comput. Methods Eng.* **2017**, *24*, 365–395. [CrossRef] [PubMed]
39. Crivelli Visconti, I.; Langella, A. Analytical modelling of pressure bag technology. *Compos. Manuf.* **1992**, *3*, 3–6. [CrossRef]

Article

Effect of Processing Temperature and the Content of Carbon Nanotubes on the Properties of Nanocomposites Based on Polyphenylene Sulfide

Kamil Dydek ^{1,*}, Paulina Latko-Durałek ¹, Agata Sulowska ¹, Michał Kubiś ², Szymon Demski ¹, Paulina Kozera ¹, Bogna Sztorch ³ and Anna Boczkowska ¹

- ¹ Faculty of Materials Science and Engineering, Warsaw University of Technology, 141 Wołoska, 02-507 Warsaw, Poland; paulina.latko@pw.edu.pl (P.L.-D.); agata.sulowska.stud@pw.edu.pl (A.S.); szymon.demski.dokt@pw.edu.pl (S.D.); paulina.kozera@pw.edu.pl (P.K.); anna.boczkowska@pw.edu.pl (A.B.)
- ² Faculty of Power and Aeronautical Engineering, Warsaw University of Technology, 24 Nowowiejska, 00-665 Warsaw, Poland; michal.kubis@pw.edu.pl
- ³ Centre for Advanced Technologies, Adam Mickiewicz University in Poznań, 10 Uniwersytetu Poznańskiego, 61-614 Poznań, Poland; bognasztorch@gmail.com
- * Correspondence: kamil.dydek@pw.edu.pl

Abstract: The study aimed to investigate the effect of processing temperature and the content of multi-wall carbon nanotubes (MWCNTs) on the rheological, thermal, and electrical properties of polyphenylene sulfide (PPS)/MWCNT nanocomposites. It was observed that the increase in MWCNT content influenced the increase of the complex viscosity, storage modulus, and loss modulus. The microscopic observations showed that with an increase in the amount of MWCNTs, the areal ratio of their agglomerates decreases. Thermogravimetric analysis showed no effect of processing temperature and MWCNT content on thermal stability; however, an increase in stability was observed as compared to neat PPS. The differential scanning calorimetry was used to assess the influence of MWCNT addition on the crystallization phenomenon of PPS. The calorimetry showed that with increasing MWCNT content, the degree of crystallinity and crystallization temperature rises. Thermal diffusivity tests proved that with an increase in the processing temperature and the content of MWCNTs, the diffusivity also increases and declines at higher testing temperatures. The resistivity measurements showed that the conductivity of the PPS/MWCNT nanocomposite increases with the increase in MWCNT content. The processing temperature did not affect resistivity.

Keywords: PPS; carbon nanotubes; thermal analysis; electrical properties; rheological properties

Citation: Dydek, K.; Latko-Durałek, P.; Sulowska, A.; Kubiś, M.; Demski, S.; Kozera, P.; Sztorch, B.; Boczkowska, A. Effect of Processing Temperature and the Content of Carbon Nanotubes on the Properties of Nanocomposites Based on Polyphenylene Sulfide. *Polymers* **2021**, *13*, 3816. <https://doi.org/10.3390/polym13213816>

Academic Editors: Somen K. Bhudolia and Sunil Chandrakant Joshi

Received: 13 October 2021

Accepted: 2 November 2021

Published: 4 November 2021

Publisher's Note: MDPI stays neutral with regard to jurisdictional claims in published maps and institutional affiliations.



Copyright: © 2021 by the authors. Licensee MDPI, Basel, Switzerland. This article is an open access article distributed under the terms and conditions of the Creative Commons Attribution (CC BY) license (<https://creativecommons.org/licenses/by/4.0/>).

1. Introduction

Modern technological developments have created a need for new materials or the expansion of parameters and functional features of currently available products. In recent years, high-performance thermoplastics, also known as engineering polymers, have been the subject of study for many scientists. This was a result of the exceptional properties of the polymers, their ease of forming, and many possibilities of modifications. Polymers containing aromatic units, such as polyether ether ketone (PEEK), polyphenylene sulfide (PPS), and poly(ether sulfone) (PES), are widely used in electrical [1], automotive [2], and chemical industries [3,4]. Polyphenylene sulfide (PPS) is one of the most used engineering semi-crystalline thermoplastic due to its properties and relatively high temperature resistance (melting point 275 °C) [5,6]. PPS has good chemical resistance to most organic solvents, including alcohols, ketones, chlorinated aliphatic compounds, esters, and liquid ammonia [7]. It is also resistant to atmospheric factors, such as moisture and UV radiation. It has a low coefficient of thermal expansion and is, therefore, a material with excellent dimensional stability. Its natural non-flammability is also an advantage in many applications [8,9]. Although neat PPS possess exceptional properties, in the case of many

applications, they are insufficient; thus, a great deal of research focuses on improving them or adding new functional properties through the modification of PPS [10].

One of the most popular methods of PPS modification is the production of polymer blends [11]. J. Z. Liang [12] manufactured PPS/Polycarbonate (PC) blends to investigate the influence of PC content on heatproof properties. It has been demonstrated that when the PC weight fraction is less than 20%, the distortion temperature of the PPS/PC blend is lower than that of neat PPS. The reason is the lower heatproof property of PC than PPS and an insufficient number of physical nodes of the macromolecular chains between the PPS and PC. The number of nodes will increase with higher PC content, resulting in an improved heatproof property. Z. Ma et al. [13] fabricated microcellular foams from high-performance PPS/PEEK blends and compared their performance with solid PPS/PEEK blends. The conclusion was that PEEK could improve the impact toughness of the PPS blend due to their interaction, and the presence of PEEK greatly accelerates the crystallization process of PPS. Microcellular foaming improves the crystallinity, specific tensile strength, and impact strength of the PPS/PEEK blends and decreases the storage modulus and loss factor. Another method of PPS modification is the production of PPS composites with inorganic fillers, i.e., TiO₂ and ZnO. This solution allows for a significant improvement in tribological properties compared to pure PPS—by adding 6 wt% of TiO₂, the material wear index was reduced 100 times, so it can be successfully used in bearings, brake pads, and gears [14,15].

Although methods of improving parameters are available and a new application of PPS blends and composites is observed, there are still areas that require new modifications, e.g., in the field of conductive materials. The electrical performance of polymer matrix composites (PMCs) can be improved by adding metal or carbon particles, i.e., carbon nanotubes (CNTs). R. K. Goyal et al. [16] prepared PPS composites with copper (Cu) particles by first mixing and then injection molding to investigate the influence of metal particles on various properties of composites, including electrical properties. The results showed that the percolation threshold is around 6 vol% of Cu particles and the electrical conductivity increases to 18.5 vol% of Cu particles due to the infinite conductive cluster in the matrix. However, on further increasing the Cu content, the conductivity decreased due to the porosity of the composite. J. Yang et al. [17] obtained (PPS)/multi-wall carbon nanotube (MWCNT) nanocomposites by melt mixing PPS with raw MWCNTs without any pre-treatment, to investigate the mechanical and electrical properties of such composites. The melt blending of PPS with MWCNTs was conducted using a mixer at a temperature of 300 °C for 10 min. Considering electrical properties, it was observed that there is a gradual decrease of resistivity before MWCNTs is increased to 5 wt%. Then, a sharp decrease of the resistivity of almost five orders of magnitude (from 10⁻¹² to 10⁻⁷ Ω·cm) was achieved, as the content was increased from 5 to 7 wt%. However, with a higher MWCNT content, only an insignificant decrease in resistivity was observed. M. Park et al. [18] investigated the enhancement of PPS composites' interfacial, electrical, and flexural properties by introducing CFs coated with MWCNTs based on electrophoresis. PPS composites filled with seized CFs or with CFs coated with MWCNTs were fabricated using a twin-screw extruder. The interfacial shear strength of the PPS composites was improved by about 41.7% due to the MWCNTs introduced on the surface of CFs. Introducing MWCNTs on the CF surface improved the electrical conductivity of the composites by about 78%, probably because MWCNTs are excellent electrically conductive fillers. Additionally, the percolation threshold of the PPS composites filled with the MWCNT coated CFs based on electrophoresis was lower than that of PPS composites filled with resized CFs. Moreover, low thermal conductivity, which is characteristic of polymers, limits a range of applications in many cases where heat dissipation is required. This parameter can also be modified by using highly thermally conductive fillers. Y. Seki et al. [19] prepared PPS-based composites modified with a maximum of 5 wt% of synthetic graphite that showed an approximately triple increase in thermal diffusivity in the through-thickness direction and the 32-fold larger increase for the in-plane direction compared with neat PPS. S. Deng et al. [20] demonstrated an impact of graphene nanoplates on the thermal conductivity of PPS.

Thermal conductivity for the neat matrix was reported as $0.219 \text{ W m}^{-1} \cdot \text{K}^{-1}$. It increased up to $1.156 \text{ W m}^{-1} \cdot \text{K}^{-1}$ in the case of 30 wt% content of graphene nanoplates. G. Junwei [21] presented even higher thermal conductivity for PPS/Graphene nanoplates composite. An almost 20-fold increase in thermal conductivity was achieved by using a similar weight fraction of filler.

Another example of processing of PPS composites is to use them in the form of fibers, which combine moderate thermal properties with excellent chemical resistance, but few studies have included the modification with a high volume of carbon nanotubes (CNT). Xing et al. [22] manufactured PPS fibers with functionalized graphene nanoplatelets (GNPs) via melt spinning to improve the oxidation resistance of the composite. The result shows that the addition of GNPs influences the surface roughness of fibers and increases the degree of crystallinity of PPS. Kulpinski et al. [6] manufactured PPS fibers and nonwovens by the melt-blown method modified with CNT and carbonyl iron microparticles at low content (up to 1 wt%). The mechanical properties of fibers with fillers were worse than neat PPS because of the chosen production method. The addition of CNTs improved the electrical properties of fibers, and manufactured nonwovens obtained electromagnetic properties. EMI shielding of nonwovens was tested and the results were satisfying. Moreover, PPS can be also used as a material for the filament to 3D printing [23]. Parans Paranthaman et al. used PPS/NbFeB composites to produce permanent magnets using the FDM technique [24].

The aim of this article is to optimize the processing temperature of PPS/MWCNT nanocomposites and the content of MWCNTs so that in the developed material, it would be possible to successfully produce nanocomposite fibers, which in the next stage will be used to produce conductive, thermoplastic nonwovens using the thermo-pressing method [25]. Thermoplastic nonwovens containing MWCNTs can be used as interlayers or surface finish to modify carbon fiber reinforced polymers (CFRPs) to improve electrical and mechanical properties [26–28]. Quan et al. [29] used PPS/MWCNT nonwovens produced wet-laid process, where the MWCNTs were applied using the airbrush technique, and then, the nonwovens were used to improve the properties of CFRP composites. In the case of improving the electrical properties, thermoplastic nonwovens with the addition of MWCNTs allow the creation of conductive paths between the layers of carbon fibers, which in turn reduces the CFRP resistivity [30]. Additionally, no reports were found in the literature about the impact of processing using a twin-screw extruder on the properties of PPS/MWCNT nanocomposites. To sum up, the use of PPS/MWCNT nanocomposites as a material for the production of thermoplastic nonwovens by thermo-pressing method is an innovative approach, so far unheard of in the literature, which justifies the need to select and optimize the processing temperature as well as the content of MWCNTs in PPS/MWCNT nanocomposites in order to verify their functional properties.

2. Materials and Methods

2.1. Materials

Fortron[®] PPS (Celanese, Pasadena, TX, USA) was used as a polymer matrix to produce PPS/MWCNT nanocomposites, whereas MWCNTs with the trade name NC7000 from Nanocyl (Sambreville, Belgium), synthesized through catalytic carbon vapor deposition process, were used as a conductive nanofiller. The average diameter of an MWCNT is 9.5 nm, its length is 1.5 μm , and its purity >95%. Additionally, Nanocyl manufactured and delivered masterbatch in the form of pellets, using a semi-industrial production line equipped with a twin-screw extruder. The masterbatch contained 10 wt% MWCNT. Then, using the laboratory twin-screw extruder HAAKE MiniLab (ThermoFisher Scientific, Waltham, MA, USA), mixing neat PPS with delivered masterbatch, nanocomposites PPS/MWCNT were produced with the following MWCNT concentrations: 2 wt%, 4 wt%, 6 wt%, and 8 wt%. Moreover, to check the impact of the processing conditions, three different temperatures were applied: 290, 305, and 320 °C at a constant rotational speed of the screws, which was 50 rpm. To investigate the effect of the processing temperature on

the dispersion of MWCNTs in the polymer matrix, the masterbatch was also extruded at three different temperatures, namely 290, 305, and 320 °C.

The test specimens were produced using a laboratory HAAKE MiniJet Pro (Thermo Fisher Scientific) injection molding machine, where the mold temperature was 140 °C, and the injection and hold pressures were 800 and 700 bar, respectively. The temperatures in the cylinder, where the material was plasticized, were 290, 305, and 320 °C, corresponding to the processed nanocomposite material.

2.2. Measurement Methods

The rheological properties of the material were measured using an oscillatory ARES rheometer (Rheometric Scientific Inc., TA Instruments, New Castle, DE, USA) in parallel plate geometry mode. Firstly, the amplitude sweep test was performed, to choose the appropriate strain values from the linear elastic range. Afterward, using the selected strain (10%), a dynamic oscillatory stress-controlled rotational test was performed at 320 °C with a frequency sweep from 0.1 to 100 Hz. To examine how the addition of MWCNTs affects the rheological properties of PPS, the complex viscosity, storage modulus, and loss modulus were collected. Specimens for the rheological analysis were prepared directly from the pellets by injection molding into rounds having a diameter of 1.5 mm and a thickness of 2 mm.

The state of MWCNTs' dispersion has been characterized by transmission optical microscopy. Samples were prepared using Ultramicrotome Leica EM UC6 (Leica Microsystems, Wetzlar, Germany) equipped with a chamber for low-temperature processing. The materials were cut with a diamond knife at the temperature -10 °C into slides with 2 μm thickness. Furthermore, samples were deposited on the surface of a microscopic glass and observed through a light transmission microscope PZO Biolar (Biolar, Warsaw, Poland). The optical micrographs were analyzed using the digital image processing software ImageJ (National Institutes of Health and the Laboratory for Optical and Computational Instrumentation, Madison, WI, USA). The MWCNTs' agglomerate area ratio was defined as the ratio of the cumulative area of the MWCNTs' agglomerate system relating to the micrograph area, and this ratio was presented in a percentage [31]. Only MWCNT agglomerates with diameters higher than 1 μm were used for analysis. To have sufficient statistics of measured values, at least seven optical illustrating micrographs were used for calculation.

The thermal stability of the PPS/MWCNT composites was investigated by thermogravimetric analysis (TGA) using a TGA Q500 (TA Instruments, New Castle, DE, USA). Samples with a weight of around 11 mg were placed in an aluminum crucible and heated from 0 to 820 °C in a nitrogen atmosphere with a heating rate of 10 °C/min and a flow rate of 10 mL/min and 90 mL/min. The degradation temperature at 2% (T2%) and 5% (T5%) weight loss, as well as the temperature of the maximum weight loss rate (Td), were determined from the obtained TGA curves.

Thermal properties of materials were studied using a Q1000 Differential Scanning Calorimeter (TA Instruments, New Castle, DE, USA). Samples with a weight of 8.0 ± 0.2 mg were placed in an aluminum hermetic pan. Firstly, the samples were equilibrated at 0 °C, then heated to 340 °C with a scan rate of 10 °C/min, and cooled to 0 °C with a scan rate of 5 °C/min. Finally, they were heated again to 340 °C with a scan rate of 10 °C/min. The process was conducted in a nitrogen atmosphere. Using the Universal V4.5A TA software, the melting point (Tm) was determined from the second heating curve and the crystallization temperature (Tc) was determined based on the cooling curve. The crystallinity content (Xc) of the PPS composites was calculated from Equation (1):

$$X_c(\%) = \frac{\Delta H_c}{\Delta H_m^\circ (1 - x)} \Delta 100\% \quad (1)$$

where ΔH_c is the enthalpy of melting taken as the area under the melting peak from the second heating curve, ΔH_m° is the melting enthalpy of 100% crystalline PPS, which is 76.5 J/g [32], and x is the weight fraction of MWCNT.

An impact of MWCNTs on thermal diffusivity of PPS-based composites was determined using the laser flash apparatus (LFA 447, Netzsch, Selb, Germany) at a temperature range from 50 °C to 250 °C with steps of 50 °C. Measurements were divided into two groups. The thermal diffusivity of each type of sample was calculated as an average of the measurements of the four samples. Moreover, at each temperature setpoint for each sample, the measurement was repeated five times. Samples had similar dimensions with an approximate diameter $d = 25$ mm and height $h = 1$ mm.

To examine the influence of the processing temperature and the MWCNT content, the electrical resistivity of the produced materials was measured using a Keithley 6221/2182A (Cleveland, OH, USA) nano voltmeter and a DC source, equipped with copper electrodes. To ensure very good contact between the samples and the electrodes, a silver conductive paste (CW7100, Chemtronics, Kennesaw, GA, USA) was used. Five samples of each material with a diameter of 25 mm and thickness of 1 mm were tested in the range from 1 nA to 1 mA; additionally, they were cleaned with ethanol before testing. To reduce noise and thermoelectric effects, the tests were performed in the delta mode using the four-point method.

3. Results and Discussion

3.1. Rheological Properties

MWCNTs are known as additives that change the rheological properties of different thermoplastic and thermoset polymers to a large degree due to their high aspect ratio [33]. For the prepared PPS-based composites, the complex viscosity, storage, and loss modulus also change in the presence of MWCNTs, which is presented in Figure 1a, b, and c, respectively. Neat PPS possess a viscosity around 10^1 Pa·s, and it is increased by about three orders of magnitude up to the value of 10^4 Pa·s after the addition of 2 wt% MWCNTs. For the higher MWCNT loadings, the viscosity increases up to 10^5 Pa·s. There is no significant difference between the MWCNT concentration, especially for 8 and 10 wt%, where the curves are practically the same. The MWCNTs' effect on the viscosity of PPS is more pronounced at low concentrations (2 wt%) and low frequencies, which has been reported in the literature for other thermoplastic polymers [34]. It should be noted that neat PPS behaves as a Newtonian liquid with no changes in the complex viscosity within the frequency range. The addition of MWCNTs causes the disappearance of a Newtonian plateau, and all PPS/MWCNT composites show a typical shear-thinning behavior with decreasing viscosity and frequency. Similar to viscosity, storage and loss modulus increase in the presence of MWCNTs. This is an effect of the increased viscosity, and strong interactions occur between the filler and the polymer. Both moduli are raised to the value of 10^3 Pa for 2 wt% MWCNTs. Higher MWCNT loadings cause an increase in storage and loss modulus of up to 10^4 Pa·s or 10^5 Pa·s, respectively. Similar to the effect of viscosity, 4, 6, 8, and 10 wt% MWCNT content has a lower effect on storage and loss modulus. The character of the curves changes from a steep course to a frequency-independent plateau-like behavior. The literature has reported the same character of both moduli at high MWCNT concentrations, e.g., above 2 wt% for PEEK [35]. This is related to the rheological percolation threshold, defined as the minimum filler concentration at which the motion of the polymer chains is restricted. It can be determined from the so-called Cole-Cole plot, which is a dependence between loss and storage modulus in a logarithmic scale, as shown in Figure 1d. Neat PPS presents a linear relationship between the moduli. There is a clear divergence from the linear dependence for all composites, which means that the filler forms the structural network resulting in a more heterogeneous system. Based on the changes in storage and loss modulus, the rheological percolation threshold can be found between 0–2 wt% MWCNTs within the same range reported for PPS/MWCNT composites prepared by direct components mixing [17]. Finally, it should be noted that for neat PPS, the loss modulus (Figure 1c) exceeds the storage modulus (Figure 1b). Within the whole frequency range, neat PPS reveals more viscous behavior of the material. The situation alters after the

addition of MWCNTs, and for all composites, the loss modulus is lower than the storage modulus, which results in a more elastic material.

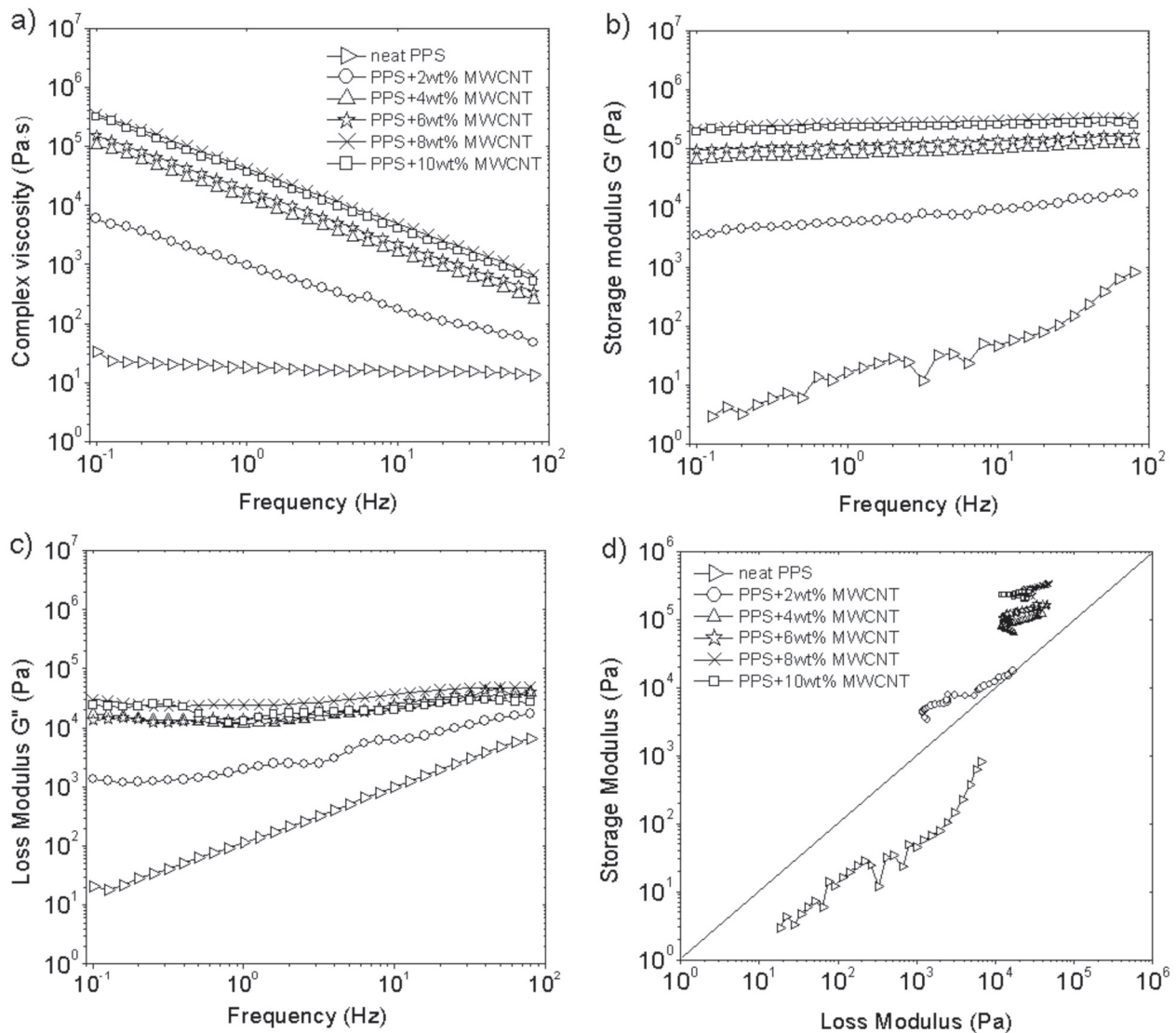


Figure 1. Rheological properties of PPS/MWCNT composites: (a) complex viscosity as a function of frequency; (b) storage modulus as a function of frequency; (c) loss modulus as a function of frequency, (d) Cole-Cole plot. The test was performed at 320 °C with 10% strain.

3.2. Microscope Observations

The optical observations of non-extruded PPS + 10 wt% of MWCNTs were performed and the result is shown in Figure 2a. To investigate the MWCNTs' agglomerate dispersion, 10 wt% MWCNT masterbatch was processed at three different temperatures: 290 °C, 305 °C, and 320 °C, and the optical microscopy observations are presented in Figure 2b–d. A slight effect of temperature on the increase in the number of agglomerates was observed. This was the effect of a decrease in viscosity with an increase in temperature. However, in each of the analyzed cases, the number of MWCNT agglomerates was at a satisfactory, low level. Moreover, the effect of MWCNT content on the agglomerates dispersion was examined for the selected temperature (320 °C), and the results are presented in Figure 2e–h. It was observed that with a lower MWCNT content, the number of agglomerates increased. This was the effect of the viscosity change, where the shear forces may be too low for lower MWCNT contents.

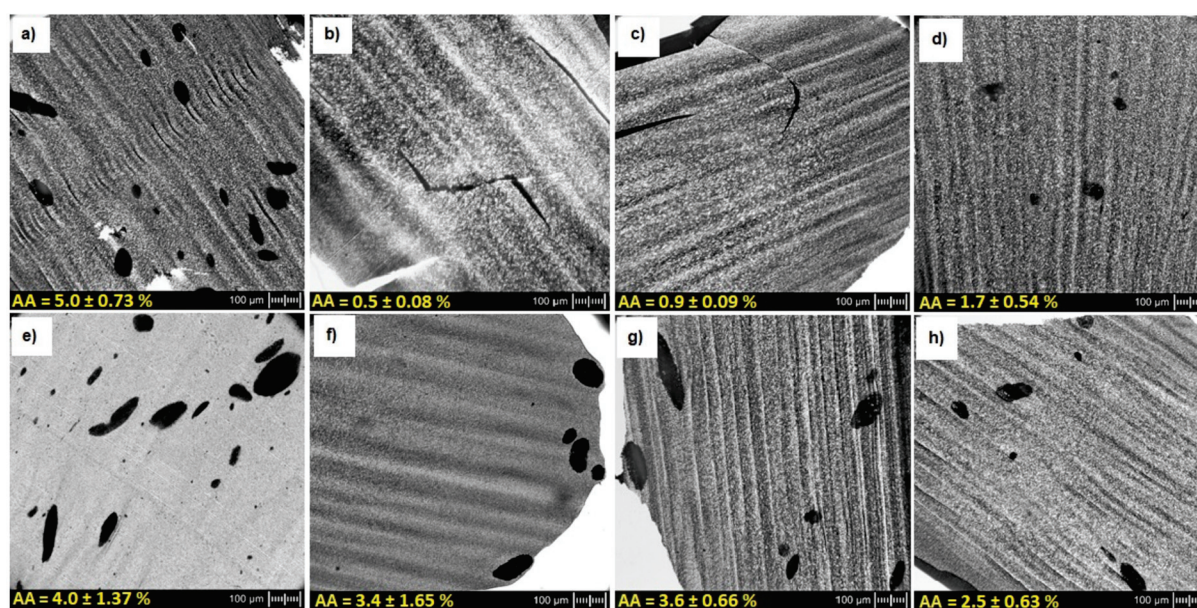


Figure 2. Optical micrographs illustrating the state of MWCNTs' agglomerate dispersion at different temperature and MWCNT content: (a) PPS + 10 wt% MWCNT masterbatch, (b) PPS + 10 wt% MWCNT (T = 290 °C), (c) PPS + 10 wt% MWCNT (T = 305 °C), (d) PPS + 10 wt% MWCNT (T = 320 °C), (e) PPS + 2 wt% MWCNT (T = 320 °C), (f) PPS + 4 wt% MWCNT (T = 320 °C), (g) PPS + 6 wt% MWCNT (T = 320 °C), (h) PPS + 8 wt% MWCNT (T = 320 °C).

To evaluate the MWCNTs' agglomerate area ratio, such optical micrographs were quantitatively evaluated by applying an image analysis procedure. The calculated CNT agglomerate area ratio confirms the decrease of agglomerates formation after applying the extrusion process to the samples and the increase in their number, along with the decrease in the content of CNTs. The influence of twin-screw extrusion conditions on nanotube dispersion is presented in the literature [36,37], which indicates that a high rotation speed and temperature are beneficial for dispersing and evenly distributing the CNT in the polymer matrix. It was found that the extrusion screw can ensure the introduction of high shear forces for CNT deagglomeration in the PPS polymer matrix. Furthermore, a better dispersion quality was achieved at higher CNT contents in the PPS matrix [38] as well as the poly(lactic acid) matrix. It was found that shear stresses as well as the viscosity of nanocomposites play an important role in destroying agglomerated nanofillers [39]. Thus, the viscosity increase resulting from the higher MWCNT content leads to higher maximum shear stresses applied to remaining CNT agglomerates. With lower CNT contents, the shear stresses can be insufficient for agglomerate breakdown.

3.3. Thermal Properties

The results of the thermal analysis were collected in Table 1. The thermal stability, which is understood as the temperatures at 2% and 5% weight loss, was determined from the TGA curves. The degradation starts at 453 °C (2%) and 481 °C (5%) for neat PPS. In the starting masterbatch containing 10 wt% MWCNTs, the degradation temperatures are shifted to about 12–14 °C, and the temperature of the maximum weight loss rate also increases by about 14 °C. Further processing of the masterbatch by extrusion process resulted in the values of T2% and T5%, which are about 3 °C higher for some of the composites, or lower for others.

Table 1. The results of the thermal analysis.

Material	Extrusion Temp. (°C)	TGA			DSC		
		T _{2%} (°C)	T _{5%} (°C)	T _d (°C)	T _m (°C)	X _c (%)	T _c (°C)
neat PPS		453	481	521	283	54.5	228
PPS + 10% masterbatch		467	493	535	286	59.3	257
PPS + 2% MWCNT	290	456	486	531	287	66.5	256
PPS + 4% MWCNT		452	484	532	287	53.2	257
PPS + 6% MWCNT		451	483	535	286	61.8	257
PPS + 8% MWCNT		453	484	533	286	58.7	257
PPS + 10% MWCNT		451	482	530	287	65.3	257
PPS + 2% MWCNT		305	454	487	535	287	57.3
PPS + 4% MWCNT	453		484	531	286	53.3	258
PPS + 6% MWCNT	454		485	534	287	58.9	257
PPS + 8% MWCNT	454		484	534	286	73.1	257
PPS + 10% MWCNT	457		486	535	286	61.1	257
PPS + 2% MWCNT	320		452	484	533	286	60.6
PPS + 4% MWCNT		457	487	532	287	67.5	257
PPS + 6% MWCNT		454	484	534	287	65.7	257
PPS + 8% MWCNT		456	486	538	287	64.1	257
PPS + 10% MWCNT		453	483	534	286	54.1	257

The temperature of the maximum weight loss is significantly improved by about 10–17 °C for all composites compared with the maximum weight loss rate. There is no apparent effect of the extrusion temperature and MWCNT content on the thermal stability of PPS/MWCNT composites. Because both T_{2%} and T_{5%} are the highest for the masterbatch, the additional processing step decreases the thermal stability in view of initiating the degradation process. The calculated amount of the agglomerates is presented in Figure 2. Many more MWCNT agglomerates were found in the masterbatch than in the composites after processing. It seems that the presence of agglomerates is more critical for thermal stability improvement than perfectly dispersed MWCNTs. More agglomerates in the composites hinder the flux of degradation products more effectively than single MWCNTs. It might also be that PPS chains near the MWCNT agglomerates degrade slowly, but only if they are homogeneously dispersed [40]. The other possible mechanism is that the second extrusion step causes some degradation of the PPS chains, and therefore, the composites start to decompose at a lower temperature. Most of the nanofiller works as a nucleating agent for the polymers.

The analysis of the effect of MWCNT addition on the crystallization phenomenon of PPS was carried out using the DSC method. The determined melting point T_m, crystallization temperature T_c, and calculated crystallinity degree X_c are included in Table 1. The melting point of neat PPS is 283 °C, and it shifts to the value of 286–287 °C. An example thermogram comparing the effect of MWCNTs on the melting point and extrusion temperature is shown in Figure 3a,b.

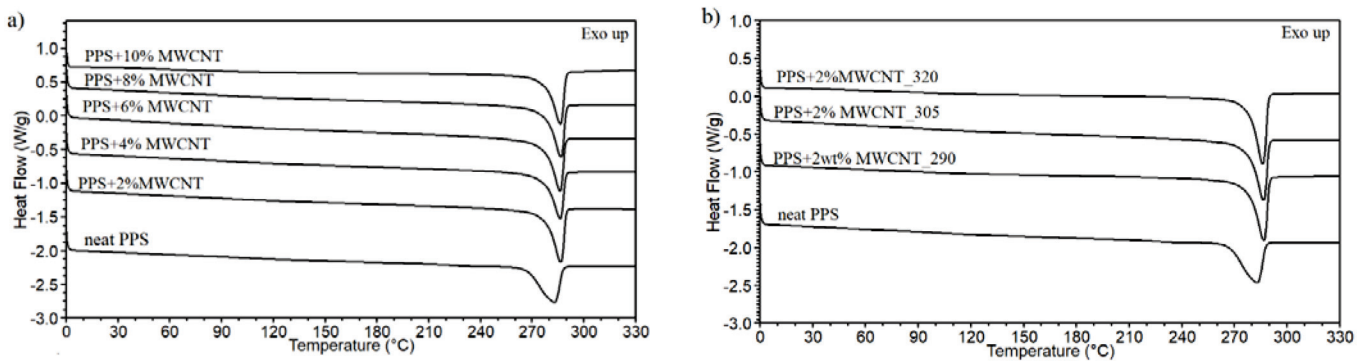


Figure 3. The second heating curve for the PPS/MWCNT composites. (a) Comparison of the MWCNT content. (b) Comparison of the extrusion temperature.

There is no effect of the MWCNT content and extrusion temperature on the melting point. Moreover, the melting peak of neat PPS is broad, and it is getting narrower for PPS/MWCNT composites, which reveals the changes in the crystal phase of the polymer, as demonstrated by an increase in the crystallinity degree and crystallization temperature. As shown in Table 1, for most of the composites, the addition of MWCNTs causes an increase in the crystallinity content at a maximum of 18% and an increase in the crystallization temperature of 29 °C. The nucleation effect of MWCNTs on PPS is visible by a significant shift in the crystallization peak, as presented in Figure 4a,b.

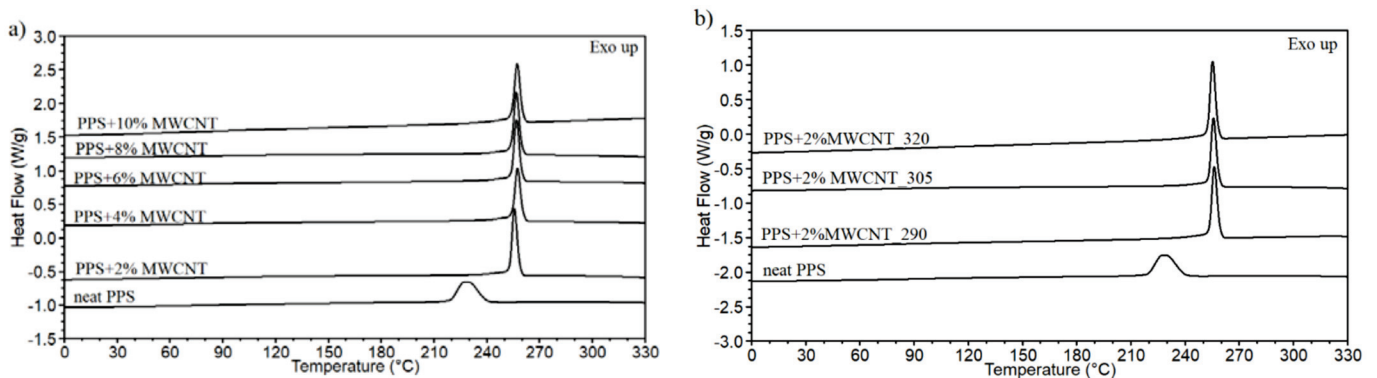


Figure 4. The cooling curves for the PPS/MWCNT composites. (a) Comparison of the MWCNT content. (b) Comparison of the extrusion temperature.

The graphs also confirm no evident influence of MWCNT concentration and extrusion temperature on the crystallization phenomena. It is confirmed by a similar value of the crystallization temperature (256–258 °C) obtained for all composites. A similar lack of linear dependence between crystallinity content and nanotube concentration was found in PA6 containing MWCNTs [41]. In the other PPS/MWCNT composites prepared by direct components mixing, the nucleating effect of MWCNTs was observed, but only for small nanotube concentrations. At higher concentrations, the melting point and crystallinity degree show a gradual decrease. Probably, the created MWCNT network hinders the movement of the polymer chains leading to forming of an imperfect crystal phase [17].

The thermal diffusivity of all PPS/MWCNT composites is shown in Figure 5a,b. Figure 5a presents the thermal diffusivity decreasing with temperature. In addition, MWCNTs affect the thermal diffusivity of PPS-based composites. The higher the weight fraction of MWCNTs, the higher the thermal diffusivity. Maximum value $a = 0.255 \text{ mm}^2 \cdot \text{s}^{-1}$ was determined for samples PPS+10 wt% MWCNT at the temperature $T = 50 \text{ °C}$. On the other hand, neat PPS has lower thermal diffusivity of $a = 0.144 \text{ mm}^2 \cdot \text{s}^{-1}$ at the same temperature. That compared with samples containing 10 wt% MWCNT gives a maximum increase of

approximately 77%. At maximum measured temperature $T = 250\text{ }^{\circ}\text{C}$, the thermal diffusivity of a sample with maximum loading increases by 38% compared with neat PPS. The increase in thermal diffusivity with an increasing MWCNT weight fraction is close to linear. The achieved increase in thermal diffusivity of PPS/MWCNT composites with this type of filler is rather low when compared with other authors [19]. However, since a different filler was used, the carbon MWCNT feature is extremely high for a specific surface area. It is higher than in other allotropes of carbon-based fillers and causes higher interfacial resistance, which deteriorates heat conduction through the material.

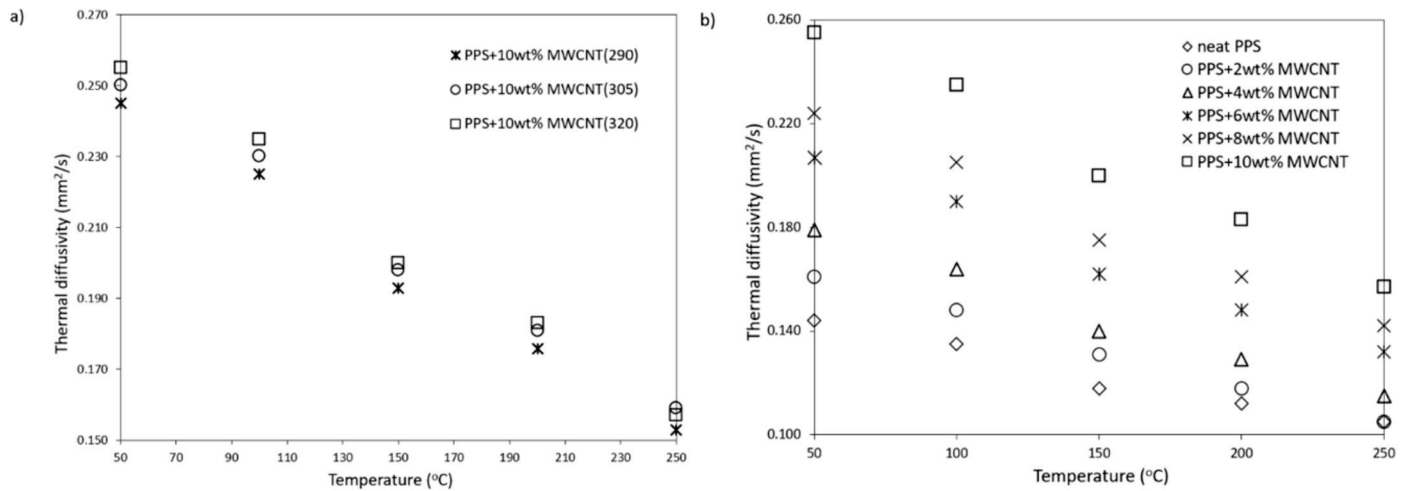


Figure 5. Thermal diffusivity vs. (a) temperature of PPS-based composites filled with MWCNT and (b) temperature of PPS-based composite manufactured with different temperature.

Figure 5b shows the impact of the extrusion temperature on the thermal diffusivity of the tested samples. The higher the temperature, the higher the thermal diffusivity, but it increases the maximum by approximately 4% for samples PPS + 10 wt% MWCNT ($T = 320\text{ }^{\circ}\text{C}$) compared with PPS + 10 wt% ($T = 290\text{ }^{\circ}\text{C}$).

3.4. Electrical Properties

The influence of the MWCNT content and processing temperature on the level of electrical conductivity of PPS/MWCNT nanocomposites has been examined and the results are presented in Figure 6. The largest increase in electrical conductivity was observed from 10^{-11} S/m for neat PPS to $7 \cdot 10^{-5}\text{ S/m}$ for 2 wt% MWCNT, and this increase was almost six orders of magnitude. Then, the increase in conductivity slowed down and increased linearly from 2 to 6% in the MWCNT content, after which it slowed significantly, and the increase in concentration from 6 to 10% of MWCNT improved by one order of magnitude, finally reaching values of about 10^0 .

By analyzing the results and the conductivity curve, the electrical percolation threshold can be established between 0–2 wt% of MWCNTs. This value is relatively low compared with the values obtained in the literature at 5% of the MWCNT content [17], which proves good MWCNT dispersion in the PPS matrix. It was achieved by the selection of appropriate temperature and double extrusion on a twin-screw extruder. It was also the effect of using MWCNTs from Nanocyl, which possess very good properties as a conductive filler. Using them to make conductive nanocomposites is known in the literature and the obtained percolation threshold for these MWCNTs is about 1wt% [42,43]. Moreover, it was observed that the change of the processing temperature from 290 $^{\circ}\text{C}$ to 320 $^{\circ}\text{C}$ did not affect the electrical conductivity. The greatest change was observed for nanocomposites with 10 wt% MWCNT content, where the electrical conductivity was $8.39 \cdot 10^{-1}\text{ S/m}$ and $1.05 \cdot 10^0\text{ S/m}$ for 290 $^{\circ}\text{C}$ and 320 $^{\circ}\text{C}$, respectively. This is the result of a slight difference in the state of MWCNTs' agglomerate dispersion, which is presented in Figure 2.

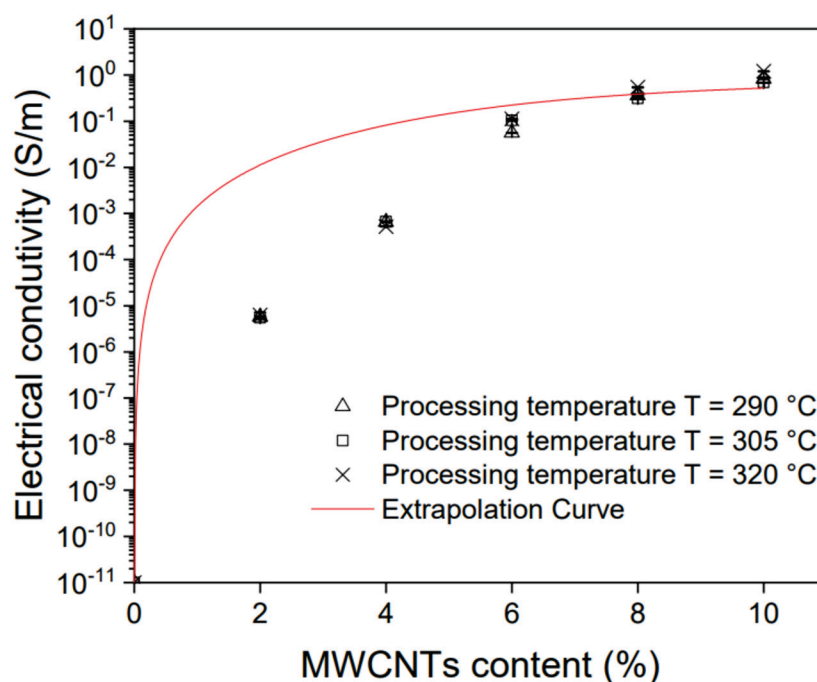


Figure 6. Electrical conductivity of PPS/MWCNT nanocomposites.

4. Conclusions

The present work investigated the effect of processing temperature and the content of carbon nanotubes on the properties of nanocomposites based on PPS. The studies aimed to select the best material and processing parameters for the production of thermoplastic veils with the addition of MWCNTs, as a unique technique to improve the properties of CFRP. For this purpose, PPS/MWCNT nanocomposites were produced at three different temperatures and with different filler contents. TGA analysis showed a slight decrease in thermal stability for the produced nanocomposites compared with a masterbatch with an MWCNT content of 10 wt%. This may be the result of the subsequent processing of the material, as the MWCNT content was not found to affect thermal stability. In the case of DSC analysis, the content of MWCNTs and the processing temperature do not affect the melting point; however, the addition of MWCNT causes an increase in the degree of crystallinity and the crystallization temperature. The highest values of thermal diffusivity and electrical conductivity were observed in nanocomposites containing 8–10 wt% MWCNTs, which was caused by the excellent thermal and electrical properties of MWCNTs. Viscosity studies showed that the addition of 2% MWCNT makes the material more elastic than plastic. Additionally, no significant effect of the amount of filler on the rheological properties was observed for higher MWCNT concentrations. In the case of microscopic observations, a larger area of agglomerates was observed for lower concentrations of MWCNTs, which is the result of lower nanocomposite viscosity, and consequently, lower shear forces during processing. The same was observed as regards the influence of the processing temperature—as the processing temperature increases, the viscosity decreases, which translates into lower shear forces and worse homogenization of the nanocomposite. Taking into account the obtained results, it was found that the content of MWCNTs within the range of 8–10 wt% and the processing temperature from 305 to 320 °C allows for obtaining the desired properties of the PPS/MWCNT nanocomposites, which will be the basis for thermoplastic nonwovens, used to improve the properties of CFRPs.

Author Contributions: Conceptualization, K.D.; methodology, K.D., P.L.-D., S.D., P.K., M.K. and A.S.; software, K.D., S.D. and A.S.; validation, K.D., P.L.-D. and B.S.; formal analysis, K.D.; investigation, K.D., P.L.-D., P.K. and M.K.; resources, K.D.; writing—original draft preparation, K.D.; writing—review and editing, A.B. and B.S.; visualization, K.D., P.L.-D., M.K. and P.K.; supervision, A.B.; project administration, K.D.; acquiring funds, K.D. All authors have read and agreed to the published version of the manuscript.

Funding: This study was carried out with funding from grant no. LIDER/46/0185/L-11/19/NCBR/2020, financed by The National Centre for Research and Development.

Institutional Review Board Statement: Not applicable.

Informed Consent Statement: Not applicable.

Data Availability Statement: All data are available in the main text.

Conflicts of Interest: The authors declare no conflict of interest.

References

1. Corea, J.R.; Flynn, A.M.; Lechêne, B.; Scott, G.; Reed, G.D.; Shin, P.J.; Lustig, M.; Arias, A.C. Screen-printed flexible MRI receive coils. *Nat. Commun.* **2016**, *7*, 1–7. [CrossRef] [PubMed]
2. Schwartz, C.J.; Bahadur, S. The role of filler deformability, filler-polymer bonding, and counterface material on the tribological behavior of polyphenylene sulfide (PPS). *Wear* **2001**, *250*, 1532–1540. [CrossRef]
3. Menzel, F.; Klein, T.; Ziegler, T.; Neumaier, J.M. 3D-printed PEEK reactors and development of a complete continuous flow system for chemical synthesis. *React. Chem. Eng.* **2020**, *5*, 1300–1310. [CrossRef]
4. Yu, L.; Yang, S.; Liu, W.; Xue, Q. Investigation of the friction and wear behaviors of polyphenylene sulfide filled with solid lubricants. *Polym. Eng. Sci.* **2000**, *40*, 1825–1832. [CrossRef]
5. Deng, Y.; Yang, Y.; Ma, Y.; Fan, K.; Yang, W.; Yin, G. Nano-hydroxyapatite reinforced polyphenylene sulfide biocomposite with superior cytocompatibility and in vivo osteogenesis as a novel orthopedic implant. *RSC Adv.* **2017**, *7*, 559–573. [CrossRef]
6. Kulpinski, P.; Czarnecki, P.; Niekraszewicz, B.; Jeszka, J.K. Functional nanocomposite poly(phenylene sulphide) fibres—Preliminary studies. *Fibres Text. East. Eur.* **2016**, *24*, 20–26. [CrossRef]
7. Zuo, P.; Tcharkhtchi, A.; Shirinbayan, M.; Fitoussi, J.; Bakir, F. Overall Investigation of Poly (Phenylene Sulfide) from Synthesis and Process to Applications—A Review. *Macromol. Mater. Eng.* **2019**, *304*, 1–27. [CrossRef]
8. Rahate, A.S.; Nemade, K.R.; Waghuley, S.A. Polyphenylene sulfide (PPS): State of the art and applications. *Rev. Chem. Eng.* **2013**, *29*, 471–489. [CrossRef]
9. Lv, C.; Wang, H.; Liu, Z.; Wang, C.; Li, H.; Zhao, Y.; Zhu, Y. A fluorine-free superhydrophobic PPS composite coating with high thermal stability, wear resistance, corrosion resistance. *Prog. Org. Coatings* **2017**, *110*, 47–54. [CrossRef]
10. Chen, G.; Mohanty, A.K.; Misra, M. Progress in research and applications of Polyphenylene Sulfide blends and composites with carbons. *Compos. Part B Eng.* **2021**, *209*, 108553. [CrossRef]
11. Yu, Y.; Xiong, S.; Huang, H.; Zhao, L.; Nie, K.; Chen, S.; Xu, J.; Yin, X.; Wang, H.; Wang, L. Fabrication and application of poly (phenylene sulfide) ultrafine fiber. *React. Funct. Polym.* **2020**, *150*, 104539. [CrossRef]
12. Liang, J.Z. Heat distortion temperature of PPS/PC blend, PPS/PC nanocomposite and PPS/PC/GF hybrid nanocomposite. *J. Polym. Eng.* **2013**, *33*, 483–488. [CrossRef]
13. Ma, Z.; Zhang, G.; Yang, Q.; Shi, X.; Li, J.; Zhang, H.; Qin, J. Tailored morphologies and properties of high-performance microcellular poly(phenylene sulfide)/poly(ether ether ketone) (PPS/PEEK) blends. *J. Supercrit. Fluids* **2018**, *140*, 116–128. [CrossRef]
14. Jiang, Z.; Gyurova, L.A.; Schlarb, A.K.; Friedrich, K.; Zhang, Z. Study on friction and wear behavior of polyphenylene sulfide composites reinforced by short carbon fibers and sub-micro TiO₂ particles. *Compos. Sci. Technol.* **2008**, *68*, 734–742. [CrossRef]
15. Zhang, Z.; Zhou, W.; Li, Y.; Yan, C. Isothermal crystallization kinetics of poly(phenylene sulfide)/ZnO composites. *Adv. Mater. Res.* **2012**, *535–537*, 243–246. [CrossRef]
16. Goyal, R.K.; Kambale, K.R.; Nene, S.S.; Selukar, B.S.; Arbuj, S.; Mulik, U.P. Fabrication, thermal and electrical properties of polyphenylene sulphide/copper composites. *Mater. Chem. Phys.* **2011**, *128*, 114–120. [CrossRef]
17. Yang, J.; Xu, T.; Lu, A.; Zhang, Q.; Tan, H.; Fu, Q. Preparation and properties of poly (p-phenylene sulfide)/multiwall carbon nanotube composites obtained by melt compounding. *Compos. Sci. Technol.* **2009**, *69*, 147–153. [CrossRef]
18. Park, M.; Park, J.H.; Yang, B.J.; Cho, J.; Kim, S.Y.; Jung, I. Enhanced interfacial, electrical, and flexural properties of polyphenylene sulfide composites filled with carbon fibers modified by electrophoretic surface deposition of multi-walled carbon nanotubes. *Compos. Part A Appl. Sci. Manuf.* **2018**, *109*, 124–130. [CrossRef]
19. Seki, Y.; Kizilkan, E.; İşbilir, A.; Sarikanat, M.; Altay, L. Enhanced in-plane and through-plane thermal conductivity and mechanical properties of polyamide 4.6 composites loaded with hybrid carbon fiber, synthetic graphite and graphene. *Polym. Compos.* **2021**, *42*, 4630–4642. [CrossRef]

20. Deng, S.; Lin, Z.; Xu, B.; Qiu, W.; Liang, K.; Li, W. Isothermal crystallization kinetics, morphology, and thermal conductivity of graphene nanoplatelets/polyphenylene sulfide composites. *J. Therm. Anal. Calorim.* **2014**, *118*, 197–203. [CrossRef]
21. Gu, J.; Xie, C.; Li, H.; Dang, J.; Geng, W.; Zhang, Q. Thermal Percolation Behavior of Graphene Nanoplatelets/Polyphenylene Sulfide Thermal Conductivity Composites Junwei. *Polym. Compos.* **2014**, *35*, 1087–1092. [CrossRef]
22. Xing, J.; Xu, Z.; Ni, Q.Q.; Ke, H. Preparation and characterization of polyphenylene sulfide/graphene nanoplatelets composite fibers with enhanced oxidation resistance. *High Perform. Polym.* **2020**, *32*, 394–405. [CrossRef]
23. Retolaza, J.; Ansola, R.; Gómez, J.L.; Diez, G. Identifying elastic constants for pps technical material when designing and printing parts using fdm technology. *Materials* **2021**, *14*, 1–19. [CrossRef] [PubMed]
24. Parans Paranthaman, M.; Yildirim, V.; Lamichhane, T.N.; Begley, B.A.; Post, B.K.; Hassen, A.A.; Sales, B.C.; Gandha, K.; Nlebedim, I.C. Additive manufacturing of isotropic NdFeB PPS bonded permanent magnets. *Materials* **2020**, *13*, 1–10. [CrossRef] [PubMed]
25. Boczkowska, A.; Latko, P. Sposób Wytwarzania Włókien i Włókniny z Nanorurkami Węglowymi. Polish Patent Pl 221848 B1, 30 June 2016.
26. Dydek, K.; Latko-Durałek, P.; Boczkowska, A.; Sałaciński, M.; Kozera, R. Carbon Fiber Reinforced Polymers Modified with Thermoplastic Nonwovens Containing Multi-Walled Carbon Nanotubes. *Compos. Sci. Technol.* **2019**, *173*, 110–117. [CrossRef]
27. Latko-Durałek, P.; Dydek, K.; Golonko, E.; Boczkowska, A. Mechanical properties of PETG fibres and their usage in carbon fibres/epoxy composite laminates. *Fibres Text. East. Eur.* **2018**, *26*. [CrossRef]
28. Latko-Durałek, P.; Dydek, K.; Bolimowski, P.; Golonko, E.; Durałek, P.; Kozera, R.; Boczkowska, A. Nonwoven fabrics with carbon nanotubes used as interleaves in CFRP. *IOP Conf. Ser. Mater. Sci. Eng.* **2018**, *406*, 012033. [CrossRef]
29. Quan, D.; Mischo, C.; Binsfeld, L.; Ivankovic, A.; Murphy, N. Fracture behaviour of carbon fibre/epoxy composites interleaved by MWCNT- and graphene nanoplatelet-doped thermoplastic veils. *Compos. Struct.* **2020**, *235*, 111767. [CrossRef]
30. Dydek, K.; Boczkowska, A.; Latko-Durałek, P.; Wilk, M.; Padykuła, K.; Kozera, R. Effect of the areal weight of CNT-doped veils on CFRP electrical properties. *J. Compos. Mater.* **2020**, *54*, 2677–2685. [CrossRef]
31. Kasaliwal, G.R.; Pegel, S.; Gödel, A.; Pötschke, P.; Heinrich, G. Analysis of agglomerate dispersion mechanisms of multiwalled carbon nanotubes during melt mixing in polycarbonate. *Polymer* **2010**, *51*, 2708–2720. [CrossRef]
32. Nohara, L.B.; Nohara, E.L.; Moura, A.; Gonçalves, J.M.R.P.; Costa, M.L.; Rezende, M.C. Study of crystallization behavior of poly(phenylene sulfide). *Polimeros* **2006**, *16*, 104–110. [CrossRef]
33. Nobile, M.R. *Rheology of Polymer-Carbon Nanotube Composites Melts*; Woodhead Publishing Limited: Sawstln, UK, 2011; ISBN 9781845697617.
34. Jin, S.H.; Choi, D.K.; Lee, D.S. Electrical and rheological properties of polycarbonate/multiwalled carbon nanotube nanocomposites. *Colloids Surf. Physicochem. Eng. Asp.* **2008**, *313–314*, 242–245. [CrossRef]
35. Bangarusampanth, D.S.; Ruckdäschel, H.; Altstädt, V.; Sandler, J.K.W.; Garray, D.; Shaffer, M.S.P. Rheological and electrical percolation in melt-processed poly(ether ether ketone)/multi-wall carbon nanotube composites. *Chem. Phys. Lett.* **2009**, *482*, 105–109. [CrossRef]
36. Pegel, S.; Pötschke, P.; Petzold, G.; Alig, I.; Dudkin, S.M.; Lellinger, D. Dispersion, agglomeration, and network formation of multiwalled carbon nanotubes in polycarbonate melts. *Polymer* **2008**, *49*, 974–984. [CrossRef]
37. Villmow, T.; Kretzschmar, B.; Pötschke, P. Influence of screw configuration, residence time, and specific mechanical energy in twin-screw extrusion of polycaprolactone/multi-walled carbon nanotube composites. *Compos. Sci. Technol.* **2010**, *70*, 2045–2055. [CrossRef]
38. Noll, A.; Burkhart, T. Morphological characterization and modelling of electrical conductivity of multi-walled carbon nanotube/poly(p-phenylene sulfide) nanocomposites obtained by twin screw extrusion. *Compos. Sci. Technol.* **2011**, *71*, 499–505. [CrossRef]
39. Villmow, T.; Pötschke, P.; Pegel, S.; Häussler, L.; Kretzschmar, B. Influence of twin-screw extrusion conditions on the dispersion of multi-walled carbon nanotubes in a poly(lactic acid) matrix. *Polymer* **2008**, *49*, 3500–3509. [CrossRef]
40. Moniruzzaman, M.; Winey, K.I. Polymer nanocomposites containing carbon nanotubes. *Macromolecules* **2006**, *39*, 5194–5205. [CrossRef]
41. Fornes, T.D.; Paul, D.R. Crystallization behavior of nylon 6 nanocomposites. *Polymer* **2003**, *44*, 3945–3961. [CrossRef]
42. Krause, B.; Villmow, T.; Boldt, R.; Mende, M.; Petzold, G.; Pötschke, P. Influence of dry grinding in a ball mill on the length of multiwalled carbon nanotubes and their dispersion and percolation behaviour in melt mixed polycarbonate composites. *Compos. Sci. Technol.* **2011**, *71*, 1145–1153. [CrossRef]
43. Socher, R.; Krause, B.; Hermasch, S.; Wursche, R.; Pötschke, P. Electrical and thermal properties of polyamide 12 composites with hybrid fillers systems of multiwalled carbon nanotubes and carbon black. *Compos. Sci. Technol.* **2011**, *71*, 1053–1059. [CrossRef]

Article

Mono–Material 4D Printing of Digital Shape–Memory Components

Dalia Niazy^{1,*} , Ahmed Elsabbagh² and Mostafa R. Ismail¹

¹ Architecture Department, Faculty of Engineering, Ain Shams University, Cairo 11566, Egypt; mostafa_ismail@eng.asu.edu.eg

² Design and Production Engineering Department, Faculty of Engineering, Ain Shams University, Cairo 11566, Egypt; elsabbagh.ahmed@eng.asu.edu.eg

* Correspondence: dalia.niazy@eng.asu.edu.eg

Abstract: Dynamic shading systems in buildings help reduce solar gain. Actuated systems, which depend on renewable energy with reduced mechanical parts, further reduce building energy consumption compared to traditional interactive systems. This paper investigates stimuli-responsive polymer application in architectural products for sustainable energy consumption, complying with sustainable development goals (SDGs). The proposed research method posits that, by varying the infill percentage in a pre-determined manner inside a 3D-printed mono-material component, directionally controlled shape change can be detected due to thermal stimuli application. Thus, motion behavior can be engineered into a material. In this study, PLA+, PETG, TPU and PA 6 printed components are investigated under a thermal cycle test to identify a thermally responsive shape-memory polymer candidate that actuates within the built environment temperature range. A differential scanning calorimetry (DSC) test is carried out on TPU 95A and PA 6 to interpret the material shape response in terms of transitional temperatures. All materials tested show an anisotropic shape-change reaction in a pre-programmed manner, complying with the behavior engineered into the matter. Four-dimensional (4D)-printed PA6 shows shape-shifting behavior and total recovery to initial position within the built environment temperature range.

Keywords: 4D printing; material programming; digital fabrication; shape-memory polymers

Citation: Niazy, D.; Elsabbagh, A.; Ismail, M.R. Mono–Material 4D Printing of Digital Shape–Memory Components. *Polymers* **2021**, *13*, 3767. <https://doi.org/10.3390/polym13213767>

Academic Editors: Somen K. Bhudolia, Andrea Ehrmann and Sunil Chandrakant Joshi

Received: 7 September 2021

Accepted: 28 October 2021

Published: 30 October 2021

Publisher's Note: MDPI stays neutral with regard to jurisdictional claims in published maps and institutional affiliations.



Copyright: © 2021 by the authors. Licensee MDPI, Basel, Switzerland. This article is an open access article distributed under the terms and conditions of the Creative Commons Attribution (CC BY) license (<https://creativecommons.org/licenses/by/4.0/>).

1. Introduction

Digital materiality is defined as the combination of digital and material disciplines in the fields of built environment design and construction [1]. The application of 3D printing digital fabrication to acquire smart spatial structures has been widely investigated [2–5]. Three-dimensional (3D) printing as an additive manufacturing (AM) method is highly preferred due to the recyclability it allows, which enhances system sustainability [6]. The application of the 3D printing method to acquire stimuli-responsive spatial deformation in a programmed manner has been classified as a 4D printing manufacturing paradigm [7,8]. Four-dimensional (4D)-printed components hold a promising method for advancing interactive architecture components by exploiting surrounding environment parameters—renewable energy resources—as stimuli for motion.

Implementing 4D polymeric material programming in architecture can enable building interactive system components, which can be achieved in six steps: system motion design, identifying the required angle of bending that corresponds with the solar radiation penetration, system component identification, allocation of active components within the system and programming the polymers by 3D printing. Four-dimensional (4D) printing manufacturing parameters are identified as final desired shape, material properties, stimulus and material structure through printing paths [8]. Material structure by bi-/multi-layered 3D-printed multi-material composites is classified as an established method for attaining a 3D stimuli-responsive structural form from 2D structures [9–12]. The act of

recovering a polymer to its initial position after actuation upon stimuli application is identified as a two-way shape-memory polymer (SMP) [4,13,14].

Most two-way shape-memory effects previously achieved in polymers required composite formation [12,15]. Thus, the material structure of multi-materials has been widely investigated. Consequently, the material structure programming parameter through control of printing paths has undergone an evolution, which started from 3D patterning of an actuating polymer above an elastomeric matrix to the complete weaving of multi-materials [12,16–20]. As an example, Zolfagharian et al. [16] achieved different angles and rates of bending of a film component by varying the pattern of chitosan hydrogel ink coated in the middle of a 3D-printed pre-strained polystyrene film. Wang et al. [17] achieved variable deployable structures of bi-layer, multi-material printed components by varying the pattern of carbon fibers on a flexible polyamide 66 matrix. In [21,22], the effect of adding fillers to an SMP enhanced the thermal and/or electric conductivity of the SMP matrix, resulting in reduced actuation and recovery time, as well as reduced electric current consumption in the case of an electro-activated SMP. Correa et al. [23] applied multi-material 4D printing to achieve an architectural-scale product by weaving a composite of wood polymer composite (WPC) with acrylonitrile butadiene styrene (ABS) in different patterns. The weaved composite showed variable directional control in correspondence with 3D-printed patterns angles. It was observed that submerging the SMP matrix, before stimuli application, in solvents modified the glass transition temperature T_g , which was identified as a plasticizing effect [24,25].

Gladman et al. [26] explored different spatial deformation from 2D to 3D structures through 3D printing nozzle path variation, expressed as patterning for a single material. The single material Gladman et al. used was a digital hydrogel composite. The cellulose fibril alignment inside the hydrogel controlled the motion direction. In general, directional motion control in self-shape-shifting components depends on stress. The shape-memory effect (SME) is defined as the proportional change to stimuli applied upon material programming [14,27]. Thermal stimuli-responsive composite manufacturing is based on volumetric thermal expansion (Equation (1)). Variable volume change due to variance in the thermal expansion coefficient (α) of each lamina/part/layer causes stress between layers, evoking directional motion control, which produces overall composite shape variation in response to stimuli application.

$$\Delta V = 3V_0 \times \alpha \times \Delta T \quad (1)$$

The complexity of 3D printing by fused deposition modeling (FDM) is increased in multi-polymeric materials. A multi-layered component for 4D printing, where the materials' required print bed temperature may vary, may pose a constraint for printing feasibility. Thus, further investigation of Gladman et al.'s method with a different approach for the printing of single material is conducted in this paper. This paper investigates thermal stimuli-responsive shape shifting by 3D printing of a single/mono-material to acquire anisotropic shape shifting through variable infill parameters during printing. Motion direction control is programmed into the material by applying variable infill parameters of nozzle path design and patterning effect. This verifies the hypotheses that, for a 4D-printed mono-material at a constant thermal expansion coefficient (α), varying the initial volume (V_0) of the separate layers/lamina of a single/mono 3D-printed material will result in an overall anisotropic volumetric change in a controlled direction and shape. The volumetric change will be induced due to the generation of internal stresses inside the sample directing the motion. Thus, 4D printing of a single/mono-material of variable infill parameters is investigated through experiments. This method presents a different patterning approach. The approach proposed differs from that of Galman et al. in that the directional motion control is achieved using variable infill parameters. As per the experiments conducted, 4D-printed samples can actuate in a preprogrammed manner, as the angle of curvature—motion direction—is affected by the infill pattern, initial volume—infill percentage—of each layer, glass transition range and Young's modulus of the material.

The computationally simulated dynamic system in Figure 1 is a bending-active system with variable angles of curvature, demonstrating possible architecture application. The system consists of two parts of 4D-printed components as sensors and motion drivers, while a textile sheet is fixed in between. Upon the programming of motion into the material, the material becomes informed to acquire an environmentally passive dynamic system, and the shading unit produced is thermally actuated. Kangaroo in the Grasshopper plugin was utilized for the model motion simulation. The angles of curvature observed from the experiments are used as motion limits in the simulation.

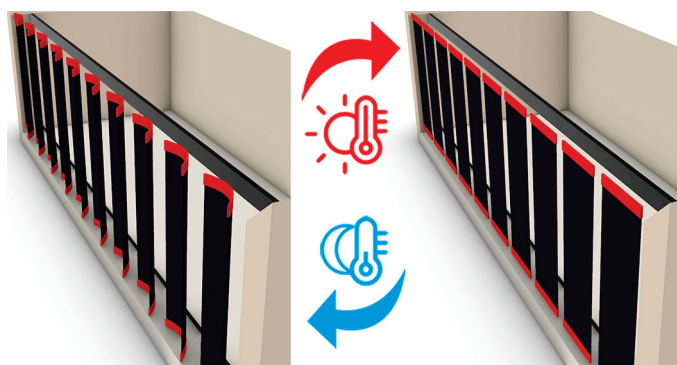


Figure 1. Sun-shading architecture interactive system. It actuates according to heat stimuli.

2. Materials and Methods

Material selection depended on the commercial availability of environmentally friendly filaments in Egypt. Polylactic acetate (PLA+)(eSUN, Shenzhen, China), polyamide 6 (eSUN PA 6), thermoplastic polyurethane 95A (eSUN TPU 95A) and recyclable polyethylene terephthalate glycol (eSUN PETG) filaments were investigated. Ester-based TPU [28] and PLA [11,28,29] are biodegradable. Thus, eSUN PLA+ filament was used. PLA+ was selected, as it has ten times higher mechanical strength than PLA. PA 6 was selected, as it is of high mechanical strength and biocompatible [29]. Due to the commercial availability of filaments, PA 6 was selected over biodegradable polyamide 11 (PA 11), and eSUN TPU 95A filament was selected over ester-based TPU. The selected filaments' elongation percentages as received by the supplier are 196%, 12%, 780% and 225% for PA 6, PLA+, TPU 95A and PETG, respectively. Young's modulus was calculated to be 225.2, 9.054, 12.09 and 6.37 N/mm² for PLA+, PETG, PA 6 and TPU 95A, respectively.

2.1. 3D Printing

All materials investigated were 3D printed using FDM 3D printers. PLA+, TPU 95A and PETG were 3D printed using the Creality CR-10 V2 FDM(Creality, Shenzhen, China) printer, while PA 6 was printed using the ANYCUBIC Chiron printer (ANYCUBIC, Shenzhen, China). The PLA+ filament printing parameters are 200 °C, 50 °C and 60 mm/s for nozzle temperature, bed temperature and printing speed, respectively. The PA 6 filament printing parameters are 255 °C, 90 °C and 50 mm/s for nozzle temperature, bed temperature and printing speed, respectively. The TPU 95A printing parameters are 220 °C, 60 °C and 30 mm/s for nozzle temperature, bed temperature and printing speed, respectively. The PETG filament printing parameters are 245 °C, 70 °C and 40 mm/s for nozzle temperature, bed temperature and printing speed, respectively.

In this paper, one of Bakradze et al.'s [30] optimization strategies were used. The low-surface-roughness optimization strategy was utilized to provide higher geometrical precision and good mechanical properties. Printing speed was lowered with higher-temperature printing. Geometrical precision is essential for the investigation of the infill pattern and percentage method, as the material distribution is a key parameter to investigate 4D printed mono-material programmed motion.

2.2. Motion Programming Methodology

The directional motion investigation utilized material allocation during 3D printing. The infill variation parameter was suitable for mono-material 4D printing. Programming was performed by designing the print path parameters—infill percentage and pattern—followed by a thermal stimuli application step for the one-way shape-memory effect. In the two-way shape-memory effect, material programming was performed through print path design, while stimuli application was for validation of recoverability. Sample component geometry was computationally modeled using Rhinoceros software. Then, Ultimaker Cura (Software, Utrecht, The Netherlands) was used to control the infill printing parameters, which was the shape-shifting stimulator. Four-dimensional (4D)-printed components were not submerged in any solvent. The 4D mono-material printing method was conducted on different materials with different mechanical parameters to investigate the resulting one-way or two-way SME.

In the thermal stimuli application, 3D-printed samples were heated in an enclosed chamber to ensure uniform heat distribution on samples. During the experiment, each sample was fixed in place using a clamp at the bottom part and left free hanging upward, as shown in Figure 2. A thermometer was placed during the heating process to determine the temperature range at which actuation occurs. At the actuation temperature of samples, the oven door was opened to allow the samples to cool to room temperature and prevent excess heating. Experiments were video recorded. Actuation and angle of curvature were determined using Kinovea software by analyzing the recorded physical experiment images. The images were recorded every 5 s.

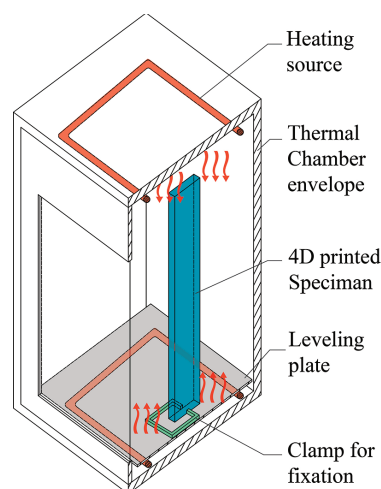


Figure 2. Sketch illustrating uniform heat distribution on 4D-printed sample during thermal programming.

The experimental model consisted of six major steps: form design, infill variation design, FDM 3D printing, thermal enclosure test, angle of curvature analysis and deducing motion direction. The investigation of method validity was carried out in three tests. In the first test, the method was applied to different materials to investigate the programmability of each while maintaining constant infill parameters for all printed samples, as found in Section 3.1. The following step was to identify the impact of varying the print path parameters on the most programmable material. The second step was divided into two tests, variation of the infill pattern and variation of infill percentage of the bottom and lower layers, as found in Section 3.2.

In the infill percentage variation test, the investigation parameters selection depended on acquiring different overall percentages of the same 4D printing material, which is further explained in Section “3D Printing”. The overall percentages selected provided a wide spectrum of iterations for testing to deduce resulting behavior.

3. Experimental Section

3.1. 3D Printing by Variable Printing Infill

3.1.1. Variable Infill Layering

Samples were designed in the form of a strip with dimensions of $200 \times 30 \times 6.4 \text{ mm}^3$, as Form Iteration 1. The strip was equally divided into lower and upper parts: the lower part of 80% infill and the upper part of 20% infill. Each layer had a thickness of 3.2 mm. The variation of print paths, which differed in infill percentage and patterning in the printed layers, is illustrated in Figure 3A. There was an upper layer above the upper part and a lower layer below the lower part. Both the upper and lower layers were fully enclosed, and no gaps between the horizontal layers were found. Additionally, there is no enclosed layer between the upper and lower infills. The overall enclosed perimeter (wall parameter) of the specimen was printed with a thickness of 0.4 mm. PLA+, TPU, PETG and PA6 were 3D printed with the material distribution design of Form Iteration 1. All printed samples were of a diagonal infill pattern. Each sample was tested in the thermal enclosure separately.

The experimental thermal stimuli application test was conducted. The graph in Figure 3B illustrates the relationship between time and the thermal cycle heating and cooling rates. The cooling rate exceeded $16 \text{ }^\circ\text{C}/\text{min}$ for the PLA, PETG and TPU samples. In the PA6 sample, the cooling rate was $2 \text{ }^\circ\text{C}/\text{min}$.

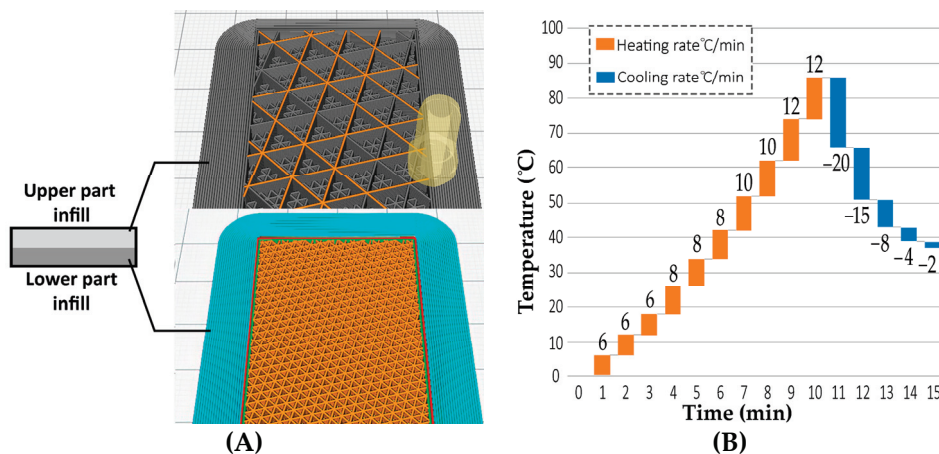


Figure 3. (A) Form Iteration 1: hypothesis validity sample modeling. Lower part (Layer 1) of 80% infill and upper (Layer 2) of 20% infill. Simulation of print paths of infill variation using Cura software between layers from bottom to top. (B) Graph illustrating heating and cooling rates during thermal programming of 4D-printed TPU.

3.1.2. Results

PLA+ and TPU show total deflection in the direction of the lower infill percentage. PETG shows total deflection in the higher infill layer direction, while PA 6 shows a recoverable curvature toward the higher infill, as shown in Figure 4. PLA+, TPU and PETG show gradient angles of curvature after actuation temperatures of $65 \text{ }^\circ\text{C}$, $\sim 80 \text{ }^\circ\text{C}$ and $\sim 60 \text{ }^\circ\text{C}$, respectively as shown in Figure 4c,e,h–k. PA 6 shows variable curvature angles at a lower actuation temperature of $28 \text{ }^\circ\text{C}$, observed in the first step of actuation Figure 4m. PETG and PLA+ show no recovery to initial position during cooling and no recovery after stimuli removal Figure 4c,f. TPU shows a recoverable 7° curvature during the test toward a higher infill percentage layer above $40 \text{ }^\circ\text{C}$, which presents the first step of actuation Figure 4h. It then deflects in the lower infill direction of 59° , which is the second step of actuation at a temperature of $108 \text{ }^\circ\text{C}$, and after cooling to room temperature, it recovers by 2° . The total attained curvature is 50° Figure 4k. TPU deflection toward a higher infill is observed to be recoverable shape memory upon stimuli removal. PA6 deflects in the 80% infill direction for 2° above $28 \text{ }^\circ\text{C}$ Figure 4m, then at 3° above $34 \text{ }^\circ\text{C}$ Figure 4n. PA6 shows total recovery to the original position during cooling Figure 4q.

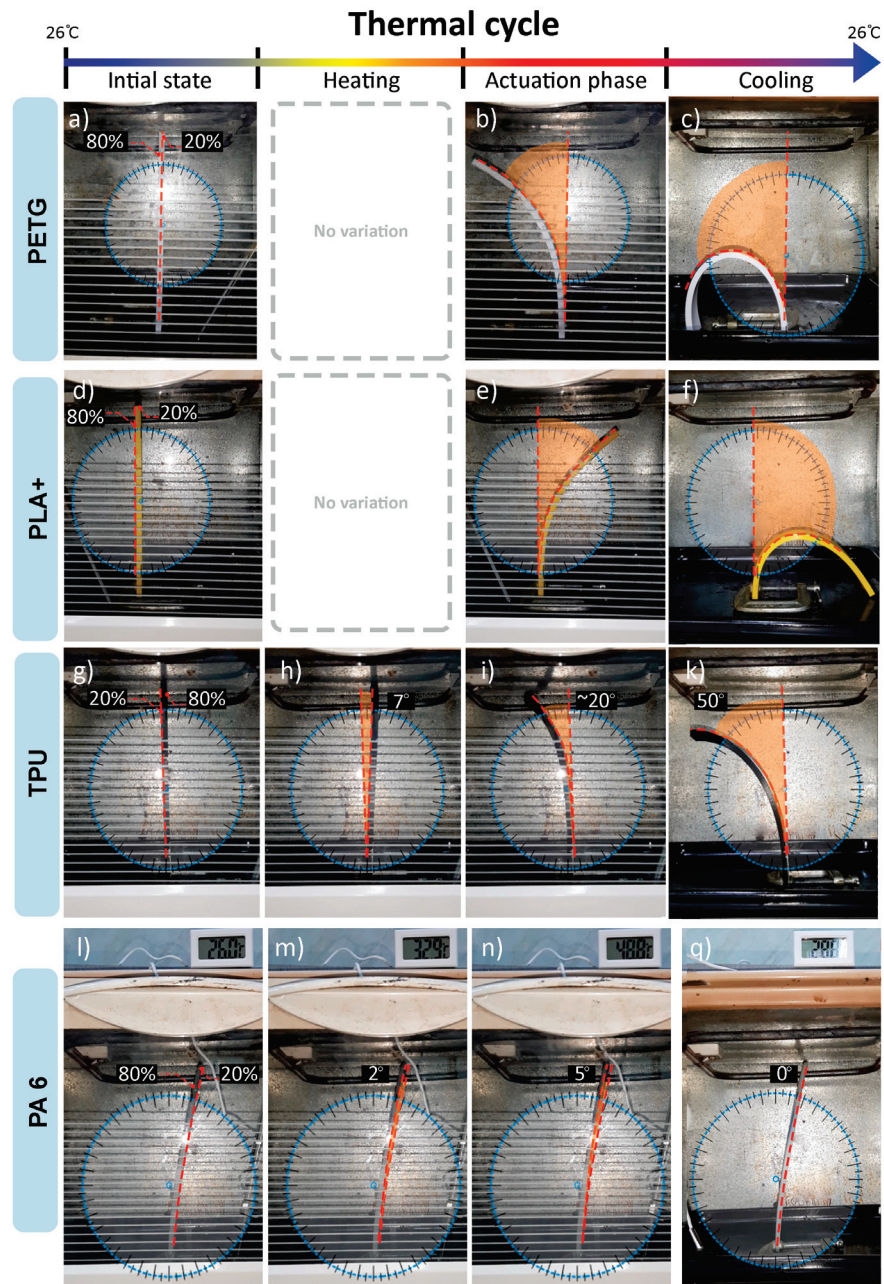


Figure 4. Comparison between PETG, PLA+, TPU and PA6 thermal test results using Kinovea to determine angles of curvature: (a) initial form of PETG; (b) actuation above 60 °C of 30° curvature, then 60° at 85 °C in 80% infill direction; (c) total curvature of 180° after cooling; (d) initial form of PLA+; (e) actuation above 65 °C of gradient curvature; (f) total curvature of 180° after cooling; (g) initial form of TPU; (h) 7° recoverable curvature toward 80% infill; (i) actuation at temperature ~80 °C, deflection toward 20% infill direction; (k) 50° total curvature in 80% infill direction after 2° recovery toward 20% infill; (l) initial form of PA 6; (m) actuation temperature above 28 °C toward 80% infill of 2° curvature; (n) actuation temperature above 40 °C toward 80% infill of 3° curvature; (q) 5° recovery in 20% infill direction.

3.2. Programming Variations Using 3D Printing Infill Parameters

3.2.1. Infill Pattern Parameter

The pattern variance effect on shape shifting was tested by comparing the angle of deflection of the TPU sample of the same spatial dimensions and two different pattern iterations, which were grid and diagonal infill patterns. A TPU sample with dimensions of

200 × 30 × 6.4 mm was 3D printed with a grid infill pattern, different from the diagonal 3D-printed pattern of the TPU sample in Section 3.1.2. As shown in Figure 5, upon heating, the grid infill pattern sample deflects in the 80% infill direction for 5° recovery Figure 5b, then deflects back in the 20% infill direction for ~25°, with a net angle of curvature of 19° Figure 4c. The total angle of curvature of the grid infill pattern is ~31° less than the diagonal infill sample.

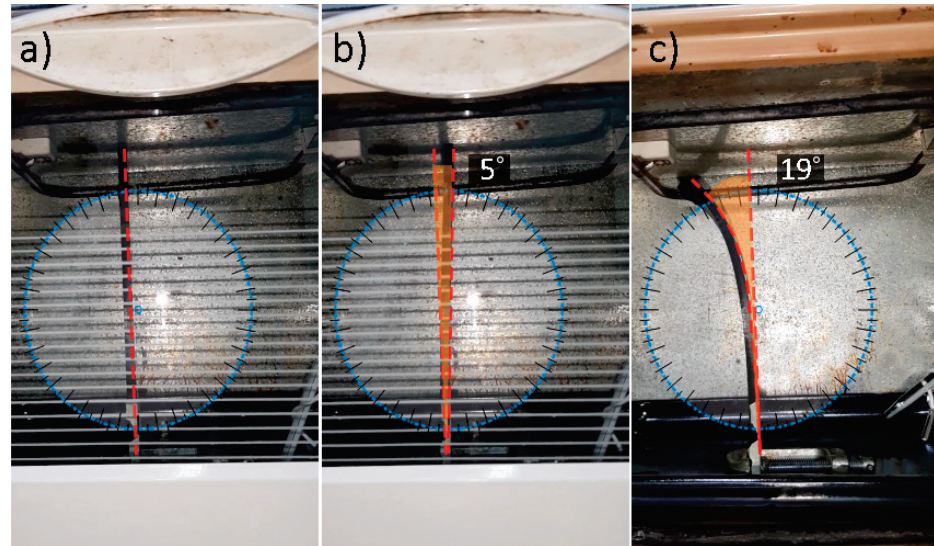


Figure 5. TPU sample of grid infill pattern: (a) initial position before heating; (b) deflection toward higher infill percentage; (c) total curvature after cooling toward lower infill percentage.

3.2.2. Infill Percentage Parameter

This section investigates the impact of varying the infill percentage of each layer on the shape-shifting behavior upon stimuli application and the resultant variance of the angle of curvature. Based on the previous results in Figure 4, it was deduced that the 3D-printed TPU shows the largest angle of curvature using the variable infill method. Thus, it was selected to investigate the infill percentage parameter effect. Samples were printed with a more variable infill percentage for each layer than in Figure 3A. Each sample was subjected to a heating cycle of ramping the thermal enclosure to 110 °C, then the enclosure was opened to allow free cooling to reach room temperature. The room temperature was kept at 25 °C.

3D Printing

The printed samples were of a diagonal infill pattern because, from the infill pattern variance test experiment, it was found that the diagonal pattern allows larger deformation. Samples of Form Iteration 1 have overall dimensions and layer thickness. Six different infill percentage iterations were 3D printed to investigate the material behavior. The iterations were designed by varying the percentages of the upper part's infill percentage with a constant lower infill percentage of 80%. The overall percentage was the ratio between the upper- and lower-part infill percentages in Equation (2), and the overall percentages tested were 10%, 20%, 25%, 30%, 40% and 50%.

$$\text{Overall percentage} = \frac{\text{Upper Part infill percentage}}{\text{Lower Part infill percentage}} \quad (2)$$

Verifying the effect of the overall percentages of the variable 3D-printed infills—upper- to lower-part infill percentages—the impact on curvature was measured by testing the same overall percentages with another constant lower infill percentage of 60%, as shown in Table 1. Three samples of each infill percentage iteration were tested separately, and the

resulting angles of the curvatures of samples of the same variable infill iteration were of a 0–1° curvature difference.

Table 1. Infill percentage parameter test results. All samples show net curvature deflection toward the lower infill percentage part.

Overall Percent	Diagonal Infill Pattern		Total Angle of Curvature	Net Motion Direction Toward	Recoverable Deflection Angle toward Higher Infill %
	Lower-Layer Infill %	Upper-Layer 2 Infill %			
10%	80	8	65°	Lower infill	7°
20%	80	16	60°		7°
25%	80	20	50°		7°
30%	80	24	37°		5°
40%	80	32	30°		7°
50%	80	40	27°		7°
10%	60	6	85°	Lower infill	5°
20%	60	12	76°		7°
25%	60	15	72°		5°
30%	60	18	67°		5°
40%	60	24	56°		5°
50%	60	30	31°		5°

Results

In all samples, deflection toward the higher infill percentage was deduced at the beginning at a temperature above ~40 °C, and following actuation toward a lower infill percentage was detected above ~80 °C. All samples of the 80% lower infill showed maximum curvature at 110 °C, while all samples of 60% lower infill showed maximum curvature at 108 °C.

As shown in Table 1, in samples of the 60% lower-layer infill, the 60–6% infill sample shows 85°, the 60–12% infill sample shows 76°, the 60–15% infill sample shows 72°, the 60–18% infill sample shows 67°, the 60–24% infill sample shows 56° and the 60–30% infill sample shows 31°. In the samples of the lower layer of 80% infill, the 80–8% infill sample shows 65°, the 80–16% infill sample shows 60°, the 80–20% infill sample shows 50°, the 80–24% infill sample shows 37°, the 80–32% infill sample shows 30° and the 80–40% infill sample shows 27°. In Figure 6, a graph is deduced from the empirical experiment results. The graph represents the relationship between the sample overall percentage and the resulting curvature due to thermal stimuli.

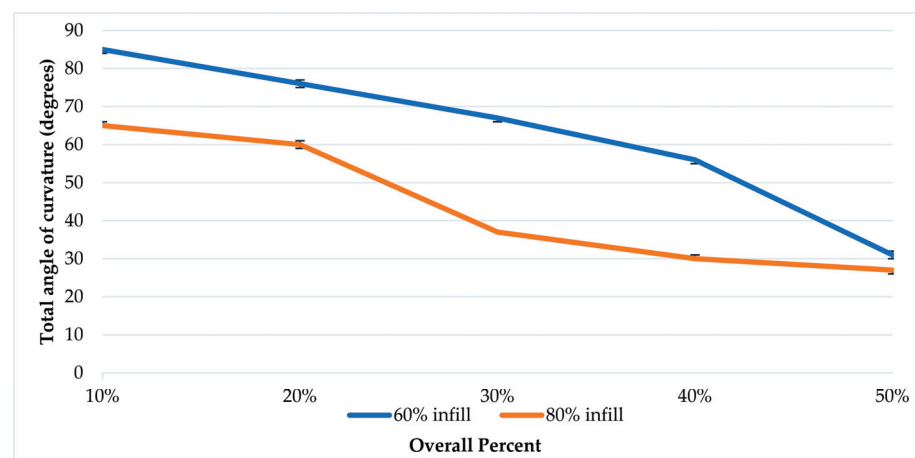


Figure 6. Overall percentage and resulting programming curvature graph. Deviations range from 0 to 1 degrees of curvature.

3.3. Differential Scanning Calorimetry (DSC) Test

TA Instrument Q2000 DSC (Mettler Toledo, Columbus, OH, USA) was used on materials showing programmability. The test was used to identify the thermal properties of TPU 95A and PA 6 to investigate the observed infill variation experiment results with the thermal properties. A cyclical heat-cool-heat pan test was applied to the polymeric TPU 95A sample with a weight of 10 mg and PA6 with a weight of 6.5 mg. Each sample was heated at a rate of 10 °C/min from −50 °C up to 350 °C under nitrogen atmosphere. Three cycles were registered for each sample, as shown in Figures 7 and 8, in which Cycle 1 represents the thermal properties of the material during the experimental tests.

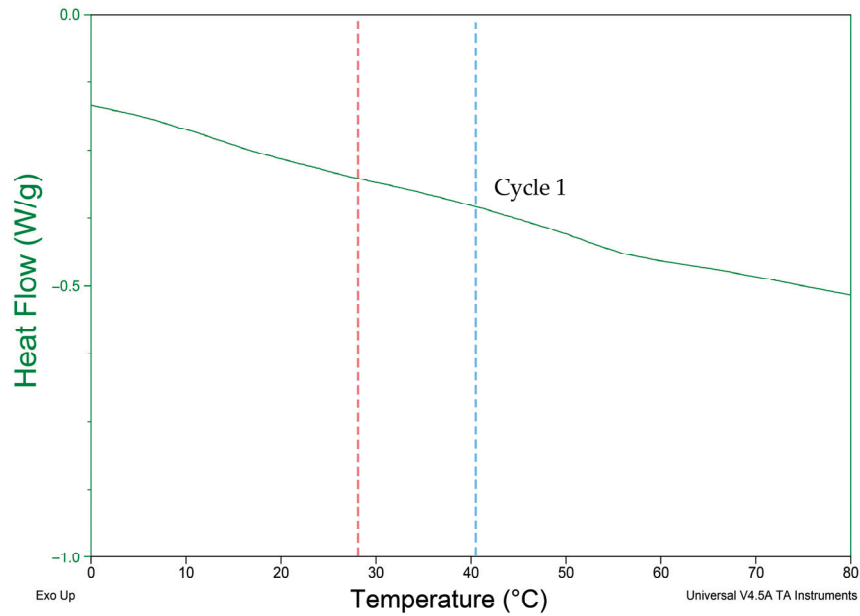


Figure 7. DSC test result of PA 6 3D-printed sample. Red line indicates first actuation step. Blue line indicates second actuation step.

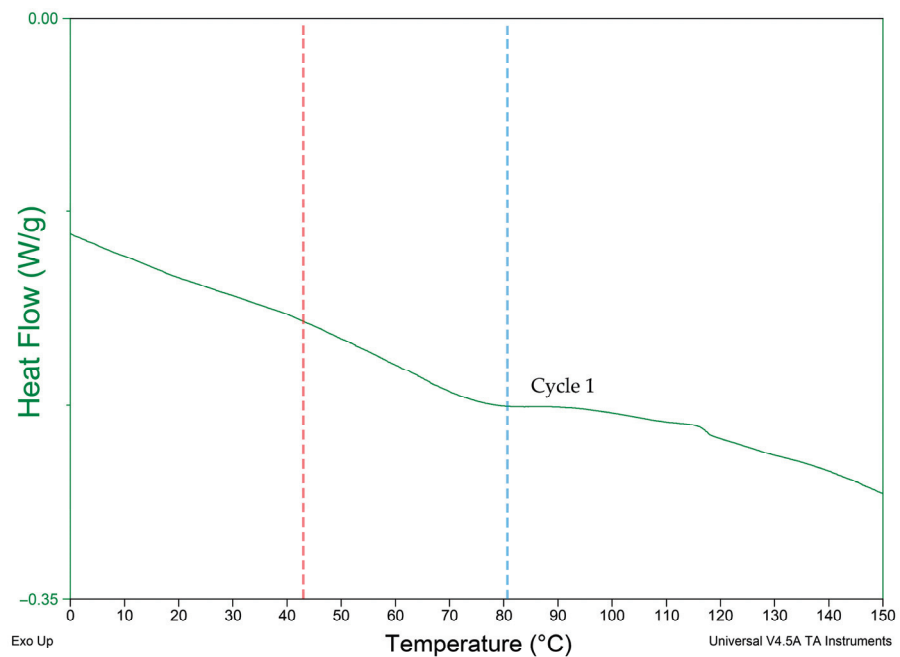


Figure 8. DSC test result of TPU. Red line indicates first actuation step. Blue line indicates second actuation step.

4. Discussion

Shape-shifting behavior was investigated by programming a 4D-printed mono-material with variable parameters of infill percentage and pattern. Infill percentage variation between the top and bottom parts of the sample was observed to control the total angle of curvature and motion direction. Upon investigation of the four polymers, it was deduced that PA 6 and TPU 95A show programmability with the proposed 4D printing method. The broad glass transition indicates the crystalline nature of PA 6 and TPU 95A. PETG and PLA are known to have an amorphous structure [31,32]. Although PA 6 has a lower elongation percentage and a higher Young's modulus than PETG, PA 6 shows recoverable programmability, while PETG does not, as shown in Figure 4. Figures 7 and 8 show that PA 6 and TPU 95A have broader glass transition ranges than PLA+ and PETG. The results present that in the low range of polymers' Young's modulus, the selection criteria of the programmable material of the mono-material 4D printing method can be referred to as the crystallinity of PA 6 and TPU 95A.

When analyzing the behavior of programmed materials using the mono-material 4D printing method, one-way and two-way shape-memory effects (SMEs) are observed. PA 6 shows two recoverable actuation steps, and the temperatures of actuation lie within the glass transition range, as shown in Figure 7. The one-way SME of PA 6 is observed upon exceeding the glass transition range. The 4D-printed TPU can be programmed as a one-way and two-way SMP. The 4D-printed TPU shows curvature toward a higher infill percentage, which is totally recoverable upon stimuli removal on the condition that the programming temperature does not exceed 80 °C as the first step of actuation. One-way 4D printing of TPU results upon exceeding 80 °C and the control of the cooling time and rate. One-way 4D-printed TPU results in the second step of actuation. The infill percentage variance in Figure 6 shows that higher angles of curvature result from samples of a constant 60% rather than 80% bottom-part infill. By comparing the behavior recorded of TPU in Figure 9 with the thermal properties graph in Figure 8, the first step of recoverable actuation is within the glass transition range, while the second step of actuation exceeds the glass transition range. Figure 9 indicates that gradient degrees of curvature can result by applying the same stimuli to several TPU 95A samples of a variable overall infill percentage. Angles of curvature deduced with 80% lower part infill in Figure 9a were lower than 60% in Figure 9b. A general behavior is deduced which is the lower the bottom-layer infill percentage, the higher the degree of curvature.

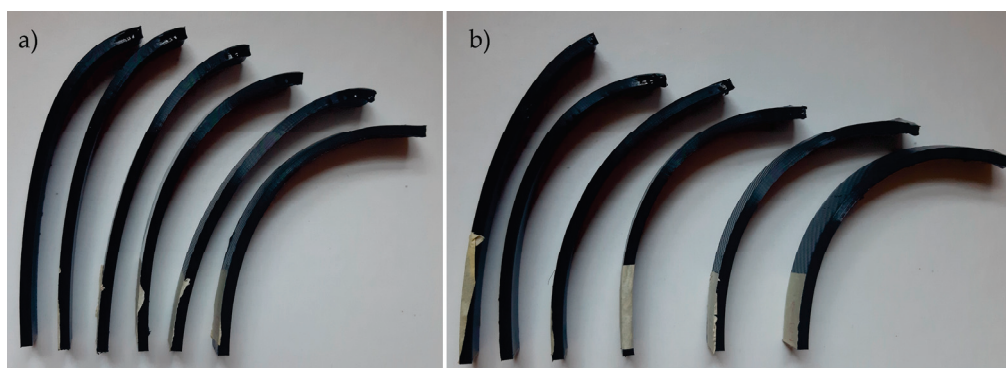


Figure 9. (a) Lower layer of 80% infill. Upper-layer infill percentages from left to right: 32%, 24%, 16% and 8%. (b) Lower layer of 60% infill. Upper-layer infill percentages from left to right: 32%, 18%, 15%, 12% and 6%.

The mono-material 4D printing method presents an upscaling approach. Programming of the 4D-printed components depends on stresses generated within the same 3D-printed layers of the material, which differ from studies in the literature on multi-material 4D printing to achieve stresses in the contact zones between different materials as motion drivers upon stimuli application. In the literature, multi-materials have mostly been actual-

ized by two separate processes of manufacturing, unlike this paper, which proposes a single 4D printing process. It is noted that although Galdman et al.'s method used single filament for 4D printing, it depended on the allocation of fibrils inside the printed filament for directional motion control; thus, directional motion programming was performed during the fabrication step of the filament as a first step, followed by the patterning effect during 3D printing. The 4D printing method presented in this research utilizes single-material 4D printing, where the directional motion programming step is performed during 3D printing only. The plasticizing effect helps control the T_g , which presents a method of investigation to achieve 4D printing components that can actuate within the built environment temperature range. The exposure of the component to the built environment can be investigated to validate the efficiency of the plasticizing effect in 4D printing architecture products. Additionally, integration of fillers in the presented 4D printing method can be investigated to enhance the efficiency of the 4D-printed component performance.

By investigating the application in architecture products, it is found that the interactive architecture system consists of sensors, actuators and a movable feature. Two-way PA 6 observed actuation temperatures lie within the built environment temperature range. Two-way TPU 95A recoverable actuation lies in the higher built environment temperature range, which can offer applications in arid climates. Thus, exploiting recoverable 4D-printed PA 6 and TPU 95A as alternatives to sensors and actuators while using renewable energy—solar radiation—as the motion driver would reduce electric energy consumption for shape-shifting façade systems, as well as reduce system pieces production. Adding the aspect of reduced production to sustainable resource consumption—electric energy consumption—would comply with the sustainable development goals of sustainable consumption and product SDGs. Another possible application would be applying one-way 4D-printed components to special tensegrity deployable architecture structures.

5. Conclusions

This paper validates the applicability of mono-material 4D printing to acquire directional motion control. The experimental tests indicate the possibility of one-way and two-way 4D printing using mono-material FDM. It is observed that the infill variation method produces a two-way SMP when applying thermal stimuli within the glass transition range, while a one-way SMP is produced by exceeding that range. It is concluded that polymeric filaments of broader glass transition range such as PA 6 and TPU 95A allow programming using the mono-material 4D printing method. The infill parameters of percentage and pattern affect the acquired angle of curvatures upon thermal stimuli application. A diagonal infill pattern allows a larger resulting angle of curvature upon stimuli application. It is deduced from Table 1 that the lower the overall upper- to lower-part infill percentages, the higher the angle of curvature. Additionally, it is concluded that the lower the infill percentage of the top part, the higher the resulting angle of curvature.

Author Contributions: Conceptualization, D.N., A.E. and M.R.I.; methodology, software, validation, formal analysis, investigation, resources, data curation, D.N.; writing—original draft preparation, A.E. and D.N.; writing—review and editing, supervision, project administration, A.E. and M.R.I. All authors have read and agreed to the published version of the manuscript.

Funding: This research received no external funding.

Institutional Review Board Statement: Not applicable.

Informed Consent Statement: Not applicable.

Acknowledgments: The authors acknowledge PolyLab in the Faculty of Engineering, Ain Shams University, Egypt, for providing the DSC test and thermal testing.

Conflicts of Interest: The authors declare no conflict of interest.



References

- Willmann, J.; Gramazio, F.; Kohler, M. Langenberg, Digital by Material. Proceedings of Rob Arch 2012, Vienna, Austria, December 2012. Available online: https://link.springer.com/chapter/10.1007/978-3-7091-1465-0_2 (accessed on 25 October 2021).
- Ge, Q.; Qi, H.J.; Dunn, M.L. Active materials by four-dimension printing. *Appl. Phys. Lett.* **2013**, *103*, 131901. [CrossRef]
- Raviv, D.; Zhao, W.; McKnelly, C.; Papadopoulou, A.; Kadambi, B.; Shi, S.; Hirsch, D.; Dikovskiy, M.; Zyracki, C.; Olguin, R.; et al. Active printed materials for complex self-evolving deformations. *Sci. Rep.* **2014**, *4*, 7422. [CrossRef] [PubMed]
- Momeni, F.; Liu, X.; Ni, J. A review of 4D printing. *Mater. Des.* **2017**, *122*, 42–79. [CrossRef]
- Li, J.; Duan, Q.; Zhang, E.; Wang, J. Applications of shape memory polymers in kinetic buildings. *Adv. Mater. Sci. Eng.* **2018**, *2018*. [CrossRef]
- Colorado, H.A.; Velásquez, E.I.G.; Monteiro, S.N. Sustainability of additive manufacturing: The circular economy of materials and environmental perspectives. *J. Mater. Res. Technol.* **2020**, *9*, 8221–8234. [CrossRef]
- Tibbits, S. 4D Printing. *Architect. Des.* **2020**, *84*, 421–433. [CrossRef]
- Momeni, F.; Ni, J. Laws of 4D Printing. *Engineering* **2020**, *6*, 10–17. [CrossRef]
- Zhang, Q.; Zhang, K.; Hu, G. Smart three-dimensional lightweight structure triggered from a thin composite sheet via 3D printing technique. *Sci. Rep.* **2016**, *6*, 22431. [CrossRef]
- Yu, K.; Ritchie, A.; Mao, Y.; Dunn, M.L.; Qi, H.J. Controlled Sequential Shape Changing Components by 3D Printing of Shape Memory Polymer Multimaterials. *Procedia IUTAM* **2015**, *12*, 193–203. [CrossRef]
- Miao, S.; Cui, H.; Nowicki, M.; Xia, L.; Zhou, X.; Lee, S.J.; Zhu, W.; Sarkar, K.; Zhang, Z.; Zhang, L.G. Stereolithographic 4D Bioprinting of Multiresponsive Architectures for Neural Engineering. *Adv. Biosyst.* **2018**, *2*, 1–10. [CrossRef] [PubMed]
- Wu, J.; Yuan, C.; Ding, Z.; Isakov, M.; Mao, Y.; Wang, T.; Dunn, M.L.; Qi, H.J. Multi-shape active composites by 3D printing of digital shape memory polymers. *Sci. Rep.* **2016**, *6*, 24224. [CrossRef]
- Yao, Y.; Zhou, T.; Wang, J.; Li, Z.; Lu, H.; Liu, Y.; Leng, J. Two way shape memory composites based on electroactive polymer and thermoplastic membrane. *Compos. Part. A Appl. Sci. Manuf.* **2016**, *90*, 502–509. [CrossRef]
- Zhang, Z.; Demir, K.G.; Gu, G.X. Developments in 4D-printing: A review on current smart materials, technologies, and applications. *Int. J. Smart Nano Mater.* **2019**, *10*, 205–224. [CrossRef]
- Westbrook, K.K.; Mather, P.T.; Parakh, V.; Dunn, M.L.; Ge, Q.; Lee, B.M.; Qi, H.J. Two-way reversible shape memory effects in a free-standing polymer composite. *Smart Mater. Struct.* **2011**, *20*, 65010. [CrossRef]
- Zolfagharian, A.; Kaynak, A.; Khoo, S.Y.; Kouzani, A. Pattern-driven 4D printing. *Sens. Actuators Appl. Phys. A* **2018**, *274*, 231–243. [CrossRef]
- Wang, Q.; Tian, X.; Huang, L.; Li, D.; Malakhov, A.V.; Polilov, A.N. Programmable morphing composites with embedded continuous fibers by 4D printing. *Mater. Des.* **2018**, *155*, 404–413. [CrossRef]
- Correa, D.; Menges, A. 3D printed hygroscopic programmable material systems. *Mater. Res. Soc. Symp. Proceed.* **2015**, *1800*, 24–31. [CrossRef]
- Correa, D.; Krieg, O.D.; Menges, A.; Reichert, S.; Rinderspacher, K. Hygroskin: A climate-responsive prototype project based on the elastic and hygroscopic properties of wood. In Proceedings of the ACADIA 2013 Adaptive Architecture—Proceeding 33rd Annual Conference Associated Computer Aided Design Architecture, Cambridge, ON, USA, 21–27 October 2013; pp. 33–42.
- Cheng, T.; Thielen, M.; Poppinga, S.; Tahouni, Y.; Wood, D.; Steinberg, T.; Menges, A.S. Bio-Inspired Motion Mechanisms: Computational Design and Material Programming of Self-Adjusting 4D-Printed Wearable Systems. *Adv. Sci.* **2021**, *2100411*, 1–12. [CrossRef]
- Lu, H.; Liang, F.; Gou, J.; Leng, J.; Du, S. Synergistic effect of Ag nanoparticle-decorated graphene oxide and carbon fiber on electrical actuation of polymeric shape memory nanocomposites. *Smart Mater. Struct.* **2014**, *23*, 85034. [CrossRef]
- Weber, E.H.; Clingerman, M.L.; King, J.A. Thermally conductive nylon 6,6 and polycarbonate based resins. I. Synergistic effects of carbon fillers. *J. Appl. Polymer Sci.* **2003**, *88*, 112–122. [CrossRef]
- Correa, D.; Poppinga, S.; Mylo, M.D.; Westermeier, A.S.; Bruchmann, B.; Menges, A.; Speck, T. 4D pine scale: Biomimetic 4D printed autonomous scale and flap structures capable of multi-phase movement. *Philosoph. Trans. R. Soc. A* **2020**, *378*, 445. [CrossRef] [PubMed]
- Huang, W.M.; Yang, B.; An, L.; Li, C.; Chan, Y.S. Water-driven programmable polyurethane shape memory polymer: Demonstration and mechanism. *Appl. Phys. Lett.* **2005**, *86*, 1–3. [CrossRef]
- Lu, H.; Leng, J.; Du, S. A phenomenological approach for the chemo-responsive shape memory effect in amorphous polymers. *Soft Matter* **2013**, *9*, 3851–3858. [CrossRef]
- Gladman, A.S.; Matsumoto, E.A.; Nuzzo, R.G.; Mahadevan, L.; Lewis, J.A. Biomimetic 4D printing. *Nat. Mater.* **2016**, *15*, 413–418. [CrossRef]
- Zhou, Y.; Huang, W.M.; Kang, S.F.; Wu, X.L.; Lu, H.B.; Fu, J.; Cui, H. From 3D to 4D printing: Approaches and typical applications. *J. Mech. Sci. Technol.* **2015**, *29*, 4281–4288. [CrossRef]
- Nath, K.; Ghosh, S.; Ghosh, S.K.; Das, P.; Das, N.C. Facile preparation of light-weight biodegradable and electrically conductive polymer based nanocomposites for superior electromagnetic interference shielding effectiveness. *J. Appl. Polymer Sci.* **2021**, *138*, 50514. [CrossRef]
- Barenberg, S.A.; Mulleur, E.P. *Biomedical Materials*, 2nd ed.; Springer International Publishing: Berlin/Heidelberg, Germany, 2021. [CrossRef]

30. Bakradze, G.; Arājs, E.; Gaidukovs, S.; Thakur, V.K. On the heuristic procedure to determine processing parameters in additive manufacturing based on materials extrusion. *Polymers* **2020**, *12*, 3009. [CrossRef] [PubMed]
31. Latko-Durałek, P.; Dydek, K.; Boczkowska, A. Thermal, Rheological and Mechanical Properties of PETG/rPETG Blends. *J. Polym. Environ.* **2019**, *27*, 2600–2606. [CrossRef]
32. Sin, L.T.; Tuen, B.S. Poly (Lactic Acid) Injection Molding and Three Dimensional Printing of Poly (Lactic Acid). In *Poly(lactic Acid)*, 2nd ed.; Sin, L.T., Tuen, B.S., Eds.; William Andrew Publishing: New York, NY, USA, 2019; pp. 325–345. [CrossRef]

Article

Rheological and Morphological Properties of Oil Palm Fiber-Reinforced Thermoplastic Composites for Fused Deposition Modeling (FDM)

Mohd Nazri Ahmad ^{1,2,3,*} , Mohamad Ridzwan Ishak ^{1,4,5,*}, Mastura Mohammad Taha ², Faizal Mustapha ¹ and Zulkiflle Leman ^{6,7} 

¹ Department of Aerospace Engineering, Faculty of Engineering, Universiti Putra Malaysia, Serdang 43400, Selangor, Malaysia; faizalms@upm.edu.my

² Faculty of Mechanical and Manufacturing Engineering Technology, Universiti Teknikal Malaysia Melaka, Hang Tuah Jaya, Durian Tunggal 76100, Melaka, Malaysia; mastura.taha@utem.edu.my

³ Centre of Smart System and Innovative Design, Universiti Teknikal Malaysia Melaka, Hang Tuah Jaya, Durian Tunggal 76100, Melaka, Malaysia

⁴ Aerospace Malaysia Research Centre (AMRC), Universiti Putra Malaysia, Serdang 43400, Selangor, Malaysia

⁵ Laboratory of Biocomposite Technology, Institute of Tropical Forestry and Forest Products (INTROP), Universiti Putra Malaysia, Serdang 43400, Selangor, Malaysia

⁶ Department of Mechanical and Manufacturing Engineering, Faculty of Engineering, Universiti Putra Malaysia, Serdang 43400, Selangor, Malaysia; zleman@upm.edu.my

⁷ Advanced Engineering Materials and Composites Research Centre, Faculty of Engineering, Universiti Putra Malaysia, Serdang 43400, Selangor, Malaysia

* Correspondence: mohdnazri.ahmad@utem.edu.my (M.N.A.); mohdridzwan@upm.edu.my (M.R.I.)

Citation: Ahmad, M.N.; Ishak, M.R.; Taha, M.M.; Mustapha, F.; Leman, Z. Rheological and Morphological Properties of Oil Palm Fiber-Reinforced Thermoplastic Composites for Fused Deposition Modeling (FDM). *Polymers* **2021**, *13*, 3739. <https://doi.org/10.3390/polym13213739>

Academic Editors: Somen K. Bhudolia and Sunil Chandrakant Joshi

Received: 26 September 2021

Accepted: 20 October 2021

Published: 29 October 2021

Publisher's Note: MDPI stays neutral with regard to jurisdictional claims in published maps and institutional affiliations.

Abstract: Fused deposition modelling (FDM) is a filament-based rapid prototyping technology that allows new composite materials to be introduced into the FDM process as long as they can be manufactured in feedstock filament form. The purpose of this research was to analyze the rheological behavior of oil palm fiber-reinforced acrylonitrile butadiene styrene (ABS) composites when used as a feedstock material, as well as to determine the best processing conditions for FDM. The composite's shear thinning behavior was observed, and scanning electron microscopy was used to reveal its composition. The morphological result found that there was a good fiber/matrix adhesion with a 3 wt% fiber loading, as no fiber pullouts or gaps developed between the oil palm fiber and ABS. However, some pores and fiber pullouts were found with a 5 and 7 wt% fiber loading. Next, the rheological results showed that the increment of fiber content (wt%) increased the viscosity. This discovery can definitely be used in the extrusion process for making wire filament for FDM. The shear thinning effect was increased by adding 3, 5, or 7 wt% of oil palm fiber. The non-Newtonian index (n) of the composites increased as the number of shear rates increased, indicating that the fiber loading had a significant impact on the rheological behavior. As the fiber loading increased, the viscosity and shear stress values increased as well. As a result, oil fiber reinforced polymer composites can be used as a feedstock filament for FDM.

Keywords: FDM; oil palm fiber; ABS; rheology



Copyright: © 2021 by the authors. Licensee MDPI, Basel, Switzerland. This article is an open access article distributed under the terms and conditions of the Creative Commons Attribution (CC BY) license (<https://creativecommons.org/licenses/by/4.0/>).

1. Introduction

Additive manufacturing (AM), also known as three-dimensional (3D) printing, has gradually gained traction in the manufacturing industry [1–3]. It can be utilized to print intricately shaped metallic, polymer, and composite items with a great design flexibility. By 2020, the market for AM products and services was estimated to exceed \$5 billion [4]. FDM is a wire-filament-based method that is frequently used to create functional parts [5–11]. The impact of the material qualities and mechanical properties of printed parts is critical for their further expansion into FDM. The filament wire is fed into the print head, which allows

for the three-dimensional dispensing of the resulting polymer melts on a platform that is lowered one layer at a time. FDM-printed parts are extremely anisotropic and this has a significant impact on the quality of the printed part [12,13]. This demonstrates that the intermolecular diffusion across the interface of the fused filaments is directly proportional to the strength of a thermoplastic interface within an FDM part. The importance of the bonding quality between consecutive filaments is determined by the printing parameters and the melt viscosity of the filament polymer. Previous researchers, such as McIlroy et al. [14,15], Murphy and Collins [16], and Cicala et al. [17], only looked into the effect of rheology on the FDM printing process. As a result, the rheological behavior of polymer melts during FDM processing is an important feature that needs to be investigated further in order to justify the impact of melt behavior on the printing quality. When manufacturing wire filaments for FDM, the flow behavior of a polymer composite material is critical, especially for custom-made composite materials.

For many years, industrial communities and academic circles have paid increasing attention to people's views of environmental issues and biodegradable polymer products [18–20]. "Rheology" refers to how materials deform and flow under stress. It is a basic concept in chemical engineering and the second-most referenced physicochemical feature in engineering research, after particle size distribution [18]. The term rheology was borrowed from Greek and defined as "flow science"—rheo ($\rho\epsilon\omega$) means "flowing". The term was created by Reiner [19], and the definition was recognized by a group of prominent scientists. A capillary rheometer is the most straightforward and oldest instrument that measures a fluid's flow through a pipe of considerable length relative to its diameter. Earlier in history, the water viscosity was measured by Hagen and Poiseuille [20]. Recently, industrial and academic communities have been paying growing attention to biodegradable polymer materials [21–24]. The capillary rheometer is currently one of the most commonly used tools for measuring the rheological properties of wood plastic composites with primarily powder fillers. Composites reinforced by fibers with a high aspect ratio, on the other hand, are too large to pass through the capillary die (commonly 1 mm in diameter). Furthermore, when simple premixed composites pass through the capillary cylinder, the natural fibers become entangled and detach from the polymer. Because of these fibers' low dispersion, the mixes are inhomogeneous, making the rheological measurements incorrect.

Many researchers have combined fibers with thermoplastic into composites, crushed them into pellets, and then used a capillary rheometer to test their rheological properties. Kalaprasad et al. used an extruder to make sisal-reinforced polymer composite granules, glass-reinforced polymer composite granules, and combined glass/sisal-reinforced polymer composites, then used a capillary rheometer to characterize the rheology of those composites [25]. The findings revealed that all three types of composites had pseudoplastic tendencies. The non-Newtonian index (n) of the glass fiber composite was lower than that of a sisal fiber composite with a similar fiber composition (20%). The non-Newtonian index of glass/sisal-reinforced composites reduced as the number of glass fibers increased, whereas the viscosity rose. These results showed that varied glass and sisal fiber morphologies had a considerable impact on rheological properties. Smita et al. [26] used a twin-screw extruder to make sisal/high-density polyethylene composites, and then used a capillary rheometer with the extruder to investigate the fiber composites' steady-state rheological characteristics. The results revealed that the entirety of each material had pseudoplastic properties, which can be described by the equation of the power law. The non-Newtonian index declined as the fiber loading increased from ten percent to thirty percent. The consistency index of the composites, on the other hand, increased. The capillary rheometer was used to assess the rheological characteristics of low-fiber-content composites (not exceeding 40% of the volume). In addition, during the premix and cutting procedures the fibers were sheared and pulled and the matrix could be degraded, all of which compromised the accuracy of the capillary rheometer's rheological data. Industries have created natural-fiber-reinforced composite (NFRC) materials. An NFRC is a composite material made up of a polymer matrix and natural fibers. Because of its lightweight quali-

ties, low cost, reduced damage to processing equipment, biodegradability, and relatively good mechanical properties, NFRC is widely employed in a variety of applications [27].

Synthetic fibers are human-made fibers that are generated by chemical synthesis and are further categorized as organic or inorganic based on their composition. Carbon fibers, glass fibers, basalt fibers, and aramid fibers are examples of synthetic fibers used in structural applications. Guijun et al. [28] discovered superior corrosive resistance in rods with a fiber random hybrid mode and a smaller diameter. Kevlar-fiber-reinforced composites have great impact strength and tensile qualities but low compression strength due to their anisotropic nature when compared to glass and carbon fibers [29]. Natural fibers are currently being employed in engineering applications as replacements for synthetic fibers. Today, natural fibers have become famous because of their advantages, such as their low cost, abundant availability, environmental friendliness, low density, and good mechanical properties [30]. Natural fibers such as flax, hemp, jute, coir, kenaf, and wood are utilized for reinforcing thermoplastics. On the other hand, natural fibers' drawbacks include a short lifetime—albeit with a minimal environmental impact when they degrade—and a limited processing temperature, which limit their performance and application [31]. Recently, there has been increased testing and exploration of the use of NFRC filaments for FDM, as well as increased concern for, and knowledge of, environmentally acceptable materials. However, one of the key difficulties for FDM is the melt flow behavior of NFRC materials. Islam et al. [32] reported with the addition of fiber and Maleic anhydride-grafted polypropylene, the melt flow index showed a downward trend. The quality of printed specimens is affected by the melt flow behavior, which is influenced by the pressure, temperature, and physical qualities, including the melting temperature and rheological behavior [33,34]. Extrusion process parameters such as screw speed and barrel temperature have an effect on the manufactured filaments, according to previous studies. Mohammad et al. [35] conducted rheological tests on kenaf fiber-reinforced recycled plastics and discovered that the presence of kenaf fiber negatively affected the flow characteristics. They also identified an indirect link between the composite's molecular weight and its viscosity. Their results showed that the higher the fiber content of the composites, the more viscous the melts became. Similarly, Mohammed et al. [27] found that the viscosity of kenaf fiber composites rose as their molecular weight increased and as their loading with kenaf fiber increased. Morphology is defined in biology as the study of the shape and structure of organisms [36]. Recently, many researchers have carried out morphological studies on fiber-reinforced polymer composites. For example, Feng et al. [37] studied the effects of sisal fiber morphology on the rheological properties of fiber-reinforced poly (butylene succinate) composites with the same fiber content. They found that the rheological properties of composites reinforced by fibers with different morphologies differed. Subsequently, Kumar et al. [38] discovered that the surface roughness of HDPE was less than that of LDPE using a scanning electron microscope (SEM).

Extrusion, injection molding, compression, and blow molding are examples of polymer processing techniques that might impact rheological behavior and affect the setting of processing parameters. Conversely, fewer published papers have analyzed the behavior of materials in the extrusion process to produce filaments for FDM, particularly for custom-made composite materials. Thus, the aim of our research is to look at the rheological and morphological properties of oil palm fiber-reinforced acrylonitrile butadiene styrene (ABS) composites used as a feedstock material for fused deposition modeling (FDM).

2. Materials and Methods

2.1. Materials

The oil palm fiber was obtained from local sources. The fibers were soaked for 2 days in water until the oily surfaces were removed. Then, the dried fiber was immersed in a sodium hydroxide (NaOH) solution for 2 h to extract the undesired soluble cellulose, hemicellulose, pectin, and lignin [39]. In natural-fiber-reinforced polymer composites, poor adhesion between the fiber and matrix is a typical issue. Thus, by removing the

cellulose, hemicellulose, pectin, and lignin using an alkali treatment, NaOH was found to improve the tensile and flexural characteristics of the material [40]. Experimental results have shown that the flexural strength of composites made from alkali (NaOH)-treated fibers were much better when compared to those of untreated fiber composites [41]. Sghaier et al. [42] studied the characterization of fibers treated by NaOH and found that morphology structure changes can be enhanced by the interaction between the matrix and fibers in composites. Acrylonitrile butadiene styrene (ABS) is a common thermoplastic polymer material that is typically used for FDM. In this study, the ABS PA-747H was used, and it was supplied by a local vendor that is imported from Chi Mei Corporation, Taiwan. A typical ABS is 15% to 35% acrylonitrile, 5% to 30% butadiene, and 40% to 60% styrene, but these proportions may vary within a relatively wide range [43]. The chemical formula for ABS is shown in Figure 1. Table 1 shows the physical and mechanical properties of ABS PA-747H and oil palm fiber.

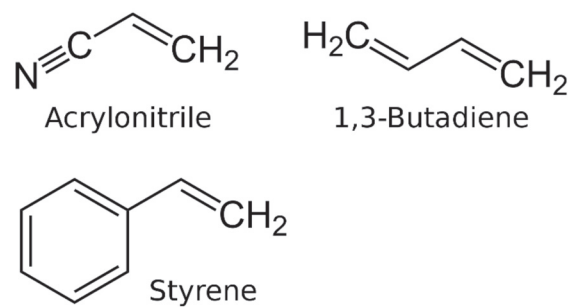


Figure 1. The chemical formula of ABS [43].

Table 1. The physical and mechanical properties of ABS PA-747H and oil palm fiber [39].

Physical and Mechanical Properties	ABS	Oil Palm Fiber
MFI (g/10 min)	13	-
Density (g/cm ³)	0.9–1.53	0.7
Melting point (°C)	No true melting (amorphous)	-
Cellulose content (%)	-	43–65
Lignin content (%)	-	13–25
Moisture content (%)	-	2.2–9.5
Tensile strength (MPa)	39.0	71.0
Elongation at break (%)	45	11

2.2. Oil Palm Fiber Composite Preparation

Figure 2 shows a flow chart for the preparation of oil-palm-fiber-reinforced polymer composites including alkaline treatment, mixing, hot press molding, and crushing. Figure 3 shows the machine used for producing the oil-palm-fiber-mixed ABS plastic in granule form. The oil palm fiber composite samples were prepared by adding the fiber by 3, 5, and 7 wt% into the ABS matrix. Then, the composite was transferred to the pre-mixing process using a high-speed mixer (Cheso model, Cheso Machinery Pte Ltd., Loyang Way, Singapore) at 3000 rpm for 5 min. The next process was a compression molding process; this technique leads the other molding techniques in terms of cost, material consumption, and production rate [44,45]. For the compression molding process, the hot press machine (Gotech model, Gotech Testing Machines Inc) from Taichung City, Taiwan, was used with parameters set at 180 °C for 20 min under a load of 1 ton. The compound resulting from the hot press process was in plate form. Therefore, it had to be crushed in order to acquire the composite material in granule form. For this purpose, a crushing machine (Cheso model, Cheso Machinery Pte Ltd., Loyang Way, Singapore) was used to produce the composite granules (with 3, 5, and 7 wt% of oil palm fiber composite), which were then ready to be used in the rheology test.

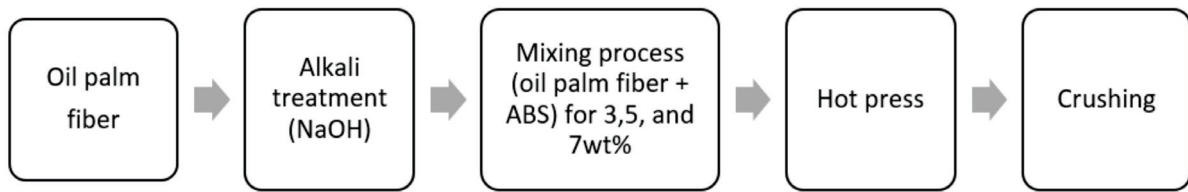


Figure 2. Flow chart for the preparation of oil-palm-fiber-reinforced thermoplastic composites.

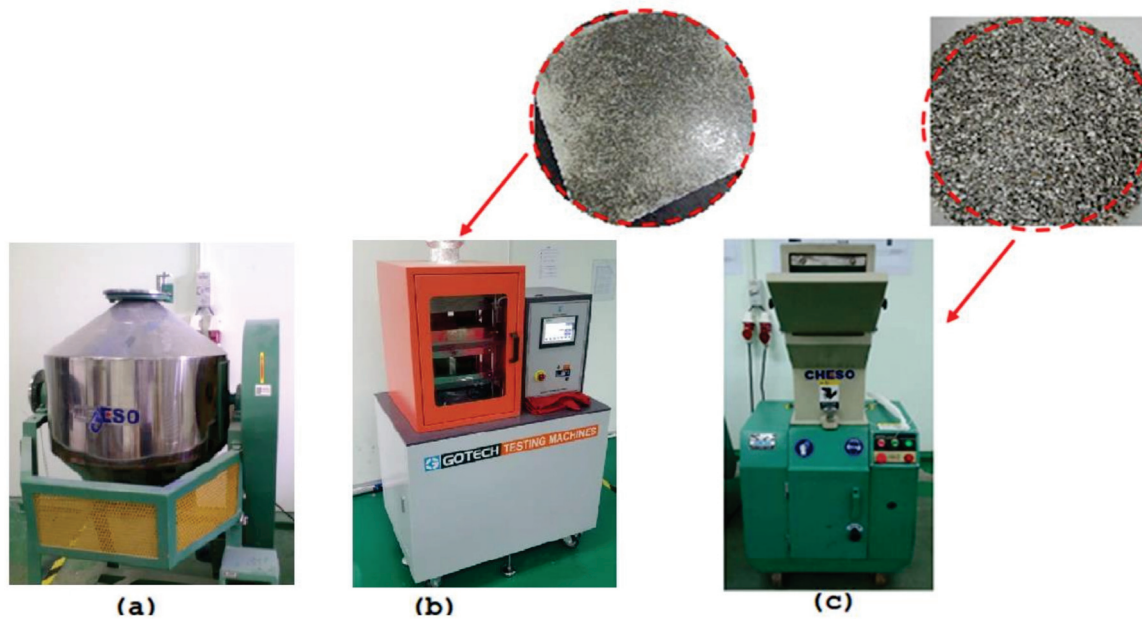


Figure 3. Some of the machines used for producing the oil-palm-fiber-mixed ABS plastic in granule form: (a) a mixer, (b) a hot pressing machine, and (c) a crusher.

2.3. Rheological Test

The rheological measurements were taken using an Instron capillary rheometer model SR20 (Instron, Norwood, MA, USA) at different piston speeds in the range of 0.00024–1200 mm/min, as shown in Figure 4. The capillary used was made of tungsten carbide with a length to diameter (L/D) ratio of 5:1. The samples with 0, 3, 5, and 7 wt% oil palm fiber composite were loaded into the barrel of the extrusion assembly and forced down into the capillary using a plunger. The experiment began by setting the die temperature to 220 °C, followed by 230 °C and 240 °C for each sample. The shear rate values were set to 200, 400, 600, 800, and 1000 s⁻¹. After allowing a resting time of 5 min, the melt was extruded through the capillary at predetermined plunger speeds. The initial position of the plunger was kept constant in all of the experiments, and shear viscosities at different shear rates were obtained from a single charge of the material [46]. Referring to the previous study by Son Y, fiber-reinforced polymers are non-Newtonian or known as shear thinning fluids [47]. For Newtonian fluids, the wall shear rate is given by:

$$\dot{\gamma}_l = \frac{4Q}{\pi r^3} \quad (1)$$

where Q is the volumetric flow rate and r is the capillary radius. However, due to the shear thinning behavior of these composites, a Rabinowitsch correction was made to obtain the true shear rate for the power law model [47]. The following is the power law equation for shear stress:

$$\tau = k\dot{\gamma}_l^{n-1} \quad (2)$$

where τ is the shear stress, k is the consistency index, $\dot{\gamma}$ is the shear rate, and n is the flow behavior index. The parameters k and n characterize the rheology of power law fluids. Rabinowitsch correction accounts for the non-Newtonian behavior of the melt in which the apparent shear rate $\dot{\gamma}_a$ was converted into the true shear rate $\dot{\gamma}_w$ by the following formula [48]:

$$\dot{\gamma}_w = \left[\frac{3n + 1}{4n} \right] \dot{\gamma}_a \quad (3)$$

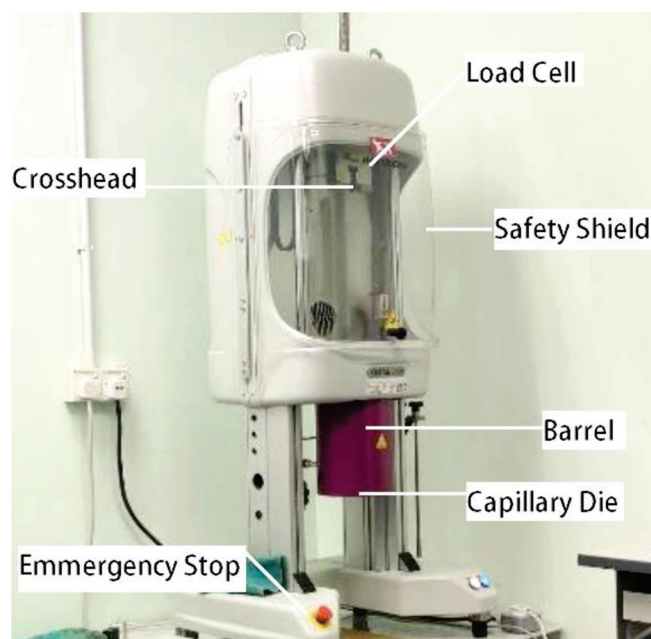


Figure 4. The capillary rheometer used (model Instron SR20).

2.4. Scanning Electron Microscope (SEM)

The morphology of the compounded oil palm fiber/ABS composite was observed using a scanning electron microscope, model JEOL (JSM 6010PLUS/LV, JEOL Ltd., Tokyo, Japan), using a platinum coating and 20 kV acceleration, as shown in Figure 5.

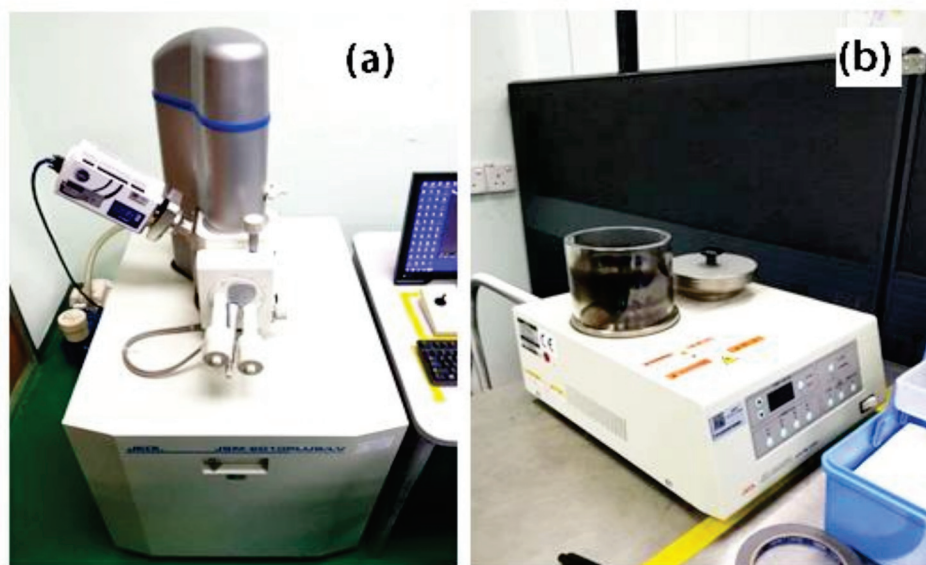


Figure 5. The laboratory setup for the morphology: (a) SEM and (b) the platinum coating machine.

3. Results and Discussion

3.1. Rheological Behavior

The purpose of performing rheological tests was to characterize the flow behavior and identify the correct melting temperature (T_m) of the oil palm fiber composite. Rheology tests were successfully performed for the oil palm fiber/ABS composites with compositions of 0, 3, 5, and 7 wt% at three different die temperatures: 220, 230, and 240 °C. Unfortunately, the composite material was able to flow out only at the 240 °C die temperature, whereas the other temperatures (220 and 230 °C) clogged the die nozzle. As a result, the recommended die temperature for the oil palm composite is 240 °C. This temperature setting was critical for the following step in the fabrication of a wire filament for FDM using the extrusion technique. The extruded samples made using capillary rheometer with a 1.0 mm diameter die are shown in Figure 6. The results show that the color of the 7 wt% sample was much darker compared to that of the 3 and 5 wt% samples. This is due to the higher percentage of oil palm fiber present in the 7 wt% sample. The outer surfaces of the 0 and 3 wt% samples appeared consistent and fine compared to those of the 5 and 7 wt% samples. This means that the surface of extruded samples may become less fine and fragile as a result of the fiber content or loading. Because all of the samples flowed smoothly out of the capillary die, oil palm fiber composite can successfully be fabricated using a twin screw extruder (i.e., for producing wire filament for FDM). Table 2 lists the rheological parameters of the oil palm fiber composite samples including the flow index (n), consistency index (k), and correlation coefficient (R^2). The values of the flow index for this composite were 0.71, 0.53, and 0.61 for the 0, 3, 5, and 7 wt% samples, respectively. However, the values of the consistency index for the 0, 3, 5, and 7 wt% samples were 0.0004, 0.0012, and 0.0008, respectively. Thus, the trend is that the n value decreased when the fiber loading (wt%) increased. In addition, the values of R^2 for all samples including the 0, 3, 5, and 7 wt% samples were greater than 0.99. Figure 7 shows the scattering data from a flow curve, including the flow index (n) and correlation coefficient (k), using the power law model. This shows that the flow curve was a satisfactory fit, with a high correlation ($R^2 > 0.99$). The flow index of the oil palm fiber composite increased as the number of shear rates increased, indicating that the fiber loading had a significant impact on the rheological behavior.

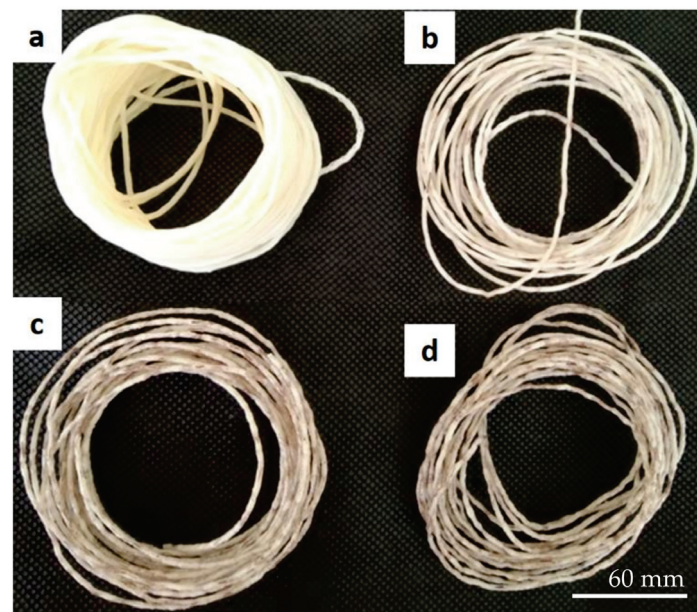
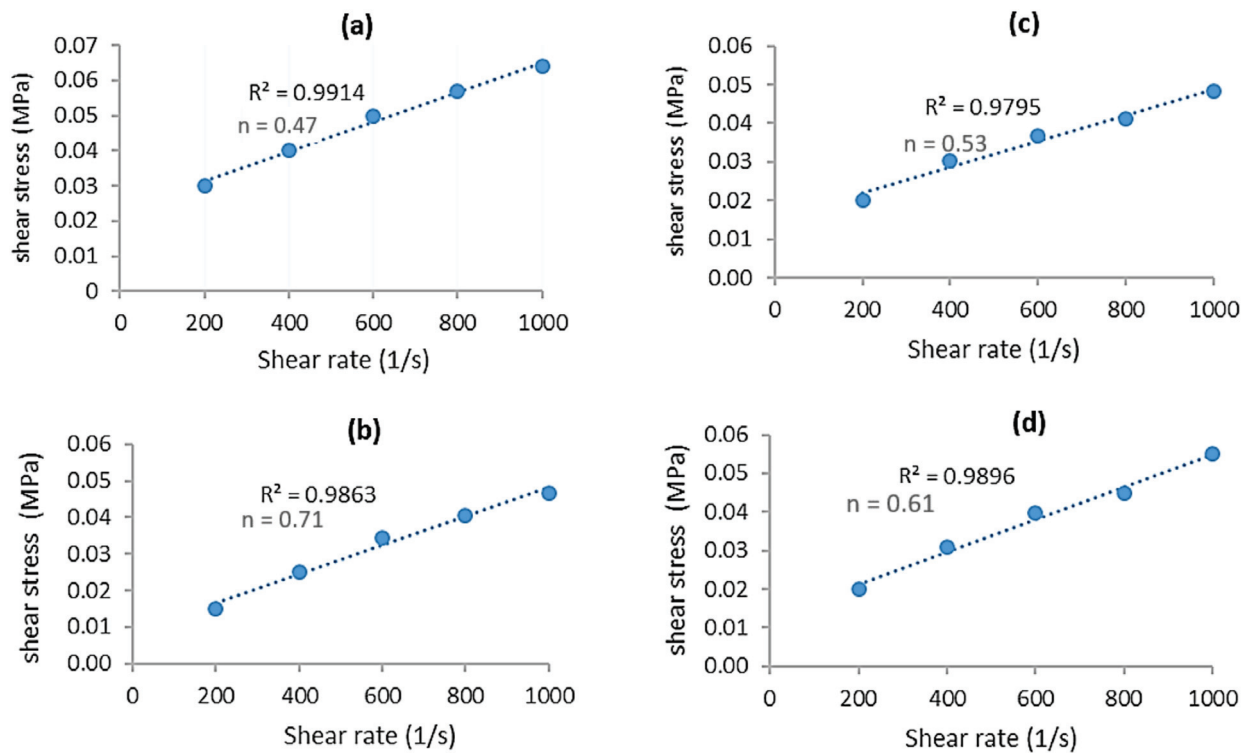


Figure 6. The rheology test samples: (a) 0 wt%, (b) 3 wt%, (c) 5 wt%, and (d) 7 wt% of oil palm fiber composite at a 240 °C die temperature.

Table 2. Rheological parameter of the power law model.

Fiber Loading (vol%)	Flow Index, n	Consistency Index, k	Correlation Coefficient, R ²
0	0.4737	0.0024	0.9972
3	0.7114	0.0004	0.9978
5	0.5342	0.0012	0.9953
7	0.6112	0.0008	0.9962

**Figure 7.** Flow curve graph for the (a) 0 wt%, (b) 3 wt%, (c) 5 wt%, and (d) 7 wt% of oil palm fiber composite samples.

In rheology, shear thinning is the non-Newtonian behavior of fluids whose viscosity decreases under shear rate. It is sometimes considered synonymous with pseudoplastic behavior [49,50]. Figure 8a shows the graph of the apparent viscosity versus shear rate. Figure 8b shows the corrected viscosity with reference to the Rabinowitsch formula. The viscosity curve for the 5 wt% sample was significantly lower and intercepted the 3 wt% sample's curve at a 900 s^{-1} shear value. This is due to the inhomogeneous distribution of the fiber in the ABS matrix. The resulting viscosity exhibited shear-thinning behavior when the flow index, n, was less than 1, and the trend of apparent viscosity was decreased with the increment in the shear rate value. Previously, Nair et al. [46] carried out a study on rheological properties of fiber composite, and found that the apparent viscosity of a sisal/PP composite decreased when the shear rate increased. In addition, the non-Newtonian index decreased linearly with an increase in fiber loading from 3 wt% to 7 wt%. Furthermore, the viscosity increased with increasing fiber content (wt%). This is similar to previous research by Mohammad et al. [35], who reported that as the loading of kenaf fiber in composites increased, the viscosity increased, because the molecular weight of the composites increased. Another finding by Qaiser et al. [48] was that the predicted behavior of non-Newtonian shear-thinning increased when the filler content increased the viscosity. The apparent viscosity was estimated to rise with an increasing concentration of fibers at low concentration levels. This was due to the growing number of collisions between particles as they become more closely packed together. Conversely, random packing is no longer achievable at a critical concentration level, and increasing fiber concentration leads

to a more ordered anisotropic structure of the fibers in suspension, allowing them to slide easily past one another.

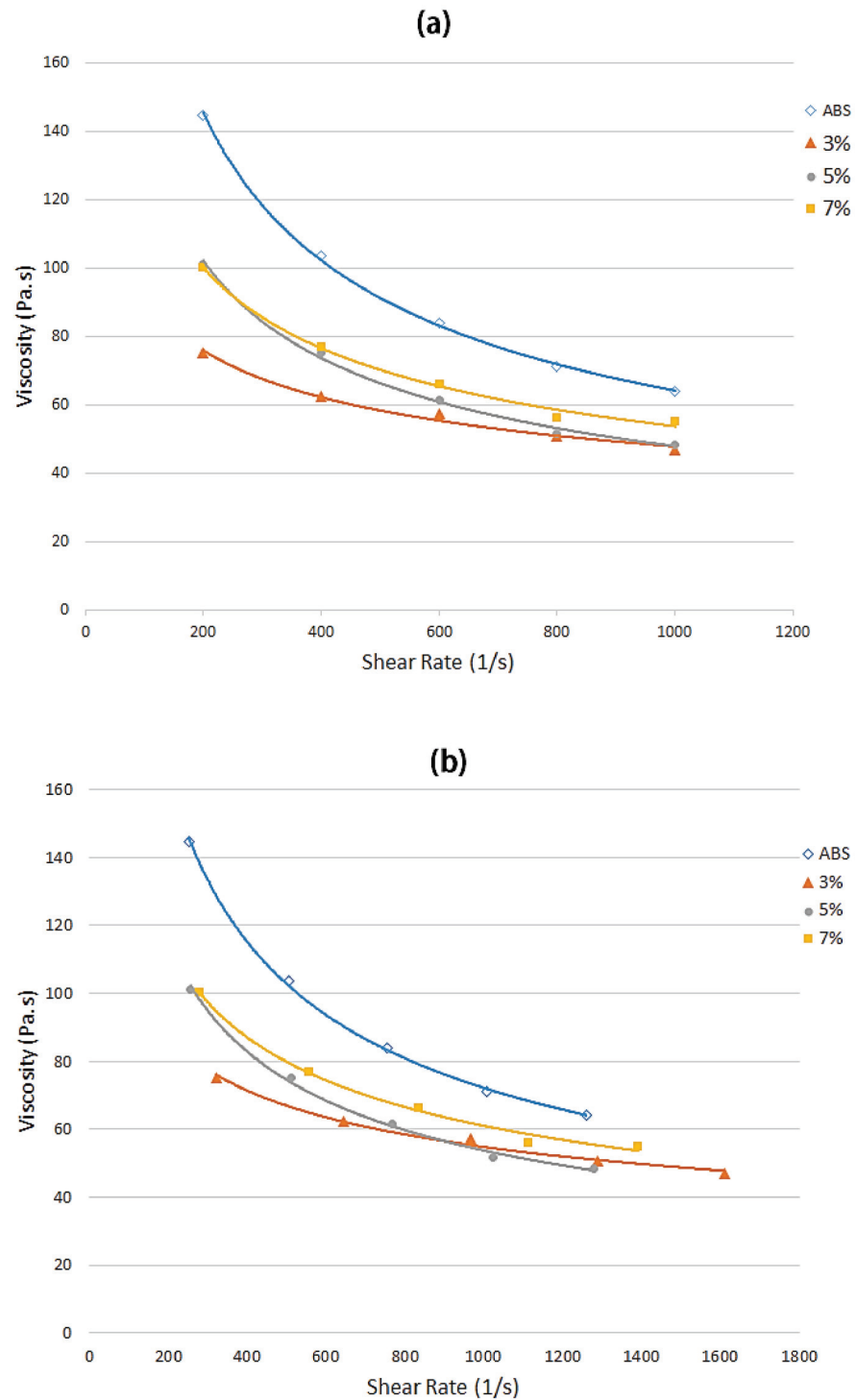


Figure 8. The apparent viscosity of the samples with oil palm fiber composite of 0, 3, 5, and 7 wt% at a 240 °C die temperature: (a) the experimental data and (b) corrected factor using the Rabinowitsch model.

Figure 9 shows the pressure drops measured at a 240 °C die temperature over the shear rate range with three different fiber loadings (vol%). The value of pressure drops declined with a decrease in the fiber content, and the values of viscosity at 5 and 7 wt% flowing through the 1.0 mm diameter dies were the same at the beginning of the stage

(with a shear rate of 200–300 s^{-1}). As a result, the oil palm composite melts' apparent viscosities dropped, and they flowed more easily through the capillary die, lowering the pressure drop value. When the content of the PP rose, the pressure drop reduced, according to Meng et al. [51]. The effects of pressure on the shear viscosity of polymer melts have been studied previously [52–55]. These findings showed that when the pressure of the polymer melt in the die increased, the free volume decreased, which was related to the availability of space between molecules. As a result, the polymer melt's density increased. As the viscosity of the polymer melts rose, the intermolecular friction increased as well. The viscosity increased as the fiber loading increased. The viscosity value increased from 50.7 (3 wt%) to 56.3 (7 wt%) Pa. s at an 800 s^{-1} apparent shear rate.

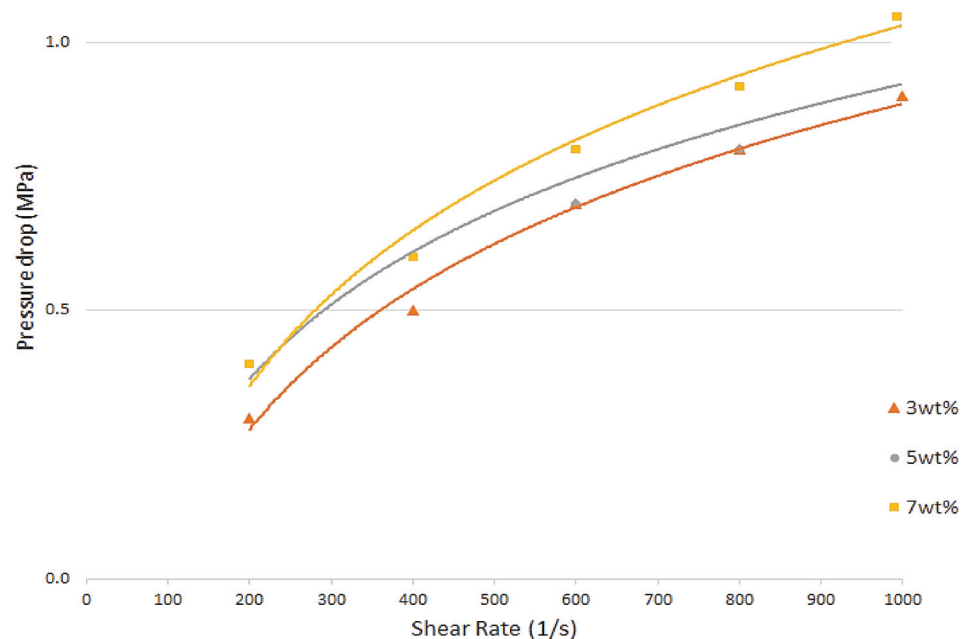


Figure 9. The pressure drop with different fiber loadings at a 240 °C die temperature.

Therefore, it is necessary to conduct a rheology characteristics analysis of new materials, such as oil palm fiber composite, in order to solve problems that arise during the extrusion process of producing wire filament for FDM. There are some problems in developing composite feed stock filaments for FDM, such as the process of extrusion damaging the fiber due to exposure to a high temperature and pressure [56]. That will cause nozzle clogging and undesirable results (e.g., over-melting, an inconsistent diameter of wire). Therefore, it is important to determine the characteristics of the fiber composite flow (via rheology analysis) as well as preparation data (e.g., temperature and speed) for the twin screw extruder process. The flow behaviors of polymer and fiber materials are vital for producing filaments for FDM, especially for custom-made composite materials [57].

3.2. Morphological Structures

Figure 10 shows SEM micrographs of the oil palm fiber composite samples with fiber loading levels of 0, 3, 5, and 7 wt%. Figure 10b shows that there was a good fiber/matrix adhesion, as no fiber pullouts or gaps appeared between the oil palm fiber and ABS. However, there were some pores and fiber pullouts at 5 and 7 wt% fiber loadings. Figure 10b also indicates that the number of pores and fractured fibers increased with the increase in the fiber content (vol%). This phenomenon was similar to that seen by Hongjie et al. [58], where the increased wood fiber content contributed to a higher number of gaps and fiber pullouts. Figure 9d obviously shows a big pore and clear fractured fiber on the surface. This is due to improper fiber/matrix bonding and the presence of higher fiber loading (7 wt%). The big pores are present because the oil palm fiber started to degrade during the heating

process within the temperature range 240–250 °C [59]. Thermal stability can be improved by chemically eliminating a certain proportion of hemicellulose and lignin elements from the fiber. Natural fiber deterioration is a significant challenge in the development of natural fiber composites in composite manufacturing, for example, during the curing process, extrusion process, and injection molding [60,61].

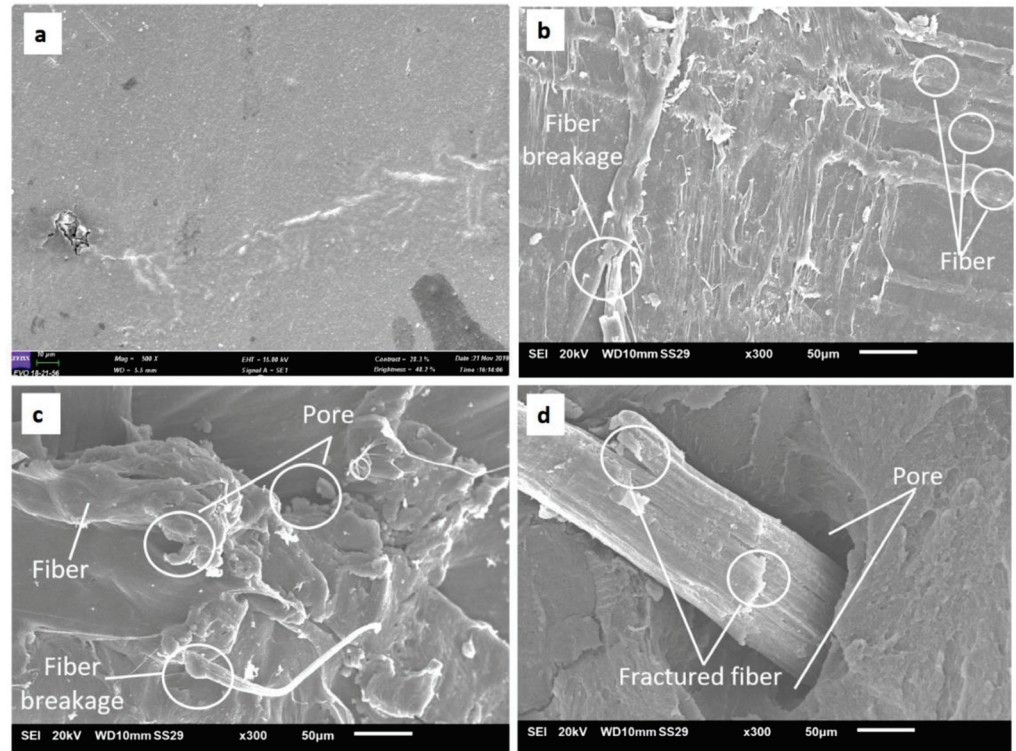


Figure 10. SEM micrographs of the oil-palm-fiber-reinforced ABS composite surfaces: (a) 0 wt%, (b) 3 wt%, (c) 5 wt%, and (d) 7wt%. The scale bar in the inset represents 50 μm .

4. Conclusions

Rheological tests on the oil palm fiber composite samples were carried out using a capillary rheometer to investigate their rheological behaviors through a capillary die (1.0 mm diameter). The results show that the viscosity of the sample with a fiber loading of 7 wt% was higher than that of samples with loadings of 3 wt% and 5 wt%. It was seen that increasing the fiber content (wt%) increased the viscosity. The apparent viscosity of these composites reduced as the shear rate value increased, indicating pseudoplastic behavior. There was good fiber/matrix adhesion for samples with a 3 wt% fiber loading in terms of morphological behavior, as no fiber pullouts or gaps developed between the oil palm fiber and ABS. However, there were some pores and fiber pullouts in the samples with 5 and 7 wt% fiber loadings. The addition of 3–7% by weight of oil palm fiber increased the shear thinning effect. Furthermore, the pressure drops of the oil palm fiber composite decreased with the decrease in the fiber content. Therefore, data such as viscosity, shear stress, shear rate, and appropriate flow temperature (240 °C) for oil palm composite were collected, and these data will purposefully be used in the next process of making wire filaments and 3D printing processes. Thus, oil-palm-fiber-reinforced polymer composites are suitable for use as a feedstock filament material for FDM.

Author Contributions: Conceptualization, M.N.A.; methodology, M.N.A.; validation, M.N.A., M.R.I., M.M.T., F.M. and Z.L.; formal analysis, M.N.A.; investigation, M.N.A.; resources, M.N.A.; data curation, M.N.A.; writing—original draft preparation, M.N.A.; writing—review and editing, M.N.A., M.R.I. and M.M.T.; visualization, M.N.A.; supervision, M.R.I., M.M.T., F.M. and Z.L.; project administration, M.N.A.; funding acquisition, M.R.I., M.M.T., F.M. and Z.L. All authors have read and agreed to the published version of the manuscript.

Funding: This research was funded by the Fundamental Research Grant Scheme (FRGS), grant no. FRGS/1/2019/TK05/UPM/02/11 (5540205). The APC was funded by Research Management Centre (RMC), Universiti Putra Malaysia.

Institutional Review Board Statement: Not applicable.

Informed Consent Statement: Not applicable.

Data Availability Statement: The data presented in this study are available on request from the corresponding author.

Acknowledgments: The authors are grateful for the help from all staff and technicians at Universiti Putra Malaysia as well as to Universiti Teknikal Malaysia Melaka and the Ministry of Higher Education (Malaysia) for providing the scholarship awarded to the principal author of this project. Additionally, we would like to thank our families and friends for their moral support during this research.

Conflicts of Interest: The authors declare no conflict of interest.

References

- Gardan, J. Additive manufacturing technologies: State of the art and trends. *Int. J. Prod. Res.* **2016**, *54*, 3118–3132. [CrossRef]
- Berman, B. 3-D printing: The new industrial revolution. *Bus. Horiz.* **2012**, *55*, 155–162. [CrossRef]
- Guo, N.; Leu, M.C. Additive manufacturing: Technology, applications, and research needs. *Front. Mech. Eng.* **2013**, *8*, 215–243. [CrossRef]
- Wohlers. *Wohlers Report 2011: Additive Manufacturing and 3D Printing State of the Industry. Annual Worldwide Progress Report*; Wohlers: Fort Collins, CO, USA, 2011.
- Turner, B.N.; Strong, R.; Gold, S.A. A review of melt extrusion additive manufacturing processes: I. Process design and modeling. *Rapid Prototyp. J.* **2014**, *20*, 192–204. [CrossRef]
- Fafenrot, S.; Grimmelsmann, N.; Wortmann, M.; Ehrmann, A. Three-dimensional (3D) printing of polymer-metal hybrid materials by fused deposition modeling. *Materials* **2017**, *10*, 1199. [CrossRef] [PubMed]
- Wong, J.Y.; Pfahnl, A.C. 3D printing of surgical instruments for long-duration space missions. *Aviat. Space Environ. Med.* **2014**, *85*, 758–763. [CrossRef]
- Comotti, C.; Regazzoni, D.; Rizzi, C.; Vitali, A. Additive Manufacturing to Advance Functional Design: An Application in the Medical Field. *J. Comput. Inf. Sci. Eng.* **2017**, *17*, 031006. [CrossRef]
- Yu, Y.Z.; Lu, J.R.; Liu, J. 3D printing for functional electronics by injection and package of liquid metals into channels of mechanical structures. *Mater. Des.* **2017**, *122*, 80–89. [CrossRef]
- Tronvoll, S.A.; Welo, T.; Elverum, C.W. The effects of voids on structural properties of fused deposition modelled parts: A probabilistic approach. *Int. J. Adv. Manuf. Technol.* **2018**, *11*, 1–12. [CrossRef]
- Villanueva, M.P.; Galindo, B.; Moliner, E.; García, S.; Ruedas, V. Biobased conductive plastic materials for manufacturing capacitive lamps. *Mater. Today Commun.* **2018**, *15*, 105–108. [CrossRef]
- Motaparti, K.P.; Taylor, G.; Leu, M.C.; Chandrashekhara, K.; Castle, J.; Matlack, M. Experimental investigation of effects of build parameters on flexural properties in fused deposition modelling parts. *Virtual Phys. Prototyp.* **2017**, *12*, 207–220. [CrossRef]
- Cicala, G.; Latteri, A.; Del Curto, B.; Lo Russo, A.; Recca, G. Engineering thermoplastics for additive manufacturing: A critical perspective with experimental evidence to support functional applications. *J. Appl. Biomater. Funct. Mater.* **2017**, *15*, 10–18. [CrossRef]
- McIlroy, C.; Olmsted, P.D. Deformation of an Amorphous Polymer during the Fused-Filament-Fabrication Method for Additive Manufacturing. *J. Rheol.* **2017**, *61*, 379. [CrossRef]
- McIlroy, C.; Olmsted, P.D. Disentanglement effects on welding behaviour of polymer melts during the fused-filament-fabrication method for additive manufacturing. *Polymer* **2017**, *123*, 376–391. [CrossRef]
- Murphy, C.A.; Collins, M.N. Microcrystalline cellulose reinforced polylactic acid biocomposite filaments for 3D printing. *Polym. Compos.* **2018**, *39*, 1311–1320. [CrossRef]
- Cicala, G.; Ognibene, G.; Portuesi, S.; Blanco, I.; Rapisarda, M.; Pergolizzi, E.; Recca, G. Comparison of Ultem 9085 used in fused deposition modelling (FDM) with polyetherimide blends. *Materials* **2018**, *11*, 285. [CrossRef] [PubMed]
- Patience, G.S. Experimental methods in chemical engineering: Preface. *Can. J. Chem. Eng.* **2018**, *96*, 2312–2316. [CrossRef]
- Reiner, M. The Deborah number. *Phys. Today* **1964**, *17*, 62. [CrossRef]

20. Ghanbari, A.; Mousavi, Z.; Heuzey, M.C.; Patience, G.S.; Carreau, P.J. Experimental methods in chemical engineering: Rheometry. *Can. J. Chem. Eng.* **2020**, *98*, 1456–1470. [CrossRef]
21. Frederick, T.T.; David, G.C.; Milan, M. Biodegradation of a synthetic co-polyester by aerobic mesophilic microorganisms. *Polym. Degrad. Stab.* **2008**, *93*, 1479–1485.
22. Nagahama, H.; New, N.; Jayakumar, R. Novel biodegradable chitin membranes for tissue engineering applications. *Carbohydr. Polym.* **2008**, *73*, 295–302. [CrossRef]
23. Kim, H.S.; Lee, B.H.; Lee, S. Enhanced interfacial adhesion, mechanical, and thermal properties of natural flour-filled biodegradable polymer bio-composites. *J. Anal. Calorim.* **2011**, *104*, 331–338. [CrossRef]
24. Yee, T.W.; Rahman, W.; Sin, L.T. Properties and morphology of poly (vinyl alcohol) blends with sago pith bio-filler as biodegradable composites. *J. Vinyl. Addit. Technol.* **2011**, *17*, 184–189. [CrossRef]
25. Kalaprasad, G.; Mathew, G.; Pavithran, C.; Thomas, S. Melt rheological behavior of intimately mixed short sisal-glass hybrid fiber-reinforced low-density polyethylene composites. I. Untreated fibers. *J. Appl. Polym. Sci.* **2003**, *89*, 432–442. [CrossRef]
26. Smita, M.; Nayak, S.K. Rheological characterization of HDPE/sisal fiber composites. *Polym. Eng. Sci.* **2007**, *47*, 1634–1642.
27. Mohammed, L.; Ansari, M.N.; Pua, G.; Jawaid, M.; Islam, M.S. A review on natural fibre reinforced polymer composite and its applications. *Int. J. Polym. Sci.* **2015**, *2015*, 243947. [CrossRef]
28. Xian, G.; Guo, R.; Li, C.; Hong, B. Effects of rod size and fiber hybrid mode on the interface shear strength of carbon/glass fiber composite rods exposed to freezing-thawing and outdoor environments. *J. Mater. Res. Technol.* **2021**, *14*, 2812–2831. [CrossRef]
29. Singh, T.J.; Samanta, S. Characterization of Kevlar Fiber and its composites: A review. *Mater. Today: Proc.* **2015**, *2*, 1381–1387. [CrossRef]
30. Ahmad, F.; Choi, H.S.; Park, M.K. A review: Natural fibre composites selection in view of mechanical, light weight, and economic properties. *Macromol. Mater. Eng.* **2015**, *300*, 10–24. [CrossRef]
31. Gallo, E.; Schartel, B.; Acierno, D.; Cimino, F.; Russo, P. Tailoring the flame retardant and mechanical performances of natural fibre-reinforced biopolymer by multi-component laminate. *Compos. Part. B Eng.* **2013**, *44*, 112–119. [CrossRef]
32. Islam, M.R.; Beg, M.D.; Gupta, A. Characterization of laccase-treated kenaf fibre reinforced recycled polypropylene composites. *BioResour* **2013**, *8*, 3753–3770. [CrossRef]
33. Ramanath, H.S.; Chua, C.K.; Leong, K.F.; Shah, K.D. Melt flow behaviour of poly- ϵ - caprolactone in fused deposition modelling. *J. Mater. Sci. Mater. Med.* **2008**, *19*, 2541–2550. [CrossRef] [PubMed]
34. Singh, R.; Singh, S.; Mankotia, K. Development of ABS based wire as feedstock filament of FDM for industrial applications. *Rapid Prototyp. J.* **2016**, *22*, 300–310. [CrossRef]
35. Mohammad, N.N.B.; Arsad, A. Mechanical, thermal and morphological study of kenaf fibre reinforced rPET/ ABS composites. *Malays. Polym. J.* **2013**, *8*, 8–13.
36. Aronoff, M.; Fudeman, K. *What Is Morphology*; John Wiley & Sons: New Jersey, NJ, USA, 2011; Volume 8.
37. Feng, Y.H.; Li, Y.J.; Xu, B.P.; Zhang, D.W.; Qu, J.P.; He, H.Z. Effect of fiber morphology on rheological properties of plant fiber reinforced poly (butylene succinate) composites. *Compos. Part B Eng.* **2013**, *44*, 193–199. [CrossRef]
38. Kumar, S.; Singh, R.; Singh, T.P.; Batish, A. On investigation of rheological, mechanical and morphological characteristics of waste polymer-based feedstock filament for 3D printing applications. *J. Thermoplast. Compos. Mater.* **2019**, *18*, 0892705719856063. [CrossRef]
39. Ahmad, M.N.; Wahid, M.K.; Maidin, N.A.; Ab Rahman, M.H.; Osman, M.H.; Alis, I.F. Mechanical characteristics of oil palm fiber reinforced thermoplastics as filament for fused deposition modeling (FDM). *Adv. Manuf.* **2020**, *8*, 72–81. [CrossRef]
40. Goud, G.; Rao, R.N. Effect of fibre content and alkali treatment on mechanical properties of Roystonea regia-reinforced epoxy partially biodegradable composites. *Bull. Mater. Sci.* **2011**, *34*, 1575–1581. [CrossRef]
41. Rokbi, M.; Osmani, H.; Imad, A.; Benseddiq, N. Effect of chemical treatment on flexure properties of natural fiber-reinforced polyester composite. *Procedia Eng.* **2011**, *10*, 2092–2097. [CrossRef]
42. Sghaier, A.E.O.B.; Chaabouni, Y.; Msahli, S.; Sakli, F. Morphological and crystalline characterization of NaOH and NaOCl treated *Agave americana* L. fiber. *Ind. Crops Prod.* **2012**, *36*, 257–266. [CrossRef]
43. Żenkiewicz, M.; Rytlewski, P.; Moraczewski, K.; Stepczyńska, M.; Karasiewicz, T.; Malinowski, R.; Ostrowicki, W. Some effects of multiple injection moulding on selected properties of ABS. *J. Achiev. Mater. Manuf. Eng.* **2009**, *37*, 361–368.
44. Jaafar, J.; Siregar, J.P.; Tezara, C.; Hamdan, M.H.; Rihayat, T. A review of important considerations in the compression molding process of short natural fiber composites. *Int. J. Adv. Manuf. Technol.* **2019**, *105*, 3437–3450. [CrossRef]
45. Tataru, R.A. Compression Molding. In *Applied Plastics Engineering Handbook*; Elsevier: Amsterdam, The Netherlands, 2011; pp. 289–309. [CrossRef]
46. Nair, K.M.; Kumar, R.P.; Thomas, S.; Schit, S.C.; Ramamurthy, K. Rheological behavior of short sisal fiber-reinforced polystyrene composites. *Compos. Part A Appl. Sci. Manuf.* **2000**, *31*, 1231–1240. [CrossRef]
47. Son, Y. Determination of shear viscosity and shear rate from pressure drop and flow rate relationship in a rectangular channel. *Polymer* **2007**, *48*, 632–637. [CrossRef]
48. Qaiser, A.A.; Qayyum, A.; Rafiq, R. Rheological properties of ABS at low shear rates: Effects of phase heterogeneity. *Malays. Polym. J.* **2009**, *4*, 29–36.
49. Mezger, T.G. *The Rheology Handbook: For. Users of Rotational and Oscillatory Rheometers*, 2nd ed.; Vincentz Network: Hannover, Germany, 2020; p. 34, ISBN 978878701743.

50. Heldman, R.; Paul, S.; Dennis, R. *Introduction to Food Engineering*, 5th ed.; Elsevier: Amsterdam, The Netherlands, 2013; p. 160, ISBN 9780124016750.
51. Meng, L.; Wu, D.; Kelly, A.; Woodhead, M.; Liu, Y. Experimental investigation of the rheological behaviors of polypropylene in a capillary flow. *J. Appl. Polym. Sci.* **2016**, *133*, 145. [CrossRef]
52. Kelly, A.L.; Gough, T.; Whiteside, B.R.; Coates, P.D. High shear strain rate rheometry of polymer melts. *J. Appl. Polym. Sci.* **2009**, *114*, 864–873. [CrossRef]
53. Couch, M.A.; Binding, D.M. High pressure capillary rheometry of polymeric fluids. *Polymer* **2000**, *41*, 6323–6334. [CrossRef]
54. Sedlacek, T.; Zatloukal, M.; Filip, P.; Boldizar, A.; Saha, P. On the effect of pressure on the shear and elongational viscosities of polymer melts. *Polym. Eng. Sci.* **2004**, *44*, 1328–1337. [CrossRef]
55. Binding, D.M.; Couch, M.A.; Walters, K. The pressure dependence of the shear and elongational properties of polymer melts. *J. Non-Newton. Fluid Mech.* **1998**, *79*, 137–155. [CrossRef]
56. Balla, V.K.; Kate, K.H.; Satyavolu, J.; Singh, P.; Tadimeti, J.G.D. Additive manufacturing of natural fiber reinforced polymer composites: Processing and prospects. *Compos. Part B Eng.* **2019**, *174*, 106956. [CrossRef]
57. Tanikella, N.G. Mechanical Testing of Fused Filament 3-D Printed Components for Distributed Manufacturing. Dissertation Master Thesis, Michigan Technological University, Michigan, MI, USA.
58. Bi, H.; Ren, Z.; Guo, R.; Xu, M.; Song, Y. Fabrication of flexible wood flour/thermoplastic polyurethane elastomer composites using fused deposition molding. *Ind. Crops Prod.* **2018**, *122*, 76–84. [CrossRef]
59. Izani, M.N.; Paridah, M.T.; Anwar, U.M.K.; Nor, M.M.; H'ng, P.S. Effects of fiber treatment on morphology, tensile and thermogravimetric analysis of oil palm empty fruit bunches fibers. *Compos. Part B Eng.* **2013**, *45*, 1251–1257. [CrossRef]
60. Sgriccia, N.; Hawley, M.; Misra, M. Characterization of natural fibre surfaces and natural fibre composites. *Compos. Part A Appl. Sci. Manuf.* **2008**, *39*, 514–522. [CrossRef]
61. Taj, S.; Munawar, M.A.; Khan, S. Review: Natural fibre reinforced polymer composites. *Proc. Pak. Acad. Sci. USA* **2007**, *44*, 129–144.

Communication

Synthesis and Properties of Copolyphenylene Sulphones with Cardo Fragments

Zhanna Kurdanova, Azamat Zhansitov * , Kamila Shakhmurzova, Azamat Slonov, Artur Baykaziev and Svetlana Khashirova

Progressive Materials and Additive Technologies Center, Kabardino-Balkarian State University Named after H.M. Berbekov, St. Chernyshevsky, 173, 360004 Nalchik, Russia; kurdanova09@mail.ru (Z.K.); shakhmurzova.kamila@yandex.ru (K.S.); azamatslonov@yandex.ru (A.S.); 2303tzoo@mail.ru (A.B.); new_kompozit@mail.ru (S.K.)

* Correspondence: azamat-z@mail.ru; Tel.: +7-928-718-9227

Abstract: Copolymers based on 4,4'-dihydroxydiphenyl, phenolphthalein and 4,4'-dichlorodiphenyl sulfone were synthesized by the method of high temperature polycondensation. The structure of the synthesized copolymers was confirmed by IR spectroscopy. Their physical, mechanical and thermal properties were investigated. It is shown that increases in the content of carded fragments lead to higher glass transition temperatures and heat resistance of the copolymers, as well as higher elastic and strength properties.

Keywords: polyphenylene sulfone; cardo fragments; IR spectroscopy; heat resistance; thermostability

Citation: Kurdanova, Z.; Zhansitov, A.; Shakhmurzova, K.; Slonov, A.; Baykaziev, A.; Khashirova, S. Synthesis and Properties of Copolyphenylene Sulphones with Cardo Fragments. *Polymers* **2021**, *13*, 3689. <https://doi.org/10.3390/polym13213689>

Academic Editors: Somen K. Bhudolia and Sunil Chandrakant Joshi

Received: 21 September 2021
Accepted: 22 October 2021
Published: 26 October 2021

Publisher's Note: MDPI stays neutral with regard to jurisdictional claims in published maps and institutional affiliations.



Copyright: © 2021 by the authors. Licensee MDPI, Basel, Switzerland. This article is an open access article distributed under the terms and conditions of the Creative Commons Attribution (CC BY) license (<https://creativecommons.org/licenses/by/4.0/>).

1. Introduction

Aromatic polysulfones are of great interest for various industries due to their particular set of valuable properties, such as heat resistance, fire resistance, high strength, etc. [1]. In order to expand the brand range of polysulfones, it is important to synthesize copolymers with both statistical and block structures [1].

Back in the thirties of the last century, the use of 4,4'-dioxiphthalophenone (phenolphthalein) as a bisphenol component in the synthesis of polyesters was proposed [2]. The first mention in the patent literature of the synthesis of polysulfones based on 4,4'-dioxiphthalophenone and 4,4'-dichlorodiphenylsulfone dates back to 1969 [3]; attention was mainly paid to the specific influence of cardo fragments on the properties of the polymer.

The introduction of cardo fragments into the structure of simple and complex aromatic polyesters gives them a number of specific properties. References [4,5]: an increase in the glass transition temperature; high values of heat resistance, which allow the copolymers to be used at higher temperatures without changing their mechanical properties; and the presence of bulky groups improves the solubility of polymers in strongly polar solvents, which makes it possible to process polymers from solutions. Thus, polymers with cardo groups, in addition to high thermal and physical-mechanical properties, are also characterized by a high transparency index and a high refractive index, along with low birefringence [6].

Studies have been carried out [7] on the effect of cardo groups on the dielectric properties of polyetherimides (PEI). These PEI-based films are characterized by good dielectric properties, with an ultra-low dielectric constant of 2.3 at 1 MHz, due to an increase in the free volume in the polymer chain. These materials are used as functional materials for the microelectronic, aerospace, electrical insulating and semiconductor industries. Another promising area developed over the last decade is the synthesis of polymer membranes used as gas separation systems and fuel cells [8,9]. The presence of cardo groups in the polymer membrane significantly affects their gas permeable characteristics due to the packing density and segmental mobility of the polymer chain. [10]. The authors of [11] cited studies on the gas barrier properties of membranes based on polyethersulfone (PES)

and cardo polyethersulfone (PES-C)— there is an increase in selectivity with respect to N_2 , which increased from 2.95 to 4.24 barrers.; O_2 permeability increased from 0.62 to 1.78 barrers and CO_2 permeability increased from 6.87 to 13.80 barrers.

In subsequent years, research in the field of carded polyesters has been extensively developed [12–16]. Moreover, most of the available scientific publications are devoted to the study of the synthesis and properties of cardo polyethersulfones based on 4,4'-dihydroxydiphenylsulfone, 4,4'-dioxypthalophenone and 4,4'-dichlorodiphenylsulfone [17–22]. Copolymers with cardo fragments based on 4,4'-dihydroxydiphenyl are mentioned in the patent technical literature without a detailed description of their physicochemical properties [23,24].

Earlier, in work [25], we reported on preliminary studies of the synthesis of cardo polyphenylene sulfones, with a content of 4,4-dihydroxyphthalophenone up to 50%. This article presents the results of a study of the whole series of copolymers of cardo polyphenylene sulfones synthesized by us in order to establish the dependence of the properties of the copolymer on the content of 4,4-dihydroxyphthalophenone.

2. Materials and Methods

2.1. Materials

4,4'-dihydroxy diphenyl and 4,4'-dichlorodiphenyl sulfone were kindly supplied by Alfa Aesar (Heysham, UK). Potassium carbonate and 4,4'-dihydroxy phthalophenone were purchased from Rechem (Moscow, Russia). N,N-dimethyl acetamide was purchased from Acros Organics (Geel, Belgium). N,N-dimethylacetamide (DMAc) was purified by distillation over calcium hydride and stored over 4-Å^o molecular sieves. All other reagents for the study were commercially obtained and used as received without further purification.

2.2. Characterization and Methods

The IR spectra of polymer samples in the form of a powder were recorded on a Fourier spectrometer Spectrum Two (PerkinElmer, Inc., Waltham, MA, USA), in the range of 4000–450 cm^{-1} with a spectral resolution of 0.4 cm^{-1} .

The thermal properties of the polymers were investigated by differential scanning calorimetry using a DSC 4000 (PerkinElmer, Inc., Waltham, MA, USA), and by thermogravimetric analysis at a heating rate of 5 $^{\circ}C\ min^{-1}$ in an air atmosphere on a TGA 4000 instrument (PerkinElmer, Inc., Waltham, MA, USA).

The melt flow index (MFI) was determined on a capillary viscometer with IIRT-5 (Moscow, Russia) at a temperature of 350 $^{\circ}C$ and a load of 5 kg.

The reduced viscosity (η) of the synthesized polymers was determined in an Ubbelohde type capillary viscometer at 25 $^{\circ}C$ for 0.5 g of polymer in 10.0 mL of chloroform.

Mechanical tests were carried out on a universal testing machine, Gotech Testing Machine CT-TCS 2000 (Taichung, Taiwan) at 23 $^{\circ}C$. Impact tests were performed with and without notch, by the Izod method on the instrument Gotech Testing Machine, Model GT-7045-MD (Taichung, Taiwan), with the energy of a pendulum, 11 J.

The Vicat softening temperature of the samples was determined on an HV-2000-M3 W Computer HDT/VICAT Tester Gotech Testing Machine (Taichung, Taiwan).

2.3. Synthesis of Polymers

2.3.1. Synthesis of PPSU

Synthesis of polyphenylene sulfones (PPSU) was carried out in a 500 mL three-necked flask equipped with a nitrogen inlet, a mechanical stirrer, a Dean–Stark trap, and a reflux condenser; 4,4'-dihydroxy diphenyl (55.86 g, 0.3 mol), 4,4'-dichlorodiphenyl sulfone (89.16 g, 0.31 mol), and potassium carbonate (51.82 g, 0.375 mol) were charged in a flask. Then, N,N-dimethyl acetamide (470 mL) was added as reaction solvent. The reaction mixture was gradually heated to 165 $^{\circ}C$ for 4 h to distill the water. After the temperature reached 165 $^{\circ}C$, the reaction mixture was allowed to proceed at this temperature for 6 h. After synthesis, the mixture was discharged and the formed salts were filtered. Then, the

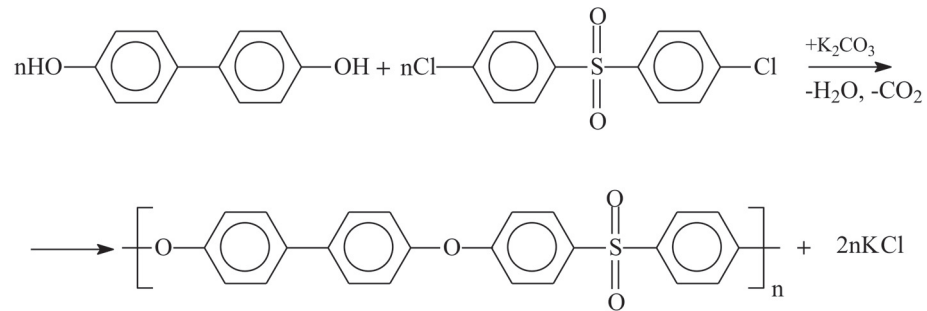
reaction solution was slowly poured into the water acidified by oxalic acid. The precipitated polymer was filtered and washed several times with water and dried in a vacuum oven at 160 °C for about 12 h.

2.3.2. Synthesis of PPSU-C

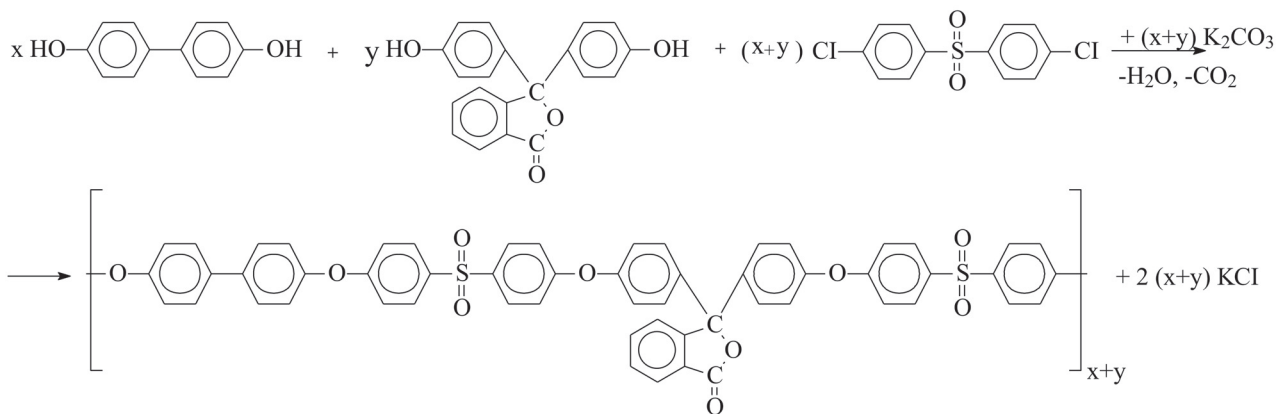
As an example of the synthesis of copolyphenylene sulfone with cardo fragments, the synthesis with 30% phenolphthalein content is given. In the preparation of copolymers, PPSU with phenolphthalein as starting monomers in a flask were charged with 4,4'-dihydroxy diphenyl (39.1 g, 0.21 mol), 4,4'-dihydroxy phthalophenone (phenolphthalein) (28.65 g, 0.09 mol), 4,4'-dichloro diphenyl sulfone (89.16 g, 0.31 mol), and potassium carbonate (51.82 g, 0.375 mol). Further synthesis was carried out as described above.

3. Results and Discussion

The synthesis of copolyphenylene sulfones was carried out by high-temperature polycondensation by the mechanism of a nucleophilic substitution reaction. PPSU was synthesized according to Scheme 1; a copolymer of polyphenylene sulfone with 4,4'-dioxiphthalophenone was synthesized according to Scheme 2.



Scheme 1. Synthesis of PPSU.



Scheme 2. Synthesis of copolymer PPSU with phenolphthalein.

The structure of the synthesized copolymers was studied by IR spectroscopy. In the spectra of synthesized PPSU, absorption bands due to stretching vibrations of C–H bonds were characterized by a weak intensity, and appeared as two peaks with maxima at 3037 and 3066 cm^{-1} (Figure 1).

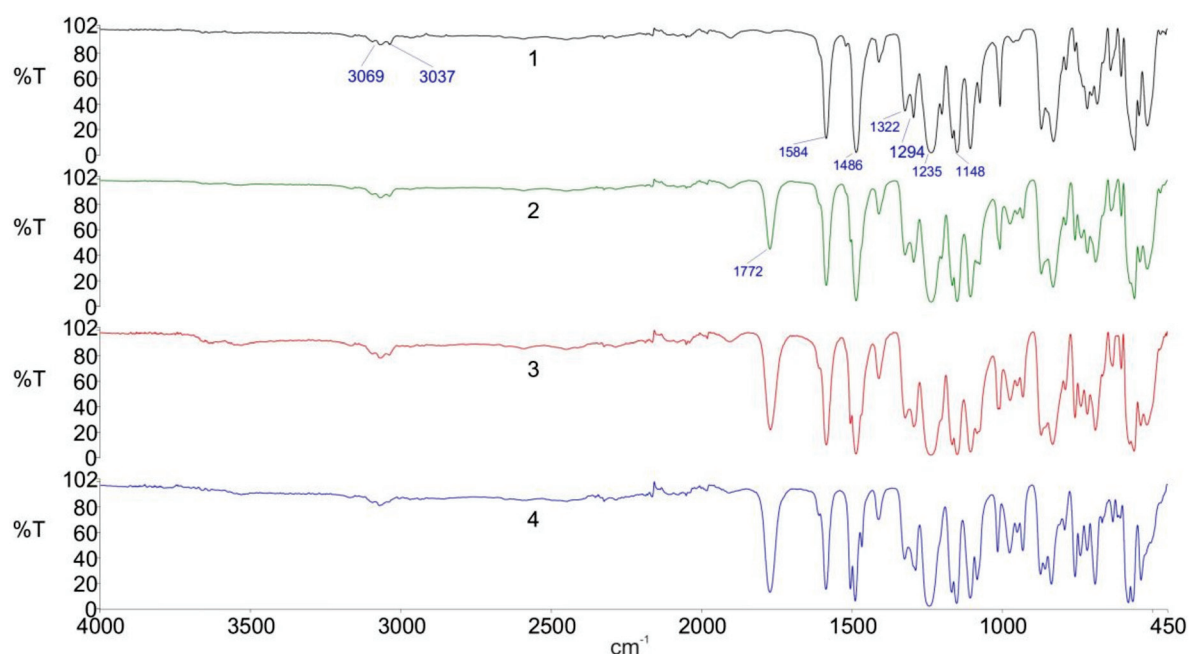
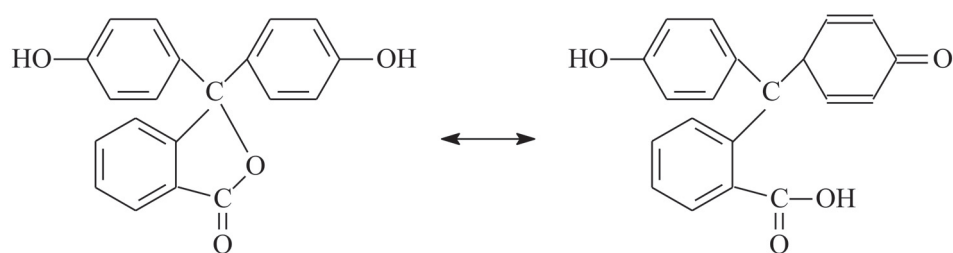


Figure 1. IR spectra: 1—PPSU; 2—PPSU-C-30; 3—PPSU-C-50; 4—PPSU-C-100.

Skeletal vibrations of aromatic C–C bonds are manifested in bands with maxima at 1584 and 1486 cm^{-1} . Polyphenylene sulfones also have a very characteristic absorption in the range of 1350–1300 cm^{-1} and 1170–1120 cm^{-1} , caused by symmetric and antisymmetric vibrations of the SO_2 group, respectively. In the spectra of the copolymers synthesized in this work, similar symmetric and antisymmetric vibrations of the SO_2 group appeared as a split band with peaks at 1322 and 1294 cm^{-1} , as well as a second split band with peaks at 1165 and 1148 cm^{-1} , respectively. An intense band at 1235 cm^{-1} is associated with asymmetric stretching vibrations of the C–O group [1,26].

The main distinguishing feature confirming the presence of the phenolphthalein component in the copolymers is the presence of a carbonyl group, which appears as a band with a maximum at 1772 cm^{-1} . In this case, the intensity of this band could also be judged on the percentage of 4,4'-dioxypthalophenone in the copolymers.

As can be seen from the data shown in Table 1, with an increase in the content of 4,4'-dihydroxyphthalophenone at the same temperature–time modes of synthesis, the reduced viscosity of the samples decreased, which is associated with the lower reactivity of 4,4'-dihydroxyphthalophenone compared to 4,4'-dihydroxydiphenol. With a strictly equivalent ratio of monomers, the final molecular mass of the polymer was determined by the acid–base properties of the monomers, the ratio of the rates of the main chain growth reaction and the side reactions limiting the chain growth. Due to the higher acidity of the cardo monomer, a side reaction occurs during polycondensation—the formation of a quinoid structure as a result of a tautomeric rearrangement in the 4,4'-dihydroxyphthalophenone molecule [27], according to the following Scheme 3:



Scheme 3. Tautomeric rearrangement in the 4,4'-dihydroxyphthalophenone molecule.

Table 1. Rheological properties.

Sample	η (dL g ⁻¹)	MFI (g min ⁻¹)
PPSU	0.50	14.0
PPSU-C-10	0.47	13.0
PPSU-C-30	0.40	12.0
PPSU-C-50	0.31	9.0
PPSU-C-70	0.31	10.0
PPSU-C-90	0.30	4.3
PPSU-C-100	0.28	5.4

In this case, the value of the MFI was also decreased by an increase in the fraction of cardo fragments of 4,4'-dihydroxyphthalophenone. This is presumably caused by the hindrance of bulky side substituents on the movement of macro molecules relative to one another in the melt.

One of the most important indicators in the use of high performance polymers is a glass transition temperature, which is directly related to the maximum possible temperature of their long-term operation.

It is known [1,28] that the introduction of large side substituents into the polymeric chain increases the heat resistance of the material. As expected, the introduction of phenolphthalein significantly increased the glass transition temperature and heat resistance (Table 2).

The temperatures at the beginning of the mass loss of the synthesized copolymers in air, as can be seen from the results presented in Table 2 and Figure 2, insignificantly decreased with an increase in the concentration of cardo fragments. Thus, the addition of 10% 4,4'-dihydroxyphthalophenone reduced the temperature of the onset of thermal degradation, corresponding to a loss of 2% of the mass, by only 13 °C, and the addition of 50% 4,4'-dihydroxyphthalophenone reduced the heat resistance by 26 °C. Further, with an increase in the content of the proportion of cardo fragments, the temperature of the onset of thermal degradation practically did not change.

Table 2. Thermal properties of PPSU and PPSU-C.

Sample	T _{2%} , °C	T _{5%} , °C	T _{10%} , °C	T _g , °C	Vicat Softening Temperature, °C
PPSU	490	517	538	219	221
PPSU-C-10	477	500	518	221	222
PPSU-C-30	470	489	504	229	229
PPSU-C-50	464	483	497	235	233
PPSU-C-70	462	480	493	241	239
PPSU-C-90	462	481	494	245	244
PPSU-C-100	465	482	494	248	248

T_{2%}, T_{5%}, T_{10%}: temperature of 2, 5 and 10% weight loss, respectively.

The main physical and mechanical properties of copolyphenylene sulfones with cardo fragments of 4,4'-dihydroxyphthalophenone are shown in Table 3.

As can be seen from Table 3, there is a direct dependence of the elastic-strength properties on the 4,4'-dihydroxyphthalophenone content: with an increase in its concentration, the elastic modulus, both in bending and in tension, gradually increased (by about 14% at 50% comonomer content). These results are consistent with the nature of the change in T_g, which characterizes the rigidity of the polymer chain. Strength characteristics also tended to increase. When the comonomer content was above 50%, the fracture became brittle, without plastic flow—which explains the increased strength at a break at 70% content of 4,4'-dihydroxyphthalophenone; however, further, due to the decrease in reduced viscosity, the strength decreased. Clearly, the observed changes in properties are the result of an

increase in the kinetic rigidity of the chain, as well as the creation of conditions for the “linkages” of structural elements due to the presence of a bulky substituent.

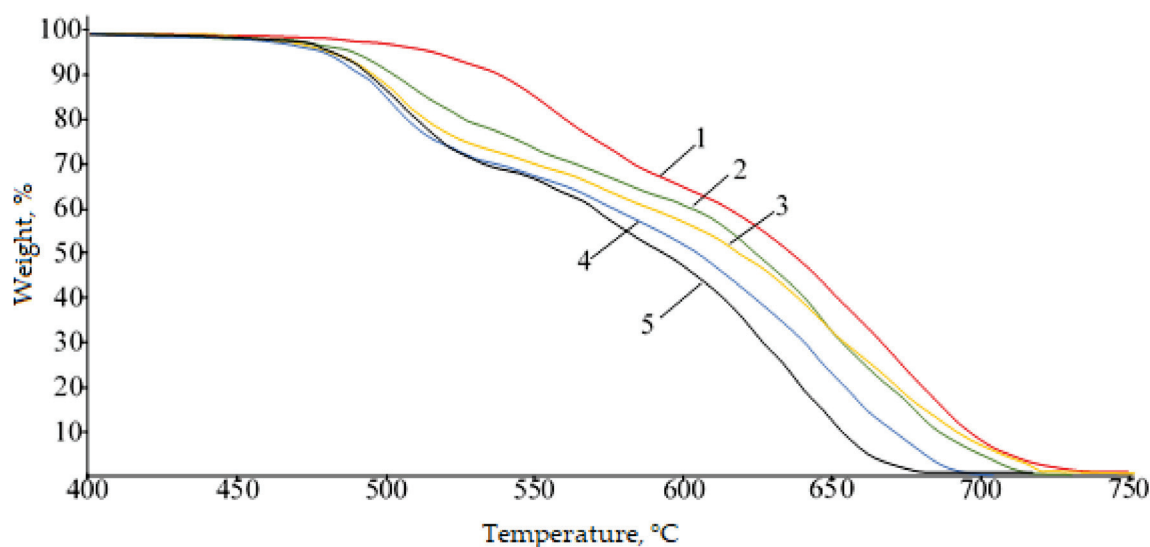


Figure 2. TGA curves: 1—PPSU; 2—PPSU-C-30; 3—PPSU-C-50; 4—PPSU-C-70; 5—PPSU-C-100.

Table 3. Mechanical properties of PPSU and PPSU-C.

Sample	Impact Strength, kJ/m ²		E_{fl} , MPa	σ_{yield} , MPa	E_{ten} , MPa	σ_{ten} , MPa	ϵ , %	Shore Hardness (D Scale)
	Unnotched	Notched						
PPSU	n/b	24.3	2390	87.5	2150	73	38.5	75
PPSU-C-10	150	14.8	2500	83.0	2230	68	12.6	76
PPSU-C-30	168	11.0	2650	87.0	2300	70	11.7	78
PPSU-C-50	88	6.2	2780	90.5	2430	73	9.8	79
PPSU-C-70	27	6.5	2970	-	2613	94	8.0	80
PPSU-C-90	15	4.5	3110	-	2330	83	4.5	80
PPSU-C-100	26	9.8	3270	-	2490	85	4.2	80

E_{fl} : flexural modulus, σ_{yield} : Yield strength, E_{ten} : tensile modulus, σ_{ten} : tensile strength, ϵ : elongation at break. n/b: not break.

Additionally, copolymers have lower values of impact strength than homopolymers, which appears to be the result of two factors. First, toughness is highly dependent on molecular weight. As shown above (Table 1), the values of the average molecular weight of the copolymers (M_w) monotonically decreased with an increase in the concentration of 4,4'-dihydroxyphthalophenone, which, in turn, can lead to a loss of impact resistance. Secondly, it can be seen from Table 3 that even at a content of 10% comonomer, the impact strength and elongation in tension were significantly lower than the corresponding properties of the homopolymer, despite the close values of the rheological and molecular weight characteristics. This suggests that the presence of 4,4'-dihydroxyphthalophenone cardo fragments in itself already leads to a decrease in plastic properties.

Shore hardness studies of the synthesized polymers showed (Table 3) that an increase in the content of the proportion of 4,4'-dihydroxyphthalophenone cardo fragments above 70 mol.% did not lead to an increase in the hardness values of the samples

4. Conclusions

As a result of the studies carried out, the influence of the concentration of 4,4'-dioxypthalophenone on the molecular weight characteristics of the obtained copolymers was revealed. Their structural features were confirmed by IR spectroscopy. It is shown that an increase in the content of cardo fragments led to an increase in the glass transition temperature and heat resistance of copolymers, as well as elastic-strength properties, due

to an increase in chain rigidity. In this case, a decrease in heat resistance, as well as the plastic properties of the copolymers, was observed.

Author Contributions: Investigation, Z.K., A.Z., K.S., A.S. and A.B.; Project administration, S.K. All authors have read and agreed to the published version of the manuscript.

Funding: This research received no external funding.

Institutional Review Board Statement: Not applicable.

Informed Consent Statement: Not applicable.

Acknowledgments: This work was done using equipment of the collective usage center «Polymers and composites» of Kh.M. Berbekov Kabardino-Balkarian State University.

Conflicts of Interest: The authors declare no conflict of interest.

References

- Zhansitov, A.A.; Khashirova, S.Y.; Slonov, A.L.; Kurdanova, Z.I.; Shabaev, A.S.; Khashirov, A.A.; Mikitaev, A.K. Development of technology of polysulfone production for 3D printing. *High Perform. Polym.* **2017**, *29*, 724–729. [CrossRef]
- Wagner, F.C. Synthetic Resin. U.S. Patent 2035578, 31 March 1936.
- Akutin, M.S. A Method of Producing a Polysulfone. SU Author's Certificate 301073. 4 June 1969.
- Li, L.; Liu, J.; Chen, G.; Xu, L.; Mushtaq, N.; Sidra, L.R.; Wang, R.; Fang, X. Synthesis of organosoluble and transparent phenolphthalein-based cardo poly(ether sulfone imide)s via aromatic nucleophilic substitution polymerization. *High Perform. Polym.* **2016**, *28*, 1263–1271. [CrossRef]
- Yang, Y.; He, T.; Yu, F. The fracture behavior of phenolphthalein polyether–ether ketone at elevated temperature for long terms. *J. Appl. Polym. Sci.* **1995**, *55*, 627–632. [CrossRef]
- Chamkure, Y.K.; Sharma, R.K. New organosoluble polyarylates containing pendent fluorene units: Synthesis, characterization and thermal behaviour. *J. Polym. Res.* **2019**, *26*, 17. [CrossRef]
- Yuan, Y.; Xie, B.; Wang, Y. An Interesting Result of Dielectric Property for Novel Polyimides with Fluorene Groups. *Mater. Sci. Forum* **2010**, *663–665*, 511–514. [CrossRef]
- Khan, M.M.; Halder, K.; Shishatskiy, S.; Filiz, V. Synthesis and Crosslinking of Polyether-Based Main Chain Benzoxazine Polymers and Their Gas Separation Performance. *Polymers* **2018**, *10*, 221. [CrossRef]
- Kim, D.; Hossain, I.; Kim, Y.; Choi, O.; Kim, T.-H. PEG/PPG-PDMS-Adamantane-based Crosslinked Terpolymer Using the ROMP Technique to Prepare a Highly Permeable and CO₂-Selective Polymer Membrane. *Polymers* **2020**, *12*, 1674. [CrossRef] [PubMed]
- Du, N.; Park, H.B.; Dal-Cin, M.M.; Guiver, M.D. Advances in high permeability polymeric membrane materials for CO₂ separations. *Energy Environ. Sci.* **2012**, *5*, 7306–7322. [CrossRef]
- Chen, G.; Zhang, X.; Zhang, S.; Chen, T.; Wu, Y. Synthesis, properties, and gas permeation performance of cardo poly(arylene ether sulfone)s containing phthalimide side groups. *J. Appl. Polym. Sci.* **2007**, *106*, 2808–2816. [CrossRef]
- Hergenrother, P.M.; Jensen, B.J.; Havens, S.J. Poly(arylene ethers). *Polymer* **1988**, *29*, 358–369. [CrossRef]
- Singh, R.; Hay, A.S. Synthesis and physical properties of soluble, amorphous poly(ether ketone)s containing the o-dibenzoylbenzene moiety. *Macromolecules* **1992**, *25*, 1017–1024. [CrossRef]
- Korycki, A.; Garnier, C.; Abadie, A.; Nassiet, V.; Sultan, C.; Chabert, F. Poly(etheretherketone)/Poly(ethersulfone) Blends with Phenolphthalein: Miscibility, Thermomechanical Properties, Crystallization and Morphology. *Polymers* **2021**, *13*, 1466. [CrossRef]
- Xueren, L.; Congjie, G. Research on polyethersulfone, polyarylsulphone and polyetheretherketone with cardo membranes. *Desalination* **1994**, *96*, 155–161. [CrossRef]
- Pulyalina, A.; Rostovtseva, V.; Faykov, I.; Toikka, A. Application of Polymer Membranes for a Purification of Fuel Oxygenated Additive. Methanol/Methyl Tert-butyl Ether (MTBE) Separation via Pervaporation: A Comprehensive Review. *Polymers* **2020**, *12*, 2218. [CrossRef] [PubMed]
- Vasoya, P.J.; Patel, V.A.; Bhuva, B.D.; Parsania, P.H. Synthesis and Physico-Chemical Study of High Performance Cardo Copoly(Ether-Sulfone-Sulfonates). *Polym. Technol. Eng.* **2008**, *47*, 828–835. [CrossRef]
- Wang, L.-M.; Guan, G.-Y.; Chen, Z.-W. Electrospun Nanofiber-Based Cardo Poly(aryl ether sulfone) Containing Zwitterionic Side Groups as Novel Proton Exchange Membranes. *Int. Polym. Process.* **2018**, *33*, 480–485. [CrossRef]
- Blanco, J.; Nguyen, Q.; Schaezel, P. Novel hydrophilic membrane materials: Sulfonated polyethersulfone Cardo. *J. Membr. Sci.* **2001**, *186*, 267–279. [CrossRef]
- Zhang, Q.; Zhang, S.; Li, S. Synthesis and characterization of novel cardo poly(aryl ether sulfone) bearing zwitterionic side groups for proton exchange membranes. *Int. J. Hydrogen Energy* **2011**, *36*, 5512–5520. [CrossRef]
- Gao, N.; Zhang, S. Phenolphthalein-based cardo poly(arylene ether sulfone): Preparation and application to separation membranes. *J. Appl. Polym. Sci.* **2013**, *128*, 1–12. [CrossRef]
- Zheng, G.; Dong, L.; Cai, Z.H.; Feng, Z.H. Synthesis of segmented copolymers with polysulfones containing bisphenol A or phenolphthalein units as hard segment. *Polym. Commun.* **1985**, *2*, 176–179.

23. Harris, J.; Maresca, L.; Metzner, M. Polyaryl Ether Sulphones. U.S. Patent No 4785072, 15 November 1988.
24. Brunelle, D.J.; Steiger, D. Polyethersulfone Compositions with High Heat and Good Impact Resistance. Patent WO 2008051651, 24 October 2006.
25. Kurdanova, Z.H.I.; Shakhmurzova, K.T.; Zhansitov, A.A.; Baykaziev, A.E.; Slonov, A.L.; Khashirova, S.Y.; Ligidov, M.K.H.; Mik-Itaev, A.K. Study of synthesis and properties of copolysulphones with cardium fragments. *Plast. Massy*. **2017**, 7–8, 23–26.
26. Steiner, G.; Zimmerer, C. Poly(aryl ether sulfone) (PAES). In *Landolt-Börnstein—Group VIII Advanced Materials and Technologies 6A1 (Polymer Solids and Polymer Melts—Definitions and Physical Properties I)*; Arndt, K.-F., Lechner, M.D., Eds.; Springer: Berlin/Heidelberg, Germany, 2013; Volume 6A1. [CrossRef]
27. Musaev, U.I.; Mikitaev, A.K. *Appreciation de Tacide Relativee des Diphenols dan le Melange de l'Alcool Tertiobuty Liquo et dimethilsulpoixide*; Revue Scientifique sur la Chimie Industrielle: Annaba, Algerie, 1979; pp. 78–81.
28. Mikitaev, A.K.; Korshak, V.V.; Shustov, G.B. Synthesis and properties of halide-containing polyarylatesulfonic block copolymers/*Vysokomol. Soedin. Seriya A* **1982**, 24, 2558–2562.

Article

Recycled Porcine Bone Powder as Filler in Thermoplastic Composite Materials Enriched with Chitosan for a Bone Scaffold Application

Marco Valente ^{1,2,*} , Jordi Puiggali ³ , Luis J. del Valle ³ , Gioconda Titolo ¹  and Matteo Sambucci ^{1,2} 

¹ Department of Chemical Engineering, Materials, Environment, Sapienza University of Rome, 00184 Rome, Italy; titologioconda@gmail.com (G.T.); matteo.sambucci@uniroma1.it (M.S.)

² INSTM Reference Laboratory for Engineering of Surface Treatments, Department of Chemical Engineering, Materials, Environment, Sapienza University of Rome, 00184 Rome, Italy

³ Departament d'Enginyeria Química, Universitat Politècnica de Catalunya, Escola d'Enginyeria de Barcelona Est-EEBE, 08019 Barcelona, Spain; jordi.puiggali@upc.edu (J.P.); luis.javier.del.valle@upc.edu (L.J.d.V.)

* Correspondence: marco.valente@uniroma1.it; Tel.: +39-06-44585582

Abstract: This work aims to synthesize biocompatible composite materials loaded with recycled porcine bone powder (BP) to fabricate scaffolds for in-situ reconstruction of bone structures. Polylactic acid (PLA) and poly(ϵ -caprolactone) (PCL) were tested as matrices in percentages from 40 wt% to 80 wt%. Chitosan (CS) was selected for its antibacterial properties, in the amount from 5 wt% to 15 wt%, and BP from 20 wt% to 50 wt% as active filler to promote osseointegration. In this preliminary investigation, samples have been produced by solvent casting to introduce the highest possible percentage of fillers. PCL has been chosen as a matrix due to its greater ability to incorporate fillers, ensuring their adequate dispersion and lower working temperatures compared to PLA. Tensile tests demonstrated strength properties (6–10 MPa) suitable for hard tissue engineering applications. Based on the different findings (integration of PLA in the composite system, improvements in CS adhesion and mechanical properties), the authors supposed an optimization of the synthesis process, focused on the possible implementation of the electrospinning technique to develop PCL-BP composites reinforced with PLA-CS microfibers. Finally, biological tests were conducted to evaluate the antibacterial activity of CS, demonstrating the applicability of the materials for the biomedical field.

Keywords: thermoplastic composites; bone scaffold; recycled bone powder; chitosan; PLA; PCL; mechanical properties; antibacterial activity

Citation: Valente, M.; Puiggali, J.; del Valle, L.J.; Titolo, G.; Sambucci, M. Recycled Porcine Bone Powder as Filler in Thermoplastic Composite Materials Enriched with Chitosan for a Bone Scaffold Application. *Polymers* **2021**, *13*, 2751. <https://doi.org/10.3390/polym13162751>

Academic Editors: Somen K. Bhudolia and Sunil Chandrakant Joshi

Received: 3 July 2021

Accepted: 10 August 2021

Published: 16 August 2021

Publisher's Note: MDPI stays neutral with regard to jurisdictional claims in published maps and institutional affiliations.



Copyright: © 2021 by the authors. Licensee MDPI, Basel, Switzerland. This article is an open access article distributed under the terms and conditions of the Creative Commons Attribution (CC BY) license (<https://creativecommons.org/licenses/by/4.0/>).

1. Introduction

Continuous advances in medical science and surgical techniques have allowed transplantation, whether of tissues or whole organs, to become one of the potential options for restoring the native functions of many damaged parts of the human body. However, transplantation techniques encountered several limitations, such as the growing demand that far exceeds the actual availability by donors of usable tissues and the possible contamination of the donor tissue [1]. Therefore, a new technique is needed to reduce this discrepancy between clinical needs and availability in healthy tissues or organs. Tissue engineering (TE) is an interdisciplinary approach which utilizes cells, bioactive factors, and biomaterials to restore required functions of tissues. TE is based on the principles of medicine, biology, material science, and engineering by integrating them into the design of biological components to repair, maintain, and improve tissue functions [2,3]. Scaffolds are an essential part of this methodology. They are 3D structures that provide a template for cell attachment in the biological tissue formation. Besides, scaffolds perform unique functions that cannot be achieved by common drugs, including providing specific

mechanical support in defect areas, stimulating cell differentiation by regulating the mechanical properties, and executing, raising, or replacing some lost physiological functions caused by diseases or impairments [2,4]. In summary, an ideal scaffold in TE applications should meet three basic requirements: (a) A porous microstructure with a tunable pore size distribution; (b) biocompatibility and degradation properties to enable cell migration and growth; (c) appropriate mechanical properties and stability of the shape to resist stresses and maintain the integrity of the designed structure [5]. According to the classification proposed by Eltom et al. [6], fabrication technologies for scaffold manufacturing can be categorized in two classes: Conventional fabrication techniques (freeze-drying, solvent casting, gas foaming, electrospinning) and rapid prototyping methods (stereolithography, selective laser sintering, fused deposition modelling, bioprinting). Table 1 shows the main advantages and limitations of these scaffold fabrication technologies compared with the transplantation approach applied in tissue surgery.

Table 1. Advantages and drawbacks of the scaffold fabrication technologies for TE and comparison with transplantation methods.

Method	Advantages	Drawbacks
Transplantation		
Autografts	Availability of all necessary genetic elements (cells, tissue-inductive growth factors, substrates) for tissue regeneration [7]	Pain and morbidity of the donor site, prolonged surgery, limited available volume, and hardly manipulation to reproduce complex anatomical structures [7]
Allogeneic grafts	Virtually unlimited amount of material obtainable in various sizes and shapes from a human tissue bank. Shorter surgery compared to autografting because the tissue harvesting procedure is not necessary. Suitable healing capabilities [7,8]	Disease transmission, toxicity associated with the sterilization, high variability in host immune response, limited supplies. Lack of scientific evidence and standardized protocols [7,8]
Conventional Fabrication Technique		
Solvent casting	Low-cost technique. High porosity (50–90%). Not need of sophisticated equipment [6,9]	Use of very toxic solvents. Residual solvent can defunctionalize the cell growth [6,9]
Freeze-drying	Possibility to manage the pore size distribution by changing the freezing method. Possibility to produce scaffold with suitable interconnectivity without implementing high working temperature [6,9]	Use of cytotoxic solvents. Generation of small and irregular pores (15–35 μm) [6,9]
Gas foaming	High porosity (up to 85%). No use of organic solvents [6,9]	Strict control of thermal operating conditions is necessary as the method is highly sensitive to the development of closed pore structures and non-porous skin layer [6,9]
Electrospinning	Possibility to produce highly porous scaffolds with small pore diameters (nano to micro scale). High tensile strength performance due to the fibers-based structure [6,9]	Use of toxic solvents. Process depends on many variables (type of solvent, polymer concentration, voltage, flow rate, needle size, temperature, pressure, needle-to-collector distance). Problematic to obtain 3D structures [6,9]
Rapid Prototyping Methods		
Stereolithography	High resolution. Uniformity in pores interconnectivity. Possibility to fabricate structures with anatomically shape [6,9]	Expensive equipment. Requiring massive amounts of monomers and post-treatment to improve the monomer conversion. Shrinkage during polymerization [6,9]
Selective laser sintering	Not using solvent. Rapid process. Excellent control over the scaffold microstructure by adapting the process parameters [6,9]	High operating temperature. High-cost equipment. Requiring many post-processing treatments to remove injected powder [6,9]
Fused deposition modelling	Low operating temperature. Solvent-free technique. Reaching of suitable strength properties. Low cost [6,9]	Medium precision. Several limitations in its application to biodegradable polymers [6,9]
Bioprinting	High accuracy and shape complexity. High cell viability (80–90%). Low costs [6]	Depends on existence of cells [6]

In the orthopedical sector, bone tissue engineering (BTE) is a rapidly growing sector aiming to create a bio-functional tissue that can integrate and degrade *in vivo* to treat lost, diseased, or damaged bone tissue, minimizing the complications deriving from the more traditional bone grafting methods [10]. According to the principles of TE, BTE is based on four key components: (a) Osteogenic cells that generate the bone matrix; (b) a scaffold that mimics the extracellular matrix (ECM) of the bone; (c) vascularization that ensures the transport of nutrient and waste products; and (d) morphogenetic signals to assist cell proliferation. Osteo-induction, osteo-conduction, osseointegration, chemical-mechanical stability in host environment, and adequate manufacturability are the main requirements that a biomaterial should possess for BTE applications [11]. In this context, several matrices have been identified as functional for scaffold applications due to their suitable mechanical and technological properties. Specifically, Polylactic acid (PLA) and poly(ϵ -caprolactone) (PCL) were recognized as promising candidates in the BTE field. They are biocompatible and biodegradable polymers whose degradation products (due to non-enzymatic hydrolysis of the esters in a physiological environment) are low molecular weight compounds, such as lactic and hydroxyhexanoic acids [12,13]. For instance, lactic acid is the main degradation product that falls within the normal metabolic pathways. In fact, it is normally

expelled by the body in the form of carbon dioxide and water [12,13]. The ability of the two thermoplastic polymers to support osseointegration without undergoing rejection from the biological environment was demonstrated in recent studies. Nazeer et al. [14] researched 3D-printed PLA scaffolds functionalized with chitosan (CS) and hydroxyapatite (HA) used as mechanical reinforcements and an osteoconductive filler, respectively. Zimina et al. [15] employed solvent casting and salt leaching methods to fabricate PLA/HA scaffolds with mechanical properties suitable for soft TE applications and minimal inflammatory response after *in vivo* implantation. Lopresti et al. [16] investigated the influence of HA concentration and size on the mechanical properties and cytocompatibility of PLA-based electrospun nanofibrous mats intended for BTE applications. The nanosized HA fillers promoted less structural defects, higher mechanical performance, and better biological behavior in terms of more homogeneous colonization of the scaffold by pre-osteoblastic cells. Trakoolwannachai et al. [17] synthesized HA from eggshell waste to produce PCL-HA composites by a conventional wet chemical method. *In-vitro* analysis showed that the scaffolds supported high levels of Saos-2 cells without causing any cytotoxic effect. Cestari et al. [18] developed PCL scaffolds, via 3D printing, functionalized with nanometric HA. The composite scaffolds showed a compressive elastic modulus between 203 MPa and 316 MPa, comparable with that of trabecular bone, and better *in vitro* bioactivity than pure PCL. Miszuk et al. [19] synthesized a 3D electrospun PCL/HA scaffold combined with biomaterials-mediated bone morphogenic proteins (BMPs) to generate a bone-forming favorable niche for BTE interventions. By *in vivo* and *in vitro* experimentation, the developed scaffolds (~96% of interconnected porosity) were able to form a system to generate more favorable microenvironments for osteogenic differentiation and BMP2-induced ectopic bone formation than plain 3D electrospun PCL scaffolds. From the previously cited literature, two noteworthy aspects can be deduced: (a) The high adaptability of the two thermoplastic polymers to be processed with a wide range of TE manufacturing methods and (b) the use of HA as a bioactive, osteoconductive, and mechanical reinforcement filler.

HA is a bioactive and bioresorbable Calcium phosphate that constitutes most of the inorganic components of bone tissue. In both natural and synthetic form, HA has an identical chemical structure that differs in terms of porosity, crystal size, and microstructure. HA directly bonds with live bone after implantation in cases of bone defects, enhancing appropriate vascularization, stem cell proliferation, and the bone regeneration without causing any local or systemic toxicity [20]. There are two common ways to obtain HA [21]: Synthetically (wet processing, dry processing, sol-gel, hydrothermal processing) or by extraction from naturally available materials (eggshells, fish scales, bovine bones). The synthetic product is still preferred for BTE applications thanks to its higher purity and biological and mechanical effectiveness [22]. However, several drawbacks were found in its employment [21–23], such as the use of expensive reagent chemicals, the involvement of time-consuming and laborious work, possible triggering of inflammatory reactions by the host system due to implanted debris or foreign substances, and the slow degradation rate that hindered the rapid osteogenesis.

To investigate alternative osteo-active fillers for the BTE field, the present work proposed a preliminary study about the possibility of integrating recycled bone powder (BP) in thermoplastic matrices (PLA and PCL), to develop biocompatible thermoplastic composite materials suitable for scaffold applications. This research is positioned in the novel perspective of industrial waste recovery to obtain new materials for TE, understanding the importance of recycling of waste materials and by-products to obtain alternative source for precursors. Indeed, BP used like an inorganic reinforcement was a fine-grain (0–500 μm) by-product of the mechanical processing of porcine bone to obtain two coarser bone fractions used by TecnoSS™ company (Turin, Italy) [24] in OsteoBiol™ technology (Figure 1).

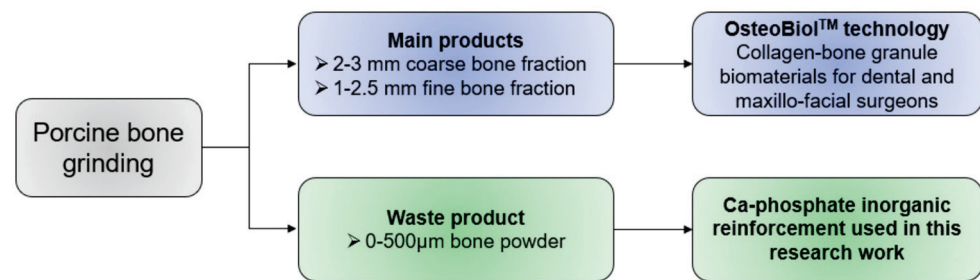


Figure 1. Origin of the BP (provided by TecnoSS™) used in this work.

Besides, the research envisaged an optimization in terms of antimicrobial properties, by the integration of Chitosan (CS), extensively used as a “platform” in BTE and other biomedical applications because of its cytocompatibility, degradability, appropriateness for cell ingrowths, and bactericidal activity [25]. As a first attempt at manufacturing the composite, the solvent-casting technique was employed to produce bio-composites. The aim of the research was to investigate the feasibility of producing composite materials with adequate reproducibility and analyze the variations in mechanical and antibacterial properties. After evaluating the most suitable polymer-BP-CS formulations, mechanical characterization by tensile tests and bacterial growth/adhesion evaluation were performed. This preliminary study lays the foundations for advanced upgrades in terms of integration of reinforcement fillers and the development of filaments potentially usable in additive manufacturing (AM) techniques.

2. Materials and Methods

2.1. Materials

PLA Ingeo Biopolymer 3001D (density of 1.24 g/cm³ at 25 °C; melt flow rate of 80 g/10 min at 210 °C; glass transition temperature of 55–60 °C) was purchased from NatureWorks (Minnetonka, MN, USA). PCL pellets (molecular weight of 80,000 g/mol; density of 1.145 g/mL; melting point of 60 °C; purity > 95%), CS (high molecular weight of 310–357 kDa, with a degree of deacetylation > 75%, viscosity of 800–2000 cps, density of 0.15–0.3 g/cm³), and 99% anhydrous Chloroform (CHCl₃) stabilized with amylene were purchased from Sigma-Aldrich (St. Louis, MO, USA). As previously mentioned, 0–500 μm porcine BP was provided by TecnoSS (Turin, Italy). The microstructure (Figure 2) and particle size distribution (Figure 3) of the particles were investigated by scanning electron microscopy (SEM), using a Mira 3 FEG-SEM (Tescan, Brno, Czech Republic), and particle size analysis by a MasterSizer 3000 (Malvern Panalytical, Malvern, UK), respectively.

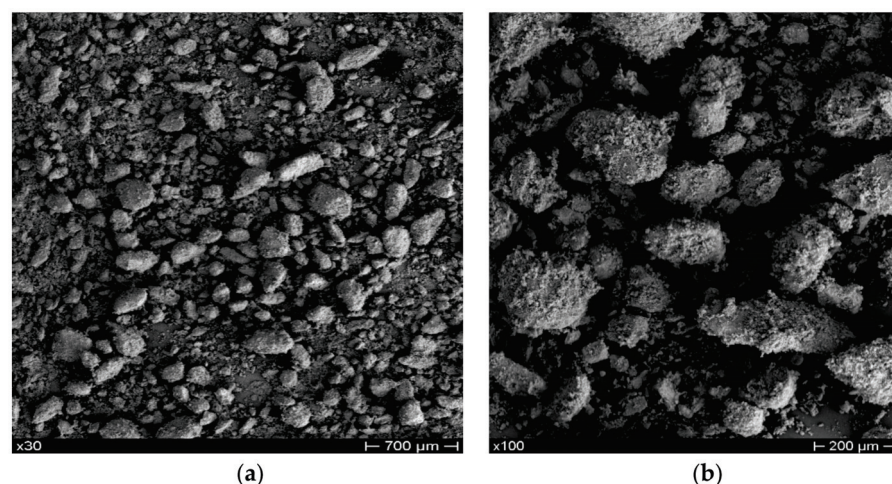


Figure 2. SEM images of BP at low (a) and high (b) magnifications.

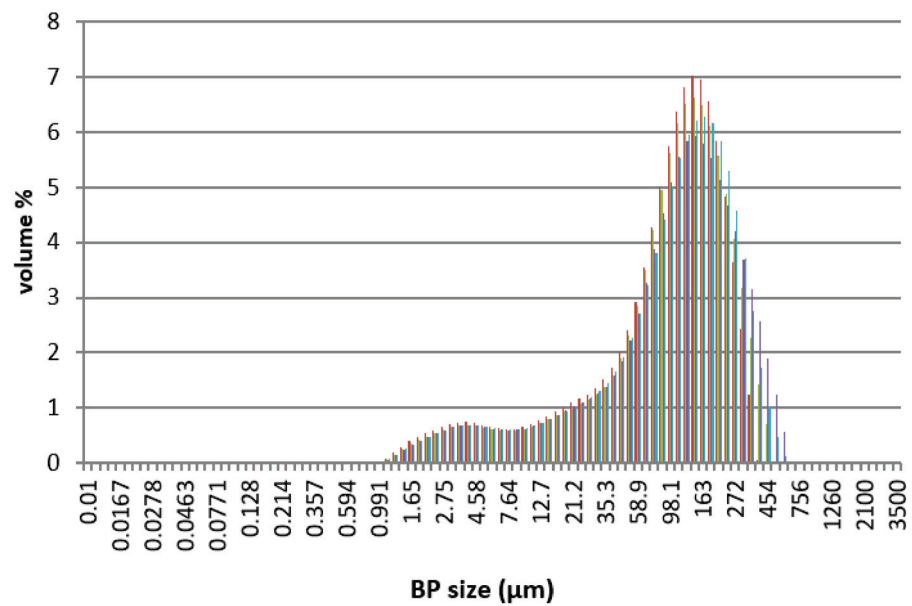


Figure 3. Dimensional distribution of the BP used in this work. Each color represents a particle size pair of BP (μm)–Volume (%) obtained from the MasterSizer analyzer.

2.2. Experimental

2.2.1. Solvent Casting

BP and CS were added to the appropriate solutions of PCL and PLA in CHCl_3 . Mixtures were then homogenized by stirring for 24 h inside a closed shaker at 37°C and 95 rpm. The final mixtures were finally poured into a glass Petri dish with a diameter of 9 cm and height of 1.5 cm, to obtain films with a maximum thickness of 1 mm after complete solvent evaporation. The solvent-casting process lasted 4 days. In accordance with the above procedure, different formulations were tested by varying the type of matrix (PCL and PLA) and the percentage of fillers (CS and BP). For each thermoplastic matrix, four weight levels of BP (from 20 wt% to 50 wt%) and three weight percentages of CS (from 5 wt% to 15 wt%) were selected and experimented with.

After the process, the solvent-casted products were subjected to quality and dimensional checks, to evaluate the characteristics of the film in terms of structural integrity and thickness homogeneity. The composite films had to be uniform, not excessively brittle, and able to incorporate BP inside. The dimensional check was performed by a MEGA-CHECK Pocket (List-Magnetik, Leinfelden-Echterdingen, Germany) thickness meter (Figure 4), taking into consideration only the films with a thickness in the central part of 0.8–1.2 mm, which appeared to be suitable for the preparation of specimens for mechanical tests.



Figure 4. Thickness measurement on solvent-casted polymer-BP films.

2.2.2. Samples Preparation for Mechanical Tests

Specimens for tensile tests were obtained from the solvent-casted films by die-cutting (Figure 5), using a MT1130 die-cutter (MinEuro, Turin, Italy) equipped with a metallic dog-bone shaped cutting edge. From each disk, it was possible to extract three samples for the mechanical characterization, with a width of 3 mm and a gauge length of 60 mm.

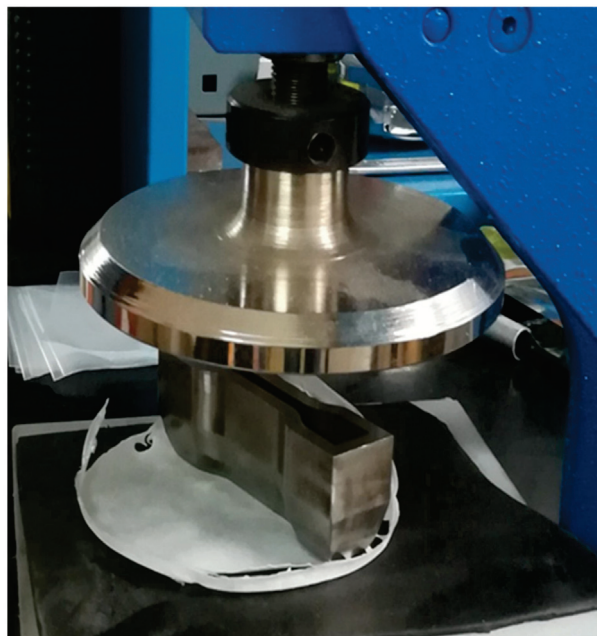


Figure 5. Dog-bone specimen preparation for tensile test: Die-cutting method.

2.3. Characterization

2.3.1. SEM

The microstructural evaluation of the samples by SEM was conducted in collaboration with the Department of Chemical Engineering, Materials, Environment (Sapienza University of Rome, Italy) and Department d'Enginyeria Química (Universitat Politècnica de Catalunya, Barcelona, Spain) employing a Mira 3 FEG-SEM (Tescan, Brno, Czech Republic) and a Phenom XL Desktop SEM (Thermo-Fisher, Waltham, MA, USA), respectively. Before SEM analyses, samples were sputter-coated with gold to obtain conductive specimens.

2.3.2. Mechanical Tests

Tensile tests were performed at room temperature using a ZwickRoell Z10 machine (Zwick-Roell, Ulm, Germany) equipped with a 1kN load cell and interfaced with the TESTXPERT II (Zwick-Roell, Ulm, Germany) software. The crosshead speed was 5 mm/min.

2.3.3. Assay of Bacterial Growth and Adhesion

Staphylococcus aureus ATCC 25923 (*S. aureus*) and *Escherichia coli* DH5 α (*E. coli*) bacteria were selected to evaluate the antimicrobial activity of CS in the PLA matrices. Bacterial inhibition was quantitatively evaluated.

The samples (i.e., each one of 100 mg) were placed into the wells of a 24-well culture plate and sterilized by UV radiation in a laminar flux cabinet for 15 min. Then, 1 mL of broth culture (Luria-Bertani medium) containing the bacteria at a concentration of 10^3 CFU/mL was added to samples for quantitative tests. Cultures were incubated at 37 °C and agitated at 80 rpm. Aliquots of 50 μ L were taken at predetermined time intervals (i.e., time 0 and 24 h) for absorbance measurement at 650 nm in a microplate reader. Each sample was analyzed in quadruplicate and the results averaged. *t*-Test with a 95% ($p < 0.05$) confidence level was performed to determine significant differences of the samples.

Turbidity was related to the relative bacterial growth by considering the maximum growth attained in the control, the sample without CS.

Bacterial adhesion on matrices has also been determined. The culture medium was aspirated after the proliferation measurements (i.e., at 72 h of culture), and the material was washed three times with distilled water. Then, 0.5 mL of sterile 0.01 M Sodium thiosulfate was added to each well to detach adhered bacteria on the sample surface. After agitation at 100 rpm and 37 °C for 1 h, samples were removed, and 1 mL of broth culture was added to each well. The first sample was taken subsequently filled with fresh broth culture (time 0 h for adhesion assay). Then, plates were incubated at 37 °C and 100 rpm for 24 h. The bacterial number was determined by absorbance measurement at 24 h.

3. Results and Discussions

3.1. Quality Check of Post-Solvent-Casted Specimens

Only some PCL-based formulations were suitable to produce suitable solvent-casted disks and dog-bone specimens for mechanical tests. PLA-based composite samples were excessively curved, too inhomogeneous, or unable to incorporate the inorganic reinforcement. In this regard, Zhou et al. [26] highlighted that one of the main concerns in the use of solvent casting techniques to integrate HA fillers in the PLA matrix concerns the low affinity between the two components: During the solvent evaporation, the particles can precipitate from the polymer solution, resulting in a non-uniform dispersion or weak incorporation. By way of example, the comparison between a PCL-based disk (30 wt% of BP) with good dimensional and mechanical characteristics and an untestable PLA-based sample (50 wt% of BP) is shown in Figure 6. This variability of results is attributable to a non-optimized solvent-casting process. A possible future development will be based on the careful study of the synthesis parameters (the polymer–solvent ratio, solvent evaporation conditions, and the mixing method) and integrating alternative technologies to incorporate BP and CS into the polymer matrix. This latter aspect will be discussed in more detail later.

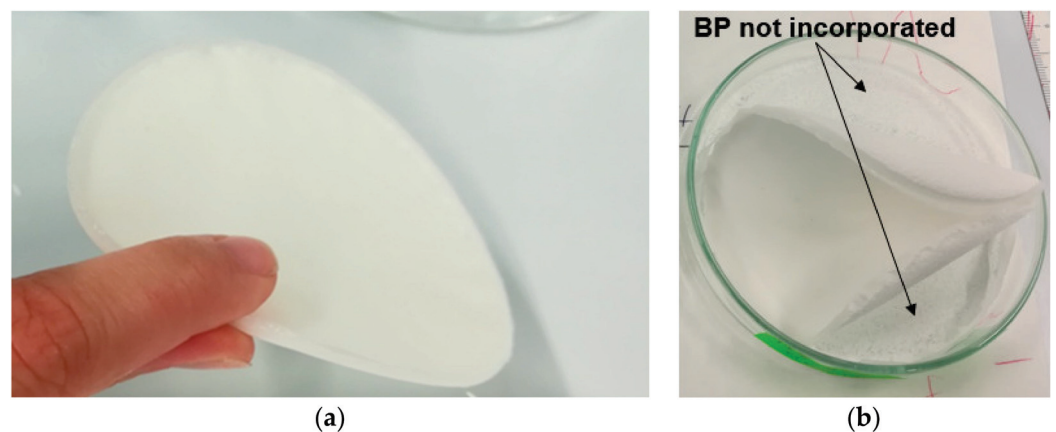


Figure 6. Comparison between a well-made disk (a) and a solvent-casted specimen with unsuitable features (b).

Table 2 lists the PCL formulations (plain and composite specimens) subjected to mechanical characterization. Here, 5 wt% was the maximum level of CS that was possible to incorporate in the composite, maintaining suitable dimensional and structural characteristics of solvent-casted films for the dog-bone specimen extraction and adequate dispersion and incorporation of the fillers into the thermoplastic matrix.

Table 2. Compositions of PCL-based samples characterized by tensile test.

ID Sample	PCL (wt%)	BP (wt%)	CS (wt%)
PCL-0	100	0	0
PCL80-BP20	80	20	0
PCL70-BP30	70	30	0
PCL50-BP50	50	50	0
PCL45-BP50-CS5	45	50	5

3.2. Microstructural Characterization by SEM

3.2.1. PLA-Based Samples Prepared by Solvent Casting

SEM analysis on samples extracted from PLA disks confirms the defects detected during the post-solvent-casting quality control. In Figure 7a, the cross section of the PLA-based composite (40 wt% of BP) shows an inhomogeneous distribution of the BP, which appears totally absent in the central part of the analyzed fragment. In addition, some small cracks are detectable. The high-magnification micrograph (Figure 7b) displays the defects, for example due to air bubbles incorporated in the solution during stirring and casting in the Petri dish. In the same figure, areas with poor solvent evaporation are evident. Figure 7c shows the air-exposed surface of the PLS sample incorporated with 50 wt% of BP. In this case, a completely polymeric surface emerges without any presence of BP. A poor interface between PLA and BP was observed in Figure 7d. This evidence agrees with the literature data [27]. The poor interface leads to a collapse of the mechanical properties of the sample, due to the absence of an interaction between the matrix and filler. Therefore, these matrices may not be ideal scaffolds, and, as mentioned above, improvements in their preparation would be required.

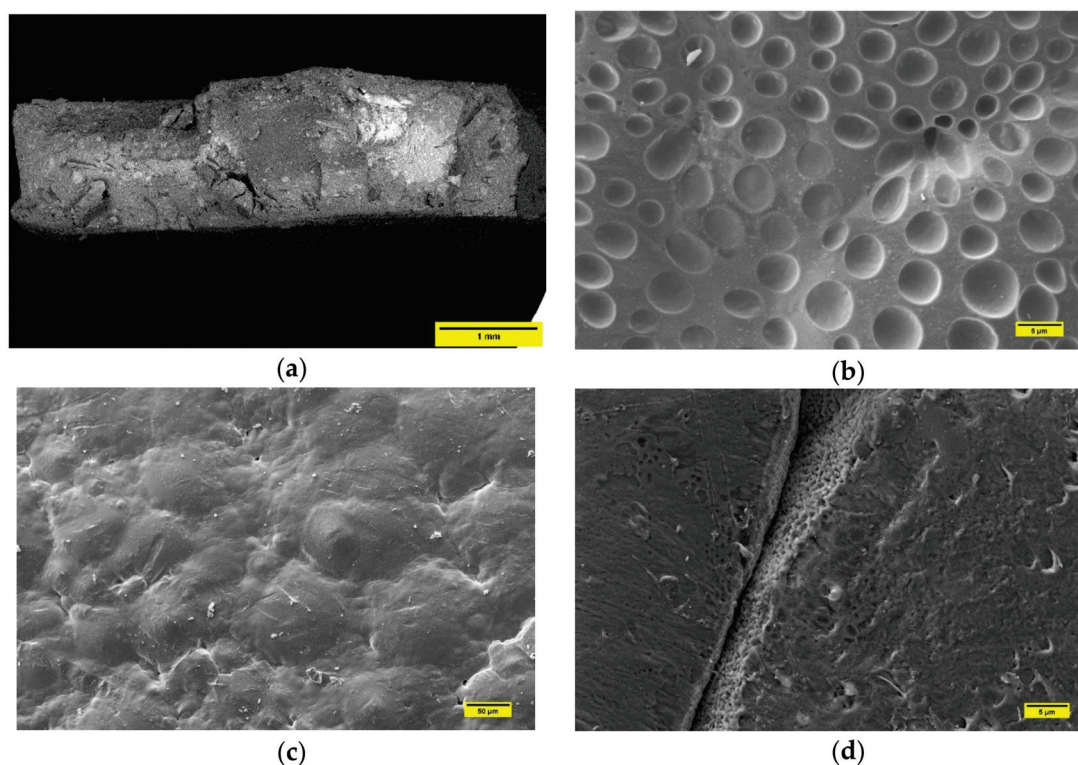


Figure 7. (a) Cross-section of PLA sample filled with 40 wt% of BP. (b) SEM micrograph PLA surface in the composite with 30 wt% of BP, highlighting air bubbles resulted from solvent casting; (c) SEM micrograph of PLA-BP sample (50 wt% of BP), where the inorganic particles are not detectable; (d) SEM image of sample constituted by 50 wt%BP and 50wt%PLA. In this case, the micrograph shows the poor cohesion between matrix and filler.

3.2.2. PCL-Based Samples Prepared by Solvent Casting

Unlike the PLA-BP composites, the solvent-casting procedure employed in this research appeared to be quite efficient for PCL matrix. From the cross-section image of PCL50-BP50 fragment, it can be seen how the polymer incorporates BP, which is homogeneously distributed over the investigated section (Figure 8a). Although the distribution of the ceramic fillers in the matrix was adequate, weak matrix–particle adhesion was noted (Figure 8b). The cross-section micrograph in Figure 8c highlights the distribution of CS filler (dashed areas) in the PCL45-BP50-CS5 sample. Figure 8d details the typical flake-like shape of CS and its interface with the PCL matrix. The tensile test results described in the next section will provide an assessment on the impact of the microstructural features on the mechanical properties.

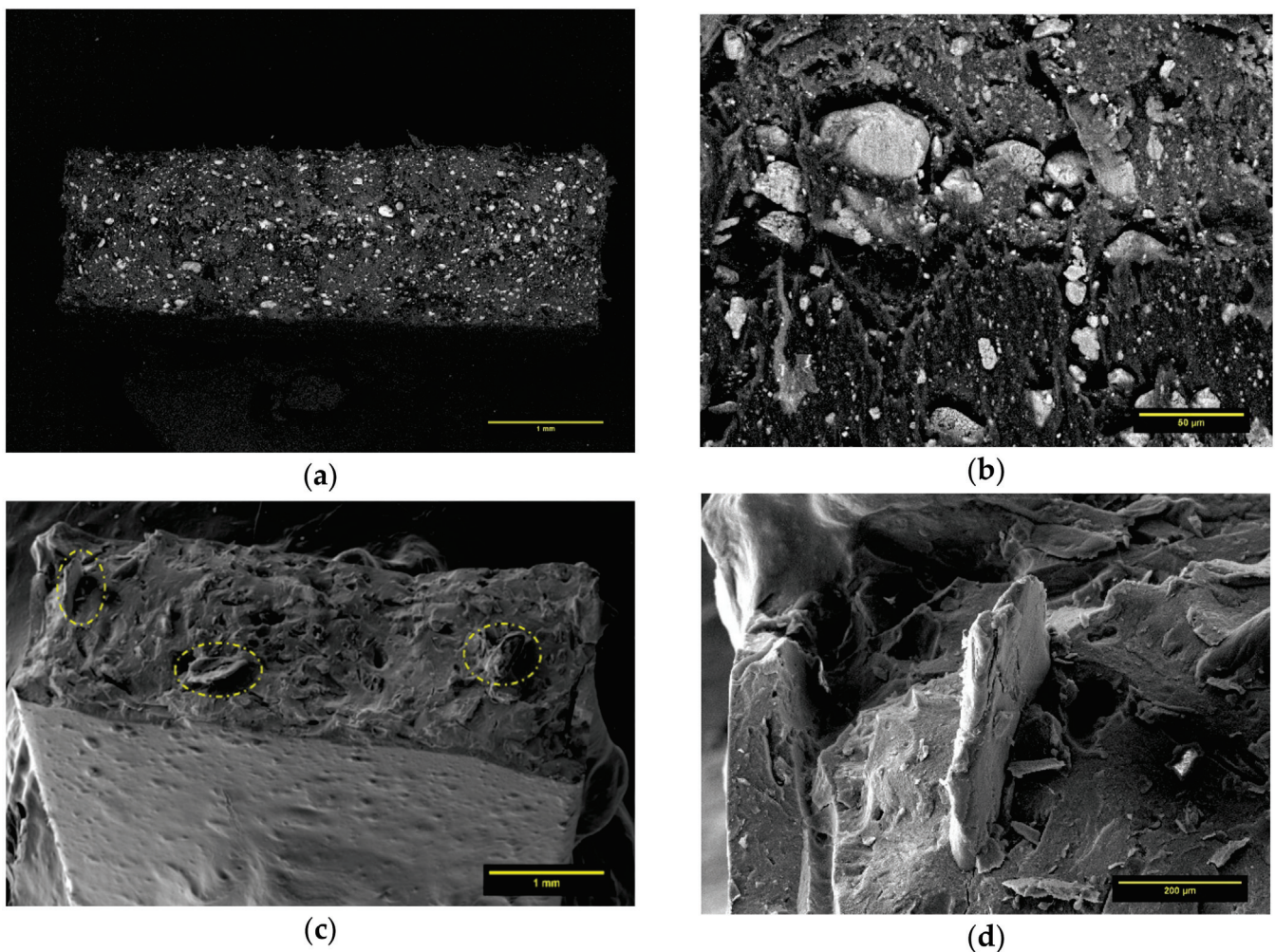


Figure 8. (a) Cross-section image of PCL50-BP50. (b) Interfacial adhesion between PCL and BP in PCL50-BP50 sample. (c) Distribution of CS filler in PCL45-BP50-CS5 specimen. (d) Detail on the interfacial adhesion of CS in PCL matrix.

3.3. Mechanical Characterization by Tensile Tests

Tensile tests were performed on the five PCL-BP-CS composites described in Table 1 and the results are summarized by histograms in Figure 9 (Tensile strength results), plots in Figure 10 (Young’s modulus and elongation-at-break results), and stress–strain curves in Figure 11.

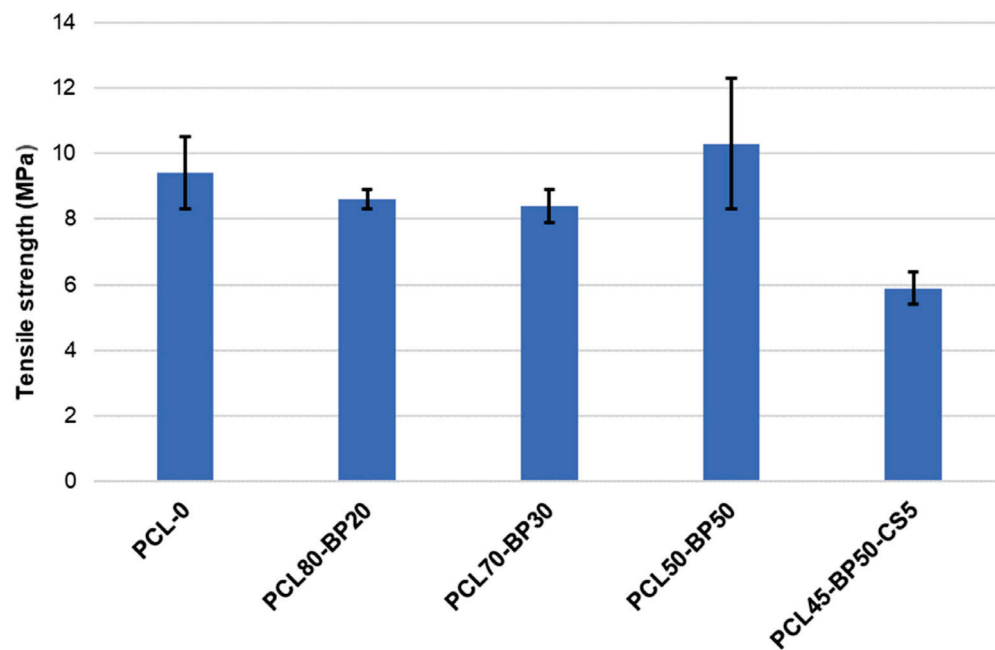


Figure 9. Tensile strength results.

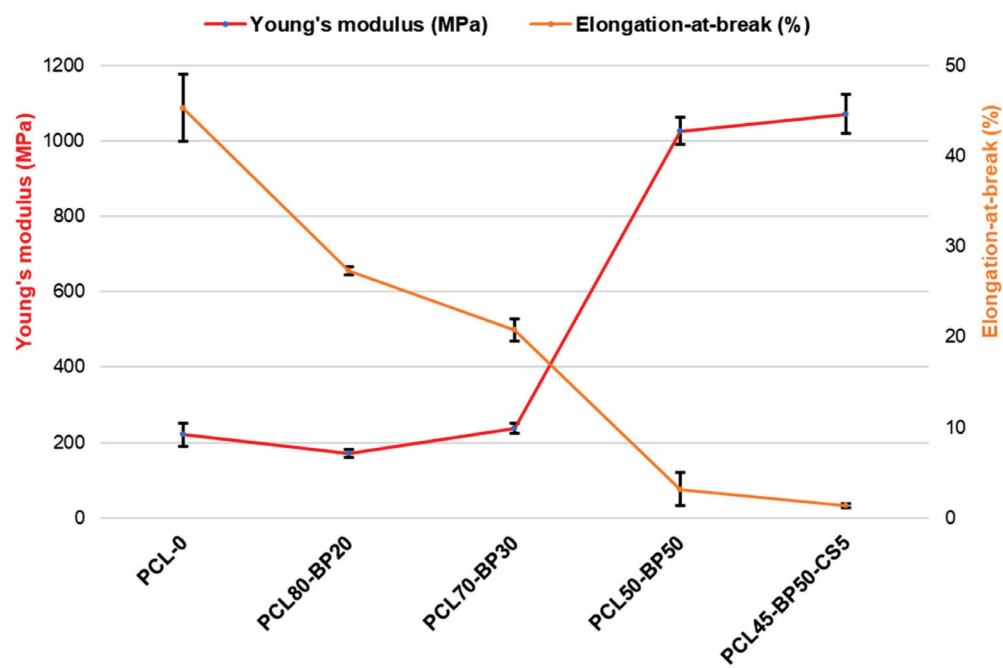


Figure 10. Young's modulus and elongation-at-break results.

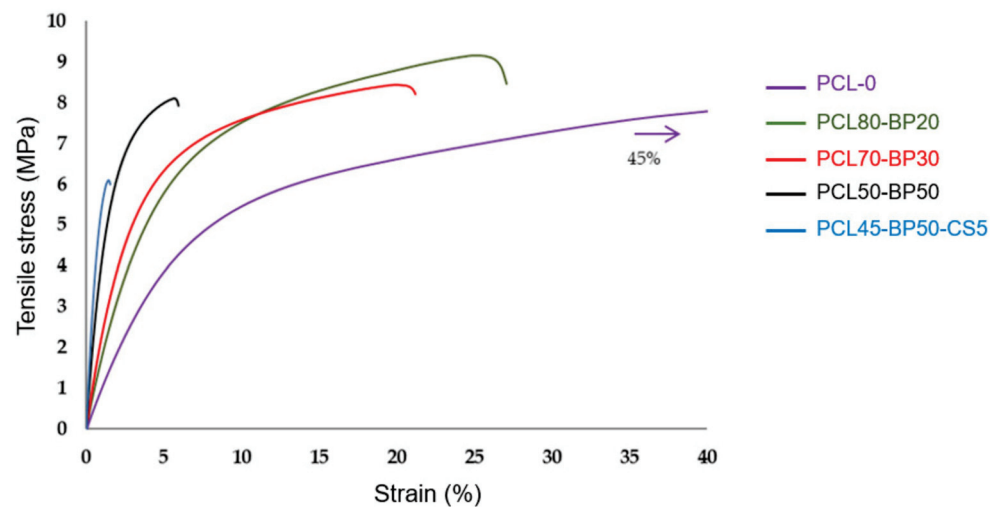


Figure 11. Stress vs. strain curves from tensile test.

Although SEM investigation on PCL-BP composites revealed some defects in matrix–ceramic interfaces, the tensile strength of the samples did not show significant drops compared to unfilled material (PCL-0). These results confirm that PCL and BP in this proportion are compatible in terms of dispersion. Tensile strength increased from 9.34 MPa to 10.32 MPa when increasing the loading of BP from 0% to 50%, indicating an effective reinforcement effect of hard-phase fillers. The most significant decrease in mechanical strength is observed in the formulation functionalized with 5 wt% of CS fillers. This behavior is attributable to several possible reasons [27,28]: (a) The flaked morphology of CS reduces the interlocking with the PCL matrix; (b) the strong difference in polarity between PCL and CS results in phase-separated composites, reducing the mechanical properties; and (c) the non-optimal concentration of CS, which could lead to an agglomeration phenomena and scarce interfacial adhesion with the matrix. As reported by [29], for hard tissue engineering applications, a minimum strength value of 100 kPa is required (depending on target tissue). All the formulations developed in this research fully satisfy such requirements.

By increasing the BP content, the material’s plasticity was decreased while stiffness increased. For BP levels below 30 wt%, the composites maintain comparable elasticity properties, indicating that the polymer matrix is in such quantities as to still govern the mechanical behavior of the material. Above this concentration, there is a sudden increase in the material’s stiffness. The maximum Young’s modulus value can be found in the PCL45-BP50-CS5 sample, where an increase of about 385% compared to the plain formulation (PCL-0) was recorded. In the CS-filled composite, the increase in stiffness did not correspond to an increase in tensile strength as usually observed, but a marked mechanical strength drop was detected. In addition to the factors mentioned above regarding the CS–PCL interaction, this behavior can be attributed to the lower PCL concentration more so than the other formulations. A similar finding was found by Fadaie et al. [30]: Reducing the concentration of the PCL solution causes a remarkable decline in tensile strength. Elongation-at-break gradually decreases with the increase of BP more incisively than the elastic modulus increase previously observed. For a low BP level (20 wt%) there is already a strong decrease in deformability (–54% of elongation-at-break) and a more brittle failure behavior compared to the unloaded PCL sample. Therefore, in accordance with previous studies [31,32], the co-presence of ductile polymer and hard ceramic fillers promotes the brittle nature of the bio-composite.

3.4. Process Upgrade

In light of the results obtained and discussed in the previous sections, this part anticipates a possible implementation of the production technology of thermoplastic–ceramic composites. Specifically, it illustrates a way to ensure the integration of PLA

into the system by overcoming the problems encountered in the solvent-casting method. The idea is based on the use of the electrospinning technique to obtain PLA microfibers loaded with CS to be deposited on the PCL-BP disk. This would allow one to minimize the CS–matrix interface issues and ensure greater mechanical strength of the composite due to the fiber-reinforcing effect. A PCL disk reinforced with electrospun PLA-CS microfibers can be reduced to pellets for subsequent extrusion, obtaining the PCL-PLA-BP-CS filament. In this case, the great advantage concerns the correct balance in the physical properties of the two biopolymers: PCL melts at about 90 °C while PLA melts at 150–160 °C. This would allow the polymeric fibers blended with CS to be kept unchanged during the extrusion, resulting in a reinforced filament with adequate fiber alignment and the proper incorporation of BP and CS fillers. A schematic illustration of the proposed production cycle is shown in Figure 12.

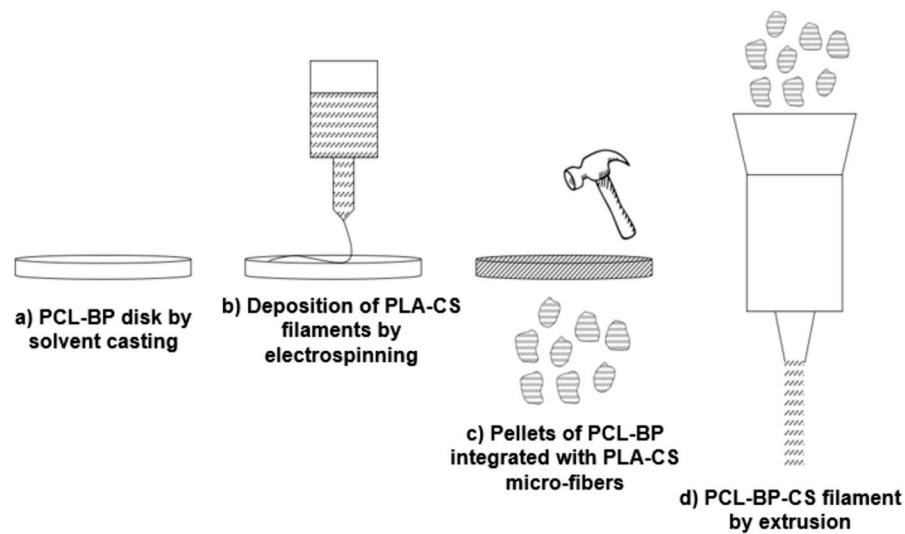


Figure 12. Implementation of the production technology of thermoplastic composites: Future upgrade.

Based on this possible implementation of the production technology, the biological investigations described below focused on the PLA-based formulations, evaluating the antibacterial efficiency of CS. Two PLA-BP-CS composites (Table 3), previously processed by solvent casting, were analyzed to evaluate the influence of different concentration of CS on the antibacterial performance.

Table 3. Compositions of PLA-based samples for biological tests.

ID Sample	PLA (wt%)	BP (wt%)	CS (wt%)
PLA65-BP30-CS5	65	30	5
PLA60-BP25-CS15	60	25	15

3.5. Antibacterial Activity of PLA-BP-CS

CS is largely known for its activity against a wide range of microorganisms. However, its antibacterial activity can be related to its structural characteristics. As reviewed by Chandrasekaran et al. [33], the antibacterial properties of low-molecular weight (MW) CS result in being higher or lower than those of high MW CS depending on the unit of measure with which concentrations are expressed. If concentrations are expressed in µg/mL, high MW CS usually results in being less potent than low molecular weight CS. Conversely, if the concentrations are expressed as µM, high MW CS results in being more potent than low molecular weight CS. Past studies evaluated the antibacterial activity of high MW CS (similar to that used in this research work) against Gram-negative and

Gram-positive bacteria. No et al. [34] demonstrated a stronger bactericidal effect for Gram-positive species than Gram-negative ones, evaluating a reduction of bacterial activities of 36% and 82% against *E. coli* and *S. aureus*, respectively. Mellegard et al. [35] observed that low MW CS (below 12 kDa) had no detectable inhibitory effect in terms of antibacterial activities towards both Gram-negative and Gram-positive cultures. On the other hand, high MW CS showed greater antibacterial activity. Specifically, the bactericidal effect, evaluated in terms of minimum bactericidal concentration (MBC), was higher against Gram-negative species (*E. coli*) than the Gram-negative strain (*B. cereus*), recording MBC values of 0.13 mg/mL and 0.95 mg/mL, respectively.

In this study, the bactericide effect of CS loaded in the matrix was determined by studying bacterial adhesion on the matrix and the bacterial growth in broth medium. As shown in Figure 13, regardless of the type of bacterial culture, the PLA60-BP25-CS15 sample promoted lower bacterial adhesion than PLA65-BP30-CS5. A higher CS concentration achieved its antimicrobial mechanism, based on the presence of charged groups in the polymer backbone and their ionic interactions with bacteria wall constituents. This interaction suggests the occurrence of hydrolysis of the peptidoglycans in the bacterial wall, provoking the leakage of intracellular electrolytes, leading the bacteria to death. The charges present in CS chains are generated by the protonation of amino groups when in an acid medium [36]. Globally, a lower bacterial adhesion rate was observed for *S. aureus* bacteria with respect to the *E. coli* strain. This finding agrees with previous studies [37,38], which revealed that CS is much more incisive on Gram-positive bacteria (i.e., *S. aureus*) than Gram negative ones (i.e., *E. coli*). Although it is widely accepted that CS inhibits bacterial growth through an electrostatic interaction between its protonated amino groups and negative residues on microbial cell membranes, it is controversial whether this activity can be increased by lowering or increasing the MW [39].

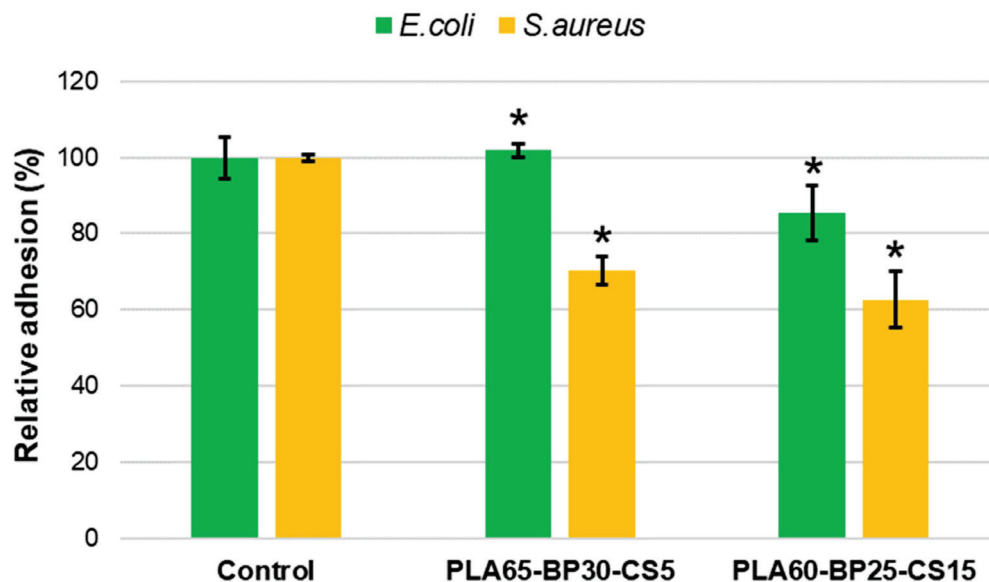


Figure 13. *S. aureus* and *E. coli* bacterial adhesion on PLA-CS-BP matrices. The inhibition of bacterial adhesion was significant with * $p < 0.05$ (*t*-Test).

Bacterial growth measurements (Figure 14) further proved the bactericide activity of CS, indicating a greater efficiency for a higher filler load (i.e., 15% vs. 4% of CS). Comparing the investigated bacterial cultures, the analysis on *E. coli* strain revealed a maximum reduction of bacterial growth of about 9%, while more relevant reduction was observed in the case of *S. aureus* bacteria (maximum reduction rate of about 16%).

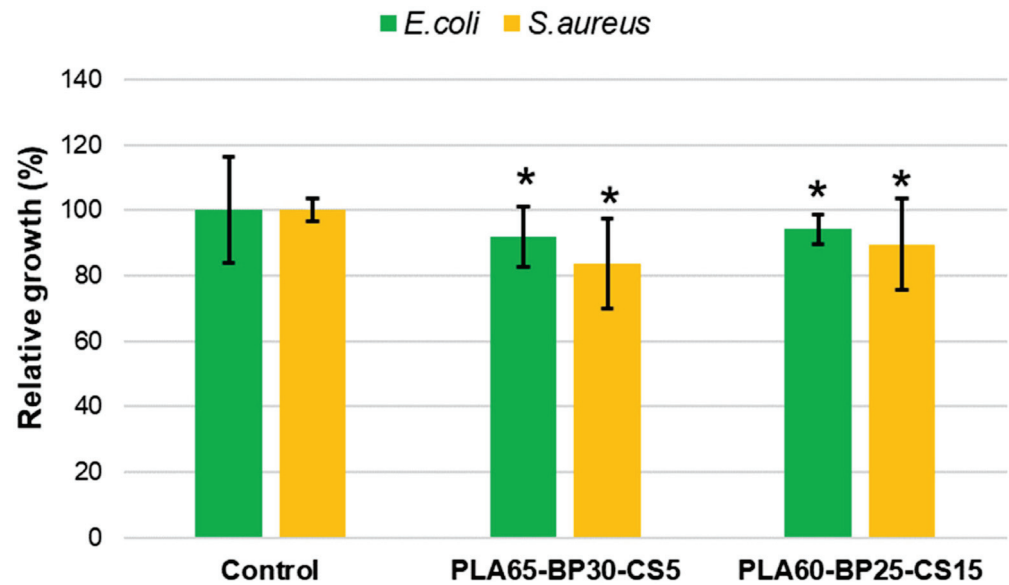


Figure 14. Relative growth of *S. aureus* and *E. coli* strains on CS loaded PLA-BP scaffolds after 24 h of culture. * $p < 0.05$ vs. control (*t*-Test).

The results obtained allow us to conclude that the CS load in the matrices prepared for bone regeneration maintain its antibacterial activity and the potency of this activity depends on its load ratio in the matrix. The presence of CS inhibits the adhesion of bacteria on the material and the release of CS from the matrix can control bacterial growth in the matrix environment. Better performance was found against the Gram-positive bacterial culture (*S. aureus*), which was recognized as a high-incidence factor for hospital infections [40].

4. Conclusions

This research work presented a preliminary investigation on the synthesis of thermoplastic composites loaded with waste BP and CS filler, to obtain bioactive materials for BTE applications. PCL-BP and PLA-BP composites (at different BP content) were processed in the form of solvent-casted films to evaluate the ability of thermoplastic matrices to incorporate the inorganic fillers and obtain homogeneous and workable composites. From a qualitative check of the films and SEM investigations, it was found that only PCL ensured an adequate incorporation of the BP and good particle dispersion. Conversely, in the case of PLA, weak structural integrity of the films and poor integration of the filler was detected. Even in relation to the lowest working temperatures compared to PLA, PCL was selected as the matrix for the bio-composite under study. Mechanical tests were performed on the PCL-BP-CS formulations to evaluate the effect of the two fillers on the mechanical performance of the material. Although several BP-PCL interfacial defects were observed, the formulations investigated show suitable mechanical strength properties for tissue engineering applications. However, a drastic decline in mechanical properties was found when the CS was incorporated into the composite, resulting in the chemical-physical incompatibility between PCL and CS. According to these findings, the authors hypothesized a proposal for the optimization of the production technology based on the integration of the electrospinning technique to fiber-reinforce the PCL-BP composites with PLA-CS micro-fibers, in order to minimize the integration problems of the PLA in the composite, promote the adhesion of CS, and obtain a potential mechanical strength improvement. Based on this upgrade, antibacterial tests were performed on the PLA-BP-CS composites, which highlighted the effective bactericidal efficiency of the CS and the potential applicability of the composite for biomedical applications.

Future research will be aimed at investigating the optimized process proposed by the authors, firstly evaluating the possibility of implementing electrospinning technology in the production of PCL-PLA-BP-CS composites. An experimental campaign focused on

the production of the fiber-reinforced composite filaments will be dedicated to this, which will be followed by the evaluation of the physical-mechanical properties suitable for the bone-integration application.

Author Contributions: Conceptualization, M.V.; data curation, L.J.d.V.; formal analysis, G.T.; funding acquisition, M.V.; investigation, L.J.d.V. and G.T.; methodology, M.S.; supervision, J.P.; validation, M.V., J.P. and M.S.; writing—original draft, G.T. and M.S.; writing—review and editing, M.V., L.J.d.V. and M.S. All authors have read and agreed to the published version of the manuscript.

Funding: This research received no external funding but has been financed by personal research.

Data Availability Statement: Not applicable.

Conflicts of Interest: The authors declare no conflict of interest.

References

1. Di Bello, C. *Biomateriali Introduzione allo Studio dei Materiali per uso Biomedico*, 1st ed.; Patron: Bologna, Italy, 2004.
2. Haleem, A.; Javaid, M.; Khan, R.H.; Suman, R. 3D printing applications in bone tissue engineering. *J. Clin. Orthop. Trauma* **2020**, *11*, S118–S124. [CrossRef]
3. Rahmati, M.; Mills, D.K.; Urbanska, A.M.; Saeb, M.; Venugopal, J.R.; Ramakrishna, S.; Mozafari, M. Electrospinning for tissue engineering applications. *Prog. Mater. Sci.* **2020**, 100721. [CrossRef]
4. Cheng, R.; Liu, L.; Xiang, Y.; Lu, Y.; Deng, L.; Zhang, H.; Santos, H.A.; Cui, W. Advanced liposome-loaded scaffolds for therapeutic and tissue engineering applications. *Biomaterials* **2020**, *232*, 119706. [CrossRef]
5. Zhao, P.; Gu, H.; Mi, H.; Rao, C.; Fu, J.; Turng, L.S. Fabrication of scaffolds in tissue engineering: A review. *Front. Mech. Eng.* **2018**, *13*, 107–119. [CrossRef]
6. Eltom, A.; Zhong, G.; Muhammad, A. Scaffold techniques and designs in tissue engineering functions and purposes: A review. *Adv. Mater. Sci. Eng.* **2019**, 2019. [CrossRef]
7. Liu, Y.; Wu, G.; de Groot, K. Biomimetic coatings for bone tissue engineering of critical-sized defects. *J. R. Soc. Interface* **2010**, *7*, S631–S647. [CrossRef]
8. Pérez-González, F.; Molinero-Mourelle, P.; Sánchez-Labrador, L.; Sáez-Alcaide, L.M.; Limones, A.; Brinkmann, J.C.B.; López-Quiles, J. Assessment of clinical outcomes and histomorphometric findings in alveolar ridge augmentation procedures with allogeneic bone block grafts: A systematic review and meta-analysis. *Med. Oral. Patol. Oral. Cir. Bucal.* **2020**, *25*, e291. [CrossRef] [PubMed]
9. Roshandel, M.; Dorkoosh, F. Cardiac tissue engineering, biomaterial scaffolds, and their fabrication techniques. *Polym. Adv. Technol.* **2021**, *32*, 2290–2305. [CrossRef]
10. Collins, M.N.; Ren, G.; Young, K.; Pina, S.; Reis, R.L.; Oliveira, J.M. Scaffold fabrication technologies and structure/function properties in bone tissue engineering. *Adv. Funct. Mater.* **2021**, *31*, 2010609. [CrossRef]
11. Bharadwaz, A.; Jayasuriya, A.C. Recent trends in the application of widely used natural and synthetic polymer nanocomposites in bone tissue regeneration. *Mater. Sci. Eng. C* **2020**, *110*, 110698. [CrossRef]
12. Vogel, C.; Siesler, H.W. Thermal Degradation of Poly(ϵ -caprolactone), Poly(L-lactic acid) and their Blends with Poly(3-hydroxybutyrate) Studied by TGA/FT-IR Spectroscopy. *Macromol. Symp.* **2008**, *265*, 183–194. [CrossRef]
13. Pang, X.; Zhuang, X.; Tang, Z.; Chen, X. Polylactic acid (PLA): Research, development and industrialization. *Biotechnol. J.* **2010**, *5*, 1125–1136. [CrossRef]
14. Nazeer, M.A.; Onder, O.C.; Sevgili, I.; Yilgor, E.; Kavakli, I.H.; Yilgor, I. 3D printed poly (lactic acid) scaffolds modified with chitosan and hydroxyapatite for bone repair applications. *Mater. Today Commun.* **2020**, *25*, 101515. [CrossRef]
15. Zimina, A.; Senatov, F.; Choudhary, R.; Kolesnikov, E.; Anisimova, N.; Kiselevskiy, M.; Orlova, P.; Strukova, N.; Generalova, M.; Manskikh, V.; et al. Biocompatibility and Physico-Chemical Properties of Highly Porous PLA/HA Scaffolds for Bone Reconstruction. *Polymers* **2020**, *12*, 2938. [CrossRef]
16. Lopresti, F.; Pavia, F.C.; Vitrano, I.; Kersaudy-Kerhoas, M.; Brucato, V.; la Carrubba, V. Effect of hydroxyapatite concentration and size on morpho-mechanical properties of PLA-based randomly oriented and aligned electrospun nanofibrous mats. *J. Mech. Behav. Biomed. Mater.* **2020**, *101*, 103449. [CrossRef]
17. Trakoolwannachai, V.; Kheolamai, P.; Ummartyotin, S. Characterization of hydroxyapatite from eggshell waste and polycaprolactone (PCL) composite for scaffold material. *Compos. Part B Eng.* **2019**, *173*, 106974. [CrossRef]
18. Cestari, F.; Petretta, M.; Yang, Y.; Motta, A.; Grigolo, B.; Sglavo, V.M. 3D printing of PCL/nano-hydroxyapatite scaffolds derived from biogenic sources for bone tissue engineering. *Sustain. Mater. Technol.* **2021**, e00318. [CrossRef]
19. Miszuk, J.M.; Xu, T.; Yao, Q.; Fang, F.; Childs, J.D.; Hong, Z.; Tao, J.; Fong, H.; Sun, H. Functionalization of PCL-3D electrospun nanofibrous scaffolds for improved BMP2-induced bone formation. *Appl. Mater. Today* **2018**, *10*, 194–202. [CrossRef]
20. Oliveira, H.L.; da Rosa, W.L.; Cuevas-Suárez, C.E.; Carreno, N.L.; da Silva, A.F.; Guim, T.N.; Odir, A.D.; Piva, E. Histological evaluation of bone repair with hydroxyapatite: A systematic review. *Calcif. Tissue Int.* **2017**, *101*, 341–354. [CrossRef]

21. Sathiyavimal, S.; Vasantharaj, S.; LewisOscar, F.; Selvaraj, R.; Brindhadevi, K.; Pugazhendhi, A. Natural organic and inorganic-hydroxyapatite biopolymer composite for biomedical applications. *Prog. Org. Coat.* **2020**, *147*, 105858. [CrossRef]
22. Tecu, C.; Antoniac, A.; Goller, G.; Gok, M.G.; Manole, M.; Mohan, A.; Moldovan, H.; Earar, K. The sintering behaviour and mechanical properties of hydroxyapatite—Based composites for bone tissue regeneration. *Rev. Chim.* **2018**, *69*, 1272–1275. [CrossRef]
23. Zheng, T.; Guo, L.; Du, Z.; Leng, H.; Cai, Q.; Yang, X. Bioceramic fibrous scaffolds built with calcium silicate/hydroxyapatite nanofibers showing advantages for bone regeneration. *Ceram. Int.* **2021**, *47*, 18920–18930. [CrossRef]
24. Osteobiol by Tecoss. Available online: <https://www.osteobiol.com/> (accessed on 28 June 2021).
25. Li, C.; Qin, W.; Lakshmanan, S.; Ma, X.; Sun, X.; Xu, B. Hydroxyapatite based biocomposite scaffold: A highly biocompatible material for bone regeneration. *Saudi J. Biol. Sci.* **2020**, *27*, 2143–2148. [CrossRef] [PubMed]
26. Zhou, H.; Lawrence, J.G.; Bhaduri, S.B. Fabrication aspects of PLA-CaP/PLGA-CaP composites for orthopedic applications: A review. *Acta Biomater.* **2012**, *8*, 1999–2016. [CrossRef]
27. Suyatma, N.E.; Copinet, A.; Tighzert, L.; Coma, V. Mechanical and barrier properties of biodegradable films made from chitosan and poly (lactic acid) blends. *J. Polym. Environ.* **2004**, *12*, 1–6. [CrossRef]
28. Zakaria, Z.; Islam, M.; Hassan, A.; Mohamad Haafiz, M.K.; Arjmandi, R.; Inuwa, I.M.; Hasan, M. Mechanical properties and morphological characterization of PLA/chitosan/epoxidized natural rubber composites. *Adv. Mater. Sci. Eng.* **2013**, *2013*. [CrossRef]
29. Malikmammadov, E.; Tanir, T.E.; Kiziltay, A.; Hasirci, V.; Hasirci, N. PCL and PCL-based materials in biomedical applications. *J. Biomater. Sci. Polym. Ed.* **2018**, *29*, 863–893. [CrossRef]
30. Fadaie, M.; Mirzaei, E.; Geramizadeh, B.; Asvar, Z. Incorporation of nanofibrillated chitosan into electrospun PCL nanofibers makes scaffolds with enhanced mechanical and biological properties. *Carbohydr. Polym.* **2018**, *199*, 628–640. [CrossRef]
31. Fu, S.Z.; Wang, X.H.; Guo, G.; Shi, S.; Fan, M.; Liang, H.; Luo, F.; Qian, Z.Y. Preparation and properties of nano-hydroxyapatite/PCL-PEG-PCL composite membranes for tissue engineering applications. *J. Biomed. Mater. Res. Part B Appl. Biomater.* **2011**, *97*, 74–83. [CrossRef]
32. Xiao, X.; Liu, R.; Huang, Q.; Ding, X. Preparation and characterization of hydroxyapatite/polycaprolactone-chitosan composites. *J. Mater. Sci. Mater. Med.* **2009**, *20*, 2375. [CrossRef]
33. Chandrasekaran, M.; Kim, K.D.; Chun, S.C. Antibacterial Activity of Chitosan Nanoparticles: A Review. *Processes* **2020**, *8*, 1173. [CrossRef]
34. No, H.K.; Park, N.Y.; Lee, S.H.; Meyers, S.P. Antibacterial activity of chitosans and chitosan oligomers with different molecular weights. *Int. J. Food Microbiol.* **2002**, *74*, 65–72. [CrossRef]
35. Mellegård, H.; Strand, S.P.; Christensen, B.E.; Granum, P.E.; Hardy, S.P. Antibacterial activity of chemically defined chitosans: Influence of molecular weight, degree of acetylation and test organism. *Int. J. Food Microbiol.* **2011**, *148*, 48–54. [CrossRef]
36. Goy, R.C.; Morais, S.T.; Assis, O.B. Evaluation of the antimicrobial activity of chitosan and its quaternized derivative on *E. coli* and *S. aureus* growth. *Revista Bras. Farmacogn.* **2016**, *26*, 122–127. [CrossRef]
37. Sarasam, A.R.; Krishnaswamy, R.K.; Madihally, S.V. Blending chitosan with polycaprolactone: Effects on physicochemical and antibacterial properties. *Biomacromolecules* **2006**, *7*, 1131–1138. [CrossRef]
38. Li, K.; Guan, G.; Zhu, J.; Wu, H.; Sun, Q. Antibacterial activity and mechanism of a laccase-catalyzed chitosan-gallic acid derivative against *Escherichia coli* and *Staphylococcus aureus*. *Food Control* **2019**, *96*, 234–243. [CrossRef]
39. Tanpichai, S.; Witayakran, S.; Wootthikanokkhan, J.; Srimarut, Y.; Woraprayote, W.; Malila, Y. Mechanical and antibacterial properties of the chitosan coated cellulose paper for packaging applications: Effects of molecular weight types and concentrations of chitosan. *Int. J. Biol. Macromol.* **2020**, *155*, 1510–1519. [CrossRef]
40. Zivanovic, S.; Li, J.; Davidson, P.M.; Kit, K. Physical, mechanical, and antibacterial properties of chitosan/PEO blend films. *Biomacromolecules* **2007**, *8*, 1505–1510. [CrossRef]

Article

Fluoropolymer/Glycidyl Azide Polymer (GAP) Block Copolyurethane as New Energetic Binders: Synthesis, Mechanical Properties, and Thermal Performance

Minghui Xu ^{1,2,*}, Xianming Lu ², Ning Liu ² , Qian Zhang ², Hongchang Mo ² and Zhongxue Ge ²

¹ State Key Laboratory of Fluorine & Nitrogen Chemicals, Xi'an Modern Chemistry Research Institute, Xi'an 710065, China

² Department of Energetic Materials Science and Technology, Xi'an Modern Chemistry Research Institute, Xi'an 710065, China; luxianming@126.com (X.L.); flackliu@163.com (N.L.); qian3545267@163.com (Q.Z.); hongchangmo@163.com (H.M.); gzx204@163.com.cn (Z.G.)

* Correspondence: hzyxb@204s.com

Citation: Xu, M.; Lu, X.; Liu, N.; Zhang, Q.; Mo, H.; Ge, Z. Fluoropolymer/Glycidyl Azide Polymer (GAP) Block Copolyurethane as New Energetic Binders: Synthesis, Mechanical Properties, and Thermal Performance. *Polymers* **2021**, *13*, 2706. <https://doi.org/10.3390/polym13162706>

Academic Editors: Somen K. Bhudolia and Sunil Chandrakant Joshi

Received: 7 July 2021

Accepted: 10 August 2021

Published: 13 August 2021

Publisher's Note: MDPI stays neutral with regard to jurisdictional claims in published maps and institutional affiliations.



Copyright: © 2021 by the authors. Licensee MDPI, Basel, Switzerland. This article is an open access article distributed under the terms and conditions of the Creative Commons Attribution (CC BY) license (<https://creativecommons.org/licenses/by/4.0/>).

Abstract: In order to enhance the application performance of glycidyl azide polymer (GAP) in solid propellant, an energetic copolyurethane binder, (poly[3,3-bis(2,2,2-trifluoro-ethoxymethyl)oxetane] glycol-*block*-glycidylazide polymer (PBFMO-*b*-GAP) was synthesized using poly[3,3-bis(2,2,2-trifluoro-ethoxymethyl)oxetane] glycol (PBFMO), which was prepared from cationic polymerization with GAP as the raw material and toluene diisocyanate (TDI) as the coupling agent via a prepolymer process. The molecular structure of copolyurethanes was confirmed by attenuated total reflectance-Fourier transform-infrared spectroscopy (ATR-FTIR), nuclear magnetic resonance spectrometry (NMR), and gel permeation chromatography (GPC). The impact sensitivity, mechanical performance, and thermal behavior of PBFMO-*b*-GAP were studied by drop weight test, X-ray photoelectron spectroscopic (XPS), tensile test, scanning electron microscopy (SEM), differential scanning calorimetry (DSC), and thermal gravimetric analysis (TGA), respectively. The results demonstrated that the introduction of fluoropolymers could evidently reduce the sensitivity of GAP-based polyurethane and enhance its mechanical behavior (the tensile strength up to 5.75 MPa with a breaking elongation of 1660%). Besides, PBFMO-*b*-GAP exhibited excellent resistance to thermal decomposition up to 200 °C and good compatibility with Al and cyclotetramethylene tetranitramine (HMX). The thermal performance of the PBFMO-*b*-GAP/Al complex was investigated by a cook-off test, and the results indicated that the complex has specific reaction energy. Therefore, PBFMO-*b*-GAP may serve as a promising energetic binder for future propellant formulations.

Keywords: energetic binder; block copolyurethane; sensitivity; mechanical property; thermal behavior

1. Introduction

A recent trend in the field of energetic material formulations (explosives/propellants) is to replace inert binders (*viz.*, hydroxy terminated poly butadiene (HTPB), carboxyl terminated polybutadiene (CTPB), and hydroxyl terminated polyether (HTPE), etc.) by energetic binders, which contain energetic groups such as $-N_3$ (azide), nitro (C-nitro, O-nitro (nitrate ester), N-nitro (nitramine) and difluoroamine groups, to impart additional energy to the systems [1–3]. Among energetic polymers, glycidyl azide polymer (GAP) has been extensively studied as a polymeric binder since it was first reported in a patent in 1972 by Vandenburg [4–6]. This is due to its high density (1.3 g cm^{-3}) with positive heat of formation of $+117.2 \text{ kcal mol}^{-1}$, low glass-transition temperature ($T_g = -45 \text{ °C}$), good thermally stability, low detonation tendency, and high burning rate (1 cm s^{-1} at 40 atmospheres) [7,8]. Thus, it offers a unique energetic binder and plasticizer system for advanced propellants and plastic bonded explosives (PBX) to achieve a higher performance,

and has become a hotspot in the field of energy materials [9]. However, traditional GAP-based binders are thermoset polymer and usually difficult to recycle. In addition, it also suffers from highly sensitive and inferior mechanical behavior (generally, the largest tensile strength σ_m was less than 2 MPa; the elongation at break ε_m was less than 200%), which is due to its high polarity of azide groups and poor flexibility of the polymer backbone [10–12].

In order to overcome these difficulties and obtain a better performance, various energetic polymers have been developed in the last two decades. Energetic thermoplastic elastomers (ETPE) as high performance recyclable polymeric binders with superior mechanical properties (σ_m : 2–5 MPa, ε_m : 200–700%), have received widespread attention in the past decades [13]. In ETPE, the crystalline hard segments forming physical cross-linking points provide mechanical strength, while the energetic soft segments provide flexibility and energy. When it heated above the melting temperature of the hard segments, the physical crosslinks between the polymer chains disappear, allowing the ETPEs to flow like a thermoplastic and fully recyclable [14,15]. Development of novel ETPE has attracted the extensive attention of many researchers in recent years [16,17].

In the past three decades, fluoropolymers have gained considerable attention in the energetic material community (such as aerial infrared decoys, igniters, tracking flares, reactive binder systems, and solid fuel rocket propellants) as high explosive binders, owing to their high densities, low coefficients of friction, long-term chemical stabilities, and good compatibility with the main ingredients (oxidizers, metal fuels, and plasticizer) [18–20]. Particularly, fluoropolymer possesses strong oxidation [21–23], for instance, the magnesium, Teflon, and Viton system (MTV) as one of the well-known compositions used in decoys and flares. The metal/fluoropolymer compositions have a special exothermic reaction heat of 9.4 kJ g^{-1} , which is higher than the control compositions based on 2,4,6-trinitrotoluene (TNT) (3.72 kJ g^{-1}) and cyclotrimethylenetrinitramine (RDX) (6.569 kJ g^{-1}) [24].

In this study, fluoropolymer/GAP block copolyurethane binders were synthesized via a prepolymer process by coupling together poly[3,3-bis(2,2,2-trifluoroethoxymethyl)oxetane] glycol (PBFMO) and GAP to decrease the sensitivity, enhance the mechanical properties, and promote the reactive efficiency with Al. The chemical structure and molecular weight of copolyurethanes were characterized by attenuated total reflectance-Fourier transform-infrared spectroscopy (ATR-FTIR), nuclear magnetic resonance spectrometry (NMR), and gel permeation chromatography (GPC). The impact sensitivity and mechanical properties of the copolyurethanes were tested by drop weight test, X-ray photoelectron spectroscopic (XPS), tensile test, and scanning electron microscopy (SEM), respectively. The thermal properties of copolyurethanes and their compatibility with Al and cyclotetramethylene tetranitramine (HMX) were also described by differential scanning calorimetry (DSC), thermal gravimetric analysis (TGA), and differential thermal analysis (DTA). The thermal performance of the PBFMO-*b*-GAP/Al complex was investigated by the cook-off test.

2. Experimental

2.1. Materials

GAP with molecular weight of 3500 g mol^{-1} and hydroxy value of 0.9% was provided from the Liming Chemical Engineering Research and Design Institute (Luoyang, China). Butane diol (BDO), BF_3 -etherate and dibutyltindilaurate (DBTDL) were purchased from J&K scientific Ltd. (Shanghai, China). Toluene diisocyanate (TDI), *N,N*-dimethylformamide (DMF), dichloromethane (DCM), and ethanol were supplied by Sinopharm Chemical Reagent Co., Ltd. (Xi'an, China). 1,2-dichloroethane was obtained from Jinshan Chemical Test Co., Ltd. (Chengdu, China). BDO and BF_3 -dimethyl ether were distilled under reduced pressure prior to use. All other solvents for the reactions were of analytical grade and distilled before use.

2.2. Polymerization of PBFMO

The PBFMO was synthesized via cationic ring-opening homopolymerization of [3,3-bis(2,2,2-trifluoroethoxymethyl) oxetane] glycol (BFMO), which was synthesized according to the literature procedure [25]. In brief, under a nitrogen atmosphere, BDO and BF₃-etherate were dissolved in dried methylene chloride in a round bottom Schlenk flask and stirred for 1 h. BFMO was added into the mixture drop by drop over a period of 8 h, and the reaction mixture was then left under stirring for an additional 24 h. After the polymerization, sodium bicarbonate solution was added to terminate the reaction, and the organic phase was collected, washed by distilled water and dried over anhydrous Na₂SO₄ overnight. Finally, the solution was dried under 45 °C vacuum to yield a viscous wax PBFMO.

2.3. Synthesis of PBFMO-*b*-GAP Copolyurethanes

PBFMO-*b*-GAP copolyurethanes were synthesized through linking of GAP and PBFMO by TDI via a prepolymer process. In a typical synthesis example, GAP, PBFMO, and freshly distilled 1,2-dichloroethane were placed in a 250 mL four-neck flask equipped with a condenser, mechanical stirrer and thermometer under a nitrogen atmosphere, and then heated to 60 °C. TDI and DBTDL were then dissolved in 1,2-dichloroethane and added dropwise into the reaction solution. After stirring for an additional 2 h, the reaction mixture was poured into 400 mL ethanol. The polymer was precipitated and separated out and dried in vacuum at 50 °C for 24 h to obtain PBFMO-*b*-GAP copolyurethanes (yield, 97%).

2.4. Characterization

ART-FTIR spectra were recorded in a Bruker Tensor 27 spectrometer. ¹H-NMR, ¹³C-NMR, and ¹⁹F-NMR were conducted on a 500 MHz Bruker spectrometer using deuterated chloroform as the solvent and tetramethylsilane as the internal standard. GPC was conducted on a Waters GPC, using tetrahydrofuran and polystyrene standards as the mobile phase and for calibration, respectively. The impact sensitivity was tested according to the national military standard GJB772-1997 method (the weight of dropping hammer 5 kg, and the drop height was between 0–1.29 m), and the characteristic drop height H_{50} (the drop hammer height of a statistical 50% probability of explosion) was taken to evaluate the impact sensitivity of samples. XPS analysis was performed using a SigmaProbe instrument (ThermoElectron Corp., Pennsylvania, UK) equipped with a nonmonochromatic Al KR (hν = 1486.6 eV) source at a power of 300 W. Mechanical test samples were prepared according to ASTM standard D-412 [26]. Mechanical properties of all the elastomers gels were measured on a Shimadzu AG-100kN X Plus universal testing machine (Shimadzu, Kyoto, Japan) in accordance with GB/T528–1998 with a tensile rate of 500 mm min⁻¹ at 293 K. The dimensions of testing gels were 20 mm (neck length) × 4 mm (width) × 2 mm (thickness). Tensile tests were conducted five times independently, and results were presented as the mean in values ± standard deviation of quintuplicate measurements for the experiment. Morphology of the gels was investigated through SEM on a Tescan Vega 3 LMU scanning electron microscope (Tescan, Brno, Czech Republic). All the elastomers gels were frozen in liquid nitrogen, snapped, and sputtered with gold until the experiment. DSC equipped with a TA instruments DSC Q1000 and TGA measurements of samples were performed in a nitrogen atmosphere using a SDT Q600 TGA instrument in the temperature range from 25 to 500 °C with heating rate of 10 K min⁻¹.

The special equipment for the slow cook-off test used in the research was designed by the Institute of Chemical Materials; its schematic diagram is shown in Figure 1. The equipment had a power of 1500 W, the heating rate of the heating cartridge wall was set at 1 °C min⁻¹, and temperature ranged from room temperature to 250 °C. In the slow cook-off test, we put PBFMO-*b*-GAP/Al complex samples in the test set-up, heated by an electric heating cord; meanwhile, the equal heating components of PBFMO-*b*-GAP were heated with an intelligent temperature controller to adjust the heating rate. Samples were well sealed, and the thermocouples were utilized to obtain their temperature vs time

curves. These experimental results were synthetically analyzed to investigate the thermal performance of the PBFMO-*b*-GAP/Al complex under slow heating stimulation.

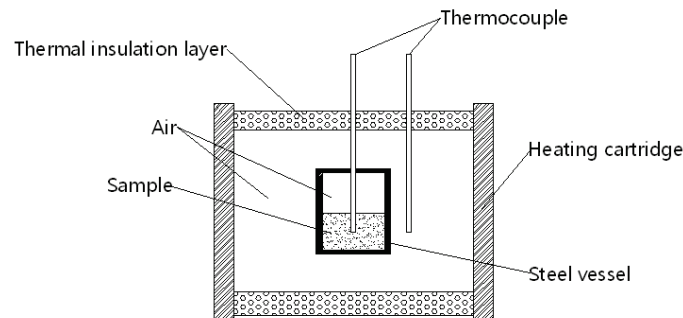


Figure 1. Schematic geometry of the cook-off test.

3. Result and Discussion

3.1. Preparation of PBFMO-*b*-GAP Copolyurethanes

The synthesis of PBFMO-*b*-GAP copolyurethanes was done via a prepolymer process, as illustrated in Figure 2. ART-FTIR and NMR were adopted to confirm the molecular structure of PBFMO-*b*-GAP. The peaks that appeared at 1135 and 1276 cm^{-1} in Figure 3 were due to the C–O–C and –CF₃ stretching vibration of PBFMO, respectively [27,28]. The new stretching band at 2093 cm^{-1} was ascribed to the –N₃ from GAP. The appearance of 3320 cm^{-1} was due to the –NH stretching vibration, the appearance of 1726 cm^{-1} , 1531 cm^{-1} and 1376 cm^{-1} were assigned to C=O and –NH stretching bands of the urethane group [29,30]. These results confirmed the successful synthesis of the PBFMO-*b*-GAP polyurethane.

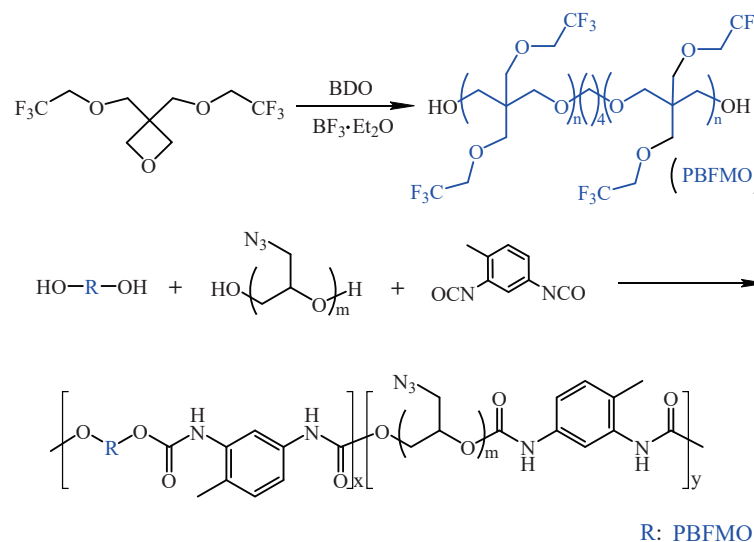


Figure 2. The synthesis route of PBFMO-*b*-GAP copolyurethanes.

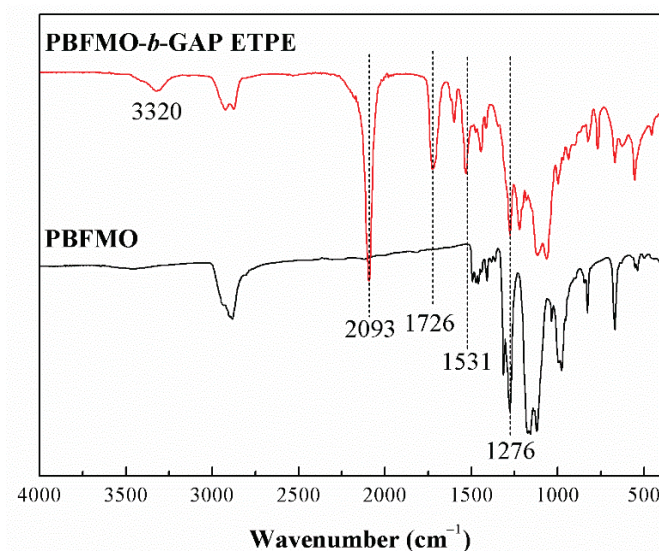


Figure 3. ART-FTIR spectra of PBFMO and PBFMO-*b*-GAP copolyurethanes.

As shown in Figure 4a, proton signals due to methylene protons of GAP and PBFMO in the 3.62 ppm region as a broad band are clearly seen; methylene protons of the PBFMO side chain appeared in the 3.33 ppm region. The corresponding ^{13}C -NMR (Figure 4b) also indicated the presence of all the carbons in GAP and PBFMO. The chemical shifts at 69.5 and 78.8 ppm are attributed to the carbons signals of methylene from GAP and PBFMO. A characteristic signal at 51.9 ppm due to the quaternary carbon atom of C-N₃ was also observed [31]. The signals at 1.77 ppm and 2.17 ppm were assigned to the methyl protons of TDI and methylene protons of BDO, respectively, and the corresponding carbon signals appearing at 17.1 ppm and 25.7 ppm were also observed. Moreover, as shown in Figure 4c of ^{19}F -NMR, the peak at -74.4 ppm was attributed to the -CF₃ of the side chain [32]. These signal positions observed in the NMR spectra of PBFMO-*b*-GAP strictly corroborated the ART-FTIR results.

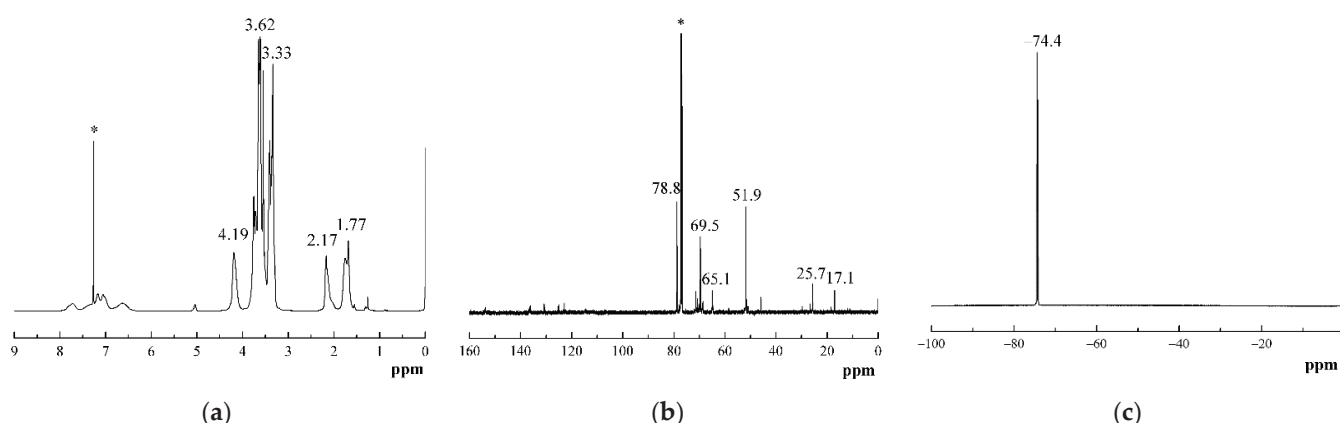


Figure 4. ^1H -NMR spectrum (a), ^{13}C -NMR spectrum (b), and ^{19}F -NMR spectrum (c) of PBFMO-*b*-GAP in CDCl_3 .

3.2. Density, Sensitivity, and XPS of PBFMO-*b*-GAP Copolyurethanes

To investigate the different PBFMO-*b*-GAP copolyurethanes, the molar ratio of PBFMO/GAP was set at 1/3, 1/9, and 1/19, during chain coupling by TDI to obtain PBFMO-*b*-GAP-1[#], 2[#] and 3[#], respectively. As shown in Table 1, the number average molecular weight (M_n) of PBFMO-*b*-GAP was around $3.0\sim 3.3\times 10^4\text{ g mol}^{-1}$, and its density was around $1.273\sim 1.308\text{ g cm}^{-3}$, which was higher than that of the control group (GAP-based polyurethane, GAP-ETPE, 1.263 g cm^{-3}). It is due to the polymers with -CF₃ that the group side chain has a higher density [33].

Table 1. Relative molecular mass, density, and H_{50} of PBFMO-*b*-GAP copolyurethanes in different molar ratios.

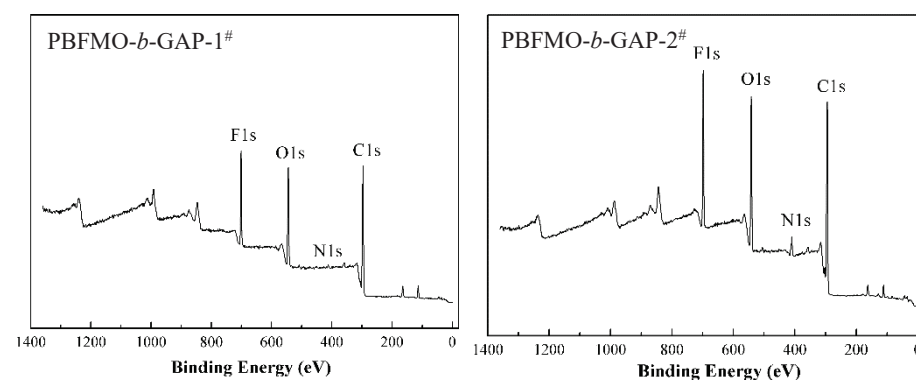
Sample	PBFMO/GAP Molar Ratio	Theoretical Content of F Element	M_n (10^3 gmol $^{-1}$)	Density (g cm $^{-3}$)	H_{50} (cm)
PBFMO- <i>b</i> -GAP-1 [#]	1/3	10.1	33	1.308	>129
PBFMO- <i>b</i> -GAP-2 [#]	1/9	4.04	31	1.290	>129
PBFMO- <i>b</i> -GAP-3 [#]	1/19	2.02	30	1.273	56.2
GAP-ETPE	0	0	32	1.263	9.55

Sensitivity of the energetic polymer is an important parameter because it is significantly connected with the safety operation and applications in the propellant [34]. In this study, the characteristic drop height H_{50} towards impact sensitivity was characterized by the drop weight test using standard procedures (listed in Table 1). It could be seen that the sensitivity of energetic materials was reduced as the mass ratio of polymer in the gel increased. Particularly noteworthy is the fact that the PBFMO/GAP molar ratio at 1/19 was markedly less sensitive than the pure GAP-based polyurethane. Therefore, it appeared that the introduction of fluoropolymer is manipulated to reduce the sensitivity of very high energy composite energetic materials made in this fashion, and it is easy to handle processability as propellant formulations.

XPS was employed to detect the change in elementary composition on the elastomers surface, and provide valuable insight into the influence between sensitivity and fluorine content [35]. The N1s, C1s, O1s, and F1s elements of the XPS spectra of the elastomers surface and its surface compositions, expressed quantitatively as atomic weight percentages, were summarized in Figure 5 and Table 2, respectively. Due to the introduction of different content of PBFMO, the concentrations of F from the elastomers surface were 5.34%, 12.91%, and 13.05%; meanwhile, the theoretical contents of F elements were 2.02%, 4.04%, and 10.01%, respectively, and the atomic weight percentage of N obviously decreased from 12.16% to 1.54%. The values of F elements at the surface were much higher than its theoretical value, which was due to F atoms segregating on the surface and generating low wettability and coefficients of friction, as was also predicted in other literature [36,37]. The results indicate that the increase in F elements on the surface and the reduction of N elements create a satisfactory sensitivity of PBFMO-*b*-GAP.

Table 2. Atomic weight percentages of XPS curves.

Sample	C (%)	O (%)	N (%)	F (%)
PBFMO- <i>b</i> -GAP-1 [#]	65.22	20.18	1.54	13.05
PBFMO- <i>b</i> -GAP-2 [#]	63.00	19.76	4.33	12.91
PBFMO- <i>b</i> -GAP-3 [#]	60.88	23.42	10.36	5.34
GAP-ETPE	63.8	24.04	12.16	0

**Figure 5.** Cont.

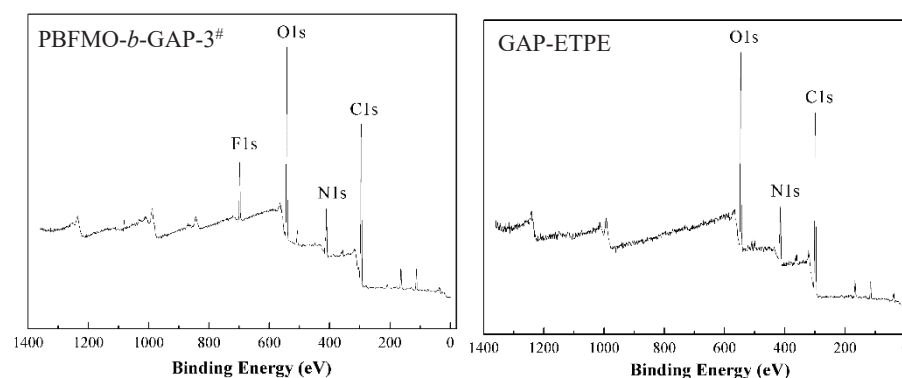


Figure 5. XPS curves of the gels prepared from GAP-based polyurethanes.

3.3. Mechanical Properties of PBFMO-*b*-GAP Copolyurethanes

Mechanical properties of the PBFMO-*b*-GAP copolyurethanes prepared from various ratio of PBFMO/GAP prepolymers were evaluated with a universal testing machine according to GB/T528-1998 (shown in Figure 6 and Table 3). It is clear that the tensile strength of PBFMO-*b*-GAP increased from 2.9 ± 0.11 to 5.75 ± 0.275 MPa, along with an increase in PBFMO content; meanwhile, the elongation at break decreased from $2056 \pm 47.3\%$ to $1660 \pm 42.3\%$. The mechanical properties of PBFMO-*b*-GAP copolyurethanes were better than the reported literature, as shown in Table S1 [38,39]. In this work, PBFMO works as a hard segment in PBFMO-*b*-GAP copolyurethanes, and aggregates with each other to form physical cross-linking points. The rise in crosslinking density causes better tensile strength and lower breaking elongation. The results reveal that the PBFMO could be competent for hard segments in GAP-based polyurethanes to improve their mechanical properties.

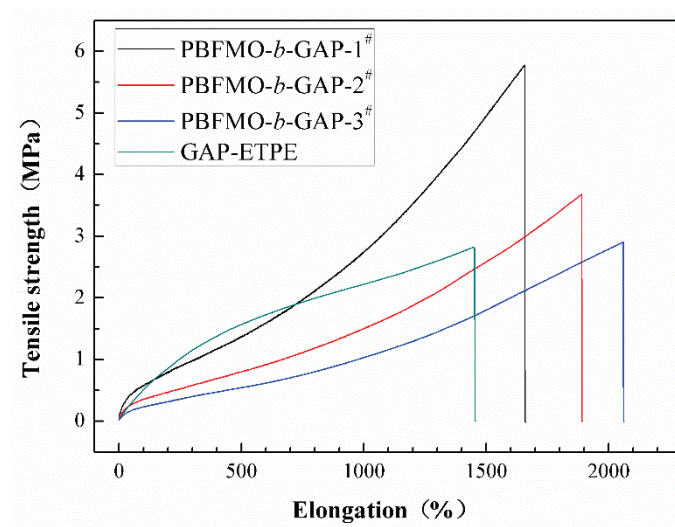


Figure 6. Mechanical properties of PBFMO-*b*-GAP copolyurethanes. (Tensile tests were conducted five times independently for each example, and the curve close to the average value was presented.)

Table 3. Mean values of PBFMO-*b*-GAP copolyurethanes in the tensile test.

Scheme	Tensile Strength (MPa)	Elongation at Break (%)
PBFMO- <i>b</i> -GAP-1 [#]	5.75 ± 0.275	1660 ± 42.3
PBFMO- <i>b</i> -GAP-2 [#]	3.65 ± 0.13	1874 ± 58
PBFMO- <i>b</i> -GAP-3 [#]	2.9 ± 0.11	2056 ± 47.3
GAP-ETPE	2.81 ± 0.124	1446 ± 52

The dispersion of hard segments and soft segments in PBFMO-*b*-GAP copolyurethanes is expected to affect their mechanical properties; SEM micrographs of freeze-fractured surfaces of the PBFMO-*b*-GAP copolyurethanes were displayed in Figure 7. The wrinkles (marked as blue square frame), representative of aggregated hard segments; and ravines (marked as red circle frame), representative of non-homogeneous soft segments, were observed in Figure 7. Generally, in ETPE, hard segments aggregate with each other to form physical cross-linking densities, and phase separation exists between the soft and hard segments. In this study, the dispersion of phase separation of hard and soft segments was obviously improved with an increase in PBFMO; meanwhile, the crosslinking density was enhanced, which was in correspondence with prior mechanical properties; the same phenomenon was found in other researches [40,41]. These results reveal that the introduction of PBFMO uniformly improved the phase separation of gels prepared from PBFMO-*b*-GAP, and resulted in good mechanical properties [42]. Considering PBFMO-*b*-GAP-1[#] possessing the best tensile strength and sufficient elongation, it was selected in the next experiment.

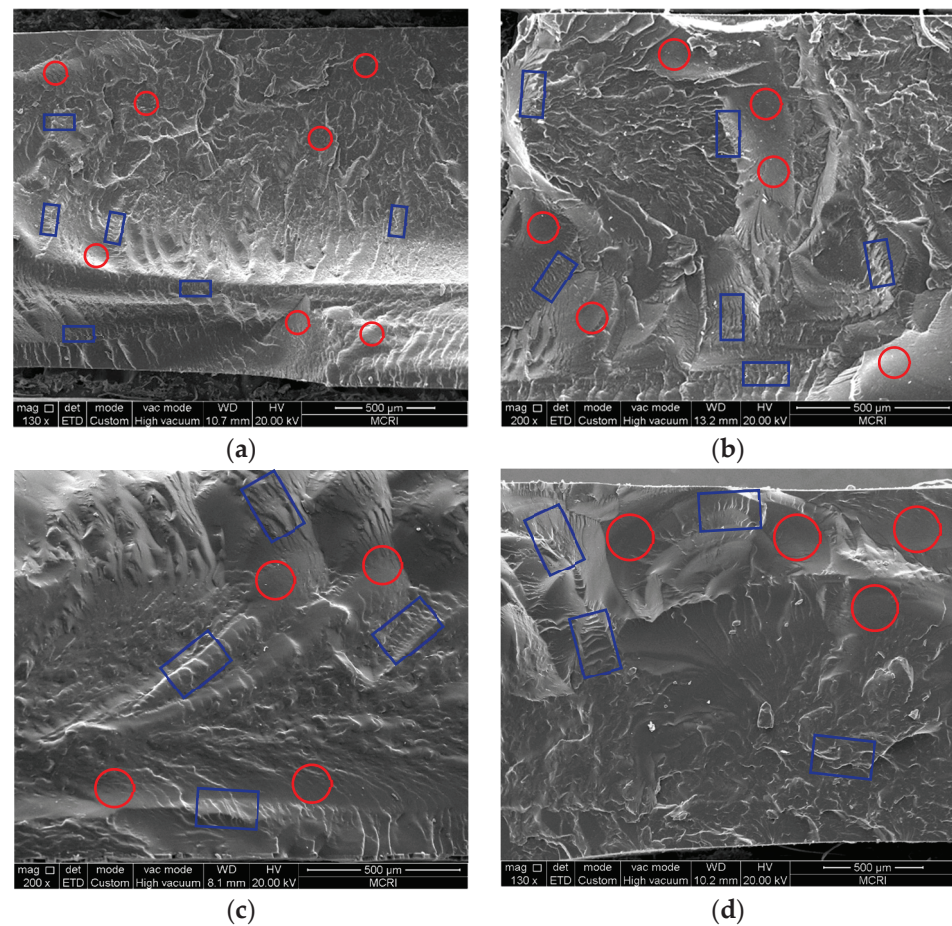


Figure 7. SEM images of the fracture surface of the gels prepared from (a) PBFMO-*b*-GAP-1[#], (b) PBFMO-*b*-GAP-2[#], (c) PBFMO-*b*-GAP-3[#], and (d) GAP-ETPE. (wrinkles were marked as blue square frame, and ravines were marked as red circle frame).

3.4. Thermal Decomposition

It is well known that the thermal stability of energetic binders plays an important role in the preparation, processing, storage, and application of energetic materials [43,44]. Thus, DSC and TGA were used to study the thermal decomposition behavior of PBFMO-*b*-GAP copolyurethanes. The DSC curve of the PBFMO-*b*-GAP is presented in Figure 8, and the DSC curve of PBFMO-*b*-GAP showed three exothermic peaks. The first exothermic peak at 40 °C was the melting point of PBFMO, the second exothermic peak at 247 °C

was caused by the decomposition of side chain azide groups on PBFMO-*b*-GAP to give nitrogen molecules, and the peak at 453 °C was due to PBFMO-*b*-GAP's main chain decomposition [45]. The TGA and DTA traces of PBFMO-*b*-GAP are shown in Figure 9, displaying two distinct regions of weight loss. The first sharp weight loss of around 25% with respect to the total was at 246 °C, which corresponded to the stripping of the azide groups of the side chain, as described in DSC. After the first sharp step, the TGA curve showed a gradual weight loss, which corresponded to the incipient degradation of the main chain of PBFMO-*b*-GAP [46,47]. After the thermal decomposition period, the remaining residue was 35.9%.

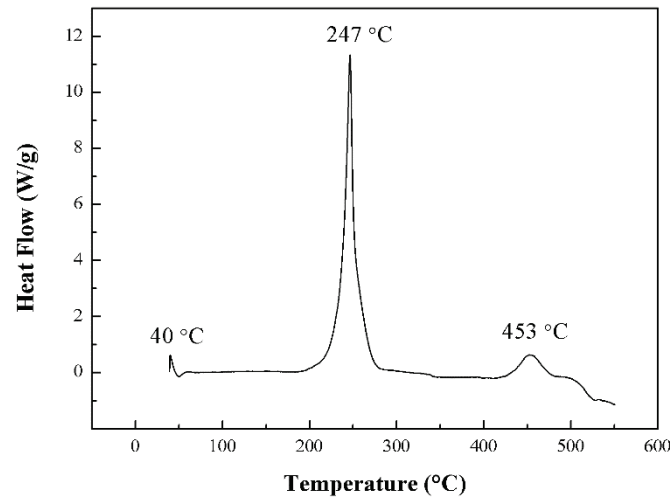


Figure 8. DSC curve of PBFMO-*b*-GAP copolyurethanes.

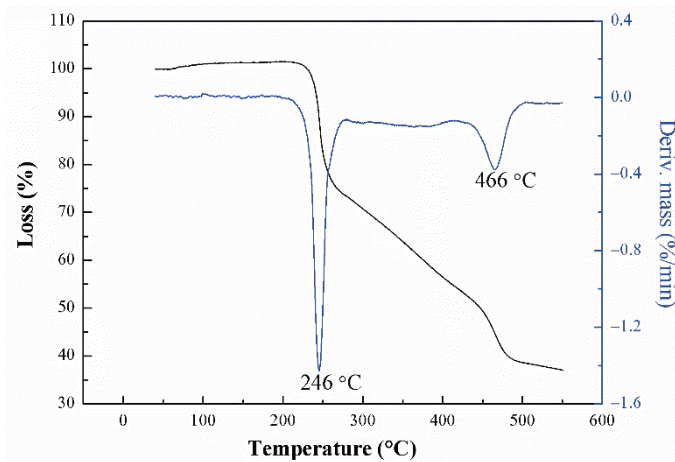


Figure 9. TG/DTA curves of PBFMO-*b*-GAP copolyurethanes.

3.5. Compatibility Testing

Compatibility is an important safety and reliability index used to evaluate the production, application, and storage performance of energetic materials [48,49]. Usually, compatibility can be evaluated from DSC curves by studying the effect of the contact materials on the exothermic decomposition temperature of the explosives. In this study, DSC curves were used to determine the compatibility of PBFMO-*b*-GAP with the main energetic components, such as HMX and Al. Typical DSC curves of binary systems PBFMO-*b*-GAP/HMX, and PBFMO-*b*-GAP/Al are shown in Figure 10. According to the standards of compatibility, the binary systems PBFMO-*b*-GAP/HMX and PBFMO-*b*-GAP/Al had good compatibility because their ΔT_p values were all less than 2 °C [30]. This indicated that PBFMO-*b*-GAP could be safely used in HMX-based propellants.

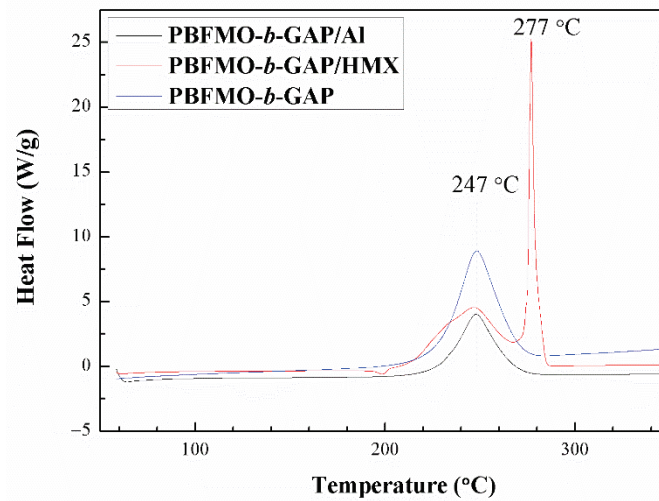


Figure 10. DSC curves of PBFMO-*b*-GAP, PBFMO-*b*-GAP/HMX complex, and PBFMO-*b*-GAP/Al complex.

3.6. Cook-Off Test

The cook-off experiment was used to investigate the thermal performance of the PBFMO-*b*-GAP/Al complex, and the cook-off curves of PBFMO-*b*-GAP/Al composition are shown in Figure 11. Generally, the thermal decomposition characteristics of the PBFMO-*b*-GAP/Al complex are close-linked with the response temperature peak of cook-off curves [50–52]. In this study, the response temperature peak of PBFMO-*b*-GAP/Al composition was up to 298 °C, which was significantly higher than that of the control group (269 °C). It was due to the decomposition process of PBFMO-*b*-GAP releasing HF; subsequently HF could react with Al and give more exothermal reactions [53].

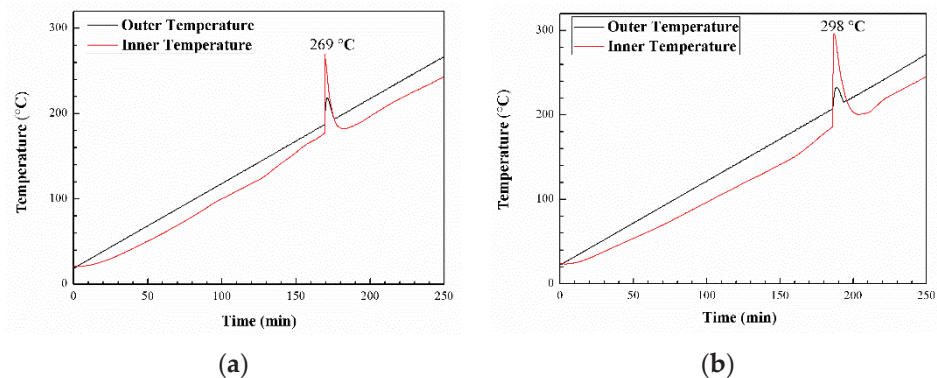


Figure 11. Cook-off curves of GAP-ETPE/Al (a) and PBFMO-*b*-GAP/Al (b).

4. Conclusions

An energetic copolyurethane binder, PBFMO-*b*-GAP, was synthesized on GAP as a soft segment and TDI-extended PBFMO as a hard segment. From FT-IR, NMR, and GPC results, the PBFMO-*b*-GAP was synthesized successfully via a prepolymer process. The drop weight test and XPS results indicated that the introduction of fluoropolymer could evidently reduce the sensitivity of the PBFMO-*b*-GAP polyurethane. The PBFMO-*b*-GAP showed an enhanced tensile strength of 5.75 MPa with a breaking elongation of 1660%, and the tensile strength of PBFMO-*b*-GAP gels was enhanced with an increase in PBFMO content. The DSC and TGA/DTA curves indicated that PBFMO-*b*-GAP had adequate resistance to thermal decomposition up to 200 °C and began to decompose gradually at about 230 °C; it also had good compatibility with Al and HMX. The PBFMO-*b*-GAP/Al complex had a significant response temperature peak of 298 °C in the cook-off curves, which indicated that the PBFMO-*b*-GAP/Al complex has specific reaction energy.

Supplementary Materials: The following are available online at <https://www.mdpi.com/article/10.3390/polym13162706/s1>, Table S1: Mechanical Properties of polymer film for SEM images in different literatures.

Author Contributions: Conceptualization, M.X. and X.L.; methodology, H.M.; software, N.L.; validation, X.L., N.L., Q.Z. and H.M.; formal analysis, Q.Z.; investigation, M.X.; resources, Z.G.; data curation, N.L.; writing—original draft preparation, M.X.; writing—review and editing, X.L. and N.L.; visualization, Q.Z. and H.M.; supervision, Z.G.; project administration, Z.G.; funding acquisition, M.X. All authors have read and agreed to the published version of the manuscript.

Funding: The authors gratefully acknowledge the financial support from the China Postdoctoral Science Foundation (2016M592851).

Institutional Review Board Statement: Not applicable.

Informed Consent Statement: Not applicable.

Data Availability Statement: The data presented in this study are available on request from the corresponding author.

Conflicts of Interest: The authors declare no conflict of interest.

References








- Cheng, T. Review of novel energetic polymers and binders-high energy propellant ingredients for the new space race. *Des. Monomers Polym.* **2019**, *22*, 54–65. [CrossRef]
- Bodaghi, A.; Shahidzadeh, M. Synthesis and characterization of new PGN based reactive oligomeric plasticizers for glycidyl azide polymer. *Propellants Explos. Pyrotech.* **2018**, *43*, 364–370. [CrossRef]
- Wang, Q.; Wang, L.; Zhang, X.; Mi, Z. Thermal stability and kinetic of decomposition of nitrated HTPB. *J. Hazard. Mater.* **2009**, *172*, 1659–1664. [CrossRef]
- Hafner, S.; Keicher, T.; Klapoetke, T.M. Copolymers based on GAP and 1,2-epoxyhexane as promising prepolymers for energetic binder systems. *Propellants Explos. Pyrotech.* **2018**, *43*, 126–135. [CrossRef]
- Boopathi, S.K.; Hadjichristidis, N.; Gnanou, Y.; Feng, X. Direct access to poly(glycidyl azide) and its copolymers through anionic (co-)polymerization of glycidyl azide. *Nat. Commun.* **2019**, *10*, 293–301. [CrossRef]
- Frankel, M.B.; Grant, L.R.; Flanagan, J.E. Historical development of glycidyl azide polymer. *J. Propuls. Power.* **1992**, *8*, 560–563. [CrossRef]
- Murali Mohan, Y.; Mani, Y.; Mohana Raju, K. Synthesis of azido polymers as potential energetic propellant binders. *Des. Monomers Polym.* **2006**, *9*, 201–236. [CrossRef]
- Selim, K.; Ozkar, S.; Yilmaz, L. Thermal characterization of glycidyl azide polymer (GAP) and GAP-based binders for composite propellants. *J. Appl. Polym. Sci.* **2000**, *77*, 538–546. [CrossRef]
- Gaur, B.; Lochab, B.; Choudhary, V.; Varma, I.K. Azido polymers-Energetic binders for solid rocket propellants. *J. Macromol. Sci. Polym. Rev.* **2003**, *43*, 505–545. [CrossRef]
- Ding, Y.; Hu, C.; Guo, X.; Che, Y.; Huang, J. Structure and mechanical properties of novel composites based on glycidyl azide polymer and propargyl-terminated polybutadiene as potential binder of solid propellant. *J. Appl. Polym. Sci.* **2014**, *131*, 40007–40014. [CrossRef]
- Li, Y.J.; Ma, S.; Deng, J.K.; Luo, Y.J. Study on bulk preparation and properties of glycidyl azide polymer with hydroxyl-terminated polyether elastomers obtained through step-wise curing process. *Colloid. Polym. Sci.* **2017**, *295*, 637–646. [CrossRef]
- Li, P.; Li, Q.; Li, X.L.; Gan, X.X.; Yu, H.J. Research on the mechanical property of GAP copolymer elastomer. *Chin. J. Explos. Propellants* **2000**, *23*, 23–28.
- Sikder, A.K.; Reddy, S. Review on energetic thermoplastic elastomers (ETPEs) for military science. *Propellants Explos. Pyrotech.* **2013**, *38*, 14–28. [CrossRef]
- Yanagisawa, Y.; Nan, Y.; Okuro, K.; Aida, T. Mechanically robust, readily repairable polymers via tailored noncovalent cross-linking. *Science* **2018**, *359*, 72–80. [CrossRef]
- Hu, Y.; Jian, X.; Xiao, L.; Zhou, W. Microphase separation and mechanical performance of thermoplastic elastomers based on poly(glycidyl azide)/poly(oxytetramethylene glycol). *Polym. Eng. Sci.* **2018**, *58*, 167–173. [CrossRef]
- Wang, G.; Luo, Y. Characterization of P(BAMO/AMMO) ETPE prepared using different diisocyanates. *Propellants Explos. Pyrotech.* **2016**, *41*, 850–854. [CrossRef]
- Zhang, Z.; Wang, G.; Wang, Z.; Zhang, Y.; Ge, Z.; Luo, Y. Synthesis and characterization of novel energetic thermoplastic elastomers based on glycidyl azide polymer (GAP) with bonding functions. *Polym. Bull.* **2015**, *72*, 1835–1847. [CrossRef]
- Lee, I.; Reed, R.R.; Brady, V.L.; Finnegan, S.A. Energy release in the reaction of metal powders with fluorine containing polymers. *J. Therm. Anal.* **1997**, *49*, 1699–1705. [CrossRef]
- Lee, J.H.; Kim, S.J.; Park, J.S.; Kim, J.H. Energetic Al/Fe₂O₃/PVDF composites for high energy release: Importance of polymer binder and interface. *Macromol. Res.* **2016**, *24*, 909–914. [CrossRef]

20. Dattelbaum, D.M.; Sheffield, S.A.; Stahl, D.; Weinberg, M.; Neel, C.; Thadhani, N. Equation of state and high pressure properties of a fluorinated terpolymer: THV 500. *J. Appl. Phys.* **2008**, *104*, 113525–113535. [CrossRef]
21. McCollum, J.; Pantoya, M.L.; Iacono, S.T. Activating aluminum reactivity with fluoropolymer coatings for improved energetic composite combustion. *ACS Appl. Mater. Interfaces* **2015**, *7*, 18742–18749. [CrossRef]
22. Gong, F.; Guo, H.; Zhang, J.; Shen, C.; Lin, C.; Zeng, C.; Liu, S. Highly thermal stable TATB-based aluminized explosives realizing optimized balance between thermal stability and detonation performance. *Propellants Explos. Pyrotech.* **2017**, *42*, 1424–1430. [CrossRef]
23. Yang, H.; Huang, C.; Chen, H. Tuning reactivity of nanoaluminum with fluoropolymer via electrospray deposition. *J. Therm. Anal. Calorim.* **2017**, *127*, 2293–2299. [CrossRef]
24. Rider, K.B.; Little, B.K.; Emery, S.B.; Lindsay, C.M. Thermal analysis of magnesium/perfluoropolyether pyrolants. *Propellants Explos. Pyrotech.* **2013**, *38*, 433–440. [CrossRef]
25. Jiang, W.C.; Huang, Y.G.; Gu, G.T.; Meng, W.D.; Qing, F.L. A novel waterborne polyurethane containing short fluoroalkyl chains: Synthesis, characterization and its application on cotton fabrics surface. *Appl. Surf. Sci.* **2006**, *253*, 2304–2309. [CrossRef]
26. Ma, S.; Li, Y.; Li, Y.J.; Li, G.P.; Luo, Y.J. Research on the mechanical properties and curing networks of energetic GAP/TDI binders. *Cent. Eur. J. Energetic Mater.* **2017**, *14*, 708–725. [CrossRef]
27. Wang, X.; Hu, J.; Li, Y.; Zhang, J.; Ding, Y. The surface properties and corrosion resistance of fluorinated polyurethane coatings. *J. Fluor. Chem.* **2015**, *176*, 14–19. [CrossRef]
28. Liu, X.; Gao, H.; Chen, X.; Hu, Y.; Pei, S.; Li, H.; Zhang, Y. Synthesis of perfluorinated ionomers and their anion exchange membranes. *J. Membr. Sci.* **2016**, *515*, 268–276. [CrossRef]
29. Tanver, A.; Rehman, F.; Wazir, A.; Khalid, S.; Ma, S.; Li, X.; Luo, Y.; Huang, M.H. Energetic hybrid polymer network (EHPN) through facile sequential polyurethane curation based on the reactivity differences between glycidyl azide polymer and hydroxyl terminated polybutadiene. *RSC Adv.* **2016**, *6*, 11032–11039. [CrossRef]
30. Ma, M.; Kwon, Y. Reactive cycloalkane plasticizers covalently linked to energetic polyurethane binders via facile control of an in situ Cu-free azide-alkyne 1,3-dipolar cycloaddition reaction. *Polym. Chem.* **2018**, *9*, 5452–5461. [CrossRef]
31. Jin, B.; Shen, J.; Gou, X.; Peng, R.; Chu, S.; Dong, H. Synthesis, characterization, thermal stability and sensitivity properties of new energetic polymers-PVTNP-g-GAPs crosslinked polymers. *Polymers* **2016**, *8*, 10. [CrossRef]
32. Shmatova, O.I.; Nenajdenko, V.G. Tetrazole-substituted five, six, and seven-membered cyclic amines bearing perfluoroalkyl groups efficient synthesis by azido-ugi reaction. *Eur. J. Org. Chem.* **2013**, *28*, 6397–6403. [CrossRef]
33. Sarangapani, R.; Reddy, S.T.; Sikder, A.K. Molecular dynamics simulations to calculate glass transition temperature and elastic constants of novel polyethers. *J. Mol. Graph. Modell.* **2015**, *57*, 114–121. [CrossRef] [PubMed]
34. Wang, X.F.; Jin, B.; Peng, R.F.; Zhang, Q.C.; Gong, W.L.; Huang, H.J.; Chu, S.J.; Dong, H.S. Synthesis, spectroscopic characterization, thermal stability and compatibility properties of energetic PVB-g-GAP copolymers. *J. Polym. Res.* **2015**, *22*, 167–177. [CrossRef]
35. Cai, T.; Yang, W.J.; Neoh, K.G.; Kang, E.T. Poly(vinylidene fluoride) membranes with hyperbranched antifouling and antibacterial polymer brushes. *Ind. Eng. Chem. Res.* **2012**, *51*, 15962–15973. [CrossRef]
36. Sangermano, M.; Bongiovanni, R.; Malucelli, G.; Priola, A.; Pollicino, A.; Recca, A. Fluorinated epoxides as surface modifying agents of UV curable systems. *Appl. Polym. Sci.* **2003**, *89*, 1524–1529. [CrossRef]
37. Xiong, J.S.; Jin, Y.Q.; Shentu, B.Q.; Weng, Z.X. Preparation and fluorine enrichment behavior of fluorinated polyester. *J. Coat. Technol. Res.* **2013**, *10*, 621–629. [CrossRef]
38. Wang, Z.; Zhang, T.F.; Zhao, B.B.; Luo, Y.J. Effect of nitrocellulose (NC) on morphology, rheological and mechanical properties of glycidyl azide polymer based energetic thermoplastic elastomer/NC blends. *Polym. Int.* **2017**, *66*, 705–711. [CrossRef]
39. Xu, M.H.; Ge, Z.X.; Lu, X.M.; Mo, H.C.; Ji, Y.P.; Hu, H.M. Structure and mechanical properties of fluorine-containing glycidyl azide polymer-based energetic binders. *Polym. Int.* **2017**, *66*, 1318–1323. [CrossRef]
40. Lee, W.J.; Cha, S.H. Improvement of mechanical and self-healing properties for polymethacrylate derivatives containing maleimide modified graphene oxide. *Polymers* **2020**, *12*, 603. [CrossRef]
41. Zirnstein, B.; Schulze, D.; Scharrel, B. Mechanical and fire properties of multicomponent flame retardant EPDM rubbers using aluminum trihydroxide, ammonium polyphosphate, and polyaniline. *Materials* **2019**, *12*, 1932. [CrossRef]
42. Malkappa, K.; Jana, T. Simultaneous improvement of tensile strength and elongation: An unprecedented observation in the case of hydroxyl terminated polybutadiene polyurethanes. *Ind. Eng. Chem. Res.* **2013**, *36*, 12887–12896. [CrossRef]
43. Landsem, E.; Jensen, T.L.; Kristensen, T.E.; Hansen, F.K.; Benneche, T.; Unneberg, E. Isocyanate-free and dual curing of smokeless composite rocket propellants. *Propellants Explos. Pyrotech.* **2013**, *38*, 75–86. [CrossRef]
44. You, J.S.; Kweon, J.O.; Kang, S.C.; Noh, S.T. A kinetic study of thermal decomposition of glycidyl azide polymer (GAP)-based energetic thermoplastic polyurethanes. *Macromol. Res.* **2010**, *18*, 1226–1232. [CrossRef]
45. Pisharath, S.; Ang, H.G. Synthesis and thermal decomposition of GAP-Poly(BAMO) copolymer. *Polym. Degrad. Stabil.* **2007**, *92*, 1365–1377. [CrossRef]
46. Guo, M.L.; Ma, Z.L.; He, L.M.; He, W.; Wang, Y.W. Effect of varied proportion of GAP-ETPE/NC as binder on thermal decomposition behaviors, stability and mechanical properties of nitramine propellants. *J. Therm. Anal. Calorim.* **2017**, *130*, 909–918. [CrossRef]
47. Wang, G.; Ge, Z.; Luo, Y.J. Thermal decomposition kinetics of poly(3,30-bisazidomethyl oxetane-3-azidomethyl-30-methyl oxetane). *J. Therm. Anal. Calorim.* **2015**, *122*, 1515–1523. [CrossRef]

48. Pei, J.F.; Zhao, F.Q.; Lu, H.L.; Song, X.D.; Zhou, R.; Yuan, Z.F.; Zhang, J.; Chen, J.B. Compatibility study of BAMO-GAP copolymer with some energetic materials. *J. Therm. Anal. Calorim.* **2016**, *124*, 1301–1307. [CrossRef]
49. Li, Y.; Li, J.; Ma, S.; Luo, Y. Compatibility, mechanical and thermal properties of GAP/P(EO-co-THF) blends obtained upon a urethane-curing reaction. *Polym. Bull.* **2017**, *74*, 4607–4618. [CrossRef]
50. Ding, X.Y.; Shu, Y.J.; Xu, H.T.; Chen, Z.Q. Study on thermal behaviour of AP/LiBH₄ energetic system. *Propellants Explos. Pyrotech.* **2018**, *43*, 267–273. [CrossRef]
51. Li, W.F.; Yu, Y.G.; Ye, R.; Yang, H.W. Three-dimensional simulation of base bleed unit with AP/HTPB propellant in fast cook-off conditions. *J. Energetic Mater.* **2017**, *35*, 265–275. [CrossRef]
52. Chen, L.; Ma, X.; Lu, F.; Wu, J.Y. Investigation of the cook-off processes of HMX-based mixed explosives. *Cent. Eur. J. Energetic Mat.* **2014**, *11*, 199–218.
53. Xu, M.H.; Ge, Z.X.; Lu, X.M.; Mo, H.C.; Ji, Y.P.; Hu, H.M. Fluorinated glycidyl azide polymers as potential energetic binders. *RSC Adv.* **2017**, *7*, 47271–47278. [CrossRef]

Article

Antimicrobial Property of Polypropylene Composites and Functionalized Copper Nanoparticles

Noemi Jardón-Maximino ¹, Gregorio Cadenas-Pliego ^{1,*}, Carlos A. Ávila-Orta ¹,
Víctor Eduardo Comparán-Padilla ¹, Luis E. Lugo-Uribe ², Marissa Pérez-Alvarez ¹,
Salvador Fernández Tavizón ¹ and Gerardo de Jesús Sosa Santillán ³

¹ Centro de Investigación en Química Aplicada (CIQA), Saltillo, Coahuila 25294, Mexico; nahomy_mimis@hotmail.com (N.J.-M.); carlos.avila@ciqa.edu.mx (C.A.Á.-O.); victor.comparan@ciqa.edu.mx (V.E.C.-P.); pamarissa@hotmail.com (M.P.-A.); salvador.fernandez@ciqa.edu.mx (S.F.T.)

² Centro de Tecnología Avanzada CIATEQ, Lerma, Estado de México 542004, Mexico; luis.lugo@ciateq.mx

³ Facultad de Ciencias Químicas, Universidad Autónoma de Coahuila, Saltillo, Coahuila 25280, Mexico; gdejsosa@uadec.edu.mx

* Correspondence: gregorio.cadenas@ciqa.edu.mx

Abstract: Copper nanoparticles (CuNPs) functionalized with polyethyleneimine (PEI) and 4-aminobutyric acid (GABA) were used to obtain composites with isotactic polypropylene (iPP). The iPP/CuNPs composites were prepared at copper concentrations of 0.25–5.0 wt % by melt mixing, no evidence of oxidation of the CuNP was observed. Furthermore, the release of copper ions from iPP/CuNPs composites in an aqueous medium was studied. The release of cupric ions was higher in the composites with 2.5 and 5.0 wt %. These composites showed excellent antibacterial activity (AA) toward *Pseudomona aeruginosa* (*P. aeruginosa*) and *Staphylococcus aureus* (*S. aureus*). The incorporation of CuNP into the iPP polymeric matrix slightly decreased the thermal stability of the composite material but improved the crystallinity and the storage modulus. This evidence suggests that CuNPs could work as nucleating agents in the iPP crystallization process. The iPP/CuNPs composites presented better AA properties compared to similar composites reported previously. This behavior indicates that the new materials have great potential to be used in various applications that can be explored in the future.

Keywords: antimicrobial; metallic ions; ligand; copper nanoparticles; polypropylene

Citation: Jardón-Maximino, N.; Cadenas-Pliego, G.; Ávila-Orta, C.A.; Comparán-Padilla, V.E.; Lugo-Uribe, L.E.; Pérez-Alvarez, M.; Fernández-Tavizón, S.; Sosa-Santillán, G.d.J. Antimicrobial Property of Polypropylene Composites and Functionalized Copper Nanoparticles. *Polymers* **2021**, *13*, 1694. <https://doi.org/10.3390/polym13111694>

Academic Editors: Somen K. Bhudolia and Sunil Chandrakant Joshi

Received: 1 May 2021
Accepted: 20 May 2021
Published: 22 May 2021

Publisher's Note: MDPI stays neutral with regard to jurisdictional claims in published maps and institutional affiliations.



Copyright: © 2021 by the authors. Licensee MDPI, Basel, Switzerland. This article is an open access article distributed under the terms and conditions of the Creative Commons Attribution (CC BY) license (<https://creativecommons.org/licenses/by/4.0/>).

1. Introduction

From an academic and industrial viewpoint, the synthesis of CuNPs has been of great interest due to their potential applications. Examples of these include the production of conductive and antibacterial materials and as a replacement of expensive materials, such as gold and silver nanoparticles [1,2]. The antimicrobial properties of copper have been well known for a long time. Recently, copper was considered the first and only metal with antimicrobial properties by the American Environmental Protection Agency (EPA) [3]. This material eliminates 99.9% of most pathogens within 2 h of contact [4]. Furthermore, in some specific cases, copper has better properties compared to other expensive metals with antimicrobial activity, such as silver and gold [5].

Recently, several research works have emphasized the importance of CuNPs in priority areas for society such as medicine (COVID-19 pandemic) [6,7], agriculture [8–11], and environment [12,13], among others.

The addition of CuNPs into iPP has given excellent results for the inhibition of the growth of a broad microorganism spectrum. Applications of such polymeric composites include among the most important ones' food packaging, medical instruments, and water treatment [14–16].

Copper/polymer composites show bactericide properties that can be attributed to their ability to release metal ions in an aqueous medium [14]. The metal ions promote an electrostatic interaction with the negatively charged bacterial cell wall, disrupting its integrity to the point of rupture. This behavior leads to leakage of intracellular material and subsequent cell death [17–23].

The release process of the metal ions from the composites starts with water diffusion into the composite bulk. This is followed by the reaction between metallic particles and water molecules that leads to the formation of metal ions. Finally, the migration of these metal ions towards the external surface of the composite allows its interaction with bacteria [14,24].

The properties of the polymeric matrix, such as crystallinity and hydrophobic behavior, may influence the capability of the composite to release metal ions [14,25]. Damm et al. argued that the diffusion of water molecules and metal ions occurs in the amorphous regions of the polymer matrix, then an increment in the hydrophilicity and decrease of the polymer matrix crystallinity could improve the release of ions [26].

Nonetheless, an important problem that can be observed frequently in composite materials obtained by melt mixing is the poor dispersion of the nanoparticles (NPs) in the polymeric matrix. The aggregation of NPs in a polymeric matrix is associated with its high surface energy. Typically, the formation of large NP aggregates involves a decrease in the mechanical, thermal, and antimicrobial properties of the composite [27].

On the other hand, the compatibility of the composite components can influence too on the aggregation of metallic NPs inside the polymeric matrix. Some strategies applied to improve the CuNPs compatibility with the polymeric matrix consist of functionalization of the NPs and dispersion by physical methods such as ultrasound [28]. A highly feasible option contemplates the functionalization of the CuNPs with ligands that contain both polar and non-polar moieties in their chemical structure. The polar moiety could interact with the CuNPs, whereas the non-polar moiety could do it with the polypropylene matrix. Yurong Wu. et al. obtained by solution mixing composites formed by iPP and Cu₂O NPs modified by silanes [28]. Ramazanov et al. produced composites of iPP and functionalized CuNPs with sodium oleate through a solution mixing process [29]. Palza et al. obtained by a melt mixing method composites formed by iPP and CuNPs functionalized by hexanethiol [30]. Molaba et al. developed a method that includes, as the first step, the mixing of silver nanoparticles (AgNPs) with a paraffinic wax followed by melt blending with iPP [31]. In all these cited works it was reported good dispersion of the CuNPs in the polymeric matrix. However, the non-polar moiety of the ligand coating the NPs could affect the release process of the metal ions from the composite in an aqueous medium.

Our research group has reported the obtention of functionalized CuNPs with nitrogenated ligands [32–34]. These modified CuNPs were employed successfully to prepare polymeric composites with nylon 6, achieving an improvement in the mechanical properties of this polymer with a low concentration of the copper nanoparticles [27]. It is expected that these composites exhibit good antimicrobial properties due to the combination of the polar nature of the polymeric matrix with the functionalized CuNPs with nitrogenated ligands. Generally, it is considered that CuNPs functionalized with polar coatings can favor the process of liberation of metal ions and the elimination of bacteria and viruses.

In this work the obtention of composites based on iPP and CuNPs functionalized with polyethyleneimine (PEI) and 4-aminobutyric acid (GABA) by a melt mixing process is reported. Several CuNP concentrations (0.25, 1.0, 2.5, and 5.0 wt %) were employed to prepare the composites. Additionally, the copper ions release was studied and its effect on the antibacterial activity toward *Pseudomonas aeruginosa* and *Staphylococcus aureus*. Finally, the mechanical and thermal properties of the composites were evaluated.

2. Materials and Methods

2.1. Materials

The isotactic polypropylene (iPP) used in this study was Valtec HS013 from Indelpro S.A. de C.V. (Altamira, México), with a melt flow index (MFI) (at 230 °C with 2.16 kg) of 11 g/10 min and an average molecular weight (M_n) of 74,784 g/mol, molecular weight distribution (MWD) of 3.9. MW and MWD were determined by gel permeation chromatography using a Waters 150 °C chromatograph eluting with 1,2,4-trichlorobenzene at 135 °C. Narrow MWD polystyrene standards were used for GPC calibration. Copper nanoparticles functionalized with polyethyleneimine and 4-aminobutyric acid (CuNPs-PEI/GABA) were obtained according to a previously reported procedure developed in our research group [35]. The nanoparticles present an average particle size of 27.0 nm and a ligand content of 8 wt %.

2.2. Composite Preparation

iPP/CuNPs composites were prepared using an internal mixer ATR Brabender Plasticorder (C.W.B. Brabender Instrument, Inc., South Hackensack, NJ, USA) at 190 °C and 100 rpm. The iPP and different samples with CuNPs concentrations of 0.25, 1.0, 2.5, and 5.0 wt % were processed in the same way in batches of 65 g. Plates were obtained from the composites in a P.H.I. Press (P.H.I., City of Industry, CA, USA), which was operated at a temperature of 180 °C and 17.0 MPA for 10 min. After this time, the plates are kept under pressure and are cooled with water at a cooling rate of approximately 18 °C/min. The obtained plates had a thickness of 3.0 mm.

For the study of copper ions releasing and antimicrobial activity, 2 cm × 2.4 cm samples were cut from the composite's plates and for the DMA analysis, 3.5 cm × 1.2 cm samples were prepared.

2.3. Characterization

Wide-angle X-ray diffraction analysis (WAXD) was employed to identify the crystalline structure of the composites. It was used a diffractometer Siemens D-5000 (SIEMENS, Berlin, Germany) operated at 35 kV and a current of 25 mA. The scan range on the 2θ scale was from 20 to 80° with a step size of 0.02°/s.

Scanning electron microscopy (SEM) was employed to observe the dispersion of the CuNPs in the polymeric matrix. A JEOL JSM-7001F electron microscope (Jeol LTD., Akishima, Tokyo, Japan) was used, applying a voltage of 8 kV, secondary electrons detector COMPO and a work distance (WD) of 8 mm. Image acquisition was performed using the backscattered electron signal detector. The samples were cryogenically broken and the fracture surfaces were electrocoated with an Au-Pd alloy to improve electron conduction.

Copper quantification of the released ions from the composite plates in an aqueous medium (15 mL deionized water) was determined using an atomic absorption spectrophotometer (Varian SPECTR AA-250 plus, Varian inc., Mulgrave, Victoria, Australia) at a wavelength of 324.4 nm that corresponds to copper. A calibration curve was prepared using multielemental standards (high-purity standards) at different concentrations (ppm).

Thermal stability of the iPP/CuNPs composites was determined by thermogravimetric analysis (TGA) using a TA Instruments Discovery TGA 5500 device (TA instruments Inc., New Castle, DE, USA). The analysis consisted of a temperature sweep from 25 to 600 °C under N₂ atmosphere of a 20 mg sample with a heating rate of 10 °C/min. From 600 to 700 °C the N₂ atmosphere was replaced by an oxygen atmosphere to assure full combustion of the residues.

Thermal transitions (melting and crystallization) of the iPP/CuNPs composites were studied by differential scanning calorimetry analysis (DSC) using a TA Instruments Discovery DSC 2500 device. Heating and cooling cycles were performed at a rate of 10 °C/min under an inert atmosphere using an N₂ flow of 50 mL/min.

Dynamical-mechanical thermal analysis (DMTA) was used to characterize the viscoelastic behavior of the iPP/CuNPs composite as a function of temperature. A TA In-

struments DMA Q800 device was employed for the analysis using a single cantilever clamp. The temperature range was from 25 to 180 °C, with a heating rate of 5 °C/min at a frequency of 1 Hz and an oscillation amplitude of 20 µm. The storage or elastic modulus (E') was determined and reported at 30 °C.

Antibacterial activity of iPP/CuNPs composites was determined according to methods reported in ASTM E2149-01. *Pseudomonas aeruginosa* Gram (-) and *Staphylococcus aureus* Gram (+) bacteria were studied. Preparation of the bacterial suspension consisted of activation and growth of the bacterial inoculum in sterile Ringer's solution at optimal conditions (37 °C for 16 h) until a final concentration (after dilution) of 1×10^5 CFU/mL was reached.

The procedure to analyze the antibacterial activity of the composites is described as follows. First, it was conducted the addition of 25 mL of the bacterial suspension (1×10^5 CFU/mL) together with the composite sample into a 250 mL flask (the composite plate was previously sterilized with UV light for 25 min); the flask was placed in an incubator at 37 °C with stirring. After the established contact time has elapsed, a sample of 0.1 mL was taken from the flask and was mixed in an Eppendorf tube with 0.9 mL of Ringer's solution. After, a sample of 0.1 mL was taken from this mix and was placed in a polystyrene Petri dish together with sterile nutrient agar. The Petri dishes were inoculated in triplicate with the bacterial solution at different contact times (0, 2, 4, 6, and 24 h) and were kept in an incubator at 37 °C for a time interval between 18 and 24 h.

Antibacterial activity of the composites was calculated using Equation (1) [26,36]

$$\text{Antibacterial activity (\%)} = \frac{C_0 - C}{C_0} \times 100 \quad (1)$$

where C_0 is the number of formed CFU (colony-forming unit) in the control dish (bacterial solution without sample) and C is the number of formed CFU in the dishes where the bacterial solution was in contact with the sample.

3. Results and Discussion

3.1. Wide Angle X-ray Diffraction (WAXD)

WAXD analysis was performed on the iPP/CuNPs composites and the unfilled polymer (iPP). Through this analysis, it was possible to determine the type of copper particle resulting in the processing of the composites.

X-ray diffractograms of iPP and a sample representative of the composites identified as iPP/CuNPs 5% (5.0 wt % of CuNPs in iPP) are shown in Figure 1. Diffractogram corresponding to iPP shows characteristic reflections of the crystals β -PP of this polymer such as $2\theta = 14.1, 16.9, 18.5, 21.2, 22.1, 25.5,$ and 28.5° associated with the (110), (040), (130), (111), (041), (060), and (220) planes, respectively. Other reflections associated with β -PP crystals are observed at $2\theta = 16.2$ and 21.2° corresponding to planes (300) and (301), respectively. Additionally, a peak at $2\theta = 42.8^\circ$ is appreciated, suggesting the presence of nucleating agents to induce the formation of β -crystals in the commercial iPP [37–39].

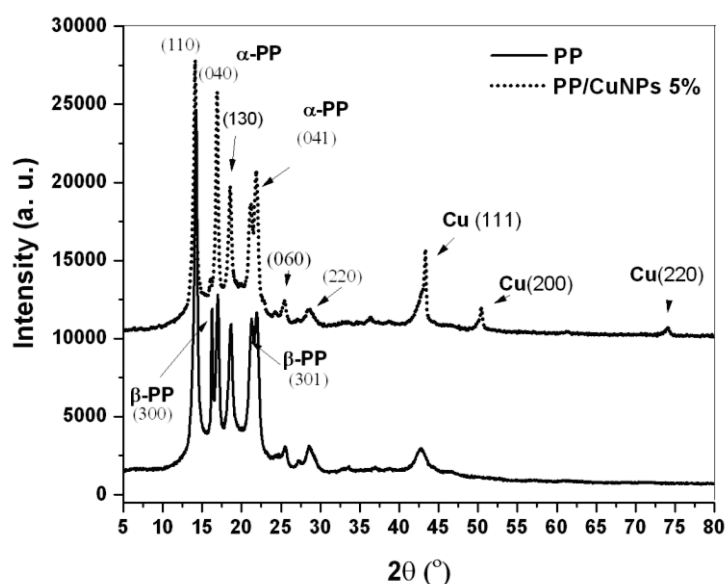


Figure 1. Diffractograms of iPP and PP/CuNPs 5 wt % composite.

The composite diffractogram shows some differences regarding that of the iPP; peaks intensity changes and even the peak at $2\theta = 16.2^\circ$ that corresponds to β -PP crystals disappears [37]. The modifications of the characteristic diffractogram of iPP can be associated with a nucleating effect of the CuNPs. Some authors have reported that the processing conditions used for preparing the CuNPs/iPP composites promoted a transformation of β -PP crystals to α -PP crystals, which is feasible too [38]. Another important change that can be observed is the presence of three new peaks associated with metallic copper (face-centered cubic structure, FCC). These peaks were found at $2\theta = 43.6, 50.7,$ and 74.6° , corresponding to planes (111), (200), and (220), respectively [40–43].

The diffractograms of the composites did not show evidence of the formation of Cu_2O and CuO . According to this analysis, it can be inferred that the oxidation of metallic copper during the iPP/CuNPs composite processing stage is avoided due to the coating based on nitrogenated ligands (PEI and GABA) formed over the CuNPs surface. This fact is important since in other works that report the preparation of polymeric composites based on CuNPs it is common to detect the oxidation of the CuNPs during the processing of the composite due to the strong tendency of metallic copper to form copper oxide under ambient conditions [36].

3.2. SEM Analysis

CuNPs dispersion in the polymeric matrix was analyzed by SEM micrographs. The composite samples were cryogenically fractured and coated with gold/platinum to allow electron conductivity. Figure 2 shows the micrograph of the iPP/CuNPs composite with 0.25 wt % of nanoparticles. The images were taken at different magnification levels with backscattered electron techniques or Z-contrast; this technique is able to differentiate individual heavy atoms from lighter [44].

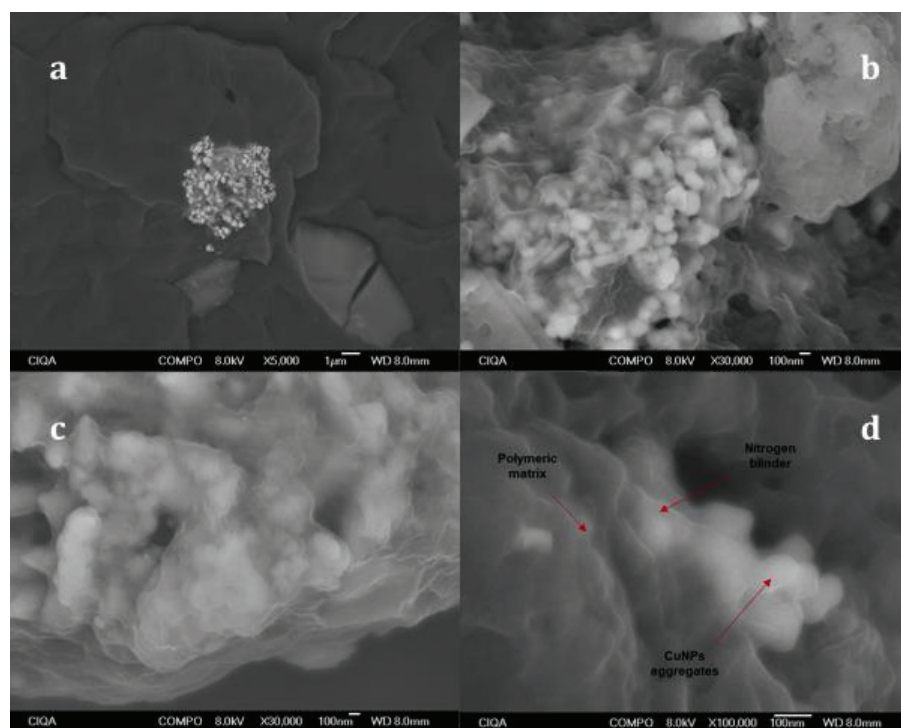


Figure 2. SEM images with different magnification (a) 5000, (b) 30,000, (c) 30,000, and (d) 100,000 times of sample iPP/CuNPs 0.25 wt %.

The polymer matrix can be detected in dark gray, while the CuNPs aggregate is observed in a bright white tone with a semispherical morphology. The analysis of the high-resolution micrographs determined the presence of irregularly shaped aggregates of an approximate size of 350 nm. These aggregates are formed of subparticles with an average particle size of 36–226 nm; the addition of 0.25 wt % of CuNPs increased the particle size compared to the original (27.0 nm). This behavior is known, CuNPs increase in size when they are mixed with a polymer in the molten state and high concentrations of copper lead to larger particle sizes [29].

It is noted a different tonality in the edges of the copper nanoparticles compared to their inner part. This tonality difference can be attributed to the nitrogenated ligand, which is approximately 7 nm thick.

3.3. TGA Analysis

The thermal stability of the iPP and iPP/CuNPs composites, as a measure of resistance to thermal degradation, was evaluated using TGA. Figure 3 shows TGA thermograms of weight loss as a function of the temperature of iPP and iPP/CuNPs composites.

All composites show greater weight loss regarding the iPP sample in the temperature range of 150–320 °C. The composites with 0.25, 1.0, and 5.0 wt % presented a lower maximum degradation temperature (T_{max}) compared to the iPP that can be observed between 320 and 470 °C. The composite with 2.5 wt % shows the T_{max} at 431.7 °C, slightly higher compared to the iPP. Figure 4 illustrates the first derivative of TG curves (DTG) that confirm the stability of the samples.

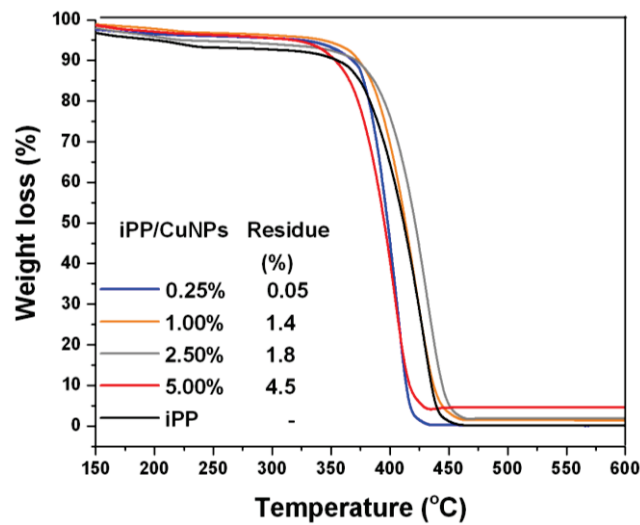


Figure 3. TGA thermographs of iPP and iPP/CuNPs composites.

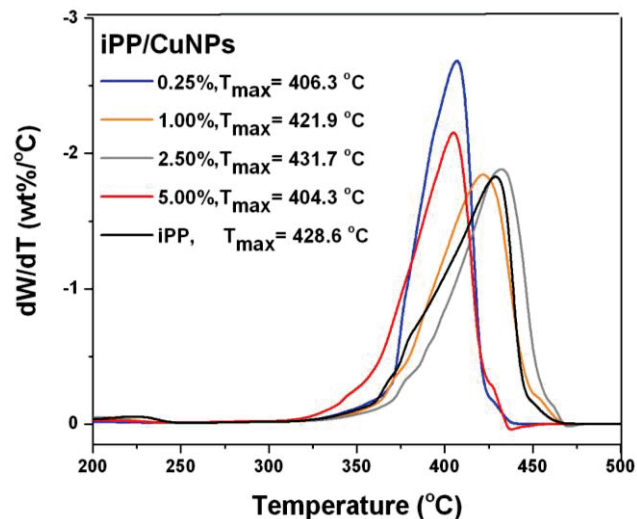


Figure 4. DTG curves of iPP and CuNPs/iPP composites.

The effect produced by copper on the stability of the polymeric matrix of iPP is not clear, reports indicate that the stability is negatively and positively affected, generally the positive effects are observed when using NPs of large size (850 nm) and CuO NPs [28].

The weight percentage observed at temperatures higher than 460 °C can be attributed to inorganic residues that cannot be degraded at this range of temperature. In this case, these residues can be associated with CuNPs. Residues values of the composite samples do not correspond to those used in the formulation for CuNPs. These variations can be attributed to a non-homogeneous distribution of the CuNPs in the iPP matrix.

3.4. DSC and DMA Analyses

The thermal transitions of the iPP/CuNPs composites at several nanoparticle concentrations were studied through DSC analysis. Besides, storage module E' at 30 °C was obtained from the DMTA analysis for these same samples. Table 1 lists the crystallization temperature (T_c), enthalpy of crystallization (ΔH_c), melting temperature (T_m), enthalpy of melting (ΔH_m), the crystalline fraction (X_c), and the storage modulus (E') of the iPP/CuNPs composites.

Table 1. DSC and DMA data corresponding to iPP/CuNPs composites.

Samples	T _c ^a (°C)	ΔH _c ^a (J/g)	T _m ^a (°C)	ΔH _m ^a (J/g)	X _c ^b	E' ^c (MPa)
PP	117.1	93.7	164.2	92.4	0.44	1764
PP/CuNPs 0.25%	118.9	99.3	163.7	97.8	0.47	3983
PP/CuNPs 1.00%	118.6	90.4	162.5	87.9	0.42	1695
PP/CuNPs 2.50%	121.1	93.4	163.6	93.5	0.45	2839
PP/CuNPs 5.00%	122.1	93.9	163.5	96.7	0.46	2699

a—Obtained by DSC, b—determined as $X_c = \Delta H_m / 209 \text{ J/g}$, and c—obtained by DMA at 30 °C.

Thermal transition data show growth with the increase of the filler in the iPP matrix, except for the composite with 1.0 wt % copper. This can be attributed to a non-homogeneous distribution of the NPs. The T_m was slightly lower compared to the unfilled iPP, while the T_c increased with the addition of CuNPs to the iPP. An increase of 5 °C was observed in the composite with 5.0 wt %. Yanying Jiang et al. observed a rise of 3 °C in the T_c of iPP/CuO composites. They attributed this increase to the low efficiency of CuONPs as nucleating agents [28]. The greater increase in T_c observed in the iPP/CuNPs composites suggests that the CuNPs have a greater nucleating effect on the crystallization rate of iPP compared to CuONPs.

The crystalline fraction (X_c) was calculated using the formula $X_c = \Delta H_m / \Delta H_f$ (100%). The enthalpy of melting for a 100% crystalline iPP was taken from the literature as ΔH_f 100% = 209 J/g [45]. In most of the analyzed samples, the CuNPs in the polymeric matrix caused an increment in the crystalline fraction (X_c). The increment of the crystalline fraction can be associated with a nucleating effect of the CuNPs on the iPP matrix. As crystallization is an exothermic process, then the copper particles can absorb and dissipate fast the heat generated by nearby polymer chains. This effect can cause the iPP chains closest to the copper particle's surface to show a faster crystallization rate. Other authors who consider that metallic nanoparticles can induce a nucleating process during the crystallization of the polymeric matrix have reported a similar explanation [46,47]. They point out that the high thermal conductivity of polymers that contains metal nanoparticles is evidence supporting this idea. However, it must be considered that copper nanoparticles do not always show the same behavior since it depends on several factors, such as the oxidation state, size, and functionalization, among others, so these reports should be taken with caution.

A comparison of the results of X_c and storage module E' indicates a good correlation. The iPP/CuNPs composites that showed higher X_c values compared to those obtained for iPP had better E' modulus values. These CuNPs composites samples showed E' values between 2700 to 4000 MPa that were superior compared to unfilled iPP that had an E' value of 1764 MPa. An increase in E' values shows a growth in the rigidity of the composite and reinforcement of the polymeric matrix, which was less significant at high concentrations of copper. By increasing the number of CuNPs in the polymer matrix, the formation of aggregates is favored, therefore, more defective points will also be produced in the matrix [48]. Aggregate formation in CuNPs composites seems inevitable even at concentrations of 0.25 wt % (Section 3.2). The functionalization of CuNPs is not enough to avoid the aggregation of particles. New research involving the use of compatibility agents for iPP and functionalized CuNPs should be carried out to contribute to the synthesis of iPP composites with high copper concentration.

In general, the data of X_c and storage module E' agree to expected values. J. A. Molefi et al. reported a similar behavior when studying polyethylene composites with CuNPs [48]. In this work, the E' values increase with rising copper concentration. The highest E' values are achieved at copper concentrations of 1 vol.%, the E' values were very similar to concentrations of 3 and 5 vol.%. This increase is attributed to several reasons, such as weak interfacial bonding between the CuNP and matrix interfaces, aggregates of Cu nanoparticles, and nanoparticle processing-related defects [48].

3.5. Cupric Ion Release from PP/CuNPs Composites

It is known that the antibacterial mechanism of these sorts of composites is based on the release of metal ions in the presence of moisture and oxygen in the air [49]. In this work, the release of copper ions from the iPP/CuNPs composites was determined by atomic absorption analysis. Figure 5 contains the plots of copper concentration in $\text{mg/L}\cdot\text{cm}^2$ released in deionized water as a function of exposition time (number of days) for the different iPP/CuNPs composites (0.25, 1.0, 2.5, and 5.0 wt %).

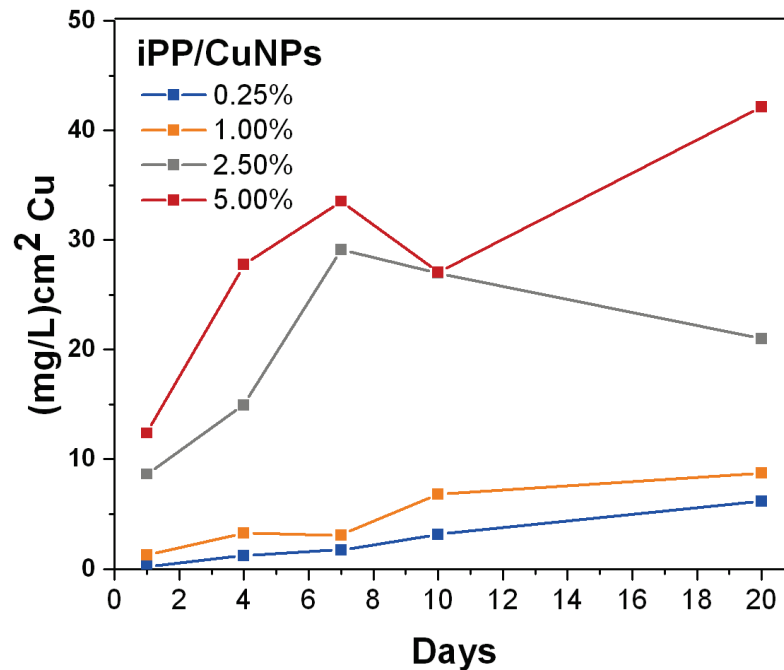


Figure 5. Concentration of released copper from iPP/CuNPs composites.

In general, it can be appreciated a raise in the copper ions release when CuNPs concentration increases. This result suggests that an increment in the crystalline fraction of the composite (see Table 1) did not affect the copper ion release capability. There was also an increase in copper concentration as the exposure time of the sample in water increased from 1 to 10 days. After the tenth day, it is not observed a significant increment in the copper concentration. The highest amount of released copper was obtained with the iPP/CuNPs composite with 5 wt % of nanoparticles, which was 12.5 and 27 $\text{mg/L}\cdot\text{cm}^2$ at 1 and 10 days, respectively. These results are in agreement with those reported by other authors, as described below.

Tamayo et al. reported a copper ions concentration of 18 and 26 $\text{mg/L}\cdot\text{cm}^2$ at 1 and 10 days, respectively, for a composite with 5.0 wt % of CuNPs in polyethylene produced by in situ polymerization [50]. Palza et al. reported copper concentrations of 22 and 80 $\text{mg/L}\cdot\text{cm}^2$ at 1 and 10 exposition days corresponding to an iPP/CuNPs composite at 5.0 wt % [30]. These composites were obtained by a melt mixing method applying an additional treatment, which could be: (a) a predispersion step of the CuNPs in ethanol, (b) preparation of a nanoparticle masterbatch with a compatibilizer, or (c) CuNPs functionalization.

It should be noted that the first hours of contact of the sample with the microorganism are relevant for the efficacy of the antibacterial activity. In the case of the composite iPP/CuNPs at 5.0 wt % that showed a copper concentration of 12.5 $\text{mg/L}\cdot\text{cm}^2$ at the first contact day, it would suggest that this composite should show a good antibacterial efficiency.

3.6. Antibacterial Activity

Table 2 shows the required contact time of the sample with the bacterial suspension to reach different antibacterial activity percentages by the iPP/CuNPs composites toward *P. aeruginosa* and *S. aureus* bacteria.

Table 2. Antibacterial activity (AA) of iPP/CuNPs composites toward.

Composite PP/CuNPs	<i>P. aeruginosa</i> Gram (-)	<i>S. aureus</i> Gram (+)
	AA(%) /h	AA(%) /h
0.25%	53/24	76/24
1.00%	100/24	98/24
2.50%	100/2	100/6
5.00%	100/2	100/4

P. aeruginosa and *S. aureus* bacteria.

For all composites, it was observed a higher antibacterial activity toward *P. aeruginosa* with respect to *S. aureus*. This behavior could be associated with differences in the cell wall of the bacteria. As has been reported by several studies, Gram (-) bacteria are more susceptible to metal ions compared to Gram (+) bacteria [19,50–52].

The composite iPP/CuNPs at 5.0 wt % of nanoparticles in iPP showed the highest antibacterial activity. It required only 2 h to achieve total antibacterial activity (100%) toward *P. aeruginosa* and 4 h toward *S. aureus*. The composite with 2.5 wt % of CuNPs in iPP also achieved total antibacterial activity toward *P. aeruginosa* at 2 h of contact and toward *S. aureus* at 6 h of contact.

It is important to mention that the iPP/CuNPs composite at 5.0 wt % showed higher antibacterial activity compared to other similar works reported in the literature. According to España et al., composites based on iPP charged with 5.0 wt % of commercial CuNPs, which were treated with plasma to increase its hydrophilicity, achieve 100% antibacterial activity at 3 h of contact toward *P. aeruginosa* and 98% at 6 h toward *S. aureus* [36]. The treatment with plasma improves the antimicrobial activity but it can reduce the mechanical properties of the composite. In another report, Palza et al. evaluated PP/CuNPs composite with 5.0 vol.% of nanoparticles, achieving antibacterial activity of 99.8% toward *P. aeruginosa* and *S. aureus* after 60 min of contact [25]. However, the quantity of CuNPs is too high, since 5.0 vol.% equals 36 wt %. This conversion agreed with the calculations used by other reports to show the equivalence between wt % with vol.% in their copper/iPP composite formulations [47,53–55].

Another important aspect that must be considered in antimicrobial activity studies is the chemical nature of the copper nanoparticles. It is known that CuNPs chemically stable to oxidation have higher antimicrobial activity and less cytotoxicity compared to CuO and Cu₂O nanoparticles. This suggests that CuNPs/iPP composites obtained in the present research work could be materials with low toxicity maintaining a high antimicrobial activity for a longer lifetime [56].

4. Conclusions

The CuNPs preserved its metallic state (no oxidation) during the processing of the composites because of the functionalization of the nanoparticles with the nitrogenated ligands. Additionally, the hydrophilic character of these functionalized nanoparticles improved the copper ions release from the composite in an aqueous medium.

The highest amount of released copper was obtained with the composites that contained 2.5 and 5 wt % of the CuNPs in the iPP matrix. Composites' capability to release copper ions agreed with the antibacterial properties; composites with 2.5 and 5.0 wt % of

CuNPs show full antibacterial activity (100%) toward *P. aeruginosa* after 2 h of contact and toward *S. aureus* after 4 h of contact.

The presence of CuNPs in the polymer matrix slightly decreased the thermal stability but improved the crystallinity and storage modulus. The copper/polymer composites could be an excellent alternative to be employed as antimicrobial materials, but it is necessary to do more detailed studies about its toxicity. The composites with the highest antibacterial activity are potential materials for wastewater disinfection, packaging, and biomedical products.

Author Contributions: Conceptualization, G.C.-P., N.J.-M., G.d.J.S.S., and C.A.Á.-O.; methodology, N.J.-M., V.E.C.-P., L.E.L.-U., and G.d.J.S.S.; formal analysis, S.F.T., M.P.-A., and N.J.-M.; investigation, G.C.-P., C.A.Á.-O., S.F.T., L.E.L.-U., and V.E.C.-P.; writing—original draft preparation, N.J.-M., G.C.-P., and C.A.Á.-O.; writing—review and editing, N.J.-M., M.P.-A., and G.C.-P. All authors have read and agreed to the published version of the manuscript.

Funding: This research was funded by Internal Project CIQA-2021, grant number 6597.

Institutional Review Board Statement: Not applicable.

Informed Consent Statement: Not applicable.

Data Availability Statement: The data presented in this study are available on request from the corresponding author.

Acknowledgments: Noemi Jardón-Maximino wishes to thank CONACYT for the Scholarship no. 263275. Finally, the authors would like to thank G. Mendez Padilla, A. Espinoza Muñoz, J.A. Mercado Silva, J. Campos Oyervides, and R. Cedillo García for their valuable technical support.

Conflicts of Interest: The authors declare no conflict of interest.

References

- Nowak, A.; Szade, J.; Talik, E.; Zubko, M.; Wasikowski, D. Physicochemical and antibacterial characterization of ionocytivity Ag/Cu powder nanoparticles. *Mat. Charact.* **2016**, *117*, 9–16. [CrossRef]
- Medellín-Banda, D.I.; Navarro-Rodríguez, D.; Fernández-Tavizón, S.; Ávila-Orta, C.A.; Cadenas-Pliego, G.; Comparán-Padilla, V.E. Enhancement of the thermal conductivity of polypropylene with low loadings of CuAg alloy nanoparticles and graphene nanoplatelets. *Mat. Tdy. Commun.* **2019**, *21*, 100695. [CrossRef]
- Prado, J.V.; Vidal, A.R.; Duran, T.C. Application of copper bactericidal properties in medical practice. *Rev. Med. Chil.* **2012**, *140*, 1325–1332. [CrossRef] [PubMed]
- Hans, M.; Erbe, A.; Mathews, S.; Chen, Y.; Solioz, M.; Mücklich, F. Role of copper oxides in contact killing of bacteria. *Langmuir* **2013**, *29*, 16160–16166. [CrossRef] [PubMed]
- Usman, M.S.; El Zowalaty, M.E.; Shameli, K.; Zainuddin, N.; Salama, M.; Ibrahim, N.A. Synthesis, characterization, and antimicrobial properties of copper nanoparticles. *Int. J. Nanomed.* **2013**, *8*, 4467–4479. [CrossRef]
- Zuniga, J.M.; Cortes, A. The role of additive manufacturing and antimicrobial polymers in the COVID-19 pandemic. *Exp. Rev. Med. Dev.* **2020**, *17*, 477–481. [CrossRef] [PubMed]
- Kumar, S.; Karmacharya, M.; Joshi, S.R.; Gulenko, O.; Park, J.; Kim, G.H.; Cho, Y.K. Photoactive Antiviral Face Mask with Self-Sterilization and Reusability. *Nan. Lett.* **2021**, *21*, 337–343. [CrossRef] [PubMed]
- Quiterio-Gutiérrez, T.; Ortega-Ortiz, H.; Cadenas-Pliego, G.; Hernández-Fuentes, A.D.; Sandoval-Rangel, A.; Benavides-Mendoza, A.; Cabrera-de la Fuente, M.; Juárez-Maldonado, A. The Application of Selenium and Copper Nanoparticles Modifies the Biochemical Responses of Tomato Plants under Stress by *Alternaria solani*. *Int. J. Mol. Sci.* **2019**, *20*, 1950. [CrossRef]
- Pérez-Labrada, F.; López-Vargas, E.R.; Ortega-Ortiz, H.; Cadenas-Pliego, G.; Benavides-Mendoza, A.; Juárez-Maldonado, A. Responses of Tomato Plants under Saline Stress to Foliar Application of Copper Nanoparticles. *Plants* **2019**, *8*, 151. [CrossRef] [PubMed]
- Hernández-Hernández, H.; Quiterio-Gutiérrez, T.; Cadenas-Pliego, G.; Ortega-Ortiz, H.; Hernández-Fuentes, A.D.; Cabrera de la Fuente, M.; Valdés-Reyna, J.; Juárez-Maldonado, A. Impact of Selenium and Copper Nanoparticles on Yield, Antioxidant System, and Fruit Quality of Tomato Plants. *Plants* **2019**, *8*, 355. [CrossRef] [PubMed]
- González-García, Y.; Cárdenas-Álvarez, C.; Cadenas-Pliego, G.; Benavides-Mendoza, A.; Cabrera-de-la-Fuente, M.; Sandoval-Rangel, A.; Valdés-Reyna, J.; Juárez-Maldonado, A. Effect of Three Nanoparticles (Se, Si and Cu) on the Bioactive Compounds of Bell Pepper Fruits under Saline Stress. *Plants* **2021**, *10*, 217. [CrossRef]
- Bashir, F.; Irfan, M.; Ahmad, T.; Iqbal, J.; Butt, M.T.; Sadeq, Y.; Moniruzzaman, M. Efficient utilization of low cost agro materials for incorporation of copper nanoparticles to scrutinize their antibacterial properties in drinking water. *Environ. Technol. Innov.* **2020**, 101228. [CrossRef]

13. Garcia, K.A.; Peroja, K.A.G.; Tuberon, N.A.L.; Cambiador, C.J.B.; Cid-Andres, A.P. Metal incorporated Philippine Abaca fiber (Manila hemp) as a potential novel filter for water disinfection. *J. Phys. Conf. Ser.* **2021**, *1*, 012064. [CrossRef]
14. Tamayo, L.; Azócar, M.; Kogan, M.; Riveros, A.; Páez, M. Copper-polymer nanocomposites: An excellent and cost-effective biocide for use on antibacterial surfaces. *Mat. Sci. Eng. C* **2016**, *69*, 1391–1409. [CrossRef]
15. Gurianov, Y.; Nakonechny, F.; Albo, Y.; Nisnevitch, M. Antibacterial Composites of Cuprous Oxide Nanoparticles and Polyethylene. *Int. J. Mol. Sci.* **2019**, *20*, 439. [CrossRef]
16. Gurianov, Y.; Nakonechny, F.; Albo, Y.; Nisnevitch, M. LLDPE Composites with Nanosized Copper and Copper Oxides for Water Disinfection. *Polymers* **2020**, *12*, 1713. [CrossRef] [PubMed]
17. Jung-Huh, A.; Jik-Kwon, Y. “Nanoantibiotics”: A new paradigm for treating infectious diseases using nanomaterials in the antibiotics resistant era. *J. Contr. Release* **2011**, *156*, 128–145. [CrossRef]
18. Hajipour, M.J.; Fromm, K.M.; Ashkarran, A.A.; Jimenez de Aberasturi, D.; Ruis de Larramendi, I.; Rojo, T.; SErpooshan, V.; Parak, W.J.; Mahmoudi, M. Antibacterial properties of nanoparticles. *Tren. Biotech.* **2012**, *30*, 499–511. [CrossRef]
19. Raffi, M.; Mehrwan, S.; Bhatti, T.M.; Akhter, J.I.; Hameed, A.; Yawar, W.; Hasan, M.M. Investigations into the antibacterial behavior of copper nanoparticles against *Escherichia coli*. *Ann. Microbiol.* **2010**, *60*, 75–80. [CrossRef]
20. Ruparelia, J.P.; Chatterjee, A.K.; Duttagupta, S.P.; Mukherji, S. Strain specificity in antimicrobial activity of silver and copper nanoparticles. *Act. Biomat.* **2008**, *4*, 707–716. [CrossRef]
21. Chen, K.L.; Bothun, G.D. Nanoparticles Meet Cell Membranes: Probing Nonspecific Interactions using Model Membranes. *Environ. Sci. Technol.* **2014**, *48*, 873–880. [CrossRef]
22. Palza, H. Antimicrobial Polymers with Metal Nanoparticles. *Int. J. Mole. Sci.* **2015**, *16*, 2099–2116. [CrossRef] [PubMed]
23. Horst, A.M.; Vukanti, R.; Priester, J.H.; Holden, P.A. An Assessment of Fluorescence and Absorbance-Based Assays to Study Metal-Oxide Nanoparticle ROS Production and Effects on Bacterial Membranes. *Small* **2013**, *9*, 1753–1764. [CrossRef] [PubMed]
24. Radheshkumar, C.; Munstedt, H. Antimicrobial polymers from polypropylene/silver composites-Ag⁺ release measured by anode stripping voltammetry. *React. Funct. Polym.* **2006**, *66*, 780–788. [CrossRef]
25. Palza, H.; Quijada, R.; Delgado, K. Antimicrobial polymer composite with copper micro and nanoparticles: Effect of particle size and polymer matrix. *J. Bioact. Compat.* **2015**, *30*, 366–380. [CrossRef]
26. Damm, C.; Münstedt, H.; Rösch, A. The antimicrobial efficacy of polyamide6/silver-nano- and microcomposites. *Mat. Chem. Phys.* **2008**, *108*, 61–66. [CrossRef]
27. Sierra-Ávila, R.; Pérez-Alvarez, M.; Valdez-Garza, J.; Avila-Orta, C.A.; Jiménez-Regalado, E.J.; Mata-Padilla, J.M.; Soto-Castruita, E.; Cadenas-Pliego, G. Synthesis and Thermomechanical Characterization of Nylon 6/Cu Nanocomposites Produced by an Ultrasound-Assisted Extrusion Method. *Adv. Mat. Sci. Eng.* **2018**, 1–10. [CrossRef]
28. Wu, Y.; Xu, L.; Jiang, Y. Preparation and Thermal Properties of Modified Cu₂O/Polypropylene (PP) Composite. *Materials* **2020**, *13*, 309. [CrossRef] [PubMed]
29. Ramazanov, M.A.; Hajiyeva, F.V. Copper and copper oxide nanoparticles in polypropylene matrix: Synthesis, characterization, and dielectric properties. *Comp. Interf.* **2020**, 1–14. [CrossRef]
30. Palza, H.; Delgado, K.; Pinochet, I. Improving the Metal Ion Release from Nanoparticles Embedded in a Polypropylene Matrix for Antimicrobial Applications. *J. App. Polym. Sci.* **2015**, *41232*, 1–8. [CrossRef]
31. Molaba, M.P.; Dudic, D.; Luyt, A.S. Influence of the presence of medium-soft paraffin wax on the morphology and properties of iPP/silver nanocomposites. *eXPRESS Polym. Lett.* **2015**, *9*, 901–915. [CrossRef]
32. Jardón-Maximino, N.; Pérez-Alvarez, M.; Sierra-Ávila, R.; Ávila-Orta, C.A.; Jiménez-Regalado, E.; Bello, A.M.; González-Morones, P.; Cadenas-Pliego, P. Oxidation of Copper Nanoparticles Protected with Different Coatings and Stored under Ambient Conditions. *J. Nanomat.* **2018**, 1–8. [CrossRef]
33. Sierra-Ávila, R.; Pérez-Álvarez, M.; Cadenas-Pliego, C.; Ávila-Orta, C.A.; Betancourt-Galindo, R.; Jiménez-Regalado, E.; Jiménez-Barrera, R.M.; Martínez-Colunga, J.G. Synthesis of Copper Nanoparticles Coated with Nitrogen Ligands. *J. Nanomat.* **2014**, 1–8. [CrossRef]
34. Sierra-Ávila, R.; Pérez-Álvarez, M.; Cadenas-Pliego, G.; Comparán-Padilla, V.E.; Ávila-Orta, C.A.; Pérez-Camacho, O.; Jiménez-Regalado, E.; Hernández-Hernández, E.; Jiménez-Barrera, R.M. Synthesis of Copper Nanoparticles Using Mixture of Allylamine and Polyallylamine. *J. Nanomat.* **2015**, 1–9. [CrossRef]
35. Cadenas-Pliego, G.; Pérez Alvarez, M.; Avila-Orta, C.A.; Ortega-Ortiz, H.; Betancourt-Galindo, R.; Comparán-Padilla, V.E.; Neira-Velázquez, M.G.; Sierra-Avila, R.; Jiménez-Regalado, E.; Rivera-Orta, V.H.; et al. Síntesis de Nanopartículas Metálicas Modificadas con Polímeros Mediante Ligantes Nitrogenados. Mx. Patent MX/E/2012/081565, 13 2012.
36. España-Sánchez, B.L.; Ávila-Orta, C.A.; Padilla-Vaca, F.; Neira-Velázquez, M.G.; González-Morones, P.; Rodríguez-Gonzalez, J.A.; Hernández-Hernández, E.; Rangel-Serrano, A. Enhanced antibacterial activity of melt processed polypropylene Ag and Cu nanocomposites by argon plasma treatment. *Plasm. Pross. Polym.* **2014**, *11*, 353–365. [CrossRef]
37. Camacho, P.H.; Morales-Cepeda, A.B.; Salas-Papayanopolos, H.; Bautista, J.E.; Castro, C.; Lozano, T. Crystallization behavior of polypropylene/silver nanocomposites using polyethylene glycol as reducing agent and interface modifier. *J. Thermopl. Comp. Mat.* **2015**, 1–16. [CrossRef]
38. Van Erp, T.N.; Balzano, L.; Peters, G.W.M. Oriented Gamma Phase in Isotactic Polypropylene Homopolymer. *ACS Macr. Lett.* **2012**, *1*, 618–622. [CrossRef]

39. Abad, M.J.; Arribas, J.M.; Gómez, M.A.; Marco, C. Análisis de la cristalización dinámica de polipropileno isotáctico en presencia de ácido pimélico. *Rev. Iber. Polim.* **2005**, *6*, 93–110.
40. Boyanova, M.; Balta-Calleja, F.J.; Fakirov, S. New aspects of the $\beta \rightarrow \alpha$ polymorphic transition in plastically deformed isotactic polypropylene studied by microindentation hardness. *J. Mat. Sci.* **2006**, *41*, 5504–5509. [CrossRef]
41. Slouf, M.; Pavlova, E.; Krejčíková, S.; Ostafinska, A.; Zhigunov, A.; Krzyzanek, V. Relations between morphology and micromechanical properties of alpha, beta and gamma phases of iPP. *Polygr. Test.* **2018**, 1–18. [CrossRef]
42. Garbarczyk, J. A study on the mechanism of polymorphic transition $\beta \rightarrow \alpha$ in isotactic polypropylene. *Makr. Chem.* **1985**, *186*, 2145–2151. [CrossRef]
43. Machado, G.; Denardin, E.L.G.; Kinast, E.J.; Goncalves, M.C.; de Luca, M.A.; Teixeira, S.R. Crystalline properties and morphological changes in plastically deformed isotactic polypropylene evaluated by X-ray diffraction and transmission electron microscopy. *Europ. Polym. J.* **2005**, *41*, 129–138. [CrossRef]
44. Lloyd, G.E. Atomic number and crystallographic contrast images with the SEM: A review of backscattered electron techniques. *Mineral. Mag.* **1987**, *51*, 3–19. [CrossRef]
45. Bai, F.; Li, F.; Clahoun, B.H.; Quirk, R.P.; Cheng, S.Z.D. *Polymer Handbook*, 4th ed.; Brandrup, J., Immergut, E.H., Grulke, E.A., Eds.; Wiley-Interscience: New York, NY, USA, 1999; Volume 1, Chapter V.
46. Sahoo, R.K.; Mohanty, S.; Nayak, S.K. Effect of silver nanoparticles on the morphology, crystallization, and melting behavior of polypropylene: A study on non-isothermal crystallization kinetics. *Polym. Sci. Ser. A* **2016**, *58*, 443–453. [CrossRef]
47. Luyt, A.S.; Molefi, J.A.; Krump, H. Thermal, mechanical and electrical properties of copper powder filled low-density and linear low-density polyethylene composites. *Polym. Deg. Stab.* **2006**, *91*, 1629–1636. [CrossRef]
48. Molefi, J.A.; Luyt, A.S.; Krupa, I. Comparison of the influence of copper micro- and nano-particles on the mechanical properties of polyethylene/copper composites. *J. Mater. Sci.* **2009**, *45*, 82–88. [CrossRef]
49. Delgado, K.; Quijada, R.; Palma, R.; Palza, H. Polypropylene with embedded copper metal or copper oxide nanoparticles as a novel plastic antimicrobial agent. *Lett. App. Microb.* **2011**, *53*, 50–54. [CrossRef] [PubMed]
50. Tamayo, L.A.; Zapata, P.A.; Vejar, N.D.; Azócar, M.I.; Gulppi, M.A.; Zhou, X. Release of silver and copper nanoparticles from polyethylene nanocomposites and their penetration into *Listeria monocytogenes*. *Mat. Sci. Eng. C* **2014**, *40*, 24–31. [CrossRef] [PubMed]
51. Kim, J.S.; Kuk, E.; Yu, K.N. Antimicrobial effects of silver nanoparticles. *Nanomed. Nanotech. Biol. Med.* **2007**, *3*, 95–101. [CrossRef]
52. Quiñones-Jurado, Z.V.; Waldo-Mendoza, M.A.; Aguilera-Bandin, H.M.; Villabona-Leal, E.G.; Cervantes-González, E.; Pérez, E. Silver nanoparticles supported on TiO₂ and their antibacterial properties: Effect of Surface confinement and nonexistence of plasmon resonance. *Mat. Sci. App.* **2014**, *5*, 895–903. [CrossRef]
53. Kori, M.A.; Kulthe, M.G.; Goyal, R.K. Influence of Cu Micro Particles on Mechanical Properties of Injection Molded Polypropylene/Cu Composites. *Int. J. Innov. Res. Sci. Eng. Techn.* **2014**, *3*, 14034–14043.
54. Boudenne, A.; Ibos, L.; Fois, M.; Majesté, J.C.; Géhin, E. Electrical and thermal behavior of polypropylene filled with copper particles. *Comp. Part A* **2005**, *36*, 1545–1554. [CrossRef]
55. Ghassan, A.N. Effect of Temperature and Nickel Concentration on the Electrical and Dielectric Properties of Polyethylene-Nickel Composites. *Int. J. Eng. Res. Dev.* **2015**, *11*, 29–38.
56. Shu, X.; Feng, J.; Liao, J.; Zhang, D.; Peng, R.; Shi, Q.; Xie, X. Amorphous carbon-coated nano-copper particles: Novel synthesis by Sol-Gel and carbothermal reduction method and extensive characterization. *J. Alloy. Compd.* **2020**, 156556. [CrossRef]

Article

Finite Element Modelling and Experimental Validation of Scratches on Textured Polymer Surfaces

Weimin Gao^{1,2,*} , Lijing Wang³, Jolanta K. Coffey⁴, Hongren Wu¹  and Fugen Daver^{1,*} ¹ School of Engineering, RMIT University, Melbourne, VIC 3001, Australia; henry.wu@rmit.edu.au² School of Metallurgy and Energy, North China University of Science and Technology, Tangshan 063600, China³ School of Fashion and Textiles, RMIT University, 25 Dawson St, Brunswick, VIC 3056, Australia; Lijing.wang@rmit.edu.au⁴ Ford Motor Company, Research and Engineering Product Development Centre, 20901 Oakwood Blvd, Dearborn, MI 48124-4077, USA; jcoffey4@ford.com

* Correspondence: weimin.gao@rmit.edu.au (W.G.); fugen.daver@rmit.edu.au (F.D.)

Abstract: Surface texturing is a common modification method for altering the surface properties of a material. Predicting the response of a textured surface to scratching is significant in surface texturing and material design. In this study, scratches on a thermoplastic material with textured surface are simulated and experimentally tested. The effect of texture on scratch resistance, surface visual appearance, surface deformation and material damage are investigated. Bruise spot scratches on textured surfaces are found at low scratch forces (<3 N) and their size at different scratch forces is approximately the same. There is a critical point between the bruise spot damage and the texture pattern damage caused by continuous scratching. Scratch resistance coefficients and an indentation depth-force pattern are revealed for two textured surfaces. A texture named “Texture CB” exhibits high effectiveness in enhancing scratch visibility resistance and can increase the scratch resistance by more than 40% at low scratch forces. The simulation method and the analysis of the power spectral density of the textured surface enable an accurate prediction of scratches.

Keywords: textured surface; scratch; scratch resistance; thermoplastic polymer; finite element modelling

Citation: Gao, W.; Wang, L.; Coffey, J.K.; Wu, H.; Daver, F. Finite Element Modelling and Experimental Validation of Scratches on Textured Polymer Surfaces. *Polymers* **2021**, *13*, 1022. <https://doi.org/10.3390/polym13071022>

Academic Editor: Somen K. Bhudolia

Received: 28 February 2021

Accepted: 22 March 2021

Published: 25 March 2021

Publisher's Note: MDPI stays neutral with regard to jurisdictional claims in published maps and institutional affiliations.



Copyright: © 2021 by the authors. Licensee MDPI, Basel, Switzerland. This article is an open access article distributed under the terms and conditions of the Creative Commons Attribution (CC BY) license (<https://creativecommons.org/licenses/by/4.0/>).

1. Introduction

Surface texturing is a common functionalization method for altering the surface properties of a material or component. The most successful application of surface texturing in engineering is in the improvement of tribological performance [1–5]. Its applications have rapidly expanded, along with contributions in various fabrication techniques [6–10]. This paper focuses on producing hard textured polymeric parts with good scratch/mar resistance and durable gloss levels through surface topography modification.

The texturing of polymeric parts can be achieved either via direct patterning or by replicating the surface of a tool with a specified topography, such as wood or leather [11,12]. It was found that certain textures could increase scratch resistance and conceal the surface damage of polymeric materials [13,14]. This has led to an increased focus on understanding how surface texture influences surface damage features, and scratch resistance and visibility [13,15–18]. The surface damage features demonstrate both brittle and ductile modes of deformation which are sensitive to the contact properties in scratching [19,20]. The contact features such as the force magnitude, the normal versors, and the principal curvatures greatly depend on the contact point, when the size of the scratch tip is lower than the grain size of the rough surface or textured surface. The scratch resistance and visibility on polymer surfaces are other major concern areas of material scientists. These are complex issues that involve the physical deformation of material, the surface damage features and the surface optical properties. These features become more complicated when scratching on rough and textured surfaces is considered. There are an extremely large

number of surface textures being used in various materials and products for different purposes, such as improving tribological performance, scratch resistance, thermal resistance, visual appearance, additive manufacturability, wettability, biocompatibility, and light absorbability.

The load scratch test is an effective and widely used method to assess surface texture and investigate the failure of substrate material. Although laboratory-based experimental testing can be used to evaluate the capability of an existing texture in terms of scratch resistance and material damage [15,21,22], it is a time-consuming and capital-intensive process for a new texture; for instance, examining a new texture on a thermoplastic polymer plaque includes mold design and making, material preparation, sample injection and cooling, scratch test, and analysis of results. Most existing surface damage models consider the scratch force, material properties, and the viscoelastic–viscoplastic behavior of material in the case of polymeric material scratches [23], but seldomly take into account the roughness and texture of the surfaces. The prediction of a new surface texture on the scratch properties of the material is also of significant interest to both academia and the manufacturing industry for scratch management. Computer simulation is a straightforward method for predicting the scratch properties of materials. However, a literature review conducted by the authors shows that only a few simulation studies are focused on the influence of surface texture. Almost all simulations are only for smooth surfaces without large material deformation and damage, and are aimed at studying the material behaviors during indentation [24,25] and scratching [26–31], the influence of material mechanical properties (elastic modulus, yield strength, Poisson’s ratio, coefficient of friction) [17,32–37], type of materials [24,26,27,38], surface texture [22,39–41] and roughness [42,43], interface interaction between rough material surface and scratch tip [44–48], and scratch visibility [18,49,50].

Textured surfaces render scratch simulation more challenging, adding to the difficulty of simulating large deformations and damage of materials [39,51]. The failure mechanisms of materials, e.g., cracking, chipping, and delamination, will greatly depend on the local contact behavior. They may include continuous deformation of the roughness zone and substrate and the deformation of only asperities. The apparent friction coefficient also varies during scratching when the characteristic wavelength of the texture is larger than the size of the scratch tip, due to the change of the ratio between the tangential force and the normal load.

In order to determine the scratch simulation of a textured surface for the investigation of a certain problem, the four characteristic lengths are associated, namely the scratch tip size, the wavelength of the texture pattern, the roughness (micro and nano roughness) of the surface, and the wavelength of the waves involved in the problem or the surface function. In the case of studying scratch visibility, the roughness should be considered in the simulation as it governs the surface–object contact and flow of light over the scratched surface. Both influence the visual appearance of the scratched surface. Contact interaction occurs between rough surfaces. In the case of most interfacial phenomena, the accuracy of simulation relies to a large extent on the accurate description of geometrical contact between surfaces of any given roughness [52]. In the case of polymer scratch, it is associated with appropriately defined friction properties. In finite element method (FEM) simulations, the influence of surface roughness on light flow that manipulates the visual appearance of the rough surface has not yet been discussed. It is desirable to compute the photorealistic appearance of the surface in the real world and, thereafter, study the ability of the texture to conceal scratches and the behavior of textured surfaces in reducing the visibility of scratches. The human ability to identify scratch damage relies on the visual capacity of the eyes. A human eye can identify a spatial pattern separated by a visual angle of $1/60^\circ$ [53], at which angle the viewing distance must be less than 10 cm for an object of $30\ \mu\text{m}$ or a resolution of ~ 900 dpi to be discerned. For instance, the size of roughness of an interior trim polymeric component used in automobiles can be as low as $20\ \mu\text{m}$. The change in surface topography that occurs at low scratch impacts is at such a level of asperity. It is well-known that human eyes show different color sensitivities [54]. The human visual perception is also

highly sensitive to the structural information in a scene; it can extract information from similar textures and similar structures [55,56]. Therefore, studies on the scratch visibility of polymers [15,18,35] show that different textures possess different visibility resistance.

The features of scratches on the surfaces with different texture patterns have been systematically studied experimentally [13,15]. It was found that texture pattern significantly influenced scratch resistance and visibility. Our previous study of scratch modelling on smooth surfaces [30,39] demonstrated the large dependence of scratching process, material deformation and material damage features on contact properties, indicating that the scratch process and material failure mechanism on a textured surface would be very different to that of scratching on a smooth surface. To study the surface deformation and damage, the failure mechanisms of materials, and the functions of textured surfaces subjected to scratching, scratch simulation needs to be carefully constructed to capture all essential aspects related to the problem. In this study, we present simulation and experimental results of scratches on thermoplastic plaques with different textured surfaces and discuss the effect of texture, as well as visual scratch identification. A simulation method and the knowledge of the power spectral density (PSD) of the textured surfaces were used to accurately predict scratches and to examine the performance of the model in capturing their texture patterns and roughness features. The simulation results are evaluated via scratch experiments at different scratch forces and show accurate prediction of scratches for commercial surface textures.

2. Experimental

The samples used are injection-molded thermoplastic plaques. The material is a commercial polypropylene product (ADX5017 supplied by Advanced Composites, Inc., Ohio, USA). The plaques were molded with different surface textures.

The power spectral density (PSD) was used to analyze the surface roughness of the plaques. PSD is a fractal method that is considered as one of the better characterization techniques of surface topography and has been used by different researchers [57,58]. A detailed discussion of PSD can be found in the references [59,60]. In brief, a surface PSD is the Fourier transform of the autocorrelation function of the 2D surface height data, decomposing the rough surface into contributions from different spatial frequencies (wavevectors). The radial average on the Fourier transform of surface topography is generally used for isotropic surfaces and a 2D power spectrum, 2D-PSD, is obtained.

The PSD provides a representation of the amplitude (C) of surface roughness as a function of the spatial frequency (q) of the roughness. The PSD can also reveal possible periodic surface features of the texture and how the features are distributed. Figure 1 shows how the PSD of a rough surface changes when it includes a texture. The left and right PSD peaks, at $q = 3 \times 10^3 - 1 \times 10^4 \text{ m}^{-1}$, of the texture and the synthesized surface in Figure 1d are the representation of the texture distribution in X and Y directions, respectively. In general, the area under the PSD curve is equal to the square of the root mean square roughness (R_{RMS}^2 , with unit of m^2), i.e., the square of the standard deviation of surface heights (σ^2) for the present case. Higher PSD values associate with rougher surface geometries. The spatial frequency of the roughness (wavevector: Q) is the inverse of the wavelength of the roughness features. The slope of the decay at higher spatial frequencies is determined by the Hurst exponent (H), which is directly related to the fractal dimension of a surface topography. A Hurst exponent with higher values indicates a smoother trend, less volatility, and less roughness [61].

Scratch tests on the plaques were conducted with the TABER® multi-finger scratch/mar tester (Model 710). The textured surfaces and scratched surfaces were captured using a Cannon SLR camera equipped with a macro lens. The camera was tilted at a fixed angle from the surface normal, and a fluorescent light source placed opposite to the camera was adjusted to best highlight the scratches.

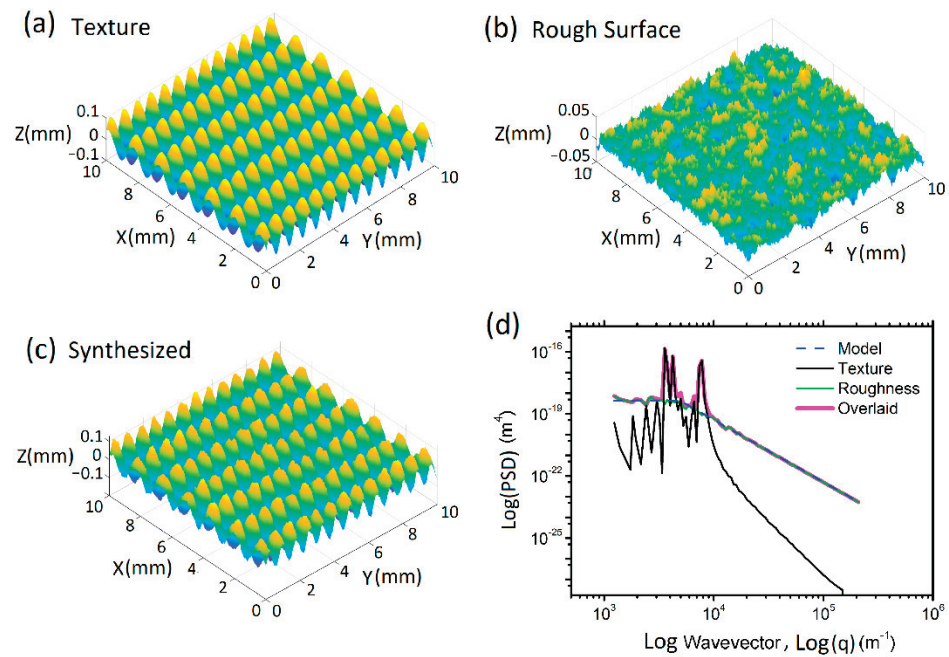


Figure 1. Example of PSD (d) for a textured surface (c) synthesized with a smooth texture (a) and a rough model (b). The smooth texture is 0.1 mm high; its wavelengths in X and Y directions are 1.58 mm and 0.79 mm, respectively. The rough surface has RMS = 10 μm , Hurst exponent $H = 0.5$, and surface resolution $dx = 20 \mu\text{m}$. q_r , q_L and q_s indicate roll-off, large and small wavelength cut-offs.

To evaluate the simulation results, the laboratorial scratch tests were conducted on different textured surfaces at fixed loads of 2 N, 3 N, 7 N, 10 N and 15 N using a steel scratch finger with a spherical tungsten carbide tip, 1 mm in diameter, and scratch speed of 100 mm/s. Images of the scratched surfaces were captured using a high-resolution camera under a light source that was adjusted to render the scratches on the surfaces noticeable. An image processing and analysis (IPA) program was developed with MATLAB and the Image Processing Toolbox to automatically identify the scratches from the textured patterns and parameterize the features of each scratch. The IPA system consists of six modules: image preparation, integration, background filtration, pattern filtration, scratch identification, and scratch characterization. The image preparation is designed to select a region for analysis and adjust the selected section if it is distorted. The image intensity is then integrated along defined coordinates. The background and pattern are filtered to eliminate the deviation of light source influence over the panel and the intensity response to the panel patterns. The identification and characterization of scratches are based on the peaks of the intensities of the filtered image data.

For instance, Figure 2a shows the image of the SB texture and five scratches on it, with the positions of the detected scratches highlighted using the IPA program. The background of the image was filtered. The intensity of each pixel in contrast to the background was then measured to calculate the features of the scratches, as shown in Figure 2b. The larger variances in pixel intensity clearly show the positions and sizes of the five scratches. The values of the differences in intensity were used to evaluate the visibility of the scratches.

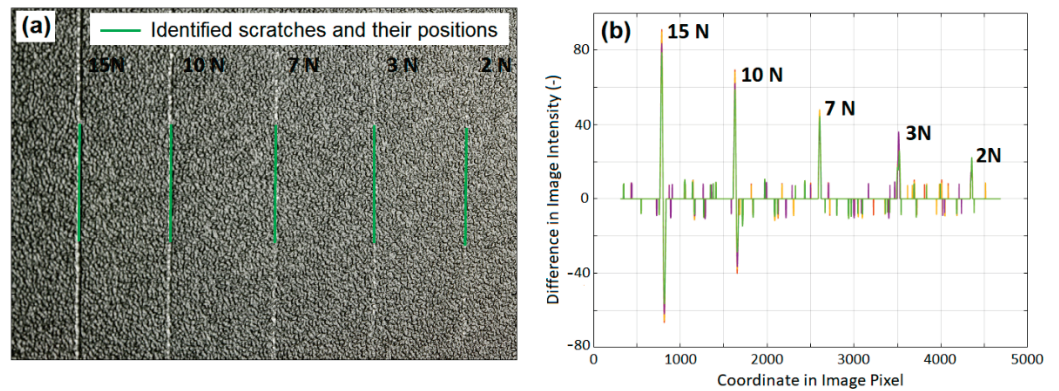


Figure 2. (a) Scratches identified and their positions (indicated by short green lines) on SB texture, and (b) Image intensity difference in contrast to background for calculating the properties of the scratches.

3. Textured Surface Model and Scratch Modelling

3.1. Textured Surfaces

Figure 3 shows two different textures. The height profile of a small surface section of each texture was also presented to identify the features of the surfaces. The textured surfaces consist of primary patterned coarse grains and random small peaks and pits on the grains. The shallow bump (SB) texture (Figure 3a) is comprised of worm-like islands with fine peaks. The coarse bump (CB) texture (Figure 3d) consists of large and tall islands with small craters densely distributed over the island surface and small bumps in the basin. The features of them are summarized in Table 1.

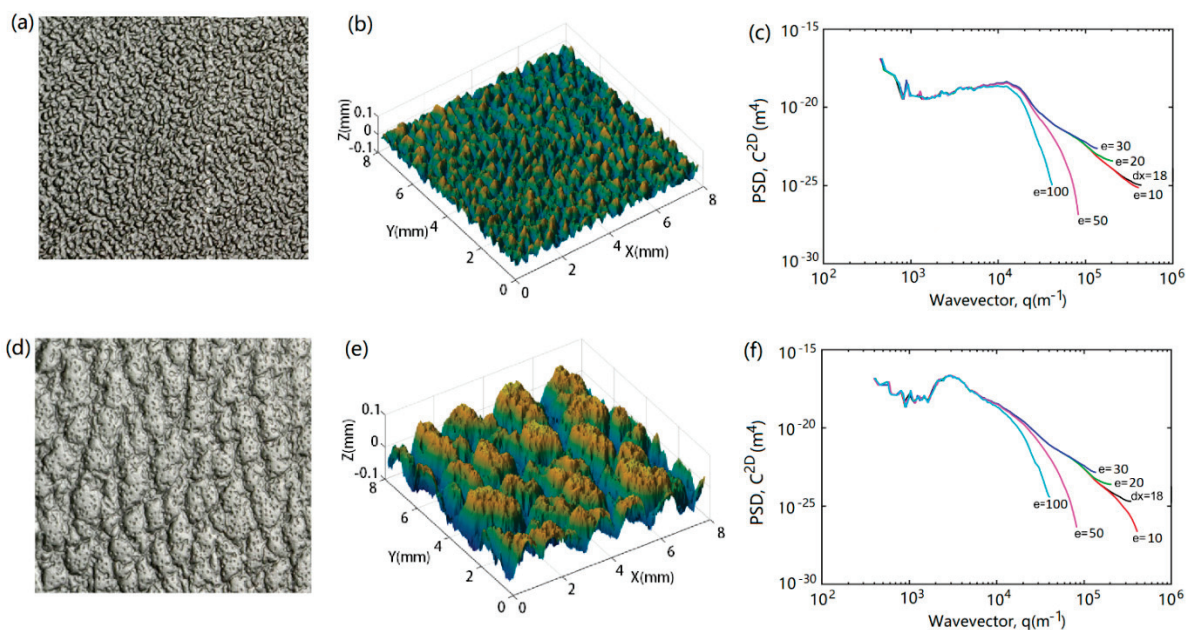


Figure 3. Images of textured surfaces of (a) shallow bump (SB), (d) coarse bump (CB), and (b,e) their respective local 3D scanned profiles and (c,f) radially averaged 2D PSD, C^{2D} , for original sample ($dx = 18 \mu\text{m}$) and square-meshed surfaces ($e = 10\text{--}100 \mu\text{m}$). The surface is isotropic such that C^{2D} is radially symmetric, and the radial average is provided; dx is the average resolution size of the 3D scanned surfaces; e is the element size of surface meshes.

The radially averaged 2D PSDs of the textured surfaces are given in Figure 3c,f, revealing the inherent characteristics of the coarse grains and surface roughness. The curves of $dx = 18 \mu\text{m}$ in Figure 3c,f show the PSDs of the original SB and CB textures, respectively. The data at about $q = 2 \times 10^3 - 2 \times 10^4 \text{ m}^{-1}$ in Figure 3c represent the size and distribution of the islands in the SB texture. The wide range of q indicates that the islands are long with varying lengths. The islands are worm-like and have average thickness of

213 μm . The spacing between islands is about 460 μm . At $q = \sim 2 \times 10^4 \text{ m}^{-1}$ the Hurst exponent H changes. H is low at $q > 2 \times 10^4 \text{ m}^{-1}$, while H becomes high at $q = 2 \times 10^4 \text{ m}^{-1}$. The drop of the PSD at low q ($< 10^4 \text{ m}^{-1}$) approximately stops at $q = \sim 2 \times 10^3$. These are attributed to the contribution of the worm-like islands in the SB texture. The obviously high values of C^{2D} at about $q = 2 \times 10^3 \text{ m}^{-1}$ in Figure 3f indicate the features of the large islands of the CB textures. These islands are approximately 120 μm high and 700 μm in width. The obviously high PSD profile at $q = 1.3 \times 10^3 - 5 \times 10^3 \text{ m}^{-1}$ is attributed to the large and tall islands. The contribution of the islands is much similar to the influence of a texture on a rough surface illustrated in Figure 1. The PSD at higher q reveals the features of the small peaks, craters, and bumps. A close comparison of the PSD data for $q > 2 \times 10^4 \text{ m}^{-1}$ in Figure 3 reveals that they are approximately the same, indicating that the peaks in the SB texture and the craters and bumps in the CB texture have approximately the same characteristic size and distribution features over the surfaces.

Table 1. Parameters of surface features (in μm).

Texture	Shape of Grain	Max Height	Grain Size *	Grain Spacing *	R_A
Shallow Bump	Sharp	0.070	213 (124)	460 (217)	3.56
Coarse Bump	Round	0.110	700 (374)	1856 (466)	2.52

* The data are the average values; standard deviations given in brackets.

3.2. Surface Models

The meshing of materials is a critical step in simulations employing the FEM. Unlike the meshing of materials with ideal smooth surfaces, whose geometrical features would be fully obtained if an appropriate mesh size were to be adapted based on the grid independent of the analysis of the simulation results, the meshing of rough surfaces becomes an important issue when the interface interaction is significant, such as, in addition to the modelling of scratch and material damage that will influence the visual perception of the polymer surface in the present work, the modelling of wear, friction, contact electrical conduction, contact thermal conduction, and fluid transport over rough solid surfaces [45,52,62]. It is difficult to build a model of a real rough surface and, generally, the rough surface is simplified to save simulation costs, including the requirement for hardware and computing time. One simplification is to describe the rough surface as consisting of larger hills and valleys, called asperities, neglecting the smaller rough peaks and pits. In other words, the contact interaction is that of asperity against asperity. In the scratching of the textured polymeric surfaces shown in Figure 3 with a spherical tip, the interaction is that of contact between a smooth sphere and a rough surface. When the scratch tip size (for instance, diameter of 1 mm) is much greater than those of the small peaks and craters (for instance, the root mean square height of the SB and CB rough surfaces, $h_{\text{RMS}} < 20 \mu\text{m}$, when eliminating the contribution of the islands), the textured surfaces, as illustrated in Figure 3, can be filtered to only include the primary patterned islands in the simulation of scratches on polymeric plaques if the aim is to study material deformation (scratch formation) and failure, or to examine the material properties, texture pattern, or scratch load [39]. However, the optical properties of the scratches cannot be accurately studied, as the smaller peaks, craters, and bumps play an important role in influencing the flow of light.

A rough surface model that accurately represents the real textured surface is essential for the scratch simulation to yield results closer to the actual changes in surface topography. Therefore, the element size for meshing the surface must be carefully determined. The model should capture all the surface features that affect the transport of light. Meshing very small peaks and tips would result in exponential increases in the number of elements and computing time. Employing unstructured surfaces and volume meshes would help capture more features of rough surfaces.

In this work, a three-dimensional laser scanning system was used to capture the surface geometry of the plaques and the standard triangulation language data was converted to a 2D surface height matrix, $Z(x, y)$, via MATLAB. The rough surface models were then generated based on the measured surface height matrix, $Z(x, y)$, of the SB and CB textures. The textured surfaces were tested using different mesh sizes and were analyzed via the PSD method, as shown in Figure 3. The results showed that when the element size was smaller than the resolution of the scanned surface ($e \leq dx$), most features of the textured surfaces could be captured. At $e = 20 \mu\text{m}$ and $e = 30 \mu\text{m}$, the Hurst exponents, H_s , are the same, but q_s reduces with the element size. This indicates that, when a $20 \mu\text{m}$ mesh was used, only very small surface roughness features were filtered out. When $e > dx$, an increasing number of small-scale roughness features was lost with an increase in mesh size. When a $30 \mu\text{m}$ mesh was used, the tops of the peaks on the worm-like islands in the SB texture and the roughness of the small craters over the large island surface and smaller bumps in the basin of the CB texture were filtered out. Hurst exponent H increases when the element size is larger than $30 \mu\text{m}$, i.e., $H(e = 100) > H(e = 50) > H(e = 10-30)$. This indicates that the surfaces become smooth with the increase in mesh size. When larger meshes (50 to $100 \mu\text{m}$) were used, the small peaks, craters, and bumps in both the textures were completely removed. A few features of the worm-like islands in the SB texture were additionally filtered, as shown in Figure 3c, when the mesh size was increased to $100 \mu\text{m}$. In short, knowledge of the PSDs of the samples and meshed surfaces can aid in the quantitative examination of the mesh size required to capture the desired features of the rough surface. For the textured surfaces used in this work, meshes smaller than $30 \mu\text{m}$ can capture the small roughness features. Meshes larger than $50 \mu\text{m}$ are not recommended for meshing the surfaces, as this would entail the loss of texture patterns to a certain extent, especially in the case of the worm-like islands in the SB texture.

3.3. Scratch Modelling

In the scratch simulations, the material is described as a hyperelastic and viscoelastic model, which was generated from its compression strain-stress curve by MCalibration. The model is a parallel rheological framework (PRF) model, which uses a Yeoh hyperelastic model for the elastic behavior of the polymer and three power-law strain flow models for modeling the viscoelastic behaviors [63]. The four networks connect in parallel. The description of the PRF model and its formulation are given [64] and the parameters are listed in Table 2.

Table 2. Yeoh and PRF constants for ADX-5017.

Yeoh Constants				PRF Constants			
C_{10}	1.71396	S_1	122.537	S_2	62.0356	S_3	12.579
C_{20}	-0.20298	τ_{Base1}	18.9996	τ_{Base2}	15.8083	τ_{Base3}	12.5455
C_{30}	0.0174978	n_1	14.2556	n_2	14.5184	n_3	11.6288
κ	2000	m_1	-0.499632	m_2	-3.01084×10^{-4}	m_3	-3.24107×10^{-6}

The model was also compared to an elastic-plastic with isotropic hardening (EPI), where the plastic model was described by 10 terms to best match the experimental data set [30]. The square of the correlation between predicted stresses and experimental stresses, R^2 , was calculated as the evaluation parameter and it shows $R^2 = 0.984$ for the PRF model and $R^2 = 0.997$ for the EPI model, respectively. The different material models have been compared for their application in modelling polyethylene terephthalate, high-density polyethylene, polytetrafluoroethylene and other polymers [65]. It shows that the parallel network model with two power flow networks and the elastic-plastic with isotropic hardening model have approximately the same model calibration error when they are applied for thermoplastic polyester.

The scratch simulation consists of two steps, as shown in Figure 4—the indentation process (step 1) and scratching (step 2). The scratch tip in contact with the material surface was first pushed down. The vertical force was linearly increased in intervals of 0.05 s up

to a specified force (from A to B). The tip then moved horizontally over the rough surface along the Y direction at a speed of 100 mm s^{-1} (travelling 6 mm in 0.06 s) at the specified force (from B to C). Then, the load-controlled scratching covered more than 10 large grains of the SB texture and more than two large islands of the CB texture. The scratch started at the point of $X = 2.5 \text{ mm}$ and $Y = 1 \text{ mm}$. The scratch tip in the X direction was restricted such that straight scratches were produced. The bottom faces were fixed, and zero displacement was applied for both +Y and -Y boundaries in the simulation, while the symmetrical boundary condition was applied for the +X and -X faces. The simulations were performed for scratch forces that were the same as those applied in the experiments. In the simulation, the friction coefficient, μ , decays exponentially from the static value, μ_s , to the kinetic value, μ_k , according to the Formula:

$$\mu = \mu_k + (\mu_s - \mu_k)e^{-d_c s} \quad (1)$$

where d_c is the decay coefficient, and s is the sliding velocity. The static friction coefficient, the kinetic friction coefficient, and the decay coefficient (μ_s , μ_k , and d_c) were experimentally measured on a smooth surface plate of the same material as the rough surfaces. They are 0.102, 0.086 and 0.25, respectively.

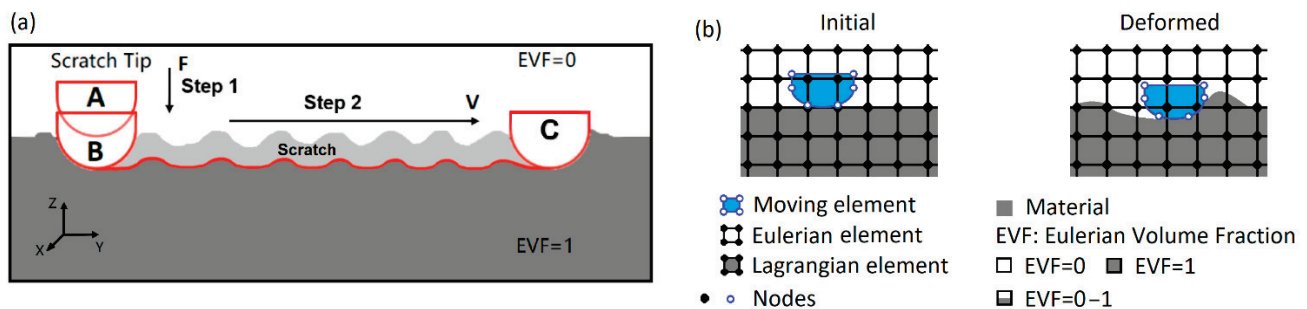


Figure 4. (a) Schematic of simulation model and (b) the concept of CEL method for scratching.

The coupled Eulerian–Lagrangian (CEL) method [66,67] was employed for the scratch simulation considering the very complex surface textures and roughness, and the extreme material deformation and damage involved in the scratching, as shown in Figure 4b. This numerical technology combines the Lagrangian and Eulerian meshes in a single analysis, wherein the material inside the Eulerian region is quantitatively represented by the Eulerian volume fraction (EVF). The Lagrangian object can move inside the Eulerian domain and interacts with the Eulerian material when they come in contact. The interaction between Eulerian and Lagrangian meshes is described with contact algorithms [63]. For the fundamental of the CEL method, the reference [68] is proposed. For scratching on the polymer surface, the Eulerian material is the polymer. The plaque domain (the grey region in Figure 4) is discretized using the Eulerian mesh and also set as Lagrangian meshes, while the domain above the rough surface (the white region in Figure 4) is the Eulerian region only. The interface between these two kinds of meshes, i.e., between the scratch tip and the polymer surface, will change with the motion of the Lagrangian scratch tip. In the present work, the contact between the scratch tip and polymeric material was expressed using a general contact algorithm based on the penalty contact method. The CEL approach combines the advantages of Lagrangian analysis in deformable mesh and Eulerian formulation in the spatial movement of continuum, and this has been demonstrated via the simulation of materials undergoing large deformations [69–71] and its merits and shortcomings in the application to model the deformation of polymers, compared to the Abaqus/Explicit arbitrary Lagrangian–Eulerian (ALE) adaptive meshing method, were discussed by Gao et al. [30].

4. Results and Discussion

4.1. Features of Modelled Texture Surfaces

A model with a surface area of 5 mm × 8 mm and thickness of 3 mm was created for each plaque, as shown in Figure 5. The scratch was performed on a 4 mm × 7 mm textured surface. The plain area extending from the rough surface makes the plaque model sufficiently large such that changes in strain/stress during scratching occur only within the center and do not spread to the boundaries of the model. Contrarily, meshing can be easily handled to reduce the number of meshes.

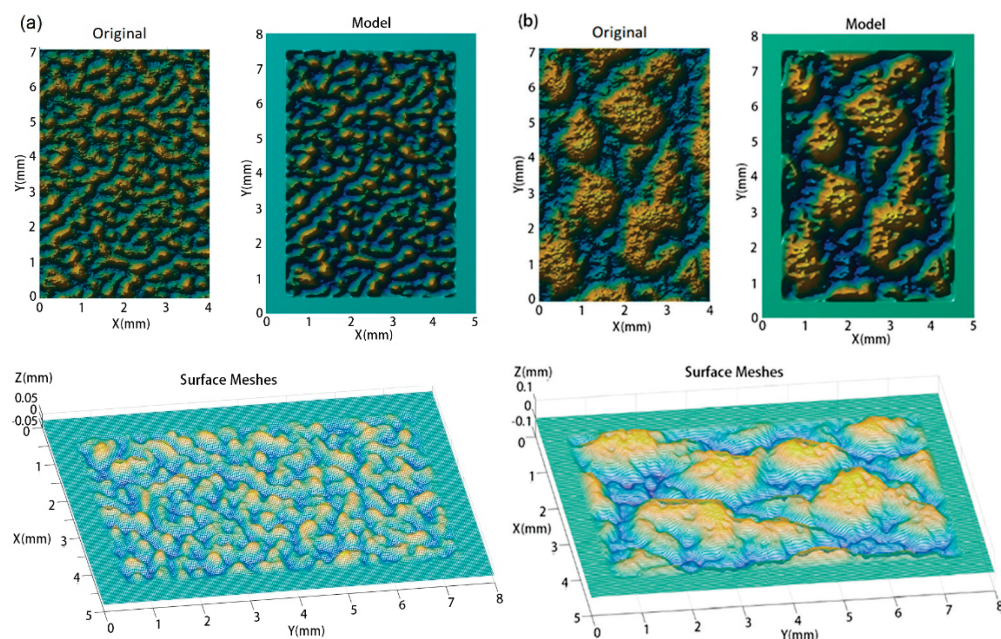


Figure 5. Original sample surface, model, and surface meshes for (a) SB texture, and (b) CB texture. The original surfaces include all small peaks. The models capture the texture features, small peaks and craters shown in the original surfaces. A 0.5 mm plain margin around the texture was created to extend the plaque model size.

The modelling results of $e = 30 \mu\text{m}$ in Figure 5 show that the model for the SB texture captured the worm-like islands and their peaks. As shown in Figure 5a (original and model), the model includes the islands and all the obvious peaks on each island, but some sharp peaks and dips were filtered out as indicated by the Z-scale, which reduced from the original scale of +0.06 mm to -0.06 mm to the scale of +0.04 mm to -0.04 mm. As shown in Figure 5b, only the sharp dips of the CB textured surface were filtered. The Z-scale changed from the original scale of +0.06 mm to -0.08 mm to the scale of +0.06 mm to -0.06 mm. Figure 3 shows that the model for the CB texture captured the islands, craters on the top of the islands, and peaks in the basin. Comparing the modelled textures with the texture surface images as presented in Figure 3, it can be concluded that the scale of roughness replicated in the models is identical to that captured by the high-resolution digital camera. This is important in studying the effect of the textured surfaces on the visibility of scratches and damage. The characteristic size of the surface grains captured is much lower than the identifiable size by a normal human eye at a viewing distance of less than 10 cm. The change in roughness that can be resolved by the human eye at very small viewing distances can, therefore, be simulated using the model.

Figure 5 clearly shows the aforementioned texture pattern features. The worm-like islands in the SB texture and the small craters on the top of the islands and small bumps in the basin in the CB texture are more clearly seen in Figure 5 than in Figure 3. The worm-like islands have a wide range of lengths, which are represented by the PSDs at $q = \sim 2 \times 10^3 - \sim 2 \times 10^4 \text{ m}^{-1}$ in Figure 3c, as described above. Their width and spacing

are small and approximately the same. These features are represented by higher PSDs at a spatial frequency of $\sim 2 \times 10^4 \text{ m}^{-1}$.

4.2. Indentation and Scratch Resistance

Figure 6 shows the displacement of the indenter at different forces and at different force-loading rates. The data were from different indentation processes, i.e., the step one in the scratching simulations, where the force was linearly increased. The surface here refers to the median plane of the surface texture, so that the initial point of contact (IPC) locates at the top of the surface, showing a negative distance from the sample surface in Figure 6. Note that IPC depends on the position of the indentation in relation to the texture pattern. The indenter moved through the textured surface of 0.08 mm in thickness and reached the substrate surface at a force of about 4 N. The displacement is shown as a nonlinear function of the force in this step. The surface deformation or damage caused by the indenter would not lead to a visually observable change of the surface appearance. The typical linear indentation regime was finally reached with a further increase in the load, as indicated in the figure.

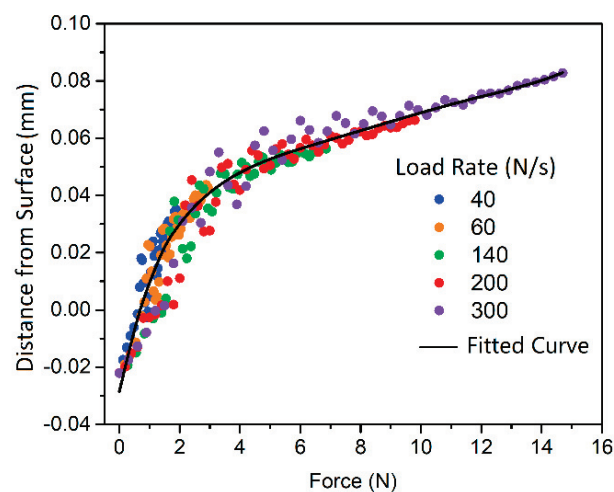


Figure 6. Force and indentation depth at different force-loading rates for rough surface.

The scratch resistance was calculated based on the forces in the scratching step of the simulations. The resistance coefficient (μ_R) is defined as the ratio of the force in the scratching direction to the scratch force. Figure 7a shows the instantaneous μ_R of pattern CB during scratching under different forces. The fluctuation of μ_R relates to the pattern and the kinetic energy of the indenter. Skipping of the indenter over the rough surfaces was observed. The zero values of μ_R at 2 N and 3 N are due to there being no interaction of the indenter with the surface. The indenter recontacted the surface at a high energy and a higher contact angle, leading to a normal contact force that is much higher than the specified scratching force. This resulted in the high values of μ_R at the recontact periods. It seems that there is a contact frequency that increases with the load. When the force approached 7 N, the contact became continuous and the main component of μ_R fluctuation was caused by the texture profile.

The resistance coefficients were averaged. Figure 7b shows the mean of μ_R of rough surfaces CB and SB to different scratch forces. The results show that the surface with texture CB has a higher scratch resistance than the surface SB. This has been demonstrated by the experiments and will be discussed in the following sections. To evaluate the function of the textures in increasing the scratch resistance, the results were compared to a smooth surface. The smooth surface shows a linear relationship of the resistance and the scratch force. It is interesting to note that texture SB resulted in a lower resistance to high scratch forces compared to the smooth force, but a higher resistance to low scratch forces. The most significant for the effect of the pattern is the substantially high resistance coefficient

of surface CB, especially at low scratch forces. It is effective in increasing the scratch resistance.

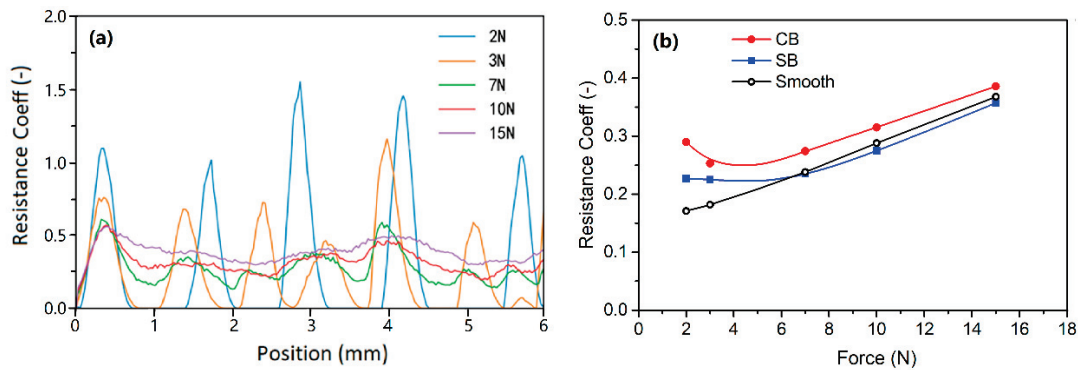


Figure 7. (a) Instantaneous resistance coefficient in scratching and (b) scratch resistance coefficients of different surfaces.

4.3. Surface Appearance

The scratches simulated on the SB and CB textures and the experimental results are presented in Figures 8 and 9, respectively. The simulated and test scratches appear the same. It is difficult for the human eye to discern the scratches at 2 N on the SB texture and at 2 N and 3 N on the CB texture from the rough textures. Moreover, the scratch at 2 N on the CB texture could not be identified, as any variation in the surface was obscured by the texture pattern and random roughness. However, it can be detected by analyzing the digital color information using the IPA technology [15]. Close observation, i.e., enlargement, of the scratches clearly shows some bruise spots among the textures. Although too minor to be observed by the human eye, they changed the profiles of grains and surface roughness, thereby influencing the flow of light and, as a result, rendering themselves detectable. At higher scratch forces (such as >10 N), continuous scratches were formed and significantly influenced the appearance of the structured polymeric surfaces.

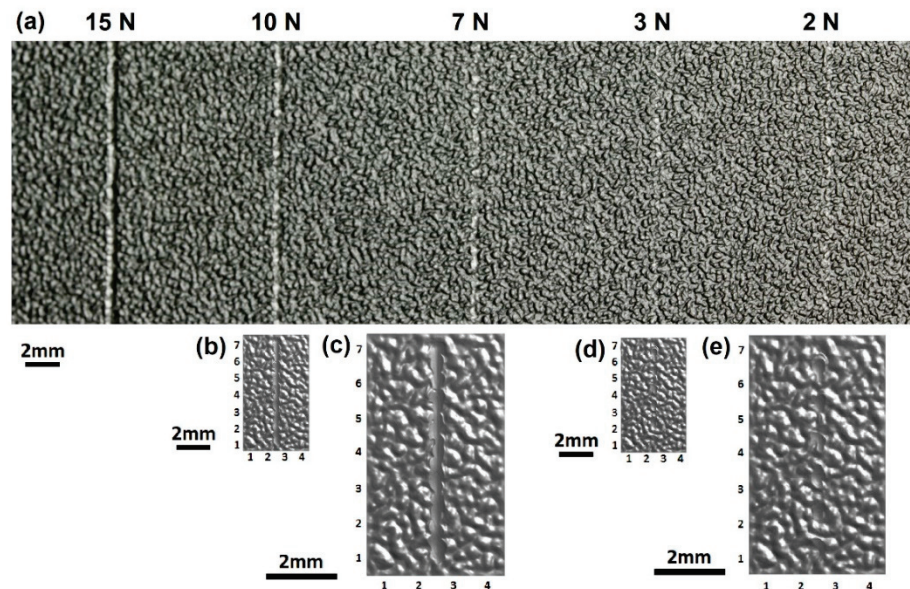


Figure 8. Images of scratches (a) produced by instrument under different forces and simulated under (b,c) 10 N and (d,e) 3 N on the SB texture. Images (c,e) are enlarged views of the simulated scratches presented in (b,d).

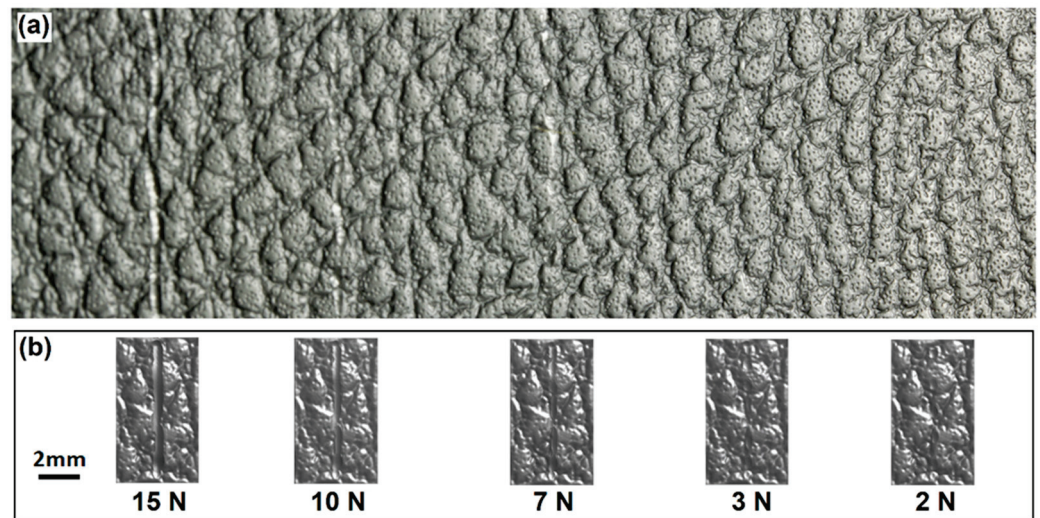


Figure 9. Images of scratches produced under different forces on the CB texture. (a) experiment and (b) simulation.

It is well-known that the visual appearances of the textured surfaces and scratches depend on the lighting condition, colors of the plaque surface, position of observation, and performance and position of the camera. The simulations produced more identifiable and clearer scratches than the experimental tests, not only because the simulation provided the geometric profile of the scratched surfaces but also because the images of the simulated scratches were produced by computer rendering with the clearest lighting. This demonstrated the merits of the finite element method in modeling scratches and the importance of the simulation result rendering in the prediction of the visual appearances of scratches, especially if the simulated scratches are rendered under lighting conditions and image capturing parameters equivalent to experiments.

4.4. Surface Damage and Scratch Size

The features of the scratches on the textured surfaces were quantitatively described by two parameters: Average width, \bar{W} and transverse (the X direction in the simulation model) width, \bar{W}_T . The average width was calculated by dividing the deformed surface area by the length of the path of the scratch tip (L_S), as shown in Figure 10a. The transverse width is the average of the maximum transverse dimensions (W_T) of the scratched areas. The surface damage was described by the scratched volume, V_S , and the debris volume, V_B , per length along the scratch, as shown in Figure 10b. The deformed surfaces, scratch volume and debris volume were determined by comparing the original and scratched surface profiles. The results are shown in Figure 11.

The simulation predicted the scratch profile and deformation of the material very well. At low forces, bruise spots on the surface grains were produced by the scratch tip, as illustrated by the scratches at 2 N, 3 N and 7 N in Figures 8, 9 and 12. The bruise spots are owed to the jump of the tip over the surfaces [72] and do not change the texture pattern, as shown by the enlarged scratches in Figures 8e and 12. The scratched volume, V_S , linearly increased with the force and no debris was produced at the low forces as shown in Figure 11b, (2 N–7 N). The micro roughness was smoothed over the bruise spots. The spots distribute linearly at a certain distance interval. An interesting finding is that the size of the spots, \bar{W}_T in Figure 11a, at 2 N and 3 N are approximately the same, and larger than that at 7 N. The interval greatly decreased when the scratch force increased to 3 N from 2 N. Figure 7 gives the details of the interval. The average intervals at 2 N and 3 N are 1.348 mm (std = 0.159 mm) and 0.954 mm (std = 0.157 mm), respectively. Figure 11a shows that the SB texture resulted in a larger scratch width than the CB texture, as its grains are small, sharp, and more directional and orientational than the large CB grains. The scratch became nearly continuous at 7 N. The no-scratch area can also be found by closely examining the

simulated scratches in Figure 12, but Figure 7 shows that the stage with zero resistance coefficient disappeared.

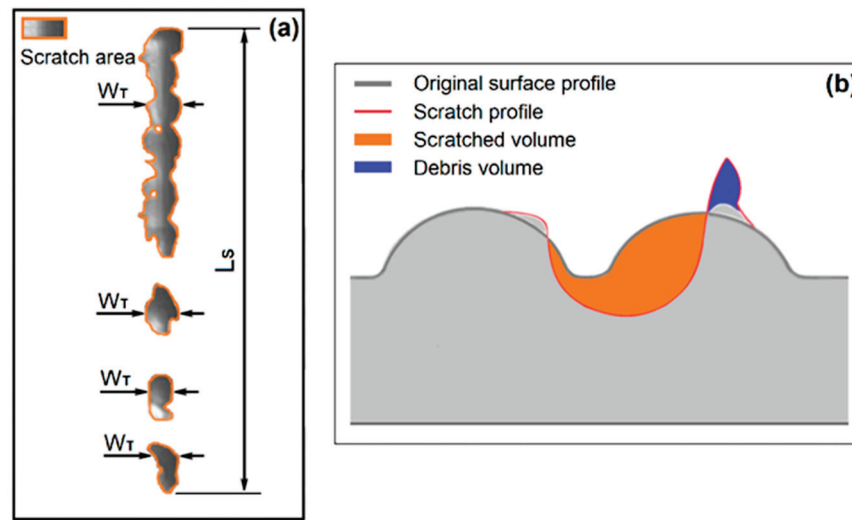


Figure 10. Evaluation parameters of scratches on a textured surface. (a) scratch size and (b) material damage. Figure b was adapted from [39].

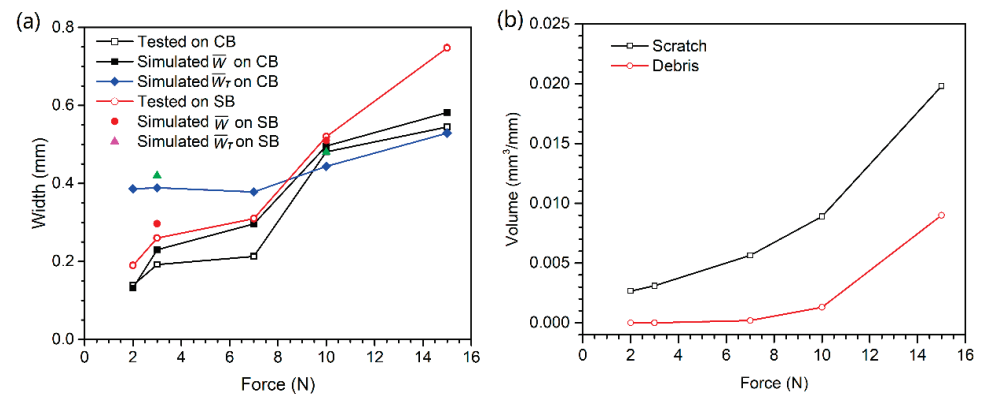


Figure 11. (a) Scratch size and (b) materials damage as a function of scratching force.

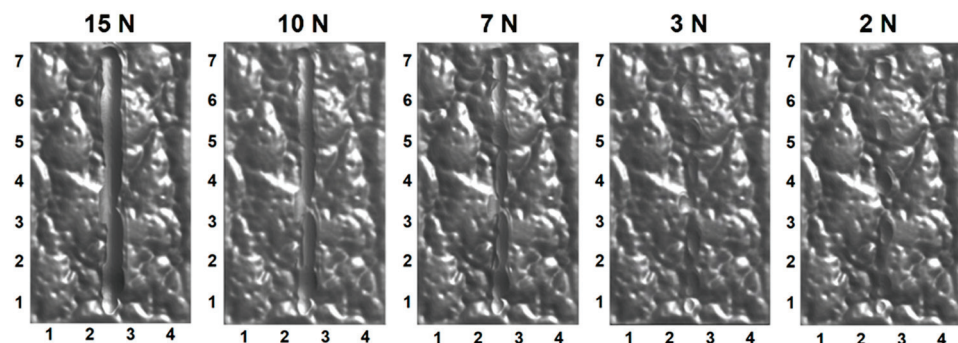


Figure 12. Simulated scratches showing the hidden bruise spots (2 N and 3 N) and continuous material damage (10 N and 15 N) of the CB textured surface.

At high forces, the primary large grains and the substrate were damaged. The body of the worm-like islands in the SB texture and the top surfaces of the coarse islands in the CB texture were obviously damaged by the scratch tip at 10 N, whereas the material deformation degree at the bottom of the CB texture is very low. The experiments show

that the damage of the substrate of plaque with CB texture is still slight at 10 N and 15 N, but large material failure occurred in the substrate of SB texture at the forces, due to the difference in the features of their grains. The grains of the CB texture are larger and rounder and have a less directional structure and less orientational distribution than the SB texture grains, as mentioned before. The simulation results show that the material damage extended to the valleys of the CB texture at 10 N. Figure 11 shows a fast increase in both the scratch volume and the debris volume with the force at the stage. The width of scratches on both textures rapidly increased as the scratching force increased from 7 N to 10 N. For the continuous scratches at high forces, their \bar{W} is larger than their \bar{W}_T due to the material deformation close to either side of the scratches and the transverse swing of them.

There is a critical force between the bruise spot damage and the texture pattern damage as shown in Figures 8, 9, 11 and 12. The \bar{W}_T of the bruise spots did not change with force, whereas \bar{W} slightly increased. The \bar{W}_T is the smallest when the scratch tip starts to creep on the rough surface. The energy is mainly consumed in friction and removing the micro roughness when the scratch tip creeps on the textured surfaces. Therefore, \bar{W}_T is a useful parameter to identify the critical point between the scratching types. The pattern and substrate damages became serious with the increase in scratch force. The energy was mainly spent by the plastic deformation of the texture and the substrate.

The simulation predicted the scratch profile, the surface damage and the quantitative scales well at the two typical scratching regions. It appears that the prediction of scratch on the SB texture is more accurate than that on the CB texture. Figure 11a shows that the simulation predicted the sizes of the scratches well on both the textures. The widths of the scratches tested were calculated using the IPA method, which was based on the intensity of each pixel in the scratches in contrast to the background. The difference in width between the experimental and simulated scratches on the CB texture is small except at 7 N.

The simulated scratch on the CB texture is more obvious than the experimental scratch both in terms of material deformation and appearance. Figure 11a shows that the simulated widths are higher than the measured values, especially on the CB texture at 3 N and 7 N. The deviation is attributed to the differences between the simulation and experiment in terms of both scratching position and scratch finger behavior. The scratch tip in the simulation was located at the position where the tip moved over the tops of a few islands, whereas the scratch tip in the experiment mainly moved along the sides of a few islands and on the bottom/basin of the texture. The former resulted in larger deformation of the material, considering that the scratch tip, a perfectly rigid object, was restricted in the X-direction motion in the simulation (for the coordinate, see Figure 5). The scratch finger in the experiment could not, however, behave as such a rigid body because it had a certain length and neither the scratch finger nor the test plaque could be mechanically fitted on the experimental setup 'perfectly'. The scratch tests were actually conducted using an elastic scratch finger with a rigid tip. The positions of the scratch tip and plaque varied in the X direction during scratching owing to the change in contact force with the position of interaction between the tip surface and grain surface. The slight swings of both the scratch finger and plaque led to crooked, i.e., not straight, scratches on the CB texture and a lower impact on the material than that caused by a perfectly rigid scratch tip.

5. Conclusions

The combination of simulations and experiments of scratching different textured surfaces with a spherical scratch tip provided a fundamental understanding of scratch behavior on textured polymeric surfaces. Jumping of the scratch tip over the textured surfaces and generation of bruise spots on the surfaces were found at low scratch forces. The continuous contact of the scratch tip with the textured surfaces occurred at only high scratch forces. The transverse widths of bruise spots at different scratch forces are approximately the same, but the interval between the spots decreases with the force. The transverse width is a useful parameter to identify the critical point between the bruise spot

damage and the texture pattern damage caused by the continuous scratching. The critical force is about 7 N for the polypropylene.

The simulations quantitatively revealed the resistance coefficients of two textured surfaces and an indentation depth-force pattern. Texture CB showed high effectiveness in enhancing the scratch visibility resistance and increased the scratch resistance by more than 40% at low scratch forces (<3 N) and 9% at high forces (>7 N). The scratch visibility was strongly influenced by the surface texture. The scratches on the CB texture showed a low visibility, but a large size.

The simulation was based on the accurate capture of the textures and surface roughness features. Meshes smaller than 30 μm could capture the small roughness features. The experimental evaluation showed that the simulation predicted the appearances and profiles of the scratched surfaces well. This is significant in computing the appearances of scratched surfaces and in modelling the influence of textured surfaces on the scratch visibility resistance.

Author Contributions: W.G., F.D., J.K.C. and L.W. proposed the conception and modelling method. W.G. performed the image processing and analysis and numerical simulations. F.D. was responsible for the experiments. J.K.C. managed the project and provided samples. H.W. assisted with the image processing and analysis. All authors contributed to the result analyses and discussion. W.G. and F.D. wrote the manuscript with revisions from all other authors. All authors have read and agreed to the published version of the manuscript.

Funding: This project was funded as part of a joint research program by the Ford Motor Company and RMIT University.

Institutional Review Board Statement: Not applicable.

Informed Consent Statement: Not applicable.

Data Availability Statement: The data presented in this study are available on request from the corresponding author.

Acknowledgments: This project was funded as part of a joint research program by the Ford Motor Company and RMIT University.

Conflicts of Interest: The authors declare that they have no conflict of interest.

References

1. Grützmacher, P.G.; Profito, F.J.; Rosenkranz, A. Multi-Scale Surface Texturing in Tribology—Current Knowledge and Future Perspectives. *Lubricants* **2019**, *7*, 95. [CrossRef]
2. Zheng, X.F.; Wang, Z.W.; Chen, M.W.; Zheng, H.H.; Wu, J.W. A Review of Surface Texture of Tribological Interfaces. *Appl. Mech. Mater.* **2010**, *37–38*, 41–45. [CrossRef]
3. Rosenkranz, A.; Grützmacher, P.G.; Murzyn, K.; Mathieu, C.; Mücklich, F. Multi-scale surface patterning to tune friction under mixed lubricated conditions. *Appl. Nanosci.* **2021**, *11*, 751–762. [CrossRef]
4. Arslan, A.; Masjuki, H.H.; Kalam, M.A.; Varman, M.; Mufti, R.A.; Mosarof, M.H.; Khuong, L.S.; Quazi, M.M. Surface Texture Manufacturing Techniques and Tribological Effect of Surface Texturing on Cutting Tool Performance: A Review. *Crit. Rev. Solid State Mater. Sci.* **2016**, *41*, 447–481. [CrossRef]
5. Rosenkranz, A.; Grützmacher, P.G.; Gachot, C.; Costa, H.L. Surface Texturing in Machine Elements—A Critical Discussion for Rolling and Sliding Contacts. *Adv. Eng. Mater.* **2019**, *21*, 1900194. [CrossRef]
6. Coblas, D.; Fatu, A.; Maoui, A.; Hajjam, M. Manufacturing textured surfaces: State of art and recent developments. *J. Eng. Tribol.* **2014**, 229. [CrossRef]
7. Kim, M.S.; Lee, J.H.; Kwak, M.K. Review: Surface Texturing Methods for Solar Cell Efficiency Enhancement. *Int. J. Precis. Eng. Manuf.* **2020**, *21*, 1389–1398. [CrossRef]
8. Zhang, J.-J.; Zhao, L.; Rosenkranz, A.; Song, C.-W.; Yan, Y.-D.; Sun, T. Nanosecond Pulsed Laser Ablation on Stainless Steel—Combining Finite Element Modeling and Experimental Work. *Adv. Eng. Mater.* **2019**, *21*, 1900193. [CrossRef]
9. Zhang, J.; Zhao, L.; Rosenkranz, A.; Song, C.; Yan, Y.; Sun, T. Nanosecond pulsed laser ablation of silicon-finite element simulation and experimental validation. *J. Micromech. Microeng.* **2019**, *29*, 75009. [CrossRef]
10. Schneider, J.; Djamiykov, V.; Greiner, C. Friction reduction through biologically inspired scale-like laser surface textures. *Beilstein J. Nanotechnol.* **2018**, *9*, 2561. [CrossRef]
11. Ignell, S.; Kleist, U.; Rigdahl, M. Visual perception and measurements of texture and gloss of injection-molded plastics. *Polym. Eng. Sci.* **2009**, *49*, 344–353. [CrossRef]

12. Piccolo, L.; Sorgato, M.; Batal, A.; Dimov, S.; Lucchetta, G.; Masato, D. Functionalization of Plastic Parts by Replication of Variable Pitch Laser-Induced Periodic Surface Structures. *Micromachines* **2020**, *11*, 429. [CrossRef]
13. Barr, C.J.; Wang, L.; Coffey, J.K.; Daver, F. Influence of surface texturing on scratch/mar visibility for polymeric materials: A review. *J. Mater. Sci.* **2017**, *52*, 1221–1234. [CrossRef]
14. De Vietro, N.; Belforte, L.; Lambertini, V.G.; Fracassi, F. Low pressure plasma modified polycarbonate: A transparent, low reflective and scratch resistant material for automotive applications. *Appl. Surf. Sci.* **2014**, *307*, 698–703. [CrossRef]
15. Barr, C.J.; Wang, L.; Coffey, J.K.; Gidley, A.; Daver, F. New technique for the quantification of scratch visibility on polymeric textured surfaces. *Wear* **2017**, *384–385*, 84–94. [CrossRef]
16. Hamdi, M.; Sue, H.-J. Effect of color, gloss, and surface texture perception on scratch and mar visibility in polymers. *Mater. Des.* **2015**, *83*, 528–535. [CrossRef]
17. Hossain, M.M.; Jiang, H.; Sue, H.-J. Effect of constitutive behavior on scratch visibility resistance of polymers—A finite element method parametric study. *Wear* **2011**, *270*, 751–759. [CrossRef]
18. Jiang, H.; Browning, R.L.; Hossain, M.M.; Sue, H.-J.; Fujiwara, M. Quantitative evaluation of scratch visibility resistance of polymers. *Appl. Surf. Sci.* **2010**, *256*, 6324–6329. [CrossRef]
19. Wong, M.; Moyses, A.; Lee, F.; Sue, H.-J. Study of surface damage of polypropylene under progressive loading. *J. Mater. Sci.* **2004**, *39*, 3293–3308. [CrossRef]
20. Ni, B.Y.; Faou, A.L. Scratching behaviour of polymer films using blunt spherical styli. *J. Mater. Sci.* **1996**, *31*, 3955–3963. [CrossRef]
21. Ali, S.H.R. Advanced Nanomeasuring Techniques for Surface Characterization. *ISRN Opt.* **2012**, *2012*, 23. [CrossRef]
22. Chivatanasootorn, V.; Tsukise, S.; Kotaki, M. Surface texture effect on scratch behavior of injection molded plastics. *Polym. Eng. Sci.* **2012**, *52*, 1862–1867. [CrossRef]
23. Le Houérou, V.; Gauthier, C.; Schirrer, R. Energy based model to assess interfacial adhesion using a scratch test. *J. Mater. Sci.* **2008**, *43*, 5747–5754. [CrossRef]
24. Cheng, Q.; Jiang, C.; Zhang, J.; Yang, Z.; Zhu, Z.; Jiang, H. Effect of thermal aging on the scratch behavior of poly (methyl methacrylate). *Tribol. Int.* **2016**, *101*, 110–114. [CrossRef]
25. Zhu, Z.; Cheng, Q.; Jiang, C.; Zhang, J.; Jiang, H. Scratch behavior of the aged hydrogenated nitrile butadiene rubber. *Wear* **2016**, *352–353*, 155–159. [CrossRef]
26. Bouvard, J.L.; Denton, B.; Freire, L.; Horstemeyer, M.F. Modeling the mechanical behavior and impact properties of polypropylene and copolymer polypropylene. *J. Polym. Res.* **2016**, *23*, 1–19. [CrossRef]
27. Şerban, D.-A.; Marşavina, L.; Modler, N. Finite element modelling of the progressive damage and failure of thermoplastic polymers in puncture impact. *Procedia Eng.* **2015**, *109*, 97–104. [CrossRef]
28. Alemi-Ardakani, M.; Milani, A.S.; Yannacopoulos, S. On Complexities of Impact Simulation of Fiber Reinforced Polymer Composites: A Simplified Modeling Framework. *Sci. World J.* **2014**, *2014*, 10. [CrossRef]
29. Jiang, H.; Wei, Y.; Cheng, Q.; Zhu, Z. Scratch behavior of low density polyethylene film: Effects of pre-stretch and aging. *Mater. Des.* **2018**, *157*, 235–243. [CrossRef]
30. Gao, W.M.; Wang, L.; Coffey, J.K.; Daver, F. Finite element simulation of scratch on polypropylene panels. *Mater. Des.* **2018**, *140*, 400–408. [CrossRef]
31. Jiang, H.; Browning, R.; Sue, H.-J. Understanding of scratch-induced damage mechanisms in polymers. *Polymer* **2009**, *50*, 4056–4065. [CrossRef]
32. Bucaille, J.L.; Gauthier, C.; Felder, E.; Schirrer, R. The influence of strain hardening of polymers on the piling-up phenomenon in scratch tests: Experiments and numerical modelling. *Wear* **2006**, *260*, 803–814. [CrossRef]
33. Jiang, H.; Lim, G.T.; Reddy, J.N.; Whitcomb, J.D.; Sue, H.J. Finite element method parametric study on scratch behavior of polymers. *J. Polym. Sci. Part B Pol. Phys.* **2007**, *45*, 1435–1447. [CrossRef]
34. Hossain, M.M.; Browning, R.; Minkwitz, R.; Sue, H.-J. Effect of asymmetric constitutive behavior on scratch-induced deformation of polymers. *Tribol. Lett.* **2012**, *47*, 113–122. [CrossRef]
35. Hossain, M.M.; Minkwitz, R.; Charoensirisomboon, P.; Sue, H.-J. Quantitative modeling of scratch-induced deformation in amorphous polymers. *Polymer* **2014**, *55*, 6152–6166. [CrossRef]
36. Zhang, J.; Jiang, H.; Jiang, C.; Kang, G.; Kan, Q.; Li, Y. Experimental and numerical investigations of evaluation criteria and material parameters' coupling effect on polypropylene scratch. *Polym. Eng. Sci.* **2017**, 118–122. [CrossRef]
37. Yeo, N.E.; Cho, W.K.; Kim, D.-I.; Jeong, M.Y. Enhanced anti-scratch performance of nanopatterned anti-reflective polymer films. *Appl. Surf. Sci.* **2018**, *458*, 503–511. [CrossRef]
38. Friedrich, K.; Sue, H.J.; Liu, P.; Almajid, A.A. Scratch resistance of high performance polymers. *Tribol. Int.* **2011**, *44*, 1032–1046. [CrossRef]
39. Gao, W.M.; Wang, L.; Coffey, J.K.; Daver, F. Understanding the scratch behaviour of polymeric materials with surface texture. *Mater. Des.* **2018**, *146*, 38–48. [CrossRef]
40. Browning, R.; Hossain, M.M.; Li, J.; Jones, S.; Sue, H.-J. Contrast-based evaluation of mar resistance of thermoplastic olefins. *Tribol. Int.* **2011**, *44*, 1024–1031. [CrossRef]
41. Yilbas, B.S.; Khaled, M.; Abu-Dheir, N.; Al-Aqeeli, N.; Said, S.A.M.; Ahmed, A.O.M.; Varanasi, K.K.; Toumi, Y.K. Wetting and other physical characteristics of polycarbonate surface textured using laser ablation. *Appl. Surf. Sci.* **2014**, *320*, 21–29. [CrossRef]

42. Feng, B. Effects of surface roughness on scratch resistance and stress-strain fields during scratch tests. *AIP Adv.* **2017**, *7*, 035217. [CrossRef]
43. Jiang, H.; Browning, R.; Fincher, J.; Gasbarro, A.; Jones, S.; Sue, H.-J. Influence of surface roughness and contact load on friction coefficient and scratch behavior of thermoplastic olefins. *Appl. Surf. Sci.* **2008**, *254*, 4494–4499. [CrossRef]
44. Jiang, C.; Jiang, H.; Zhang, J.; Kang, G. Analytical model of friction behavior during polymer scratching with conical tip. *Friction* **2019**, *7*, 466–478. [CrossRef]
45. Yastrebov, V.A.; Durand, J.; Proudhon, H.; Cailletaud, G. Rough surface contact analysis by means of the Finite Element Method and of a new reduced model. *C. R. Méc.* **2011**, *339*, 473–490. [CrossRef]
46. Yu, C.; Yu, H.; Liu, G.; Chen, W.; He, B.; Wang, Q.J. Understanding Topographic Dependence of Friction with Micro- and Nano-Grooved Surfaces. *Tribol. Lett.* **2014**, *53*, 145–156. [CrossRef]
47. Pelletier, H.; Gauthier, C.; Schirrer, R. Strain and stress fields during scratch tests on amorphous polymers: Influence of the local friction. *Tribol. Lett.* **2008**, *32*, 109–116. [CrossRef]
48. Jiang, H.; Cheng, Q.; Jiang, C.; Zhang, J.; Yonghua, L. Effect of stick-slip on the scratch performance of polypropylene. *Tribol. Int.* **2015**, *91*, 1–5. [CrossRef]
49. Chu, J.; Rumao, L.; Coleman, B. Scratch and mar resistance of filled polypropylene materials. *Polym. Eng. Sci.* **1998**, *38*, 1906–1914. [CrossRef]
50. Weon, J.-I.; Song, S.-Y.; Choi, K.-Y.; Lee, S.-G.; Lee, J.H. Quantitative determination of scratch-induced damage visibility on polymer surfaces. *J. Mater. Sci.* **2010**, *45*, 2649–2654. [CrossRef]
51. Gao, W.; Wang, L.; Coffey, J.K.; Wu, H.; Daver, F. An attempt to simulate structure and realistic images of scratches on rough polymeric surfaces. *J. Polym. Sci.* **2020**, *58*, 3209–3218. [CrossRef]
52. Yastrebov, V.A.; Anciaux, G.; Molinari, J.-F. On the accurate computation of the true contact-area in mechanical contact of random rough surfaces. *Tribol. Int.* **2017**, *114*, 161–171. [CrossRef]
53. Roberts, M. *Biology: A Functional Approach*, 4th ed.; Oxford University Press: Oxford, UK, 1986.
54. Buchsbaum, W.H. *Color. TV Servicing*, 3rd ed.; Prentice Hall: Bergen County, NJ, USA, 1975.
55. Pappas, T.N.; Neuhoff, D.L.; Ridder, H.d.; Zujovic, J. Image Analysis: Focus on Texture Similarity. *Proc. IEEE* **2013**, *101*, 2044–2057. [CrossRef]
56. Zhou, W.; Bovik, A.C.; Sheikh, H.R.; Simoncelli, E.P. Image quality assessment: From error visibility to structural similarity. *IEEE Trans. Image Process.* **2004**, *13*, 600–612. [CrossRef]
57. Mwema, F.M.; Akinlabi, E.T.; Oladijo, O.P.; Oladijo, O.P. The Use of Power Spectrum Density for Surface Characterization of Thin Films. In *Photoenergy and Thin Film Materials*; Scrivener Publishing LLC: Beverly, MA, USA, 2019; pp. 379–411. [CrossRef]
58. Ariño, I.; Kleist, U.; Barros, G.G.; Johansson, P.-Å.; Rigdahl, M. Surface texture characterization of injection-molded pigmented plastics. *Polym. Eng. Sci.* **2004**, *44*, 1615–1626. [CrossRef]
59. Tevis, D.B.J.; Till, J.; Lars, P. Quantitative characterization of surface topography using spectral analysis. *Surf. Topogr.* **2017**, *5*, 013001.
60. Zhao, Y.; Wang, G.C.; Lu, T.-M. *Characterization of Amorphous and Crystalline Rough Surface: Principles and Applications*; Elsevier Science Publishing Co Inc.: Amsterdam, The Netherlands, 2001; Volume 37, p. 15.
61. Mandelbrot, B.B. *The Fractal Geometry of Nature*; W.H. Freeman: New York, NY, USA, 1983; Volume 173.
62. Thompson, M.K.; Thompson, J.M. Considerations for the incorporation of measured surfaces in finite element models. *Scanning* **2010**, *32*, 183–198. [CrossRef]
63. ABAQUS Abaqus 6.13. *User's Guide*; Dassault Systèmes Simulia: Providence, RI, USA, 2013.
64. Hurtado, J.; Lapczyk, I.; Govindarajan, S. Parallel rheological framework to model non-linear viscoelasticity, permanent set and Mullins effect in elastomers. *Const. Models Rubber* **2013**, *8*, 95–100.
65. Bergström, J. 11—Material Modeling Case Studies. In *Mechanics of Solid Polymers*; Bergström, J., Ed.; William Andrew Publishing: Amsterdam, The Netherlands, 2015; pp. 455–497. [CrossRef]
66. Qiu, G.; Henke, S.; Grabe, J. Application of a Coupled Eulerian–Lagrangian approach on geomechanical problems involving large deformations. *Comput. Geotech.* **2011**, *38*, 30–39. [CrossRef]
67. Ducobu, F.; Rivière-Lorphèvre, E.; Filippi, E. Application of the Coupled Eulerian-Lagrangian (CEL) method to the modeling of orthogonal cutting. *Eur. J. Mech. A-Solid* **2016**, *59*, 58–66. [CrossRef]
68. Benson, D.J. Computational methods in Lagrangian and Eulerian hydrocodes. *Comput. Methods Appl. Mech. Eng.* **1992**, *99*, 235–394. [CrossRef]
69. Gullerud, A.; Hollenshead, J. Coupled Euler-Lagrange simulations of metal fragmentation in pipe bomb configurations. *Procedia Eng.* **2017**, *204*, 202–207. [CrossRef]
70. Ansari, M.A.; Samanta, A.; Behnagh, R.A.; Ding, H. An efficient coupled Eulerian-Lagrangian finite element model for friction stir processing. *Int. J. Adv. Manuf. Tech.* **2018**. [CrossRef]
71. Chmelnizkij, A.; Nagula, S.; Grabe, J. Numerical Simulation of Deep Vibration Compaction in Abaqus/CEL and MPM. *Procedia Eng.* **2017**, *175*, 302–309. [CrossRef]
72. Li, K.; Ni, B.Y.; Li, J.C.M. Stick-slip in the scratching of styrene-acrylonitrile copolymer. *J. Mater. Res.* **2011**, *11*, 1574–1580. [CrossRef]

Article

Fibre Alignment and Void Assessment in Thermoplastic Carbon Fibre Reinforced Polymers Manufactured by Automated Tape Placement

Tamer A. Sebaey^{1,2,*} , Mohamed Bouhrara³ and Noel O'Dowd⁴ 

¹ Engineering Management Department, College of Engineering, Prince Sultan University, Riyadh 66833, Saudi Arabia

² Mechanical Design and Production Department, Faculty of Engineering, Zagazig University, Zagazig P.O. Box 44519, Sharkia, Egypt

³ Saudi Aramco, Research & Development Center, Dhahran 31311, Saudi Arabia; MohamedmmBouhrara@aramco.com

⁴ Irish Composites Centre (IComp), Bernal Institute, University of Limerick, V94 T9PX Limerick, Ireland; Noel.dowd@ul.ie

* Correspondence: sebaey@hotmail.com or tsebaey@psu.edu.sa; Tel.: +966-(0)-11-494-8644

Abstract: Automated Tape Placement (ATP) technology is one of the processes that is used for the production of the thermoplastic composite materials. The ATP process is complex, requiring multiple melting/crystallization cycles. In the current paper, laser-assisted ATP was used to manufacture two thermoplastic composites (IM7/PEEK and AS4/PA12). Those specimens were compared to specimens that were made of thermoset polymeric composites (IM7/8552) manufactured while using a standard autoclave cycle. In order to assess the quality, void content, fibre distribution, and fibre misalignment were measured. After manufacturing, specimens from the three materials were assessed using optical microscopy and computed tomography (CT) scans. The results showed that, as compared to the thermoset composites, thermoplastics that are manufactured by the ATP have a higher amount of voids. On the other hand, manufacturing using the ATP showed an improvement in both the fibre distribution inside the matrix and the fibre misalignment.

Keywords: thermoplastic composites; automated tape placement; fibre misalignment; voids; CT scan; circular distribution

Citation: Sebaey, T.A.; Bouhrara, M.; O'Dowd, N. Fibre Alignment and Void Assessment in Thermoplastic Carbon Fibre Reinforced Polymers Manufactured by Automated Tape Placement. *Polymers* **2021**, *13*, 473. <https://doi.org/10.3390/polym13030473>

Academic Editor: Luigi Sorrentino and Somen K. Bhudolia

Received: 10 December 2020

Accepted: 28 January 2021

Published: 2 February 2021

Publisher's Note: MDPI stays neutral with regard to jurisdictional claims in published maps and institutional affiliations.



Copyright: © 2021 by the authors. Licensee MDPI, Basel, Switzerland. This article is an open access article distributed under the terms and conditions of the Creative Commons Attribution (CC BY) license (<https://creativecommons.org/licenses/by/4.0/>).

1. Introduction

Fibre-reinforced plastic (FRP) composites are extensively used in aerospace, submarine, automotive, and petrochemical industries for their high strength and stiffness to weight ratios, chemical stability, and ability to tailor strength and stiffness properties by tailoring the fibre orientation [1,2]. For more than half a century, most of the polymer composite parts were designed of thermoset matrix, due to their thermal stability and strength. During the last two decades, interest in thermoplastic composites has increased due to their superior properties, such as short processing times, long-term storage, ease of recycling, and impact properties [3–5]. The manufacturing of thermoplastic composite parts requires a heating process, either directly before the final moulding process, where a heat source plus a cool tool is used (non-isothermal processing), or in a hot mould (isothermal processing) [6]. Laser-assisted automated tape placement (ATP) is one of the non-isothermal processes that uses laser as a heat source to melt the thermoplastic matrix while tapes are laid-up on a tool, and then consolidated under a roller [7].

Many factors influence the final quality of the FRP, including resin viscosity, difference in thermal expansion coefficient, and control of processing parameters. Therefore, several types of defects can be found, such as porosity (void content), fibre waviness (misalignment), and poor distribution of fibres in the matrix, which results in resin-rich areas [8,9].

The effect of these defects on the mechanical properties of the composite parts is well documented in the literature [10–12]. During the manufacturing of FRP, if both pressure and application time are not optimized, voids could arise in the laminate [13]. The presence of voids reduces the interlaminar shear, longitudinal compressive, and transverse tensile strengths, in addition to inducing local stress concentrations, with consequent severe degradation of strength and stiffness in-service [12,14]. For aeronautical and other safety critical applications, the void content is limited to 1%, whereas, for other applications, 5% can be accepted, depending on the application [15].

The inhomogeneous distribution of fibres inside the polymer matrix results in areas with a lower volume of fibre. These areas are called resin-rich areas. The manufacturing technique [16,17] and the fibre architecture [18] are the main contributors to this lack of “perfect” uniform distribution. The resin rich areas are another source of stress concentration that need to be avoided for better quality of the manufactured composites [19]. In a numerical analysis, Ghayoor et al. [20] showed that, at the same fibre volume fraction, the failure initiation strain in the matrix is 20% lower for samples with resin rich areas when compared to samples without resin pockets.

Fibre misalignment is the third manufacturing defect that is taken into consideration in this paper. It results from the improper manufacturing parameters and thermal stress during the curing/crystallization [21]. The misalignment is considered as an initial fibre-kinking and, consequently, it directly affects the compression strength [22]. For a multidirectional laminate under general loading conditions, Fedulov et al. [23] numerically studied the effect of the ply misalignment in unidirectional (UD) composites and showed that it leads to a reduction of up to 49% in the laminate compressive strength. This effect was experimentally confirmed by Wilhelmsson et al. [24]. The fibre misalignment can be measured by many techniques, including ultrasonic array [25], mathematical representation of ellipse resulting from cutting the individual fibre [26], optical microscopy [27], and computed tomography (CT) scan [28].

The development of the manufacturing technology leads to improvements in the type and impact of the manufacturing defects. Most of the data that are reviewed are for thermoset-based composites and there are little data available on thermoplastic based composites [29]. In the current paper, the aim is to assess the quality of thermoplastic-based carbon fibre-reinforced composites manufactured using automatic controlled laser-assisted ATP. The parameters used in the assessments are the defects mentioned in the introduction; the measurement techniques are optical microscopy and CT scan.

2. Materials Manufacturing and Measurements

2.1. Materials and Manufacturing Techniques

Two thermoplastic-based composite systems are used in this study. The first one is IM7/PEEK, with poly(etheretherketone) as the polymeric matrix and IM7 carbon fibre. The second one is AS4/PA12, with polyamide 12 as the thermoplastic matrix and AS4 as the carbon fibre. Both of the material systems are in the form of tape (of the fibres embedded in the matrix) ready to be processed by the ATP. In addition, a thermoset-based composite is used as a reference, namely IM7/8552 in the form of prepreg (of the fibres embedded in the matrix), to be processed in an autoclave. The matrix and fibre properties can be found on the material data sheets [30–32]. Table 1 shows some of the characteristics of the three materials systems that were used in this study. Table 2 summarizes the properties of the three matrix systems, as per the materials data sheets.

Table 1. Characteristics of the IM7/PEEK, AS4/PA12, and IM7/8552 CFRP composites.

Material	Fibre Volume Fraction %	Ply Thickness mm	Density g/cm ³	Tape/Prepreg Width mm
IM7/PEEK	60.0	0.14	1.588	12
AS4/PA12	60.0	0.133	1.48	12
IM7/8552	60.0	0.131	1.57	400

Table 2. Characteristics of the three matrix materials, as per the material data sheets [30–32].

Property	PEEK	PA12	8552 Epoxy Resin
Trade name	VICTREX PEEK 150UF10	VESTOSINT 2159	HexPly 8552
Supplier	Suprem	Suprem	Hexcel
Melting point (°C)	343	184	—
Glass transition (°C)	143	49	200
Density (g/cm ³)	1.30	1.02	1.30
Tensile strength (MPa)	100	73	121
Tensile Modulus (GPa)	4.00	1.96	4.67

The standard autoclave cycle was used to manufacture the IM7/8552 composites. Firstly, squares of 200 × 200 mm were cut from the prepreg and manually laid, with the corresponding stacking sequence. For this study, all of the specimens are designed to be [0₂/90₄]_S, with 12 layers in total. This stacking sequence was selected with a cluster of 8 layer of 90° in the middle to be able to clearly see the fibre cross-section with the different scanning techniques. The idea behind the 0° layers was to give strength to the samples while manufacturing and handling. The plies were laid and placed in an autoclave. The autoclave cycle consists of the following steps [32]: (1) apply full vacuum (1 bar), (2) apply 7 bar gauge autoclave pressure, (3) reduce the vacuum to a safety value of 0.2 bar when the autoclave pressure reaches approximately 1 bar gauge, (4) heat at 1–3 °C/min to 110 °C, (5) hold at 110 °C for 60 min., (6) heat at 1–3 °C/min to 180 °C, (7) hold at 180 °C for 120 min., (8) cool at 2–5 °C/min, and (9) vent autoclave pressure when the component reaches 60 °C. After curing, 30 mm were trimmed from all laminate edges using a numerically controlled diamond cutter with a hydraulic specimen holding mechanism.

The thermoplastic composites were manufactured by automated tape placement ATP. The machine uses a laser-assisted tape placement head (AFPT, GmbH) that was attached to a robot arm (Kuka, KR240 L210-2) and it is placed in a closed clean room. The manufacturing using the ATP starts by placing the tape in the right position through the robot arm. The laser beam melts, in situ, the laid tape and, consequently, a silicone consolidation roller applies pressure and cooling to finalise the process. The silicon roller applies pressure through a pneumatic cylinder. The roller is cooled externally using compressed air to avoid the tape to adhere the roller. Studies on the process parameters of the ATP can be found elsewhere [33,34]. Those processing parameters include: (a) the laser power, (b) the laser applied angle, (c) roller material and pressure, (d) tool temperature, (e) lay-down speed, and (f) roller temperature. For the current study, the processing parameters were selected based on the previous parametric study [35] and Table 3 shows the results.

Table 3. Manufacturing parameters that are used by the ATP to manufacture IM7/PEEK and AS4/PA12 CFRP composites.

Lay-Down Speed	Target Temperature	Roller Material	Pressure
12 m/min	420 °C for IM7/PEEK 210 °C for AS4/PA12	Silicone	1.2 Bar

Securing the flatness of the plates manufactured while using this technology is a challenge, given that the plate is under in-situ thermal stresses through the whole manufacturing cycle. This thermal stress causes several deformations to the plate. A mechanical solution is proposed for solving this problem by manufacturing using a prismatic mould with square cross-section to lay the first two layers [0₂] around the whole circumference. The next eight layers [90₈] were laid on only one side of the square cross-section. Finally, the last two layers [0₂] were applied to the whole circumference. Figure 1 shows the manufacturing details. The benefit of this procedure is to ensure a flat laminate surface

that is maintained by the four $[0_2]$ layers surrounding the structure. After complete consolidation, the three non-effective sides of the mould were removed to leave a flat panel with the required stacking sequence.

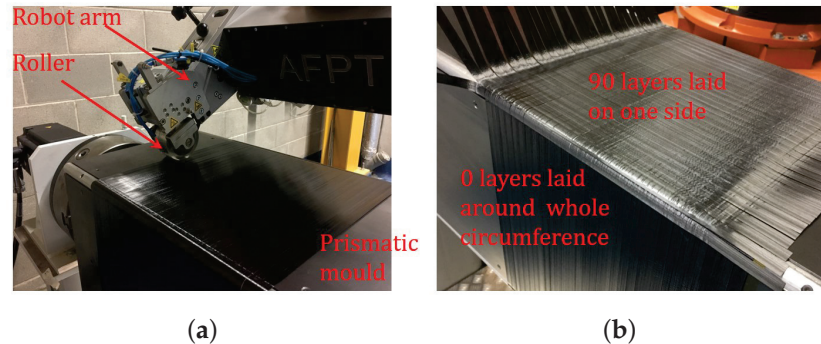


Figure 1. Using the prismatic mould with the robotic arm to manufacture the thermoplastic composite; (a) Laying the 0° . (b) Laying the 90° .

Because of the multiple in situ melting/crystallization process during the manufacturing of thermoplastic composites using ATP, the resulting panel is not perfectly flat. In addition to panel flatness, the void content of ATP composite panels can be high [36]. To minimise void content and improve specimen flatness, two panels (one IM7/PEEK and one AS4/PA12) were subjected to autoclave cycles of 1 bar maximum pressure for three hours and maximum temperature of 400°C and 200°C , respectively. The cool down rate that was used for this process was $4^\circ\text{C}/\text{min}$. This autoclave cycle melts the pre-manufactured (using ATP) panels under vacuum and pressure, and allows for it to solidify, which releases the thermal induced residual stresses and reduces the void volume. By adding these two panels, our test matrix was composed of a thermoset-based composite panel, two thermoplastic-based panels manufactured using ATP, and other two thermoplastic-based panels manufactured using ATP, and then treated using autoclave. In total, five conditions are tested.

In an earlier study, Rao et al. [37] studied the mechanical properties and damage mechanisms of the five conditions that were adopted in the current study through in-situ tensile loading. For the AS4/PA12 without autoclave treatment, the failure load and stress were 0.98 kN and 288 MPa, respectively. For the specimens with autoclave treatment, the failure load and stress were 1.48 kN and 363 MPa, respectively. This improvement in both the load carrying capacity and strength was governed by reducing the amount of voids and thickness reduction resulting from the compression in the autoclave cycle.

2.2. Measurements

Two non-destructive testing techniques were used to assess the quality of the composites. The first one was optical microscopy. Three specimens of 15 mm were cut from each panel and then mounted in silicon moulds of 50 mm diameter. The moulds were filled with epoxy resin (Transparent epoxy resin from Resineco) and left overnight for curing. After curing, the mounted specimens were grinded (with P600 for 5 min, P1200 for 10 min, and P2500 for 10 min) and then polished (with 0.3 microns polishing media for 30 min and 0.05 microns polishing media for 10 min) for the optical microscopy scans. The optical microscope (Axio imager MAT microscope from Zeiss) was used to monitor the specimens with different magnification factors ($5\times$ – $50\times$). The images that were obtained from the optical microscope were processed using ImageJ software [38] to calculate the percentage of the area covered by the fibres and/or voids with respect to the total image area. The average of this value was taken as the fibre/void volume fraction. In addition, the tolerance in this measurement was used as a rubric to assess the fibre distribution i.e., the higher the tolerance means that the variation in the amount of fibre between the different images is high, which is an indication of the non-uniform distribution of the fibre inside the matrix.

The second tool used was the μ CT scan, which was mainly used to assess the fibre misalignment. A total of nine scans were considered for each material. The values of the voltage and current of the X-ray were 80 kV and 87 μ A, respectively. The images obtained were 924×924 pixels, with a pixel size of 0.36 μ m. The result of this scan is a cylinder of 300 μ m diameter and 300 μ m length. Each scan resulted in 3201 projections (images), with an exposure time of 5 s, and specimen rotation of 360° . Each scan required approximately 270 min. to be completed. The images of the cross-section, taken during the previous step, were then reconstructed into a 3D shape using ImageJ software [39]. Slices, parallel to the fibre direction, were taken and the fibre pass was followed by segments of 30 μ m each. The angles of these segments were measured, with reference to the principal direction, and they were collected for the same material and then plotted to show the distribution of the fibre misalignment. These data were fitted using the von Mises circular distribution as [40,41]:

$$P(\alpha, \mu, \kappa) = \frac{1}{2 \cdot \pi \cdot I_0(\kappa)} \cdot e^{(\kappa \cdot \cos \alpha - \mu)} \quad (1)$$

where α is the parameter being analysed, which is the misalignment in our study (in radians), μ represents the mean, at which the distribution is clustered around, and κ is the concentration parameter. I_0 is the modified Bessel function of order 0. For κ equals zero, the von Mises distribution is uniform. On the other hand, for small values of κ , the distribution is close to uniform. For a higher value of κ , the distribution becomes very concentrated regarding the angle μ . In our application, the higher the value of κ , the closer the fibres are to the zero angle, which represents an excellent alignment of the fibres to the desired angle.

3. Results and Discussion

3.1. Thermoset- vs. Thermoplastic-Based Composites

Figure 2 shows a sample of the images that were obtained from the optical microscopy scan for the thermoset- and the two thermoplastic-based composite panels. The first observation is the amount of voids. In the thermoset composites (Figure 2a), for more than 50 images, there are no visible voids, which reflects the well-established quality of the autoclave processing of the thermoset composites. This result can be justified by the vacuum and pressure applied to the specimen during the solidification process inside the autoclave. For the material that was manufactured with ATP (Figure 2b,c), the voids are obvious and appear to be a feature of thermoplastic composites manufactured by ATP. For the AS4/PA12, the voids are coloured with purple to enhance visibility. For the others, the voids are clear without changing the colour. These remarkable voids give evidence that the pressure that is applied by the roller is not enough and/or the flow of the matrix in the liquid state needs more control to fill in all of the areas inside the composites.

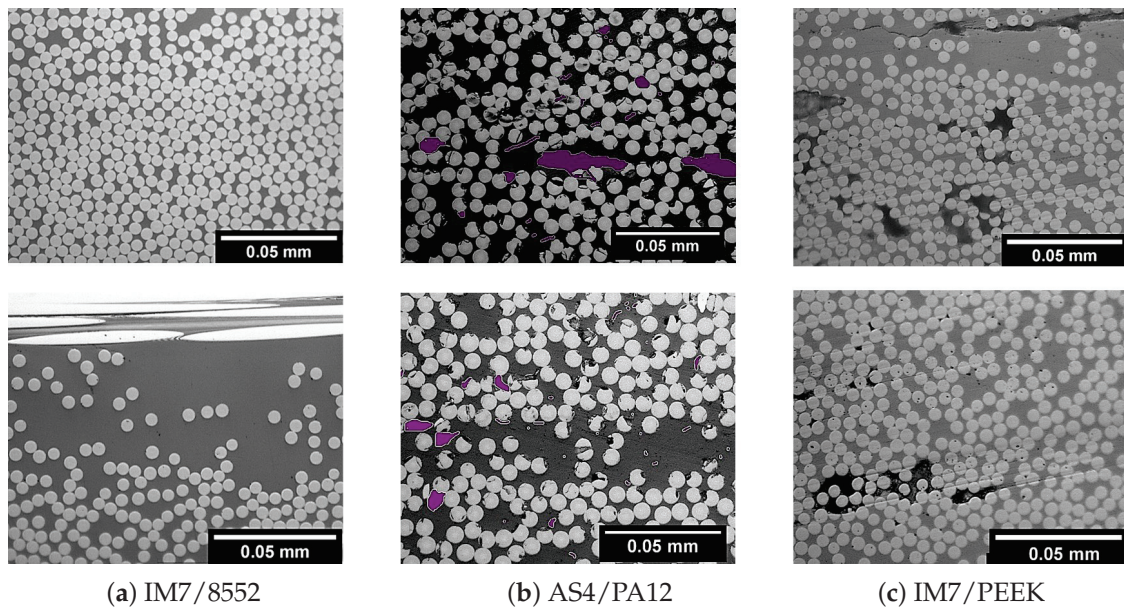


Figure 2. Sample of the optical microscope images that were obtained for the three material systems (Voids in AS4/PA12 are covered with purple for easy identification).

By phase separation on the ImageJ software, the amount of voids are estimated for both the IM7/PEEK and AS4/PA12 as $5.1 \pm 0.6\%$ and $5.1 \pm 0.9\%$, respectively. With the same phase separation technique, the amount of fibres in each image is calculated and its area is divided by the image area in order to calculate the fibre volume fraction. The values of the fibre volume fraction measured for the three materials are $61 \pm 16\%$, $55 \pm 8\%$, and $53 \pm 10\%$ for the IM7/8552, AS4/PA12, and IM7/PEEK, respectively (Table 4). Those numbers are obtained from at least 50 images for each material. These numbers give an indication on the amount of fibre in the matrix, although, due to the high tolerance in the measurements, other techniques [42,43] give higher precision. The numbers showed that the specimens manufactured by the autoclave (the thermosets) contained the same fibre volumes fraction, as delivered by the prepreg manufacturer (see Table 1), which reflects the quality of the autoclave process and minimum void contents. On the other hand, the results for the volume fraction of the thermoplastic material is about 10% lower than the desired values, as per the material data sheets, as in Table 1. This is highly affected by the void content, as it increases the total plate volume.

The tolerance (scatter) in the measurement of the fibre volume fraction is used as an indication of the distribution of the fibres in the matrix. A higher variation corresponds to higher deviation of the volume % in between the images taken for the same materials. The values of the tolerance are 16%, 8%, and 10 % for the IM7/8552, AS4/PA12, and IM7/PEEK, respectively. This result indicates that the distribution of the fibres in specimens manufactured by ATP is better than that of the autoclave, which results in more resin rich areas in the thermoset composites.

Table 4. Measured void contents and volume fraction of the three composite materials.

Property	IM7/PEEK	AS4/PA12	IM7/8552
Void contents (%)	5.1 ± 0.6	5.1 ± 0.9	0.0
Fibre volume fraction (%)	53 ± 10	55 ± 8	61 ± 16

Figure 3 shows samples of the CT scans that were obtained for each material. The first observation is the amount of voids that appears in IM7/PEEK and AS4/PA12. This method could also be used for the void content measurements [44], but, due to the high cost and limited sample size, the authors decided to proceed with the data from the optical

microscopy. This observation is correlated to the lower volume fraction obtained for both of the thermoset-based composites.

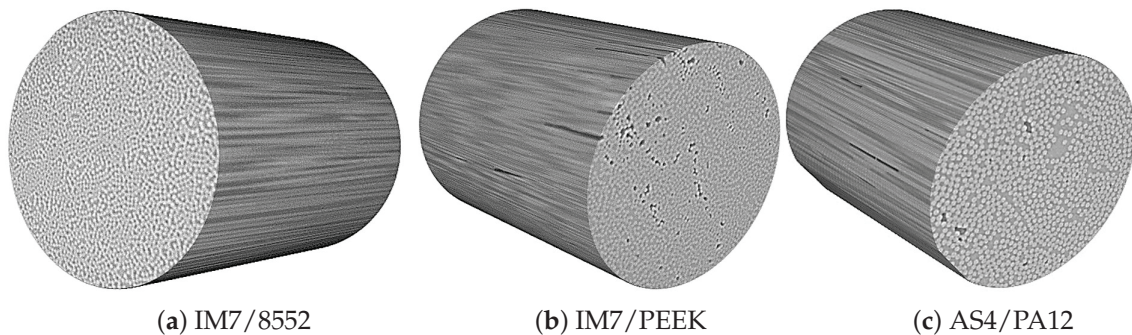


Figure 3. Samples of the constructed computed tomography (CT) scans for the entire test campaign.

The main result of the CT scans is the fibre misalignment measurement. From the 3D images, sections at different locations that are parallel to the fibre direction were analysed in order to determine the fibre waviness/deviation from zero. Samples of the 2D sections are shown in Figure 4. Using Image-J, the footprint of each individual fibre was followed to measure the angle of the single fibre at an average of 8–10 different locations. The result of this process was a set of angles of almost 200 data points for each 2D image. Of the three 3D images presented in Figure 3, at least 4000 data points were considered to plot the distribution of the fibre waviness for each material. Figure 5 shows the distributions for the materials under consideration.

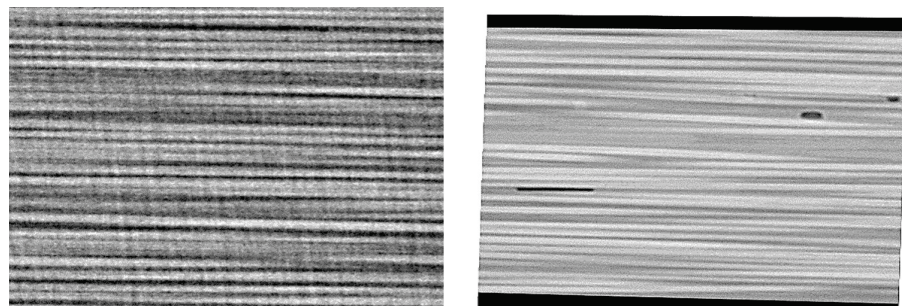


Figure 4. Samples of the two-dimensional (2D) images obtained through the fibre direction from the three-dimensional (3D) images resulting from the CT scan.

The results for the different material systems are analysed while using the circular toolbox [41] to find the von Mises concentration parameter (κ). The value of κ is listed on each distribution, Figure 5. Again, the statistical data that were obtained from fitting the measured misalignment angles with the von Mises distribution confirm that the samples with the highest fibre alignment are those of the IM7/PEEK (thermoplastic matrix) with a concentration parameter $\kappa = 2070$. This value is close to the one that was obtained for the AS4/PA12 ($\kappa = 2020$), which suggests that this improved alignment is related to the manufacturing process, rather than being a material-related issue. When compared to the thermoplastic-based composites, the thermoset composite IM7/8552 shows a lower value of the concentration parameter ($\kappa = 1560$). In summary, the standard autoclave cycle that is used in the processing of thermosets seems to lead to some local waviness/misalignment of individual fibres due to the applied pressure. On the other hand, in the ATP process, the composite is being solidified, while the individual fibres are in tension. This provides a constraint on the fibres, which reduces the misalignment.

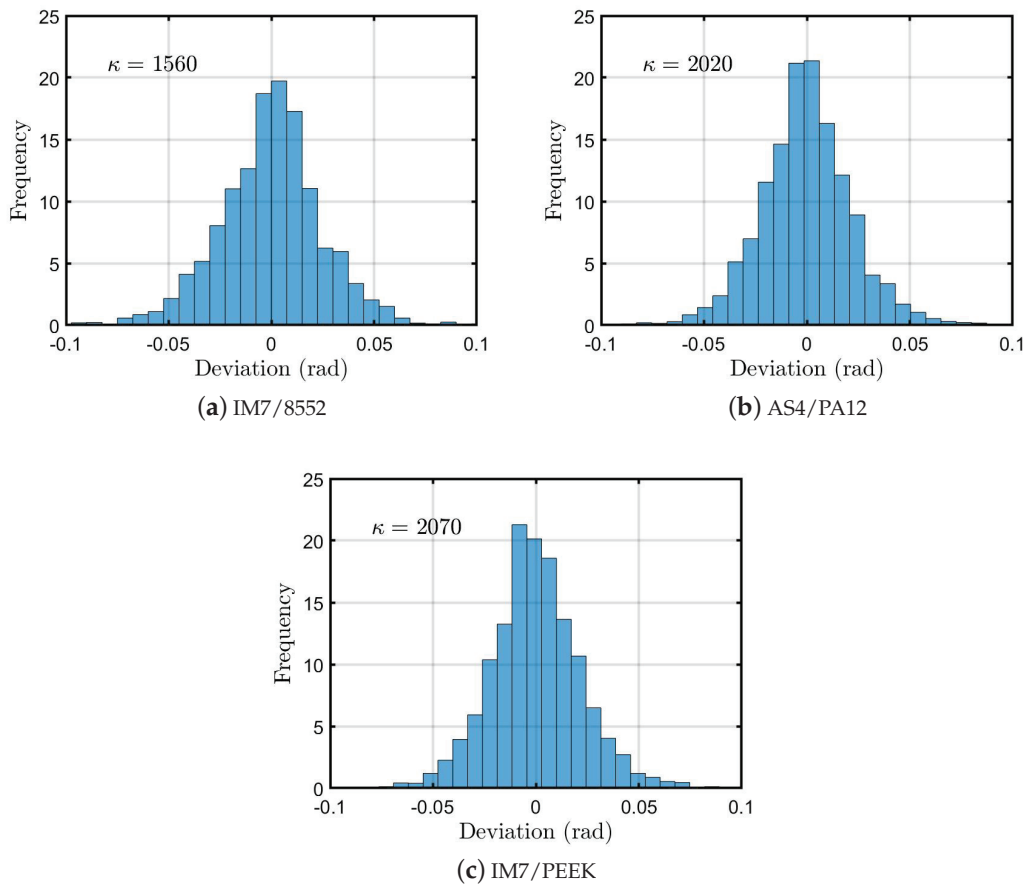


Figure 5. Fibre misalignment distribution for the IM7/8552, AS4/PA12, and IM7/PEEK, and the corresponding concentration parameter κ .

3.2. Thermoplastics Treated by Autoclave after ATP Manufacturing

The samples of the images obtained from the specimens treated by the autoclave, after being manufactured by ATP, are shown in Figures 6 and 7 for the AS4/PA12 and IM7/PEEK, respectively. Autoclave post processing of the AS4/PA12 (Figure 6) shows a significant impact on the void content (both size and number). No large voids appear, as compared to the ones that are shown in Figure 2. Other feature is the uniform fibre distribution. The observation is the same for the images in Figure 7 when compared to the images without treatment in Figure 2 for the IM7/PEEK composites. This finding of the lack of voids is also confirmed from the 3D CT scans for both materials.

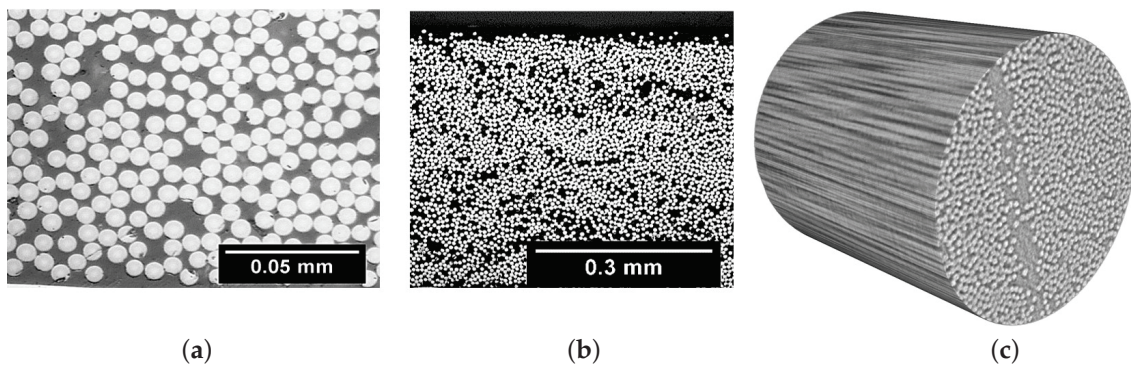


Figure 6. Inspection of AS4/PA12; (a) A high magnification. (b) A low magnification. (c) 3D CT image.

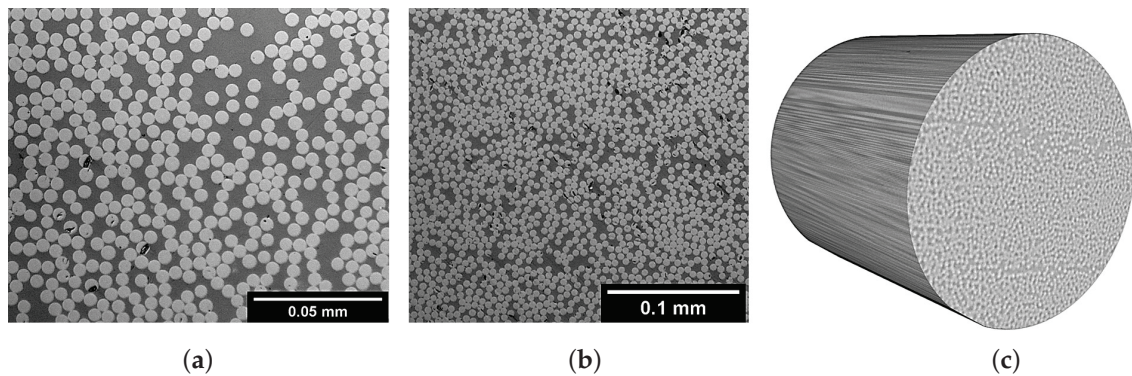


Figure 7. Inspection of IM7/PEEK; (a) A high magnification. (b) A low magnification. (c) 3D CT image.

The measured fibre volume fraction is $59\pm 4\%$ and $60\pm 7\%$ for the AS4/PA12 and IM7/PEEK, respectively. The values of the fibre volume fraction are closer to the ones that were supplied by the supplier (Table 1), as compared to the values that were obtained without autoclave treatment. In addition, deviations are less for those specimens treated by autoclave. This result implies that the fibre distribution is better in the treated specimens. This improvement can be justified by the pressure that is applied to the thermoplastic specimens in the autoclave that squeezes the fibres in the liquid matrix.

Figure 8 represents the misalignment distribution obtained from the specimens post processed by autoclave after ATP manufacturing. The readings of the current samples show higher values of misalignment angle with less concentration around the zero degree (the ideal UD lamina) as compared to the samples without post processing (Figure 5). As a result, the corresponding values of the concentration parameters κ are smaller than that of the specimens without treatment, which implies more fibre misalignment/waviness.

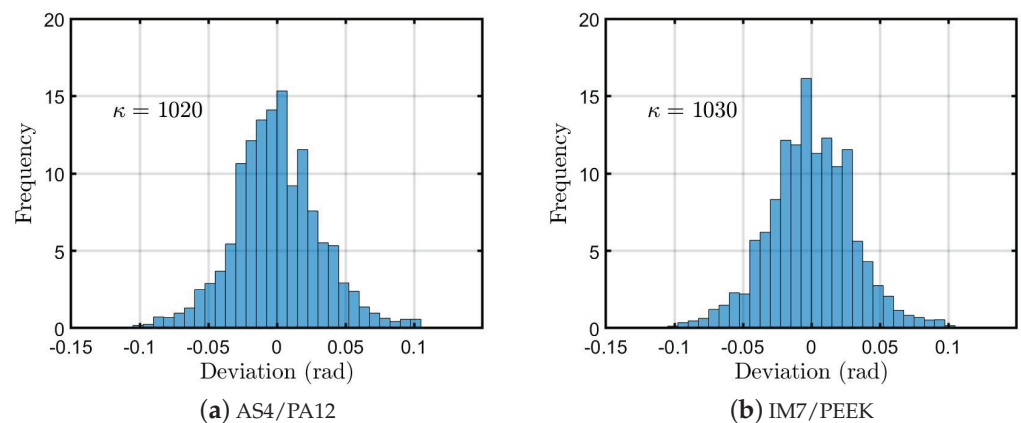


Figure 8. Fibre misalignment distribution for the samples treated by autoclave after being manufactured by ATP and the corresponding concentration parameter κ .

In the autoclave post-processing, the thermoplastic matrix is fully melted and then pressed in order to minimize the voids. As a side effect of this process, the fibres experience micro and sometimes macro unconstrained movement. This justifies the smaller values of the concentration parameter, which is a result of the poor alignment of the fibres. This result shows that, although it reduces the void content, the autoclave cycle has a negative effect on the fibre alignment.

4. Conclusions

This paper examines the quality of composite parts that are manufactured by the automated tape placement (ATP) technology. Two thermoplastic composites manufactured by ATP were used herein, namely IM7/PEEK and AS4/PA12. For reference, the authors used the well-known thermoset aeronautical composites, IM7/8552, manufactured by

standard autoclave cycle. The parameters that were used in the assessment were the distribution of the fibre inside the matrix, the void contents, and the misalignment of the fibres. The methodology that was used for the assessment consists of optical microscopy scans and CT scans followed by statistical analysis.

The results showed that using the ATP with the prescribed manufacturing parameters results in a higher volume fraction of voids, when compared to the autoclave cycle used in the manufacturing of the thermoset-based composites. This is a challenge to be addressed in order to fully benefit from the huge capability of this automated manufacturing technique.

On the other hand, as compared to the epoxy-based composite (IM7/8552), the thermoplastic composites (IM7/PEEK and AS4/PA12) showed improved quality in terms of the distribution of the fibres inside the matrix as well as the fibre misalignment. The crystallization in ATP occurs while the fibres are under tension, which justifies this improved fibre misalignment in the automated tape placement of thermoplastic composites.

The specimens that were treated by autoclave cycle with 1 bar pressure and a temperature higher than the melting temperature showed improvements in the void contents and the fibre distribution in the matrix. However, the autoclave treatment also results in a degradation in the fibre misalignment, as the process melts the polymeric matrix and allow under pressure solidification while the individual fibres are unconstrained.

Author Contributions: Data curation, M.B., Formal analysis, T.A.S.; Funding acquisition, N.O., Investigation, T.A.S. and N.O., Methodology, T.A.S., Project administration, M.B. and N.O., Resources, M.B. and N.O., Writing—review & editing, T.A.S. and N.O., Writing—review & editing, T.A.S. and M.B. All authors have read and agreed to the published version of the manuscript.

Funding: This work has received funding from Enterprise Ireland (EI) and the European Union Horizon 2020 Research and Innovative Programme under the Marie Skłodowska-Curie grant agreement No. 713654. The first author would like to acknowledge the support of Prince Sultan University under the S&M LAB research laboratory grant. The technical assistance of Mr. David Jones of the School of Engineering at the University of Limerick is acknowledged.

Data Availability Statement: The data presented in this study are available on request from the corresponding author.

Conflicts of Interest: The authors declare no conflict of interest.

References

- Gürdal, Z.; Haftaka, R.T.; Hajela, P. *Design and Optimization of Laminated Composite Materials*; John Wiley & Sons, Inc.: New York, NY, USA, 2009.
- Rajak, D.P.; Pagar, D.D.; Menezes, P.L.; Linul, E. Fiber-Reinforced Polymer Composites: Manufacturing, Properties, and Applications. *Polymers* **2019**, *11*, 1667. [CrossRef] [PubMed]
- Legrand, X.; Cochrane, C.; Koncar, V. A Complex Shaped-Reinforced Thermoplastic Composite Part Made of Commingled Yarns with an Integrated Sensor. In *Smart Textiles and their Applications*; Koncar, V., Ed.; Elsevier: Amsterdam, The Netherlands, 2016; pp. 353–374.
- Rubino, F.; Nistico, A.; Tucci, F.; Carlone, P. Marine Application of Fiber Reinforced Composites: A Review. *J. Mar. Sci. Eng.* **2020**, *8*, 26. [CrossRef]
- Cui, J.; Wang, S.; Wang, S.; Li, G.; Wang, P.; Liang, C. The Effects of Strain Rates on Mechanical Properties and Failure Behavior of Long Glass Fiber Reinforced Thermoplastic Composites. *Polymers* **2019**, *11*, 2019. [CrossRef] [PubMed]
- Wakeman, M.D.; Mason, J.A.E. Composites Manufacturing—Thermoplastics. In *Design and Manufacture of Textile Composites*; Long, A., Ed.; Elsevier: Amsterdam, The Netherlands, 2005; pp. 197–241.
- Maurer, D.; Mitschang, P. Laser-Powered Tape Placement Process—Simulation and Optimization. *Adv. Manuf. Polym. Compos. Sci.* **2015**, *1*, 129–137.
- Hou, W.; Zhang, W. Advanced Composite Materials Defects/Damages and Health Monitoring. In Proceedings of the Prognostics & System Health Management Conference (PHM-2012 Beijing), Beijing, China, 23–25 May 2012.
- Antin, K.; Laukkanen, A.; Andersson, T.; Smyl, D.; Vilaca, P. A Multiscale Modelling Approach for Estimating the Effect of Defects in Unidirectional Carbon Fiber Reinforced Polymer Composites. *Materials* **2019**, *12*, 1885. [CrossRef] [PubMed]
- Muramatsu, M.; Nakasumi, S.; Harada, Y. Characterization of Defects in Carbon Fiber-Reinforced Plastics by Inverse Heat Conduction Analysis Using Transfer Matrix Between Layers. *Adv. Compos. Mater.* **2016**, *25*, 541–555. [CrossRef]
- Potter, K.; Khan, B.; Wisnom, M.; Bell, T.; Stevens, J. Variability, Fibre Waviness and Misalignment in the Determination of the Properties of Composite Materials and Structures. *Compos. Part A* **2008**, *39*, 1343–1354. [CrossRef]

12. Mehdikhani, M.; Gorbatiikh, L.; Verpoest, I.; Lomov, S.V. Voids in Fiber-Reinforced Polymer Composites: A Review on their Formation, Characteristics, and Effects on Mechanical Performance. *J. Compos. Mater.* **2019**, *53*, 1579–1669. [CrossRef]
13. Ouarhim, W.; Zari, N.; Bouhfid, R.; Qaiss, A. Mechanical Performance of Natural Fibers-Based Thermosetting Composites. In *Mechanical and Physical Testing of Biocomposites, Fibre-Reinforced Composites and Hybrid Composites*; Jawaid, M.; Thariq, M.; Saba, N., Eds.; Elsevier: Amsterdam, The Netherlands, 2019; pp. 43–60.
14. Meola, C.; Toscano, C. Flash Thermography to Evaluate Porosity in Carbon Fiber Reinforced Polymer (CFRPs). *Materials* **2014**, *7*, 1483–1501. [CrossRef]
15. Liu, L.; Zhang, B.M.; Wang, D.F.; Wu, Z.J. Effects of Cure Cycles on Void Content and Mechanical Properties of Composite Laminates. *Compos. Struct.* **2006**, *73*, 303–309. [CrossRef]
16. Kuriyama, T.; Mizoguchi, M.; Ogawa, T. Effect of Injection Speed on Internal Structure and Mechanical Properties in Short Glass Fibre Reinforced Polyamide Injection Mouldings. *Polym. Polym. Compos.* **2004**, *12*, 423–431. [CrossRef]
17. Mouritz, A.P. Review of Z-Pinned Composite Laminates. *Compos. Part A* **2007**, *12*, 2383–2397.
18. Greenhalgh, E.S. *Failure Analysis and Fractography of Polymer Composites*; Woodhead Publishing Limited: Cambridge, UK, 2009.
19. Stickler, P.B.; Ramulu, M. Investigation of Mechanical Behaviour of Transverse Stitched T-Joints with PR520 Resin in Flexure and Tension. *Compos. Struct.* **2001**, *52*, 307–314. [CrossRef]
20. Ghayoor, H.; Marsden, C.C.; Hoa, S.V.; Melro, A.R. Numerical Analysis of Resin-Rich Areas and their Effects on Failure Initiation of Composites. *Compos. Part A* **2019**, *117*, 125–133. [CrossRef]
21. Nimbale, S.S.; Banker, M.M.; Roopa, A.; Varughese, B.; Sundaram, R. Effect of Gap Induced Waviness on Compressive Strength of Laminated Composites. *Mater. Today Proc.* **2016**, *4*, 8355–8369. [CrossRef]
22. Christian, W.J.R.; DiazDelaO, F.A.; Atherton, K.; Patterson, E.A. An Experimental Study on the Manufacture and Characterization of In-Plane Fibre-Waviness Defects in Composites. *R. Soc. Open Sci.* **2018**, *5*, 180082. [CrossRef]
23. Fedulov, B.N.; Antonov, F.K.; Safonov, A.A.; Ushakov, A.E.; Lomov, S.V. Influence of Fibre Misalignment and Voids on Composite Laminate Strength. *J. Compos. Mater.* **2015**, *49*, 2887–2896. [CrossRef]
24. Wilhelmsson, D.; Gutkin, R.; Edgren, F.; Asp, L.E. An Experimental Study of Fibre Waviness and its Effects on Compressive Properties of Unidirectional NCF Composites. *Compos. Part A* **2018**, *107*, 665–674. [CrossRef]
25. Pain, D.; Drinkwater, B.W. Detection of Fibre Waviness Using Ultrasonic Array Scattering Data. *J. Nondestruct. Eval.* **2013**, *32*, 215–227. [CrossRef]
26. Clarke, A.R.; Archenhold, G.; Davidson, N.C. A Novel Technique for Determining the 3D Spatial Distribution of Glass Fibres in Polymer Composites. *Compos. Sci. Technol.* **1995**, *55*, 75–91. [CrossRef]
27. Kratmann, K.K.; Sutcliffe, M.P.F.; Lilleheden, L.T.; Pyrz, R.; Thomsen, O.T. A Novel Image Analysis Procedure for Measuring Fibre Misalignment in Unidirectional Fibre Composites. *Compos. Sci. Technol.* **2009**, *69*, 228–238. [CrossRef]
28. Sebaey, T.A.; Catalanotti, G.; O'Dowd, N. An Integrated Approach to Measure and Model Fibre Misalignment in Carbon/Epoxy Composites. *Compos. Sci. Technol.* **2019**, *183*. [CrossRef]
29. Han, Z.; Sun, S.; Li, W.; Zhao, Y.; Shao, Z. Experimental Study of the Effect of Internal Defects on Stress Waves During Automated Fiber Placement. *Polymers* **2018**, *10*, 413. [CrossRef] [PubMed]
30. Suprem. *Product Data Sheet 10037, Suprem T60% AS4/PA12-2159*; Technical Report; Suprem: Yverdon-les-Bains, Switzerland, 2009.
31. Suprem. *Product Destination Sheet 10192, Suprem T60%IM7/PEEK 150*; Technical Report; Suprem: Yverdon-les-Bains, Switzerland, 2014.
32. Hexcel. *HexPly 8552 Epoxy Matrix (180 °C/356 °F Curing Matrix) Product Data Sheet*; Technical Report; Hexcel Corporation: Stamford, CT, USA, 2016.
33. Comer, A.J.; Ray, D.; Obande, W.O.; Jones, D.; Lyons, J.; Rosca, I.; O'Higgins, R.M.; McCarthy, M.A. Mechanical Characterisation of Carbon Fibre/PEEK Manufactured by Laser-Assisted Automated-Tape-Placement and Autoclave. *Compos. Part A* **2015**, *69*, 10–20. [CrossRef]
34. Ray, D.; Comer, A.J.; Lyons, J.; Obande, W.; Jones, D.; O'Higgins, R.M.; McCarthy, M.A. Fracture Toughness of Carbon Fiber/Polyether Ether Ketone Composites Manufactured by Autoclave and Laser-Assisted Automated Tape Placement. *J. Appl. Polym. Sci.* **2015**, *132*. [CrossRef]
35. Clancy, G.; Peeters, D.; Oliveri, V.; Jones, D.; O'Higgins, R.M.; Weaver, P.M. A Study of the Influence of Processing Parameters on Steering of Carbon Fibre/PEEK Tapes Using Laser-Assisted Tape Placement. *Compos. Part B* **2019**, *163*, 243–251. [CrossRef]
36. Groupe, W.A.; Warnet, L.L.; Rietman, B.; Visser, R.A.; Akkerman, R. Optimization of the Tape Placement Process Parameters for Carbon/PPS Composites. *Compos. Part A* **2013**, *50*, 44–53. [CrossRef]
37. Rao, P.S.; Hardiman, M.; O'Dowd, N.; Sebaey, T.A. Comparison of Progressive Damage between Thermoset and Thermoplastic CFRP Composites under In-Situ Tensile Loading. *J. Compos. Mater.* **2020**. [CrossRef]
38. Rueden, C.T.; Schindelin, J.; Hiner, M.C.; DeZonia, B.E.; Walter, A.E.; Arena, E.T.; Eliceiri, K.W. IMAGEJ2: ImageJ for the Next Generation of Scientific Image Data. *BMC Bioinform.* **2017**, *18*, 529. [CrossRef]
39. Schneider, C.A.; Rasband, W.S.; Eliceiri, K.W. NIH Image to ImageJ: 25 Years of Image Analysis. *Nat. Methods* **2012**, *9*, 671–675. [CrossRef]
40. Van Doorn, E.; Dhruva, B.; Sreenivasan, K.R.; Cassella, V. Statistics of Wind Directions and its Increments. *Phys. Fluids* **2000**, *12*, 1529–1534. [CrossRef]
41. Berens, P. CircStat: A MATLAB Toolbox for Circular Statistics. *J. Stat. Softw.* **2009**, *31*, 1–21. [CrossRef]

42. ASTM-D3529. *Standard Test Methods for Constituent Content of Composite Prepreg*; Astm International, American Society for Testing and Materials: West Conshohocken, PA, USA, 2016.
43. ASTM-D3171. *Standard Test Methods for Constituent Content of Composite Materials*; Astm International, American Society for Testing and Materials: West Conshohocken, PA, USA, 2011.
44. Mehdikhani, M.; Petrov, N.A.; Straumit, I.; Melro, A.R.; Lomov, S.V.; Gorbatikh, L. The Effect of Voids on Matrix Cracking in Composite Laminates as Revealed by Combined Computations at the Micro- and Meso-Scales. *Compos. Part A* **2019**, *117*, 180–192. [CrossRef]

Review

Different Production Processes for Thermoplastic Composite Materials: Sustainability versus Mechanical Properties and Processes Parameter

Marco Valente ^{1,2,*} , Ilaria Rossitti ^{1,2} and Matteo Sambucci ^{1,2} 

¹ Department of Chemical Engineering, Materials, Environment, Sapienza University of Rome, 00184 Rome, Italy

² INSTM Reference Laboratory for Engineering of Surface Treatments, UdR Rome, Sapienza University of Rome, 00184 Rome, Italy

* Correspondence: marco.valente@uniroma1.it

Abstract: Up to now, fiber-reinforced composites with thermoplastic matrix have seen limited fields of use in the structural scope due to their high viscosity in the molten state, which results in poor impregnability of the reinforcement, leading to mechanical properties of the finished product that are not comparable to those of thermosets. Although the latter still dominate the various sectors of automotive, aerospace, transportation and construction, new applications involving the production of thermoplastic composites are growing rapidly, offering new approaches to the solution of this problem. The aim of this work is to study and evaluate the state of the art on the manufacturing processes of thermoplastic matrix composite, analyzing the parameters that come into play and that most influence the process and material performance. The advantages of film stacking and powder impregnation techniques are contrasted by the versatility of hybrid fabrics and, at the same time, parameters such as pressure and temperature must be carefully considered. A description of different thermoplastic composite processes such as powder impregnation, film stacking molding, hybrid woven fabric, hybrid yarn and products follows, which represent the current possibilities to move from a thermosetting matrix composite to a thermoplastic one, upon which the concept of sustainability is based. This article wants to present an overview of research that has been done in manufacturing thermoplastic reinforced composites and will serve as a baseline and aid for further research and development efforts.

Keywords: thermoplastic matrix composites; impregnation processes; manufacturing; fiber reinforced; processing

Citation: Valente, M.; Rossitti, I.; Sambucci, M. Different Production Processes for Thermoplastic Composite Materials: Sustainability versus Mechanical Properties and Processes Parameter. *Polymers* **2023**, *15*, 242. <https://doi.org/10.3390/polym15010242>

Academic Editor: Zina Vuluga

Received: 2 December 2022

Revised: 28 December 2022

Accepted: 30 December 2022

Published: 3 January 2023



Copyright: © 2023 by the authors. Licensee MDPI, Basel, Switzerland. This article is an open access article distributed under the terms and conditions of the Creative Commons Attribution (CC BY) license (<https://creativecommons.org/licenses/by/4.0/>).

1. Introduction

Thermoplastic composites (TPCs) offer some advantages over thermosets, such as higher toughness, faster production and, first of all, their recyclable nature [1]. Many novel techniques have been proposed, developed and evaluated for thermoplastic applications in the last 20 years and, in recent years, continuous fiber reinforced thermoplastic matrix composites have been successfully employed in the aircraft, military and aerospace industries due to their excellent properties [2]. In these and many other commercial engineering applications, they can replace other materials, such as thermoset composites [3]. Since the late 1990s, an ever-increasing number of aerospace products in these materials have moved into series production. They allow a completely new and automated production since they can be heated and formed repeatedly [4]. They have several advantages over other materials, including excellent fire resistance, significant strain-to-failure, better impact tolerance, higher resistance to fatigue, short molding time and longer shelf life of prepreg [5]. However, the high cost and difficulties of impregnating continuous fiber thermoplastic composites, resulting from polymer melting or the use of solvents, still limits their use in

commercial applications. Therefore, cost savings and mechanical properties largely depend on developing more efficient methods for impregnating fibers due to the thermoplastic's high viscosity and processing the final composite parts [3]. Furthermore, their use has been limited by the lack of good processing techniques to make flexible prepreg tapes. The general intractability of these matrices due to their high viscosity and high processing temperatures gives rise to a series of problems, such as the manufacture of stiff tape, devolatilization of the solution which leads to the formation of voids with the consequent loss of mechanical properties, and dishomogeneous resin content prepreg tapes [6]. A solution to improve fiber impregnation is to bring the matrix and fibers into contact as much as possible before the final molding step or, in other words, reducing the flux length required by the polymeric matrix. Various concepts of these intermediates have been developed [1], such as commingled textiles that consist of both reinforcing and polymer fibers, textiles made of powder coated fibers and partially or fully consolidated panels. As Figure 1 shows, in the general context of thermoplastic polymer matrix composite manufacturing, two approaches can be taken: the most direct, Reactive Processing, which starts from the fabric impregnation with the monomer and involves in-situ polymerization. We will not discuss this process in this paper as it has been addressed and explored in detail in another work [7] by our research group. Instead, our attention will be focused, in this article, on the second technique, Melt Processing. It is important to emphasize the fact that in-situ polymerization can be the best performing route as it might be able to limit as much as possible the porosity and difficulties arising from Melt Processing, e.g., the inability to achieve optimal impregnation due to high viscosities of thermoplastic melt material. This, in turn, could lead to lower mechanical properties and a fair amount of defectiveness, which needs to be minimized. While Reactive Processing is better performing, the monomers that can fulfill this function with feasible and economically viable industrial processes are limited. To date, it is only possible with PA6, starting with ϵ -caprolactam monomer and PMMA. With Melt Processing, therefore, it is more difficult to get a defect-free composite, but it is possible to use a multitude of polymers and thus dose the properties of the final product.

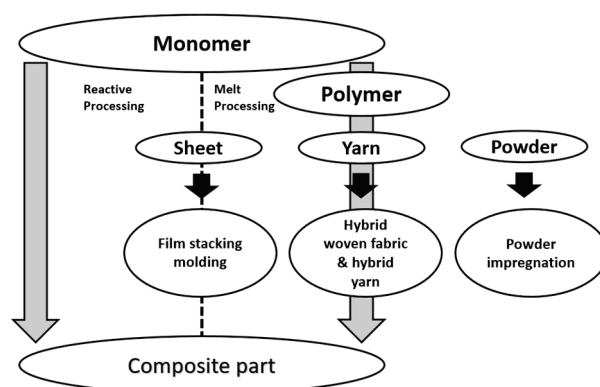


Figure 1. Processing steps for manufacturing thermoplastic composite parts through melt and reactive processing. Author's own figure.

Nevertheless, one of the most effective solutions lies precisely in their production, in order to move toward eco-sustainable and circular composites. The strong commitment of world organizations in the field of safeguarding the planet has directed the research of these materials toward production processes with a lower environmental impact and a strong propensity to recycle the polymeric part [8]. The development of eco-sustainable composites has involved the study of glass/polymer [9], carbon/polymer [10], metal/polymer [11], polymer/polymer [12], ceramic/polymer [13], and concrete/polymer [14] interactions for the optimization of the final mechanical properties and the inclusion of these products in the perspective of environmental and economic circularity.

The rapid increase in the application of fiber-reinforced polymer matrix composites is creating a challenge for waste recycling. The use of high-performance thermosetting poly-

mers as a matrix makes the recovery of fibers and resins extremely difficult. Implementing a circular economy able to eliminate waste and reuse resources ensures the use of efficient processes to recycle thermoset composites components and manufacturing wastes [15].

Definitely, the outstanding performance of conventional thermosets arising from their covalently cross-linked networks directly results in a limited recyclability. The available commercial or close-to-commercial techniques facing this challenge can be divided into mechanical, thermal and chemical processing. However, these methods typically require a high energy input and do not take the recycling of thermoset matrix itself into account. Rather, they focus on retrieving the more valuable fibers, fillers, or substrates [16]. This push in the use of thermosetting composites is now raising awareness of their fate: a direct consequence is, in fact, a strong increase in the relative waste, coming from the production processes (prepreg waste; cuttings and scraps of vulcanized composites, which represent approximately 30–40% by weight of total materials) and, belatedly, by end-of-life products (EoL). In fact, carbon fiber reinforced polymers worldwide are projected to reach up to 20 ktons per year by 2025 [17]. With approximately 6000–8000 commercial aircrafts reaching their end-of-life by 2030 [18], there is a clear and demanding request in order to develop economically-sustainable waste management and recycling techniques for fiber reinforced polymer matrix [15]. As shown in Figure 2, the global epoxy composite market size was valued at USD 28.40 billion in 2020 and is expected to grow at a compound annual growth rate (CAGR) of 8.3% from 2021 to 2028 [19]. Rapid replacement of conventional materials in automotive and aerospace applications is expected to drive the market in the coming years. Furthermore, it should also be emphasized that the current European Union (EU) legislation still lacks specific regulation for the treatment of composite waste. Some hints are included in the 2000/53/EC EU Directive, which provides for a recovery of 95% and a recycling rate of 85% of the total weight of the EoL vehicle and limits the use of non-metallic components if they do not comply with the requirements of the Directive, but no specific instruction on how to treat EoL carbon fiber reinforced polymers is specifically addressed [15] or these reasons, industry and researchers have shown a growing interest in new approaches for the recycling of thermosetting composites or, in the most innovative solutions, on the potential of manufacturing thermoplastic composites.

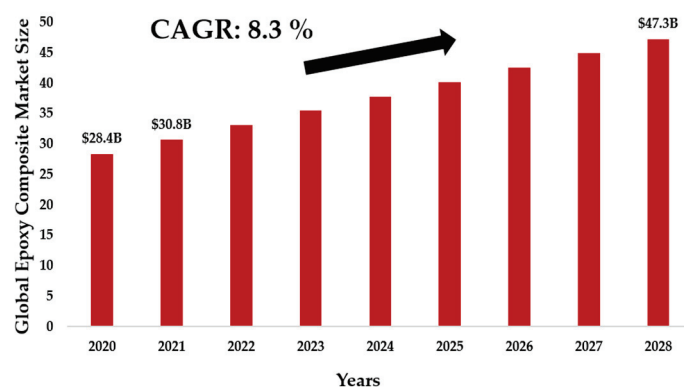


Figure 2. Epoxy Composites Market Size and Forecast. Authors' own figure from Reference [19].

It is a fact that, when taking into account factors such as climate change, global warming, environmental sustainability and circular economy, the landfill or incineration of thermoset component wastes must be avoided. In this context, more efforts are required to improve the technology readiness level of the processes in place and their scalability should be economically accessed. To develop commercially viable recycling activities, the future research studies must be focused on the following points: achievement of consistent quality of recycled fibers; reuse of them as reinforcement in thermoplastic polymers, also from renewable sources; study of mechanical properties after reuse and remanufactured technologies evaluation of the potential to close the life cycle loop of CFRPs and reducing energy consumption and recycling cost. In this field, innovation is multifaceted and can

come both from the constituent materials (high-performance engineering thermoplastic matrices, commingled semi-preg of recycled carbon, and glass fibers/thermoplastics) and production processes (film stacking, dry powder impregnation, fiber commingling).

This review will be focused on the latest advances and development of reinforced thermoplastic, mainly referring to continuous fibers and non-woven fabric composites and related processing technologies: relationships between impregnation mechanisms, consolidation quality and resulting mechanical properties of composites manufactured from film stacking, commingled fabrics and dry powder impregnation systems will be investigated. This paper highlights how these materials can be processed, adopting a completely different paradigm in comparison to that of the thermosetting matrix, the former not requiring a reaction to set the properties but complex thermal cycles, often performed in a short time span.

2. Impregnation Methods from Molten Polymer Matrices

It is possible to make an important distinction between various impregnation methods: we distinguish those that precede it, called pre-impregnation, and those that follow it, called post-impregnation. In the former, the fibers impregnation takes place in a single step using a polymer in the molten state. The various layers thus obtained are stacked and subsequently consolidated due to the application of heat and pressure. In the latter, however, it is expected that the impregnation occurs during the processing of the piece starting from a polymer in the shape of a film, powder or filament [20]. In this article we will focus only on the post-impregnation phase starting from semi-impregnated forms.

Figure 3 presents several methods for wetting the fibers with a thermoplastic polymer. Different methods have been employed to make thermoplastic pre-impregnated tapes. The most common processes for combining the polymer and the reinforcement that will be addressed in this work are:

1. Film stacking, technique that consists in alternating thin polymer sheets with the reinforcement and, subsequently, compacting them;
2. Powder impregnation technique consists in covering and, therefore, impregnating the fiber fabric with the polymeric matrix in the shape of a dry powder [21];
3. Hybrid woven fabrics;
4. Hybrid yarns.

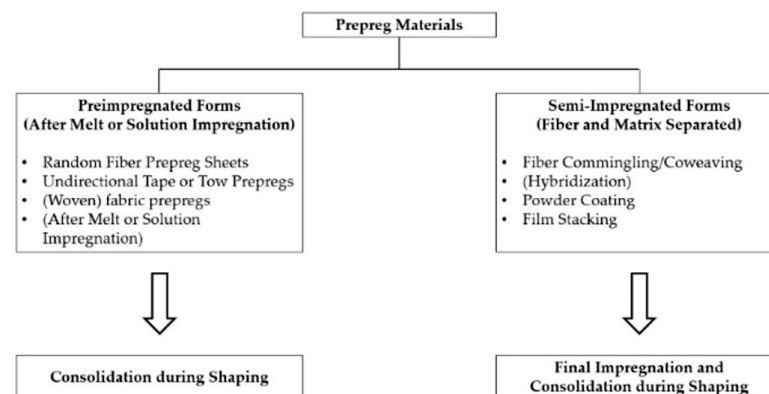


Figure 3. Typical impregnation techniques for thermoplastic composites materials. Authors' own figure from Reference [6].

2.1. Film Stacking

Film stacking consists in heating and compressing a sequence of alternated layers of thermoplastic films and dry fabric reinforcements (Figure 4). The resulting thermoplastic laminates serve as a semi-finished product subsequently intended to thermoforming processes to obtain the desired shape of the final composite component. Film stacking process involves three main phases [22]:

1. Heating of the press to lower the matrix viscosity;

2. Increasing of the pressure to force the liquid-state thermoplastic matrix to impregnate the fabric;
3. Cooling of the press to solidify the laminate.

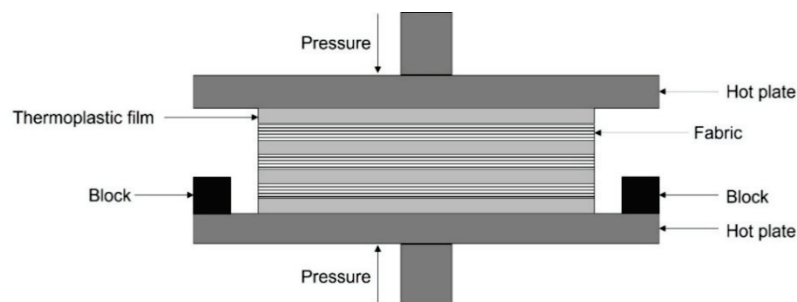


Figure 4. Schematic of film stacking process for thermoplastic composite laminates. Author's own figure.

Temperature, pressure, and holding time are the core parameters to control the process. Their values depend on the nature of the polymer, mainly melting temperature and viscosity, as well as on the fabric tortuosity and the load and temperature the fibers can sustain [23]. Below a comprehensive literature survey on the influence of these process parameters on the properties of film-stacked thermoplastic composites is reported.

2.1.1. Influence Mechanism of Processing Temperature

Processing temperature considerably affects the mechanical and microstructural properties of the composite produced. It is known that the use of thermoplastic resins introduces the issue of adequate fiber bed impregnation because of the higher viscosity of thermoplastic melts than thermosetting ones. Optimization in processing temperature is crucial. High temperature pressing scheme promote a lower resin's viscosity and therefore greater mobility and fluidity to penetrate between the fibers and impregnate them. On the other hand, the use of high temperatures potentially clashes with the thermal stability of the materials constituting the composite. Then, an optimal condition will exist where adequate resin flow occurs during consolidation (i.e., good impregnation and composite quality) and thermal degradation of the constituents is kept at a minimum [24].

Hu et al. [25] explored the influence of molding temperature (360–400 °C) on the mechanical strength of carbon fiber fabric reinforced polyether ether ketone (CFF-PEEK) thermoplastic composites. The tensile and flexural properties exhibited the char of first increase and then decrease in the temperature range under investigation. From 360 to 390 °C the tensile and flexural strengths increased from 412.63 MPa and 487.45 MPa (+15.35%) and from 663.21 to 808.32 MPa (+17.95%), respectively. At 400 °C, a negative influence in mechanical properties was detected, with a decrease in tensile and flexural strengths of 9.95% and 11.88%, respectively. The authors explained the results monitoring the viscosity of PEEK melt under different isothermal conditions. At the molding temperature of 390 °C, the resin showed the lower viscosity and the higher fluidity, adequately impregnating the fibers and providing the composite the best performance. At 400 °C, PEEK converged to a rapid increase in viscosity because to thermal crosslinking of macromolecular chains induced by excessively higher temperature. Consequently, the increment in viscosity hindered the proper impregnation of carbon fabric, worsening the mechanical performance. Kim and Park [26] investigated the effect of process temperature (205, 215, and 225 °C) on the impregnation quality of flax fiber reinforced polypropylene (FFR-PP) composites. The authors discovered that, at the lowest temperature, the flax fabric was not completely impregnated. Although the higher temperatures are advantageous with respect to the resin flow, the void content in the laminate fabricated at 225 °C (5.1%) was greater than the process temperature of 215 °C (3.2%). In this case, the thermal degradation of flax fiber induced by the highest processing temperature was recognize as the main reason for the increment of void concentration at the matrix-fiber interface. Then, detrimental

effects were detected in terms of flexural properties. Zal et al. [27] studied the effective processing temperature (160–240 °C) on the strength and microstructural properties of glass fiber reinforced polyvinyl chloride (GF-PVC) composites. Due to the reduction of PVC viscosity, impregnation and flexural strength of the samples get better by increasing the processing temperature up to 220 °C (from 59.4 MPa at 160 °C to 146 MPa at 220 °C). The highest temperature (240 °C) involved degradation of PVC matrix, weakening the bonding between fibers and matrix and dramatically diminishing the flexural performance (39.3 MPa). Figure 5 elucidates the different failure mechanism as a function of processing temperature (at the same pressure and holding time). At the lowest processing temperature (160 °C) the impregnation quality was low, causing inter-laminar sliding failure (Figure 5a). By increasing the processing temperature, the adhesion between matrix and GF gradually improved. At 180 °C, both inter-laminar sliding and fibers fracture occur simultaneously like failure mechanism of the composite (Figure 5b). For the laminate produced at 240 °C, the failure mode was governed by the degradation due to the weak adhesiveness and integrity of matrix (Figure 5c).

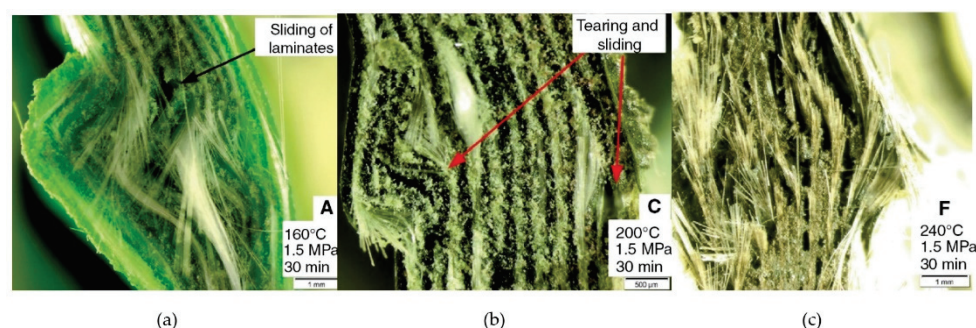


Figure 5. Failure mechanism in GF-PVC laminate as a function of processing temperature: (a) 160 °C, (b) 200 °C, (c) 240 °C. Adapted with permission from Reference [27].

2.1.2. Influence Mechanism of Pressure

The pressure drives the thermoplastic resin to infiltrate into the compliant fabric while simultaneously deforming it, altering the infiltration kinetics [28]. This parameter plays counteracting roles to determine the resin impregnation in the fibrous medium. Too low compression pressure can increase the impregnation time, forming dry spots inside the composite. Conversely, if too high pressure is applied on the fibrous bed, the fiber volume fraction increases decreasing the fabric's permeability due to the reduction of the pores volume between the bundles and between the fibers [23,26]. Additionally, the pressure must be carefully selected to avoid excessive compression loads exerted on the fibers, which lead to damage or failure to the reinforcement prior the composite's fabrication [29].

Suresh and Kumar [30] researched the effect of forming pressure (4 MPa, 7 MPa, and 9 MPa) on the mechanical properties of glass fiber reinforced polypropylene (GF-PP) laminates. Keeping fixed the processing temperature at 190 °C, the authors observed that an increase in the forming pressure initially increased the flexural and tensile strengths (+17% in tensile and +63% in bending, moving from 4 MPa to 7 MPa of pressure), then decreased the properties of the composite laminates (−12% in tensile and −30% in bending, moving from 7 MPa to 9 MPa of pressure). The optimal pressure condition of 7 MPa, also corroborated by Design of Experiment (DOE) computational analysis, revealed an improved wetting of the glass fibers and therewith good bonding to the matrix in the GF-PP system. Katayama et al. [31] optimized a film stacking process to fabricate jute fabric reinforced poly-lactic acid (JF-PLA) composites. Investigating among a range of compaction pressures (1 MPa, 2 MPa, 3 MPa, and 4 MPa) at 160 °C as a processing temperature, the authors discovered that that the higher moulding pressure than 3 MPa did not significantly affect the impregnation and density of composite structure. Moulding pressure of 3 MPa was consider optimum in terms of moulding time (300 s), microstructural compaction, and mechanical strength reaching approximately 115 MPa in flexural strength. Kazano et al. [32]

investigated the relation among mould pressure conditions in film-stacking process and resin impregnation to fiber yarns in carbon fiber fabric reinforced polyimide (CFF-PI) composites. The impregnation ratio, predicted by the Kobayashi et al. [33] model, and the microstructural analysis of the laminate were assessed as a function of five pressure conditions (0 MPa, 1 MPa, 2 MPa, 4 MPa, 8 MPa). The photograph in Figure 6 highlights that since the polymer impregnation was not improved after the pressure 4 MPa, this condition was indicated as the optimum molding pressure. Interestingly, it is possible to verified different void size and distribution as a function of processing pressure. At 0 MPa (no compaction), a large void can be detected at the center of the yarn (Figure 6a). By increasing the pressure, fine voids are formed inside the fabric and their dimensions tend to gradually diminish. This is because the pressure disassembles the large-sized gap in the uncompacted laminate to the fine voids, which tend to disperse in the composite. The increase in mould pressure also promotes the expulsion of excess air resulting in smaller void sites. Consistently, at the optimum pressure of 4 MPa, the impregnation ratio converged to 100%.

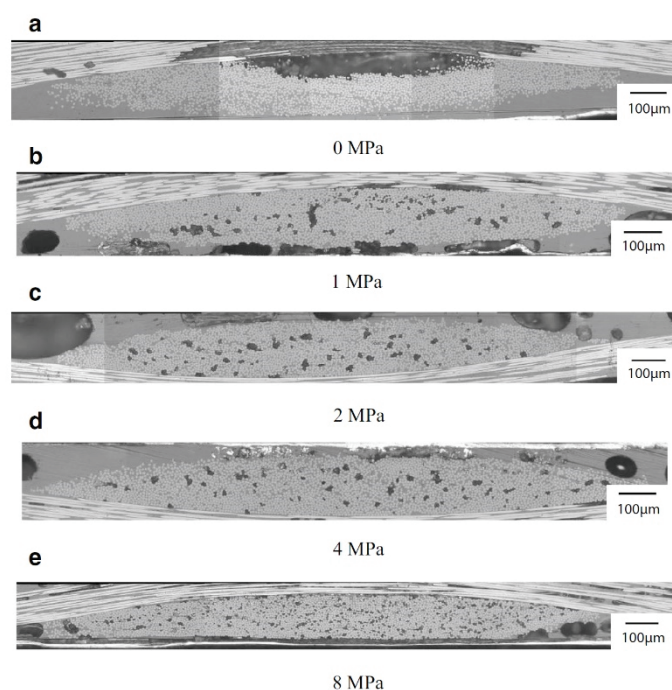


Figure 6. Cross section of CFF-PI laminate as a function of mould pressure: (a) 0 MPa, (b) 1 MPa, (c) 2 MPa, (d) 4 MPa, and (e) 8 MPa. Reprinted with permission from Reference [32].

2.1.3. Influence Mechanism of Holding Time

Other than temperature and pressure, the application time for these parameters is another critical consideration in the film stacking process. Insufficient holding time could compromise the laminate's microstructural quality, producing defects on the sample, which are associated with inadequate pressure and temperature [34].

As with processing pressure, Katayama et al. [31] investigated the influence of different holding times (30–600 s) on the impregnation of JF-PLA laminates. Cross section photos of the film-stacked composites processed at 1 MPa and 160 °C revealed that the high melt viscosity of PLA as well as the twist architecture of natural fiber bundles required almost 300 s for an adequate and defect-free impregnation. After 300 s the polymer impregnated into fiber bundles but no significant improvement in flexural strength occurred, verifying that a “threshold” duration for compression exists which provides short working time and good mechanical performance, see Figure 7.

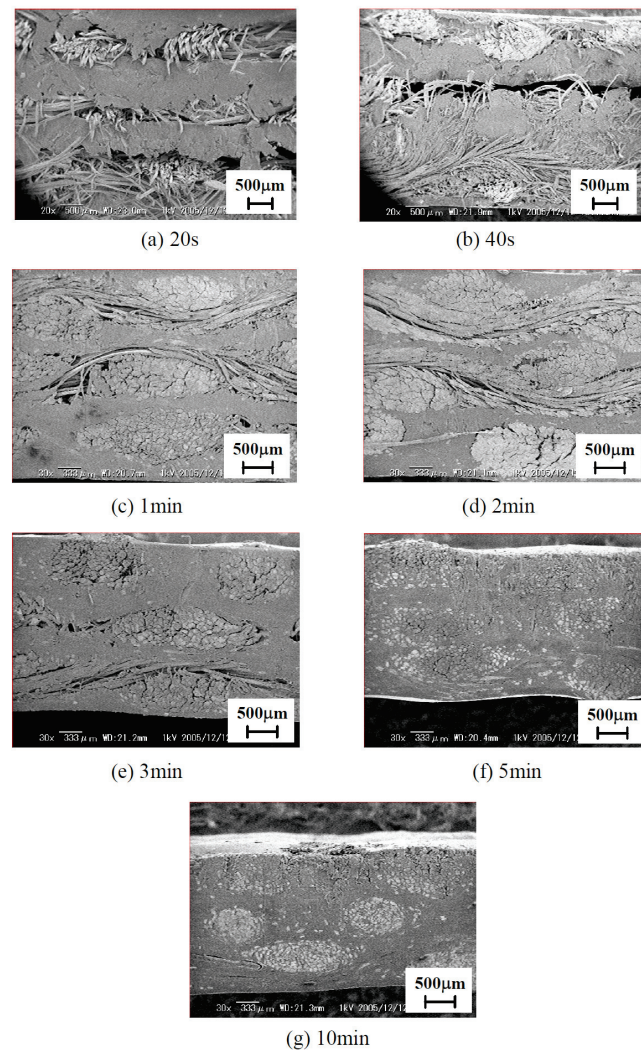


Figure 7. Cross section of JF-PLA laminate as a function of holding time: (a) 20 s, (b) 40 s, (c) 1 min, (d) 2 min, and (e) 3 min, (f) 5 min, and (g) 10 min. Reprinted from Reference [31] under Creative Commons license.

Yang et al. [35] analyzed the influence of holding time on the mechanical behavior of ultra-thin carbon fiber fabric reinforced polycarbonate (CFF-PC) composites. The examined moulding times ranged from 0.5 min to 5 min at increments of 1.5 min, considering a processing temperature of 240 °C and pressure of 6 MPa. Although, long holding time would seem to promote the wettability and interfacial bonding between the matrix and reinforcement, maximum tensile properties were identified at 3.5 min (tensile strength of approximately 450 MPa) while the strength decreased when the parameter reached the higher value of 5 min. The authors explained the detected results by considering the excessive increase in flowability of PC matrix for the highest process parameters (temperature, pressure, and holding time). The resulting rheology of the melt polymer would generate an extremely high scouring force, disturbing the carbon fiber location and the pre-determined uniformity. Then, misalignment of the reinforcement would act as a manufacturing defect, negatively altering the strength of the laminates. Vitiello et al. [36] implemented two impregnation procedures, in terms of duration and intensity, for the fabrication of basalt fiber-reinforced polyamide 11 (BF-PA) laminates. Regarding “slow” procedure the laminate was compacted at lower pressure (3 MPa) and for longer times (13 min), suffering from the growing viscosity of the matrix. The “fast” procedure applied high pressure (4.5 MPa) at short time (7 min), that is, when the polymer viscosity is low. The differences in fabric impregnation resulted in substantial differences in the mechanical

properties of the laminates: “fast” procedure sample exhibited better fiber impregnation, lower porosity, higher flexural modulus (+20%) and strength (+60%), and even the damages following impact and indentation stresses were lower than those recorded in the sample realized with the slow procedure.

2.2. Powder Impregnated Tow

The use of thermoplastic composites has been limited by the lack of reliable techniques to make prepregs of consistent quality. Dry powder impregnation methods offer a new approach to the solution of this problem. This process was identified as the technique with the greatest potential for success as a valid alternative to produce prepreg thermoplastic tapes [6]. Various research groups have developed several ways to disperse polymer powder and impregnate a fiber tow as summarized in Table 1.

Table 1. Reference values of thermoplastic polymers. Authors’ own table from [20].

Materials (Thermoplastic Polymer)	Tensile Modulus, GPa	Tensile Strength (Yield), MPa	Melt Flow, g/10 min	Melting Point, °C	Density, g/cm ⁻³
Polypropylene (PP)	1.50–1.75	28–39	0.47–350	134–165	0.89–0.91
Polyethylene (PE)	0.15	10–18	0.25–2.6	104–113	0.918–0.919
Polyamide (PA)	0.7–3.3	40–86	15–75	211–265	1.03–1.16
Poly ether ether ketone (PEEK)	3.1–8.3	90–11	4–49.5	340–344	1.3–1.44

These processes differ mainly in the way in which the particles of the matrix are deposited on the fibers and in the forces of particle/fiber interaction responsible for their adhesion. In most dry processes, the fibers are passed through an air suspension of particles. Some of the main factors that influence the mode and rate of deposition of the powder are:

- Fiber tow spreading;
- Particulate flow pattern;
- Particle size;
- Dielectric properties of fibers and particles;
- Particle cloud concentration [21,37].

It is expected that the powder is introduced into a fiber tow which is processed by heating to sinter the particles onto the fibers. Price [38] was the first to employ this technique, that provides for the passage of the glass roving through a bed (fluidized or loosely packaged) of thermoplastic powder. The particles attach themselves to the fibers due to electrostatic attraction. The tow is then heated and passed through a mold to produce an impregnated tow. The impregnation is macroscopic, i.e., the particles cover fiber groups rather than single fibers and is mainly aimed at the production of short fiber reinforced thermoplastics. Polypropylene particles with an average diameter of 250 microns were used. Ganga [6] fluidized polyamide particles smaller than 20 microns in a fluidization chamber, impregnated glass rovings and then coated it with an outer sheath of a second material with a lower melting point than the impregnated particles. The second sheath was extruded onto the tow. Muzzy et al. [39] demonstrated the ability to manufacture the prepreg by passing a scattered tow through an electrostatic fluid bed of PEEK powder (50 microns). Allen et al. [40] impregnated the fibers in a recirculation chamber with annular walls to aid dust recovery and a fan on the bottom to disperse the thermo-plastic polyimide particles (5–20 microns, LaRC-TPI) [6].

Powder polymer matrix and reinforcement can contact each other electrostatically. The impregnation takes place thanks to the charged powder particles deposited on the fabric surface [20,39,41]. In this case as well, the consolidation occurs through the simultaneous application of heat and pressure in order to obtain continuous fiber prepregs [6,41]. Rath et al. [42] produced prepregs with a Nylon-12 matrix and a reinforcing volumetric content between 20% and 50% in continuous aramid fibers [20]. Padaki and Drzal [37,43]

identified heating, compression and cooling as the three necessary steps for the process. This method is discussed in detail in literature.

The flowchart for the manufacture of powder-impregnated thermoplastic composites is shown in Figure 8 and lists the two basic steps:

1. Tape manufacture, which involves the fiber tows impregnation with thermoplastic particles and their subsequent coalescence on the fibers to form a flexible prepreg tape;
2. Consolidation, which involves laying prepreg tapes into a mold followed by heat and pressure application to form void-free composites. An important aspect for optimizing the processing cycle is the characterization of the different properties of the thermoplastic matrix and the reinforcing fiber.

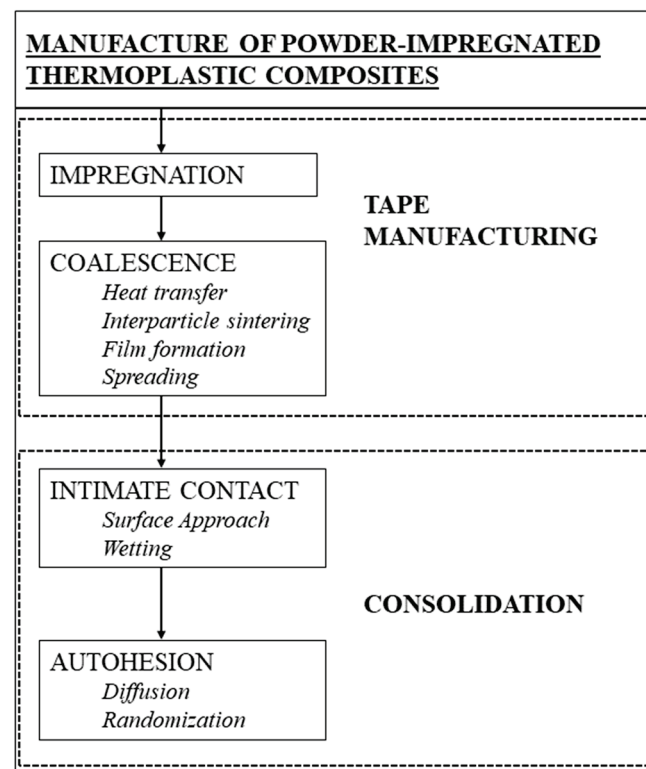


Figure 8. Flowchart for the manufacture of powder-impregnated thermoplastic composites. Authors' own figure from Reference [6].

Dry powder processes have numerous advantages for the production of thermoplastic prepreg tape. An ideal process would have the following advantages over other processes:

- It would be little affected of the viscosity of the matrix. Most high-performance thermoplastic matrices are highly viscous (104 to 105 Poise) above their softening point (amorphous) or melting point (semi-crystalline). A good dry powder process would circumvent this problem by coating the fibers individually so that flow occurs over very short distances of the order of microns;
- It would avoid the use of binders, solvents or water that must be evaporated during the last stages of the processing cycle. Incomplete removal can result in voids which have a detrimental effect on the mechanical properties of the composite;
- The introduction of secondary material processing operations such as fiber spinning which could increase the cost of the final product would be avoided [6].

2.3. Hybrid Woven Fabrics

Hybrid woven fabrics (HWFs) are characterized by orthogonal interlacing of two sets of yarns: polymer filaments and reinforcing long fibers in different architectures (carbon, glass, aramid, and natural fibers) constituting the fill (warp) and weft, respectively. There

are many types of weaving patterns employed to create HWFs: plain weave, twill, and satin [44]. According to Figure 9 the woven fabric involves periodicity in its microstructure, thus permitting identification of a repeating unit, defined as unit cell. The index n_g can be defined to indicate the interlacing counts between the fill (polymer) and weft (reinforcement) yarns. The n_g index is equals two for plain weave, three for twill weave, and four or greater for satin weave [45].

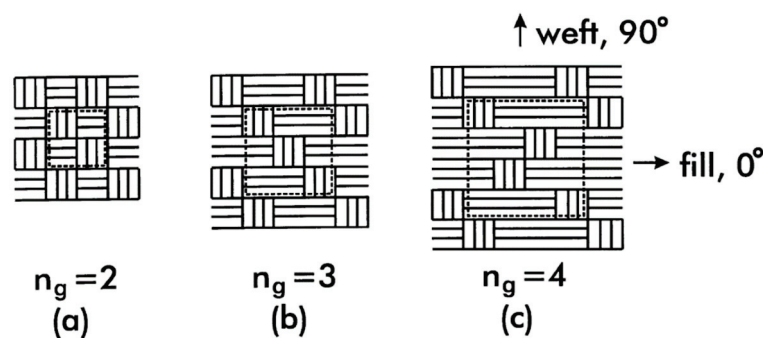


Figure 9. Different weaving patterns in hybrid woven fabrics: (a) plain, (b) twill, and (c) stain. Reprinted with permission from Reference [45].

Irrespective of the type of polymer matrix and reinforcing fibers, the weave pattern used for making the HWF contributes to the mechanical properties of the composite. For instance, research conducted by Alavudeen et al. [46] on natural fiber-reinforced hybrid polyester fabric highlighted that plain pattern exhibited higher tensile strength than the twill weave pattern due to a more uniform distribution of stress transfer with the application of tensile load in both the longitudinal and transverse directions. Indeed, in the plain weave configuration, fibers are interlaced one-to-one in both the warp and weft directions whereas there is no interlacing of filament in the weft direction in the twill pattern, which in turn reduces the strength properties of the composite. Fabrics are transformed by hot-pressing consolidation process into rigid composite structures of fibers embedded in a continuous polymer matrix. Using HWF in composite materials, the manufacturing process stay the same with respect to the film-stacking technique. Processing cycle consists of heating a stack of several layers of hybrid fabrics above the melting point of the matrix fibers, applying sufficient pressure to reduce the thickness of the laminate to the fully consolidated thickness and then cooling below the glass transition temperature of the matrix while maintaining pressure. The time to reach full consolidation depends on the time taken to fully impregnate the reinforcing fiber bundles. Processing cycles may be prolonged to improve the fiber impregnation and matrix-to-fiber adhesion or to achieve the desired level of crystallinity in the polymer matrix. Pressure, temperature, and holding time are the main process parameters governing the characteristics of the final composite [47].

Compared with the common unidirectional laminates, HWF composites provide better dimensional stability over a large temperature range, more balanced properties in the fabric plane and the interlacing of yarns results in higher out-of-plane strength, better impact resistance, and tolerance [48]. In the warp-weft configuration, after thermo-compression, the different filaments scatter amongst one another, as a result, the resin flow distance for impregnation can be greatly reduced and consequently the applied pressure and time are limited compared to film stacking and even considering the powder-based impregnation technique, leading to a saving in manufacturing costs [49]. However, intercalation of the polymer filament in the fiber bed by weaving would establish a fixed matrix-to-reinforcement proportion ratio in each hybrid fabric produced, limiting the management freedom in designing composites at varying reinforcement level.

On the best authors' knowledge, recent literature regarding optimization of the manufacturing process of hybrid fabric as well as the effect of thermo-forming parameters on the final composite's characteristics is very limited. Below, some topical studies are reviewed.

2.3.1. CF-GF/Thermoplastic (PP/PET) HWFs: Weaving Process Optimization for Electromagnetic Shielding Applications

Lin et al. [50] combined PET and PP yarns and CFs and GFs to form woven fabrics by rotor twister method. Specifically, the authors investigated various rotary rate (from 9000 rpm to 15,000 rpm) during the manufacturing stage to optimize the structure of the fabric in terms of compaction between the wrapped yarns and tensile properties. The highest rotatory speed (15,000 rpm) yielded the slightest thickness of yarn and optimal tensile strength along the weft direction. In addition, the compact interior structure of hybrid fabric already achieved at 13,500 rpm enhanced the reflection and refraction of electromagnetic waves, conferring optimal shielding properties. Comparing GFs and CFs, the latter possessed higher electromagnetic effectiveness because of their greater electric conductivity that make the fibers able to shield the waves by absorbing them.

2.3.2. GF/PP HWFs: Assessment of the Moulding Technology and Stacking Sequence

Formisano et al. [51] studied the influence of the manufacturing technology (isothermal and non-isothermal moulding methods) on the mechanical behavior of laminates from commercial hybrid fabrics of GF (60 *w/w%*) and PP fibers (40 *w/w%*) (Figure 10). The composite laminates (from 1 to 5 mm thickness) were realized with two stacking sequence, (1) 45–0–90 and (2) 0–90, to also evaluate the effect of laminate orientations on the mechanical characteristics. At the same moulding technology, 0–90 samples showed a higher peak force, penetration energy, and peak deformation values than 45–0–90 specimens. This result was attributed to several factors: higher bending stiffness and lower stiffness mismatch between adjacent layers in 0–90 configuration and greater sensitivity to delamination and interlaminar damage of 45–0–90 specimen. Considering the moulding methods, isothermal procedure was demonstrated better in term of strength, leading to a flexural strength almost 25% higher than those achieved by non-isothermal method.

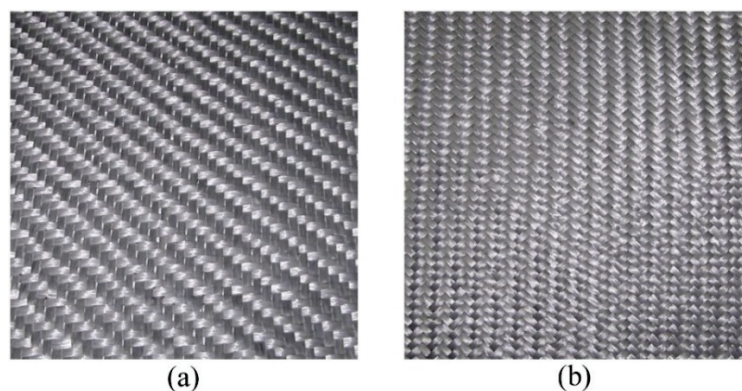


Figure 10. PP-GF fabrics investigated by Formisano et al.'s research [8]: (a) 0/90 ply and (b) ± 45 ply. Adapted with permission from Reference [51].

2.3.3. CF/PA6 HWF: Assessment of Impact Energy Absorption Capability

Di Benedetto et al. [52] developed a multiple regression model to predict the low-velocity impact behavior of CF/PA6 composite laminates obtained by compression moulding of five HWFs with stacking sequence 0° .

The purpose of this study was to optimize the energy absorption properties of composite and then increase their crashworthiness for using on automotive components. Five consolidation temperature (240 °C, 250 °C, 260 °C, 270 °C, and 280 °C) and two pressure conditions (<0.3 MPa and 0.3 MPa) were investigated to build the predictive model.

Processing temperatures above 260 °C negatively affected the dynamic mechanical response of the composite due to thermos-oxidative degradation phenomena that the polymer matrix underwent.

Indeed, in accordance with the thermal degradation kinetics method implemented by the authors, the material crashworthiness is highly associated with the degradation kinetics. The composite is more resistant when the degradation rates are reduced. With regard to the pressure, the laminates manufactured at 0.3 MPa provided a homogeneous and defects-free microstructure (Figure 11a) compared to the sample processed with pressure below 0.3 MPa (Figure 11b).

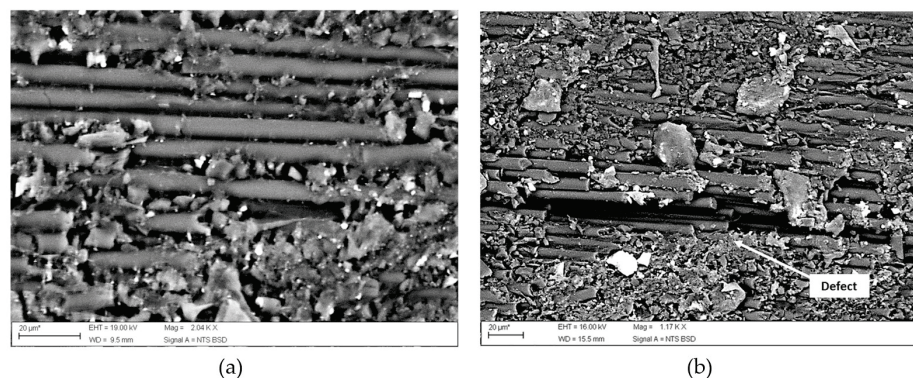


Figure 11. CF/PA6 laminates processed with pressure (a) of 0.3 MPa and (b) below 0.3 MPa. Adapted with permission from Reference [52].

2.3.4. Jute/PP HWF: Manufacturing and Characterization

Souza et al.'s research work [53] proposed the manufacture of Jute/PP (40 *v/v%* Jute–60 *v/v%* PP) HWFs as preforms for bio-composite laminates fabrication. The woven architecture and the cross-sectional optical micrographs of the laminate obtained by compression moulding (processing temperature of 190 °C, pressure of 0.2 MPa, and holding time of 20 min) are reported in Figure 12, respectively.

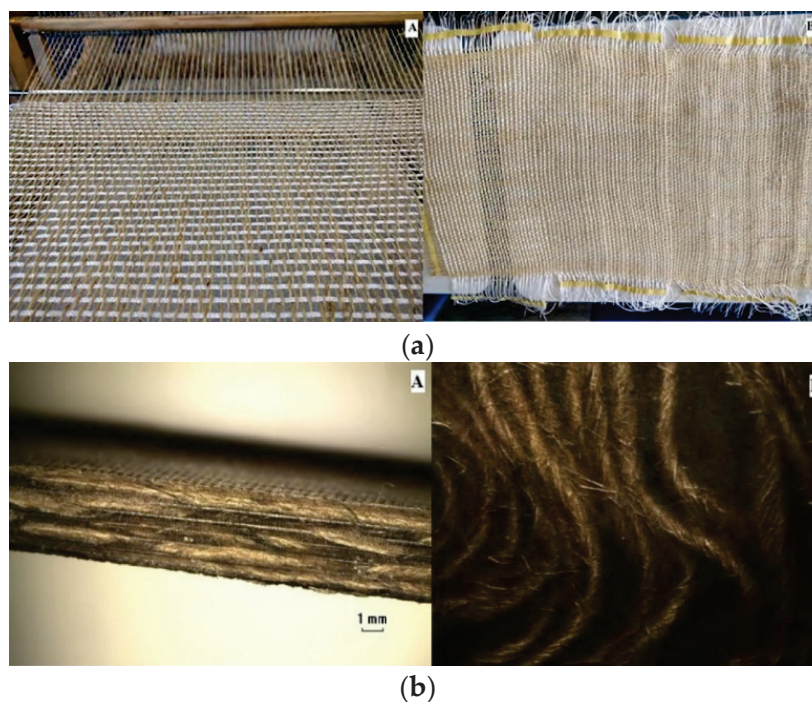


Figure 12. (a) Jute/PP HWF architecture and (b) cross-sectional optical micrographs of the laminate Adapted from Reference [53] under Creative Commons license.

The HWF technique was successfully applied in the manufacturing of Jute/PP hybrid bio-composites by compression moulding. The obtained composites presented moderate

mechanical properties of tensile strength (44.62 MPa) and elastic modulus (7.1 GPa), which were slightly better than the values found in literature on non-continuous fiber Jute/PP composites with same fiber/matrix proportion ratio. These performances suggest their possible application in non-structural components for reducing weight, costs, and environmental impact. The HWF has also presented interesting properties of malleability and strength required by textile industries for weaving processes.

2.4. Hybrid Yarns

The use of hybrid yarns is one of the most promising routes for producing structural thermoplastic composites due to a low-cost manufacturing of complex shaped parts. This process can offer a very good distribution of matrix and reinforcement in a non-molten state before processing. To take advantages of the processing and fabrication reductions that can be provided by textile technology, the thermoplastic matrix should be incorporated into the yarns before their conversion into preforms. In hybrid yarns, indeed, matrix and fabric are blended intimately at the filament level, such as the polymer flow distance for impregnation is reduced when matrix and fibers are commingled each other. To obtain an excellent and rapid impregnation, it is important that reinforcement and matrix are in direct contact as much as possible and distributed in a homogeneous way, reducing the distance that the molten matrix must take to wrap the reinforcement. [54]. To benefit from these advantages, it is necessary to take into account process parameters, identify and optimize them.

There are many methods by which the hybrid yarns can be manufactured such as co-wrapping and commingling. These techniques involve bringing the matrix and reinforcement into close contact with the aim not only to obtain, as already mentioned, a uniform distribution but also to limit the detrimental effects.

2.4.1. Co-Wrapping Method

The yarns made by the co-wrapping method, called co-wrapped yarns, have a feature in which the reinforcing fibers are intimately combined with the thermoplastic matrix fibers using a self-assembled winding apparatus [55]. Referring to the process scheme presented by Zhai et al. [56], the co-wrapped yarns (CWYs) are fabricated by a hollow spindle spinning loom. Reinforcing fiber roving passes through the roving condenser and drafting rollers as a core roving then is guided into the hollow spindle; at the same time, matrix filament wraps around fiber roving then passes together in the hollow spindle. Reinforcing fiber roving and polymeric filament both have false twist since the hollow spindle rotated speedily. After passing through the twisting hook, the false twist of reinforcing fiber roving become untwisted, while matrix filament wraps remain twisted (Figure 13). A crucial parameter for co-wrapping method is the cover factor (CF), which represents the percentage of fiber roving surface covered by polymer filaments and the related to the proportion ratio between matrix and reinforcement [56]. CF can be estimated as follows (Equation (1)):

$$CF = 1 - \left(1 - \frac{W_M \times T_M}{1000}\right)^2 \quad (1)$$

where W_M is the polymer filament width (mm) and T_M is the polymer wrapping turns per meter (turns/m).

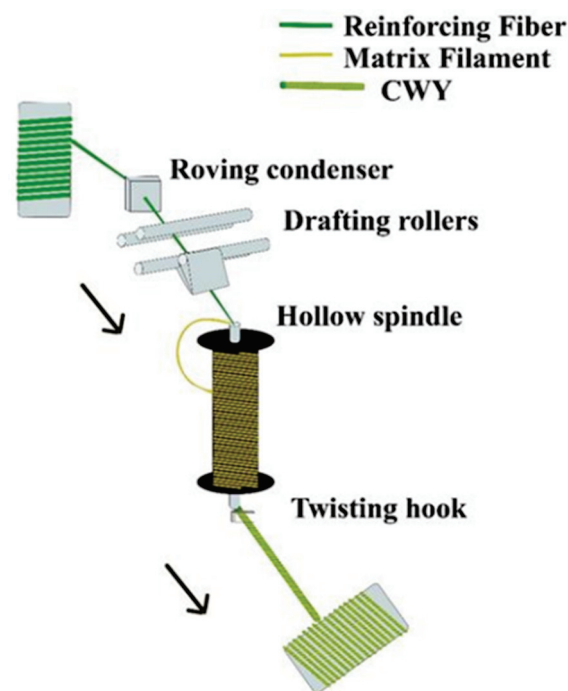


Figure 13. Schematic of co-wrapping process for hybrid yarns. Adapted from Reference [56] under Creative Commons license.

With respect to other hybrid yarn production methods, such as commingling process, co-wrapping ensures better protection for the reinforcing fibers during manufacturing. However, the distribution of the reinforcing fibers and the matrix fibers is still a challenge, requiring higher processing temperature and pressure to improve impregnation [57]. As for commingled, in co-wrapped fabric the impregnation takes place mainly by resin flow perpendicular to the fibers so the impregnation time are generally longer than powder-based process. In addition, one of the main advantages of co-wrapped fabrics is their freedom design. Hybrid yarns are drapable to a variety of complex and their dimensional shaped parts avoiding further forming/moulding processes [58]. A recent literature survey on co-wrapping technology revealed a lot of research work investigating both the synthesis parameters to produce the hybrid yarn and the optimization of compression molding processing to achieve the composite laminates. Mirdehghan et al. [59] investigated the influence of linear densities (16, 50.67, and 67.11 tex) and wrapping densities (115, 180, and 230 turns/m) of polyester fibers on the tensile performance of glass/polyester co-wrapped hybrid yarns. The authors found that the breaking load and tenacity of yarn increased with an increase in the wrapping density until an optimum point (180 turns/m). After that, increment in wrapping density produced a decrease in mechanical properties. Excessive twisting of glass fibers would lead to morphological alteration and damage, negatively affecting the tensile strength.

In addition, the intermediate value of linear density (50.67) was discovered as optimal in terms of mechanical properties, providing the best condition for the radial compressive force exerted by the wrapped filament to interact with glass core. At the optimal process conditions, co-wrapped yarns provided breaking load and tenacity 62% and 46% higher than those of the neat glass fibers (not wrapped with polyester). Baghaei et al. [60] studied PLA-hemp co-wrapped hybrid yarns evaluating the effect of wrap density (150 wraps/m and 250 wraps/m), and PLA/hemp mass ratios (10/90, 20/80, 35/65, and 45/55) on the hot compacted laminate composites. Tensile test results (Figure 14) revealed that composites with a wrapping density of 250 showed a significant improvement in tensile modulus over the composites fabricated at 150 wraps/m, across the whole range of fiber fraction ratios investigated. At a low reinforcement level (<25% by mass), the improvement was approximately 4.6%; at higher fiber fraction (>40% by mass), the improvement increased

to approximately 14.7%. This increase could be attributed to the better fiber alignment. Increasing wrapping density improved the tensile modulus of the composites because the tortuosity of the hybrid yarns decreases as wrap twist increases, and consequently the reinforcement alignment would be improved. Xu et al. conducted a comparative study between PEEK-based co-wrapped yarns using carbon [57] and glass fibers [55] as reinforcement materials. Specifically, the authors researched the optimal laminate manufacturing process investigating the following process parameters: molding temperature (370–450 °C), holding time (10–150 min), and cooling rate (from −2 °C/min, −10 °C/min, and −20 °C/min). The best results of the above-mentioned works are reported in Table 2. In both cases, intermediate values of the process parameters provided the maximum mechanical performance. Temperatures and holding times higher than the optimal value were deleterious for the mechanical behavior of the composites due to the thermal degradation that the PEEK matrix underwent. A cooling rate of 10 °C/min was detected as an optimum condition in terms of crystallinity degree achieved in the examined matrix [55,57]. It is worth mentioning that the carbon-based laminates were processed at lower temperatures and holding times than the glass-based counterpart.

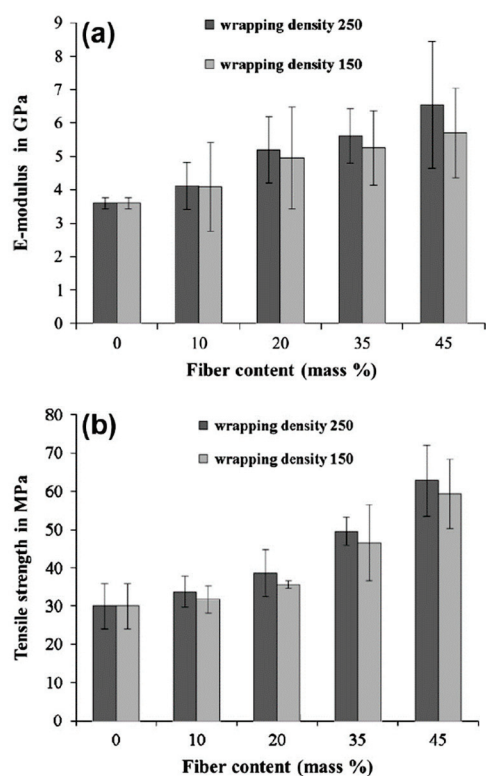


Figure 14. Mechanical properties in tensile of co-wrapped PLA-hemp laminates: (a) elastic modulus and (b) tensile strength. Adapted with permission from Reference [60].

Table 2. Optimal process parameters and performance.

Laminate	Temperature	Time	Cooling Rate	Tensile Strength	Tensile Modulus
PEEK-glass [55]	430 °C	120 min	−10 °C/min	1.24 GPa	29.62 GPa
PEEK-carbon [57]	400 °C	60 min	−10 °C/min	1.51 GPa	161 GPa

This is to be attributed to the higher thermal conductivity of carbon fiber (~1.31 W/m × K) compared to glass (~0.25 W/m × K) which would sanction a more effective heat transfer at the fiber–matrix interface and therefore not requiring higher temperatures to drive the melting of the matrix and the consequent impregnation of the reinforcement [61].

2.4.2. Commingling

Commingling is one of the most promising techniques founded on the principle of uniform distribution of continuous matrix and reinforcement filaments during melt spinning [62]. The homogeneous fiber/matrix distribution of commingled yarns in particular leads to short impregnation routes and low void contents reflected by the high mechanical performance of the thermoplastic composites [63]. This method allows for acceptable levels of impregnation to be attained, but relatively long cycles are required. In the follow Figure 15 [64] is shown the yarn cross section. Another important advantage is that commingled yarns can be processed and produced entirely with almost all existing known technologies for the fabrics manufacture. Combined with the developments in textile structures, the use of commingled yarns considerably improves the mechanical properties of the resulting composite parts [65]. As Figure 16 [66] shows, commingling process can be schematized as follows: the multifilament yarns cross through a section on which a jet of compressed air acts, so that tangles are created inside them. The result at the section is the intermingled yarn, obtained by processing several yarns from which the single thread is obtained. The Figure 16, precisely, draws the intermilling process of a polymer-metal yarn carried out by Özkan et al. [66] for composites intended for electromagnetic applications.

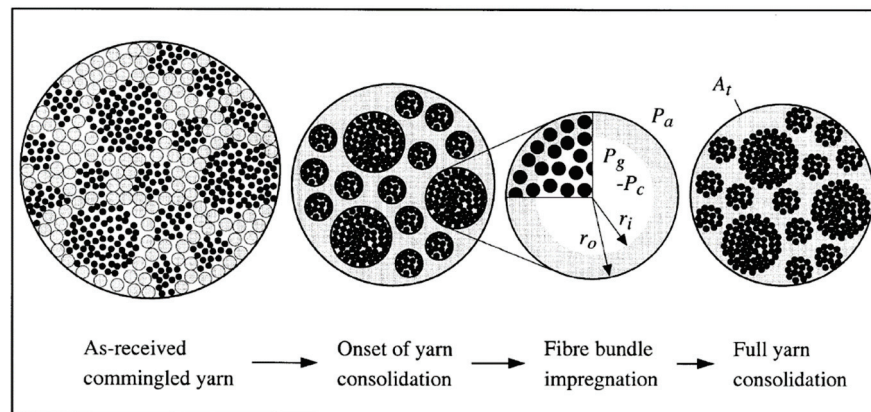


Figure 15. Representative commingled yarn cross-section and assumed consolidation mechanism. Reprinted with permission from Reference [64].

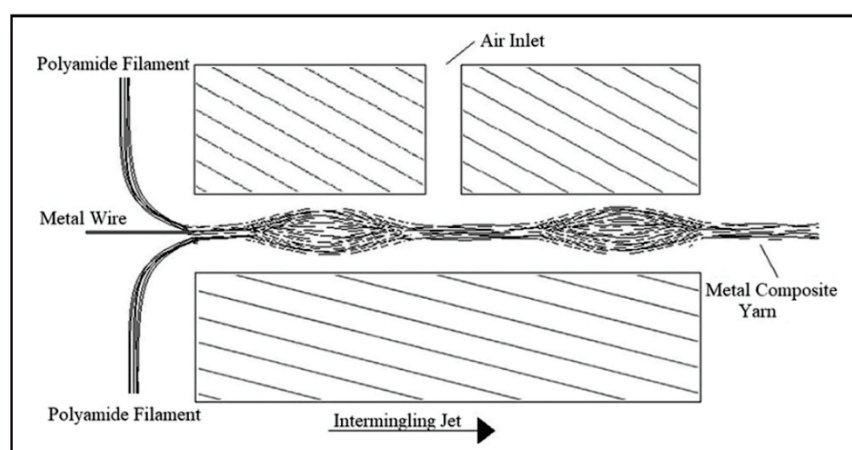


Figure 16. Intermingling process. Reprinted from Reference [66] under Creative Commons license.

Due to the commingling process, both reinforcing and polymer fibers can be combined, representing great potential [67,68]. The desired ratio of fiber to matrix can be achieved by varying the number of constituent yarns during the production of the hybrid yarn itself.

Nevertheless, the process involves technological challenges concerning the impregnation as well as wetting of the fibers hence a decrease in the quality of the consolidation [69].

The atmospheric pressure, production speed, machine configuration and designing of the nozzle, filament stiffness, fiber cross-sectional area and the ratio of the diameter [69], density of the matrix forming fibers, the cross-section of matrix forming filaments, the number of filaments in yarn bundle, filament diameter, diameter ratio of reinforcing and matrix forming filaments influence the degree of commingling and structural attributes of hybrid yarns [20]. The mixing quality of commingled yarn increases and decreases directly with the rate of overfeeding and processing speed, respectively, which is given by

$$D_{ov} = \left(\frac{V_{DG} - V_{TG}}{V_{TG}} \right) \times 100 \% \quad (2)$$

where V_{DG} and V_{TG} represents, respectively, the speed of delivery godet and the take-off godet [70]. Numerous studies have concentrated on commingled materials, yarn manufacturing and preforming, and mechanical properties of commingled composites [71,72]. Jumaev et al. [73] reported a wide range of experimental and analytical investigations into parameters that affect the performance of commingled composites, such as damping properties, hardness, coefficient of friction, moisture absorption, and other mechanical properties. However, by employing a highly dissipative epoxy resin, it is feasible to obtain a high flexural modulus and a loss factor in the case of carbon-reinforced unidirectional plastic composite. Conversely, maximum energy dissipation occurs near the glass transition temperature, which also significantly reduces the other mechanical properties. Mankodi et al. [74] examined the impact of commingling parameters on PP/GF composites properties. According to their study, the linear density value of the resulting composite is significantly affected by overfeeding and air pressure, which in turn results in poor quality and high material failure. The overfeed value also affects the toughness of PP/GF hybrid yarns. At low take-up, speed tenacity improves as a function of pressure as well as overfeed, whereas the higher winding speed leads to poor yarn tenacity with reduced nip frequency and poor regularity. Di Benedetto et al. [52] reported energy dissipation from low velocity impact test considering processing parameters, material properties and degradation kinetic of the matrix of polyamide/carbon fiber commingled composite, that is the capability to absorb energy and then increase crashworthiness. In this study it is seen that the energy absorption capability must be increased to promote thermoplastics materials composites reliability for using on automotive components. The viscosity of the PA6 multifilament yarn undergoes a significant decrease after the temperature of 220 °C, due probably to the molecular mobility caused by the polymer melting. In this case, intermolecular forces of attraction were not sufficiently strong to resist the forces induced by the rheometer. The increase of the temperature up to 220 °C increased the vibrational motion in the polymer molecules causing them to lose their intermolecular forces of attraction and undergo easy movement. The increase of the processing temperature causes a reduction of the resistance force and total energy of the material. A processing temperature above 260 °C affects dissipated energy values due to the matrix degradation. Lu et al. [75] analyzed four parameters for hot-compacted CF/PEEK plain weave fabric composites: melting temperature, molding pressure, crystallization temperature and the mass content of resin. It is seen that a higher compaction temperature leads to more matrix creation and better layer bonding; indeed, a suitable molding pressure causes bubbles to be discharged from composites and helps to form a uniform surface, but when the pressure becomes too high, this is expected to result in loss of resin content, resin outflow, and probable distortion of fiber bundles. Moreover, the melting temperature has a non-negligible effect on the static contact angle of PEEK on CF mats and it means that the smaller the contact angle, the better the wettability. Samples crystallized at 300 °C show excellent tensile properties and crystallinity. Resin mass content is also an important parameter in the fabrication of composites: The high mass ratio of PEEK material provides good interfacial strength, whereas the increased resin content causes loss of resin, dispersion of carbon fiber, and creates defects while processing. Lekube et al. [76] investigated the influence of porosity, fiber content and fiber length as well as processing parameters on the properties of partially

compacted nonwoven composites based on polypropylene and glass fibers. The study showed an increasing density with increasing glass fiber content. Moreover, stiffness and strength of the composites increase as well when glass fiber content increases. In addition, both the elastic modulus and tensile strength increase with increasing initial glass fiber length. Furthermore, important factors for restriction of void content are the number of stacked layers and applied pressure during processing. The study of Bernet et al. [77,78] has foreseen the numerical simulation of the impregnation and consolidation process in order to obtain composite materials made with hybrid yarns. The developed model involved the use of both carbon fibers reinforcement and PA12 polymer fibers matrix. At the beginning of the impregnation it is assumed that the commingled yarn is like a molten resin surrounding the reinforcing fibers [79], as shown in Figure 17 [63]. The consolidation is regulated by the impregnation of the fiber agglomerations by the resin, at a rate which is presumed to follow Darcy's law [20]. Specifically, the following figure illustrates the scheme processing of online commingled yarns (thermoplastics + glass fibers) proposed by Wiegand and Mäder [63]. In their work, the authors investigated different matrices (PP, PLA, and PA) and sizing chemistry on the mechanical performance and consolidation behavior of glass fiber-based commingled yarns. For all examined matrices, significant improvements in fiber/matrix compatibility were detected by using pure silane coupling agents as sizing component.

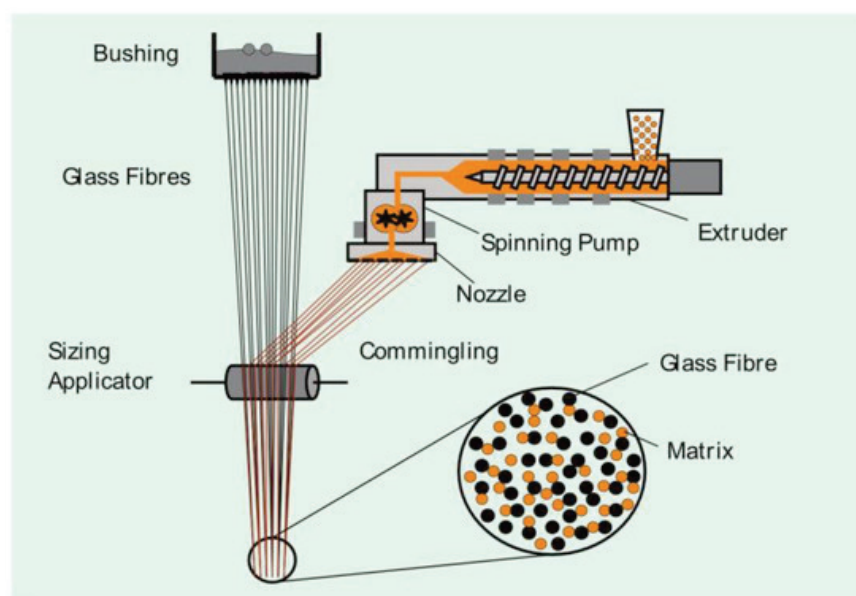


Figure 17. Processing scheme for commingled yarn. Reprinted from Reference [63] under Creative Commons license.

Compared to the production processes analyzed so far, the hybrid yarns technique is certainly the most ambitious and promising since they have some non-negligible advantages such as high flexibility, and this allows to obtain more complex parts [20]. Commingled composite is an innovative and inventive systems with research from industries and academia still at work to study and fabricate new commingled composite, characterize them for perfect function, making them exemplary candidates, particularly in structural applications. However, in the enduring literature, no coalescence of comprehensive details is available to the author's foremost information and understanding.

3. Key Characteristics, Pros and Cons of Investigated Techniques

Thermoplastic composites can play a key role in 21st century industry, as new materials are emerging day by day, while manufacturing processes are evolving to meet the stringent industrial performance requirements, production and multifunctionality. This section aims to summarize and highlight the key aspects of each technique, the various advantages,

disadvantages and the parameters that most influence and drive processes choices that cannot be ignored. Film stacking molding is widely used due to the relative ease of manufacture. Disadvantages include high resin content, the uneconomic nature of the process, and the difficulty in impregnating the fiber tow (high pressure forces the fibers together) with high-viscosity matrix material. We have seen how important processing temperature, pressure and holding time are, as the core parameters to control the process. The higher the temperature, the lower the resin viscosity, an advantage that guarantees better mobility and fluidity through the fiber bed. On the other hand, however, high temperatures can degrade the material, nullifying its contribution. Pressure represents a crucial parameter: if too low, the impregnation time increases with the consequence to obtain dry spot inside the composite. Nevertheless, an excessive increase would cause a reduction in the fabric permeability. In the powder impregnation process sufficient pressure and time must be applied to force the resin to impregnate the fiber tows in order to achieve fully consolidated composite parts. Poor impregnation and consolidation will result in a significant reduction in the mechanical properties of the final composites [80]. We report some of the most important factors influencing the process: particle size, fiber tow spreading, particulate flow pattern. Regarding hybrid woven fabrics, composites manufactured with this technique offer an effective way of increasing ultimate strain and impact properties while reducing the cost of an advanced composite material. By combining two or more types of fibers, it is possible to obtain the advantages of both the fibers while simultaneously mitigating their fewer desirable qualities. The mechanical properties of a hybrid composite can be varied by changing composite volume fraction and stacking sequence of different plies. Fibers such as carbon or boron are widely used in many aerospace applications because of their high specific modulus [80]. Hybrid yarns, consisting of reinforcing and matrix fibers, are one kind of basic material (semi-finished product) with which to construct continuous-fiber-reinforced thermoplastic composites [81,82]. Composite properties are influenced mainly by the arrangement of the reinforcing fibers and the homogeneity of the fiber's distribution in the composite, as well as by impregnation of the glass fibers with the polymer matrix. Hybrid yarns are usually manufactured into thermoplastic composites by hand lay-up [83], filament winding [84] or—as done recently—by the pultrusion process [85]. The incredible advantage of this technique, which distinguishes it from the others and makes it the most prestigious is the possibility to low-cost manufacture complex shaped parts, owing to reduced impregnation times and applied pressures during processing.

An aspect of extreme importance lies in the fact that these are industrial production processes and that allows to start from thermoplastics obtained from recycled material.

4. Conclusions

This review article investigated the main production technologies to produce thermoplastic matrix composite materials. The reason lies in a principle that is now more important than ever, sustainability: the opposite nature of thermoplastic matrix composites compared to thermosets, i.e., the possibility to recycle them. The thermosetting polymer certainly guarantees the best mechanical characteristics but it can no longer be reworked and reused for other purposes. Conversely, thermoplastic polymer can be remelted and subjected to a new type of processing. The goal is to produce high-performance thermoplastic matrix composite materials, with high volume-based quantities of reinforcement, to allow a real comparison with thermosetting materials. There are two process techniques to manufacture thermoplastic composite parts: reactive and melt processing. The first solution focuses on in-situ polymerization, starting from water-like viscosity monomers that could potentially provide an optimal reinforcement impregnation, and a subsequent polymerization reaction triggered by temperature increase [7]. The second one lies in melt processing, discussed in detail in this article. Four main technologies have been revised such as film stacking molding, powder impregnation, hybrid fabrics, hybrid yarns and the respective parameters that most influence the processes. Hybrid yarn is certainly the most technologically advanced but hard process. It opened a new era by kicking off the

research area with their unique advantage of easy production and prodigious application. Commingling is the most favorable method for several industrial applications owing to their process simplicity and cost-effectiveness, which is imperative for combining its advantage with other conventional technologies [69]. Numerous combinations of materials and reinforcements are now available on a wide range of length, innovative material shapes and different processing possibilities for both designers and fabricators.

Author Contributions: Conceptualization, M.V.; methodology, M.S. and I.R.; validation, M.V.; formal analysis, I.R.; resources, I.R.; data curation, I.R., M.S. and M.V.; writing—original draft, I.R. and M.S.; writing—review and editing, M.V. and M.S.; supervision, M.V.; funding acquisition, M.V. All authors have read and agreed to the published version of the manuscript.

Funding: This research received no external funding but has been financed by personal research funds.

Acknowledgments: The authors of this review thank Pietro Russo (senior researcher of the National Research Center) of the Institute for Polymers, Composites and Biomaterials in Naples (IPCB) for technical support and exchange of views. Additional warm thanks go to the two companies Carbon-Task (in the person of Christian Scopinich) and 2Gamma srl composites division (in the person of Stefano Forzano).

Conflicts of Interest: The authors declare no conflict of interest.

References

- van Rijswijk, K.; Bersee, H.E.N. Reactive processing of textile fiber-reinforced thermoplastic composites—An overview. *Compos. Part A Appl. Sci. Manuf.* **2007**, *38*, 666–681. [CrossRef]
- Malcolm, W.; Todd, E. Carbon Fiber Reinforced PPS Thermoplastic Materials Implemented in Cost Sensitive Commercial Applications. In Proceedings of the 38th International SAMPE Symposium, Anaheim, CA, USA, 10 May 1993; pp. 2055–2065.
- Nunes, J.P.; Silva, J.F.; Marques, A.T.; Crainic, N.; Cabral-Fonseca, S. Production of Powder-Coated Towpregs and Composites. *J. Thermoplast. Compos. Mater.* **2003**, *16*, 231–248. [CrossRef]
- Offringa, A.R. Thermoplastic composites-rapid processing applications. *Compos. Part A Appl. Sci. Manuf.* **1996**, *27*, 329–336. [CrossRef]
- McMahon, P.E. *Developments in Reinforced Plastics—4*; Springer: Berlin/Heidelberg, Germany, 1984.
- Iyer, S.R.; Drzal, L.T. Manufacture of Powder-Impregnated Thermoplastic Composites. *J. Thermoplast. Compos. Mater.* **1990**, *3*, 325–355. [CrossRef]
- Valente, M.; Rossitti, I.; Biblioteca, I.; Sambucci, M. Thermoplastic Composite Materials Approach for More Circular Components: From Monomer to In Situ Polymerization, a Review. *J. Compos. Sci.* **2022**, *6*, 132. [CrossRef]
- Weteringe, B.J.; van Dongen, W.A.; Bersee, H.E.N. Rubber forming of thermoplastic composite parts for the eaglet rudder. In Proceedings of the 15th International Conference on Composite Materials, Durban, South Africa, 27 June–1 July 2005; pp. 1–10.
- Laura, D.M.; Keskkula, H.; Barlow, J.W.; Paul, D.R. Effect of glass fiber surface chemistry on the mechanical properties of glass fiber reinforced, rubber-toughened nylon 6. *Polymer* **2002**, *43*, 4673–4687. [CrossRef]
- Seo, J.; Kim, D.Y.; Kim, D.C.; Park, H.W. Recent Developments and Challenges on Machining of Carbon Fiber Reinforced Polymer Composite Laminates. *Int. J. Precis. Eng. Manuf.* **2021**, *22*, 2027–2044. [CrossRef]
- Grujicic, M.; Sellappan, V.; Omar, M.A.; Seyr, N.; Obieglo, A.; Erdmann, M.; Holzleitner, J. An overview of the polymer-to-metal direct-adhesion hybrid technologies for load-bearing automotive components. *J. Mater. Process. Technol.* **2008**, *197*, 363–373. [CrossRef]
- Kazan, H.; Farahani, S.; Zheng, T.; Pilla, S. Experimental analysis on the bonding conditions of thermoset-thermoplastic composite parts manufactured by the hybrid single shot method. *J. Compos. Mater.* **2022**, *56*, 57–68. [CrossRef]
- Valente, M.; Sambucci, M.; Chougan, M.; Ghaffar, S.H. Reducing the emission of climate-altering substances in cementitious materials: A comparison between alkali-activated materials and Portland cement-based composites incorporating recycled tire rubber. *J. Clean. Prod.* **2022**, *333*, 130013. [CrossRef]
- Sambucci, M.; Valente, M. Ground waste tire rubber as a total replacement of natural aggregates in concrete mixes: Application for lightweight paving blocks. *Materials* **2021**, *14*, 7493. [CrossRef]
- Zhang, J.; Chevali, V.S.; Wang, H.; Wang, C.H. Current status of carbon fibre and carbon fibre composites recycling. *Compos. B Eng.* **2020**, *193*, 108053. [CrossRef]
- Post, W.; Susa, A.; Blaauw, R.; Molenveld, K.; Knoop, R.J.I. A Review on the Potential and Limitations of Recyclable Thermosets for Structural Applications. *Polym. Rev.* **2020**, *60*, 359–388. [CrossRef]
- Yang, Y.; Boom, R.; Irion, B.; van Heerden, D.J.; Kuiper, P.; de Wit, H. Recycling of composite materials. *Chem. Eng. Process. Process Intensif.* **2012**, *51*, 53–68. [CrossRef]
- McConnell, V.P. Launching the carbon fibre recycling industry. *Reinf. Plast.* **2010**, *54*, 33–37. [CrossRef]

19. Saitta, L.; Tosto, C.; Dattilo, S.; Puglisi, C.; Cicala, G. *Chemical Recycling of Bioepoxy Matrices for Composites: Novel Processing Route and Reuse Strategies to Obtain New Matrices*; XVI Convegno Nazionale AIMAT: Cagliari, Italy, 2021.
20. Vaidya, U.K.; Chawla, K.K. Processing of fibre reinforced thermoplastic composites. *Int. Mater. Rev.* **2008**, *53*, 185–218. [CrossRef]
21. Vodermayr, A.; Kaerger, J.; Hinrichsen, G. Manufacture of high performance fibre-reinforced thermoplastics by aqueous powder impregnation. *Compos. Manuf.* **1993**, *4*, 123–132. [CrossRef]
22. Groupe, W.J.B.; Akkerman, R. Consolidation process model for film stacking glass/PPS laminates. *Plast. Rubber Compos.* **2010**, *39*, 208–215. [CrossRef]
23. Ouagne, P.; Bizet, L.; Baley, C.; Bréard, J. Analysis of the film-stacking processing parameters for PLLA/flax fiber biocomposites. *J. Compos. Mater.* **2010**, *44*, 1201–1215. [CrossRef]
24. Mukhopadhyay, S.; Srikanta, R. Effect of ageing of sisal fibres on properties of sisal-Polypropylene composites. *Polym. Degrad. Stab.* **2008**, *93*, 2048–2051. [CrossRef]
25. Hu, J.; Zhang, H.; Li, S.; Ji, C.; Chen, S.; Zhou, Z.; Wang, B. Process parameter–mechanical property relationships and influence mechanism of advanced CFF/PEEK thermoplastic composites. *Polym. Compos.* **2022**, *43*, 5119–5132. [CrossRef]
26. Kim, S.H.; Park, C.H. Direct impregnation of thermoplastic melt into flax textile reinforcement for semi-structural composite parts. *Ind. Crop. Prod.* **2017**, *95*, 651–663. [CrossRef]
27. Zal, V.; Moslemi Naeni, H.; Bahramian, A.R.; Abdollahi, H.; Behraves, A.H. Investigation of the effect of processing temperature on the elastic and viscoelastic properties of PVC/fiberglass composite laminates. *Modares Mech. Eng.* **2016**, *15*, 9–16.
28. Groupe, W.J.B.; Akkerman, R. Multi-scale effects in the consolidation of thermoplastic laminates. *Int. J. Mater. Form.* **2009**, *2*, 157–160. [CrossRef]
29. Khondker, O.A.; Ishiaku, U.S.; Nakai, A.; Hamada, H. Fabrication mechanical properties of unidirectional jute/PP composites using jute yarns by film stacking method. *J. Polym. Environ.* **2005**, *13*, 115–126. [CrossRef]
30. Suresh, S.; Senthil Kumar, V.S. Experimental determination of the mechanical behavior of glass fiber reinforced polypropylene composites. *Procedia Eng.* **2014**, *97*, 632–641. [CrossRef]
31. Katayama, T.; Tanaka, K.; Murakami, T.; Uno, K. Compression moulding of jute fabric reinforced thermoplastic composites based on PLA non-woven fabric. *WIT Trans. Built Environ.* **2006**, *85*, 159–167. [CrossRef]
32. Kazano, S.; Osada, T.; Kobayashi, S.; Goto, K. Experimental and analytical investigation on resin impregnation behavior in continuous carbon fiber reinforced thermoplastic polyimide composites. *Mech. Adv. Mater. Mod. Process.* **2018**, *4*, 6. [CrossRef]
33. Kobayashi, S.; Tsukada, T.; Morimoto, T. Resin impregnation behavior in carbon fiber reinforced polyamide 6 composite: Effects of yarn thickness, fabric lamination and sizing agent. *Compos. Part A Appl. Sci. Manuf.* **2017**, *101*, 283–289. [CrossRef]
34. Jaafar, J.; Siregar, J.P.; Tezara, C.; Hamdan, M.H.M.; Rihayat, T. A review of important considerations in the compression molding process of short natural fiber composites. *Int. J. Adv. Manuf. Technol.* **2019**, *105*, 3437–3450. [CrossRef]
35. Yang, B.; Lu, L.; Liu, X.; Xie, Y.; Li, J.; Tang, Y. Uniaxial tensile and impact investigation of carbon-fabric/polycarbonate composites with different weave tow widths. *Mater. Des.* **2017**, *131*, 470–480. [CrossRef]
36. Vitiello, L.; Papa, I.; Lopresto, V.; Mocerino, D.; Filippone, G.; Russo, P. Manufacturing of bio-polyamide 11/basalt thermoplastic laminates by hot compaction: The key-role of matrix rheology. *J. Thermoplast. Compos. Mater.* **2022**, 1–16. [CrossRef]
37. Padaki, S.; Drzal, L.T. A consolidation model for polymer powder impregnated tapes. *J. Compos. Mater.* **1997**, *31*, 2202–2227. [CrossRef]
38. Svensson, N.; Shishoo, R.; Gilchrist, M. Manufacturing of thermoplastic composites from commingled yarns—A review. *J. Thermoplast. Compos. Mater.* **1998**, *11*, 22–56. [CrossRef]
39. Muzzy, J.; Varughese, B.; Thamrongkol, V.; Tincher, W. Electrostatic prepregging of thermoplastic matrices. *SAMPE J.* **1989**, *25*, 15–21.
40. Allen, L.E.; Edie, D.D.; Lickfield, G.C.; McCollum, J.R. Thermoplastic coated carbon fibers for textile preforms. *J. Thermoplast. Compos. Mater.* **1988**, *1*, 371–379. [CrossRef]
41. Werner, E. Powder Based Prepreg Fabric: What, How, Why? In Proceedings of the 42nd International SAMPE Symposium, Anaheim, CA, USA, 4–8 May 1997; pp. 706–719.
42. Rath, M.; Kreuzberger, S.; Hinrichsen, G. Manufacture of aramid fibre reinforced nylon-12 by dry powder impregnation process. *Compos. Part A Appl. Sci. Manuf.* **1998**, *29*, 933–938. [CrossRef]
43. Padaki, S.; Drzal, L.T. A simulation study on the effects of particle size on the consolidation of polymer powder impregnated tapes. *Compos. Part A Appl. Sci. Manuf.* **1999**, *30*, 325–337. [CrossRef]
44. Raji, M.; Abdellaoui, H.; Essabir, H.; Kakou, C.-A.; Bouhfid, R. Prediction of the cyclic durability of woven-hybrid composites. In *Durability and Life Prediction in Biocomposites, Fibre-Reinforced Composites and Hybrid Composites*; Elsevier: Amsterdam, The Netherlands, 2019; pp. 27–62.
45. Alif, N.; Carlsson, L.A.; Boogh, L. The effect of weave pattern and crack propagation direction on mode I delamination resistance of woven glass and carbon composites. *Compos. B Eng.* **1998**, *29*, 603–611. [CrossRef]
46. Alavudeen, A.; Rajini, N.; Karthikeyan, S.; Thiruchitrabalam, M.; Venkateshwaren, N. Mechanical properties of banana/kenaf fiber-reinforced hybrid polyester composites: Effect of woven fabric and random orientation. *Mater. Des.* **2015**, *66*, 246–257. [CrossRef]
47. van West, B.P.; Pipes, R.B.; Advani, S.G. The consolidation of commingled thermoplastic fabrics. *Polym. Compos.* **1991**, *12*, 417–427. [CrossRef]

48. Jamshaid, H.; Mishra, R. Thermomechanical characteristics of basalt hybrid and nonhybrid woven fabric–reinforced epoxy composites. *Polym. Compos.* **2016**, *37*, 2982–2994. [CrossRef]
49. Liu, D.; Ding, J.; Fan, X.; Lin, X.; Zhu, Y. Non-isothermal forming of glass fiber/polypropylene commingled yarn fabric composites. *Mater. Des.* **2014**, *57*, 608–615. [CrossRef]
50. Lin, T.A.; Chuang, Y.C.; Lin, J.Y.; Lin, M.C.; Lou, C.W.; Lin, J.H. Weaving carbon fiber/recycled polypropylene selvages to reinforce the polymer-based protective composite fabrics: Manufacturing techniques and electromagnetic shielding effectiveness. *Polym. Compos.* **2019**, *40*, E1910–E1917. [CrossRef]
51. Formisano, A.; Papa, I.; Lopresto, V.; Langella, A. Influence of the manufacturing technology on impact and flexural properties of GF/PP commingled twill fabric laminates. *J. Mater. Process. Technol.* **2019**, *274*, 116275. [CrossRef]
52. di Benedetto, R.M.; Botelho, E.C.; Gomes, G.F.; Junqueira, D.M.; Junior, A.C.A. Impact energy absorption capability of thermo-plastic commingled composites. *Compos. B Eng.* **2019**, *176*, 107307. [CrossRef]
53. Souza, B.R.; di Benedetto, R.M.; Hirayama, D.; Raponi, O.; Barbosa, L.; Ancelotti, A. Manufacturing and characterization of jute/PP thermoplastic commingled composite. *Mater. Res.* **2017**, *20*, 458–465. [CrossRef]
54. Alagirusamy, R.; Fanguero, R.; Ogale, V.; Padaki, N. Hybrid yarns and textile preforming for thermoplastic composites. *Text. Prog.* **2006**, *38*, 1–71. [CrossRef]
55. Xu, Z.; Wang, G.; Hu, J.; Zhang, M.; Zhang, S.; Gai, X.; Li, Y.; Yu, R.; Luan, J. Influence of processing conditions on tensile property of continuous glass fiber–reinforced PEEK composites fabricated by the co-wrapped yarn method. *High Perform. Polym.* **2018**, *30*, 489–499. [CrossRef]
56. Zhai, W.; Wang, P.; Legrand, X.; Soulat, D.; Ferreira, M. Effects of micro-braiding and co-wrapping techniques on characteristics of flax/polypropylene-based hybrid yarn: A comparative study. *Polymers* **2020**, *12*, 2559. [CrossRef]
57. Xu, Z.; Zhang, M.; Gao, S.H.; Wang, G.; Zhang, S.; Luan, J. Study on mechanical properties of unidirectional continuous carbon fiber-reinforced PEEK composites fabricated by the wrapped yarn method. *Polym. Compos.* **2019**, *40*, 56–69. [CrossRef]
58. Gibson, A.G.; Manson, J.-A. Impregnation technology for thermoplastic matrix composites. *Compos. Manuf.* **1992**, *3*, 223–233. [CrossRef]
59. Mirdehghan, A.; Nosraty, H.; Shokrieh, M.M.; Akhbari, M. The structural and tensile properties of glass/polyester co-wrapped hybrid yarns. *J. Ind. Text.* **2018**, *47*, 1979–1997. [CrossRef]
60. Baghaei, B.; Skrifvars, M.; Berglin, L. Manufacture and characterisation of thermoplastic composites made from PLA/hemp co-wrapped hybrid yarn prepregs. *Compos. Part A Appl. Sci. Manuf.* **2013**, *50*, 93–101. [CrossRef]
61. Zhang, S.; Li, Y.; Zheng, Z. Effect of physiochemical structure on energy absorption properties of plant fibers reinforced composites: Dielectric, thermal insulation, and sound absorption properties. *Compos. Commun.* **2018**, *10*, 163–167. [CrossRef]
62. Mäder, E.; Rausch, J.; Schmidt, N. Commingled yarns—processing aspects and tailored surfaces of polypropylene/glass composites. *Compos. Part A Appl. Sci. Manuf.* **2008**, *39*, 612–623. [CrossRef]
63. Wiegand, N.; Mäder, E. Commingled yarn spinning for thermoplastic/glass fiber composites. *Fibers* **2017**, *5*, 26. [CrossRef]
64. Bernet, N.; Michaud, V.; Bourban, P.-E.; Ènson, J.-A.E.M. Commingled yarn composites for rapid processing of complex shapes. *Compos. Part A Appl. Sci. Manuf.* **2001**, *32*, 1613–1626. [CrossRef]
65. Lauke, B.; Bunzel, U.; Schneider, K. Effect of hybrid yarn structure on the delamination behaviour of thermoplastic composites. *Compos. Part A Appl. Sci. Manuf.* **1998**, *29*, 1397–1409. [CrossRef]
66. Özkan, I.; Telli, A. The effects of metal type, number of layers, and hybrid yarn placement on the absorption and reflection properties in electromagnetic shielding of woven fabrics. *J. Eng. Fibers Fabr.* **2019**, *14*, 1–13. [CrossRef]
67. Bunzel, U.; Lauke, B.; Schneider, K. Air Textured Hybrid Yarn Structures and Their Influence on the Properties of Long Fiber Reinforced Thermoplastic Composites. *Tech. Text.* **1999**, *42*, 10–12.
68. Long, A.C.; Wilks, C.E.; Rudd, C.D. Experimental characterisation of the consolidation of a commingled glass/polypropylene composite. *Compos. Sci. Technol.* **2001**, *61*, 1591–1603. [CrossRef]
69. Kandasubramanian, V.N.B. Advanced polymeric composites via commingling for critical engineering applications. *Polym. Test.* **2020**, *91*, 106774. [CrossRef]
70. Kravaev, P.; Stolyarov, O.; Seide, G.; Gries, T. Influence of process parameters on filament distribution and blending quality in commingled yarns used for thermoplastic composites. *J. Thermoplast. Compos. Mater.* **2014**, *27*, 350–363. [CrossRef]
71. Choi, B.D.; Diestel, O.; Offermann, P.; Hübner, T.; Mäder, E. Advancement for Commingling Hybrid Yarns for Fiber Reinforced Thermoplastics. In Proceedings of the Techtexsil-Symposium, Frankfurt, Germany, 23–26 April 2001; pp. 23–26.
72. Nygard, P.; Gustafson, C.-G. Continuous glass fiber–polypropylene composites made by melt impregnation: Influence of processing method. *J. Thermoplast. Compos. Mater.* **2004**, *17*, 167–184. [CrossRef]
73. Djumaev, A.; Takahashi, K. Effect of moisture absorption on damping performance and dynamic stiffness of NY-6/CF commingled yarn composite. *J. Mater. Sci.* **1994**, *29*, 4736–4741. [CrossRef]
74. Mankodi, H.; Patel, P. Study the effect of commingling parameters on glass/polypropylene hybrid yarns properties. *Autex Res. J.* **2009**, *9*, 70–74.
75. Lu, C.; Xu, N.; Zheng, T.; Zhang, X.; Lv, H.; Lu, X.; Xiao, L.; Zhang, D. The optimization of process parameters and characterization of high-performance CF/PEEK composites prepared by flexible CF/PEEK plain weave fabrics. *Polymers* **2018**, *11*, 53. [CrossRef]

76. Lekube, B.M.; Hermann, W.; Burgstaller, C. Partially compacted polypropylene glass fiber non-woven composite: Influence of processing, porosity and fiber length on mechanical properties and modeling. *Compos. Part A Appl. Sci. Manuf.* **2020**, *135*, 105939. [CrossRef]
77. Bernet, N.; Wakeman, M.D.; Bourban, P.-E.; Manson, J.-A. An integrated cost and consolidation model for commingled yarn based composites. *Compos. Part A Appl. Sci. Manuf.* **2002**, *33*, 495–506. [CrossRef]
78. Bernet, N.; Michaud, V.; Bourban, P.E.; Manson, J.A.E. An impregnation model for the consolidation of thermoplastic composites made from commingled yarns. *J. Compos. Mater.* **1999**, *33*, 751–772. [CrossRef]
79. Wakeman, M.D.; Zingraff, L.; Bourban, P.-E.; Manson, J.-A.; Blanchard, P. Stamp forming of carbon fibre/PA12 composites—A comparison of a reactive impregnation process and a commingled yarn system. *Compos. Sci. Technol.* **2006**, *66*, 19–35. [CrossRef]
80. Ye, L.; Friedrich, K. Processing of Thermoplastic Composites from Powder/Sheath-Fibre Bundles. *J. Mater. Process. Technol.* **1995**, *48*, 317–324. [CrossRef]
81. Pandya, K.S.; Veerajulu, C.; Naik, N.K. Hybrid composites made of carbon and glass woven fabrics under quasi-static loading. *Mater. Des.* **2011**, *32*, 4094–4099. [CrossRef]
82. Mader, E.; Bunzel, U.; Mally, A. Einfluss der Struktur textiler Vorprodukte auf die Eigenschaften langfaserverstärkter Thermoplaste. *Tech. Text.* **1995**, *38*, 205–208.
83. Fujita, A.; Maekawa, Z.; Hamada, H.; Matsuda, M.; Matsuo, T. Mechanical behavior and fracture mechanism of thermoplastic composites with commingled yarn. *J. Reinf. Plast. Compos.* **1993**, *12*, 156–172. [CrossRef]
84. Lauke, B.; Friedrich, K. Evaluation of processing parameters of thermoplastic composites fabricated by filament winding. *Compos. Manuf.* **1993**, *4*, 93–101. [CrossRef]
85. Michaeli, W.; Jirss, D. Thermoplastic pull-braiding: Pultrusion of profiles with braided fibre lay-up and thermoplastic matrix system (PP). *Compos. Part A Appl. Sci. Manuf.* **1996**, *27*, 3–7. [CrossRef]

Disclaimer/Publisher’s Note: The statements, opinions and data contained in all publications are solely those of the individual author(s) and contributor(s) and not of MDPI and/or the editor(s). MDPI and/or the editor(s) disclaim responsibility for any injury to people or property resulting from any ideas, methods, instructions or products referred to in the content.

Review

Green Nanocomposites Based on Thermoplastic Starch: A Review

Katherine E. Rivadeneira-Velasco , Christian A. Utreras-Silva, Antonio Díaz-Barrios, Alicia E. Sommer-Márquez , Juan P. Tafur and Rose M. Michell * 

School of Chemical Sciences & Engineering, Yachay Tech University, Urcuquí 100119, Ecuador; katherine.rivadeneira@yachaytech.edu.ec (K.E.R.-V.); christian.utreras@yachaytech.edu.ec (C.A.U.-S.); adiaz@yachaytech.edu.ec (A.D.-B.); asommer@yachaytech.edu.ec (A.E.S.-M.); jtafur@yachaytech.edu.ec (J.P.T.)
* Correspondence: rmichell@yachaytech.edu.ec

Abstract: The development of bio-based materials has been a consequence of the environmental awareness generated over time. The versatility of native starch is a promising starting point for manufacturing environmentally friendly materials. This work aims to compile information on the advancements in research on thermoplastic starch (TPS) nanocomposites after the addition of mainly these four nanofillers: natural montmorillonite (MMT), organically modified montmorillonite (OMMT), cellulose nanocrystals (CNC), and cellulose nanofibers (CNF). The analyzed properties of nanocomposites were mechanical, barrier, optical, and degradability. The most important results were that as the nanofiller increases, the TPS modulus and strength increase; however, the elongation decreases. Furthermore, the barrier properties indicate that the incorporation of nanofillers confers superior hydrophobicity. However, the optical properties (transparency and luminosity) are mostly reduced, and the color variation is more evident with the addition of these fillers. The biodegradability rate increases with these nanocompounds, as demonstrated by the study of the method of burial in the soil. The results of this compilation show that the compatibility, proper dispersion, and distribution of nanofiller through the TPS matrix are critical factors in overcoming the limitations of starch when extending the applications of these biomaterials. TPS nanocomposites are materials with great potential for improvement. Exploring new sources of starch and natural nano-reinforcement could lead to a genuinely eco-friendly material that can replace traditional polymers in applications such as packaging.

Citation: Rivadeneira-Velasco, K.E.; Utreras-Silva, C.A.; Díaz-Barrios, A.; Sommer-Márquez, A.E.; Tafur, J.P.; Michell, R.M. Green Nanocomposites Based on Thermoplastic Starch: A Review. *Polymers* **2021**, *13*, 3227. <https://doi.org/10.3390/polym13193227>

Academic Editor: Somen K. Bhudolia

Received: 30 August 2021

Accepted: 18 September 2021

Published: 23 September 2021

Publisher's Note: MDPI stays neutral with regard to jurisdictional claims in published maps and institutional affiliations.



Copyright: © 2021 by the authors. Licensee MDPI, Basel, Switzerland. This article is an open access article distributed under the terms and conditions of the Creative Commons Attribution (CC BY) license (<https://creativecommons.org/licenses/by/4.0/>).

Keywords: thermoplastic starch; nanocomposites; biopolymers; properties; packaging; nanofiller

1. Introduction

Plastic production has been increasing over time (Figure 1a) [1]. It is currently one of the most used materials worldwide due to its excellent flexibility, durability, and resistance. This type of material also allows the modeling of various products that can be applied in different fields of human activities (e.g., electronics, medical supplies, building, and packaging, among others) [2]. However, plastic represents a potential pollutant for the planet because of poor recycling methods and the limited capacity of storage facilities. As a result, the plastic accumulation is greater than the decomposition rate of this material in landfills or the environment [1].

According to the UN Environment Programme (UNEP) [3], from the 1950s to the present, more than 8.3 billion tonnes of plastic have been produced, of which around 60% has ended up in the natural environment and a part of them in the oceans (4 to 12 million metric tonnes [1]), which tend to produce substantial damage to marine species. Generally, carbon-based products are from non-renewable sources. Another problem with plastic is that many of the additives used in its manufacture are not biodegradable, and in some cases, they can be toxic [4]. Furthermore, waste disposal and the depletion of fossil sources are the major drawbacks of maintaining non-biodegradable single-use products [5]. Therefore,

the replacement of oil-based products with bio-based products is the driving force behind these initiatives.

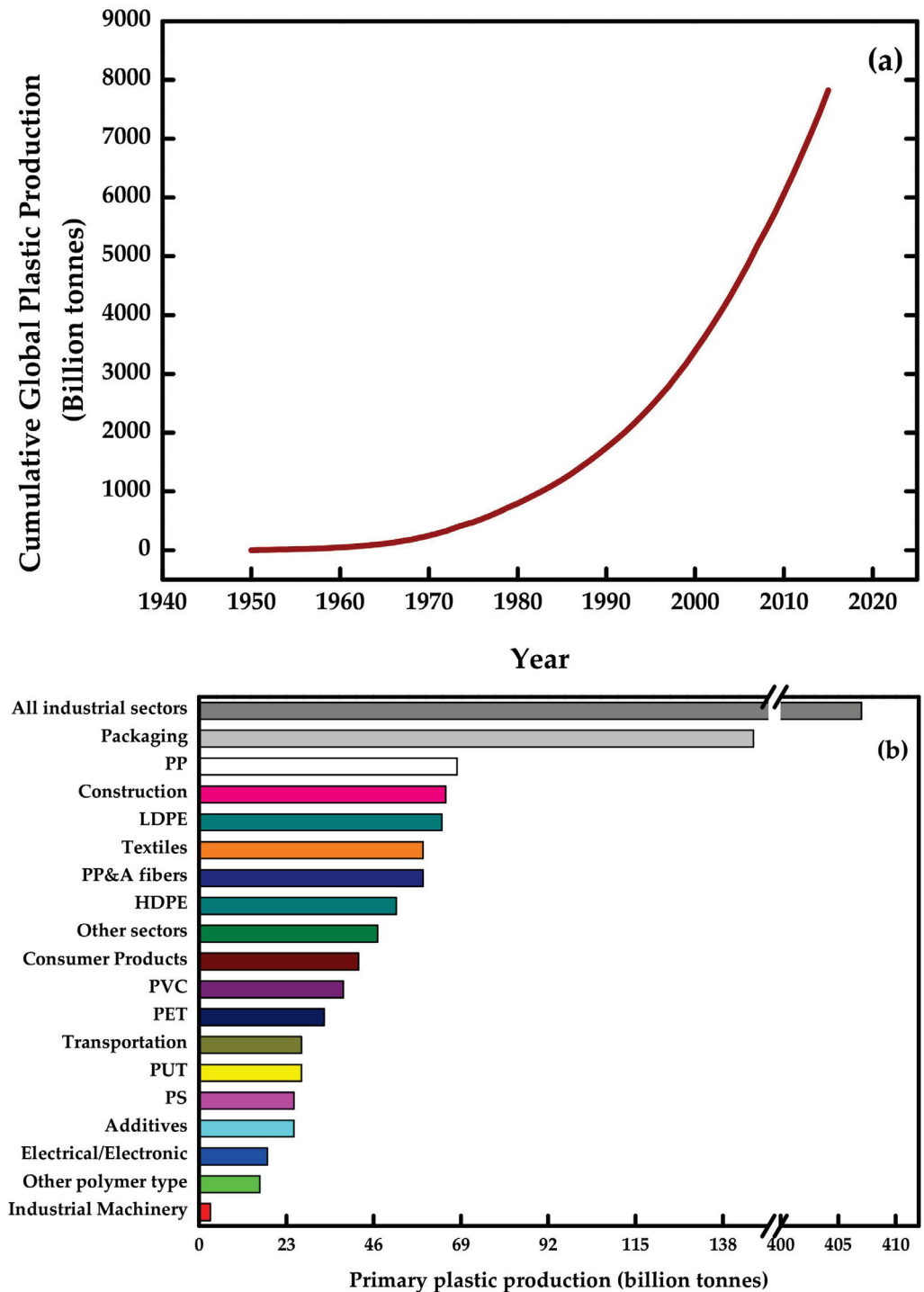


Figure 1. Plastic production: (a) global cumulative from 1950 to 2015, (b) primary in different entities at 2015. Prepared from data in [1].

Numerous studies have been conducted in search of sustainable and ecological alternatives to deal with the excessive production of plastic derived from fossil hydrocarbons [6–10]. The main objective is to find low-cost and biodegradable materials with good mechanical properties and high quality [11]. One of the alternatives is biopolymers manufactured from biomass or organic waste, which come from natural sources because they are abundantly available and inexpensive. Consequently, they are economically viable

compared to synthetic oil-based products [2,12]. Thermoplastic starch (TPS) is becoming an interesting option to achieve this goal.

TPS is a biopolymer prepared from native starch after its granular structure transformation using a plasticizer (water, glycerol, and sorbitol, among others) [13]. Native starch is abundant in nature and takes advantage of these low-cost resources obtained from agroindustrial waste. TPS alone is not suitable as a work material due to its poor performance. To enhance the final product, blending with other polymers and incorporating additives into the matrix is mandatory. The most common blends of TPS/polymer are prepared with poly(lactic acid) (PLA) [14–18], polyethylene varieties [19–26], poly(ethylene-co-vinyl alcohol) (EVA) [27,28], polycaprolactone [29], poly(vinyl alcohol) (PVA) [30], polyester [31], and polypropylene [32]. Additionally, a promising additive employed to reinforce the TPS is nanofillers to obtain nanocomposites-type materials. Consequently, they have been widely developed because of the synergistic merging of nanofillers in the polymer matrix of TPS.

The nanofillers that can be used for TPS reinforcement could be extracted from natural sources: cellulose [33–37], native starch [38–42], clays [43–48], and chitosan [49]. The most used nanofillers are natural montmorillonite (MMT), organically modified montmorillonite (O-MMT), cellulose nanocrystals (CNC), and cellulose nanofibers (CNF). Nanofillers (nanofibers, nanocrystals, and nanoparticles) obtained from polysaccharide materials are among the best options because they have similar chemical structures to TPS and are easy to extract.

Furthermore, green nanocomposites based on TPS help to reduce the environmental impact caused by oil-based products, and they can have several applications in different fields, such as the food industry [47,50,51], packaging (one of the largest plastics markets, as shown in Figure 1b) [1,52,53], drug delivery [54], biosensors, and electronic shielding [55], and tissue engineering [56].

Some reviews have been organized around different approaches to or related to TPS. Processing techniques for TPS with emphasis on the importance of plasticizer [9] and TPS nanocomposites (highlighting the novel water-assisted technique) [7] have been reviewed. In the same way, there are some others that present the characterization of TPS-based materials, including polyblends (e.g., PVA/starch) [4] and composites [6,8,10,57]. Recently, the use of TPS as a food packaging material has been studied [9,58]. However, no reviews exclusively focus on completely natural-based materials reinforcement for TPS and its potential packaging application.

For the above reason, this study will conduct a critical literature review on TPS-based nanocomposites and how these materials could substitute for conventional packaging plastics. It will present an overview of natural nanofillers (MMT, O-MMT, CNC, and CNF) and how they improve the TPS properties, mainly mechanical, barrier, and optical, as well as the degradability. Finally, this review could be a starting point for future research on environmentally friendly packaging materials based on TPS.

2. Thermoplastic Starch

Native starch is a renewable natural resource, which can be extracted from different parts of the plants, such as seeds, fruits, leaves, tubers, and roots. It may come from a variety of vegetables and greens [56], including potato [34,46,59–64], cassava [65–71], maize [28,38,72–76], wheat [58], pea [5,45,77–80], tapioca [2,81,82], corn [33,35,36,43,47,48,83–89], pomegranate [90], sweet potato [53], and avocado [91–93]. Figure 2 shows the world production of some of the mentioned sources, which have been increasing over time [94], looking forward to promoting the usage of their residues.

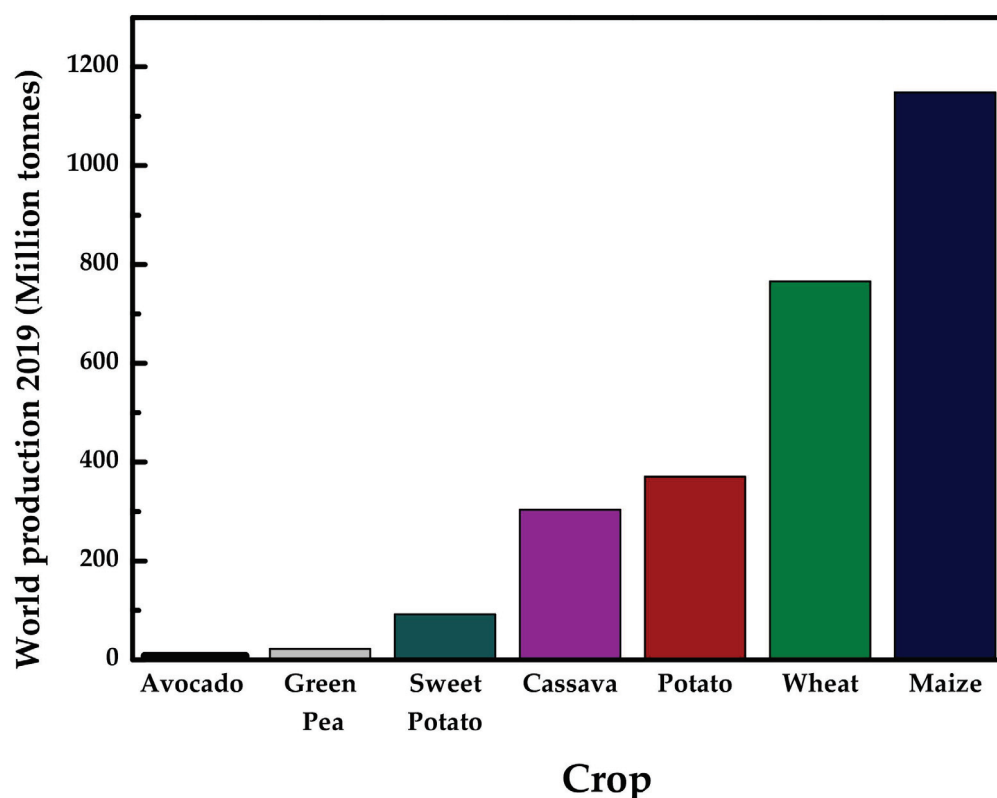


Figure 2. World production of main starch crops in 2019 (million tonnes). Prepared from data in [94].

Starch granules are mainly composed of amylose (linear component) and amylopectin (branched component). The functionality and applicability of starch are given by its two high-molecular-weight components. They vary depending on the natural source: 20–30% of amylose and 70–80% of amylopectin [8]. The amylose/amylopectin ratio and the non-starch components (such as lipids, proteins, and phosphate groups) from the natural source will determine the properties of the starch [95]. In general, the functional properties of starch are associated to its water absorption, which is related to the amylose amylopectin ratio [96].

Starch has a semicrystalline structure (the crystallinity degree varies between 15% and 45% [97]), in which the amorphous region comprises amylose and long amylopectin chains, while the crystalline region comprises short amylopectin chains [98]. If there is a higher content of amylose, it directly affects the organization of the crystalline lamellae in the granules as well as the amylopectin packaging degree [96]. Consequently, the ratio of amylose and amylopectin affects the granular shape and morphology of starch.

The crystalline structure of starch shows three polymorphisms; these are classified into types A, B, and C (see Figure 3). Type A is formed from orthogonally packed double helices with a firm inclusion of structural water, type B presents the double helices in a wider orthogonal packing with 36 water molecules per unit cell (some of them are located in the channels formed by the hexagonal packing), and type C exhibits both polymorphisms, A and B [99].

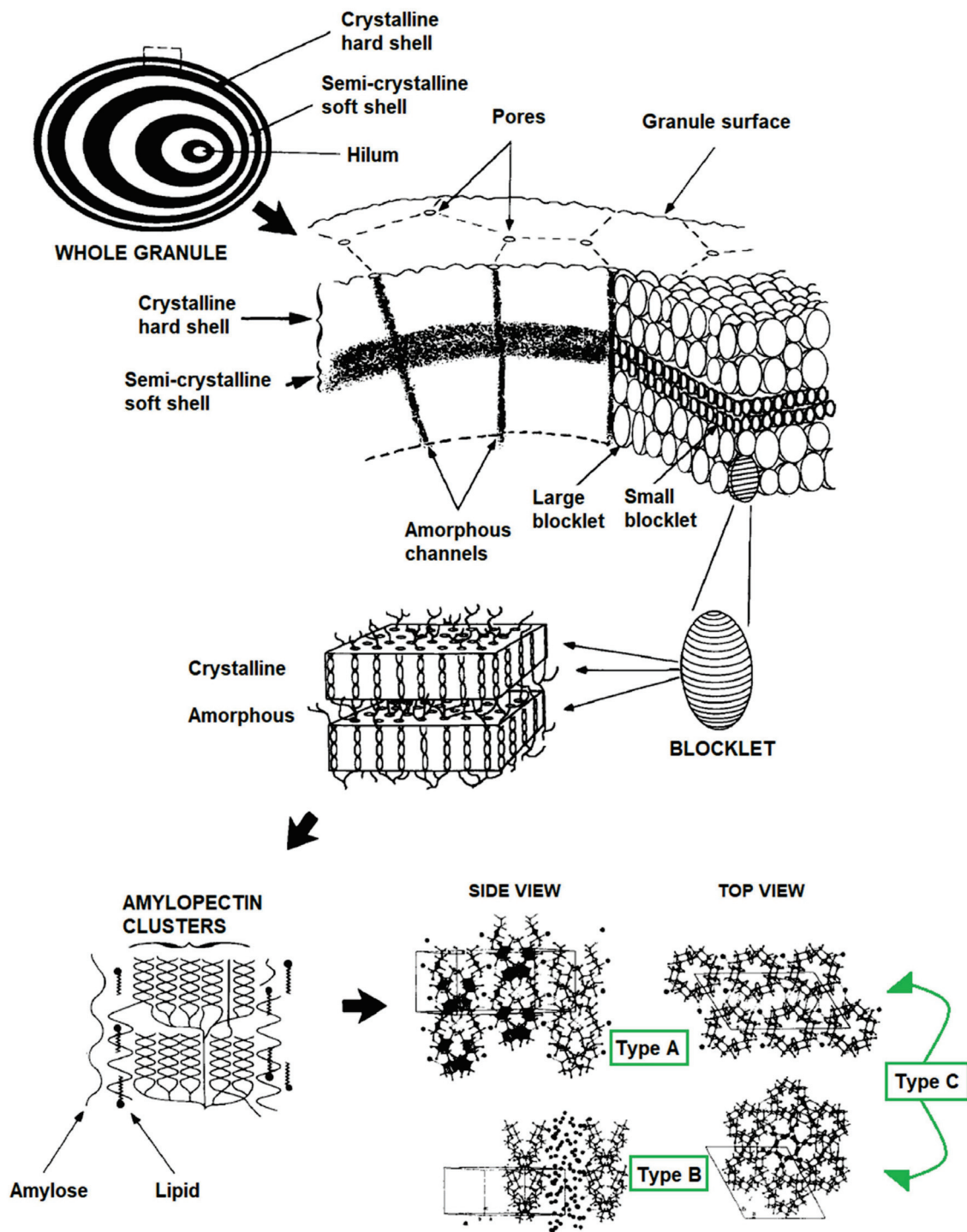


Figure 3. Crystallographic description of the native starch granule. Reproduced with permission from Carbohydr. Polym., 32 (3–4), Gallant et al., Microscopy of Starch: Evidence of a New Level of Granule Organization, 177–191, 1997 [99].

One of the principal industrial applications of starch is plastics when transformed into TPS. It has been developed under specific heat, pressure, and moisture conditions to overcome the impossibility of processing the granular starch using traditional plastic methods. In Figure 4, it can be seen that native starch is discontinuous, and the granules are explicitly shown, while TPS looks like a homogeneous surface with almost no apparent irregularities [100].

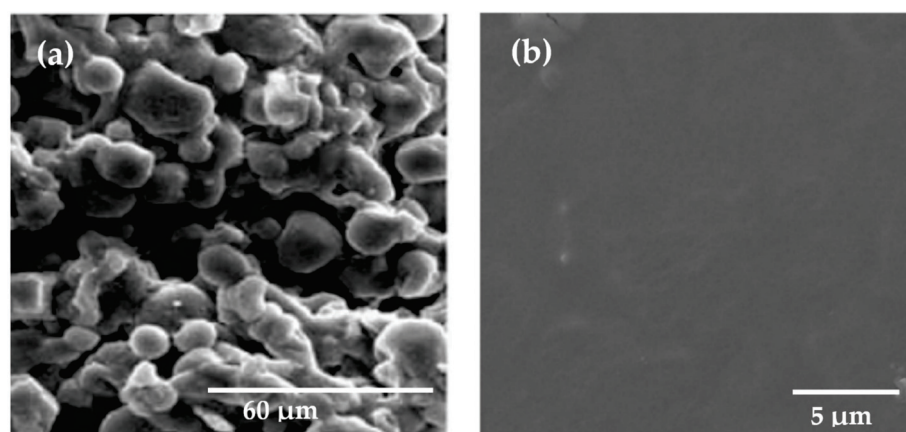


Figure 4. (a) SEM representation of native granular starch. Reproduced with permission from *Polym. Environ.*, 17, Ren et al., Study on biodegradable starch/OMMT nanocomposites for packaging applications, 203–207, 2009 [53]. (b) SEM representation of thermoplastic starch. Reproduced with permission from *Fibers*, 6, Asrofi et al., Mechanical properties of a water hyacinth nanofiber cellulose-reinforced thermoplastic starch bionanocomposite: Effect of ultrasonic vibration during processing, 1–9, 2018 [101].

TPS preparation differs based on starch source and final product usage, but it may follow the general process below. Materials include extracted starch from natural sources and plasticizers. Assuming that it is necessary to increase the properties, then the use of additives is mandatory. TPS is prepared using the extracted native starch, adding the plasticizer, and taking it to a system equipped with a mixer. Typically, a two-step procedure is followed: the premix is made from a native starch/plasticizer (proportions vary depending on the goal) and held as long as it takes (plasticizer-dependent) to swell the granular starch molecules. The swollen mixture is transferred to the mixer at a certain roller speed to induce gelatinization until the gelatinization temperature is reached. Conditions must be monitored during the process. The final mixture needs to be cooled down and pelletized to be subsequently blended with the additives, improving the properties of the final product [102].

The role of a plasticizer is critical for achieving the desired product characteristics. It causes microstructural changes in native starch, as can be seen in Figure 5. The molecular size of the plasticizer must be smaller than starch to diffuse within the intermolecular spaces of the polymer and start the interaction [9]. The hydroxy groups of the most common plasticizers (water, glycerol, or sorbitol) make them compatible with starch, generating an adequate interaction [56]. These alter the initial crystallographic structure by breaking the hydrogen bonds that join the macromolecules, with partial depolymerization of the starch structure, allowing the amylose and amylopectin chains to flow with the temperature increase and making the starch thermoplastic [103].

The most common plasticizer for TPS preparation is glycerol due to its properties, such as polarity, hydrophilicity, compatibility, and boiling point lower than the gelatinization temperature. These properties facilitate the gelatinization process by adding flexibility, which implies reducing the viscosity of the molten material [56]. The glass transition temperature, the degree of crystallinity, the amylose content, the type and amount of plasticizer, and the storage conditions are the main parameters involved in the mechanical properties of the obtained TPS materials [8]. Zhang and Han [61,104] studied the properties of pea starch with various plasticizers (monosaccharides and polyols) proportions from 0 to 25% and after 14 days of storage at 50% of relative humidity (RH). Films were prepared by aqueous starch dispersion, keeping them at the boiling point of the starch dispersion during the process. In the case of glycerol (Figure 6) as a plasticizer, it shows an uncommon anti-plasticizing effect on pea starch at low concentrations (less than 10%), while at higher concentrations (around 25%), plasticity was improved and fracture stress was reduced. This phenomenon affects the mechanical properties of starch because at low concentrations

(less than 10%), the starch crystals tend to act as physical crosslinking points and produce internal stress, leading to a faster rupture. Based on this example, it is suggested that an optimal amount of plasticizer should be considered to obtain the desired properties of TPS, bearing in mind the nature of starch and/or plasticizer.

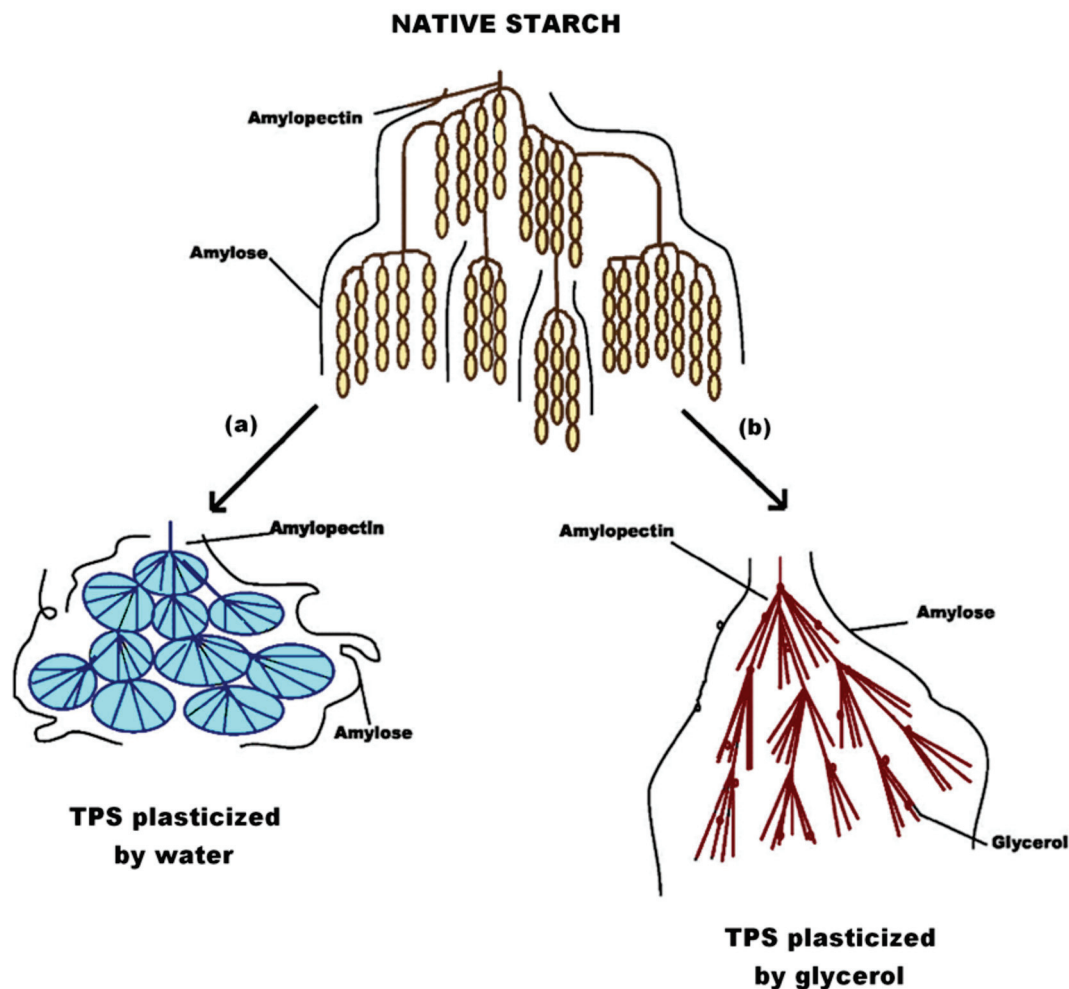


Figure 5. Microstructural change in native starch processing to TPS plasticized with (a) water and (b) glycerol. Reproduced with permission from *J. Food Process Eng.*, 40, Khan et al., Thermoplastic Starch: A Possible Biodegradable Food Packaging Material—A Review, 2017 [9].

In order to promote the microstructural changes on starch, it is necessary to apply temperature, pressures, and shear, typically by extruders or internal mixers. The target temperature of these types of equipment (around 140 and 160 °C) [105] is below the starch decomposition point (230 °C) [103], which implies reducing the glass transition and melting temperatures. The most common methods for TPS transformation are extrusion [106], compression molding [107], and film casting [108]. Injection is not suitable due to the high viscosity and low flow properties of the material. Extrusion is used for film packaging materials, mainly when the twin-screw configuration is used, since it allows adequate feeding and temperature control with a widespread shear. Compression molding is widely used for foam packaging, which involves the gelatinization of starch and lubricating additives to prevent the mold from sticking. Film casting is used to obtain thin sheets approximately 0.02–0.1 mm thick [8].

After transformation, the general characterization of TPS nanocomposites is carried out by X-Ray Diffraction (XRD), Scanning Electron Microscopy (SEM), Thermogravimetric Analysis (TGA), Differential Scanning Calorimetry (DSC), and Atomic Force Microscopy (AFM), among other techniques [102]. Then, the mechanical characterization is generally

based on the International Organization for Standardization (ISO) [32,49] or American Society for Testing and Materials (ASTM) [48,62,70,109] and conducted in special machinery for this purpose. With the use of these standards, the performance of the material can be adequately assessed. Using standardized specimens, the most common tests to report mechanical properties are tensile, compression, and flexion [110].

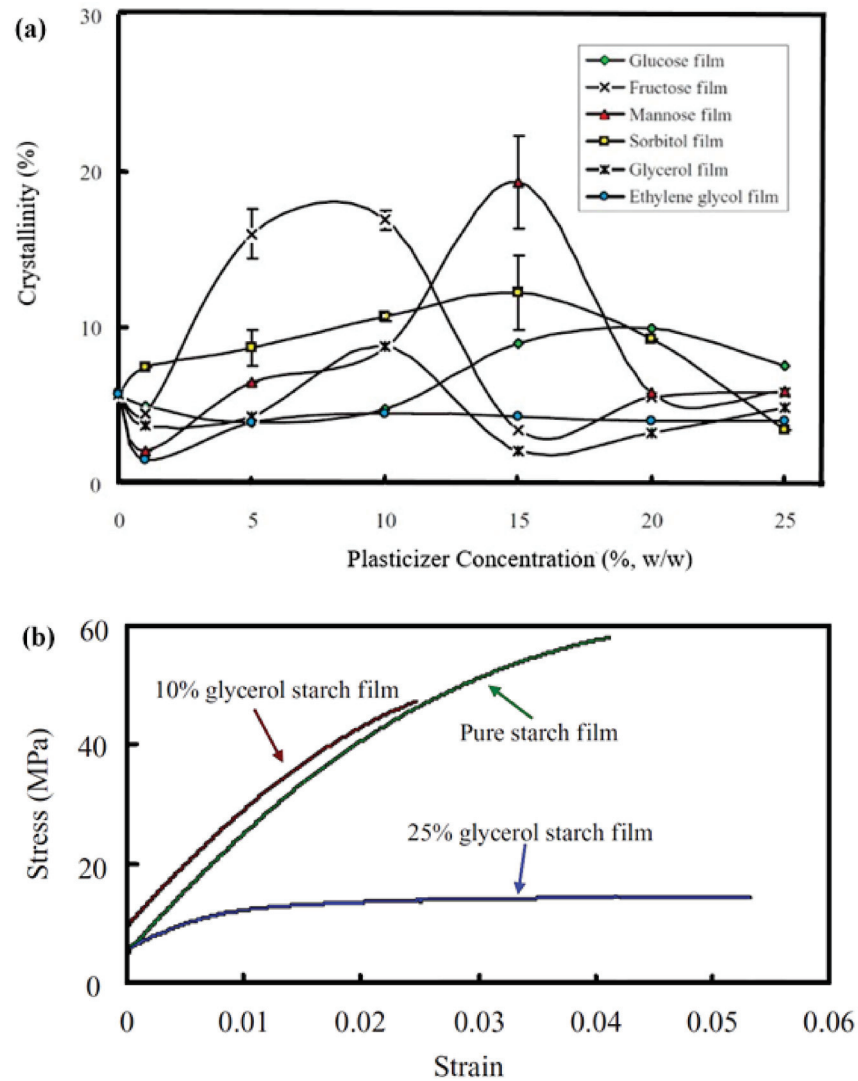


Figure 6. (a) Crystallinity dependence of different plasticizers (monosaccharides and polyols) at concentrations from 0 to 25 wt %. (b) Tensile test results for starch films varying glycerol concentrations (0, 10, and 25 wt %). Reproduced with permission from *J. Food Sci.*, 75 (1), Zhang and Han, Crystallization of high-amylose starch by the addition of plasticizers at low and intermediate concentrations, 2010 [104].

Some of the weaknesses of TPS are the low mechanical, barrier, rheological, and thermal-resistant properties. To improve the performance of TPS, a transformation of this material into nanocomposites is a well-known alternative. These significant drawbacks lead to finding the best options for co-components and nanofillers for the TPS matrix [12]. These nanocomposites are currently applied in different fields because of their properties such as tissue engineering [54], drug delivery systems [54], and packaging [47,111].

3. Nanocomposites: General Trend in the Main Properties

The primary purpose of employing fillers is to enhance the properties of TPS. The most common nanofillers found in the literature are CNF, CNC, MMT, and O-MMT. The

highest impact of adding nanocompounds to the TPS matrix is improving mechanical, barrier, optical properties, and degradability performance.

Figure 7 shows a reported mechanical properties compilation of these nanocomposites. The presented values are calculated employing Equation (1) for comparative purposes.

$$\Psi_{\pm} = \left(\frac{\Psi_{\text{filler}}}{\Psi_{\text{blank}}} - 1 \right) \times 100\% \quad (1)$$

where Ψ_{\pm} is the reported parameter, Ψ_{filler} is the value of the parameter at a specific filler concentration, and Ψ_{blank} is the value of the parameter for neutral TPS.

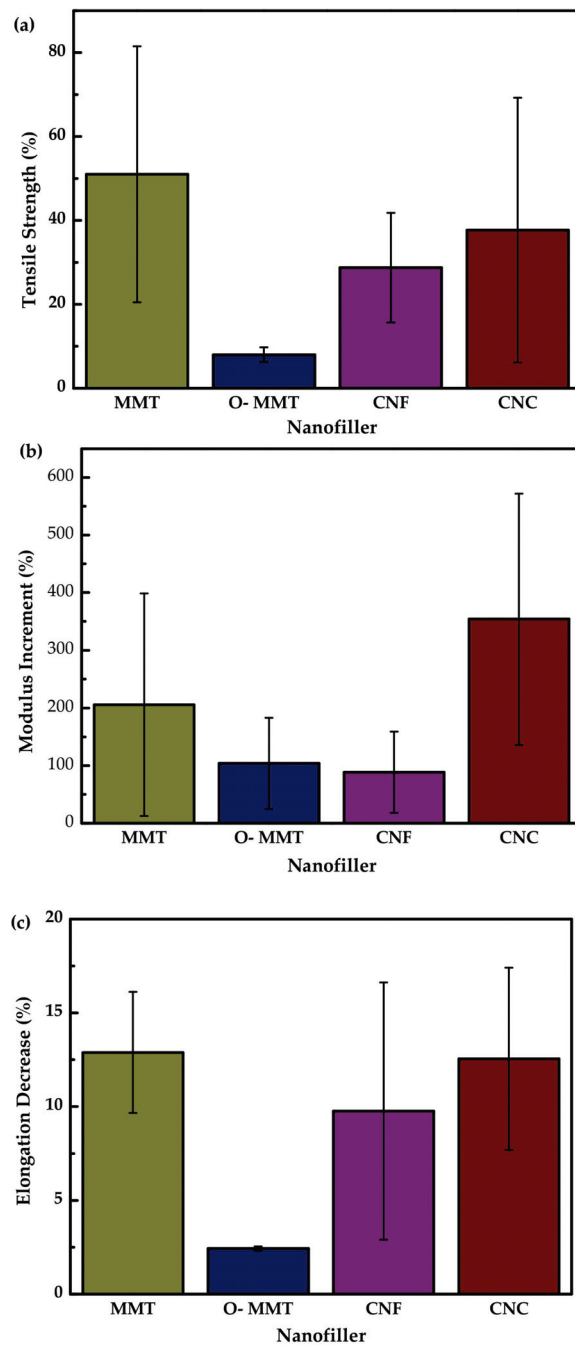


Figure 7. Mechanical properties for the main nanocompounds (MMT, O-MMT, CNF, CNC): (a) tensile strength, (b) modulus increment, (c) elongation decrease. Prepared from data (fixed at 5% of nanofiller) in [20,24–26,30,58,66–68,74,87,89,90,106,109].

The graphs show the relative increase for strength (Figure 7a) and modulus (Figure 7b) and the decrease in elongation (Figure 7c) for the different nanofillers. It can be deduced that CNC is the one that improves the modulus in a greater way, while MMT shows the highest value of the increase in tensile strength but also the most significant elongation decrease. These results agree with the common trend in the mechanical properties after adding a nanofiller in the TPS matrix, which increases the modulus and tensile strength while reducing elongation. This behavior is related to the exfoliation of the filler (Figure 8). It means that more exfoliation favors modulus and tensile strength, while less exfoliation favors elongation. This fact could help achieve high performance for future applications of this type of material.

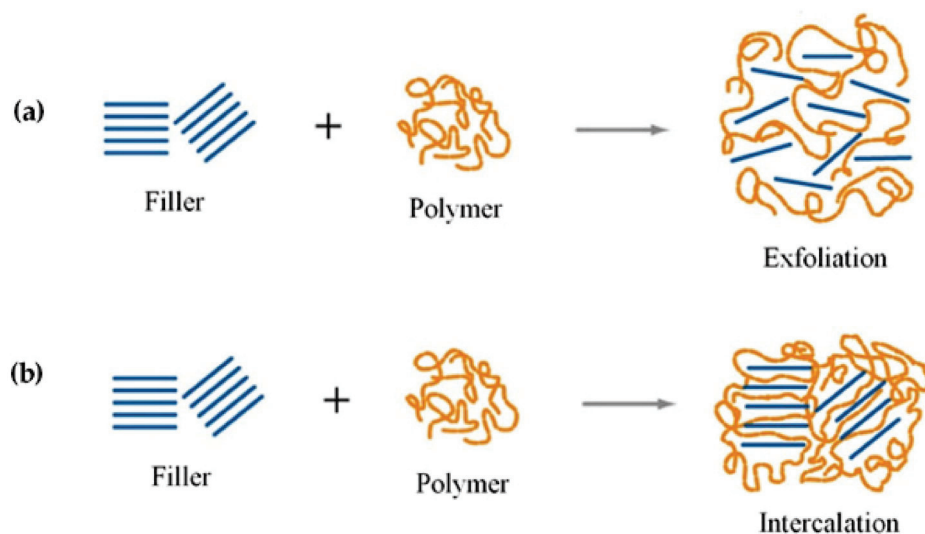


Figure 8. Representation of filler (a) exfoliation and (b) intercalation within the polymer matrix. Reproduced with permission from *Mater. Sci. Eng. R Reports*, 28, Alexandre and Dubois, Polymer-layered silicate nanocomposites: Preparation, properties and uses of a new class of materials, 1–63, 2000 [112].

These nanofillers also improve the barrier properties, such as water vapor permeability (WVP), oxygen permeability (OP), and aroma permeability (AP). They are essential parameters to predict the shelf life of the material on the packaging. However, the most studied barrier property is WVP. In general, bio-based materials exhibit poor WVP [8], so nanocompounds are added to overcome this inconvenience. These nanofillers also prevent the pass of fluids (water, oxygen, and/or aroma) through the film, avoiding the affectation of a marketed product as represented in Figure 9 (the nanofillers cause a torturous path for the molecules).

The nanofillers modify the aesthetic of the final product, and it is related to optical properties. For example, the transparency of nanocomposites is assessed by transmittance in UV-Vis analysis. When the specific particle size is exceeded (40 nm), the opacity is progressively increased. The Beer–Lambert law can be applied to quantify the loss of clarity [33,44]. In addition, optical transparency can be attributed to light dispersion due to the size of particles that affect the transmittance of light [106]. Bigger particles produce a blockage of visible light, leading to material opacity [22], compared to net TPS that is highly transparent with 90% transmittance at 600 nm [33]. This trend can be represented in Figure 10; the increment of nanofiller percentage in the nanocomposite produces an increase in opacity.

Materials based on TPS meet the degradation standard, which means that this material can be converted into biomass, carbon dioxide, and water by the action of biological enzymes in a given environmental exposure time [113]. It should not be confused with the mineralization process because it includes one more end product, methane. This process may never reach 100%, because a part of the polymer will be incorporated into microbial biomass. The polymer degradation path will be determined by environmental conditions (aerobic or anaerobic) [114]. There are many ways in which this property is evaluated

for materials, including gravimetric weight changes, morphological changes, mechanical characteristics, and carbon dioxide emission [115]. Figure 11 represents a schematic degradation process for conventional polymers versus eco-friendly/green materials.

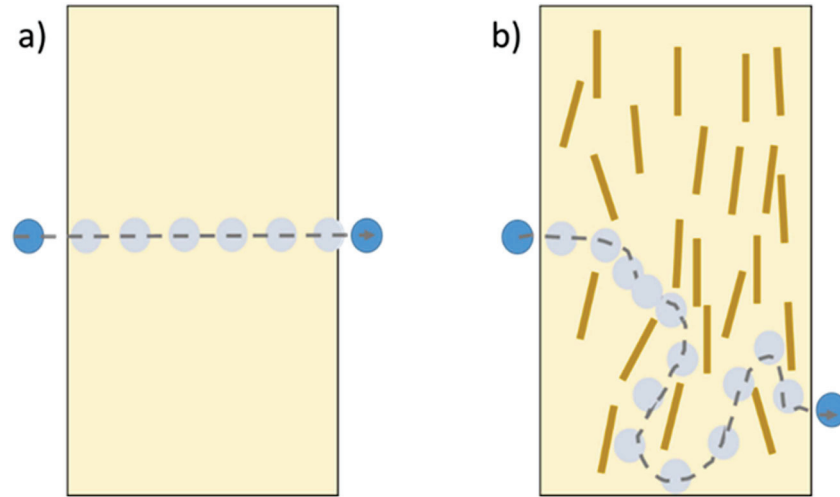


Figure 9. Schematic representation of molecular diffusion through (a) TPS and (b) TPS nanocomposite.

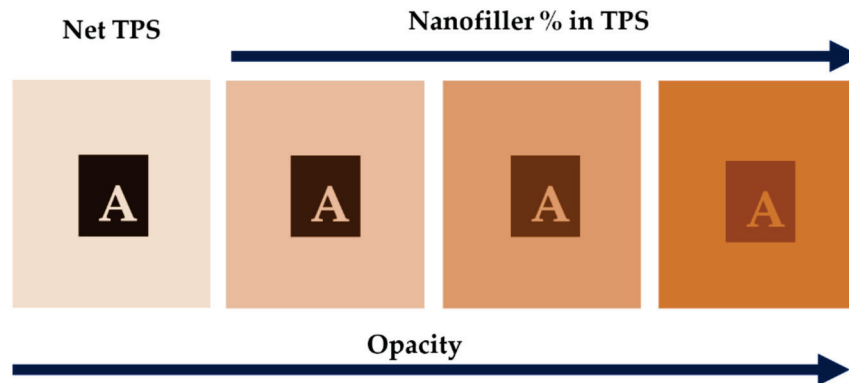


Figure 10. Schematic representation of opacity from net TPS to an increasing percentage of nanofiller in TPS nanocomposite.

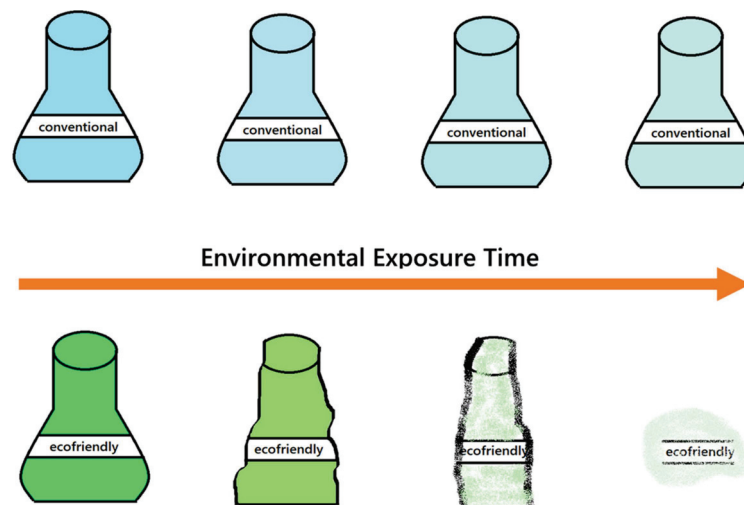


Figure 11. Schematic representation of environmental exposure of a conventional and green (ecofriendly) container with the increase on the environmental exposure time.

4. Cellulose Nanofibers (CNF)

Cellulose and starch are the two most abundant polysaccharides in nature; due to their similarity in their structures, there are expected to be no compatibility problems when preparing blends with these components [37]. In this way, the cellulose nanofibers (CNF) could be extracted from various parts of plants, such as pulp, bagasse, husk, and leaves. Table 1 shows the different sources of starch and CNF. The methods for extracting the fibers can be chemical (e.g., acid hydrolysis) and/or mechanical (e.g., high-intensity ultrasonication, high-pressure refiner, grinder treatment, cryocrushing, or electrospinning) [77]. The main advantages of CNF include that they are highly available, easy to degrade, and recyclable.

Table 1. Plasticizers and cellulose nanofibers as nanofillers (including their wt %) in most used TPS sources.

Starch Source	Plasticizer	Nanofiller	Wt %	Reference
NI	Glycerol	Cotton nanofibers	0.1–1	[116]
Cassava	Glycerol/Sorbitol (1:1)	Cellulose cassava bagasse nanofibers	5–20	[70]
		Cellulose nanofibers (eucalyptus pulp)	2–15	[33]
	Glycerol	Cellulose nanofibers	2–12	[35]
	Glycerol	Cellulose nanofibers	1–30	[36]
Corn	Glycerol	Cellulose nanofibers	5	[12]
	Glycerol	Cellulose nanofibers	10	[117]
	Glycerol	Cotton cellulose nanofibers	0.5–5	[118]
	Glycerol	Graphene oxide nanoplatelets, Cellulose nanofibers	1–5, 5–15	[119]
	Glycerol	Lignin cellulose nanofibers	5–15	[120]
Corn, cassava, sago	Glycerol, formaldehyde	Oil palm empty fruit bunches cellulose nanofibers	1–3	[121]
		Sugarcane bagasse cellulose Nanofibers	4–20	[77]
Maize	Glycerol and sorbitol	Cotton nanofibers	5–20	[122]
		Cellulose nanofibers	5–15	[123]
Merck-modified starch	Glycerol	Rice straw cellulose nanofibers	5–15	[124]
	Glycerol	Cellulose nanofibers and nanocrystals	1–3	[37]
	Water/Glycerol	Sisal cellulose nanofibers	2.5–20	[62]
	Glycerol	Wheat straw cellulose nanofibers	2–10	[64]
Potato	Glycerol	Pineapple leaf cellulose nanofibers	1–4	[52]
	D-Sorbitol	Cellulose nanofibers	5–20	[106]
	Glycerol	Bleached eucalyptus pulp cellulose nanofibers	0.18–0.36	[125]
Tapioca	Glycerol	Cellulose nanofibers	0.3–1.5	[81]
Waxy maize	Glycerol	Cellulosic nanofibers	2–10	[73]

NI: No information reported.

According to the compiled information, CNF is added to the TPS matrix in 0.1 to 20 wt %, showing that in most studies, the presence of CNF increases the stiffness (improvement in Young's modulus and a slight to moderate decrease in the elongation at break) of the TPS. The corresponding changes are attributed to an adequate filler dispersion in the matrix. Furthermore, the formation of a rigid hydrogen bonds network between the matrix and filler confers adequate stress transfer. This network also implies that an excess of this filler will produce agglomeration, which will lead to poor mechanical properties (Figure 12) [124]. However, Teixeira et al. [70] reported unusual behavior in cassava starch-based TPS and cassava bagasse CNF composites. The main difference in the mechanical properties was the increase in the elongation at break, which was originated by a plasticizing effect of sugars present in the nanofiber suspension through the mixing process, developing a hydrolysis degradation of starch during acid extraction [118].

As was previously discussed, TPS has poor barrier properties; then, with the aid of CNF and its nanometric size, a positive impact on the barrier properties can be observed. A reduction in WVP values is evidenced by promoting a hydrogen bond network between filler and starch chains (Figure 13). This network causes a restriction of diffusion through starch films. Cellulose confers a hydrophilic character to TPS films because of its high crystallinity and compact microfibrillar arrangement [8].

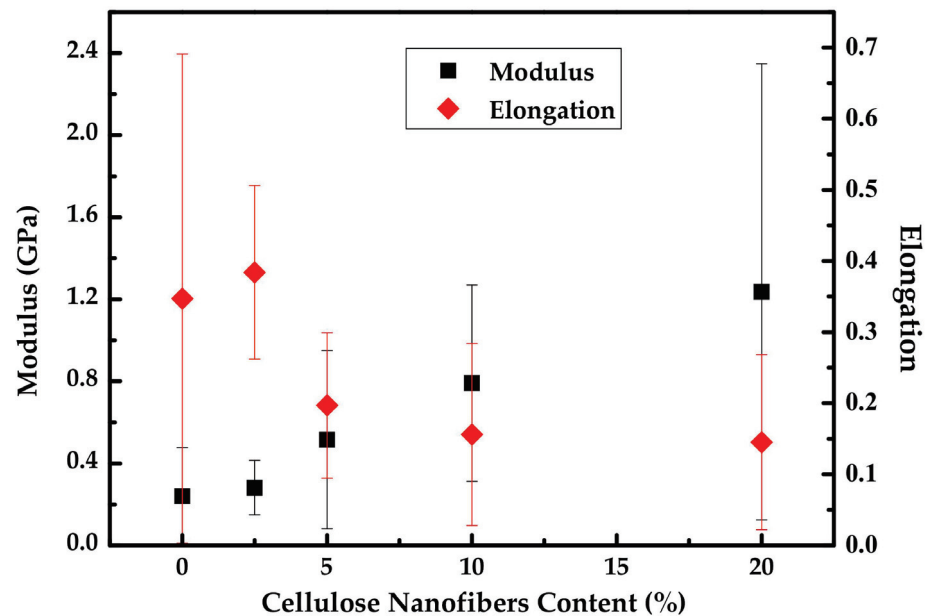


Figure 12. Modulus and elongation trend as CNF content increases in TPS matrix. Prepared from data in [62].

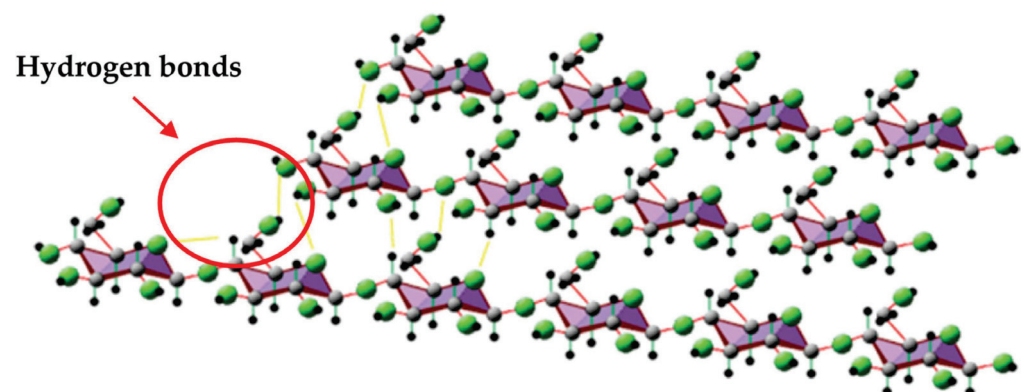


Figure 13. Hydrogen bonds interaction between β -glucose molecules in a segment of cellulose. Reproduced with permission from *Compos. from Renew. Sustain. Mater.*, Pérez-Pacheco et al., Thermo-plastic Starch (TPS)–Cellulosic Fibers Composites: Mechanical Properties and Water Vapor Barrier: A Review, 2016 [8].

For example, Fourati et al. [33] studied WVP in nanocomposites based on corn TPS with glycerol (30 wt %) and CNF-oxidized eucalyptus pulp (2–15 wt %). As shown in Figure 14, the expected behavior is obtained; an increase in CNF in the TPS matrix improves the barrier properties, causing lower water uptake.

The presence of CNF will affect the optical properties as well; this nanofiller in the TPS matrix could produce opacity in films as its content increases and depends on the quality of the dispersion of CNF in the matrix. Figure 15 shows the decrease in transmittance and clarity with the CNF addition; the authors agree that the poor dispersion of the CNF and the presence of agglomerates is the origin of the loss in the transparency [33,106].

In some studies, the CNF improves the transparency of the composite. It is possible to increase the dispersion by improving the blending mechanism or applying chemical modifications. For example, Pitiphatharaworachot et al. [81] studied the TEMPO-oxidized (TEMPO stands for 2,2,6,6-tetramethylpiperidine-1-oxyl radical) bamboo cellulose nanofibrils (TOBCNFs) in tapioca TPS matrix (starch: glycerol 4:1). All films with the different nanofiller contents were homogeneous and transparent, owing to the good dispersion and bonding with the TPS matrix, increasing transparency by 3% at 600 nm (see Figure 16).

This improvement is due to the nanometric size of TOBCNFs (3–4 nm of diameter), which is lower than optical wavelengths.

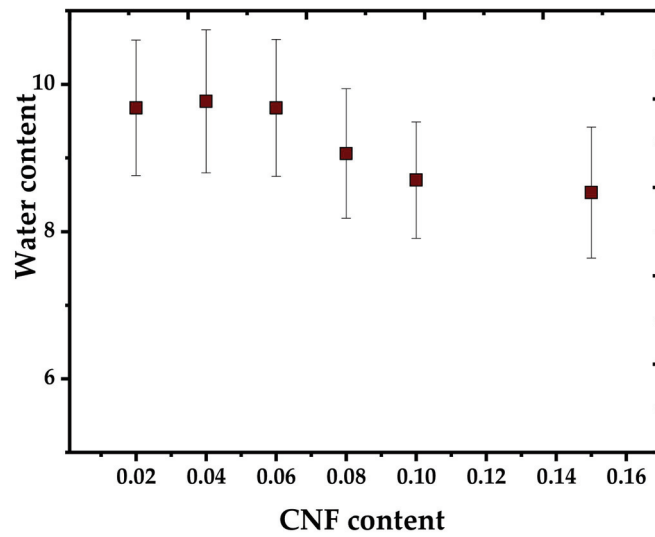
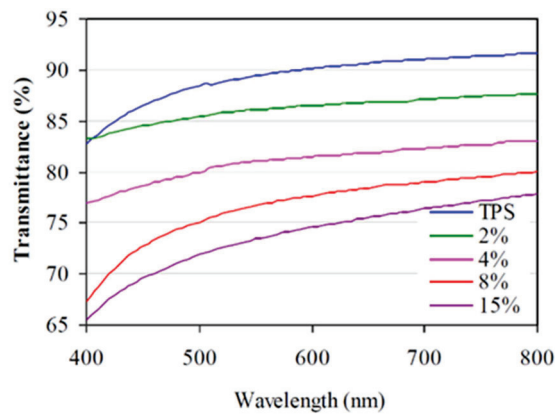
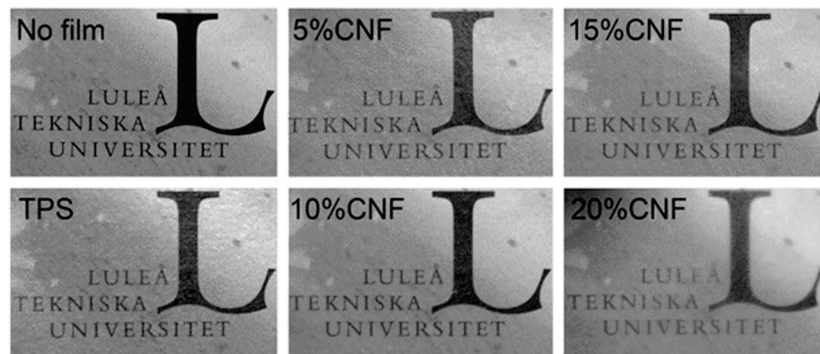


Figure 14. Water uptake trend in respect to CNF content in TPS matrix. Prepared from data in [33].



(a)



(b)

Figure 15. (a) UV-Vis transmittance spectra for TPS/CNF films. Reproduced with permission from *Carbohydr. Polym.*, 229, Fourati et al. One-Step Processing of Plasticized Starch/Cellulose Nanofibrils Nanocomposites via Twin-Screw Extrusion of Starch and Cellulose Fibers, 2020 [33]. (b) Visual aspect and transparency for TPS/CNF films at different wt %. Reproduced with permission from *Eur. Polym. J.*, 49, Hietala et al., Bionanocomposites of thermoplastic starch and cellulose nanofibers manufactured using twin-screw extrusion, 950–956, 2013 [106].

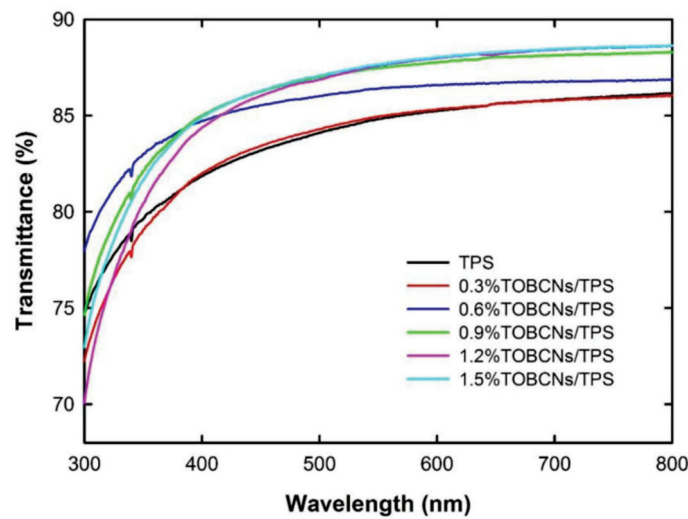


Figure 16. Light transmittance spectra of TOBCNs/TPS nanocomposite films. Reproduced with permission from *BioResources*, 14, Pitiphatharaworachot et al., Starch nanocomposites reinforced with TEMPO-oxidized cellulose nanofibrils derived from bamboo holocellulose, 2784–2797, 2019 [81].

Another important characteristic is the degradability of the nanocomposite once the CNF is added. According to the reported studies, these nanocomposites are biodegradable. However, adding a highly crystalline phase to the TPS leads to a slight decrease in the biodegradation rate. This behavior was reported by Babae et al. [117], who studied corn TPS nanocomposites with modified kenaf bast CNF. They degraded the samples using white-rot fungus, which consists of a laboratory incubator with purified fungi at 25 °C. These microorganisms are placed in a Petri dish until they are completely spread on the medium; then, the samples are placed on the medium on a platform to avoid direct contact. They are taken to an incubator at room temperature and 75% of relative humidity during the study time with periodic monitoring, recording the final weight after exposure.

Figure 17 shows the weight loss over time for TPS and nanocomposites with acetylated CNF and sole CNF. The compactness of the films is reduced after exposure by 50% within the 20 first days. Complete fungal degradability is different for the cases shown: for TPS, it is day 30, with CNF, it is at day 40, and acetylated CNF is day 60. CNF increases the crystallinity of the material, thus giving more resistance to degradation. These additions can restrict the destructive enzymatic activity and enzymatic hydrolysis of cellulose, increasing the degradation time compared to net TPS [117].

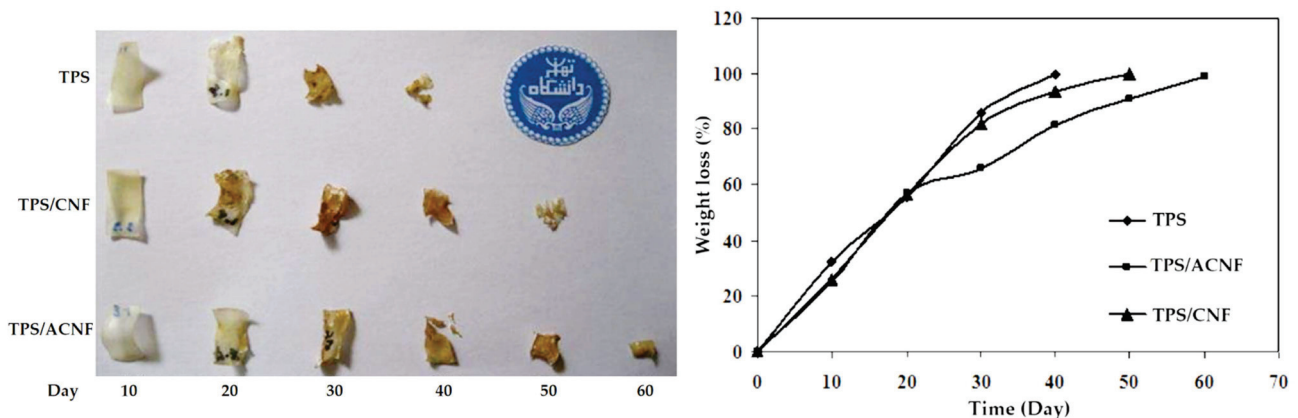


Figure 17. Visual and graphical fungal degradation of TPS and its nanocomposites. Reproduced with permission from *Carbohydr. Polym.*, 132, Babee et al., Biodegradability and mechanical properties of reinforced starch nanocomposites using cellulose nanofibers, 1–8, 2015 [117].

5. Cellulose Nanocrystals (CNC)

Similar to CNF, CNC can be obtained from a wide variety of natural sources. Table 2 shows the different starch and CNC sources extracted from several raw materials. These can be produced by a two-step mechanism that begins with acid hydrolysis, commonly HCl or H₂SO₄. This treatment is done to separate the amorphous region of the cellulose polymer, stabilizing the CNC in solution and preventing agglomeration. As the second step, and to obtain CNC, mechanical stress is required [76]. Some of the main key advantages of CNC include its easy combustion recyclability, low manufacturing energy, high availability, low density, non-abrasive nature (easy processability), and low cost [85].

Table 2. Plasticizers and cellulose nanocrystals as nanofillers (including their wt %) in most used TPS sources.

Starch Source	Plasticizer	Nanofiller	Wt %	Reference
NI	Glycerol	Cellulose nanocrystals	5	[126]
Corn	Glycerol	Waxy corn starch nanocrystals	1–5	[40]
	Glycerol	Cellulose nanocrystal	1–2	[127]
	Glycerol	Starch nanocrystals	1–2	[41]
Field pea	Glycerol, concentrated sulfuric acid, and sodium hypochlorite solution	Hemp cellulose nanocrystals	5–30	[79]
		Glycerol	Waxy starch nanocrystals (WSNC)/Cellulose cellulose nanocrystals	1–5
Maize	Glycerol	Cotton cellulose nanocrystals	4–8	[74]
	Glycerol	Cellulose nanocrystals	5–25	[75]
	Glycerol	Waxy maize starch nanocrystals	2.5	[42]
	Glycerol	Cellulose nanocrystals	1.5–10	[34]
Potato	Glycerol	Cellulose nanofibers and nanocrystals	1–3	[37]
	Glycerol	Cellulose nanocrystals	1–2	[128]
	Glycerol	Waxy maize nanocrystals	5–15	[39]
Potato, corn, pea	Glycerol	Cellulose nanocrystals	2–5	[5]

NI: No information reported.

From Table 2, we can deduce that the content of CNC on the TPS-based nanocomposites is similar to the employed in CNF, between 1 and 30%. The primary purpose is to increase the mechanical strength and elastic modulus. Achieving the desired properties requires homogeneous dispersion and strong hydrogen bonding between the filler and matrix molecules (reinforcement effect). Similarly, the decrease in elongation is present because of the strong interactions that reduce mobility between nanocrystals and the TPS matrix. On the other hand, a lack of interaction between the matrix and the fillers causes weak force transmission with rapid rupture propagation. A good balance is obtained by Cao et al. [79], who studied hemp cellulose nanocrystals (acid-catalyzed hydrolysis) in pea starch with glycerol matrix. They found in a range from 0 to 30 wt % of nanofiller values of 3.9 to 11.5 MPa for tensile strength, 31.9 to 823.9 MPa for modulus, and 68.2 to 7.5% for elongation at break.

The mechanical properties and the overall performance of the nanocomposites are affected by the water uptake, since it facilitates the retrogradation process due to the increased molecular motion of starch molecules. It is necessary to determine the relative humidity (RH) at room temperature to evaluate the absorption capacity of the film. Figure 18 shows the water uptake trends at different values of RH for potato, pea, and corn TPS with glycerol 30 wt % and CNC at 5 wt % studied by Montero et al. [5]. This work was done by placing the films in different RH chambers (20 °C) at 95%, 75%, and 54%. Data are reported within 300 h, showing that the absorption rate is the same regardless of the starch source. Water is absorbed in the beginning of exposure until equilibrium is reached; then, retrogradation occurs, and water is released (turning material opaque, yellowish, and softer). It is shown that the filler content helped reduce the water diffusion through the

material owing to hydrogen bonds between the filler and the matrix as well as increasing the crystallinity of the composite [5].

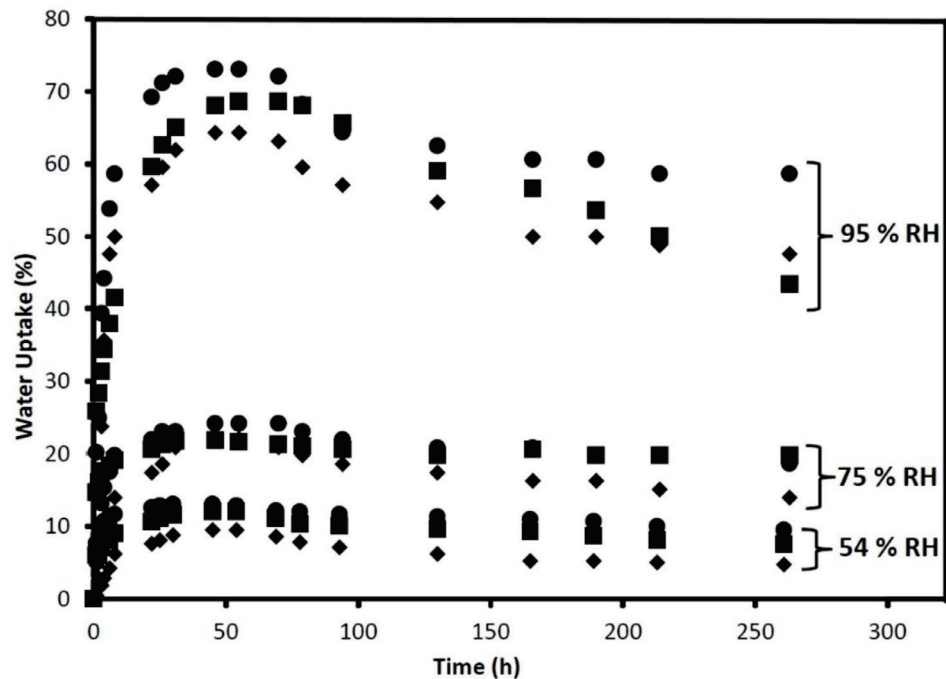


Figure 18. Water uptake trend through time considering the relative humidity (RH) at 20 °C for potato, pea, and corn TPS with CNC 5 wt %. Reproduced with permission from *Carbohydr. Polym.*, 157, Montero et al., Effect of Nanocellulose as a Filler on Biodegradable Thermoplastic Starch Films from Tuber, Cereal, and Legume, 1094–1104, 2017 [5].

The addition of CNC potentially modifies the optical properties of TPS in terms of optical transparency, which is due to its size (nanofiller width); since it is smaller than the visible light wavelength, CNC allows the transmission of light in the matrix, making it a more transparent material [129]. The high transparency is given by the width of the nanocrystal and the adequate distribution and dispersion of the nanofiller in the matrix [130]. The effect is similar to that observed with a proper CNF incorporation.

As expected, the TPS–CNC nanocomposites are biodegradable, and their degradability is related to the process of depolymerization of nanocomposite by water and the hydrophilic character of CNC. The study mentioned above establishes that CNC increases the crystallinity of the material, and consequently, the hydrophobicity [5]. In contrast, Vaezi et al. [129] mentioned that CNC has a double effect: the first is the one indicated above, and the second is the increase in the rates of disintegration caused by the hydrophilic nature of the nanofiller after a period time of exposure to the environment. This evidence suggests that the degradation process started earlier in the nanocomposite than in net TPS.

Comparing the effect of adding CNC or CNF to TPS, it is possible to find some differences; for example, the level of mechanical reinforcement is higher when the CNF is added; however, transparency tends to be reduced. The main reason for the difference is the nanofiller morphology. Figure 19 shows a short structure for CNC, while the suspension of CNF exhibits a higher L/D ratio. In addition, the crystallinity of the nanofiller is another critical factor; CNC has a higher crystallinity degree than CNF due to the elimination of amorphous regions in cellulosic arrays [37].

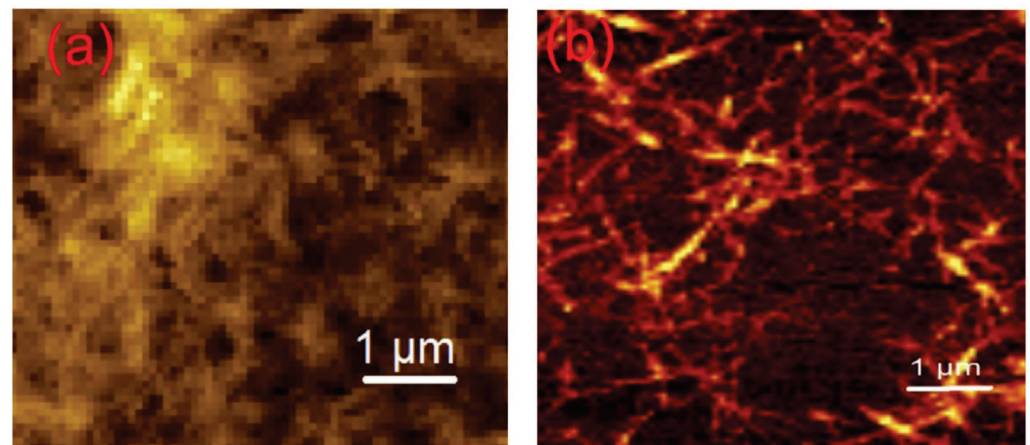


Figure 19. AFM of cellulose: (a) nanocrystals (CNC), (b) nanofibers (CNF). Reproduced with permission from *Macromol. Symp.*, 380 (1), Balakrishnan et al., Cellulose Nanofiber vs. Nanocrystals From Pineapple Leaf Fiber: A Comparative Studies on Reinforcing Efficiency on Starch Nanocomposites, 1–7, 2018 [37].

6. Natural Montmorillonite (MMT)

As a result of the TPS weaknesses, such as its hydrophilic nature, rapid degradation, and low performance, nanosized clays are a suitable option considering their properties. MMT shows an adequate distribution in the TPS matrix thanks to intercalation or exfoliation (Figure 8) [109]. Table 3 shows the different starch sources of TPS additivated with MMT that have been studied.

To prepare thermoplastic starch with nanoclays such as MMT, it is necessary to carry out a previous gelatinization process. Therefore, a starch/glycerol/nanoclay suspension is taken into an oven before the internal mixing process. This step is carried out to facilitate plasticization and optimize production by reducing process energy use during internal mixing [110].

The most noteworthy addition of MMT can be seen by the mechanical properties in the final product. An increase in elastic modulus and strength is observed as the nanofiller increases; this could be associated with the degree of exfoliation of MMT. Therefore, compatibility and dispersion with the TPS matrix are higher [109]. MMTs can withstand the effect of physical crosslinking with TPS and reinforcing it due to their surface area [131]; MMT decreases the elongation value, causing the applications of the material obtained to be restricted [132]. The main contribution of MMT is to the crystalline region (reducing the polymer chains' mobility), thanks to the nucleation effect of the layers [133], but it does not affect the flexibility, which makes it ideal for their use in packaging [109].

Table 3. Plasticizers and montmorillonite as nanofiller (including their wt %) in most used TPS sources.

Starch Source	Plasticizer	Nanofiller	wt %	Reference
Acetylated cassava	Water	Montmorillonite	1–10	[69]
	Glycerol	Montmorillonite, alumina trihydrate	26–37, 1–6	[67]
	Glycerol	Montmorillonite	3–5	[133]
Cassava	Glycerol	Montmorillonite, Cloisite 30B	5	[68]
	Glycerol	Na-montmorillonite (Cloisite® Na+)	1–2	[71]
	Glycerol	Montmorillonite	2–4	[134]
	Glycerol	Sodium montmorillonite, modified organo-montmorillonite	NI	[135]
Cationic starch	Glycerol	Sodium montmorillonite, ZnO	3–5, 0.5–1	[44]
Cereal	Glycerol	Montmorillonite/Chitosan	3–5/0.6–1	[49]

Table 3. Cont.

Starch Source	Plasticizer	Nanofiller	wt %	Reference
	Glycerol	Sodium montmorillonite	1	[43]
	Glycerol/water	Montmorillonite clay	3–4.5	[86]
	Glycerol/water	Hydrophilic bentonite, sodium montmorillonite/Essential oils constituents	0.5	[47]
	Glycerol	Walnut shell flour/Montmorillonite (MMT)	30–50/3–5	[89]
	Glycerol	Montmorillonite	0–5	[83]
	Glycerol	Montmorillonite	1–6	[84]
	Glycerol	Sodium montmorillonite	3–5	[136]
	Glycerol	Montmorillonite	1–5	[137]
	Glycerol	Sodium montmorillonite	2–5	[138]
	Glycerol	Sodium montmorillonite	2–8	[138]
	Glycerol	Montmorillonite clay	1–5	[51]
	Glycerol/water	Montmorillonite clay	1–9	[139]
	Glycerol	Montmorillonite clay	1–5	[109]
	Water	Sodium montmorillonite clay	5	[140]
	Glycerol	Montmorillonite (natural and glycerol-activated)	1–9	[141]
	Glycerol	Natural montmorillonite	2–6	[97]
	Glycerol	Sodium montmorillonite	1–9	[142]
	Water, partially hydrolyzed polyvinyl alcohol	Natural montmorillonite	1–5	[143]
	Sorbitol, formamide	Sodium montmorillonite	2–10	[131]
	Water	Natural montmorillonite, fluorohectorite	1–3.2	[144]
	Citric acid, formamide, and ethanolamine	Sodium montmorillonite	2–10	[145]
	Glycerol	Montmorillonite	0.03–0.1 (g)	[146]
Corn, wheat, potato Granular Maize	Glycerol	Natural montmorillonite, Cloisite 30B	3–15	[147]
	Glycerol	Montmorillonite	1–7	[72]
Maize	Glycerol	Natural montmorillonite, Cloisite 30B	5	[148]
	Glycerol	Montmorillonite	10–20	[149]
Merck starch	Glycerol	Natural montmorillonite	1–5	[150]
Pearl silver corn starch	Glycerol	Natural montmorillonite, Cloisite 30B	1, 1–5	[80]
	Glycerol	Sodium montmorillonite	2–5	[63]
	Urea	Montmorillonite		[151]
	Glycerol	Montmorillonite, kaolinite, hectorite and treated hectorite	6–22/5–18/5–20/5–19	[152]
Potato	Glycerol	Organically modified montmorillonite (Cloisite 30B), Natural montmorillonite Sodium montmorillonite	2.5–10	[153]
	Glycerol	Sodium montmorillonite	2–5	[63]
	Glycerol/water	Sodium montmorillonite	1–1.5	[154]
	Glycerol	Montmorillonite	4–8	[155]
	Glycerol/water	Cloisite 30B, Cloisite 10A, Cloisite 6A and Sodium montmorillonite	5	[102]
Sweet potato	Carbamide and ethanolamine	Sodium montmorillonite	2–8	[148]
Tapioca (Acetylated)	Glycerol	Natural and organically modified montmorillonite	5	[150]
	Glycerol	Sodium montmorillonite, Aminododecanoic-acid-treated organophilic clays	Silicate content: 0.5–7 (vol)	[80]
Wheat	Water/Glycerol	Montmorillonite	2–5	[87]
	Glycerol	Montmorillonite, Cloisite 30B, Cloisite 10A	1–5	[156]

Note: Natural montmorillonite and sodium montmorillonite refer to the same nanofiller. NI: No information reported.

Figure 20 represents the elastic modulus, strength, and elongation to break concerning the MMT content, which is the most used nanofiller in the TPS matrix due to the high performance obtained. In the case of elastic modulus and strength (Figure 20a,b, respectively), they increase with the MMT content, and the dispersion cloud is higher between 2 and 6 wt % of MMT. However, the decrease in elongation (Figure 20c) does not follow a trend in its scattering. The behavior in the range (2 to 6 wt %) is due to the dispersion and distribution of the filler being adequate to improve the properties of the polymer. When the content is higher, agglomerates can be produced, decreasing the mechanical properties

by reducing the stress distribution and increasing the rigidity. As the nanofiller content decreases, no significant change in the matrix is observed.

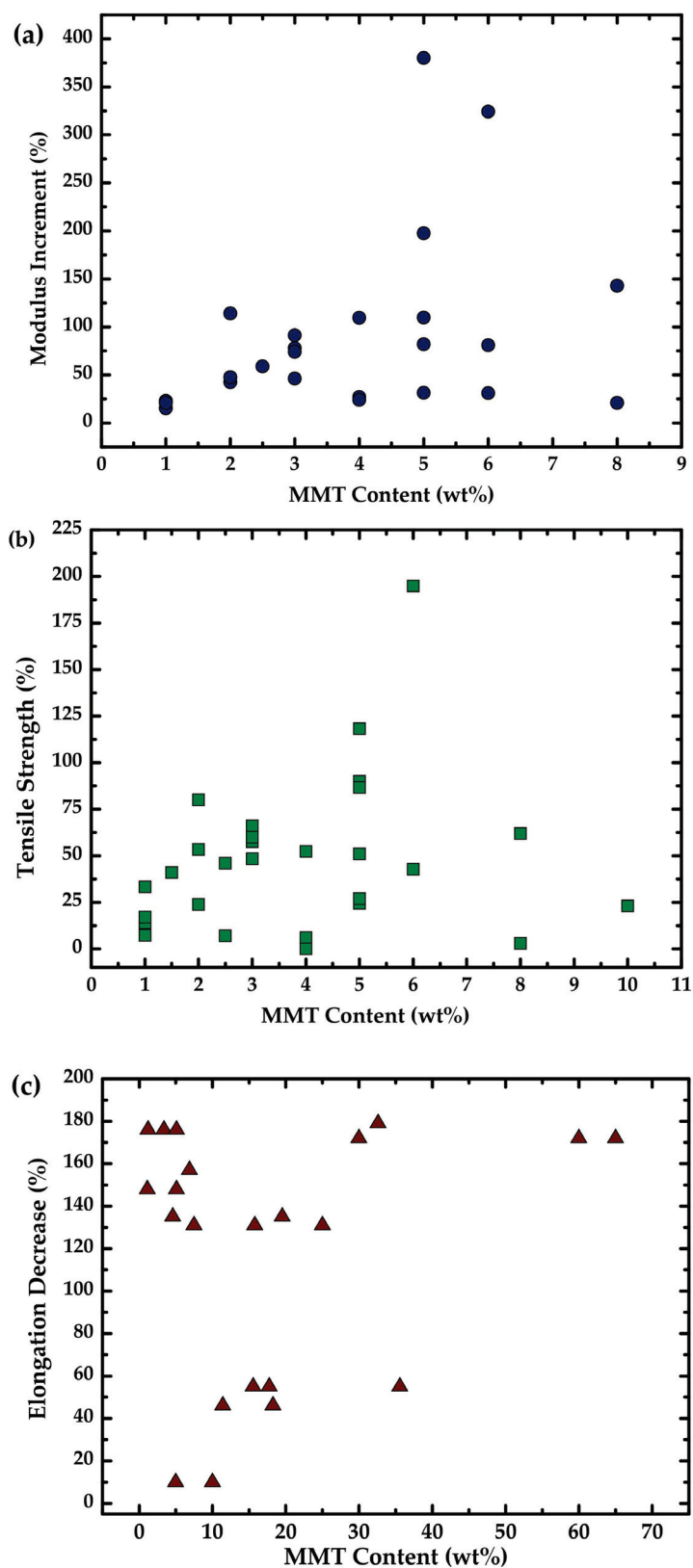


Figure 20. Mechanical properties with respect to montmorillonite (MMT) content: (a) tensile strength, (b) modulus increment, and (c) elongation decrease. Prepared from data in [43,44,49,53,63,83,100,109,131,136,143,154,155,157].

Ma et al. [131] studied corn TPS/MMT (2–10 wt %) nanocomposites (plasticized by sorbitol 0–20 wt %). They found the expected behavior for these nanocomposites. The Young modulus increased from 19.8 to 84.0 MPa, the tensile strength tripled to 12.27 MPa, and elongation decreased from 138.0% to 93.0%. This trend could be due to the adequate interaction between the matrix and the filler, which was intercalated (Figure 8b) and presenting a nano-scale dispersion. In addition, MMT presents physical crosslinking and TPS reinforcement, absorbing starch molecules thanks to its extensive specific surface. As mentioned above, it can be seen that the addition improves the elastic modulus and strength of the nanofiller. In this way, the mechanical properties are increased.

In order to consider different nanocomposite applications, water absorption is one of the main parameters in barrier properties to take into account. Huang et al. [158] studied corn starch/glycerol (1:3, *w/w*) with MMT content from 0 to 30% by extrusion. Figure 21 shows the water content through exposure to 50% RH environment for nanocomposites with MMT. It is observed that the rate of absorption gradually increases until reaching equilibrium around days 12 to 15 after exposure. A higher MMT content results in lower water uptake; this is described as stronger hydrogen bonds between the polymeric matrix and the nanofiller. This result can also be related to the mechanical properties: in a range from 5 to 50% of water content, the stress first increases (with a maximum at 13% of water content) and then decreases rapidly. It suggests that with the lowest and highest water content, the poor mechanical performance of the material will be exhibited.

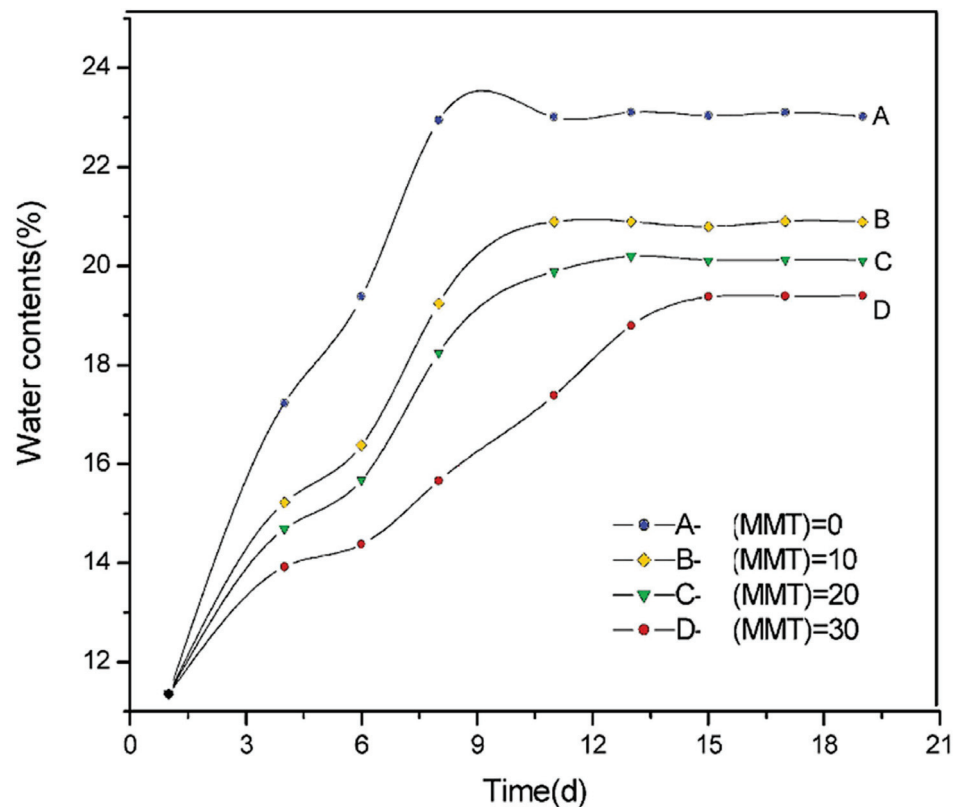


Figure 21. Water content of nanocomposites at 50% RH for different MMT in wt % (0, 10, 20, 30). Reproduced with permission from *Polymer (Guildf)*, 45, Huang et al., Studies on the properties of montmorillonite-reinforced thermoplastic starch composites, 7017–7023, 2004 [158].

In terms of optical properties, incorporating MMT in the TPS matrix decreases the luminosity and transparency due to the increase in light dispersion and diffuse reflectance, resulting in an opaquer nanocomposite. This behavior is highlighted by using rosemary essential oil (as an antioxidant) studied by Azevedo et al. [43] in corn TPS. It occurs due to a possible light scattering in the interface of oil droplets.

Additionally, ZnO nanoparticles along with MMT were studied by Vaezi et al. [44] in cationic starch (with glycerol) prepared by the solvent casting method. Although these nanoparticles reduce luminosity, the opacity is enhanced by the concentration of ZnO particles because it is considered a whitening agent. They also accentuated the difference in the color of the materials. TPS/MMT films additivated with ZnO particles can be UV-shielding and thermal insulators in the packaging industry.

For the degradability study, Behera [159] prepared corn TPS with MMT from 0 to 5 wt % by extrusion. According to standard procedures, the biodegradation analysis was performed using the soil-burial method, and the results were studied by field-emission (FE) SEM (Figure 22). It is shown that after 60 days of burial, the weight loss of net TPS to TPS nanocomposite, with 3 wt % of MMT, is 9% greater for the latter. This improvement is attributed to microorganism attack burial in the first place (circled cavity in Figure 22b). Furthermore, it is evident that before degradation, the surface is smoother (Figure 22a) than after it. Since it is highly biodegradable, the potential replacement of conventional plastics is foreseen.

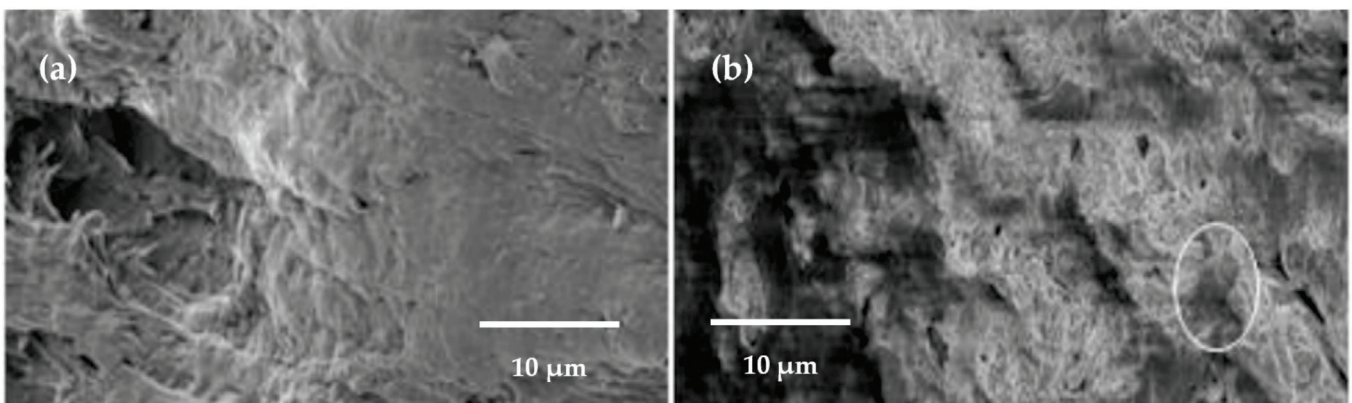


Figure 22. FE-SEM micrograph for TPS nanocomposite with 3 wt % of MMT (a) before degradation and (b) after degradation (60 days). Reproduced with permission from *IOP Conf. Ser. Mater. Sci. Eng.*, 410, Behera, Mechanical and biodegradation analysis of thermoplastic starch reinforced nano-biocomposites, 2018 [159].

7. Organically Modified Montmorillonite (O-MMT)

To increase the compatibility of the nanofiller with the matrix, MMT is organically modified to form intercalated or exfoliated structures with suitable interlayer distances [131]. Table 4 shows different sources of starch with O-MMT with various treatments. An example of organic treatments includes the modification of MMT by Ren et al. [53] via an activation method with dodecyl benzyl dimethyl ammonium bromide (12-OREC). The O-MMT solution is heated slowly to 50 °C; then, 12-OREC is added, and this solution is brought to 90 °C for 5 h. Finally, the solution is cooled to room temperature, filtered, dried, and pulverized. Even though there are many variations of O-MMT, Cloisite 30B is the most commercially available and used.

Adequate mechanical performance of the O-MMT nanocomposite requires proper dispersion and distribution through the matrix. The general tendency to use low concentrations (up to 3 wt %) follows that the properties are optimized, while higher concentrations tend to form agglomerates in the matrix. For example, Mohan and Kanny [48] studied corn TPS with Cloisite 30B; when 1 and 2 wt % of nanoclay is present in the matrix, a uniform and exfoliated structure can be observed because of the well-separated and randomly dispersed filler. For higher contents, meaning 3 and 5 wt %, the level of agglomeration of the nanolayers is elevated, which leads to an intercalated nanocomposite structure (Figure 23).

Table 4. Plasticizers and organically modified montmorillonite as nanofiller (including their wt %) in most used TPS sources.

Starch Source	Plasticizer	Nanofiller	wt %	Reference
NI	Glycerol	Cloisite 30B	3	[160]
Cassava	Glycerol	Montmorillonite, Cloisite 30B	5	[68]
	Glycerol	Sodium montmorillonite, modified organo-montmorillonite	NI	[135]
	Glycerol	Cloisite 30B	1–5	[48]
	Sorbitol	Cloisite 30B	1–5	[161]
Corn	Glycerol	Montmorillonite clay	1–5	[51]
	Glycerol	Cloisite 30B	2.5–10	[162]
	Glycerol	Montmorillonite (natural and glycerol-activated)	1–9	[141]
	Glycerol	Pristine clay (p-clay), Cloisite 93A	3	[163]
Corn, wheat, potato	Glycerol	Natural montmorillonite, Cloisite 30B	3–15	[147]
	Glycerol/distilled water	Bentonite and organically modified montmorillonite	40–50	[76]
Maize	Glycerol	Natural montmorillonite, Cloisite 30B	5	[148]
Pearl silver corn starch	Glycerol	Natural montmorillonite, Cloisite 30B	1, 1–5	[80]
	Glycerol/water	Cloisite (organoclay)	5	[164]
Potato	Glycerol	Cloisite 30B, natural sodium montmorillonite	2.5–10	[100]
	Glycerol/water	Cloisite 30B, Cloisite 10A, Cloisite 6A and Sodium montmorillonite	5	[102]
Tapioca (Acetylated)	Glycerol	Natural and organically modified montmorillonite	5	[82]
Wheat	Glycerol	Sodium montmorillonite, aminododecanoic-acid-treated organophilic clays	Silicate content: 0.5–7 (vol)	[153]
	Glycerol	Montmorillonite, Cloisite 30B, Cloisite 10A	1–5	[156]

Note: Natural montmorillonite and sodium montmorillonite refers to the same nanofiller. NI: No information reported.

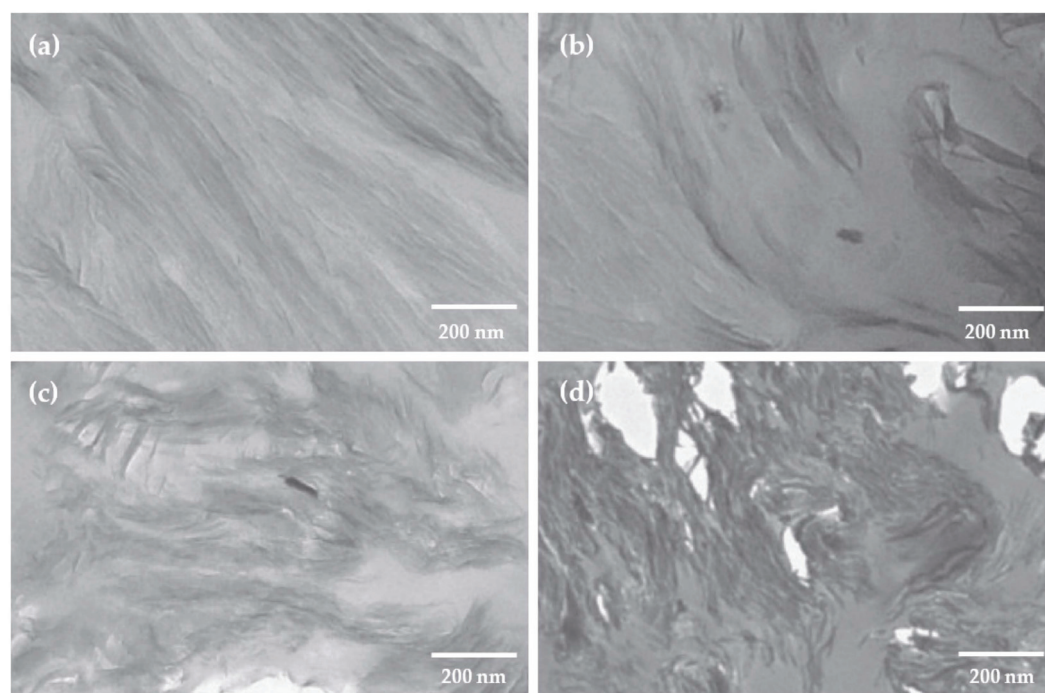


Figure 23. TEM micrographs of TPS matrix with different nanoclay concentrations in wt %: (a) 1, (b) 2, (c) 3, (d) 5. Reproduced with permission from *J. Plast. Film Sheeting*, 32, Mohan and Kanny, Thermoforming studies of corn starch-derived biopolymer film filled with nanoclays, 163–188, 2016 [48].

The barrier and mechanical properties are better for exfoliated than intercalated arrangements (8). This improvement may be due to the aspect ratio (length/thickness); more contact surface of the clay with the matrix is shown in an exfoliated structure,

reducing the net thickness and improving the dispersion. On the other hand, intercalated configurations exhibit a particular orientation of the clay layers, increasing net thickness and reducing the area of the contact surface of the filler with the matrix [48].

The influence of the nanoclay configuration within the TPS matrix is evidenced by the work of Ren et al. [53]; they studied the effect of different content of modified MMT on the mechanical behavior and crystallinity of the TPS, finding an increase in the restriction of the granular, crystalline structure of starch in the nanocomposite with the rise of O-MMT, as can be seen in Figure 24. When the filler content increases in a moderate range, the elastic modulus and strength tend to improve, but elongation decreases with filler content. Although the TPS morphology is modified by the action of the filler, the low clay contents produce excellent dispersion in the TPS matrix, but high clay contents lead to agglomeration.

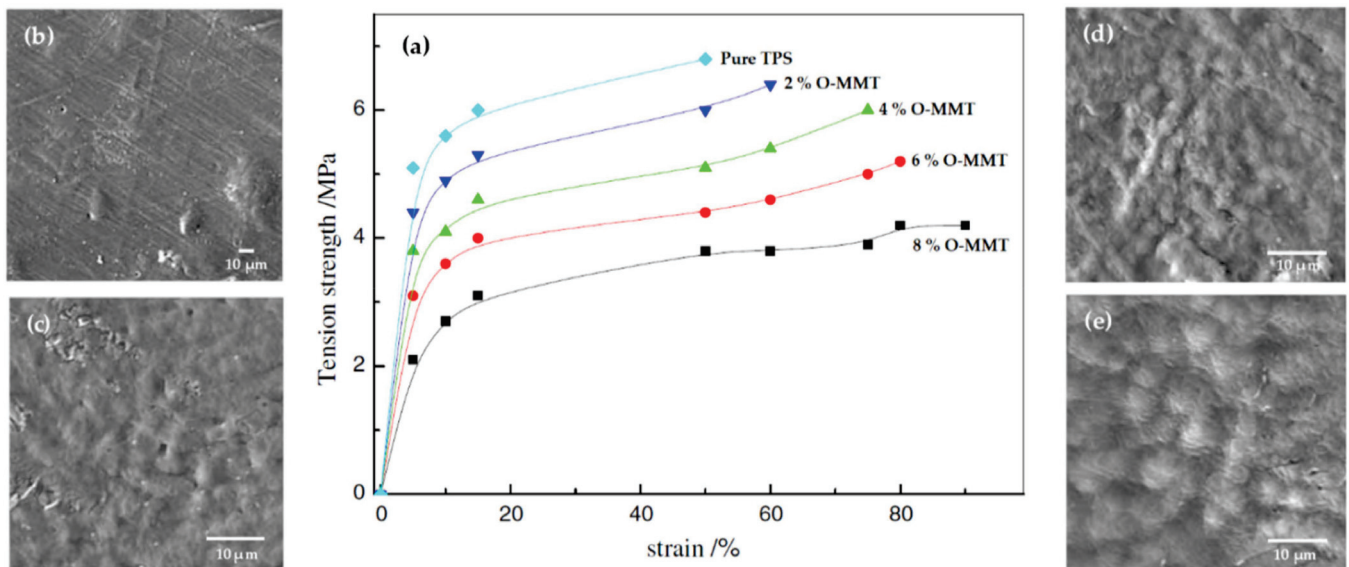


Figure 24. (a) Tension strength versus strain for neat TPS and the TPS/O-MMT nanocomposites indicated. SEM images of (b) 2% O-MMT, (c) 4% O-MMT, (d) 6% O-MMT, (e) 8% O-MMT. Reproduced with permission from *Polym. Environ.*, 17, Ren et al., Study on biodegradable starch/OMMT nanocomposites for packaging applications, 203–207, 2009 [53].

The agglomeration and nanoclay configuration affect the barrier properties as well. Boonprasith et al. [135] compared MMT and Cloisite 30B (5 pph) in TPS with poly(butylene succinate) (PBS) matrix (75/25% *w/w*) plasticized with glycerol (30 wt %). They found that WVP could not be measured because TPS is the major component in matrix, and it is sensibly hydrophilic. In terms of oxygen permeability, changes are not significant regardless of the clay type.

Gao et al. [165] studied films made by extrusion blown with hydroxypropyl starch, glycerol, O-MMT, and sugars (10 or 20%) as co-plasticizing agents (sucrose, fructose, and glucose). Figure 25 shows an increase in WVP with sugars due to their hydrophilic nature and molecular expansion effect in the plasticization phase.

In the case of optical properties and biodegradability of TPS/O-MMT nanocomposites, more research should be conducted because there is little information in the literature, mainly studying these nanofillers in other matrixes. However, Mohan and Kanny [48] point out that Cloisite 30B increases the degradation rate in the soil burial test when compared with MMT-based TPS and net TPS.

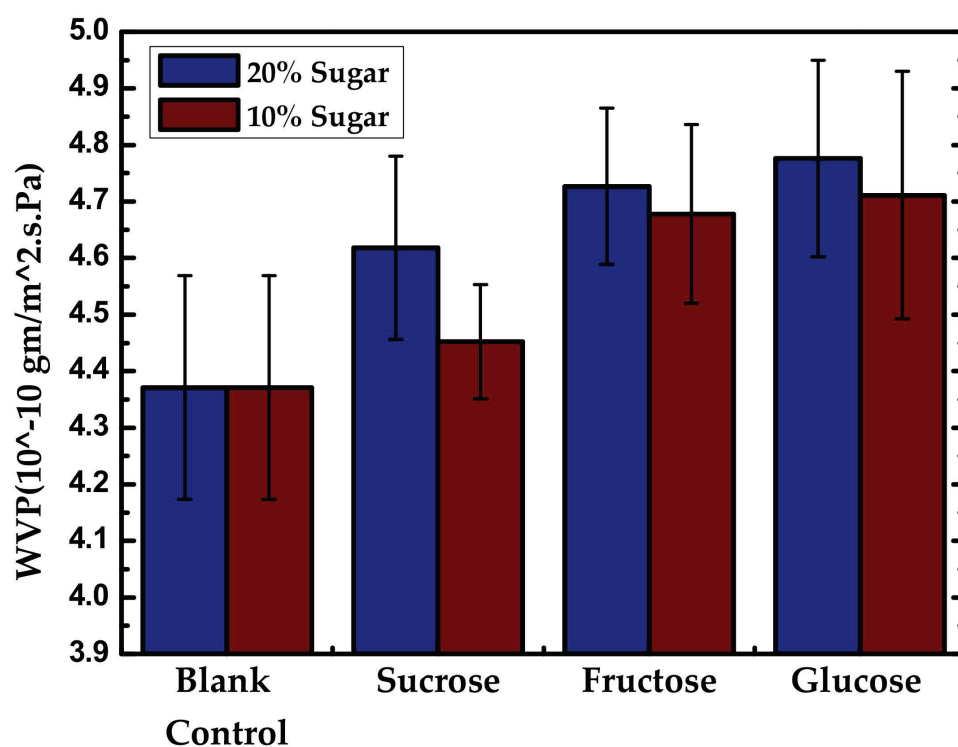


Figure 25. WVP of starch-based nanocomposite films with 20% and 10% sugar content at 6 wt % of modified MMT. Reproduced with permission from *Int. J. Biol. Macromol.*, 133, Gao et al., The Co-Plasticization Effects of Glycerol and Small Molecular Sugars on Starch-Based Nanocomposite Films Prepared by Extrusion Blowing, 1175–1181, 2019 [165].

8. Other Nanofillers

In addition to the main nanofillers mentioned above, studies were conducted with various nanofillers and starch sources, as can be seen in Table 5. In this section, some examples regarding their mechanical properties and degradability will be briefly presented, which are the main parameters to consider for TPS nanocomposites analysis and end-product applications.

As shown in Table 5, the TPS has been blended with other natural nanofillers such as chitosan, bacterial cellulose, bentonite, kaolinite, and synthetic ones such as carbon nanotubes, silver, and graphene quantum dots. In most cases, the amount employed was low, around 5 wt %.

In all the studies, the mechanical properties were affected. For example, the tensile and flexural properties are enhanced by multi-walled carbon nanotubes (MWCNTs). In general, they are acid-functionalized with a mixture of sulfuric and nitric acids [2] to improve their merging into the matrix. This chemical modification increases the filler hydrophilicity and reduces the agglomerations in the matrix, which contributes to hydrogen bonding interactions and compatibility. Cao et al. [118] studied this filler in pea starch plasticized with glycerol and water. They obtained in a range from 0 to 3 wt % of nanofiller, 2.85 to 4.73 MPa for tensile strength, 20.74 to 39.18 MPa for elastic modulus, 41.99% (maximum) at 1 wt % of filler for elongation at break (if the filler exceeds 1 wt %, elongation slightly decreases).

Table 5. Plasticizers and other nanofillers (including their wt %) in most used TPS sources.

Starch Source	Plasticizer	Nanofiller	wt %	Reference
NI	Glycerol	Chitin nanofibers	3–10	[166]
	Glycerol	Silver nanoparticles	0.5–1	[90]
Cassava	Glycerol	Chitosan-modified Veegum® HS clay (smectite)	2.5–5	[65]
	Glycerol	Sepiolite	1–5	[66]
	Glycerol	Sepiolite	1–5	[167]
	Glycerol	Silver nanoparticles	0.006–0.15	[168]
	Glycerol	Halloysite nanotubes	2	[169]
	Glycerol	Halloysite nanoclay	1–5	[170]
	Glycerol	Halloysite nanotubes	2–8	[171]
	Glycerol	Talc nanoparticles	1–5	[87]
	Glycerol	Graphene quantum dots (GQD)	0.05–0.5	[88]
	Glycerol	Laponite Carboxylate	1–5	[172]
Corn	Glycerol	multi-walled carbon nanotubes (CMWNTs)	0.5–3	[173]
	Glycerol	Bentonite, chitosan	4	[174]
	Glycerol	Talc nanoparticles	0–5	[175]
	Glycerol	Bacterial cellulose nanowhiskers (BCNW)	2–20	[50]
	Glycerol	Talc	1–5	[176]
	Glycerol	Bentonite, organically modified	40–50	[76]
	Glycerol	montmorillonite Beta-tricalcium phosphate nanoparticles	3–10	[177]
	Glycerol	Nanoclay: bentonite (H ₂ Al ₂ O ₆ Si)	1–5	[178]
	Sorbitol	Cardanol oil, in situ silver nanoparticles	0.2–0.6, 1–4 (mmol)	[179]
	Glycerol	Graphene oxide nanoplatelets, cellulose nanofibers	1–5, 5–15	[119]
Maize	Glycerol	Lanthanum hydroxide nanoparticles	1–3	[180]
	Ethyl vinyl acetate	Bentonite		[45]
	Glycerol	Zirconium glycine-N,N- dimethylphosphonate (ZGDMP)	0.2–1	[77]
Pea	Glycerol	Acid-treated multi-walled carbon nanotubes (MWCNTs)	0.1–3	[80]
	Glycerol	Natural bentonite	1	[78]
Pomegranate	Polyethylene glycol and glycerol	Particles of AgNO ₃ , Silver	2.5–5, 0.5–1	[90]
	Glycerol	Halloysite nanoclay	3–7	[46]
	Glycerol	Talc, bentonite	1–5, 1–5	[59]
Potato	Glycerol	Bacterial cellulose (BC) nanoribbons		[60]
	Glycerol	Kaolin clay	5–15	[181]
Tapioca	Glycerol	Multi-walled carbon nanotubes (MWCNT)	0.25–10	[2]
	Glycerol	Kaolinite	10–60	[182]
	Glycerol, urea, ethanolamine	Halloysites nanotubes	6	[54]

NI: No information reported.

Although the general increasing trend mentioned in the other system for elastic modulus and strength and a decreasing trend for elongation is maintained in most studies, it sometimes does not follow that rule. That is the case of the work of Kwaśniewska et al. [181], showing that in the nanocomposite with 15% kaolinite in potato TPS matrix (with 20 wt % of glycerol), the modulus and strength is lower than the base film, and the elongation increases. These changes could be due to the intercalation of kaolinite in the TPS matrix.

As was discussed for the other nanofillers, the biodegradation of these nanocomposites is worth mentioning. Its behavior should depend on the nature and amount of the nanofiller. However, there is not enough data to establish a general trend. One example of the TPS-based biodegradation behavior is the study of Sessini et al. [45], who prepared EVA/pea TPS (50:50) blend nanocomposites with glycerol (25 wt %) and distilled water (20 wt %) reinforced with natural bentonite (1 wt %). Figure 26 shows the visual disintegration process of TPS under aerobic conditions until its complete disappearance at day 56. A yellowish tone and breakable structure are reached even on day 1 (Figure 26a), which is caused by the enzymatic attacks of microorganisms that break the bonds of long-chain sugar units. In addition, the opaque tone is caused by the hydrolytic disintegration process. The environmental impact can be improved because these materials take less time to degrade, considering that composting conditions would be required.

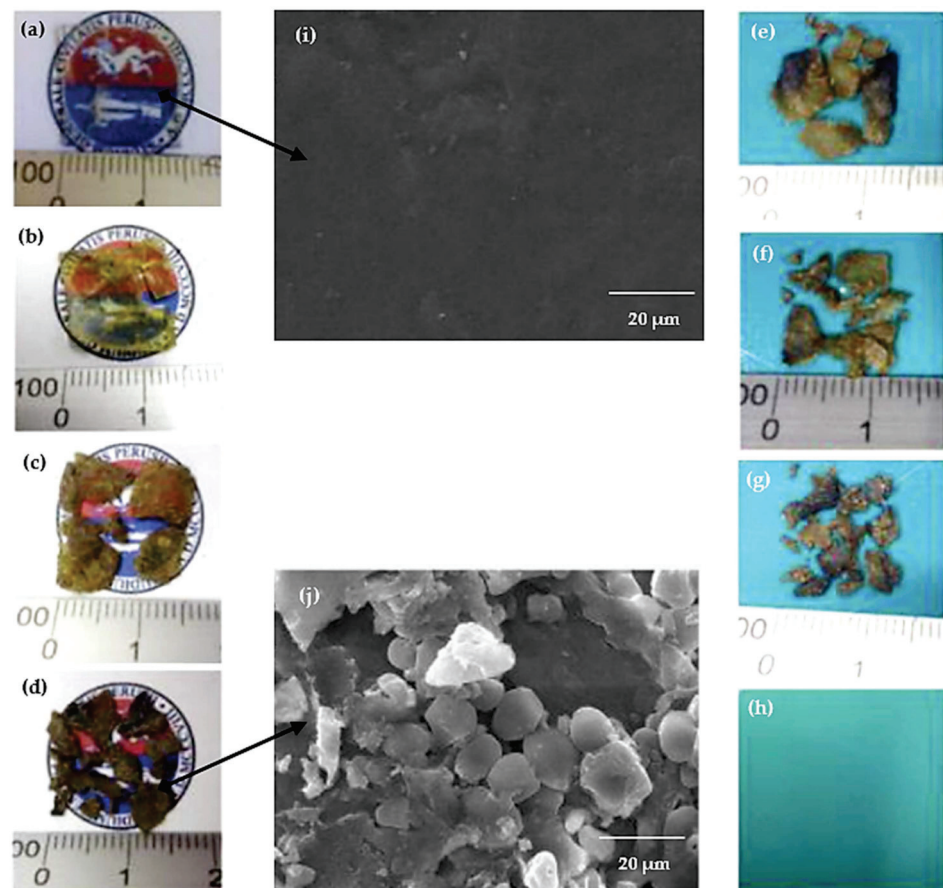


Figure 26. Disintegration process under composting conditions of TPS film at day (a) 0, (b) 1, (c) 11, (d) 18, (e) 25, (f) 32, (g) 39, and (h) 56. SEM micrograph of the disintegration process at day (i) 0 and (j) 18. Reproduced with permission from *Polym. Degrad. Stab.*, 159, Sessini et al. Thermal and composting degradation of EVA/Thermoplastic starch blends and their nanocomposites, 184–198, 2019 [45].

Different arrangements can be made as test options for degradability studies. One of the most common is to bury the material in a mixture that reproduces outdoor aerobic conditions of the environment. For example, composting conditions may include a solid

synthetic waste made of 10% compost, 30% rabbit food, 10% starch, 5% sugar, 4% corn oil, 1% urea, and 40% sawdust with a humidity content of 50%. The material is cut into small samples and placed on a textile to perform the disintegrability test under these parameters. This arrangement allows for quick removal after the test and easy access to moisture and microorganisms. The synthetic residue is buried 4 to 6 cm deep, and the synthetic waste is incubated under aerobic conditions (58 °C). Weight normalization is necessary to measure disintegrability, which is relative to the initial day after the cleaning and drying [45].

9. Analysis and Discussion for Packaging Purposes

It seems impossible to think of life without plastic, but it is one of the major pollutants in many aspects of daily life and industries. Currently, landfills are the most widely applied method to reduce packaging waste disposal; however, more methods include incineration, recycling, and compost. According to American Society for Testing and Materials (ASTM), biodegradable and compostable are not equivalent terms. Biodegradation considers the environment (temperature, moisture, oxygen, pH) in which the material is placed and the chemical nature of the polymer, while composting refers to a material that suffers degradation by microorganisms to produce biomass, water, carbon dioxide, and inorganic compounds at a consistent rate. All compostable materials are biodegradable, but the opposite does not come into effect [183].

Bio-based polymers have been extensively developed with new technologies to address this problem, reducing costs and improving performance. In addition, studies suggest that multi-layer arrangements or blends accomplish better performance for bio-based materials. In order to meet the standards for synthetic polymers, requirements include adequate water vapor permeability, resistance to water, acids, oils, UV light, machinability, transparency, and anti-fogging capacity availability, among others [184].

TPS nanocomposites reinforced with CNF, CNC, MMT, and O-MMT will be analyzed for this application regarding the items presented above and considering the main factors for ideal packaging material. TPS nanocomposites are an excellent option for packaging thanks to their high availability, easy processability, biodegradability, and compostability; however, the addition of fillers enhanced these properties [12].

TPS/CNF nanocomposites may be suitable for packaging material because they meet the requirements mentioned above. Adequate plasticizer and proper dispersion, distribution, and interaction with the matrix lead to favored mechanical and barrier properties, using on average 15 wt % [33]. However, if aesthetic characteristics are required for the end usage material, it is essential to know that an excessive CNF (around 5–20 wt %) confers opacity [106], while low content (less than 1.5 wt %) results in increased transparency [81]. The degradation rate will be related to a modification in CNF; e.g., if the material will be needed for prolonged use, the acetylated CNF confers a longer degradation time after exposure than sole CNF (short-term use) [117].

Crystallinity is the main factor in CNC because, unlike CNF, its incorporation directly affects the crystalline region of TPS [37]. The stiffness of the material will increase, causing a more pronounced reduction in elongation due to reduced mobility of starch molecules, and it will maintain strength and the modulus capacity under competent conditions [79]. Improvements in barrier properties are observed when the material begins to be exposed to the environment [5], but the hydrophilic nature of CNC produces earlier degradability than the rest of the TPS matrix after a specific exposure time [129]. Considering that CNC is smaller than the optical wavelength, they are useful for packaging applications when the esthetic factor is the most determinant in the final product (they improve material transparency) [130].

Likewise, the increase in CNC and MMT crystallinity in TPS materials does not drastically affect flexibility, which improves mechanical properties (around 2–10 wt %) [109,131]. For this reason, field packaging is notably considered among their applications. Furthermore, the strong interaction between the nanofiller and the matrix leads to adjusting barrier properties in a relative range of 0 to 30 wt %. The chosen MMT content is crucial for the

WVP and, as a consequence, for the mechanical performance of the nanocomposites [158]. On the other hand, the appearance of the material will be affected by this nanofiller because it causes an increment in opacity, so it has to be considered if transparency is of importance for the packaging [44]. These nanocomposites fulfill the characteristics of biodegradable packaging, as was shown by the soil-burial tests that have been carried out [159].

In TPS/O-MMT, these nanocomposites can be applied in the packaging industry, specially reinforced with Cloisite 30B because of the high commercial availability (organic modification is already done), reducing processing costs. In addition, the mechanical and barrier properties are optimized thanks to a good interaction with the matrix, forming exfoliated structures. The inclusion of O-MMT produces a higher biodegradation rate, making it efficient for packaging use [48]. In order to analyze the esthetics of the final product, it is necessary to carry out more studies in optical properties.

10. Final Remarks and Future Perspectives

TPS is a suitable option to replace conventional thermoplastic polymers; however, the lack of mechanical properties exhibited by TPS alone can be overcome by adding nanofillers. This review focused on the following four common ones: MMTs (natural and organically modified), CNC, and CNF. These fillers must have a good dispersion and distribution in the TPS matrix, which leads to better mechanical properties (increased modulus and strength while decreasing elongation) and barrier properties (greater hydrophobic character). On the other hand, the optical properties (transparency and luminosity) are mostly reduced, and the color variation with these fillers needs further study. In the case of biodegradability, few studies have been carried out with the soil-burial method.

Despite that, more research of new methods to reproduce different conditions is needed or even implementing the material in real scenarios to obtain more information on the degradation rate. The study of different starch blends can be useful to redirect the potential of TPS usages in terms of properties and morphology. Other unconventional sources for starch and different type of fillers could be explored further. The interaction of the polymer with nanofiller is another potential prospect for considerable studies in order to reduce deformation at break. This improvement could be made by chemical modification of either the TPS or the nanofiller. Due to its good performance, TPS with nanofillers is a promising option for new advanced materials for the packaging industry. Finally, the processing methods for these nanocomposites and other similar systems should be systematically studied to establish their applicability in real life.

Author Contributions: Conceptualization, formal analysis, data curation, investigation, writing—original draft preparation, K.E.R.-V. Rivadeneira and C.A.U.-S.; writing—review and editing, A.D.-B., A.E.S.-M. and J.P.T.; Conceptualization, methodology, supervision, project administration, funding acquisition, writing—review and editing, R.M.M. All authors have read and agreed to the published version of the manuscript.

Funding: This research was funded by *Corporación Ecuatoriana para el Desarrollo de la Investigación y Academia, CEDIA, through its CEPRA program, grant number CEPRA 2021–012 Hacia la economía circular: desarrollo de eco-empaques a partir de desechos agroindustriales* and The APC was funded by *Corporación Ecuatoriana para el Desarrollo de la Investigación y Academia, CEDIA*.

Institutional Review Board Statement: Not applicable.

Informed Consent Statement: Not applicable.

Conflicts of Interest: The authors declare no conflict of interest. The funders had no role in the design of the study; in the collection, analyses, or interpretation of data; in the writing of the manuscript, or in the decision to publish the results.

References

- Geyer, R.; Jambeck, J.R.; Law, K.L. Production, use, and fate of all plastics ever made. *Sci. Adv.* **2017**, *3*, e1700782. [CrossRef]
- Deepthi, M.V.; Sailaja, R.R.N.; Ananthapadmanabha, G.S.; Avadhani, G.S. Cross-linked Chitosan/Thermoplastic Starch Reinforced with Multiwalled Carbon Nanotubes Using Maleate Esters as Coupling Agent: Mechanical, Tribological and Thermal Characteristics. *Polym.-Plast. Technol. Eng.* **2014**, *53*, 1476–1486. [CrossRef]
- #BeatPlasticPollution This World Environment Day. Available online: <https://www.unenvironment.org/interactive/beat-plastic-pollution/> (accessed on 20 October 2020).
- Tang, X.; Alavi, S. Recent advances in starch, polyvinyl alcohol based polymer blends, nanocomposites and their biodegradability. *Carbohydr. Polym.* **2011**, *85*, 7–16. [CrossRef]
- Montero, B.; Rico, M.; Rodríguez-Llamazares, S.; Barral, L.; Bouza, R. Effect of nanocellulose as a filler on biodegradable thermoplastic starch films from tuber, cereal and legume. *Carbohydr. Polym.* **2017**, *157*, 1094–1104. [CrossRef]
- Palza, H. Antimicrobial Polymers with Metal Nanoparticles. *Int. J. Mol. Sci.* **2015**, *16*, 2099–2116. [CrossRef]
- Karger-Kocsis, J.; Kmetty, Á.; Lendvai, L.; Drakopoulos, S.X.; Bárány, T. Water-Assisted Production of Thermoplastic Nanocomposites: A Review. *Materials* **2015**, *8*, 72–95. [CrossRef] [PubMed]
- Pérez-Pacheco, E.; Canto-Pinto, J.C.; Moo-Huchin, V.M.; Estrada-Mota, I.A.; Estrada-León, R.J.; Chel-Guerrero, L. Thermoplastic Starch (TPS)-Cellulosic Fibers Composites: Mechanical Properties and Water Vapor Barrier: A Review. In *Composites from Renewable and Sustainable Materials*; Intech Open: London, UK, 2016. [CrossRef]
- Khan, B.; Bilal Khan Niazi, M.; Samin, G.; Jahan, Z. Thermoplastic Starch: A Possible Biodegradable Food Packaging Material—A Review. *J. Food Process. Eng.* **2017**, *40*, e12447. [CrossRef]
- Zhong, Y.; Godwin, P.; Jin, Y.; Xiao, H. Biodegradable polymers and green-based antimicrobial packaging materials: A mini-review. *Adv. Ind. Eng. Polym. Res.* **2020**, *3*, 27–35. [CrossRef]
- Hammache, Y.; Serier, A.; Chaoui, S. The effect of thermoplastic starch on the properties of polypropylene/high density polyethylene blend reinforced by nano-clay. *Mater. Res. Express* **2020**, *7*, 025308. [CrossRef]
- Balakrishnan, P.; Geethamma, V.; Gopi, S.; Thomas, M.G.; Kunaver, M.; Huskić, M.; Kalarikkal, N.; Volova, T.; Rouxel, D.; Thomas, S. Thermal, biodegradation and theoretical perspectives on nanoscale confinement in starch/cellulose nanocomposite modified via green crosslinker. *Int. J. Biol. Macromol.* **2019**, *134*, 781–790. [CrossRef]
- Valle, U.; Jose, H.; Pedro, J.; Valle, U. Influencia del tiempo de almacenamiento en las propiedades estructurales de un almidón termoplástico de yuca (TPS). *Ing. Compet.* **2009**, *11*, 1–27.
- Shayan, M.; Azizi, H.; Ghasemi, I.; Karrabi, M. Influence of modified starch and nanoclay particles on crystallization and thermal degradation properties of cross-linked poly(lactic acid). *J. Polym. Res.* **2019**, *26*, 238. [CrossRef]
- Solati, M.; Saeidi, A.; Ghasemi, I. The effect of graphene nanoplatelets on dynamic properties, crystallization, and morphology of a biodegradable blend of poly(lactic acid)/thermoplastic starch. *Iran. Polym. J.* **2019**, *28*, 649–658. [CrossRef]
- Shayan, M.; Azizi, H.; Ghasemi, I.; Karrabi, M. Effect of modified starch and nanoclay particles on biodegradability and mechanical properties of cross-linked poly lactic acid. *Carbohydr. Polym.* **2015**, *124*, 237–244. [CrossRef] [PubMed]
- Manepalli, P.H.; Alavi, S. Mathematical modeling of mechanical and barrier properties of poly(lactic acid)/poly(butylene adipate-co-terephthalate)/thermoplastic starch based nanocomposites. *J. Food Eng.* **2019**, *261*, 60–65. [CrossRef]
- Nofar, M.; Sacligil, D.; Carreau, P.J.; Kamal, M.R.; Heuzey, M.-C. Poly (lactic acid) blends: Processing, properties and applications. *Int. J. Biol. Macromol.* **2019**, *125*, 307–360. [CrossRef]
- Afkhami, A.; Rezaei, M.; Malmiri, H.J. Effect of chitosan incorporation on crystallinity, mechanical and rheological properties, and photodegradability of PE/TPS blends. *J. Thermoplast. Compos. Mater.* **2021**, *34*, 780–800. [CrossRef]
- Ahmadi, M.; Behzad, T.; Bagheri, R. Reinforcement effect of poly (methyl methacrylate)-g-cellulose nanofibers on LDPE/thermoplastic starch composites: Preparation and characterization. *Iran. Polym. J.* **2017**, *26*, 733–742. [CrossRef]
- Sabetzadeh, M.; Bagheri, R.; Masoomi, M. Effect of nanoclay on the properties of low density polyethylene/linear low density polyethylene/thermoplastic starch blend films. *Carbohydr. Polym.* **2016**, *141*, 75–81. [CrossRef]
- López, O.V.; Castillo, L.A.; Barbosa, S.E.; Villar, M.A.; Alejandra García, M.A. Processing-properties-applications relationship of nanocomposites based on thermoplastic corn starch and talc. *Polym. Compos.* **2018**, *39*, 1331–1338. [CrossRef]
- Inceoglu, F.; Menciloglu, Y.Z. Transparent low-density polyethylene/starch nanocomposite films. *J. Appl. Polym. Sci.* **2013**, *129*, 1907–1914. [CrossRef]
- Sharif, A.; Aalaie, J.; Shariatpanahi, H.; Hosseinkhanli, H.; Khoshniyat, A. Study on the structure and properties of nanocomposites based on high-density polyethylene/starch blends. *J. Polym. Res.* **2011**, *18*, 1955–1969. [CrossRef]
- Kumanayaka, T.; Parthasarathy, R.; Jollands, M. Accelerating effect of montmorillonite on oxidative degradation of polyethylene nanocomposites. *Polym. Degrad. Stab.* **2010**, *95*, 672–676. [CrossRef]
- Chiu, F.-C.; Lai, S.-M.; Ti, K.-T. Characterization and comparison of metallocene-catalyzed polyethylene/thermoplastic starch blends and nanocomposites. *Polym. Test.* **2009**, *28*, 243–250. [CrossRef]
- Mahdieh, Z.; Bagheri, R.; Eslami, M.; Amiri, M.; Shokrgozar, M.A.; Mehrjoo, M. Thermoplastic starch/ethylene vinyl alcohol/forsterite nanocomposite as a candidate material for bone tissue engineering. *Mater. Sci. Eng. C* **2016**, *69*, 301–310. [CrossRef]
- Sessini, V.; Raquez, J.-M.; Re, G.L.; Mincheva, R.; Kenny, J.M.; Dubois, P.; Peponi, L. Multiresponsive Shape Memory Blends and Nanocomposites Based on Starch. *ACS Appl. Mater. Interfaces* **2016**, *8*, 19197–19201. [CrossRef] [PubMed]

29. Guarás, M.P.; Alvarez, V.A.; Ludueña, L.N. Biodegradable nanocomposites based on starch/polycaprolactone/compatibilizer ternary blends reinforced with natural and organo-modified montmorillonite. *J. Appl. Polym. Sci.* **2016**, *133*, 6–11. [CrossRef]
30. Majdzadeh-Ardakani, K.; Nazari, B. Improving the mechanical properties of thermoplastic starch/poly(vinyl alcohol)/clay nanocomposites. *Compos. Sci. Technol.* **2010**, *70*, 1557–1563. [CrossRef]
31. Bordes, P.; Pollet, E.; Averous, L. Nano-biocomposites: Biodegradable polyester/nanoclay systems. *Prog. Polym. Sci.* **2009**, *34*, 125–155. [CrossRef]
32. Tessier, R.; Lafranche, E.; Krawczak, P. Development of novel melt-compounded starch-grafted polypropylene/polypropylene-grafted maleic anhydride/organoclay ternary hybrids. *Express Polym. Lett.* **2012**, *6*, 937–952. [CrossRef]
33. Fourati, Y.; Magnin, A.; Putaux, J.-L.; Boufi, S. One-step processing of plasticized starch/cellulose nanofibrils nanocomposites via twin-screw extrusion of starch and cellulose fibers. *Carbohydr. Polym.* **2020**, *229*, 115554. [CrossRef] [PubMed]
34. Nessi, V.; Falourd, X.; Maigret, J.-E.; Cahier, K.; D'Orlando, A.; Descamps, N.; Gaucher, V.; Chevigny, C.; Lourdin, D. Cellulose nanocrystals-starch nanocomposites produced by extrusion: Structure and behavior in physiological conditions. *Carbohydr. Polym.* **2019**, *225*, 115123. [CrossRef] [PubMed]
35. Fazeli, M.; Simão, R.A. Preparation and characterization of starch composites with cellulose nanofibers obtained by plasma treatment and ultrasonication. *Plasma Process. Polym.* **2019**, *16*, e1800167. [CrossRef]
36. Park, C.W.; Han, S.Y.; Seo, P.N.; Youe, W.J.; Kim, Y.S.; Choi, S.K.; Kim, N.H.; Lee, S.H. Property comparison of thermoplastic starch reinforced by cellulose nanofibrils with different chemical compositions. *BioResources* **2019**, *14*, 1564–1578. [CrossRef]
37. Balakrishnan, P.; Gopi, S.; Geethamma, V.G.; Kalarikkal, N.; Thomas, S. Cellulose Nanofiber vs Nanocrystals from Pineapple Leaf Fiber: A Comparative Studies on Reinforcing Efficiency on Starch Nanocomposites. *Macromol. Symp.* **2018**, *380*, 1–7. [CrossRef]
38. González, K.; Retegi, A.; González, A.; Eceiza, A.; Gabilondo, N. Starch and cellulose nanocrystals together into thermoplastic starch bionanocomposites. *Carbohydr. Polym.* **2015**, *117*, 83–90. [CrossRef] [PubMed]
39. Angellier, H.; Molina-Boisseau, S.; Dole, A.P.; Dufresne, A. Thermoplastic Starch-Waxy Maize Starch Nanocrystals Nanocomposites. *Biomacromolecules* **2006**, *7*, 531–539. [CrossRef]
40. González, K.; Iturriaga, L.; González, A.; Eceiza, A.; Gabilondo, N. Improving mechanical and barrier properties of thermoplastic starch and polysaccharide nanocrystals nanocomposites. *Eur. Polym. J.* **2020**, *123*, 109415. [CrossRef]
41. Ren, L.; Fu, Y.; Chang, Y.; Jiang, M.; Tong, J.; Zhou, J. Performance improvement of starch films reinforced with starch nanocrystals (SNCs) modified by cross-linking. *Starch Stärke* **2017**, *69*, 1600025. [CrossRef]
42. Garcia, N.L.; Ribba, L.; Dufresne, A.; Aranguren, M.I.; Goyanes, S. Effect of glycerol on the morphology of nanocomposites made from thermoplastic starch and starch nanocrystals. *Carbohydr. Polym.* **2011**, *84*, 203–210. [CrossRef]
43. Azevedo, V.M.; Carvalho, R.A.; Borges, S.; Claro, P.I.C.; Hasegawa, F.K.; Yoshida, M.I.; Marconcini, J.M. Thermoplastic starch/whey protein isolate/rosemary essential oil nanocomposites obtained by extrusion process: Antioxidant polymers. *J. Appl. Polym. Sci.* **2019**, *136*, 1–12. [CrossRef]
44. Vaezi, K.; Asadpour, G.; Sharifi, H. Effect of ZnO nanoparticles on the mechanical, barrier and optical properties of thermoplastic cationic starch/montmorillonite biodegradable films. *Int. J. Biol. Macromol.* **2019**, *124*, 519–529. [CrossRef] [PubMed]
45. Sessini, V.; Arrieta, M.P.; Raquez, J.-M.; Dubois, P.; Kenny, J.M.; Peponi, L. Thermal and composting degradation of EVA/Thermoplastic starch blends and their nanocomposites. *Polym. Degrad. Stab.* **2019**, *159*, 184–198. [CrossRef]
46. Ren, J.; Dang, K.M.; Pollet, E.; Avérous, L. Preparation and Characterization of Thermoplastic Potato Starch/Halloysite Nano-Biocomposites: Effect of Plasticizer Nature and Nanoclay Content. *Polymers* **2018**, *10*, 808. [CrossRef] [PubMed]
47. Campos-Requena, V.H.; Rivas, B.L.; Pérez, M.A.; Figueroa, C.; Figueroa, N.E.; Sanfuentes, E.A. Thermoplastic starch/clay nanocomposites loaded with essential oil constituents as packaging for strawberries – In vivo antimicrobial synergy over Botrytis cinerea. *Postharvest Biol. Technol.* **2017**, *129*, 29–36. [CrossRef]
48. Mohan, T.; Kanny, K. Thermoforming studies of corn starch-derived biopolymer film filled with nanoclays. *J. Plast. Film Sheeting* **2016**, *32*, 163–188. [CrossRef]
49. Kelnar, I.; Kaprálková, L.; Brozova, L.; Hromádková, J.; Kotek, J. Effect of chitosan on the behaviour of the wheat B-starch nanocomposite. *Ind. Crop. Prod.* **2013**, *46*, 186–190. [CrossRef]
50. Fabra, M.J.; López-Rubio, A.; Ambrosio-Martín, J.; Lagaron, J.M. Improving the barrier properties of thermoplastic corn starch-based films containing bacterial cellulose nanowhiskers by means of PHA electrospun coatings of interest in food packaging. *Food Hydrocoll.* **2016**, *61*, 261–268. [CrossRef]
51. Aouada, F.A.; Mattoso, L.H.; Longo, E. Enhanced bulk and superficial hydrophobicities of starch-based bionanocomposites by addition of clay. *Ind. Crop. Prod.* **2013**, *50*, 449–455. [CrossRef]
52. Balakrishnan, P.; Sreekala, M.; Kunaver, M.; Huskić, M.; Thomas, S. Morphology, transport characteristics and viscoelastic polymer chain confinement in nanocomposites based on thermoplastic potato starch and cellulose nanofibers from pineapple leaf. *Carbohydr. Polym.* **2017**, *169*, 176–188. [CrossRef]
53. Ren, P.; Shen, T.; Wang, F.; Wang, X.; Zhang, Z. Study on Biodegradable Starch/OMMT Nanocomposites for Packaging Applications. *J. Polym. Environ.* **2009**, *17*, 203–207. [CrossRef]
54. Schmitt, H.; Creton, N.; Prashantha, K.; Soulestin, J.; Lacrampe, M.; Krawczak, P. Melt-blended halloysite nanotubes/wheat starch nanocomposites as drug delivery system. *Polym. Eng. Sci.* **2015**, *55*, 573–580. [CrossRef]
55. Ning, W.; Xingxiang, Z.; Xuechen, W.; Haihui, L. Ionic liquids modified montmorillonite/thermoplastic starch nanocomposites as ionic conducting biopolymer. *Macromol. Res.* **2009**, *17*, 285–288. [CrossRef]

56. Janssen, L.; Moscicki, L. *Thermoplastic Starch: A Green Material for Various Industries*; Janssen, L., Moscicki, L., Eds.; Wiley-VCH Verlag GmbH & Co. KGaA: Weinheim, Germany, 2009; ISBN 978-3-527-32528-3.
57. Dufresne, A.; Castaño, J. Polysaccharide nanomaterial reinforced starch nanocomposites: A review. *Starch Stärke* **2017**, *69*, 1500307. [CrossRef]
58. Bangar, S.P.; Whiteside, W.S.; Ashogbon, A.O.; Kumar, M. Recent advances in thermoplastic starches for food packaging: A review. *Food Packag. Shelf Life* **2021**, *30*, 100743. [CrossRef]
59. Castillo, L.A.; López, O.V.; Ninago, M.D.; Versino, F.; Barbosa, S.E.; García, M.A.; Villar, M.A. Effect of Mineral and Organic Fillers on Processing, Structure, and Final Properties of Starch. In *Composites and Nanocomposites Based on Starches*; Elsevier Inc.: Amsterdam, The Netherlands, 2017; ISBN 9780128122570.
60. Osorio, M.A.; Restrepo, D.; Velásquez-Cock, J.A.; Zuluaga, R.O.; Montoya, U.; Rojas, O.; Gañán, P.F.; Marín, D.; Castro, C.I. Synthesis of Thermoplastic Starch-Bacterial Cellulose Nanocomposites via in situ Fermentation. *J. Braz. Chem. Soc.* **2014**, *25*, 1607–1613. [CrossRef]
61. Zhang, Y.; Rempel, C.; Liu, Q. Thermoplastic Starch Processing and Characteristics—A Review. *Crit. Rev. Food Sci. Nutr.* **2014**, *54*, 1353–1370. [CrossRef]
62. Morán, J.I.; Vazquez, A.; Cyras, V.P. Bio-nanocomposites based on derivatized potato starch and cellulose, preparation and characterization. *J. Mater. Sci.* **2013**, *48*, 7196–7203. [CrossRef]
63. Cyras, V.P.; Manfredi, L.B.; Ton-That, M.-T.; Vázquez, A. Physical and mechanical properties of thermoplastic starch/montmorillonite nanocomposite films. *Carbohydr. Polym.* **2008**, *73*, 55–63. [CrossRef]
64. Alemdar, A.; Sain, M. Biocomposites from wheat straw nanofibers: Morphology, thermal and mechanical properties. *Compos. Sci. Technol.* **2008**, *68*, 557–565. [CrossRef]
65. Perotti, G.; Kijchavengkul, T.; Auras, R.; Constantino, V. Nanocomposites Based on Cassava Starch and Chitosan-Modified Clay: Physico-Mechanical Properties and Biodegradability in Simulated Compost Soil. *J. Braz. Chem. Soc.* **2017**, *28*, 649–658. [CrossRef]
66. Olivato, J.; Marini, J.; Yamashita, F.; Pollet, E.; Grossmann, M.; Avérous, L. Sepiolite as a promising nanoclay for nanobiocomposites based on starch and biodegradable polyester. *Mater. Sci. Eng. C* **2017**, *70*, 296–302. [CrossRef] [PubMed]
67. Ahamed, F.; Phang, S.W.; Sin, L.T. Mechanical behaviour of thermoplastic starch/montmorillonite/alumina trihydrate nanocomposites. *J. Eng. Sci. Technol.* **2016**, *11*, 1344–1359.
68. DeLeo, C.; Pinotti, C.A.; do Gonçalves, M.C.; Velankar, S. Preparation and Characterization of Clay Nanocomposites of Plasticized Starch and Polypropylene Polymer Blends. *J. Polym. Environ.* **2011**, *19*, 689–697. [CrossRef]
69. Schlemmer, D.; Angélica, R.S.; Sales, M.J.A. Morphological and thermomechanical characterization of thermoplastic starch/montmorillonite nanocomposites. *Compos. Struct.* **2010**, *92*, 2066–2070. [CrossRef]
70. Teixeira, E.D.M.; Pasquini, D.; Curvelo, A.A.; Corradini, E.; Belgacem, M.N.; Dufresne, A. Cassava bagasse cellulose nanofibrils reinforced thermoplastic cassava starch. *Carbohydr. Polym.* **2009**, *78*, 422–431. [CrossRef]
71. De Takahashi, G.C.S.; Barbosa, H.D.; De Bergamasco, R.C.; Madrona, G.S.; Tonon, L.A.C.; Yamashita, F.; Scapim, M.R.D.S. Development and active biodegradable film evaluation incorporated with oregano essential oil and nanoclay. *Chem. Eng. Trans.* **2017**, *57*, 403–408. [CrossRef]
72. Cucinelli Neto, R.P.; da Rocha Rodrigues, E.J.; Bruno Tavares, M.I. Proton NMR relaxometry as probe of gelatinization, plasticization and montmorillonite-loading effects on starch-based materials. *Carbohydr. Polym.* **2018**, *182*, 123–131. [CrossRef]
73. Karimi, S.; Abdulkhani, A.; Tahir, P.M.; Dufresne, A. Effect of cellulosic fiber scale on linear and non-linear mechanical performance of starch-based composites. *Int. J. Biol. Macromol.* **2016**, *91*, 1040–1044. [CrossRef]
74. Kaushik, A.; Kumra, J. Morphology, thermal and barrier properties of green nanocomposites based on TPS and cellulose nanocrystals. *J. Elastomers Plast.* **2014**, *46*, 284–299. [CrossRef]
75. Vigiúé, J.; Molina-Boisseau, S.; Dufresne, A. Processing and Characterization of Waxy Maize Starch Films Plasticized by Sorbitol and Reinforced with Starch Nanocrystals. *Macromol. Biosci.* **2007**, *7*, 1206–1216. [CrossRef]
76. Lendvai, L.; Apostolov, A.; Karger-Kocsis, J. Characterization of layered silicate-reinforced blends of thermoplastic starch (TPS) and poly(butylene adipate-co-terephthalate). *Carbohydr. Polym.* **2017**, *173*, 566–572. [CrossRef]
77. Rani, A.; Monga, S.; Bansal, M.; Sharma, A. Bionanocomposites reinforced with cellulose nanofibers derived from sugarcane bagasse. *Polym. Compos.* **2018**, *39*, E55–E64. [CrossRef]
78. Sessini, V.; Raquez, J.-M.; Lourdin, D.; Maigret, J.-E.; Kenny, J.M.; Dubois, P.; Peponi, L. Humidity-Activated Shape Memory Effects on Thermoplastic Starch/EVA Blends and Their Compatibilized Nanocomposites. *Macromol. Chem. Phys.* **2017**, *218*, 1700388. [CrossRef]
79. Cao, X.; Chen, Y.; Chang, P.R.; Stumborg, M.; Huneault, M.A. Green composites reinforced with hemp nanocrystals in plasticized starch. *J. Appl. Polym. Sci.* **2008**, *109*, 3804–3810. [CrossRef]
80. Raquez, J.-M.; Nabar, Y.; Narayan, R.; Dubois, P. Preparation and characterization of maleated thermoplastic starch-based nanocomposites. *J. Appl. Polym. Sci.* **2011**, *122*, 639–647. [CrossRef]
81. Pitiphatharaworachot, S.; Chitbanyong, K.; Sungkaew, S.; Pisutpiched, S.; Khantayanuwong, S.; Puangsin, B. Starch nanocomposites reinforced with TEMPO-oxidized cellulose nanofibrils derived from bamboo holocellulose. *BioResources* **2019**, *14*, 2784–2797. [CrossRef]
82. Qiao, X.; Jiang, W.; Sun, K. Reinforced Thermoplastic Acetylated Starch with Layered Silicates. *Starch Stärke* **2005**, *57*, 581–586. [CrossRef]

83. García, N.L.; Famá, L.; D'Accorso, N.B.; Goyanes, S. Biodegradable Starch Nanocomposites. In *Eco-Friendly Polymer Nanocomposites: Processing and Properties*; Springer: Berlin/Heidelberg, Germany, 2015; pp. 17–77, ISBN 978-81-322-2469-3.
84. Zicans, J.; Meri, R.M.; Kalnins, M.; Maksimovs, R.; Jansons, J. Modeling and experimental investigations of elastic and creep properties of thermoplastic polymer nanocomposites. *ZAMM* **2015**, *95*, 1110–1198. [CrossRef]
85. Teacă, C.-A.; Bodîrlău, R. Multicomponent Polymer Composite/Nanocomposite Systems Using Polymer Matrices from Sustainable Renewable Sources. In *Eco-Friendly Polymer Nanocomposites: Processing and Properties*; Springer: Berlin/Heidelberg, Germany, 2015; pp. 469–494, ISBN 978-81-322-2469-3.
86. Campos-Requena, V.H.; Rivas, B.L.; Pérez, M.A.; Garrido-Miranda, K.A.; Pereira, E.D. Release of essential oil constituent from thermoplastic starch/layered silicate bionanocomposite film as a potential active packaging material. *Eur. Polym. J.* **2018**, *109*, 64–71. [CrossRef]
87. Arroyo, O.; Huneault, M.; Favis, B.; Bureau, M. Processing and properties of PLA/thermoplastic starch/montmorillonite nanocomposites. *Polym. Compos.* **2010**, *31*, 114–127. [CrossRef]
88. Javanbakht, S.; Namazi, H. Solid state photoluminescence thermoplastic starch film containing graphene quantum dots. *Carbohydr. Polym.* **2017**, *176*, 220–226. [CrossRef]
89. Sarsari, N.A.; Pourmoussa, S.; Tajdini, A. Physical and Mechanical Properties of Walnut Shell Flour-Filled Thermoplastic Starch Composites. *Bioresources* **2016**, *11*, 6968–6983. [CrossRef]
90. Mohseni, M.S.; Khalilzadeh, M.; Mohseni, M.; Hargalani, F.Z.; Getso, M.I.; Raissi, V.; Raiesi, O. Green synthesis of Ag nanoparticles from pomegranate seeds extract and synthesis of Ag-Starch nanocomposite and characterization of mechanical properties of the films. *Biocatal. Agric. Biotechnol.* **2020**, *25*, 101569. [CrossRef]
91. Fu, D.; Netravali, A.N. Green composites based on avocado seed starch and nano- and micro-scale cellulose. *Polym. Compos.* **2020**, *41*, 4631–4648. [CrossRef]
92. Lubis, M.; Harahap, M.B.; Hendra, M.; Ginting, S.; Sartika, M.; Azmi, H. *Effect of Microcrystalline Cellulose (MCC) from Sugar Palm Fibres and Glycerol Addition on Mechanical Properties of Bioplastic from Avocado Seed Starch (Persea Americana Mill)*; Academic Fora: Kuala Lumpur, Malaysia, 2016; Volume 331, pp. 1–10.
93. Lacerda, L.G.; Colman, T.A.D.; Bauab, T.; Da Silva Carvalho Filho, M.A.; Demiate, I.M.; De Vasconcelos, E.C.; Schnitzler, E. Thermal, structural and rheological properties of starch from avocado seeds (*Persea americana*, Miller) modified with standard sodium hypochlorite solutions. *J. Therm. Anal. Calorim.* **2014**, *115*, 1893–1899. [CrossRef]
94. FAOSTAT. Available online: <http://www.fao.org/faostat/en/#data/QC/visualize> (accessed on 20 October 2020).
95. Ellis, R.P.; Cochrane, M.P.; Dale, M.F.B.; Duffus, C.M.; Lynn, A.; Morrison, I.M.; Prentice, R.D.M.; Swanston, J.S.; Tiller, S.A. Starch production and industrial use. *J. Sci. Food Agric.* **1998**, *77*, 289–311. [CrossRef]
96. Copeland, L.; Blazek, J.; Salman, H.; Tang, M.C. Form and functionality of starch. *Food Hydrocoll.* **2009**, *23*, 1527–1534. [CrossRef]
97. Nayak, S.K. Biodegradable PBAT/Starch Nanocomposites. *Polym.-Plast. Technol. Eng.* **2010**, *49*, 1406–1418. [CrossRef]
98. Chung, Y.-L.; Lai, H.-M. Recent Progress in the Development of Starch-Layered Silicate Nanocomposites. In *Handbook of Polymernanocomposites. Processing, Performance and Application*; Springer: Berlin/Heidelberg, Germany, 2014; pp. 69–86, ISBN 9783642386497.
99. Gallant, D.J.; Bouchet, B.; Baldwin, P.M. Microscopy of starch: Evidence of a new level of granule organization. *Carbohydr. Polym.* **1997**, *32*, 177–191. [CrossRef]
100. Park, H.-M.; Lee, W.-K.; Park, C.-Y.; Cho, W.-J.; Ha, C.-S. Environmentally friendly polymer hybrids Part I Mechanical, thermal, and barrier properties of thermoplastic starch/clay nanocomposites. *J. Mater. Sci.* **2003**, *38*, 909–915. [CrossRef]
101. Asrofi, M.; Abrial, H.; Kasim, A.; Pratoto, A.; Mahardika, M.; Hafizulhaq, F. Mechanical Properties of a Water Hyacinth Nanofiber Cellulose Reinforced Thermoplastic Starch Bionanocomposite: Effect of Ultrasonic Vibration during Processing. *Fibers* **2018**, *6*, 40. [CrossRef]
102. Park, H.-M.; Li, X.; Jin, C.-Z.; Park, C.-Y.; Cho, W.-J.; Ha, C.-S. Preparation and Properties of Biodegradable Thermoplastic Starch/Clay Hybrids. *Macromol. Mater. Eng.* **2002**, *287*, 553–558. [CrossRef]
103. Raquez, J.-M.; Nabar, Y.; Narayan, R.; Dubois, P. New Developments in Biodegradable Starch-based Nanocomposites. *Int. Polym. Process.* **2007**, *22*, 463–470. [CrossRef]
104. Zhang, Y.; Han, J. Crystallization of High-Amylose Starch by the Addition of Plasticizers at Low and Intermediate Concentrations. *J. Food Sci.* **2010**, *75*, N8–N16. [CrossRef]
105. Carvalho, A.J. Starch: Major Sources, Properties and Applications as Thermoplastic Materials. In *Monomers, Polymers and Composites from Renewable Resources*; Elsevier: Amsterdam, The Netherlands, 2008; pp. 321–342. [CrossRef]
106. Hietala, M.; Mathew, A.P.; Oksman, K. Bionanocomposites of thermoplastic starch and cellulose nanofibers manufactured using twin-screw extrusion. *Eur. Polym. J.* **2013**, *49*, 950–956. [CrossRef]
107. Van Soest, J.J.G.; Borger, D.B. Structure and properties of compression-molded thermoplastic starch materials from normal and high-amylose maize starches. *J. Appl. Polym. Sci.* **1997**, *64*, 631–644. [CrossRef]
108. Osman, A.F.; Ashafee, A.M.T.; Adnan, S.A.; Alakrach, A. Influence of Hybrid Cellulose/Bentonite Fillers on Structure, Ambient, and Low Temperature Tensile Properties of Thermoplastic Starch Composites. *Polym. Eng. Sci.* **2020**, *60*, 810–822. [CrossRef]
109. Aouada, F.A.; Mattoso, L.H.; Longo, E. New strategies in the preparation of exfoliated thermoplastic starch-montmorillonite nanocomposites. *Ind. Crop. Prod.* **2011**, *34*, 1502–1508. [CrossRef]

110. Tunjano, V.; Salcedo, F.; Jiménez, I.; Medina, J.; Alvarez, O.; Prieto, E. Estudio de las propiedades térmicas y mecánicas del almidón termoplástico (TPS) reforzado con nanoarcilla. *Rev. Latinoam. Metal. Mater.* **2009**, *1*, 29–36.
111. Brody, A.L.; Bugusu, B.; Han, J.H.; Sand, C.K.; McHugh, T.H. Innovative food packaging solutions. *J. Food Sci.* **2008**, *73*, 107–116. [CrossRef]
112. Alexandre, M.; Dubois, P. Polymer-layered silicate nanocomposites: Preparation, properties and uses of a new class of materials. *Mater. Sci. Eng. R: Rep.* **2000**, *28*, 1–63. [CrossRef]
113. Mehta, A.; Bhardwaj, K.K.; Gupta, R. *Biodegradable Polymers for Industrial Applications*; Elsevier: Amsterdam, The Netherlands, 2017; ISBN 9781536122527.
114. Shah, A.A.; Hasan, F.; Hameed, A.; Ahmed, S. Biological degradation of plastics: A comprehensive review. *Biotechnol. Adv.* **2008**, *26*, 246–265. [CrossRef] [PubMed]
115. Li, G.; Sarazin, P.; Orts, W.J.; Imam, S.H.; Favis, B.D. Biodegradation of Thermoplastic Starch and its Blends with Poly(lactic acid) and Polyethylene: Influence of Morphology. *Macromol. Chem. Phys.* **2011**, *212*, 1147–1154. [CrossRef]
116. Savadekar, N.; Mhaske, S. Synthesis of nano cellulose fibers and effect on thermoplastics starch based films. *Carbohydr. Polym.* **2012**, *89*, 146–151. [CrossRef]
117. Babae, M.; Jonoobi, M.; Hamzeh, Y.; Ashori, A. Biodegradability and mechanical properties of reinforced starch nanocomposites using cellulose nanofibers. *Carbohydr. Polym.* **2015**, *132*, 1–8. [CrossRef] [PubMed]
118. Cao, X.; Chen, Y.; Chang, P.R.; Huneault, M.A. Preparation and properties of plasticized starch/multiwalled carbon nanotubes composites. *J. Appl. Polym. Sci.* **2007**, *106*, 1431–1437. [CrossRef]
119. Ramezani, H.; Behzad, T.; Bagheri, R. Synergistic effect of graphene oxide nanoplatelets and cellulose nanofibers on mechanical, thermal, and barrier properties of thermoplastic starch. *Polym. Adv. Technol.* **2020**, *31*, 553–565. [CrossRef]
120. Zhang, C.-W.; Nair, S.S.; Chen, H.; Yan, N.; Farnood, R.; Li, F.-Y. Thermally stable, enhanced water barrier, high strength starch bio-composite reinforced with lignin containing cellulose nanofibrils. *Carbohydr. Polym.* **2020**, *230*, 115626. [CrossRef]
121. Lisdayana, N.; Fahma, F.; Sunarti, T.C.; Iriani, E.S. Thermoplastic Starch–PVA Nanocomposite Films Reinforced with Nanocellulose from Oil Palm Empty Fruit Bunches (OPEFBs): Effect of Starch Type. *J. Nat. Fibers* **2020**, *17*, 1069–1080. [CrossRef]
122. Kaushik, A.; Kaur, R. Thermoplastic starch nanocomposites reinforced with cellulose nanocrystals: Effect of plasticizer on properties. *Compos. Interfaces* **2016**, *23*, 701–717. [CrossRef]
123. Kaushik, A.; Singh, M.; Verma, G. Green nanocomposites based on thermoplastic starch and steam exploded cellulose nanofibrils from wheat straw. *Carbohydr. Polym.* **2010**, *82*, 337–345. [CrossRef]
124. Nasri-Nasrabadi, B.; Mehra, M.; Rafienia, M.; Bonakdar, S.; Behzad, T.; Gavanji, S. Porous starch/cellulose nanofibers composite prepared by salt leaching technique for tissue engineering. *Carbohydr. Polym.* **2014**, *108*, 232–238. [CrossRef] [PubMed]
125. Granda, L.A.; Oliver-Ortega, H.; Fabra, M.J.; Tarrés, Q.; Pelach, M.À.; Lagarón, J.M.; Méndez, J.A. Improved Process to Obtain Nanofibrillated Cellulose (CNF) Reinforced Starch Films with Upgraded Mechanical Properties and Barrier Character. *Polymers* **2020**, *12*, 1071. [CrossRef] [PubMed]
126. Metzger, C.; Briesen, H. Thermoplastic Starch Nanocomposites Reinforced with Cellulose Nanocrystal Suspensions Containing Residual Salt from Neutralization. *Macromol. Mater. Eng.* **2021**, *306*, 2100161. [CrossRef]
127. Gray, N.; Hamzeh, Y.; Kaboorani, A.; Abdulkhani, A. Influence of cellulose nanocrystal on strength and properties of low density polyethylene and thermoplastic starch composites. *Ind. Crop. Prod.* **2018**, *115*, 298–305. [CrossRef]
128. Chen, D.; Lawton, D.; Thompson, M.; Liu, Q. Biocomposites reinforced with cellulose nanocrystals derived from potato peel waste. *Carbohydr. Polym.* **2012**, *90*, 709–716. [CrossRef]
129. Vaezi, K.; Asadpour, G.; Sharifi, S.H. Bio nanocomposites based on cationic starch reinforced with montmorillonite and cellulose nanocrystals: Fundamental properties and biodegradability study. *Int. J. Biol. Macromol.* **2020**, *146*, 374–386. [CrossRef] [PubMed]
130. Mariano, M.; El Kissi, N.; Dufresne, A. Cellulose nanocrystals and related nanocomposites: Review of some properties and challenges. *J. Polym. Sci. Part B Polym. Phys.* **2014**, *52*, 791–806. [CrossRef]
131. Ma, X.; Yu, J.; Wang, N. Production of Thermoplastic Starch/MMT-Sorbitol Nanocomposites by Dual-Melt Extrusion Processing. *Macromol. Mater. Eng.* **2007**, *292*, 723–728. [CrossRef]
132. Chivrac, F.; Pollet, E.; Schmutz, M.; Avérous, L. New Approach to Elaborate Exfoliated Starch-Based Nanobiocomposites. *Biomacromolecules* **2008**, *9*, 896–900. [CrossRef]
133. Müller, C.; Laurindo, J.B.; Yamashita, F. Composites of thermoplastic starch and nanoclays produced by extrusion and thermopressing. *Carbohydr. Polym.* **2012**, *89*, 504–510. [CrossRef] [PubMed]
134. Lara, S.C.; Salcedo, F. Gelatinization and retrogradation phenomena in starch/montmorillonite nanocomposites plasticized with different glycerol/water ratios. *Carbohydr. Polym.* **2016**, *151*, 206–212. [CrossRef] [PubMed]
135. Boonprasith, P.; Wootthikanokkhan, J.; Nimitsiriwat, N. Mechanical, thermal, and barrier properties of nanocomposites based on poly(butylene succinate)/thermoplastic starch blends containing different types of clay. *J. Appl. Polym. Sci.* **2013**, *130*, 1114–1123. [CrossRef]
136. Katerinopoulou, K.; Giannakas, A.; Grigoriadi, K.; Barkoula, N.M.; Ladavos, A. Preparation and characterization of acetylated corn starch–(PVOH)/clay nanocomposite films. *Carbohydr. Polym.* **2014**, *102*, 216–222. [CrossRef]
137. Nistor, M.-T.; Vasile, C. TG/FTIR/MS study on the influence of nanoparticles content upon the thermal decomposition of starch/poly(vinyl alcohol) montmorillonite nanocomposites. *Iran. Polym. J.* **2013**, *22*, 519–536. [CrossRef]

138. Dai, H.; Chang, P.R.; Geng, F.; Yu, J.; Ma, X. Preparation and Properties of Thermoplastic Starch/Montmorillonite Nanocomposite Using N-(2-Hydroxyethyl)formamide as a New Additive. *J. Polym. Environ.* **2009**, *17*, 225–232. [CrossRef]
139. Paglicawan, M.A.; Basilia, B.A.; Navarro, M.T.V.; Emolaga, C.S. Influence of Nanoclay on the Properties of Thermoplastic Starch/Poly(lactic acid) Blends. *J. Biobased Mater. Bioenergy* **2013**, *7*, 102–107. [CrossRef]
140. Dean, K.M.; Petinakis, E.; Goodall, L.; Miller, T.; Yu, L.; Wright, N. Nanostabilization of thermally processed high amylose hydroxylpropylated starch films. *Carbohydr. Polym.* **2011**, *86*, 652–658. [CrossRef]
141. Wang, X.; Zhang, X.; Liu, H.; Wang, N. Impact of Pre-Processing of Montmorillonite on the Properties of Melt-Extruded Thermoplastic Starch/Montmorillonite Nanocomposites. *Starch Stärke* **2009**, *61*, 489–494. [CrossRef]
142. Wang, N.; Zhang, X.; Han, N.; Bai, S. Effect of citric acid and processing on the performance of thermoplastic starch/montmorillonite nanocomposites. *Carbohydr. Polym.* **2009**, *76*, 68–73. [CrossRef]
143. Dean, K.M.; Do, M.D.; Petinakis, E.; Yu, L. Key interactions in biodegradable thermoplastic starch/poly(vinyl alcohol)/montmorillonite micro- and nanocomposites. *Compos. Sci. Technol.* **2008**, *68*, 1453–1462. [CrossRef]
144. Dean, K.; Yu, L.; Wu, D.Y. Preparation and characterization of melt-extruded thermoplastic starch/clay nanocomposites. *Compos. Sci. Technol.* **2007**, *67*, 413–421. [CrossRef]
145. Huang, M.; Yu, J.; Ma, X. High mechanical performance MMT-urea and formamide-plasticized thermoplastic cornstarch biodegradable nanocomposites. *Carbohydr. Polym.* **2006**, *63*, 393–399. [CrossRef]
146. De Souza, A.G.; dos Santos, N.M.A.; da Silva Torin, R.F.; dos Santos Rosa, D. Synergic antimicrobial properties of Carvacrol essential oil and montmorillonite in biodegradable starch films. *Int. J. Biol. Macromol.* **2020**, *164*, 1737–1747. [CrossRef]
147. Majdzadeh-Ardakani, K.; Navarchian, A.H.; Sadeghi, F. Optimization of mechanical properties of thermoplastic starch/clay nanocomposites. *Carbohydr. Polym.* **2010**, *79*, 547–554. [CrossRef]
148. Bocchini, S.; Battezzore, D.; Frache, A. Poly (butylsuccinate co-adipate)-thermoplastic starch nanocomposite blends. *Carbohydr. Polym.* **2010**, *82*, 802–808. [CrossRef]
149. Mansour, G.; Zoumaki, M.; Marinopoulou, A.; Tzetzis, D.; Prevezanos, M.; Raphaelides, S.N. Characterization and properties of non-granular thermoplastic starch—Clay biocomposite films. *Carbohydr. Polym.* **2020**, *245*, 116629. [CrossRef]
150. Taghizadeh, M.T.; Abbasi, Z.; Nasrollahzade, Z. Study of enzymatic degradation and water absorption of nanocomposites starch/polyvinyl alcohol and sodium montmorillonite clay. *J. Taiwan Inst. Chem. Eng.* **2012**, *43*, 120–124. [CrossRef]
151. Chen, M.; Chen, B.; Evans, J.R.G. Novel thermoplastic starch—Clay nanocomposite foams. *Nanotechnology* **2005**, *16*, 2334–2337. [CrossRef] [PubMed]
152. Chen, B.; Evans, J.R. Thermoplastic starch—clay nanocomposites and their characteristics. *Carbohydr. Polym.* **2005**, *61*, 455–463. [CrossRef]
153. Bagdi, K.; Müller, P.; Pukánszky, B. Thermoplastic starch/layered silicate composites: Structure, interaction, properties. *Compos. Interfaces* **2006**, *13*, 1–17. [CrossRef]
154. Ayana, B.; Suin, S.; Khatua, B. Highly exfoliated eco-friendly thermoplastic starch (TPS)/poly (lactic acid)(PLA)/clay nanocomposites using unmodified nanoclay. *Carbohydr. Polym.* **2014**, *110*, 430–439. [CrossRef]
155. Zhang, Y.; Liu, Q.; Hrymak, A.; Han, J.H. Characterization of Extruded Thermoplastic Starch Reinforced by Montmorillonite Nanoclay. *J. Polym. Environ.* **2013**, *21*, 122–131. [CrossRef]
156. Derungs, I.; Rico, M.; López, J.; Barral, L.; Montero, B.; Bouza, R. Influence of the hydrophilicity of montmorillonite on structure and properties of thermoplastic wheat starch/montmorillonite bionanocomposites. *Polym. Adv. Technol.* **2021**. [CrossRef]
157. Mondragón, M.; Hernández, E.; Rivera-Armenta, J.; Rodríguez-González, F. Injection molded thermoplastic starch/natural rubber/clay nanocomposites: Morphology and mechanical properties. *Carbohydr. Polym.* **2009**, *77*, 80–86. [CrossRef]
158. Huang, M.-F.; Yu, J.-G.; Ma, X.-F. Studies on the properties of Montmorillonite-reinforced thermoplastic starch composites. *Polymer* **2004**, *45*, 7017–7023. [CrossRef]
159. Behera, A.K. Mechanical and biodegradation analysis of thermoplastic starch reinforced nano-biocomposites. *IOP Conf. Ser. Mater. Sci. Eng.* **2018**, *410*, 012001. [CrossRef]
160. Hanifi, S.; Oromiehie, A.; Ahmadi, S.; Farhadnejad, H. (Corn Starch and Montmorillonite Nanocomposite)-Reinforced Polypropylene: Preparation, Properties, and Biodegradability. *J. Vinyl Addit. Technol.* **2014**, *20*, 16–23. [CrossRef]
161. Ebrahimi, H.; Najafi, F.S.A.; Shahabadi, I.; Garmabi, H. A response surface study on microstructure and mechanical properties of poly(lactic acid)/thermoplastic starch/nanoclay nanocomposites. *J. Compos. Mater.* **2016**, *50*, 269–278. [CrossRef]
162. Magalhães, N.F.; De Andrade, C.T. Properties of melt-processed poly(hydroxybutyrate-co-hydroxyvalerate)/starch 1:1 blend nanocomposites. *Polímeros* **2013**, *23*, 366–372. [CrossRef]
163. Zhang, Q.-X.; Yu, Z.-Z.; Xie, X.-L.; Naito, K.; Kagawa, Y. Preparation and crystalline morphology of biodegradable starch/clay nanocomposites. *Polymer* **2007**, *48*, 7193–7200. [CrossRef]
164. Park, H.-M.; Kim, G.-H.; Ha, C.-S. Preparation and characterization of biodegradable aliphatic polyester/thermoplastic starch/organoclay ternary hybrid nanocomposites. *Compos. Interfaces* **2007**, *14*, 427–438. [CrossRef]
165. Gao, W.; Liu, P.; Li, X.; Qiu, L.; Hou, H.; Cui, B. The co-plasticization effects of glycerol and small molecular sugars on starch-based nanocomposite films prepared by extrusion blowing. *Int. J. Biol. Macromol.* **2019**, *133*, 1175–1181. [CrossRef] [PubMed]
166. Bahrami, B.; Behzad, T.; Salehinik, F.; Zamani, A.; Heidarian, P. Incorporation of Extracted *Mucor indicus* Fungus Chitin Nanofibers into Starch Biopolymer: Morphological, Physical, and Mechanical Evaluation. *Starch-Stärke* **2021**, *73*, 2000218. [CrossRef]

167. Olivato, J.; Marini, J.; Pollet, E.; Yamashita, F.; Grossmann, M.; Avérous, L. Elaboration, morphology and properties of starch/polyester nano-biocomposites based on sepiolite clay. *Carbohydr. Polym.* **2015**, *118*, 250–256. [CrossRef]
168. Ceballos, R.L.; von Bilderling, C.; Guz, L.; Bernal, C.; Famá, L. Effect of greenly synthesized silver nanoparticles on the properties of active starch films obtained by extrusion and compression molding. *Carbohydr. Polym.* **2021**, *261*, 117871. [CrossRef]
169. Da Silva, G.L.P.; Morais, L.C.D.A.; Olivato, J.B.; Marini, J.; Ferrari, P.C. Antimicrobial dressing of silver sulfadiazine-loaded halloysite/cassava starch-based (bio)nanocomposites. *J. Biomater. Appl.* **2021**, *35*, 1096–1108. [CrossRef]
170. Dang, K.M.; Yoksan, R.; Pollet, E.; Avérous, L. Morphology and properties of thermoplastic starch blended with biodegradable polyester and filled with halloysite nanoclay. *Carbohydr. Polym.* **2020**, *242*, 116392. [CrossRef]
171. Peres, A.M.; Orefice, R. Effect of incorporation of Halloysite nanotubes on the structure and properties of low-density polyethylene/thermoplastic starch blend. *J. Polym. Res.* **2020**, *27*, 1–10. [CrossRef]
172. Aouada, F.; Mattoso, L.H.; Longo, E. A simple procedure for the preparation of laponite and thermoplastic starch nanocomposites: Structural, mechanical, and thermal characterizations. *J. Thermoplast. Compos. Mater.* **2013**, *26*, 109–124. [CrossRef]
173. Liu, Z.; Zhao, L.; Chen, M.; Yu, J. Effect of carboxylate multi-walled carbon nanotubes on the performance of thermoplastic starch nanocomposites. *Carbohydr. Polym.* **2011**, *83*, 447–451. [CrossRef]
174. Merino, D.; Gutiérrez, T.; Alvarez, V.A. Structural and Thermal Properties of Agricultural Mulch Films Based on Native and Oxidized Corn Starch Nanocomposites. *Starch Stärke* **2019**, *71*, 1–9. [CrossRef]
175. Castillo, L.A.; López, O.V.; García, M.A.; Barbosa, S.E.; Villar, M.A. Crystalline morphology of thermoplastic starch/talc nanocomposites induced by thermal processing. *Heliyon* **2019**, *5*, e01877. [CrossRef] [PubMed]
176. Castillo, L.; López, O.; López, C.; Zaritzky, N.; García, M.A.; Barbosa, S.; Villar, M. Thermoplastic starch films reinforced with talc nanoparticles. *Carbohydr. Polym.* **2013**, *95*, 664–674. [CrossRef]
177. Taherimehr, M.; Bagheri, R.; Taherimehr, M. In-vitro evaluation of thermoplastic starch/ beta-tricalcium phosphate nano-biocomposite in bone tissue engineering. *Ceram. Int.* **2021**, *47*, 15458–15463. [CrossRef]
178. Trinh, B.M.; Chang, C.C.; Mekonnen, T.H. Facile fabrication of thermoplastic starch/poly (lactic acid) multilayer films with superior gas and moisture barrier properties. *Polymer* **2021**, *223*, 123679. [CrossRef]
179. Yahia, R.; Owda, M.E.; Abou-Zeid, R.E.; Abdelhai, F.; Gad, E.S.; Saleh, A.K.; El-Gamil, H.Y. Synthesis and characterization of thermoplastic starch/ PVA /cardanol oil composites loaded with in-situ silver nanoparticles. *J. Appl. Polym. Sci.* **2021**, *2021*, 51511. [CrossRef]
180. Ochigbo, S.S.; Luyt, A.S.; Mofokeng, J.P.; Antić, Ž.; Dramićanin, M.D.; Djoković, V. Dynamic mechanical and thermal properties of the composites of thermoplastic starch and lanthanum hydroxide nanoparticles. *J. Appl. Polym. Sci.* **2013**, *127*, 699–709. [CrossRef]
181. Kwaśniewska, A.; Chocyk, D.; Gładyszewski, G.; Borc, J.; Świetlicki, M.; Gładyszewska, B. The Influence of Kaolin Clay on the Mechanical Properties and Structure of Thermoplastic Starch Films. *Polymers* **2020**, *12*, 73. [CrossRef]
182. Lu, P.; Zhang, M.; Qian, P.; Zhu, Q. Preparation and characterization of thermoplastic starch-kaolinite nanocomposite films. *Polym. Compos.* **2012**, *33*, 889–896. [CrossRef]
183. Kale, G.; Kijchavengkul, T.; Auras, R.; Rubino, M.; Selke, S.E.; Singh, S.P. Compostability of Bioplastic Packaging Materials: An Overview. *Macromol. Biosci.* **2007**, *7*, 255–277. [CrossRef] [PubMed]
184. Weber, C.J.; Haugaard, V.; Festersen, R.; Bertelsen, G. Production and applications of biobased packaging materials for the food industry. *Food Addit. Contam.* **2002**, *19* (Supp. S1), 172–177. [CrossRef] [PubMed]

Review

Investigating Physio-Thermo-Mechanical Properties of Polyurethane and Thermoplastics Nanocomposite in Various Applications

Tyser Allami *, Ahmed Alamiery, Mohamed H. Nassir and Amir H. Kadhum

Department of Chemical and Process Engineering, Faculty of Engineering and Built Environment, Universiti Kebangsaan Malaysia, Bangi 43600, Selangor Darul Ehsan, Malaysia; dr.ahmed1975@ukm.edu.my (A.A.); mhnassir1949@gmail.com (M.H.N.); amir8@ukm.edu.my (A.H.K.)

* Correspondence: gaaz@ukm.edu.my; Tel.: +60-1157-733-927

Abstract: The effect of the soft and hard polyurethane (PU) segments caused by the hydrogen link in phase-separation kinetics was studied to investigate the morphological annealing of PU and thermoplastic polyurethane (TPU). The significance of the segmented PUs is to achieve enough stability for further applications in biomedical and environmental fields. In addition, other research focuses on widening the plastic features and adjusting the PU–polyimide ratio to create elastomer of the poly(urethane-imide). Regarding TPU- and PU-nanocomposite, numerous studies investigated the incorporation of inorganic nanofillers such as carbon or clay to incorporating TPU-nanocomposite in several applications. Additionally, the complete exfoliation was observed up to 5% and 3% of TPU–clay modified with 12 amino lauric acid and benzidine, respectively. PU-nanocomposite of 5 wt.% Cloisite®30B showed an increase in modulus and tensile strength by 110% and 160%, respectively. However, the nanocomposite PU-0.5 wt.% Carbone Nanotubes (CNTs) show an increase in the tensile modulus by 30% to 90% for blown and flat films, respectively. Coating PU influences stress-strain behavior because of the interaction between the soft segment and physical crosslinkers. The thermophysical properties of the TPU matrix have shown two glass transition temperatures (T_g 's) corresponding to the soft and the hard segment. Adding a small amount of tethered clay shifts T_g for both segments by 44 °C and 13 °C, respectively, while adding clay from 1 to 5 wt.% results in increasing the thermal stability of TPU composite from 12 to 34 °C, respectively. The differential scanning calorimetry (DSC) was used to investigate the phase structure of PU dispersion, showing an increase in thermal stability, solubility, and flexibility. Regarding the electrical properties, the maximum piezoresistivity (10 S/m) of 7.4 wt.% MWCNT was enhanced by 92.92%. The chemical structure of the PU–CNT composite has shown a degree of agglomeration under disruption of the sp² carbon structure. However, with extended graphene loading to 5.7 wt.%, piezoresistivity could hit 10^{−1} S/m, less than 100 times that of PU. In addition to electrical properties, the acoustic behavior of MWCNT (0.35 wt.%)/SiO₂ (0.2 wt.%)/PU has shown sound absorption of 80 dB compared to the PU foam sample. Other nanofillers, such as SiO₂, TiO₂, ZnO, Al₂O₃, were studied showing an improvement in the thermal stability of the polymer and enhancing scratch and abrasion resistance.

Keywords: nanocomposite; physio-thermo-mechanical properties; polyurethane; polymers; bio-applications

Citation: Allami, T.; Alamiery, A.; Nassir, M.H.; Kadhum, A.H. Investigating Physio-Thermo-Mechanical Properties of Polyurethane and Thermoplastics Nanocomposite in Various Applications. *Polymers* **2021**, *13*, 2467. <https://doi.org/10.3390/polym13152467>

Academic Editor: Victor Tcherdyntsev

Received: 27 February 2021

Accepted: 22 March 2021

Published: 27 July 2021

Publisher's Note: MDPI stays neutral with regard to jurisdictional claims in published maps and institutional affiliations.



Copyright: © 2021 by the authors. Licensee MDPI, Basel, Switzerland. This article is an open access article distributed under the terms and conditions of the Creative Commons Attribution (CC BY) license (<https://creativecommons.org/licenses/by/4.0/>).

1. Introduction

A range of research has been conducted on the ongoing discussion of the effect of chemical structure and annealing of the morphology of polyurethanes (PUs) on experimental and theoretical work on phase-separation kinetics [1]. Phase separation is the most crucial reason for the PUs' microphase separation as the powerful hydrogen link between the urethane hard parts [2]. The main components of PUs are macrodiol, diisocyanate, and chain extender [3]. The chemistry of PU synthesis depends on the reactions of isocyanate.

The hydrolysis resistance of PUs and the noting of the diol chemistry on molecular weight stability in water are discussed by Gomez et al. [4].

PUs belong to a group of elastomers that are linked to a urethane material with a distinctive feature of being hard and soft parts in the macromolecule [5]. In addition, the environmental issue that involves PU recycling was a concern of researchers [6]. The synthesis of PU is the main theme of the studies in the field of working towards environmentally based materials such as PU, using the short-chain diol called diisocyanate [7]. Polyurethane is widely considered as the biggest polymer product which is categorized under plastics [8]. Plastic and modular construction industries produce big quantities of PU wastes in the fabrication process during either processing or utilization of materials [9]. The structure and properties of PU parts have been investigated to achieve better biocompatibility and are characterized by surface and bulk morphology [10]. Traditionally, PU items are equipped with many organic solvents and free isocyanate monomers [11]. In the production of PU foams, catalysts are employed in the polyaddition reaction [12]. It has been reported that two simultaneous reactions could occur during PU manufacturing that involves the isocyanates and polyols during gas liberation or a foaming reaction [13]. As an example, paints from modified PU are extensively used as topcoats for corrosion and weather resistance. The aliphatic PU is sensitive to acrylic ester comprising hydroxyl which is widely considered as having good adhesion and being aging-resistant [14]. These processes involve building up strong hydrogen links of the PU matrix, raising the rigidity of the matrix, and negatively affecting the relaxation of dipoles [15]. The particles dispersed in aqueous phase dispersion, classified as anionic PU, are binary colloidal systems, cationic, and non-ionic systems [16]. Regarding the nanomaterials, the antibacterial polyurethane activity of composite nanofibers has been assessed in food-borne pathogenic bacteria and staphylococcus aureus, using various techniques [17]. The focus is on the formation of soft, long-chain diol segments, whereas the construction of the hard segment belongs to the microdomain of segmented PU copolymers [18].

The organization of this review paper is explained in Figure 1. The introduction is followed by shedding the light on the general properties of PU composite, TPU composite, a comparison between PU and TPU, and PU clay. The other main section of the paper is presented to discuss the properties of the nanofillers in both PU and TPU. These properties include morphology, mechanical properties, thermal properties, electrical properties, acoustic properties, and viscoelastic properties. The last main section of the paper is devoted to highlighting some applications in various fields.

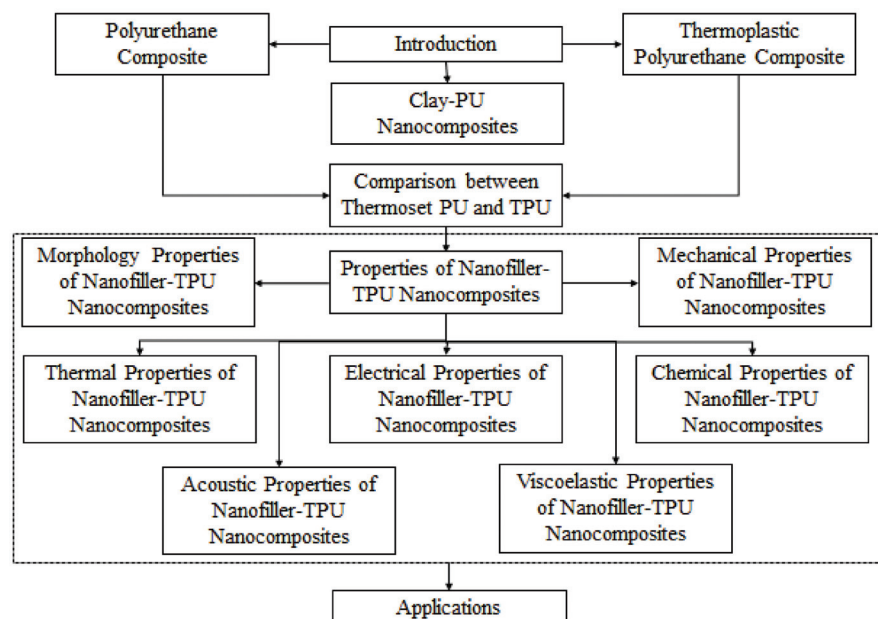


Figure 1. Organization of the paper.

2. Polyurethane Composite

The soft segment relative to the hard segment of the lower air-interfacial polymer has made the appearance of PU in polyol structure [19]. The size of the dispersed PU particle reduces the concentration of the ionic group per unit chain length of the PU prepolymer [20]. On the other hand, the increase of the ratio of hard to soft parts of the PU chains results in increasing the viscosity of the prepolymer [21]. The reduction of the ionic group concentration and the increase in the viscosity could cause a stiffer PU chain, lowering the solubility of the polymer, enhance the phase separation, and make coarse particles at the surface [22]. The above behavioural changes increase the hysteresis values of the quaternized polymers compared to the base PUs. The effect then causes a noticeable rearrangement surface that changes the hydration [23].

PUs are industrially crucial polymers with a range of structures and uses [24]. The acrylics PU polymer is known by a table of Newtonian rheological features [25]. Regarding the aging of the PU film, Sanchis et al. [26] have shown that the PU structure plays an important role in addressing the age issue.

The poor elasticity of the two segmented PUs was caused by their low molecular weight which, in turn, influences the morphology of the segmented PUs [27]. Hetflejš et al. [28] illustrated that the stabilizing efficiency of polymer-linked structures could be compared with that of their low-molecular-weight analogs, physically admixed with the PU. In another field, a sufficient mixing of the fluoro acrylic and PU polymers in the film properties could produce better results [29]. In this regard, it was found that modifying the ratio of PU and polyimide parts results in widening the range of properties from plastic to elastomer of the poly(urethane-imide) [30]. The solubility of the polyimide is enhanced as a result of adding isocyanate-terminated PU prepolymer, making a gelatine solution [31].

3. Thermoplastic Polyurethane Composite

Thermoplastic polyurethanes (TPUs) are linear segmented copolymers composed of hard and soft segments separated by a microphase, which complicates the investigation of its relevant microstructure [32]. The difficulty of this investigation shortening the research of the microstructure to extension behaviour [33]. Thermoplastic polyurethane (TPU) and the thermoset PU are chemically similar to each other; however, they have different features [34]. TPU is characterized by unique physical-chemical properties due to the reformation ability from melting state which makes it elastic, highly flexible, and suitable for many industrial applications [35]. On the other hand, the sensitivity of TPU to oil is smaller than that of thermoset PU, as the latter is easy to tear with abrasive applications [36]. TPU becomes soft at high temperatures and can hold low pressure, possessing a higher tensile modulus in comparison to rubber [37].

TPU is generally described as “bridging the gap between rubber and plastics” and imparts high elasticity combined with high abrasion resistance, and, hence, becomes suitable to a variety of biomedical applications [38]. TPUs are conventionally not degradable; however, they become susceptible to hydrolytic and oxidative under vacuum [39]. The TPUs’ susceptibility to such degradation causes a problem for long-lasting biomedical implants which exploit designing biodegradable PUs [40].

TPU displays a very wide range of properties, ranging from very soft to strong, rigid thermoplastics that depend on the chemical compositions, backbone structures, and resultant microphase morphologies [41]. The 40-year investigation revealed that there are various morphological models for segmented PUs [42]. TPU has become one of the most versatile engineering thermoplastics that have constituted developing more interesting polymers due to specific structures of TPU macromolecules, interphase interactions, and microphase transformations [43]. Several researchers have addressed that blending TPU with nanomaterials enhances its physical properties and toughness [44]. The TPU’s good compatibility with polycarbonate or acrylonitrile butadiene styrene was behind using TPU as a modifier to create new blends [45]. The effect of using special additives can be

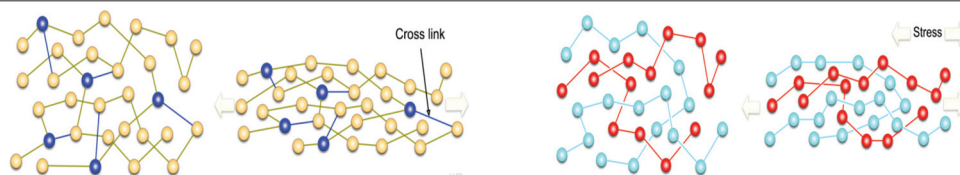
seen in creating properties necessary to achieve flame retardance, antistatic, and radiation crosslinking ability [46]. Besides, exposing TPU to severe conditions results in significant structural changes depending on the structure and morphology; however, such changes deteriorate the physical properties [47].

4. Comparison between Thermoset PU and TPU

Thermoset PU and TPU belong to two different classes of polymers; however, they show some differences; for example, the thermoplastic has low melting points while the thermoplastic can withstand high temperature. TPU can be remoulded, while thermoset cannot be reformed, remoulded, or recycled. Table 1 shows the main differences between thermoset PU and TPU [48].

Table 1. Comparison property between thermoset polyurethane (PU) and thermoplastic polyurethane (TPU) (partially from Kopal et al. [48]).

Thermoset PU	Thermoplastic PU
Less hardness	High hardness
Burns easily	Difficult to burn
Soft and delicate	Rough, strong
Moderate abrasion resistance	High abrasion resistance
Withstands temperatures up to 250 °C	Softens and deforms above 250 °C
Hold a large amount of weight	Unable hold a large amount of weight
Specific gravity: 1 to 1.2	Specific gravity: 1.2
Shore hardness (HV): 10–85	Shore hardness (HV): 55
Tensile strength (MPa): 1–12	Tensile strength (MPa): 48–83
Elongation at break (%): 10–510	Elongation at break (%): 500
Tear strength (N/m): 6–48	Tear strength (N/m): 200



5. Clay–PU Nanocomposites

The valuable and key properties of TPU that have been collected by Tehran et al. [49] were articulated in Table 2. There were three ways to enhance these key properties: the first is via manipulating the three basic building blocks, which are polyester/polyether polyol, diisocyanates, and chain extender; secondly, blending with an appropriate polymer; and thirdly, incorporation of inorganic fillers, particularly nanofillers, into the PU matrix. Amongst these three techniques, the incorporation of inorganic nanofillers was found to be the best, in terms of both commercial effectiveness and technical viability of the process [46]. This is because nanofillers have great advantages for improving barrier and mechanical properties, as well as thermal stability [50].

Table 2. Basic and valuable properties of TPU (Partially from Tehran et al. [49]).

Property	Value
Density	1224 kg/m ³
Shore hardness	55 A
Tensile strength	20 MPa
Melting temperature	200 °C
Ultimate elongation	500 %
Glass transition temperature	−42 °C
Low temperature brittle point	≤ −68 °C
Injection molding–melt temperature	200–220 °C
Injection molding–mold temperature	20–40 °C
Maximum drying temperature	110 °C

It has been observed that montmorillonite clay modified with long-chain onium ions exhibited excellent compatibility with several polyols that are commonly used for PU synthesis [51]. Additionally, an increase in the chain length of alkyl groups that are present in the long-chain onium ions causes an increase in interlayer distance between the clay platelets in the nanocomposites. Clay–polymer nanocomposites may be prepared by three distinct methods, e.g., melt blending, solution mixing, and in-situ synthesis. In the case of the melt blending technique, nanoclay is mixed with the molten polymer in an internal mixer or extruder. Meanwhile, solution mixing involves the intermixing of a solution of polymer and the solvated nanoclay, utilizing mechanical stirring and/or ultrasonic vibration, followed by the evaporation of the solvent. In the case of the in-situ synthesis technique, clay is dispersed either with the polyol or with the prepolymer followed by a further course of polymerization. Several factors that are responsible for the dispersion of nanoclay [52] in the polymer matrix such as the method of preparation, mixing temperature and thermal history, mixing time, shear rate, the extent of deformation, the solvent used (particularly in solution mixing as well as in-situ preparation), the concentration of polymer solution (again in solution mixing and in-situ preparation), the molecular weight of the monomer (for the in-situ preparation method) or polymer, the types of modifier used for modification of nanoclay and the extent of modification of the nanoclay [53].

6. Properties of Nanofiller–TPU Nanocomposites

The main application of TPU is in the medical field due to its exceptional mechanical properties and biocompatibility. The siloxane-based TPU is one of the most important nanocomposites. TPU nanocomposites were vigorously studied based on the nanofiller aspect ratio, surface modification, and percentage loading. The mechanical properties were increased at an even small amount of loading. In this section, several TPU nanocomposites will be discussed. The mechanism of the nanofillers is explained schematically, as shown in Figure 2 [54]. The effect on nanofillers will be investigated in terms of morphology, mechanical properties, thermal properties, chemical properties, electrical properties, acoustic properties, and viscoelastic properties.

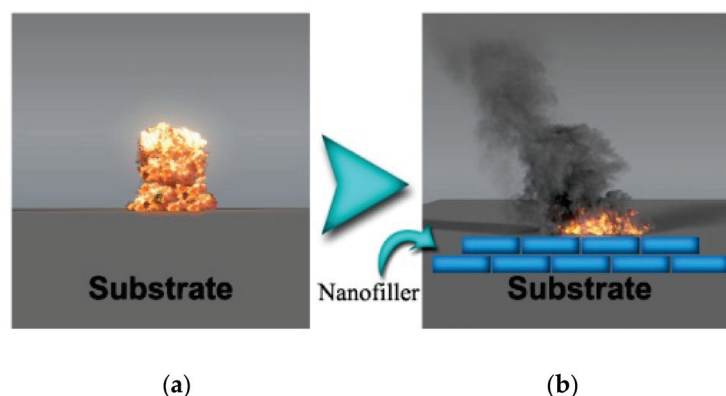


Figure 2. (a) The mechanism of nanofiller on the substrate and (b) corresponding morphology [54].

6.1. Morphology Properties of Nanofiller–TPU Nanocomposites

The first-ever successful attempt of dispersion of nanoclays in the TPU matrix has resulted in incredibly high interest amongst the scientific community [55]. It was seen that the morphology of clay platelets plays a crucial role in the improvement of the properties of the clay–TPU nanocomposites. The effect of hard segment content along with the amount of clay on the morphology has been discussed by Xu et al. [56]. Increased hard segment content has been seen to result in an increase of the basal spacing of the clay platelets at a lower clay content. However, the opposition has been observed to occur at higher clay contents, where increased hard segment content reduces the basal spacing. Two varieties of modified montmorillonite (MMT) have been dispersed in the TPU matrix [57]; the first is clay modified with 12 amino lauric acids and the second is clay modified with benzidine. This was done in order to study the effect of the modifier on the morphology and properties of the resulting nanocomposites [57]. Complete exfoliation was observed of up to 5% and 3% for clay modified with 12 amino lauric acid and benzidine, respectively.

An investigation into an intercalated to exfoliated morphology was carried out, in which there was the incorporation of clay modified with dialuryldimethyl ammonium bromide and 4,4'-diaminodiphenylmethane, respectively [58]. Intercalated structures were mainly observed when the clay was used as a pseudo chain extender [59]. However, the prevalence was as follows: firstly, intercalated morphology with nontethered clay (clay that was mixed physically), and secondly, exfoliated morphology with the tethered clay (clay that had the active functional group)—where both were for nanocomposite prepared by in-situ preparation technique [60]. It has also been shown by many other researchers that tethering of the clay leads to exfoliation of the clay platelets [61]. Of note is the fact that highly exfoliated morphology occurrence up to 40 wt.% of nanoclay was demonstrated by using clay as a pseudo chain extender [62]. The effect of changing the number of end-tethered–OH functional groups on the tail of the modifier (the modification of montmorillonite) has been studied previously [63]. The morphology of the clay changes from intercalated to exfoliated, with the increase in the number of [–OH] groups in the modifier. The MMT with tris (hydroxymethyl) aminomethane was modified so that a tethered clay with three [–OH] groups may be prepared [62]. It is of importance to note that the intercalate-to-exfoliate morphology was for all the nanocomposites and increased aggregation tendency was also seen but only at higher clay contents [64]. High mechanical shearing (not the tethering of the clay) was found by Adak et al. [52] as a complete exfoliation of the nanoclay. The clay that possessed the in-house synthesized organizer was modified before subsequently being dispersed into the TPU matrix [52].

Figure 3 shows the overall impact of nanofillers on the morphology of C30B-CPN and CA-CPN, highlighting the state of dispersion of clay layers in the PU matrix. In the case of CACPN, an intercalated and flocculated morphology was obtained where the clay layers were oriented in the PU matrix by edge–edge interaction. Good dispersion was observed at lower clay concentrations. However, at higher clay-loadings, clusters or particles were

formed due to agglomeration of clay-layers, leading to non-uniform dispersion in the PU matrix. Other effects can be seen in the subsequent parts of Figure 3 [52].

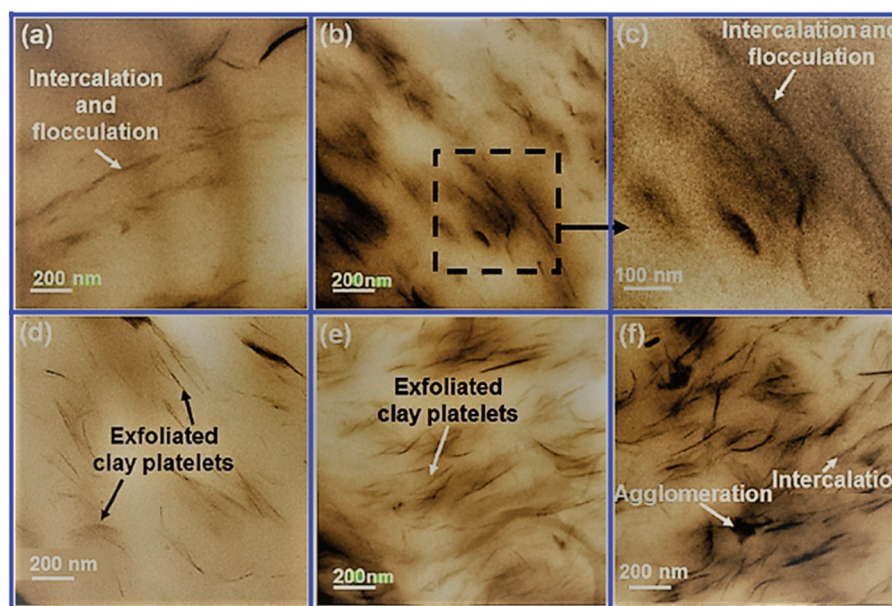


Figure 3. Images showing dispersion of clay-platelets in CPN: (a) PU-CA-1, (b,c) PU-CA-3, (d) PU-C30B-1, (e) PU-C30B-3, (f) PU-C30B-5. [52].

6.2. Mechanical Properties of Nanofiller–TPU Nanocomposites

The mechanical properties of modified TPU are extremely important because of the usefulness of modified TPU in many engineering applications. It has been observed that the addition of nanoclay into the PU matrix improves the tensile properties to a significant degree [65]. As an example, adding 10 wt.% of modified clay increases the tensile strength, modulus, and strain at the break by more than 100% [45,56]. Young's modulus of the nanoclay–TPU nanocomposites has previously been seen to increase with the addition of modified nanoclays [66]. Nonetheless, improved Young's modulus coupled with a reduction in tensile strength and elongation at break with the addition of clay has also been reported in previous studies [67]. Besides that, the destruction of hydrogen bonds in the hard segment of TPU due to the incorporation of tethered nanoclays has also been observed [67]. The destruction in H-bonding occurs due to the H-bond formation between the carbonyl group of the TPU and the [–OH] group present on the tail of the modifier to the clay. However, modulus and tensile strength are increased by 110 and 160%, respectively, for the nanocomposite containing 5 wt.% of Cloisite[®]30B. The reaction of the surface [–OH] group of the MMT with the isocyanate during in situ synthesis, which leads to an improvement in tensile strength, as well as elongation at break, has been observed from experimentation [56].

The effect of the modifier on the improvement in the properties of the TPU has been studied using three types of modifier [68]. With the increase in the degree of exfoliation, the tensile strength and elongation at break have been found to increase. However, increasing the mixing time (in order to achieve exfoliation) is found to cause degradation in the TPU matrix [69]. It is reported that better properties are obtained when the degree of exfoliation of the clay platelets is higher. This is due to an increase in the mass-to-volume interaction between the clay and polymer in the exfoliated state of clay in the polymer matrix, which in turn is highly dependent on the type of modifier used. The samples with 0.5 wt.% CNTs, an increase of the tensile modulus concerning the TPU matrix was estimated between 90 to 30% for flat and blown films, respectively. It is also shown that the samples of CNT–TPU nanocomposites show that the stiffness and tensile strength increase with increasing content of CNTs at the expense of elongation at break which is reduced by

more than 40%. The typical stress–strain curves for the sample films containing 0, 0.2, 0.5, and 1 wt.% multiwall carbon nanotubes (MWNs). Results show a non-monotonic trend of mechanical properties with the filler loading [70].

It has been previously reported that the rate and degree of separation have a direct correlation with the tensile features of PU elastomers [71]. The significant finding of this current work was depicting the role diisocyanate symmetry played in the stage of development of microphase separated morphology and the resultant new mechanical properties of the PU [5]. The method deemed to be best to improve the PUs' mechanical properties is the chemical linking of the PU chain with functionalized dendritic polymers through crosslinking [72]. Energy recovery and mechanical, chemical, and thermochemical recycling were some of the ways identified for recycling PU [73]. The findings may be linked to the high porosity, as well as the weak compressive toughness of alveolar PU. The high decrease in the strength was because of the rise in PU foam content which in turn was a result of an increase in mass loss [74]. Moreover, the static tensile features and toughness of the PUs are depicted in Table 3 [75].

Table 3. Mechanical properties of PUs with different hard segment contents [75].

Type of PU	Rm (MPa)	E (MPa)	ϵ (%)	Hardness ($^{\circ}$ Sh D)
PU2PCL2000	$>24 \pm 1$	39 ± 1	$>763 \pm 41$	41 ± 2
PU2PCL1250	23 ± 2	17 ± 3	643 ± 40	22 ± 1
PU4PCL2000	33 ± 3	36 ± 2	440 ± 56	27 ± 2
PU4PCL1250	48 ± 3	39 ± 2	356 ± 11	38 ± 2
PU2PCL530	41 ± 2	38 ± 0.9	420 ± 28	43 ± 2
PU4PCL530	1.6 ± 0.4	32 ± 0.4	-	61 ± 3

Linear poly(urethane-imide) elastomers were achieved [76]. They showed significantly better mechanical features and greater thermal stability when compared to the typical linear PU [76]. The patterns were the same as the flexible PU but accompanied by a reduction in stiffness and strength in the wet condition where new samples showed enhanced features for all aging states [77]. By catalytically balancing two deeply understood reaction schemes, flexible PU foams are made. Flexible PU foams are produced by balancing two well-understood reaction schemes through catalytic balancing. Besides that, an analysis of the orientation-elongation feature of linear PU elastomers was shown as having low deformation with the hard segment's base transversing to the stretching direction [78]. As a pigment grinding medium, the phosphate PU acrylics were shown to be well-suited for this function because of their sheer stability [79]. It has been stated that there may be improved cracking when steroids were adsorbed on PUs [80]. Looking at drying time, PU resin-coated panels were tested for four different properties, which were scratch hardness, impact hardness, flexibility, and chemical barrier [81]. It should be noted that for PUs comprising both hydrophobic fluorinated chain as well as hydrophilic phosphatidylcholine group, the need existed for the utilization of the average tapping mode to examine the difference of surface stiffness between hard and soft PU segments [82]. Arrieta et al. [83] maintained that higher modulus was seen compared to DCE-based PUs, but equal tensile strength was also present due to higher Mn content [83]. Xu et al. [84] observed that the rubbery plateau modulus segmented PUs increased with an increase in the hard segment content due to the rise of more continuous hard phase morphology. Figure 4 shows the ambient stress–strain behavior of the four segmented PUs, which were uniaxially deformed until failure [84].

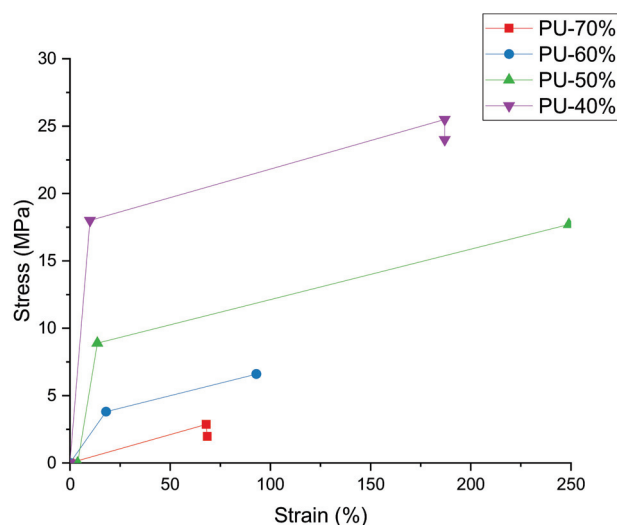


Figure 4. Stress–strain behavior of segmented PUs [84].

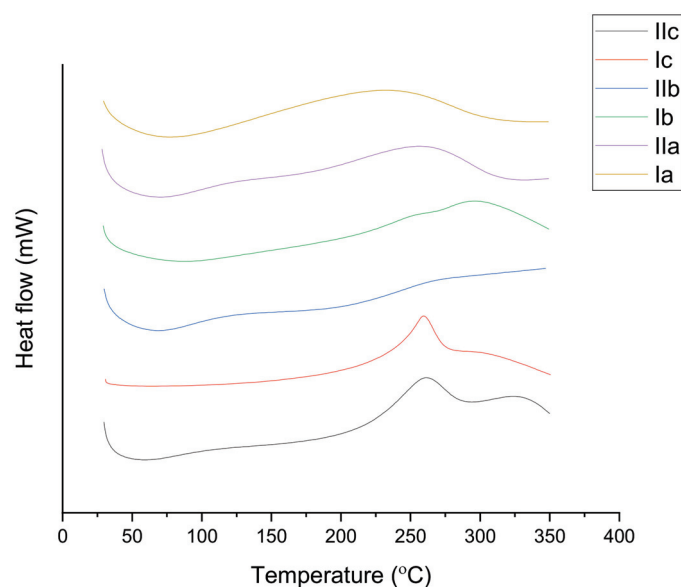
6.3. Thermal Properties of Nanofiller–TPU Nanocomposites

The thermal stability of the TPU matrix is of great importance since its degradation commences around 230–300 °C. It is important to note that a TPU matrix possesses two glass transition temperatures (T_g) corresponding to the soft and the hard segments, while it is known that the hard segment temperature T_g is not always observed due to the dominance of the soft segment and ordered hard domains [85]. It also appears that the addition of a small amount of tethered clay could increase T_g of the hard segment by 44 °C [52] while a 13 °C rise was observed in the T_g value of the soft segment with the addition of Cloisite® 20A [86]. TPU was found to exhibit two stages of degradation during decomposition. The first stage of degradation relates to the degradation of the hard segment and the second stage of degradation relates to the degradation of the soft segment [87]. In some other studies, a lower T_g of the nanocomposite, as compared to the TPU matrix, has been reported [88]. The thermal stability of the clay–TPU nanocomposite will increase after the complete decomposition of the modifier compared to that of the TPU matrix [89]. An increase in the amount of clay from 1 to 5 wt.% was reported to increase the thermal stability of the TPU matrix from 12 to 34 °C, respectively [52]. The increase in thermal stability with an increase for MMT in the TPU matrix has also been reported in previous studies [56]. The improvement in thermal stability of the clay–TPU nanocomposite was found to be directly connected to the degree of dispersion of the nanoclay in the TPU matrix [89]. Enhancement of the thermal stability, along with the flame-retardant property of the clay–TPU nanocomposite, has been observed [90]. The thermal stability was enhanced by 25 °C with 5 wt.% clay. The heat release rate (HRR) decreased by 63% with the addition of 6% clay as compared to that of the TPU matrix. However, HRR decreased with further increase in the clay content. The degradation of the modified wt.% of carbon nanofiber (CNF) loading (PR-24-HHT-XT-LD) shows that the first- and second-onset degradation temperatures (T_{d1} and T_{d2}) are significantly increased. It was also shown that the 50% weight loss degradation temperature (T_{50} wt.%) was positively shifted from about 400 °C for TPU matrix to 425 °C in a case of CNF-reinforced materials.

Kariduraganavar et al. [15] demonstrated that cross-linked PUs with azobenzene chromophores show improved thermal stability. Besides that, it was discovered that no T_g could be seen for the PUs that had thiadiazole chromophores as part of their composition before they decompose, which infers that the T_g was above the decomposition temperatures (T_d). In order to investigate this stability, they controlled the temporal and thermal stability of the second harmonic generation signs for the PUs. This data obtained as operations of the time were their findings, as presented in a straightforward and simplified manner in Table 4. The differential scanning calorimetry (DSC) and thermal gravimetric analysis (TGA) thermograms are presented in Figure 5 [15].

Table 4. Physical properties of PUs [15].

PUs	T_g (°C)	T_{opt} (°C)	Field Applied (kV)	T_d (°C)
Ia	140	140	2.0	207
IIa	147	145	3.0	221
Ib	155	150	3.0	227
IIb	165	170	3.0	273
Ic	-	180	2.5	250
IIc	-	205	3.0	276

**Figure 5.** Differential scanning calorimetry (DSC) thermograms of PUs at a heating rate of 10 °C/min under a nitrogen atmosphere [15].

Longer durations of soil exposure and vermiculite media produce harmful effects on the PU thermomechanical features and the composite, with a fall in the T_g and in the storage modulus. In addition, a move towards higher temperatures for the initial thermal degradation occurred in the TGA curves of the composite and the neat PU linked to the lower concentration of dangling chains in the materials' content of the exposed degrading media, as shown in Figure 6 [91].

Temperature operations show the PU effects on gas selectivity along with the penetrability of membranes. Previous research has centred on the modified chemical PU structure membrane to enhance its gas transport features [92]. Efforts to enhance the PUs' thermal stability have been undertaken for a long period of time. One technique utilized to improve PU's heat resistance is that of the structural chemical change via the introduction of thermally stable parts [93]. The flexible PU enables predictions to be used even for lower temperatures (assuming that this linear extrapolation was reliable for the entire temperature range) [94]. The thermal features, microstructure, mesomorphic features, and thermal degradation were examined for the PUs [95]. Findings from a dynamic contact angle showed enhanced hydrophobicity of the PU acrylic dispersion films [96]. The endotherm of this fluorinated phosphatidylcholine PUs was not seen at higher temperature areas in DSC curves, which are shown in Figure 6.

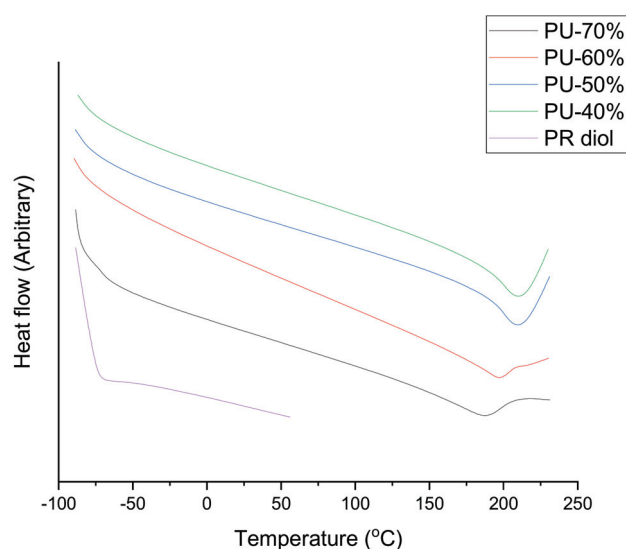


Figure 6. DSC thermograms of PUs at a heating rate of 10 °C/min [84].

Based on the thermogravimetric experiments, PUs that were made with the use of a catalyst in nitrogen were more stable [97]. This cured hybrid showed higher thermal stability and more favourable mechanical strength as compared to pure PU [76]. In terms of PU, for many polymers, it is used as a flame-retardant new additive [98,99]. The use of the polyimide composition in PU improved the decaying temperature of PU for higher temperatures [100]. Czech et al. [100] put forward the finding that PU's increase of length by raising the macrodiol length or by increasing the quantity of repeating units enabled the polymer to be softer at high temperatures. The reported T_g of the systems derived by DSC are listed in Table 5, together with the definition of the samples' nomenclature [100].

Table 5. The T_g determined from the DSC second scans for the PU-based networks crosslinked with hyperbranched polyester (Boltorn H40) [100].

PU Network Name	Number of Repeating Units in the PU Chain	Molecular Weight of Terathane (g/mol)	T_g (°C)
20-T650	20	650	−43.5
20-T1000	20	1000	−59.5
20-T2000	20	2000	−77.3
20-T2900	20	2900	−82.1
04-T2000	4	2000	−77.7
10-T2000	10	2000	−77.0

It is noted that minicolumns in flow systems, which are filled with loaded PU foam, did not depict any overpressure or swelling, although this often occurs with the utilization of other sorbents [101]. Madru et al. [102] had the contention that the water swelling of PU membranes was related to both its aggregation condition, as well as the temperature [102].

6.4. Electrical Properties of Nanofiller–TPU Nanocomposites

The electrical properties of a material are characterized by the ability of the material to conduct or insulate electricity based on the parameters such as its resistivity, conductivity, dielectric strength, temperature coefficient of resistance, and thermoelectricity [103]. Conductive fibres are known to improve electrical conductivity in polymer composites [104]. Examples of these are carbon, silver, gold, copper, and nickel, which are found in many different shapes and sizes [104]. In the composite field, the maximum electrical conduc-

tivity of 10 S/m at a loading of 7.4 wt.% of MWCNT and 0.3 wt.% as the percolation threshold for MWCNT/polyimide (MWCNT/PI) composite was achieved using the in situ polymerization method based on a study by Jiang et al. [105]. This concluded the ability of CNT to improve the EC of a polymer composite [106].

In the study of Vaithyalingam et al. [107], the EC value of 0.33 S/m was noted to have been achieved at 7 wt.% loadings of MWCNT, and 5 wt.% was the percolation threshold for MWCNT/PU composite using the three-roll milling machine technique. It was determined that this technique is fast, simple, and easy, and compatible with standard industrial techniques enabling the production of high percolation threshold composite compared to in situ polymerization, solution compound, and combination of different techniques [107]. The addition of CNT can result in high dielectric strength at a very low loading fraction (<5 wt.%) being achieved. CNT adding may also change the electrical resistance of the composite under applied load/strain. This is called piezoresistivity and can be measured using a two-probe method. The composite with 5 wt.% loadings of MWCNT showed 92.92%, piezoresistivity, the largest percentage achieved [107]. Further loading of CNT into the composite may actually decrease the EC, piezoresistivity, and dielectric strength because of entanglement and agglomeration [107]. Based on Fu et al. [108], the degree of agglomeration of the 1-dimensional CNT can be reduced using two-dimensional graphite oxide (GO) as a novel dispersant to promote the adhesion between the CNT and PU matrix. The discovery of single-layer graphite, which is commonly known as graphene, has brought great improvements in the electrical properties of polymer composites [109].

In order to obtain high-yield graphene, top-down methods such as the combination of oxidation, exfoliation, and reduction of graphite are often practiced. GO is produced from exfoliation and oxidation of graphite. GO consists of a great number of versatile oxygen functional groups on its edge and basal planes [110]. This leads to stable dispersion in an aqueous solution [110]. Nevertheless, the disruption of the sp² carbon structure by the oxygen functional groups results in GO with poor electrical conductivity. Chemical reduction is an effective method of obtaining reduced graphene oxide (RGO) which can be dispersed in aqueous or solvent media and solve the disruption of sp² carbon structure [111]. Nevertheless, GO tends to aggregate and re-stack due to large van der Waals forces as well as π - π interactions [112]. Compatibilization of graphene via non-covalent and/or covalent interactions is an effective way to enhance surface adhesion with the polymer matrix and prevent aggregation. The existence of functional groups such as hydroxyl, carbonyl, and carboxyl promotes the covalent interaction. Hydroxyl groups can react with silicone coupling agents to result in better graphene adhesion to the polymer matrix [113]. Under the investigation of incorporating modified expanded graphene (EG), the electrical conductivity of 10⁻¹ S/m at 8 wt.% loadings and 5.7 wt.% was taken as the percolation threshold for EG/PU composite using the in situ polymerization method [107].

In recent years, sulfonated graphite oxide (SGO) has been found to be of higher efficacy in facilitating the oxygen reduction reaction of GO. Hydroiodic acid (HI) may be used as a strong reducing agent since it is an environmentally friendly inorganic acid. The strength, as well as conductivity of GO and filled polymers increases after reduction with HI because of the reaction with the epoxy groups in GO. Hence, the reduced SGO (RSGO) has very good potential to improve the electrical and thermal conductivity of polymer composites [114]. Similar to CNT, introducing graphene to the polymer matrices improves the EC, piezoresistivity, and dielectric strength of the composite by a substantial degree [115].

In the past few years, silver nanoparticles (AgNP) have drawn much attention as it is widely used as conductive fibers for electrically conductive composites. A_g is known for its high aspect ratio which is beneficial to form electrically conductive networks while having a relatively low percolation threshold in polymer composite. Nonetheless, A_g has a tendency to agglomerate because of its fine size and large specific surface area, which could result in a reduction of the conductive path. A_g is also prone to sedimentation as the density of A_g (10.53 g/cm³) is higher than the polymer density (around 1.0 g/cm³).

Therefore, is it required to address the A_g sedimentation and agglomeration issue before proceeding with the preparation of Ag/polymer composite with high EC. The usage of Nanosilica (SiO_2) as a dispersant may not be an option in this case because SiO_2 is more of an electrical insulator. As a step to improve the performance of Ag/PU composite, GO or LDH may be used as a novel dispersant to improve the EC of said composite [107].

It was shown by Vaithyalingam et al. [107] that the Ag/GO/PU composite exhibits superior electrical property ($<10 \Omega/\text{sq}$) [116]. As global warming issues are on the rise, employing piezoelectric generator composites is able to convert vibration and mechanical energy source from human activities such as pressure, bending, and stretching motion into electrical energy. This is becoming a topic of high interest in recent composite studies. Material like zinc oxide (ZnO) and barium titanate (BaTiO_3) can be used as fibers to improve the piezoelectric properties of the polymer composite. Based on the investigation by Vaithyalingam et al. [107], the generator composite prepared using ZnO incorporated in the PU matrix showed the greatest peak voltage value of 40.45 V upon cyclic loading.

6.5. Chemical Properties of Nanofiller-TPU Nanocomposites

Chemical properties are conventionally used to determine the ability to resist or comply in a chemical reaction based on the parameters like toxicity, corrosion-resistance, chemical stability, flammability, and enthalpy of formation that governs composite classification [107]. The behaviour of the materials varies in terms of their resistance to corrosion such as monolithic materials. Prevention of corrosion can be performed by organic-based coatings. However, these materials may fail due to electrolyte exposure which is responsible for cathodic delamination and physical damage like impact, scratching, or wear during service. This allows direct contact of underlying steel substrates to aggressive environment and electrochemical reaction taking place at the coating-substrate interface [117]. The increase in hydroxide ions concentration results in alkalization weakening the adhesion of steel substrate and coating. In addition, it was found that transporting water and oxygen molecules through organic coatings could be critical in reducing oxygen [118].

Recent research has shown that adding nanoparticles (NP) such as SiO_2 , TiO_2 , ZnO, Al_2O_3 , MWCNT, and CaCO_3 in coatings results in improving the thermal stability of the polymer and enhancing scratch and abrasion resistance [119]. As an example, incorporating MWCNT in polymer matrices improves the wear resistance and reduces the friction of the composite when upgraded [120]. It was reported that increasing MWCNT content from 0 to 0.5 wt.% causes decreasing of the PU cathodic delamination which is caused by making a dense barrier of MWCNT, which, in turn, blocks the oxygen and water molecule pathways through the coating [58].

6.6. Acoustic Properties of Nanofiller-TPU Nanocomposites

In the acoustic behaviour of materials, the cellular structure can be used to absorb sound [121]. The determination of the acoustic properties of a material depends on the ability to perform as either insulator or conductor by involving vibration, ultrasound, and infrasound [122]. Examples of acoustic materials include nanoclay, titania nanoparticles (TiO_2), and MWCNT which can be incorporated into the PU matrix to enhance sound absorption [93,123]. It has been reported that the MWCNT/ SiO_2 /PU composite showed remarkable sound insulation properties compared to pristine PU where the addition of 0.2 wt.% SiO_2 and 0.35 wt.% CNT to the PU composition improved sound transmission loss up to 80 dB that of pure PU foam sample [124]. Surprisingly, the continuous addition of CNT of up to 2 wt.% had poorer sound insulation than the pristine PU foam due to the high loading of CNT effectively preventing the interactions between the polyol and isocyanate [125].

6.7. Viscoelastic Properties of Nanofiller-TPU Nanocomposites

Viscoelastic properties of a composite refer to the ability to exhibit both viscous and elastic characteristics when undergoing deformation [126]. These materials are resisting

the shear flow and strain linearly upon stretching; yet, they can retain their shapes as the stress is removed [127].

Research in this field has led to the discovery of smart materials such as electro active polymers (EAP).

EAPs have the ability to change their size or shape when stimulated by the right external electrical activation mechanism by converting the electric signal into energy [128]. PU-based composites are very favourable when taking viscoelastic properties into consideration as they are flexible, lightweight, biocompatible, easy to process, and have the ability to be moulded into various shapes [129]. The authors investigated incorporating grafted CNT into the PU matrix using the “grafting onto” technique to increase the interfacial adhesion, dielectric strength, permittivity, and 5 wt.% as the percolation threshold of the CNT/PU composite. Further, the electromechanical performance of the composite was also increased by a factor of 2, thus enabling high viscoelastic behaviour.

7. Applications

TPU fortified by its exceptional mechanical properties and biocompatibility is widely considered for the construction of implantable medical components by replacing silicon for implantation [44,130]. The reason for this potential replacement is mainly due to TPU’s superior tensile and tear strength which allows thinner insulation and more intricate design, while still maintaining structural integrity [131]. Figure 7 shows the general applications of TPU.

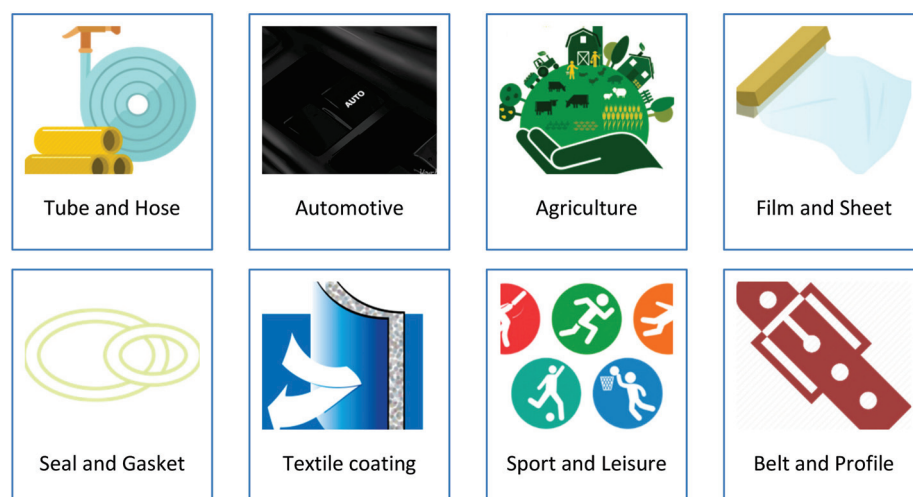


Figure 7. Applications of TPU [132].

7.1. Additive Manufacturing (AM)

AM is layer-by-layer 3D object printing. AM is mainly related to using polymers and their composites in modern industries and it has been proven that AM has vast potential for various applications, especially in the medical, aerospace, and automotive industries. AM techniques have been developing due to the creation of new materials and techniques such as photo polymerization, material jetting, powder bed fusion, material extrusion, binder jetting, and sheet lamination. The focus of most research in the AM field is to investigate the possibility to conduct a specific application, process, or type of material. The first step in this search is to highlight the progress of the corresponding materials and the methodology of the preparation of these materials. However, there are many challenges in using AM technology for polymer materials [54].

7.2. PU in Human Soft Tissues

The PU composite has a greater amount of water (over long timescales) when compared to both media due to the extremely hygroscopic properties of wood flour particles,

commonly known as sawdust [133]. One of the applications of TPU could be possibly related to biocompatible tough hydrogels in medical devices, such as prosthetics. The important key that causes the hard and soft segments located in the topography of the PU parts is what determines the strength of the hydrogen bonds [134]. In addition, the average particle size can be changed or modified by varying the emulsification procedures, such as the revolution speed of the mixer or temperature in PU dispersions. Furthermore, water absorption into the particles showed an increase in concurrence with the increasing hydrophilicity of the PU [135]. There is a series of biocompatible tough hydrogels whose mechanical properties can be adjusted by fabricating a physically crosslinked poly(ethylene glycol)-based polyurethane and a copolymer. There is a significant effect of varying the chain length of the chemical crosslinkers and the chain length of the hydrophilic soft segments in the physically crosslinked polyurethane. This effect is linked to the physico-chemical properties of the hydrogels which are widely used in determining the swelling, stiffness, strength, and toughness. The manipulation of the length of polyethylene glycol results in changing the length of polyethylene oxide; the networks become tightened or loosened, as depicted in Figure 8 [136].

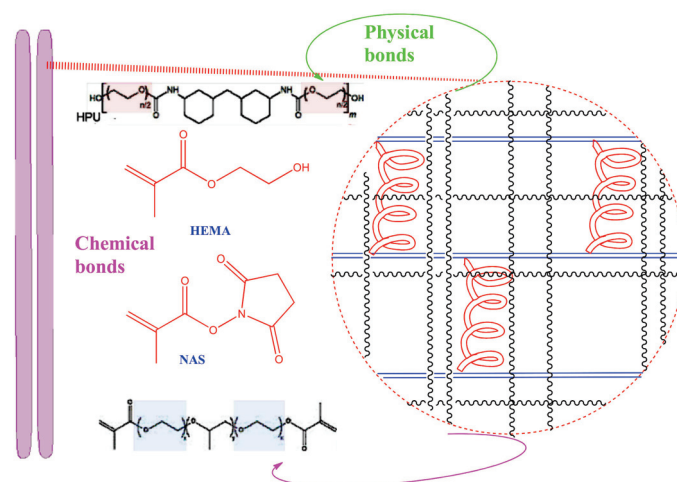


Figure 8. Hydrogel PU used in soft human tissues [136].

7.3. Coating and Anti-Corrosion and Anti-Bacterial Properties

Another application is the use of the modified polyurethane (PU) in Figure 9 which was prepared by using polyol with toluene diisocyanate in NCO/OH = 0.7 ratios. Investigation of the prepared polymer by spectroscopic studies has confirmed the modification process. The anti-corrosive properties of the galvanized steel with PU coating surpassed the steel in an aqueous (3.5 wt%) NaCl solution environment. Atomic Force Microscopy (AFM) showed the surface hydrophobicity, roughness, and morphology. The moiety cross-link in the PU backbone chain has expressed better physicochemical properties compared to the unmodified PU. In addition, the thermal stability of modified coated PU was investigated by differential scanning calorimetry (DSC) and thermal gravimetric analysis (TGA). The results have shown better surface qualities in terms of corrosion [137].

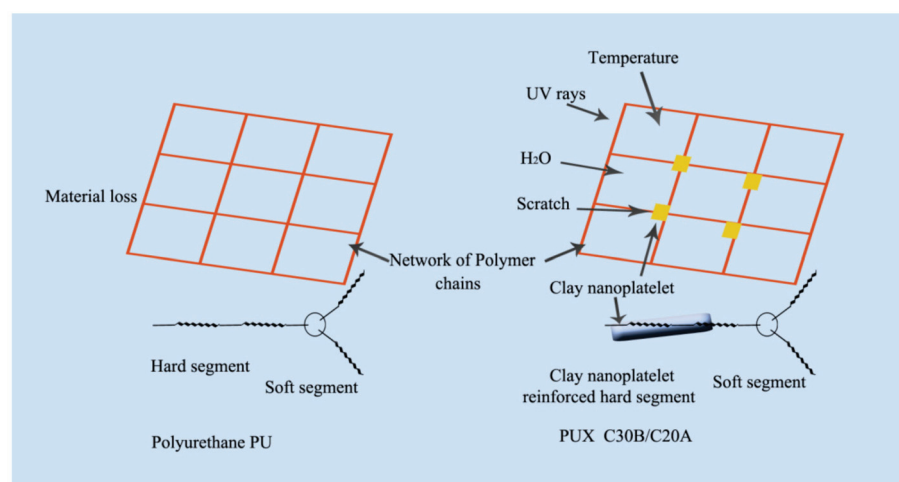


Figure 9. Atomic Force Microscopy (AFM) investigation of modified PU morphology [137].

7.4. PU Foam Uses

The weight loss of PUs decreases with increasing spacer lengths. Asensio et al. [42] showed that the patterns in flexible PU foams correlate with their plaque which provides the rationale for the utilization of plaques. The radiolabel that is released from incubations is normalized based on the radioactivity of the PU used [87]. The depolymerized oligoesters could be esterified with coco fatty acid so that a polymeric precursor, polyester polyol for PU can be built [138]. Wang et al. [139] mentioned the need and importance of hydrogen linking and inductive elements in determining the phase of PUs. The structure of PUs is depicted in the insert of Table 1. A wide variety of elements can be achieved by tuning the structure of the PU [140]. It was concluded that nitrogen plasma was the correct and best approach for improving the wetting properties of a PU film [141]. This was supported by Datta and Kasprzyk [142] who showed that polyricinoleate-segmented PU was stable enough to be processed using injection molding and extrusion [142]. This is of concept if traditional stabilizers were additions, as is the practice in the industry [143]. According to another study [144], the incorporation of PETpc particles into the PU foam resulted in a reduction in the mass loss for both top and bottom layers while cycling [144].

Both elastomers, as well as thermal degradation of PU foams, have been extensively studied in the last half a century, with differences and inconsistencies in results and findings because of a variety of PU compositions, materials, and products. Isocyanate, polyol, and chain extender have been used to produce the PUs, with the different linkages in the polymer chain resulting in different thermal dissociation temperatures [145]. Early degradation temperature in hard segments for PUs has been successfully reduced through the decreased composition of the soft segment [146,147]. Furthermore, the thermal degradation of PUs was examined thoroughly for the different types of diisocyanate (aliphatic or aromatic), polyol (polyester or polyether), and chain extender, where diisocyanates may be aliphatic or aromatic and polyols may be polyesters or polyethers.

7.5. Environmental Applications

The degradation system was also seen to be very complex due to the variety of products in the process. However, this seems to be the case only at the beginning stage of degradation which may be due to the high quantity of aromaticity in the polyester backbone causing the PU chains to be susceptible to scission, and this solved challenges of the structure crowing. The degradation of the PU films may not be a result of the polymer backbone's breakage but may instead be due to reduced cohesive energy within the hydrazo PU chains [148]. Ourique et al. [149] stated that the degradation kinetics were slower for the structured material when compared to the supple PU. The very slow degradation kinetics that was measured shows that the PUs fit long-term underwater applications [149,150]. It was clear that the other PUs would continuously degrade following testing, beyond the

test period. PUs with these isocyanates showed unfavourable mechanical features when compared to PUs with traditional isocyanates and hydrolytic degradation of PUs that were slow [151].

The thermal degradation of PU was noted by the decomposition of urethane links, the degradation of soft segments, and the volatile components' evolution [152]. The same authors have mentioned that this was not due to only pure thermal oxidation but rather also to prior degradation of the PU sample. Degradation of PUs may cause unfavourable issues by hydrolytic reactions which are of importance in polyester-based PUs [153]. Khadivi et al. [154] maintained that the degradation products via the PUs and nanocomposites showed no cytotoxic effect. Furthermore, steady differences in cytotoxicity of the by-products from polymers were not seen. Moreover, it was predicted that the polymers would be viable for ophthalmological uses. In simulated physiological situations, PU samples showed a more substantial weight loss when in vitro degradation assessments were undertaken [155]. The polyether with PUs had no significant signs of cell-mediated degradation under the same conditions as determined by radiolabel release. A live cell culture system used to test the susceptibility of PUs to degradation was an important measure in studying and understanding the mechanism of biodegradation [87]. The findings depict that the nanocomposites degradation rates turned slightly slower as compared to PU, implying PU's improvement of thermal stability, as the inorganic material could be a barrier for the heat to expand fast and limit further degradation [156].

8. Conclusions

The chemical structure and morphological annealing of PU have been reviewed experimentally and theoretically to investigate the phase-separation kinetics in terms of the influence of the powerful hydrogen link between the hard and soft segments of urethane. Controlling the interaction between hard and soft segments through hydrogen linking plays a crucial role in featuring the amorphous structure of PU and the thermally labile thermoplastic polyurethane (TPU), which is chemically similar to PU with a better heat resistivity. TPU has become the most versatile engineering thermoplastic with exceptional mechanical properties and biocompatibility that could be utilized to develop more interesting polymers due to specific structures of TPU macromolecules, interphase interactions, and microphase transformations. In addition, polydimethylsiloxane (PDMS)-based PUs were investigated and it was found that it is well-equipped with bio stability caused by the mixed macrodiol technique.

TPU and PU were investigated commercially and technically to highlight the incorporation of inorganic nanofillers such as carbon or clay using a process. The most important step is to incorporate TPUs in many possible applications relying on biocompatibility properties. Meanwhile, exfoliated morphology occurred when a 40 wt. % nanoclay was used to utilize a pseudo chain extender. The resulting PU-nanocomposite of 5 wt.% Cloisite[®]30B has shown an increase in modulus and tensile strength by 110 and 160%, respectively, compared to the 30–90% increase of the nanocomposite PU–0.5 wt.% CNTs. Adversely, the high decrease in the strength was attributed to the rise in PU foam content, which in turn was a result of an increase in mass loss. Coating PU was found to influence stress–strain behaviour due to the interaction between the soft segment and physical crosslinkers.

The thermophysical properties of the TPU matrix have shown two glass transition temperatures (T_g 's) corresponding to the soft and the hard segment. T_g for both segments is influenced by adding a small amount of tethered clay shifting temperature for hard and soft segments by 44 °C and 13 °C, respectively. Meanwhile, an increase of clay content from 1 to 5 wt.% results in increasing the thermal stability of the TPU matrix from 12 to 34 °C, respectively. The shifting temperature of TPU–CNF nanocomposites from 400 °C to 425 °C could be caused by experiencing 50% weight loss. The phase structure of PU dispersion investigated by DSC suggested enhancing properties such as thermal stability, solubility, and flexibility. The maximum piezoresistivity measured by the electrical conductivity of PU composites of 7.4 wt.% MWCNT could hit 10 S/m, reaching 92.92%.

The chemical structure of the PU–CNT composite has shown a degree of agglomeration which, under disruption of the sp² carbon structure, shows poor electrical conductivity. However, with expanded graphene loading at 5.7 wt.%, piezoresistivity could hit 10^{−1} S/m, less than 100 times than PU. Another composite, MWCNT (0.35 wt.%)/SiO₂ (0.2 wt.%)/PU, has shown excellent sound absorption of 80 dB compared to the PU foam sample. Recently, adding nanoparticles such as SiO₂, TiO₂, ZnO, Al₂O₃ results in improving the thermal stability of the polymer and enhancing scratch and abrasion resistance.

Author Contributions: The manuscript was written by T.A., A.A. and M.H.N. were the principal investigators, and A.H.K. was a co-investigator. This manuscript is known to all writers and they have agreed to its publication. All authors have read and agreed to the published version of the manuscript.

Funding: This research received no external funding.

Acknowledgments: This work was supported by the Universiti Kebangsaan Malaysia, Selangor, Malaysia.

Conflicts of Interest: The authors declare no conflict of interest.

References

- Shafeeq, V.; Unnikrishnan, G. Experimental and theoretical evaluation of mechanical, thermal and morphological features of EVA-millable polyurethane blends. *J. Polym. Res.* **2020**, *27*, 1–11. [CrossRef]
- Mocan, M.; Kamperman, M.; Leermakers, F.A. Microphase segregation of diblock copolymers studied by the self-consistent field theory of Scheutjens and Fleer. *Polymers* **2018**, *10*, 78. [CrossRef] [PubMed]
- Akram, N.; Zia, K.M.; Saeed, M.; Usman, M.; Saleem, S. Impact of macrodiols on the adhesion strength of polyurethane pressure-sensitive adhesives. *J. Appl. Polym. Sci.* **2018**, *135*, 46635. [CrossRef]
- Gomez, C.M.; Gutierrez, D.; Asensio, M.; Costa, V.; Nohales, A. Transparent thermoplastic polyurethanes based on aliphatic diisocyanates and polycarbonate diol. *J. Elastomers Plast.* **2017**, *49*, 77–95. [CrossRef]
- Parcheta, P.; Głowińska, E.; Datta, J. Effect of bio-based components on the chemical structure, thermal stability and mechanical properties of green thermoplastic polyurethane elastomers. *Eur. Polym. J.* **2020**, *123*, 109422. [CrossRef]
- Ikutegbe, C.A.; Farid, M.M. Application of phase change material foam composites in the built environment: A critical review. *Renew. Sustain. Energy Rev.* **2020**, *131*, 110008. [CrossRef]
- Xie, F.; Zhang, T.; Bryant, P.; Kurusingal, V.; Colwell, J.M.; Laycock, B. Degradation and stabilization of polyurethane elastomers. *Prog. Polym. Sci.* **2019**, *90*, 211–268. [CrossRef]
- Somarathna, H.M.; Raman, S.N.; Mohotti, D.; Mutalib, A.A.; Badri, K.H. The use of polyurethane for structural and infrastructural engineering applications: A state-of-the-art review. *Constr. Build. Mater.* **2018**, *190*, 995–1014. [CrossRef]
- Groover, M.P. *Fundamentals of Modern Manufacturing: Materials, Processes, and Systems*; John Wiley & Sons: Hoboken, NJ, USA, 2020.
- Abbasi, A.; Mir, M.S.; Ghasemi, I.; Shahrsvand, M. Shape memory performance of green in situ polymerized nanocomposites based on polyurethane/graphene nanoplatelets: Synthesis, properties, and cell behavior. *Polym. Compos.* **2018**, *39*, 4020–4033. [CrossRef]
- Utomo, R.N.C.; Li, W.-J.; Tiso, T.; Eberlein, C.; Doeker, M.; Heipieper, H.J.; Jupke, A.; Wierckx, N.; Blank, L.M. Defined Microbial Mixed Culture for Utilization of Polyurethane Monomers. *ACS Sustain. Chem. Eng.* **2020**, *8*, 17466–17474. [CrossRef]
- Zhu, S.; Chen, K.; Xu, J.; Li, J.; Mo, L. Bio-based polyurethane foam preparation employing lignin from corn stalk enzymatic hydrolysis residues. *RSC Adv.* **2018**, *8*, 15754–15761. [CrossRef]
- Saleh, S.; Yunus, N.Z.M.; Ahmad, K.; Ali, N. Improving the strength of weak soil using polyurethane grouts: A review. *Constr. Build. Mater.* **2019**, *202*, 738–752. [CrossRef]
- Athavale, S.P. *Hand Book of Pressure Sensitive Adhesives and Coatings: Pressure Sensitive Adhesives Technology*; Notion Press: Chennai, India, 2018.
- Kariduraganavar, M.Y.; Tambe, S.M.; Tasaganva, R.G.; Kittur, A.A.; Kulkarni, S.S.; Inamdar, S.R. Studies on nonlinear optical polyurethanes containing heterocyclic chromophores. *J. Mol. Struct.* **2011**, *987*, 158–165. [CrossRef]
- Shin, E.J.; Choi, S.M. Advances in waterborne polyurethane-based biomaterials for biomedical applications. *Novel Biomater. Regener. Med.* **2018**, *1077*, 251–283.
- Pant, B.; Park, M.; Ojha, G.P.; Kim, D.-U.; Kim, H.-Y.; Park, S.-J. Electrospun salicylic acid/polyurethane composite nanofibers for biomedical applications. *Int. J. Polym. Mater. Polym. Biomater.* **2018**, *67*, 739–744. [CrossRef]
- Gaaz, T.S.; Sulong, A.B.; Akhtar, M.N.; Raza, M.R. Morphology and tensile properties of thermoplastic polyurethane-halloysite nanotube nanocomposites. *Int. J. Autom. Mech. Eng.* **2015**, *12*, 2844–2856. [CrossRef]
- Maji, P.K.; Bhowmick, A.K. Structure–property correlation of polyurethane nanocomposites: Influence of loading and nature of nanosilica and microstructure of hyperbranched polyol. *J. Appl. Polym. Sci.* **2013**, *127*, 4492–4504. [CrossRef]
- Son, S.-H.; Lee, H.-J.; Kim, J.-H. Effects of carboxyl groups dissociation and dielectric constant on particle size of polyurethane dispersions. *Colloids Surf. A Physicochem. Eng. Asp.* **1998**, *133*, 295–301. [CrossRef]

21. Babaie, A.; Rezaei, M.; Sofla, R.L.M. Investigation of the effects of polycaprolactone molecular weight and graphene content on crystallinity, mechanical properties and shape memory behavior of polyurethane/graphene nanocomposites. *J. Mech. Behav. Biomed. Mater.* **2019**, *96*, 53–68. [CrossRef]
22. Jabbari, E.; Khakpour, M. Morphology of and release behavior from porous polyurethane microspheres. *Biomaterials* **2000**, *21*, 2073–2079. [CrossRef]
23. Grapski, J.A.; Cooper, S.L. Synthesis and characterization of non-leaching biocidal polyurethanes. *Biomaterials* **2001**, *22*, 2239–2246. [CrossRef]
24. Golling, F.E.; Pires, R.; Hecking, A.; Weikard, J.; Richter, F.; Danielmeier, K.; Dijkstra, D. Polyurethanes for coatings and adhesives—chemistry and applications. *Polym. Int.* **2019**, *68*, 848–855. [CrossRef]
25. Bhavsar, R.A.; Nehete, K.M. Rheological approach to select most suitable associative thickener for water-based polymer dispersions and paints. *J. Coat. Technol. Res.* **2019**, *16*, 1089–1098. [CrossRef]
26. Sanchis, M.; Calvo, O.; Fenollar, O.; Garcia, D.; Balart, R. Characterization of the surface changes and the aging effects of low-pressure nitrogen plasma treatment in a polyurethane film. *Polym. Test.* **2008**, *27*, 75–83. [CrossRef]
27. Marcano, A.; Fatyeyeva, K.; Koun, M.; Dubuis, P.; Grimme, M.; Marais, S. Recent developments in the field of barrier and permeability properties of segmented polyurethane elastomers. *Rev. Chem. Eng.* **2019**, *35*, 445–474. [CrossRef]
28. Hetflejš, J.; Šabata, S.; Podešva, J.; Kovářová, J.; Prokůpek, L.; Netopilík, M.; Spěvák, J.; Sýkora, J. Novel stabilisers acting simultaneously as molecular-weight regulators in soluble elastomeric polyurethanes. *Polym. Degrad. Stab.* **2010**, *95*, 579–586. [CrossRef]
29. Li, J.-W.; Lee, H.-T.; Tsai, H.-A.; Suen, M.-C.; Chiu, C.-W. Synthesis and Properties of Novel Polyurethanes Containing Long-Segment Fluorinated Chain Extenders. *Polymers* **2018**, *10*, 1292. [CrossRef]
30. Didenko, A.; Smirnova, V.E.; Popova, E.N.; Vaganov, G.V.; Kuznetsov, D.A.; Elokhovskii, V.; Ivanov, A.G.; Svetlichnyi, V.M.; Yudin, V.E.; Kudryavtsev, V.V. Heat Resistance and Dynamic Mechanical and Rheological Properties of a Blend of Crystallizing Polymers Polyimide and Copoly (urethane—imide), at Identical Chemical Structure of the Imide Blocks in the Initial Polymers. *Russ. J. Appl. Chem.* **2020**, *93*, 45–56. [CrossRef]
31. Zuo, M.; Takeichi, T. Preparation and characterization of poly (urethane–imide) films prepared from reactive polyimide and polyurethane prepolymer. *Polymer* **1999**, *40*, 5153–5160. [CrossRef]
32. Jouibari, I.S.; Haddadi-Asl, V.; Mirhosseini, M.M. A novel investigation on micro-phase separation of thermoplastic polyurethanes: Simulation, theoretical, and experimental approaches. *Iran. Polym. J.* **2019**, *28*, 237–250. [CrossRef]
33. Andrew, J.J.; Srinivasan, S.M.; Arockiarajan, A.; Dhakal, H.N. Parameters influencing the impact response of fiber-reinforced polymer matrix composite materials: A critical review. *Compos. Struct.* **2019**, *224*, 111007. [CrossRef]
34. Wang, S.; Liu, Z.; Zhang, L.; Guo, Y.; Song, J.; Lou, J.; Guan, Q.; He, C.; You, Z. Strong, detachable, and self-healing dynamic crosslinked hot melt polyurethane adhesive. *Mater. Chem. Front.* **2019**, *3*, 1833–1839. [CrossRef]
35. Xiang, D.; Zhang, X.; Li, Y.; Harkin-Jones, E.; Zheng, Y.; Wang, L.; Zhao, C.; Wang, P. Enhanced performance of 3D printed highly elastic strain sensors of carbon nanotube/thermoplastic polyurethane nanocomposites via non-covalent interactions. *Compos. Part. B Eng.* **2019**, *176*, 107250. [CrossRef]
36. Varnava, C.K.; Patrickios, C.S. Polymer Networks One Hundred Years after the Macromolecular Hypothesis: A Tutorial Review. *Polymer* **2020**, *215*, 123322. [CrossRef]
37. Szefer, E.; Stafin, K.; Leszczyńska, A.; Zając, P.; Hebda, E.; Raftopoulos, K.N.; Pieliowski, K. Morphology, dynamics, and order development in a thermoplastic polyurethane with melt blended POSS. *J. Polym. Sci. Part. B Polym. Phys.* **2019**, *57*, 1133–1142. [CrossRef]
38. Princi, E. *Rubber: Science and Technology*; Walter de Gruyter GmbH & Co KG.: Berlin, Germany, 2019.
39. Yuan, S.; Shen, F.; Chua, C.K.; Zhou, K. Polymeric composites for powder-based additive manufacturing: Materials and applications. *Prog. Polym. Sci.* **2019**, *91*, 141–168. [CrossRef]
40. Herzberger, J.; Sirrine, J.M.; Williams, C.B.; Long, T.E. Polymer design for 3D printing elastomers: Recent advances in structure, properties, and printing. *Prog. Polym. Sci.* **2019**, *97*, 101144. [CrossRef]
41. Solouki Bonab, V. *Polyurethane (PU) Nanocomposites Interplay of Composition Morphology and Properties*; Case Western Reserve University: Cleveland, OH, USA, 2019.
42. Asensio, M.; Costa, V.; Nohales, A.; Bianchi, O.; Gómez, C.M. Tunable structure and properties of segmented thermoplastic polyurethanes as a function of flexible segment. *Polymers* **2019**, *11*, 1910. [CrossRef]
43. Ren, M.; Zhou, Y.; Wang, Y.; Zheng, G.; Dai, K.; Liu, C.; Shen, C. Highly stretchable and durable strain sensor based on carbon nanotubes decorated thermoplastic polyurethane fibrous network with aligned wave-like structure. *Chem. Eng. J.* **2019**, *360*, 762–777. [CrossRef]
44. Lin, W.; Qu, J.-P. Enhancing impact toughness of renewable poly (lactic acid)/thermoplastic polyurethane blends via constructing cocontinuous-like phase morphology assisted by ethylene–methyl acrylate–glycidyl methacrylate copolymer. *Ind. Eng. Chem. Res.* **2019**, *58*, 10894–10907. [CrossRef]
45. Lu, F.; Liu, Y.; Wang, F.; Mai, Y.-l.; Li, D.-y. Effect of Organo-Modified Montmorillonite on the Morphology and Properties of SEBS/TPU Nanocomposites. *Polym. Eng. Sci.* **2020**, *60*, 850–859. [CrossRef]

46. Müller, K.; Bugnicourt, E.; Latorre, M.; Jorda, M.; Echegoyen, Y.; Lagaron, J.M.; Miesbauer, O.; Bianchin, A.; Hankin, S.; Bözl, U. Review on the processing and properties of polymer nanocomposites and nanocoatings and their applications in the packaging, automotive and solar energy fields. *Nanomaterials* **2017**, *7*, 74. [CrossRef]
47. Kim, K.-S.; Choi, S.B.; Kim, D.U.; Lee, C.-R.; Kim, J.-W. Photo-induced healing of stretchable transparent electrodes based on thermoplastic polyurethane with embedded metallic nanowires. *J. Mater. Chem. A* **2018**, *6*, 12420–12429. [CrossRef]
48. Kopal, I.; Harničárová, M.; Valíček, J.; Krmela, J.; Lukáč, O. Radial basis function neural network-based modeling of the dynamic thermo-mechanical response and damping behavior of thermoplastic elastomer systems. *Polymers* **2019**, *11*, 1074. [CrossRef]
49. Tehran, A.C.; Shelesh-Nezhad, K.; Barazandeh, F.J. Mechanical and thermal properties of TPU-toughened PBT/CNT nanocomposites. *J. Thermoplast. Compos. Mater.* **2019**, *32*, 815–830. [CrossRef]
50. Majdoub, M.; Essamlali, Y.; Amadine, O.; Ganetri, I.; Zahouily, M. Organophilic graphene nanosheets as a promising nanofiller for bio-based polyurethane nanocomposites: Investigation of the thermal, barrier and mechanical properties. *New J. Chem.* **2019**, *43*, 15659–15672. [CrossRef]
51. Joshi, M.; Adak, B.; Butola, B. Polyurethane nanocomposite based gas barrier films, membranes and coatings: A review on synthesis, characterization and potential applications. *Prog. Mater. Sci.* **2018**, *97*, 230–282. [CrossRef]
52. Adak, B.; Butola, B.S.; Joshi, M. Effect of organoclay-type and clay-polyurethane interaction chemistry for tuning the morphology, gas barrier and mechanical properties of clay/polyurethane nanocomposites. *Appl. Clay Sci.* **2018**, *161*, 343–353. [CrossRef]
53. Behnood, A.; Gharehveran, M.M. Morphology, rheology, and physical properties of polymer-modified asphalt binders. *Eur. Polym. J.* **2019**, *112*, 766–791. [CrossRef]
54. George, J.; Ishida, H. A review on the very high nanofiller-content nanocomposites: Their preparation methods and properties with high aspect ratio fillers. *Prog. Polym. Sci.* **2018**, *86*, 1–39. [CrossRef]
55. Mokhothu, T.H.; Mtibe, A.; Mokhena, T.C.; Mochane, M.J.; Ofosu, O.; Muniyasamy, S.; Tshifularo, C.A.; Motsoeneng, T.S. Mechanical, Thermal and Viscoelastic Properties of Polymer Composites Reinforced with Various Nanomaterials. In *Sustainable Polymer Composites and Nanocomposites*; Springer: Berlin, Germany, 2019; pp. 185–213.
56. Xu, J.; Cheng, L.; Zhang, Z.; Zhang, L.; Xiong, C.; Huang, W.; Xie, Y.; Yang, L. Highly exfoliated montmorillonite clay reinforced thermoplastic polyurethane elastomer: In situ preparation and efficient strengthening. *RSC Adv.* **2019**, *9*, 8184–8196. [CrossRef]
57. Chen, T.-K.; Tien, Y.-I.; Wei, K.-H. Synthesis and characterization of novel segmented polyurethane/clay nanocomposites. *Polymer* **2000**, *41*, 1345–1353. [CrossRef]
58. Gaaz, T.S.; Sulong, A.B.; Kadhum, A.A.H.; Nassir, M.H.; Al-Amiery, A.A. Surface improvement of halloysite nanotubes. *Appl. Sci.* **2017**, *7*, 291. [CrossRef]
59. Caminade, A.-M.; Beraa, A.; Laurent, R.; Delavaux-Nicot, B.; Hajjaji, M. Dendrimers and hyper-branched polymers interacting with clays: Fruitful associations for functional materials. *J. Mater. Chem. A* **2019**, *7*, 19634–19650. [CrossRef]
60. Oğuz, O.; Zanjani, J.S.M.; Soytaş, S.H.; Menciloğlu, Y.Z. *Specific Interactions and Self-Organization in Polymer/Functionalized Nanoparticle Systems, in Polymer Composites with Functionalized Nanoparticles*; Elsevier: Amsterdam, The Netherlands, 2019; pp. 85–117.
61. Suter, J.L.; Coveney, P.V. Chemically Specific Multiscale Modeling of the Shear-Induced Exfoliation of Clay–Polymer Nanocomposites. *ACS Omega* **2018**, *3*, 6439–6445. [CrossRef]
62. Uddin, F. *Montmorillonite: An Introduction to Properties and Utilization*; IntechOpen: London, UK, 2018.
63. Kuo, S.-W. *Hydrogen Bonding in Polymeric Materials*; John Wiley & Sons: Hoboken, NJ, USA, 2018.
64. Zhang, G.; Wu, T.; Lin, W.; Tan, Y.; Chen, R.; Huang, Z.; Yin, X.; Qu, J. Preparation of polymer/clay nanocomposites via melt intercalation under continuous elongation flow. *Compos. Sci. Technol.* **2017**, *145*, 157–164. [CrossRef]
65. Wang, X.-C.; Zhu, Q.-S.; Dong, B.-B.; Wu, H.-H.; Liu, C.-T.; Shen, C.-Y.; Turng, L.-S.; Geng, T. The effects of nanoclay and deformation conditions on the inelastic behavior of thermoplastic polyurethane foams. *Polym. Test.* **2019**, *79*, 106043. [CrossRef]
66. Yeh, S.-K.; Liu, Y.-C.; Chu, C.-C.; Chang, K.-C.; Wang, S.-F. Mechanical properties of microcellular and Nanocellular thermoplastic polyurethane nanocomposite foams created using supercritical carbon dioxide. *Ind. Eng. Chem. Res.* **2017**, *56*, 8499–8507. [CrossRef]
67. Amirikiai, A.; Panahi-Sarmad, M.; Sadeghi, G.M.M.; Arjmand, M.; Abrisham, M.; Dehghan, P.; Nazockdast, H. Microstructural design for enhanced mechanical and shape memory performance of polyurethane nanocomposites: Role of hybrid nanofillers of montmorillonite and halloysite nanotube. *Appl. Clay Sci.* **2020**, *198*, 105816. [CrossRef]
68. Bi, H.; Ren, Z.; Guo, R.; Xu, M.; Song, Y. Fabrication of flexible wood flour/thermoplastic polyurethane elastomer composites using fused deposition molding. *Ind. Crop. Prod.* **2018**, *122*, 76–84. [CrossRef]
69. Sheng, X.; Zhao, Y.; Zhang, L.; Lu, X. Properties of two-dimensional Ti₃C₂ MXene/thermoplastic polyurethane nanocomposites with effective reinforcement via melt blending. *Compos. Sci. Technol.* **2019**, *181*, 107710. [CrossRef]
70. Russo, P.; Acierno, D.; Marletta, G.; Destri, G.L. Tensile properties, thermal and morphological analysis of thermoplastic polyurethane films reinforced with multiwalled carbon nanotubes. *Eur. Polym. J.* **2013**, *49*, 3155–3164. [CrossRef]
71. Somarathna, H.; Raman, S.N.; Mohotti, D.; Mutalib, A.A.; Badri, K.H. Rate dependent tensile behavior of polyurethane under varying strain rates. *Constr. Build. Mater.* **2020**, *254*, 119203. [CrossRef]
72. Xu, W.J.; Wang, J.J.; Zhang, S.Y.; Sun, J.; Qin, C.X.; Dai, L.X. Tuning chain extender structure to prepare high-performance thermoplastic polyurethane elastomers. *RSC Adv.* **2018**, *8*, 20701–20711. [CrossRef]
73. Kemona, A.; Piotrowska, M. Polyurethane Recycling and Disposal: Methods and Prospects. *Polymers* **2020**, *12*, 1752. [CrossRef]

74. Członka, S.; Bertino, M.F.; Strzelec, K.; Strąkowska, A.; Masłowski, M. Rigid polyurethane foams reinforced with solid waste generated in leather industry. *Polym. Test.* **2018**, *69*, 225–237. [CrossRef]
75. Bil, M.; Ryszkowska, J.; Woźniak, P.; Kurzydłowski, K.J.; Lewandowska-Szumieł, M. Optimization of the structure of polyurethanes for bone tissue engineering applications. *Acta Biomater.* **2010**, *6*, 2501–2510. [CrossRef] [PubMed]
76. Liu, L.; Wang, Z. High performance nano-zinc amino-tris-(methylenephosphonate) in rigid polyurethane foam with improved mechanical strength, thermal stability and flame retardancy. *Polym. Degrad. Stab.* **2018**, *154*, 62–72. [CrossRef]
77. Zepp, R.; Ruggiero, E.; Acrey, B.; Davis, M.; Han, C.; Hsieh, H.-S.; Vilsmeier, K.; Wohlleben, W.; Sahle-Demessie, E. Fragmentation of polymer nanocomposites: Modulation by dry and wet weathering, fractionation, and nanomaterial filler. *Environ. Sci. Nano* **2020**, *7*, 1742–1758. [CrossRef]
78. Niu, Y.; Liu, G.; Fu, M.; Chen, C.; Fu, W.; Zhang, Z.; Xia, H.; Stadler, F.J. Designing a multifaceted bio-interface nanofiber tissue-engineered tubular scaffold graft to promote neo-vascularization for urethral regeneration. *J. Mater. Chem. B* **2020**, *8*, 1748–1758. [CrossRef]
79. Gupta, H.; Texter, J. Stimuli-Responsive Polyurethane Dispersions—Aqueous Auto-Dispersion. *Isr. J. Chem.* **2018**, *58*, 1338–1346. [CrossRef]
80. Pergal, M.V.; Balaban, M. Synthesis and structure–property relationships of biodegradable polyurethanes. In *Biodegradable Polymers: Recent Developments and New Perspectives*; IAPC Publishing: Zagreb, Croatia, 2017; Chapter 5.
81. Patil, A.M.; Jirimali, H.D.; Gite, V.V.; Jagtap, R.N. Synthesis and performance of bio-based hyperbranched polyol in polyurethane coatings. *Prog. Org. Coat.* **2020**, *149*, 105895. [CrossRef]
82. Xu, C.-A.; Qu, Z.; Tan, Z.; Nan, B.; Meng, H.; Wu, K.; Shi, J.; Lu, M.; Liang, L. High-temperature resistance and hydrophobic polysiloxane-based polyurethane films with cross-linked structure prepared by the sol-gel process. *Polym. Test.* **2020**, *86*, 106485. [CrossRef]
83. Arrieta, M.P.; Sessini, V.; Peponi, L. Biodegradable poly (ester-urethane) incorporated with catechin with shape memory and antioxidant activity for food packaging. *Eur. Polym. J.* **2017**, *94*, 111–124. [CrossRef]
84. Xu, Y.; Petrovic, Z.; Das, S.; Wilkes, G.L. Morphology and properties of thermoplastic polyurethanes with dangling chains in ricinoleate-based soft segments. *Polymer* **2008**, *49*, 4248–4258. [CrossRef]
85. Sarver, J.; Kiran, E. Foaming of Polymers with Carbon Dioxide—The year-in-review—2019. *J. Supercrit. Fluids* **2021**, *173*, 105166. [CrossRef]
86. Bocchio, J.A.; Escobar, M.M.; Amado, J.C.Q. Ablative properties of polyurethanes reinforced with organoclay. *Polym. Eng. Sci.* **2020**, *60*, 630–635. [CrossRef]
87. Magnin, A.; Pollet, E.; Phalip, V.; Avérous, L. Evaluation of biological degradation of polyurethanes. *Biotechnol. Adv.* **2020**, *39*, 107457. [CrossRef]
88. Arenas, J.P.; Castaño, J.L.; Troncoso, L.; Auad, M.L. Thermoplastic polyurethane/laponite nanocomposite for reducing impact sound in a floating floor. *Appl. Acoust.* **2019**, *155*, 401–406. [CrossRef]
89. Khalifa, M.; Anandhan, S.; Wuzella, G.; Lammer, H.; Mahendran, A.R. Thermoplastic polyurethane composites reinforced with renewable and sustainable fillers—A review. *Polym. Plast. Technol. Mater.* **2020**, *59*, 1751–1769. [CrossRef]
90. Sut, A.; Metzsch-Zilligen, E.; Großhauser, M.; Pfaendner, R.; Schartel, B. Rapid mass calorimeter as a high-throughput screening method for the development of flame-retarded TPU. *Polym. Degrad. Stab.* **2018**, *156*, 43–58. [CrossRef]
91. Aranguren, M.; González, J.; Mosiewicki, M. Biodegradation of a vegetable oil based polyurethane and wood flour composites. *Polym. Test.* **2012**, *31*, 7–15. [CrossRef]
92. Sazanova, T.S.; Otvagina, K.V.; Kryuchkov, S.S.; Zarubin, D.M. Fukina, D.G.; Vorotyntsev, A.V. Vorotyntsev, I.V. Revealing the Surface Effect on Gas Transport and Mechanical Properties in Nonporous Polymeric Membranes in Terms of Surface Free Energy. *Langmuir* **2020**, *36*, 12911–12921. [CrossRef] [PubMed]
93. Liu, C. *Development of Nanocomposites Based Sensors Using Molecular/Polymer/Nano-Additive Routes*; University of Dayton: Dayton, OH, USA, 2019.
94. Ionita, D.; Cristea, M.; Gaina, C. Prediction of polyurethane behaviour via time-temperature superposition: Meanings and limitations. *Polym. Test.* **2020**, *83*, 106340. [CrossRef]
95. Wen, Z.-B.; Liu, D.; Li, X.-Y.; Zhu, C.-H.; Shao, R.-F.; Visvanathan, R.; Clark, N.A.; Yang, K.-K.; Wang, Y.-Z. Fabrication of liquid crystalline polyurethane networks with a pendant azobenzene group to access thermal/photoresponsive shape-memory effects. *Acs Appl. Mater. Interfaces* **2017**, *9*, 24947–24954. [CrossRef]
96. Zhao, H.; She, W.; Shi, D.; Wu, W.; Zhang, Q.-C.; Li, R. Polyurethane/POSS nanocomposites for superior hydrophobicity and high ductility. *Compos. Part. B Eng.* **2019**, *177*, 107441. [CrossRef]
97. Oprea, S.; Timpu, D.; Oprea, V. Design-properties relationships of polyurethanes elastomers depending on different chain extenders structures. *J. Polym. Res.* **2019**, *26*, 1–15. [CrossRef]
98. Bhoiyate, S.; Ionescu, M.; Radojicic, D.; Kahol, P.K.; Chen, J.; Mishra, S.R.; Gupta, R.K. Highly flame-retardant bio-based polyurethanes using novel reactive polyols. *J. Appl. Polym. Sci.* **2018**, *135*, 46027. [CrossRef]
99. Vahabi, H.; Rastin, H.; Movahedifar, E.; Antoun, K.; Brosse, N.; Saeb, M.R. Flame retardancy of bio-based polyurethanes: Opportunities and challenges. *Polymers* **2020**, *12*, 1234. [CrossRef]
100. Tian, H.; Yao, Y.; Zhang, S.; Wang, Y.; Xiang, A. Enhanced thermal stability and flame resistance of rigid polyurethane-imide foams by varying copolymer composition. *Polym. Test.* **2018**, *67*, 68–74. [CrossRef]

101. De Sousa, J.M.; Couto, M.T.; Cassella, R.J. Polyurethane foam functionalized with phenylfluorone for online preconcentration and determination of copper and cadmium in water samples by flame atomic absorption spectrometry. *Microchem. J.* **2018**, *138*, 92–97. [CrossRef]
102. Mandru, M.; Bercea, M.; Gradinaru, L.M.; Ciobanu, C.; Drobotu, M.; Vlad, S.; Albulescu, R. Polyurethane/poly (vinyl alcohol) hydrogels: Preparation, characterization and drug delivery. *Eur. Polym. J.* **2019**, *118*, 137–145. [CrossRef]
103. Rajagopalan, M.; Darling, K.A.; Kale, C.; Turnage, S.A.; Koju, R.K.; Hornbuckle, B.C.; Mishin, Y.; Solanki, K.N. Nanotechnology enabled design of a structural material with extreme strength as well as thermal and electrical properties. *Mater. Today* **2019**, *31*, 10–20. [CrossRef]
104. Alemour, B.; Badran, O.; Hassan, M.R. A review of using conductive composite materials in solving lightning strike and ice accumulation problems in aviation. *J. Aerosp. Technol. Manag.* **2019**, *11*. [CrossRef]
105. Jiang, S.; Li, Q.; Zhao, Y.; Wang, J.; Kang, M. Effect of surface silanization of carbon fiber on mechanical properties of carbon fiber reinforced polyurethane composites. *Compos. Sci. Technol.* **2015**, *110*, 87–94. [CrossRef]
106. Khan, F.S.A.; Mubarak, N.M.; Khalid, M.; Walvekar, R.; Abdullah, E.C.; Ahmad, A.; Karri, R.R.; Pakalapati, H. Functionalized multi-walled carbon nanotubes and hydroxyapatite nanorods reinforced with polypropylene for biomedical application. *Sci. Rep.* **2021**, *11*, 1–10. [CrossRef]
107. Vaithyalingam, R.; Ansari, M.; Shanks, R.A. Recent advances in polyurethane-based nanocomposites: A review. *Polym. Plast. Technol. Eng.* **2017**, *56*, 1528–1541. [CrossRef]
108. Fu, S.; Sun, Z.; Huang, P.; Li, Y.; Hu, N. Some basic aspects of polymer nanocomposites: A critical review. *Nano Mater. Sci.* **2019**, *1*, 2–30. [CrossRef]
109. Singh, N.P.; Gupta, V.; Singh, A.P. Graphene and carbon nanotube reinforced epoxy nanocomposites: A review. *Polymer* **2019**, *180*, 121724. [CrossRef]
110. Aliyev, E.; Filiz, V.; Khan, M.M.; Lee, Y.J.; Abetz, C.; Abetz, V. Structural characterization of graphene oxide: Surface functional groups and fractionated oxidative debris. *Nanomaterials* **2019**, *9*, 1180. [CrossRef]
111. Jing, X.; Mi, H.-Y.; Peng, X.-F.; Turg, L.-S. Biocompatible, self-healing, highly stretchable polyacrylic acid/reduced graphene oxide nanocomposite hydrogel sensors via mussel-inspired chemistry. *Carbon* **2018**, *136*, 63–72. [CrossRef]
112. Sarno, M.; Scarpa, D.; Senatore, A.; Ahmed, W. rGO/GO Nanosheets in Tribology: From the State of the Art to the Future Prospective. *Lubricants* **2020**, *8*, 31. [CrossRef]
113. Wang, H.; He, Y.; Fei, G.; Wang, C.; Shen, Y.; Zhu, K.; Sun, L.; Rang, N.; Guo, D.; Wallace, G.G. Functionalizing graphene with titanate coupling agents as reinforcement for one-component waterborne poly (urethane-acrylate) anticorrosion coatings. *Chem. Eng. J.* **2019**, *359*, 331–343. [CrossRef]
114. Jun, Y.-S.; Park, M.G.; Um, J.G.; Habibpour, S.; Sy, S.; Park, C.B.; Yu, A. The conductivity of polydimethylsiloxane/graphene nano-ribbon foam composite with elongation. *Carbon* **2020**, *162*, 328–338. [CrossRef]
115. Costa, P.; Nunes-Pereira, J.; Oliveira, J.; Silva, J.; Moreira, J.A.; Carabineiro, S.A.C.; Buijnsters, J.G.; Lanceros-Mendez, S. High-performance graphene-based carbon nanofiller/polymer composites for piezoresistive sensor applications. *Compos. Sci. Technol.* **2017**, *153*, 241–252. [CrossRef]
116. Hsiao, S.-T.; Ma, C.-C.; Tien, H.-W.; Liao, W.-H.; Wang, Y.-S.; Li, S.-M.; Chuang, W.-P. Preparation and characterization of silver nanoparticle-reduced graphene oxide decorated electrospun polyurethane fiber composites with an improved electrical property. *Compos. Sci. Technol.* **2015**, *118*, 171–177. [CrossRef]
117. Chauhan, D.S.; Quraishi, M.A.; Ansari, K.R.; Saleh, T.A. Graphene and graphene oxide as new class of materials for corrosion control and protection: Present status and future scenario. *Prog. Org. Coat.* **2020**, *147*, 105741. [CrossRef]
118. Khun, N.; Frankel, G. Cathodic delamination of polyurethane/multiwalled carbon nanotube composite coatings from steel substrates. *Prog. Org. Coat.* **2016**, *99*, 55–60. [CrossRef]
119. Radhamani, A.; Lau, H.C.; Ramakrishna, S. Nanocomposite coatings on steel for enhancing the corrosion resistance: A review. *J. Compos. Mater.* **2020**, *54*, 681–701. [CrossRef]
120. Gaaz, T.S.; Sulong, A.B.; Kadhun, A.A.H.; Al-Amiery, A.A.; Nassir, M.H.; Jaaz, A.H. The impact of halloysite on the thermo-mechanical properties of polymer composites. *Molecules* **2017**, *22*, 838. [CrossRef]
121. Ren, X.; Wang, J.; Sun, G.; Zhou, S.; Liu, J.; Han, S. Effects of structural design including cellular structure precision controlling and sharp holes introducing on sound absorption behavior of polyimide foam. *Polym. Test.* **2020**, *84*, 106393. [CrossRef]
122. Fediuk, R.; Amran, M.; Vatin, N.; Vasilev, Y.; Lesovik, V.; Ozbakkaloglu, T. Acoustic Properties of Innovative Concretes: A Review. *Materials* **2021**, *14*, 398. [CrossRef]
123. Liu, L.; Xu, Y.; Li, S.; Xu, M.; He, Y.; Shi, Z.; Li, B. A novel strategy for simultaneously improving the fire safety, water resistance and compatibility of thermoplastic polyurethane composites through the construction of biomimetic hydrophobic structure of intumescent flame retardant synergistic system. *Compos. Part. B Eng.* **2019**, *176*, 107218. [CrossRef]
124. Yuvaraj, L.; Jeyanthi, S.; Kadam, D.D.; Ajai, R.G. Influence of Magnesium Hydroxide Fillers on Acoustic, Thermal, and Flame Retardant Properties of Pu Foam. *Trends Manuf. Eng. Manag.* **2021**, *208*, 393–408.
125. Orfali, W.A. Acoustic properties of polyurethane composition reinforced with carbon nanotubes and silicon oxide nano-powder. *Phys. Procedia* **2015**, *70*, 699–702. [CrossRef]

126. Lagos-Varas, M.; Movilla-Quesada, D.; Arenas, J.P.; Raposeiras, A.C.; Castro-Fresno, D.; Calzada-Pérez, M.A.; Vega-Zamanillo, A.; Maturana, J. Study of the mechanical behavior of asphalt mixtures using fractional rheology to model their viscoelasticity. *Constr. Build. Mater.* **2019**, *200*, 124–134. [CrossRef]
127. El Saeed, A.M.; El-Fattah, M.A.; Azzam, A.M. Synthesis of ZnO nanoparticles and studying its influence on the antimicrobial, anticorrosion and mechanical behavior of polyurethane composite for surface coating. *Dye. Pigment.* **2015**, *121*, 282–289. [CrossRef]
128. Bar-Cohen, Y. Electroactive polymers: Current capabilities and challenges. In *Smart Structures and Materials 2002: Electroactive Polymer Actuators and Devices (EAPAD)*; SPIE's 9th Annual International Symposium on Smart Structures and Materials; International Society for Optics and Photonics: San Diego, CA, USA, 2002.
129. Thompson, D.G.; Osborn, J.C.; Kober, E.M.; Schoonover, J.R. Effects of hydrolysis-induced molecular weight changes on the phase separation of a polyester polyurethane. *Polym. Degrad. Stab.* **2006**, *91*, 3360–3370. [CrossRef]
130. Nemati, S.; Kim, S.-j.; Shin, Y.M.; Shin, H. Current progress in application of polymeric nanofibers to tissue engineering. *Nano Converg.* **2019**, *6*, 1–16. [CrossRef]
131. Defonseka, C. *Two-Component Polyurethane Systems: Innovative Processing Methods*; Walter de Gruyter GmbH & Co KG.: Berlin, Germany, 2019.
132. Zhang, H.; Zhang, F.; Wu, Y. Robust stretchable thermoplastic polyurethanes with long soft segments and steric semisymmetric hard segments. *Ind. Eng. Chem. Res.* **2020**, *59*, 4483–4492. [CrossRef]
133. De Avila Delucis, R.; Magalhães, W.L.E.; Petzhold, C.L.; Amico, S.C. Forest-based resources as fillers in biobased polyurethane foams. *J. Appl. Polym. Sci.* **2018**, *135*, 45684. [CrossRef]
134. Li, J.W.; Cheng, Y.-H.; Lee, H.-T.; Wang, C.-C.; Chiu, C.-W.; Suen, M.-C. Synthesis and properties of castor oil-based polyurethane containing short fluorinated segment. *J. Appl. Polym. Sci.* **2020**, *137*, 49062. [CrossRef]
135. Dai, M.; Wang, J.; Zhang, Y. Improving water resistance of waterborne polyurethane coating with high transparency and good mechanical properties. *Colloids Surf. A Physicochem. Eng. Aspects* **2020**, *601*, 124994. [CrossRef]
136. Oveissi, F.; Naficy, S.; Le, T.Y.L.; Fletcher, D.F.; Dehghani, F. Tough hydrophilic polyurethane-based hydrogels with mechanical properties similar to human soft tissues. *J. Mater. Chem. B* **2019**, *7*, 3512–3519. [CrossRef]
137. Verma, G. Weathering, salt spray corrosion and mar resistance mechanism of clay (nano-platelet) reinforced polyurethane nanocomposite coatings. *Prog. Org. Coat.* **2019**, *129*, 260–270. [CrossRef]
138. Furtwengler, P.; Avérous, L. Renewable polyols for advanced polyurethane foams from diverse biomass resources. *Polym. Chem.* **2018**, *9*, 4258–4287. [CrossRef]
139. Ulbricht, M. Advanced functional polymer membranes. *Polymer* **2006**, *47*, 2217–2262. [CrossRef]
140. Sarkar, D. *Development and Characterization of L-Tyrosine Based Polyurethanes for Tissue Engineering Applications*; University of Akron: Akron, OH, USA, 2007.
141. Barz, J.; Haupt, M.; Oehr, C.; Hirth, T.; Grimmer, P. Stability and water wetting behavior of superhydrophobic polyurethane films created by hot embossing and plasma etching and coating. *Plasma Process. Polym.* **2019**, *16*, 1800214. [CrossRef]
142. Datta, J.; Kasprzyk, P. Thermoplastic polyurethanes derived from petrochemical or renewable resources: A comprehensive review. *Polym. Eng. Sci.* **2018**, *58*, E14–E35. [CrossRef]
143. Eling, B.; Tomović, Ž.; Schädler, V. Current and future trends in polyurethanes: An industrial perspective. *Macromol. Chem. Phys.* **2020**, *221*, 2000114. [CrossRef]
144. Kaur, G.; Pavia, S. Physical properties and microstructure of plastic aggregate mortars made with acrylonitrile-butadiene-styrene (ABS), polycarbonate (PC), polyoxymethylene (POM) and ABS/PC blend waste. *J. Build. Eng.* **2020**, *31*, 101341. [CrossRef]
145. Lee, C.-F.; Chen, C.-W.; Rwei, S.-P.; Chuang, F.-S. Thermal Behavior and Morphology of Thermoplastic Polyurethane Derived from Different Chain Extenders of 1, 3-and 1, 4-Butanediol. *Appl. Sci.* **2021**, *11*, 698. [CrossRef]
146. Ospina, A.C.; Orozco, V.H.; Giraldo, L.F.; Fuensanta, M.; Martín-Martínez, J.M.; Mateo-Oliveras, N. Study of waterborne polyurethane materials under aging treatments. Effect of the soft segment length. *Prog. Org. Coat.* **2020**, *138*, 105357. [CrossRef]
147. Nishiyama, Y.; Kumagai, S.; Motokucho, S.; Kameda, T.; Saito, Y.; Watanabe, A.; Nakatani, H.; Yoshioka, T. Temperature-dependent pyrolysis behavior of polyurethane elastomers with different hard-and soft-segment compositions. *J. Anal. Appl. Pyrolysis* **2020**, *145*, 104754. [CrossRef]
148. Zhang, Z.P.; Rong, M.Z.; Zhang, M.Q. Polymer engineering based on reversible covalent chemistry: A promising innovative pathway towards new materials and new functionalities. *Prog. Polym. Sci.* **2018**, *80*, 39–93. [CrossRef]
149. Ourique, P.A.; Ornaghi, F.G.; Ornaghi, H.L.; Wanke, C.H.; Bianchi, O. Thermo-oxidative degradation kinetics of renewable hybrid polyurethane-urea obtained from air-oxidized soybean oil. *J. Therm. Anal. Calorim.* **2019**, *137*, 1969–1979. [CrossRef]
150. Wang, F.; Liu, J.; Yu, Q. Synthesis and characterization of poly (siloxane-ether-urethane) copolymers. *Colloid Polym. Sci.* **2017**, *295*, 1243–1249. [CrossRef]
151. Griffin, M.; Castro, N.; Bas, O.; Saifzadeh, S.; Butler, P.; Hutmacher, D.W. The current versatility of polyurethane three-dimensional printing for biomedical applications. *Tissue Eng. Part. B Rev.* **2020**, *26*, 272–283. [CrossRef]
152. Javaid, M.A.; Rizwan, M.; Khera, R.A.; Zia, K.M.; Saito, K.; Zuber, M.; Iqbal, J.; Langer, P. Thermal degradation behavior and X-ray diffraction studies of chitosan based polyurethane bio-nanocomposites using different diisocyanates. *Int. J. Biol. Macromol.* **2018**, *117*, 762–772. [CrossRef]

153. Yamane, S.; Watanabe, R.; Ata, S.; Mizukado, J.; Shinzawa, H. Solvent-induced degradation of polyurethane studied by two-dimensional (2D) infrared (IR) correlation spectroscopy. *Vib. Spectrosc.* **2020**, *108*, 103062. [CrossRef]
154. Khadivi, P.; Salami-Kalajahi, M.; Roghani-Mamaqani, H.; Sofla, R.L.M. Polydimethylsiloxane-based Polyurethane/cellulose Nanocrystal Nanocomposites: From Structural Properties Toward Cytotoxicity. *Silicon* **2021**, 1–9. [CrossRef]
155. Liu, C.-H.; Lee, H.-T.; Tsou, C.-H.; Wang, C.-C.; Gu, J.-H.; Suen, M.-C. Preparation and characterization of biodegradable polyurethane composites containing oyster shell powder. *Polym. Bull.* **2020**, *77*, 3325–3347. [CrossRef]
156. Xiong, J.; Liu, Y.; Yang, X.; Wang, X. Thermal and mechanical properties of polyurethane/montmorillonite nanocomposites based on a novel reactive modifier. *Polym. Degrad. Stab.* **2004**, *86*, 549–555. [CrossRef]

Review

Clay-Based Polymer Nanocomposites: Essential Work of Fracture

Edgar Adrian Franco-Urquiza 

National Council for Science and Technology (CONACYT—CIDESI), Center for Engineering and Industrial Development, Carretera Estatal 200, km 23, Querétaro 76265, Mexico; edgar.franco@cidesi.edu.mx

Abstract: This work details the general structure of the clays used as a reinforcement phase in polymer nanocomposites. Clays are formed by the molecular arrangement of atomic planes described through diagrams to improve their visualization. The molecular knowledge of clays can facilitate the selection of the polymer matrix and achieve a suitable process to obtain clay-based polymer nanocomposite systems. This work highlights the development of polymer nanocomposites using the melt intercalation method. The essential work of fracture (EWF) technique has been used to characterize the fracture behavior of materials that show ductility and where complete yielding of the ligament region occurs before the crack propagation. In this sense, the EWF technique characterizes the post-yielding fracture mechanics, determining two parameters: the specific essential work of fracture (w_e), related to the surface where the actual fracture process occurs, and the specific non-essential work of fracture (w_p), related to the plastic work carried out in the outer zone of the fracture zone. The EWF technique has been used successfully in nano-reinforced polymers to study the influence of different variables on fracture behavior. In this work, the fundamentals of the EWF technique are described, and some examples of its application are compiled, presenting a summary of the most relevant contributions in recent years.

Citation: Franco-Urquiza, E.A. Clay-Based Polymer Nanocomposites: Essential Work of Fracture. *Polymers* **2021**, *13*, 2399. <https://doi.org/10.3390/polym13152399>

Academic Editors: Somen K. Bhudolia and Sunil Chandrakant Joshi

Received: 20 May 2021
Accepted: 15 June 2021
Published: 22 July 2021

Publisher's Note: MDPI stays neutral with regard to jurisdictional claims in published maps and institutional affiliations.



Copyright: © 2021 by the author. Licensee MDPI, Basel, Switzerland. This article is an open access article distributed under the terms and conditions of the Creative Commons Attribution (CC BY) license (<https://creativecommons.org/licenses/by/4.0/>).

Keywords: EWF; polymer-layered silicates; oMMT; clay minerals; mechanical properties

1. Introduction

Thermoplastic polymers are commonly reinforced with inorganic fillers to improve various properties and reduce costs. Conventional inorganic fillers include talc, calcium carbonate, silica, mica, among others. Achieving a significant improvement in the properties of the reinforced polymer often requires incorporating a relatively large amount of filler, which leads to a loss of transparency and increases the volume and density of the polymers. Depending on the dimensions of the phases involved, the particle-filled polymers are classified as microcomposites. However, the technological demand in innovation and materials engineering allows the constant development of polymers reinforced with inorganic particles to increase their mechanical resistance and integrate other functionalities such as thermal conductivity, heat capacity, thermal diffusion, and self-healing [1].

This review collects information on the influence of clay minerals on the fracture behavior of ductile nanocomposites, employing the essential work of fracture (EWF) approach and focusing on the process-properties relationship. There is extensive literature on the structure and characterization of clay minerals. However, studies on relevant aspects such as the arrangement of atomic planes, which are results of interest for the preparation of clay-based polymer nanocomposite systems, have not been published. On the other hand, the influence of clay minerals on the ductile fracture behavior of polymer nanocomposites has not been fully explored, and this is the gap that this review intends to cover.

Although vast amounts of information about clay-based polymer nanocomposite systems is available, this review aims to disseminate knowledge in a very didactic way. Therefore, it is addressed primarily at graduate students entering the exciting field of developing new clay-based polymer nanocomposite systems.

2. Clay-Based Polymer Nanocomposites

Clay-based polymer nanocomposites are often referred to as polymer layered silicates, nanostructured polymers, or simply polymer nanocomposites. These polymers are reinforced with inorganic particles containing at least one dimension in the nanometric scale (<100 nm). Compared to traditional composites (macro- or microscale), polymer nanocomposites offer the opportunity to explore new behaviors and functionalities beyond conventional polymers. Nanoparticles often strongly influence the mechanical properties of polymers in very low volume fractions due to the relatively short distance between nanoparticles, molecular compatibility, and interfacial interaction between the particles and the polymer chains.

Clay minerals are known as phyllosilicates, or lamellar silicates, which are the inorganic particles most commonly used to prepare clay-based polymer nanocomposites [2–4]. It is necessary to highlight that the clay particles are not by themselves nanometric scale particles, but instead that they are formed by the stacking of several layers that leads to the development of irregular aggregates, as schematized in Figure 1. Each layer has a high aspect ratio between 100 and 800 nm in length and approximately 1 nm in thickness. Its uniform dispersion within the polymer matrix favors developing a very high interfacial area per unit volume, which is the primary reinforcement mechanism of clay-based polymer nanocomposites. However, the layer dispersion mechanism is complex since different aspects must be considered, and that is why the specialized literature focuses on evaluating processing conditions to achieve the maximum level of dispersion [2,5–8].

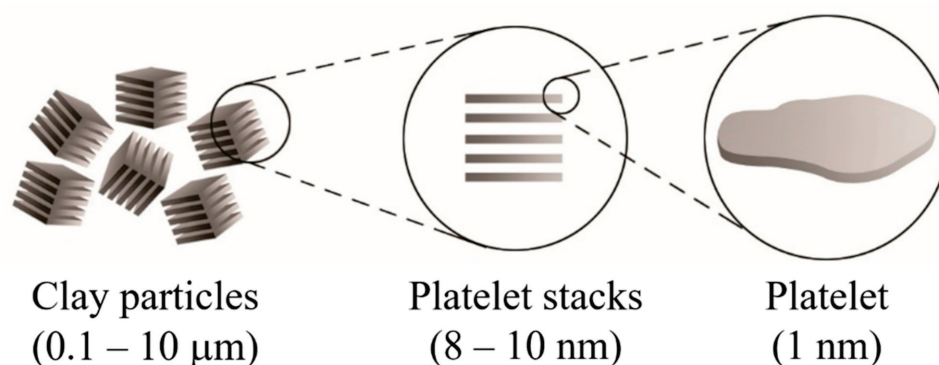


Figure 1. Schematic representation of the arrangement of the platelet stacks that conform to the clay particles.

Clay layers have a molecular structure based on the stacking sequence. Interesting and complete information is available on the web page of Professor Dorronsoro Fernández from the University of Granada, Spain (Department of Soil Science and Agricultural Chemistry, <https://www.edafologia.net/>, last visited 12 May 2021).

The basic compositional unit is the silicon–oxygen (Si–O) tetrahedron, as outlined in Figure 2a. It consists of one silicon cation (Si^{+4}) surrounded by four oxygen anions (O^{-2}). Chemically, the Si–O tetrahedron has a net electrical charge of -4 , $(\text{SiO}_4)^{-4}$, so it is balanced by adding other cations to neutralize their charges (Figure 3a). For this, each vertex of the basal plane belongs to two tetrahedra, since each oxygen is in coordination with two silicones, forming tetrahedral layers distributed under the configuration of hexagons, as can be seen in detail in Figure 4. Sheet silicates (also called layered silicates or phyllosilicates) are obtained when three oxygens on each tetrahedron link to other tetrahedra to form tetrahedral planes.

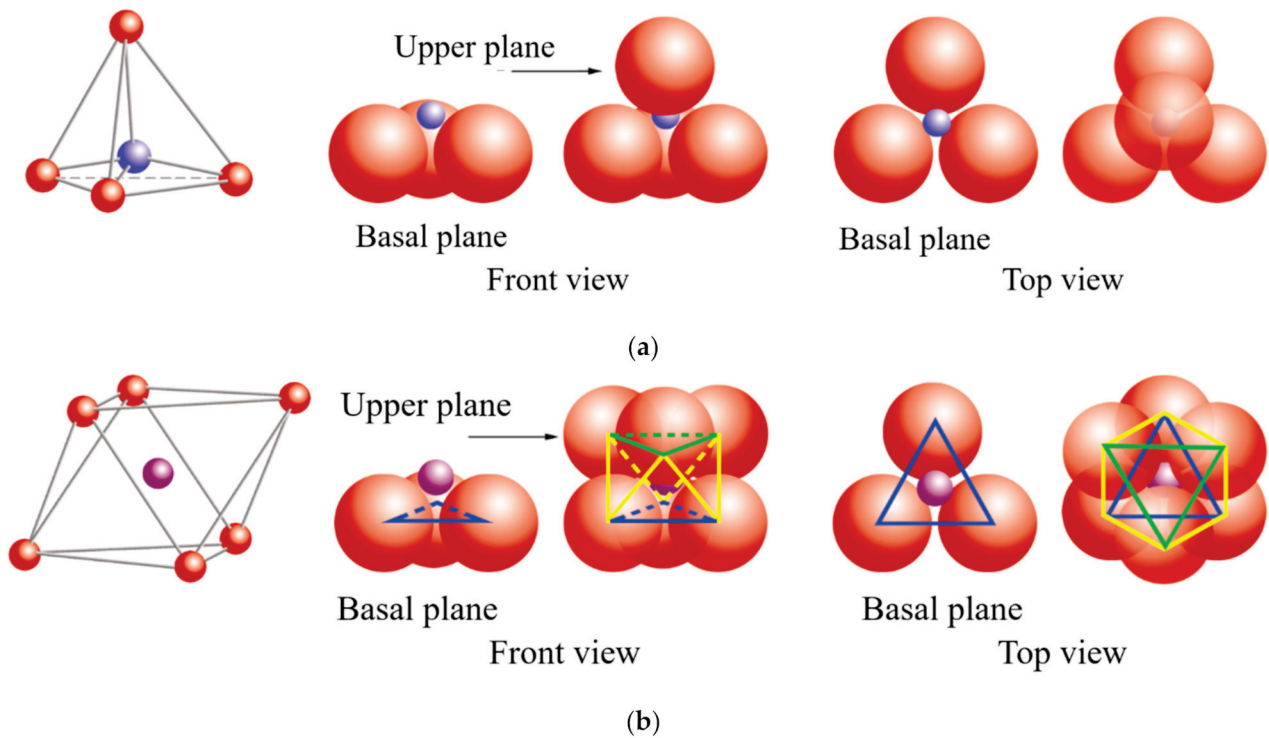


Figure 2. Schematic representation: (a) silicon tetrahedron, (b) magnesium and/or aluminum octahedron. In both cases, a general diagram is presented, a front view and a top view. ● oxygen, ● silicon, ● magnesium/aluminum. Adapted from <https://www.edafologia.net/>, last visited 12 May 2021.

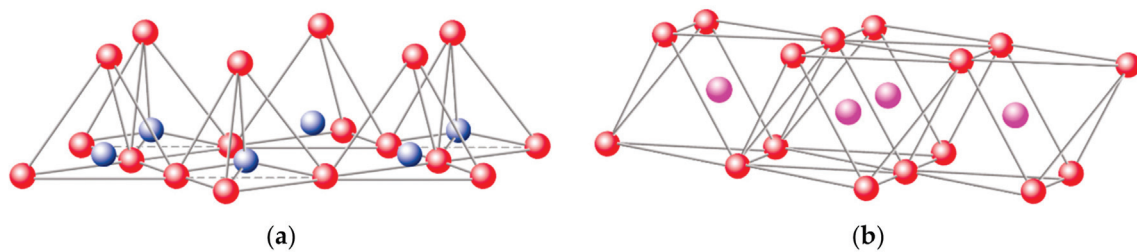


Figure 3. Schematic representation of the structural layers of clays: (a) silicon tetrahedron, (b) magnesium and/or aluminum octahedron. ● oxygen, ● silicon, ● magnesium/aluminum. Adapted from <https://www.edafologia.net/>, last visited 12 May 2021.

Sheet silicates are planar structures containing different kinds of layer that can accommodate cations of all sizes. Tetrahedral layers (labeled T in this work) consist primarily of SiO_4 tetrahedra. Octahedral layers (labeled O in this work) contain divalent and trivalent cations (Mg^{2+} or Al^{3+}) in 6-fold coordination, where each octahedron is supported on one of its faces, which represents the octahedral basal plane, as schematized in Figure 2b. Octahedral sheets are composed of individual octahedra that share edges composed of oxygen and hydroxyl anion groups, with Mg or Al typically serving as the coordinating cation, as presented in Figure 3b. In two dimensions, anions can fit together in symmetrical patterns to form hexagonal patterns (Figure 4).

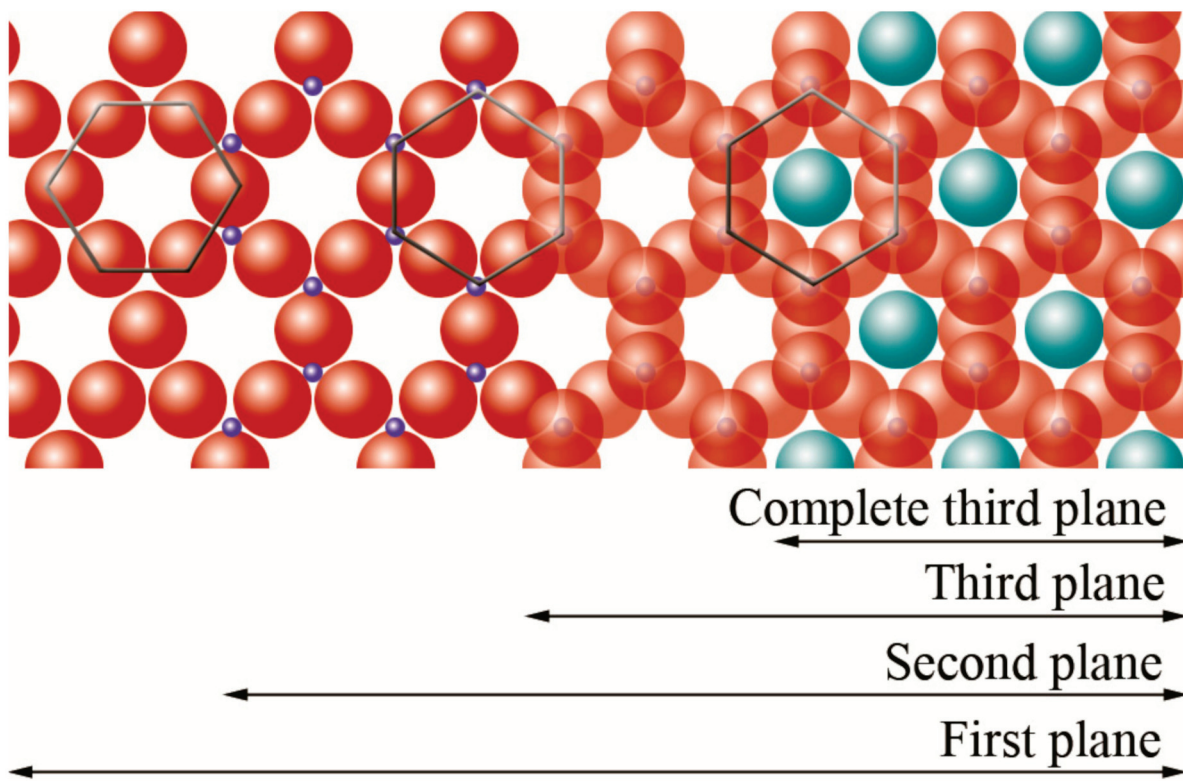


Figure 4. Schematic representation from the top view of the planes formed by the union of tetrahedral and octahedral layers. ● oxygen, ● silicon, ● hydroxyl groups. Adapted from <https://www.edafologia.net/>, last visited 12 May 2021.

In three dimensions, tetrahedral (T) and octahedral (O) layers may stack in various ways. The arrangement of both layers can be better understood if they are represented through atomic planes, as outlined in Figure 5.

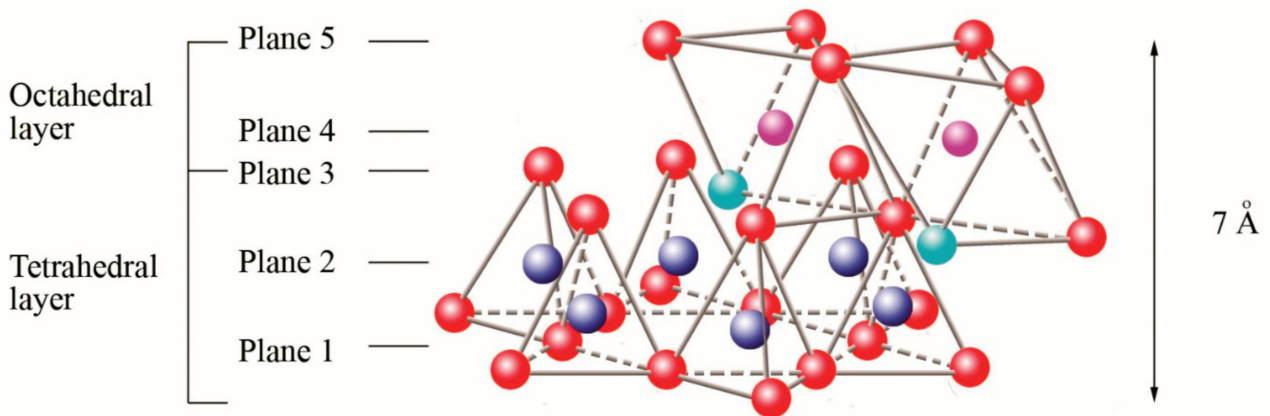


Figure 5. Schematic representation of the final structure corresponding to sheet 1:1. ● oxygen, ● silicon, ● magnesium/aluminum, ● hydroxyl groups. Adapted from [9].

The first plane corresponds to the basal plane of the tetrahedral layer. Silicon atoms are placed in the second plane, occupying part of the space in the basal plane of each tetrahedron (Figure 4). In a third plane, the unshared oxygens (also called apical oxygen) are located just above the silicon, ending up occupying the remaining space, as depicted in Figure 4. In this way, the arrangement of these three planes constitutes the fundamental unit of the tetrahedral layers (Figure 5).

The union between tetrahedral and octahedral sheets occurs with the apical oxygen, linked to Mg^{2+} or octahedral Al^{3+} . However, not all the vertices of the octahedral basal plane, formed in part by the apical oxygen, would be shared with the silicon atoms contained in the tetrahedra, so the charge balance occurs when they bind to a hydrogen atom (H), forming hydroxyl groups (OH), as shown in Figures 4 and 5. Thus, the basal plane of the octahedron forms part of the superior plane of the tetrahedra and completes the third plane. It should be noted that all planes represent a hexagonal lattice, while the third plane forms a centered hexagonal lattice, as shown in Figure 4.

The fourth plane consists of the arrangement of octahedral Mg^{2+} or Al^{3+} atoms. These atoms are located in the small free spaces left by every two apical oxygens and one OH group, as shown in Figure 6.

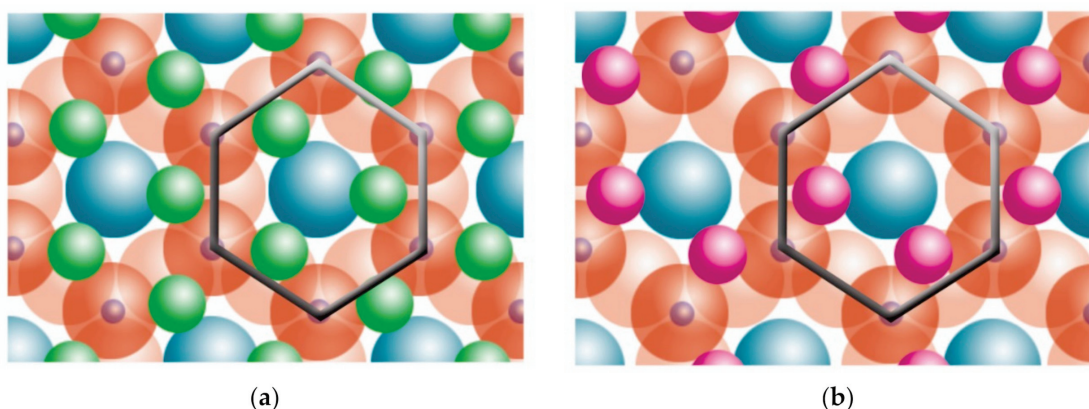


Figure 6. Schematic representation from the top view of the planes: (a) trioctahedral, (b) dioctahedral. ● oxygen, ● silicon, ● magnesium, ● aluminum, ● hydroxyl groups. Adapted from <https://www.edafologia.net/>, last visited 12 May 2021.

The octahedral Mg^{2+} covers all positions in the trioctahedral plane (Figure 6a). However, the octahedral Al^{3+} covers just two positions of three vacancies, and it is called the dioctahedral plane (Figure 6b). Nonetheless, this plane is within hexagonal networks.

The fifth plane corresponds to the superior plane of the octahedra (showed in Figure 5). If the structure ends in this plane, the clay has a T:O sequence (also known as 1:1 structure). However, if another tetrahedral layer is added, a sandwich-type T:O:T sequence is formed. The 1:1 sheet silicate is 7 Å thick, while the 2:1 sheet silicate is about 9 Å thick (Figure 7). Thus, the sheet silicates originate from the stacking of parallel planes with hexagonal symmetries, alternating the planes of ions (O and OH) and cations (Si^{4+} , Al^{3+} , and Mg^{2+}).

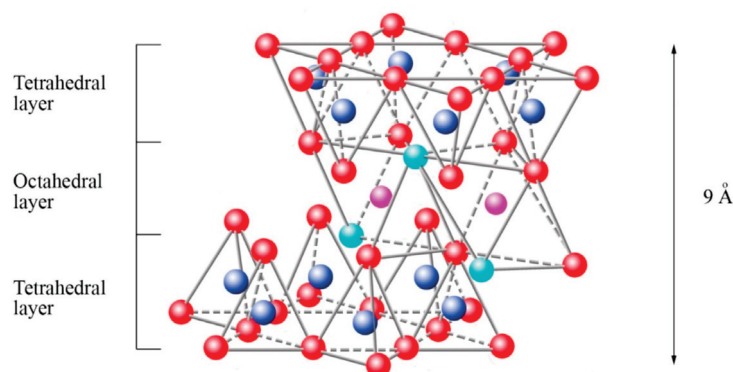


Figure 7. Schematic representation of the final structure corresponding to sheet 2:1. ● oxygen, ● silicon, ● magnesium/aluminum, ● hydroxyl groups. Adapted from <https://www.edafologia.net/>, last visited 12 May 2021.

Most sheet silicates are monoclinic or triclinic, and have several different polymorphs related to how T:O:T and T:O sheets stack to each other. Figure 8 shows a representative diagram of the 1:1 and 2:1 sheet silicates to better visualize the structural arrangement described. Table 1 shows the classification of clay minerals according to their structural configuration.

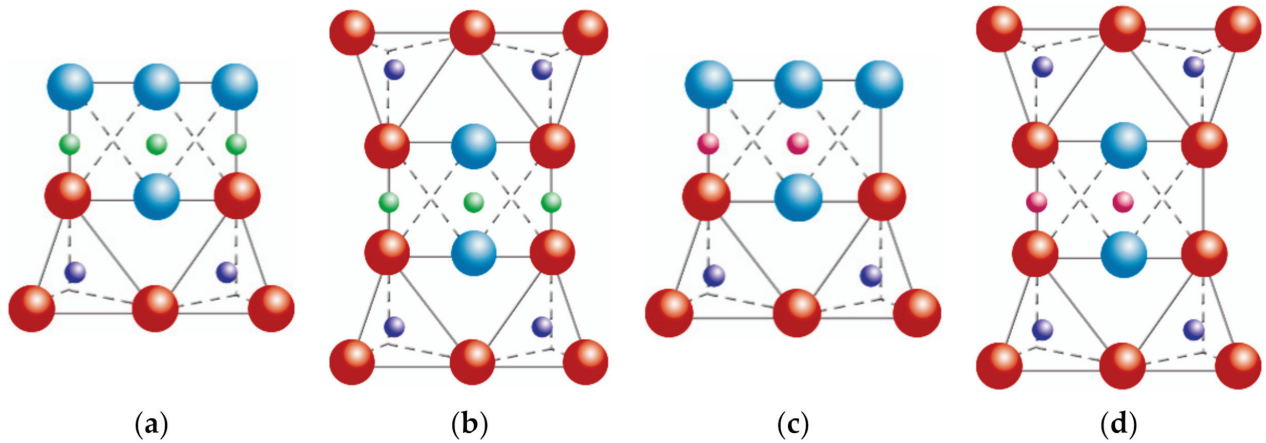


Figure 8. Schematic representation of the arrangement of the atomic planes: (a) 1:1 trioctahedral sheets, (b) 2:1 trioctahedral sheets, (c) 1:1 dioctahedral sheets, (d) 2:1 dioctahedral sheets. ● oxygen, ● silicon, ● magnesium/aluminum, ● hydroxyl groups. Adapted from <https://www.edafologia.net/>, last visited 12 May 2021.

Table 1. Classification of clay minerals.

Structure	Dioctahedral	Trioctahedral
T:O	Kaolinite group [10–26] Pyrophyllite	Serpentine group [27–29] Talc
	Montmorillonite [45–77] Beidellite Nontronite	Smeectite group [30–44] Saponite Hectorite Stevensite
T:O:T	Muscovite Paragonite	Vermiculite group [14,78–82] Illite Mica group [81,83–126] Biotite Phlogopite Lepidolite
	Paligorskite	Chlorite group [127–135] Sepiolite

Montmorillonite (discovered by Damour and Salvetat in Montmorillon, France) is currently the most widely used mineral clay to prepare polymer nanocomposites. It is a smectite-type clay belonging to the 2:1 sheet silicates and is composed of aluminosilicates (Al^{3+}). Montmorillonite clay has a high reaction capacity, exceptional resistance, and a large aspect ratio.

2.1. Cation Exchange Capacity

The ability to absorb a certain amount of cations and retain them in an exchangeable state is known as the cation exchange capacity (CEC), expressed in terms of milliequivalents per 100 g (meq/100 g) [Formatting Citation]. The charge of the layer is not locally constant as it varies from layer to layer and must instead be considered an average value over the whole crystal. The importance of knowing the CEC is that the sheets are not electrically neutral due to isomorphous substitutions, where others replace cations such as Si^{4+} with a

lower charge (Al^{3+}), promoting an excess of negative charge. In this case, the load balance is maintained by the presence of individual cations (as in the micas group) or hydrated cations (as in the case of vermiculites and smectites) in the interlaminar space, which is the existing space between two consecutive sheets, also known as “galleries” (Figure 9a). When the hydrated cations are ion-exchanged with organic cations such as more bulky alkylammonium, it usually results in a larger interlayer spacing.

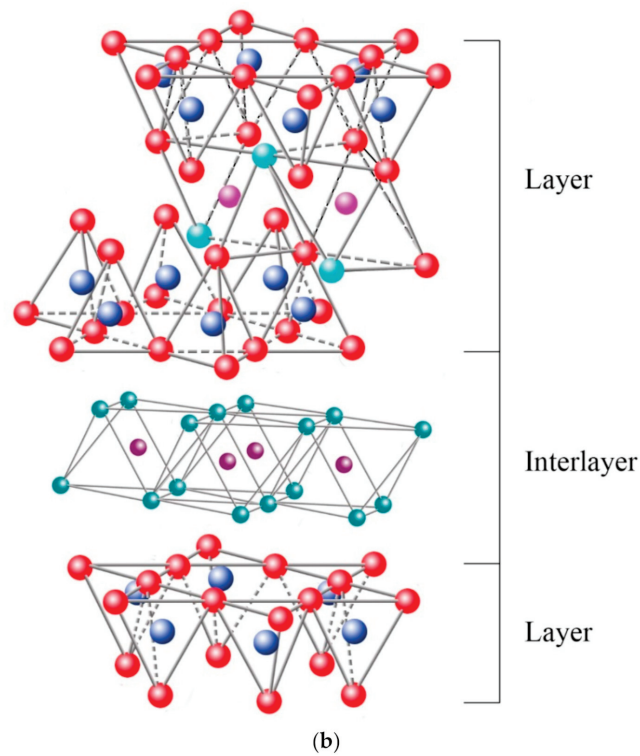
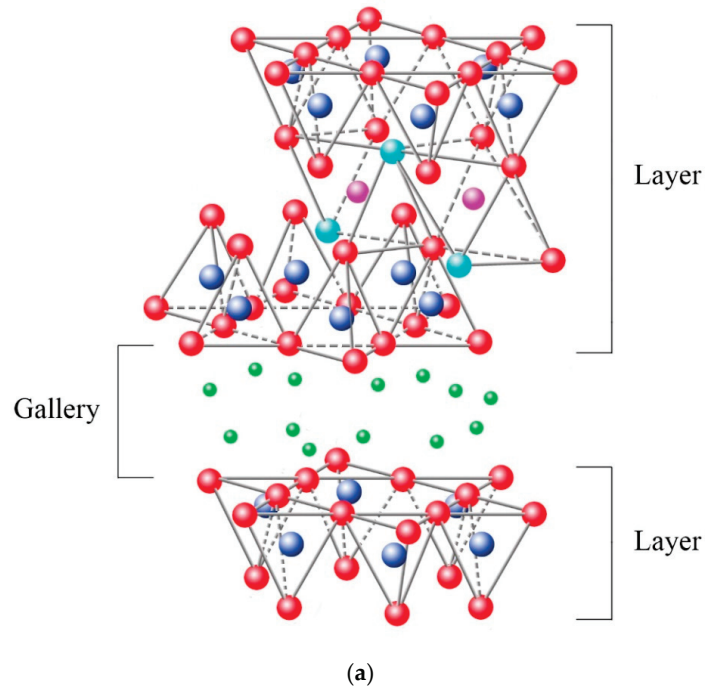


Figure 9. Schematic representation of the clay structure whose charge balance is maintained by: (a) inter-change cations, (b) interlaminar octahedral layer. ● oxygen, ● silicon, ● magnesium/aluminum, ● hydroxyl groups. Schematic sketch based on Beyer [136] with permission from Elsevier.

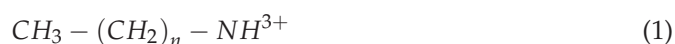
Among the most frequent interlamellar cations are alkalines (Na^+ and K^+) and alkaline earth (Mg^{2+}). The hydrated cations such as water and different polar liquids increase the interlamellar space by swelling effect. If the interlamellar cations coordinate with OH groups, an octahedral layer would be formed within the interlamellar space (as chlorites, Table 1), developing structures T:O:T:o or 2:1:1, as represented in Figure 9b. In this case, the number 2 represents the two tetrahedral layers, while 1:1 indicates that the layers of the octahedra differ from each other since the interlamellar octahedra do not share vertices with the tetrahedra.

The bonding forces that join the sheets with the interlayer are weaker than those existing between the ions of the same sheet, so the phyllosilicates have a clear parallel direction of exfoliation.

2.2. Coupling Agents

In the first instance, clay minerals can only be miscible with hydrophilic polymers. Therefore, the use of coupling agents is necessary to make both phases compatible. These agents are fundamental molecules constituted by a hydrophilic functionality (related to clays) and by an organophilic functionality (related to the polymer), which favors the molecular compatibility between the sheets of the clay and the polymer chains.

The first coupled agents used to obtain nanocomposites were amino acids [137]. However, the most popular are alkylammonium ions, since they can easily be exchanged with the cations in the galleries. The alkylammonium ions are primary alkylamines [138,139]. Its basic formula is:



where n represents the chain length, which ranges from 1 to 18 carbons. Lan et al. [140] highlighted that the exfoliation of the sheets is favored when ions with a chain length greater than eight carbon atoms are used, while with shorter chains, it led to the formation of agglomerated structures.

Ideally, the alkylammonium ions can be accommodated in various ways within the galleries, depending on the charge density of the clay minerals. Thus, the ions adopt monolayer, bilayer, or paraffin-like monolayers [141], as outlined in Figure 10.

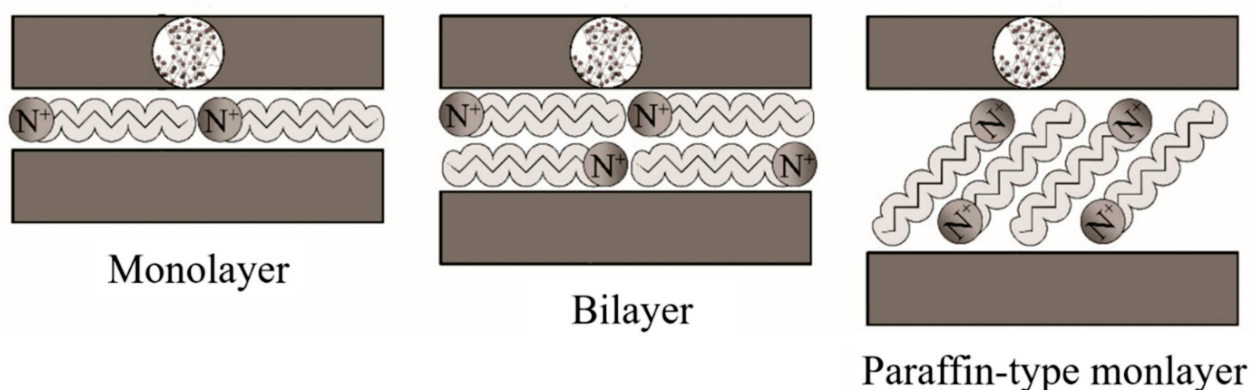


Figure 10. Schematic representation of the configuration of alkylammonium ions within the galleries of clays. Schematic figure based on Lagaly [142] with permission from Elsevier.

2.3. Nanocomposite Structures

Depending on the nature of the composite constituents (layered silicate, organic cation, and polymer matrix) and the method of preparation, three main types of composite may be obtained. Thus, polymer nanocomposites can be classified according to their morphology into agglomerates, intercalated, and exfoliated structures, as represented in Figure 11.

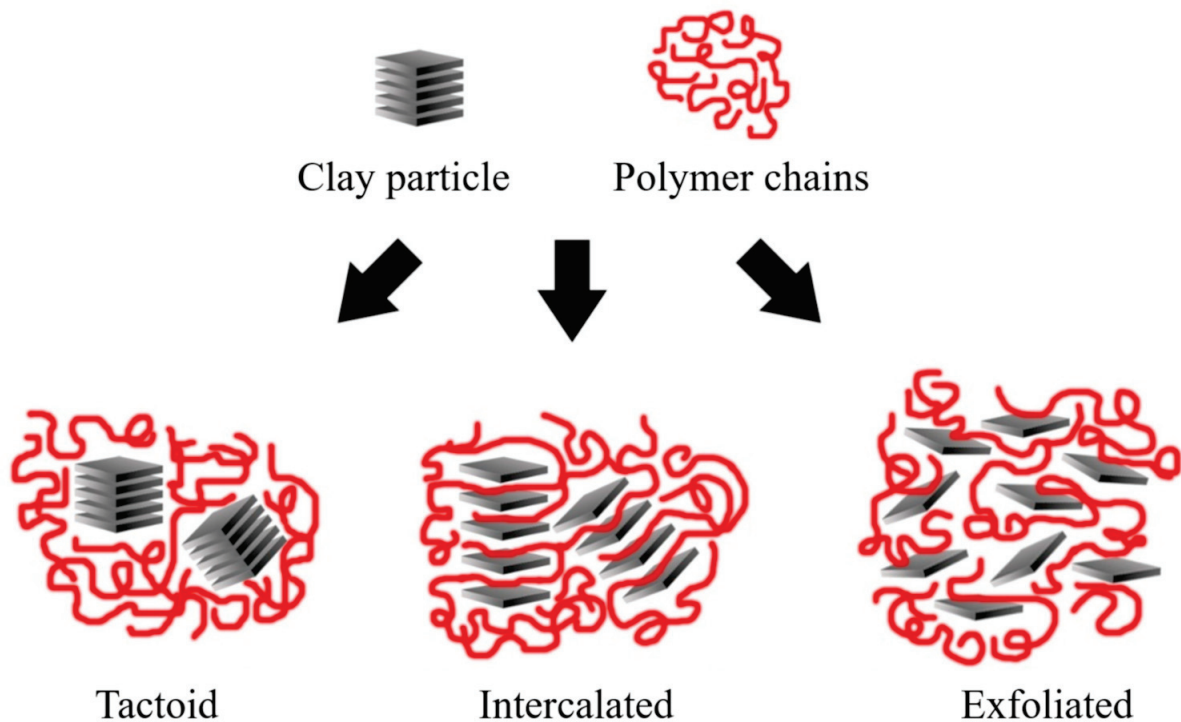


Figure 11. Schematic representation of the nanocomposite structures. Schematic figure based on Beyer [136] with permission from Elsevier.

Agglomerated composites are formed when the polymer is unable to intercalate between the sheets of clay. In this way, two separate and well-defined phases are obtained, where the sheets remain joined and aligned parallel to each other. It is common to classify the properties of these materials within the microcomposites. Some authors refer to the agglomerated composites as tactoids [2,141] or low-packing nanocomposites since there are no variations in the interlaminar space [2,6].

In the case of intercalated composites (also classified as flocculated [3]), the polymer chains are intercalated between the sheets of the clay, increasing the interlaminar space, obtaining a morphology of multiple highly ordered sheets.

Exfoliated nanocomposites contain sheets entirely separated and dispersed within the polymer matrix. This type of exfoliated structure presents relevant mechanical properties due to the high aspect ratio of single sheets. However, this structure is difficult to obtain, and three main processing strategies are commonly used.

2.4. Polymer Intercalation in Solution

The clay mineral is suspended in a polar organic solvent such as water, toluene, ethanol, etc., forming a gel-like structure. Subsequently, the polymer is dissolved and dispersed in the same type of solution, and the reaction is initiated by mixing the solutions, where polymer chains start to fill spaces in the galleries. Then, the solvent is removed by evaporation, obtaining the nanocomposite with a multilayered structure, as outlined in Figure 12.

The nanocomposites obtained through this method are highly selective since the polymer and clay minerals possess different physical and chemical properties. The solvent is also essential because it is expensive and not environmentally friendly for large-scale production.

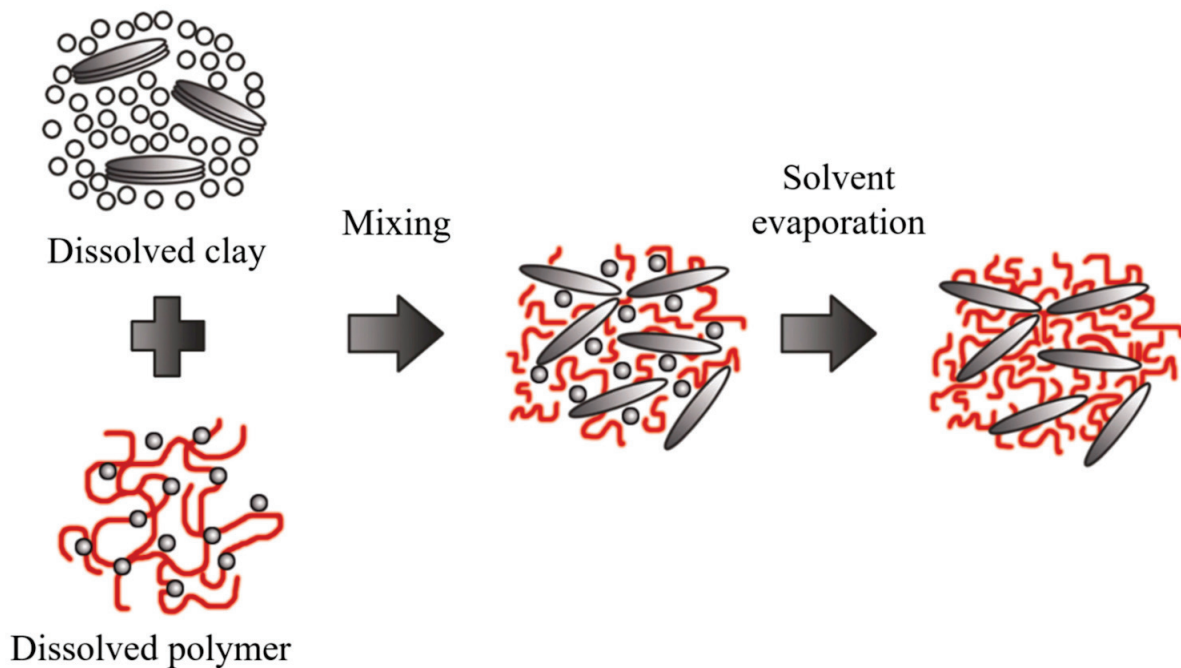


Figure 12. Schematic representation of polymer intercalation in solution. Schematic figure based on Zanetti [143] with permission from John Wiley and Sons, and Unalan [144] from RSC Adv. Open Access.

2.5. In Situ Polymerization

In this method, the galleries are expanded using a liquid monomer or a monomer in solution. The polymerization starts by the diffusion of an organic initiator or by catalysis through exchangeable cations (Figure 13) [145]. After polymerization termination, the solvent is evaporated, and the nanocomposite is ready for further modification. The in situ polymerization should be the best method to obtain high intermolecular distance between the clay layers. However, this method contains similar drawbacks to the solution-based method due to large-scale difficulties and environmental considerations.

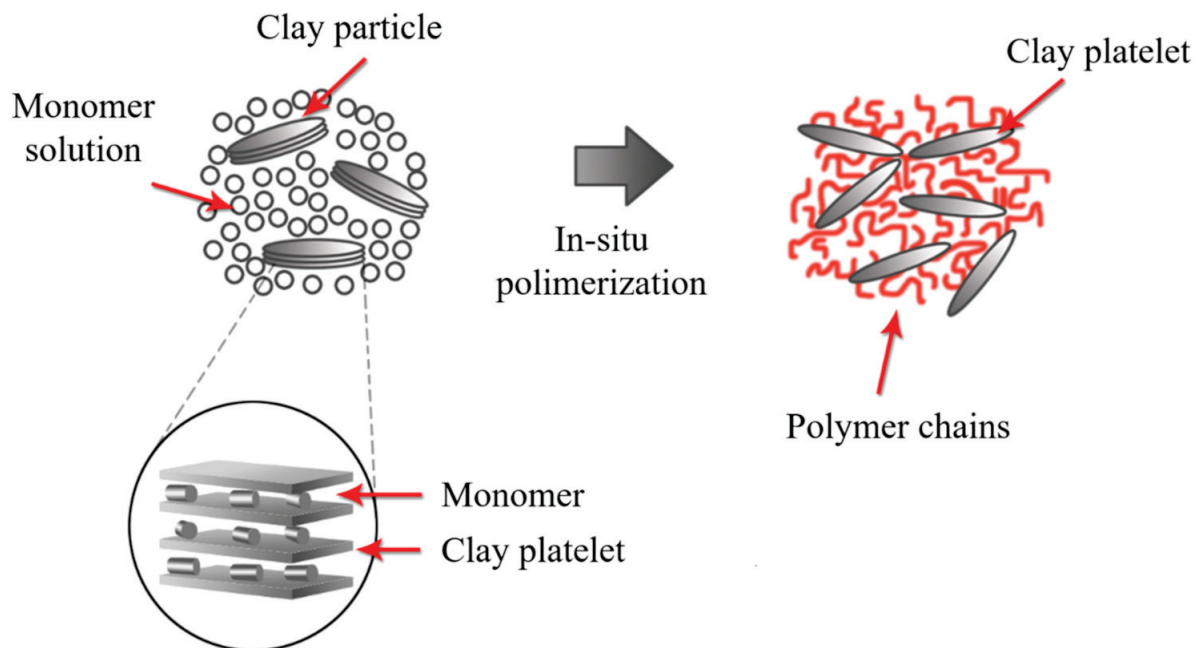


Figure 13. Schematic representation of in situ polymerization. Schematic figure based on Zanetti [143] with permission from John Wiley and Sons, and Unalan [144] from RSC Adv. Open Access.

2.6. Melt Blending Process

This method consists of mixing both phases (polymer and clay minerals) under the action of a high-temperature shear force. Melt intercalation is used for synthesizing thermoplastic polymer nanocomposites at a large scale. This procedure is compatible with industrial processes such as extrusion, making it more economical, convenient, and environmentally friendly because solvents are not required. However, the high temperatures during the extrusion process (up to 220 °C) can degrade the coupling agents (clay minerals modified with alkylammonium).

In a broad definition, the extrusion process refers to any transformation operation in which molten material is forced through a die to produce an article of constant cross-section and, in principle, indefinite length. In addition to plastics, many other materials are processed by extrusion, such as metals, ceramics, or food, obtaining very varied products such as aluminum or PVC window frames, pipes, pasta, etc. From a plastics point of view, extrusion is one of the essential transformation processes. The polymer is generally fed in solid form (commonly dust or pellet) in the hopper section and exits the extruder in the molten state. On some occasions, the polymer can be fed in molten form from a reactor where the extruder acts as a pump, providing the necessary pressure to pass the polymer through the nozzle. The extrusion process is frequently used to mix distinct materials, additives, and fillers to add better performance, reduce costs, and obtain multiple functionalities. These new formulations are further processed to create components or preforms using injection molding, blow molding, or thermoforming techniques.

Although there are various types of extruders, the most widely used are single-screw and twin-screw extruders. Specifically, a single-screw extruder can perform six main functions: transporting the solid material towards the melting zone, melting the polymer, pumping the melt, mixing, degassing, and forming. However, not all of the above functions necessarily take place during the operation of the extruder. According to the purpose, the extrusion process starts with the material feeding system, a melting-plasticizing system, the pumping, and a pressurization system, generating a mixing effect.

It is common to find in the literature that single-screw extruders have poor material mixing due to their design. However, it is essential to consider many other factors that affect the end product, such as the wear of extruder working parts, rotational speed, pressure, nozzle type, and many more. In addition, the extruders are not just used for mixing but also for producing various materials, e.g., direct molding at the nozzle, injection into the die, etc. Ekielski et al. [146] evaluated the wear status of the single-screw extruder working elements based on die pressure and screw load values changes. The changes to these parameters were analyzed as a frequency spectrum using wavelet analysis tools. Due to the dynamic characteristics of the process in determining natural frequencies, the authors used the Morlet wavelet transform, observing that it is possible to accurately evaluate the degree of wear of the friction elements in a single-screw extruder.

Extrusion technology is also used in the food processing industry, known as extrusion-cooking, to produce so-called engineered foods and special feed. Leszek Moscicki and Dick J. van Zuilichem detailed an interesting work related to extrusion-cooking using single-screw extrusion technology [147]. The authors mentioned that the shear exerted by the rotating screw and the additional heating of the barrel promote a rheological modification. The physical aspects such as heat transfer, mass transfer, impulse transfer, residence time, and residence time distribution have a substantial impact on the properties of food and feed during extrusion-cooking and can drastically influence the quality of the final product.

Twin-screw extruders provide a much higher degree of shear than single-screw extruders, and the screw rotation can be co-rotating or counter-rotating. Therefore, this process can be too aggressive for some applications; even so, the high shear promotes twin-screw extrusion to prepare clay-based polymer nanocomposites (Figure 14). However, the single-screw extrusion should be considered for producing starch-based bionanocomposites or other natural composites.

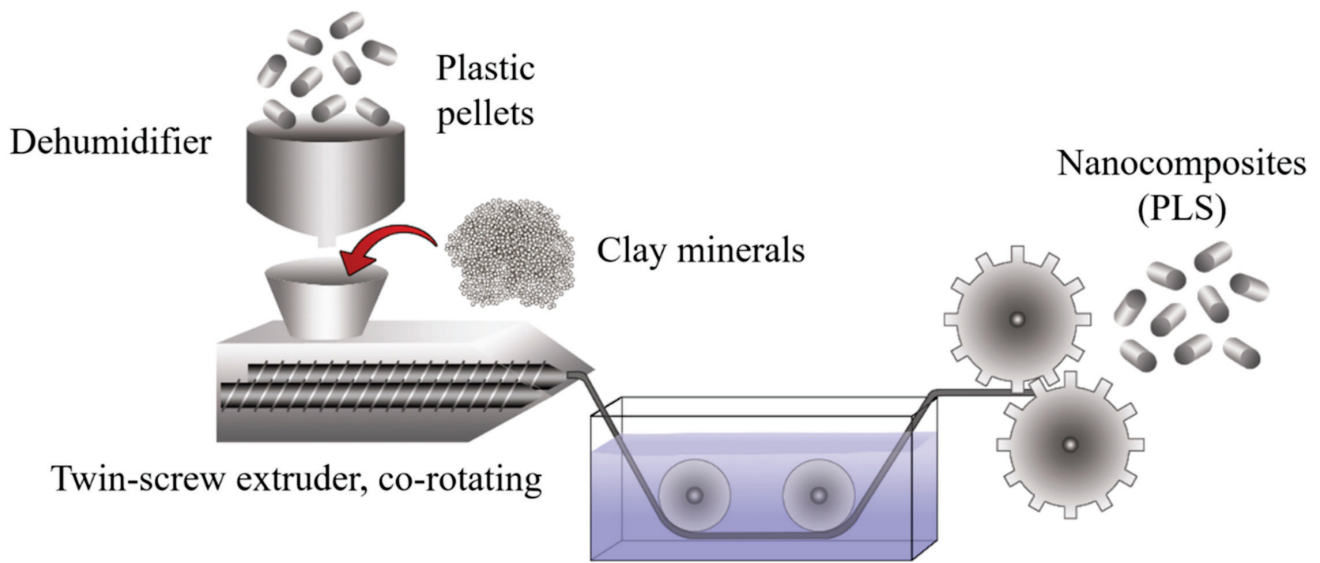


Figure 14. Schematic representation of the production process using twin-screw extrusion.

The literature is consistent in stating that the extrusion process leads to the development of intercalated structures. However, exfoliated structures can develop if there is high molecular compatibility between the phases, and in many instances, the use of additives is required (Figure 15).

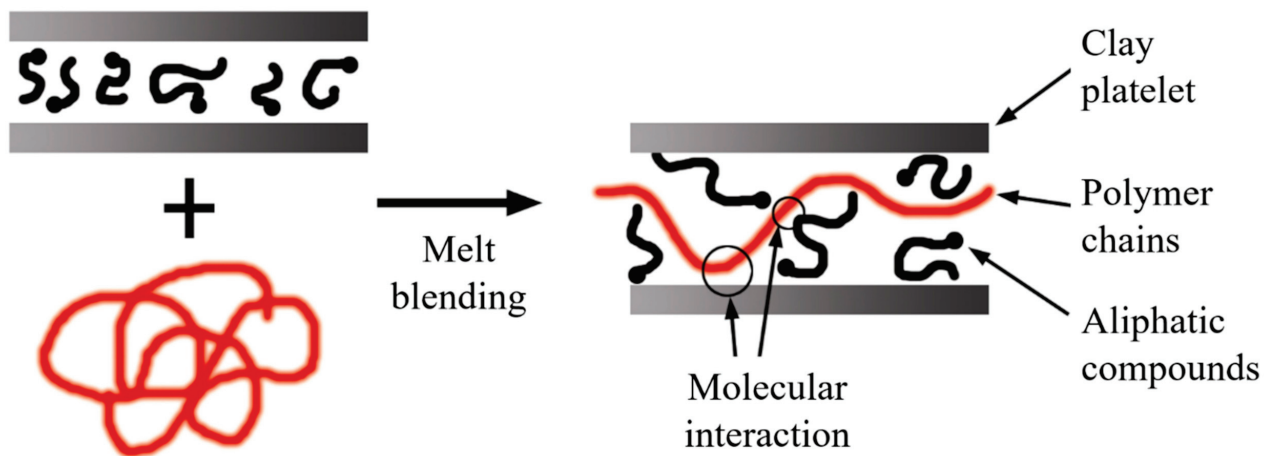


Figure 15. Schematic representation of intercalated structures for melt blending. Schematic figure based on Vaia [148] with permission from American Chemical Society, Copyright 1997.

Some authors [149–151] evaluated the influence of the extrusion process on the morphology of polymer nanocomposites. In this way, Dennis et al. [150] observed that a single screw extruder did not provide sufficient shear to separate or fracture the clay layers and did not offer an adequate residence time for layer dispersion. On the other hand, intercalated structures and some agglomerations are present when using a twin-screw extruder under the co-rotating configuration. By using the counter-rotating configuration, a high level of exfoliation was achieved.

Fornes et al. [151] found that the design of the extrusion screws also conditioned the morphology of the nanocomposites. The low- and medium-cut spindles developed interleaved structures, while a high-shear design obtained a high level of exfoliation.

Based on the previous studies, it is possible to consider that using a counter-rotating twin-screw extruder with high- or medium-shear screws should favor the exfoliation of

the clay sheets. Nonetheless, it is important to consider that factors such as molecular compatibility and good processing conditions (dosage rate, temperature, and residence time, among others) are necessary for optimal exfoliation [152].

During the twin-screw extrusion process, the exfoliation mechanism begins with the fracture of the particles and the sliding of the sheets until they become stacked sheets of smaller size, as schematized in Figure 16a. This first phase requires a high shear intensity. Subsequently, the polymer is sandwiched between the sheets, taking advantage of their flexibility to increase the distance between them. This second phase requires both high shear and good molecular compatibility (Figure 16b). Finally, the exfoliated sheets are randomly dispersed within the matrix (Figure 16c), requiring adequate residence time [8,153].

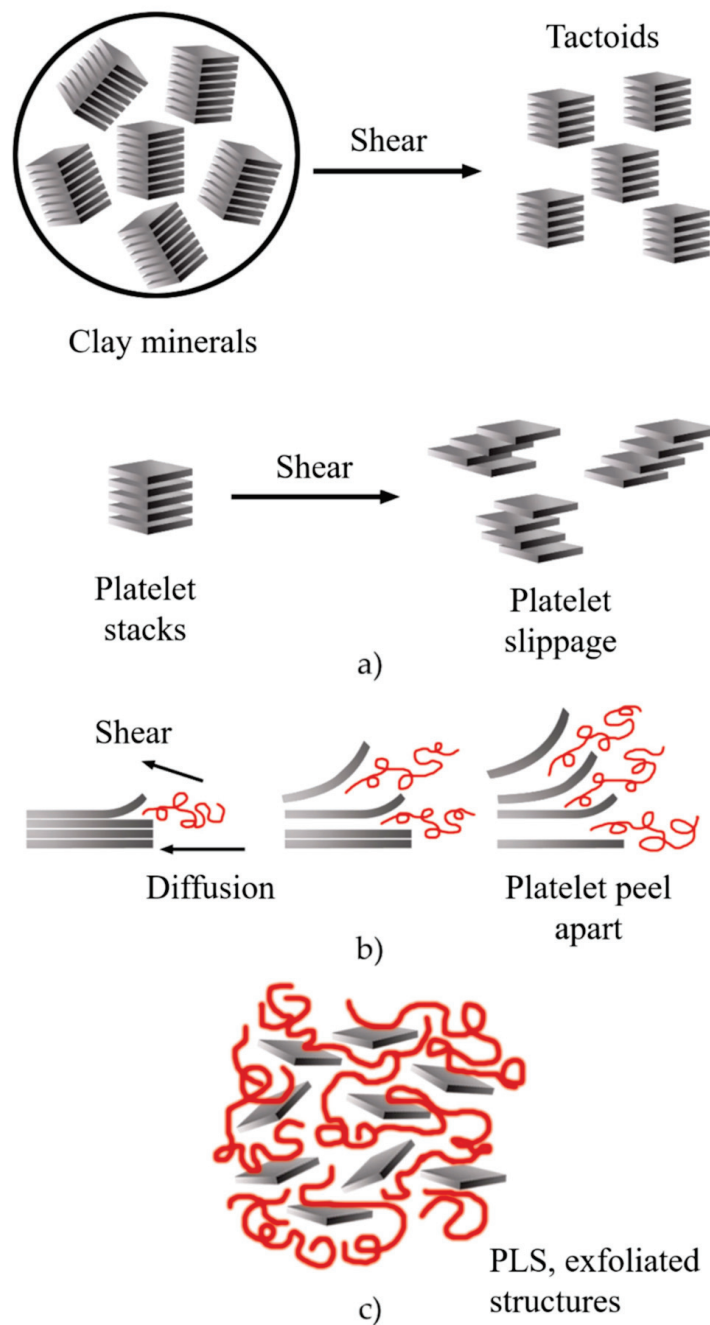


Figure 16. Schematic representation of the exfoliation mechanism of the clay platelets during the twin-screw extrusion process: (a) fracture and sliding of the sheets, (b) intercalation, (c) exfoliation. Schematic figure based on Fornes [154] with permission from Elsevier.

It is important to note that an intense shear does not guarantee a more significant number of exfoliated sheets. Similarly, a longer residence time does not provide better dispersion. For this reason, a large number of studies have focused on developing processing conditions that allow for increasing the level of exfoliation by using the melt intercalation process [1,5,8,151,153,155].

It is possible to consider the average dimensions of each particle: length (ℓ_p), thickness (t_p), and aspect ratio (ℓ_p/t_p). Some authors [8] detailed that the increase in ℓ_p can be related to the sliding of the sheets that occurred during the twin-screw extrusion process, which can be defined as effective particle length, as shown in Figure 17.

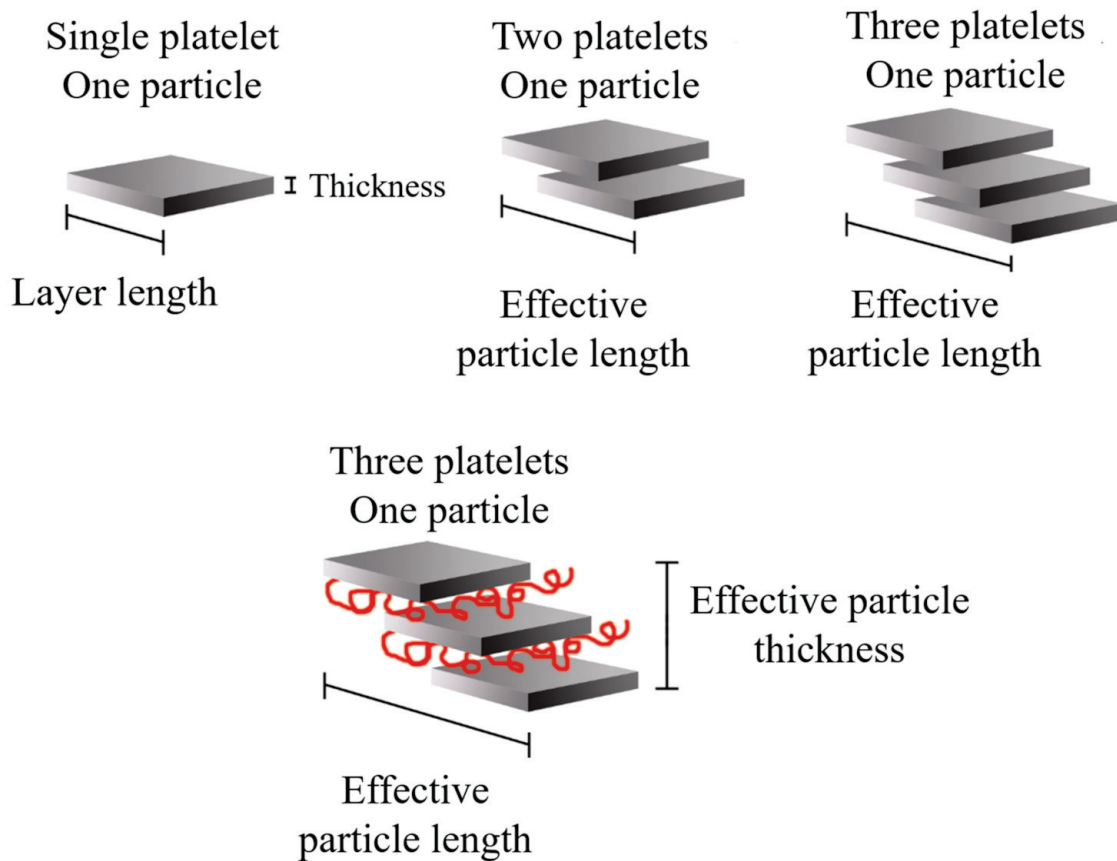


Figure 17. Schematic representation of the effective length and thickness of the clay particles present in nanocomposites with a certain degree of intercalation. Schematic figure based on Fornes [154] and Chavarria [156] with permission from Elsevier.

The clay-based polymer nanocomposites have gained the attention of academics and industry in recent decades. Integrating small percentages of clay minerals into the polymer matrix improves the mechanical properties compared to neat polymers. Properly dispersed and aligned clay platelets have proven to be very effective for increasing stiffness without altering the polymer density. There is extensive literature regarding the mechanical properties of polymers enhanced by low clay content, as summarized in Table 2.

Table 2. Mechanical properties for clay-based polymer nanocomposites.

Mechanical Test	References
Tensile	[3,157–187]
Compression	[164,181]
Bending	[188–193]

3. Fracture Mechanics

Fracture mechanics is based on the need to analyze the flaws present due to a part or component's manufacturing and machining processes. Different manufacturing processes induce failures or small internal or surface cracks, and the fracture mechanics allows for characterizing those cracks that can propagate (instability) and cause failures in the structure.

Fracture mechanics involves three complementary theories: linear elastic, elastic-plastic, and post-yielding fracture mechanics. Practically, the main difference is in the development of plastic deformations around the crack-tip of notched specimens during the fracture process, as presented in Figure 18.

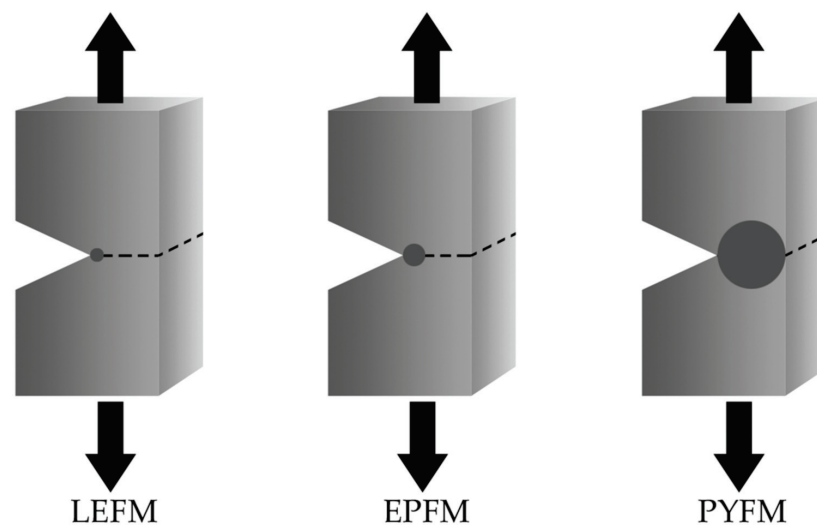


Figure 18. Schematic representation of the three approaches to fracture mechanics: linear-elastic fracture mechanics (LEFM), elasto-plastic fracture mechanics (EPFM) and post-yield fracture mechanics (PYFM). The shaded area represents the extent of the plastic deformation that develops during the fracture process.

Generally, a crack in a solid body can propagate in three different ways depending on the applied load and with respect to the crack plane, as shown in Figure 19. Mode I (opening mode) represents the opening of the crack due to stresses perpendicular to the plane of the crack. Mode II (sliding mode) refers to the displacement of the crack under shear forces that act parallel to the plane of the crack and perpendicular to the crack front. Mode III (tear mode) is produced by shear forces that act perpendicular to the plane of the crack and parallel to the crack front. It is common to indicate the fracture mode employing a subscript I, II, or III.

Fracture mechanics theory is relatively new, beginning in 1913 when Charles E. Inglis [194] studied the stress behavior of plates with ellipse-shaped defects. Considering an infinite isotropic plate in uniaxial tension, Inglis proposed the linear elastic solution for the ellipse's tension field. Later, in 1920, Griffith [195] used the work of Inglis to calculate the stress concentrations around the ellipse and to predict the resistance to fracture. However, Inglis's solution poses a mathematical difficulty considering that the stresses approach infinity at the crack-tip in the limit of a perfectly sharp crack, which is physically impossible. Thus, Griffith proposed the energy-balance approach, which is based on balancing the reduction in potential energy during fracture with the increase in surface energy due to creating new free surfaces when a crack grows. Griffith's theory provides excellent agreement with experimental data for brittle materials and is the fundamental base for the linear elastic fracture mechanics (LEFM) theory.

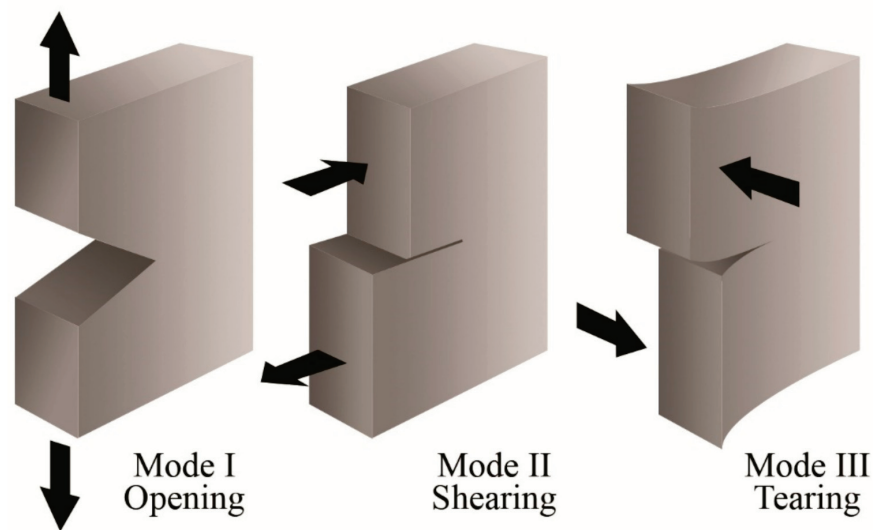


Figure 19. Schematic representation of the three modes for crack propagation.

After Griffith's work, in 1950, G. R. Irwin observed that ductile materials develop a plastic zone at the crack-tip. The plastic zone increases with the applied load and leads to the dissipation of energy in the form of heat. Therefore, a dissipative term must be added to the energy-balance relationship for brittle materials. In physical terms, ductile materials require additional energy for crack growth. Thus, Irwin extended the theory to some ductile materials through the concept of energy release rate (G_c) [196]. Subsequently, Irwin used Westergaard's approach [197] to demonstrate that local stresses and displacements near the crack-tip had a general solution. He introduced the stress intensity factor (K), which relates the local mechanical state near to the crack-tip with macroscopic characteristics in a continuous process of stable crack growth until the onset of instability.

After the fundamentals of linear elastic fracture mechanics (LEFM) were established (around the 1960s), several scientists began to study the plasticity that developed at the crack-tip. Wells [198], in 1961, presented the concept of crack tip opening displacement (CTOD) for materials that can show some plastic deformation at the crack-tip during the fracture process. In 1968, Rice [199] developed the J-integral approach as a parameter for the characterization of the crack propagation under elastic-plastic fracture mechanics (EPFM) conditions. The J-integral initially emerged as a fracture criterion for small-scale plasticity conditions at the crack-tip. Later, it was considered a fracture criterion in large-scale plasticity for fracture initiation and stable crack growth. The J-integral approach considers the elastic and plastic parts separately to characterize near-crack-tip deformation filed in linear and non-linear elastic materials. Experimentally, the J-integral shows an energetic contour path integral, independent of the path around a crack, and it enables determining the strain energy release rate. The J-integral and CTOD are the parameters most often used to correlate mechanically short and long crack growth rates.

Broberg [200,201], in 1968, observed changes in the distribution of plastic deformation near the crack-tip in materials with considerable plastic deformation before fracture. These changes contribute to a gradually increasing screening of the energy flow through the plastic region towards the crack-tip, leading to stable crack growth accompanied by plastic collapse. Thus, Broberg established the beginning of the post-yielding fracture mechanics (PYFM) criteria based on the stable crack growth.

In 1977, Cotterell and Reddel [202] developed Broberg's ideas and proposed the essential work of fracture (EWF) method, which allows for determining the fracture properties of ductile materials.

3.1. Essential Work of Fracture

The EWF approach considers the total energy involved during the ductile fracture process, where the plastic deformation is fully developed around the ligament region before the crack growth. The EWF consists of using deeply double notched in tension (DDENT) specimens to determine the energy absorbed by fracturing the DDENT specimens. The total fracture energy (W_f) can be separated into two terms: the essential work of fracture (W_e) performed in the inner fracture process zone (FPZ) and the non-essential work of fracture (W_p) performed in the outer plastic zone (OPZ):

$$W_f = W_e + W_p \tag{2}$$

Both areas are easily identifiable, as outlined in Figure 20.

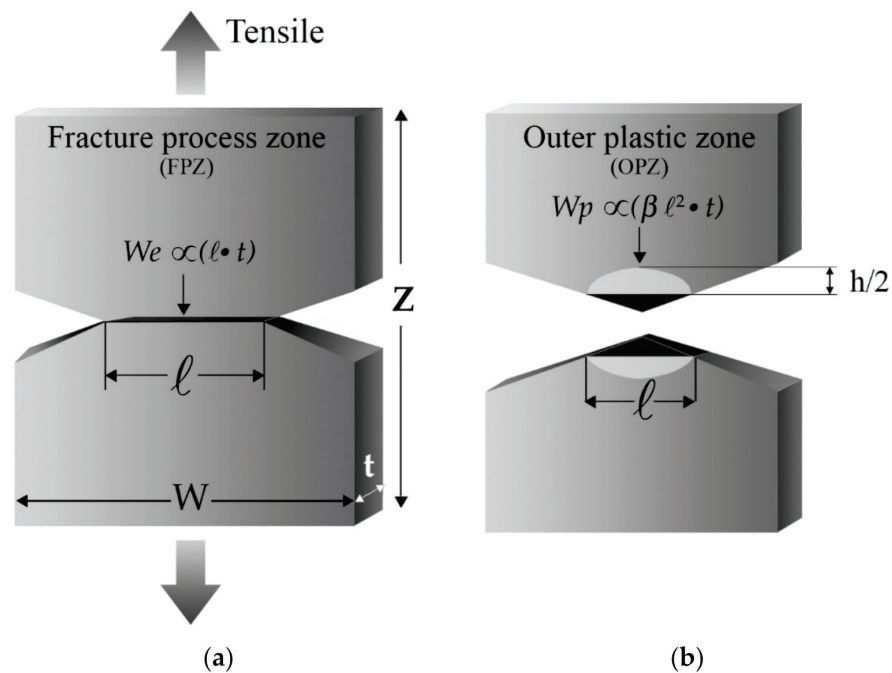


Figure 20. Schematic representation of the DDENT specimen: (a) before being tensile tested and (b) after being tensile tested.

W_e is associated with the FPZ (where the real fracture process occurs) and represents the energy involved in creating two new surfaces during the crack propagation. This term is proportional to the ligament section $l \cdot t$, as depicted in Figure 20a.

The W_p term is also named “plastic work” and is related to the OPZ, where the rest of the phenomena associated with the ductile fracture, such as plastic deformation, and other dissipative processes such as shear, crazing, or cracks, occur. This term is proportional to the volume of the deformed region (Figure 20b).

The previous concepts enable rewriting the Equation (2) in the following expression:

$$W_f = W_e + W_p = w_e \cdot l \cdot t + \beta \cdot w_p \cdot l^2 \cdot t \tag{3}$$

where w_e is the specific essential work of fracture per unit area of the ligament ($l \cdot t$), l is the length of the ligament, t is the thickness of the specimen, β is the shape factor of the plastic zone, and w_p is the specific non-essential work of fracture per unit volume ($l^2 \cdot t$). Dividing both terms of Equation (3) by the ligament section ($l \cdot t$), we find that the specific work of fracture work (w_f) is:

$$w_f = \frac{W_f}{l \cdot t} = w_e + \beta w_p \tag{4}$$

The experimental procedure consists of testing several DDENT specimens with different ligament lengths. The fracture energy (W_f) is determined as the area under the experimental load vs. displacement curves (Figure 21a).

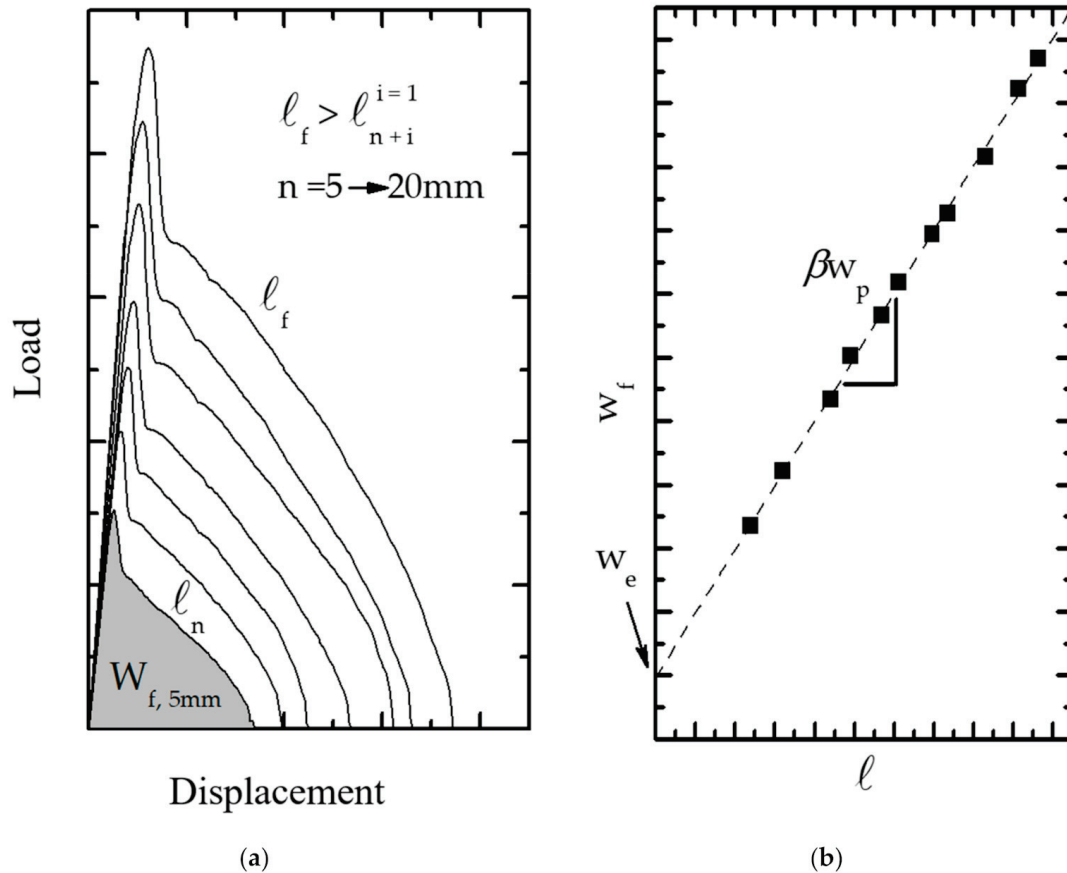


Figure 21. Schematic representation of the EWF fracture process: (a) the shape of the L–d curves, necessary to represent (b) w_f vs. l and obtain the linear regression.

According to Equation (4), we can calculate w_e and βw_p terms by representing the w_f values in front of l . These points are subject to linear regression, where w_e is the intercept of the fitting line with the y-axis, while βw_p is the slope of the fitting line, as presented in Figure 21b.

Theoretically, w_e is an intrinsic material constant that depends only on the thickness and is equivalent to J_{IC} [203], which has been supported experimentally by different authors [204–207] and contrasted with the CTOD values [17]. However, compared to the J-integral approach, the EWF method has certain procedural advantages, such as its simplicity in experimental testing or its applicability to very thin thicknesses such as thin sheets or films [208,209].

The EWF method is currently attractive for several research projects that deal with fracture toughness for polymer materials. However, its application is limited since there are currently no mathematical models that allow the use of the data obtained by the EWF technique to simulate the fracture of ductile materials. Therefore, it is necessary to highlight the works performed by Knockaert, Pardoen, Chen, and Cotterell [207,210–212] in the numerical simulation for the fracture of DDENT-type specimens. Furthermore, Chen et al. [213] investigated the correlation between fracture parameters and the molecular structure of amorphous and ductile polymers.

It is also noteworthy that the application of the EWF method has been extended from Mode I to the other two crack propagation modes: shear (Mode II) [214,215] and tear

(Mode III) [216,217]. Additionally, the EWF method was applied to evaluate the adhesion energy in joints [218,219].

3.1.1. Experimental Considerations for the EWF Method

In 1993, Gray [220] made the first attempt to standardize the EWF method within the technical committee number 4 of the European Structural Integrity Society (ESIS TC-4), where the following recommendations were established:

- Under tensile load, the full ligament yielding should be reached before the crack is initiated
- Equation (3) can be applied if the DDENT specimen is in a plane stress fracture condition, which is verified by applying Hill's criterion [221].
- Self-similarity of the experimental load–displacement curves for each l , which supports the development of a fracture geometry common to all DDENT specimens.
- For materials with ductile fracture, the FPZ undergoes a necking process which then breaks into a fracture surface. So, the required conditions involve the specimen thickness (t), the width of DDENT specimen (W), and the plastic zone size (r_p):

$$(3 - 5)t \leq \ell \leq \min\left(\frac{W}{3}\right) \text{ or } 2r_p \quad (5)$$

where r_p is the radius of the plastic zone, which is defined as

$$2r_p = \left(\frac{\pi}{8}\right) \left(\frac{Ew_e}{\sigma_y^2}\right) \quad (6)$$

where E and σ_y are the elastic modulus and the tensile strength, respectively.

In addition, the height of the plastic zone (h in Figure 20) must be measured to determine the shape factor (β), where three primary geometric forms were established: rhombus, circle, or ellipse.

This first standard protocol was revised in 1997 and later in 2001 [222], emphasizing that the similar stress condition could improve Hill's criterion. This is verified through σ_{\max} , which must be similar in all the tested specimens, regardless of ℓ .

Despite all the reviews and work carried out by the TC-4 committee of the ESIS, some issues cause controversy, representing a challenge for research. Table 3 lists some of these topics.

Table 3. Issues related to the validity and evaluation of the EWF technique.

Issues	Evaluation	References
Tested specimens	DDENT specimen dimensions. Use of a video extensometer. Notch sharpening. Ligament lengths Test rate.	[223–226]
Test conditions	Test temperature EWF in mode III.	[208,217,227–234]
Analysis of the results	Energy partitioning. Other geometries for β . w_e - J_0 relationship	[235–244]

3.1.2. Dimensions of the DDENT Specimen

According to the theory of the essential work of fracture, w_e represents the material's toughness, and so it is independent of specimen geometry. Maspocho et al. [245] detailed the effect of the DDENT specimen dimensions by applying the EWF method testing an isotactic polypropylene (iPP). They concluded that the width of the specimen does not

drastically influence the values of w_e or βw_p , which would indicate that both fracture parameters are intrinsic properties of the material. Similarly, the length of the specimen does not seem to influence the EWF parameters. Regarding ℓ , the authors observed that the minimum length does not seem to be subject to the criterion $\ell > (3-5)t$, since ℓ was valid for values between 5 and 6 mm, and independent of the specimen thickness. Finally, the thickness had a significant effect on the fracture parameters of the iPP studied, since an increase in t produced an apparent decrease in the values of w_e that may be related to both the morphology and the fracture mechanisms, as could be appreciated through scanning electron microscopy (SEM).

3.1.3. Use of Video Extensometer

The essential fracture work theory indicates that all the energy involved during the fracture process is absorbed in both the fracture process zone (FPZ) and the plastic zone (OPZ). However, it is possible to argue that part of the viscoelastic energy can be stored in the DDENT specimen (outside the OPZ), and is released slowly after the fracture [246]. Fung et al. [247] demonstrated that the viscoelastic energy is not included in total fracture energy and proposed to measure the plastic deformation using a videoextensometer. They found the use of videoextensometer does not significantly affect the values of w_e but reduces the βw_p values.

Other authors detected and quantified the plastic deformations during the EWF test using a digital image correlation system (GOM-Aramis™) that allowed visualizing the field of deformations in 3D.

One of the most common interests for experimental fracture mechanics characterization is evaluating the influence of the notching quality on the fracture parameters. Martinez et al. [244] proposed a new procedure for sharpening the notches of the DDENT specimens, which was based on pulsed laser ablation in periods of femtoseconds (femtolaser). This procedure was compared to the conventional notch sharpening method by a razor blade. The results show that the radius of the bottom of the notch appears to be critical below 10 μm . However, the fracture parameters are susceptible to plastic deformation induced during notching, altering the w_e values.

3.1.4. Energy Partitioning

According to the EWF theory, w_f considers all the energy dissipated divided by the ligament section $\ell \cdot t$ (Equation (3)), and the fracture process is related to the shape of the load–displacement curves. Therefore, it is possible to suggest the energy contribution separation in terms of fracture initiation and propagation. Mai et al. [248] partitioned the total work into two distinct parts: the energy for initiate fracture and the fracture work for crack growth, including crack propagation and necking. Karger-Kocsis et al. [249] proposed that the maximum load (Figure 22a) divides the fracture energy into two components: the yield work ($W_{f,y}$) and the necking and propagation work ($W_{f,n}$):

$$w_f = w_{f,y} + w_{f,n} = (w_{e,y} + \beta w_{p,y} \cdot \ell) + (w_{e,n} + \beta w_{p,n} \cdot \ell) \quad (7)$$

Ferrer-Balas et al. [250] proposed the initiation work method, limiting the partition energy at the end of necking (Figure 22b), just before starting the crack propagation. Thus, the fracture energy is separated into two terms, WI (initiation process, which refers to the full ligament yield, which is a phenomenon of plastic deformation) and WII (crack propagation and energy dissipation in the plastic zone). The elastic energy absorbed during the ligament yield is consumed during the crack propagation; hence, it is considered part of WII (propagation) and is subtracted from WI (initiation), as schematically depicted in Figure 20.

$$w_f = w_{f,I} + w_{f,II} = (w_{e,I} + \beta w_{p,I} \cdot \ell) + (w_{e,II} + \beta w_{p,II} \cdot \ell) \quad (8)$$

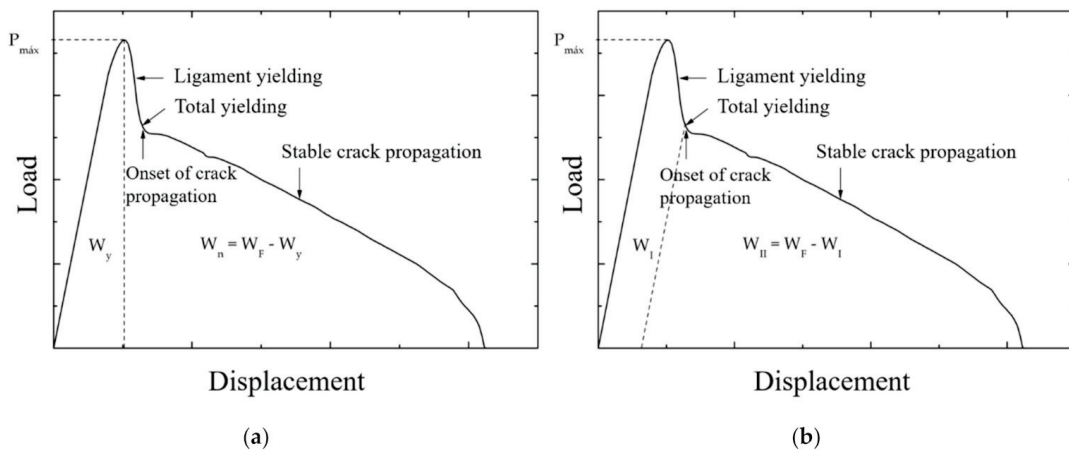


Figure 22. Energy partitioning methods: (a) method at yield, (b) method of initiation.

3.1.5. Proposal for the New Shape of the Plastic Zone

Under similar geometric and test conditions, the plastic term (βw_p) can be used as a comparative parameter between different materials. The shape factor depends on the material and is related to the geometry of the plastic zone developed during the fracture of the DDENT specimens. On the other hand, the value of w_p cannot be determined directly through the linear regression obtained from the graphical representation of w_f vs. ℓ , which justifies the need to measure β accurately. It is common to observe that the plastic zone develops an intermediate shape between elliptical and rhomboid geometries [251], identified as the intersection between two parabolas and defined using the following equation:

$$h = k \cdot \beta \cdot \ell \tag{9}$$

where k is a constant that depends on the shape of the plastic zone and takes values of 1.27 for circular and elliptical geometries, and 2 and 1.5 for rhomboid and parabolic shapes, respectively (Figure 23).

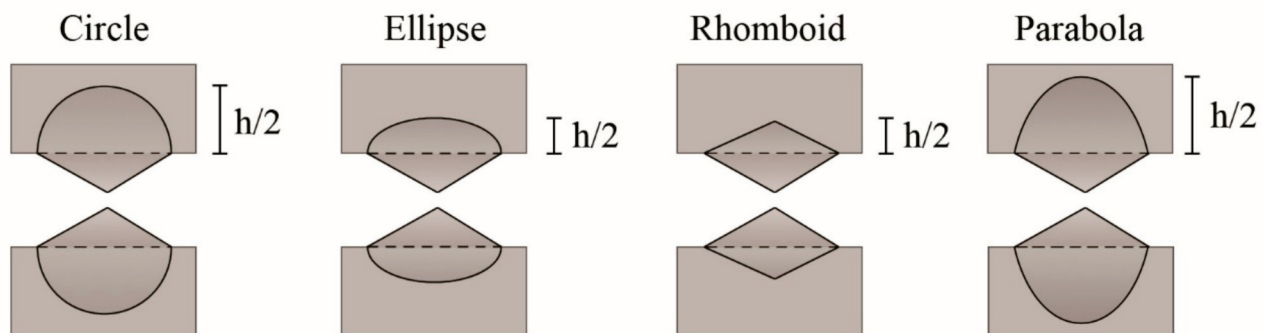


Figure 23. Schematic representation of the different ways in which the plastic zone can develop during the process of fracturing DDENT specimens. Schematic figure based on Ferrer-Balas [251] with permission from Elsevier.

In this way, β can be determined as the slope of the linear regression obtained by representing the total height of the plastic zone (h) versus the ligament length (ℓ), divided by the factor k .

The EWF method allows us to relate the fracture processes with distinct microstructural parameters. Thus, some studies related to complex phenomena such as aging or degradation [252,253] and the ductile–brittle transition [254,255] use the EWF approach.

The high sensitivity of the EWF method makes it of particular interest to study the processing–properties relationship to optimize the processing parameters [256], and even to evaluate the influence of annealing in different polymer systems [236,257,258]. Further-

more, the EWF technique is appropriate to study the influence of different morphological parameters such as molecular weight, anisotropy, molecular entanglement density, and crystalline structure have on the fracture toughness of films and thin sheets.

Even though the numerous published works demonstrate the satisfactory application of the EWF on ductile materials (polymers and metals included), there are still some controversies about the influence of some experimental variables such as the test speed, the DDENT specimen thickness, and the notching quality, which may limit the applicability of the EWF method.

3.2. EWF for Clay-Based Polymer Nanocomposites

Recently, the EWF method began to be used in clay-based polymer nanocomposites [188,224,259–261]. The high sensitivity of the EWF technique is attractive to evaluate the influence of distinct variables such as the type of organic modifier, the filler content, the platelets' orientation, and the exfoliation degree on the fracture toughness of polymer nanocomposites. Table 4 presents a summary of the literature found for the applicability of the EWF method in polymer nanocomposites.

Table 4. Summary of the literature regarding to the EWF method applied to polymer nanocomposites.

Polymer	Filler	References
Polypropylene	Montmorillonite clay	[232,259,262–266]
	Boehmite clay	[267–269]
	mica	[270]
	Innosilicate	[271]
	Carbon nanotubes	[272–276]
	Graphene	[277]
Polyethylene	Other nanoparticles	[257,278,279]
	Montmorillonite clay	[260,280–282]
	Boehmite	[283]
	Mg–Al layered double hydroxide (LDH)	[284]
Styrene	Other nanoparticles	[285–289]
	Montmorillonite clay	[261,290]
Polyamide	Carbon nanotubes	[291,292]
	Montmorillonite clay	[227,293–299]
Polycarbonate	Other nanoparticles	[300–303]
	Carbon nanotubes	[304,305]
Biodegradable polymers (PLA and others)	Monmorillonite clay	[224,306–308]
	Boehmite	[307]
Thermoplastic natural rubber (TPNR)	Montmorillonite clay	[309]

Polyolefins such as polypropylene and polyethylene are the most common thermoplastics for EWF evaluation. Similarly, montmorillonite is a clay mineral mainly used as a reinforcement for thermoplastic resins.

Saminathan et al. [232,233] evaluated the effect of loading rates on the EWF parameters. The PP/MMT nanocomposites were prepared by melt mixing using a twin-screw extruder. The compatibilizer was maleic anhydride grafted polypropylene (MA-g-PP). The commercial nanoclay Cloisite®15A was used as a nanofiller. The concentration of nanoclay was 5 wt.%, and the ratio between the nanoclay and MA-g-PP was 1:1. The nanocomposites were injection molded to obtain 1.5 mm thick plates. The EWF tests were conducted at room temperature with loading rates varying from 1 to 20 mm/min. The authors mechanically characterized the nanocomposite. The results obtained show an increase in tensile modulus, flexural modulus, yield strength by 25%, 20% and 10%, respectively, compared to pure PP. Nevertheless, the authors observed the maximum percent strain reduced by 41%. According to the EWF results, the authors revealed that the specific work of fracture increases 25% with respect to pure PP, and as the loading rate increases, the specific EWF for yielding increases, but the specific EWF for necking decreases.

Nekhlaoui et al. [259] studied the fracture of polypropylene nanocomposites. In this work, the authors compared the fracture behavior using the EWF approach in PP mixtures with and without a compatibilizer. The nanofiller percentage was 5, 10, 15, 20, 25, 30 and 35 wt.%, through the intercalation method with PP and PP-SEBS-g-MA. The DDENT specimens were obtained by injection molding with a thickness of 2 mm. The authors observed that the presence of clay particles at higher content (30 wt.%) leads to a reduction in both the essential and plastic work of fracture due to the rigid character of the clay.

The EWF approach is widely used to determine the plane stress fracture toughness of highly ductile polymers. To understand how the presence of nanofillers influences fracture toughness, Karger-Kocsis et al. [269] mixed amorphous copolyester and polypropylene block copolymer with multiwall carbon nanotube (MWCNT), graphene (GR), boehmite alumina (BA), and organoclay (oMMT) at one wt.% each. They performed the EWF test, and the data reduction occurred by energy partitioning between yielding and necking. The fracture zone showed some tearing morphology. The EWF prerequisites were not met with the nanocomposites containing MWCNT and GR, by contrast to those with BA and oMMT. Therefore, the fracture toughness of nanocomposites with homogeneous clay dispersion was properly determined using the EWF method. The authors also found that incorporating oMMT may result in an adverse effect between the w_e and w_p terms.

Some authors [265] used the EWF method to compare the effect of the clay content and the coupling agent on the fracture toughness of polypropylene films. The authors found that the addition of mineral clay led to a considerable reduction in the w_e term compared with the unfilled PP, and the coupling agent did not influence the fracture parameters. However, the presence of clay promoted an appreciable increase in dissipated plastic work, regardless of the clay content.

Other authors applied the EWF method to evaluate molecular compatibility, morphology, and clay content on the fracture parameters [178,180,213,232,233,259,260,310,311].

Bureau et al. [263] discussed the failure mechanisms of polypropylene/clay nanocomposites. The fracture behavior of these nanocomposites, based on polypropylene with organo-modified clays (2 wt.%) and different coupling agents, was evaluated using the EWF procedure. The microstructure revealed an acceptable level of intercalation with partial exfoliation (<100 nm). Furthermore, the mechanical properties increased by 25–50% due to the reinforcing effect of the nanoparticles. The authors evaluated the trends observed in the specific work of fracture for the crack initiation–ligament length ($w_{e,init}$ and $\beta w_{p,init}$). The results show a flat slope of the $w_{e,init}$ curve obtained for PP, which was caused by the difficulty of developing a plane stress condition in PP, and the authors considered this value a reference. The authors suggested that $w_{e,init}$ varies considerably among the materials tested. The addition of clay to PP without coupling agents leads to a decrease in $w_{e,init}$ by more than 75%, depending on the type of coupling agent used. The authors pointed out the quality in clay dispersion could be correlated with $w_{e,init}$. The nanocomposites with lower micron-scale clay particles proved to be those with the highest $w_{e,init}$. However, such a correlation could not be established between $w_{e,init}$ and surface density in sub-micron-scale clay particles. So, the authors underlined that the reinforcement or toughening effects are related to the nanoscale particles, as concluded from tensile results analysis. The authors also analyzed the fracture surfaces. They observed the fracture occurred by void initiating at larger clay particles, followed by void growth and coalescence as the surrounding matrix stretched into ligaments. Thus, toughness improvements were attributed to higher voiding stresses and improved matrix resistance attributed to finer, more oriented clay nanoparticles.

More recently, other authors applied the EWF technique on PP nanocomposites reinforced with Boehmite clay [267,268]. Pedrazzoli et al. [267] studied the influence of boehmite nanoparticles with various surface treatments on the mechanical properties and fracture behavior of polypropylene copolymer nanocomposites. The boehmite was used in pristine and surface-treated forms, adding 2.5, 5, and 10 wt.% using a co-rotating twin-screw extruder. The nanocomposites were successively blow molded to produce films

with a thickness of about 0.05 mm. The authors performed an extensive morphological, rheological, thermal, and mechanical characterization. The results obtained were related to fracture behavior. Thus, the authors found that the specific EWF (w_e) of PP increased after incorporating boehmite. Since the crystalline morphology did not show significant changes, the reinforcing effect was mainly attributed to the nano-reinforcement. However, the increase in the filler content induces a reduction in the w_e values, resulting from an excessive filler content that contributes to the agglomeration of the nanoparticles. According to the authors, this effect was also reflected in the reduction in yield stress.

Regarding the treated boehmite, the nanocomposites showed an increase in resistance with low reinforcement content. However, w_e did not show significant variations and even decreased. The authors declared that these results are in accordance to observed by other authors [237] regarding the direct proportion between w_e and $e_0 \cdot \sigma_y$, where e_0 is the ordinate intercept of extension-at-break versus ligament length linear regression plots. In addition, the authors also reported lower βw_p values when compared with unfilled PP. Therefore, the nanofillers do not influence the dissipative plastic work.

Turcsán et al. [268] used the EWF procedure to determine the fracture toughness of poly (propylene-blockethylene) (EPBC)-based nanocomposites with different boehmite content (0.5, 1, 2.5, 5 wt.%) using a twin-screw extruder. The nanocomposites were compression molded to obtain sheets of 0.5 mm thickness. The degree and quality of the dispersion of the boehmite reinforcement were analyzed using transmission electron microscopy, revealing good distribution and particle agglomerations. The manuscript detailed the efforts to carry out the energy partition method, even though the authors observed that the yield is not instantaneous but develops over time due to the blunting effect. Consequently, the authors indicated that yielding and necking/tearing processes are somewhat superimposed, and only the maximum load may serve for their separation. The results show that a maximum value of w_e is reached with 1 wt.% of boehmite content. Higher concentrations lead to a reducing w_e parameter, similar to those obtained by the unreinforced EPBC.

Similarly, βw_p decreases as the reinforcement content increases. The authors separated the w_p values from the shape factor β , considering the plastic zone as an ellipse. The results indicate a marked reduction in w_p with the filler content, while β remained practically constant, with values very similar to the unfilled EPBC. The authors concluded the dispersion and the filler content have a significant impact on the necking section. The boehmite nanoparticles did not act as a reinforcement, but it hinders the initiation and growth of cracks.

Haghnegahdar et al. [277] evaluated the fracture toughness of polypropylene (PP)/ethylene propylene diene monomer (EPDM)/graphene nanocomposites prepared by melt mixing process via an internal mixer. The authors used multi-layer graphene (MLG) and few-layer graphene (FLG) with 0.5 wt.% as reinforcement. The DENT specimens were obtained by compression molding with a thickness of 1 mm. The essential work of fracture (EWF) method was used to describe the deformation mechanism and fracture toughness behavior of PP/EPDM and its nanocomposites based on FLG or MLG in two systems (vulcanized and un-vulcanized). The results indicate that w_e and βw_p of the PP/EPDM fracture enhanced by dynamic vulcanization and also FLG platelets were more efficient in relation to MLG platelets. The SEM micrographs from the fractured surface and subsurface of DENT specimens in the EWF test revealed that the fracture mechanism of PP/EPDM and its nanocomposites were changed by dynamic vulcanization. In the case of vulcanized samples, the fracture toughness mechanism originated from creating cavitation in the dispersed phase, which caused the formation of nanovoids inside the EPDM droplets. This phenomenon caused the dilatation of shear bands and the development of shear yielding of PP matrix. However, in un-vulcanized specimens, the formation of that dilatation band was more prominent due to debonding of rubber droplets from the surrounding PP matrix. In the PP/EPDM nanocomposites, graphene type played a different role in the fracture toughness mechanism. The MLG acted as a suitable domain for crack initiation, which

decreased the essential work of fracture. Therefore, FLG platelets hindered the crack path and prevented the crack propagation, leading to increased plastic work of fracture.

Franco-Urquiza et al. [260] evaluated the influence of oriented platelets for intercalated and exfoliated morphologies on the fracture parameters of EVOH/oMMT films through transmission electron microscopy (TEM). The observations revealed that the longitudinal axis of the whole particles was disposed parallel to the melt direction (MD). In order to evaluate the effect of the particle orientation on the fracture parameters, DDENT specimens were cut in the melt and transverse directions (TD). Considering this, the FPZ was perpendicular or parallel to the length of the whole particles, as presented in Figure 24.

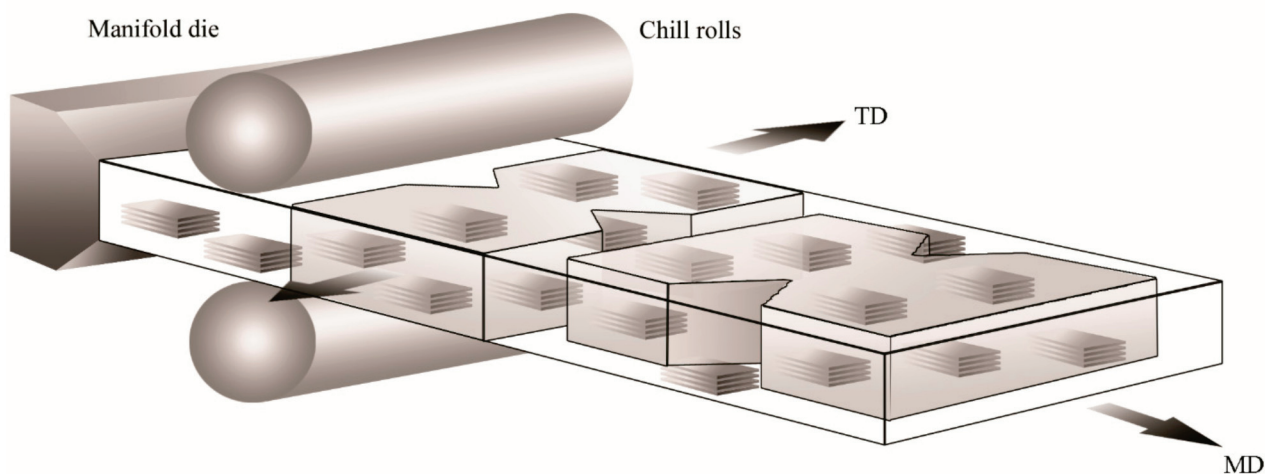


Figure 24. Schematic representation of the cast film extrusion and the orientation of DDENT specimens in MD and TD. The figure represents the clay particle orientation and its influence on the fracture behavior.

The fracture surfaces of DDENT specimens in both configurations (MD and TD) showed distinct behavior related to the orientation of the oMMT particles. According to the SEM observations, the FPZ of the polymer film containing 2.5 wt.% of oMMT in MD showed a necking ligament section notoriously lower than the nanocomposites tested in TD. At higher magnifications, the fracture surfaces of the nanocomposites showed a high level of fibrillation, being more evident for the DDENT specimens tested in MD than in TD, which was attributed to the orientation of the clay particles within the polymer matrix that hinder the plastic flow during the fracture process. Regarding the fracture parameters, the results show that the clay particles act as effective reinforcement since the toughness increased in both configurations (MD and TD). However, βw_p did not show an evident tendency, and it was necessary to calculate the shape factor. Thus, β increased with the clay content in MD and decreased in TD because the longest longitudinal axis was oriented parallel to the crack propagation, promoting lower stress transfer than in MD. On the other hand, w_p decreased for both configurations (MD and TD) because the clay particles restrict the plastic flow during the fracture process.

Many commercial clay minerals contain organic modifiers. This modification favors molecular diffusion as long as there is an affinity between the organic modifier and the polymer chains. Franco-Urquiza et al. [281] demonstrated that molecular compatibility could dramatically influence the morphology of clay sheets (Figure 25) and their degree of exfoliation. They used two distinct organo-montmorillonite (oMMT) clays in ethylene-vinyl alcohol (EVOH) copolymer film. The affinity between EVOH and the modifier within oMMT resulted in intercalated morphology because of well-dispersed and oriented platelets due to the sliding during processing (Figure 25a). The low affinity between EVOH and organoclay led to immiscible systems with tactoids by folding the platelets from the clay stacks (Figure 25b). Both morphologies altered the mechanical parameters and the fracture behavior in different ways. The specific essential fracture work (w_e) was influenced by the clay content and crystallinity in both cases. The shape factor increased with the clay

content, which implies that the oMMT transfers the stresses for affinity nanocomposites. In inadequate affinity systems, clay particles promoted plastic deformation at low stress levels, according to the values obtained from the specific plastic work (w_p) and observations by SEM. On the other hand, it was observed that the degree of exfoliation decreased as the clay content increased, promoting the development of agglomerated particles.

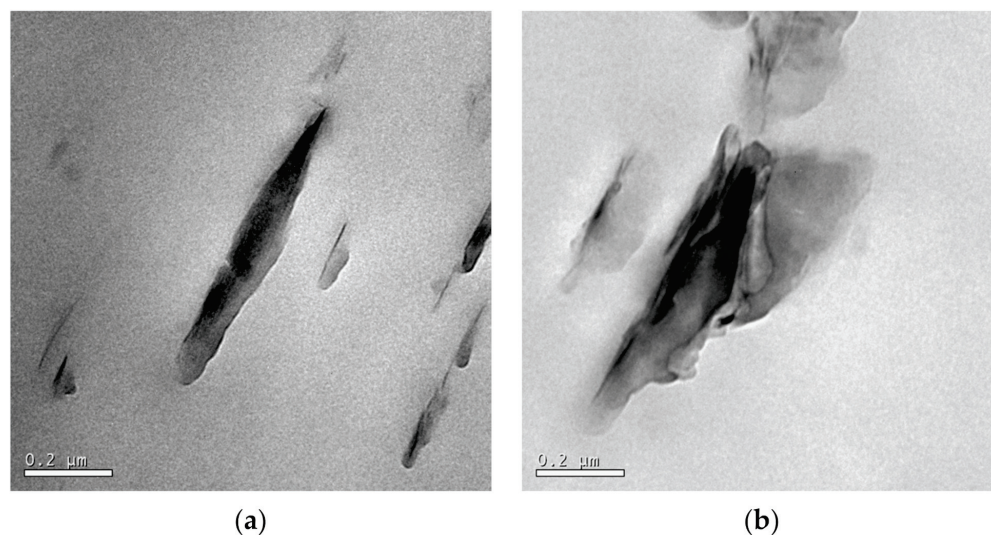


Figure 25. TEM micrographs showing distinct morphologies: (a) laminar, (b) rolled. The micrographs intend to represent the effect of molecular compatibility between polymer and organomodified clays.

Block copolymers represent a particular class of self-assembled nanostructured materials, the structure and size of whose morphology can be controlled by molecular architecture, molecular weight, and composition. Martin Ganß et al. [261] studied the influence of oligostyrene-modified montmorillonite (os-MMT) on the morphological, mechanical, and fracture behavior of styrene-butadiene-based block copolymer. They performed the EWF tests to evaluate the crack propagation using a pseudo-single specimen. TEM observations detected a high degree of exfoliation of MMT against well-distributed tactoids with gallery spacings of approximately 10 nm. The authors observed a maximum in the resistance to crack propagation at 3 wt.% of os-MMT accompanied by a change in deformation mechanism from homogenous plastic flow (drawing and micro-necking of microdomains) in the block copolymer nanocomposite (BCP-NC) with 0 to 1 wt.% of os-MMT to a craze-like deformation (microvoid formation and stretching of polymer fibrils) for the BCP-NC with 3 to 5 wt.% of os-MMT. Furthermore, above 5 wt.% os-MMT content a tough-to-brittle type transition attributed to the micro-sized aggregates combined with increased content of rigid PS phase controlling the fracture process BCP-NC with 10 wt.% nanofillers could be ascertained. The authors made an in-depth analysis of the fracture surface, and carried out the correlations between the structural attributes, mechanical behavior and the crack toughness behavior of the developed nanocomposites. They highlighted that the crack initiation behavior, characterized by the magnitude of the specific essential fracture work w_e , changes from being dominated by the polymeric matrix to being dominated by the nano-reinforcement close to 1 wt.%. By increasing the filler content, (3–5 wt.%), the intercalated silicate platelets favored a higher fraction of nano-confined layers in morphology and therefore improved the overall hard phase content, leading to a three-fold reduction in the value of w_e . However, resistance to crack propagation βw_p increases. The authors attributed these results to a change in the deformation mechanism of the homogeneous plastic flow. Finally, the authors observed that higher concentrations of reinforcement, above 5 wt.%, the transition from toughness to brittle observed in the fracture behavior was attributed to the aggregates micrometers in size and the increase in the hard phase content.

Polyamides contain a repeated CO-NH group within the chain. They are well-known engineering thermoplastic materials widely used in industrial applications because of their remarkable mechanical and thermal properties. However, moisture absorption is a relevant limitation. The incorporation of nanometer-scale reinforcement improves the stiffness and toughness of PA.

Baldi et al. [277] evaluated the rubber toughening of polyamide 6 (PA6)/layered-silicate nanocomposites. Nanocomposites with different reinforcing contents were prepared by melt intercalation. For this, a 20 wt.% masterbatch was extruded, which was then diluted in PA6 matrix using a co-rotating twin-screw extruder to obtain concentrations of 4 and 6 wt.%. Three rubber contents were used (0, 5, and 10% by weight). The authors also evaluated the influence of humidity, analyzing the behavior of the various nanocomposites at three humidity levels: dry, slightly humid, and very humid. The authors found that silicate layers in the PA6 matrix strongly influenced the creep and fracture behavior of the material, increasing the elastic limit and reducing the resistance to fracture, depending on the moisture content. The addition of a rubbery phase increased the fracture strength of the nanocomposites under slightly humid conditions, providing evidence of a hardening effect. At the same time, they did not observe a significant increase in fracture toughness in the materials under dry conditions. The authors concluded that a good balance between stiffness and toughness can be obtained under certain humidity conditions, using a suitable rubber-to-silicate layer content ratio.

There is an extensive literature review regarding evaluating the EWF technique for thermoplastic polymers, especially for polyolefins, as previously indicated. However, there is a wide field of opportunities to test the fracture toughness in thermoplastic natural rubber (TPNR) reinforced with clay minerals. An extensive literature review has been carried out, and just one reference on the fracture behavior of these nanocomposites was found. TPNR is a blended material made from natural rubber (NR) and a thermoplastic, such as polypropylene, polystyrene, and polyethylenes, which provides intermediate properties between NR and plastics. Currently, TPNR is used for several industrial applications. Ahmad et al. [309] performed the analysis of the mechanical properties and fracture toughness of TPNR nanocomposites. The nanocomposites were prepared in a twin-screw extruder, varying the concentration of the MMT clay content intercalated with octadecylamine. The authors developed two nanoclay dispersion methods. In the first method, called the direct method (DM), the nanoclay was incorporated into the fused TPNR matrix. In the second method, called the indirect method (IDM), the organoclay was pre-mixed in liquid natural rubber (LNR) before mixing in extrusion. The fracture toughness was evaluated through the EWF technique using 1 mm thick sheets. The addition of optimum organoclay content led to a substantial improvement in stiffness. However, the authors note that the addition of organo-clay reduced the total work of fracture w_f for both nanocomposites. The EWF results show that incorporating 4 wt.% organo-clay causes a notable reduction in βw_p for IDM nanocomposites compared to the TPNR matrix. In the case of DM nanocomposites, the authors observed the same trend with the decrease in the values of both specific fracture parameters. The authors attributed these trends to the stiff nature of the clay, which prevents plastic deformation from occurring and the constrained mobility of polymer chains in the presence of organo-clay particles.

Poly(lactic acid), or polylactide (PLA), is a biodegradable, biocompatible, and renewable thermoplastic polyester, which is mainly derived from corn starch. PLA is classified as an aliphatic polyester because of the ester bonds that connect the monomer units. This bio thermoplastic is the most comprehensively explored biodegradable and renewable thermoplastic polyester. However, uncontrolled degradation, poor thermal properties, and brittleness are the significant drawbacks of PLA. Consequently, PLA nanocomposite systems have been widely exploited to address some of the shortcomings.

Arroyo et al. [308] investigated the processing and fracture behavior of PLA/thermoplastic starch/montmorillonite nanocomposites. Thermoplastic wheat starch (TPS) and PLA were combined with a non-organic MMT clay, using a twin-screw extrusion process to investi-

gate the structure and properties of these nanocomposites. The method of incorporation and gelatinization of starch was based on the technique developed by Rodríguez-González and collaborators [312].

The authors also paid particular attention to moisture content to assess the degree of intercalation/exfoliation of MMT platelets. The authors evaluated the mechanical properties of these biodegradable nanocomposites and their fracture behavior using DDENT specimens and following the EWF protocol. The authors made two relevant observations. The first is that the data obtained met the criteria of self-similarity. Yield stress increased with the ligament length and the general shape of the stress–strain curves was similar. The second general observation is that all the investigated materials exhibited relatively brittle behavior. The initiation energy was significantly higher than the propagation energy, which resulted in both polymers showing a relatively small plastic term, expressed at a low coefficient of linearity. This observation allows the authors to express their questions about whether the plane stress conditions were fully developed during the EWF tests.

The results indicate that PLAG (PLA with maleic anhydride grafted) has lower $w_{e,ini}$ and $w_{e,tot}$ values than neat PLA, which the authors attributed to a lower molecular weight. The authors also found that the presence of TPS in PLA led to a considerable reduction in $w_{e,ini}$ and $w_{e,tot}$ while βw_p increased dramatically. However, the presence of TPS in PLAG did not lead to such a reduction in $w_{e,ini}$ and $w_{e,tot}$ parameters but did lead to a similar increase in βw_p values.

The clay particles showed a higher affinity with the TPS phase. The clay in the TPS phase remains in it, while the clay in the PLA phase migrates to the interface of the blend or even crosses the interface to the TPS phase. The addition of MMT clay increased the tensile modulus of the materials. This observation was most noticeable in the blend with higher TPS content because the tensile modulus of TPS is much lower than PLA. Fracture toughness and elongation at break decreased with the addition of clay. The authors concluded that clay at the interface of the mixtures could reduce the interaction between the PLA and TPS phases in compatibilized mixtures, resulting in a lower stress transfer from the PLA matrix to the disperse TPS phase.

Maspoch et al. [224] employed the EWF methodology to evaluate the ductile–brittle transition behavior of biodegradable polymers. The authors confirmed that the EWF was successfully applied in the organo-modified montmorillonite-based poly(lactic acid) films (PLA/oMMT). In order to evaluate the fracture behavior, the PLA/oMMT films were subjected to a de-aging process. According to differential scanning calorimetry (DSC) results, physical aging at 30 °C of PLA/o-MMT samples exhibited slower enthalpy relaxation kinetics than the neat PLA, which pointed to the toughening mechanisms promoted by oMMT. Similarly, Rodríguez et al. [306] used the PLA/oMMT to evaluate the specific essential work of fracture and compare it with the small punch test (SPT) methodology. The results show that the SPT is an effective tool for the mechanical characterization of these materials because it is possible to perform, from one test with a small sample, the mechanical characterization, and the fracture toughness. The straightforwardness of both the testing procedure and the preparation of the specimens facilitates the rapid characterization. However, the results also reveal that the SPT test is susceptible to prior defects and the oMMT content, allowing the applicability of the EWF method for fracture characterization in ductile materials.

4. Conclusions

This work compiles a relevant amount of information on the influence of clay minerals on the fracture behavior of ductile nanocomposites using the EWF technique. From the literature collected, some conclusions can be highlighted:

1. Although clay minerals are commonly used in the development of clay-based polymer nanocomposites, the montmorillonite clay is widely studied. Therefore, there is a wide field of research to explore with the rest of the phyllosilicates.

2. Most clay-based polymer nanocomposites are processed by twin-screw extrusion, leaving aside the use of single-screw extruders. Although the shear stress generated by the twin-screw technology is very efficient in the exfoliation and dispersion of nanoclays (especially polyamides), it promotes the degradation of both the polymer matrix and the organic compounds contained in the modified clays. However, references about processing-induced degradation and its effect on the fracture toughness of polymer nanocomposites were not found.
3. The EWF approach allows the evaluation of the fracture behavior of ductile polymers. However, most of the literature focuses on polyolefins and polyamides. One field that is currently being explored is the study of toughness in bio-based polymer nanocomposites. PLA is the most widely used material, but there are many research opportunities in evaluating the fracture behavior of green polymer nanocomposites.

Funding: This work was supported by the Secretary of Public Education (SEP) and National Council of Science and Technology (CONACYT) through the Basic Science Fund (SEP-CONACYT Ciencia Basica) (grant number 257458) and funded by CONACYT through the Institutional Fund for Regional Promotion for Scientific, Technological and Innovation Development (FORDECYT), grant number 297708. The APC was funded by FORDECYT, grant number 297708.

Institutional Review Board Statement: Not applicable.

Informed Consent Statement: Not applicable.

Data Availability Statement: This study did not report any data.

Acknowledgments: Edgar Franco conveys special appreciation to the “CONACYT Researchers Program (Catedras CONACYT)”.

Conflicts of Interest: The author declare no conflict of interest.

References

1. Mittal, V. Polymer layered silicate nanocomposites: A review. *Materials* **2009**, *2*, 992–1057. [CrossRef]
2. Alexandre, M.; Dubois, P. Polymer-layered silicate nanocomposites: Preparation, properties and uses of a new class of materials. *Mater. Sci. Eng. R Rep.* **2000**, *28*, 1–63. [CrossRef]
3. Sinha Ray, S.; Okamoto, M. Polymer/layered silicate nanocomposites: A review from preparation to processing. *Prog. Polym. Sci.* **2003**, *28*, 1539–1641. [CrossRef]
4. Minerals, S.; Page, I.; The, S.M.; Guggenheim, S.; Martin, R.T.; Alietti, A.; Drits, V.A.; Formoso, M.L.L.; Galán, E.; Köster, H.M.; et al. Clays, nanoclays, and montmorillonite minerals. *Dev. Clay Sci.* **2017**, *148*, 255–256. [CrossRef]
5. Camargo, P.H.C.; Satyanarayana, K.G.; Wypych, F. Nanocomposites: Synthesis, structure, properties and new application opportunities. *Mater. Res.* **2009**, *12*, 1–39. [CrossRef]
6. Giannelis, E.P. Polymer layered silicate nanocomposites. *Adv. Mater.* **1996**, *8*, 29–35. [CrossRef]
7. Hanemann, T.; Szabó, D.V. Polymer-Nanoparticle Composites: From Synthesis to Modern Applications. *Materials* **2010**, *3*, 3468–3517. [CrossRef]
8. Paul, D.R.; Robeson, L.M. Polymer nanotechnology: Nanocomposites. *Polymer* **2008**, *49*, 3187–3204. [CrossRef]
9. Giannelis, E.P.; Krishnamoorti, R.; Manias, E. Polymer-Silicate Nanocomposites: Model Systems for Confined Polymers and Polymer Brushes. In *BT—Polymers in Confined Environments*; Granick, S., Binder, K., de Gennes, P.-G., Giannelis, E.P., Grest, G.S., Hervet, H., Krishnamoorti, R., Léger, L., Manias, E., Raphaël, E., et al., Eds.; Springer: Berlin/Heidelberg, Germany, 1999; pp. 107–147, ISBN 978-3-540-69711-4.
10. Papp, S.; Szucs, A.; Dékány, I. Colloid synthesis of monodisperse Pd nanoparticles in layered silicates. *Solid State Ion.* **2001**, *141–142*, 17169–17211. [CrossRef]
11. Papp, S.; Szel, J.; Dékány, I. Stabilization of rhodium nanoparticles in an aqueous medium by polymer and layered silicates. *Nanotechnology* **2003**, *5118*, 646–656.
12. Ruiz-Hitzky, E.; Aranda, P.; Darder, M. Hybrid and Biohybrid Materials Based on Layered Clays. In *Tailored Organic-Inorganic Materials*; John Wiley & Sons, Inc.: Hoboken, NJ, USA, 2015; pp. 245–297, ISBN 9781118792223.
13. Ouchiar, S.; Stoclet, G.; Cabaret, C.; Georges, E.; Smith, A.; Martias, C.; Addad, A.; Gloaguen, V. Comparison of the influence of talc and kaolinite as inorganic fillers on morphology, structure and thermomechanical properties of polylactide based composites. *Appl. Clay Sci.* **2015**, *116–117*. [CrossRef]
14. Sleptsova, S.A.; Okhlopko, A.A.; Kapitonova, I.V.; Lazareva, N.N.; Makarov, M.M.; Nikiforov, L.A. Spectroscopic study of tribooxidation processes in modified PTFE. *J. Frict. Wear* **2016**, *37*. [CrossRef]

15. Iqbal, S.; Inam, F.; Iqbal, N.; Jamil, T.; Bashir, A.; Shahid, M. Thermogravimetric, differential scanning calorimetric, and experimental thermal transport study of functionalized nanokaolinite-doped elastomeric nanocomposites. *J. Therm. Anal. Calorim.* **2016**, *125*. [CrossRef]
16. Malkappa, K.; Rao, B.N.; Jana, T. Functionalized polybutadiene diol based hydrophobic, water dispersible polyurethane nanocomposites: Role of organo-clay structure. *Polymer* **2016**, *99*. [CrossRef]
17. Neto, J.C.M.; Kimura, S.P.R.; Adeodato, M.G.; Neto, J.E.; Do Nascimento, N.R.; Lona, L.M.F. Intercalation and exfoliation mechanism of kaolinite during the emulsion polymerization. *Chem. Eng. Trans.* **2017**, *57*. [CrossRef]
18. Youssef, A.M.; El-Sayed, S.M. Bionanocomposites materials for food packaging applications: Concepts and future outlook. *Carbohydr. Polym.* **2018**, *193*. [CrossRef]
19. Cabedo, L.; Plackett, D.; Giménez, E.; Lagarón, J.M. Studying the degradation of polyhydroxybutyrate-co-valerate during processing with clay-based nanofillers. *J. Appl. Polym. Sci.* **2009**, *112*. [CrossRef]
20. Letaief, S.; Christian, D. Functionalization of the interlayer surfaces of kaolinite by alkylammonium groups from ionic liquids. *Clays Clay Miner.* **2009**, *57*. [CrossRef]
21. Sun, D.; Li, Y.; Zhang, B.; Pan, X. Preparation and characterization of novel nanocomposites based on polyacrylonitrile/kaolinite. *Compos. Sci. Technol.* **2010**, *70*. [CrossRef]
22. Rhim, J.W.; Park, H.M.; Ha, C.S. Bio-nanocomposites for food packaging applications. *Prog. Polym. Sci.* **2013**, *38*. [CrossRef]
23. Weiss, S.; Hirsemann, D.; Biersack, B.; Ziadeh, M.; Müller, A.H.E.; Breu, J. Hybrid Janus particles based on polymer-modified kaolinite. *Polymer* **2013**, *54*. [CrossRef]
24. Kirillina, I.V.; Nikiforov, L.A.; Okhlopko, A.A.; Sleptsova, S.A.; Yoon, C.; Cho, J.H. Nanocomposites based on polytetrafluoroethylene and ultrahigh molecular weight polyethylene: A brief review. *Bull. Korean Chem. Soc.* **2014**, *35*. [CrossRef]
25. Cui, Y.; Kumar, S.; Rao Kona, B.; Van Houcke, D. Gas barrier properties of polymer/clay nanocomposites. *RSC Adv.* **2015**, *5*. [CrossRef]
26. Poikelispää, M.; Das, A.; Dierkes, W.; Vuorinen, J. The effect of coupling agents on silicate-based nanofillers/carbon black dual filler systems on the properties of a natural rubber/butadiene rubber compound. *J. Elastomers Plast.* **2015**, *47*. [CrossRef]
27. Dang, W.; Lorenzelli, L.; Vinciguerra, V.; Dahiya, R. Hybrid structure of stretchable interconnect for reliable E-skin application. In Proceedings of the IEEE International Symposium on Industrial Electronics, Edinburgh, UK, 19–21 June 2017.
28. Dolgoplov, K.N.; Lyubimov, D.N. Evaluation of tribological properties of components of polymer composite selflubricating materials. *MATEC Web Conf.* **2018**, *226*, 01005. [CrossRef]
29. Valentin, T.M.; Dubois, E.M.; Machnicki, C.E.; Bhaskar, D.; Cui, F.R.; Wong, I.Y. 3D printed self-adhesive PEGDA-PAA hydrogels as modular components for soft actuators and microfluidics. *Polym. Chem.* **2019**, *10*. [CrossRef]
30. Kotsilkova, R.; Petkova, V.; Pelovski, Y. Thermal analysis of polymer-silicate nanocomposites. *J. Therm. Anal. Calorim.* **2001**, *64*, 591–598. [CrossRef]
31. Kotsilkova, R. Rheology-structure relationship of polymer/layered silicate hybrids. *Mech. Time-Depend. Mater.* **2002**, *6*. [CrossRef]
32. Kiersnowski, A.; Serwaczak, M.; Kułaga, E.; Futoma-Kołoch, B.; Bugla-Płoskońska, G.; Kwiatkowski, R.; Doroszkiewicz, W.; Pięłowski, J. Delamination of montmorillonite in serum-A new approach to obtaining clay-based biofunctional hybrid materials. *Appl. Clay Sci.* **2009**, *44*. [CrossRef]
33. Szczerba, M.; Środoń, J.; Skiba, M.; Derkowski, A. One-dimensional structure of exfoliated polymer-layered silicate nanocomposites: A polyvinylpyrrolidone (PVP) case study. *Appl. Clay Sci.* **2010**, *47*. [CrossRef]
34. Lan, Y.F.; Lee, R.H.; Lin, J.J. Aqueous dispersion of conjugated polymers by colloidal clays and their film photoluminescence. *J. Phys. Chem. B* **2010**, *114*. [CrossRef] [PubMed]
35. Tamura, K.; Yamada, H. Morphology Generation in Polymer Nanocomposites Using Various Layered Silicates. *Optim. Polym. Nanocomposite Prop.* **2010**, *198*. [CrossRef]
36. Pascua, C.S.; Ohnuma, M.; Matsushita, Y.; Tamura, K.; Yamada, H.; Cuadros, J.; Ye, J. Synthesis of monodisperse Zn-smectite. *Appl. Clay Sci.* **2010**, *48*. [CrossRef]
37. Chang, Y.C.; Chou, C.C.; Lin, J.J. Emulsion intercalation of smectite clays with comb-branched copolymers consisting of multiple quaternary amine salts and a poly(styrene-butadiene-styrene) backbone. *Langmuir* **2005**, *21*. [CrossRef]
38. Dudkina, M.M.; Tenkovtsev, A.V.; Pospiech, D.; Jehnichen, D.; Häußler, L.; Leuteritz, A. Nanocomposites of NLO chromophore-modified layered silicates and polypropylene. *J. Polym. Sci. Part B Polym. Phys.* **2005**, *43*. [CrossRef]
39. Leroux, F. Organo-modified anionic clays into polymer compared to smectite-type nanofiller: Potential applications of the nanocomposites. *J. Nanosci. Nanotechnol.* **2006**, *6*. [CrossRef]
40. Wang, H.W.; Dong, R.X.; Liu, C.L.; Chang, H.Y. Effect of clay on properties of polyimide-clay nanocomposites. *J. Appl. Polym. Sci.* **2007**, *104*. [CrossRef]
41. Liu, T.; Chen, B.; Evans, J.R.G. Ordered assemblies of clay nano-platelets. *Bioinspir. Biomim.* **2008**, *3*. [CrossRef]
42. Darder, M.; Aranda, P.; Ruiz, A.I.; Fernandes, F.M.; Ruiz-Hitzky, E. Design and preparation of bionanocomposites based on layered solids with functional and structural properties. *Mater. Sci. Technol.* **2008**, *24*, 1100–1110. [CrossRef]
43. Watanabe, H.; Matsushima, H.; Fuji, M.; Takahashi, M. Electrophoretic Deposition of Smectite Particles onto Copper Plate. *Key Eng. Mater.* **2009**, *412*, 195–200. [CrossRef]
44. Maiti, M.; Bhowmick, A.K. Synthesis and properties of new fluoroelastomer nanocomposites from tailored anionic layered magnesium silicates (hectorite). *J. Appl. Polym. Sci.* **2009**, *111*. [CrossRef]

45. Suh, D.J.; Park, O.O.; Mun, J.; Yoon, C.S. Photorefractive behaviors in a polymer composite including layered silicates. *Appl. Clay Sci.* **2002**, *21*. [CrossRef]
46. Wang, K.; Liang, S.; Du, R.; Zhang, Q.; Fu, Q. The interplay of thermodynamics and shear on the dispersion of polymer nanocomposite. *Polymer* **2004**, *45*. [CrossRef]
47. Shi, X.; Gan, Z. Preparation and characterization of poly(propylene carbonate)/montmorillonite nanocomposites by solution intercalation. *Eur. Polym. J.* **2007**, *43*. [CrossRef]
48. Dornelas, C.B.; Resende, D.K.; Tavares, M.I.B.; Gomes, A.S.; Cabral, L.M. Preparation and reactional evaluation of formation of PVP K-30 - Montmorillonite (natural and organophilic) by X ray diffraction. *Polímeros* **2008**, *18*. [CrossRef]
49. Wang, C.A.; Long, B.; Lin, W.; Huang, Y.; Sun, J. Poly(amic acid)-clay nacrelite composites prepared by electrophoretic deposition. *J. Mater. Res.* **2008**, *23*. [CrossRef]
50. Galimberti, M.; Martino, M.; Guenzi, M.; Leonardi, G.; Citterio, A. Thermal stability of ammonium salts as compatibilizers in polymer/layered silicate nanocomposites. *E-Polymers* **2009**. [CrossRef]
51. Buruiana, T.; Melinte, V.; Buruiana, E.C.; Mihai, A. Synthesis and characterization of polyurethane cationomer/MMT hybrid composite. *Polym. Int.* **2009**, *58*. [CrossRef]
52. Gao, J.; Guo, N.; Liu, Y.; Li, J.; Hu, H.; Sun, L.; Zhang, X. Effect of compound technology on polyethylene/montmorillonite composites. In Proceedings of the IEEE International Conference on Properties and Applications of Dielectric Materials, Harbin, China, 19–23 July 2009.
53. Soundararajah, Q.Y.; Karunaratne, B.S.B.; Rajapakse, R.M.G. Mechanical properties of poly(vinyl alcohol) montmorillonite nanocomposites. *J. Compos. Mater.* **2010**, *44*. [CrossRef]
54. Chang, M.K.; Hsieh, H.H.; Li, S.J. A Study of Thermal Stability and Electromagnetic Shielding Behavior of Polyaniline-P-Toluene Sulfonic Acid/Montmorillonite Nanocomposites. *Appl. Mech. Mater.* **2011**, *52–54*, 180–185. [CrossRef]
55. Monsiváis-Barrón, A.J.; Bonilla-Rios, J.; Ramos De Valle, L.F.; Palacios, E. Oxygen permeation properties of HDPE-layered silicate nanocomposites. *Polym. Bull.* **2013**, *70*. [CrossRef]
56. Shiravand, F.; Hutchinson, J.M.; Calventus, Y. Influence of the isothermal cure temperature on the nanostructure and thermal properties of an epoxy layered silicate nanocomposite. *Polym. Eng. Sci.* **2014**, *54*. [CrossRef]
57. Wooster, T.J.; Abrol, S.; MacFarlane, D.R. Cyanate ester polymerization catalysis by layered-silicates. *Polymer* **2004**, *45*. [CrossRef]
58. Jin, X.; Hu, X.; Wang, Q.; Wang, K.; Yao, Q.; Tang, G.; Chu, P.K. Multifunctional cationic polymer decorated and drug intercalated layered silicate (NLS) for early gastric cancer prevention. *Biomaterials* **2014**, *35*. [CrossRef]
59. Riaz, U.; Ashraf, S.M.; Verma, A. Influence of Conducting Polymer as Filler and Matrix on the Spectral, Morphological and Fluorescent Properties of Sonochemically Intercalated poly(o-phenylenediamine)/Montmorillonite Nanocomposites. *Recent Pat. Nanotechnol.* **2016**, *10*. [CrossRef]
60. Ghosh, S.K.; Rahman, W.; Middya, T.R.; Sen, S.; Mandal, D. Improved breakdown strength and electrical energy storage performance of γ -poly(vinylidene fluoride)/unmodified montmorillonite clay nano-dielectrics. *Nanotechnology* **2016**, *27*. [CrossRef]
61. Pu, W.F.; Yang, Y.; Yuan, C.D. Gelation performance of poly(ethylene imine) crosslinking polymer-layered silicate nanocomposite gel system for potential water-shutoff use in high-temperature reservoirs. *J. Appl. Polym. Sci.* **2016**, *133*. [CrossRef]
62. Saldábola, R.; Merijs Meri, R.; Zicans, J.; Ivanova, T.; Berzina, R. PC/ABS Nanocomposites with Layered Silicates Obtaining, Structure and Properties. *Key Eng. Mater.* **2016**, *721*, 38–42. [CrossRef]
63. Hernandez-Guerrero, O.; Castillo-Pérez, R.; Hernández-Vargas, M.L.; Campillo-Illanes, B.F. Study of Thermal and Mechanical Properties of Clay/Polymer Nanocomposite Synthesized Via Modified Solution Blending. *MRS Adv.* **2017**, *2*, 2757–2762. [CrossRef]
64. El-Sheikhy, R.; Al-Shamrani, M. Interfacial bond assessment of clay-polyolefin nanocomposites CPNC on view of mechanical and fracture properties. *Adv. Powder Technol.* **2017**, *28*. [CrossRef]
65. İlk, S.; Şener, M.; Vural, M.; Serçe, S. Chitosan/Octadecylamine-Montmorillonite Nanocomposite Containing Nigella arvensis Extract as Improved Antimicrobial Biofilm Against Foodborne Pathogens. *Bionanoscience* **2018**, *8*. [CrossRef]
66. Ashok Gandhi, R.; Jayaseelan, V.; Raghunath, B.K.; Palanikumar, K.; Ramachandran, S. Nano indentation hardness testing of PP-CNT composites. *Mater. Today Proc.* **2019**, *16*, 1372–1377. [CrossRef]
67. Shuai, C.; Li, Y.; Feng, P.; Yang, W.; Zhao, Z.; Liu, W. Montmorillonite reduces crystallinity of poly-l-lactic acid scaffolds to accelerate degradation. *Polym. Adv. Technol.* **2019**, *30*. [CrossRef]
68. Chou, C.C.; Lin, J.J. One-step exfoliation of montmorillonite via phase inversion of amphiphilic copolymer emulsion. *Macromolecules* **2005**, *38*. [CrossRef]
69. Attia, N.F.; Nour, M.; Hassan, M.; Mohamed, G.; Oh, H.; Mahmoud, M. Effect of type of organic modifier on the clay layered-based nanocomposites flammability and toxic gases emission. *J. Thermoplast. Compos. Mater.* **2020**. [CrossRef]
70. Zubair, M.; Ullah, A. Recent advances in protein derived bionanocomposites for food packaging applications. *Crit. Rev. Food Sci. Nutr.* **2020**, *60*. [CrossRef]
71. Meng, N.; Zhang, M.; Ge, M.Q.; Zhou, N.; Chi, C.; Chu, X.; Sun, B.; Gao, X. Montmorillonite-lecithin-heparin/PDMS films with enhanced mechanical and antithrombogenic properties. *Polym. Compos.* **2020**, *41*. [CrossRef]
72. Sheu, Z.; Cheng, Y.B.; Simon, G.P. Sequential and simultaneous melt intercalation of poly(ethylene oxide) and poly(methyl methacrylate) into layered silicates. *Macromolecules* **2005**, *38*. [CrossRef]

73. Qin, H.; Zhang, S.; Liu, H.; Xie, S.; Yang, M.; Shen, D. Photo-oxidative degradation of polypropylene/montmorillonite nanocomposites. *Polymer* **2005**, *46*. [CrossRef]
74. Rehab, A.; Salahuddin, N. Nanocomposite materials based on polyurethane intercalated into montmorillonite clay. *Mater. Sci. Eng. A* **2005**, *399*. [CrossRef]
75. Hao, X.; Gai, G.; Liu, J.; Yang, Y.; Zhang, Y.; Nan, C.W. Flame retardancy and antidripping effect of OMT/PA nanocomposites. *Mater. Chem. Phys.* **2006**, *96*. [CrossRef]
76. Zhu, Y.; Wang, B.; Gong, W.; Kong, L.; Jia, Q. Investigation of the hydrogen-bonding structure and miscibility for PU/EP IPN nanocomposites by PALS. *Macromolecules* **2006**, *39*. [CrossRef]
77. Román, F.; Montserrat, S.; Hutchinson, J.M. On the effect of montmorillonite in the curing reaction of epoxy nanocomposites. *J. Therm. Anal. Calorim.* **2007**, *87*, 113–118. [CrossRef]
78. Vasilev, A.P.; Struchkova, T.S.; Nikiforov, L.A.; Okhlopkova, A.A.; Grakovich, P.N.; Shim, E.L.; Cho, J.H. Mechanical and tribological properties of polytetrafluoroethylene composites with carbon fiber and layered silicate fillers. *Molecules* **2019**, *24*, 224. [CrossRef]
79. Wan, Y.; Fan, Y.; Dan, J.; Hong, C.; Yang, S.; Yu, F. A review of recent advances in two-dimensional natural clay vermiculite-based nanomaterials. *Mater. Res. Express* **2019**, *6*. [CrossRef]
80. Leont'ev, L.B.; Shapkin, N.P.; Leont'ev, A.L. Effect of the Chemical Composition and Structural Characteristics of Vermiculite-Based Tribotechnical Materials on the Operating Ability of the Coatings Formed. *J. Mach. Manuf. Reliab.* **2020**, *49*. [CrossRef]
81. Mittal, V. High CEC generation and surface modification in mica and vermiculite minerals. *Philos. Mag.* **2013**, *93*. [CrossRef]
82. Sleptsova, S.A.; Afanas'eva, E.S.; Grigor'eva, V.P. Structure and tribological behavior of polytetrafluoroethylene modified with layered silicates. *J. Frict. Wear* **2009**, *30*. [CrossRef]
83. Mehrotra, V.; Giannelis, E.P. Metal-insulator molecular multilayers of electroactive polymers: Intercalation of polyaniline in mica-type layered silicates. *Solid State Commun.* **1991**, *77*. [CrossRef]
84. Gaylarde, P.; Gaylarde, C. Deterioration of siliceous stone monuments in Latin America: Microorganisms and mechanisms. *Corros. Rev.* **2004**, *22*. [CrossRef]
85. Heinz, H.; Koerner, H.; Anderson, K.L.; Vaia, R.A.; Farmer, B.L. Force field for mica-type silicates and dynamics of octadecylammonium chains grafted to montmorillonite. *Chem. Mater.* **2005**, *17*. [CrossRef]
86. Zhang, X.; Lin, G.; Abou-Hussein, R.; Hassan, M.K.; Noda, I.; Mark, J.E. Some novel layered-silicate nanocomposites based on a biodegradable hydroxybutyrate copolymer. *Eur. Polym. J.* **2007**, *43*. [CrossRef]
87. Zhang, Y.H.; Su, Q.S.; Yu, L.; Liao, L.B.; Zheng, H.; Huang, H.T.; Zhang, G.G.; Yao, Y.B.; Lau, C.; Chan, H.L.W. Preparation of Low-K Fluorinated Polyimide/Phlogopite Nanocomposites. *Adv. Mater. Res.* **2008**, *47–50*, 987–990. [CrossRef]
88. Bae, S.H.; Yoo, S.I.; Bae, W.K.; Lee, S.; Lee, J.K.; Sohn, B.H. Single-layered films of diblock copolymer micelles containing quantum dots and fluorescent dyes and their fluorescence resonance energy transfer. *Chem. Mater.* **2008**, *20*. [CrossRef]
89. Miwa, Y.; Drews, A.R.; Schlick, S. Unique structure and dynamics of poly(ethylene oxide) in layered silicate nanocomposites: Accelerated segmental mobility revealed by simulating ESR spectra of spin-labels, XRD, FTIR, and DSC. *Macromolecules* **2008**, *41*. [CrossRef]
90. Fujii, K.; Ishihama, Y.; Sakuragi, T.; Ohshima, M.A.; Kurokawa, H.; Miura, H. Heterogeneous catalysts immobilizing α -diimine nickel complexes into fluorotetrasilicic mica interlayers to prepare branched polyethylene from only ethylene. *Catal. Commun.* **2008**, *10*. [CrossRef]
91. Pacheco-Torgal, F.; Castro-Gomes, J.; Jalali, S. Tungsten mine waste geopolymeric binder: Preliminary hydration products investigations. *Constr. Build. Mater.* **2009**, *23*. [CrossRef]
92. Cheng, H.Y.; Jiang, G.J.; Hung, J.Y. Enhanced mechanical and thermal properties of PS/mica and PMMA/mica nanocomposites by emulsion polymerization. *Polym. Compos.* **2009**, *30*. [CrossRef]
93. Tamura, K.; Uno, H.; Yamada, H.; Umeyama, K. Layered silicate-polyamide-6 nanocomposites: Influence of silicate species on morphology and properties. *J. Polym. Sci. Part B Polym. Phys.* **2009**, *47*. [CrossRef]
94. Herzog, E.; Caseri, W.; Suter, U.W. Adsorption of polymers with crown ether substituents on muscovite mica. *Colloid Polym. Sci.* **1994**, *272*. [CrossRef]
95. Möller, M.W.; Handge, U.A.; Kunz, D.A.; Lunkenbein, T.; Altstädt, V.; Breu, J. Tailoring shear-stiff, mica-like nanoplatelets. *ICS Nano* **2010**, *4*, 717–724. [CrossRef]
96. Lin, J.J.; Chan, Y.N.; Lan, Y.F. Hydrophobic modification of layered clays and compatibility for epoxy nanocomposites. *Materials* **2010**, *3*, 2588–2605. [CrossRef]
97. Manias, E.; Heidecker, M.J.; Nakajima, H.; Costache, M.C.; Wilkie, C.A. Poly(ethylene terephthalate) nanocomposites using nanoclays modified with thermally stable surfactants. *Therm. Stable Flame Retard. Polym. Nanocompos.* **2011**, *9780521190*, 100.
98. Schütz, M.R.; Kalo, H.; Lunkenbein, T.; Gröschel, A.H.; Müller, A.H.E.; Wilkie, C.A.; Breu, J. Shear stiff, surface modified, mica-like nanoplatelets: A novel filler for polymer nanocomposites. *J. Mater. Chem.* **2011**, *21*. [CrossRef]
99. Fu, Y.T.; Zartman, G.D.; Yoonessi, M.; Drummy, L.F.; Heinz, H. Bending of layered silicates on the nanometer scale: Mechanism, stored energy, and curvature limits. *J. Phys. Chem. C* **2011**, *115*. [CrossRef]
100. Ahmad Rasyid, M.F.; Hazizan, M.A.; Sharif, J.M. Influence of Organo-Clay on Mechanical and Thermal Properties of O-Muscovite/PP Layered Silicate Nanocomposite. *Adv. Mater. Res.* **2011**, *364*, 174–180. [CrossRef]

101. Xu, X.; Ding, H.; Wang, Y.B.; Liang, Y.; Jiang, W. Preparation and Characterization of Activated Sericite Modified by Fluorosilicate. *Adv. Mater. Res.* **2012**, *427*, 70–76. [CrossRef]
102. Wang, X.Y.; Liu, B.; Tang, Y.F.; Su, H.J.; Han, Y.; Sun, R.C. New progress on rectorite/polymer nanocomposites. *Wuji Cailiao Xuebao J. Inorg. Mater.* **2012**, *27*. [CrossRef]
103. Kudus, M.H.A.; Akil, H.M.; Rasyid, M.F.A. Muscovite-MWCNT hybrid as a potential filler for layered silicate nanocomposite. *Mater. Lett.* **2012**, *79*. [CrossRef]
104. Mittal, V. Surface modification of layered silicates. II. Factors affecting thermal stability. *Philos. Mag.* **2012**, *92*. [CrossRef]
105. Olson, B.G.; Peng, Z.L.; Srithawatpong, R.; McGervey, J.D.; Ishida, H.; Jamieson, A.M.; Manias, E.; Giannelis, E.P. Free volume in layered organosilicate-polystyrene nanocomposites. *Mater. Sci. Forum* **1997**, 255–257. [CrossRef]
106. Livi, S.; Duchet-Rumeau, J.; Gérard, J.F. Effect of ionic liquid modified synthetic layered silicates on thermal and mechanical properties of high density polyethylene nanocomposites. *Macromol. Symp.* **2014**, *342*. [CrossRef]
107. Omar, M.F.; Abd Wahab, N.S.; Akil, H.M.; Ahmad, Z.A.; Rasyid, M.F.A.; Noriman, N.Z. Effect of Surface Modification on Strain Rate Sensitivity of Polypropylene/Muscovite Layered Silicate Composites. *Mater. Sci. Forum* **2014**, *803*, 343–347. [CrossRef]
108. Omar, M.F.; Jaya, H.; Akil, H.M.; Ahmad, Z.A.; Rasyid, M.F.A.; Noriman, N.Z. Effect of Organic Modification on Dynamic Compression Properties of Polypropylene/Muscovite Layered Silicate Composites. *Mater. Sci. Forum* **2014**, *803*, 282–287. [CrossRef]
109. Ding, J.; Huang, Z.; Luo, H.; Qin, Y.; Shi, M. The role of microcrystalline muscovite to enhance thermal stability of boron-modified phenolic resin, structural and elemental studies in boron-modified phenolic resin/ microcrystalline muscovite composite. *Mater. Res. Innov.* **2015**, *19*. [CrossRef]
110. Kovalevsky, V.; Shchiptsov, V.; Sadovnichy, R. Unique natural carbon deposits of shungite rocks of Zazhogino Ore Field, Republic of Karelia, Russia. In Proceedings of the International Multidisciplinary Scientific GeoConference Surveying Geology and Mining Ecology Management, SGEM, Albena, 30 June–6 July 2016; Volume 1.
111. Xia, L.; Wu, H.; Guo, S.; Sun, X.; Liang, W. Enhanced sound insulation and mechanical properties of LDPE/mica composites through multilayered distribution and orientation of the mica. *Compos. Part A Appl. Sci. Manuf.* **2016**, *81*. [CrossRef]
112. Zhang, X.; Yuan, L.; Guan, Q.; Liang, G.; Gu, A. Greatly improving energy storage density and reducing dielectric loss of carbon nanotube/cyanate ester composites through building a unique tri-layered structure with mica paper. *J. Mater. Chem. A* **2017**, *5*. [CrossRef]
113. Michal, O.; Mentlik, V. Influence of Thermal Degradation on the Dielectric Properties of Polymer Composites. In Proceedings of the International Conference on Diagnostics in Electrical Engineering, Diagnostika, Pilsen, Czech Republic, 4–7 September 2018; pp. 1–5.
114. Bae, H.J.; Goh, Y.; Yim, H.; Yoo, S.Y.; Choi, J.W.; Kwon, D.K. Atomically thin, large area aluminosilicate nanosheets fabricated from layered clay minerals. *Mater. Chem. Phys.* **2019**, *221*. [CrossRef]
115. Lü, R.; Wang, Y.; Wang, J.; Ren, W.; Li, L.; Liu, S.; Chen, Z.; Li, Y.; Wang, H.; Fu, F. Soliton and bound-state soliton mode-locked fiber laser based on a MoS₂/fluorine mica Langmuir–Blodgett film saturable absorber. *Photonics Res.* **2019**, *7*. [CrossRef]
116. Geke, M.O.; Shelden, R.A.; Caseri, W.R.; Suter, U.W. Ion exchange of cation-terminated poly(ethylene oxide) chains on mica surfaces. *J. Colloid Interface Sci.* **1997**, *189*. [CrossRef]
117. Mohammadi, H.; Moghbeli, M.R. Effect of ethylene-1-butene copolymer on tensile properties and toughness of polypropylene/mica/organoclay hybrid nanocomposites. *J. Vinyl Addit. Technol.* **2019**, *25*. [CrossRef]
118. Fu, Y.; Wang, Y.; Wang, S.; Gao, Z.; Xiong, C. Enhanced breakdown strength and energy storage of PVDF-based dielectric composites by incorporating exfoliated mica nanosheets. *Polym. Compos.* **2019**, *40*. [CrossRef]
119. Mohammadi, H.; Moghbeli, M.R. Polypropylene/organically modified-grafted mica/organoclay hybrid nanocomposites: Preparation, characterization, and mechanical properties. *Polym. Compos.* **2019**, *40*. [CrossRef]
120. Wang, B.; Tang, M.; Wu, Y.; Chen, Y.; Jiang, C.; Zhuo, S.; Zhu, S.; Wang, C. A 2D Layered Natural Ore as a Novel Solid-State Electrolyte. *ACS Appl. Energy Mater.* **2019**, *2*. [CrossRef]
121. Kuznetsov, V.; Ottermann, K.; Helfricht, N.; Kunz, D.; Loch, P.; Kalo, H.; Breu, J.; Papastavrou, G. Surface charge density and diffuse layer properties of highly defined 2:1 layered silicate platelets. *Colloid Polym. Sci.* **2020**, *298*. [CrossRef]
122. Tani, M.; Fukushima, Y. Properties of organic/inorganic hybrid clay-like polymers with epoxy groups. *Kobunshi Ronbunshu* **2002**, *59*. [CrossRef]
123. Imai, Y.; Nishimura, S.; Abe, E.; Tateyama, H.; Abiko, A.; Yamaguchi, A.; Aoyama, T.; Taguchi, H. High-modulus poly(ethylene terephthalate)/expandable fluorine mica nanocomposites with a novel reactive compatibilizer. *Chem. Mater.* **2002**, *14*. [CrossRef]
124. Maiti, P.; Yamada, K.; Okamoto, M.; Ueda, K.; Okamoto, K. New polylactide/layered silicate nanocomposites: Role of organoclays. *Chem. Mater.* **2002**, *14*. [CrossRef]
125. McNally, T.; Murphy, W.R.; Lew, C.Y.; Turner, R.J.; Brennan, G.P. Polyamide-12 layered silicate nanocomposites by melt blending. *Polymer* **2003**, *44*. [CrossRef]
126. Sinha Ray, S.; Yamada, K.; Okamoto, M.; Ogami, A.; Ueda, K. New polylactide/layered silicate nanocomposites. 3. High-performance biodegradable materials. *Chem. Mater.* **2003**, *15*. [CrossRef]
127. Bokobza, L. Elastomeric composites. I. Silicone composites. *J. Appl. Polym. Sci.* **2004**, *93*. [CrossRef]
128. Zhang, D.; Zhou, C.H.; Lin, C.X.; Tong, D.S.; Yu, W.H. Synthesis of clay minerals. *Appl. Clay Sci.* **2010**, *50*. [CrossRef]

129. Fukushima, K.; Wu, M.H.; Bocchini, S.; Rasyida, A.; Yang, M.C. PBAT based nanocomposites for medical and industrial applications. *Mater. Sci. Eng. C* **2012**, *32*. [CrossRef]
130. Fukushima, K.; Tabuani, D.; Camino, G. Poly(lactic acid)/clay nanocomposites: Effect of nature and content of clay on morphology, thermal and thermo-mechanical properties. *Mater. Sci. Eng. C* **2012**, *32*. [CrossRef]
131. Ruiz-Hitzky, E.; Darder, M.; Wicklein, B.; Fernandes, F.M.; Castro-Smirnov, F.A.; Martín del Burgo, M.A.; del Real, G.; Aranda, P. Advanced biohybrid materials based on nanoclays for biomedical applications. In Proceedings of the Nanosystems in Engineering and Medicine; Choi, S.H., Choy, J.-H., Lee, U., Varadan, V.K., Eds.; SPIE: Incheon, Korean, 2012; Volume 8548, p. 85480D.
132. Vahabi, H.; Sonnier, R.; Otazaghine, B.; Le Saout, G.; Lopez-Cuesta, J.M. Nanocomposites of polypropylene/polyamide 6 blends based on three different nanoclays: Thermal stability and flame retardancy. *Polim. Polym.* **2013**, *58*. [CrossRef]
133. Ruiz-Hitzky, E.; Aranda, P. Novel architectures in porous materials based on clas. *J. Sol-Gel Sci. Technol.* **2014**, *70*, 307–316. [CrossRef]
134. Ruiz-Hitzky, E.; Darder, M.; Alcântara, A.C.S.; Wicklein, B.; Aranda, P. Recent advances on fibrous clay-based nanocomposites. *Adv. Polym. Sci.* **2014**, *267*. [CrossRef]
135. Frindy, S.; Primo, A.; Quiss, A.E.K.; Bouhfid, R.; Lahcini, M.; Garcia, H.; Bousmina, M.; El Kadib, A. Insightful understanding of the role of clay topology on the stability of biomimetic hybrid chitosan-clay thin films and CO₂-dried porous aerogel microspheres. *Carbohydr. Polym.* **2016**, *146*. [CrossRef]
136. Beyer, G. Nanocomposites: A new class of flame retardants for polymers. *Plast. Addit. Compd.* **2002**, *4*, 22–28. [CrossRef]
137. Kojima, Y.; Usuki, A.; Kawasumi, M.; Okada, A.; Kurauchi, T.; Kamigaito, O. Synthesis of nylon 6–clay hybrid by montmorillonite intercalated with ϵ -caprolactam. *J. Polym. Sci. Part A Polym. Chem.* **1993**, *31*, 983–986. [CrossRef]
138. Jordan, J.W. Organophilic Bentonites. I. Swelling in Organic Liquids. *J. Phys. Colloid Chem.* **1949**, *53*, 294–306. [CrossRef]
139. Weiss, A. Organic Derivatives of Mica-type Layer-Silicates. *Angew. Chem. Int. Ed. Engl.* **1963**, *2*, 134–144. [CrossRef]
140. Lan, T.; Kaviratna, P.D.; Pinnavaia, T.J. Mechanism of Clay Tactoid Exfoliation in Epoxy-Clay Nanocomposites. *Chem. Mater.* **1995**, *7*, 2144–2150. [CrossRef]
141. Vaia, R.A.; Teukolsky, R.K.; Giannelis, E.P. Interlayer Structure and Molecular Environment of Alkylammonium Layered Silicates. *Chem. Mater.* **1994**, *6*, 1017–1022. [CrossRef]
142. Lagaly, G. Interaction of alkylamines with different types of layered compounds. *Solid State Ion.* **1986**, *22*, 43–51. [CrossRef]
143. Zanetti, M.; Lomakin, S.; Camino, G. Polymer layered silicate nanocomposites. *Macromol. Mater. Eng.* **2000**, *279*, 1–9. [CrossRef]
144. Unalan, I.U.; Cerri, G.; Marcuzzo, E.; Cozzolino, C.A.; Farris, S. Nanocomposite films and coatings using inorganic nanobuilding blocks (NBB): Current applications and future opportunities in the food packaging sector. *RSC Adv.* **2014**, *4*, 29393–29428. [CrossRef]
145. Mrah, L.; Meghabar, R. In situ polymerization of styrene–clay nanocomposites and their properties. *Polym. Bull.* **2020**. [CrossRef]
146. Ekielski, A.; Żelaziński, T.; Durczak, K. The use of wavelet analysis to assess the degree of wear of working elements of food extruders. *Eksploat. Niezawodn. Maint. Reliab.* **2017**, *19*, 560–564. [CrossRef]
147. Mościcki, L.; van Zuilichem, D.J. Extrusion-Cooking and Related Technique. In *Extrusion-Cooking Techniques*; Wiley Online Books; Wiley-VCH Verlag GmbH & Co. KGaA: Weinheim, Germany, 2011; pp. 1–24, ISBN 9783527634088.
148. Vaia, R.A.; Giannelis, E.P. Lattice Model of Polymer Melt Intercalation in Organically-Modified Layered Silicates. *Macromolecules* **1997**, *30*, 7990–7999. [CrossRef]
149. Chavarria, F.; Shah, R.K.; Hunter, D.L.; Paul, D.R. Effect of melt processing conditions on the morphology and properties of nylon 6 nanocomposites. *Polym. Eng. Sci.* **2007**, *47*, 1847–1864. [CrossRef]
150. Dennis, H.R.; Hunter, D.L.; Chang, D.; Kim, S.; White, J.L.; Cho, J.W.; Paul, D.R. Effect of melt processing conditions on the extent of exfoliation in organoclay-based nanocomposites. *Polymer* **2001**, *42*, 9513–9522. [CrossRef]
151. Fornes, T.D.; Paul, D.R. Modeling properties of nylon 6/clay nanocomposites using composite theories. *Polymer* **2003**, *44*, 4993–5013. [CrossRef]
152. Lertwimolnun, W.; Vergnes, B. Influence of screw profile and extrusion conditions on the microstructure of polypropylene/organoclay nanocomposites. *Polym. Eng. Sci.* **2007**, *47*, 2100–2109. [CrossRef]
153. Fornes, T.; Yoon, P.; Hunter, D.; Keskkula, H.; Paul, D. Effect of organoclay structure on nylon 6 nanocomposite morphology and properties. *Polymer* **2002**, *43*, 5915–5933. [CrossRef]
154. Fornes, T.D.; Yoon, P.J.; Keskkula, H.; Paul, D.R. Nylon 6 nanocomposites: The effect of matrix molecular weight. *Polymer* **2001**, *42*, 9929–9940. [CrossRef]
155. Cabedo, L.; Villanueva, M.P.; Lagarón, J.M.; Giménez, E. Development and characterization of unmodified kaolinite/EVOH nanocomposites by melt compounding. *Appl. Clay Sci.* **2017**, *135*, 300–306. [CrossRef]
156. Chavarria, F.; Paul, D.R. Comparison of nanocomposites based on nylon 6 and nylon 66. *Polymer* **2004**, *45*, 8501–8515. [CrossRef]
157. Wang, Z.; Pinnavaia, T.J. Hybrid Organic-Inorganic Nanocomposites: Exfoliation of Magadiite Nanolayers in an Elastomeric Epoxy Polymer. *Chem. Mater.* **1998**, *10*. [CrossRef]
158. Ganguly, A.; De Sarkar, M.; Bhowmick, A.K. Thermoplastic elastomeric nanocomposites from poly[styrene-(ethylene-co-butylene)-styrene] triblock copolymer and clay: Preparation and characterization. *J. Appl. Polym. Sci.* **2006**, *100*. [CrossRef]
159. Zhu, L.; Wool, R.P. Nanoclay reinforced bio-based elastomers: Synthesis and characterization. *Polymer* **2006**, *47*. [CrossRef]

160. Százdi, L.; Pozsgay, A.; Pukánszky, B. Factors and processes influencing the reinforcing effect of layered silicates in polymer nanocomposites. *Eur. Polym. J.* **2007**, *43*. [CrossRef]
161. Rehab, A.; Akelah, A.; Agag, T.; Shalaby, N. Polyurethane-nanocomposite materials via in situ polymerization into organoclay interlayers. *Polym. Adv. Technol.* **2007**, *18*. [CrossRef]
162. Chu, D.; Nguyen, Q.; Baird, D.G. Effect of matrix molecular weight on the dispersion of nanoclay in unmodified high density polyethylene. *Polym. Compos.* **2007**, *28*. [CrossRef]
163. Wilkinson, A.N.; Man, Z.; Stanford, J.L.; Matikainen, P.; Clemens, M.L.; Lees, G.C.; Liauw, C.M. Tensile properties of melt intercalated polyamide 6-Montmorillonite nanocomposites. *Compos. Sci. Technol.* **2007**, *67*. [CrossRef]
164. Sarkar, M.; Dana, K.; Ghatak, S.; Banerjee, A. Polypropylene-clay composite prepared from Indian bentonite. *Bull. Mater. Sci.* **2008**, *31*. [CrossRef]
165. Kiliaris, P.; Paspapirides, C.D.; Pfaendner, R. Polyamide 6 filled with melamine cyanurate and layered silicates: Evaluation of flame retardancy and physical properties. *Macromol. Mater. Eng.* **2008**, *293*. [CrossRef]
166. Zhang, Y.; Liu, W.; Han, W.; Guo, W.; Wu, C. Preparation and properties of novel natural rubber/ organo-vermiculite nanocomposites. *Polym. Compos.* **2009**, *30*. [CrossRef]
167. Schmidt, D.F.; Giannelis, E.P. Silicate dispersion and mechanical reinforcement in polysiloxane/layered silicate nanocomposites. *Chem. Mater.* **2010**, *22*. [CrossRef]
168. Lebaron, P.C.; Wang, Z.; Pinnavaia, T.J. Polymer-layered silicate nanocomposites: An overview. *Appl. Clay Sci.* **1999**, *15*. [CrossRef]
169. Zhu, L.; Wool, R.P. Bio-based elastomers from soy oil and nanoclay. In *Nanocomposites with Biodegradable Polymers*; Oxford University Press: Oxford, UK, 2011; Volume 9780199581, pp. 189–208.
170. Lipinska, M.; Hutchinson, J.M. Elastomeric epoxy nanocomposites: Nanostructure and properties. *Compos. Sci. Technol.* **2012**, *72*. [CrossRef]
171. Marega, C.; Causin, V.; Saini, R.; Marigo, A.; Meera, A.P.; Thomas, S.; Devi, K.S.U. A direct SAXS approach for the determination of specific surface area of clay in polymer-layered silicate nanocomposites. *J. Phys. Chem. B* **2012**, *116*. [CrossRef]
172. Mallakpour, S.; Dinari, M. The effects of reactive organoclay on the thermal, mechanical, and microstructural properties of polymer/layered silicate nanocomposites based on chiral poly(amide-imide)s. *J. Therm. Anal. Calorim.* **2013**, *114*. [CrossRef]
173. Stojšić, J.; Raos, P.; Kalendova, A. A study of structure and tensile properties of polyamide 12/clay nanocomposites. *Polym. Compos.* **2016**, *37*. [CrossRef]
174. Ghanbari, A.; Heuzey, M.C.; Carreau, P.J.; Ton-That, M.T. Morphology and gas barrier properties of polymer nanocomposites. *Polym. Morphol. Princ. Charact. Process.* **2016**, *394–417*. [CrossRef]
175. Rahman, M.R.; Hamdan, S.B.; Hossen, M.F. The effect of clay dispersion on polypropylene nanocomposites: Physico-mechanical, thermal, morphological, and optical properties. In *Silica and Clay Dispersed Polymer Nanocomposites*; Elsevier: Cambridge, UK, 2018; pp. 201–257.
176. Msekh, M.A.; Cuong, N.H.; Zi, G.; Areias, P.; Zhuang, X.; Rabczuk, T. Fracture properties prediction of clay/epoxy nanocomposites with interphase zones using a phase field model. *Eng. Fract. Mech.* **2018**, *188*. [CrossRef]
177. Rauschendorfer, J.E.; Thien, K.M.; Denz, M.; Köster, S.; Ehlers, F.; Vana, P. Tuning the Mechanical Properties of Poly(Methyl Acrylate) via Surface-Functionalized Montmorillonite Nanosheets. *Macromol. Mater. Eng.* **2021**, *306*. [CrossRef]
178. Chang, M.-K.; Wei, H.-L.; Wu, K.-S. The Strength and Thermal Stability of Low-Density Polyethylene Grafted Maleic Anhydride/Montmorillonite Nanocomposites. *Adv. Sci. Lett.* **2012**, *13*, 240–244. [CrossRef]
179. Kuchta, F.D.; Lemstra, P.J.; Keller, A.; Batenburg, L.F.; Fischer, H.R. Polymer crystallization studied in confined dimensions using nanocomposites from polymers and layered minerals. *Mater. Res. Soc. Symp. Proc.* **2000**, *628*. [CrossRef]
180. Filippone, G.; Dintcheva, N.T.; Acierno, D.; La Mantia, F.P. The role of organoclay in promoting co-continuous morphology in high-density poly(ethylene)/poly(amide) 6 blends. *Polymer* **2008**, *49*, 1312–1322. [CrossRef]
181. Tillekeratne, M.; Jollands, M.; Cser, F.; Bhattacharya, S.N. Role of mixing parameters in the preparation of poly(ethylene vinyl acetate) nanocomposites by melt blending. *J. Appl. Polym. Sci.* **2006**, *100*, 2652–2658. [CrossRef]
182. Liao, B.; Song, M.; Liang, H.; Pang, Y. Polymer-layered silicate nanocomposites. 1. A study of poly(ethylene oxide)/Na⁺-montmorillonite nanocomposites as polyelectrolytes and polyethylene-block-poly(ethylene glycol) copolymer/Na⁺-montmorillonite nanocomposites as fillers for reinforcement of po. *Polymer* **2001**, *42*. [CrossRef]
183. Lim, S.K.; Lim, S.T.; Kim, H.B.; Chin, I.; Choi, H.J. Preparation and Physical Characterization of Polyepichlorohydrin Elastomer/Clay Nanocomposites. *J. Macromol. Sci. Phys.* **2003**, *42*. [CrossRef]
184. Li, X.; Mishra, J.K.; Seul, S.D.; Kim, I.; Ha, C.S. Microstructure and properties of poly (butylene terephthalate) based nanocomposites. *Compos. Interfaces* **2004**, *11*, 335–346. [CrossRef]
185. Ahmadi, S.J.; Huang, Y.D.; Li, W. Synthetic routes, properties and future applications of polymer-layered silicate nanocomposites. *J. Mater. Sci.* **2004**, *39*. [CrossRef]
186. Song, L.; Hu, Y.; Tang, Y.; Zhang, R.; Chen, Z.; Fan, W. Study on the properties of flame retardant polyurethane/organoclay nanocomposite. *Polym. Degrad. Stab.* **2005**, *87*. [CrossRef]
187. Li, J.; Zhao, L.; Guo, S. Ultrasonic preparation of polymer/layered silicate nanocomposites during extrusion. *Polym. Bull.* **2005**, *55*. [CrossRef]
188. Chang, M.-K. Mechanical properties and thermal stability of low-density polyethylene grafted maleic anhydride/montmorillonite nanocomposites. *J. Ind. Eng. Chem.* **2015**, *27*, 96–101. [CrossRef]

189. Sinha Ray, S.; Okamoto, M. Biodegradable polylactide and its nanocomposites: Opening a new dimension for plastics and composites. *Macromol. Rapid Commun.* **2003**, *24*. [CrossRef]
190. Vlasveld, D.P.N.; Daud, W.; Bersee, H.E.N.; Picken, S.J. Continuous fibre composites with a nanocomposite matrix: Improvement of flexural and compressive strength at elevated temperatures. *Compos. Part A Appl. Sci. Manuf.* **2007**, *38*. [CrossRef]
191. Akbari, B.; Bagheri, R. Deformation mechanism of epoxy/clay nanocomposite. *Eur. Polym. J.* **2007**, *43*. [CrossRef]
192. Yamagata, S.; Iida, J.; Watari, F. FRP Esthetic Orthodontic Wire and Development of Matrix Strengthening with Poly(methyl methacrylate)/Montmorillonite Nanocomposite. In *Handbook of Polymernanocomposites. Processing, Performance and Application*; Springer: Berlin/Heidelberg, Germany, 2014; pp. 319–328, ISBN 9783642386497.
193. Tasan, C.C.; Kaynak, C. Mechanical performance of resol type phenolic resin/layered silicate nanocomposites. *Polym. Compos.* **2009**, *30*. [CrossRef]
194. Inglis, C.E. Stress in a plate due to the presence of cracks and sharp corners. *Trans. R. Inst. Nav. Archit.* **1913**, *60*, 219–241.
195. Griffith, A.A. The Phenomena of Rupture and Flow in Solids. *Philos. Trans. R. Soc. London Ser. A* **1921**, *221*, 163–198.
196. Irwin, G.R. Analysis of stresses and strains near the end of a crack traversing a plate. *J. Appl. Mech.* **1957**, *24*, 361–364. [CrossRef]
197. Westergaard, H.M. Bearing Pressures and Cracks. *J. Appl. Mech.* **1939**, *6*, 49–53. [CrossRef]
198. Wells, A.A. Application of fracture mechanics at and beyond general yielding. *Br. Weld. J.* **1961**, *11*, 563–570.
199. Rice, J.R. A path independent integral and the approximate analysis of strain concentrations by notches and cracks. *J. Appl. Mech.* **1968**, *35*, 379–389. [CrossRef]
200. Broberg, K.B. On stable crack growth. *J. Mech. Phys. Solids* **1975**, *23*, 443–445. [CrossRef]
201. Broberg, K.B. Crack-Growth Criteria and Non-linear Fracture Mechanics. *J. Mech. Phys. Solids* **1971**, *19*, 407. [CrossRef]
202. Cotterell, B.; Reddel, J.K. The Essential Work of Plane Stress Ductile Fracture. *Int. J. Fract.* **1977**, *13*, 267–277.
203. Mai, Y.W.; Cotterell, B. The Essential Work of fracture for tearing of ductile metals. *Int. J. Fract.* **1984**, *24*, 229–236. [CrossRef]
204. Paton, C.A.; Hashemi, S. Plane-stress essential work of ductile fracture for polycarbonate. *J. Mater. Sci.* **1992**, *27*, 2279–2290. [CrossRef]
205. Wu, J.; Mai, Y.W. Cotterell Fracture toughness and fracture mechanisms of PBT/PC/IM blend (Part I: Fracture properties). *J. Mater. Sci.* **1993**, *28*, 3373–3384. [CrossRef]
206. Sanchez, J.J.; Santana, O.O.; Gordillo, A.; Maspoch, M.L.; Martinez, A.B. Essential work of fracture of injection moulded samples of PET and PET/PC blends. *Fract. Polym. Compos. Adhes.* **2003**, *32*, 77–88.
207. Pardoën, T.; Marchal, Y.; Delannay, F. Essential work of fracture compared to fracture mechanics—towards a thickness independent plane stress toughness. *Eng. Fract. Mech.* **2002**, *69*, 617–631. [CrossRef]
208. Rae, P.J.; Brown, E.N.; Orlor, E.B. The mechanical properties of poly(ether-ether-ketone) (PEEK) with emphasis on the large compressive strain response. *Polymer* **2007**, *48*, 598–615. [CrossRef]
209. Arkhireyeva, A.; Hashemi, S. Fracture behaviour of polyethylene naphthalate (PEN). *Polymer* **2002**, *43*, 289–300. [CrossRef]
210. Knockaert, R.; Doghri, I.; Marchal, Y.; Pardoën, T.; Delannay, F. Experimental and numerical investigation of fracture in double-edge notched steel plates. *Int. J. Fract.* **1996**, *81*, 383–399. [CrossRef]
211. Cotterell, B.; Pardoën, T.; Atkins, A.G. Measuring toughness and the cohesive stress-displacement relationship by the essential work of fracture concept. *Eng. Fract. Mech.* **2005**, *72*, 827–848. [CrossRef]
212. Chen, Y.H.; Mai, Y.W.; Tong, P.; Zhang, L.C. Numerical Simulation of the Essential Fracture Work Method. In *Fracture of Polymers, Composites and Adhesion*; Williams, J.G., Pavan, A., Eds.; Elsevier: Amsterdam, The Netherlands, 2000; Volume 27, p. 175.
213. Chen, H.B.; Wu, J.S. Understanding the underlying physics of the essential work of fracture on the molecular level. *Macromolecules* **2007**, *40*, 4322–4326. [CrossRef]
214. Kwon, H.J.; Jar, P.Y.B. Fracture toughness of polymers in shear mode. *Polymer* **2005**, *46*, 12480–12492. [CrossRef]
215. Kwon, H.J.; Jar, P.Y.B. Toughness of high-density polyethylene in shear fracture. *Int. J. Fract.* **2007**, *145*, 123–133. [CrossRef]
216. Kim, H.S.; Karger-Kocsis, J. Tearing resistance of some co-polyester sheets. *Acta Mater.* **2004**, *52*, 3123–3133. [CrossRef]
217. Wong, J.S.S.; Ferrer-Balas, D.; Li, R.K.Y.; Mai, Y.W.; Maspoch, M.L.; Sue, H.J. On tearing of ductile polymer films using the essential work of fracture (EWF) method. *Acta Mater.* **2003**, *51*, 4929–4938. [CrossRef]
218. Schuller, T.; Lauke, B. Finite-element simulation of interfacial crack propagation: Methods and tools for the complete failure process under large scale yielding. *Eng. Fract. Mech.* **2006**, *73*, 2252–2263. [CrossRef]
219. Haughie, D.W.; Buckley, C.P.; Wu, J.J. The integrity of welded interfaces in ultra-high molecular weight polyethylene: Part 2 - Interface toughness. *Biomaterials* **2006**, *27*, 3875–3881. [CrossRef]
220. Gray, A. Testing protocol for Essential Work of Fracture. *ESIS-TC4* **1993**.
221. Hill, R. On discontinuous plastic states, with special reference to localized necking in thin sheets. *Journa Mech. Phys. Solids* **1952**, *1*, 19–30. [CrossRef]
222. Clutton, E.Q. ESIS TC4 experience with the essential work of fracture method. In *European Structural Integrity Society*; Williams, J.G., Pavan, A., Eds.; Elsevier Science, Ltd.: Oxford, LB, USA, 2000; Volume 27, pp. 187–199.
223. Maspoch, M.L.; Gamez-Perez, J.; Gordillo, A.; Sánchez-Soto, M.; Velasco, J.I. Characterisation of injected EPBC plaques using the essential work of fracture (EWF) method. *Polymer* **2002**, *43*, 4177–4183. [CrossRef]
224. Maspoch, M.L.; Santana, O.O.; Cailloux, J.; Franco-Urquiza, E.; Rodriguez, C.; Belzunce, J.; Martínez, A.B. Ductile-brittle transition behaviour of PLA/o-MMT films during the physical aging process. *Express Polym. Lett.* **2015**, *9*, 185–195. [CrossRef]

225. Martínez, A.B.; Segovia, A.; Gamez-Perez, J.; Maspoch, M.L. Essential work of fracture (EWF) analysis of the tearing of a ductile polymer film. *Eng. Fract. Mech.* **2010**, in press. [CrossRef]
226. Pettarin, V.; Frontini, P.M.; Elicabe, G.E. Optimal ligament lengths in impact fracture toughness estimation by the essential work of fracture method. *Polym. Test.* **2005**, *24*, 189–196. [CrossRef]
227. Tjong, S.C.; Bao, S.P. Impact fracture toughness of polyamide-6/montmorillonite nanocomposites toughened with a maleated styrene/ethylene butylene/styrene elastomer. *J. Polym. Sci. Part B Polym. Phys.* **2005**, *43*. [CrossRef]
228. Ozkoc, G.; Bayram, G.; Bayramli, E. Impact essential work of fracture toughness of ABS/polyamide-6 blends compatibilized with olefin based copolymers. *J. Mater. Sci.* **2008**, *43*, 2642–2652. [CrossRef]
229. Bao, S.P.; Tjong, S.C. Fracture characterization of high density polyethylene/organoclay nanocomposites toughened with SEBS-g-MA. *Key Eng. Mater.* **2006**, *312*, 187–192. [CrossRef]
230. Fayolle, B.; Tcharkhtchi, A.; Verdu, J. Temperature and molecular weight dependence of fracture behaviour of polypropylene films. *Polym. Test.* **2004**, *23*, 939–947. [CrossRef]
231. Wainstein, J.; Fasce, L.A.; Cassanelli, A.; Frontini, P.M. High rate toughness of ductile polymers. *Eng. Fract. Mech.* **2007**, *74*, 2070–2083. [CrossRef]
232. Saminathan, K.; Selvakumar, P.; Bhatnagar, N. Fracture studies of polypropylene/nanoclay composite. Part I: Effect of loading rates on essential work of fracture. *Polym. Test.* **2008**, *27*, 296–307. [CrossRef]
233. Saminathan, K.; Selvakumar, P.; Bhatnagar, N. Fracture studies of polypropylene/nanoclay composite. Part II: Failure mechanism under fracture loads. *Polym. Test.* **2008**, *27*, 453–458. [CrossRef]
234. Santana, O.O.; Maspoch, M.L.; Martinez, A.B. Plane strain essential work of fracture in SENB geometry at low and high strain rates of PC/ABS blends. *Polym. Bull.* **1997**, *39*, 511–518. [CrossRef]
235. Maspoch, M.L.; Gamez-Perez, J.; Karger-Kocsis, J. Effects of thickness, deformation rate and energy partitioning on the work of fracture parameters of uPVC films. *Polym. Bull.* **2003**, *50*, 279–286. [CrossRef]
236. Arkhireyeva, A.; Hashemi, S. Effect of temperature on work of fracture parameters in poly(ether-ether ketone) (PEEK) film. *Eng. Fract. Mech.* **2004**, *71*, 789–804. [CrossRef]
237. Arkhireyeva, A.; Hashemi, S. Combined effect of temperature and thickness on work of fracture parameters of unplasticized PVC film. *Polym. Eng. Sci.* **2002**, *42*, 504–518. [CrossRef]
238. Korsunsky, A.M.; Kim, K. Determination of essential work of necking and tearing from a single tensile test. *Int. J. Fract.* **2005**, *132*, L37–L44. [CrossRef]
239. Korsunsky, A.M.; Nguyen, G.D.; Houlsby, G.T. Analysis of essential work of rupture using non-local damage-plasticity modelling. *Int. J. Fract.* **2005**, *135*, L19–L26. [CrossRef]
240. Karger-Kocsis, J.; Ferrer-Balas, D. On the plane-strain essential work of fracture of polymer sheets. *Polym. Bull.* **2001**, *46*, 507–512. [CrossRef]
241. Kwon, H.J.; Jar, P.Y.B. New energy partitioning approach to the measurement of plane-strain fracture toughness of high-density polyethylene based on the concept of essential work of fracture. *Eng. Fract. Mech.* **2007**, *74*, 2471–2480. [CrossRef]
242. Kwon, H.J.; Jar, R.Y.B. Application of essential work of fracture concept to toughness characterization of high-density polyethylene. *Polym. Eng. Sci.* **2007**, *47*, 1327–1337. [CrossRef]
243. Pegoretti, A.; Ricco, T. On the essential work of fracture of neat and rubber toughened polyamide-66. *Eng. Fract. Mech.* **2006**, *73*, 2486–2502. [CrossRef]
244. Martinez, A.B.; Segovia, A.; Gamez-Perez, J.; Maspoch, M.L. Influence of femtolaser notch sharpening technique in the determination of essential work of fracture (EWF) parameters. *Eng. Fract. Mech.* **2009**, *76*, 1247–1254. [CrossRef]
245. Maspoch, M.L.; Ferrer, D.; Gordillo, A.; Santana, O.O. Effect of the Specimen Dimensions and the test Speed on the Fracture Toughness of iPP by the Essential Work of Fracture (EWF) Method. *J. Appl. Polym. Sci.* **1999**, *73*, 177–187. [CrossRef]
246. Gamez-Perez, J.; Santana, O.; Martinez, A.B.; Maspoch, M.L. Use of extensometers on essential work of fracture (EWF) tests. *Polym. Test.* **2008**, *27*, 491–497. [CrossRef]
247. Fung, K.L.; Li, R.K.Y. A study on the fracture characteristics of rubber toughened poly(ethylene terephthalate) blends. *Polym. Test.* **2005**, *24*, 863–872. [CrossRef]
248. Mai, Y.-W.; Cotterell, B.; Horlyck, R.; Vigna, G. The essential Work of Plane Stress Ductile Fracture of Linear Polyethylenes. *Polym. Eng. Sci.* **1987**, *27*, 804. [CrossRef]
249. Karger-Kocsis, J.; Czigány, T.; Moskala, E.J. Thickness Dependence of work of fracture Parameters of an Amorphous Copolyester. *Polymer* **1997**, *38*, 4587. [CrossRef]
250. Ferrer-Balas, D.; Maspoch, M.L.; Martínez, A.B.; Santana, O.O. On the essential work of fracture method: Energy partitioning of the fracture process in iPP films. *Polym. Bull.* **1999**, *42*, 101–108. [CrossRef]
251. Ferrer-Balas, D.; Maspoch, M.L.; Martínez, A.B.; Santana, O.O. Influence of annealing on the microstructural, tensile and fracture properties of polypropylene films. *Polymer* **2001**, *42*, 1697–1705. [CrossRef]
252. Casellas, J.J.; Frontini, P.M.; Carella, J.M. Fracture characterization of low-density polyethylenes by the essential work of fracture: Changes induced by thermal treatments and testing temperature. *J. Appl. Polym. Sci.* **1999**, *74*, 781–796. [CrossRef]
253. Ho, C.H.; Vu-Khanh, T. Physical aging and time-temperature behavior concerning fracture performance of polycarbonate. *Theor. Appl. Fract. Mech.* **2004**, *41*, 103–114. [CrossRef]

254. Kayano, Y.; Keskkula, H.; Paul, D.R. Fracture behaviour of some rubber-toughened nylon 6 blends. *Polymer* **1998**, *39*, 2835–2845. [CrossRef]
255. Van der Wal, A.; Mulder, J.J.; Thijs, H.A.; Gaymans, R.J. Fracture of polypropylene: 1. The effect of molecular weight and temperature at low and high test speed. *Polymer* **1998**, *39*, 5467–5475. [CrossRef]
256. Yamakawa, R.S.; Razzino, C.A.; Correab, C.A.; Hage, E., Jr. Influence of notching and molding conditions on determination of EWF parameters in polyamide 6. *Polym. Test.* **2004**, *23*, 195–202. [CrossRef]
257. Baldi, F.; Bignotti, F.; Fina, A.; Tabuani, D.; Riccò, T. Mechanical characterization of polyhedral oligomeric silsesquioxane/polypropylene blends. *J. Appl. Polym. Sci.* **2007**, *105*. [CrossRef]
258. Arencon, D.; Velasco, J.I.; Realinho, V.; Sanchez-Soto, M.; Gordillo, A. Fracture toughness of glass microsphere-filled polypropylene and polypropylene/poly (ethylene terephthalate-co-isophthalate) blend-matrix composites. *J. Mater. Sci.* **2007**, *42*, 19–29. [CrossRef]
259. Nekhlaoui, S.; Essabir, H.; Bensalah, M.O.; Fassi-Fehri, O.; Qaiss, A.; Bouhfid, R. Fracture study of the composite using essential work of fracture method: PP-SEBS-g-MA/E1 clay. *Mater. Des.* **2014**, *53*. [CrossRef]
260. Maspoch, M.L.; Franco-Urquiza, E.; Gamez-Perez, J.; Santana, O.O.; Sánchez-Soto, M. Fracture behaviour of poly[ethylene-(vinyl alcohol)]/organo-clay composites. *Polym. Int.* **2009**, *58*. [CrossRef]
261. Ganß, M.; Staudinger, U.; Satapathy, B.K.; Leuteritz, A.; Weidisch, R. Mechanism of strengthening and toughening of a nanostructured styrene-butadiene based block copolymer by oligostyrene-modified montmorillonites. *Polymer* **2021**, *213*, 123328. [CrossRef]
262. Bao, S.P.; Tjong, S.C. Impact essential work of fracture of polypropylene / montmorillonite nanocomposites toughened with SEBS-g-MA elastomer. *Compos. Part A Appl. Sci. Manuf.* **2007**, *38*, 378–387. [CrossRef]
263. Bureau, M.N.; Perrin-sarazin, F. Essential work of fracture and failure mechanisms of polypropylene–clay nanocomposites. *Eng. Fract. Mech.* **2006**, *73*, 2360–2374. [CrossRef]
264. Lim, J.W.; Hassan, A.; Rahmat, A.R.; Wahit, M.U. Mechanical behaviour and fracture toughness evaluation of rubber toughened polypropylene nanocomposites. *Plast. Rubber Compos.* **2006**, *35*, 37–46. [CrossRef]
265. Bureau, M.N.; Perrin-Sarazin, F.; Ton-That, M.T. Polyolefin nanocomposites: Essential work of fracture analysis. *Polym. Eng. Sci.* **2004**, *44*, 1142–1151. [CrossRef]
266. Tjong, S.C.; Ruan, Y.H. Fracture behavior of thermoplastic polyolefin/clay nanocomposites. *J. Appl. Polym. Sci.* **2008**, *110*. [CrossRef]
267. Pedrazzoli, D.; Tuba, F.; Khumalo, V.M.; Pegoretti, A.; Karger-Kocsis, J. Mechanical and rheological response of polypropylene/boehmite nanocomposites. *J. Reinf. Plast. Compos.* **2014**, *33*. [CrossRef]
268. Turcsán, T.; Mészáros, L.; Khumalo, V.M.; Thomann, R.; Karger-Kocsis, J. Fracture behavior of boehmite-filled polypropylene block copolymer nanocomposites as assessed by the essential work of fracture concept. *J. Appl. Polym. Sci.* **2014**, *131*. [CrossRef]
269. Karger-Kocsis, J.; Khumalo, V.M.; Bárány, T.; Mészáros, L.; Pegoretti, A. On the toughness of thermoplastic polymer nanocomposites as assessed by the essential work of fracture (EWF) approach. *Compos. Interfaces* **2013**, *20*, 395–404. [CrossRef]
270. Wang, L.; Xie, B.H.; Yang, W.; Yang, M.B. Grafted polyolefin-coated synthetic mica-filled polypropylene-co-ethylene composites: A study on the interfacial morphology and properties. *J. Macromol. Sci. Part B Phys.* **2010**, *49*. [CrossRef]
271. Fu, Z.; Dai, W.; Yu, H.; Zou, X.; Chen, B. Effect of composition on fracture behavior of polypropylene-wollastonite- polyolefin elastomer system. *J. Mater. Sci.* **2011**, *46*. [CrossRef]
272. Mouzakis, D.E.; Papanicolaou, G.C.; Giannadakis, K.; Zuburtikudis, I. On the toughness response of iPP and sPP/MWNT nanocomposites. *Strain* **2013**, *49*. [CrossRef]
273. Das, D.; Satapathy, B.K. Designing tough and fracture resistant polypropylene/multi wall carbon nanotubes nanocomposites by controlling stereo-complexity and dispersion morphology. *Mater. Des.* **2014**, *54*. [CrossRef]
274. Khodabandelou, M.; Razavi Aghjeh, M.K.; Mazidi, M.M. Fracture toughness and failure mechanisms in un-vulcanized and dynamically vulcanized PP/EPDM/MWCNT blend-nanocomposites. *RSC Adv.* **2015**, *5*. [CrossRef]
275. Khodabandelou, M.; Razavi Aghjeh, M.K.; Khonakdar, H.A.; Mehrabi Mazidi, M. Effect of localization of carbon nanotubes on fracture behavior of un-vulcanized and dynamically vulcanized PP/EPDM/MWCNT blend-nanocomposites. *Compos. Sci. Technol.* **2017**, *149*. [CrossRef]
276. Satapathy, B.K.; Ganß, M.; Weidisch, R.; Po, P.; Jehnichen, D.; Keller, T.; Jandt, K.D. Ductile-to-Semiductile Transition in PP-MWNT Nanocomposites. *Macromol. Rapid Commun.* **2007**, *28*, 834–841. [CrossRef]
277. Haghnegahdar, M.; Naderi, G.; Ghoreishy, M.H.R. Fracture toughness and deformation mechanism of un-vulcanized and dynamically vulcanized polypropylene/ethylene propylene diene monomer/graphene nanocomposites. *Compos. Sci. Technol.* **2017**, *141*. [CrossRef]
278. Zhang, H.; Zhang, Z.; Park, H.W.; Zhu, X. Influence of surface-modified TiO₂ nanoparticles on fracture behavior of injection molded polypropylene. *Front. Mater. Sci. China* **2008**, *2*. [CrossRef]
279. Hajibabazadeh, S.; Razavi Aghjeh, M.K.; Palahang, M. Study on the fracture toughness and deformation micro-mechanisms of PP/EPDM/SiO₂ ternary blend-nanocomposites. *J. Compos. Mater.* **2020**, *54*. [CrossRef]
280. Tjong, S.C.; Bao, S.P. Fracture toughness of high density polyethylene/SEBS-g-MA/montmorillonite nanocomposites. *Compos. Sci. Technol.* **2007**, *67*. [CrossRef]

281. Franco-Urquiza, E.; Perez, J.G.; Sánchez-Soto, M.; Santana, O.O.; Maspocho, M.L. The effect of organo-modifier on the structure and properties of poly[ethylene-(vinyl alcohol)]/organo-modified montmorillonite composites. *Polym. Int.* **2010**, *59*. [CrossRef]
282. Na, S.; Spatari, S.; Hsuan, Y.G. Fracture characterization of recycled high density polyethylene/nanoclay composites using the essential work of fracture concept. *Polym. Eng. Sci.* **2016**, *56*. [CrossRef]
283. Pedrazzoli, D.; Ceccato, R.; Karger-Kocsis, J.; Pegoretti, A. Viscoelastic behaviour and fracture toughness of linear-low-density polyethylene reinforced with synthetic boehmite alumina nanoparticles. *Express Polym. Lett.* **2013**, *7*. [CrossRef]
284. Costa, F.R.; Satapathy, B.K.; Wagenknecht, U. POLYMER Morphology and fracture behaviour of polyethylene/Mg–Al layered double hydroxide (LDH) nanocomposites. *Eur. Polym. J.* **2006**, *42*, 2140–2152. [CrossRef]
285. Liao, C.Z.; Bao, S.P.; Tjong, S.C. Microstructure and fracture behavior of maleated high-density polyethylene/ silicon carbide nanocomposites toughened with poly(styrene-ethylene-butylene- styrene) triblock copolymer. *Adv. Polym. Technol.* **2011**, *30*. [CrossRef]
286. Dorigato, A.; Pegoretti, A. Fracture behaviour of linear low density polyethylene-fumed silica nanocomposites. *Eng. Fract. Mech.* **2012**, *79*. [CrossRef]
287. Pedrazzoli, D.; Pegoretti, A.; Thomann, R.; Kristóf, J.; Karger-Kocsis, J. Toughening linear low-density polyethylene with halloysite nanotubes. *Polym. Compos.* **2015**, *36*. [CrossRef]
288. Mohsenzadeh, M.S.; Mazinani, M.; Zebarjad, S.M. Evaluation of fracture behavior of polyethylene/CaCO₃ nanocomposite using essential work of fracture (EWF) approach. *Nanocomposites* **2015**, *1*. [CrossRef]
289. Shir Mohammadi, M.; Hammerquist, C.; Simonsen, J.; Nairn, J.A. The fracture toughness of polymer cellulose nanocomposites using the essential work of fracture method. *J. Mater. Sci.* **2016**, *51*. [CrossRef]
290. Tjong, S.C.; Bao, S.P.; Liang, G.D. Polypropylene/montmorillonite nanocomposites toughened with SEBS-g-MA: Structure-property relationship. *J. Polym. Sci. Part B Polym. Phys.* **2005**, *43*. [CrossRef]
291. Heidari, F.; Aghalari, M.; Chalabi Tehran, A.; Shelesh-Nezhad, K. Study on the fluidity, mechanical and fracture behavior of ABS/TPU/CNT nanocomposites. *J. Thermoplast. Compos. Mater.* **2020**. [CrossRef]
292. Liao, C.Z.; Tjong, S.C. Effects of carbon nanofibers on the fracture, mechanical, and thermal properties of PP/SEBS-g-MA blends. *Polym. Eng. Sci.* **2011**, *51*. [CrossRef]
293. Baldi, F.; Bignotti, F.; Tieghi, G.; Riccò, T. Rubber toughening of polyamide 6/organoclay nanocomposites obtained by melt blending. *J. Appl. Polym. Sci.* **2006**, *99*. [CrossRef]
294. Xu, W.; Lv, R.; Na, B.; Tian, N.; Li, Z.; Fu, Q. Micro-FTIR study of molecular orientation at crack tip in nylon 6/clay nanocomposite: Insight into fracture mechanism. *J. Phys. Chem. B* **2009**, *113*. [CrossRef]
295. Dayma, N.; Jaggi, H.S.; Satapathy, B.K. Post-yield fracture behaviour of PA-6/LDPE-g-MA/nanoclay ternary nanocomposites: Semiductile-to-ductile transition. *J. Polym. Res.* **2012**, *19*. [CrossRef]
296. Dayma, N.; Jaggi, H.S.; Satapathy, B.K. Post-yield crack toughness behavior of polyamide-6/polypropylene grafted maleic anhydride/nanoclay ternary nanocomposites. *Mater. Des.* **2013**, *49*. [CrossRef]
297. González, I.; Zabaleta, A.; Eguiazábal, J.I. Toughening and brittle-tough transition in polyamide 12-organoclay/maleated styrene-ethylene-co-butylene-styrene nanocomposites. *Polym. Eng. Sci.* **2013**, *53*. [CrossRef]
298. Dayma, N.; Kumar, S.; Das, D.; Satapathy, B.K. Melt-mixed PA-6/LDPE-g-MA/nanoclay ternary nanocomposite: Micro-mechanisms from post-yield fracture kinetics and strain field analysis. *Mater. Chem. Phys.* **2013**, *142*. [CrossRef]
299. Nakhaei, M.R.; Naderi, G.; Reza Ghoreishy, M.H. Experimental investigation of mechanical properties, fracture mechanism and crack propagation of PA6/NBR/Clay nanocomposites. *Iran. J. Polym. Sci. Technol.* **2020**, *33*. [CrossRef]
300. Fu, L.D.; Chen, S.; Wang, Y.J.; Wang, X.D.; Wang, X. Fracture toughness of polyamide 6/maleated ethylene-propylene-diene terpolymer rubber/nano calcium carbonate ternary composites according to essential work of fracture analysis. *J. Appl. Polym. Sci.* **2011**, *120*. [CrossRef]
301. Prashantha, K.; Schmitt, H.; Lacrampe, M.F.; Krawczak, P. Mechanical behaviour and essential work of fracture of halloysite nanotubes filled polyamide 6 nanocomposites. *Compos. Sci. Technol.* **2011**, *71*. [CrossRef]
302. Liao, C.Z.; Tjong, S.C. Fracture Toughness of Polyamide 6/ Maleated Styrene-Ethylene-Butylene-Styrene/Silicon Carbide Nanocomposites. *Adv. Mater. Res.* **2011**, *275*, 229–233. [CrossRef]
303. Liao, C.Z.; Tjong, S.C. Mechanical and thermal behaviour of polyamide 6/silicon carbide nanocomposites toughened with maleated styrene-ethylene-butylene-styrene elastomer. *Fatigue Fract. Eng. Mater. Struct.* **2012**, *35*, 56–63. [CrossRef]
304. Satapathy, B.K.; Weidisch, R.; Po, P.; Janke, A. SCIENCE AND Tough-to-brittle transition in multiwalled carbon nanotube (MWNT)/polycarbonate nanocomposites. *Compos. Sci. Technol.* **2007**, *67*, 867–879. [CrossRef]
305. Janke, A. Crack Toughness Behaviour of Multiwalled Carbon Nanotube (MWNT)/Polycarbonate Nanocomposites. *Macromol. Rapid Commun.* **2005**, 1246–1252. [CrossRef]
306. Rodríguez, C.; Arencón, D.; Belzunce, J.; Maspocho, M.L. Small punch test on the analysis of fracture behaviour of PLA-nanocomposite films. *Polym. Test.* **2014**, *33*, 21–29. [CrossRef]
307. Tuba, F.; Khumalo, V.M.; Karger-Kocsis, J. Essential work of fracture of poly(μ -caprolactone)/boehmite alumina nanocomposites: Effect of surface coating. *J. Appl. Polym. Sci.* **2013**, *129*. [CrossRef]
308. Arroyo, O.H.; Huneault, M.A.; Favis, B.D.; Bureau, M.N. Processing and properties of PLA/Thermoplastic starch/Montmorillonite nanocomposites. *Polym. Compos.* **2010**, *31*. [CrossRef]

309. Ahmad, S.H.; Rasid, R.; Surip, S.N.; Anuar, H.; Czigany, T.; Razak, S.B.A. Mechanical and fracture toughness behavior of TPNR nanocomposites. *J. Compos. Mater.* **2007**, *41*. [CrossRef]
310. Penalzoa, D.P. Review on the preparation and properties of clay-based nanocomposites with covalently-bound polymer architecture. *Philipp. J. Sci.* **2019**, *148*, 813–824.
311. Peres, F.M.; Schon, C.G. Application of the essential work of fracture method in ranking the performance in service of high-density polyethylene resins employed in pressure pipes. *J. Mater. Sci.* **2008**, *43*, 1844–1850. [CrossRef]
312. Rodriguez-Gonzalez, F.; Ramsay, B.; Favis, B. High performance LDPE/thermoplastic starch blends: A sustainable alternative to pure polyethylene. *Polymer* **2003**, *44*, 1517–1526. [CrossRef]

Review

Review: Filament Winding and Automated Fiber Placement with In Situ Consolidation for Fiber Reinforced Thermoplastic Polymer Composites

Yi Di Boon * , Sunil Chandrakant Joshi  and Somen Kumar Bhudolia * 

School of Mechanical and Aerospace Engineering, Nanyang Technological University, 50 Nanyang Avenue, Singapore 639798, Singapore; mscjosshi@ntu.edu.sg

* Correspondence: ydboon@ntu.edu.sg (Y.D.B.); somenkum001@e.ntu.edu.sg (S.K.B.)

Abstract: Fiber reinforced thermoplastic composites are gaining popularity in many industries due to their short consolidation cycles, among other advantages over thermoset-based composites. Computer aided manufacturing processes, such as filament winding and automated fiber placement, have been used conventionally for thermoset-based composites. The automated processes can be adapted to include in situ consolidation for the fabrication of thermoplastic-based composites. In this paper, a detailed literature review on the factors affecting the in situ consolidation process is presented. The models used to study the various aspects of the in situ consolidation process are discussed. The processing parameters that gave good consolidation results in past studies are compiled and highlighted. The parameters can be used as reference points for future studies to further improve the automated manufacturing processes.

Keywords: thermoplastic resin; process modeling; filament winding; automated fiber placement

Citation: Boon, Y.D.; Joshi, S.C.; Bhudolia, S.K. Review: Filament Winding and Automated Fiber Placement with In Situ Consolidation for Fiber Reinforced Thermoplastic Polymer Composites. *Polymers* **2021**, *13*, 1951. <https://doi.org/10.3390/polym13121951>

Academic Editor: Victor Tcherdintsev

Received: 19 May 2021

Accepted: 9 June 2021

Published: 11 June 2021

Publisher's Note: MDPI stays neutral with regard to jurisdictional claims in published maps and institutional affiliations.



Copyright: © 2021 by the authors. Licensee MDPI, Basel, Switzerland. This article is an open access article distributed under the terms and conditions of the Creative Commons Attribution (CC BY) license (<https://creativecommons.org/licenses/by/4.0/>).

1. Introduction

Fiber reinforced polymer (FRP) composites have very high specific strength and stiffness. These favorable properties led to FRP composites becoming more popular in many industries, such as aerospace, automotive, sports, construction, offshore, and so on [1–7]. Advancements in computer aided manufacturing processes for FRP composites, such as automated fiber placement (AFP) and filament winding (FW), have greatly improved the production throughput and the quality of FRP composite components. Epoxy, a thermoset polymer, is commonly used as the matrix material in FRP composites because of its excellent mechanical strength. However, one of the major drawbacks of thermoset based FRP composites is their long curing cycle, which results in increased manufacturing costs. In contrast, the manufacturing of fiber reinforced thermoplastic polymer (FRTP) composites is generally much less time consuming due to their short consolidation cycles. Besides this, FRTP composites also have other advantages over thermoset based FRP composites, including higher toughness, long shelf life, ease of repairing and potential for recycling [4]. High performance thermoplastic polymers, such as polyether ether ketone (PEEK), can also maintain their mechanical properties in environments with elevated temperature and moisture [8,9]. For FRTP composite components, their fabrication using AFP and FW processes can include in situ consolidation (ISC) to further shorten the processing time required.

Many studies have been carried out on the manufacturing of FRTP composites using AFP and FW with ISC. Researchers used various material forms and ISC methods in their studies, leading to different heat transfer and consolidation mechanisms. In this review, a comprehensive overview on the topic, encompassing the different material forms and ISC methods, is presented. Experimental and numerical studies on the factors affecting the ISC process are discussed, with attention given to recent studies. The optimization of the AFP and FW processes with ISC is deliberated, with emphasis given to the physical

and mechanical properties of the FRTP component fabricated, as well as the productivity of the process. A summary of the optimized processing parameters from past studies is also presented, providing a basis for future studies on further improving the fabrication of FRTP components using AFP and FW with ISC.

2. Manufacturing of FRTP Composites

The manufacturing of FRTP components generally involves three stages, namely heating, consolidation and cooling. In the heating stage, the thermoplastic matrix is melted or softened so that bonding can occur. Pressure is applied in the consolidation stage to produce components with low void content. During the cooling stage, the cooling rate is controlled to obtain the desired microstructure in the thermoplastic [4].

The autoclave process and compression molding are two commonly used manufacturing processes for FRTP composites in the industry. For the autoclave process, the FRTP preform is laid on a tool, by hand or using AFP, and sealed in a vacuum bag assembly. The vacuum bag assembly can include release films, a bleeder, a breather, a vacuum bag and sealants. The assembly is then put into an autoclave where heat and pressure are applied to the FRTP composite [4,10]. Advantages of the autoclave process include being able to fabricate large and complex components, as well as the consistency in the quality of components produced [10]. However, the process is difficult to automate. Consolidation also takes longer due to the convection heating involved [4]. For FRTP composites with high performance thermoplastic matrix, high-temperature vacuum bagging materials, which are difficult to handle, need to be used [10].

In compression molding, the FRTP component is formed from a preform using a compression press and a mold set. Similar to the autoclave process, the preform can be made by hand layup or using AFP. Prior to molding, the preform can be preheated in an oven. The preform is then compressed between the upper and lower molds (or 'core and cavity') using a compression press to give the component its shape. Heat is also applied during this stage [4,11]. Advantages of compression molding include its short processing cycles and being suitable for automation [4,11]. However, FRTP components fabricated using automated compression molding tend to have defects caused by wrinkles and waviness in the fiber reinforcement [11].

Computer aided manufacturing processes such as AFP and FW have several advantages over the autoclave process and compression molding. One of the advantages is the better precision in the fiber orientation that can be achieved. AFP and FW can also include ISC to enable the fabrication of FRTP composite components in a single step, thus potentially reducing production times. The AFP and FW processes with ISC are discussed in more detail in the next sections.

2.1. Automated Fiber Placement

A schematic diagram of the AFP process for FRTP composites is shown in Figure 1. Strips of FRTP prepreg tapes are laid on a tool usually by a robot arm equipped with a fiber placement head. The feeding unit on the fiber placement head guides the prepreg tapes onto the tool. The tape is heated at the nip point by a heat source and pressed onto the substrate by a compaction roller for ISC. The tape is cut into strips of specified lengths by the cutting unit. The AFP process is controlled by a computer program to lay the FRTP prepreg tapes in the designed layup configuration.

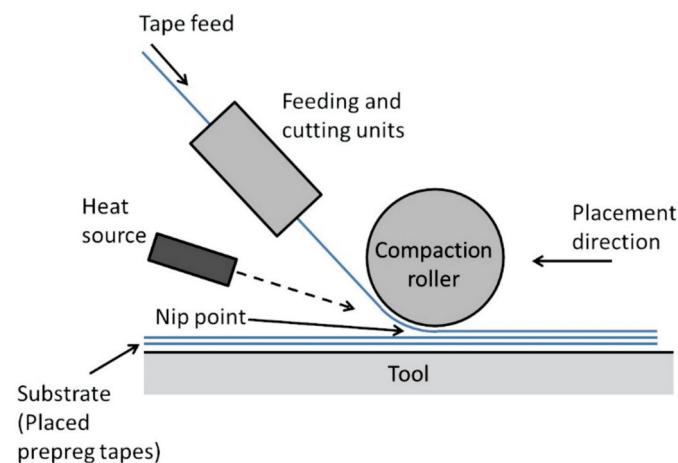


Figure 1. Automated fiber placement with in situ consolidation.

Advancements in AFP technology enabled the fabrication of FRTP composite components with improved fiber direction accuracy compared to conventional fabrication methods, such as hand layup, while reducing material wastage [12]. Advanced AFP machines allow for fiber placement speeds (or line speeds) of up to 3 m/s [13]. For the fabrication of large components, multiple tapes can be placed simultaneously to increase the productivity of the process [12]. For the fabrication of more complexed parts, the process is constrained by factors such as the size of the compaction roller, the arrangements of the feeding and cutting units, and the size of the heat source [13,14]. Some of the constraints can be overcome by designing the fiber placement head with features such as multiple compaction rollers with adjustable heights [13].

One of the major limiting factors to increasing the productivity of AFP processes is the incidence of manufacturing defects requiring inspections and corrections [13]. One strategy to alleviate the problem is to improve the defect detection using tools such as laser positioning systems [15] or online process monitoring methods such as thermographic imaging [13]. Sacco et al. presented a method using machine learning techniques in image processing to detect and classify defects in AFP processes [16]. Another strategy is to gain a better understanding of the effects of the defects on the performance of the FRP composite component and develop defect tolerant designs. Croft et al. conducted experiments to study the impacts of four different defect configurations, namely gap, overlap, half gap/overlap and twisted tow [17]. Nguyen et al. expanded on the study and investigated defects of various sizes [18]. Zhang et al. studied the tape wrinkling when placing prepreg tapes in curves and developed a set of placement criteria to avoid wrinkling [19]. Reviews on the effects of manufacturing defects in AFP and the methods for defect detection have been presented by Oromiehie et al. [20] and Sun et al. [21].

2.2. Filament Winding

Figure 2 shows a schematic of a FW setup with ISC. FRTP yarns or prepreg tapes are directed by the carriage and wound onto a rotating mandrel. For the fabrication of cylinders or pipes, a simple 2-axis FW machine (as shown in Figure 2) is sufficient. For the fabrication of parts with more complex geometry, such as pressure vessels with hemispherical end domes, a FW machine with more axes of motions, such as a robot arm with a FW head, is required. Similar to AFP, ISC is carried out using a heat source and a compaction roller. FW is a continuous process where cutting the FRTP yarns or prepreg tapes is not required during winding. As such, the yarns or tapes are usually tensioned throughout the process by tensioners.

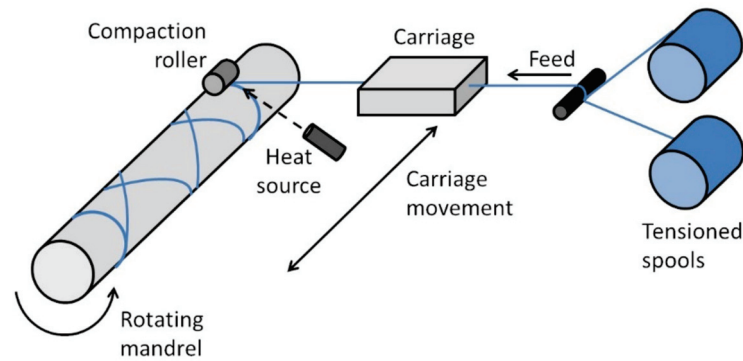


Figure 2. Filament winding with in situ consolidation.

FW has been used for decades to make axisymmetric FRP components, such as pipes, pressure vessels, pipe fittings and drive shafts [22,23]. Recently, advancements in robotics have made it possible to make components with more complex shapes. Sorrentino et al. used FW to fabricate a helicopter “fork” (a structural component connecting the helicopter blade to the rotor) which is not axisymmetric [24]. The authors highlighted the considerations in designing the FW process, including the winding trajectory, the winding tool, the mold and the winding pattern. Beck et al. used FW to fabricate a 3D fiber skeleton which is then overmolded through injection molding to form the final part [25]. The continuous fibers in the 3D skeleton are oriented strategically to be aligned to the load path.

3. Materials

The fiber reinforcement in FRP composites is the main load bearing component. Fiber reinforcements that are commonly used include carbon, glass and aramid. Carbon fibers have very high stiffness and tensile strength, making them suitable for applications in the aerospace industry. The reinforcement fibers need to be surface treated with the proper sizing to ensure good fiber-matrix bonding in the FRP composite [26,27].

There are two types of thermoplastic polymers, namely semi-crystalline and amorphous thermoplastics. Semi-crystalline thermoplastics experience thermal transitions from a solid or glassy state to a rubbery state at the glass transition temperature, T_g , and subsequently to a liquid state at the melting temperature, T_m . On the other hand, amorphous thermoplastics only exhibit a T_g . Thermoplastic polymers are generally categorized into two groups based on their performances, namely low cost thermoplastics and high performance thermoplastics. Low cost thermoplastics include polypropylene (PP), polyethylene (PE) and polyamides, such as PA6, PA66, and PA12. High performance thermoplastics include polyether ether ketone (PEEK), polyether ketone ketone (PEKK), polyphenylene sulphide (PPS), polyetherimide (PEI) and high temperature polyimides (TPI) [4,8,28]. The mechanical properties of high performance thermoplastics are comparable or better than conventionally used thermosets such as epoxy. High performance thermoplastics also have high T_g and high chemical resistance, allowing them to maintain their mechanical properties in harsh environments [8,9]. Gabrion et al. reported that a carbon/TPI composite retained its strengths in tensile and fatigue tests at temperatures up to 200 °C [28].

For the processing of FRTP composites using FW and AFP, semi-finished forms of the material system are generally used. For AFP, prepreg tapes are commonly used. For FW, in addition to prepreg tapes, commingled yarns and powder impregnated fibers can also be used [29]. The various semi-finished forms of FRTP composites are shown in Figure 3.

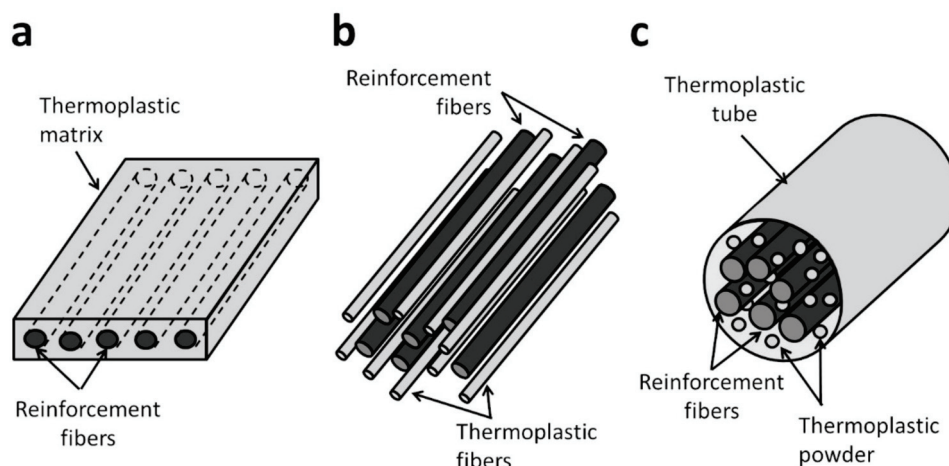


Figure 3. (a) Prepreg tape, (b) commingled yarn, (c) powder impregnated fibers.

Prepreg tapes are commonly produced through hot melt coating or pultrusion. High pressure is applied during the coating to ensure good thermoplastic impregnation. The resulting tapes are fully consolidated with very low void content [8]. Prepreg tapes with uniform tape width and smooth tape surfaces are suitable for use in FW and AFP. For FW and AFP using prepreg tapes, ISC only involves the bonding between the tapes and not impregnation, thus allowing for higher line speeds [29]. The FRTP component fabricated from prepreg tapes is also generally of better quality compared to using other semi-finished forms [4,29]. One disadvantage of prepreg tapes is their low flexibility making it difficult to form complex parts with them [4,8]. Prepreg tapes are also more expensive than commingled yarns and powder impregnated fibers [29,30]. Many FRTP materials, such as carbon/PEEK, carbon/PA6 and carbon/PPS, are currently available in prepreg tape form, and research on prepreg tapes for new material systems are ongoing. Iannone et al. proposed a hybrid prepreg tape consisting of carbon/PEEK tapes with PEI films added on the tape surfaces [31]. The hybrid prepreg tapes enable the fabrication of laminates with PEEK matrix at the desired degree of crystallinity and amorphous PEI at the interlaminar regions.

Commingled yarns are produced by intermingling reinforcement fibers with thermoplastic fibers. The reinforcement and thermoplastic fibers need to be distributed evenly in the yarn to minimize the thermoplastic flow distance required to achieve good impregnation during consolidation. The intermingling process is usually performed using air jets at room or elevated temperatures [32]. More recently, the production of commingled yarns using an online hybrid melt spinning technique is developed [26]. The technique enables excellent intermingling of the fibers without damaging them, and sizing can be applied in the same process. The use of commingled yarns allows for the fabrication of FRTP components with uniform fiber volume content. Commingled yarns are also flexible and can be woven into highly drapeable fabrics which can be used in stamp forming [32–34]. For FW using commingled yarns, researchers have studied the use of various heat sources such as ultrasonic welding and hot gas torch for ISC [29,35,36].

Powder impregnated fibers are made of reinforcement fibers with fine dispersed thermoplastic powder. In some products, an outer tube made of the same thermoplastic material is added. However, the outer tube can lead to composite components with large matrix rich region [9]. Powder impregnated fibers are produced by passing the reinforced fibers through a fluidized bed (air fluidization) or an aqueous bath where thermoplastic powders are dispersed onto the fibers [8,37,38]. The deposition of the powders is aided by ionizing the powders or adding surfactants. This process enables thermoplastics with very high melt viscosities to be used in FRTP composites [9]. Similar to commingled fibers, powder impregnated fibers are flexible and can be woven into fabric forms [8,9].

Henninger et al. proposed an FW process with online impregnation [39,40]. The reinforcement fibers and thermoplastic matrix are used in their raw forms. The online impregnation is performed by passing the reinforcement fibers through porous impregnation wheels. Molten thermoplastic polymer is squeezed from the inside of the wheels through to the surface to impregnate the fibers. A hot air gun and a consolidation roller are used for ISC. Henninger et al. reported that the FW process with online impregnation led to lower costs overall due to the raw materials used [39]. By controlling the online impregnation parameters, the process can be used to fabricate FRTP components with varying fiber volume contents. However, the productivity is lower than FW processes using semi-finished FRTP products because the line speed is limited by the fiber pretension [40].

4. Heat Sources for In Situ Consolidation

Temperature and dwell time (or exposure time) are two related parameters crucial to the consolidation of FRTP composites. Low temperatures or short dwell times lead to insufficient bonding, whereas temperatures which are too high or dwell times that are overly long result in degradation and decomposition of the thermoplastic matrix [36,41,42]. The temperatures and dwell times achievable in the ISC process are limited by the heating rate and the heating zone of the heat source. Therefore, the choice of the ISC heat source affects the productivity of the AFP and FW processes, as well as the quality of the FRTP composite component fabricated. Many different types of heat sources have been used for ISC, including hot gas torch, infrared (IR) heater, laser and ultrasonic welder.

Hot gas torch has been widely used in AFP and FW due to its low capital cost [43,44]. It can also be attached to the AFP or FW heads easily [45]. Heat is transferred to the thermoplastic through forced convection. Factors affecting the heat transfer include the hot gas temperature, the gas flow rate and the distance of the nozzle to the nip point [45]. For consolidation requiring high temperatures, an inert gas, such as nitrogen, needs to be used to prevent oxidation. This results in a significant increase in the operating costs [43,44]. Another drawback of the hot gas torch is its low energy efficiency [43,46]. In order to improve the heating process, hot gas heating can be used together with methods such as preheating of the composite fibers or tapes [36,47] and using a heated mandrel or tool [48].

An IR heater is another inexpensive option for heating FRTP composites. They are also easy to operate. They have been used both for the preheating of incoming fibers or tapes and as the main heat source for ISC. For the latter, IR spot heaters can output more focused heating to achieve results that are better or comparable to a hot gas torch [44,49]. IR heaters transfer heat mainly through radiation. For the heating of powder impregnated fibers with outer tubes using IR heaters, only the outer surface is exposed to IR radiation. The heat needs to be transferred from the outer tube to the powders and the fibers through conduction or convection, thus leading to a delay in the heating process [47]. Another disadvantage of IR heaters is the inconsistent heating due to the residual heat in the heaters after they are switched off [50]. The heat transfer from IR heaters is also less focused, leading to inefficiencies [44].

Laser has been studied by many researchers for ISC. Lasers are characterized by their very high radiation intensity which allows fast heating at a localized point [43,44]. Researchers have used CO₂ lasers for the consolidation FRTP composites such as carbon/PEEK and glass/PPS in early studies [42,43]. However, using CO₂ lasers can cause burning and oxidizing at the surface of FRTP prepreg tapes as the radiation from CO₂ lasers is absorbed by the thermoplastic matrix [44]. More recently, high powered lasers such as near infrared (NIR) diode lasers are used [51–53]. Diode lasers do not cause oxidation at the prepreg tape surface as the radiation from diode lasers is absorbed by the carbon fibers instead of the thermoplastic matrix [44]. The high power ratings of modern lasers (e.g., 3 kW [41]) compared to those used in early studies (e.g., 80 W [42]) allow AFP or FW to be performed at very high line speeds. Lasers are considerably more expensive than hot gas torch and IR heaters [43], thus they are generally reserved for the processing of FRTP composites requiring high temperatures, where other heating methods are considered insufficient. The implementation of a laser

heating system is also more difficult. Additional processing parameters such as the laser angle, the laser beam profile and the distance between the laser and the nip point need to be taken into consideration [41,44,54]. Additionally, safety measures, such as having an enclosed environment, need to be implemented.

Ultrasonic welding is a relatively new technique for ISC of FRTP composites. The technique has been proven to be effective in the joining and repairing of thermoplastic-based components [55]. In ultrasonic welding, high frequency, low-amplitude ultrasonic vibration is applied to the thermoplastic surface through a sonotrode or horn to cause surface and intermolecular friction, resulting in the heating and melting of the thermoplastic polymer [35,56]. The advantages of ultrasonic welding include short processing time, good localized heating and low energy requirement [55,56]. For ultrasonic ISC, the horn also acts as a compaction unit to apply pressure onto the FRTP composite. Additional rollers can be added to increase the contact time [35]. Researchers have studied the ultrasonic ISC of FRTP composites in the forms of commingled yarns and prepreg tapes, with thermoplastic matrices including poly(ethylene terephthalate) (PET), PP and high density polyethylene (HDPE) [35,46,56,57]. One of the limitations of ultrasonic welding is the dependence of the heat transfer process on the FRTP material properties, including stiffness, hardness and damping response [55]. Rizzolo and Walczyk reported that ultrasonic welding is effective for the consolidation of carbon/PET but less so for glass/HDPE [46].

Heraeus Noblelight developed a new flashlamp heating system named, humm3[®], based on pulsed light technology [58]. The humm3[®] has very high heating rate and excellent temperature control. The heating performance of the humm3[®] is comparable to high powered lasers. However, unlike lasers, there is no restrictive safety requirements for its application. Another advantage of the heating system is the small flashlamp head which allows it to be used for the fabrication of complex parts using AFP. Nguyen et al. used the flashlamp technology in the AFP of a hybrid material made for lightning protection, consisting of a FRTP prepreg layer, a copper layer (expanded or perforated foil) and a thermoplastic layer [59]. The line speed of 2400 mm/min was achieved for the process temperature of 380 °C.

5. Modeling Heat Transfer

The heat transfer process is a crucial part of the ISC of FRTP composites. Heat transfer mechanisms are categorized into conduction, convection and radiation. For AFP and FW with ISC, due to the various mechanisms involved and the complexity of the process, heat transfer is often studied using numerical methods, such as finite element (FE) simulations and finite difference methods (FDMs). In numerical simulations, the temperature field for the material being studied is obtained by solving the heat equation, with the heat transfer between the material and the environment modeled as boundary conditions. From the energy balance principle, the general heat equation can be written as shown in Equation (1) [60]:

$$\rho C \frac{\partial T}{\partial t} = -\nabla \cdot \mathbf{q} + \phi \quad (1)$$

where ρ is the material density, C is the specific heat capacity of the material, T is temperature, t is time, \mathbf{q} is the heat flux vector and ϕ is the volumetric rate of heat generation. For semi-crystalline thermoplastic polymers, the latent heat of fusion and heat related to crystallization can be modeled as a heat sink and a heat source respectively [61]. However, they are small compared to other heat exchange mechanisms involved and thus are often ignored [62,63]. The heat flux vector through the material, \mathbf{q}_{mat} , can be obtained using Fourier's law of heat conduction shown in Equation (2) [60]:

$$\mathbf{q}_{mat} = -k \nabla T \quad (2)$$

where k is the thermal conductivity of the material and ∇T is the temperature gradient. For FRTP composites, the thermal conductivity in the fiber direction is different from the

thermal conductivity in the transverse direction. Therefore, the heat flux in the fiber and transverse directions need to be considered separately [62,64].

For the heat transfer boundary conditions, the heat flux vector, q_{bc} , is often described using a linear relation shown in Equation (3) [60]:

$$q_{bc} \cdot n = h(T_1 - T_2) \quad (3)$$

where n is the unit normal vector, h is the film heat transfer coefficient at the boundary, T_1 is the temperature of the material and T_2 is the temperature of the heat source or the environment. For heat transfer through conduction, radiation and convection, h is substituted by thermal conductivity at the boundary, k_{bc} , the radiation heat transfer coefficient, h_r , and the convection heat transfer coefficient, h_{conv} , respectively. For the radiation heat exchange between the material and the environment, h_r is approximated by representing the material as a small body in a large enclosure. Using this representation, h_r is defined as shown in Equation (4) [65]:

$$h_r = 4\epsilon\sigma T_{ref}^3 \quad (4)$$

where ϵ is the emissivity of the material, σ is the Stefan-Boltzmann constant and $T_{ref} = \frac{1}{2}(T_1 + T_2)$. For convection, two types of convection are considered, namely forced and free convection. Forced convection is the heat transfer between a surface and a flow of fluid that is driven by an external agency, such as a pump, whereas free convection is the heat transfer caused by fluid flow due to buoyancy [60,65]. For free convection in air, h_{conv} is typically in the range of 1 to 50 W/(m²·K) [63,65].

For the modeling of ISC using forced convection heaters such as hot gas torch, many researchers used constant heat coefficient values (h_{heater}) to model the heat transfer between the heater and the FRTP material [66–68]. Tafreshi et al. discussed the determination of the h_{heater} value for ISC using hot gas torch using two approaches, namely (i) calculating h_{heater} from the Nusselt number and the Reynold number based on impinging jet theories, and (ii) obtaining h_{heater} by considering the energy absorbed by the material and then fitting numerical calculations to experimental data [45]. The authors compiled the h_{heater} values for different nozzle temperatures, hot gas flow rates, and nozzle-substrate distances for AFP with and without a roller. The data is useful for determining h_{heater} for future studies on the topic. In a recent study, Zacherl et al. noted that assuming a constant h_{heater} for the heating process using hot gas torch can lead to satisfactory predictions for the maximum temperature, but the predicted heating and cooling rates differ from experiments [69]. A similar observation was reported by Tafreshi et al. [68]. In particular, the cooling rate is important in determining the degree of crystallization of the thermoplastic in the ISC process. Therefore, Zacherl et al. introduced two distribution functions to model the h_{heater} distributions along the length and width of the FRTP tape near the nip point [69]. Using the h_{heater} distributions, the authors showed that the heating and cooling rates predicted agreed well with experiment. However, four additional parameters need to be determined through experimental data fitting, making the use of the distribution functions more complex.

For the modeling of ISC using radiant heating (lasers or IR heaters), the heat transfer from the heater to the FRTP composite is modeled using a heat flux distribution near the nip point. In earlier studies, researchers assumed a uniform heat flux distribution for ISC using radiant heating [61,70]. However, this is not an accurate representation due to factors such as reflection. The portion of radiation reflected can be calculated from the index of refraction of the material and the incident angle of the radiation using Fresnel's relations [64,71]. For laser ISC, Stokes-Griffin and Compston presented a model which includes a spatial emittance function to simulate the divergent beam and a micro-half-cylinder surface model to represent the surface of the FRTP tape for determining reflections [54]. The authors reported that the heat flux distribution predicted by the model agreed well with experiments. Baho et al. used a ray-tracing algorithm to determine the incident beam distribution for laser ISC and study the effect of reflected beams on the heat flux distribution near the nip point [64]. The authors reported that the laser heat flux is underestimated by 38% if reflection is neglected, 19% if only the first reflection is

considered, 6% if reflections up to the second reflection are considered and 2% if reflections up to the third reflection are considered.

Several approaches have been used by researchers to model the relative movement of the heat source to the FRTP material. Many researchers modeled the ISC process using the nip point as the Eulerian reference and including a velocity vector in the heat equation to simulate the mass flow in the material [61–64,72]. This approach is limited to modeling ISC at a constant line speed. Fricke and Fischer modeled the moving heat source in ISC using a boundary condition that is a function of time and space [73]. A script was used to generate a table to activate or deactivate the boundary condition at different locations and time steps in the process simulation. Another approach used by Liu et al. in their study involved the use of elements with life and death settings in FE simulation [66]. The tape laying process is simulated by having elements representing the tape in the death state initially and activating the elements at the appropriate time steps.

6. Modeling FRTP Consolidation

6.1. Consolidation of Prepreg Tapes

The determining factor in the consolidation of FRTP composites made using prepreg tapes is the bonding between the tapes, as full consolidation is already realized within the tapes. Two conditions need to be met: (i) intimate contact between the FRTP tapes or layers and (ii) autohesion or polymer chain inter-diffusion [44,74,75]. The models developed to study the two conditions are discussed next.

6.1.1. Intimate Contact Model

Figure 4 shows the schematic diagram of the interface between a newly placed FRTP layer and the substrate. Initially, gaps exist between the layers due to the rough surfaces of both the new layer and the substrate. The gaps prevent the autohesion of the thermoplastic at the interface [74,75]. Pressure needs to be applied to close the gaps and bring the surfaces together. The thermoplastic matrix also needs to be heated to lower its viscosity.

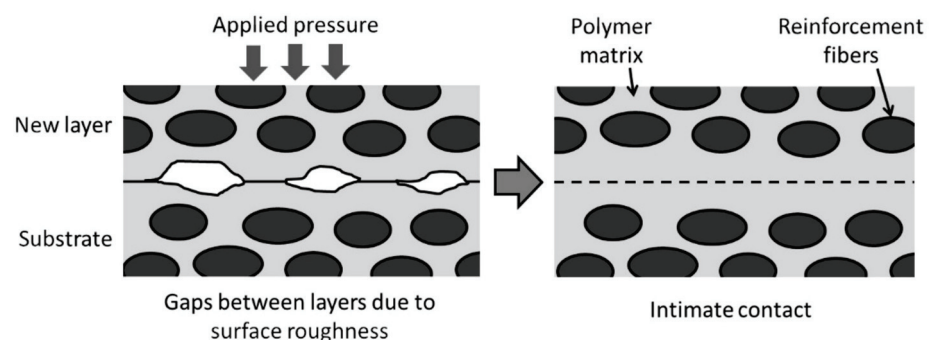


Figure 4. Establishing intimate contact at the interface between FRTP layers.

Dara and Loos developed an intimate contact model to study the effects of pressure, temperature and contact time on the degree of intimate contact, D_{ic} [74]. D_{ic} is defined as the ratio of the area in contact to the total area of the interface. This follows that $D_{ic} = 1$ when intimate contact is achieved. In their model, Dara and Loos used a statistical distribution to describe the roughness at the interface. The viscoelastic behavior of the thermoplastic is modeled as a squeezing flow of homogenous fluid between two plates. Lee and Springer simplified the model by representing the surface roughness as a series of rectangles with uniform width (b_0) and height (a_0) spaced evenly apart (w_0) [76]. The simplified representation of the surface is given in Figure 5 [76].

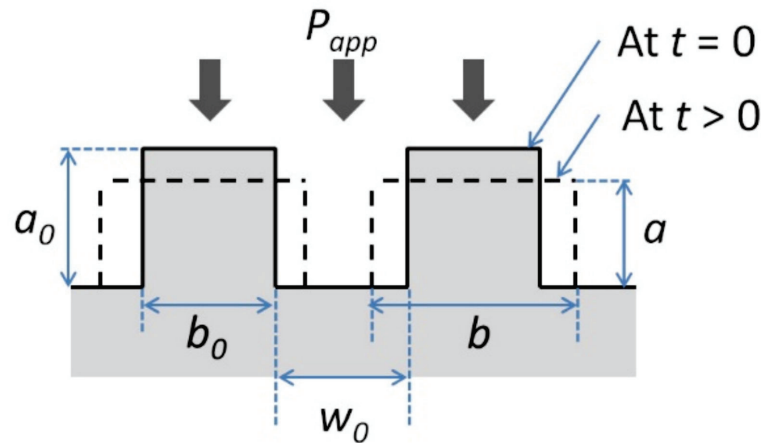


Figure 5. Simplified surface representation used by Lee and Springer for their intimate contact model.

Using this simplification, D_{ic} is given by Equation (5) [76]:

$$D_{ic} = \frac{1}{1 + \frac{w_0}{b_0}} \left[1 + \frac{5P_{app}}{\mu_{mf}} \left(1 + \frac{w_0}{b_0} \right) \left(\frac{a_0}{b_0} \right)^2 t \right]^{1/5} \tag{5}$$

where P_{app} is the applied pressure, μ_{mf} is the viscosity of the matrix-fiber mixture, and t is time. Here, it is assumed that P_{app} and μ_{mf} are constant over time. Mantell and Springer later expanded the model to include changes of P_{app} and μ_{mf} with time [77]. The resulting more generalized expression for D_{ic} is given by Equation (6) [77]:

$$D_{ic} = \frac{1}{1 + \frac{w_0}{b_0}} \left[1 + 5 \left(1 + \frac{w_0}{b_0} \right) \left(\frac{a_0}{b_0} \right)^2 \int_0^{t_c} \frac{P_{app}}{\mu_{mf}} dt \right]^{1/5} \tag{6}$$

where t_c is the contact time in which pressure is applied.

Yang and Pitchumani proposed an intimate contact model using fractal Cantor set construction to represent the surface roughness of FRTP prepreg tapes [78]. The Cantor set surface consists of generations of asperities with decreasing sizes controlled by a scaling factor f . The intimate contact process is modeled as the flattening of the asperities generation by generation following the squeeze flow model. In other words, the flattening of the $(n + 1)$ th generation asperities is completed before the (n) th generation asperities start to deform and become flattened. The degree of intimate contact for the (n) th generation asperities at time t , $D_{ic}^n(t)$, is given by Equation (7) [78]:

$$D_{ic}^n(t) = \frac{1}{f^n} \left[\frac{5}{4} \left(\frac{h_0}{L_0} \right)^2 \frac{f^{(\frac{2nD}{2-D} + n + 4)}}{(f + 1)^2} \int_{t_{n+1}}^t \frac{P_{app}}{\mu} dt + 1 \right]^{1/5}, \quad t_{n+1} \leq t \leq t_n \tag{7}$$

where μ is the viscosity of the thermoplastic matrix, L_0 is the total length of the Cantor set surface, h_0 is the height of the first-generation asperities and D is the fractal dimension of the Cantor set surface. For the models developed in [76,77], the parameters describing the surface roughness are obtained through experimental data fitting. In contrast, the parameters L_0 , h_0 , D and f required for Yang and Pitchumani’s model can be obtained from surface roughness measurements [78].

The models shown in Equations (5)–(7) have been used by researchers to study the FW and AFP processes with ISC [41,72,79]. Yassin and Hojatti highlighted the concerns that need to be accounted for when applying the intimate contact models [44]. For FW and AFP with ISC, the pressure is applied through the compaction roller. Factors such as the size and material (rigid or deformable) of the roller and the line speed affect the consolidation

pressure applied and the contact time. Besides this, the temperature of the FRTP composite, and in turn the composite viscosity, are also affected by the roller when they are in contact. These factors should be taken into consideration when using the models to study the ISC process, especially for processes with short contact times.

6.1.2. Autohesion Model

Figure 6 shows a schematic diagram of the autohesion or healing process for the consolidation of thermoplastic polymers. When a new thermoplastic layer is brought into intimate contact with the substrate and heat is applied, polymer chain inter-diffusion across the interface can occur. Over time, enough polymer chain inter-diffusion take place and the interface becomes indistinguishable from the bulk polymer [74,75]. This results in strong bonding between the thermoplastic layers. Autohesion can occur at temperatures above T_g for amorphous thermoplastics and above T_m for semi-crystalline thermoplastics [80,81].

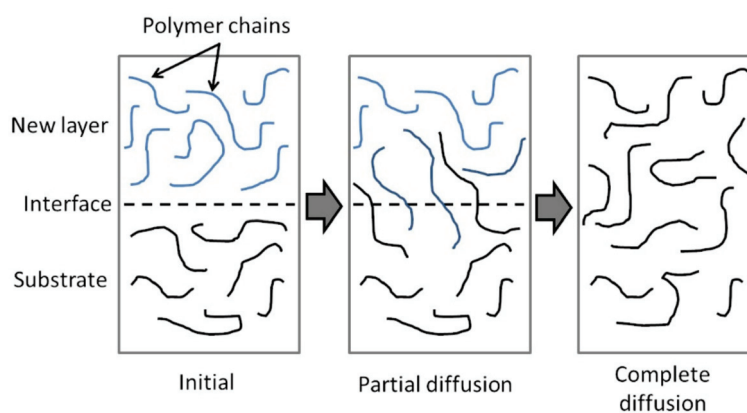


Figure 6. Polymer chain diffusion in the autohesion process.

The diffusion of polymer chains is modeled based on the reptation theory detailed by De Gennes [82]. A polymer chain entangled with many other chains is restricted to wriggling motions in a tube-like region at small time scales. At larger time scales, the ends of the polymer chain can move away from the tube, forming minor chains. Eventually, the polymer chain has a new position out of the initial tube. The time to reach this state is the renewal or reptation time, t_r [82,83]. The degree of autohesion, D_{ah} , is defined as the ratio of the interfacial bond strength to the fracture strength of the virgin thermoplastic polymer. Kim and Wool considered the interfacial bond strength as a function of the length of minor chains through the interface [83]. For time $t < t_r$, D_{ah} was found to be proportional to $t^{1/4}$ and $M^{4/3}$, where M is the molecular weight of the polymer.

Yang and Pitchumani proposed an autohesion model for non-isothermal condition [80]. Bonding at the interface is dependent on the critical entanglement molecular weight, M_C . M_C is a function of the number of monomers, the polymer chain length, the monomer weight, the number of C-C bonds per monomer, the bond length and the characteristic ratio [84]. For thermoplastic polymers with molecular weight $M > 8M_C$, the maximum bond strength is reached at the welding time, t_w with $t_w < t_r$. This is the case for most engineering thermoplastic polymers. The degree of autohesion for non-isothermal healing is given by Equation (8) [80]:

$$D_{ah}(t) = \left[\int_0^t \frac{1}{t_w(T)} dt \right]^{\frac{1}{4}} \quad (8)$$

where T is the temperature. For polymers with $M < 8M_C$, the welding time is the same as the reptation time ($t_w = t_r$). t_w is dependent on T , with their relationship described by an Arrhenius law [80]. At higher temperatures, the polymer chains can diffuse more easily, leading to shorter welding times.

6.1.3. Bonding Model

For the bonding of FRTP prepreg tapes, intimate contact has to occur before autohesion can take place. Yang and Pitchumani described the bonding process as the healing of incremental intimate contact areas. The degree of bonding, D_b , is thus given as shown in Equation (9) [85]:

$$D_b(t_b) = D_{ic}(0) \cdot D_{ah}(t_b) + \int_0^{t_b} D_{ah}(t_b - t) \cdot \frac{dD_{ic}(t)}{dt} dt \quad (9)$$

where t_b is the total bond time, $D_{ic}(0)$ is the initial intimate contact area and $(t_b - t)$ is the time available for autohesion for an incremental intimate contact area. For cases where the time required to achieve full intimate contact is much larger than the time required for autohesion (e.g., as reported in [41]), D_b is taken to be the same as D_{ic} .

6.2. Consolidation of Commingled Yarns

The consolidation process of FRTP composites made from commingled yarns involves the impregnation of fiber bundles by the thermoplastic matrix, in addition to the intimate contact and autohesion of the thermoplastic. The impregnation step is usually the limiting step [86], thus researchers have focused on the impregnation step in studying the consolidation of commingled yarns.

Klinkmuller et al. developed an impregnation model for commingled yarns [87]. The commingled yarns are modeled as consisting of several fiber agglomerations of the same size surrounded by the thermoplastic matrix (Figure 7). Consolidation is achieved when the voids in the fiber agglomerations are filled by the matrix.

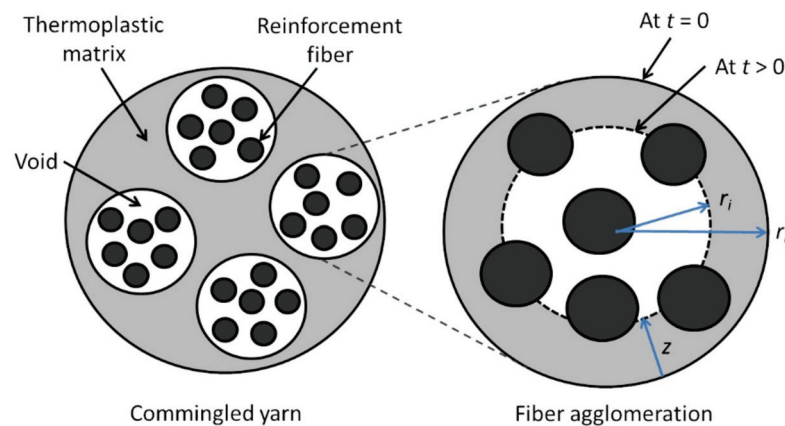


Figure 7. Cross section of commingled yarn modeled as a group of fiber agglomerations.

The Darcy’s law is used to describe the flow of the thermoplastic polymer through the reinforcement fibers (functioning as a porous bed). For the transverse permeability through the reinforcement fibers, the model presented by Gutowski et al. is used for cases with high fiber volume content [88]. The impregnation time, t , required to reach a penetration length, z , is given by Equation (10) [87]:

$$t = \frac{2\mu k_{zz} z^2 \left(\frac{V_a}{V_f} + 1 \right)}{r_f^2 (p_a - p_0) \left(\sqrt{\frac{V_a}{V_f}} - 1 \right)^3} \quad (10)$$

where:

- μ is the viscosity of the thermoplastic matrix dependent on the temperature through an Arrhenius law,
- V_a is maximum fiber volume content (0.83 for carbon fibers [88]),
- V_f is the pressure dependent fiber volume content,

- r_f is the radius of the reinforcement fiber,
- p_a is the applied pressure,
- p_0 is the atmospheric pressure, and
- k_{zz} is the transverse permeability constant through the fibers.

For fiber agglomerations with circular cross sections (Figure 7), z is related to void content, X_v , by Equation (11) [87]:

$$z = r_0 - \sqrt{\frac{X_v A_t}{\pi n (1 - V_f)}} \tag{11}$$

where r_0 is the radius of the fiber agglomeration, n is the number of fiber agglomerations in the yarn and A_t is the total cross sectional area of the commingled yarn.

For fiber agglomerations with rectangular cross sections, the relationship between z and X_v is given by Ye et al. [89], and also reported by Friedrich [32]. The relationship is shown in Equation (12) [32,89]:

$$z = \frac{h_0 (1 - V_f) - h_{1(z,0)} X_v}{(1 - V_f)(1 - X_v)} \tag{12}$$

where h_0 is the half height of the fiber agglomeration and $h_{1(z,0)}$ is the half height of the total agglomeration, which includes the surrounding thermoplastic matrix, at time, $t = 0$. The models (Equations (10)–(12)) can give satisfactory predictions for the impregnation time required to achieve a target void content, but require many parameters determined through experiments and empirical data fitting. In particular, the experiments required to determine k_{zz} is difficult to carry out [88].

Another model for the consolidation of commingled fibers is proposed by Bernet et al. [33,86]. The commingled yarn is also modeled as a group of fiber agglomerations, but the agglomerations can have different sizes. The fiber volume fraction, V_f , is assumed to be constant after some pressure is applied, thus permeability of the fiber bed, K_p , is also constant. The position of the thermoplastic flow front, r_i , is used in the model (Figure 7). For unimpregnated fiber agglomerations, the voids are considered open pores. As impregnation progresses, the thermoplastic matrix connects the fibers causing air to be trapped in the voids. At this stage, the voids are considered closed pores. A parameter, r_c , is defined such that when $r_i \geq r_c$, voids are open pores, and when $r_i < r_c$, voids are closed pores. Using the Darcy’s law, the relationship between r_i and time, t , is given by Equation (13) [33,86]:

$$\Delta t = \frac{\mu (1 - V_f)}{K_p (P_a + P_c - P_g(r_i))} \left[\frac{r_i^2}{2} \ln\left(\frac{r_i}{r_0}\right) - \frac{R_i^2}{2} \ln\left(\frac{R_i}{r_0}\right) - \frac{r_i^2}{4} + \frac{R_i^2}{4} \right] \tag{13}$$

where P_c is the capillary pressure (defined as positive when enhancing flow), P_a is the applied pressure, R_i is the thermoplastic flow front before the time increment, Δt , and μ is the viscosity of the thermoplastic matrix. $P_g(r_i)$ is the internal void pressure given by Equation (14) [33,86]:

$$P_g(r_i) = P_0 \text{ for } r_i \geq r_c, P_g(r_i) = P_0 \left(\frac{r_c}{r_i}\right)^2 \text{ for } r_i < r_c \tag{14}$$

where P_0 is the ambient pressure in the fiber agglomeration before void closing. Equation (13) is obtained through numerical integration where $P_g(r_i)$ is assumed to be constant over the time increment, Δt . Total impregnation time for $r_i < r_c$ is the sum of the time increments. P_c is small compared to P_a and can usually be neglected [86].

The fiber agglomerations are grouped according to the agglomeration size. For agglomeration size group j , N_a^j is the number of agglomerations in the group and r_i^j is

the thermoplastic flow front. The void content of the yarn, X_v , is then computed using Equation (15) [33,86]:

$$X_v = \frac{\sum_{j=1}^n \pi N_a^j r_i^2 (1 - V_f)}{A_t + \sum_{j=1}^n \pi N_a^j r_i^2 (1 - V_f)} \quad (15)$$

where n is the number of agglomeration sizes and A_t is the cross section area of a fully consolidated yarn. The number of agglomerations and their sizes can be determined from microscopic observations of the commingled yarn. For the determination of K_p , Bernet et al. used Gebart's model [90] given in Equation (16):

$$K_p = C_1 \left(\sqrt{\frac{V_{f,max}}{V_f}} - 1 \right)^{2.5} R_f^2 \quad (16)$$

where C_1 is a constant, $V_{f,max}$ is the maximum fiber volume fraction corresponding to zero permeability and R_f is the fiber radius. C_1 and $V_{f,max}$ are related to the fiber arrangement. Bernet et al. used their model to study the consolidation of carbon/PA12 commingled fibers [33,86]. The authors showed that the model is applicable for processes with consolidation times in the order of 1 min, 0.1 min and 10 s [33].

Thomann and Ermanni expanded on the model proposed by Bernet et al. [34]. The authors used a logarithmic normal distribution to better describe the fiber distribution within a commingled yarn with good blending. The frequency of occurrence for a fiber agglomeration of size j is given by Equation (17) [34]:

$$\phi(N_a^j) = \frac{1}{s\sqrt{2\pi} \sum_{j=1}^n N_a^j} \exp\left(-\frac{1}{2} \left(\frac{\ln(N_f^j) - \zeta^*}{s}\right)^2\right) \quad (17)$$

where N_f^j is the number of fibers in the agglomeration of size group j , s^2 is the variance and ζ^* is the predictand of $\ln(N_f^j)$. The parameters defining the fiber distribution are estimated from microscopic observations of the commingled yarn. Thomann and Ermanni used the model to study the stamp forming of FRTP composite components made from carbon/PA12 and carbon/poly(butylene-terephthalate) (PBT) commingled yarns [34].

6.3. Consolidation of Powder Impregnated Fibers

Similar to commingled fibers, the impregnation of the reinforcement fibers by the thermoplastic matrix is the limiting step in the consolidation of powder impregnated fibers.

Ye et al. developed a model to study the consolidation of powder impregnated fibers [91]. The thermoplastic flow is assumed to occur only in the radial direction (transverse flow through the fiber bed). Therefore, the impregnation process is modeled similar to that of commingled yarns (as reported in [32,87,89]) with a representative fiber agglomeration or tow. Using Darcy's law, the time, t , required for the thermoplastic flow front to reach a position r_i is given by Equation (18) [91]:

$$t = \frac{\mu r_0^2}{4K_p(p_a - p_0)} \left[2 \left(\frac{r_i}{r_0}\right)^2 \ln\left(\frac{r_i}{r_0}\right) + 1 - \left(\frac{r_i}{r_0}\right)^2 \right] \quad (18)$$

where r_0 is the radius of the fiber tow, p_0 is the pressure within the tow (taken as atmospheric pressure), p_a is the applied pressure, K_p is the permeability and μ is the viscosity

of the thermoplastic matrix. The void content, X_v , can be calculated from r_i using Equation (19) [91]:

$$X_v = \frac{\pi r_0^2 \left(\frac{r_i}{r_0}\right)^2 (1 - V_f - V_{mp})}{\pi r_0^2 \left(1 + \left(\frac{r_i}{r_0}\right)^2 (1 - V_f - V_{mp})\right)} \quad (19)$$

where V_f is the fiber volume fraction and V_{mp} is the volume fraction of the matrix powder. Ye et al. used the Carman-Kozeny equation to determine K_p [91]. The authors reported good correlation between the model predictions and experimental results in their study on glass/PP composites [91].

Steggall-Murphy et al. used a similar model to that of Ye et al. [92]. In their study, Steggall-Murphy et al. investigated the consolidation of an FRTP composite made with glass fiber fabric as reinforcement and HDPE powders as matrix. A rectangular cross section was used to model a powder impregnated fiber bundle. The deformation of the fiber tow is assumed to be negligible. The authors used an empirical approach to determine the ratio of K/μ , where K is the permeability of the fiber bundle and μ is the viscosity of the thermoplastic. The consolidation was divided into two stages, namely the ramp stage where pressure is increased to a setpoint and the dwell stage where pressure is held constant. The authors reported that the model gave good predictions of the laminate void content for consolidation carried out at low applied pressure (0.345 MPa). However, for consolidation performed at high pressure (0.690 MPa), the void content is overestimated by the model. This is because the effects of fiber tow deformation become significant when the applied pressure is high [92].

Connor et al. used a different approach in their impregnation model for powder impregnated fibers [93]. During consolidation, the thermoplastic matrix powders melt and form resin bridges between the reinforcement fibers. The impregnation process is modeled as the thermoplastic flow along the length of the fibers (axial flow), as shown in Figure 8. The distance between the reinforcement fibers, d , decreases as impregnation occurs. The assumptions made by the authors include: (i) transverse thermoplastic flow through the fibers is negligible compared to the axial flow, (ii) the center of the molten matrix powder is fixed and its volume is constant, and (iii) all of the resin bridges can be modeled using the same geometry.

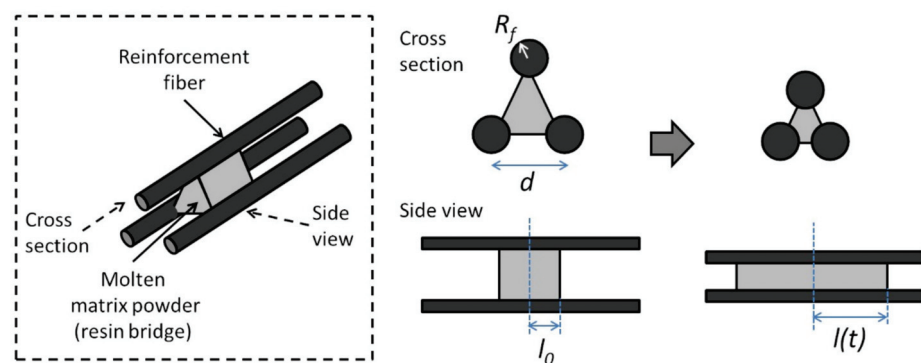


Figure 8. Model of resin bridge between fibers during the consolidation of powder impregnated fibers.

For the consolidation process, the applied pressure (P_a) is counteracted by the capillary pressure (P_C), viscous pressure from the thermoplastic (P_v) and the spring-like pressure from the fiber bundle (P_s). P_s is due to the compression of the fiber bundle as reported

by Gutowski et al. [88]. Connor et al. applied the Hagen-Poiseuille equation to relate the thermoplastic flow to P_v . The flow rate is then expressed as shown in Equation (20) [93]:

$$\frac{d}{dt} \left(\frac{l}{L} \right) = \frac{27}{128\mu} \left(\frac{R_f}{R_m} \right)^6 \left(\frac{V_m}{V_f} \right)^4 \left(\frac{l}{L} \right)^4 (P_a - P_s - P_c) \quad (20)$$

where l is the time dependent thermoplastic half length (Figure 8), L is the half length of the molten thermoplastic powder when consolidation is completed ($l = L$ at full consolidation), R_f is the radius of the reinforcement fiber, R_m is the thermoplastic powder radius, μ is the thermoplastic viscosity, V_f and V_m are the final fiber and matrix volume contents. P_c is usually much smaller than P_a and thus can be neglected. For the carbon/PEEK and carbon/PEI composites studied, the authors also found that P_s was insignificant compared to P_a . In cases where P_c and P_s are small, the time to reach full consolidation, t_1 , can be determined from Equation (21) [93]:

$$\left(\frac{t_1 P_a}{\mu} \right) = \frac{128}{135} \left(\frac{V_f}{V_m} \right)^4 \left(\frac{R_m}{R_f} \right)^6 \quad (21)$$

For cases where P_c or P_s is comparable to P_a , Equation (20) needs to be integrated numerically. In the model, the effect of different wetting behaviors in different material systems is absent as P_c is neglected. However, the authors stressed that the wetting behaviors are important for the fiber-matrix bonding and need to be taken into consideration in studying the consolidation of powder impregnated fibers [93].

7. Modeling Crystallization and Other Aspects of FRTP In Situ Consolidation

For FRTP with semi-crystalline thermoplastic matrices, the morphology of the thermoplastic affects the mechanical properties of the composite. Factors affecting the morphology include the degree of crystallinity, spherulite size and crystalline orientation [8]. Many researchers use the degree of crystallinity as a means of studying the morphology [51,53,94,95]. For PEEK, tensile strength and stiffness increases with increasing crystallinity but fracture toughness decreases at the same time [8]. Therefore, the consolidation process, especially the cooling rate, needs to be controlled properly to achieve the desired crystallinity [8,69].

Ozawa derived an expression for non-isothermal crystallization given in Equation (22) [96]:

$$\log[-\ln(1 - c_r)] = \log X(T) + n \log \left(\frac{dT}{dt} \right) \quad (22)$$

where c_r is the relative crystallinity, T is the temperature, t is time, $X(T)$ is the cooling function, and n is a constant. $X(T)$ and n can be obtained by analyzing differential scanning calorimetry (DSC) curves of the crystallization process occurring at different cooling rates. The crystallinity, c_a , is related to c_r through Equation (23) [76]:

$$\frac{c_a}{c_r} = \frac{H_T}{H_U} \quad (23)$$

where H_T is the total heat of crystallization at a given cooling rate and H_U is the theoretical ultimate heat of crystallization for the thermoplastic. Researchers have used the Ozawa model to simulate the crystallization process of FRTP composites such as carbon/PEEK [76,97]. For the APC-2 carbon/PEEK composite, $n = 0.8$, $X(T) = \exp(-0.037 T + 11.3)$, and the ratio H_T/H_U can be calculated using $H_T/H_U = -0.03 \ln(dT/dt) + 0.42$ [76,97].

Another non-isothermal crystallization model was derived by Choe and Lee [98]. The model is based on phase transition kinetics formulated by Tobin, which includes

the growth site impingement phenomena [99–101]. The non-isothermal crystallization expression derived by Choe and Lee is given in Equation (24) [98]:

$$\begin{aligned} \dot{\alpha}(t) = & \kappa_1 \exp\left(-\frac{3E_d}{RT}\right) \exp\left(-\frac{3\psi_1 T_m^0}{T(T_m^0 - T)}\right) t^2 [1 - \alpha(t)]^2 \\ & + \kappa_2 \exp\left(-\frac{4E_d}{RT}\right) \exp\left(-\frac{(3\psi_1 + \psi_2) T_m^0}{T(T_m^0 - T)}\right) \\ & \cdot [1 - \alpha(t)]^2 \int_0^t (t - \omega)^2 [1 - \alpha(\omega)] d\omega \end{aligned} \quad (24)$$

where $\alpha(t)$ is the relative crystallinity at time t , T is the temperature, T_m^0 is the equilibrium melting temperature, E_d is the activation energy of diffusion of crystallization segments across the phase boundary, ψ_1 is a constant related to the free energy of formation of a critical nucleus, ψ_2 is a constant related to the free energy of formation of a growth embryo, κ_1 and κ_2 are kinematic parameters. The expression is applicable for crystallization through the formation 3D spherulites. The first part of Equation (24) describes the rate of crystallization through heterogenous nucleation and growth, while the second part gives the rate of crystallization through homogenous nucleation and growth. Choe and Lee varied the temperatures and cooling rates in DSC to control the crystallization mechanisms of PEEK. The values of T_m^0 , E_d , κ_1 , κ_2 , ψ_1 , ψ_2 for PEEK were then determined analyzing the DSC results with the use of regression methods [98].

In a study on AFP with laser ISC, Sonmez and Hahn used Choe and Lee's model to simulate the crystallization in the FRTP tape in the cooling phase [61]. For the crystal melting process occurring in the heating phase, the model proposed by Maffezzoli et al. [102] was used. From the model, the crystallinity at time t , $c_a(t)$, is given by Equation (25) [61,102]:

$$c_a(t) = c_a(t_{init}) \left(1 - 0.5 \int_{t_{init}}^t \bar{K} dt\right)^2 \quad (25)$$

where t_{init} is the initial time and \bar{K} is given by $\bar{K} = \bar{K}_0 \exp(-E_{am}/RT)$. For APC-2 composite, the constant $\bar{K}_0 = 5.05 \times 10^{31} \text{ s}^{-1}$ and the activation energy for melting, E_{am} , is 397 kJ/mol [72,77]. Sonmez and Hahn's approach was also used by Song to simulate the crystallization process in FW of carbon/PEEK with ISC using hot gas torch [72].

Gordnian used a 'semi model-free' approach in modeling the crystallization and melt kinetics of the carbon/PEEK composite [103]. Multiple isothermal and non-isothermal DSC experiments were carried out. Using the DSC results, Gordnian plotted the 'iso-conversional' graphs for the crystallization rate to study its dependence on crystallinity and the temperature. An empirical model was then introduced with the model parameters determined through experimental data fitting. For cases where the crystallinity is below 0.001, an induction time need to be calculated to determine the onset of the crystallization process. Gordnian also studied the melt kinetics using the same procedure. Two peaks were observed in the melting DSC experiments. The author deduced that recrystallization and melting occurred simultaneously in the process, resulting in the two peaks observation. A master melt curve was then obtained using the DSC results and the results calculated from the crystallization model. The combined model was shown to give good predictions for the crystallinity in isothermal and non-isothermal crystallizations and melting.

Besides crystallinity, researchers have also modeled other aspects of FRTP composites fabricated using AFP and FW with ISC. Schlottermuller et al. studied the thermal residual stresses in glass/PP specimens made using FW with hot gas torch ISC [104]. The thermal expansion coefficients are included in the stress-strain submodel to calculate the stress distributions across the composite layers. Dedieu et al. used the same approach to study the residual stresses in carbon/PEEK composites fabricated using FW with laser ISC [105]. Nam and Seferis presented a model for the degradation kinetics in thermoplastic composites [106]. The degradation model is defined by a rate constant, $k(T)$, and a conversion dependence function, $f(\alpha)$. The temperature dependence of $k(T)$ is described by an Arrhenius expression. For $f(\alpha)$, the effects of different reaction mechanisms are included using

weighting factors. Nam and Seferis obtained the kinetic parameters for the degradation of PEEK from thermogravimetric analysis (TGA) experiments and showed that the model gave good predictions. The model developed by Nam and Seferis was adopted by Sonmez and Hahn in their studies on AFP with ISC [61,107].

8. Studies on Factors Affecting In Situ Consolidation Quality

Many researchers have carried out experimental and numerical studies on the fabrication of FRTP composites using AFP and FW with ISC. Many researchers compared the composite components fabricated using AFP and FW with components fabricated using more established methods for FRTP composites, such as compression molding and autoclave. The quality of the fabricated component is evaluated by its void content as well as mechanical properties measured from tests such as the short beam shear (SBS) test, peel tests, bending tests and delamination tests (such as the double cantilever beam (DCB) test).

Comer et al. compared the mechanical performance of carbon/PEEK laminates fabricated using AFP with laser ISC with laminates fabricated using autoclave [51]. Carbon/PEEK prepreg tapes with a width of 12 mm were used in the AFP process. For the laminates fabricated using autoclave, wide carbon/PEEK tapes (width of 150 mm) were used to make the pre-forms by hand lay-up. The pre-forms were then sealed in a high temperature vacuum bag and consolidated in an autoclave. The specimens fabricated using the AFP process have higher interlaminar fracture toughness compared to the autoclave specimens. However, the AFP specimens have lower crystallinity (17.6%) than the recommended level (33%). This led to the specimens having lower flexural strength, interlaminar shear strength, and open-hole compression strength compared to autoclave specimens (crystallinity 40%). The authors suggested the high cooling rate and insufficient through thickness heating as two possible causes for the low crystallinity in the specimens fabricated using laser ISC.

Hoa et al. studied the fabrication of carbon/PEEK laminates using AFP with ISC using a hot gas torch [48]. Carbon/PEEK prepreg tapes were used in the study. The mechanical properties of carbon/PEEK laminates consolidated using the autoclave method from literature were used for comparison. The authors reported increased fiber waviness in the laminates fabricated using AFP compared to laminates fabricated using autoclave, leading to worse compressive strength in the AFP laminates. This is due to excessive compressive pressure from the rigid compaction roller. Another problem inherent to AFP with ISC is the uneven temperature distributions in the through thickness direction of the laminate, causing warpage. The authors recommended heating the mandrel or tool above the T_g of the thermoplastic matrix to circumvent the warpage problem.

Stokes-Griffin and Compston studied various aspects of the AFP process with laser ISC for carbon/PEEK prepreg tapes [52,79]. Laminates fabricated using a lower line speed (100 mm/s) exhibited better fiber-matrix bonding compared to laminates fabricated using a higher line speed (400 mm/s). The authors attributed this to the higher crystallinity in the laminates fabricated at 100 mm/s. For the compaction roller, a deformable roller (silicone roller) resulted in better consolidation compared to a rigid roller (brass roller). This is due to the large laser shadow produced by the rigid roller. For the modeling of the consolidation process, the authors showed that the temperature threshold for autohesion of PEEK to occur is T_g instead of T_m if the PEEK is completely melted at the heating phase.

Doan and Mertiny studied the creep response of FRTP components fabricated using FW with hot air blower ISC [108]. Glass/HDPE prepreg tapes with a width of 49 mm were used. Two batches of specimens were fabricated. For batch 1, the heater setting of 400 °C was used for the first 7 layers and 420 °C was used for layers 8 to 10. For batch 2, the heater was set to 400 °C for the first 4 layers, 420 °C for layers 5 to 8, and 440 °C for layers 9 to 10. The batch 2 specimens exhibited better fiber packing and greater resistance to creep. The authors explained that the higher processing temperatures in the batch 2 specimens led to higher crystallinity, thus resulting in improved creep resistance.

Samak et al. studied the ILSS and void content of ring specimens with layup configurations $[0/90]_n$, $[0/\pm 30]_n$ and $[0/\pm 45]_n$ fabricated using FW with laser ISC [109]. Carbon/PEEK prepreg tapes were wound on a mandrel with a diameter of 400 mm. Gaps between the FRTP tapes was programmed into the FW process. For 90° layers, the gap was set to 1.6 mm while for all other layers, the gap was 1.4 mm. The width of the prepreg tape was not reported. The processing parameters, 7 m/min line speed, 430°C laser temperature and 600 N compaction force, were kept constant across the specimens. The authors reported the $[0/\pm 45]_n$ specimens had the highest ILSS (average of 48.2 MPa) and lowest void content. This suggests that the processing parameters need to be optimized for specimens with different layup configurations.

Peeters et al. studied the fabrication of FRTP composite stiffeners using AFP with laser ISC [14]. For the fiber placement at the corners of the stiffeners, a second pass or repass, where heat and compaction pressure are applied to the FRTP layer without adding new material, was required. The repass was performed to ensure that the prepreg tapes could bond well at the corners. Shadmehri et al. also studied the application of repass treatments in the AFP process with hot gas torch ISC [95]. The repass treatment was found to reduce the surface roughness of the resulting FRTP component. However, the crystallinity of the thermoplastic matrix was also reduced. The authors recommended applying the repass treatment for FRTP components used in aerodynamic applications but doing the repass only at the outermost layer.

Another study on the effect of repass in AFP with laser ISC was conducted by Chanteli et al. [94]. Four repass methods were compared, namely single repass, double repass, perpendicular repass (repass applied perpendicular to the fiber direction) and tool-side repass (repass applied on the ply already laid on the tool). Specimens fabricated using AFP without repass, with and without an additional consolidation step using autoclave, were also tested. The repass treatments improved the physical properties of the composites (lower void content, lower surface roughness, higher crystallinity) compared to AFP specimens without repass. For the mechanical properties, the single repass treatment was found to improve the open hole compression and in-plane shear performances of the specimens, while the double repass treatment resulted in the worst performance. However, specimens consolidated using autoclave showed the best performance for all the properties studied, especially for the mechanical properties. Comparing the findings from [95] and [94], it can be seen that the effect of the repass treatment depends on the heat source used. For laser ISC, due to the high heating and cooling rate, a repass treatment was required to increase the crystallinity.

Zhao et al. studied the effect of the multi-pass layup process on the interlaminar bonding of FRTP laminates fabricated using AFP [110]. Hot gas torch was used for ISC. For the fabrication of laminates with multiple FRTP layers, the applied heat and compaction pressure affects not only the current layer being placed, but also the substrate as well. Therefore, the applied compaction pressure needs to be varied between layers to achieve uniform interlaminar bonding across the different layers. The authors calculated the optimized compaction pressure for each layup pass by analyzing the intimate contact at the interlaminar regions.

Many heat transfer studies have been conducted to investigate the temperature field in the FRTP composite during FW or AFP with ISC. Weiler et al. presented an analytical solution to the transient thermal analysis of AFP with laser ISC [62]. The authors showed that in the cooling stage of laser ISC (after the nip point), the heat transfer between the FRTP tape and the environment is negligible compared to the internal conduction within the tape. Therefore, the tape can be considered insulated in the cooling stage, thus simplifying the analysis. The authors found that for high speed processes with high laser intensity, the pool of molten polymer is small due to rapid cooling. The authors suggested that this can be improved by increasing the heating length. This can be achieved using laser systems with adjustable heating lengths, such as vertical-cavity surface-emitting lasers (VCSELs) and diode lasers with motorized zoom homogenizer.

Obtaining an analytical solution for the heat transfer analysis in ISC require some simplifications to the problem. On the other hand, numerical simulations enable various boundary conditions, heat flux distributions and temperature-dependent material properties to be considered, thus leading to more accurate predictions provided the simulations are set up properly. Kollmannsberger et al. discussed using numerical simulation to obtain the temperature profile at the nip point for AFP with laser ISC [71]. FDM was used to solve the heat equations. For accurate temperature predictions, the authors recommended using values obtained from experiments for the transverse thermal conductivity of the prepreg tape and the thermal contact resistance between the tapes.

Baho et al. studied the effect of the compaction force on the heat flux distribution at the nip point for laser ISC using a ray tracing algorithm [64]. Higher compaction force resulted in larger deformation in the compaction roller. This in turn causes the heated length to be shorter and the heating to be more focused, leading to higher temperature in the material. The increased temperature due to high compaction force need to be taken into consideration to prevent overheating and material degradation.

Cao et al. studied the heat transfer processes in AFP with ISC using hot gas torch for carbon/PEEK by conducting FE simulations and experiments for verification [67]. In particular, the effect of tool temperature on the consolidation of the first layer was investigated. The authors recommended setting the tool temperature to 150 °C, which is slightly above the T_g of PEEK, for placing the first layer. Liu et al. also presented a numerical study on the placement of the first layer in AFP with ISC using hot gas torch for carbon/PEEK [66]. The simulated AFP was performed on a convex tool with a radius of curvature of 600 mm. The authors suggested a line speed of 5 mm/s, hot gas temperature of 750 °C and tool temperature of 145 °C for the first layer. The suggested parameters were similar to those recommended by Cao et al. [67]. In addition, Liu et al. also recommended using a Teflon tape to protect the rubber compaction roller for the AFP process [66].

Schlottermuller et al. studied the thermal residual stresses in FRTP components fabricated using FW with ISC [104]. Both simulations and experiments were carried out in the study. The winding angle, the annealing process after winding, the number of layers and mandrel heating were identified as the main factors affecting thermal residual stresses. Dedieu et al. developed FE models to determine the residual stresses in carbon/PEEK rings fabricated using FW with ISC [105]. For the hoop wound rings, residual stresses due to heat were insignificant because the coefficient of thermal expansion (CTE) for carbon/PEEK is small in the fiber direction. The tape tension, the curvature of the tapes during winding and the compaction pressure were the main contributors to residual stresses.

Fricke and Fischer performed the simulations of flat CFRTP panels fabrication using AFP with laser ISC to study the crystallinity and thermal residual stresses [73]. The prepreg tape studied consisted of carbon fibers and low-melt polyaryletherketone (LM-PAEK) as matrix. The crystallization model developed by Gordnian was included in the material model [103]. Crystallization parameters for LM-PAEK were obtained from DSC experiments. Using the process simulation, the researchers found that the unidirectional CFRTP panels exhibited high thermal residual stresses at the interlaminar regions. This caused warpage in the panel, with a calculated maximum deformation of 42 mm.

For the optimization of FW and AFP processes with ISC, due to the large number of variables involved, many researchers used mathematical models and numerical methods such as FE simulations [35,41,66]. Dobrzanski et al. used the Taguchi method in optimizing the processing parameters for FW with ISC [111]. The material system studied was glass/PP commingled tapes. The authors reported optimal nip point temperatures of 230 °C and 210 °C for best tensile strength and best shear performance respectively. This suggests that optimization studies using different performance indicators can lead to different optimized parameters.

Few studies have been conducted on the fabrication of complex FRTP composite components using AFP with ISC. Clancy et al. studied the fabrication of variable angle tow (VAT) laminates using AFP with laser ISC [94,112]. The authors showed that the AFP

process can produce carbon/PEEK VAT laminates with no significant defects for a steering radius of 400 mm and above. However, further studies are required to better understand the effects of AFP processing parameters on the fabrication of FRTP VAT laminates.

Zenker and Gnaedinger studied the application of AFP with laser ISC in making FRTP preforms with variable fiber orientations [113]. Preforms with steered fiber configurations with steering radii in the range of 221 to 1290 mm were laid. Two nip point temperature settings, 220 and 290 °C, were investigated. Carbon/PA6 prepreg tapes with a width of 6.35 mm (or $\frac{1}{4}$ ") were used. The authors reported that the gaps in the preforms grew larger as steering radius decreased below 500 mm. For the lower nip point temperature of 220 °C, the placed tapes exhibited a pattern with local waviness connected by short straight sections. This is due to the lower bond strength in the tape, caused by the lower nip point temperature. For the nip point temperature of 290 °C, continuous waviness in the placed tapes was observed, indicating stronger bonding.

Tannous et al. studied the effects of FRTP prepreg tape surface friction on the FW process with ISC [114]. The FW process was simulated using FE modeling. The authors showed that friction forces between the prepreg tape, the compaction roller and the mandrel are important in keeping the placed tape in position. Insufficient friction can lead to poor bonding, especially in cases such as components with concave shapes and FW of helical layers.

Kollmannsberger studied the AFP process with laser ISC for the fabrication of 2D and 3D FRTP composite parts [115]. For 3D parts featuring corners with a small radius, using processing parameters optimized for 2D parts will lead to overheating and degradation of the thermoplastic. This is due to the short laser heating length on the substrate at the corner. Kollmannsberger investigated two control strategies for the laser to prevent overheating, namely predictive closed loop control (PCLC) and coordinate controlled process parameters (CCPP). In PCLC, the laser power is lowered when the start of overheating is detected (using an IR camera). In CCPP, the laser power and the laser angle are controlled based on the position of the AFP head. Both strategies were able to prevent overheating in the fabrication of 3D FRTP composite parts.

A summary of the optimized processing parameters used in past studies is shown in Table 1. Using the AFP and FW processing parameters, researchers were able to fabricate FRTP composite parts with properties better than or comparable to parts fabricated using conventional methods. Many researchers used FRTP prepreg tapes in their studies. For the ISC heat source, the use of high powered lasers enables the AFP and FW processes to be carried out at high line speeds.

It is noted that the optimization of the processing parameters is dependent on the machine set up and the material system used. Additionally, the optimized processing parameters can vary when optimized based on different performance indicators. Therefore, the parameters shown in Table 1 should be used only as guides in future studies.

Table 1. Summary of optimized processing parameters from past studies.

Year	Matrix	Material form	Process	Heat Source	Nip Point Temperature (°C)	Line Speed (mm/s)	Compaction Force/Pressure	Other Processing Parameters	Physical and Mechanical Properties Studied	Ref.
2017	PA6	Aramid/PA6 commingled yarns	FW	Hot gas torch	320	10	190 N	Preheating of yarns to 330 °C	Void content, SBS strength, flexural modulus	[36]
2019	PA6	Carbon/PA6 prepreg tapes	AFP	NIR diode laser	260	100	130 N		Wedge peel strength	[53]
2019	PA6	Carbon/PA6 prepreg tapes	FW	Laser	280 (hoop layer), 300 (axial layer)	105 (hoop layer), 50 (axial layer)	0.3 MPa		Void content, compression modulus, implosion strength (for composite tube)	[6]
1993	PA12	Glass/PA12 powder impregnated fibers	FW	Hot gas torch	360	25	157 N	IR preheating of fibers at power 9.6 kW, mandrel temperature 100 °C	Interlaminar shear, fracture toughness (from DCB tests)	[47]
2016	PP	E-glass/PP commingled yarns	FW	Ultrasonic welding	223	52.5	85 N (applied at sonotrode)	Compaction roller located 45 mm from the sonotrode	Void content, shear modulus	[35]
2017	PP	E-glass/PP prepreg tapes	AFP	Ultrasonic welding	260	1	0.15 MPa (applied at compaction roller)	Ultrasonic amplitude 3 µm, frequency 40 kHz	SBS strength, fracture toughness (from DCB tests), impact toughness	[56]
2011	PP	Glass/PP commingled fibers	FW	Hot gas torch	125	42	54 N	Preheating of fibers to 195 °C	Flexural modulus and strength, Charpy impact toughness	[116]
2013	PPS	Carbon/PPS prepreg tapes	AFP	Laser	480	125	450 N	Laser power 1700 W	Fracture toughness (using mandrel peel test)	[41]
1995	PEI	Carbon/PEI powder impregnated fibers	FW	IR spot heater	960	80	Nil	Fiber tension 5 N per 1000 filaments, mandrel temperature 150 °C	Void content	[49]
1996	PEEK	AS4 carbon/PEEK prepreg tapes	FW	CO ₂ laser	475	15	13.8 MPa	Laser power 50 W	SBS strength, fracture toughness (from DCB tests), wedge peel force	[42]
2015	PEEK	AS4 carbon/PEEK prepreg tapes	AFP	NIR diode laser	500	100	500 N	Laser power 920 W	SBS strength	[52]
2019	PEEK	Carbon/PEEK prepreg tapes	AFP	NIR diode laser	485	100	0.34 MPa (for 1st ply), 0.46 MPa (for plies 2-7)	Laser power up to 4 kW	Lap shear strength	[117]

9. Future Perspectives

Towards the quest for automating the manufacturing process for composite structural parts, both FW and AFP are providing significant benefits in terms of improved production time. However, it is also important to make the processes more flexible to accommodate various design choices. For both processes, there is a growing challenge to meet industrial requirements to accommodate more complex component shapes and material microstructures [118]. For the fabrication of components with complex shapes, the size of the heat source used for ISC needs to be small. Particular attention also needs to be given to the heat transfer and consolidation processes, especially when the component shape involves sharp corners and curves with low radii of curvature [113,115]. Further research on process modeling techniques, including machine learning based methods, can aid in the design and fabrication of composite components with complex shapes [16,119,120].

Besides this, the development of new textile architectures such as thin spread tow fabrics [121–123] and the usage of novel resin systems can be coupled to ease the challenges associated with producing high performance composite parts. The development of thin ply fabrics is interesting for many industrial applications due to their potential to significantly improve the in situ mechanical properties and make the composite parts lighter. They have been mostly used in conjunction with liquid injection processes [124–128]. Recently, thin ply thermoplastic prepreg tapes and thin ply dry tapes have been manufactured successfully and made available [129–132]. However, challenges remain in adapting the FW and AFP processes to use the tapes. Most importantly, the laying mechanisms, the filament wetting and solidification processes are major areas of research which require critical attention. For the processing of thin ply thermoplastic prepreg tapes, the effect of the reduced tape thickness on the heat transfer process during ISC needs to be considered. On the other hand, recently developed liquid resin systems such as the reactively processed thermoplastic Elium from Arkema can be used in conjunction with thin ply dry tapes. Elium is a thermoplastic acrylic based resin in liquid state which can be processed at room temperature [55,124,128,133,134]. It can be used in the FW process with ISC using ultraviolet rays [135]. The development and qualification of the FW process and potentially also the AFP process to effectively use this kind of reactively processed thermoplastic resin systems could be an intriguing research topic.

10. Concluding Remarks

The fabrication of FRTP composite components using AFP or FW with ISC is a complex process involving many interconnected factors. Implementing the AFP and FW processes requires careful considerations on the material system and its form, as well as the heat source for ISC. When prepreg tapes are used, the FRTP consolidation process only involves the bonding between the tapes. Hence, it is faster compared to consolidation processes using other semi-finished forms, which require an impregnation step. For the ISC heat source, high powered lasers, with their very high heating rates, enable the AFP and FW processes to be carried out at high line speeds. However, using prepreg tapes and high powered lasers also leads to higher costs. Therefore, there is a need to strike a balance between costs and productivity for the manufacturing process.

Researchers have developed various models to relate the processing parameters to the degree of consolidation and other aspects of FRTP composites. Using the models, along with experimental methods and numerical simulations, many researchers have fabricated good quality FRTP composite components using AFP and FW with ISC. For the quality assessment of the FRTP composite components, many researchers focused on the void content and the interlaminar bonding of the components. However, some researchers have reported components with low void content and good interlaminar bonding showing poor in-plane mechanical properties. Therefore, for a comprehensive assessment, other properties of the FRTP composite components need to be evaluated as well. The processing parameters used in past studies are optimized for specific machine set ups and material

systems. Using the reported processing parameters as guidance, the productivity of the AFP and FW processes can be further improved in future studies.

Currently, many studies have focused on composite parts with simple shapes, such as flat plates and tubes with constant radii. For the fabrication of complex parts, additional aspects, such as the heating length at sharp corners, need to be considered in the process controls. More studies on the fabrication of complex FRTP composite components are required to fully realize the potential of the AFP and FW processes. Further research is also needed to expand the application of the manufacturing processes to accommodate the use of innovative material systems, such as thin ply composites and liquid thermoplastic resins.

Author Contributions: Conceptualization, Y.D.B., S.C.J., and S.K.B.; investigation, Y.D.B.; writing—original draft preparation, Y.D.B.; writing—review and editing, S.C.J., and S.K.B.; supervision, S.C.J.; funding acquisition, Y.D.B., and S.C.J. All authors have read and agreed to the published version of the manuscript.

Funding: This research was partially funded by the Agency for Science, Technology and Research (A*STAR), Singapore under the Polymer Matrix Composites Programme, Grant no. A19C9a0044.

Institutional Review Board Statement: Not applicable.

Informed Consent Statement: Not applicable.

Data Availability Statement: The data presented in this study are available on request from the corresponding author.

Acknowledgments: The authors would like to acknowledge the resources and support provided by the School of Mechanical and Aerospace Engineering, Nanyang Technological University, Singapore.

Conflicts of Interest: The authors declare no conflict of interest.

References

1. Boon, Y.D.; Joshi, S.C.; Ong, L.S. Interfacial bonding between CFRP and mechanically-treated aluminum liner surfaces for risers. *Compos. Struct.* **2018**, *188*, 374–386. [CrossRef]
2. Ishikawa, T.; Amaoka, K.; Masubuchi, Y.; Yamamoto, T.; Yamanaka, A.; Arai, M.; Takahashi, J. Overview of automotive structural composites technology developments in Japan. *Compos. Sci. Technol.* **2018**, *155*, 221–246. [CrossRef]
3. Bhudolia, S.K.; Perrotey, P.; Joshi, S.C. Experimental investigation on suitability of carbon fibre thin plies for racquets. *Proc. Inst. Mech. Eng. Part P J. Sports Eng. Technol.* **2015**, *230*, 64–72. [CrossRef]
4. Arhant, M.; Davies, P. 2-Thermoplastic matrix composites for marine applications. In *Marine Composites*; Pemberton, R., Summerscales, J., Graham-Jones, J., Eds.; Woodhead Publishing: Cambridge, UK, 2019; pp. 31–53.
5. Mahieux, C.A. Cost effective manufacturing process of thermoplastic matrix composites for the traditional industry: The example of a carbon-fiber reinforced thermoplastic flywheel. *Compos. Struct.* **2001**, *52*, 517–521. [CrossRef]
6. Arhant, M.; Briançon, C.; Burtin, C.; Davies, P. Carbon/Polyamide 6 thermoplastic composite cylinders for deep sea applications. *Compos. Struct.* **2019**, *212*, 535–546. [CrossRef]
7. Khennane, A. 8-Filament winding processes in the manufacture of advanced fibre-reinforced polymer (FRP) composites. In *Advanced Fibre-Reinforced Polymer (FRP) Composites for Structural Applications*; Bai, J., Ed.; Woodhead Publishing: Cambridge, UK, 2013; pp. 187–206.
8. Beland, S. *High Performance Thermoplastic Resins and Their Composites*; Noyes Data Corporation: Park Ridge, NJ, USA, 1990.
9. Chang, I.Y.; Lees, J.K. Recent development in thermoplastic composites: A review of matrix systems and processing methods. *J. Thermoplast. Compos. Mater.* **1988**, *1*, 277–296. [CrossRef]
10. Fernández, I.; Blas, F.; Frövel, M. Autoclave forming of thermoplastic composite parts. *J. Mater. Process. Technol.* **2003**, *143–144*, 266–269. [CrossRef]
11. Sherwood, J.A.; Fettatsidis, K.A.; Gorczyca, J.L. 6-Fabric thermostamping in polymer matrix composites. In *Manufacturing Techniques for Polymer Matrix Composites (PMCs)*; Advani, S.G., Hsiao, K.-T., Eds.; Woodhead Publishing: Cambridge, UK, 2012; pp. 139–181.
12. Kozaczuk, K. Automated fiber placement systems overview. *Trans. Inst. Aviat.* **2016**, *4*, 52–59. [CrossRef]
13. Denkena, B.; Schmidt, C.; Weber, P. Automated fiber placement head for manufacturing of innovative aerospace stiffening structures. *Procedia Manuf.* **2016**, *6*, 96–104. [CrossRef]
14. Peeters, D.; Clancy, G.; Oliveri, V.; O’Higgins, R.; Jones, D.; Weaver, P.M. Concurrent design and manufacture of a thermoplastic composite stiffener. *Compos. Struct.* **2019**, *212*, 271–280. [CrossRef]
15. He, K.; Nie, H.; Yan, C. The intelligent composite panels manufacturing technology based on tape-laying automatic system. *Procedia CIRP* **2016**, *56*, 610–613. [CrossRef]

16. Sacco, C.; Baz Radwan, A.; Anderson, A.; Harik, R.; Gregory, E. Machine learning in composites manufacturing: A case study of automated fiber placement inspection. *Compos. Struct.* **2020**, *250*, 112514. [CrossRef]
17. Croft, K.; Lessard, L.; Pasini, D.; Hojjati, M.; Chen, J.; Yousefpour, A. Experimental study of the effect of automated fiber placement induced defects on performance of composite laminates. *Compos. Part A Appl. Sci. Manuf.* **2011**, *42*, 484–491. [CrossRef]
18. Nguyen, M.H.; Vijayachandran, A.A.; Davidson, P.; Call, D.; Lee, D.; Waas, A.M. Effect of automated fiber placement (AFP) manufacturing signature on mechanical performance of composite structures. *Compos. Struct.* **2019**, *228*, 111335. [CrossRef]
19. Zhang, P.; Sun, R.; Zhao, X.; Hu, L. Placement suitability criteria of composite tape for mould surface in automated tape placement. *Chin. J. Aeronaut.* **2015**, *28*, 1574–1581. [CrossRef]
20. Oromiehie, E.; Prusty, B.G.; Compston, P.; Rajan, G. Automated fibre placement based composite structures: Review on the defects, impacts and inspections techniques. *Compos. Struct.* **2019**, *224*, 110987. [CrossRef]
21. Dhinakaran, V.; Surendar, K.V.; Hasunfur Riyaz, M.S.; Ravichandran, M. Review on study of thermosetting and thermoplastic materials in the automated fiber placement process. *Mater. Today Proc.* **2020**, *27*, 812–815. [CrossRef]
22. Gonzalez Henriquez, R.; Mertiny, P. 3.21 Filament winding applications. In *Comprehensive Composite Materials II*; Beaumont, P.W.R., Zweben, C.H., Eds.; Elsevier: Oxford, UK, 2018; pp. 556–577.
23. Bhudolia, S.; Fischer, S.; He, P.; Yue, C.Y.; Joshi, S.C.; Yang, J. Design, manufacturing and testing of filament wound composite risers for marine and offshore applications. *Mater. Sci. Forum* **2015**, *813*, 337–343.
24. Sorrentino, L.; Anamateros, E.; Bellini, C.; Carrino, L.; Corcione, G.; Leone, A.; Paris, G. Robotic filament winding: An innovative technology to manufacture complex shape structural parts. *Compos. Struct.* **2019**, *220*, 699–707. [CrossRef]
25. Beck, B.; Tawfik, H.; Haas, J.; Park, Y.B.; Henning, F. Automated 3D skeleton winding process for continuous-fiber-reinforcements in structural thermoplastic components. In *Advances in Polymer Processing 2020, Proceedings of the International Symposium on Plastics Technology, Aachen, Germany, 10 March 2020*; Springer: Berlin/Heidelberg, Germany, 2020; pp. 150–161.
26. Wiegand, N.; Mäder, E. Commingled yarn spinning for thermoplastic/glass fiber composites. *Fibers* **2017**, *5*, 26. [CrossRef]
27. Boon, Y.D.; Joshi, S.C. A review of methods for improving interlaminar interfaces and fracture toughness of laminated composites. *Mater. Today Commun.* **2020**, *22*, 100830. [CrossRef]
28. Gabrion, X.; Placet, V.; Trivaudey, F.; Boubakar, L. About the thermomechanical behaviour of a carbon fibre reinforced high-temperature thermoplastic composite. *Compos. Part B Eng.* **2016**, *95*, 386–394. [CrossRef]
29. Mack, J.; Schledjewski, R. 7-Filament winding process in thermoplastics. In *Manufacturing Techniques for Polymer Matrix Composites (PMCs)*; Advani, S.G., Hsiao, K.-T., Eds.; Woodhead Publishing: Cambridge, UK, 2012; pp. 182–208.
30. Volk, M.; Wong, J.; Arreguin, S.; Bar, C.; Schmuck, F.; Ermanni, P. Thermoplastic composite materials for high voltage insulator applications. In *Proceedings of the ECCM18—18th European Conference on Composite Materials, Athens, Greece, 25–28 June 2018*.
31. Iannone, V.; Barile, M.; Lecce, L. Automated fabrication of hybrid thermoplastic prepreg material to be processed by in-situ consolidation automated fiber placement process. *MATEC Web Conf.* **2018**, *188*, 01024. [CrossRef]
32. Friedrich, K. Commingled yarns and their use for composites. In *Polypropylene: An A–Z Reference*; Karger-Kocsis, J., Ed.; Springer: Dordrecht, The Netherlands, 1999; pp. 81–89.
33. Bernet, N.; Michaud, V.; Bourban, P.E.; Manson, J.A.E. Commingled yarn composites for rapid processing of complex shapes. *Compos. Part A Appl. Sci. Manuf.* **2001**, *32*, 1613–1626. [CrossRef]
34. Thomann, U.I.; Ermanni, P. The influence of yarn structure and processing conditions on the laminate quality of stampformed carbon and thermoplastic polymer fiber commingled yarns. *J. Thermoplast. Compos. Mater.* **2004**, *17*, 259–283. [CrossRef]
35. Lionetto, F.; Dell’Anna, R.; Montagna, F.; Maffezzoli, A. Modeling of continuous ultrasonic impregnation and consolidation of thermoplastic matrix composites. *Compos. Part A Appl. Sci. Manuf.* **2016**, *82*, 119–129. [CrossRef]
36. Wong, J.C.H.; Blanco, J.M.; Ermanni, P. Filament winding of aramid/PA6 commingled yarns with in situ consolidation. *J. Thermoplast. Compos. Mater.* **2017**, *31*, 465–482. [CrossRef]
37. Vodermayr, A.M.; Kaerger, J.C.; Hinrichsen, G. Manufacture of high performance fibre-reinforced thermoplastics by aqueous powder impregnation. *Compos. Manuf.* **1993**, *4*, 123–132. [CrossRef]
38. Goud, V.; Alagirusamy, R.; Das, A.; Kalyanasundaram, D. Dry electrostatic spray coated towpregs for thermoplastic composites. *Fibers Polym.* **2018**, *19*, 364–374. [CrossRef]
39. Henninger, F.; Friedrich, K. Thermoplastic filament winding with online-impregnation. Part A: Process technology and operating efficiency. *Compos. Part A Appl. Sci. Manuf.* **2002**, *33*, 1479–1486. [CrossRef]
40. Henninger, F.; Hoffmann, J.; Friedrich, K. Thermoplastic filament winding with online-impregnation. Part B. Experimental study of processing parameters. *Compos. Part A Appl. Sci. Manuf.* **2002**, *33*, 1684–1695. [CrossRef]
41. Groupe, W.J.B.; Warnet, L.L.; Rietman, B.; Visser, H.A.; Akkerman, R. Optimization of the tape placement process parameters for carbon-PPS composites. *Compos. Part A Appl. Sci. Manuf.* **2013**, *50*, 44–53. [CrossRef]
42. Agarwal, V.; McCullough, R.L.; Schultz, J.M. The thermoplastic laser-assisted consolidation process-mechanical and microstructure characterization. *J. Thermoplast. Compos. Mater.* **1996**, *9*, 365–380. [CrossRef]
43. Funck, R.; Neitzel, M. Improved thermoplastic tape winding using laser or direct-flame heating. *Compos. Manuf.* **1995**, *6*, 189–192. [CrossRef]
44. Yassin, K.; Hojjati, M. Processing of thermoplastic matrix composites through automated fiber placement and tape laying methods: A review. *J. Thermoplast. Compos. Mater.* **2018**, *31*, 1676–1725. [CrossRef]

45. Tafreshi, O.A.; Hoa, S.V.; Shadmehri, F.; Hoang, D.M.; Rosca, D. Determination of convective heat transfer coefficient for automated fiber placement (AFP) for thermoplastic composites using hot gas torch. *Adv. Manuf. Polym. Compos. Sci.* **2020**, *6*, 86–100. [CrossRef]
46. Rizzolo, R.H.; Walczyk, D.F. Ultrasonic consolidation of thermoplastic composite prepreg for automated fiber placement. *J. Thermoplast. Compos. Mater.* **2015**, *29*, 1480–1497. [CrossRef]
47. Lauke, B.; Friedrich, K. Evaluation of processing parameters of thermoplastic composites fabricated by filament winding. *Compos. Manuf.* **1993**, *4*, 93–101. [CrossRef]
48. Hoa, S.V.; Hoang, M.D.; Simpson, J. Manufacturing procedure to make flat thermoplastic composite laminates by automated fibre placement and their mechanical properties. *J. Thermoplast. Compos. Mater.* **2017**, *30*, 1693–1712. [CrossRef]
49. Romagna, J.; Ziegmann, G.; Flemming, M. Thermoplastic filament winding—An experimental investigation of the on-line consolidation of poly(ether imide) fit preforms. *Compos. Manuf.* **1995**, *6*, 205–210. [CrossRef]
50. Deden, D.; Bruckner, F.; Brandt, L.; Fischer, F. Comparison of heat sources for automated dry fibre placement: Xenon flashlamp vs. infrared heating. In Proceedings of the 22nd International Conference on Composites Materials ICCM22, Melbourne, Australia, 11–16 August 2019.
51. Comer, A.J.; Ray, D.; Obande, W.O.; Jones, D.; Lyons, J.; Rosca, I.; O’ Higgins, R.M.; McCarthy, M.A. Mechanical characterisation of carbon fibre—PEEK manufactured by laser-assisted automated-tape-placement and autoclave. *Compos. Part A Appl. Sci. Manuf.* **2015**, *69*, 10–20. [CrossRef]
52. Stokes-Griffin, C.M.; Compston, P. The effect of processing temperature and placement rate on the short beam strength of carbon fibre—PEEK manufactured using a laser tape placement process. *Compos. Part A Appl. Sci. Manuf.* **2015**, *78*, 274–283. [CrossRef]
53. Stokes-Griffin, C.M.; Kollmannsberger, A.; Compston, P.; Drechsler, K. The effect of processing temperature on wedge peel strength of CF/PA6 laminates manufactured in a laser tape placement process. *Compos. Part A Appl. Sci. Manuf.* **2019**, *121*, 84–91. [CrossRef]
54. Stokes-Griffin, C.M.; Compston, P. A combined optical-thermal model for near-infrared laser heating of thermoplastic composites in an automated tape placement process. *Compos. Part A Appl. Sci. Manuf.* **2015**, *75*, 104–115. [CrossRef]
55. Bhudolia, S.K.; Gohel, G.; Leong, K.F.; Islam, A. Advances in ultrasonic welding of thermoplastic composites: A review. *Materials* **2020**, *13*, 1284. [CrossRef] [PubMed]
56. Chu, Q.; Li, Y.; Xiao, J.; Huan, D.; Zhang, X.; Chen, X. Processing and characterization of the thermoplastic composites manufactured by ultrasonic vibration-assisted automated fiber placement. *J. Thermoplast. Compos. Mater.* **2017**, *31*, 339–358. [CrossRef]
57. Dell’Anna, R.; Lionetto, F.; Montagna, F.; Maffezzoli, A. Lay-Up and consolidation of a composite pipe by in situ ultrasonic welding of a thermoplastic matrix composite tape. *Materials* **2018**, *11*, 786. [CrossRef] [PubMed]
58. Heraeus Noblelight. humm3®—Intelligent Heat for Automated Fibre Placement (AFP). Available online: https://www.heraeus.com/en/hng/products_and_solutions/arc_and_flash_lamps/humm3/humm3.html (accessed on 29 April 2020).
59. Nguyen, C.; Kolbe, A.; Bans, C. Application of lightning strike protection on thermoplastic structures by automated fiber placement. In Proceedings of the 5th International Conference and Exhibition on Thermoplastic Composites ITHEC, Bremen, Germany, 13–14 October 2020.
60. Whitaker, S. *Fundamental Principles of Heat Transfer*; Pergamon Press Inc.: Elmsford, NY, USA, 1977.
61. Sonmez, F.O.; Hahn, H.T. Modeling of heat transfer and crystallization in thermoplastic composite tape placement process. *J. Thermoplast. Compos. Mater.* **1997**, *10*, 198–240. [CrossRef]
62. Weiler, T.; Emonts, M.; Wollenburg, L.; Janssen, H. Transient thermal analysis of laser-assisted thermoplastic tape placement at high process speeds by use of analytical solutions. *J. Thermoplast. Compos. Mater.* **2017**, *31*, 311–338. [CrossRef]
63. Stokes-Griffin, C.M.; Compston, P.; Matuszyk, T.I.; Cardew-Hall, M.J. Thermal modelling of the laser-assisted thermoplastic tape placement process. *J. Thermoplast. Compos. Mater.* **2013**, *28*, 1445–1462. [CrossRef]
64. Baho, O.; Ausias, G.; Grohens, Y.; Férec, J. Simulation of laser heating distribution for a thermoplastic composite: Effects of AFP head parameters. *Int. J. Adv. Manuf. Technol.* **2020**, *110*, 2105–2117. [CrossRef]
65. Venkateshan, S.P. *Heat Transfer*, 3rd ed.; ANE Books Pvt. Ltd.: New Delhi, India; Springer: Cham, Switzerland, 2021.
66. Liu, X.L.; Han, Z.Y.; Zhao, Z.Y.; Sun, S.Z. Thermal analysis of cylindrical molds using thermoplastic composite during robotic fiber placement. *J. Phys. Conf. Ser.* **2021**, *1765*, 012023. [CrossRef]
67. Cao, Z.; Dong, M.; Liu, K.; Fu, H. Temperature field in the heat transfer process of PEEK thermoplastic composite fiber placement. *Materials* **2020**, *13*, 4417. [CrossRef]
68. Tafreshi, O.A.; Hoa, S.V.; Shadmehri, F.; Hoang, D.M.; Rosca, D. Heat transfer analysis of automated fiber placement of thermoplastic composites using a hot gas torch. *Adv. Manuf. Polym. Compos. Sci.* **2019**, *5*, 206–223. [CrossRef]
69. Zacherl, L.; Shadmehri, F.; Rother, K. Determination of convective heat transfer coefficient for hot gas torch (HGT)-assisted automated fiber placement (AFP) for thermoplastic composites. *J. Thermoplast. Compos. Mater.* **2021**. [CrossRef]
70. Agarwal, V.; Guçeri, S.I.; McCullough, R.L.; Schultz, J.M. Thermal characterization of the laser-assisted consolidation process. *J. Thermoplast. Compos. Mater.* **1992**, *5*, 115–135. [CrossRef]
71. Kollmannsberger, A.; Lichtinger, R.; Hohenester, F.; Ebel, C.; Drechsler, K. Numerical analysis of the temperature profile during the laser-assisted automated fiber placement of CFRP tapes with thermoplastic matrix. *J. Thermoplast. Compos. Mater.* **2017**, *31*, 1563–1586. [CrossRef]



72. Song, X. Modeling of Thermoplastic Composite Filament Winding. Master's Thesis, Virginia Polytechnic Institute and State University, Blacksburg, VA, USA, 2000.
73. Fricke, D.; Fischer, F. Process simulation of the in-situ automated fiber placement process for thermoplastic composites. In Proceedings of the SAMPE Europe Conference, Amsterdam, The Netherlands, 30 September–1 October 2020.
74. Dara, P.H.; Loos, A.C. *Thermoplastic Matrix Composite Processing Model*; Center for Composite Materials and Structures, Virginia Polytechnic Institute and State University: Blacksburg, VA, USA, 1985.
75. Loos, A.C.; Dara, P.H. Processing of thermoplastic matrix composites. In *Review of Progress in Quantitative Nondestructive Evaluation*; Springer: Boston, MA, USA, 1987; pp. 1257–1265.
76. Lee, W.I.; Springer, G.S. A model of the manufacturing process of thermoplastic matrix composites. *J. Compos. Mater.* **1987**, *21*, 1017–1055. [CrossRef]
77. Mantell, S.C.; Springer, G.S. Manufacturing process models for thermoplastic composites. *J. Compos. Mater.* **1992**, *26*, 2348–2377. [CrossRef]
78. Yang, F.; Pitchumani, R. A fractal Cantor set based description of interlaminar contact evolution during thermoplastic composites processing. *J. Mater. Sci.* **2001**, *36*, 4661–4671. [CrossRef]
79. Stokes-Griffin, C.M.; Compston, P. Investigation of sub-melt temperature bonding of carbon-fibre/PEEK in an automated laser tape placement process. *Compos. Part A Appl. Sci. Manuf.* **2016**, *84*, 17–25. [CrossRef]
80. Yang, F.; Pitchumani, R. Healing of thermoplastic polymers at an interface under nonisothermal conditions. *Macromolecules* **2002**, *35*, 3213–3224. [CrossRef]
81. Boiko, Y.M.; Guérin, G.; Marikhin, V.A.; Prud'homme, R.E. Healing of interfaces of amorphous and semi-crystalline poly(ethylene terephthalate) in the vicinity of the glass transition temperature. *Polymer* **2001**, *42*, 8695–8702. [CrossRef]
82. De Gennes, P.G. Reptation of a polymer chain in the presence of fixed obstacles. *J. Chem. Phys.* **1971**, *55*, 572–579. [CrossRef]
83. Kim, Y.H.; Wool, R.P. A theory of healing at a polymer-polymer interface. *Macromolecules* **1983**, *16*, 1115–1120. [CrossRef]
84. Wool, R.P.; Yuan, B.-L.; McGarel, O.J. Welding of polymer interfaces. *Polym. Eng. Sci.* **1989**, *29*, 1340–1367. [CrossRef]
85. Yang, F.; Pitchumani, R. Nonisothermal healing and interlaminar bond strength evolution during thermoplastic matrix composites processing. *Polym. Compos.* **2003**, *24*, 263–278. [CrossRef]
86. Bernet, N.; Michaud, V.; Bourban, P.E.; Manson, J.A.E. An impregnation model for the consolidation of thermoplastic composites made from commingled yarns. *J. Compos. Mater.* **1999**, *33*, 751–772. [CrossRef]
87. Klinkmüller, V.; Um, M.K.; Steffens, M.; Friedrich, K.; Kim, B.S. A new model for impregnation mechanisms in different GF/PP commingled yarns. *Appl. Compos. Mater.* **1994**, *1*, 351–371. [CrossRef]
88. Gutowski, T.G.; Cai, Z.; Bauer, S.; Boucher, D.; Kingery, J.; Wineman, S. Consolidation experiments for laminate composites. *J. Compos. Mater.* **1987**, *21*, 650–669. [CrossRef]
89. Ye, L.; Friedrich, K.; Kästel, J. Consolidation of GF/PP commingled yarn composites. *Appl. Compos. Mater.* **1994**, *1*, 415–429. [CrossRef]
90. Gebart, B.R. Permeability of unidirectional reinforcements for RTM. *J. Compos. Mater.* **1992**, *26*, 1100–1133. [CrossRef]
91. Ye, L.; Klinkmüller, V.; Friedrich, K. Impregnation and consolidation in composites made of GF/PP powder impregnated bundles. *J. Thermoplast. Compos. Mater.* **1992**, *5*, 32–48. [CrossRef]
92. Steggall-Murphy, C.; Simacek, P.; Advani, S.G.; Yarlagadda, S.; Walsh, S. A model for thermoplastic melt impregnation of fiber bundles during consolidation of powder-impregnated continuous fiber composites. *Compos. Part A Appl. Sci. Manuf.* **2010**, *41*, 93–100. [CrossRef]
93. Connor, M.; Toll, S.; Manson, J.A.E.; Gibson, A.G. A Model for the consolidation of aligned thermoplastic powder impregnated composites. *J. Thermoplast. Compos. Mater.* **1995**, *8*, 138–162. [CrossRef]
94. Chanteli, A.; Bandaru, A.K.; Peeters, D.; O'Higgins, R.M.; Weaver, P.M. Influence of repass treatment on carbon fibre-reinforced PEEK composites manufactured using laser-assisted automatic tape placement. *Compos. Struct.* **2020**, *248*, 112539. [CrossRef]
95. Shadmehri, F.; Hoa, S.V.; Fortin-Simpson, J.; Ghayoor, H. Effect of in situ treatment on the quality of flat thermoplastic composite plates made by automated fiber placement (AFP). *Adv. Manuf. Polym. Compos. Sci.* **2018**, *4*, 41–47. [CrossRef]
96. Ozawa, T. Kinetics of non-isothermal crystallization. *Polymer* **1971**, *12*, 150–158. [CrossRef]
97. Joshi, S.C.; Lam, Y.C. Integrated approach for modelling cure and crystallization kinetics of different polymers in 3D pultrusion simulation. *J. Mater. Process. Technol.* **2006**, *174*, 178–182. [CrossRef]
98. Choe, C.R.; Lee, K.H. Nonisothermal crystallization kinetics of poly(etheretherketone) (PEEK). *Polym. Eng. Sci.* **1989**, *29*, 801–805. [CrossRef]
99. Tobin, M.C. Theory of phase transition kinetics with growth site impingement. I. Homogeneous nucleation. *J. Polym. Sci. Polym. Phys. Ed.* **1974**, *12*, 399–406. [CrossRef]
100. Tobin, M.C. The theory of phase transition kinetics with growth site impingement. II. Heterogeneous nucleation. *J. Polym. Sci. Polym. Phys. Ed.* **1976**, *14*, 2253–2257. [CrossRef]
101. Tobin, M.C. Theory of phase transition kinetics with growth site impingement. III. Mixed heterogeneous-homogeneous nucleation and nonintegral exponents of the time. *J. Polym. Sci. Polym. Phys. Ed.* **1977**, *15*, 2269–2270. [CrossRef]
102. Maffezzoli, A.M.; Kenny, J.M.; Nicolais, L. Welding of PEEK/carbon fiber composite laminates. *SAMPE J.* **1989**, *25*, 35–39.
103. Gordnian, K. Crystallization and Thermo-Viscoelastic Modelling of Polymer Composites. Ph.D. Thesis, The University of British Columbia, Vancouver, BC, Canada, 2017.

104. Schlottermuller, M.; Lu, H.; Roth, Y.; Himmel, N.; Schledjewski, R.; Mitschang, P. Thermal residual stress simulation in thermoplastic filament winding process. *J. Thermoplast. Compos. Mater.* **2003**, *16*, 497–519. [CrossRef]
105. Dedieu, C.; Barasinski, A.; Chinesta, F.; Dupillier, J.-M. About the origins of residual stresses in in situ consolidated thermoplastic composite rings. *Int. J. Mater. Form.* **2017**, *10*, 779–792. [CrossRef]
106. Nam, J.-D.; Seferis, J.C. Generalized composite degradation kinetics for polymeric systems under isothermal and nonisothermal conditions. *J. Polym. Sci. Part B Polym. Phys.* **1992**, *30*, 455–463. [CrossRef]
107. Sonmez, F.O.; Hahn, H.T. Analysis of the on-line consolidation process in thermoplastic composite tape placement. *J. Thermoplast. Compos. Mater.* **1997**, *10*, 543–572. [CrossRef]
108. Doan, H.G.M.; Mertiny, P. Creep testing of thermoplastic fiber-reinforced polymer composite tubular coupons. *Materials* **2020**, *13*, 4637. [CrossRef] [PubMed]
109. Samak, S.; Risteska, S.; Dukovski, V.; Trajkoski, S. Some experimental investigation of products from thermoplastic composite materials manufactured with robot and LAFP. *Int. J. Eng. Res. Technol.* **2020**, *9*, 1082–1088.
110. Zhao, P.; Shirinzadeh, B.; Shi, Y.; Cheuk, S.; Clark, L. Multi-Pass layup process for thermoplastic composites using robotic fiber placement. *Robot. Comput. Integr. Manuf.* **2018**, *49*, 277–284. [CrossRef]
111. Dobrzanski, L.A.; Domagala, J.; Silva, J.F. Application of Taguchi method in the optimisation of filament winding of thermoplastic composites. *Arch. Mater. Sci. Eng.* **2007**, *28*, 133–140.
112. Clancy, G.; Peeters, D.; Oliveri, V.; Jones, D.; O'Higgins, R.M.; Weaver, P.M. A study of the influence of processing parameters on steering of carbon Fibre/PEEK tapes using laser-assisted tape placement. *Compos. Part B Eng.* **2019**, *163*, 243–251. [CrossRef]
113. Zenker, T.; Gnaedinger, M. Consolidation behavior of fiber steered thermoplastic automated fiber placement preforms. In Proceedings of the 5th International Conference and Exhibition on Thermoplastic Composites ITHC, Bremen, Germany, 13–14 October 2020.
114. Tannous, M.; Barasinski, A.; Binetruy, C.; Courtemanche, B. Contribution of thermo-mechanical parameters and friction to the bonding of thermoplastic tapes in the tape winding process. *J. Mater. Process. Technol.* **2016**, *229*, 587–595. [CrossRef]
115. Kollmannsberger, A. Heating Characteristics of Fixed Focus Laser Assisted Thermoplastic-Automated Fiber Placement of 2D and 3D Parts. Ph.D. Thesis, Technische Universitat Munchen, Munich, Germany, 2019.
116. Gennaro, R.; Montagna, F.; Maffezzoli, A.; Fracasso, F.; Fracasso, S. On-Line consolidation of commingled polypropylene/glass roving during filament winding. *J. Thermoplast. Compos. Mater.* **2011**, *24*, 789–804. [CrossRef]
117. Engelhardt, R.; Ehard, S.; Wolf, T.; Oelhafen, J.; Kollmannsberger, A.; Drechsler, K. In situ joining of unidirectional tapes on long fiber reinforced thermoplastic structures by thermoplastic automated fiber placement for scientific sounding rocket applications. *Procedia CIRP* **2019**, *85*, 189–194. [CrossRef]
118. Frketic, J.; Dickens, T.; Ramakrishnan, S. Automated manufacturing and processing of fiber-reinforced polymer (FRP) composites: An additive review of contemporary and modern techniques for advanced materials manufacturing. *Addit. Manuf.* **2017**, *14*, 69–86. [CrossRef]
119. Boon, Y.D.; Joshi, S.C.; Bhudolia, S.K.; Gohel, G. Recent advances on the design automation for performance-optimized fiber reinforced polymer composite components. *J. Compos. Sci.* **2020**, *4*, 61. [CrossRef]
120. Sun, S.; Han, Z.; Zhang, J.; Jin, H.; Wang, Y. Multiscale collaborative process optimization method for automated fiber placement. *Compos. Struct.* **2021**, *259*, 113215. [CrossRef]
121. Bhudolia, S.K.; Kam, K.K.C.; Perrotey, P.; Joshi, S.C. Effect of fixation stitches on out-of-plane response of textile non-crimp fabric composites. *J. Ind. Text.* **2018**, *48*, 1151–1166. [CrossRef]
122. Bhudolia, S.K.; Joshi, S.C.; Bert, A.; Gohel, G.R.; Raama, M. Energy characteristics and failure mechanisms for textile spread tow thin ply thermoplastic composites under low-velocity impact. *Fibers Polym.* **2019**, *20*, 1716–1725. [CrossRef]
123. Cugnoni, J.; Amacher, R.; Kohler, S.; Brunner, J.; Kramer, E.; Dransfeld, C.; Smith, W.; Scobbie, K.; Sorensen, L.; Botsis, J. Towards aerospace grade thin-ply composites: Effect of ply thickness, fibre, matrix and interlayer toughening on strength and damage tolerance. *Compos. Sci. Technol.* **2018**, *168*, 467–477. [CrossRef]
124. Bhudolia, S.K.; Gohel, G.; Leong, K.F.; Joshi, S.C. Damping, impact and flexural performance of novel carbon/Elium® thermoplastic tubular composites. *Compos. Part B Eng.* **2020**, *203*, 108480. [CrossRef]
125. Bhudolia, S.; Joshi, S.; Bert, A.; Boon, Y.D.; Makam, R.; Gohel, G. Flexural characteristics of novel carbon methylmethacrylate composites. *Compos. Commun.* **2019**, *13*. [CrossRef]
126. Bhudolia, S.K.; Joshi, S.C. Low-Velocity impact response of carbon fibre composites with novel liquid Methylmethacrylate thermoplastic matrix. *Compos. Struct.* **2018**, *203*, 696–708. [CrossRef]
127. Bhudolia, S.K.; Perrotey, P.; Joshi, S.C. Mode I fracture toughness and fractographic investigation of carbon fibre composites with liquid Methylmethacrylate thermoplastic matrix. *Compos. Part B Eng.* **2018**, *134*, 246–253. [CrossRef]
128. Bhudolia, S.K.; Gohel, G.; Joshi, S.C.; Leong, K.F. Quasi-Static indentation response of core-shell particle reinforced novel NCCF/Elium® composites at different feed rates. *Compos. Commun.* **2020**, *21*, 100383. [CrossRef]
129. Ricard, T. Automated preform manufacture at an affordable price. *Reinf. Plast.* **2017**, *61*, 149–152. [CrossRef]
130. Casanovas, J.; Costa, J.; Mayugo, J.A.; Llongueras, A. Fabrication of hybrid thin ply tapes. *IOP Conf. Ser. Mater. Sci. Eng.* **2018**, *406*, 012067. [CrossRef]
131. Galos, J. Thin-Ply composite laminates: A review. *Compos. Struct.* **2020**, *236*, 111920. [CrossRef]

132. Yamashita, S.; Hirano, Y.; Sonehara, T.; Takahashi, J.; Kawabe, K.; Murakami, T. Residual mechanical properties of carbon fibre reinforced thermoplastics with thin-ply prepreg after simulated lightning strike. *Compos. Part A Appl. Sci. Manuf.* **2017**, *101*, 185–194. [CrossRef]
133. Kazemi, M.E.; Shanmugam, L.; Li, Z.; Ma, R.; Yang, L.; Yang, J. Low-Velocity impact behaviors of a fully thermoplastic composite laminate fabricated with an innovative acrylic resin. *Compos. Struct.* **2020**, *250*, 112604. [CrossRef]
134. Bhudolia, S.K.; Gohel, G.; Kah Fai, L.; Barsotti, R.J. Fatigue response of ultrasonically welded carbon/Elium®thermoplastic composites. *Mater. Lett.* **2020**, *264*, 127362. [CrossRef]
135. Arkema. Elium Resin: A Disruptive Innovation in the World of Composites? Available online: <https://www.arkema.com/global/en/webzine/post/elium-resin-a-disruptive-innovation-in-the-world-of-composites/> (accessed on 6 June 2021).

Technical Note

Innovation in Aircraft Cabin Interior Panels. Part II: Technical Assessment on Replacing Glass Fiber with Thermoplastic Polymers and Panels Fabricated Using Vacuum Forming Process

Edgar Adrián Franco-Urquiza ^{1,*}, Perla Itzel Alcántara Llanas ², Victoria Rentería-Rodríguez ², Raúl Samir Saleme ², Rodrigo Ramírez Aguilar ², Cecilia Zarate Pérez ², Mauricio Torres-Arellano ² and Saúl Piedra ¹

¹ National Council for Science and Technology, Center for Engineering and Industrial Development (CONACYT-CIDESI), Carretera Estatal 200, km 23, Querétaro 76265, Mexico; saul.piedra@cidesi.edu.mx

² Center for Engineering and Industrial Development (CIDESI), Carretera Estatal 200, km 23, Querétaro 76265, Mexico; perla.alcantara@cidesi.edu.mx (P.I.A.L.); ana.renteria@cidesi.edu.mx (V.R.-R.); raul.saleme@cidesi.edu.mx (R.S.S.); rodrigo.ramirez@cidesi.edu.mx (R.R.A.); cecilia.zarate@cidesi.edu.mx (C.Z.P.); mauricio.torres@cidesi.edu.mx (M.T.-A.)

* Correspondence: edgar.franco@cidesi.edu.mx

Citation: Franco-Urquiza, E.A.; Alcántara Llanas, P.I.; Rentería-Rodríguez, V.; Saleme, R.S.; Ramírez Aguilar, R.; Zarate Pérez, C.; Torres-Arellano, M.; Piedra, S. Innovation in Aircraft Cabin Interior Panels. Part II: Technical Assessment on Replacing Glass Fiber with Thermoplastic Polymers and Panels Fabricated Using Vacuum Forming Process. *Polymers* **2021**, *13*, 3258. <https://doi.org/10.3390/polym13193258>

Academic Editors: Somen K. Bhudolia and Sunil Chandrakant Joshi

Received: 15 August 2021

Accepted: 9 September 2021

Published: 24 September 2021

Publisher's Note: MDPI stays neutral with regard to jurisdictional claims in published maps and institutional affiliations.



Copyright: © 2021 by the authors. Licensee MDPI, Basel, Switzerland. This article is an open access article distributed under the terms and conditions of the Creative Commons Attribution (CC BY) license (<https://creativecommons.org/licenses/by/4.0/>).

Abstract: The manufacturing process of the aircraft cabin interior panels is expensive and time-consuming, and the resulting panel requires rework due to damages that occurred during their fabrication. The aircraft interior panels must meet structural requirements; hence sandwich composites of a honeycomb core covered with two layers of pre-impregnated fiberglass skin are used. Flat sandwich composites are transformed into panels with complex shapes or geometries using the compression molding process, leading to advanced manufacturing challenges. Some aircraft interior panels are required for non-structural applications; hence sandwich composites can be substituted by cheaper alternative materials and transformed using disruptive manufacturing techniques. This paper evaluates the feasibility of replacing the honeycomb and fiberglass skin layers core with rigid polyurethane foams and thermoplastic polymers. The results show that the structural composites have higher mechanical performances than the proposed sandwich composites, but they are compatible with non-structural applications. Sandwich composite fabrication using the vacuum forming process is feasible for developing non-structural panels. This manufacturing technique is fast, easy, economical, and ecological as it uses recyclable materials. The vacuum forming also covers the entire panel, thus eliminating tapestries, paints, or finishes to the aircraft interior panels. The conclusion of the article describes the focus of future research.

Keywords: aircraft cabin interior panels; vacuum forming; non-structural composite panels; thermoplastic face sheets

1. Introduction

The interiors of aircraft cabins play an essential role in improving the comfort of passengers on board [1–3]. Based on the type of interior, the aircraft cabin interior market has been segmented into aircraft seating, inflight entertainment and connectivity, cabin lighting, galley equipment, aircraft lavatories, aircraft windows and windshields, overhead compartments, and aircraft interior panels [4,5]. The current cabin interior industry is moving to modernize cabin interiors satisfying three main criteria: commercial viability, certification, and passenger experience. Some of the most notable moves are the development of lightweight and custom cabin solutions to enhance the overall passenger experience; an expansion of the overhead storage compartments to accommodate more luggage per passenger; and the design of a maximum cabin space that allows comfort and the feeling of space, while optimizing the space to add more seats. In this sense, composite materials

represent an indispensable focus area for the aircraft cabin design without sacrificing performance, safety, and cost.

Aircraft seats are the most demanded product in the aircraft cabin interior market, while galley equipment is the most expensive. The interior panels of aircraft cabins are a combination of different products, and each product has its function. The aircraft interior panels are floor panels, roof panels, side panels, and cabin dividers [1,6–8]. The requirements of the aircraft cabin interior panels present a good balance between strength, low density, high stiffness, and durability [9–13]. In addition, most panels require contoured forms, which lead to several defects induced during the manufacturing process. Aircraft cabin interior panels are manufactured using typical sandwich composites configuration made with aramid honeycomb core bonded to outer layers or face sheets, commonly glass fiber epoxy prepreg. Lightweight, low-density core between thin sheets dramatically increases panel rigidity with little added weight. Complex panels are fabricated using both single-opening and multi-opening presses. For molds with complex geometries, the one-step compression molding leads to distinct types of induced failures, such as breaks, holes, and the absence of impregnated zones or areas with excessive resin accumulation in the contours of the mold [14]. The previous occurs when the sandwich composite is placed in a large press and crushed to a predetermined shape and thickness [15]. Then, the crushed honeycomb acts as multiple blades that break the glass fiber prepreg during the transformation process. Several research articles deal with the evaluation of sandwich composite fabrication [13,15–18]. However, the replacement of fiberglass layers with thermoplastic polymers and the substitution of honeycomb for structural foams oriented to the aircraft cabin interior panels are not profoundly studied, and this is the gap this work pretends to fill.

A previous work entitled “Innovation in aircraft cabin interior panels part I: Technical assessment on replacing the honeycomb with structural foams and evaluation of optimal curing of prepreg fiberglass” [19] was focused on the evaluation of the primary components for structural sandwich panels such as aramid paper honeycomb, vinyl foam, and glass fiber prepreg skin. In addition, the paper evaluates the optimal curing processing parameters through the Differential Scanning Calorimetry (DSC) technique by varying the processing manufacturing conditions.

This work evaluates the feasibility of using thermoplastic polymers to replace the fiberglass faces in the foam core to produce alternative aircraft interior panels.

2. Materials

The sandwich panel used as reference consists of honeycomb core faced with two skin plies of fiberglass fabric epoxy prepreg DA 4080 purchased to Adhesive Prepregs for Composite Manufacturers (APCM, Plainfield, CT, USA). DA 4080 is a one-sided pre-impregnated E-glass made up of a 200 gsm layer of bidirectional fabric and 3702 filaments/yarn. DA 4080 is a 200 °F low-temperature cure recommended for laminating and honeycomb sandwich construction. In this work, the glass fiber was labeled as GF.

The core used was the PN1 honeycomb, manufactured by DuPont Nomex[®] (Wilmington, DE, USA) and purchased to Plascore. The PN1 is a sheet with regular hexagonal cell configuration, approximately 0.5-inch/13 mm thick, and a 0.12-inch/3 mm cell size.

In this work, the PN1 honeycomb (HC) is replaced by the 3 lb. density lightweight DIAB 1022 Vynil foam Divinycell[®] (Helsingborg, Sweden) supplied by Fibreglast. According to the supplier, the DIAB 1022 (Foam) offers the highest strength to density ratio, insulative properties, improved stiffness, and impact resistance. The 0.5 (12.7 mm) thick foam is best when only additional impact resistance is required. This foam can be easily thermoformed with a heat gun or oven. Other properties of this foam are excellent adhesion/peel strength, chemical resistance, good dimensional stability, and temperature performance. The operating temperature can reach from –200 °C to 70 °C, although the processing temperature depends on time and pressure conditions.

The Acrylonitrile–Butadiene–Styrene (ABS) is a plastic used in engineering due to its excellent combination of mechanical properties. ABS is a two-phase terpolymer; one is a styrene–acrylonitrile rigid copolymer, and the other is a styrene–butadiene rubber-like copolymer. The plastic name is derived from the three initial monomers, which are mixed in different proportions.

Clariant Renol Gray ABS with 30% fiberglass of weight content as reinforcement was used in this work. According to the supplier, the ABS has molding temperatures between 65.6–93.3 °C, a specific gravity of 1.04 cm³, a tensile stress of 39.3 MPa, elongation of 40%, and a flexural modulus of 20.7 GPa.

Figure 1 shows the GF prepreg and the ABS sheets before using to form the panels. The honeycomb and foam cores were presented in a previous work [19].



Figure 1. Pictures of the ABS (left) and GF prepreg (right) sheets used to manufacture distinct sandwich composite panels.

This work will manufacture prototype panels using a V-shaped mold to simulate one of the complex shapes manufactured in the aeronautical cabin interiors sector. The mold was made of aluminum 6061-T6 and adapted to a CARVER model 4122 hot plate press to fabricate composite sandwich panels at 256 °F with a constant pressure of 20 psi for one hour.

Composite materials are characterized by being designed according to their final application and the physical, mechanical, and chemical phenomena to which they will be exposed. The configuration of panels or sandwich composites stands out in structural applications thanks to their properties against compression and bending forces [20,21]. These panel structures were evaluated following the procedure indicated in the ASTM C393/C393M–20 [22], which considers the stresses that affect the mean span of 150 mm length in a flat specimen with suggested dimensions of 75 mm in width and 203 mm in length. ASTM C393 indicates that the results must be reported through the load versus crosshead displacement plots to determine if there is any significant compliance change (change in slope of the force–displacement curve, sometimes referred to as a transition region) before ultimate failure. However, for non-standard configurations, it is suggested that the width should not be less than twice the total thickness nor more than six times the total thickness [23,24]. The bending tests were performed in a universal testing machine MTS Insight with a cell load of 30 kN at room temperature and a crosshead speed of 0.5 mm/min.

Two support bars are placed under the sample, and a force is applied vertically on the specimen (Figure 2).

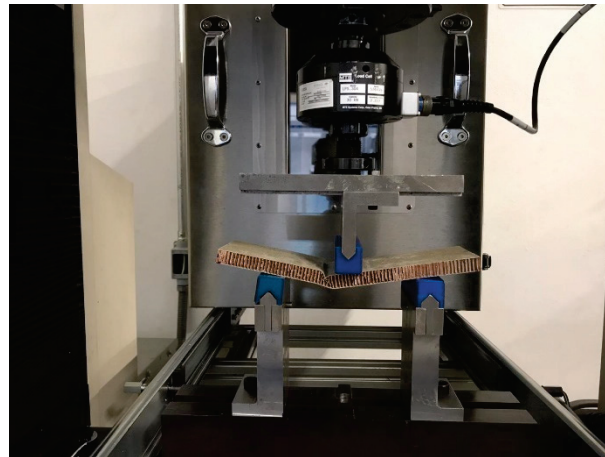


Figure 2. Photograph corresponding to the arrangement for the flexural test in reference panels according to the ASTM C393/C393M-20 standard.

The distance between the support bars should be 150 mm (6.9 in). Pressure pads are used between the load bars and the specimen to prevent localized damage to the faces of the specimen. The following equation is used to calculate the maximum shear stress of the core:

$$F_s^{ult} = \frac{P_{max}}{(d + c) \cdot b} \quad (1)$$

where F_s^{ult} represents the maximum shear stress of the core in MPa, P_{max} is the maximum force prior to failure (N), d is the thickness of the sandwich (mm), c is the thickness of the core (mm, $c = d - 2t$), t the nominal thickness of the faces (mm), and b the width of the sandwich (mm).

For core materials that have a yield above 2% strain, the yield shear stress equation should be used:

$$F_s^{yield} = \frac{P_{yield}}{(d + c) \cdot b} \quad (2)$$

where F_s^{yield} is the maximum core shear stress (MPa), and the P_{yield} is the force at 2% offset shear strain (N). To calculate the stress of the faces:

$$\sigma = \frac{P_{max} \cdot S}{2t \cdot (d + c) \cdot b} \quad (3)$$

where t is the thickness of the faces (mm) and S the length of the span (mm).

The sandwich composite panels evaluated in this work are listed in Table 1.

Table 1. Description of the panel configurations evaluated in this work.

Panel Configuration	Faces	Core	Representation
GF/HC/GF	Glass fiber prepreg	Honeycomb	Reference panels
GF/Foam/GF	Glass fiber prepreg	Foam	Experimental panels
ABS/Foam/ABS	Thermoplastic ABS	Foam	Disruptive panels

3. Manufacturing Panels

The manufacturing of V-shaped composite panels consisted of the following steps:

1. Three layers of mold release agent were applied to the two components of the V-shaped mold. With that covered, two layers of prepreg fiberglass were carefully stacked on both faces of the V-shaped mold, as presented in Figure 3.
2. Two layers of GF prepreg were placed on one of the faces of the V-shaped mold.

3. The HC specimen was placed on the GF prepreg layers, and two additional layers were placed on the top of the HC to build the sandwich composite configuration.
4. The mold is closed slowly to transfer the temperature from the hot plates to the V-shaped mold. The preheated process consisted of 256 °F during 30 min.
5. After the preheated process, the mold is closed, supplying a constant pressure of 20 psi and a temperature of 256 °F for one hour. Digital temperature recorder and thermocouples on both sides of the V-shape mold were used to monitor and verify the adequate pressure and temperature during the curing process.

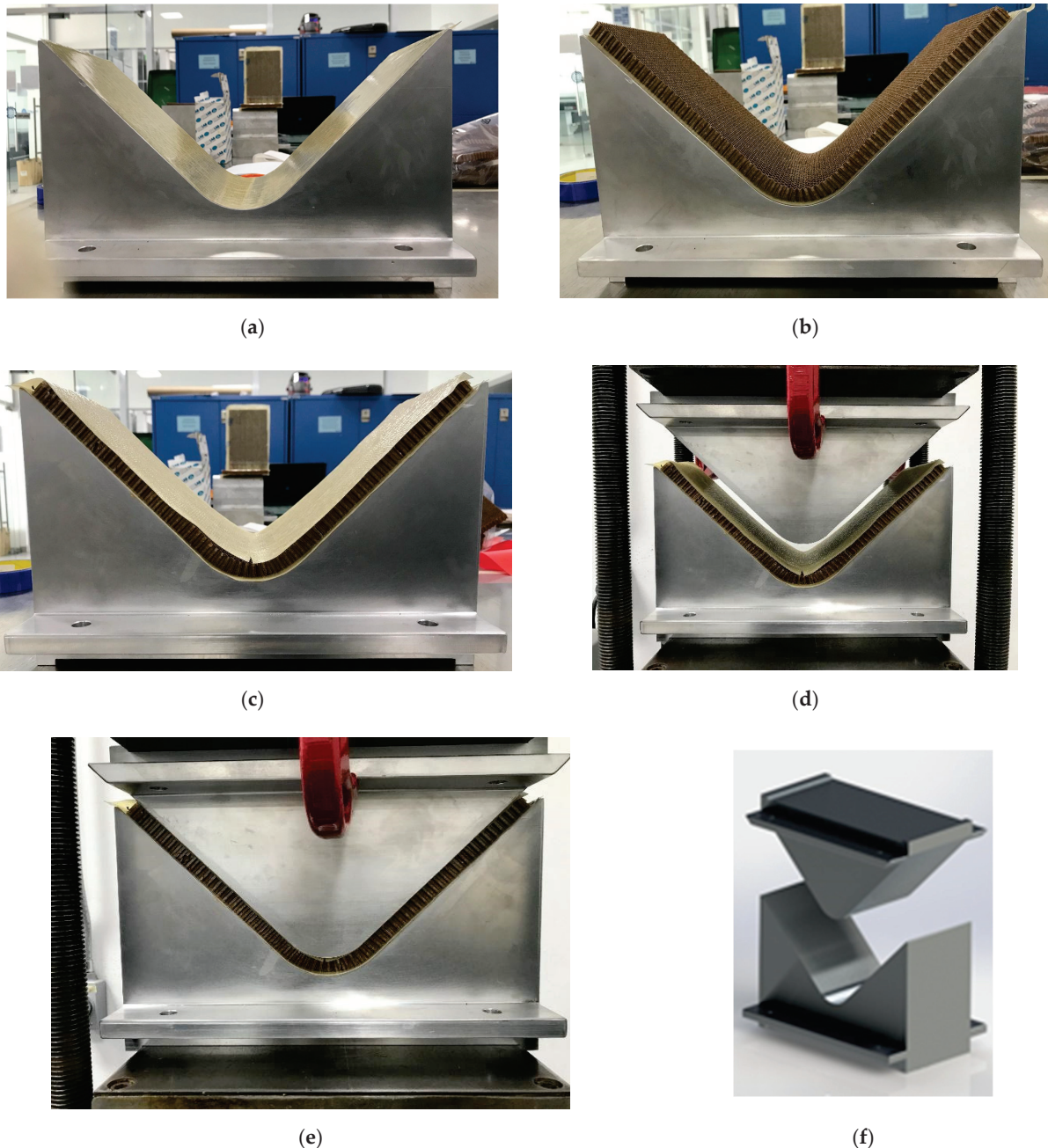


Figure 3. Schematic representation of the V-shaped mold to produce composite sandwich panels: (a) Two layers of GF prepreg (step two), (b) HC placement (step three), (c) complete sandwich structure (step three), (d) preheated process (step four), (e) manufacturing of V-shaped panel (step five), and (f) digital rendering of the V-shaped mold.

The manufacturing process was applied to all configurations listed in Table 1.

It is essential to underline that the HC is flexible and easy to place and adapt to the V-shaped mold. However, the foam is a rigid structure, and it is impossible to blend at room temperature without damage or breaking the specimen. Therefore, two strategies were followed. The first one uses a heat gun to apply heat to the foam surface to soften the material. After that, the foam specimen can be mold into the V-shaped mold, as shown in Figure 4.

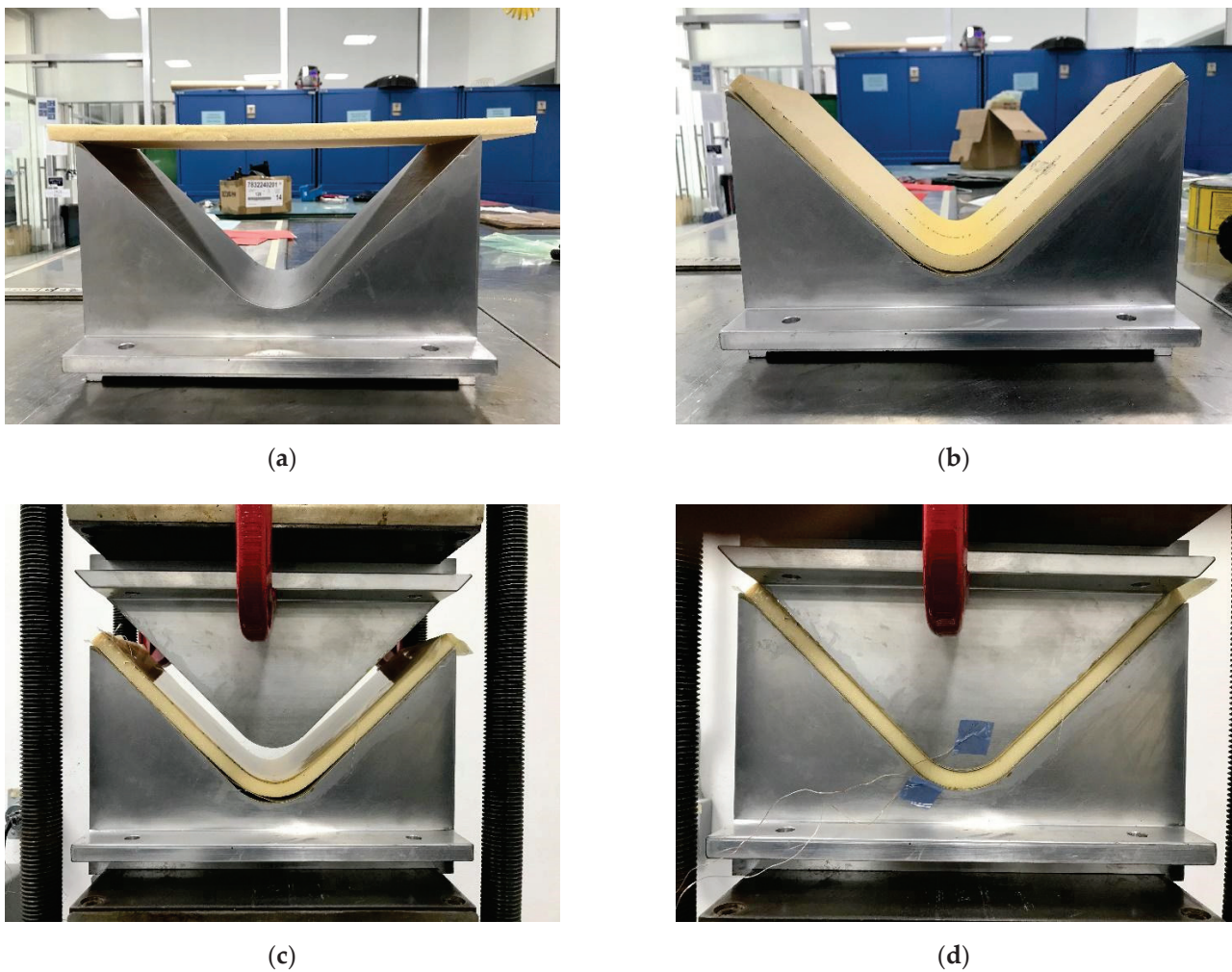


Figure 4. Schematic representation of the V-shaped mold to produce the foam sandwich panels: (a) Unbending foam specimen, (b) foam specimen adapted to the V-shaped mold, (c) preheated process, and (d) manufacturing of V-shaped foam panel.

The second strategy consisted of cutting the foam specimen in a grid, without completing the cut, just enough to bend the foam specimen in different directions, as presented in Figure 5.

The gridding foam allows its correct arrangement on the walls of the mold, avoids the material having to be softened with heat to bend it, and its handling when placing the pre-impregnated fiberglass saves time. However, from Figure 5, it can be seen that the gridding foam does not cover the entire surface of the mold, leaving spaces that are not in solid contact with the fiberglass that could weaken the structure of the panel [25]. Figure 6 shows the sandwich panels prepared.



Figure 5. Picture corresponding to the gridding foam specimen placement in the V-shaped mold before the preheated process.

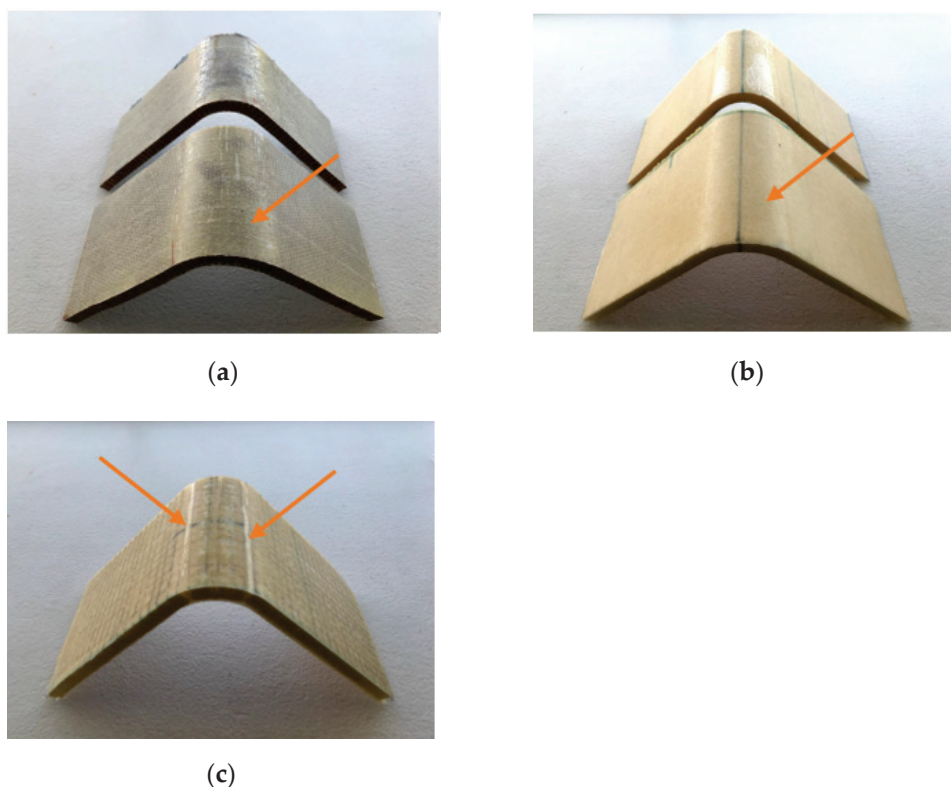


Figure 6. Pictures corresponding to the V-shaped panels of: (a) GF/HC/GF, (b) GF/Foam/GF, and (c) GF/gridding foam/GF.

It is possible to appreciate the base of the V-shaped panels presenting similar features such as the build-up of epoxy resin in the top fold, indicated by an arrow in Figure 6a,b. This defect is attributed to the non-homogeneous contact between core and GF prepreg during the panel fabrication. The core is deformed to fit the V-shaped mold. This defect is not observed in the panel made with gridding foam as it has more significant contact with the fiberglass. However, the gridding foam panel shows an evident defect, indicated by arrows in Figure 6c, which occurs due to the non-contact of the GF prepreg, as shown more evident in Figure 5.

4. Results

The GF/HC/GF, GF/Foam/GF, and GF/Gridding foam/GF systems were evaluated according to the ASTM C393. The panels were placed in a three-point bending configuration, with a span of 150 mm and a crosshead speed of 1 mm/min. The mechanical behavior of the panels is shown in Figure 7.

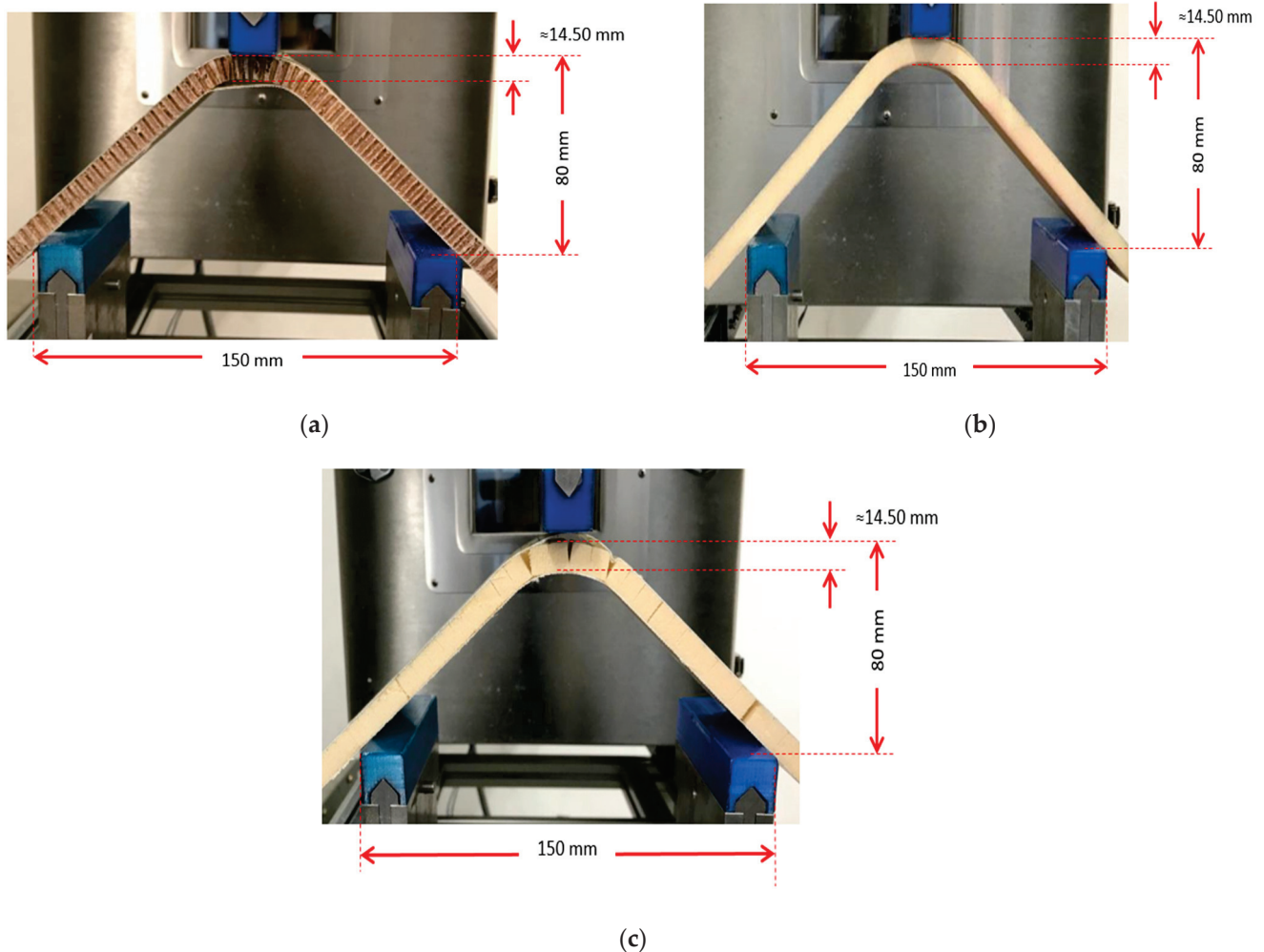


Figure 7. Pictures of the three-point bending test performed to: (a) GF/HC/GF, (b) GF/Foam/GF, (c) GF/Gridding foam/GF. The pictures present the damages that occurred during the test.

During the bending test, the GF/HC/GF reference composites showed high resistance to breakage, remaining firm until the fiberglass skin debonds. Similarly, the experimental composites GF/Foam/GF showed resistance to delamination. However, a failure of the foam core was noted, showing cracks and subsequent failure of the debonding between the fiberglass skin and the core.

As might be expected, the experimental GF/Gridding foam/GF laminate presented a collapse of the structure, attributed to the empty areas produced by the gridding (as noted in Figure 5), which weakened the structure [26].

Figure 8 shows the load versus displacement curves obtained from the bending tests for the GF/HC/GF, GF/Foam/GF, and GF/Gridding foam/GF systems. Table 2 presents the mechanical parameters determined. The ASTM C393/C393M-20 requires the load versus displacement plots from representative specimen behavior. The stress versus strain curves, calculated following the procedure proposed by Barbero et al. [27] are also added.

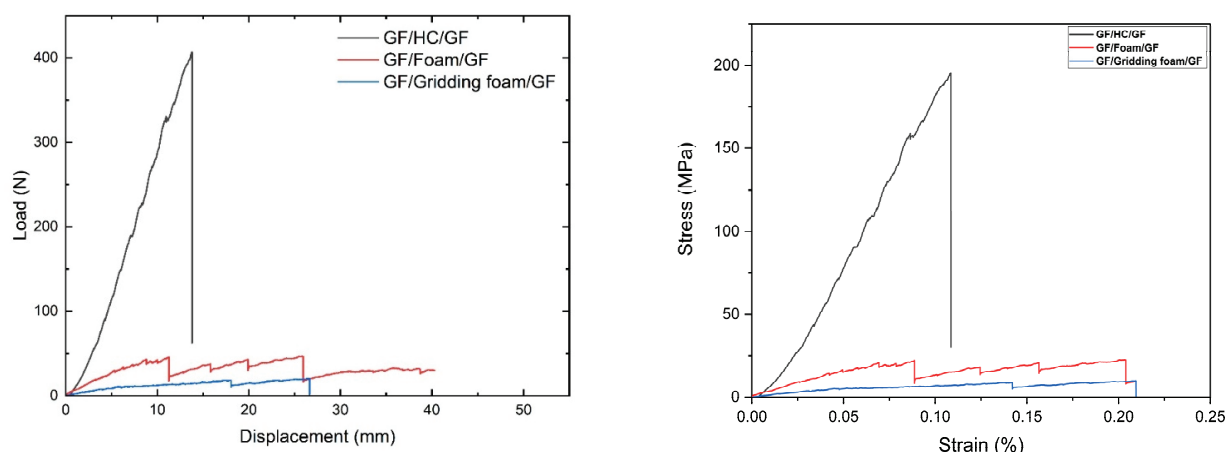


Figure 8. Representative load vs. displacement (left) and stress vs. strain (right) curves registered during the bending tests of GF/HC/GF, GF/Foam/GF, and GF/Gridding foam/GF panels.

Table 2. Bending parameters.

Composite Panel	Max Normal Strength (MPa)	Max Shear Strength (kPa)	Max Deflection (mm)
GF/HC/GF	17.44 ± 0.62	57.5 ± 0.62	13.80 ± 0.62
GF/Foam/GF	2.22 ± 0.62	56.1 ± 0.62	41.39 ± 0.62
GF/gridding foam/GF	0.90 ± 0.62	62.3 ± 0.62	37.87 ± 0.62
ABS/HC/ABS	6.52 ± 0.02	240.3 ± 0.12	32.71 ± 2.50
ABS/Foam/ABS	10.48 ± 0.03	390.4 ± 0.10	34.29 ± 0.43
ABS/gridding foam/ABS	5.14 ± 0.87	170.2 ± 0.09	51.65 ± 2.63
ABS-T/Foam/ABS-T	9.29 ± 1.47	320.2 ± 5.96	15.87 ± 3.71
ABS-TA/Foam/ABS-TA	7.13 ± 2.68	253.6 ± 8.53	15.37 ± 2.31

It is evident that better mechanical performance is obtained with the GF/HC/GF panel (Figure 9a), which is attributed to the intrinsic mechanical properties of the honeycomb structure and the molecular compatibility between the aramid in the HC and the epoxy resin from the GF prepreg [17]. The foam is a rigid material with limited mechanical performance compared to the HC. According to Figure 9b, the primary damage of the GF/Foam/GF panel is the failure of the foam and not the adhesive, which could be associated with some thermal degradation induced with the heat gun previous during the manufacturing process [17]. The GF/Gridding foam/GF panel is interesting as this material has the lowest bending properties, as expected, but avoids possible foam degradation that influences the shear strength properties (Table 2). This panel fails with the adhesive delamination, similar to the GF/HC/GF panel, as observed in Figure 9c.

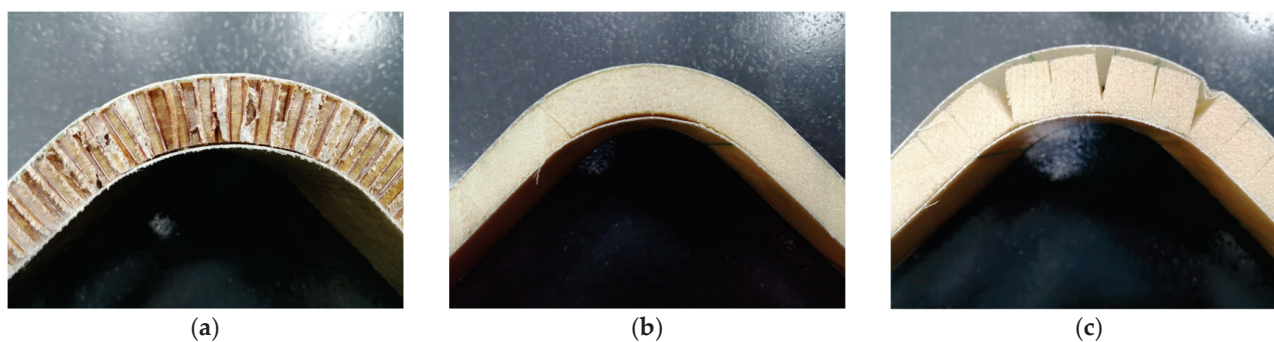


Figure 9. Pictures corresponding to the V-shaped panels after bending tests of (a) GF/HC/GF, (b) GF/Foam/GF, and (c) GF/gridding foam/GF.

The ABS sheets were molded using a square frame of $300 \times 300 \times 1$ mm thick, previously calculating the volume of the square frame considering the density of the ABS (1.03 g/cm^3) according to the technical datasheet. The ABS sheets were prepared in the CARVER hot plate press model 4122 at a temperature of $200 \text{ }^\circ\text{C}$ and pressure of 20 psi for 3 min. The unloading and loading procedure was performed to eliminate trapped air. Subsequently, the square frame was placed in a plate press at $30 \text{ }^\circ\text{C}$ and pressure of 200 psi for 2 min to cool the ABS sheets.

Several methodologies were followed to prepare ABS/foam/ABS and ABS/HC/ABS flat panels in just one step. However, it was not possible to adhere the ABS to the foam or to the HC. The methodologies are not the scope of this work.

Therefore, the foam and HC specimens were sprayed with Hi-Tack 71 from 3M™, a mist aerosol adhesive recommended by 3M for its use for the manufacturing composites, including infusion and dry lamination. Spraying was carried out at a 45° angle before ABS sheets placement and subsequently put in the V-shaped mold to proceed with the panel manufacturing, as shown in Figure 10.

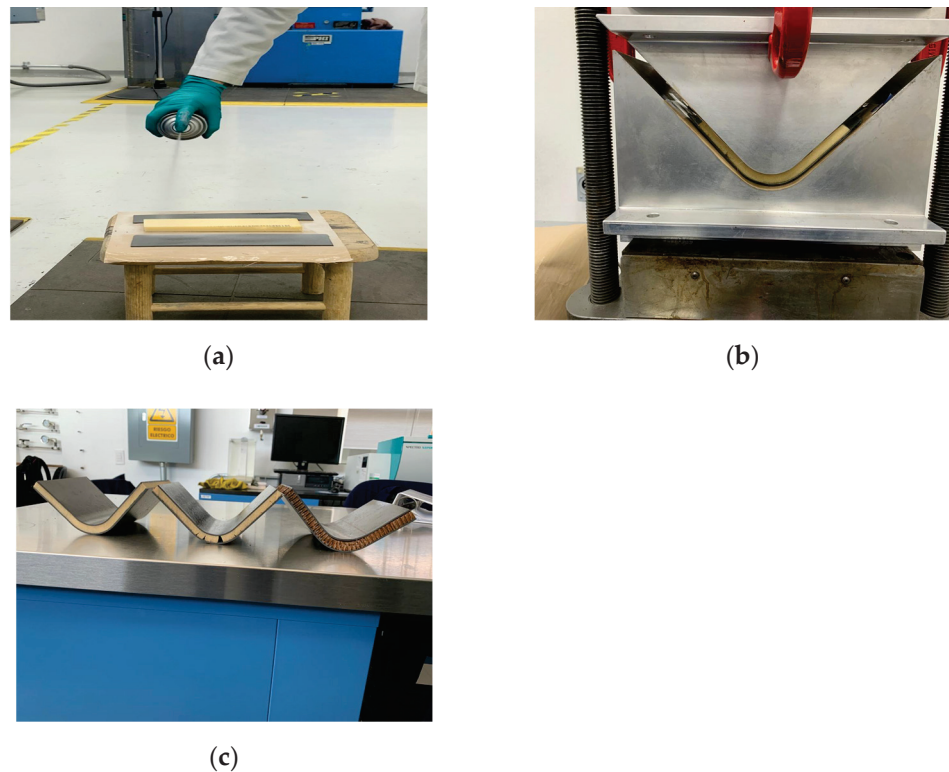


Figure 10. Pictures corresponding to the manufacturing procedure of V-shaped ABS panels: (a) spraying adhesive mist aerosol to the foam and ABS sheets, (b) ABS/foam/ABS compression molding process, and (c) V-shaped sandwich panels with face ABS sheets.

Figure 11 shows the bending tests of the sandwich composites using ABS as face sheets. Due to the restrictions in the size of the compressed molded ABS sheets, the span was fit to 120 mm. The mechanical parameters are reported in Table 2.

Based on the results, it is possible to suggest that the core acts actively more than the panels with GF prepreg in panels with ABS as face sheets. After the first delamination of the ABS, the load applied is supported by the core. That is the reason the ABS/HC/ABS presents lower mechanical performance than ABS/Foam/ABS. The foam is more rigid than HC. Considering the V-shape of the specimens, the HC under this configuration is less restrictive than the foam.

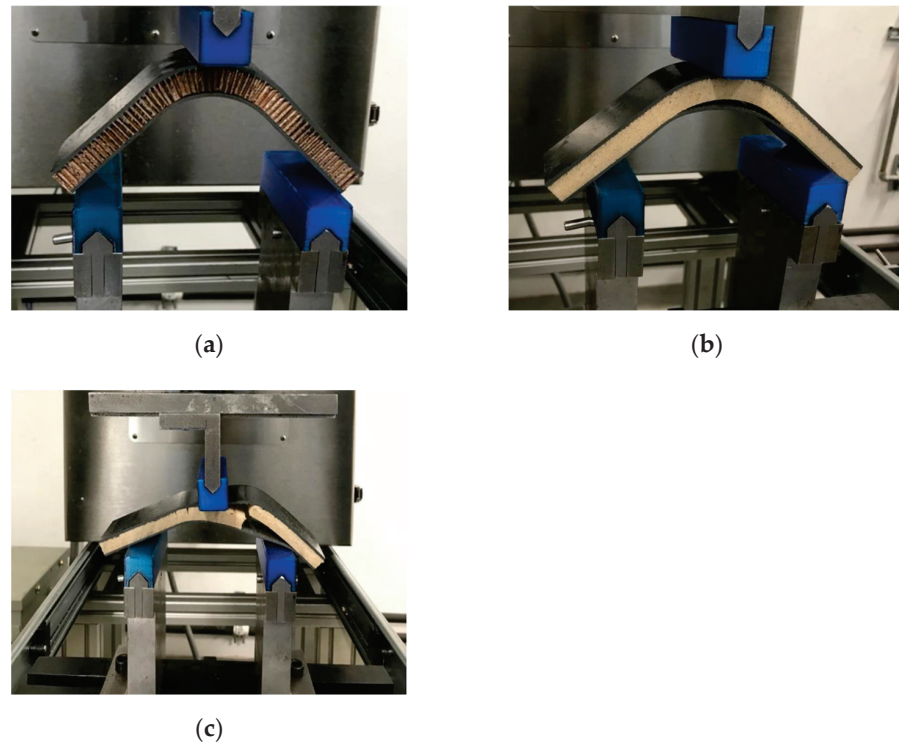


Figure 11. Pictures of the three-point bending test performed to (a) ABS/HC/ABS, (b) ABS/Foam/ABS, and (c) ABS/gridding foam/ABS. The pictures present the damages that occurred during the test.

Nonetheless, the spray adhesive seems to be more effective in the foam than HC, as the ABS/Foam/ABS supports higher load values (Figure 12). The previous is attributed to the surface contact, higher in the foam than HC structure. Similar is observed with the gridding foam, which loses rigidity and surface contact during cutting—the more flexibility, the lower mechanical resistance.

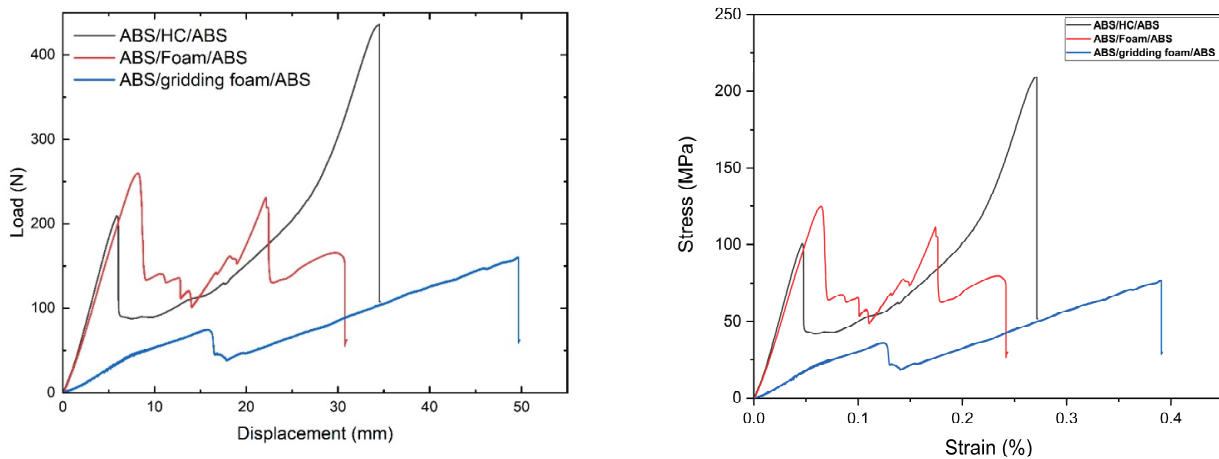


Figure 12. Representative load vs. displacement (left) and stress vs. strain (right) curves registered during the bending tests of: ABS/HC/ABS (green line), ABS/Foam/ABS (red line), and ABS/gridding foam/ABS panels (blue line).

Thermoforming, or vacuum forming, is a process where a flat thermoplastic sheet is heated and molded into the desired shape. The process is widely used for packaging consumer products and making large items such as bathtubs, contour reflectors, and interior door liners for refrigerators.

It is considered as a secondary forming process; the primary process is when molded sheets or films. Only thermoplastics can be thermoformed, as extruded sheets of thermoset or elastomeric polymers are already cross-linked and cannot be molded by reheating.

In this work, the vacuum forming process was used to build panels oriented to the aircraft interiors. The panels were fabricated in a vacuum-formed machine Formech 508FS (Floor-Standing) with reduced window process, and quartz heaters for better forming performance. The optimal conditioning parameters for vacuum formed were 6 bar of vacuum pressure, 50% of power quartz heaters, and 160 s of heating time.

The compressed molded ABS sheets with $30 \times 30 \times 1 \text{ mm}^3$ were used for the thermoformed foam panels ABS-T/Foam/ABS-T. The foam was formed with the heat gun as described previously in Figure 4. The foam acts as a mold, and it was laid in the working platform base. The ABS sheets were placed in the reduced processing window of the Formech 508FS, and the system was closed. The quartz heaters transfer the heat to the ABS sheet, and the auto-level display avoids material sag during the heating cycle and maintains an even distance between heater and sheet. When the ABS sheet is ready to form, the working platform base releases, the vacuum starts, and the cooling fan is activated. This procedure is summarized in Figure 13.

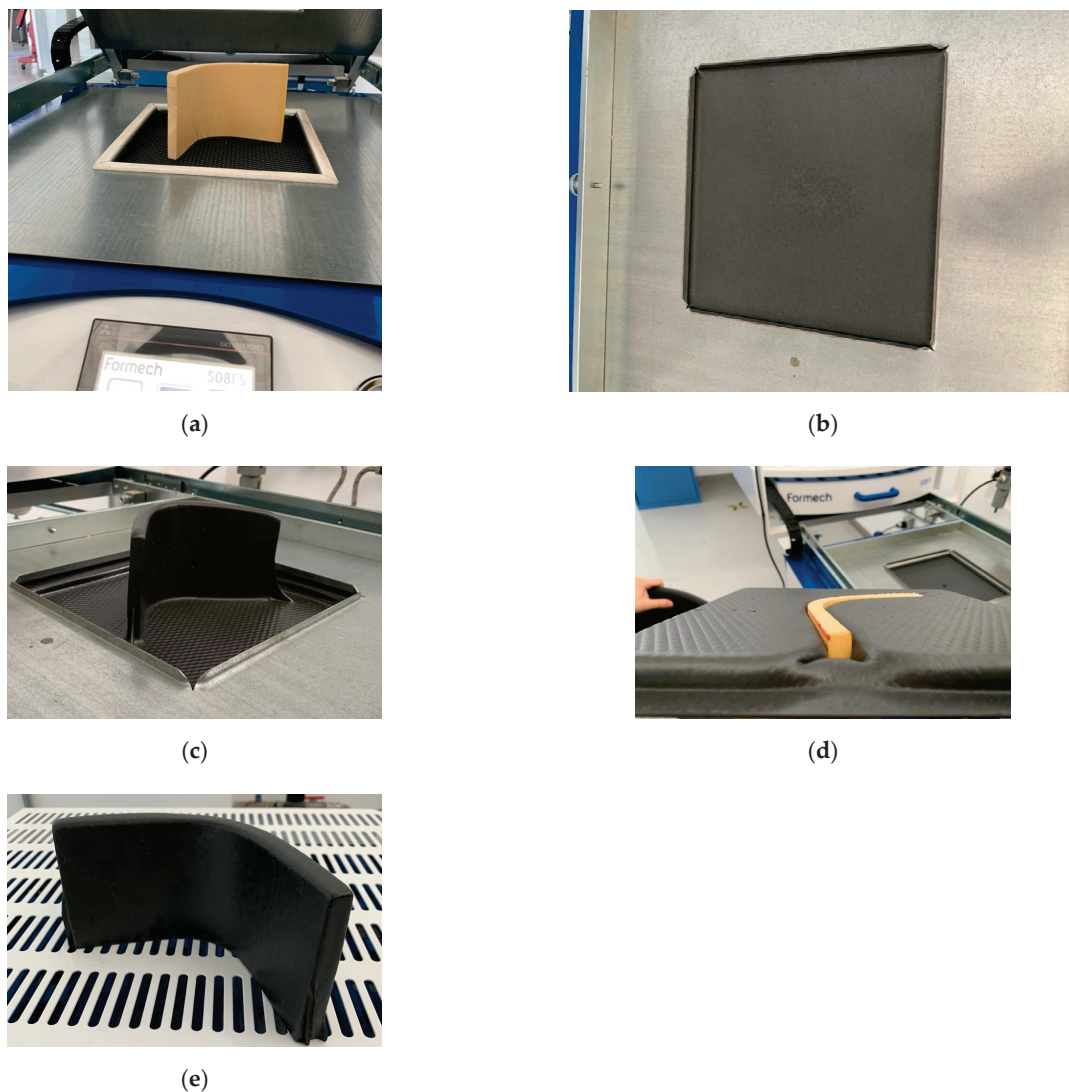


Figure 13. Schematic representation of the V-shaped vacuum forming panels: (a) foam core lays on the work platform, (b) ABS sheet places in the reduced processing window, (c) ABS-T/Foam/ABS-T panel, (d) bottom of the vacuum forming panel, and (e) panel after removing the excess of material. The panel is covered with the ABS sheet.

Vacuum forming is an alternative manufacturing process to the development of aircraft cabin interior panels. The technology is faster and cheaper than compression molding. Furthermore, the cores act as molds and are covered for all sides, which can be helpful for one-step decorative processes and avoid the use of tapestries. However, the vacuum process does not offer self-adhesion between the mold and the plastic sheets, and the ABS is not entirely compatible with polyurethane foam. Therefore, 3M™ Hi-Tack 71 spray adhesive was applied to the foam and ABS sheets before the vacuum process (ABS-TA/Foam/ABS-TA).

The mechanical properties of ABS-T/Foam/ABS-T and ABS-TA/Foam/ABS-TA panels were evaluated according to the ASTM C393, with a span of 120 mm due to the restrictions in the ABS sheets size, and a crosshead speed of 1 mm/min. Figure 14 shows the mechanical response, and the mechanical parameters are presented in Table 2.

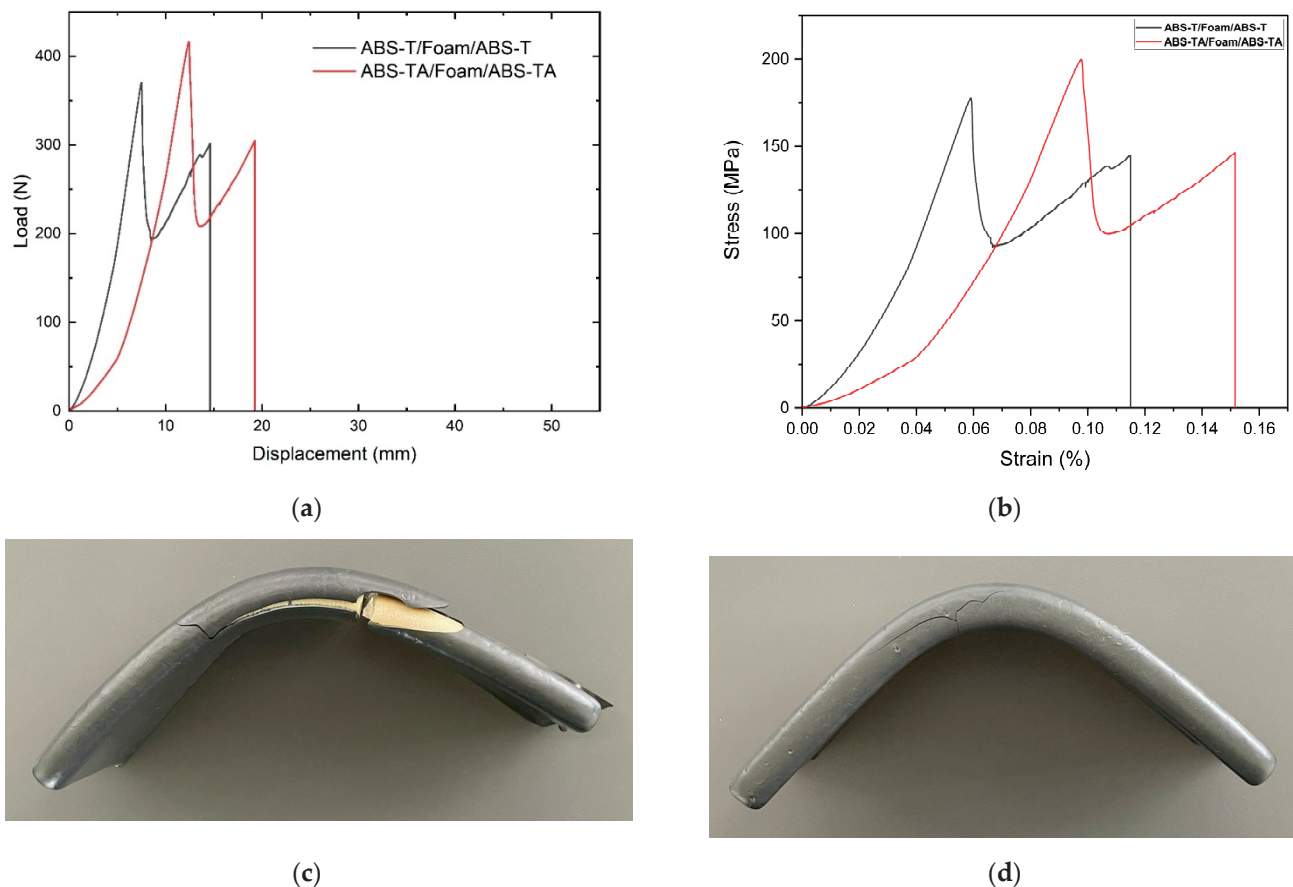


Figure 14. Mechanical behavior and failure: (a) representative load vs. displacement curves, (b) representative stress vs. strain curves registered during the bending tests, (c) failure of the ABS-T/Foam/ABS-T panels, and (d) failure of ABS-TA/Foam/ABS-TA panels. The pictures present the damages that occurred during the test.

It can be observed that there are no significant variations in the shape of the curves, which allows us to suggest that both panels have similar mechanical behavior. However, according to the mechanical parameters obtained from the mechanical tests (Table 2), the standard deviation of the normal strength results considerably higher in the ABS-TA/Foam/ABS-TA than the ABS-T/Foam/ABS-T, which should imply that the adhesive could be influencing the mechanical parameters in a non-homogeneous way. In any case, the spray adhesive interferes with the mechanical behavior of the panels manufactured with the vacuum forming process as the ABS remains adhere to the foam, which is an interesting result as, assuming an impact on the panel during service, the aircraft interior panel maintains its aesthetics until it is removed or repaired (Figure 14d).

5. Conclusions

In previous work (Innovation in aircraft cabin interior panels part I: Technical assessment on replacing the honeycomb with structural foams and evaluation of optimal curing of prepreg fiberglass, under review), the use of analytical tools such as DSC and DMA allowed a complete evaluation of the curing conditions of fiberglass prepreg in the manufacture of sandwich composites. That knowledge allows us to evaluate the feasibility of replacing the honeycomb and fiberglass skin layers core with rigid polyurethane foams and thermoplastic polymers.

In this work, the sandwich composites were transformed into complex V-shaped panels. The structural composites formed with HC and fiberglass showed higher mechanical properties than the proposed sandwich composites, although the new composites fit with the non-structural applications.

The vacuum forming process proposed and analyzed in this work was feasible for developing non-structural panels. This manufacturing technique is fast, easy, economical, and ecological as it uses recyclable materials. The vacuum forming also covers the entire panel and avoids subsequent rework such as upholstery and painting of the panels. The results lead to more detailed research on materials and manufacturing processes that may be feasible in developing and optimizing panels for aircraft cabin interiors.

Author Contributions: Conceptualization, E.A.F.-U., S.P. and M.T.-A. Funding acquisition, E.A.F.-U. and M.T.-A. Writing—original draft, E.A.F.-U. Formal analysis, P.I.A.L., V.R.-R., R.S.S., R.R.A. and C.Z.P. Validation, P.I.A.L., V.R.-R., C.Z.P. and S.P. Project administration, P.I.A.L. Investigation, V.R.-R., S.P. and M.T.-A. Data curation, R.S.S. and R.R.A. Methodology, M.T.-A. All authors have read and agreed to the published version of the manuscript.

Funding: This work was supported by the National Council of Science and Technology (CONACYT) through the Institutional Fund for Regional Promotion for Scientific, Technological and Innovation Development (FORDECYT), grant number 297708. The APC was funded by FORDECYT, grant number 297708.

Institutional Review Board Statement: Not applicable.

Informed Consent Statement: Not applicable.

Data Availability Statement: This study did not report any data.

Acknowledgments: Edgar Franco and Saul Piedra convey special appreciation to the “CONACYT Researchers Program (Catedras CONACYT)”.

Conflicts of Interest: The authors declare no conflict of interest.

References

1. Egan, B.; McCarthy, C.T.; McCarthy, M.A.; Gray, P.J.; O’Higgins, R.M. Static and high-rate loading of single and multi-bolt carbon-epoxy aircraft fuselage joints. *Compos. Part A Appl. Sci. Manuf.* **2013**, *53*, 97–108. [CrossRef]
2. Soutis, C. Carbon fiber reinforced plastics in aircraft construction. *Mater. Sci. Eng. A* **2005**, *412*, 171–176. [CrossRef]
3. McCarthy, C.; McCarthy, M. Experimental and Computational Studies of Mechanically Fastened Joints in Composite Aircraft Structures Dept. of Mechanical and Aeronautical Engineering University of Limerick. In Proceedings of the 1st CEAS European Air and Space Conference, Berlin, Germany, 10–13 September 2007. [CrossRef]
4. Impact, R.; Store, K.; Reserved, A.R. *Aircraft Cabin Interiors Market—Global Forecast to 2025*; ASDR-559916; MarketsandMarkets: Hadapsar, India, 2020.
5. Hiemstra-van Mastrigt, S.; Smulders, M.; Bouwens, J.M.A.; Vink, P. Chapter 61—Designing aircraft seats to fit the human body contour. In *DHM and Posturography*; Scataglini, S., Paul, G., Eds.; Academic Press: Cambridge, MA, USA, 2019; pp. 781–789, ISBN 9780128167137.
6. Piedra, S.; Martinez, E.; Escalante-Velazquez, C.A.; Jimenez, S.M.A. Computational aerodynamics analysis of a light sport aircraft: Compliance study for stall speed and longitudinal stability certification requirements. *Aerosp. Sci. Technol.* **2018**, *82–83*, 234–242. [CrossRef]
7. Torres, M.; Piedra, S.; Ledesma, S.; Escalante-Velázquez, C.A.; Angelucci, G. Manufacturing process of high performance-low cost composite structures for light sport aircrafts. *Aerospace* **2019**, *6*, 11. [CrossRef]

8. Lyon, R.E. 20—Materials with reduced flammability in aerospace and aviation. In *Advances in Fire Retardant Materials*; Woodhead Publishing Series in Textiles; Horrocks, A.R., Price, D.B., Eds.; Woodhead Publishing: Sawston, UK, 2008; pp. 573–598, ISBN 9781845692629.
9. Di Franco, G.; Fratini, L.; Pasta, A. Influence of the distance between rivets in self-piercing riveting bonded joints made of carbon fiber panels and AA2024 blanks. *Mater. Des.* **2012**, *35*, 342–349. [CrossRef]
10. Torres, M.; Franco-Urquiza, E.A.; Hernández-Moreno, H.; González-Villa, M.A. Mechanical Behavior of a Fuselage Stiffened Carbon-Epoxy Panel under Debonding Load. *J. Aeronaut. Astronaut. Eng.* **2018**, *7*, 2–6. [CrossRef]
11. Found, M.S.; Friend, M.J. Evaluation of CFRP panels with scarf repair patches. *Compos. Struct.* **1995**, *32*, 115–122. [CrossRef]
12. Kradinov, V.; Hanauska, J.; Barut, A.; Madenci, E.; Ambur, D.R. Bolted patch repair of composite panels with a cutout. *Compos. Struct.* **2002**, *56*, 423–444. [CrossRef]
13. Whitty, J.P.M.; Alderson, A.; Myler, P.; Kandola, B. Towards the design of sandwich panel composites with enhanced mechanical and thermal properties by variation of the in-plane Poisson's ratios. *Compos. Part A Appl. Sci. Manuf.* **2003**, *34*, 525–534. [CrossRef]
14. Seibert, H.F. Applications for PMI foams in aerospace sandwich structures. *Reinf. Plast.* **2006**, *50*, 44–48. [CrossRef]
15. Castanie, B.; Bouvet, C.; Ginot, M. Review of composite sandwich structure in aeronautic applications. *Compos. Part C Open Access* **2020**, *1*, 100004. [CrossRef]
16. Birman, V.; Kardomateas, G.A. Review of current trends in research and applications of sandwich structures. *Compos. Part B Eng.* **2018**, *142*, 221–240. [CrossRef]
17. Alila, F.; Casari, P. Fatigue damage and failure analysis of honeycomb sandwich. *Procedia Struct. Integr.* **2019**, *19*, 101–105. [CrossRef]
18. Mills, N. (Ed.) Sandwich panel case study. In *Polymer Foams Handbook*; Elsevier: Oxford, UK, 2007; pp. 425–447, ISBN 9780750680691.
19. Franco-Urquiza, E.A.; Dollinger, A.; Torres-Arellano, M.; Piedra, S.; Alcántara Llanas, P.I.; Rentería-Rodríguez, V.; Zarate Pérez, C. Innovation in Aircraft Cabin Interior Panels Part I: Technical Assessment on Replacing the Honeycomb with Structural Foams and Evaluation of Optimal Curing of Prepreg Fiberglass. *Polymers* **2021**, *13*, 3207. [CrossRef]
20. Han, B.; Wang, W.; Zhang, Z.; Zhang, Q.; Jin, F.; Lu, T. Performance enhancement of sandwich panels with honeycomb–corrugation hybrid core. *Theor. Appl. Mech. Lett.* **2016**, *6*, 54–59. [CrossRef]
21. Shahdin, A.; Mezeix, L.; Bouvet, C.; Morlier, J.; Gourinat, Y. Fabrication and mechanical testing of glass fiber entangled sandwich beams: A comparison with honeycomb and foam sandwich beams. *Compos. Struct.* **2009**, *90*, 404–412. [CrossRef]
22. *ASTM C393/C393M-20 Standard Test Method for Core Shear Properties of Sandwich Constructions by Beam Flexure*; ASTM International: West Conshohocken, PA, USA, 2020. [CrossRef]
23. Ogorkiewicz, R.M. *Analysis and Design of Structural Sandwich Panels*; Howard, G., Ed.; Allen Pergamon Press: Oxford, UK, 1969; 283p.
24. Zenkert, D. *Handbook of Sandwich Construction*; Engineering Materials Advisory Services Ltd.: Worcester, UK, 1997.
25. Laustsen, S.; Lund, E.; Kühlmeier, L.; Thomsen, O.T. Failure behaviour of grid-scored foam cored composite sandwich panels for wind turbine blades subjected to realistic multiaxial loading conditions. *J. Sandw. Struct. Mater.* **2014**, *16*, 481–510. [CrossRef]
26. Sun, Z.; Shi, S.; Guo, X.; Hu, X.; Chen, H. On compressive properties of composite sandwich structures with grid reinforced honeycomb core. *Compos. Part B Eng.* **2016**, *94*, 245–252. [CrossRef]
27. Barbero, E.J. *Finite Element Analysis of Composite Materials Using Ansys®*; CRC Press: Boca Raton, FL, USA, 2013; Volume 3, ISBN 9780429185250.

Technical Note

Innovation in Aircraft Cabin Interior Panels Part I: Technical Assessment on Replacing the Honeycomb with Structural Foams and Evaluation of Optimal Curing of Prepreg Fiberglass

Edgar Adrián Franco-Urquiza ^{1,*}, Annika Dollinger ², Mauricio Torres-Arellano ³, Saúl Piedra ¹, Perla Itzel Alcántara Llanas ³, Victoria Rentería-Rodríguez ³ and Cecilia Zarate Pérez ³

¹ National Council for Science and Technology (CONACYT—CIDESI), Center for Engineering and Industrial Development, Carretera Estatal 200, km 23, Querétaro 76265, Mexico; saul.piedra@cidesi.edu.mx

² Institute of Aviation, Department of Engineering, University of Applied Sciences, FH JOANNEUM GmbH, 8020 Graz, Austria; annika.dollinger@edu.fh-joanneum.at

³ Center for Engineering and Industrial Development (CIDESI), Carretera Estatal 200, km 23, Querétaro 76265, Mexico; mauricio.torres@cidesi.edu.mx (M.T.-A.); perla.alcantara@cidesi.edu.mx (P.I.A.L.); ana.renteria@cidesi.edu.mx (V.R.-R.); cecilia.zarate@cidesi.edu.mx (C.Z.P.)

* Correspondence: edgar.franco@cidesi.edu.mx

Citation: Franco-Urquiza, E.A.; Dollinger, A.; Torres-Arellano, M.; Piedra, S.; Alcántara Llanas, P.I.; Rentería-Rodríguez, V.; Zarate Pérez, C. Innovation in Aircraft Cabin Interior Panels Part I: Technical Assessment on Replacing the Honeycomb with Structural Foams and Evaluation of Optimal Curing of Prepreg Fiberglass. *Polymers* **2021**, *13*, 3207. <https://doi.org/10.3390/polym13193207>

Academic Editors: Somen K. Bhudolia and Sunil Chandrakant Joshi

Received: 15 August 2021

Accepted: 7 September 2021

Published: 22 September 2021

Publisher's Note: MDPI stays neutral with regard to jurisdictional claims in published maps and institutional affiliations.



Copyright: © 2021 by the authors. Licensee MDPI, Basel, Switzerland. This article is an open access article distributed under the terms and conditions of the Creative Commons Attribution (CC BY) license (<https://creativecommons.org/licenses/by/4.0/>).

Abstract: Sandwich composites are widely used in the manufacture of aircraft cabin interior panels for commercial aircraft, mainly due to the light weight of the composites and their high strength-to-weight ratio. Panels are used for floors, ceilings, kitchen walls, cabinets, seats, and cabin dividers. The honeycomb core of the panels is a very light structure that provides high rigidity, which is considerably increased with fiberglass face sheets. The panels are manufactured using the compression molding process, where the honeycomb core is crushed up to the desired thickness. The crushed core breaks fiberglass face sheets and causes other damage, so the panel must be reworked. Some damage is associated with excessive build-up of resin in localized areas, incomplete curing of the pre-impregnated fiberglass during the manufacturing process, and excessive temperature or residence time during the compression molding. This work evaluates the feasibility of using rigid polyurethane foams as a substitute for the honeycomb core. The thermal and viscoelastic behavior of the cured prepreg fiberglass under different manufacturing conditions is studied. The first part of this work presents the influence of the manufacturing parameters and the feasibility of using rigid foams in manufacturing flat panels oriented to non-structural applications. The conclusion of the article describes the focus of future research.

Keywords: aircraft cabin interior panels; optimal curing of prepreps; foams; non-structural composite panels

1. Introduction

The composite materials market is continually growing in the aerospace sector. Other industries such as automobiles, trains, and components such as tanks or pressure vessels, require these materials with excellent mechanical properties [1]. The extraordinary characteristics of composite materials, also known as fiber-reinforced polymer (FRP) composites, provide new approaches in designing and fabricating complex structures [2–5]. These composites are already ingrained in current engineering, but research is still in its infancy. According to Market & Markets Global Aircraft Cabin Interiors Market Forecast, airline expenditures account for more than 30% of total fuel operating costs, increasingly demanding more fuel-efficient aircraft [6]. This led to a focus on lighter materials in aircraft, and therefore fiberglass and carbon fiber composites have been used for the past several decades to reduce the weight of panels for cabin interiors. According to the market analysis, composite panels in aircraft interiors could double, from 20–25% currently used to 30–40% [7].

The aeronautical industry is moving today to modernize cabin interiors satisfying three main criteria: commercial viability, certification, and passenger experience. Some of the most notable moves are the development of lightweight and custom cabin solutions to enhance the overall passenger experience; an expansion of the overhead storage compartments to accommodate more luggage per passenger; the design of a maximum cabin space that allows comfort and the feeling of space, but optimizing the space to add more seats. In this sense, composite materials represent an indispensable focus area for the aircraft cabin design without sacrificing performance, safety, and cost [8,9].

Aircraft cabin interiors have witnessed a significant and impactful evolution over the past decades as composite materials have taken a disruptive journey and played a critical role in enhancing cabin interiors in general. The interiors of aircraft cabins play an essential role in improving the comfort of passengers on board. Based on the type of interior, the aircraft cabin interior market has been segmented into aircraft seating, inflight entertainment and connectivity, cabin lighting, galley equipment, aircraft lavatories, aircraft windows and windshields, overhead compartments, and divider panels. However, the materials used in the cabin interiors are similar regardless of airline or type of aircraft since all passenger-carrying craft must meet the flammability requirements [10–12].

Aircraft seats are the product most in demand in the aircraft cabin interior market, while galley equipment is the most expensive [8,9,13]. The interiors of aircraft cabins are a combination of different products, and each product has its function. In this sense, the primary function of aircraft seats is to provide comfort and safety to passengers. The requirements of the aircraft cabin interior panels present a good balance between strength, low density, high stiffness, and durability. In addition, most panels require contoured forms, which lead to several defects induced during the manufacturing process [14]. Aircraft cabin interior panels are manufactured using typical sandwich composites configuration made with aramid honeycomb core bonded to outer layers or face sheets, commonly glass fiber epoxy prepreg. A lightweight, low-density core between thin sheets dramatically increases panel rigidity with little added weight. Flat and complex panels are fabricated using single-opening and multi-opening presses, respectively. For molds with complex geometries, the one-step compression molding leads to distinct types of induced failures, such as breaks, holes, and the absence of impregnated zones or areas with excessive resin accumulation in the contours of the mold [15–17]. This occurs when the sandwich composite is placed in a large press and crushed to a predetermined shape and thickness. Then, the crushed honeycomb acts like multiple blades that break the glass fiber prepreg during the transformation process.

The use of new alternative composite materials and diverse manufacturing technologies boasts many opportunities to develop composite panels, addressing significant challenges like reducing manufacturing costs, ensuring defect-free and repeatable manufacturing, increasing the efficiency of joining technologies, and developing structural maintenance and repair technologies.

This work evaluates the optimal curing conditions of prepreg fiberglass and the mechanical properties of honeycomb and vinyl foam cores to evaluate their viability in developing sandwich composites. This first part aims to show the thermal and mechanical results for the development of sandwich panels, which are mechanically evaluated, and their results are presented in the second part of this work in a later article.

2. Materials and Methods

The prepreg fiberglass DA 4080 from APCM (Adhesive Prepregs for Composite Manufacturers), LLC, was used as the skins of the sandwich composites evaluated in this work. DA 4080 is a one-sided pre-impregnated modified epoxy prepreg with a cure temperature of 200 °F (93 °C). The prepreg reinforcement is an E-glass fabric made up of a 200 gsm layer of bidirectional fabric.

The core used was the PN1 honeycomb, manufactured by DuPont Nomex[®] and purchased to Plascore. The PN1 is a sheet with regular hexagonal cell configuration, approximately 0.5 inch/13 mm thick, and a 0.12 inch/3 mm cell size.

The another core used was the 3 lb. density lightweight DIAB 1022 Vynil foam Divinycell[®] supplied by Fibreglast. According to the supplier, the DIAB 1022 offers the highest strength to density ratio, insulative properties, improved stiffness, and impact resistance. The 0.5" (12.7 mm) thick foam is best when only additional impact resistance is required. This foam can be easily thermoformed with a heat gun or oven. Other properties of this foam are excellent adhesion/peel strength, chemical resistance, good dimensional stability, and temperature performance. The operating temperature can reach from $-200\text{ }^{\circ}\text{C}$ to $70\text{ }^{\circ}\text{C}$. The processing temperature depends on time and pressure conditions. Figure 1 shows some pictures of the materials used.

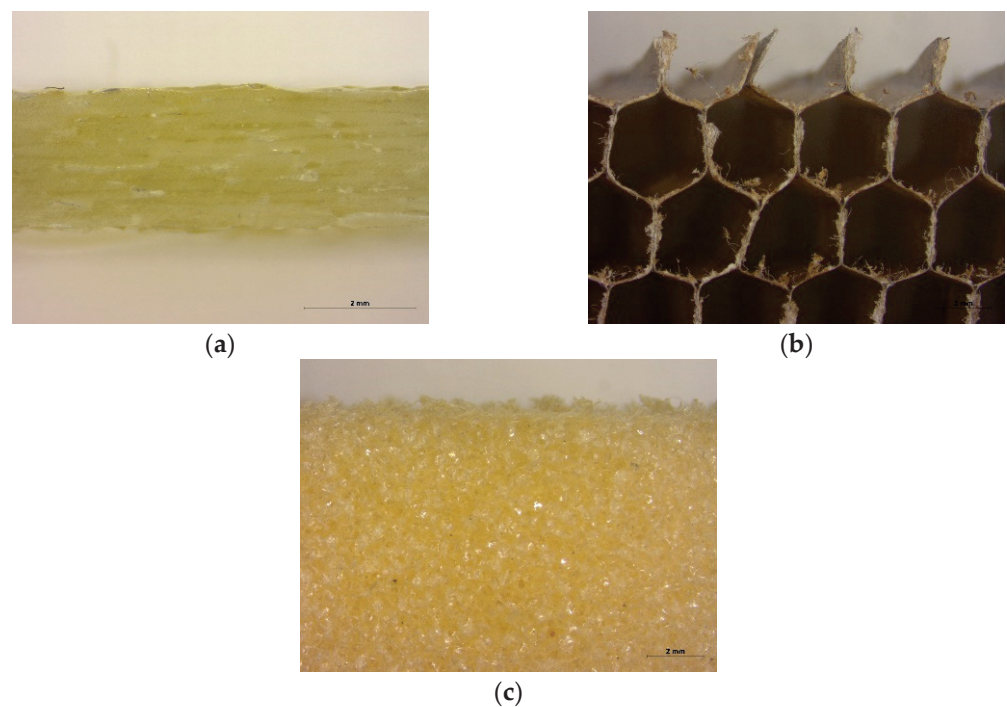


Figure 1. Pictures of the individual materials used to manufacture distinct sandwich composites: (a) glass fiber prepreg, (b) honeycomb core, (c) foam core.

Three different manufacturing methods for sandwich constructions are autoclave, press, or vacuum bag molding. For processing within an autoclave or press, all parts of a sandwich panel are cured in a single process, called co-curing. In vacuum bag molding, more stages of lay-up and curing are necessary. Co-curing means that face sheet composite and the adhesive are cured simultaneously. This work will mainly address the co-curing method with the production technology compression molding.

Fiberglass fabric epoxy prepreg (GF) laminates of two plies with the same configuration ($0/90^{\circ}$) were fabricated using a hot plate press CARVER model 4122, at $200\text{ }^{\circ}\text{F}$ ($93\text{ }^{\circ}\text{C}$) with a constant pressure of 20 psi during 1 h, as recommended by the supplier. Additionally, the manufacturing parameters on the fiberglass prepreg DA 4080 (GF) curing process were evaluated. Therefore, distinct combinations of time and temperature were used to fabricate several GF laminates (Table 1) in order to find the optimal curing parameters. For reference, the GF laminate labeled as 0 corresponds to the non-cured GF. A temperature of $200\text{ }^{\circ}\text{F}$ is recommended on the prepreg fiberglass technical datasheet. According to the manufacturer, the temperature of $300\text{ }^{\circ}\text{F}$ is the maximum service temperature of the honeycomb. The $250\text{ }^{\circ}\text{F}$ temperature is half of both initially proposed temperatures. In an attempt to investigate a different temperature range between 200 and $250\text{ }^{\circ}\text{F}$, it was

decided to increase the curing temperature of the prepreg fiberglass by 19 °F, having 219 and 238 °F. In addition, it was determined to evaluate the temperature above and below 250 °F in ± 6 °F intervals, resulting in 256 and 244 °F

Table 1. Manufacturing parameters of glass fiber (GF) laminates.

GF Laminate	Pressure (psi)	Compression Temperature (°F/°C)	Pressure Time (h)
0	-	-	-
1 *	20	200/93	1
2	20	300/149	1
3	20	256/124	1
4	20	200/93	2
5	20	256/124	2
6	20	300/149	2
7	20	219/104	1
8	20	238/114	1
9	20	244/118	1
10	20	250/121	1

* Manufacturing parameters recommended by the supplier.

Differential scanning calorimetry (DSC) was used to obtain information about the optimal curing process of GF. Since epoxy reactions release energy during cure due to their exothermic behavior, DSC can monitor their cure process. The curing evaluation was performed in a DSC 250 of TA Instruments. Samples of the GF laminates of approximately 5 mg were placed in an aluminum pan with a sealed lid and placed opposite the empty reference pan in the oven chamber. The DSC method used was first heating-cooling-second heating, from 10 to 200 °C, and the heating rate of 10 °C/min.

Dynamic mechanical analysis (DMA) tests were performed to determine the GF laminates' glass transition temperature (T_g). Specimens with 50 mm \times 12 mm \times 3 mm nominal dimensions were tested using the single cantilever geometry to conduct measurements from room temperature to 190 °C with a heating ramp of 5 °C/min in a DMA Discovery 850 from TA Instruments. Storage modulus (E') and damping factor ($\tan \delta$) curves were obtained following the ASTM-D7028. Figure 2 shows the pictures of samples and specimens before tests in DSC and DMA.



Figure 2. Pictures of representative tests of: (a) samples in the aluminum pan before hermetic close and test by differential scanning calorimetry (DSC), (b) specimen of glass fiber before testing in dynamic mechanical analysis (DMA).

Uniaxial compression tests were performed following the ASTM D1621-16 and ASTM C365/C365M-16 for the PN1 honeycomb core (HC) and the rigid cellular polyurethane foam DIAB 1022 (foam), respectively. Square HC and foam (80 \times 80 \times 12.7 mm) specimens were cut using a universal cutting tool ZUND XL-3200 and tested in a universal testing machine MTS. Insight with a cell load of 30 kN. The tests were performed at room temperature and a crosshead speed of 0.5 mm/min.

The analysis of sandwich composite panels follows a particular procedure in the software package called ANSYS Composite PrepPost (ACP), the workflow of which can be seen in Figure 3. The first step is to import the geometry and look for any required geometry repair to provide a good mesh before linking it to ACP (Pre). In ACP (Pre) the engineering data are specified, that is to say the material data of the composite like glass fiber prepreg, foam, and honeycomb core. These data can be selected from the Composite Materials Library at Engineering Data Sources. Also, it is possible to generate new material data. In ANSYS Mechanical, the shell mesh of the component is generated, and the last step of ACP (Pre) is to set up composite material fabric, element orientations, or ply lay-up. After this setup, a range of analyses can be solved.

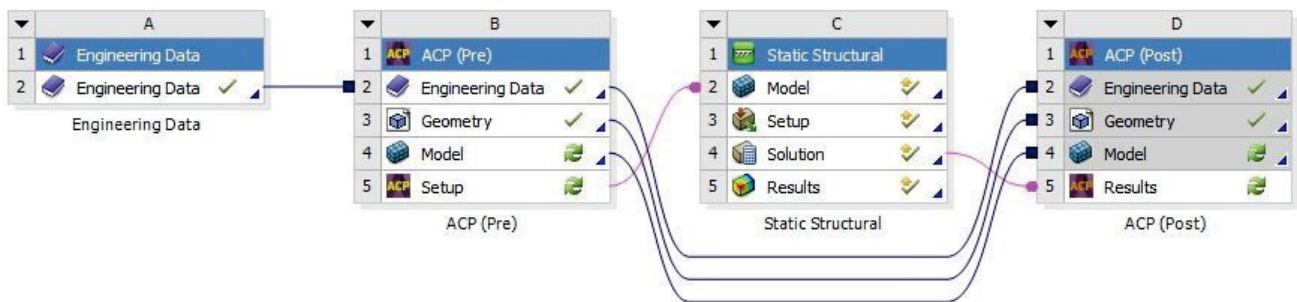


Figure 3. Workflow for the typical ACP usage of a sandwich analysis in ANSYS.

In the static structural analysis loads, boundary conditions and global post-processing of the solution are simulated, and post-processing of composite-specific results like failure criteria and stress or strain fields through the thickness of the component then follows.

3. Results

The GF laminates prepared using distinct manufacturing parameters did not show relevant physical properties like changes in color or uniformity (Figure 4).

The curing process of thermosetting resin is complex, involves a series of chemical reactions, and finally transforms the low molecular weight monomer into the macromolecular crosslinked network [18]. Figure 5 shows the DSC curves corresponding to the samples 0 to 6 (Table 1). The sample labeled as 0 corresponds to the uncured GF. The samples 1 and 4, 2 and 6, and 3 and 5 have similar time and temperature parameters.

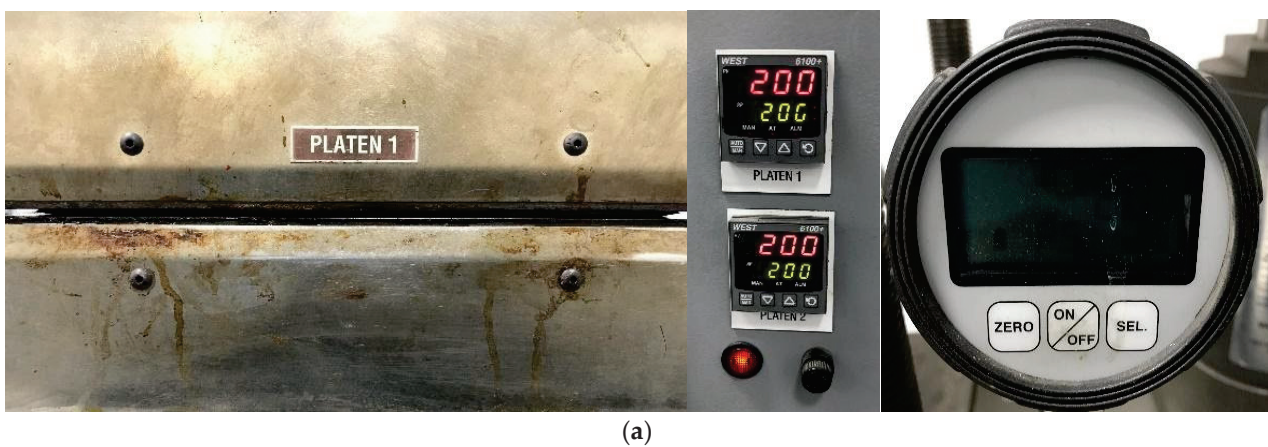


Figure 4. Cont.

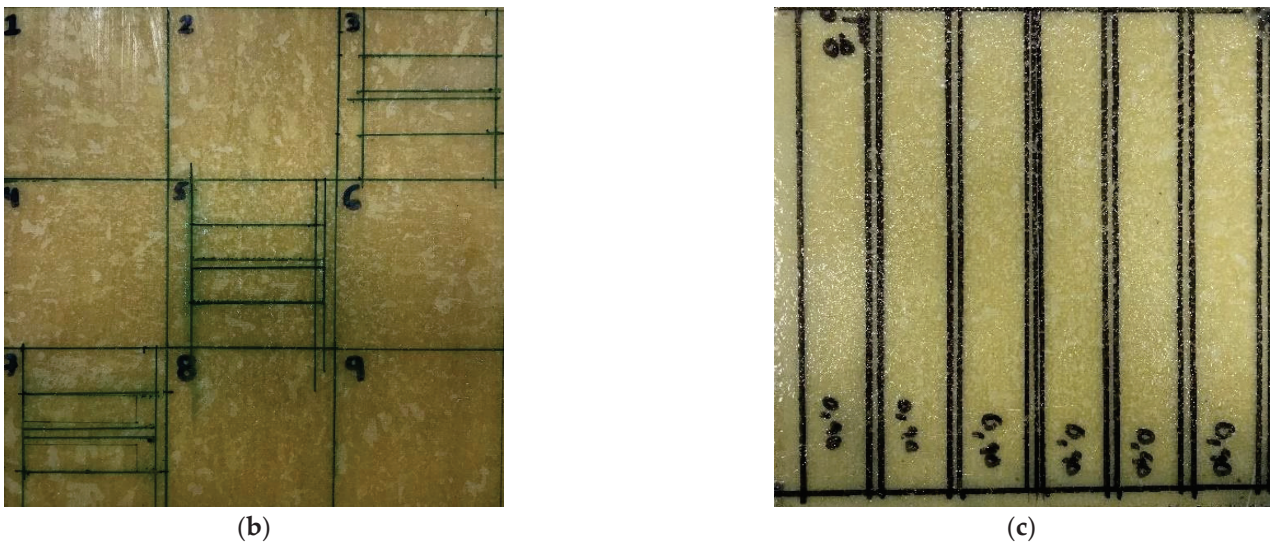


Figure 4. Pictures corresponding to the GF laminates manufacturing: (a) front view of closed hot plates with temperature and pressure displays, (b) GF laminate fabricated at 200 °F (93 °C) during 1 h, (c) GF laminate fabricated at 300 °F (149 °C) during 2 h.

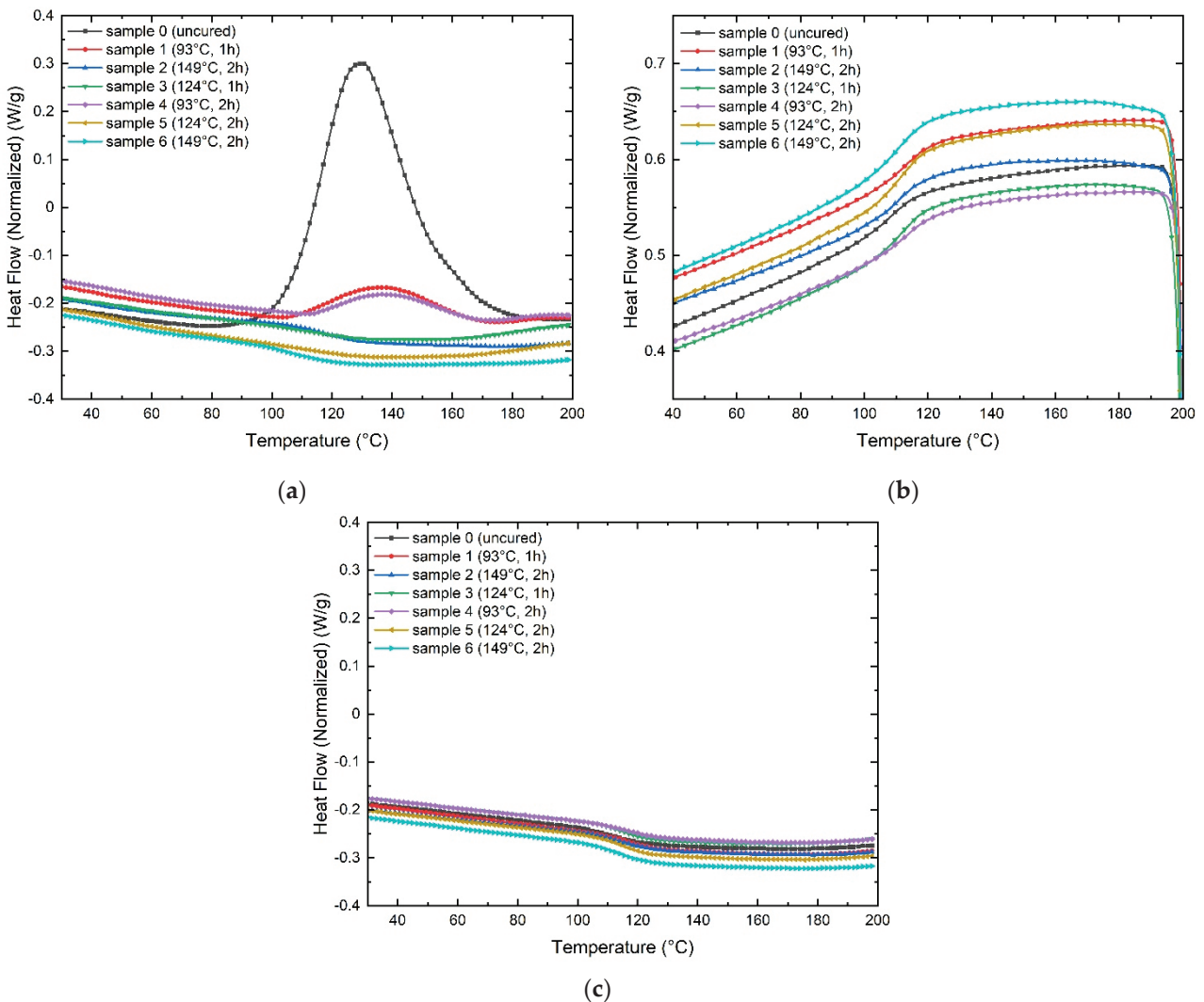


Figure 5. DSC curves corresponding to the samples 0 to 6: (a) first heating scan, (b) cooling step, (c) second heating scan.

It can be seen that sample 0 displays a significant peak from 80 °C to 190 °C. The peak is associated with the uncured GF curing process, and it is the reference for the rest of the samples. The samples 1–4 show an evident shoulder signal, which indicates the temperature of 200 °F (93 °C) is not sufficient to complete curing. The samples 2–6 reveal a slope change from approximately 115 and 100 °C, respectively. The samples 2–6 and 3–5 do not reveal any peak or shoulder signals, representing the manufacturing parameters used for the fabrication of these GF laminates that are effective for the curing process. The cooling scan does not reveal relevant changes in the curing process of GF laminates. The second heating scan reveals that the GF laminate samples are entirely cured. Lvtao Zhu et al. [19] presented similar results in a recent work.

The previous observations show that time is not relevant for the curing process, the reason sample 4 can be discarded. The downward slope of the sample curves 2 and 6, manufactured at 300 °F (149 °C), represents the fact that these GF laminates were cured with excessive energy. The slope change was not so pronounced in samples 3 and 5. Therefore, the next step is to find the optimal cure temperature set at 200 psi pressure and 1 h for cure time, but reducing the temperature within a 6 °F range (250, 244 and 238 °F) (121, 118 and 114 °C), and the half between 238 °F (114 °C) and 200 °F (93 °C) because it was observed that curing temperature of 200 °F (93 °C) represents uncured GF. Figure 6 shows the DSC curves corresponding to the samples 7 to 10 (Table 1).

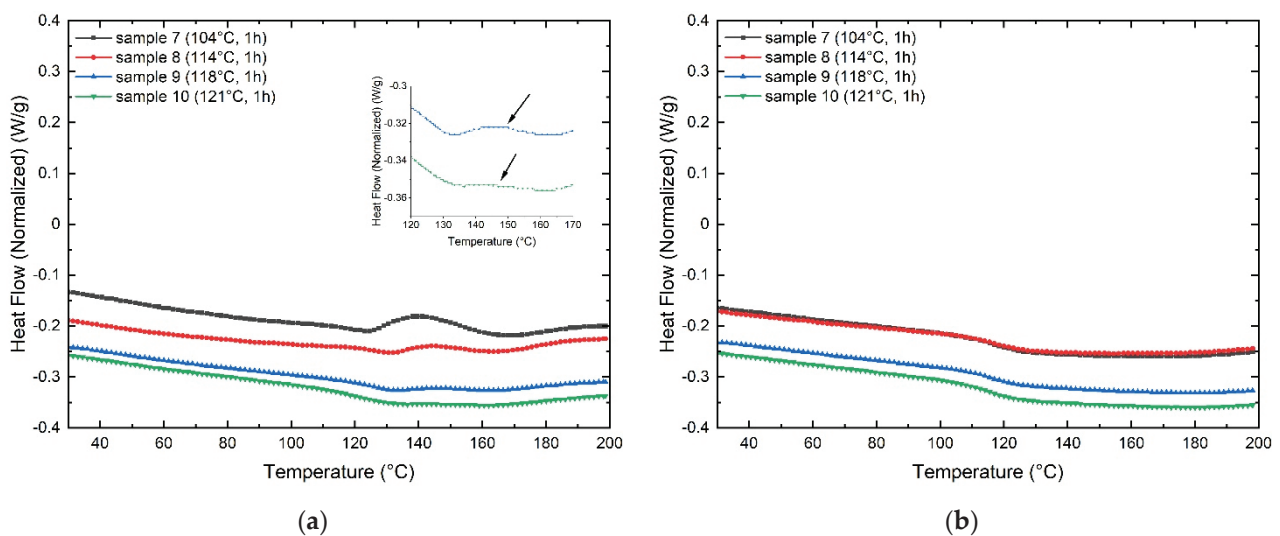


Figure 6. DSC curves corresponding to the samples 7 to 10: (a) first heating scan, (b) second heating scan.

The samples 7 and 8 display an evident shoulder signal, which is much less evident in sample 9. Sample 10 shows imperceptible features of uncured GF laminate. However, an inset graph allows visualizing the presence of a very slight shoulder pointed by an arrow. The second heating scan does not present significant variations, representing that the GF laminate samples are entirely cured. Therefore, the optimal manufacturing process for the GF laminates results in 200 psi of pressure at 256 °F (124 °C) for 1 h.

The viscoelastic properties like storage modulus and the loss factor, or $\tan \delta$, were obtained as a function of the temperature from the glassy state to the rubbery plateau. The DMA curves show the viscoelastic response of GF laminates fabricated with distinct manufacturing parameters, as presented in Figure 7.

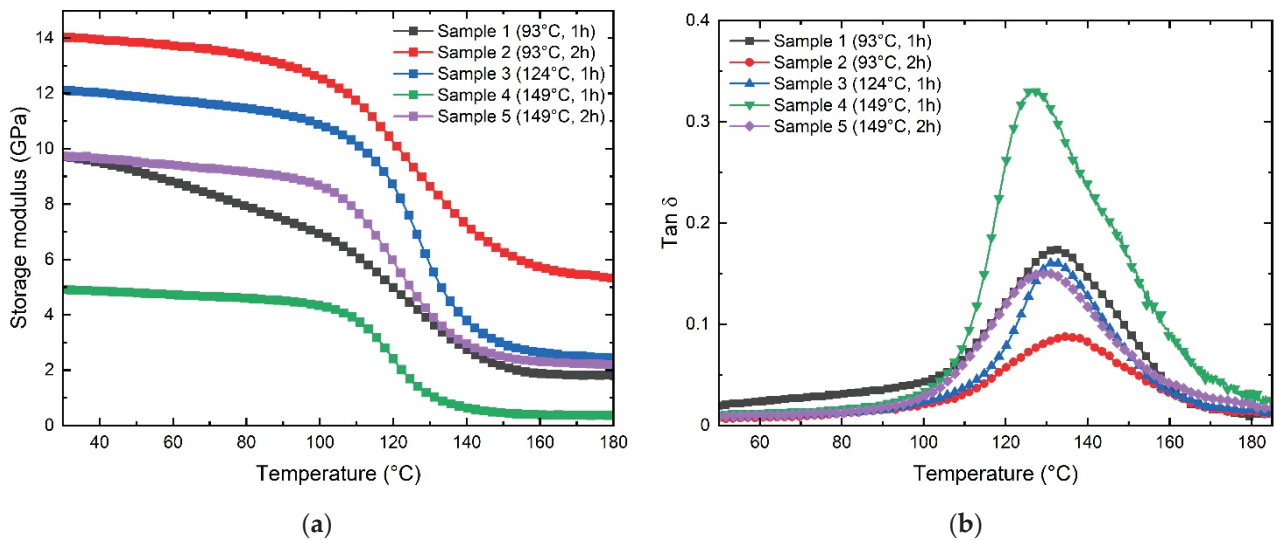


Figure 7. DMA curves corresponding to the samples 1 to 5: (a) storage modulus, (b) $\tan \delta$.

From Figure 5a, it is possible to appreciate that the manufacturing parameters strongly influence GF laminates' mechanical properties. The storage modulus varies depending on the manufacturing parameters. When comparing samples 1–2 and 4–5, it is observed that the storage modulus increases markedly with the cure time by 44% and 98%, respectively. When comparing samples 1–4 and 2–5, it is appreciated that the storage modulus decreases notoriously when the GF laminates are cured at elevated temperatures by 48% and 67%, respectively. Despite similar modulus values being obtained in samples 1–5, the behavior of the storage modulus of sample 1 reveals that the stiffness decreases markedly with increasing temperature. In fact, the value of the starting temperature (T_{onset}) of the transition from the glassy phase to the rubber region could not be determined. This behavior is attributed to incomplete curing. Table 2 presents the values obtained from the storage modulus, the starting temperature (T_{onset}), and the T_g obtained from the $\tan \delta$ plot (Figure 7b).

Table 2. DMA parameters obtained.

Sample	Temperature (°F/°C)	Time (h)	Storage Modulus (GPa)	T_{onset} (°C)	T_g (°C)
1	200/93	1	9.72	—	132.3
2	200/93	2	14	98.5	134.7
3	256/124	1	12.1	107.4	132.6
4	300/149	1	4.91	106.4	126.7
5	300/149	2	9.74	102.4	129.8

The glass transition temperature (T_g) of laminate composites is commonly obtained from the $\tan \delta$ peak in the glass transition region, where the material changes from rigid to more elastic. It is associated with the intermolecular movement of polymer chains [20,21]. Figure 7b shows the effect of the manufacturing parameters on the T_g of GF laminates. Sample 4 shows the lowest T_g value located at 126.7 °C, and sample 2 the highest one at 134.7 °C. The rest of the samples do not present significant variations.

Compression tests for HC were performed under displacement control at a crosshead speed of 0.5 mm/min. The HC followed the ASTM C365/C365M–16 procedures to determine compressive strength and modulus of sandwich cores.

The region of AC in Figure 8 is caused by the take-up of slack and alignment or seating of the specimen and does not represent the material properties. The zero points on the displacement axis have to be corrected. The linear region CD has to be extended and

constructed through the zero-force axis to receive point B, the corrected zero displacement point ($\delta = 0.0000$) from which to measure all displacements.

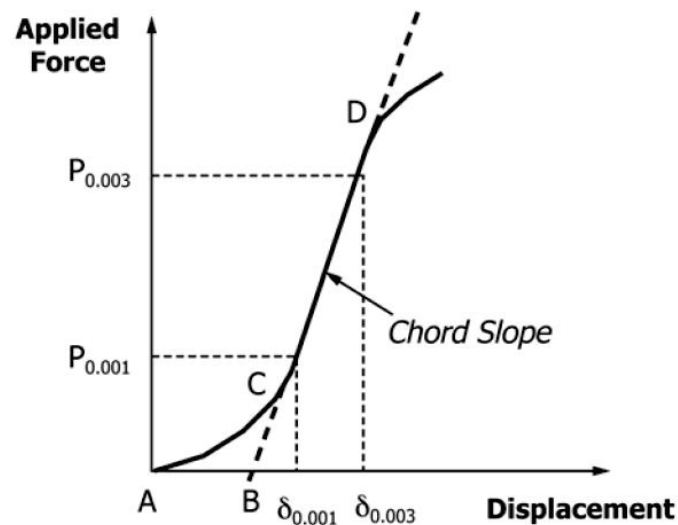


Figure 8. Force vs. displacement with Hookean region of core material.

For the 2% deflection stress, the load-displacement curve is altered by removing the toe region in the first segment. A linear curve achieves this between the 25% and 50% of maximal load points [22]. All data before this new zero point are removed and divided by the honeycomb thickness. Afterward, the nearest value to 0.02 is searched, and displacement and load at this point are extracted from the data. As the standard demands for the compressive modulus, the displacement values should be such that δ/t is closest to 0.003 and 0.001.

Following the procedure stated in the ASTM D1621.1873 [23], foam's compressive modulus and apparent modulus are calculated. Additionally, the ultimate compressive strength is derived from the test data. By continuing the linear region of the load-displacement curve with load values at 25% and 50% of maximal load, the toe region in the first segment is compensated by obtaining the new zero point where the linear curve intersects with the x -axis. With this new zero point, the compressive strength is calculated to be like that outlined in the standard. As this compressive strength accounts for the maximal load when the foam cells are not fully compressed, the ultimate compressive strength at the highest load has been calculated. At this point, the cells are fully compressed, and there are no air bubbles within the material. The compression is conducted until a yield point or until the specimen has been compressed 13% of original thickness is reached. Figure 9 shows the stress vs. strain curves corresponding to the HC and foam cores.

As expected, the HC structure contains a rigid element configuration that promotes remarkable strength under the compression test. The foam results in meager strength due to the intrinsic properties of the material and the multicellular configuration that collapses with a low level of stress. However, the foam shows large deformations and some remaining strength (crushed strength) after cells are compressed. The previous phenomenon was encountered by Rene Roy et al. [24]

The compressive modulus of the HC was 99.3 MPa, while the modulus of the foam was 11.8 MPa. The HC can support a load greater than 13% of its compression compared to the foam. However, foam shows greater elasticity due to the plastic structure with the air cavities that form it [25].

In CATIA V5[®] the shape of a basic business or first-class seat panel is modeled. The model's thickness is composed of two plies of prepreg on each facesheet with core in between, following 13.3 mm total thickness. The panel is imported into ANSYS[®] as a .stp file to use the shell structure.

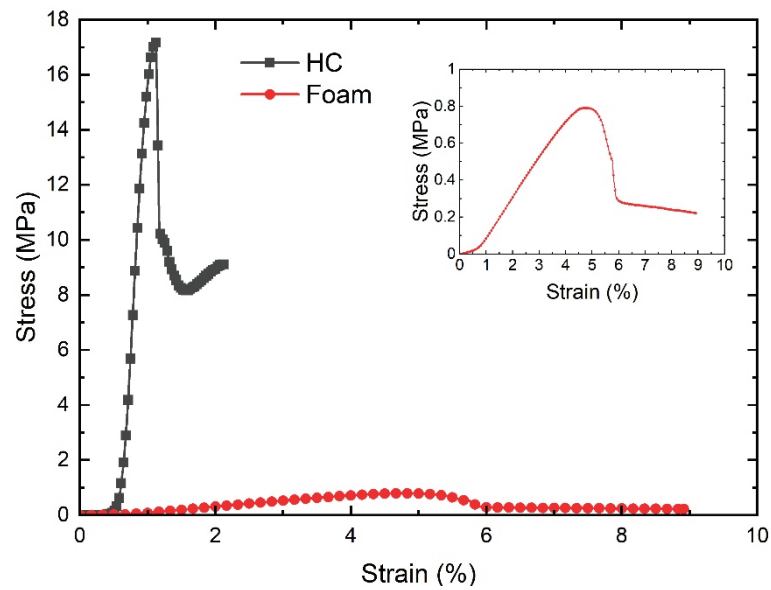


Figure 9. Stress vs. strain curves corresponding to the honeycomb core (HC) and foam tested under compression.

In order to compare the new material approach of GF face sheets and foam core, a baseline sandwich material is used and computed with the same fixtures and load. The baseline sandwich material consists of material in ANSYS Engineering Data Sources where Epoxy E-Glass Wet for the facesheets and an essential honeycomb core are selected. For the study case of glass fiber with foam core, the experimental data are inserted in Engineering Data Sources.

The model in ACP (Pre) will mesh with a mesh size of 10 mm, and subsequently, in the setup, the material data with fabrics and stack-ups are defined. After the ACP (Pre) process is completed, this building block is linked to Static Structural and the ACP post-processor. In the Static Structural setup a force with the magnitude half of the max. sandwich load resulting in 400 N is introduced to one edge, and the panel is fixed with fixed supports at the three outer edges, as seen in Figure 10.

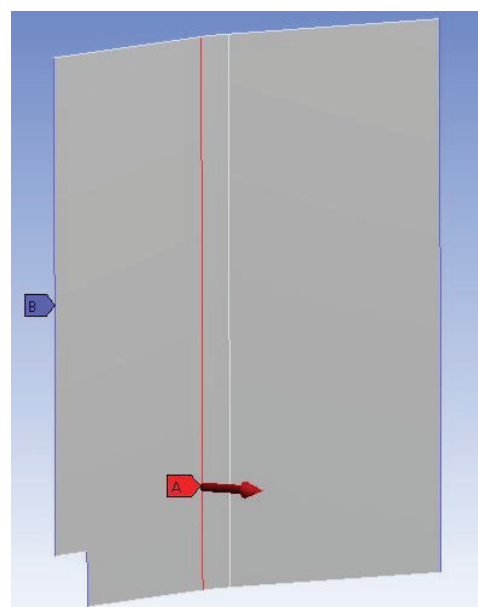


Figure 10. Side panel with fixed support and applied load.

With Static Structural it is possible to compute a ply-wise solution of composites. Here the total deformation, equivalent elastic strain, and equivalent stress were computed and displayed and we describe the stress results in more detail below.

In ACP (Post), a more suitable analysis for composites is possible, so this post-processor was used to visualize some detailed results. Total deformation, stress, and strain, as well as ply-wise stress and strain, were computed. With the failure criteria tool in ANSYS some reinforced ply criteria and sandwich criteria can be selected like Tsai-Wu, Hashin, Puck, Max. Strain, Max. Stress or Face Sheet Wrinkling, Core Failure, and Shear Crimping. These failure criteria give some additional information on which criteria are applicable for which ply, as seen in Figure 11.

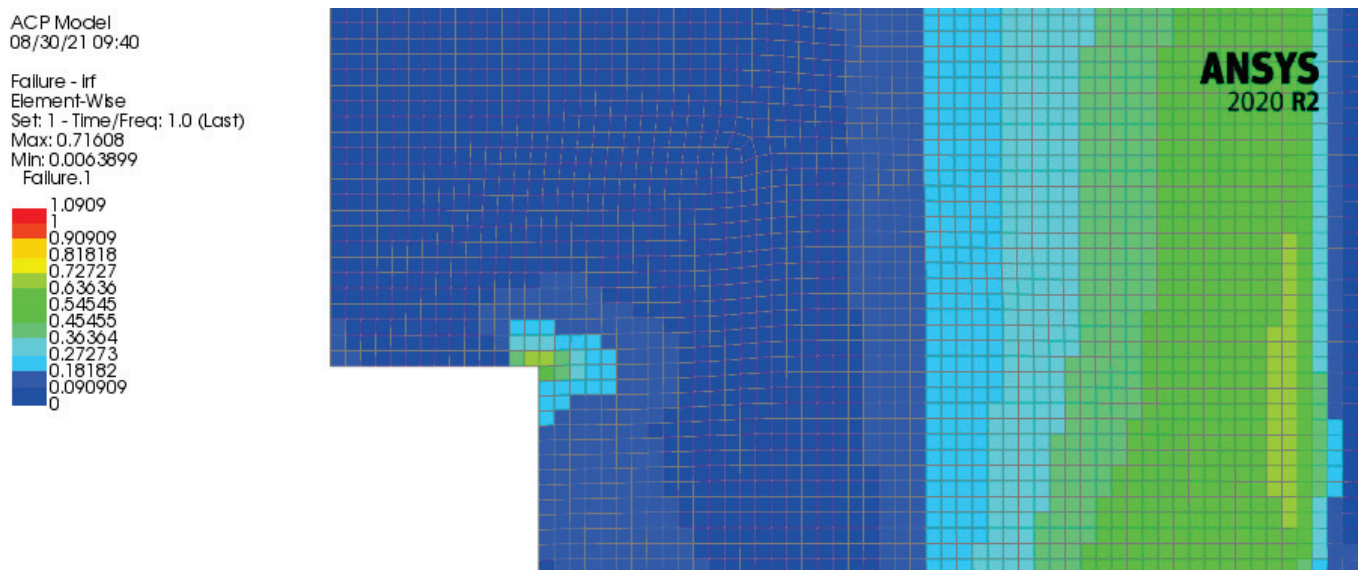


Figure 11. Applicable failure criterion and related ply in brackets in the bottom left corner of the baseline panel.

In Figures 12 and 13, the baseline and the second study case solution of total stress are displayed. As the load was applied in the middle of the panel, it shows mirrored displacement, stress, and strain. For the total stress in the baseline panel, a maximum value of 11.282 MPa and a maximum negative value of -33.102 MPa, which means compression stress, are calculated. Stress peaks occur because the panel is bent, and there is material missing in the bottom left corner. The undulation of the panel with the additional force in the middle of the panel leads to the high-stress values in the center. The high stresses derive from an edge effect on the upper and lower sides for baseline and study case panel.

The study case panel with the glass fiber prepreg and foam core exhibits a much lower stress magnitude than the baseline panel. The center does not show any additional maximum stresses and has a maximum positive stress value of 2.0084 MPa and a maximum negative stress value of -4.3769 MPa.

What has to be considered is the lower-left corner, where some material is missing in the panel. Here stress peaks occur, which are analyzed with a composite failure criteria in ACP(Post). These compression stress peaks will result in the zone of the panel shown in Figure 13. The green color of the section in the corner refers to a value between 0.6–0.725. For the Tsai-Wu criterion, which will be looked at, the panel will fail if the magnitude of the factor reaches the red area (values up to 1). In the baseline panel larger values of the failure criterion are exhibited with respect to the study case panel with a maximum of 0.25 in the zone analyzed in Figure 11.

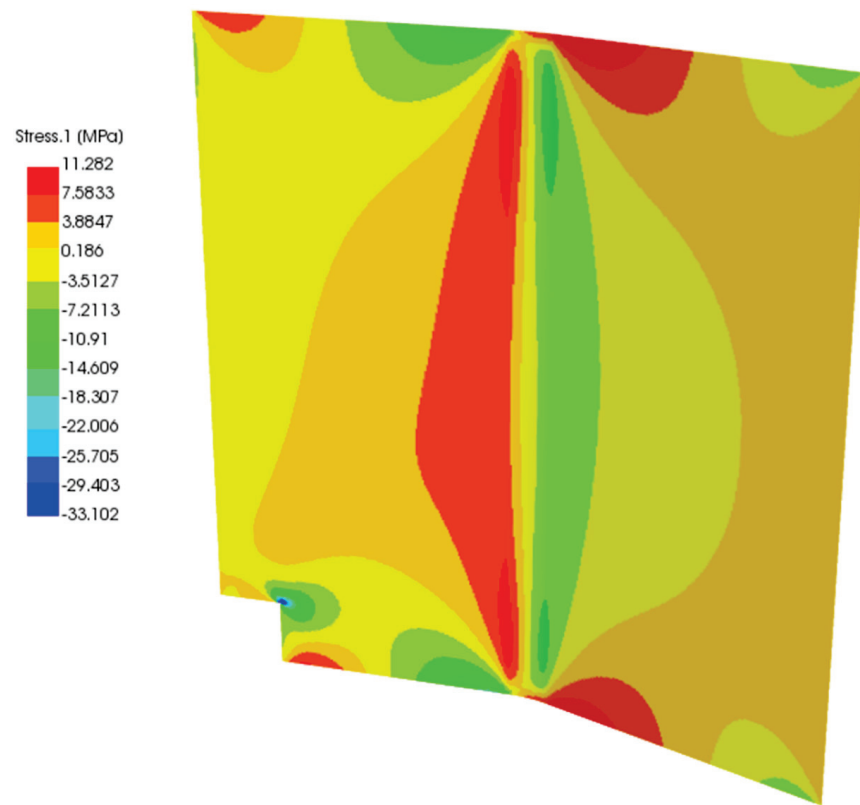


Figure 12. Total stress of the baseline panel in ACP.

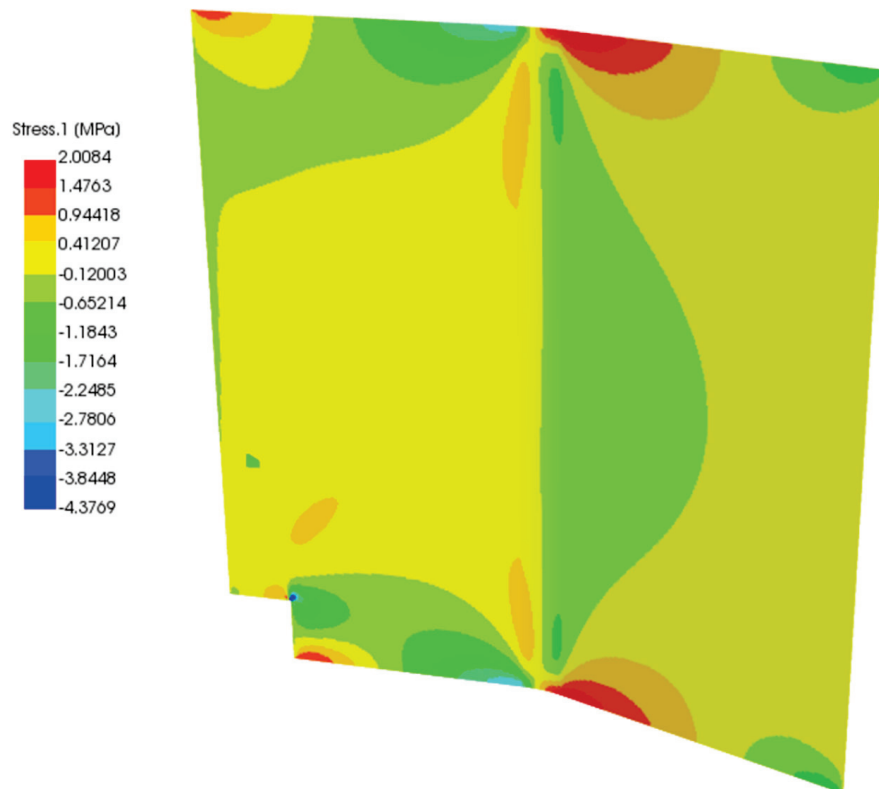


Figure 13. Total stress of the study case panel in ACP.

4. Conclusions

Ever more research is being undertaken on composite material processing geared towards the aviation industry. Composites are used in aircraft interiors due to their advanced features and their ability to reduce the aircraft's overall weight, optimizing fuel consumption.

This work evaluated the different manufacturing parameters for fiberglass prepreg curing. The technical sheets of the materials provide a starting point but should not be considered for the development of industrial parts. The detailed analysis allows finding the optimal manufacturing conditions that affect the mechanical performance of the compounds and the useful life of the components. The use of analytical tools such as DSC and DMA allows a complete evaluation of the curing conditions of fiberglass prepreg in the manufacture of sandwich compounds.

Polymeric foams do not provide remarkable mechanical strength compared to honeycomb structures. However, the foams showed much more significant deformation if they did break or permanently deform, allowing their use for non-structural applications.

Modeling mechanical behavior with the finite element method in ANSYS and any other modeling software requires a deep understanding of the theoretical background. Otherwise, the evaluation will not be productive. A variety of options are possible, the direction of stress or strain of which should be analyzed ply-wise or for the whole panel. The evaluation with the same load and supports was presented for the baseline and the study case (proposed material) panels. It was shown that the proposed material in the study case panel exhibits areas with lower stress concentrations with respect to the baseline, especially in the middle zone of the panel. This is also reflected when the Tsai-Wu failure criterion is applied to the panels, in which the maximum value of the failure factor is substantially smaller in the study case panel with respect to the baseline.

The panel modeled in this work is thought to be an approximation of a seat panel as it was not possible to use original dimensions. Also, the student version is limited to a defined node number and does not use the whole software capabilities. Further research should be undertaken for specific data by evaluating a unique panel with expected loads for different use cases.

The results allow the continuation of research activities in the development of panels at the prototype level. A second article will provide relevant information on the manufacturing processes and alternative materials to manufacture non-structural panels for aircraft cabin interiors, based on the results obtained in this article.

Author Contributions: Conceptualization, E.A.F.-U., S.P., and M.T.-A. Funding acquisition, E.A.F.-U. and M.T.-A. Writing—original draft, E.A.F.-U. Formal analysis, P.I.A.L., V.R.-R., A.D., and C.Z.P. Validation, P.I.A.L., V.R.-R., C.Z.P., and S.P. Project administration, P.I.A.L. Investigation, V.R.-R., S.P., and M.T.-A. Data curation, A.D. and C.Z.P., Methodology, M.T.-A. All authors have read and agreed to the published version of the manuscript.

Funding: This work was supported by the National Council of Science and Technology (CONACYT) through the Institutional Fund for Regional Promotion for Scientific, Technological and Innovation Development (FORDECYT), grant number 297708. The APC was funded by FORDECYT, grant number 297708.

Institutional Review Board Statement: Not applicable.

Informed Consent Statement: Not applicable.

Data Availability Statement: This study did not report any data.

Acknowledgments: Edgar Franco and Saul Piedra convey special appreciation to the "CONACYT Researchers Program (Catedras CONACYT)".

Conflicts of Interest: The authors declare no conflict of interest.

References

1. Mouritz, A.P. Manufacturing of fibre–polymer composite materials. In *Introduction to Aerospace Materials*; Elsevier: Amsterdam, The Netherlands, 2012; pp. 303–337, ISBN 978-1-85573-946-8.
2. Torres, M.; Piedra, S.; Ledesma, S.; Escalante-Velázquez, C.A.; Angelucci, G. Manufacturing process of high performance-low cost composite structures for light sport aircrafts. *Aerospace* **2019**, *6*, 11. [CrossRef]
3. Soutis, C. Carbon fiber reinforced plastics in aircraft construction. *Mater. Sci. Eng. A* **2005**, *412*, 171–176. [CrossRef]
4. Reis, J.M.L.; Coelho, J.L.V.; Monteiro, A.H.; Da Costa Mattos, H.S. Tensile behavior of glass/epoxy laminates at varying strain rates and temperatures. *Compos. Part B Eng.* **2012**, *43*, 2041–2046. [CrossRef]
5. Torres, M.; Franco-Urquiza, E.A.; Hernández-Moreno, H.; González-Villa, M.A. Mechanical behavior of a fuselage stiffened carbon-epoxy panel under debonding load. *J. Aeronaut. Aerosp. Eng.* **2018**, *7*, 2–6. [CrossRef]
6. *Final Report: Plastics and Composites Sector*; Academy of Science Malaysia: Kuala Lumpur, Malaysia, 2016.
7. Torkashvand, G.; Stephane, L.; Vink, P. Aircraft Interior Design And Satisfaction For Different Activities; A New Approach Toward Understanding Passenger Experience. *Int. J. Aviat. Aeronaut. Aerosp.* **2019**, *6*. [CrossRef]
8. Lyon, R.E. 20-Materials with reduced flammability in aerospace and aviation. In *Woodhead Publishing Series in Textiles*; Horrocks, A.R., Price, D., Eds.; Woodhead Publishing: Sawston, UK, 2008; pp. 573–598, ISBN 978-1-84569-262-9.
9. Ebnesajjad, S. 12-Aerospace applications. In *Plastics Design Library*; William Andrew Publishing: Norwich, NY, USA, 2013; pp. 275–294, ISBN 978-1-4557-7885-0.
10. Szolnoki, B.; Bocz, K.; Sóti, P.L.; Bodzay, B.; Zimonyi, E.; Toldy, A.; Morlin, B.; Bujnowicz, K.; Wladyka-Przybylak, M.; Marosi, G. Development of natural fibre reinforced flame retarded epoxy resin composites. *Polym. Degrad. Stab.* **2015**, *119*, 68–76. [CrossRef]
11. Geng, Z.; Yang, S.; Zhang, L.; Huang, Z.; Pan, Q.; Li, J.; Weng, J.; Bao, J.; You, Z.; He, Y.; et al. Self-extinguishing resin transfer molding composites using non-fire-retardant epoxy resin. *Materials* **2018**, *11*, 2554. [CrossRef] [PubMed]
12. Mittal, G.; Rhee, K.Y.; Mišković-Stanković, V.; Hui, D. Reinforcements in multi-scale polymer composites: Processing, properties, and applications. *Compos. Part B Eng.* **2018**, *138*, 122–139. [CrossRef]
13. Hiemstra-van Mastrigt, S.; Smulders, M.; Bouwens, J.M.A.; Vink, P. Chapter 61—Designing Aircraft Seats to Fit the Human Body Contour; Scataglini, S., Paul, G., Eds.; Academic Press: Cambridge, MA, USA, 2019; pp. 781–789, ISBN 978-0-12-816713-7.
14. Torres-Arellano, M.; Bolom-Martínez, M.D.J.; Franco-Urquiza, E.A.; Pérez-Mora, R.; Jiménez-Arévalo, O.A.; Olivier, P. Bearing strength and failure mechanisms of riveted woven carbon composite joints. *Aerospace* **2021**, *8*, 105. [CrossRef]
15. Birman, V.; Kardomateas, G.A. Review of current trends in research and applications of sandwich structures. *Compos. Part B Eng.* **2018**, *142*, 221–240. [CrossRef]
16. Castanie, B.; Bouvet, C.; Ginot, M. Review of composite sandwich structure in aeronautic applications. *Compos. Part C Open Access* **2020**, *1*, 100004. [CrossRef]
17. Whitty, J.P.M.; Alderson, A.; Myler, P.; Kandola, B. Towards the design of sandwich panel composites with enhanced mechanical and thermal properties by variation of the in-plane Poisson's ratios. *Compos. Part A Appl. Sci. Manuf.* **2003**, *34*, 525–534. [CrossRef]
18. Mphahlele, K.; Ray, S.S.; Kolesnikov, A. Cure kinetics, morphology development, and rheology of a high-performance carbon-fiber-reinforced epoxy composite. *Compos. Part B Eng.* **2019**, *176*, 107300. [CrossRef]
19. Zhu, L.; Wang, Z.; Rahman, M.B.; Shen, W.; Zhu, C. The Curing kinetics of e-glass fiber/epoxy resin prepreg and the bending properties of its products. *Materials* **2021**, *14*, 4673. [CrossRef] [PubMed]
20. Gheith, M.H.; Aziz, M.A.; Ghori, W.; Saba, N.; Asim, M.; Jawaaid, M.; Alothman, O.Y. Flexural, thermal and dynamic mechanical properties of date palm fibres reinforced epoxy composites. *J. Mater. Res. Technol.* **2019**, *8*, 853–860. [CrossRef]
21. Dhar Malingam, S.; Lin Feng, N.; Chan, K.; Subramaniam, K.; Selamat, M.; Zakaria, K.A. The static and dynamic mechanical properties of kenaf/glass fibre reinforced hybrid composites. *Mater. Res. Express* **2018**, *5*, 95304. [CrossRef]
22. ASTM C365/C365M-16. *Standard Test Method for Flatwise Compressive Properties of Sandwich Cores*; ASTM: West Conshohocken, PA, USA, 2016.
23. ASTM D1621-16. *Standard Test Method for Compressive Properties of Rigid Cellular Plastics*; ASTM: West Conshohocken, PA, USA, 2016.
24. Roy, R.; Park, S.-J.; Kweon, J.-H.; Choi, J.-H. Characterization of nomex honeycomb core constituent material mechanical properties. *Compos. Struct.* **2014**, *117*, 255–266. [CrossRef]
25. Kim, K.S.; Chin, I.J.; Sung, I.K.; Min, K.S. Curing of nomex/phenolic and kraft/phenolic honeycombs. *Korea Polym. J.* **1995**, *3*, 35–40.

MDPI
St. Alban-Anlage 66
4052 Basel
Switzerland
Tel. +41 61 683 77 34
Fax +41 61 302 89 18
www.mdpi.com

Polymers Editorial Office
E-mail: polymers@mdpi.com
www.mdpi.com/journal/polymers





Academic Open
Access Publishing

www.mdpi.com

ISBN 978-3-0365-8058-6